Proceedings

34th ASPE Annual Meeting

October 28 - November 1, 2019

Wyndham Grand Downtown Pittsburgh
Pittsburgh, Pennsylvania, USA

American Society for
Precision Engineering

3801 Lake Boone Trail, Ste 190, Raleigh, NC 27607
919-839-8444

Proceedings of

The Thirty-Fourth Annual Meeting of the American Society for Precision Engineering

October 28 – November 1, 2019
Wyndham Grand Downtown Pittsburgh
Pittsburgh, Pennsylvania, USA

The American Society for Precision Engineering (ASPE) is a multidisciplinary professional and technical society concerned with research and development, design, manufacture, and measurement of high accuracy components and systems. ASPE activities encompass relevant aspects of mechanical, electronic, optical and production engineering, physics, chemistry, and computer and materials science. Membership is open to anyone interested in any aspect of precision engineering.

Founded in 1986, the ASPE provides a focus for the diverse but important community. Other professional organizations have covered aspects of precision engineering, always as a sideline to their principal goals. ASPE is based on the core of generic concepts necessary to achieve precision in an application: independent of discipline, ASPE intends to be the focus for precision technology – and to represent all facets from research to application.

The Annual Meeting has evolved into an international forum for the exchange of ideas and presentation of research results relating to precision engineering, metrology, controls and system integration. Precision engineers and scientists from private industry, government laboratories, and universities meet to learn about the latest developments and to exchange ideas about the future directions of these technologies.

ASPE – The American Society for Precision Engineering
3801 Lake Boone Trail, Ste 190
Raleigh, NC 27607
919-839-8444
www.aspe.net

Preface

This book comprises the proceedings of the 34th ASPE Annual Meeting. The contributions reflect the authors'; opinions and are published as presented to ASPE, without change. Their inclusion in this publication does not necessarily constitute endorsement by the ASPE, or its editorial staff.

Individual readers of this book and nonprofit libraries acting for them are permitted to make fair use of the material contained in this book to be used in teaching or research; provided they copy said paper in total, as written by the author. Permission is granted to quote excerpts from the scientific or technical works in this book with proper acknowledgement of the source to include: the author's name, the book name, and the ASPE tag line. Reproduction of figures and tables is likewise permitted from the contents of this book, provided that the same acknowledgement of the same source and content is permitted.

Any other type of reproduction, systematic coping, or multiple reproduction of any material in this book is expressly prohibited except with the written permission of the ASPE editorial staff, addressed to the Society's headquarters.

ISBN 978-1-887706-78-0

2019

The American Society for Precision Engineering
3801 Lake Boone Trail, Ste 190
Raleigh, NC 27607

Printed in the United States of America

Organizing and Technical Program Committee

Annual Meeting Chairperson
Dr. Stephen J. Ludwick, Aerotech, Inc.

Technical Program Committee Chairpersons
Prof. Jonathan D. Ellis, University of Arizona
Metrology Systems

Dr. Stephen J. Furst, Smart Material Solutions
Precision Manufacturing

Dr. Brandon M. Lane, National Institute of Standards and Technology
Characterization

Prof. Chinedum E. Okwudire, University of Michigan
Controls and Mechatronics

Dr. Robert M. Panas, Lawrence Livermore National Laboratory
Micro-Nano Technologies

Dr. Richard M. Seugling, Lawrence Livermore National Laboratory
Precision Design

Tutorials Chairs
Prof. Don A. Lucca, Oklahoma State University
Dr. Vivek G. Badami, Zygo Corporation

Business Forum Chair
Mr. Dan E. Luttrell, Kriterion, LLC

Exhibits and Commercial Session Chairs
Dr. Byron R. Knapp, Professional Instruments Company
Mr. Brian P. O'Connor, Aerotech, Inc.

Students and Young Members Chairs
Mr. Luis A. Aguirre, 3M Company
Prof. Stuart T. Smith, University of North Carolina – Charlotte

Local Arrangements Chairs
Prof. Mark Bedillion, Carnegie Mellon University
Prof. Xiayun (Sharon) Zhao, University of Pittsburgh

Scientific Review Committee

Luis Aguirre, 3M Company
Vivek Badami, Zygo Corporation
Martin Bamberger, DWFritz
Chris Barns, DWFritz
Mark Bedillion, Carnegie Mellon University
Eric Belski, Aerotech, Inc.
Charan Bodlapati, Micro-LAM, Inc.
Dannis Brouwer, University of Twente
Christopher Brown, Worcester Polytechnic Institute
Eric Buice, Lawrence Berkeley National Labratory
Benjamin Bulla, Son-X GmbH
Nelson Cardenas, Oculus
Qunyi Chen, 3M Company
Shih-Chi Chen, The Chinese University of Hong Kong
Benny Cheung, The Hong Kong Polytechnic University
Liam Connolly, The University of Texas at Austin
Nicholas Duncan, Aerotech, Inc.
Kevin Elliot, Corning
Kaan Erkorkmaz, University of Waterloo
Christopher Evans, University of North Carolina-Charlotte
Ronnie Fesperman, US Conec Ltd.
Pete Fitsos, Lawrence Livermore National Laboratory
Jason Fox, National Institute of Standards & Technology
Stephen Furst, Smart Material Solutions, Inc.
Tony Gatica, M3 Design
Tyler Hamer, MIT
Jonathan Hopkins, UCLA
Byron Knapp, Professional Instruments Company
Mark Kosmowski, Electro Scientific Ind (ESI)
Brandon Lane, National Institute of Standards & Technology
Richard Leach, University of Nottingham
Jihyun Lee, Korea Institute of Machinery & Materials (KIMM)
Dan Luttrell, Kriterion
Reg Maas, Coorstek
Eric Marsh, Pennsylvania State University
Glenn Miller, Cranfield Precision
Hossein Mohammadi, Micro-LAM, Inc.
Chris Morgan, Moore Nanotech Systems
Marijn Nijenhuis, Univ. of Twente
Brian O'Connor, Aerotech, Inc.
Chinedum Okwudire, University of Michigan
Robert Panas, Lawrence Livermore National Laboratory
Ton Peijnenburg, VDL Enabling Technologies Group
Suresh Kumar Ramasamy, Apple Inc.
Jeff Roblee, AMETEK Precitech
Theo Ruijl, MI-Partners
Joerg Schmuetz, Beuth Hochschulle Fur Technik Berlin
Lars Schoeneman, Leibniz Institute for Materials Engineering
Burak Sencer, Oregon State University
Richard Seugling, Lawrence Livermore National Laboratory
Hossein Shahinian, Micro-LAM, Inc.
Hongliang Shi, Stanford University
Deming Shu, Argonne National Laboratory
Stuart Smith, University of North Carolina-Charlotte
Mark Stocker, Cranfield Precision
John Taylor, Lawrence Livermore National Laboratory / University of North Carolina-Charlotte
David Trumper, MIT
Jan van Eijk, MICE bv
Deokkyun Yoon, University of Michigan
Rayne Zheng, Virginia Polytechnic Institute

ASPE gratefully acknowledges the time and the effort given by the Organizing and Technical Program Committee to bring the precision engineering community this program.

Contents

Preface....ii

Organizing and Technical Program Committee....iii-iv

Table of Contents....v

ASPE Lifetime Achievement Award....vi

ASPE Distinguished Service Award....vii

2019 Student Scholarship Recipients....viii

Sustaining Corporate Sponsors....ix-x

Corporate Sponsors....xi

Technical Papers Index....1-11

Technical Papers....12-506

Author Index....507

ASPE Lifetime Achievement Award

Stephen J. Botos

Aerotech, Inc.

The Lifetime Achievement Award was conceived to honor particularly noteworthy contributions to the advancement of the discipline and/or Society over a career of service in precision engineering, and this year, ASPE is pleased to present this very special award to **Stephen J. Botos** for leadership in advancements in the field of intraocular lens manufacturing.

Stephen J. Botos, trained as a tool and die maker, left his native Hungary after the 1956 revolution and subsequent Russian occupation. After settling in the U.S. and serving two years in the U.S. military, Stephen did his first design work with Goerz Optical Co., in Pittsburgh, while at the same time attending night courses in Mechanical Engineering at the University of Pittsburgh. Among the products he worked on were sophisticated inertial guidance test systems for the aerospace industry. Soon after receiving his mechanical engineering degree in 1969, he and two of his engineer friends pooled their resources to form Aerotech, Inc.

Beginning with Stephen's first patent and subsequent introduction of a manual optical mount which allowed for both extremely high resolution and large range of motion, Aerotech grew rapidly in the 1970's.

Manual positioners were soon followed by the company's first lines of electronic controls and motorized positioners. These products saw increasing demand and broadening applications in both the R&D market and commercial use in manufacturing and testing.

International expansion began in the 1980's with Aerotech establishing subsidiaries in the United Kingdom and Germany. During this period, the company's technologies found increasing use in a broadening range of industries including: medical devices, semiconductor and electronics, data storage, and laser processing among others.

During the 1990's and early 2000's, Stephen guided Aerotech's efforts to address the rapidly expanding semiconductor and telecom industries by heading development of the company's air bearing and linear-motor-based product technologies in order to address these market's needs for ever higher precision and throughput.

After 2008/09, Stephen initiated Aerotech's next wave of international expansion with the company opening subsidiaries and representative offices in the Asia / Pacific region to address the increasingly sophisticated manufacturing and testing emerging from that part of the world.

Though retired from Aerotech, Stephen's guiding principles continue to direct the company today: a dedication to engineering research and development; a steadfast commitment to American manufacturing; a focus on employee development and retention; and, a long term view to business planning and investment.

Over the duration of his long career, Stephen has mentored many engineers and encouraged employee participation in ASPE to further their professional development. Aerotech employees, local communities, students and the broader engineering and manufacturing communities have been strengthened and supported by his ethical governance, altruism and passionate leadership.

Stephen is the holder of eleven U.S. patents. He is a recipient of the University of Pittsburgh's Distinguished Engineering Alumnus Award. He is also the recipient of the ACMS Benjamin Rush Award for his work in improving vision around the world though advancements in the field of intraocular lens manufacturing.

ASPE Distinguished Service Award

Leonard E. Chaloux

The Distinguished Service Award was conceived to honor noteworthy contributions and service to the Society, and this year, ASPE is pleased to present this award to **Leonard E. Chaloux**.

Len Chaloux began his career in 1972 as an apprentice machinist with Pneumo Precision while he also earned an Associates Degree in Manufacturing Process Technology from Keene State College, part of the University of New Hampshire system. At Pneumo Precision, Len held various positions including Assembly Foreman, Field Service Manager, Technical Services Manager, Sales Manager, Vice President of Sales & Marketing, and finally President & Chief Executive Officer of Taylor Hobson / Pneumo's North American operations, which included Taylor Hobson's precision metrology division in Chicago, IL.

In October 1997, Len became founding President & CEO of Moore Nanotechnology Systems, LLC in Swanzey, New Hampshire, USA as a stand-alone subsidiary of the Moore Tool Company located in Bridgeport, CT. Moore Nanotechnology Systems develops, designs, and manufactures state-of-the-art ultra-precision manufacturing systems for the production of advanced optics – primarily for the consumer electronics, defense, aerospace, lighting, medical, and automotive sectors. The company is a world leader in the supply of advanced machine tools and processes for the production of complex optical components and has remained one of New Hampshire's top 100 private companies since 2010. The company was also named NH Company of the Year in 2008.

Throughout his career Len traveled extensively to 27 industrialized nations throughout the world working with hundreds of leading companies in the field of precision optics fabrication. He is a charter member of the American Society for Precision Engineering (ASPE) founded in 1986 and has served two 3-year terms on its Board of Directors, most recently as President of the society in 2017. Len has published numerous technical papers and articles in the fields of ultra-precision machine design, single point diamond turning, and deterministic micro-grinding and holds two US patents for related developments in this field. In 2017 he received the NH Business Excellence Award for small group manufacturing, and in 2018 was a New England semifinalist in Ernst & Young's nationwide competition for Entrepreneur of the Year.

Len retired from Nanotech in January 2019 and was awarded an Honorary Doctor of Science Degree from Keene State College in May 2019 for his contributions in the field of precision manufacturing systems and processes, as well as his leadership, business acumen, technical expertise, and dedication to workforce development.

2019 Scholarships Recipients

Graham J. Siddall ASPE Student Scholarship

The winner of the 2019 Graham J. Siddall ASPE Student Scholarship is **David Cayll**, University of Texas at Austin (Michael Cullinan, Advisor). This award includes the ASPE Annual Meeting registration fee, 4 tutorial fees, lodging and travel expenses to the Annual Meeting.

With a 10-year student endowment, Graham Siddall will recognize a student scholar in the field of precision engineering. This prestigious award is valued at $2,500 and will support the student winner in the form of waived conference and tutorial fees and a stipend to cover the travel costs to the ASPE Annual Meeting.

Graham Siddall received his BS degree in Production Engineering and Management with First Class honors from the University of Nottingham in England. He received his M.Sc. and Ph.D. degrees in Natural Philosophy (Physics) in 1971 and 1975, respectively, working under the guidance of Professor R.V. Jones at the University of Aberdeen in Scotland.

ASPE Student Scholarships

ASPE is proud to award two students scholarships for the 34th Annual Meeting in Pittsburgh, Pennsylvania. This year's scholarship recipients are **Dipankar Behera**, University of Texas at Austin (Michael Cullinan, Advisor) and **Emma Betters**, UNC - Charlotte (Tony Schmitz, Advisor). The ASPE Student Scholarships include a waiver of the Annual Meeting registration fee and 4 tutorials fees. It also includes an honorarium to cover travel and lodging expenses to the meeting.

ASPE 2019 Sustaining Corporate Sponsors

3M Company St. Paul, MN 55144 www.mmm.com	Aerotech, Inc. 101 Zeta Drive Pittsburgh, PA 15238 412-963-7470 Motion Control Manufacturer
Ametek Precitech, Inc. 44 Blackbrook Road Keene, NH 03431 603-357-2511 www.precitech.com	ASM Pacific Technology Ltd. 20/F, Gateway ts, 8 Cheung Fai Road Tsing Yi, New Territories Hong Kong 852-2619 2000 www.asmpacific.com
Carl Zeiss Industrial Metrology 6250 Sycamore Lane North Maple Grove, MN 55369 763-744-2400 www.zeiss.com/metrology	Chardon Tool 115 Parker Court Chardon, OH 44024 440-286-6440 www.ChardonTool.com
Cranfield Precision Division of Fives Landis Ltd. Woburn House, Adams Close Kempston, Bedford, MK42 7JE United Kingdom 44-0-1234-312820 www.cranfieldprecision.com	Lion Precision 7166 4th Street North Oakdale, MN 55128 651-484-6544 800-250-9297 www.lionprecision.com

Mahr, Inc.
1144 Eddy Street
Providence, RI 02905
401-782-3168
www.mahr.com

Makino
7680 Innovation Way
Mason, OH 45040
513-573-7200
www.makino.com

Moore Nanotechnology Systems, LLC
230 Old Homestead Highway
Swanzey, NH 03446
603-352-3030
www.nanotechsys.com

New Way Air Bearings
50 McDonald Boulevard
Aston, PA 19014
610-494-6700
www.newwayairbearings.com

Physik Instrumente
16 Albert Street
Auburn, MA 01501
508-832-3456
www.pi-usa.us

Specialty Components, Inc.
14 Village Lane
Wallingford, CT 06492
203-284-9112
www.specialtycomponents.com

VDL Enabling Technologies Group USA
3758 Spinnaker Court
Fremont, CA 94538-1706
510-996-4662
www.vdletg.com

ASPE would like to thank our Sustaining Corporate Sponsors

Through its support of ASPE, encourages the Society's activities and thereby participates in advancing the art and science of Precision Engineering.

ASPE 2019 Corporate Sponsors

ADCOLE Corporation
669 Forest Street
Marlborough, MA 01752
508-485-9100
www.adcole.com

Contour Fine Tooling, Inc.
143 Jaffrey Road
Marlborough, NH 03455
603-876-4908
www.contour-diamonds.com

Corning, Inc.
Corning, NY 14831
607-974-3842
www.corning.com

K & Y Diamond
2645 Diab
Laurent, Quebec H4S 1E7
Canada
514-333-5606
www.kydiamond.ca

Parker Hannifin Corporation
1140 Sandy Hill Road
Irwin, PA 15642
724-861-8200
www.parker.com/emn

Prior Scientific, Inc.
80 Reservoir Park Drive
Rockland, MA 02370
781-878-8442
www.prior.com

Professional Instruments Company
7800 Powell Road
Hopkins, MN 55343
952-933-3315
www.airbearings.com

University of North Carolina-Charlotte
Center for Precision Metrology
9201 University City Blvd.
Charlotte, NC 28223-0001
704-687-8499
cpm.uncc.edu

Zygo Corporation
Laurel Brook Road
Middlefield, CT 06455-0448
860-347-8506
Toll-free: (800) ZYGO-NOW
www.zygo.com

ASPE would like to thank our Corporate Sponsors. Through its support of ASPE, encourages the Society's activities and thereby participates in advancing the art and science of Precision Engineering

ASPE 2019 Annual Meeting
Oral and Poster Sessions

Technical Session 1 – Micro and Nano Technologies
Wednesday, October 30, 2019, 8:00 AM - 9:30 AM
Session Chairs:
Robert Panas (Lawrence Livermore National Laboratory),
Michael Cullinan (The University of Texas at Austin)

1. **Precision Engineering Challenges in Superconducting Quantum Computing***
   Hatridge, M. J. (University of Pittsburgh)

2. **Towards the Microfabrication of Thermally Compensated Monolithically Integrated Devices Using Ultrafast Lasers**.....12
   Vlugter, P. (EPFL)

3. **Breaking the Resolution Versus Throughput Tradeoff in Nanoscale Additive Manufacturing**.....18
   Saha, S. K. (Georgia Institute of Technology);
   Nguyen, V. H. (Lawrence Berkeley National Laboratory);
   Wang, D. (The Chinese University of Hong Kong);
   Oakdale, J. (Lawrence Livermore National Laboratory,);
   Chen, S. S. (Georgia Institute of Technology)

4. **Microfabrication Via Holographic Optical Tweezers and Two-Photon Polymerization**.....24
   Chizari, S. N.; Hopkins, J. B.; Shaw, L.; Farzaneh A.; Lim, M.; Austin, S. (University of California – Los Angeles)

5. **Observation of Polymer Flow Behavior in Real Time by Light Interference in Laser-Assisted Thermal Imprinting**.....26
   Tendo, H.; Nagato, K.; Ebihara, Y. N.; Takahashi, N.; Nakao, M. (The University of Tokyo)

6. **Design, Fabrication, and Calibration of a Stiffness Programmable Metamaterial**.....32
   Luo, C. C. (University of Texas at Austin); Song, I. (The University of California - Los Angeles); Ladner, I. S. (Lawrence Livermore National Laboratory); Cullinan, M. A.; Hopkins, J. B.; Jayatilaka, G. C. (The University of Texas at Austin)

***No abstract included**

Technical Session 2 - Additive Manufacturing
Wednesday, October 30, 2019, 10:30 AM - 12:00 PM
Session Chairs: John Taylor (University of North Carolina - Charlotte), Bradley Jared (Sandia National Laboratories)

1. **Distortion Compensation for Additive Manufactured Components Via Modified Inherent Strain Method**.....37
   To, A. C.; Tran, H. T.; Zhou, Z.; Lemon, J. (University of Pittsburgh)

2. **Additive Manufacturing of Internal Features for Manipulation of Structural Dynamics**.....43
   Schmitz, T. L.; Betters, E. D. (University of Tennessee, Knoxville); West, J. (University of North Carolina – Charlotte); Noakes M.; Nycz A.; Smith S. (Oak Ridge National Laboratory)

3. **Influence of the Density of Powder Layer on Melt Solidification Phenomenon in Selective Laser Melting**.....49
   Ohyama, K.; Nagato, K.; Nakao, M. (The University of Tokyo)

4. **Coaxial Near-Infrared Camera Measurements for Process Control in Selective Laser Melting**.....54
   Shkoruta, A. O.; Mishra, S.; Rock, S. (Rensselaer Polytechnic Institute)

5. **Detecting Process Defects in Laser-Powder Bed Fusion** 61
   Jared, B. H.; Madison, J.; Mitchell, J.; Ivanoff, T.; Saiz, D.; Koepke, J.; Dagel, D. (Sandia National Laboratories)

Technical Session 3 - Precision Manufacturing
Thursday, October 31, 2019, 8:00 AM - 9:30 AM
Session Chairs: Stephen Furst (Smart Material Solutions, Inc.), Hossein Shahinian (Micro-LAM Inc.)

1. **Machine Learning with Updating for Milling Stability**.....63
   Schmitz, T. L. (University of Tennessee, Knoxville); Jiang, J.; Nogueira, M.; Greis, N. (University of North Carolina – Charlotte); Bhattacharya, S. (Fayetteville State University)

2. **Analysis of Rotor Behavior in Ultra-Precision High Speed Cutting**.....69
   Dörgeloh, T.; Schoenemann, L.; Riemer, O. (Leibniz Institute for Materials Engineering – IWT); Brinksmeier, E. (University of Bremen)

3. **Sculpturing of Colored Basso-Relievo with Elliptical Vibration Texturing** 75
   Guo, P. (Northwestern University); Wang, J. (Chinese University of Hong Kong); Yang, Y; Liao, W. (Chinese University of Hong Kong)

4. **High-Efficiency Planarization of GaN Wafer by Catalyst-Referred Etching with Positive-Biased Photo-Electrochemical Oxidation** 79
Ohnishi, R.; Toh, D.; Matsuyama, S.; Ohashi, A.; Sano, Y.; Yamauchi, K. N. (Graduate School of Engineering, Osaka University)

5. **Fabrication of Edge-Lit Light Guide Tooling by Surface Structuring by Laser Remelting**.....84
Bordatchev, E. V.; Milliken, N (National Research Council of Canada); Küpper, M. (RWTH Aachen University); Cvijanovic, S.; Tutunea-Fatan, R. O. (Western University, Canada); Willenborg, E. (Fraunhofer Institute for Laser Technology); Temmler, A. (Tsinghua University)

Technical Session 4 - Precision Design
Thursday, October 31, 2019, 10:30 AM - 12:00 PM
Session Chairs:
Richard Seugling (Lawrence Livermore National Laboratory),
Kevin Elliott (Corning Inc.)

1. **Enabling Bearing Technologies for High-Power Oil-Free Turbomachinery** 90
Ertas, B. H. (GE Research Center)

2. **Carbon-Graphite Gas Bearings for Turbomachinery**..... 95
Devitt, A. J. (New Way Air Bearings)

3. **Cross-Axis Dynamic-Coupling Analysis for 6-DoF Magnetically-Levitated Stage Design**..... 100
Nguyen, V. H. (Lawrence Berkeley National Laboratory);
Kim, W. (Texas A&M University)

4. **A Study of Micro-Mechanical Logic Elements** 106
Sun, F. N.; Panas, R. M.; Pascall, A. (Lawrence Livermore National Laboratory); Hopkins, J. B. (University of California - Los Angeles)

5. **Design of a Capacitive-Sensor-Array-Based Real-Time Mirror Profiler for Elliptically Dynamic Bent Mirror for Hard X-Ray Zoom Optics**.....111
Shu, D. N.; Anton, J.; Kearney, S.; Harder, R.; Shi, X.; Mooney, T.; Mashrafi, S.; Qian, J.; Shi, B.; Assoufid, L. (Argonne National Laboratory)

Technical Session 5 - Controls and Mechatronics
Friday, November 1, 2019, 8:00 AM - 9:30 AM
Session Chairs: Chinedum Okwudire (University of Michigan),
Burak Sencer (Oregon State University),
Ping Guo (Northwestern University)

1. Sensing and Commutation of a Spherical Permanent Magnetic Dipole Actuator .. 115
Hamer, T. T.; Trumper, D. L.; Chabot, J. A. (Massachusetts Institute of Technology)

2. Finite Element Model for Pre-Magnetized Linear Hysteresis Motors 121
Zhou, L. (Mitsubishi Electric Research Labs);
Trumper, D. L. (Massachusetts Institute of Technology)

3. Friction Isolated Rotary System for High-Precision Roll-To-Roll Manufacturing 127
Kang, D. (Korea Institute of Machinery and Materials);
Dong, X. D.; Okwudire, C. E. (University of Michigan)

4. Learning Based Pre-Compensation of Pre-Sliding Friction and Servo Tracking Errors For Precision Motion Control ..... .133
Dumanli, A.; Sencer, B. (Oregon State University)

5. Deep Learning-Based Precision Control for Six-Axis Compliant Nanopositioner .. 139
Liu, X.; Li, C. L.; Li, H.; Wang, X.; Chen, S. S.
(The Chinese University of Hong Kong)

Technical Session 6 - Metrology Systems and Characterization

Friday, November 1, 2019, 10:30 AM - 12:00 PM

Session Chairs: Jonathan Ellis (University of Arizona),
Steven Gillmer (MIT Lincoln Laboratory)

1. Intelligent Systems for Optical Form Measurement: Automated Assessment of Pose and Coverage 145
Catalucci, S.; Leach, R. K.; Piano, S. (University of Nottingham);
Senin, N. (University of Perugia)

2. Kinematic Error Analysis of Stage Tracking Using Stereo Vision 151
Isa, M. A.; Piano, S.; Leach, R. K.; Sims-Waterhouse, D. (University of Nottingham)

3. Retrace Error Calibration Algorithm for Non-Null Interferometric Testing..... 157
Tangari Larrategui, M.; Zhang, Y.; Brown, T. (University of Rochester);
Ellis, J. D. (University of Arizona)

4. Dual-Mode Multi-Wavelength Snapshot Interferometric System for On-Machine Metrology.....162
Liang, R. R.; Tian, X. N. (University of Arizona); Sohn, A. (Facebook Reality Labs);
Wang, D. (China Jiliang University)

5. Design of the QEMMS Kibble Balance..... 166
Marangoni, R. R.; Haddad, D.; Seifert, F.; Chao, L. S.; Newell, D.;
Schlamminger, S. N. (National Institute of Standards & Technology)

Poster Session 1
Wednesday, October 30, 2019, 3:30 PM - 5:00 PM

Controls and Mechatronics

1. **Efficient Interpolator with Minimal Feedrate Fluctuation for Parametric Toolpath** 171
Jiang, J. J.; Lin, F. (China University of Mining and Technology); Zhang, Y.; Zhang, H.; Ye, P. (Tsinghua University)

2. **Ultra-Precision Angle Sensors and Multi-Axis Closed-Loop Control** 175
Dowski, R. E. (Ascentia Imaging, Inc)

3. **Practical Feedforward Techniques for Accurate Desktop 3D Printing** 181
Dumanli, A.; Shannon, T. L.; Sencer, B. (Oregon State University); Tajima, S.(Tokyo Institute of Technology)

4. **Design of a 5-Axis Manipulator for the Automatic Lapping Process** 184
Park, S.; Lee, S.; Koh, D.; Shim, J.; Kim, J. (Gwangju Institute of Science & Technology)

5. **Levitation Height Control of Levitation Actuator Using Proportional Control** 191
Nakazato, A.; Torii, A. A.; Kae, D.; Suguru, M. (Aichi Institute of Technology)

6. **Rotation of an Inchworm Using Piezoelectric Elements and Electromagnets** 195
Miyake, H.; Torii, A. A.; Suguru, M.; Kae, D. (Aichi Institute of Technology)

Metrology & Characterization

7. **Influence of Preparation Process on Surface Topography and Nanotribological Properties of Molecular Films on Dlc Substrate** 199
Guo, S. (Center for Precision Engineering); Sun, T. (Harbin Institute of Technology); Cao, Y.; Gu, L.; Zhang, C. (School of Mechatronics Engineering); Xu, Z.; Li, H. (Beijing Institute of Aerospace Control Devices)

8. **Tool Edge Geometry from Structured Light Scanning** 204
Schmitz, T. L.; No, T. (University of Tennessee, Knoxville)

9. **Compressive Sensing for Fast 3-D Two-Photon Microscopy** 209
Wen, C.; Ren, M.; Chen, S. S. (The Chinese University of Hong Kong)

10. **Reverse Task in Surface Metrology - Simulation of Initial One-Process Profile Based on Resulted Two-Process Profile** 214
Pawlus, P. P.; Reizer, R. R. (Rzeszów University of Technology)

11. **A Multi-Scopic 3D Precision Measurement System for Deep Blind Holes** 220
Cheung, C. B.; Li, D. N. (The Hong Kong Polytechnic University)

12. **Methods for Optically Profiling Surfaces** 225
Caviness, A. N.; Arumugam, K.; Newman, T. L.; Shabahang, F.; Smith, S. T.; Her, T. (University of North Carolina - Charlotte)

Micro and Nano Technologies

13. **Modeling Approach for Characterization of Decomposition Behavior in Powder Injection Molding Process** 232
Han, J.; Jeong, J.; Choi, D.; Je, T. (Korea Institute of Machinery and Materials); Park, S. (POSTECH)

14. **YSZ Forest Structured Film Using Centrifugal Molding Method for SOFC Performance Improvement** 235
Okamura, T. N.; Nagato, K.; Tomizawa, M.; Nakao, M. (The University of Tokyo)

15. **Towards Embedded High-Speed Control for Dynamic Tip-Based Nanometrology in Roll-To-Roll Manufacturing** 238
Connolly, L. G.; Cullinan, M. A. (The University of Texas at Austin)

16. **MEMS Dynamic Mechanical Analyzer for In Situ Viscoelastic Characterization of 3D Printed Microstructures** 244
Cayll, D. R.; Cullinan, M. A. (The University of Texas at Austin); Ladner, I. S.; Cho, J. H. (Lawrence Livermore National Laboratory); Saha, S. K. (Georgia Institute of Technology)

17. **High Speed Stimulated Raman Scattering Microscope with Shot Noise Limited Detection** 249
Li, H. N.; Wang, P. (Huazhong University of Science and Technology)

18. **Parallel Positioning Device for X-Ray Diffraction Laboratory Use** 250
Olea, G. (HUBER Positioning & Diffraction GmbH & Co.KG)

19. **Research On The Modeling Of Burr Formation Process In Micro-Flat Milling Operation On Ti-6Al-4V** 254
Chen, N. X.; Wu, Y.; Li, Z.; Li, L. (Nanjing University of Aeronautics and Astronautics)

Precision Design

20. **Pressure-Fed Mechanisms for Nanopositioning Stage Applications** 259
Lee, C.; Han, J. (Texas A&M University); Kim, G. (Tri-N Co., Ltd); Villarraga-Gómez, H. (Nikon Metrology, Inc.)

21. **Modeling the Dynamic Stiffness of an Air Bearing Spindle Using Frequency Response Functions** 264
Knapp, B. R.; Arneson, D. A.; Oss, D. (Professional Instruments Company)

Precision Manufacturing

22. **Toolpath Generation: Freeform Surface Blending and Extrapolation** 268
Naples, N. J. (Facebook Reality Labs); Yi, A. (The Ohio State University)

23. **Double-Sided Polishing Conditions to Suppress Edge Roll-Off of Silicon Wafer** ... 274
Harada, S.; Satake, U.; Enomoto, T. (Osaka University)

24. **Experimental Study of the Probe Pre-Travel Bending Error** 279
Li, S. S.; Zeng, L.; Feng, P. (Tsinghua University)

25. **Low Cost Platform for Hybrid Manufacturing of Light Metals** 283
Schmitz, T. L.; Betters, E. D. (University of Tennessee, Knoxville);
West, J. (University of North Carolina - Charlotte)

26. **Development of Temperature Control System for Machine Tools** 289
Kodaka, S. S. (Kanagawa University)

27. **Finite Element Modeling of the Flash Thermography for Sub-Surface Defect Detection in Metals**.....295
Patel, K. A. (Academic, USA);
Evans, C. J.; Cherukuri, H.; Davies, A. D. (University of North Carolina – Charlotte)

28. **Error Motion Testing of a Bare 4R Blockhead Air Bearing Spindle** 301
Arneson, D. C. (Professional Instruments Company)

29. **Modelling of Powder Spreading to Optimize Compaction Consistency** 304
Groen, A. M.; Vlasea, M.; Erkorkmaz, K.(University of Waterloo, Canada)

30. **Design and Features of the 4 Inch Blockhead Air Bearing Spindle** 310
Arneson, S. O. (Professional Instruments Company)

31. **Addressing Precision Challenges to Fabricate 3D Parts Using Microscale Selective Laser Sintering**.....314
Behera, D. N.; Cullinan, M. A. (The University of Texas at Austin);
Roy, N. K. (Canon Nanotechnologies)

32. **High Speed Micro Laser Assisted Machining of Single Crystal Germanium**..... 319
Shahinian, H. N.; Navare, J.; Bodlapati, C. S.; Zaytsev, D.; Kang, D.; Mohammadi, H.; Arlt, M.; Ravindra, D. M. (Micro-LAM Inc.)

33. **One-Side Cutting Strategy for Ultraprecise Single Point Cutting of V-Grooves; Case 2: Constant Cutting Area** 325
Bordatchev, E. V.; Milliken, N (National Research Council of Canada); Joao, D. A.; Tutunea-Fatan, R. O. (Western University, Canada)

34. **Machine Learning Approach Prediction of Stress-Strain Curves for Low-Temperature Annealed Carbon Steels** 331
Ito, N. R.; Niho, T.; Nagato, K.; Nakao, M. (The University of Tokyo)

35. **Study on Laser-Induced Oxidation of Ti6Al4V Alloy Under Two Different Reactive Atmospheres** 337
Zhao, W.; Zhao, G.; Li, L.; He, N. (Nanjing University of Aeronautics and Astronautics); Iqbal, A. (Universiti Brunei Darussalam)

36. **Fundamental Analysis on Thermal Characteristics of High-Speed Aerostatic Spindle** 343
Wakiya, S. S.; Satsuki, Y.; Kusuyama, J.; Fedorynenko, D.; Nakao, Y. Y. (Kanagawa University, Japan)

37. **Crack Propagation in Nanocrystalline Alloy Sheet by Laser Spot Irradiation** 347
Tagata, H. (The University of Tokyo)

Poster Session 2
Thursday, October 31, 2019, 3:30 PM - 5:00 PM

Controls and Mechatronics

1. **Development of Compact Maglev Stage System for Nanometer-Scale Positioning** 352
Takahashi, M. M. (Hitachi, Ltd.)

2. **Force Control for Hybrid Electric-Pneumatic Ultra-Precision Vertical Positioning Device** 358
Kato, T.; Tanaka, T. T.; Xu, Y. W.; Shimazaki, K. (Fukuoka Institute of Technology)

3. **Study on an Active Vibration Isolation with Respect to Inertia** 362
Kim, H. Y. (Korea Institute of Industrial Technology); Choi, J.; Kim, K.; Lee, S.; Park, J. (Korea Polytechnic University)

4. **Noise, Resolution, and Sampling Rate Characterization of a Low-Cost Eddy-Current Position Sensing System for Bearingless Motor Suspension Control** 366
Weinreb, B. S.; Noh, M.; Trumper, D. L. (Massachusetts Institute of Technology); Fyler, D. (The Charles Stark Draper Laboratory)

5. **Aspects of Design and Performance of a Thermally Actuated Linear Translation Stage** 371
Fan, C. S.; Hastings, D.; Smith, S. T. (University of North Carolina – Charlotte)

6. **Prediction of Feed Drive Control Parameter Effect at the Machine Tool Cutting Point Dynamics**.....375
Franco, O.; Erkorkmaz, K. (University of Waterloo, Canada);
Beudaert, X.; Munoa, J. (IK4 IDEKO)

Metrology Systems and Characterization

7. **Procedure to Determine Linearity Deviations of a Large Range Vertical Axis of Topography Measurement Instruments Using Simple Step Height Standards** 376
Bauer, W. J.; Gerbert, D. (Polytec GmbH);
Hueser, D. (Physikalisch-Technische Bundesanstalt PTB)

8. **Measurement Uncertainty Evaluation of Cosine Error-Free Surface Profile Measuring System**.....380
Guo, X. (Texas A&M University);
Han, J.; Lee, C.; Tarbutton, J. (University of North Carolina - Charlotte)

9. **Effect of Particle Agglomeration Level in Reusing CMP Slurry at Various Pressures and Their Impact on Polishing Behavior**.....385
Kubota, M.; A, Dunn, K. (SUNY Polytechnic Institute, SUMCO Co)

10. **Sensor and Instrumentation Applied to Spindle Health Monitoring** 390
Han, J.; Lee, C. (Texas A&M University)

11. **Description of the Shape of Ordinate Distribution of Two-Process Profile**..... 394
Pawlus, P. P.; Reizer, R. R. (Rzeszów University of Technology)

Micro and Nano Technologies

12. **Experimental Characterization of Lightfield Directing Array Elements** 398
Panas, R. M.; Enstrom, K. G; Nguyen, V. (Lawrence Livermore National Laboratory);
Simonelli, J. M.; Karburn, J.; Hopkins, J. B. (University of California - Los Angeles)

13. **Sub-Wavelength Periodic Surface Structures Fabricated by Temporally Focused Femtosecond Laser** 403
Fu, Z.; Zhang, N.; Chen, S. S. (The Chinese University of Hong Kong);
Zhang, N. (Nankai University)

14. **Liquid Capsule-Based Pressure Sensor for Precision Cardiovascular Monitoring**. 407
Fan, X. N.; Ren, M.; Huang, Y.; Zhao, N.; Chen, S. S.
(The Chinese University of Hong Kong)

15. **Metrology of Nano and Micro-Scale Features Created with a Large-Area Indenting Process – Nanocoining** 412
Miller, N. C.; Furst, S. J. (Smart Material Solutions, Inc.)

16. **Wafer Scale Exfoliation of Monocrystalline Micro-Scale Silicon Films** 417
Ward, M. J.; Cullinan, M. A. (The University of Texas at Austin)

Precision Design

17. **Design of a Six-Axis Parallel Nanopositioner Using Decoupled Flexural Legs** 422
Li, C. L.; Liu, X.; Chen, S. S.; (The Chinese University of Hong Kong)

18. **Motorization of a Large Aperture Airbearing for Use in a New X-Ray Microscope**. 427
Arneson, H. D. (Professional Instruments Company);
Preissner, C. A. (Argonne National Laboratory)

Precision Manufacturing

19. **Experimental Analysis of Nickel Adhesion Process During Wire-Sawing of Rock in Vacuum by Friction Test**.....431
Furutani, K. (Toyota Technological Institute)

20. **Structured Light Scanning for Endmill Modeling** 435
Schmitz, T. L.; No, T.; Gomez, M. F. (University of Tennessee, Knoxville);
Copenhaver, R. W. (University of North Carolina – Charlotte)

21. **Laser Doppler Vibrometry for Machining Dynamics Analysis**.....441
Schmitz, T. L.; Gomez, M.; Betters, E. D. (University of Tennessee, Knoxville);
Eichenberger, J. (Polytec); Delio, T. (MLI)

22. **Study on the Protective Effect of Built-Up Layer in Dry Cutting Of SUS304 Stainless Steel**.....447
Song, X.; Tohru, I. N; Yukio, T. (Chuo University); Weiming, H.
(University of Shanghai for Science and Technology)

23. **Direct Control of Machine Tools Using 3D-CAD** 453
Sagesaka, K.; Morimoto, Y. S.; Hayashi, A. (Kanazawa Institute of Technology)

24. **Machine Learning Approach Prediction of Stress-Strain Curves for Low-Temperature Annealed Carbon Steels** 457
Ito, R. N.; Nagato, K.; Niho, T.; Nakao, M. (The University of Tokyo)

25. **Manufacturing Technology of Metamaterial with Double Square Loop Array Filled Conductive Carbon Ink for Microwave Absorption** 463
Je, T.; Jeong, J. Han, J.; Choi, D.; Jonghwa, S.
(Korea Advanced Institute of Science and Technology)

26. **Numerically Controlled Plasma Chemical Vaporization Machining Using Array-Type Electrode Toward High-Throughput Deterministic Machining**..... 466
Nishida, K.; Okayama, S.; Matsuyama, S.; Yamauchi, K. N.; Sano, Y.
(Osaka University)

27. **Fundamental Analysis on Thermal Characteristics of High-Speed Aerostatic Spindle** 470
Wakiya, S. S. (Kanagawa University)

28. **Development of an Abrasive-Free Polishing Method for Optical Material Using Pure Water and Ni Catalyst** 474
Toh, D.; Ohnishi, R.; Bui, P. V.; Isohashi, A.; Matsuyama, S.; Sano, Y.; Yamauchi, K. N. (Graduate School of Engineering, Osaka University)

29. **Fabrication of Micro Infrared Fresnel Lens Arrays by Virtual Spindle Based Tool Servo Diamond Turning and Precision Glass Molding** 478
Zhang, L. N. (The Ohio State University)

30. **Design and Fabrication of Multi-Element Diffractive Optical Array for Imaging Applications** 479
Zhou, W. N.; Yi, A. (The Ohio State University)

31. **Identification for the Feed Drive Dynamics of a 5-Axis Laser Drilling Machine Via In-Process Data** 480
Wang, C. W.; Erkorkmaz, K.; McPhee, J. (University of Waterloo, Canada)

32. **Grinding a Workpiece to Sub-Micron Roundness in a 100 Year Old Grinder** 484
Arneson, D. A.; Liebers, M. J.; Arneson, C. D.
(Professional Instruments Company, USA)

33. **Ceramics Additive Manufacturing of a Simple Plano Mirror** 488
Jared, B. H.; Saiz, D.; Choi, J.; Cook, A.; Reinholtz, W.; Saavedra, M.; Arrington, C.
(Sandia National Laboratories)

34. **Volumetric Data Analysis: Inspection and Experimental Design for Additive Manufacturing** 491
Geng, Z.; Bidanda, B. (University of Pittsburgh)

35. **Effect of Laser-Assisted Diamond Turning (Micro-Lam) on Non-Optimally Oriented Calcium Fluoride Crystal** 497
Shahinian, H. N.; Bodlapati, C. S.; Navare, J.; Zaytsev, D.; Kang, D.; Mohammadi, H.; Ravindra, D. M.; Arlt, M. (Micro-LAM Inc.)

36. **Accuracy Analysis on Weld Specifications Using Confocal Microscopy** 501
Valdez, M. O.; Arguero, C.; Sikkink, R.; Keim, D. E.; Cassidy, L.
(Los Alamos National Laboratory)

Towards the microfabrication of thermally compensated monolithically integrated devices using ultrafast lasers

Pieter Vlugter, and Yves Bellouard
Galatea Lab, STI/IMT, Ecole Polytechnique Fédérale de Lausanne (EPFL), Neuchâtel, Switzerland

Introduction

Tightly focused ultrashort laser pulses focused inside a transparent material trigger non-linear absorption events eventually leading to localized bulk modifications [1]. For a variety of transparent materials, different types of modification may be found depending on exposure conditions, such as pulse length, pulse energy, pulse frequency or confocal parameters. For instance, in fused silica, for relatively low pulse energies (<~200 nJ) and short pulse lengths (<~200 fs), homogeneous modifications associated with a refractive index increase are found [2] while increasing the pulse energies and/or the pulse lengths, leads to a second characteristic modification characterized by self-organized nanostructures with nanoscale periodicity, referred as 'nanograting' or 'type II modification' [3].

The very nature of non-linear absorption that confined energy in the bulk of the material makes it possible the writing of 3D patterns, opening the door to new types of applications exploiting the three dimension design space. As an illustration, writing a line pattern inside silica may change the refractive index, so that it behaves as a 3D waveguide. Another interesting property of this second type of modification is the local increase of etching rate when immersed in low-concentration hydrofluoric acid [4] or KOH [5]. The etching rate increases significantly with respect to the unexposed material, typically to a ratio of 1:100 or even more with KOH, making possible the fabrication of arbitrary high-aspect ratio structures [6]. Furthermore, the symbiotic combination of optical functions and structural one using a single process leads to multifunctional monolithically devices [7], such as optomechanical or optofluidic devices. In this new manufacturing paradigm, assembly steps are omitted, and hence positioning errors when transferring from one process to another are avoided.

Using brittle materials such as glass for fabricating mechanical structures may sound counterintuitive, as fused silica – like other glass, has a low toughness. This problem is mitigated by the fact that the femtosecond laser combined with chemical etching manufacturing process yields to high quality, defect-free surfaces, preventing the occurrence of crack nucleation sites. The tensile strength of femtosecond micro-machined fused silica show values well in above 1 GPa with low failure probability, and eventually reaching 2.4 GPa [8], substantially above ordinary metals. Furthermore, fused silica happens to have one of the lowest internal friction coefficient, because of his high purity, and hence no measurable stress-strain hysteresis. Together with its low thermal expansion, fused silica makes for a perfect construction material for high-precision mechanics. In Fig. 1, a femtosecond laser fabricated 3D notch-hinge is depicted in Fig. 1 [9]. This structure illustrates the true 3D nature of this technology: It could not be fabricated with conventional 2D-1/2 lithography methods. Fig .1 (right) shows a bending test of the notch hinge at an estimated maximum stress level of 1.9 GPa, measured by means of photoelasticity.

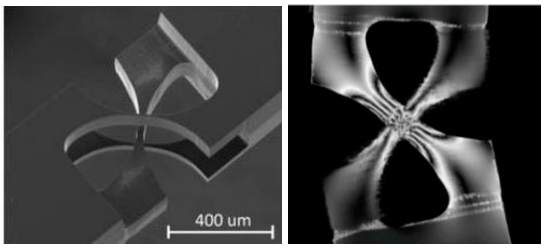

FIGURE 1. (left): SEM image of a femtosecond laser fabricated 3D notch-hinge [9]. (right) stress-induced retardance map of a loaded notch-hinge, where stress levels as high as 1.9 GPa are measured.

To further expand the applicability of this technology to the field of precision instruments, we investigate the use of femtosecond laser to modify the thermal expansion of fused silica. Being able to change the local coefficient of

thermal expansion (CTE), in any given location of a device, would give the freedom to design arbitrary thermal expansion compensation schemes in a system approach – and potentially at the material level. A classic example of thermal expansion compensation system is the gridiron pendulum.

This manuscript covers the characterization of the CTE properties of femtosecond laser exposed fused silica. Along the *local* change of CTE properties, the knowledge the elastic properties of the same laser-modified volumes is essential for determining the *global* thermal expansion of structural element consisting of laser-exposed and pristine material. Therefore, we subdivide the experimental characterization of laser-exposed patterns in two set of experiments: 1) the thermal expansion, using a bimorph structure, and 2) the elastic properties using a resonant cantilevers. For both characterizations methods, we use micromechanics to extract the relevant material properties. These micromechanical test-structure are themselves fabricated using the same laser that is also used to modify them locally.

Let us now discuss CTE measurements, starting with a detailed description of specifically designed environmental chamber that we used to control the temperature accurately.

Thermal expansion measurement

To study the change of thermal expansion of laser-modified volume, we use a method based on micro-mechanisms fabricated with ultrafast laser machining process. According this method, illustrated in Fig. 2, a cantilever, clamped on one end, is laser-exposed near its top-surface, defining the equivalent of a bimorph structure. In practice this layer consists out of an array of lines written parallel one to another as depicted in the magnified view of Fig. 2. The thermal expansion coefficient of the pristine material is denoted α_s, while the one of the laser modified material is noted α_l.

The temperature-dependent bending behavior of this structure is attributed to two separate effects: the first one due to the CTE difference between modified and pristine materials and the second one due to the constant stress introduced during laser exposure (as a consequence of the volume expansion of exposed regions [10]), leading to a thermally dependent strain since the Young's modulus evolves with temperature. A detailed differentiation of the thermally dependent behavior is further discussed in [11].

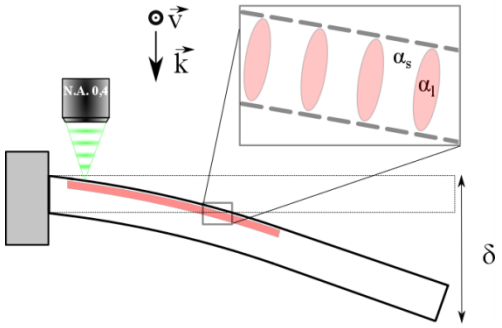

FIGURE 2 Schematic cross-section of a cantilever where the near top layer is exposed to femtosecond laser pulses. The red zone represents laser-affected zones (LAZs). As a result to the laser exposure, the cantilever bends with the radius r. δ defines the amplified motion of the cantilevers tip. The inset represents a magnified sketch showing single written lines cross-section depicted as red ellipses. α_s and α_l are the coefficients of thermal expansion of the pristine material, of the modified material, and of the modified layer (which is a composition of laser-affected and -unaffected material), respectively.

The out-of-plane motion of the bimorph is measured using an experimental setup comprising an environmental chamber and a digital holographic microscope as illustrated in Fig 3. To investigate the thermal-dependent cantilever deflection, a stable and uniform temperature distribution is required, which is particularly challenging considering the intrinsic low-thermal conductivity of fused silica. To achieve this goal, a dedicated environmental chamber was realized. The low-thermal conductivity excludes the use of temperature control based on thermal conduction across the specimen as it would induce an inhomogeneous temperature distribution.

To be able to probe optically the out-of-plane motion of the bimorph structure, an optical viewport is needed on top of the chamber. This window represents a thermal leak as it is as well isolated as the main chamber body. This may create a temperature gradient across the volume where the specimen is placed. To overcome these two issues, we choose an approach based on gas convection. In practice, a pre-heated (or pre-cooled) inert gas (N_2) flows in a laminar

regime across the chamber volume and thermalizes the specimen by heat convection.

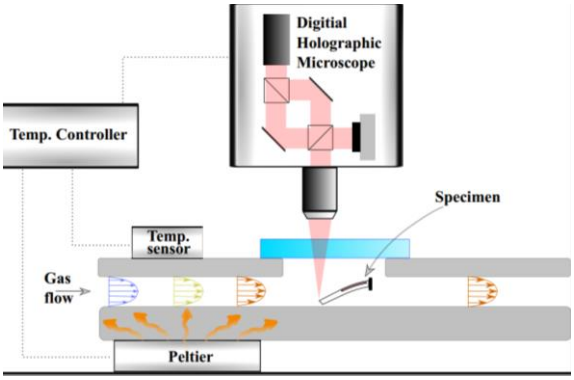

FIGURE 3. Schematic of the experimental setup for measuring the cantilever thermal deflections. The exposed cantilever is placed in a "miniature" environmental chamber and thermalized, thanks to a laminar flow of a preheated/precooled inert gas (N_2). The deflection is measured using a commercial digital holographic microscope (DHM from Lyncee Tec) that measures the motion of the cantilever's tip through a window.

A close-loop control algorithm is used to keep the gas at the desired temperature and to apply controlled-temperature heating or cooling ramps. Heating and cooling of the gas is done in an elongated 1m-long serpentine channel made out of an aluminum block, itself cooled or heated up using thermoelectric devices. In Fig. 4, exploded views of the environmental chamber are shown. The left part shows the aluminum base plate that contains the gas channels. This part is manufactured by conventional CNC milling. An aluminum cover plate and thermal conductive sealant hermetically covers the gas channels. The three components on top is the ensemble that forms the viewport. The right section shows how the aluminum body is thermally isolated using a thick housing made out of Bakelite – a material with low thermal conductivity and reasonable machinability. Finally, two thermoelectric devices - in white in Fig. 4, are in thermal contact with the aluminum core and themselves further covered with water-cooled-copper blocks for heat extraction.

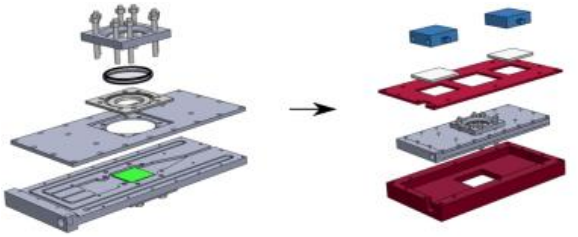

FIGURE 4. Exploded views of the thermal chamber. Left: aluminum base plate containing the gas flow channels. The green square illustrates the specimen location. Right: isolating housing (dark red) and thermoelectric heat exchanger devices (in white).

Finite element simulations are conducted to simulate the temperature distribution in the test specimen volume to optimize the chamber design. Fig. 5 left illustrates the temperature distribution for a given flowing gas, while Fig. 5 right shows a line graph of the temperature distribution across the specimen volume. In this simulation, a set point temperature of 100°C (ΔT=75°C) is used. As the gas flows through the sample volume, and hence on the viewport surface, a decrease in temperature along the propagation direction of a maximum of 1°C is observed. Increasing the flow velocity to 5 mm/s decreases the temperature gradient resulting from the presence of the viewport below 0.02 °C.

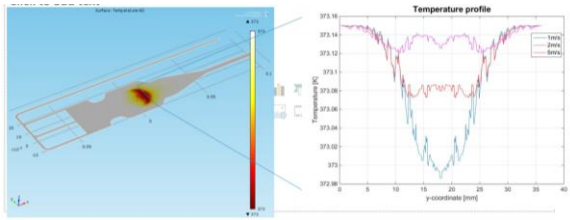

FIGURE 5. (left) Thermal-flow FEM simulation showing the gas temperature distribution across the chamber, (right) temperature distribution across the specimen volumes for a set of gas flow rates.

The temperature control operation is validated by measuring the gas temperature with a NTC thermistor. Thermal fluctuations are measured over a period of ~15 min for set points ranging from -10°C to 100°C, as depicted in Fig. 6. A PID-controller of the temperature is tuned over the complete temperature range in order to minimize temperature fluctuations. A maximum deviation of 0.07°C, at 95°C, and a minimum one of 0.0045°C, at 15°C are found. With the help of gain scheduling, the performance at high temperatures could be further enhanced.

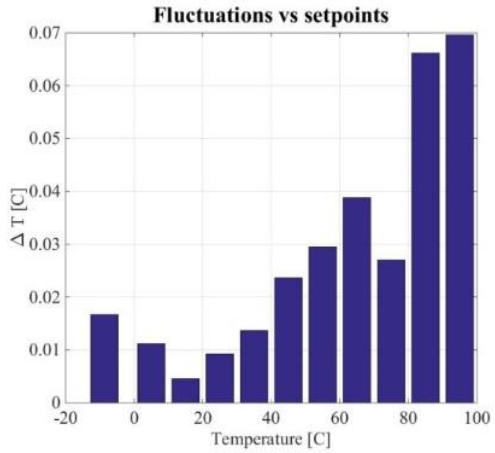

FIGURE 6. Validation of the temperature control in the specimen space of the thermal chamber. The thermal fluctuations are validated over a set of set points covering the [-10, 100] °C temperature domain.

To precisely measure the cantilever deflections, and hence small CTE differences, a digital holographic method is used. The DHM (Lyncee Tec), records holograms from a reflective 2D plane. The hologram contains intensity and phase information, as seen in Fig. 7. The phase image contains vertical distance information. When the temperature is changed, the specimen moves spatially due the thermal expansion of the chamber itself, which further interferes with the measurement. To measure only the deflection of the bimorph structure, the position and orientation of the specimen is recorded and subtracted from the measurement. The in-plane motion, of the specimen is then retrieved from the intensity image by tracking down the edge and the tip, out of which tilt and vertical movements are retrieved based on the phase image.

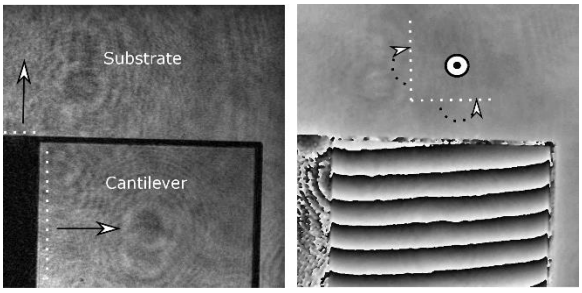

FIGURE 7. The intensity (left) and phase image (right). The parasitic motion of the substrate (caused by the thermal expansion of the environmental chamber itself) is recorded. The intensity image is further used to track down the in-plane motion and finally, the phase image is used for capturing the out-of-plane motion.

To prevent further parasitic thermally induced stress, the specimen is placed on a kinematic mount supported by precision ruby spheres, ensuring three well-defined contact points. With this strategy, the specimen can expand freely.
To study a wide range of exposure conditions, two femtosecond laser systems, having different pulse characteristics, are used. The first one emits 50 fs-pulses (an OPA from Amplitude Systèmes, emitting at 850 nm) and is capable of producing regime-I-type transformations (i.e. a localized increase of density), while the second laser is an Yb-doped fiber amplified system (Amplitude Systèmes, 380 fs at a wavelength of 1030 nm) and is capable of producing regime-II-type transformations (i.e. the nanogratings). Furthermore, a fixed pulse energy is chosen while the scanning speed is varied to investigate the CTE behavior at different laser deposited energies. The result are given in Fig. 8. Where α_l is estimated based on an analytical model described in [11].

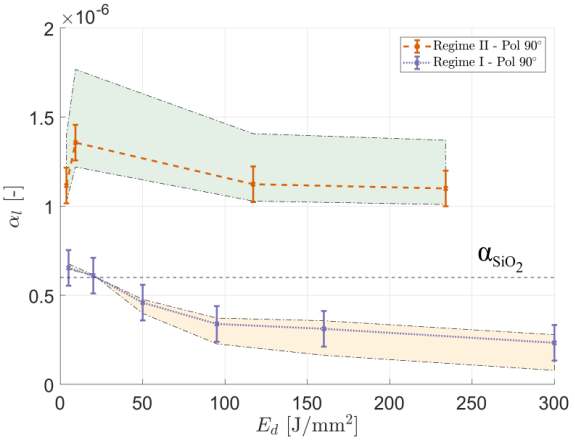

FIGURE 8. Estimation of the CTE for the laser modified material. The orange graph depicts the CTE for regime II modification while the blue one, the CTE for the regime I modification. The shaded areas depict the uncertainty due to the uncertainty of the Young's modulus in laser affected zones. The CTE value for pristine silica is shown as reference.

Noticeably, the CTE of regime I modifications reduces as the deposited energy increases, eventually reaching a value twice lower than the one of fused silica. For regime II, an opposite behavior is observed. For low deposited energies the CTE increases more than twice the

one of pristine silica, and after approximately 20 J/mm^2 the CTE decreases and saturates to twice the value of silica. The subsequent decrease in CTE observed after a peak value is accounted to a stress relaxation phenomenon, via crack formation, due to the high level of deposited energy. The shaded areas around the graphs represent the estimation uncertainty. This uncertainty is due the uncertainty for the Young's modulus value, E_I, that we further characterize in the following section.

Young's modulus measurement

In this section, we discuss preliminary results for the Young's modulus of laser modified material. The resonance frequency of a cantilever is dependent on its mass and stiffness ($f \sim \sqrt{k/m}$) (neglecting external forces possibly induced by the surrounding environment). Modifying the bulk material by laser exposure is expected to induce a frequency shift as Young's modulus and mass distribution changes occur. We estimate that the mass-distribution change is negligible, such that we can assume that the change in resonance frequency is mostly due to a change in Young's modulus. In Fig. 9 a schematic overview of the setup is given for a free-clamped cantilever with the red volume representing the laser modified volume.

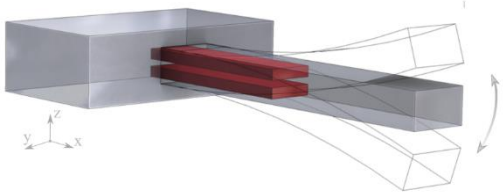

FIGURE 9. Schematic of a femtosecond laser exposed resonator. The elongated structure is a free-clamped cantilever with inside, shown in red, the femtosecond laser exposed regions.

One approach is to modify the bulk material of the cantilevers in a post-exposure step, i.e. after the fabrication step. Consequently, the cantilever bends due the volume expansion of laser affected zones. As a layer-by-layer exposure strategy is applied, meaning that the second exposure layer is applied on an already pre-stressed structure. This leads to a position error of subsequent layers (second, third and so on). To avoid this effect, we choose rather to do the fabrication and modifying exposure in *one step* and then we perform the etching step. Appropriate buffer zones are designed between laser exposed regions and the cantilever contour, to prevent laser exposed regions, used for tuning the Young modulus, to be themselves etched. In this fabrication strategy, the accumulated stress will be released during the etching step, causing the structure to move with respect to the substrate. To prevent damage on critical parts of cantilever, sacrificial fixtures are added to absorb the excess of stress.

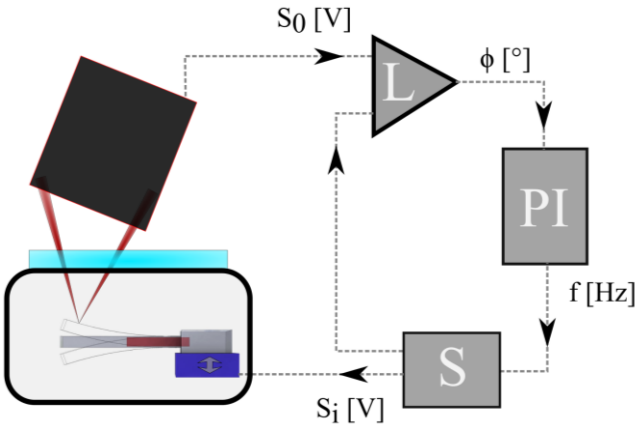

FIGURE 10 *Schematic of the experimental setup for Young's modulus characterization. The resonator is placed in the environmental chamber described previously to maintain the temperature constant at 25°C and to reduce the moist content. The resonator is excited by a piezoelectric actuator, shown in dark blue, and the cantilever vibration is measured using a laser triangular displacement sensor. Furthermore, the resonator is kept at its resonance using a closed-loop arrangement. The phase (φ) between the input (S_i) and output signal (S_o) is monitored using a lock-in amplifier (block L), and the loop is closed using a PI controller (Block PI), keeping track of the excitation frequency (f) sent to the signal generator (Block S). The frequency f is stored for further analysis.*

The resonator is placed on a piezoelectric actuator and excited with a sinusoidal signal (Fig. 11). The response of the resonator is measured using a triangulation laser-based displacement sensor (Keyence LKH022), which has sub-micrometer resolution. A lock-in amplifier (Stanford Res. Sys. SR850) is used to filter the analog signal of the sensor. In order to

accurately trace and maintain the resonance frequency, a closed-loop based method is applied. The phase shift between input and output signals - determined by the lock-in amplifier - is used as an input to a PI controller and controlled on a -90° phase delay. The resonant ensemble is placed in the environmental chamber described previously, used at a well-controlled temperature and fed with a nitrogen-rich environment to minimize external disturbances such as moisture.

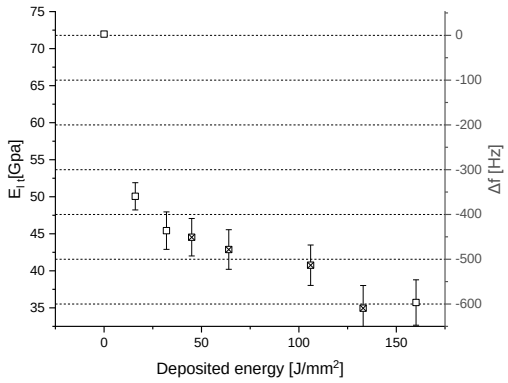

FIGURE 11. Right axis: measured frequency shift as a function of deposited energy. Left axis: estimated laser modified Young's modulus.

Fig. 11 depicts preliminary results on Young's modulus measurements. In this example, the exposure conditions corresponds to a type II modification, done using the Yb-doped fiber amplified system. In this study, the scanning speed is varied in order to study the effect of deposited energy in the specimen. As it turns out the Young's modulus decay's in an inverse proportional fashion as a function of the increased deposited energy.

Conclusion

In this work, we have demonstrated that the local CTE of fused silica can be altered using the femtosecond laser irradiation. Furthermore, we have shown a reduction by nearly a factor two of the CTE for regime I modification, and an opposite behavior for the regime II modification. This result suggests that a CTE contrast of a factor four can be obtained, which is particularly useful for thermally compensating a monolithic element made out of silica. The characterization of the Young modulus in the modified volume further completes the description of ultrafast exposed fused silica.

REFERENCES

[1] C. B. Schaffer, A. Brodeur, J. F. García, E. Mazur, Micromachining bulk glass by use of femtosecond laser pulses with nanojoule energy. *Opt. Lett.* **26**, 93–95 (2001).

[2] K. M. Davis, K. Miura, N. Sugimoto, K. Hirao, Writing waveguides in glass with a femtosecond laser. *Opt. Lett.* **21**, 1729–1731 (1996).

[3] Y. Shimotsuma, P. G. Kazansky, J. Qiu, K. Hirao, Self-organized nanogratings in glass irradiated by ultrashort light pulses. *Phys. Rev. Lett.* **91**, 247405 (2003).

[4] A. Marcinkevi Ius, S. Juodkazis, M. Watanabe, M. Miwa, S. Matsuo, H. Misawa, and J. Nishii, Femtosecond laser-assisted three-dimensional microfabrication in silica, *Opt. Lett*. **26**, 277 (2001).

[5] S. Kiyama, S. Matsuo, S. Hashimoto, and Y. Morihira, Examination of Etching Agent and Etching Mechanism on Femotosecond Laser Microfabrication of Channels Inside Vitreous Silica Substrates, *J. Phys. Chem. C* **113**, 11560 (2009).

[6] Y. Bellouard, A. Said, M. Dugan, and P. Bado, Fabrication of high-aspect ratio, micro-fluidic channels and tunnels using femtosecond laser pulses and chemical etching , *Opt. Express* **12**, 2120 (2004).

[7] R. R. Gattass, E. Mazur, Femtosecond laser micromachining in transparent materials. *Nat. Photonics*. **2**, 219–225 (2008).

[8] C.-E. Athanasiou, Y. Bellouard, A Monolithic Micro-Tensile Tester for Investigating Silicon Dioxide Polymorph Micromechanics, Fabricated and Operated Using a Femtosecond Laser. *Micromachines*. **6**, 1365–1386 (2015).

[9] V. Tielen and Y. Bellouard, Three-Dimensional Glass Monolithic Micro-Flexure F abricated by Femtosecond Laser Exposure and Chemical Etching, *Micromachines*, **5**, 697-710, (2014)

[10] A. Champion, Y. Bellouard, Direct volume variation measurements in fused silica specimens exposed to femtosecond laser. *Opt. Mater. Express, OME*. **2**, 789–798 (2012).

[11] P. Vlugter, E. Block, Y. Bellouard, Local tuning of fused silica thermal expansion coefficient using femtosecond laser. *Phys. Rev. Materials*. **3**, 053802 (2019).

BREAKING THE RESOLUTION VERSUS THROUGHPUT TRADEOFF IN NANOSCALE ADDITIVE MANUFACTURING

Vu H. Nguyen[1], Dien Wang[2], James S. Oakdale[1], Shih-Chi Chen[2], and Sourabh K. Saha[1]

[1]Lawrence Livermore National Laboratory
Livermore, California, U.S.A

[2]The Chinese University of Hong Kong
Shatin, Hong Kong

INTRODUCTION

Two-photon lithography (TPL) is a promising additive manufacturing technique for fabrication of millimeter scale complex 3D structures with nanoscale features [1-12]. TPL relies on nonlinear two-photon absorption to generate features smaller than the diffraction-limited focused light spot. This unique capability of TPL has been leveraged in diverse fields to fabricate functional micro- and nanoscale 3D structures, such as photonic crystals, optical and mechanical metamaterials, micromachines, miniaturized optics, and flexible electronics. Unfortunately, the practical import of TPL is limited by the tradeoff that exists between feature resolution and throughput.

The most common implementation of TPL involves serially scanning a tightly focused laser spot in a photopolymer resist to fabricate 3D structures by overlapping the individual submicron volumetric pixels (i.e., voxels) that are generated in the focal volume. The serial and slow writing scheme of these existing TPL implementations makes production scaleup beyond one-off demonstrations impractical. Due to the challenging ultrafast light-matter interactions that underlie TPL, past attempts at parallelization have either compromised its submicron resolution or its ability to pattern complex structures. As a result, TPL has remained a niche fabrication technique with limited adoption beyond academic and research laboratories. Here, we present a parallel TPL process based on femtosecond projection that increases the rate of 3D printing by two to three orders of magnitude without compromising the submicron resolution. In addition, our technique allows one to access previously unexplorable geometric design space by enabling the printing of thinnest-ever nanowires at widths smaller than 175 nm along all cross-sectional axes, over an area a million times larger than the nanowire's cross-sectional area, and within single-digit millisecond time scales. This transforms TPL from an expensive niche technique to a widely applicable cost-effective high-throughput high-resolution 3D printing process.

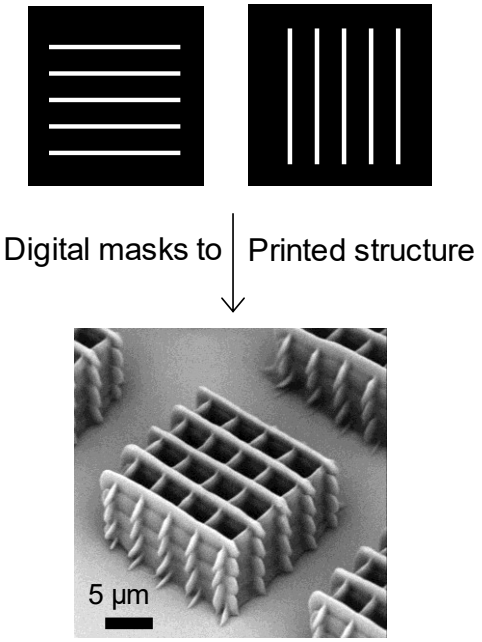

FIGURE 1. Layer-by-layer printing in FP-TPL.

FEMTOSECOND PROJECTION TPL

In our femtosecond projection two-photon lithography (FP-TPL) technique, 3D structures are fabricated via a layer-by-layer printing of patterned 2D layers that range in thickness from less than a micrometer to more than 4 μm. Each 2D layer is up to 165 μm × 165 μm in size and is written in millisecond time scales. Such thin 2D layers are generated by projecting a patterned 2D

light sheet (i.e., equivalent to a planar point cloud containing more than a million points) that is focused in both the space and time domains. The light sheet can be patterned into arbitrary 2D patterns through a digital micromirror device (DMD), a standard grating-like component of digital projectors. A schematic of the layer-by-layer printing technique is illustrated in Figure 1.

We have harnessed the broadband nature of femtosecond lasers and diffraction from the DMD to achieve temporal focusing, i.e., focusing in the time domain. During temporal focusing, a pre-stretched ultrashort light pulse is progressively shortened (in the time domain) as it travels through the photopolymer resist so that the shortest pulse (i.e., the highest light intensity) is achieved only at the spatial focal plane. The intensity gradient generated via temporal focusing ensures that writing is spatially restricted to the focal plane, without causing polymerization above or below the focal plane. Without this temporal focusing, depth resolution is lost, i.e., instead of forming a thin sheet, all material in the path of the projected beam polymerizes to form thick "extruded" solid structures such as those observed in previous demonstrations of TPL parallelization [2]. Here, we have used the temporal focusing technique with custom photopolymer resists to fabricate single-micron scale polymerized layers in arbitrarily complex 3D structures. The printing of sub-diffraction 3-D structures are consistently achieved over large-areas by exploiting the ultra-thin and uniform femtosecond light sheet and the optimized voxel aspect ratio.

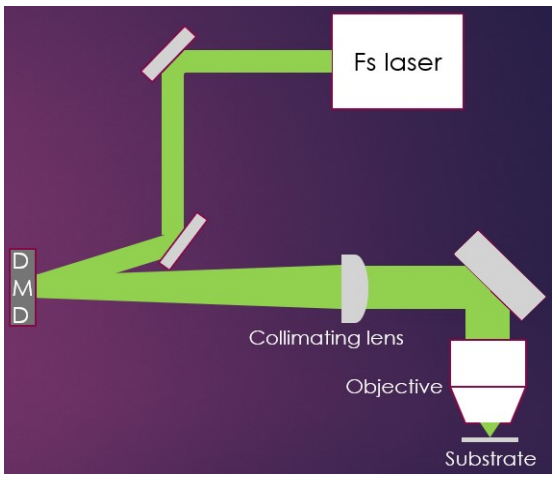

FIGURE 2. Schematic of FP-TPL.

A schematic of our FP-TPL implementation is shown in Figure 2. The key functional components of the system are (i) a laser source, (ii) a digitally tunable dynamic mask, (iii) collimating optics, (iv) a focusing objective lens, and (v) motion stages. The laser source generates near-IR femtosecond pulses centered at 800 nm with a broad wavelength spectrum (~tens of nm) and provides the light that drives the writing process. The light from the laser illuminates the digital mask, which is an array of individually-switchable micromirrors. When switched 'on', the intensity of light emerging from a micromirror along a predetermined direction is high, and when 'off', low. The collimating optics convert the diverging beam that emerges from the DMD into a collimated beam. The collimated beam passes through the objective lens and is focused onto a plane inside the photopolymer resist material. At the image plane inside the resist, the intensity of light at each point corresponding to an 'on' micromirror in the DMD is above the threshold writing intensity, and the intensity at points corresponding to the 'off' micromirrors is below the threshold. Thus, a pixelated image of the digital mask is written in the resist via photopolymerization, which contains distinct or overlapping cured, volumetric pixels (i.e., voxels). 3D structures are fabricated by moving the focused image plane relative to the resist by using the motion stages.

RESOLUTION OF FP-TPL

In our FP-TPL system, each DMD pixel is projected to an area of 151×151 nm^2 in the work field; as such, super-resolution features can be printed via thresholding the laser dosage. To experimentally verify the submicron resolution of FP-TPL, we have printed nanowire features that are thinner than the optical diffraction limit along both the lateral and the axial dimensions by varying the projected line thickness, the beam power (i.e., the focal spot intensity), and the duration of exposure. As shown in Figure 3, features as thin as 142 nm (along the lateral dimension) and as short as 175 nm (along the axial dimension) can be printed with FP-TPL.

The nanowire features printed here are the thinnest-ever polymer nanowires to be printed with any form of parallel multi-photon lithography systems and comparable in width to the features printed with high-resolution serial-scanning TPL systems [6]. In addition, the height of the thinnest line (at 175 nm tall) is smaller than past

demonstrations of both parallel [10-12] and serial TPL [6]; this is achievable here in FP-TPL due to the sub-diffraction sizes of the projected patterns in combination with the fine laser dose control. Notably, the aspect ratio of the voxel induced by projecting DMD pixels is closer to 1 as compared with the typical point spread function of serial scanning systems that are larger than 2 and closer to 3 [1]. This provides significant advantage in terms of resolution and structural strength when fabricating sub-diffraction structures.

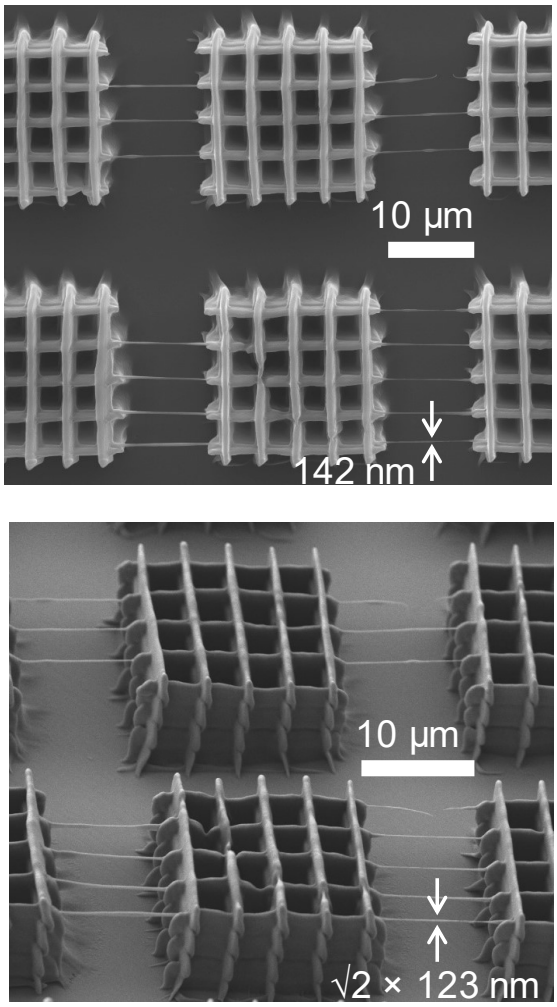

FIGURE 3. Nanowire features demonstrating nanoscale resolution of FP-TPL. All nanowires were printed in a single exposure lasting 5 milliseconds.

THROUGHPUT OF FP-TPL

Unlike the serial TPL process, the throughput of FP-TPL is insensitive to the number of voxels written per layer due to its ability to project an entire 2D layer at once. The volumetric throughput of FP-TPL is determined by the area of projection, layer thickness, and the time interval between projection of subsequent layers; whereas, the areal throughput is determined by the area of projection and the duration of exposure per projection. For our system, up to ~1 million pixels can be projected per exposure, the maximum area of projection is 165 µm × 165 µm, the layer thickness varies from below 1 µm and up to ~4 µm, the time interval between projection of subsequent layers is 20 ms including the time taken for stage motion, and the duration of exposure per projection lies in the range of 3 ms and higher. Thus, the voxel generation rate is ~333 million voxels/s, areal 2D printing rate is ~ 9 mm^2/s, the single-layer volumetric processing rate is between 33 mm^3/hr to 131 mm^3/hr depending on the layer thickness, and the volumetric 3D printing rate (including the time taken for moving the stages) is between 5 mm^3/hr to 20 mm^3/hr. All these rates are for printing configurations that maintain the submicron in-plane (i.e., lateral) printing resolution and are independent of the in-plane geometry of the layers.

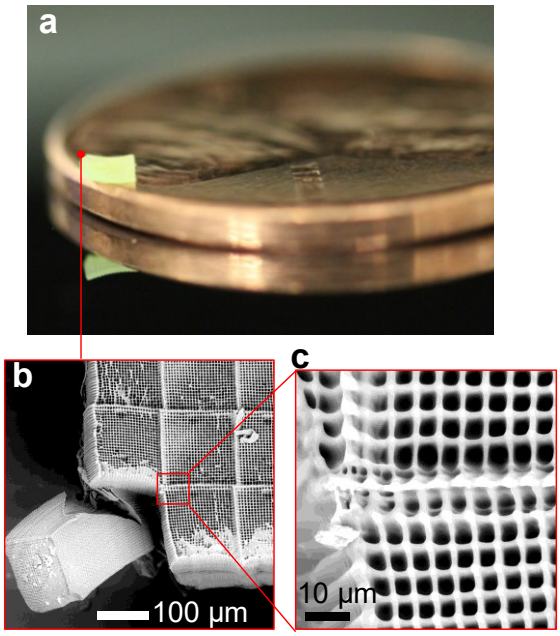

Figure 4: Millimeter scale structure with submicron features supported on a US penny on top of a reflective surface.

We have printed mm-scale structures to demonstrate the throughput scale-up achievable via FP-TPL. One such structure is shown in

Figure 4. The 2.20 mm × 2.20 mm × 0.25 mm cuboid was printed in 8 minutes 20 seconds demonstrating a 3D printing rate of 8.7 mm^3/hr. In contrast, serial techniques would require several hours to print this cuboid.

While maintaining sub-500 nm feature sizes, the single-layer volumetric processing rate of FP-TPL exceeds that of the existing serial techniques by at least 3 orders of magnitude whereas the 3D printing rate (i.e., printing rate including delays due to stage motion) exceeds that of the fastest serial system by at least 90 times for porous structures and by at least 450 times for non-porous structures.

CONCLUSIONS

In summary, we have demonstrated parallelization of the two-photon lithography process through a temporally-focused femtosecond projection technique that breaks the traditional resolution versus throughput tradeoff of nanoscale additive manufacturing. The combination of high-throughput and fine resolution makes FP-TPL superior to serial-scanning TPL and a viable technique to massively scale up nanoscale additive manufacturing of functionally-relevant complex 3D structures.

ACKNOWLEDGMENTS

This work was performed under the auspices of the U.S. Department of Energy by Lawrence Livermore National Laboratory under contract DE-AC52-07NA27344 and by the Chinese University of Hong Kong under subcontracts. (Document release #LLNL-PROC-773404). Funding was available from LLNL's LDRD project #16-ERD-047. The authors thank Dr. Robert Panas and Dr. Christopher Spadaccini at LLNL for helpful discussions.

REFERENCES

[1] Saha SK, Oakdale JS, Cuadra JA, Divin C, Ye J, Forien J-B, Bayu Aji LB, Biener J, and Smith WL. Radiopaque resists for two-photon lithography to enable submicron 3D imaging of polymer parts via X-ray computed tomography. ACS Applied Materials & Interfaces. 2018; 10(1), pp. 1164-1172.

[2] Mills B, Grant-Jacob JA, Feinaeugle M, and Eason RW. Single-pulse multiphoton polymerization of complex structures using a digital multimirror device. Optics Express. 2013; 21(12), pp. 14853-14858.

[3] Oakdale JS, Smith RF, Forien JB, Smith WL, Ali SJ, Bayu Aji LB, Willey TM, Ye J, van Buuren AW, and Worthington MA. Direct Laser Writing of Low-Density Interdigitated Foams for Plasma Drive Shaping. Advanced Functional Materials. 2017; 27, 1702425.

[4] Meza LR, Das S, and Greer JR. Strong, lightweight, and recoverable three-dimensional ceramic nanolattices. Science. 2014; 345(6202), pp. 1322-1326.

[5] Shaw LA, Chizari S, Shusteff M, Naghsh-Nilchi H, Di Carlo D, and Hopkins JB. Scanning two-photon continuous flow lithography for synthesis of high-resolution 3D microparticles. Optics Express. 2018; 26(10), pp. 13543-13548.

[6] Lu W-E, Dong X-Z, Chen W-Q, Zhao Z-S, and Duan X-M. Novel photoinitiator with a radical quenching moiety for confining radical diffusion in two-photon induced photopolymerization. Journal of Materials Chemistry. 2011; 21(15), pp. 5650-5659.

[7] Fischer J, Mueller JB, Kaschke J, Wolf TJA, Unterreiner A-N, and Wegener M. Three-dimensional multi-photon direct laser writing with variable repetition rate. Optics Express. 2013; 21(22), pp. 26244-26260.

[8] Malinauskas M, Žukauskas A, Bičkauskaitė G, Gadonas R, and Juodkazis S. Mechanisms of three-dimensional structuring of photo-polymers by tightly focussed femtosecond laser pulses. Optics Express. 2010; 18(10), pp. 10209-10221.

[9] Li Y-C, Cheng L-C, Chang C-Y, Lien C-H, Campagnola PJ, and Chen S-J. Fast multiphoton microfabrication of freeform polymer microstructures by spatiotemporal focusing and patterned excitation. Optics Express. 2012; 20(17), pp. 19030-19038.

[10] Yang L, Li J, Hu Y, Zhang C, Lao Z, Huang W, and Chu J. Projection two-photon polymerization using a spatial light modulator. Optics Communications. 2014; 331, pp. 82-86.

[11] Vizsnyiczai G, Kelemen L, and Ormos P. Holographic multi-focus 3D two-photon polymerization with real-time calculated holograms. Optics Express. 2014; 22(20), pp. 24217-24223.

[12] Yang L, El-Tamer A, Hinze U, Li J, Hu Y, Huang W, Chu J, and Chichkov BN. Parallel direct laser writing of micro-optical and photonic structures using spatial light modulator. Optics and Lasers in Engineering. 2015; 70, pp. 26-32.

Microfabrication via Holographic Optical Tweezers and Two-photon Polymerization

Samira Chizari, Lucas A. Shaw, Miles P. Lim, Amin Farzaneh, Sydney Austin, Jonathan B. Hopkins
Mechanical and Aerospace Engineering
University of California, Los Angeles
Los Angeles, CA, USA

ABSTRACT

The purpose of this work is to demonstrate concurrent use of holographic optical tweezers (HOT) and two-photon polymerization (2PP) with closed-loop automation routines for (1) fabrication of microgranular crystals and (2) fabrication and actuation of microstructures with embedded strain energy. The HOT approach provides the ability to manipulate (i.e., move and deform) microparticles and micro-mechanisms with high precision. Furthermore, the 2PP approach allows for high-resolution additive manufacturing of microstructures as well as joining of microparticles. This work also utilizes image processing-based automation routines that enable repeatable assembly of microparticles. This automated system holds potential to enable fabrication of energy-storing materials and multi-material microgranular crystals, and paves the way for further progress in the field of architected metamaterials.

INTRODUCTION

Microfabrication technologies are advancing to meet the demands for new and increasingly complex designs that are not possible with existing manufacturing techniques. Optical tweezing [1] has proven to be a powerful technique for manipulation of micro- or nano-particles of different materials such as polymers [2] and metals [3]. The broad applications of this technique in biology [4,5] led to the 2018 Nobel Prize in Physics [6] for its innovator, Arthur Ashkin [7]. By introducing a diffractive light element such as spatial light modulator (SLM) in the optical tweezing setup, creation of multiple optical traps for simultaneous handling of numerous microparticles has become possible. This technique, which is utilized in this work, is called holographic optical tweezers (HOT) [8].

An ultrafast pulsed laser is also used in this work for additive fabrication of microsturctures with nano-scale resolution via two-photon polymerization (2PP) [9]. Coincidentally, the development of the ultrafast laser led to the other 2018 Nobel Prize in Physics for Gérard Mourou and Donna Strickland [6].

This paper demonstrates how the combination of the HOT and 2PP approaches enables unprecedented capabilities needed for many new applications in microsciences.

MICROFABRICATION SYSTEM

The 2PP setup used in this work (Figure 1) includes a femtosecond pulsed laser (fs laser, Spectra Physics MaiTai eHP DS), an acousto-optic modulator (AOM, IntraAction ATM-802DA2) and a scanning galvanometer mirror system (galvo, Thorlabs GVS012).

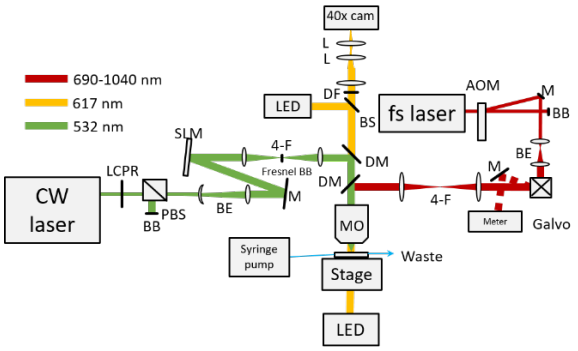

FIGURE 1. Schematic of combined HOT/ 2PP setup. L: lens, BB: beam block, PBS: polarizing beam-splitter, M: mirror, BE: beam expander, 4-F: telescope system, DM: dichroic mirror, MO: microscope objective, Meter: power meter.

The HOT system consists of a 532 nm continuous-wave laser (CW Laser, Quantum Opus), SLM (Meadowlark Optics 1920 × 1152), a liquid crystal polarization rotator (LCPR, Meadowlark Optics LPR-100-0532). A 100x microscope objective (MO, NA 1.45) is used for

both HOT and 2PP systems, and the fabrication area is imaged using a 40X camera (Basler ace acA1300-75gm). The combined HOT/2PP system is controlled with image-processing-based automation routines developed in MATLAB.

MICROSTRUCTURES WITH EMBEDDED STRAIN ENERGY

In this section, examples of microstructures that are fabricated, deformed, or actuated using the combined 2PP/HOT system's capabilities are discussed. These structures are printed by layer-by-layer scanning of the femtosecond laser in a custom photopolymer solution that consists of 1.1%wt. TPO-Li (Colorado Photopolymer Solutions), 38.4%wt. ethoxylated (15) trimethylolpropane triacrylate (Sartomer SR9035), and 60.5%wt. deionized (DI) water. The structures are subsequently handled via HOT, which uses optical forces to deform the polymeric elements, leading to stored strain energy within these microstructures.

Microscale Jack-in-the-box

A microscale Jack-in-the-box (Figure 2) is fabricated to demonstrate the ability of polymer microstructures to store and release strain energy.

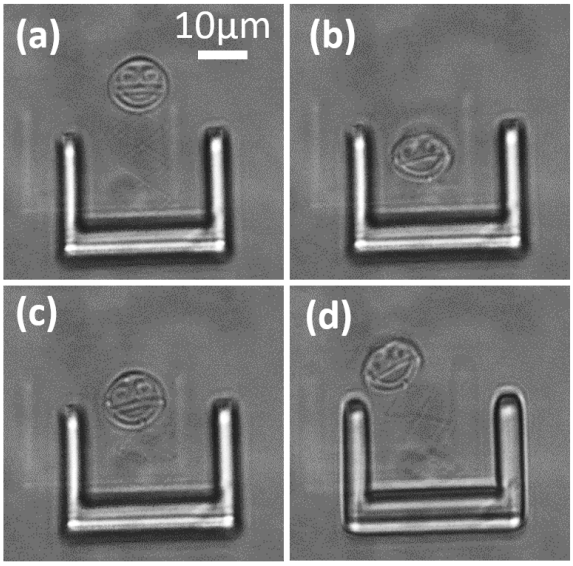

FIGURE 2. Fabrication of a functional microscale Jack-in-the-box using the combined 2PP/HOT microfabrication system.

Once the microstructure is fabricated by 2PP (Figure 2(a)), HOT is used to compress the planar spring by optical trapping of the face and forcing it into the box (Figure 2(b-c)). In the final step, the optical traps are removed, and the microstructure springs out of the box as a result of release of its stored energy (Figure 2(d)).

Rolling Cam Structure

A rolling cam structure (Figure 3) is a mechanism that uses the stored energy in its deformed constituent elements to achieve shape reconfigurability with minimal activation energy. This structure was first inspired by compliant rolling contact elements introduced by Cannon *et al* [10]. By implementing the same principles, a shape-morphing metamaterial can be designed if such elements are tessellated with different arrangements [11]. This type of metamaterial cannot be made by any conventional microfabrication methods, as it requires simultaneous fabrication and deformation of the microstructures. However, by utilizing our 2PP/HOT system we demonstrated fabrication of a 2×2 lattice of this metamaterial. The fabrication process is achieved by printing the microstructure with undeformed straps between the cams (Figure 4(a)), subsequently four optical traps are used to move the cams close to each other and deform the flexures between them, which will result in stored strain energy in these structures (Figure 4(b)). This stored energy facilitates rolling of the cams with minimal actuation force.

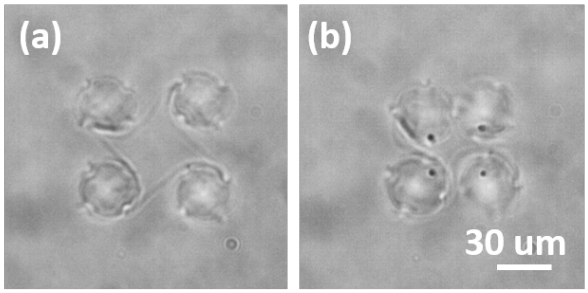

FIGURE 3. Microscale shape reconfigurable structure based on the compliant rolling cam mechanism (a) Microstructure is fabricated undeformed by 2PP (b) HOT is used to move the cams close to each other resulting in strained straps.

Negative Poisson's Ratio Structure

The presented hybrid HOT/2PP system can also be used for fabrication and actuation of structures to study their mechanical properties such as the Poisson's ratio. Here we fabricated a planar auxetic structure [12] using the 2PP approach and actuated it by using six precisely-located optical traps that are generated automatically after the lithographic process is complete. Optical

traps then slowly (i.e., quasi-statically) move outward to stretch the structure. The Poisson's coefficient of this structure was calculated to be -0.054 by image-processing based measurements.

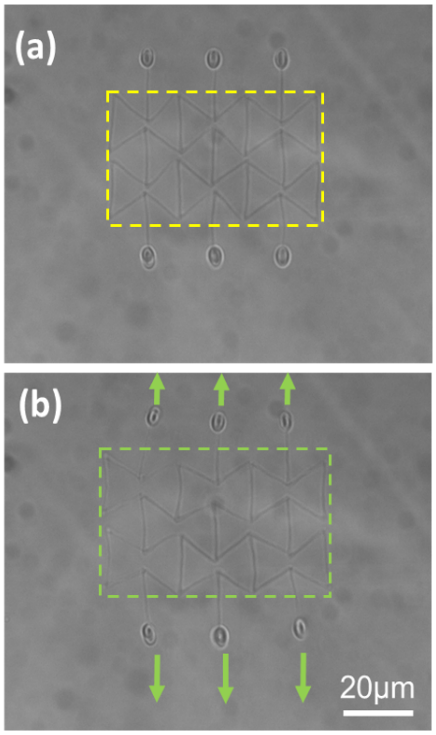

FIGURE 4. Planar auxetic lattice with negative Poisson's coefficient is (a) fabricated with 2PP and (b) actuated by HOT.

Embedded Strain Energy Metamaterial

Structures that can store energy within their elements and release it upon impacts are interesting candidates in shock mitigation devices such as absorbers, dampers, and isolators [13]. If such structures are used as the unit cell in a lattice, a novel architectured metamaterial can be achieved [14]. This type of metamaterial cannot be fabricated with any conventional microfabrication technique as it requires multiple interspersed steps of lithography and deformation during the fabrication process. However, the combined 2PP/HOT system can fabricate such structure automatically. First, a unit cell of the structures is printed on the substrate with one free floating side by using 2PP (Figure 5(a)). This microstructure has four 'V' shaped flexures connecting its two sides. Next, using HOT, the free-floating side of the cell is brought into contact with the fixed side and the contact points are fused together using 2PP. This way strain energy is "printed" into the unit cell. It is worth noting that the simultaneous use of the two techniques is the key to fabricate such a structure with embedded strain energy.

MICROGRANULAR CRYSTALS

A different category of the combined HOT/2PP system's applications is fabrication of microgranular crystals, which are closely packed arrangements of microparticles [15]. These structures possess unique nonlinear mechanical, photonic and acoustic properties. Self-assembly is the common microfabrication technique for these crystals [16], however, it is not able to produce structures with multiple materials or achieve certain packing arrangements with controlled irregularities or vacancies. The ability to pattern microparticles from variety of materials with HOT and join them together in any desired 3D configuration using 2PP are the unique features required for fabrication of engineered microgranular crystals with high precision. Our system is equipped with a closed loop control feedback system [17], that uses image processing to detect the particles and utilizes solutions to the bottleneck assignment problem for optimized path planning of the particles in a way that it can automatically produce custom crystals with large numbers of microparticles (Figure 6). Further improvements in the post-process treatments are required to avoid damages to the crystals initiating from stiction forces during the drying process.

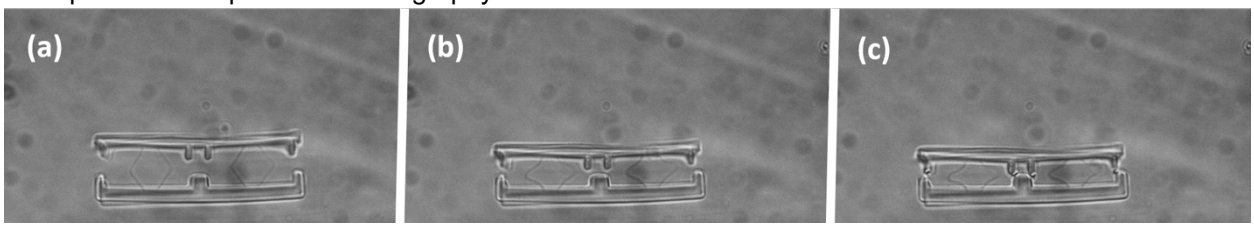

FIGURE 5. a cell of embedded strain energy metamaterial is (a) printed using 2PP with four V-shaped flexures (b) compressed and held in strained position via HOT (c) fused at four contact interfaces by 2PP

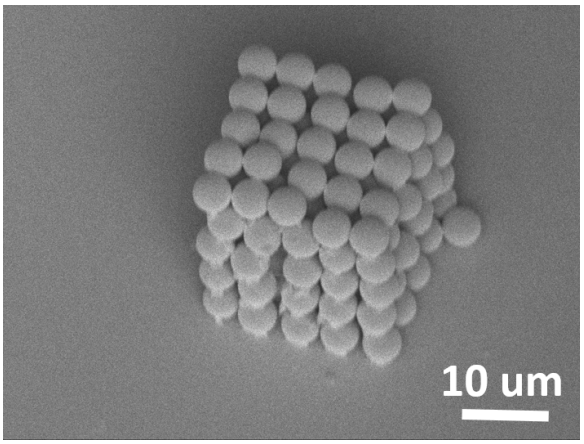

FIGURE 6. A 5×5×5 microgranular crystal made using HOT for assembly and 2PP for sticking the microparticles together. Slight deformation to the final structure was caused by post-processing steps.

CONCLUSION

This work demonstrated an advanced microfabrication method that seamlessly combined the HOT and 2PP approaches to enable fabrication of micro-granular crystals and microscale structures that can store strain energy. This approach holds potential for fabrication of metamaterials with complex engineered architectures that are not feasible with conventional microfabrication methods.

ACKNOWLEDGMENT

This work is supported by Air Force Office of Science Research under award number FA9550-18-1-0459 and by National Science Foundation Graduate Research Fellowship under Grant No. DGE-1650604. Byung “Les” Lee, Professor John Fourkas, and Professor Farah Dawood are gratefully acknowledged.

[1] Grier DG. A revolution in optical manipulation. Nature 2003;424:810–6. doi:10.1038/nature01935.

[2] Ghadiri R, Weigel T, Esen C, Ostendorf A. Microassembly of complex and three-dimensional microstructures using holographic optical tweezers. J Micromechanics Microengineering 2012;22:65016. doi:10.1088/0960-1317/22/6/065016.

[3] Sato S, Harada Y, Waseda Y. Optical trapping of microscopic metal particles. Opt Lett 1994;19:1807. doi:10.1364/OL.19.001807.

[4] Molloy JE, Padgett MJ. Lights, action: Optical tweezers. Contemp Phys 2002;43:241–58. doi:10.1080/00107510110116051.

[5] Zhang H, Liu K-K. Optical tweezers for single cells. J R Soc Interface 2008;5:671–90. doi:10.1098/rsif.2008.0052.

[6] All Nobel Prizes in Physics n.d. https://www.nobelprize.org/prizes/lists/all-nobel-prizes-in-physics.

[7] Ashkin A. Acceleration and Trapping of Particles by Radiation Pressure. Phys Rev Lett 1970;24:156–9. doi:10.1103/PhysRevLett.24.156.

[8] Dufresne ER, Spalding GC, Dearing MT, Sheets SA, Grier DG. Computer-generated holographic optical tweezer arrays. Rev Sci Instrum 2001;72:1810. doi:10.1063/1.1344176.

[9] Maruo S, Nakamura O, Kawata S. Three-dimensional microfabrication with two-photon-absorbed photopolymerization. Opt Lett 1997;22:132. doi:10.1364/OL.22.000132.

[10] Cannon JR, Lusk CP, Howell LL. Compliant Rolling-Contact Element Mechanisms. Vol. 7 29th Mech. Robot. Conf. Parts A B, vol. 2005, ASME; 2005, p. 3–13. doi:10.1115/DETC2005-84073.

[11] Shaw LA, Chizari S, Dotson M, Song Y, Hopkins JB. Compliant rolling-contact architected materials for shape reconfigurability. Nat Commun 2018;9:4594. doi:10.1038/s41467-018-07073-5.

[12] Alderson A, Alderson KL. Auxetic materials. Proc Inst Mech Eng Part G J Aerosp Eng 2007;221:565–75. doi:10.1243/09544100JAERO185.

[13] Hu N, Burgueño R. Buckling-induced smart applications: recent advances and trends. Smart Mater Struct 2015;24:63001. doi:10.1088/0964-1726/24/6/063001.

[14] Chizari S, Shaw LA, Hopkins JB. Simultaneous printing and deformation of microsystems via two-photon lithography and holographic optical tweezers. Mater Horizons 2019;6:350–5. doi:10.1039/C8MH01100A.

[15] Porter MA, Kevrekidis PG, Daraio C. Granular crystals: Nonlinear dynamics meets materials engineering. Phys Today 2015;68:44–50. doi:10.1063/PT.3.2981.

[16] Chen Q, Bae SC, Granick S. Directed self-assembly of a colloidal kagome lattice. Nature 2011;469:381–4. doi:10.1038/nature09713.

[17] Shaw LA, Chizari S, Hopkins JB. Improving the throughput of automated holographic optical tweezers. Appl Opt 2018;57:6396. doi:10.1364/AO.57.006396.

OBSERVATION OF POLYMER FLOW BEHAVIOR IN REAL TIME BY LIGHT INTERFERENCE IN LASER-ASSISTED THERMAL IMPRINTING

Haruto Tendo[1], Keisuke Nagato[1], Yusuke Ebihara[1], Nana Takahashi[1], and Masayuki Nakao[1]
[1]Department of Mechanical Engineering
The University of Tokyo
Bunkyo-ku, Tokyo, Japan

INTRODUCTION

Nanoimprint lithography (NIL) was proposed as a high-throughput and low-cost printing technology by Chou S Y in 1996 [1,2]. The process is quite simple. First, a mold with nanostructures and a thermoplastic polymer are pressed together and heated. The polymer subsequently melts and fills the nanostructures of the mold. Then, they are cooled and separated. By following these steps, we can print nanostructures on the polymer exactly as required.

Laser-assisted thermal imprinting (LATI) was also proposed as an improved printing technology. It could shorten the printing time, especially heating and cooling time, because local heating was performed by a laser [3,4]. FIGURE 1 shows the schematic of NIL and LATI.

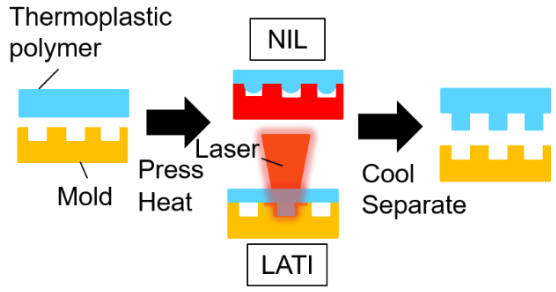

FIGURE 1. Schematic of NIL and LATI.

In LATI, some parameters such as the shape of the mold, laser power, pressure between the mold and the polymer, and irradiation time greatly influence various physical phenomena, such as the viscosity of the polymer, wetting on the wall of the mold, and capillary effects. In addition, as a result of the changes in these phenomena, the polymer flow changes significantly. Thus, the optimal values of these parameters must be identified. To achieve this, we should understand how the polymer flow behaves in LATI.

Numerical analyses are one of the means to clarify the polymer flow behavior. This behavior is exhibited during laser irradiation, and many studies have examined it. For example, Shimizu E used the moving particle semi-implicit method [5] and Jeong J H used CFD-ACE [6]. They compared the results of their numerical analyses to those of experiments conducted under the same conditions. However, the experimental results involved the effects of polymer shrinkage and residual heat during the cooling process, but the analytical ones did not. Thus, these results could not be compared correctly. In other words, as these results are different, it is unclear whether the analyses are wrong, or the cooling effects have a great influence on the results. Therefore, the flow behavior needs to be observed in real time to obtain the polymer flow behavior before the cooling process.

Moreover, it was said that videos were very useful for observing the flow behavior [7,8]. In this research, we observed the polymer flow behavior in real time by videos and then attempted to demonstrate that the height of the polymer (polymer filling height) could be calculated from it.

EXPERIMENTAL

We defined the image of the polymer from above as upper image (UI) and image of the cross section as sectional image (SI). FIGURE 2 shows the definition of UI and SI.

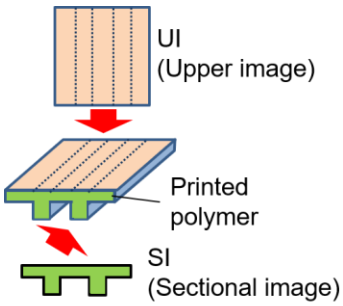

FIGURE 2. Schematic of definition of UI and SI.

FIGURE 3 shows the LATI experimental system used. It can observe UI during laser irradiation, because a microscope (VMU-LB, Mitutoyo) can match the focus of itself and the laser. The mold was made of Nickel and its surface shape was line and space (L/S). The polymer was acrylic resin (PMMA) and its thickness was 75 μm. We used a single-mode fiber laser (JL-SP0178, SPI Lasers), and its wavelength and beam diameter were 1070 nm and 484 μm, respectively. The laser power was 15 W. The laser light irradiated through the microscope, and when we measured the laser power after this, 30% of the power could be measured. In other words, 70% of the power was absorbed by the microscope. Both the mold and the polymer were pressed by an air cylinder at 30–35 MPa. We used two cameras. One was a USB camera (L-835, Hozan) that could record color videos and the other was a high-speed camera (FASTCOM, SA3, Photron) that could record monochromatic videos.

In this research, (a) we observed UI in LATI by the system and attempted to reveal the relationship between UI and SI. Then, (b) we calculated the polymer filling height in SI from UI and compared it to the real UI measured by a laser microscope (OLS4100, OLYMPUS).

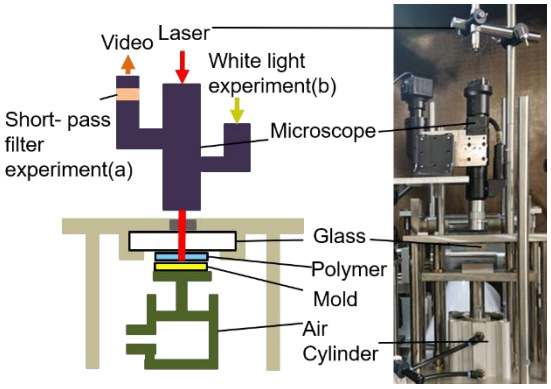

FIGURE 3. Schematic of LATI experimental system.

(a)Light interference confirmation experiment

FIGURE 4(B) shows the schematic of experiment(a). The irradiation time was 7 s and both the L/S pitches were 5 μm. The video was taken by the USB camera. We used white light as the light source and cut the laser light by a short-pass filter. It may be assumed that there was light interference in the UI, because the light waves reflected from the lower surface of the polymer (LSP) and the space part of the mold (SSM) interfered with one another (FIGURE 4(A)). Moreover, the white light contains various colors with varying wavelengths. Thus, each position of the bright lines of these colors may be different. Therefore, we made a hypothesis that colorful circular light interference can be observed in the UI like Newton rings, because the shape of the area where equal amount of heat was given was a circle due to the Gaussian distribution of the laser beam. In addition, the line parts of the mold and the center position of the irradiated area, which was perfectly filled by the polymer, were supposed to be white or the color of the mold, because the light resource reflected perfectly in those areas. Further, the colors may be arranged from the center in an ascending order of wavelengths. It was because the distance between the LSP and SSM decreased with increasing distance from the center. FIGURE 4(C) shows the expected UI based on these hypotheses.

(b)Comparison of polymer filling height experiment

After experiment(a), we observed the interference using monochromatic light. FIGURE 5 shows the schematic of the experiment(b). The high-speed camera was used to take a monochromatic video. The laser light was used as the light source, because the high-speed camera could capture the laser light in the infrared range. As for the mold, both the L/S pitches were 30 μm. The irradiation time was 4 s. Because the wavelength of the laser was 1070 nm, the difference in the polymer height between the positions of the dark lines in the UI should be 535 nm. Therefore, we could calculate and plot the expected polymer filling height based on the dark lines (EPFH) in one part of the mold. In addition, we also obtained the real polymer filling height (RPFH) by the laser microscope. Furthermore, the EPFH had error bars that showed the range of dark lines. Finally, we compared the EPFH and RPFH.

However, the EPFH included cooling effects such as shrinkage of the polymer and residual heat, unlike the RPFH. Therefore, investigating the influence of the cooling effects is necessary. Thus, a video of the UI was taken during the process when the polymer and mold were irradiated for 4 s with the laser, cooled, and then irradiated again. Next, the comparison between the EPFH, which was based on the UI at the end of the first irradiation and that at the beginning of the second irradiation was performed. The difference

between them would show the change in the cooling effects. Although the laser was used as the light source and it would change the filling height during the second irradiation, the UI at the beginning of the second irradiation appeared to be hardly affected. Therefore, the outcome of the comparison indicated the influence of the cooling effects correctly. Moreover, the reason why we did not compare the RPFH before cooling to the one after cooling was that it was very difficult to exactly attach the filled polymer to the mold again after they were separated to measure the filling height and investigate the RPFH before cooling.

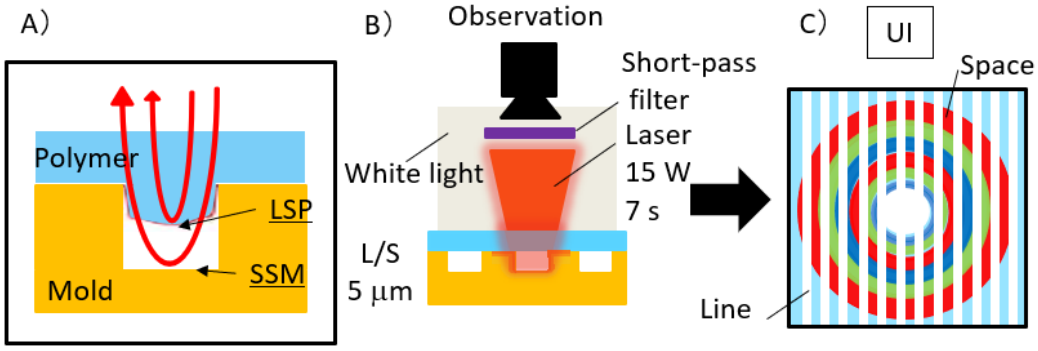

FIGURE 4. Schematic of (A) two reflected lights and definition of LSP and SSM, (B) experiment(a), and (C) hypothesis in the UI.

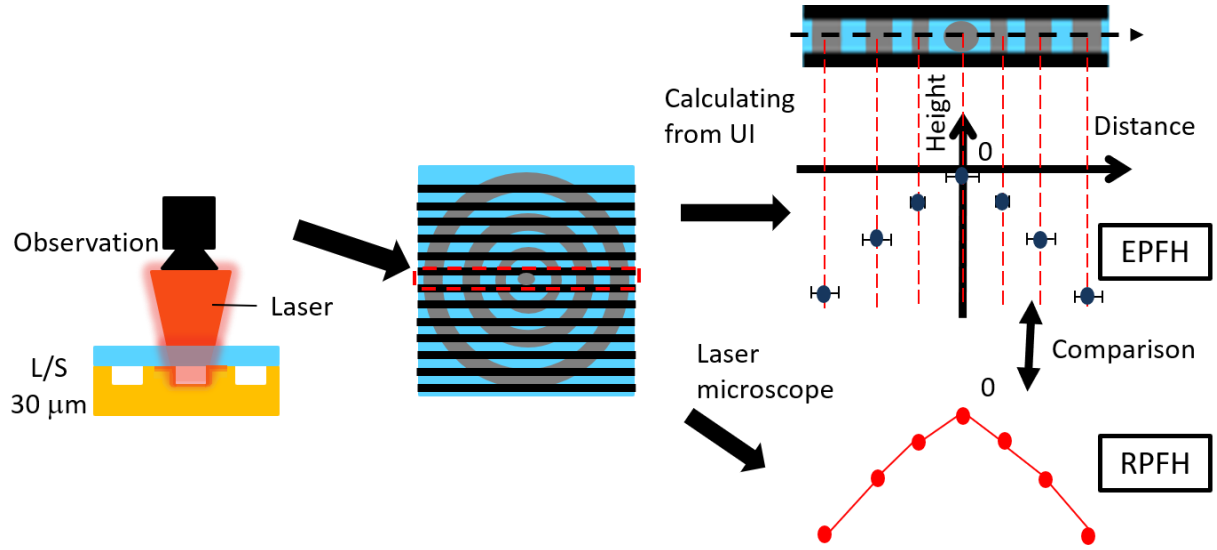

FIGURE 5. Schematic of experiment(b), and definition of the EPFH and RPFH.

RESULTS AND DISCUSSION

Experiment(a)

FIGURE 6(A) shows the results of the observation. The center was the color of the mold, and it was filled completely by the laser microscope. In addition, the circles of each color spread out on the space parts of the mold from the center. Therefore, colorful circular light interference was observed in the UI. FIGURE 6(B), (C) shows the enlarged view on the area surrounded by red dotted lines in (A), and the RGB in (B). In FIGURE 6(B), positions 2, 4, and 6 are represented in red, green, and blue, respectively. Therefore, the data presented in FIGURE 4(C) seemed to be correct. However, when we measured their RGB, the RGB of blue was lower than those of others and the blue peak was not clear. It could be assumed that because the range of color wavelength was wide, many colors were interfering there. In other words, the blue we saw was not pure blue, but a mix of many colors. Therefore, we suggested that the light

source should be changed from white light to monochromatic light. The fact that no interference was observed on the line parts of the mold was consistent with the hypothesis that there could be interference caused by the lights reflected from the LSP and SSM. Therefore, the optical path difference could be twice as long as the distance between the LSP and SSM.

Experiment(b)

FIGURE 7 shows the results of the observation. The interference fringes, dark lines and bright lines, by the monochromatic light were easier to see than those by the white light. We observed them on the space parts of the mold in UI, but not on the line parts. It agreed with the results of experiment(a). In the video, these dark lines moved along the space parts from the center.

FIGURE 7 also shows the results of the comparison between the EPFH and RPFH. The blue plots and red line indicate the EPFH and RPFH, respectively. When the EPFH and RPFH were overlaid, these graphs matched in the range of -50 to 90 μm. In this experiment, the center was the brightest, and, because of the laser properties, areas further away from the center were increasingly darker. This difference in the amount of light may be the reason why the two graphs did not match in the range of -90 to -50 μm. Moreover, the asymmetry of the graphs may be caused by the inclination of the incident light. The parallel ray from the laser was refracted by the objective lens, and the influence of the light from the right side may be stronger in this experiment. In addition, there was a difference around the centers of the EPFH and RPFH. This difference could be due to interference of several reflected lights, because the shape there was round. FIGURE 8 shows the change in the cooling effects. According to it, the cooling hardly has any effects under these conditions. Therefore, these results showed that we could calculate the polymer filling height from the interference fringes observed in the UI by the monochromatic light source.

The results of experiment(a) and experiment(b) showed that we could observe the interference in which the light waves reflected from the LSP and SSM interfered with one another, and we may be able to determine the polymer filling height in real time from the interference fringes in the UI. Furthermore, when the height is calculated through the video, the flow behavior from the beginning to the end will become clear. Next, using this method, a comparison between the results of the proposed numerical analyses and the experimental results without cooling effects would allow us to judge whether the analyses are correct or not. If causes of the cooling effects are revealed, the results of the cooling effects could be included in further analyses. Moreover, during this time, we focus only on the dark lines; however, it will be necessary to calculate the polymer filling height from the lines of any brightness from now on.

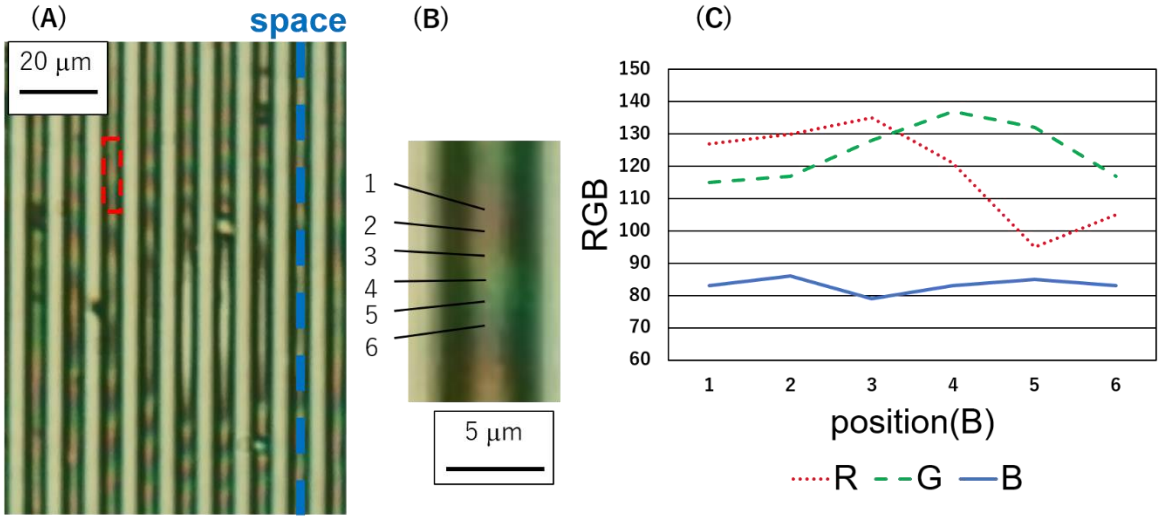

FIGURE 6. (A) Results of observation in experiment(a), (B) enlarged view of the area surrounded by red dotted lines in (A), and (C) RGB in (B).

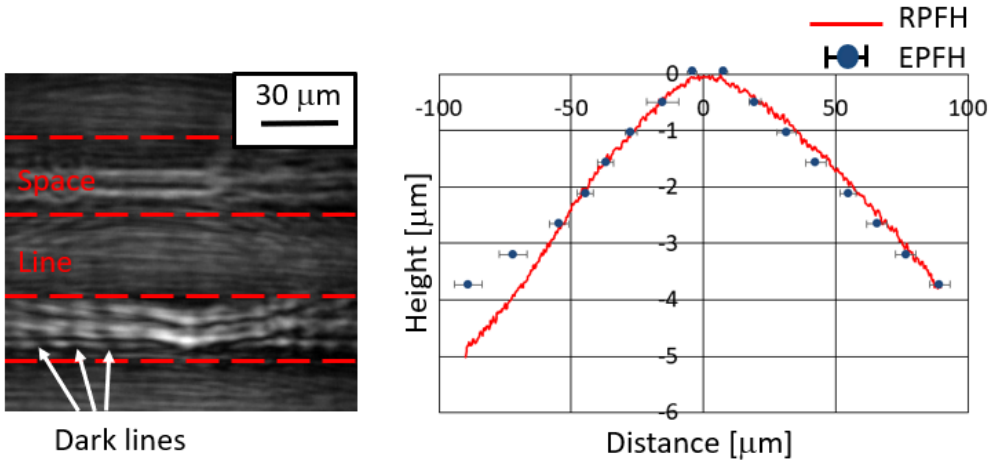

FIGURE 7. Results of observation in experiment(b) (left) and comparison graph between EPFH and RPFH (right).

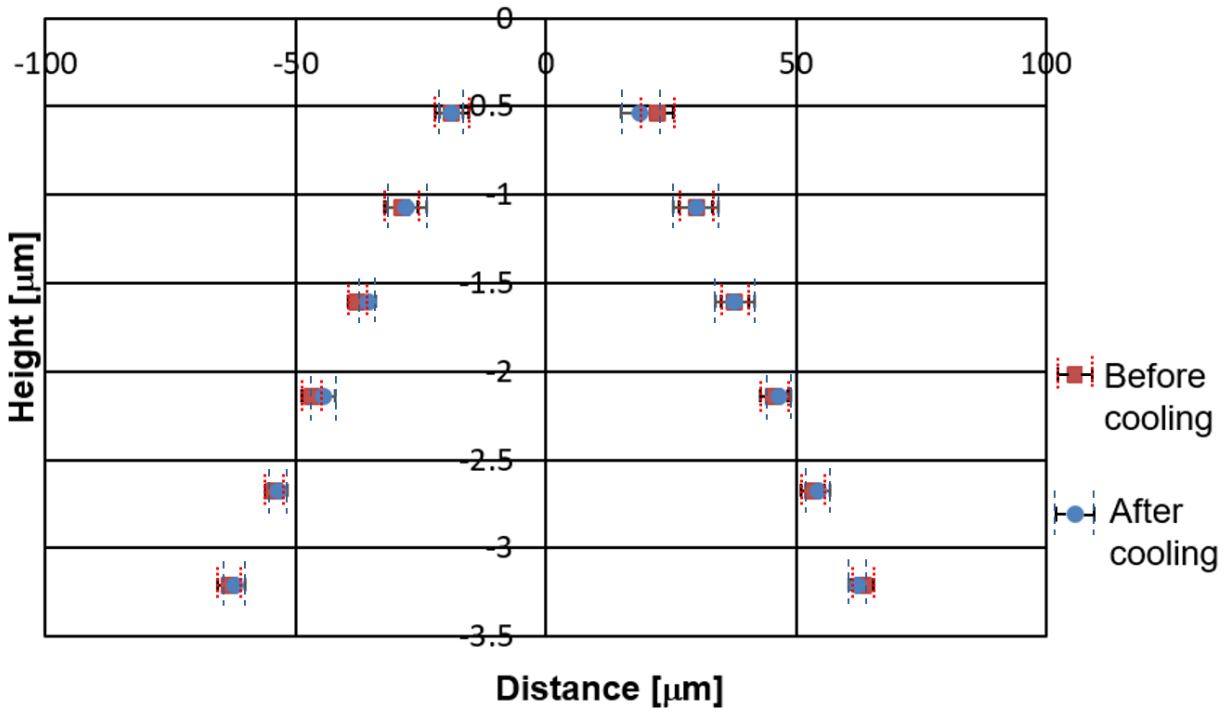

FIGURE 8. Comparison between the EPFHs before and after cooling.

CONCLUSIONS

In this research, we observed the polymer flow behavior in real time in LATI by taking a video, and showed the light interference, which consisted of the lights reflected from the LSP and SSM, observed in the UI. Moreover, we also demonstrated that the height of the polymer could be calculated from the interference fringes in UI, particularly dark lines. Therefore, this indicated that we could understand the flow behavior in LATI by calculating the height from the interference fringes seen in the video.

However, as only L/S molds were used in this study, it is necessary to demonstrate that the calculation is sufficiently robust to be applied to a variety of molds. In future work, we are planning to change the size, shape, thickness, and

material of the mold to determine the polymer filling height in any mold. Moreover, the calculation from only the dark lines was not accurate. Therefore, systems that can calculate the height of a polymer in real time from lines of any brightness should be developed. Furthermore, the calculation of height from the interference fringes should be used to compare results of the proposed analyses to those of the experiments without cooling effects.

REFERENCES

[1] Chou S Y, Krauss P R, Renstrom P J. Imprint of Sub-25 nm Vias and Trenches in Polymers. Applied Physics Letters. 1995; 67: 3114-3116.

[2] Chou S Y, Krauss P R, Renstrom P J. Nanoimprint Lithography. Journal of Vacuum Science & Technology B: Microelectronics and Nanometer Structures Processing, Measurement, and Phenomena. 1996; 14: 4129-4133.

[3] Xia Q, Keimel C, Ge H, Yu Z, Wu W, Chou S Y. Ultrafast Patterning of Nanostructures in Polymers using Laser Assisted Nanoimprint Lithography. Applied Physics Letters. 2003; 83: 4417-4419.

[4] Nagato K, Takahashi K, Sato T, Choi J, Hamaguchi T, Nakao M. Laser-Assisted Replication of Large-Area Nanostructures. J. Mater. Process. Technol. 2014; 214: 2444-2449. http://dx.doi.org/10.1016/j.jmatprotec.2014.05.025

[5] Shimizu E, Nagato K, Nakano H, Yajima Y, Nakao M. Numerical Analysis of Resin Flow in Laser-Assisted Imprinting of Various-Sized Microstructures by MPS Method. Micro Nano Engineering. 2017; 20:18-22.

[6] Jeong J H, Choi Y S, Shin Y J, Lee J J, Park K T, Lee E S, Lee S R. Flow Behavior at the Embossing Stage of Nanoimprint Lithography. Fibers and Polymers. 2002; 3: 113-119.

[7] Schift H, Bellini S, Mikkelsen M B, Gobrecht J. Visualization of Mold Filling Stages in Thermal Nanoimprint by Using Pressure Gradients. Journal of Vacuum Science & Technology B: Microelectronics and Nanometer Structures Processing Measurement, and Phenomena. 2007; 25: 2312-2316.

[8] Schift H, Kim G, Lee J, Gobrecht J. 3D Visualization of Mold Filling Stages in Thermal Nanoimprint by white Light Interferometry and Atomic Force Microscopy. Nanotechnology. 2009; 20: 355301.

Design, Fabrication, and Calibration of a Stiffness Programmable Metamaterial

Chenyang Luo[1], Gehan C. Jayatilaka[1], Yuanping Song[2], Ian S. Ladner[1], Michael A. Cullinan[1], Jonathan B. Hopkins[2]

[1]Department of Mechanical Engineering

The University of Texas at Austin

[2]Department of Mechanical and Aerospace Engineering

The University of California, Los Angeles

Abstract

This paper presents a novel MEMS-based metamaterial which is programmable using active closed-loop feedback control to achieve any desired stiffness within a given design envelope. In this device, piezoresistive strain gauges sensors are used to measure the displacement in real time and corporate with the thermal actuator to control the stiffness of bent beam with sufficient sensitivity and resolution. This paper presents the first successfully proof of concept demonstration of the metamaterial design at the MEMS scale.

Introduction

The development of mechanical meta-materials is a rapidly growing area of research with new designs progressing from passively achieved behaviors of microstructures assembled at a system level to programmable micro-size metamaterial structures with sensors and actuators embedded into the lattice. In most situations, those actuators and sensor embedded system need high level feedback and accurate control of system with external power such as batteries to perform extremely behaviors.

The idea of programmable metamaterials was proposed by Goldstein et al [1], with many small cells robots combined into a large lattice which can change its shape by changing the position of its own cells. A lot of programmable metamaterial designs have been proposed, however, many of them are not repeatable or practical. Most current metamaterial designs are built for applications with system level control (Poisson's ratio, damping ratio, etc) without controlling the individual structures within the lattice. Variety of programmable

Fig(1) Parameter sweep of 4 different version of beam designs that we made by nano-fabrication

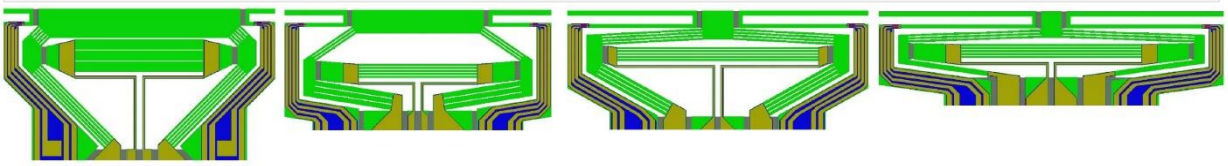

metamaterial design has been proposed with individual cell control using an embedded processor, but those applications have not been demonstrated at the microscale [2-5].

This work demonstrates the successful trial of a 3D programmable micro-size metamaterial with a feedback control sensor. Four different beam designs were used to demonstrate the different tradeoffs between maximum stress and strain that the mechanical metamaterials can achieve (Fig(1)).

Fig(3) MEMS device Process Flow

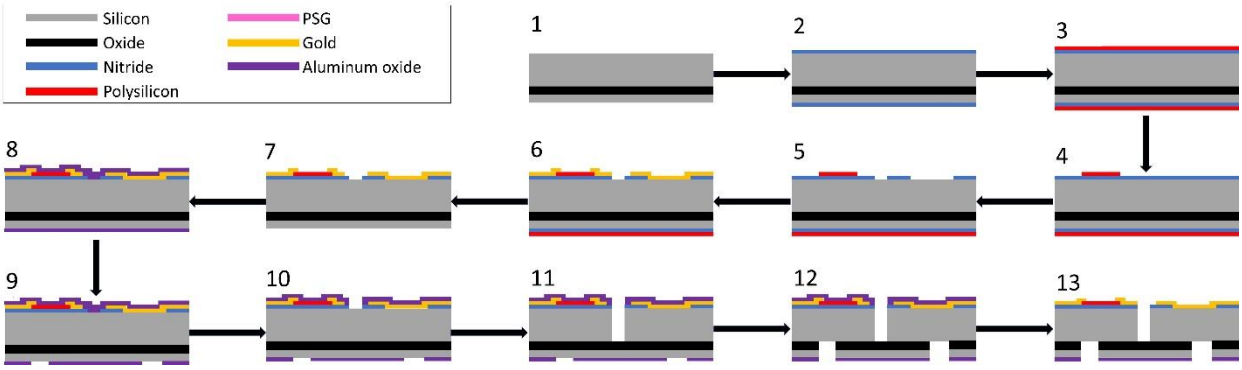

Sensor Design

The metamaterial structure uses a set of piezoresistors in a Wheatstone bridge configuration to sense the motion of the individual unit cells. The main signal in the sensor is from the motion of the shuttle on the thermal actuator creating strain in the piezoresistor as the flexure beam that the resistor sits on deforms. The force applied to the thermal actuator can be calculated by

$$F = \frac{\left(\frac{\Delta R}{R}\right) * W^3 * H}{6 * \pi_1 * z * (L - l)} \qquad (1)$$

where ΔR is the chance in resistance of the piezoresistor, R is piezo resistance, W is the width of the beam, H is the height of the beam, π_1 is piezoresistive coefficient with a value of $55.8 * 10^{-11}$ [6], L is length of beam and l is length of Piezo resistor, z is the distance from the piezo resistor to the neutral axis of the beam.

There are two main noises affecting resolution of the device: (1) Johnson noise and (2) instrument amplifier noise. Johnson noise is caused by the thermal agitation of the electrons within the piezoresistor and is given by equation (2)

$$\mathrm{Vn} = \mathrm{A} * \sqrt{4 * K_b * T * R} \ \ \mathrm{V}/\sqrt{Hz} \quad (2)$$

where A is the amplifier ratio, K_b is Bolztmann's constant, T is resistor's tempurature in Kevin and R is the resistance in ohms. An instrumentation amplifier with an input noise of $4\mathrm{nV}/\sqrt{Hz}$ and a 500 times amplification is used to boost the signal output from the Wheatston bridge into the analog-to-digital convertor.

Fig(2) (a) Bridge configurations (b) Half bridge Design

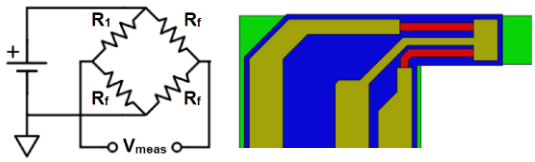

(a) (b)

The combined instrument amplifier noise and Johnson noise are calculated [7] to be $12e^{-6}\mathrm{V}/\sqrt{Hz}$ which results in a minimum force resolution of ~10 μN for the unit cells tested in this paper. Considering the stiffness the tested devices, the displacement resolution is ~8 nm

Manufacturing

All the MEMS fabrication steps were done in the Microelectronics research center (MER) at J.J Pickle research campus. This device includes a polysilicon piezoresistance layer, a silicon nitride insulation layer, a gold electrode layer with a thin Ti adhesion layer, and Si device cantilever layer. Figure (3) shows the fab flow for the device.

The MEMS device starts with a silicon-on-insulator (SOI) wafer with a 400 μm Si device layer, a 4 μm silicon oxide (box) layer, and 50 μm silicon handle layer. 200nm of silicon nitride are then grown by low pressure chemical vapor deposition (LPCVD) followed by a 200nm amorphous silicon layer also grown by LPCVD. After removing native oxide using a quick hydrofluoric acid (HF) dip, the amorphous silicon is doped using phosphoryl chloride diffusion at 900°C and annealing at 1050°C. Phosphosilicate glass layer (PSG) formed during diffusion process is then cleaned using a buffer oxide etch (BOE). Piezoresistive strain gauge shape is then defined by a lithography step (MA6). Transfer the pattern from photoresist into polysilicon layer is then done using reactive ion etching (Plasmatherm 790RIE). Another RIE is used to expose the Si layer from top side silicon nitride layer. A lift-off pattern is transferred from photoresist to deposit 200nm gold trace on 30nm Ti adhesion layer by e-beam evaporation (CHA industries SE-1000-RAP). Cleaning the backside polysilicon and silicon nitride are finished by RIE and a 200nm Al_2O_3 layer is deposited using atomic layer deposition (ALD, Cambridge NanoTech SavannahTM 200) to make hard mask for the device layer. After defining the geometry by RIE (Oxford ICP RIE 100) on the Al_2O_3 layer, the top side and bottom side are etched by deep reactive ion etching (Nordson March px-250) to define the thermal actuator and flexures. Finally, the Al_2O_3 layer is cleaned by RIE to expose the gold layer.

Calibration Results

To calibrate the sensors and actuators on the fabricated MEMS devices, the fabricated devices were wire bonded to a custom designed PCB and were tested using the MPS150 manual probe system. The actuator drive voltage was varied from 0V to 21V (voltage supply limit) to measure the expansion and compression travel displacement of the actuator. Video footage of the microscope was recorded and analyzed using digital image correlation in the NI vision software package, which can compare and analyze different pictures with sub-pixel resolution.

Fig(4) (left) Measurement of device shuttle displacement (right) Device mounted on chip

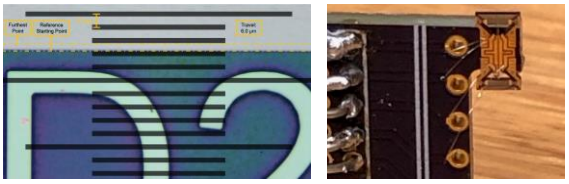

The tip shuttle displacement was observed to increase with the expected quadratic function with a uniform increasing voltage input in Fig (5). The maximum positive travel displacement of the softest device (device 4) was 24 μm. The 3rd stiffest device was able to reach a displacement of 16 μm, the 2nd stiffest device was able to reach a

displacement of 7 μm and the stiffest device (device 1) was able to reach a displacement of 3 μm. Repeated testing of devices at high voltage (>16v) is limited because the electrode trace starts to melt at these high temperatures.

Fig(5) Voltage drive-in vs Shuttle displacement for 4 different beam design

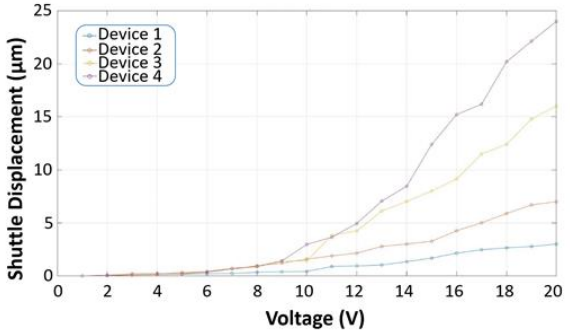

The temperature of device body and its beam was also measured and recorded using a Flir thermal camera as shown in Fig (6). The beam temperatures are similar to the FEA simulation (Fig (6)) (within 10%).

Fig (6) Temp calibration between FEA and real test

	FEA(°C)	Test(°C)	diff(%)
TopBeamTipEnd	329	366	10.10929
TopBeamAnchorEnd	356	365	2.465756
BottomBeamAnchorEnd	337	366	7.92348
BottomBeambaseEnd	326	365	10.68493
MiddleTopBeam	687	725	5.241379
Middleside	413	465	11.18128

Cube Assembly

Each of the individual MEMS chips were assembled into cubes with each MEMS device acting as a face of that cube as shown in Fig(7). This configuration allows each cube

Fig(7) (a) model of single cube with 6 devices surrounded (b)fabricated singe cube (c)) fabricated 2x2x2 cube latice (d) Temperature measurement with Flir thermal camera

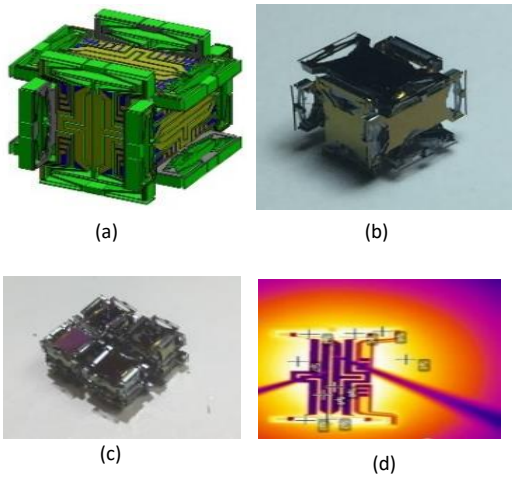

to expand or compress with programmable stiffness in all 3 different axies. After assembling each cube into a larger superstructure, the whole NxNxN lattice can have larger adjustable displacement while maintaining the same controllable stiffness.

Conclusion

We have demonstrated the concept of a programmable MEMS-based metamaterial fabricated by traditional silicon fabrication technology. In the future work, we are going to develop more sensitive and accurate piezoresistive sensors by changing the doping of the polysilicon layer [8]. This will allow us to achieve better feedback control on the programed stiffness of the devices that are fabricated.

Acknowledgements

This work was supported by AFOSR award number FA9550-18-1-0459 and based on work accomplished at Texas Nanofabrication Facilities supported in part by the National

Science Foundation under The National Nanotechnology Coordinated Infrastructure (grant EECS-1542159). The authors acknowledge program officer Byung “Les” Lee.

References

[1] S. C. Goldstein, J. D. Campbell and T. C. Mowry(2005), IEEE computer, 38, 99-101, DOI: 10.1109/MC.200-5.198

[2] D. Rus and M. Vona, in Proceedings 1999 IEEE International Conference on Robotics and Automation (Cat.No.99CH36288C), IEEE, vol. 4, pp. 2513–2520 DOI: 10.1109/ROBOT.199-9.773975

[3] P. J. White and M. Yim, in 2007 IEEE/RSJ International Conference on Intelligent Robots and Systems, IEEE, 2007, pp. 2773–2778, https://doi.org/10.1177/0278364909351942

[4] E. Hawkes, B. An, N. M. Benbernou, H. Tanaka, S. Kim, E. D. Demaine, D. Rus and R. J. Wood, Proc. Natl. Acad. Sci., 2010, 107, 12441–12445. Doi: 10.1073/pnas.0914069107

[5] L. A. Shaw and J. B. Hopkins, J. Mech. Robot., 2015, 8, 021019.

[6] P. J. French, Sensors Actuators, A Phys., vol. 99, no. 1–2, pp. 3–12, 2002. DOI: 10.1016/S0924-4247(01)00876-7

[7] Robert M. Panas, Michael A. Cullinan, Martin L. Culpepper, Precision Engineering, DOI:10.101-6/j.precisioneng.

[8] P.J.French, A.G.R.Evans, Solid-State Electronics,32,no 1, 1-10, 1989, https://doi.org/10.1016/0038-1101(89)90041-5

DISTORTION COMPENSATION FOR ADDITIVE MANUFACTURED COMPONENTS VIA MODIFIED INHERENT STRAIN METHOD

Hai T. Tran, Zekai Zhou, John Lemon, and Albert C. To
Department of Mechanical Engineering and Materials Science, University of Pittsburgh, PA 15261

INTRODUCTION

One of the most challenging issues in laser power bed fusion (l-pbf) additive manufacturing (AM) is residual distortion in as-built components. Residual distortion can be described as the change of the component's design geometry during and after AM processing. Residual distortion can also be seen as an inhomogeneous shrinkage, i.e. the shrinkage of the component depends on direction and location [1].

The origin of residual distortion in AM is mainly attributed to high local energy input, i.e. high temperature gradient, which results in high thermal stress within the part. When the local stress exceeds the material's yielding stress, distortion occurs [2]. In other words, when the material expands due to the heat provided by the deposition, compressive plastic distortion occurs at the area ahead of the moving heat source. On cooling, the material contracts resulting in tensile residual stresses along the deposition direction [3]. Another source for distortion is from the fact that the solidification speed of boundary areas is higher than in bulk material resulting from a higher evaporation rate at the part's surfaces [4].

To address this issue, some different approaches have been developed to minimize distortion in additive manufactured parts. For example, Bagg et al have tried different tool-path strategies to minimize the distortion by rebalancing the residual stress in the material [5]. Another method is to optimize the AM process parameters in order to reduce the heat input to the material which would result in smaller residual stress. In other words, this method seeks to decrease the thermal gradient in the material to get a lower level of residual stress [6, 7]. Since the build direction can affect the level of residual stress significantly due to the change of the stiffness orientation in the material, some research groups have investigated optimization of building direction and support structure design [8-10].

The aforementioned approaches aim to reduce residual distortion; however, another approach called the "distortion compensation" method compensates for the expected residual distortion. In that method, the original design geometry model is modified (or deformation compensated) before printing in such a way that the compensated geometry model will deform to the original design geometry after printing to improve its dimensional accuracy. To implement the distortion compensation method, the final deformed geometry has to be obtained either by simulation or experiment. The most common approach to do that is utilizing finite element (FE) simulations [11, 12]. The main idea of this approach is to invert the predicted distortion by changing the displacements of all the nodes of the FE mesh. Although some studies have been done on this approach but the main issues are the accuracy and the robustness (which relates to cost and time), especially for complex geometries. Afazov et al and Schmutzler et al have developed a method for distortion compensation based on 3D optical scanning [4, 12, 13]. However, this method cannot be directly applied to complex geometries which have interior features. To deal with interior features, computed tomography scanning is required [14, 15]. In addition, in most cases, several iterations are necessary, and thus compensation is not directly mapped to the later model. Therefore, this method is pretty time consuming and costly. Seidel and co-workers have developed a heat input modeling method to obtain the vector sums of displacement for each node then apply them to the original CAD (computer aided design) model for distortion reduction [16]. A solidus temperature was applied for a determined load time as boundary condition on selected nodes of the layer of interest. However, this method has been proved to underestimate distortion, resulting in needing scale factors in different directions, which makes the result strongly geometry dependent.

In this work, a simulation-based compensation method is developed based on the modified inherent strain method, and the results are then confirmed by 3D laser scanning. The modified inherent strain method has been developed in our previous work to efficiently and accurately predict residual distortion of an AM component [17, 18] by performing a series of quasi-static layer-by-layer analysis. In this work, first, this method is implemented in ANSYS APDL to obtain the residual distortion. Afterwards, using ANSYS Workbench, the predicted distortion is compensated by modifying the original CAD geometry. To make a comparison, the distortion is also obtained by the commercial module developed by ANSYS especially for AM, namely the AM Wizard.

SIMULATIONS

The inherent strains for Inconel 718 processed by l-pbf process have been obtained previously by a representative small-scale detailed thermal-mechanical simulation [18]. Using the 2019 ANSYS R1 release, the strains are loaded to the FE model as thermal strains with theoretical coefficients of thermal expansion in the condition of unity temperature change [18]. The technique of using birth-and-death elements is used.

In this work, a hollow thin walled (500 microns) cylinder of 30 mm in diameter and 60 mm high is used as a case study (Figure 1 and 3). After convergence analysis, the FE model has 17,640 elements of Solid186 of hexahedral type (each element has 20 nodes). The large deformation option and full integration option are employed. In the inherent strain analysis, numerical layers of 0.5 mm, which lumps 12.5 real layers (40 micron each), are deposited in a layer-by-layer manner. This method has been demonstrated to effectively predict the residual distortion of components produced by the l-pbf process [17, 18].

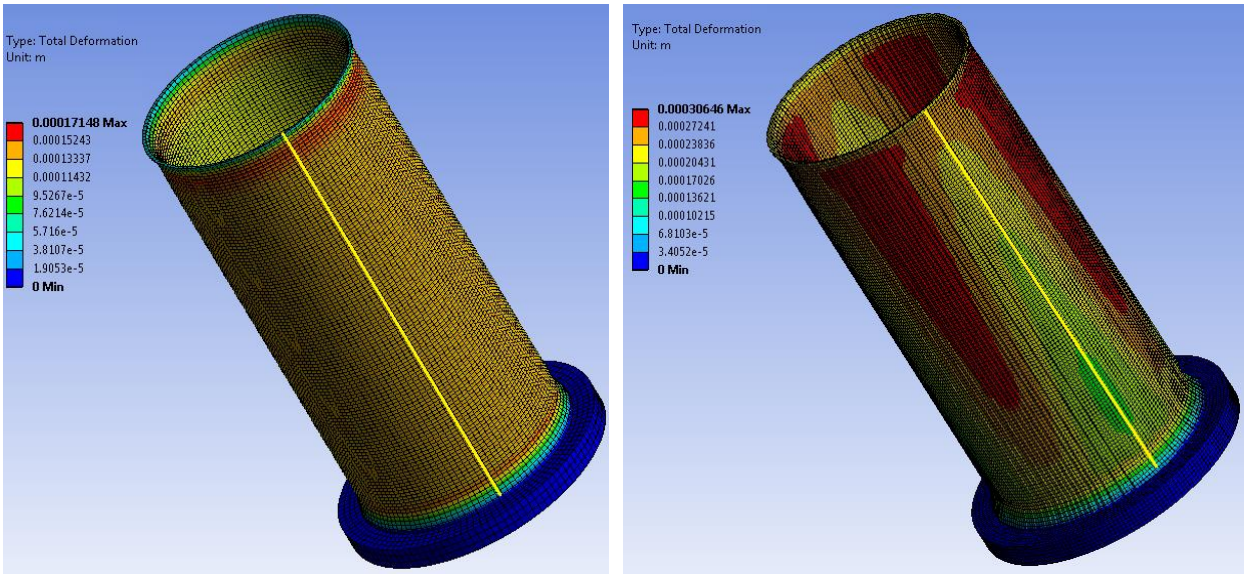

FIGURE 1. Total deformation (m) obtained by (left) Modified inherent strain method, and (right) Ansys AM Wizard.

Afterwards, the distorted model is exported to ANSYS Workbench (version 2019 R1), where all the displacement vectors of all nodes are extracted. These values are then treated as external loadings to the original CAD model in order to compensate for the distortion. To obtain the compensated model, the loadings (i.e. displacement vectors) are applied in the reverse directions. A scale factor of -1 is chosen and applied to the displacement vectors initially. Note that, for the best result the mesh and the boundary conditions should be maintained the same as they are in the previous simulation (i.e. modified inherent strain analysis). After applying boundary conditions and solving, the pre-deformed model is then exported to an stl (stereolithography) file for the printing process.

To make a comparison, the displacement vectors of all nodes are also extracted from the

AM wizard simulation. In the AM wizard model, a solid hexahedral mesh of 0.51 mm element size which composes of 120 numerical layers is used. The projection factor is set to be 0.4 so that the mesh elements could best fit the original model and kept the simulation solvable (if the projection factor is too close to 1, ANSYS may encounter errors when generating meshes at corners or the contact surfaces between the building part and the substrate). The machine settings are all determined according to the real building conditions.

EXPERIMENTS

The two stl files of the original CAD model and the compensated model resulting from the modified inherent strain simulation are loaded to the AM machine EOS M290 DMLS system (Figure 2) for printing. The printing parameters are listed in Table 1. The parts are built on a C45U steel substrate.

FIGURE 2. (left) 3D printing machine EOS M290, and (right) Faro 3D laser scanner.

TABLE 1. EOS M290 default parameters for IN718

Laser Power/W	285
Velocity/mm·s^{-1}	1000
Hatching Space/mm	0.11
Stripe Width/mm	10
Stripe Overlap/mm	0.8

Figure 3 shows the printed part of the original CAD model and its scanning data generated by the Faro 3D laser scanner (Figure 2) and the software Geomagic Control (version 2014). The scanning data is aligned with the original CAD model to obtain its deformation. To have the best alignment, four small spheres (Figure 3) are used as references. The same procedure is performed with the compensated cylinder based on the modified inherent strain method results. That means that the scanning data of the compensated cylinder is aligned with the original CAD model to evaluate its deformation.

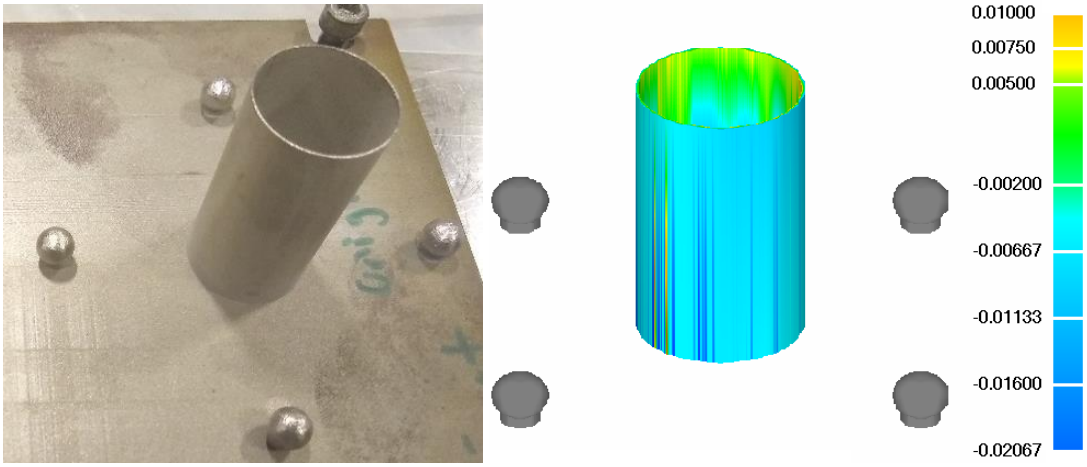

FIGURE 3. (left) The AM printed cylinder by EOS M290, and (right) its scanning data (inch) generated by Geomagic Control.

RESULTS AND DISCUSSION

Figure 4 shows the distortion along the cylinder in the simulation models (yellow lines in Figure 1) and printed parts. Comparing with the scanning result of the original cylinder (red), the modified inherent strain simulation (blue) shows better result than the AM Wizard simulation (black), both in shape and magnitude. In addition, as shown in the right picture of Figure 1, the deformation of the AM Wizard simulation is not uniform on the circumference. Therefore, the modified inherent strain simulation is chosen to do the compensation. The scanning result of the compensated cylinder (green) shows that the compensation by modified inherent strain simulation can decrease the distortion of the cylinder significantly, i.e. about 63% (from maximum deformation of 0.135 in the original printed part to maximum deformation of 0.05 in the compensated part).

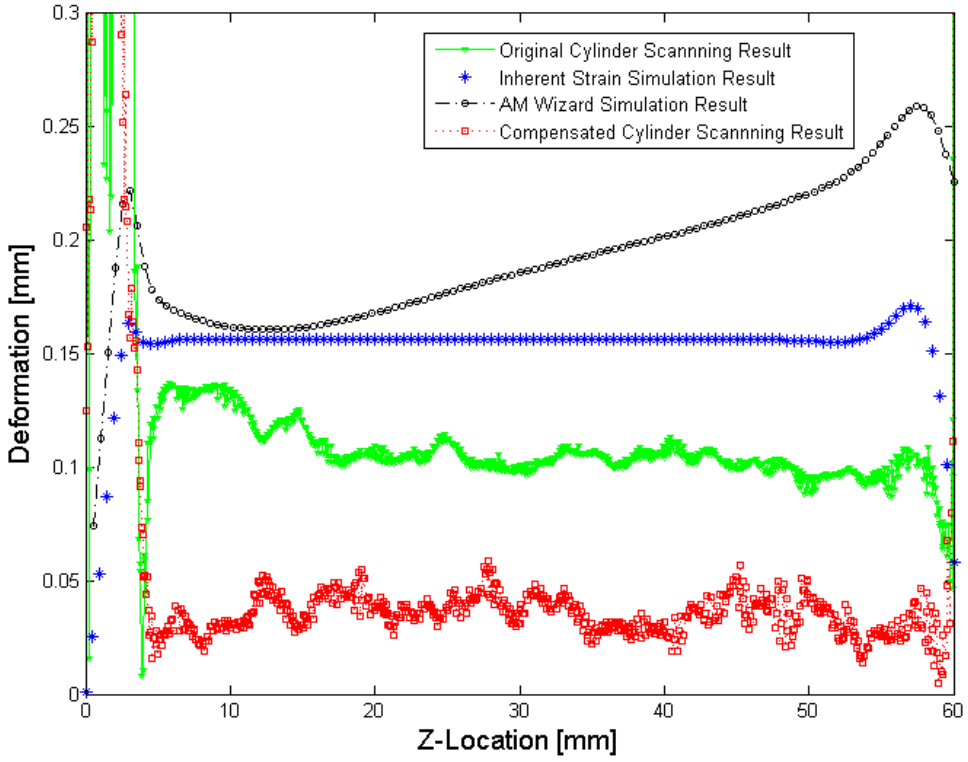

FIGURE 4. Deformation along the cylinder in the simulation models and printed parts.

Based on the scan data of the compensated part, to obtain better compensation, a different scale factor for compensation can be applied to the original CAD file. Note that the original printed part (red) shrinks, while the compensated part expands (green). In other words, the modified inherent strain simulation over-estimates the distortion. In this case study, we suggest to change the scale factor from -1 to (-1+x/y), where x is the absolute value of the deformation of the point of interest of the compensated part (from the green line) and y is the absolute value of the deformation of the point of interest of the simulation model (from the blue line). This will be confirmed by future experiment. For other unsymmetrical structures, different scale factors with respect to three coordinate directions can be applied. In summary, the schematic flow of the approach can be expressed in the Figure 5.

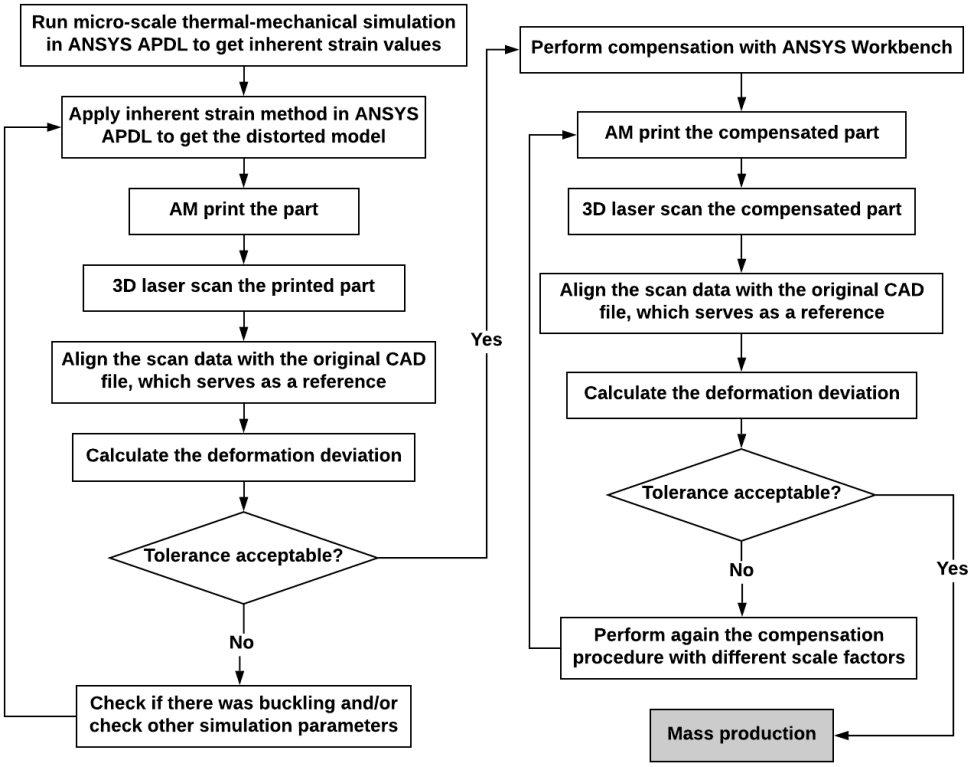
Run micro-scale thermal-mechanical simulation in ANSYS APDL to get inherent strain values
Apply inherent strain method in ANSYS APDL to get the distorted model
AM print the part
3D laser scan the printed part
Align the scan data with the original CAD file, which serves as a reference
Calculate the deformation deviation
Tolerance acceptable?
Yes
No
Check if there was buckling and/or check other simulation parameters
Perform compensation with ANSYS Workbench
AM print the compensated part
3D laser scan the compensated part
Align the scan data with the original CAD file, which serves as a reference
Calculate the deformation deviation
Tolerance acceptable?
No
Yes
Perform again the compensation procedure with different scale factors
Mass production

FIGURE 5. Schematic flow of the approach.

CONCLUSIONS

A distortion compensation methodology using the modified inherent strain method and 3D laser scanning is developed for PBF AM components. The results confirm that the distortion resulting from PBF AM process can be successfully compensated by 63% for such symmetric geometry of a thin walled cylinder. The approach can offer some significant benefits to industry such as reducing number of prototypes, which would result in time and cost savings. It also opens up design freedom since the distortion does not need to be minimized at the design stage and reduces post-processing time and cost due to heat treatments, if applicable. More experiments (printing) should be performed to confirm the mentioned above scale factor changing strategy, especially for unsymmetrical models. Moreover, to confirm the applicability of this approach to more complex geometries, future research should be conducted to incorporate computed tomography scans to this current methodology to include internal features of the geometries.

ACKNOWLEDGEMENT

The support by the National Science Foundation (CMMI-1634261) for this project is gratefully acknowledged. The authors also acknowledge

the technical guidance from Dr. Zack Francis of ANSYS.

REFERENCES

[1] Jacobs, P., The effects of random noise shrinkage on rapid tooling accuracy. Materials & Design, 2000. 21(2): p. 127-136.
[2] Mercelis, P., and Kruth, J., Residual Stresses in Selective Laser Sintering and Selective Laser Melting. Rapid Prototyping Journal 2006. 12(5): p. 254-65.
[3] Colegrove, P.A., et al., Application of bulk deformation methods for microstructural and material property improvement and residual stress and distortion control in additively manufactured components. Scripta Materialia, 2017. 135: p. 111-118.
[4] Schmutzler, C., A. Zimmermann, and M.F. Zaeh, Compensating Warpage of 3D Printed Parts Using Free-form Deformation. Procedia CIRP, 2016. 41: p. 1017-1022.
[5] Bagg SD, S.-K.L., Bunn JR, The effect of laserscan strategy on distortion and residual stresses of arches made withselective laser melting. American Society of Precision Engineering, 2016.
[6] Murr, L.E., et al., Metal Fabrication by Additive Manufacturing Using Laser and Electron Beam Melting Technologies. Journal of Materials Science & Technology, 2012. 28(1): p. 1-14.
[7] Buchbinder, D., et al., Investigation on reducing distortion by preheating during manufacture of aluminum components using selective laser melting. Journal of Laser Applications, 2014. 26(1): p. 012004.
[8] Morgan, H.D., et al., Part orientation optimisation for the additive layer manufacture of metal components. The International Journal of Advanced Manufacturing Technology, 2016. 86(5): p. 1679-1687.
[9] Cheng, L. and A. To, Part-scale build orientation optimization for minimizing residual stress and support volume for metal additive manufacturing: Theory and experimental validation. Computer-Aided Design, 2019. 113: p. 1-23.
[10] Cheng, L., et al., On utilizing topology optimization to design support structure to prevent residual stress induced build failure in laser powder bed metal additive manufacturing. Additive Manufacturing, 2019. 27: p. 290-304.
[11] Patil, N., et al., A Generalized Feed Forward Dynamic Adaptive Mesh Refinement and Derefinement Finite Element Framework for Metal Laser Sintering—Part I: Formulation and Algorithm Development. Journal of Manufacturing Science and Engineering, 2015. 137(4): p. 041001-041001-15.
[12] Afazov, S., et al., A methodology for precision additive manufacturing through compensation. Precision Engineering, 2017. 50: p. 269-274.
[13] Schmutzler C, B.F., Janson S, Seidel C, Zaeh MF, Pre-compensation of Warpage for Additive Manufacturing. Journal of Mechanics Engineering and Automation, 2016. 6: p. 392-399.
[14] Villarraga-Gómez, H., C. Lee, and S.T. Smith, Dimensional metrology with X-ray CT: A comparison with CMM measurements on internal features and compliant structures. Precision Engineering, 2018. 51: p. 291-307.
[15] Kempen K, W.F., Qian J, Kruth JP, Dimensional accuracy of internal channels in SLM produced parts. Proceedings - ASPE 2014 Spring Topical Meeting: Dimensional Accuracy and Surface Finish in Additive Manufacturing, 2014. 57.
[16] Seidel, C. and M.F. Zaeh, Multi-scale Modelling Approach for Contributing to Reduced Distortion in Parts Made by Laser-based Powder Bed Fusion. Procedia CIRP, 2018. 67: p. 197-202.
[17] Liang, X., et al., A modified method for estimating inherent strains from detailed process simulation for fast residual distortion prediction of single-walled structures fabricated by directed energy deposition. Additive Manufacturing, 2018. 23: p. 471-486.
[18] Chen, Q., et al., An inherent strain based multiscale modeling framework for simulating part-scale residual deformation for direct metal laser sintering. Additive Manufacturing, 2019. 28: p. 406-418.

ADDITIVE MANUFACTURING OF INTERNAL FEATURES FOR MANIPULATION OF STRUCTURAL DYNAMICS

Emma D. Betters[1], Justin West[1], Mark Noakes[2], Andrzej Nycz[2], Scott Smith[2], and Tony L. Schmitz[1]
[1]Department of Mechanical, Aerospace, and Biomedical Engineering
University of Tennessee, Knoxville, TN
[2]Manufacturing Demonstration Facility
Oak Ridge National Laboratory, Oak Ridge, TN

ABSTRACT
A component was designed and manufactured in two configurations using a wire arc additive process. The first configuration was an open channel, while the second contained a dynamic absorber in the internal cavity. Dynamic measurements of the two components demonstrated the ability to print internal features which, when designed appropriately, can be used to increase the dynamic stiffness of structures.

Keywords: Additive manufacturing, machining, frequency response function, dynamic absorber

INTRODUCTION
In machining processes, the machine structure, spindle, holder, tool, and workpiece collectively compose a dynamic system that defines permissible cutting parameters. Exceeding the limiting depth of cut for a particular spindle speeds leads to chatter, or self-excited vibration that yields large forces, poor surface finish, and, potentially, damage to the workpiece, tool, or spindle. In an effort to improve dynamic stiffness, the machine base can be designed specifically for higher stiffness and damping. However, traditional casting processes for machine bases are geometrically limited, labor intensive, and expensive.

An alternative approach is to use an additive manufacturing process to produce the machine base. The additive approach offers significant design freedom for internal features which can be used to alter the dynamic characteristics of the system or to maximize the dynamic stiffness at a given frequency, for example.

A pair of components was designed and fabricated to demonstrate the ability of the Metal Big Area Additive Manufacturing (mBAAM) process to print internal features intended to modify the structure's dynamics (e.g., by altering the natural frequency or increasing the dynamics stiffness). The first component was an open channel attached to a base. The second component was identical, except for the addition of a dynamic absorber inside the open cavity. The absorber was designed to maximize the dynamic stiffness at the natural frequency of the original, open channel design. Figure 1 describes the parameterized component geometries; Table 1 lists the dimensions.

This paper presents: the design and finite element analysis validation of the dynamic absorber; the additive and subtractive manufacturing processes; and the measured frequency response functions (FRFs) for the final components.

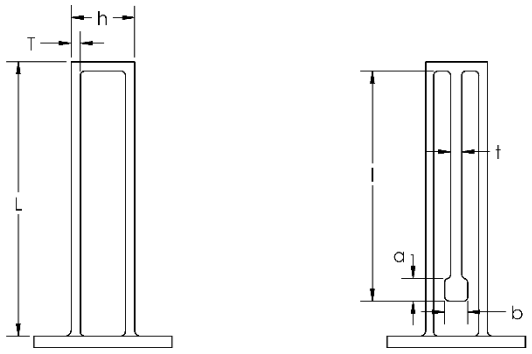

Figure 1: Dimensions of the (left) open channel and (right) open channel with dynamic absorber designs. w is the dimension into the page.

Table 1: Initial design dimensions (mm).

L	300
T	10
h	69
w	50
l	225
t	12
a	25
b	25

DESIGN AND MODELING
The dimensions of the open channel were based on the wire arc additive process resolution and a

minimum recommended printed wall thickness of 12 mm to enable the outer surfaces to be finish machined. The final machined dimensions (rather than rough printed dimensions) are provided in Table 1. The first natural frequency of the open channel was determined using finite element analysis (FEA). This frequency was used as the design point for the dynamic absorber.

FEA was completed using SOLIDWORKS and Abaqus, where a fixed boundary condition was set for the base as shown in Fig. 2. The natural frequency of the first bending mode was predicted to be 137 Hz for the open channel.

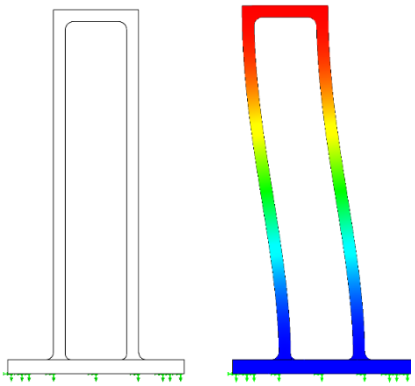

Figure 2: The first bending for the open channel is shown (137 Hz natural frequency).

For the dynamic absorber design, the open channel was modeled as a single degree of freedom (SDOF) spring-mass system with an associated natural frequency $\omega_{n1} = \sqrt{\frac{k_1}{m_1}}$. Similarly, the dynamic absorber element was modeled as a SDOF spring-mass system. The composite structure was therefore modeled by two spring-mass systems connected in series; see Fig. 3 [1].

For a harmonic force input, f_1, applied to the free end of the open channel model, the intent was to minimize the associated displacement, x_1, for a forcing frequency, ω_f, equal to the original structure's natural frequency, ω_{n1}. The parameters for the dynamic absorber were selected such that the natural frequency of the absorber was equal to the first natural frequency of the open channel, $\omega_{n2} = \omega_{n1}$. This yields a new 2DOF system with natural frequencies that appear above and below the original natural frequency. The spacing of the new frequencies is controlled by the size of the dynamic absorber mass (a small mass provides a small separation, while a mass close to the modal mass of the original system causes a larger separation).

The absorber was modeled with a fixed-free boundary condition as shown in Fig. 4, where its length (i.e., the dimension *l* shown in Fig. 1) was varied in FEA to obtain the desired natural frequency. The final values for the dynamic absorber are listed in Table 1.

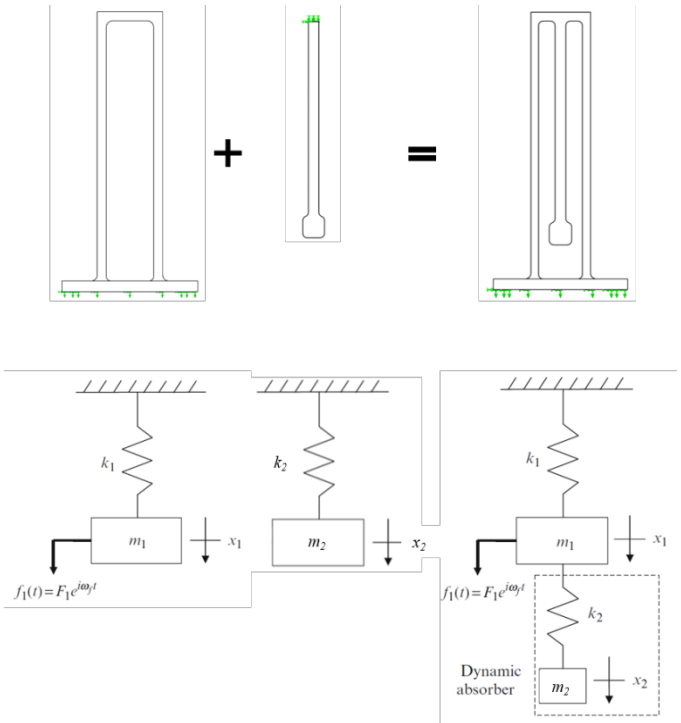

Figure 3: The open channel and the dynamic absorber were modeled as SDOF systems. The channel-absorber has a 2DOF dynamic response.

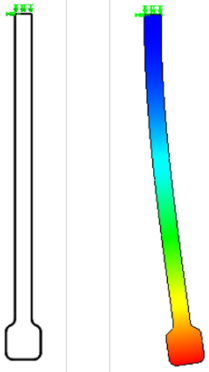

Figure 4: The dynamic absorber was designed with a first bending natural frequency equal to the original open channel's natural frequency.

MANUFACTURING

The hybrid manufacturing for the demonstration components was a joint effort between Oak Ridge National Laboratory (ORNL), which completed the additive process, and the University of Tennessee, Knoxville (UTK), which machined the near net shape parts. The internal features of each component were left as-printed to demonstrate a broader application

of this approach to systems where they cannot be accessed for further processing.

Additive

As noted, mBAAM is a wire arc-based process that uses gas metal arc welding (GMAW) with a robotic arm to carry the deposition torch [2-6]. The system is comprised of: IRB 2600 ABB manipulator, ABB IRC5 controller, PowerWave R500 Lincoln Electric welder, ABB IRBP-A750 positioner, safety system, desktop host workstation, shielding gas delivery system, and ventilation. The main components are enclosed by a protective wall that shields the operator from harmful UV radiation, heat, mechanical injury, and welding fumes as shown in Fig. 5.

Figure 5. mBAAM system. (Left) external protective walls. (Right) deposition head over printing position.

Similar to most AM processes, mBAAM creates parts in a layer-by-layer fashion. Each layer consists of sets of sequenced beads. The sequence, among many variables, is dictated by the cross-sectional shape, function, and type of material. The same applies to bead length, width, and overlap.

The first step is to match the initial design with the printing process. This involves comparing the process resolution and expected dimensions for post-machining. Considering the natural surface texture and material for machining, the printed part is designed to be slightly oversized where needed.

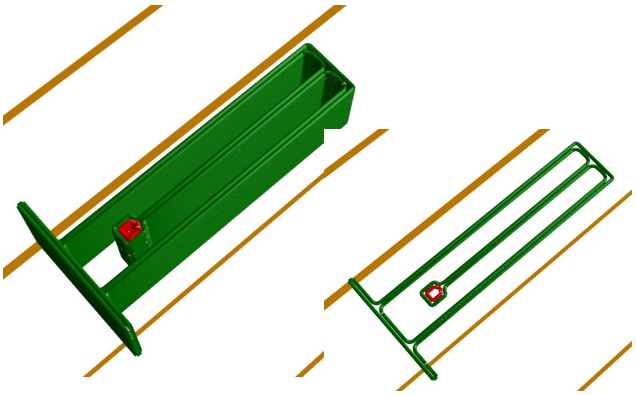

Figure 6. Dynamic absorber printed part created with ORNL slicer.(Left) entire part. (Right) single layer.

The next step is to create the toolpath for printing; this is known as slicing. The part was built with a two-bead thick structure; see Fig. 6. The vertical print orientation of the part was chosen along the width of the part in order to avoid overhangs. This approach also minimized printing time since a single layer consisted of only two beads. The part toolpath was generated using the ORNL Slicer, a software suite used for both metal and polymer BAAM printers.

The printing process requires a base plate, a substrate with similar welding properties to start the process, to conduct the welding current and to serve as a heat sink/transmitter. The substrate is mounted to the print bed with toe clamps. The bed and clamps are selected to provide proper mounting force and strength to counteract the warping forces associated with the wire arc process. The bed also serves as the ultimate heat sink for the process.

Since the base plate can be mounted in any location or orientation on the deposition bed, a localization and orientation process is required. This is completed by directing the arm to three points which represent the origin and two axes of the new coordinate frame. Then the system automatically recalculates the toolpath to match the part position and orientation with the base plate.

The material (wire) used for manufacturing was Lincoln wire L59 (AWS ER70-S6) [7]. As noted, two parts were printed using this methodology: one with the dynamic absorber and one without. Figure 7 displays the as-printed open channel with no absorber.

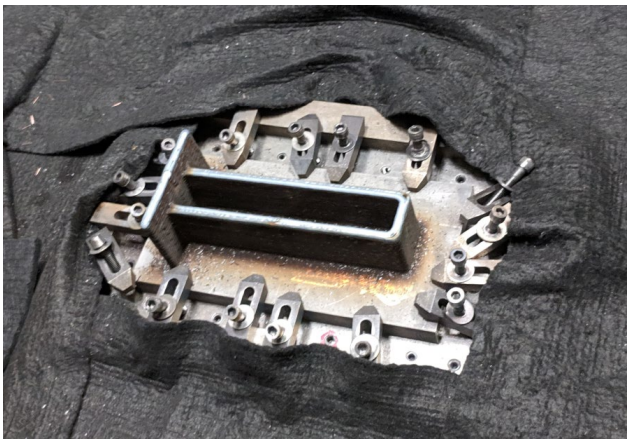

Figure 7. As-printed open channel (no absorber) on the deposition bed.

Subtractive

Upon receipt of the additively manufactured components, all features were measured and compared to the nominal dimensions. The FEA

model was updated using actual dimensions for the dynamic absorber. Due to the surface variation of the wire arc additive process, an average of measurements at ten locations along each feature was applied. The updated model was used to determine the amount of material to be removed from each face. The predicted natural frequency of the finish machined open channel was 137.4 Hz.

The primary machining challenge was the lack of a clear datum. In the first operation, the build plate was assumed to be flat. It was stoned to remove macro height deviations and was clamped directly to the machine table. Each part was then faced to provide a reference once the build plate was removed; see Fig. 8. Next, the base plate was machined away and the associated surface machined to produce two parallel surfaces which could then be used for fixturing during the machining of the remaining sides.

POORLY LIGHTED WORK AREAS.
NEVER PLACE YOUR HAND ON THE TOOL IN THE SPINDLE AND PRESS ATC FWD, ATC REV, NEXT TOOL, OR CAUSE A TOOL CHANGE CYCLE. THE TOOL CHANGER WILL MOVE IN AND CRUSH YOUR HAND !!
NEVER MODIFY
DO NOT
HOLD-TO-RUN SWITCH
WARNING !! WARNING !! WARNING !!

Figure 8: To machine the first side, the build plate was clamped to the machine table. The top surface was then faced.

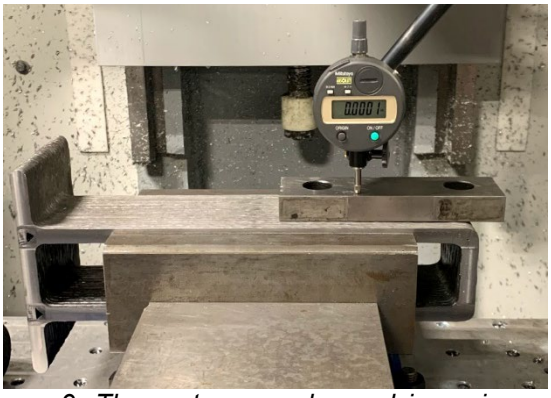

Figure 9: The parts were clamped in a vise and a machining parallel was used as an indicating surface for the dial indicator.

Prior to machining, the walls were sanded and stoned to remove debris and protrusions from the wire arc process. The previously machined front and back surfaces were clamped in a vise and a digital dial indicator was used to align the part; see Fig. 9. Each remaining surface was indicated and finished in the same way; see Fig. 10.

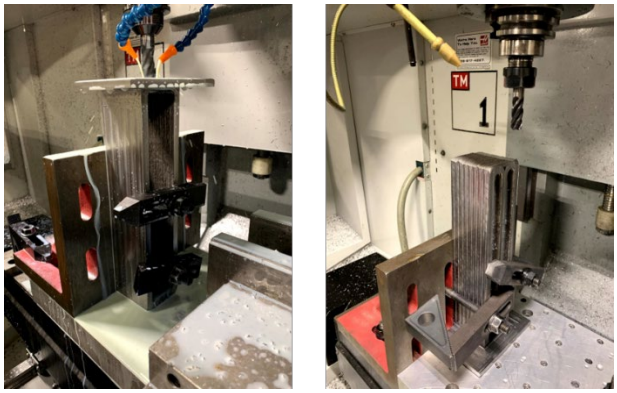

Figure 10: The parts were fixtured to an angle plate to finish the top and bottom surfaces.

Figure 11: Impact testing was used to measure the final part FRFs.

The finished parts were clamped to a rigid table and a direct FRF was measured for both the open channel and the channel with the internal dynamic absorber. Impact testing was used for the FRF measurements, where an instrumented hammer is used to excite the structure and a low mass accelerometer is used to record the vibration response; see Fig. 11.

RESULTS

The measured FRF for the open channel is shown in Fig. 12, where the first natural frequency is 127.8

Hz. The predicted first natural frequency was 137.4 Hz.

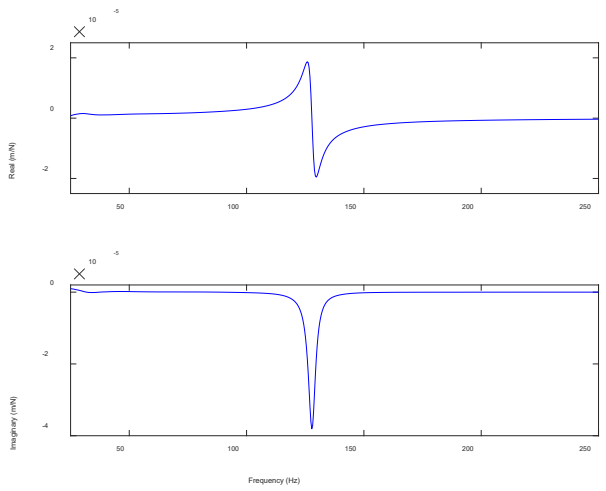

Figure 12: The real (top) and imaginary (bottom) parts of the measured FRF for the open channel.

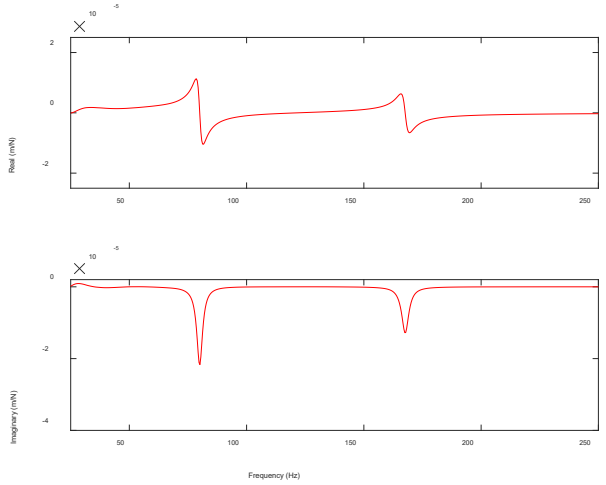

Figure 13: The real (top) and imaginary (bottom) parts of the measured FRF for the channel with the dynamic absorber.

The measured FRF for the channel with the dynamic absorber is shown in Fig. 13, where the first and second natural frequencies are 80.1 Hz and 167.5 Hz. The predicted values for these modes were 83.0 Hz and 180.4 Hz. Figure 14 superimposes the magnitudes of the measured FRFs for both components, where it is observed that the response of the system with the dynamic absorber is minimized at the natural frequency of the original open channel structure.

ADDED POLYMER DAMPING

To provide additional damping, a polymer was injected into the cavity surrounding the dynamic absorber; see Fig. 15. This represents a strategy where both structural modifications and material addition are used to maximize the dynamics stiffness of the final structure.

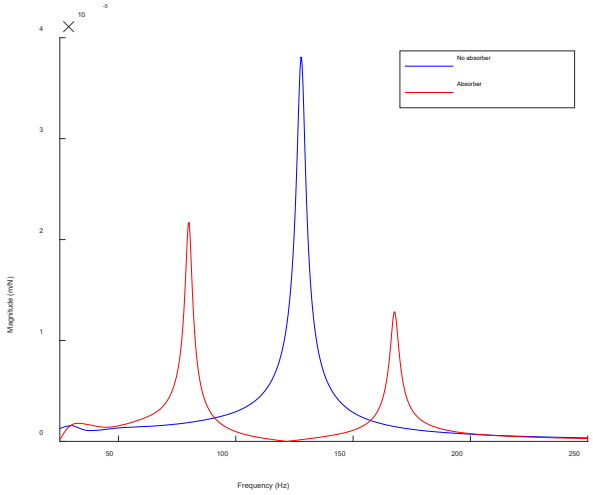

Figure 14: Magnitudes of the measured FRFs for both structures.

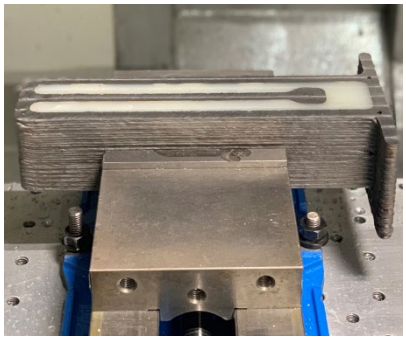

Figure 15: Polymer was injected around the dynamic absorber to increase damping.

The FEA model was updated to include the added polymer material. The measured first natural frequency for the filled channel with the dynamic absorber was 148.0 Hz and the predicted first natural frequency was 148.2 Hz.

The density and elastic modulus were required inputs to the FEA model. For the added material, the density was calculated from the measured mass and volume of the polymer. The range of elastic modulus values for the polymer was 30 MPa to 100 MPa. The best match for natural frequencies was obtained for an elastic modulus of 52 MPa. The viscous damping ratio of 0.07 was calculated from the measured FRF

by peak picking. This value provided a close match between the measured and predicted FRFs.

Figure 16 shows the three results: open channel with no absorber; open channel with absorber; and filled channel with absorber. It is observed that the dynamic stiffness is dramatically increased by the polymer addition. A comparison between predicted and measured natural frequencies for the three structures is provided in Table 2. Good agreement is observed.

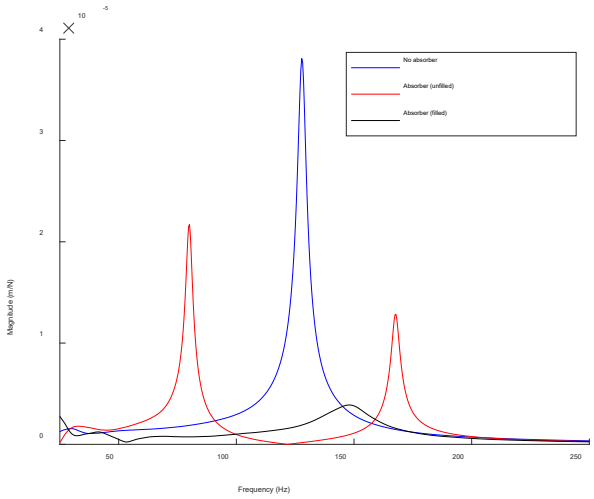

Figure 16: The magnitude of the measured FRFs for each of the three designs.

Table 2: Comparison of predicted and measured natural frequencies (Hz).

Structure	Predicted frequency	Measured frequency	% difference	Damping ratio (%)
No absorber	137.4	127.8	7.0	1.5
Absorber (unfilled) (f_{n1})	83.0	80.1	3.5	1.9
Absorber (unfilled) (f_{n2})	180.4	167.5	7.2	1.0
Absorber (filled)	148.2	148.0	0.1	7.0

CONCLUSIONS

Two Metal Big Area Additive Manufacturing (mBAAM) components were produced to demonstrate design modifications that increase dynamic stiffness. Here, an internal dynamics absorber was designed and incorporated as part of the printed part. It was shown that the system response with the added dynamic absorber was minimized at the natural frequency of the original open channel. Polymeric damping material was then added to further increase the dynamic stiffness.

The disagreement between predicted and measured natural frequency is attributed to the error in dimensions used to produce the finite element model. In future work, a structured light scanner will be implemented in the initial metrology and modeling effort to more accurately capture variations in part geometry which may arise during the additive process.

REFERENCES

[1] Schmitz, T. and Smith, K.S., 2012, *Mechanical Vibrations: Modeling and Measurement*. New York, NY: Springer.

[2] Nycz, A., Noakes, M. and Cader, M., 2018, March. Additive Manufacturing – A New Challenge for Automation and Robotics. In *Conference on Automation* (pp. 3-13). Springer, Cham.

[3] Shassere, B., Nycz, A., Noakes, M.W., Masuo, C. and Sridharan, N., 2019, Correlation of Microstructure and Mechanical Properties of Metal Big Area Additive Manufacturing. *Applied Sciences*, *9*(4), p.787.

[4] Nycz, A., Noakes, M.W., Richardson, B., Messing, A., Post, B., Paul, J., Flamm, J. and Love, L., 2017, Challenges in Making Complex Metal Large-scale Parts for Additive Manufacturing: A Case Study Based on the Additive Manufacturing Excavator. In *Proceedings of the 28th Annual International Solid Freeform Fabrication Symposium – An Additive Manufacturing Conference*.

[5] Greer, C., Nycz, A., Noakes, M., Richardson, B., Post, B., Kurfess, T. and Love, L., 2019, Introduction to the Design Rules for Metal Big Area Additive Manufacturing. *Additive Manufacturing*, *27*, pp.159-166.

[6] Nycz, A., Adediran, A.I., Noakes, M.W. and Love, L.J., 2016, January, Large Scale Metal Additive Techniques Review. In *Proceedings of the 27th Annual International Solid Freeform Fabrication Symposium*.

[7] https://www.lincolnelectric.com/assets/global/Products/Consumable_MIGGMAWWires-SuperArc-SuperArcL-59/c4104.pdf.

INFLUENCE OF THE DENSITY OF POWDER LAYER ON MELT SOLIDIFICATION PHENOMENON IN SELECTIVE LASER MELTING

Kenta Ohyama[1], Keisuke Nagato[1], and Masayuki Nakao[1]
[1]Department of Mechanical Engineering,
The University of Tokyo,
Bunkyo-ku, Tokyo, Japan

INTRODUCTION

Selective laser melting (SLM) is one of the additive manufacturing techniques that is used to produce solid structures directly from 3D data. The feature of SLM is that it can produce complex-shape components compared to the conventional producing methods such as casting, forging and cutting. In SLM, the laser beam is used to selectively irradiate a thin powder layer. Powder particles are subsequently melted together by laser beam (FIGURE 1(a), (b)). Next, powder is spread as a thin layer using a roller (FIGURE 1(c)). Repetition of these processes results in the production of an object [1]; the shape of beads depends on various condition parameters such as laser power, laser scanning speed, spot diameter, powder layer thickness and powder material [2, 3, 4]. In general, very low energy input to the powder layer causes a balling effect; when the input is too high, spatter and convection in the molten pool occur, resulting in a non-uniform shape of the beads. As each metal material has its own process-window, it is necessary to determine the process-window experimentally. Observation and understanding of the phenomena during SLM process are very important for the optimization of condition parameters [5, 6, 7]. On the other hand, SLM has a disadvantage that the cycle time is very long. At present, the cycle time of SLM is approximately 10 to 100 times that of forging; thus, reduction of the cycle time is required. However, because the process-window is limited, the laser scanning speed cannot be increased beyond a certain value, prolonging the cycle time. It is considered that thermal conductivity of the powder layer affects the process-window. According to previous research, the thermal conductivity of the powder layer is approximately 100 times smaller than that of the bulk [8]. As the thermal conductivity of the powder layer is extremely low, the temperature of the top of the powder layer is very different from that of the substrate. The wettability between the powder layer and the substrate deteriorates, causing the balling effect. In addition, since heat is likely to be accumulated within specific particles, spatter is likely to be formed.

In this research, we increased the density of the powder layer, bringing it closer to the bulk (FIGURE 1). It is expected that the contact area between particles increases with density, enhancing the thermal conductivity. In this manner, we increased the thermal conductivity of the powder layer. Thereafter, the shape of beads, the amount of spatters, and the fabricating efficiency were observed. The fabricating efficiency is the fabricated volume per unit of energy supplied to the powder layer, and is correlated with cycle time of SLM.

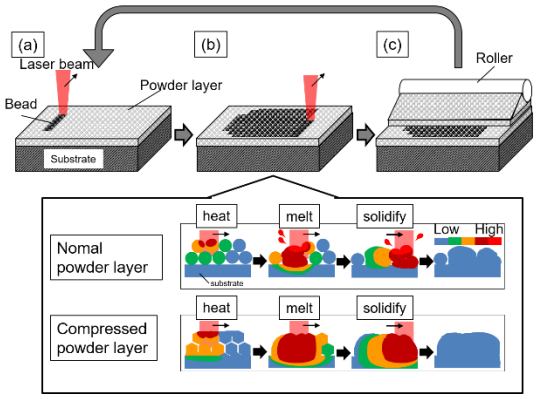

FIGURE 1. Procedure of SLM and overview of this research.

EXPERIMENTAL

Density

The powder layer was pressed using a press machine in order to obtain powder layers with different densities. The powder was SKD61 atomized powder, with an average particle size of 25 μm. In addition, to facilitate changes in density, annealing was performed in advance under an N_2 atmosphere at a maximum temperature of 870 °C. The pressure of the press machine was adjusted as 0, 68, 136, 203, and 271 MPa.

The shape of beads

We scanned a laser beam over the powder layers with different densities, and the behavior of a

laser-interaction zone was observed in real-time. In addition, the shape of beads was observed using a laser microscope (OLS4100, OLYMPUS Co.). Figure 2 shows schematics of the real-time observation system and the laser microscope system. In the real-time observation, the laser-interaction zone was observed by a high-speed camera, and the behavior of spatters was observed. In this study, spatter is defined as powder particles and molten particles which fly away from the molten pool. Frame rate and shutter speed used were 10000 fps and 20 μs, respectively. In addition, a laser illumination with a pulse width of 20 μs and a wavelength of 810 nm was used. By using a bandpass filter of 810 nm, the scattered light from the laser and the molten pool was removed. Powder layers with different densities were manufactured using a press die. The press die has an inner diameter of 15 mm. For each pressure, 0.30 g powder was used. We scanned a laser beam over the powder layer on SKD61 plate. A single-mode fiber laser (JL-SP0178, SPI Lasers Co.) was used, and wavelength, spot diameter, and scan speed were 1070 nm, 60 μm, and 10 mm/s, respectively. Linear energy density (LED) was varied consistently. LED is defined as

$$\mathrm{LED} = \frac{\mathrm{P}}{\mathrm{v}}\ [\mathrm{J/mm}]$$

where P is laser power [W], and v is scan speed [mm/s]. LED is the laser power supplied to the powder layers per the unit length of the layer. LED is considered as an important factor to fabricate objects in SLM [2, 3, 9]. In this experiment, LED was adjusted as 0.1, 0.5, 1, 5 and 10 J/mm.

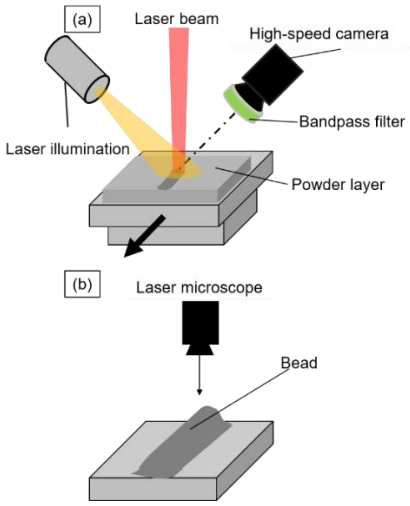

FIGURE 2. Schematics of the real-time observation system and the laser microscope system.

Thermal conductivity

To calculate thermal conductivity, we measured thermal diffusivity of the powder layer using a laser flash method device (LFA 447 Nanoflash, NETZSCH Co.). To measure thermal diffusivity, the powder layer was sandwiched between copper plates, each with a thickness of 0.1 mm. The thermal diffusivity was measured at a temperature of 25.5 °C, and the thermal conductivity was calculated by

$$\text{thermal conductivity}\left[\frac{\mathrm{W}}{\mathrm{mK}}\right] = \alpha\left[\frac{\mathrm{m}^2}{\mathrm{s}}\right] \times \mathrm{C_p}\ \left[\frac{\mathrm{J}}{\mathrm{K\cdot kg}}\right] \times \rho\left[\frac{\mathrm{kg}}{\mathrm{m}^3}\right]$$

where α is the thermal diffusivity, ρ is the density, and C_p is the specific heat.

RESULTS AND DISCUSSION

Density

As shown in FIGURE 3, the densities at 0, 68, 136, 203, and 271 MPa were 3.68, 4.59, 4.67, 5.05, and 5.15 g/cm^3, respectively. It is found that density increases with pressure.

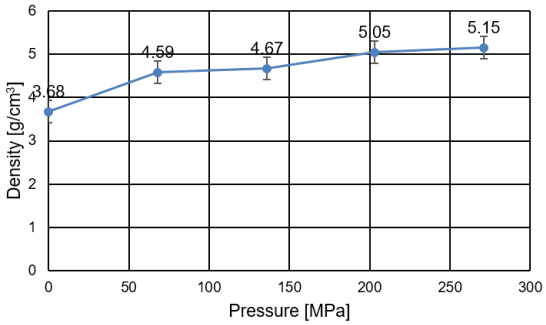

FIGURE 3. Relationship between pressure and density of the powder layer.

The shape of beads

As seen in FIGURE 4, based on the shape of beads, five process-windows could be defined over the considered range of the LED and the density.

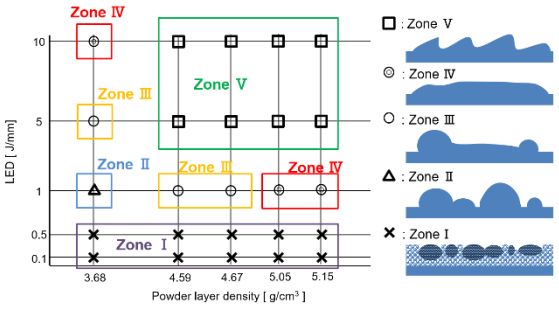

FIGURE 4. Five process-windows based on the shape of beads.

- Zone-I: No adhesion area
- Zone-II: Balling effect area
- Zone-III: Partial balling effect area
- Zone-IV: Continuous area
- Zone-V: Convection area

Based on cross-sectional profile data at the center of laser-scanned tracks and the maximum-minimum ratio of the bead width, the shape of beads was classified into these five categories. As shown in FIGURE 5, we defined the H_{index} and W_{index} as follows. H_{index} is the ratio of the difference between the maximum and minimum heights to the average particle size. W_{index} is the ratio of the maximum width to the minimum width. The boundaries of these five process-windows is as follows.

- Zone-I: No adhesion to the plate after removing surrounding powder
- Zone-II: $6 < H_{index}$ and $4 < W_{index}$
- Zone-III: $4 < H_{index} \leq 6$
- Zone-IV: $H_{index} \leq 4$
- Zone-V: $6 < H_{index}$ and $W_{index} \leq 4$

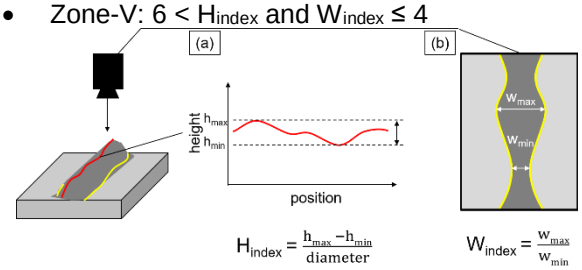

FIGURE 5. Classification criteria of the shape of beads.

From FIGURE 4, we confirm that the Zone-IV area moved to the lower LED side as the density increased. The thermal conductivity of the powder layer seemed to improve. It can be inferred that as the density of the powder layer increases, the contact area between particles increases and thermal conductivity improves. When thermal conductivity is high, the temperature gradient between the top of the powder layer and the substrate is small, and the wettability between the powder layer and the substrate is enhanced. Therefore, the Zone-IV area moved to the lower LED side. In addition, the Zone-V area was observed when the density was high. In the powder layer with 3.68 g/cm^3, Zone-V area is supposed observed in areas where the LED is larger than 10 J/mm. Not only the Zone-IV area but also all process-windows moved to the lower LED side as density improved, implying that the dense powder layer requires lower LED when fabricating all shapes of beads.

FIGURE 6 shows high-speed camera images of the laser-interaction zone. FIGURES 6(a)(b) show the images of the powder layers with densities of 3.68 g/cm^3 (a) and 5.15 g/cm^3 (b), respectively, while LED was 1 J/mm. Comparing FIGURE 6(a) with FIGURE 6(b), it can be seen that the amount of spatter is very small when the density is high. In FIGURE 6, it can be seen that, the molten pool became larger as density increased, despite the same LED.

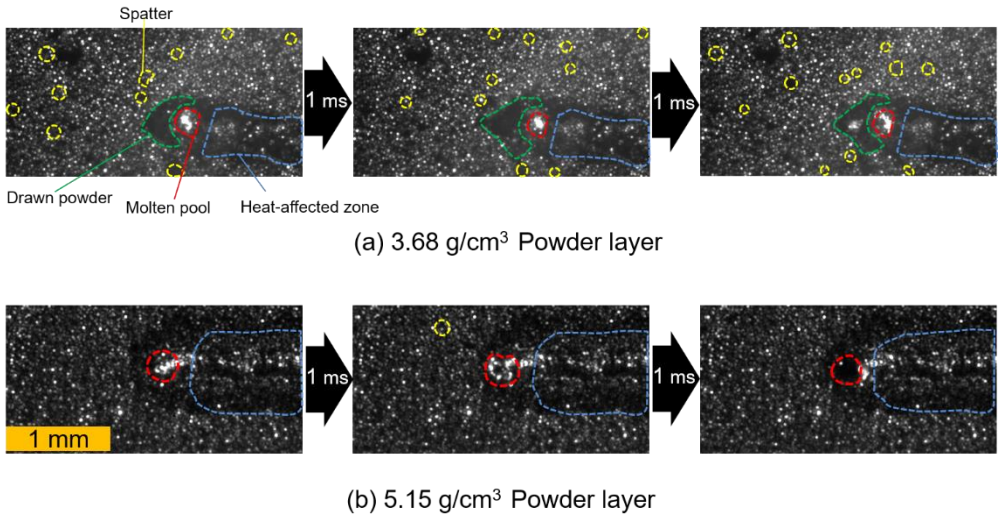

FIGURE 6. High-speed camera images of laser-interaction zone while LED is 1 J/mm. (a) 3.68 g/cm^3 (b) 5.15 g/cm^3

The number of spatters was estimated visually. The powder layer with a density of 3.68 g/cm^3 has about 1050 pieces of spatters in 150 frames, and the powder layer with a density of 5.15 g/cm^3 has about 4 pieces of spatters in 150 frames, differing by about 100 times. This is because thermal conductivity is improved, and heat is less likely to accumulate within specific particles, so the number of high temperature particles is reduced. Another reason is likely that as the density increases, the contact area between particles increases and the frictional force that prevents scattering increases.

In this experiment, the fabricating efficiency was calculated only for the beads in Zone-IV. The fabricating efficiency was calculated based on only the widths of beads. As shown in FIGURE 7, when the density was 3.68, 5.05, and 5.15 g/cm^3, the fabricating efficiency was 653, 1610, and 1640 μm^3/J, respectively. Thus, it was found that by increasing the density of the powder layer, the fabricating efficiency can be improved by about three fold.

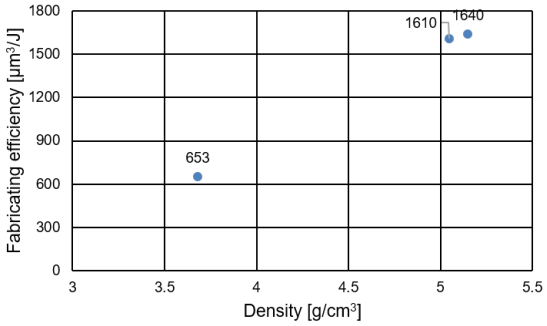

FIGURE 7. Relationship between density and fabricating efficiency.

In summary, by increasing the density of the powder layer, the process-window moved to the lower LED side, the amount of spatter decreased, and the fabricating efficiency improved.

Thermal conductivity

The thermal diffusivities of the powder layers with densities of 3.68 g/cm^3 and 5.15 g/cm^3 were 0.057 and 0.141 mm^2/s, respectively. The specific heats were 742 J/K·kg and 636 J/K·kg respectively. Thus, the thermal conductivities can be calculated as 0.16 W/m·K and 0.46 W/m·K, respectively.

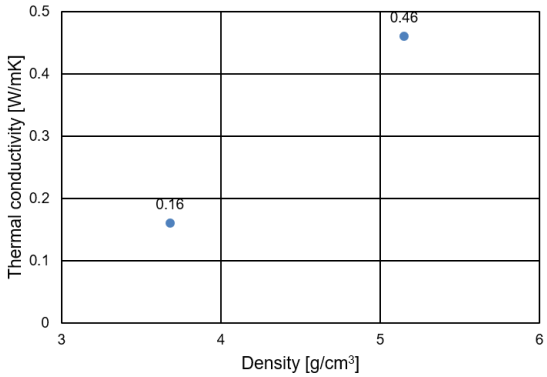

FIGURE 8. Relationship between density and thermal conductivity.

As shown in FIGURE 8, it is confirmed that by increasing the density, the thermal conductivity improved three fold. In the previous section, it is found that process-windows moved to the lower LED side, the amount of spatter decreased, and the fabricating efficiency improved, likely due to the improvement of the thermal conductivity. In this experiment, it is found that the thermal conductivity is about 3 times larger, which confirms the validity of the results of the previous section experiment.

CONCLUSIONS

In order to investigate the effects of powder density on the melt solidification phenomenon during the process of SLM, we scanned the laser beam over the different density powder layers and observed the shape of the beads.

It was found that the process-window moved to the lower LED side as density increased. It was also found that the amount of spatter is reduced when the density is high, and the fabricating efficiency improved by about three times. It is assumed that these results are caused by improvements in the thermal conductivity.

REFERENCES

[1] Kruth JP, Merceils P, Vaerenbergh JV. Froyen L, Rombouts M. Binding Mechanisms in Selective Laser Sintering and Selective Laser Melting. Rapid Prototyping Journal. 2005; 11: 26-36.

[2] Scipioni B U, Wolfer A J, Matthews M J, Delplanque J P R, Schoenung J M. On the Limitations of Volumetric Energy Density as a Design Parameter for Selective Laser Melting. Material and Design. 2017; 113: 331-340.

[3] Williams J D, Deckard C R. Advances in Modeling the Effects of Selected

Parameters on the SLS Process. Rapid Prototyping Journal. 1998; 4: 2-90-100.
[4] Song B, Dong S, Deng S, Liao H, Coddet C. Microstructure and Tensile Properties of Iron Parts Fabricated by Selective Laser Melting. Optics & Laser Technology. 2014; 56: 451-460.
[5] Lauri T, Heidi P, Olli N, Antti S. Correlation between Pyrometer Monitoring and Active Illumination Imaging of Laser Assisted Additive Manufacturing of Stainless Steel. ICALEO. 2011; 404: 196-204.
[6] Okunkova A A, Peretyagin P Y, Podrabinnik P A, Zhirnov I V, Gusarov A V. Development of Laser Beam Modulation Assets for the Process Productivity Improvement of Selective Laser Melting. Procedia IUTAM. 2017; 23: 177-186.
[7] Zhao C, Fezzaa K, Cunningham R W, Wen H, Francesco D C, Chen L, Anthony D, Sun T. Real-time Monitoring of Laser Powder Bed Fusion Process using High-speed X-ray Imaging and Diffraction. SCIENTIFIC REPORTS. 2017; 7: 3602.
[8] Samuel S S, Joel W B. The Prediction of the Emissivity and Thermal Conductivity of Powder Beds. Particulate Science and Technology. 2004; 22: 427-440.
[9] Wei P, Wei Z, Chen Z, Du J, He Y, Li J, Zhou Y. The AlSi10Mg Samples Produced by Selective Laser Melting: Single Track, Densification, Microstructure and Mechanical Behavior. Applied Surface Science. 2017; 408: 38-50.

COAXIAL NEAR-INFRARED CAMERA MEASUREMENTS FOR PROCESS CONTROL IN SELECTIVE LASER MELTING

Aleksandr Shkoruta[1], Sandipan Mishra[1], Stephen Rock[2]
[1]Mechanical, Aerospace & Nuclear Engineering
[2]Center for Automation Technologies and Systems
Rensselaer Polytechnic Institute, Troy, NY, USA

INTRODUCTION

Selective laser melting (SLM) is an additive manufacturing (AM) technology that enables the production of complex shapes out of the metal powder. Currently, closed-loop process control schemes of the SLM process are not widely implemented, in part due to challenges in in-situ process measurement and real-time laser control. In this paper, we present the results of the SLM process monitoring using near-infrared (NIR) camera integrated into the optical path of our open-source SLM machine, concentrating on the potential application of these measurements to the closed-loop feedback control. After a brief description of the hardware setup, we report the monitoring results of the single track and multi-layered parts' scans. We also discuss the response of the NIR images to a step change in laser power, as well as layer-to-layer coaxial image evolution. Coaxial images clearly register changes in process emissions due to varying process inputs, as well as changes due to varying material conditions or presence of defects. Therefore, the NIR CMOS camera is established as a credible output sensor for the real-time feedback control of the SLM process.

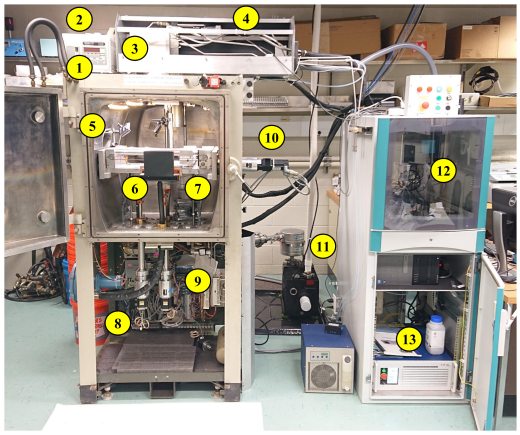

FIGURE 1. Open-source SLM machine. 1 - oxygen analyser, 2 - off-axis camera (not visible), 3 - scanner, 4 - coaxial camera, 5 - mirrors for the off-axis camera, 6 - dust collector, 7 - recoater, 8 - powder piston (left) and build platform piston (right), 9 - motion controller, 10 - recoater drive, 11 - roughing pump, 12 - industrial PC cabinet, 13 - laser.

HARDWARE SETUP

The SLM testbed used in this study is shown in Figure 1. It was designed and built in-house at Rensselaer Polytechnic Institute's Center for Automation Technologies and Systems to enable full control of the SLM process, including the ability to change the laser power on the fly at any point in time, incorporate novel sensing modalities, and test new materials and applications for AM. The laser beam is focused using an $f\theta$ lens, while a 2D scanner is used to move laser spot in the focal plane, as is typical for SLM machines. Table 1 summarizes all of the equipment used in the testbed. The user and hardware interfaces were implemented using LabVIEW [1]. A detailed description of the testbed can be found in [2].

Coaxial NIR camera setup

To monitor the process, we use a coaxially mounted NIR camera setup (as shown in Figure 2) because it is simultaneously cost-effective and achieves sufficiently high temporal and spatial resolution in observation of the *thermal* emission from the heat affected zone (HAZ). In SLM, the melt pool is small $(100\,\mu m)$ but rapidly moving $(1\,m/s)$, thus the sensor must have an instantaneous field of view (IFOV) around $10\,\mu m$ per pixel and a temporal resolution of kilo-frames per second. Such temporal requirements are cost-prohibitive or impossible for full-size infrared sensor readout. But in the coaxial monitoring setup, the full sensor readout is not necessary. The camera views the HAZ through the same optics that focus the laser (as illustrated in Figure 2). As a result, the sensor's FOV is always aligned with the melt pool location, thus the region of interest can be made very small (sub-windowed). This, in

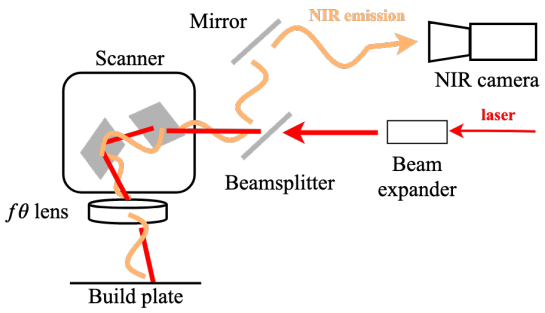

FIGURE 2. Coaxial monitoring setup for NIR camera. The beam splitter is transparent for wavelengths above $950\,nm$ and is reflective to everything below it. The laser and NIR emission go through exactly same optical path before the beam splitter.

turn, dramatically increases the achievable frame rate.

Our setup is similar to the coaxial setups reported in literature [3, 4, 5]. Peak thermal emission of the molten metals occurs near $1000\,nm$ but observation around this wavelength is impossible due to the presence of laser emission ($1070\,nm$). Thus, process observation is possible either below $1000\,nm$ (NIR), or above $1100\,nm$. While it is possible to use conventional Si-based detectors in NIR ($700 - 1000\,nm$), observation at $1100\,nm$ and above requires significantly more expensive InGaAs detectors. Therefore, we employ a conventional CMOS camera and image the HAZ at NIR.

We use an off-the-shelf $100\,mm$ achromatic lens to image the HAZ. As the distances from the build area to $f\theta$ lens ($500\,mm$), as well as from $f\theta$ lens to the camera location (estimated to be no less than $320\,mm$) are significantly large, magnification is approximately $BFL_{achromat}/BFL_{f\theta}$, i.e. 1:3. With a pixel pitch of $5\,\mu m$, estimate of IFOV is then $15\,\mu m$. Such IFOV was deemed sufficient, considering uncertainties in the optical distances (especially within the proprietary scanner), and the presence of $f\theta$ lens aberrations for wavelengths different from the $1070\,nm$.

Resolution characterization

The optical setup was focused manually using a USAF 1951 test artifact back-lit with $870\,nm$ diode (Figure 3a). The artifact was placed at the build level in the process chamber and imaged through the scanning optics.

TABLE 1. Equipment list

Laser	IPG Photonics $1070\,nm$ $40 - 400\,W$
Beam expander	Sill Optics S6EZM5076/328 up to $8\times$ magnification
Scanner	SCANLAB intelli*SCAN*$_{de}$ 20 typical marking speed $1\,m/s$ step response (1% F.S.) $0.7\,ms$ aperture $20\,mm$
$f\theta$ lens	Sill Optics S4LFT1420 focal length $420\,mm$ spot $\varnothing 60\,\mu m$ ($\varnothing 14\,mm$ beam)
Camera	Basler acA2000-165umNIR minimal exposure $40\,\mu s$ 32×32 subwindow, $2000\,Hz$ Thorlabs AC254-100-B-ML lens imaging at $800 - 950\,nm$

Based on the known geometry of the USAF target's features, the IFOV is $21\,\mu m$ per pixel[1]. Group 3, element 5 triplet can be barely resolved, i.e. resolution is $12\,lp/mm$ ($41\,\mu m$ stripes spaced $83\,\mu m$ apart).

Using the USAF test target, we estimated the point spread function (PSF) and used it to "deconvolve" the NIR image. The PSF can be interpreted as the impulse response of the imag-

[1]Group 3, element 5 lines are $50\,\mu m$ wide, while group 2, element 3 lines are $100\,\mu m$ wide.

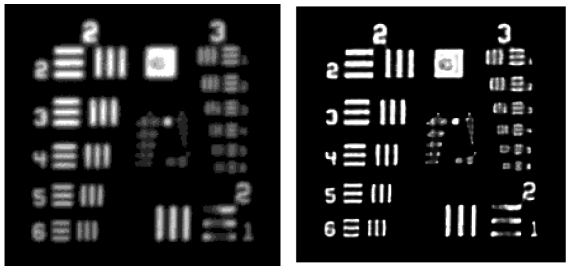

(a) (b)

FIGURE 3. (a): Image of the USAF 1951 chart seen by the coaxial camera after focusing. Iris opening and the variable length extension tube were adjusted to achieve the best focus. (b): The same image sharpened via deconvolution.

ing system, i.e. the "kernel" that blurs the "ideal" image and produces the measurement result through convolution. To determine the PSF, we calculated the line spread function for vertical and horizontal edges of a square (to the right of the three vertical bars of group 2, element 2 in the top row of Figure 3a) and assumed PSF separability [6]. The deconvolved image (using MATLAB's built-in `deconvlucy` function) of the USAF target is shown in Figure 3b. A sharper image comes with the price of more computationally expensive image processing. While longer image processing times can be justified in some cases, in this paper, we only report NIR images "as acquired".

In the following sections, we present the results from the SLM process observation using the NIR coaxial camera setup.

LOCAL EFFECTS

In this section, we report the results of single track tests, both on solid metal and powder substrates. This way, we sought to establish if coaxial NIR images are a suitable measurement modality for in-situ process control. Variety of local effects can be captured by the coaxial camera in this setting.

We address observed part-scale effects in the subsequent section.

Preliminary tests on solid metal plate

Tracks scanned on the bare metal surface are very consistent, thus they can be used as the tool to assess the influence of the process variables (such as location on the build plate, camera's exposure time, and so on) on the coaxial images. This way, we established that color aberrations of the $f\theta$ lens do not seem to distort the image at our level of resolution, and that there is no motion blur in the coaxial images. We also observed that contours of constant intensity ("level sets") exhibit extended comet-like shape, as is expected from literature [7]. Finally, increase of the exposure time "re-numbers" these level sets, i.e. they maintain their shapes but corresponding values rise proportionally (unless saturation is reached).

To assess how the coaxial images change with varying process inputs, 20 lines with nominal powers of $100 - 250\,W$[2] and speeds of $300 - 2000\,mm/s$ were scanned on the solid steel substrate. A coaxial image from $200\,W$, $600\,mm/s$ line is shown in Figure 4. From this experiment, it

[2]All powers are "nominal", i.e. as commanded via LabVIEW interface. Actual power reaching the build area is lower.

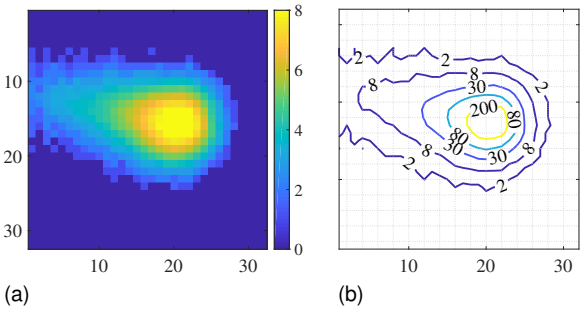

FIGURE 4. (a): NIR image, as acquired, logarithmic scale of intensity (base 2). Exposure $150\,\mu s$. (b): Contour plot of the same image (image is created using MATLAB's `contour` function).

was clear that the NIR emission pattern from the HAZ strongly depends on laser power and speed, and coaxial measurement system is able to capture this effect.

Trends in selected level sets' width and length are shown in Figure 5. Predictably, dimensions generally decrease with decreasing energy input (either decreased power or increased speed). However, "bright spot" (threshold 100, the right column of Figure 5) stays practically constant in size for higher powers and lower speeds. The behavior of the "comet length" (left column of Figure 5) is also peculiar, as for some laser powers the length decreases with speed, while for others it increases.

Remark: Following the above study, we attempted to map digital levels and melt temperature, as in [8]. Knowing spatial resolution of the NIR images, we sought to find an intensity value I

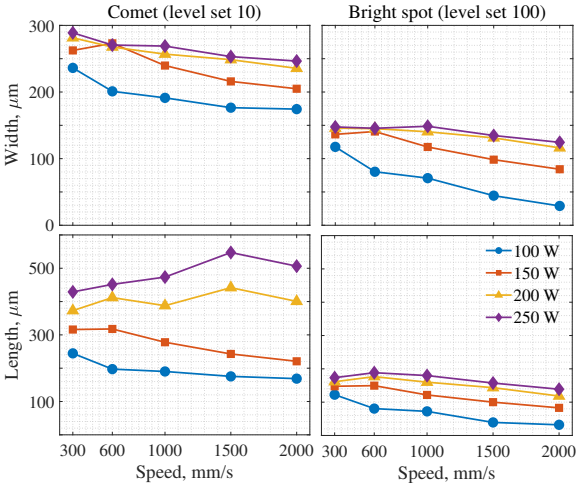

FIGURE 5. Width and length of selected level sets, depending on process parameters.

such that widths of corresponding level sets were equal to the melt track width, measured post factum with an optical microscope. However, we could not establish a universal value to link NIR coaxial images and melt pool dimensions. One possible reason for this could be unexplained behavior at higher energy densities.

Laser scanning over a defect

Not only does coaxial image signature change with variation of laser power and speed, but it also responds to external disturbances, e.g. defects. Consider Figure 10: here, the laser scanned over the surface defect (a hole, as shown on the left). When the laser passes over the defect (frames 3 through 8), coaxial images clearly differ from the typical steady-state ones (frames 1 and 9).

Laser power step change and time delay

As the long-term focus of this research is feedback process control, the following test was performed to assess delays in the control loop and the response of the coaxial image to the change of laser power: 6 lines were scanned[3] such that there was a step change in commanded laser power in the middle of each line. Initial power level (100, 150, 200, 300, 350 and $400\,W$ correspondingly) was changed to $250\,W$ at the same point within each line. Results are shown in Figure 7, where a frame's average pixel value is plotted against time. Here, all the plots are aligned such that the step change of power occurred at time 0. The behavior is obviously nonlinear, as the step from $400\,W$ to $250\,W$ is not equal in height to the one of $100\,W$ to $250\,W$. Nonlinear effects (such as keyhole drilling) might have been occurring, as $400\,W$ in combination with $300\,mm/s$ provided high energy density. In the figure, the solid lines represent a moving average

[3]Length: $20\,mm$, speed: $300\,mm/s$.

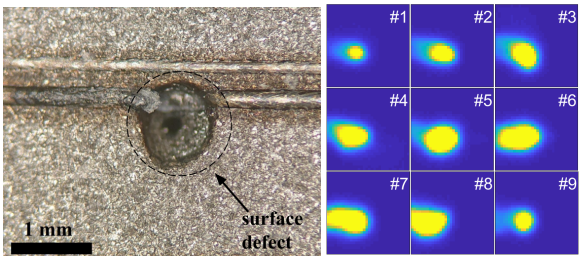

(a) (b)

FIGURE 6. (a): Surface defect, after the laser scanned over it. (b): Frames captured when laser was transitioning over the defect, exposure $50\,\mu s$.

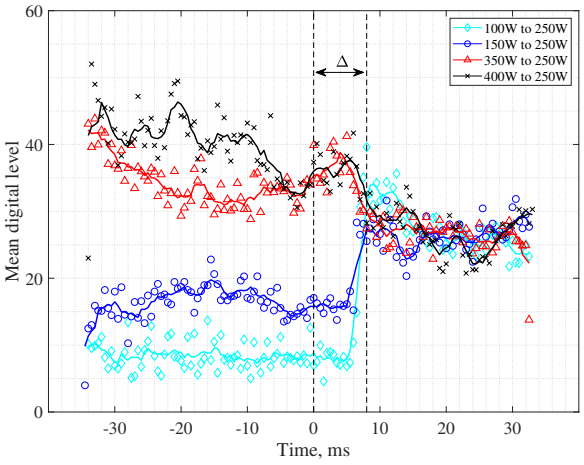

FIGURE 7. Response of the coaxial image to the step change in laser power, $200\,\mu s$ exposure. Delay Δ is consistent between all lines.

of 6 measurements. A delay of $\Delta \approx 7\,ms$ between the time of power change and the corresponding time of coaxial image reaction is observed in all of the lines. As the laser command has to go from high-level LabVIEW interface through the operating system down to the PCI laser control board, such delay is expected. Fortunately, the value of the delay is consistent. Otherwise, the implementation of the real-time feedback control schemes would become more difficult.

Material ejection in powder tests

The advantage of solid plate tests is that NIR images are consistent. On the other hand, images taken during laser scans of the powder exhibit significant stochastic behavior due to discrete particle-related events. In Figure 8, a split of the coaxial NIR level sets into separate entities

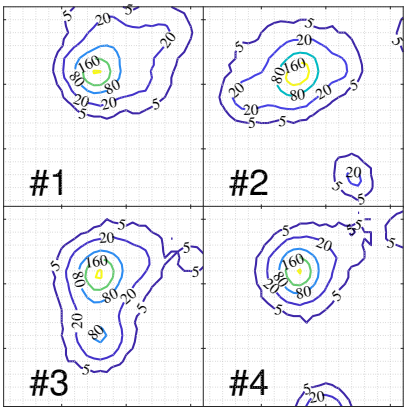

FIGURE 8. Subsequent frames with apparent material ejection when scanning over powder surface.

can be observed[4]. We believe this to be a material ejection from the melt pool. In the image, the laser is scanning from the top right corner diagonally downwards, with separate NIR source leading the hot spot. Prevalence of this effect seems to depend on the process parameters, but further quantitative analysis is required, which is outside the scope of this paper.

Laser scanning of an overhang

An overhang (also known as a down-facing surface) is a section of the part that does not have solid metal underneath and rests on the powder during the build. Such areas present a known challenge to the SLM process due to significantly different effective thermal properties of powdered and solid metal.

To observe the process signature during transition to an overhang section, we ran single lines over the single powder layer (spread manually) such that first half of each line rested on the solid part underneath, while second half was powder-supported[5]. It has been reported that the melt pool elongates when not supported by solid material [3], thus we sought to see if we can observe the same effect. Results from this test are presented in Figure 9. The NIR level sets *do* elongate after transition. Simultaneously, level sets in the center (circles corresponding to higher emission values) became smaller, i.e. there was less emission coming from the center of the HAZ.

[4]This image was taken during the part build, as described in the following section, and is not a result of a single line test. Exact part and layer number are: square 1, layer 16.

[5]Powder depth $500\,\mu m$.

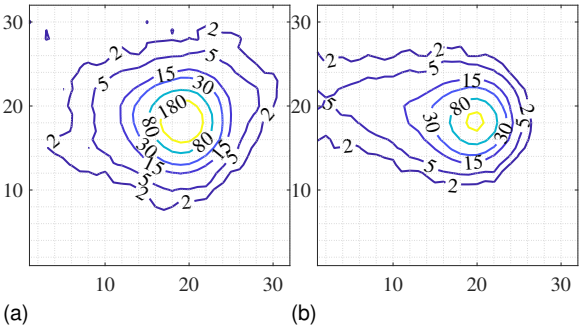

FIGURE 9. Temporarily averaged NIR images for solid-supported (a) and powder-supported (b) tracks. Process parameters: power $160\,W$*, speed* $600\,mm/s$*. Exposure* $200\,\mu s$*.*

In summary, we have demonstrated that coaxial NIR images pick up the changes in process emissions due to the different process control inputs, such as laser power or scanning speed. Images also show a difference in process emissions due to surface defects, as well as changing environmental conditions, i.e. change of the surrounding medium from solid-supported to powder-supported. Apparent material ejection can also be observed (depending on process parameters). Thus, NIR coaxial camera is a credible output sensor for the process control.

PART-SCALE EFFECTS

In this section, we briefly present some monitoring results of a multi-layer part build. In this test, CoCr powder was used to make 4 geometrically identical blocks, shown in Figure 10a. All blocks were scanned with the same nominal power of $250\,W$, but different speeds: 600, 800, 1000, and $1500\,mm/s$ (squares 1, 2, 3, 4 correspondingly). All layers (17 total) were hatched the same way (diagonally from top to bottom, as indicated in the bottom right corner). There were 8,400 non-trivial frames acquired per each layer of square 1. All layers of all 4 parts, combined, amounted to 400,000 images. To show "average-looking" NIR images, temporarily averaged frames (middle of the each square's scan, layer 6), are shown in Figure 10b.

A large number of acquired frames is prohibitive for a manual analysis, thus automated image processing methods are necessary. However, we can still manually analyze simpler descriptive statistics of the data: for example, the evolution of the maximum intensity of the image. Given the maximum digital level (M) in an image of the particular layer, we can study the evolution of the

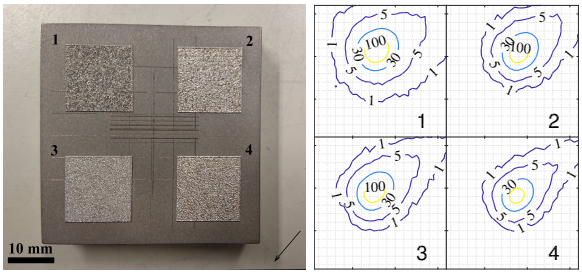

FIGURE 10. (a): CoCr test. Lines present on the plate are left from the previous test and do not influence the build result. (b): Representative images, exposure time $100\,\mu s$*.*

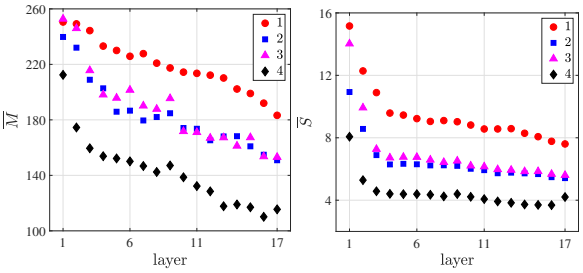

(a) (b)

FIGURE 11. (a): Maximum digital level decreases with layer number. (b): Average frame intensity stabilizes after several layers for all but square 1.

mean value of M as a function of layer number. The same could be done with the average amount of light captured, i.e. the average intensity S:

$$M(i) = \max_{r,c} I(r,c,i),\ \overline{M} = \frac{1}{N}\sum_{i=1}^{i=N} M(i),$$

$$S(i) = \frac{1}{RC}\sum_{r,c} I(r,c,i),\ \overline{S} = \frac{1}{N}\sum_{i=1}^{i=N} S(i),$$

where $r = 1 \ldots R, c = 1 \ldots C$ are row and column indices within a single image, i is the image index in the sequence of all layer frames, $i = 1 \ldots N$, and $I(r,c,i)$ is the intensity of the pixel at position r,c in the frame i.

The evolution of $\overline{M}$ and $\overline{S}$ with layer number is shown in Figures 11a and 11b. Interestingly enough, while total amount of captured NIR emission stabilizes after a couple of layers, $\overline{M}$ is decrescent throughout, clearly demonstrating layer-to-layer evolution.

CONCLUSION

In this paper, we presented a coaxial measurement setup for online SLM process monitoring and control. The coaxial images capture changes in process emissions due to different process control inputs and variations in process conditions (e.g. local defects). The exact relationship between NIR images and true melt pool dimensions is not established, but coaxial images are still deemed to be a valid process signature for the in-situ feedback control. Plans for future work include in-situ power control for SLM parts using data-driven control methodologies to ensure consistent measurement signatures.

REFERENCES

[1] 4039 Development & demonstration of open-source protocols for powder bed fusion AM - America Makes. [Online]. Available: https://www.americamakes.us/portfolio/4039-development-demonstration-open-source-protocols-powder-bed-fusion-additive-manufacturing-pbfam/. [Accessed: 22-Feb-2019].

[2] A. Shkoruta, W. Caynoski, S. Mishra, and S. Rock, “Iterative learning control for power profile shaping in selective laser melting”, in press.

[3] T. Craeghs, S. Clijsters, E. Yasa, F. Bechmann, S. Berumen, and J. P. Kruth, “Determination of geometrical factors in Layerwise Laser Melting using optical process monitoring”, Opt. Lasers Eng., vol. 49, no. 12, pp. 14401446, 2011.

[4] S. Grantham, B. Lane, J. Neira, S. Mekhontsev, M. Vlasea, and L. Hanssen,“Optical design and initial results from NISTs AMMT/TEMPS facility”, Proc. SPIE 9738, Laser 3D Manufacturing III, 97380S, 2016.

[5] M. Doubenskaia, S. Grigoriev, I. Zhirnov, and I. Smurov, “Parametric analysis of SLM using comprehensive optical monitoring”, Rapid Prototyp. J., vol. 22, no. 1, pp. 4050, 2016.

[6] R. Qin, J. Gong. “A robust method of calculating point spread function from knife-edge without angular constraint in remote sensing images”, Yaogan Xuebao - Journal of Remote Sensing 15.5 pp. 895-907, 2011.

[7] G. Gladush, I. Smurov. “Physics of laser materials processing: theory and experiment”. Heidelberg: Springer, 2011, pp. 132-135.

[8] I. Smurov, M. Dubenskaya, I. Zhirnov, and V. Teleshevskii, “Determination of the true temperature during selective laser melting of metal powders based on measurements with an infrared camera”, Measurement Techniques, vol. 59, no. 9, Springer US, pp. 14, 05-Dec-2016.

DETECTING PROCESS DEFECTS IN LASER-POWDER BED FUSION

Bradley H. Jared, Jonathan D. Madison, John A. Mitchell, Daryl Dagel, Thomas A. Ivanoff, David J. Saiz, Josh R. Koepke
Sandia National Laboratories
Albuquerque, NM

Metal additive manufacturing (AM) continues its growth and advancement into a range of industries and applications. To facilitate its adoption into precision engineering applications, fundamental questions regarding the intrinsic reliability and determinism of additive metals must be answered. Defects are a commonly cited challenge for metal AM processes; particularly laser-powder bed fusion (L-PBF). A critical aspect of L-PBF process development involves parameter optimization to reduce and minimize process defects. The stochastic nature of metal L-PBF, however, introduces significant uncertainty in the presence of process defects within any printed material and part. Therefore, defect "signatures" have been and are being investigated to provide a predictive capability for identifying process defects in-situ [1-5].

Work was performed in 316L stainless steel produced by metal L-PBF using a 3D Systems ProX 200. Two-color pyrometry was performed to monitor the build melt pool using a Stratonics Therma-Viz mounted inside the ProX 200 build chamber, Figure 1. The Therma-Viz relies on two CMOS imagers with roughly 21µm pixel resolution which are filtered with 50nm bandpass filter, once centered at 750nm and the other at 900nm. The build configuration of the ProX required fixed field imaging at an angle of roughly 20º relative to the build plate normal. A field of view of 80 x 65 pixels (1.6x1.3mm) was selected to maximize the Therma-Viz data

FIGURE 1. Stratonics ThermaViz installed inside the 3D Systems ProX 200.

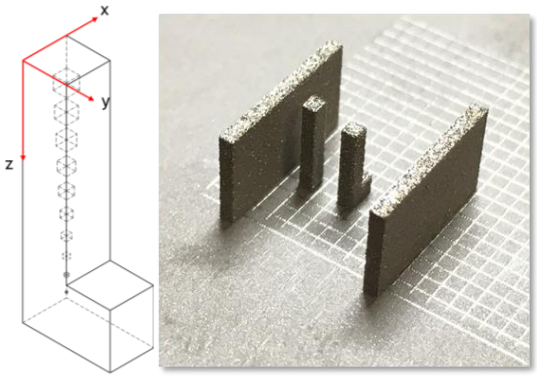

FIGURE 2. 1x1x5.25mm intentional captured holes L-column design (left) and printed part in 316L stainless steel (right).

capture rate, roughly 6-7kHz, with an exposure rate of 90µsec. Figure 2 shows a 1x1x5.25mm L-shaped column that was printed and monitored with the Therma-Viz. Printing was performed at 1060nm using a 100µm diameter laser beam with 130W of power, a 1.4m/sec scan velocity, a 50µm hatch spacing, and a 30µm nominal powder layer thickness. The L-column included ten intentional cubic pore structures that ranged in nominal size from 30 to 300µm in 30µm increments (i.e. equivalent to one to ten layer thicknesses). After printing and removal from the base plate, computed tomography (CT) of the L-column was performed using a Zeiss Xradia 520 Versa micro CT system. Voxel resolution for the measurement was roughly 2µm. Extensive data processing was performed to transform the resulting CT data into volumetric porosity maps of the defects contained within the L-column part, Figure 3.

Figure 4 shows a single temperature field from the pyrometry data at a single point in time during printing. Managing and processing the full data set for the L-column bracket proved to be challenging. Although a relatively small geometry, the 1x1x5.25mm L-column represents 175 layers which resulted in 87,500 individual thermal images during printing. Processing of

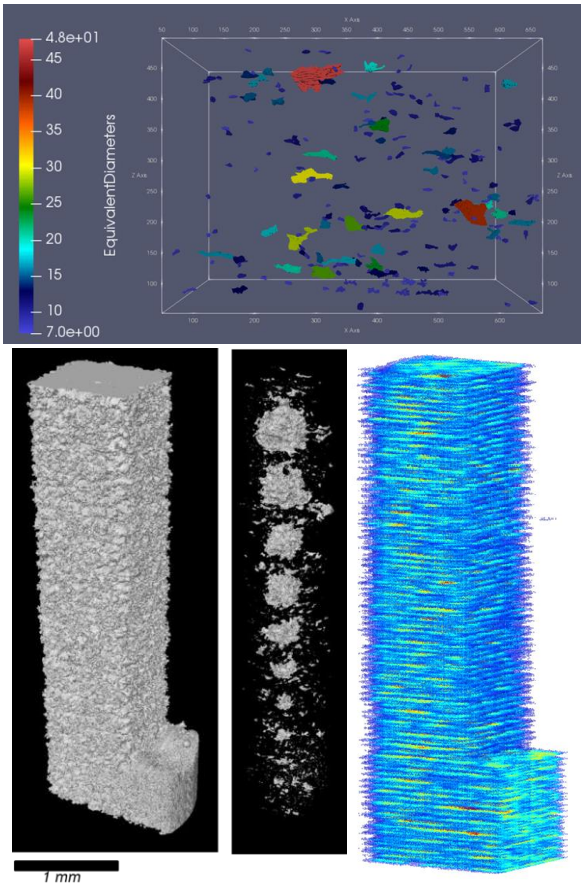

FIGURE 3. Volumetric maps of porosity in the L-column. High resolution near the bottom of the part (top) and the full part with the intentional pore features (bottom left and center). Pyrometry data reconstruction of the entire part is also provided (bottom right)

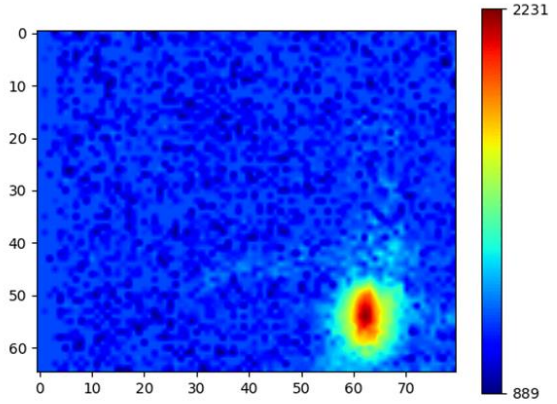

FIGURE 4. Two-color pyrometry temperature field at a single point in time during printing.

these was performed using Python scripting to improve analysis throughput and to customize temperature calculations from the raw pyrometry data sets. From these calculations, composite

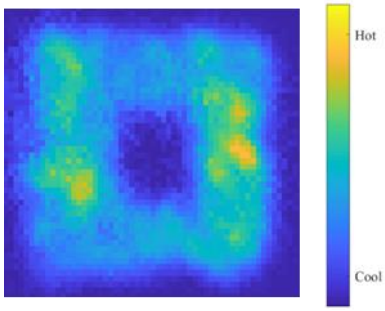

FIGURE 5. Composite normalized temperature map across a single print layer of the L-column.

images, Figure 5, were compiled for each process layer. These were then compiled into a large volumetric representation, Figure 3.

The first data comparison performed was to understand the limits of CT and pyrometry to identify the intentional features printed into the L-column. Figure 3 shows these intentional flaws in the full part volume, as well as a higher magnification image with unintentional process porosity. Not surprising, the larger voids are relatively easily identified. While the pyrometry data under-predicts the size of the intentional voids, it is capable of observing features down to roughly 60µm.

A much more challenging analysis problem was to correlate pyrometry data with the CT data. This is the heart of what was desired from the work to develop a robust in-stiu monitoring capability necessary to reduce uncertainties in metal L-PBF materials and parts. Essentially, the goal is take spatial and temporal two-color pyrometry thermal data (X,Y,Z, time) and attempt to build process-structure correlations with a spatial porosity field (X,Y,Z). Registration and orientation of the two data sets was a critical first step and was ultimately based on knowledge from individual process layers. A key step in building data correlations was examining the pyrometry data. In the end, melt pool outliers were identified using a machine learning analysis based on melt pool aspect ratio and orientation angles. The location of these outlier melt pools were then evaluated in comparison with the location of pores from the CT data. Results are encouraging as pores larger than 40µm ESD can be predicted 70% of the time, while every pore larger than 70µm was positively identified. Results will be provided in much greater detail during the presentation and have

already been documented in a peer reviewed journal article [6].

CONCLUSIONS

Work has been performed using two-color pyrometry to identify process defects in metal L-PBF for a 316L stainless steel test part. Data analysis techniques have been developed and demonstrated for both CT and pyrometry data sets. The ability of pyrometry and CT to identify and characterize intentional void porosity was examined. Work has also been demonstrated to provide positive correlation of melt pool outliers with structural process porosity.

ACKNOWLEDGMENTS

Sandia National Laboratories is a multimission laboratory managed and operated by National Technology and Engineering Solutions of Sandia LLC, a wholly owned subsidiary of Honeywell International Inc. for the U.S. Department of Energy's National Nuclear Security Administration under contract DE-NA0003525. This document has been reviewed and approved for unclassified, unlimited release, SAND2019-10674 A.

REFERENCES

[1] J.B. Forien, P.J. Depond, G.M. Guss, B.H. Jared, J.D. Madison, M.J. Matthews, Effect of laser power on roughness and porosity in laser powder bed fusion of stainless steel 316L alloys measured by X-ray tomography, International Journal of Materials Research (2019).

[2] T. Stockman, C. Knapp, K. Henderson, J. Carpenter, J. Schneider, Stainless Steel 304L LENS AM Process Monitoring Using In-Situ Pyrometer Data, Jom 70(9) (2018) 1835-1843.

[3] A.J. Dunbar, A.R. Nassar, Assessment of optical emission analysis for in-process monitoring of powder bed fusion additive manufacturing, Virtual and Physical Prototyping 13(1) (2017) 14-19.

[4] B. Lane, E. Whitenton, S. Moylan, Multiple sensor detection of process phenomena in laser powder bed fusion, SPIE Commercial+ Scientific Sensing and Imaging, International Society for Optics and Photonics, 2016, pp. 986104-986104-9.

[5] L. Scime, J. Beuth, Using machine learning to identify in-situ melt pool signatures indicative of flaw formation in a laser powder bed fusion additive manufacturing process, Additive Manufacturing 25 (2019) 151-165.

[6] Mitchell J, Ivanoff T, Dagel D, Madison J, Jared B, Linking Pyrometry to Porosity in Additively Manufactured Metals, Additive Manufacturing, submitted, 2019.

MACHINE LEARNING WITH UPDATING FOR MILLING STABILITY

Jessie Jiang[1], Monica Nogueira[2], Noel Greis[2], Sambit Bhattacharya[3], and Tony Schmitz[4]
[1]University of North Carolina at Charlotte, Charlotte, NC, USA
[2]North Carolina State University, Raleigh, NC, USA
[3]Fayetteville State University, Fayetteville, NC, USA
[4]University of Tennessee, Knoxville, TN, USA

INTRODUCTION

Although many advances in machining have been achieved in recent decades, challenges for high productivity machining remain. First, CAD/CAM software generally treats machining as a geometric effort. Provided the cylindrical tool follows the required path through the prismatic work material to leave the desired geometry, it is assumed that the machining process is acceptable. This approach does not consider the constraints imposed by the process dynamics. For example, some spindle speed-depth of cut combinations will exhibit self-excited vibrations (or chatter, which produces large forces, large vibrations, unacceptable surface finish, and potential damage to the tool, part, and spindle), while others will not [1]. Additionally, even if stable behavior is obtained (i.e., forced vibration only), the geometric accuracy of the machined part may or may not satisfy design tolerances, again depending on the selected spindle speed-depth of cut pair [1]. Machining dynamics models are therefore required to select spindle speed-depth of cut combinations that avoid chatter, while providing the required geometric accuracy.

Second, the requirement for the vibration behavior of the tool (and sometimes the part) to predict process behavior imposes a specific measurement need. The vibration behavior is traditionally described by the frequency response function (FRF), which is obtained through modal testing. A popular approach is to excite the structure in question using an instrumented hammer and a low mass accelerometer attached to the structure to record the subsequent time domain vibration response. The frequency domain displacement-to-force ratio is the FRF, or receptance, for the tool or part. While the measurement procedure is well-understood, the lack of widespread availability of modal testing equipment and the associated expertise has hindered the implementation of machining modeling on the shop floor. This points to a second modeling need: the tool point receptances must be identified without a measurement of each. Because the tool is clamped in a holder and the holder is inserted in a spindle, which is attached to the machine, the tool point receptance prediction is not trivial [1-3].

Third, the tool point receptance and machining models are deterministic, but include inherent uncertainties. The predicted operating parameters are therefore also uncertain. This establishes the need for uncertainty reduction through testing. In this research, the (uncertain) physics-based process models are used to train machine learning models. Once these machine learning models are created, they are updated as process data is gathered. This leverages Industry 4.0, where data collected during and after machining is used to achieve process improvement. In this way, each part becomes an experiment and operating parameter uncertainty can be reduced over time. The physics-guided machine learning approach is summarized in Fig. 1.

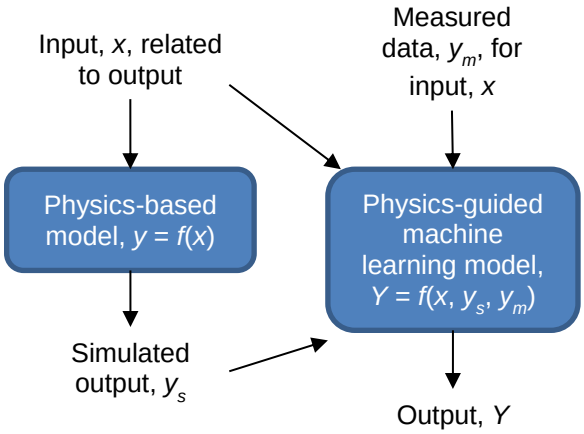
Input, x, related to output
Measured data, y_m, for input, x
Physics-based model, $y = f(x)$
Physics-guided machine learning model, $Y = f(x, y_s, y_m)$
Simulated output, y_s
Output, Y

FIGURE 1. Physics-guided machine learning approach.

PHYSICS-BASED MODEL DESCRIPTIONS

In this effort, three physics-based models are used collectively to predict the stability limit for milling. First, receptance coupling substructure analysis (RCSA) is used to predict the tool point receptance. Second, a mechanistic force model is used to relate the cutting force to the commanded chip area through cutting force coefficients. Third, a mean force frequency domain analysis is used to predict the stability limit using the first two models as input.

RCSA

Three-component RCSA for tool point dynamics prediction has been demonstrated. In prior efforts, the free-free boundary condition tool and holder were modeled as cylindrical cross-section Timoshenko beams. These beam receptances were coupled analytically to measured receptances of the spindle-machine [1-3].

The sequence of steps for tool point receptance prediction are: 1) calculate the tool receptances (free-free boundary conditions) using the Timoshenko beam model; 2) calculate the holder receptances (free-free boundary conditions) using the Timoshenko beam model; 3) measure the spindle-machine receptances using impact testing; and 4) couple these receptances to predict the tool-holder-spindle-machine assembly dynamics using either rigid or flexible-damped compatibility conditions.

Force model

In mechanistic force modeling for milling, the cutting force components, *k*, are calculated using the commanded axial depth of cut, *b*, and chip thickness, *h*. The model shown in Eq. 1 includes force components that are tangential, *t*, and normal, *n*, to the rotating cutting edge. Force coefficients that relate the force to chip area, *bh*, are identified by a *c* subscript (cutting or shearing force). Those that relate the force to axial depth alone have an *e* subscript (edge or rubbing force).

$$\begin{aligned} F_t &= k_{tc} bh + k_{te} b \\ F_n &= k_{nc} bh + k_{ne} b \end{aligned} \quad (1)$$

These coefficients may be determined by experiments where the cutting force is measured using a force dynamometer and the commanded axial depth of cut and chip thickness are known. Linear regression over a range of chip thickness values and nonlinear least squares fitting to the time domain force have been applied [4]. As an alternative, the material behavior can be defined using a constitutive model (e.g., Johnson-Cook) and the cutting force predicted using finite element simulation [5].

Frequency domain stability analysis

The analytical stability limit may be determined using the mean Fourier force analysis [6] to transform the dynamic milling equations into a time invariant, but radial immersion dependent system. This analysis expands the frequency domain dynamic milling equations into a Fourier series and then the series is truncated to include only the mean component. This analysis uses the tool point receptance and force model as inputs. The output is the limiting axial depth of cut as a function of spindle speed for a selected radial depth of cut, milling orientation (up and down), and number of teeth on the endmill.

PHYSICS-BASED MODEL UNCERTAINTY

The deterministic models described in the previous section include uncertainty. For example, the actual extension length of the endmill from the holder is subject to setup and measurement uncertainties [7]. This results in uncertainty in the tool point receptance which, in turn, leads to uncertainty in the stability limit. Propagation of uncertainties in the tool and holder models, spindle receptances, and cutting force coefficients to uncertainty in the stability limit may be completed using Monte Carlo simulation [8]. This provides a predictive model, where a probabilistic, rather than deterministic, stability limit is presented. However, if a test is performed to determine the actual stability behavior of a spindle speed-axial depth combination, there is no straightforward mapping between this result and the model input parameters.

This motivates a new approach for stability model updating using milling experiments. The approach evaluated in this study is to use the (uncertain) physics-based stability model to train a machine learning (ML) algorithm. This ML model is defined in the desired test domain of spindle speed-axial depth. Updating can then proceed directly by collecting stability results and modifying the dataset used to re-train the ML stability model. This new approach falls under the emerging paradigm of data science called theory-guided data science (TGDS) that uses physical theory to augment big data techniques such as machine learning. TGDS leverages physical knowledge embedded in derived equations with experimental data to improve the predictive capability of data-driven machine learning models. In this work, domain knowledge relevant to milling stability is used to estimate the stability limit model as represented in the stability lobe diagram (SLD). The SLD accuracy is increased by the addition of “true” sampled data, which represents experiments, to the original ML training dataset.

PHYSICS-GUIDED MACHINE LEARNING

Machine learning, a subset of artificial intelligence (AI), comprises a set of algorithms that are able to perform a specific task or model a process without being explicitly programmed, relying instead on recognizing patterns or making inferences from large sets of data. These algorithms can be grouped broadly into three categories based on the learning style. In supervised learning, algorithms map input data to corresponding known output data.

Unsupervised approaches develop models or functions from input data without knowing the corresponding outputs. Reinforcement learning approaches learn to achieve a goal through a series of decisions for which they are rewarded. Broadly, all of these approaches are designed to perform two tasks: classification in which data are separated into classes; or regression in which a continuous relationship is developed.

TGDS, or physics-guided machine learning, has emerged as an approach that addresses the specific limitations of both data learning models and physics-based models. Many data learning models, including ML, are black box models that do not provide insight into the underlying physics and do not reveal physical constraints for the modeled system. On the other hand, many physical processes are not completely understood, so physics-based models must make simplifying assumptions that compromise accuracy. Physics-guided machine learning offers a new approach to stability modeling that leverages experimental data while incorporating decades of process modeling efforts.

NUMERICAL CASE STUDY

The goal of this research is to explore how physics-based milling stability models, with their associated uncertainty, can be updated with experimental data to reduce uncertainty in parameter selection for a particular milling machine operating in a factory environment under specific conditions. A numerical case study is presented, where the physics-based machine learning model is trained using an initial approximation of the system and then updated with experimental data to better approximate the underlying true model. Errors are intentionally introduced into the inputs to the physics-based model so that the predicted stability limit used to train the machine learning model includes uncertainty. However, because the input errors are known, it is possible to determine the true (zero uncertainty) stability limit. This error-free stability model is used to generate experimental data, which replaces the uncertain data in the original uncertain training dataset during the updating step.

The physics-based stability model is created by adding uncertainty to both the RCSA and force models. Errors are added to the extension length from the holder in the RCSA model and to the cutting force coefficients in the force model. The stability model with errors is then created from the error-induced inputs of both these models; the result is presented in a stability lobe diagram (SLD) that provides the limiting axial depth of cut as a function of spindle speed for a given radial depth of cut, milling orientation, and number of teeth on the endmill. A second stability model is created without errors, representing the unknown true stability limit. Experimental points are selected for updating the ML model from this true stability limit. Example SLDs for the physics-based stability model (with errors) and the “true” model are shown in Fig. 2.

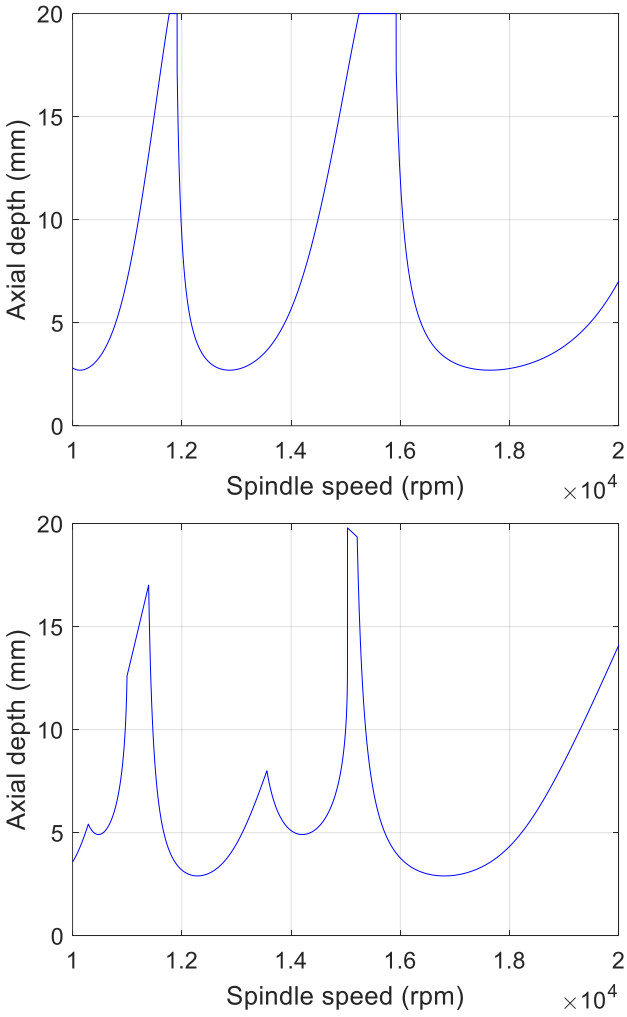

FIGURE 2. Comparison of (top) physics-based SLD with errors and (bottom) true SLD without errors.

In Fig. 2, the model parameters for the tool were: 12 mm diameter, 4 teeth, 50 mm extension from the holder (with errors); and 12 mm diameter, 4 teeth, 53 mm extension (without errors). The force model coefficients were: k_{tc} = 649.0 N/mm^2, k_{nc} = 262.2 N/mm^2, k_{te} = 0, and k_{ne} = 0 (with errors); andk_{tc} = 692.8 N/mm^2, k_{nc} = 400.0 N/mm^2, k_{te} = 0, and k_{ne} = 0 (without errors). The same spindle and holder receptances were used in both cases. Up milling with a radial depth of 2 mm was applied.

Data points below the stability limit represent stable behavior while data points above the stability limit give unstable behavior (chatter). Using the dataset created from the physics-based model with errors, the physics-guided machine learning model is trained. During subsequent updating, data points are sampled from the true experimental dataset and added to the training dataset. As the physics-guided machine learning model is updated using true experimental points, it is expected that the "learned" stability model will approach the underlying and unknown "true" model. Correspondingly, as true experimental data is added to the physics-guided machine learning model during updating, the number of correct stability predictions is expected to increase. This increasing number of correct predictions is defined as the convergence of the physics-based ML model to the true model.

The training and updating steps are summarized.

1. *Build a physics-based milling stability model.* This model is populated by the best information about the structural dynamics, relationship between the cutting force and chip area, and other process parameters. Using these inputs, the model predicts the limiting axial depth of cut to avoid chatter over a range of spindle speeds (i.e., the stability boundary). For the case study, known errors are intentionally inserted in the input data. This enables the incorrect model to be later updated with new points, corresponding to experimental data, which are generated using the true error-free stability limit (step 4).
2. *Generate training data from the physics-based model.* The stability boundary separates the spindle speed-axial depth of cut domain into two zones: stable and unstable (chatter). For the purposes of training, testing, and updating the model, a grid of 2020 points was defined using: 101 spindle speeds from 10000 rpm to 20000 rpm in increments of 100 rpm; and 20 axial depths of cut from 1 mm to 20 mm in increments of 1 mm. Each combination of depth of cut and spindle speed is associated with a stability value (stable or chatter).
3. *Train the physics-guided machine learning model.* A physics-guided ML model is trained to evaluate baseline performance in predicting the stability value for combinations of spindle speed and axial depth of cut. For the purposes of training, 70% of the population of points is randomly selected for training; the remaining 30% is reserved for testing. Prediction accuracy is determined by computing the percent of the test points for which a correct prediction is obtained by the physics-guided ML model.
4. *Generate true experimental data*. The true stability model (without errors) is used to predict the limiting axial depth of cut. Experimental points are then defined using this stability limit. The same spindle speed-axial depth points are selected, but the stability behavior is defined with the true stability limit.
5. *Update the physics-guided ML model with true experimental data and retrain*. Using the designated updating strategy, select experimental data points from the population of true data points for updating. Correct the stability values in the training dataset with the true stability values, as necessary, and retrain the physics-guided ML model.
6. *Evaluate performance of the updating strategy*. To evaluate performance of the updated physics-guided ML model, convergence, *C* (%) is used, where *CP* is the number of correct predictions compared to the true stability value and *TP* is the total number of predictions; see Eq. 2. A higher *C* value means that the machine learning model agrees more closely with the true stability limit. This indicates that updating has improved the model's predictive ability.

$$C = \frac{CP}{TP} \cdot 100\% \quad (2)$$

TRAINING THE PHYSICS-GUIDED MACHINE LEARNING MODEL

Many ML classification algorithms are available to train the stability model and predict the stability outcome (chatter or stable) for input combinations of axial depth of cut and spindle speed. In this study, k-nearest neighbors (KNN) was used. KNN is one of the simplest classification algorithms, which makes decisions by referring to the k data points closest to the data point of interest [9]. The distance between any two data points is calculated using several approaches. Common choices are Manhattan, Euclidean, and Minkowski distances. Euclidean was applied here.

UPDATING THE PHYSICS-GUIDED MACHINE LEARNING MODEL

Updating the physics-guided ML model simulates the process by which experimental results are used to reduce prediction uncertainty (i.e., converge to the true stability condition). In this research, a "climbing" strategy was implemented.

In the first update, all points in the training set with a user-selected low depth of cut are chosen and their stability status is assessed and updated. For the stable points only, the depth of cut is increased and the stability is determined at the same spindle

speeds. If the new cutting parameters are in the training set, the incorrect stability status is replaced by the true stability status. The process is then repeated by again increasing the depth of cut for the stable points. For each updating point, additional information is available. If an experimental point (at a selected spindle speed-axial depth pair) is stable, then all points for that spindle speed at lower axial depths are also stable. Conversely, if a point is unstable, then all points for that spindle speed at higher axial depths are also unstable. These updates are also incorporated.

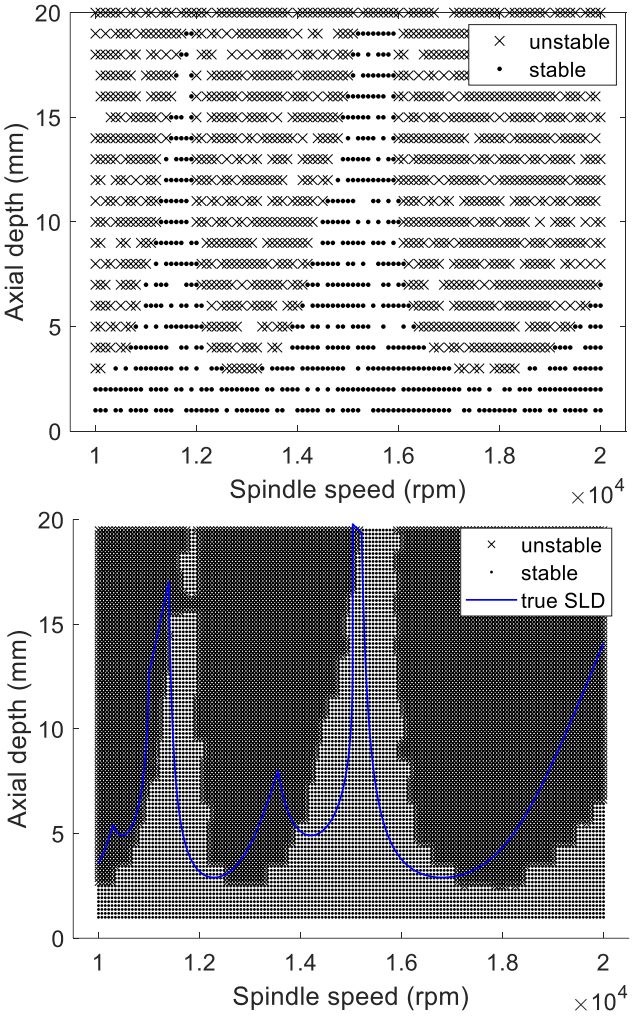

FIGURE 3. (Top) dataset used for updating the KNN model. (Bottom) Initial KNN model compared to the stability limit without errors.

Figure 3 displays the original KNN dataset used for updating. Note that the gaps in the grid appear because 30% of the original points were extracted to measure the accuracy of the original training (i.e., a comparison between the initial KNN model and the stability limit with errors). This figure also compares the initial KNN model (k = 3) to the stability limit without errors.

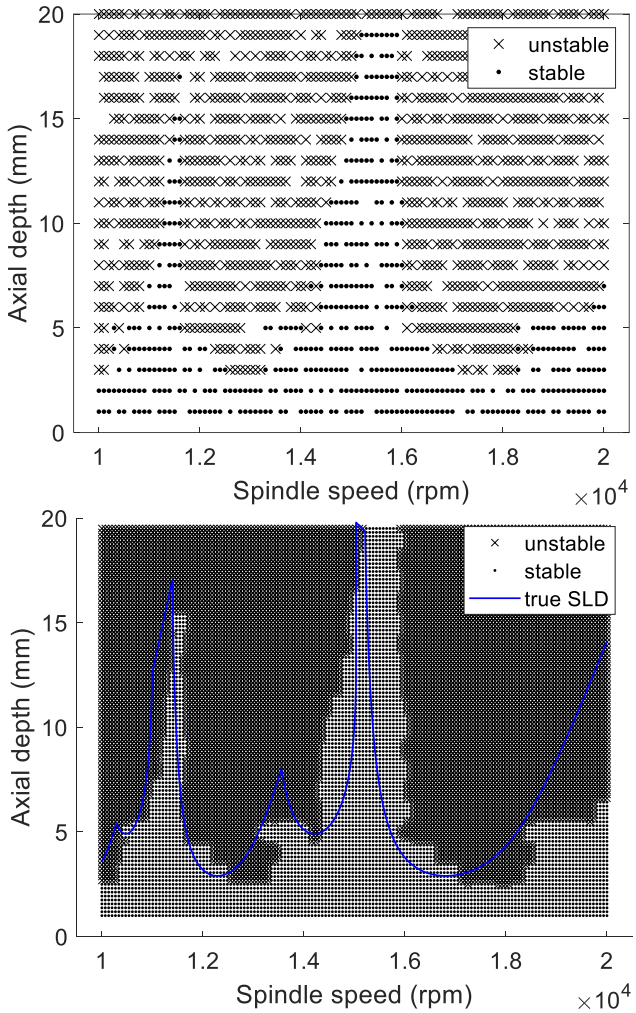

FIGURE 4. (Top) dataset after first update at a 5 mm axial depth. (Bottom) Updated KNN model compared to the stability limit without errors.

Figure 4 displays the results after updating the points at an axial depth of 5 mm. For each point, the true stability behavior was determined using the true stability limit (this represents an experiment). If the point was stable, all points at the same spindle speed with lower axial depths were also set to stable. If the point was unstable, all points at the same spindle speed with higher axial depths were set to unstable.

Figure 5 displays the results after sequential updating at axial depths of {5, 7, 10, and 13} mm. Collectively, this included 133 experiments, which yielded 1239 additional data point updates due to the strategy of modifying the state of points above

and below experiments depending on a stable or unstable outcome. The KNN model now matches the true stability limit with a convergence value of 88.37%. The results are summarized in Table 1.

TABLE 1: Updating results for climbing with KNN.

# experimental points	# additional points	Total update points	*C* (%)
Training			
-	-	-	76.47
Updating			
77	726	803	84.16
112	1041	1153	86.14
125	1160	1285	88.12
133	1239	1372	88.37

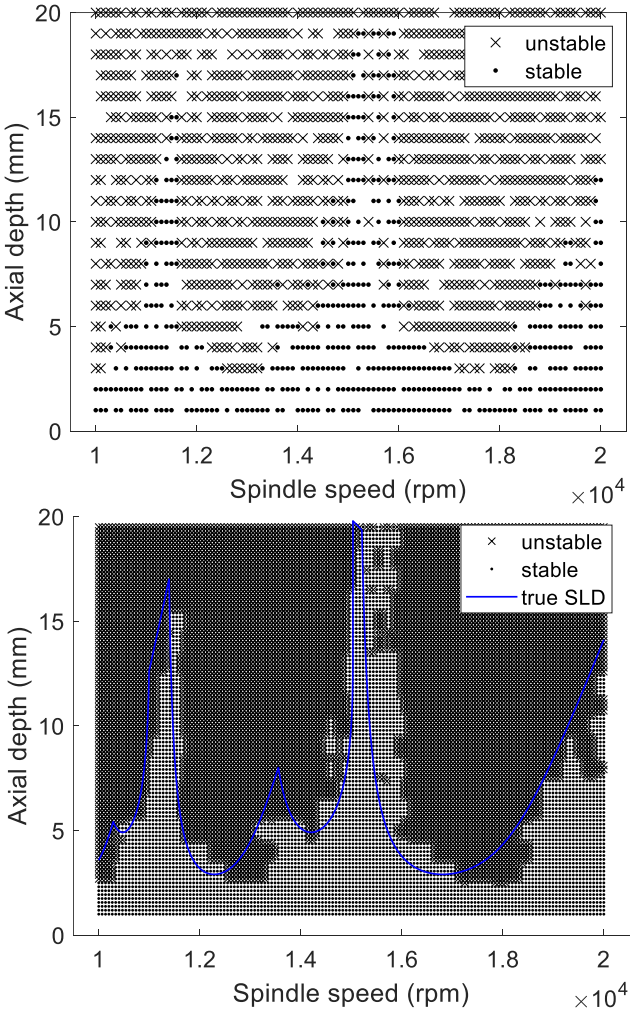

FIGURE 5. (Top) dataset after four update at axial depths of {5, 7, 10, and 13} mm. (Bottom) Updated KNN model compared to the stability limit without errors.

CONCLUSIONS

This paper described the use of uncertain physics-based milling stability models to train a machine learning stability model and then updating this model with new data to reduce uncertainty in parameter selection. A numerical case study was presented where the machine learning model was trained using an initial approximation of the system (with errors) and then updated with new data (without errors) to better approximate the underlying true model. It was shown that the model accuracy was improved with updates and converged to the true stability behavior.

ACKNOWLEDGEMENTS

This work was supported by UNC ROI.

REFERENCES

[1] Schmitz, T.L. and Smith, K.S., 2009, Machining Dynamics: Frequency Response to Improved Productivity, Springer, New York, NY.

[2] Schmitz, T. and Donaldson, R., 2000. Predicting high-speed machining dynamics by substructure analysis. Annals of the CIRP, 49/1: 303-308.

[3] Schmitz, T. and Duncan, G.S., 2005. Three-component receptance coupling substructure analysis for tool point dynamics prediction. Journal of Manufacturing Science and Engineering, 127/4: 781-790.

[4] Rubeo, M. and Schmitz, T., 2016. Mechanistic force model coefficients: A comparison of linear regression and nonlinear optimization. Precision Engineering, 45: 311-321.

[5] Shi, J. and Liu, C.R., 2004. The influence of material models on finite element simulation of machining. Journal of manufacturing science and engineering, 126/4: 849-857.

[6] Altintaş, Y. and Budak, E., 1995. Analytical prediction of stability lobes in milling. Annals of the CIRP, 44/1: 357-362.

[7] Vieira Junior, M., Baptista, E.A., Araki, L., Smith, S., and Schmitz, T., 2018, The role of tool presetting in milling stability uncertainty, Procedia Manufacturing, 26: 164-172.

[8] Karandikar, J., Zapata, R., and Schmitz, T., 2010, Incorporating stability, surface location error, tool wear, and uncertainty in the milling super diagram, Transactions of the NAMRI/SME, 38: 229-236.

[9] Cover, T.M. and Hart, P.E., 1967, Nearest neighbor pattern classification, IEEE Transactions on Information Theory, 13/1: 21-27.

ANALYSIS OF ROTOR BEHAVIOR IN ULTRA-PRECISION HIGH SPEED CUTTING

Timo Dörgeloh[1], Lars Schönemann[1,2],Oltmann Riemer[1], and Ekkard Brinksmeier[1,2]
[1]Leibniz Institute for Materials Engineering IWT, Division Manufacturing Technologies, Badgasteiner Straße 3, 28359 Bremen, Germany
[2]University of Bremen, MAPEX Center for Materials and Processes, Bibliothekstraße 1, 28359 Bremen, Germany

INSTRUCTIONS

For the manufacturing of freeform surfaces, ultra-precision single tooth circumferential milling, also known as raster milling or flycutting, is a proven technology. Naturally, numerous research has already addressed the influences and possibilities to improve the surface finish when using this process. Obviously, process dynamics play an important role in this context. For instance, Zhang and To [1] investigated the influence of cutting force induced spindle vibration on surface finish in ultra-precision raster milling. Marsh et al. [2] studied the effect of structural dynamics and its influence on the workpiece flatness in diamond flycutting. The effect of the workpiece material on surface finish in ultra-precision raster milling was investigated by Wang et al. [3]. So far, all these investigations have one feature in common: they were conducted at cutting velocities $v_c < 1,000\ m/min$. However, by increasing the cutting velocity in ultra-precision machining to $v_c \geq 2,000\,m/min$, various benefits become obvious, as has been proven recently. Brinksmeier et al. [4] identified reduced abrasive tool wear and smaller step heights between grain boundaries as a result of cutting non-ferrous materials at $v_c \geq 2,000\ m/min$. Berger et al. [5] detected superior surface finish in machining monocrystalline silicon with cutting velocities of $v_c \geq 4,000 m/min$. The mentioned studies were part of a larger comprehensive research on "Ultra-Precision High Performance Cutting (UP-HPC)" which aims at reducing primary and secondary process times, inter alia by high speed cutting (HSC) [6] and by designing and using milling tools with multiple cutting edges [7]. However, for cutting at velocities $v_c \geq 2,000\ m/min$ in single tooth radial circumferential milling, either the rotational speed of the air-bearing spindle n or the swing radius r_s of the tool have to be increased significantly. Due to the relatively low axial and radial stiffness of air-bearings in comparison to ball bearings and the quadratic influence of the angular velocity ω on the centrifugal force, the precision balancing of air-bearing spindles is essential to avoid bearing damages. Additionally, an in-situ adjustment of multiple cutting edges on the same swing radius as presented by Schönemann et al. [7] requires a continuous balancing to compensate for changing mass distribution. However, the impact of rotor unbalances on the surface finish and the process behavior in ultra-precision high speed cutting has not been investigated so far. Also, knowledge of the influence of rotor unbalances on rotor displacement is essential for an optimal process control when using tools with multiple cutting edges. Therefore, the influence of various intentionally adjusted residual rotor unbalances U_{res} on the surface finish of non-ferrous metals at high ($v_c \approx 4,000\,m/min$) and low ($v_c \approx 1,000\,m/min$) cutting velocities has been investigated for an air-bearing spindle in this study.

EXPERIMENTAL SETUP

The investigations were carried out on an ultra-precision milling and turning machine (Moore Nanotech 350FG) with an additionally mounted air-bearing spindle (Professional Instruments model ISO 3.375B) on the Z axis. The spindle specifications at 6.9 bar air pressure are shown in Table 1.

TABLE 1. Spindle specifications of applied air-bearing spindle.

Specification	ISO 3.375B
maximum rotational speed n_{max}	$20,000\ min^{-1}$
axial stiffness S_{axial}	$90\ N/\mu m$
radial stiffness S_{radial}	$40\ N/\mu m$
rotor weight m_{rot}	$32\ N$

For the cutting experiments, four non-ferrous metals were selected as workpiece materials (aluminium AlMg3, OFHC copper, brass CuZn39Pb3/MS58 and German silver CuNi18Zn19Pb1/ N37). All specimens ($30 \cdot 20 \cdot 15\ mm^3$) were mounted on the work spindle at the same time using a joint fixture

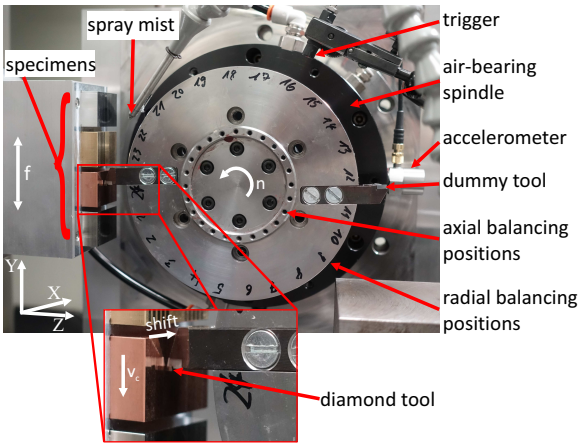

FIGURE 1. Experimental setup with flycutter, mounted workpieces, air-bearing spindle, trigger and accelerometer

(see Fig. 1, left) and were ultra-precision face turned to ensure an even surface plane and thus a constant depth of cut of $a_p = 20\ \mu m$ for the subsequent cutting experiments.
The flycutter (swing radius $r_s = 82\ mm$), which was mounted to the ISO 3.375B spindle for machining the flats, was equipped with two tool holders, one of which holds a single-crystal diamond tool with a nose radius $r_\varepsilon = 0.797\ mm$. The second tool holder holds a "dummy tool" and serves as counter mass for pre-balancing. For precise balancing, the flycutter provides 24 evenly distributed axial M3 and radial M4 screw threads in the front and shell surface, respectively.

The balancing state was detected by a commercial balancing measurement system, based on the influence coefficient method and the use of highly sensitive acceleration sensors with a sensitivity of $1000\,mV/g \pm 10\%$. According to the DIN ISO 21940 11:2016 standard, the balancing quality grade G is defined over a broad range of rotational speeds for various applications and can be calculated by using the following equation [8]:

$$G = e_{per} \cdot \Omega = \frac{U_{per}}{m} \cdot \Omega = const. \qquad (1)$$

where the permissible residual specific unbalance e_{per} can be substituted by the permissible residual unbalance U_{per} over the rotor mass m and is multiplied with the angular velocity Ω. Due to the different specifications and therefore varying dynamic behavior of air-bearing spindles, the use of the balancing quality grade G as a variable in the experiments is considered unsuitable.

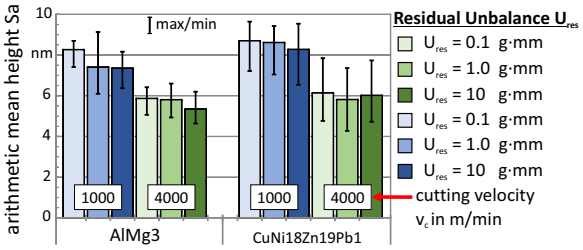

FIGURE 2. Measured surface roughness Sa for machined flats using the ISO 3.375B spindle and intentionally adjusted rotor unbalances for aluminium and German silver.

Hence, the residual unbalance U_{res} is used as a variable, due to its independency of any spindle specification. For the cutting experiments, the residual unbalance U_{res} was intentionally adjusted to $0.1\,g \cdot mm$, $1\,g \cdot mm$ or $10\,g \cdot mm$ for each cutting velocity. The surface finish of each machined flat was measured by using a white light interferometer at three positions along each flat and was processed with an image processing and analysing software.

RESULTS AND DISCUSSION

The results of the experiments using all materials and the ISO 3.375B spindle are quite similar, hence only selected representative results will be shown. In Fig. 2 the arithmetic mean height Sa (applied L-Filter of 80 μm) of the measured surface against the specimen material, cutting velocity v_c and residual unbalance U_{res} is displayed for aluminium and German silver. Each bar in the graph displays the mean of four measurements. The error bars display the maxima and minima of those.
As it can be expected, the arithmetic mean height Sa in Fig. 2 decreases by increasing the cutting velocity v_c from 1000 m/min to 4000 m/min. This is the case for both materials with the amount of decrease being between 22 % and 32 %.
However, an adverse influence of the rotor unbalance on the arithmetic mean height Sa could not be observed in all experiments. Instead, even a decrease of the Sa values with higher unbalances is visible for aluminium for both cutting velocities and German silver at $v_c = 1000\ m/min$, although it is deemed negligible, since the difference is smaller than the spread of Sa values as depicted by the error bars.

The results are surprising as they suggest that spindle unbalances are not affecting the arithmetic mean height Sa significantly in ultra-precision radial fly-cutting. A simple explanation

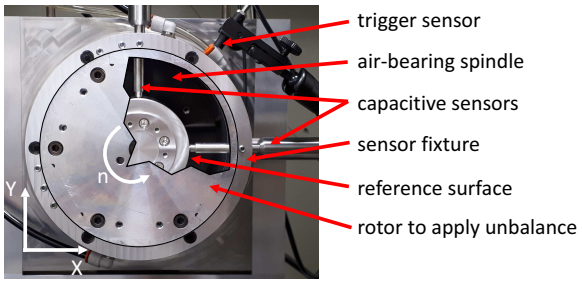

FIGURE 3. Experimental setup for measurement of rotor displacement in X and Y direction after intentionally adjusting of rotor unbalances.

for these results is not obvious, since a greater rotor unbalance should induce greater eccentricities to the rotary centre of mass and therefore, change the spindle error motion as well as induce greater vibrations to the machining system.

For further investigations and to explain these unexpected findings, specific experiments were designed and performed which aimed at directly measuring the rotor displacements induced by the residual unbalances without cutting tool engagement to later simulate a surface generation based on the measured rotor displacement. Similar investigations were already performed for a different air-bearing spindle in Ref. [9] and are here carried out for the first time for the ISO 3.375B air-bearing spindle.

The experimental setup for measuring the rotor displacement is shown in Fig. 3. Highly sensitive capacitive sensors were mounted on a static fixture to detect the rotor displacement in X and Y direction. The sensors were positioned against an ultra-precisely turned reference surface. The cut out area shows the location of the capacitive probes measuring against the reference surface. This element was mounted after the turning operation between the face plate of the spindle and a rotor, to intentionally apply adjusted residual unbalances. For comparability between the displacement measurements and the cutting experiments, the residual unbalance U_{res} was adjusted to $0.1\,g \cdot mm$, $1\,g \cdot mm$ and $10\,g \cdot mm$ as well as the rotational speed met the cutting velocities $v_c = 1000\,m/min$ and $v_c = 4000\,m/min$.

Due to the superimposed noise on the measurement data, the measured rotor displacement was processed by use of the complementary ensemble empirical mode decomposition (CEEMD) [10]. The extractable signal from CEEMD consists of the rotor displacement over multiple rotations with significantly reduced noise and eliminated higher

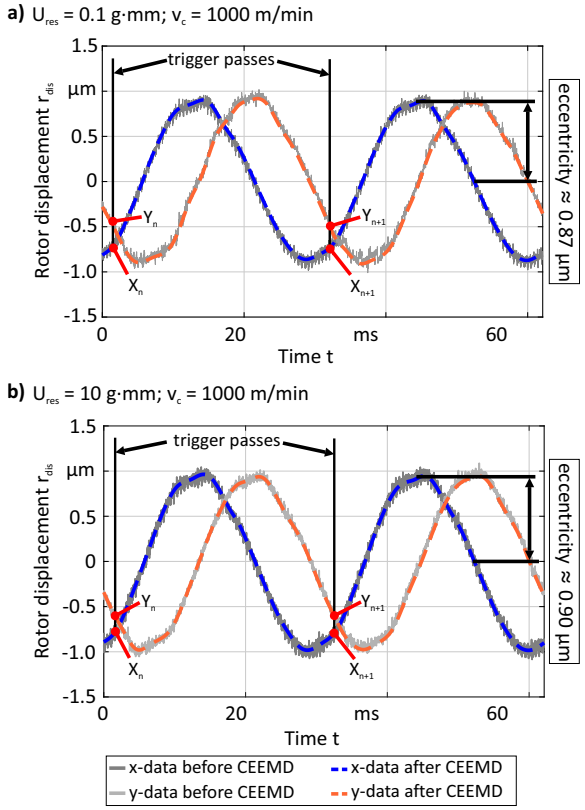

FIGURE 4. Comparison of the recovered rotor displacement signal and the original signal for a) $0.1\,g \cdot mm$, $4000\,m/min$ *and b)* $10\,g \cdot mm$, $4000\,m/min$.

order harmonics (cf. Fig. 4 – X and Y data before and after CEEMD). Nevertheless, the synchronous and asynchronous spindle error motion is intentionally included in the displacement signal. This has been done in separation from the ISO230-7 standard [11], since absolute tool positions are assumed in subsequent simulations and not mean values or relative to them as occurs in the calculation of synchronous and asynchronous spindle error motion, respectively.

The displacement signals in X and Y direction recovered by CEEMD in Fig. 4 a) and b) display an increase of rotor eccentricity from approx. $0.87\,\mu m$ to $0.90\,\mu m$ for an increased residual unbalance from $0.1\,g \cdot mm$ to $10\,g \cdot mm$ at $1000\,m/min$. This is consistent to the theory, since higher unbalances result in higher centrifugal forces, hence in increased eccentricities of the rotor. Since in the flycutting process only one tool is used, a greater eccentricity results obviously in an enlargement of the tool swing radius. However, the eccentricity is not static and changes with each further rotation which shifts the contact

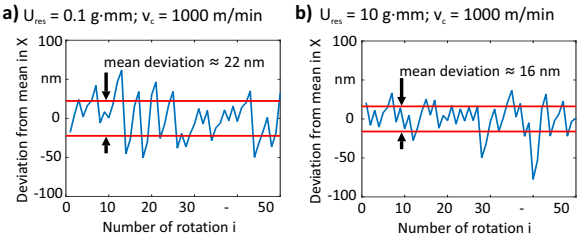
a) U_res = 0.1 g·mm; v_c = 1000 m/min
b) U_res = 10 g·mm; v_c = 1000 m/min
mean deviation ≈ 22 nm
mean deviation ≈ 16 nm
Deviation from mean in X
nm
Number of rotation i

FIGURE 5. Deviation in eccentricity at a) U_{res} = 0.1 $g \cdot mm$ and b) U_{res} = 10 $g \cdot mm$ for a calculated cutting velocity of v_c = 4000 m/min.

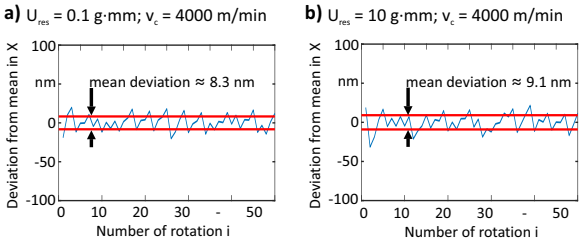
a) U_res = 0.1 g·mm; v_c = 4000 m/min
b) U_res = 10 g·mm; v_c = 4000 m/min
mean deviation ≈ 8.3 nm
mean deviation ≈ 9.1 nm
Deviation from mean in X
nm
Number of rotation i

FIGURE 6. Deviation in eccentricity at a) U_{res} = 0.1 $g \cdot mm$ and b) U_{res} = 10 $g \cdot mm$ for a cutting velocity of v_c = 4000 m/min.

point between tool and workpiece continuously.

To determine the deviation of the eccentricity, the trigger pass position is used to determine the X and Y value in the recovered displacement signals at this position. This position will be defined as point of contact between tool and workpiece in the following surface generation simulations.

In Fig. 4 a) and b) X_n, Y_n, X_{n+1} and Y_{n+1} depict the positions of detection, extracted for each rotation in the recovered signal. The detected values in X direction of multiple rotations for 0.1 $g \cdot mm$ and 10 $g \cdot mm$, both at 1000 m/min, are displayed in Fig. 5 a) and b) (blue line), respectively. The data in Fig. 5 a) and b) show a decrease of the mean deviation of the eccentricity change in X direction from 22 nm at 0.1 $g \cdot mm$ to 16 nm at 10 $g \cdot mm$. The Y data are processed similar but not presented in this paper. They show a mean deviation of 37 nm and 36 nm for 0.1 $g \cdot mm$ and 10 $g \cdot mm$, respectively.

In Fig. 6 the deviation in eccentricity at the trigger pass positions are shown for the X direction at a) U_{res} = 0.1 $g \cdot mm$ and b) U_{res} = 10 $g \cdot mm$, both at v_c = 4000 m/min. The results in Fig. 6 indicate significantly lower deviation in X direction for v_c = 4000 m/min than in Fig. 5 for v_c = 1000 m/min. At U_{res} = 0.1 $g \cdot mm$ the mean deviation of the eccentricity calculates to 8.3 nm and at U_{res} = 10 $g \cdot mm$ to 9.1 nm. The mean deviation in the Y direction increases from 28 nm for U_{res} = 0.1 $g \cdot mm$ to 35 nm for U_{res} = 10 $g \cdot mm$ at 4000 m/min. This is different to the mean deviation at 1000 m/min where the changes in the Y direction are negligible.

In order to verify the impact of the unbalance-induced rotor displacement on the machining process, the resulting surface was calculated numerically using a geometric model of a milling process. For this, the milling tool was modelled as a torus, featuring the swing radius of the milling tool (r_s = 82 mm) as its primary and the nose radius of the tool (r_ε = 0.792 mm) as its secondary radius. This torus was positioned to intersect with a planar surface at equidistant intervals defined by the feed and the raster spacing (f = 80 μm and s = 8 μm, respectively) while the difference to the previous result was kept for the subsequent iteration. In addition to the "perfect" motion of the tool (no spindle error motion), which results in a nominal value of Sa = 3.44 nm, the disturbance caused by the rotor displacement was introduced as a deviation in feed and infeed direction. For this, the calculated absolute eccentricity and the changes in X and Y direction were used. The resulting surfaces are shown in Fig. 7.

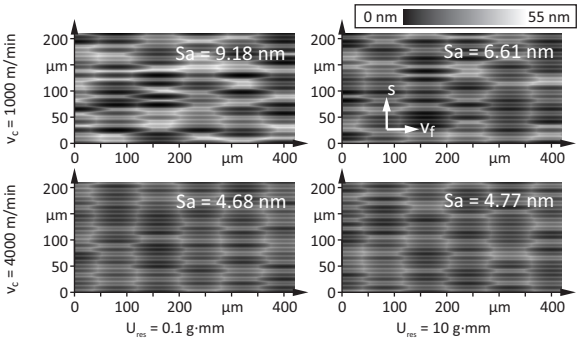

FIGURE 7. Simulated surface geometry considering the calculated tool positions for selected cutting speeds and unbalances.

The larger deviations in the measured displacement signals for the low cutting speeds cause a considerable deviation of the cutting depth, which is expressed by an increase of the surface roughness to Sa = 9.18 nm and 6.61 nm (with detected spindle error motion). The spindle error motion at higher spindle speeds turns out to be lower, thus the simulated surfaces feature a more regular pattern and a lower surface roughness ($Sa \approx$ 4.7 nm). As a result a significant effect of the unbalance cannot be derived from the simulations, which is consistent with the previous cutting experiments (cf. Fig. 2).

These unexpected results of the cutting experiments and the subsequent surface generation simulations have multiple reasons, some of which are listed here:

1. The magnitude of the eccentricity caused by the unbalance is only of minor importance in single-tool diamond milling, because the point of contact to the workpiece always occurs at the same angle, i.e. with the same eccentricity. Thus, the disturbance of the process is primarily caused by the deviation (noise) of the eccentricity.

2. According to Dupont, the bearing stiffness of air-bearings increases with increasing rotor eccentricity [12]. The reason is that an increasing centrifugal force, induced by an increased unbalance or rotational speed, results in a reduced air gap of the air-bearing. Hence, the air will be compressed and the stiffness increased. Although the eccentricity is only minimally changed by the unbalance, this seems to have a positive influence on the micro scale for a flycutting process with one single-tool.

3. The reduced contact time between cutting tool and workpiece at $v_c = 4000\,m/min$ in comparison to $v_c = 1000\,m/min$ leads to a reduced impact time of cutting forces to the rotor and thus decreasing the displacement. Therefore the cutting process is influenced to such an extent that with the same mass inertia, the increased cutting speed leads to a situation where the rotor is not stimulated to any significant displacement.

CONCLUSION AND OUTLOOK

In this paper, the relevance of spindle unbalance in ultra-precision high speed cutting has been investigated. Multiple cutting experiments with an air-bearing spindle and various process parameters have been carried out and the machined surfaces were analysed. The results indicate that the most influencing factor of the surface generation in ultra-precision single tooth circumferential milling is the cutting velocity v_c, which is consistent to further conducted surface generation simulations by the use of directly measured rotor displacement data. An effect of the rotor unbalance on the surface generation cannot be derived from these results. However, the rotor unbalance has a significant influence on the spindle error motion, which could be important for applications using multiple cutting edges as presented in Ref. [7]. A Possible explanation for the shown results is that an increased rotor eccentricity, which has minor influence on the surface generation than the deviation of it, increases the air-bearing stiffness, which in turn leads to a lower susceptibility from the cutting process.

ACKNOWLEDGMENTS

The authors thank the German Research Foundation (DFG) for funding this work as part of the subproject “Balancing of spindles for ultra-precision high-speed milling” within the research unit FOR1845 “Ultraprecision High Performance Cutting”.

REFERENCES

[1] Zhang SJ, To S (2013) A theoretical and experimental study of surface generation under spindle vibration in ultra-precision raster milling. International Journal of Machine Tools and Manufacture, 75:36-45.

[2] Marsh E, Arneson D, Blystone S, Van Doren M, Vallance R (2005) The Effects of Spindle Dynamics on Precision Flycutting. Proceedings of the American society for precision engineering.

[3] Wang SJ, To S, Cheung CF (2012) Effect of workpiece material on surface roughness in ultraprecision raster milling. Materials and Manufacturing Processes, 27(10):1022-1028.

[4] Brinksmeier E, Preuss W, Riemer O, Rentsch R, 2017, Cutting forces, tool wear and surface finish in high speed diamond machining. Precision Engineering, 49:293-304.

[5] Berger D, Schönemann L, Riemer O, Brinksmeier E (2018) High Speed Cutting of Monocrystalline Silicon by Offaxis Diamond Turning, 33rd ASPE annual meeting, 70:184-189.

[6] Brinksmeier E, Riemer O, Schönemann L (2015) High performance cutting for ultra-precision machining. International Journal of Nanomanufacturing, 11:245-260.

[7] Schönemann L, Riemer O (2019) Thermo-mechanical tool setting mechanism for ultra-precision milling with multiple cutting edges. Precision Engineering, 55:171-178.

[8] International Standard. ISO 21940-11:2016. Mechanical vibration – Rotor balancing – Part 11: Procedures and tolerances for rotors with rigid behaviour. 2016.

[9] Cao H, Dörgeloh T, Riemer O, Brinksmeier E (2017) Adaptive Separation of Unbalance Vibration in Air Bearing Spindles. Procedia CIRP, 62: 357-362.

[10] Yeh J-R, Shieh J-S, Huang NE (2010) Complementary ensemble empirical mode decomposition: A novel noise enhanced data analysis method. Advances in Adaptive Data Analysis, 02(02):135-156.

[11] International Standard. ISO 230-7:2015(E). Test code for machine tools – Part 7: Geometric accuracy of axes of rotation. 2015.

[12] Dupont R (2003) On an isotropic and centrifugal force invariant layout of a conically shaped gas-lubricated high-speed spiral-groove bearing. Precision Engineering, 27(4):346-361.

SCULPTURING OF COLORED BASSO-RELIEVO WITH ELLIPTICAL VIBRATION TEXTURING

Jianjian Wang[1, 2], Yang Yang[2], Wei-Hsin Liao[2] and Ping Guo[1,*]

[1] Department of Mechanical Engineering, Northwestern University, Evanston, IL, USA
[2] Department of Mechanical and Automation Engineering, The Chinese University of Hong Kong, Hong Kong, China

INTRODUCTION

Basso-relievo refers to the sculptural relief with a very shallow image extended from the background. Colored basso-relievo fabricated on the metal surface is well-received for functional decoration. The fabrication of colored basso-relievo usually replies on a multiple-steps procedure to create concave-convex topography and surface color step by step. The concave-convex topography of basso-relievo is firstly sculptured out through milling [1], and then the surface color is produced by pigmented coloration. In addition to the pigmented coloration, structural coloration is another widely involved principle of color production in our nature [2], which utilizes micro/nanostructured surfaces to manipulate the visible lights through diffraction, interference, and scattering [3]. Structural coloration shows unique visual effects compared with pigmented coloration; it is more dazzling, brighter, and has the viewing-angle dependent iridescent effect [4]. Inspired by nature, structural coloration has an array of breakthrough applications in decoration, anti-counterfeiting, information storage, etc. [5]. It is promising to apply the structural coloration to the colored basso-relievo for new functional performance.

To provide structural coloration, several kinds of artificial methods are used for fabrication of micro/nanostructures on metal, including lithography [6], femtosecond laser-induced periodically structuring (LIPSS) [7]. Lithography is highly productive for mass replication, but it is limited in the capacity to texture a continuously covered surface, thus not suitable for the structurally colorizing of concave-convex basso-relievo. The LIPSS can texture various kinds of metal surfaces suitable for colorizing the basso-relievo surface after the milling process. However, the LIPSS suffers from low color quality due to the semi-random nature of the structures, and it is too expensive for industrial application due to the high cost of a femtosecond laser system. Recently, elliptical vibration texturing, which is a kind of metal cutting method, has also been successfully applied in the structural coloration of metal surfaces [8]. In elliptical vibration texturing, the diamond cutter vibrates with an elliptical shape under a nominal cutting speed to form overlapping trajectories, which can generate conjunctive micro-structures of near-subwavelength [9]. Compared with LIPSS, elliptical vibration texturing is cost-effective, and highly flexible due to its capacity to texture large-area and freeform surfaces without changing the material properties. Moreover, elliptical vibration texturing has the potential to sculpture colored basso-relievo in one-step due to its nature of cutting.

This study is to investigate the feasibility of utilizing a modulated elliptical vibration texturing process to fabricate colored basso-relievo in one step by substituting the conventional milling process. The depth-of-cut and nominal cutting speed in elliptical vibration texturing are controllably modulated to provide structural coloration and concave-convex visual effect synergistically.

PROCESS PRINCIPLE

The principle of the proposed sculpturing process of colored basso-relievo can be mainly ascribed to the synergistic modulation of depth-of-cut and nominal cutting speed in elliptical vibration texturing, as shown in FIGURE 1(a). The modulation of depth-of-cut is used to adjust the relative height variation of microgrooves to provide the concave-convex visual effect of basso-relievo as illustrated in FIGURE 1(b). Meanwhile, the modulation of nominal cutting speed is used to generate microgrooves with

controllable spacing distances, which can serve as gratings to diffract the visible lights to provide structural color. The spacing distance d of the microgrooves is controlled by the nominal cutting speed V_c at a fixed vibration frequency f as:

$$d = \frac{V_c}{f} \tag{1}$$

According to the principle of light diffraction, as shown in FIGURE 1(c), the relationship between the incident angle θ_i and diffractive angle θ_k of light with a wavelength λ can be expressed as:

$$\lambda = \frac{d \cdot (\sin\theta_k + \sin\theta_i)}{K} \tag{2}$$

where K is the order of diffraction. In this study, considering the balance between energy loss in spectral reflection and the angular dispersion, the incident angle is fixed to be 45º, and K is assumed to be 1. Notably, when the observing direction is rightly perpendicular to the machined surface (θ_k = 0º), Eq.(2) can be reduced to $d = \sqrt{2}\lambda$.

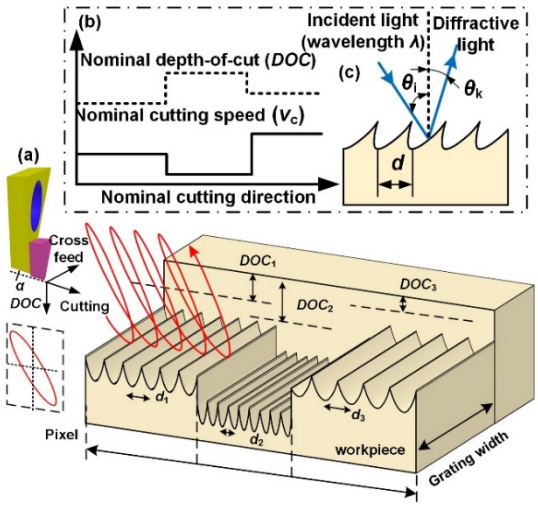

FIGURE 1. Illustration of basso-relievo fabrication using elliptical vibration texturing. (a) Process principle; (b) modulation of cutting speed and depth-of-cut (DOC); (c) grating diffraction.

EXPERIMENTAL SETUP

The procedure for sculpturing a colored basso-relievo from a 3D image is illustrated in FIGURE 2. A colored 3D model can be developed according to the customized requirement of visual effects using a professorial software-JD painting. The colored 3D model consists of the information of relative height variation and colors of every pixel. Using JD painting, the height variation information can be exported as a 2D grayscale image, while color information can be exported as a 2D colored image. The grayscale image is expressed using a matrix *Gray*(*X, Y*), which can be used to control the modulation of depth-of-cut through a function g1. On the other hand, the hue axis of color information (HSV) of the 2D colored image can be expressed using a matrix *Hue*(*X, Y*) [10], which can be used to control the modulation of nominal cutting speed through a function g_2. g_1 and g_2 can be expressed as:

$$\begin{cases} g_1 : DOC(X,Y) = DOC_{\max}\left(1 - Gray(X,Y)/255\right) \\ g_2 : V_c(X,Y) = \sqrt{2}\cdot\lambda\left(Hue(X,Y)\right)\cdot f \end{cases} \tag{3}$$

where (X, Y) is the pixel coordinate; $DOC(X, Y)$ is the depth-of-cut of an individual pixel; DOC_{max} is the maximum height variation of basso-relievo. g_2 is obtained based on Eq. (1) and Eq. (2) when K=1, θ_i=45º, θ_k=0º. $\lambda(Hue)$ establishes the relationship between the image hue and the wavelength of diffractive light [10].

$$\lambda(Hue) = \begin{cases} -0.26\cdot Hue + 0.64 & Hue \in [0, 0.9) \\ 0.7 Hue + 0.01 & Hue \in [0.9, 1) \end{cases} \tag{4}$$

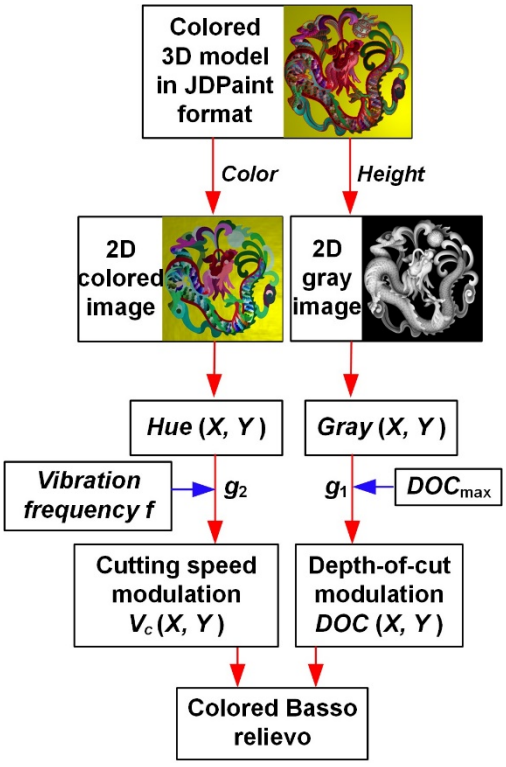

FIGURE 2. 3D Image rendering process.

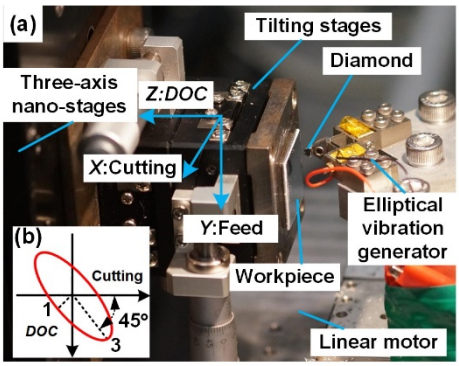

FIGURE 3. (a) Experimental setup; (b) designed elliptical trajectory when f=4 kHz.

The experimental setup is shown in FIGURE 3. The sculpturing test is performed on an ultraprecision motion platform, which consists of a linear motor (ACT165DL, Aerotech, USA) and a three-axis nano-stages (ANT130LZ-060 and ANT130XY, Aerotech, USA). The elliptical vibration of the diamond cutter is generated using an ultrafast non-resonant elliptical vibration generator, which has a frequency bandwidth of 6 kHz with a full stroke of 10 μm ×15 μm. The ultrafast 2-D vibration cutting tool is mounted on the linear motor. The aluminum workpiece is mounted on a three-axis nano-stage through a two-degree-of-freedom tilt stage, which is used for level adjustment with the help of a capacitance displacement sensor. The linear motor is used to control the modulation of nominal cutting speed of the tool with a position-velocity-time interpolation method [10], while the three-axis nano-stage is used to control the modulation of depth-of-cut and to provide feed motion.

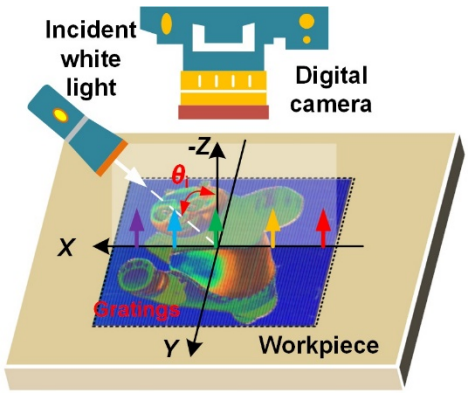

FIGURE 4. Optical system for image observation.

The diamond cutter used for cutting in this study has a nose radius of 500 μm, a rake angle of 12º and a clearance angle of 10º. The adopted elliptical vibration trajectory (f =4 kHz) is shown in FIGURE 3(b). According to Eq. (3) and Eq. (4), when f = 4 kHz, the nominal cutting speed range can be determeind to be from 2.3 to 4.0 mm/s, which characterizes the writing speed for the sculpturing and coloration process. An optical system, which is illustrated in FIGURE 4, is used to observe the rendered images, where the observing direction is perpendicular to the machined surface.

RESULTS AND DISCUSSION

We compared the visual effects of sculptured basso-relievo between without and with depth-of-cut modulation (DOC_{max} = 10 μm, cross feed = 30 μm, pixel length = 30 μm). As shown in FIGURE 5(c), with the depth-of-cut modulation, colored basso-relieve can be produced presenting both the concave-convex and colorful visual effects. Compared with the results in FIGURE 5(a) and (b) that only show the structural coloration or the concave-convex basso-relievo respectively, the colored basso-relievo in FIGURE 5(c) is more stimulating and eye-catching. The results in FIGURE 5 verify the feasibility of the proposed one-step sculpturing method for the fabrication of colored basso-relievo with the utilization of elliptical vibration texturing. We then demonstrate more results of machined colored basso-relievos, as shown in FIGURE 6.

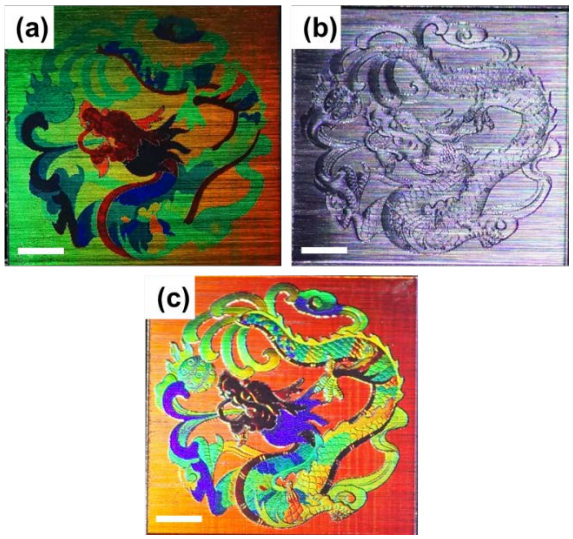

FIGURE 5. Comparison between without and with depth-of-cut (DOC) modulation (scale bar = 2 mm). (a) Without DOC modulation (θ_i = 45°); (b) with DOC modulation (θ_i = 90°); (c) with DOC modulation (θ_i = 45°).

The proposed sculpturing method is aiming at the fabrication of colored basso-relievo on metals.

Due to the low machinability of polymer to get acceptable surface integrity, which is another widely used material in the industry and consumer products, the proposed sculpturing method cannot be used to fabricate colored basso-relievo on polymer. However, using the proposed sculpturing method, we can fabricate colored intaglio on metals, by modifying the '-' to '+' in the expression of g_1 in Eq. (3), we can fabricate colored intaglio on metals, which be used as a die for injection molding to manufacture colored basso-relievos on polymers.

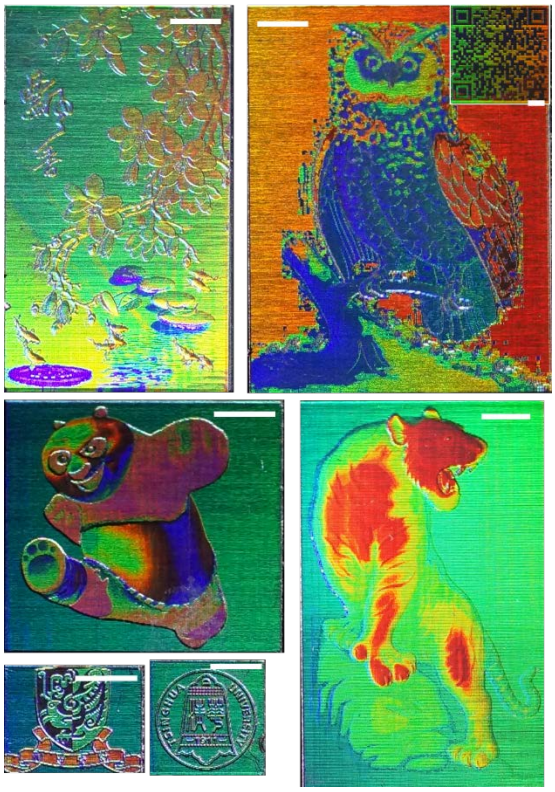

FIGURE 6. Results of basso-relievo sculpturing on aluminum (scale bar = 2 mm).

CONCLUSION

This study proposed a one-step sculpturing process for the fabrication of colored-basso-relievo on metal by modulating the depth-of-cut and nominal cutting speed in elliptical vibration texturing. The modulation of nominal cutting speed can generate grating-type microgrooves with controllable spacing distances to provide vivid structural coloration, while the modulation of depth-of-cut can provide the concave-convex visual effect on the metal surface. Sculpturing tests with a line writing speed of 2.3~4.0 mm/s on aluminum verified the feasibility of the process.

ACKNOWLEDGMENTS

This research was supported by the start-up fund from McCormick School of Engineering, Northwestern University, Evanston, IL, USA; and the Innovation and Technology Fund, Hong Kong, #ITS/076/17.

REFERENCES

[1] Tunc L T. Smart tool path generation for 5-axis ball-end milling of sculptured surfaces using process models. Robotics and Computer-Integrated Manufacturing. 2019; 56: 212-221.

[2] Williams T L, Senft S L, Yeo J, et al. Dynamic pigmentary and structural coloration within cephalopod chromatophore organs. Nature communications. 2019; 10(1): 1004.

[3] Sun J, Bhushan B, Tong J. Structural coloration in nature. RSC Advances. 2013; 3: 3(35): 14862-14889.

[4] Andreeva Y M, Luong V C, Lutoshina D S, et al. Laser coloration of metals in visual art and design. Optical Materials Express, 2019, 9(3): 1310-1319.

[5] Zhao Y, Zhao Y, Hu S, et al. Artificial structural color pixels: A review. Materials. 2017; 10(8): 944.

[6] Wu H, Jiao Y, Zhang C, et al. Large area metal micro-/nano-groove arrays with both structural color and anisotropic wetting fabricated by one-step focused laser interference lithography. Nanoscale. 2019; 11(11): 4803-4810.

[7] Müller F, Kunz C, Gräf S. Bio-inspired functional surfaces based on laser-induced periodic surface structures. Materials. 2016; 9(6): 476.

[8] Yang Y, Pan Y, Guo P. Structural coloration of metallic surfaces with micro/nano-structures induced by elliptical vibration texturing. Applied Surface Science. 2017; 402: 400-409.

[9] Guo P, Ehmann K F. An analysis of the surface generation mechanics of the elliptical vibration texturing process. International Journal of Machine Tools and Manufacture. 2013; 64: 85-95.

[10] Yang Y, Guo P. Global tool path optimization of high-resolution image reproduction in ultrasonic modulation cutting for structural coloration. International Journal of Machine Tools and Manufacture. 2019; 138: 14-26.

High-efficiency planarization of GaN wafer by catalyst-referred etching with positive-biased photo-electrochemical oxidation

Ryosuke Ohnishi[1], Daisetsu Toh[1], Satoshi Matsuyama[1], Ai Isohashi[2], Yasuhisa Sano[1] and Kazuto Yamauchi[1,3]
[1]Department of Precision Science and technology
Graduate school of Engineering, Osaka University
Suita, Osaka, Japan
[2]Nanoscience and Nanotechnology Center
Institute of Scientific and Industrial Research, Osaka University
Ibaraki, Osaka, Japan
[3]Research Center of Ultra-Precision Science and Technology
Graduate School of Engineering, Osaka University
Suita, Osaka, Japan

INSTRUCTIONS

Gallium nitride (GaN) has excellent physical properties such as wide bandgap, high breakdown field, and high thermal conductivity and has applications not only in light-emitting devices but also for power control devices. In order to produce devices with a theoretically expected performance, atomically well-ordered surface is required. We developed a novel polishing method called catalyst-referred etching (CARE). Here, pure water and Pt are used as an etchant and a catalyst, respectively. A Pt firm is deposited on an elastic pad surface as a catalyst to induce the etching reaction. The substrate surface is pushed onto the catalyzed pad and slid on it. In this configuration, topmost sites on the substrate are preferentially etched off [1-3] because such sites are in contact with the catalyst surface more frequently as indicated in Figure 1. Using this method, we obtain highly a geometrically and crystallographically ordered surface with a step-terrace structure on GaN, as shown in Figure 2 [4]. This characteristic means that the removal proceeds as a step-flow etching, and the accordingly the removal rate depends on the step density.

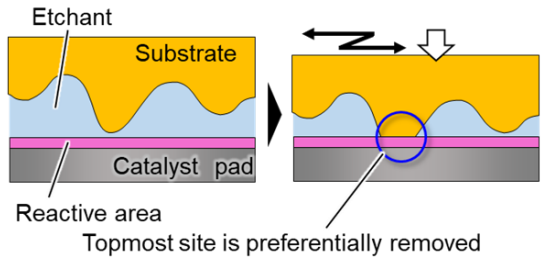

FIGURE 1. Conceptual diagram of CARE

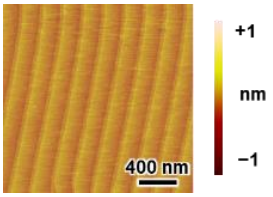

FIGURE 2. AFM image of GaN (0001) surface after CARE. We obtain an ordered surface with a step-terrace structure on GaN surface.

In this research, to enhance the removal rate, we tried to increase the step density by using photo-electrochemical (PEC) oxidation during CARE which is called PEC-CARE. In this method, the GaN surface is irradiated by ultraviolet (UV) light which has photon energy higher than the bandgap energy of GaN and generates electron-hole pairs in the surface layer. The hole generated can assist the surface oxidation, which can be represented by the following chemical equation [5]:

$$2GaN + 6OH^- + 6h^+ \rightarrow Ga_2O_3 + N_2 + 3H_2O$$

Atomic scale oxidations proceed even on the terrace, and atomically oxidized sites are quickly removed due to the higher removal rate of the oxide. Peripheral sites of the atomic pit as a foot print of the oxidation act as a new reaction site to be a newly introduced atomic step. In our previous research, the removal rate of the PEC-CARE was about 100 times higher than that of the CARE that did not use UV irradiation [6]. However, in some cases, we cannot remove the surface roughness due to a crystallographic ununiformity on the GaN surface. Figure 3(a) is the height distribution on a roughened surface

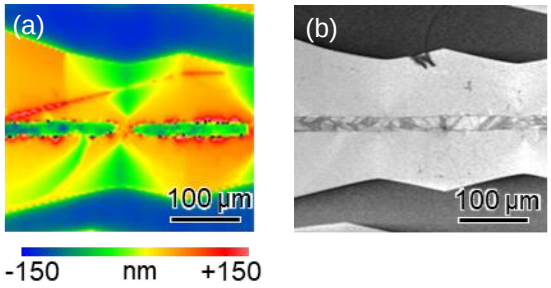

FIGURE 3. (a) Ununiformity removal rate depending on crystallographical characteristics. In PEC-CARE processing. (b) CL image of the same position. Removal rates and CL properties are strongly correlated.

during PEC-CARE, and Figure 3(b) shows the intensity map of the light emission obtained by a cathode luminescence (CL) measurement on the same surface, as shown in Fig. 3(a). The light emission intensity relates to concentrations of oxygen impurity. The dark area in Fig. 3(b) represents the area of low oxygen concentration, the fluctuation of which is induced by a mode difference of the crystal growth. The oxygen concentration is low in the case of c-axis oriented growth. Surfaces of GaN substrates comprise different crystallographic areas, the growth modes of which are different. The removal rates in the PEC-CARE strongly depend on the oxygen concentration, evidenced by the correlation between the images of Fig.3 (a) and (b), and the oxygen acts as a donor in GaN. The photochemical oxidation rate becomes higher as the donor concentration decreases.

A NEW PROPOSAL of BPEC-CARE

Figure 4 shows a conceptual diagram of the band structure of GaN surface in a water solution. The width of depletion layer varies depending on the donor concentration. The depletion layer becomes thicker with decreasing donor concentration. On the other hand, the holes generated in the depletion layer can drift to the surface, assisted by the electric field in the layer. Accordingly, removal rates become higher at the area, the depletion layer of which is thicker. Based on this understanding, we propose an application of positive bias to the GaN surface during PEC-CARE. In the case of no bias, the number of holes drifting to the surface fluctuates depending on the donor concentration as understood from Fig.4 (a). In contrast, under the sufficiently positive-biased condition, the depletion layer expands to be sufficiently thicker than the penetration depth of UV light. The

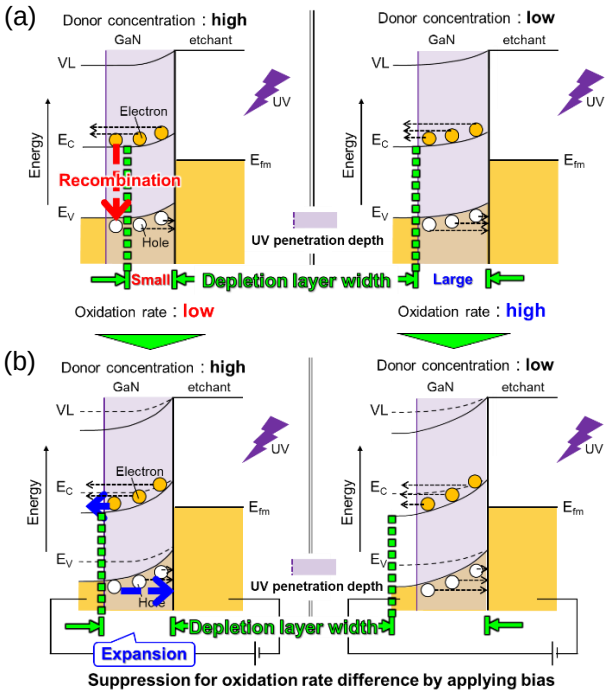

FIGURE 4. Conceptual diagram of band structure of GaN in solution when the surface is irradiated by ultraviolet. (a) In the case of no applied voltage, the number of holes drifting to the surface depends on the width of the depletion layer. (b) In the case with bias voltage to extend the depletion layer width thicker than the penetration depth of UV light, the number of holes drifting to the surface becomes equal to suppress the fluctuation of oxidation rate.

number of the photo-generated holes, which drift to the surface, becomes equal independently of the donor concentration. Positive bias application during UV light irradiation can suppress the fluctuation of oxidation rate. We named the modified method biased PEC-CARE (BPEC-CARE).

EXPERIMENTAL SETUP

The processing conditions are listed in Table 1. Figure 5 shows the schematic of a BPEC-CARE system. The polishing pad has many holes, through which UV light irradiates the GaN surface. The Pt wire is placed under the pad to work as a cathode. The GaN surface is positively biased against the Pt wire.

TABLE 1. Processing conditions

Sumple	HVPE or Na flux on point seeds
Catalyst	Pt
Process pressure	40 kPa
Rotation speed	15 rpm
Etchant	PBS (Ga ion additive)
Power of UV lamp	0.8 mW/cm^2

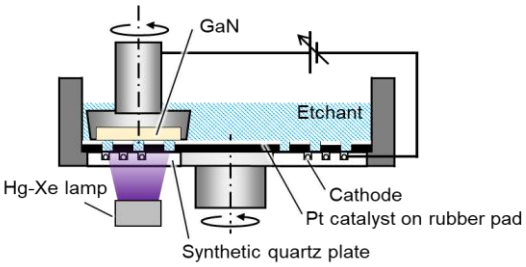

FIGURE 5. Schematic of BPEC-CARE apparatus. The substrate was pressed against the catalyst pad. The substrate and polishing pad rotate independently.

EMPLOYED GaN SUBSTRATE

In recent years, various crystal growth methods have been developed. In these methods, HVPE (Hydride vapor phase epitaxy) and Na-flux methods have received attention. The HVPE method is suitable for the mass production because the growth rate is much higher than other techniques. Na-flux method can realize GaN substrate with large diameters and low dislocation concentration. We employed GaN substrates prepared by these two methods, the properties of which are summarized in Table 2.

TABLE 2. Comparison of leading methods for growth of GaN crystals.

	HVPE	Na-flux on point seed
Growth rate (μm/h)	> 200	10~40
Dislocation density (cm^{-2})	10^5~10^6	10^2~10^5
Dopant density (cm^{-3})	10^{16}~10^{18}	10^{17}~10^{19}
Wafer size (inch)	4	8

RESULT

Figure 6(a) and (b) are the surface profiles after BPEC-CARE processing of GaN substrates prepared by HVPE and Na-flux methods, respectively. On the substrate prepared by the HVPE method, a flat surface was obtained by the BPEC-CARE under a bias voltage of 1.5 V. This means that the oxidation rate fluctuation could be suppressed by applying the positive bias, and 1.5V is considered to be high enough to expand the depletion layer to be thicker than the penetration depth of UV light. In contrast, on the substrate grown by Na-flax method, removal rate still fluctuates, and surface is not flattened even with a higher bias of 3V. These results reveal an application limitation of this method to extremely high donor concentration cases. We discuss the application limitation of this method quantitatively and propose improvements in the next session.

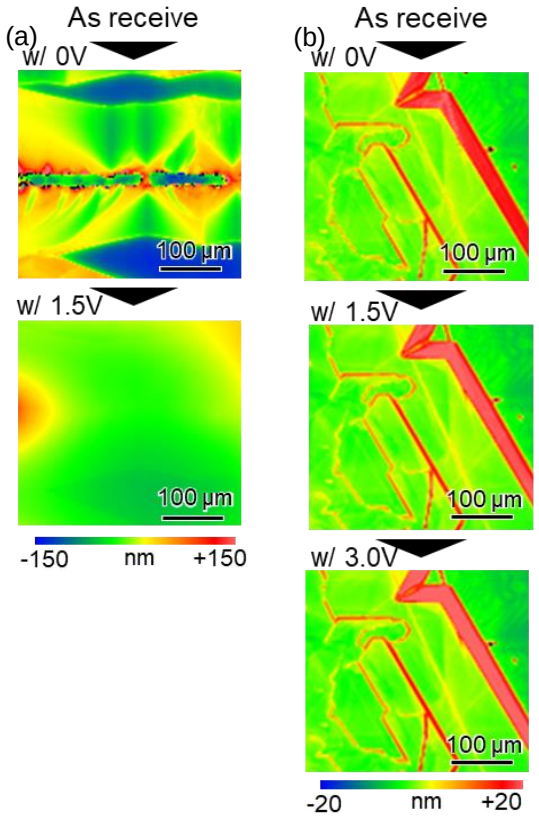

FIGURE 6. Interferometer images after BPEC-CARE: (a) HVPE GaN, (b) Na-flux GaN on point seeds.

CONSIDERATION

As mentioned above, to suppress the ununiformity of oxidation rate, the depletion layer must be thicker than the penetration depth of UV light without depending on the donor concentration. The width of depletion layer is expressed by following equation [7]:

$$W = \sqrt{\frac{2\varepsilon_s\varepsilon_0}{eN_D}(V_D + V)} \qquad (1)$$

ε_s : Specific dielectric
ε_0 : Dielectric constant under vacuum (Fm^{-1})
V_D : Diffusion potential (V)
V : Applying voltage (V)
e : Elementary electrical charge (C)
N_D : Dopant density (m^{-3})

In the equation, we see that the depletion layer becomes thinner as the donor concentration becomes higher. The degree of expansion of depletion layer by positive bias is also lower. The penetration depth of UV light is expressed by following equation:

$$I(x) = I(0)\exp(-\alpha x) \qquad (2)$$

$I(x)$: Light intensity at depth of x
α : Absorbance coefficient (cm^{-1})

The penetration depth is defined as x satisfying $I(x)/I(0)$ =1/e. The penetration depth at the absorption edge of GaN (364 nm) is 75 nm [8]. The depletion layer widths in the 3 different donor concentrations are calculated with a function of bias voltage using eq. (1) and shown in Fig. 7. Curves of (a), (b), and (c) relate to areas of HVPE GaN with a donor concentration (oxygen concentration) of $4x10^{17}$ cm^{-3}, lower concentration area on Na-flux GaN with $7x10^{17}$ cm^{-3}, and higher concentration area on the Na-flux GaN with $1x10^{19}$ cm^{-3}. In areas (a) and (b), the depletion layer becomes sufficiently thicker than the penetration depth of UV light under appropriate positive bias, such as 1V for the area (a) and 3V for the area (b). In contrast, in the area (c), the depletion layer is still thinner than the penetration depth. Although a much larger bias can expand the depletion layer, it is not ideal to apply such a large bias to avoid gaseous products that disturb the process conditions. To solve this problem, we attempt to reduce the penetration depth to be shallower than the width of depletion layer by employing UV light with shorter wavelength. As an instrumental modification, a high-pass filter, through which short wavelength UV light can pass, is planned to be installed.

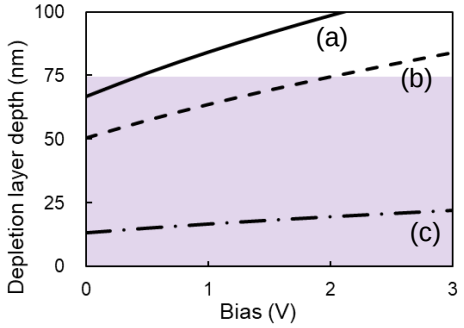

FIGURE 7. Estimated depletion layer width: (a) HVPE GaN with a donor concentration (oxygen concentration) of $4x10^{17}$ cm^{-3}, (b) smaller concentration area on Na-flux GaN with $7x10^{17}$ cm^{-3}, (c) higher concentration area on Na-flux GaN with $1x10^{19}$ cm^{-3}. Penetration depth of the UV light is 75 nm or less where the photoexcitation occurs.

CONCLUSION

Ununiformity of the removal rate in PEC-CARE is caused by the oxidation rate fluctuation due to the donor concentration difference. We proposed a positively biased PEC-CARE named BPEC-CARE to suppress the fluctuation. In the case that the donor concentration is not so high such as lower than $1x10^{18}$ cm^{-3}, the removal rate fluctuation could be completely suppressed. However, in the case that the donor concentration is higher, the depletion layer could not be expanded sufficiently, and the removal rate of the BPEC-CARE still fluctuates. To solve this problem, we attempt to reduce the penetration depth of UV light by employing shorter wavelength UV light.

REFERENCES

[1] H. Hara, Y. Sano, H. Mimura, K. Arima, A. Kubota, K. Yagi, et al. Novel abrasive-free planarization of 4H-SiC (0001) using catalyst. J. Electron. Mater. 2006; 35: 11-14.

[2] K. Arima, H. Hara, J. Murata, T. Ishida, R. Okamoto, K. Yagi, et al. Appl. Phys. Lett. Atomic-scale flattening of SiC surfaces by electroless chemical etching in HF solution with Pt catalyst. 2007; 90: 202106.

[3] P. V. Bui, A. Isohashi, H. Kizaki, Y. Sano, K. Yamauchi, Y. Morikawa. Appl. Phys. Lett. Study on the mechanism of platinum-assisted hydrofluoric acid etching of SiC using density functional theory calculations. 2015; 107: 201601.

[4] J. Murata, S. Sadakuni, T. Okamoto, A. N. Hattori, K. Yagi, Y. Sano, et al. J. Crystal Growth. Structural and chemical characteristics of atomically smooth GaN surfacesprepared by abrasive-free polishing with Pt catalyst. 2012; 349: 83-88.

[5] G. Nowak, X. H. Xia, J. J. Kelly, J. L. Weyher and S. Porowski. J. Cryst. Growth. Electrochemical etching of highly conductive GaN single crystals. 2001; 222: 735.

[6] S. Sadakuni, J. Murata, K. Yagi, Y. Sano, K. Arima, A. N. Hattori, et al. Material Science Forum. Influence of the UV Light Intensity on the Photoelectrochemical Planarization Technique for Gallium Nitride. 2009; 645: 795-798.

[7] R. Sakata. Busseikagaku. Baifukan, editor. 1989.

[8] G. Yu, G. Wang, H. Ishikawa, M. Umeno, T. Soga, T. Egawa, et al. Appl. Phys. Lett. 1997; 70: 3209-3211.

FABRICATION OF EDGE-LIT LIGHT GUIDE TOOLING BY SURFACE STRUCTURING BY LASER REMELTING

Evgueni V. Bordatchev[1*], Moritz Küpper[2*], Srdjan J. Cvijanovic[3], Edgar Willenborg[4], Nicolas Milliken[1], André Temmler[5], and Remus O. Tutunea-Fatan[3]
[1]Automotive and Surface Transportation Research Center
National Research Council of Canada
London, Ontario, Canada
[2]Chair for Laser Technology, RWTH Aachen University
Aachen, Germany
[3]Mechanical and Materials Engineering Department, Western University
London, Ontario, Canada
[4]Fraunhofer Institute for Laser Technology
Aachen, Germany
[5]School of Mechanical Engineering
Tsinghua University
Beijing, China

INTRODUCTION

Advanced tooling (e.g. dies, molds, inserts, stamps) for mass-scale production of lighting and optical products, such as, light guides and pipes, light collectors and concentrators, retroreflective optics and emblems, has strict technical requirements to the surface quality and form geometry accuracy. Performance of such optical and lighting products is a result of a complex combination of the form accuracy and surface quality, where form accuracy is responsible for focusing, direction and redirection of rays. However, surface quality delivers optical phenomena, such as definite reflection, refraction and total internal reflection instead of the light scattering. With introduction and wide use of micro/nano-optical structures, conventional paradigm of optical fabrication is changing from two consecutive operations – roughing and finishing towards using one combined process resulting in optical surface quality. This paper presents an attempt to demonstrate the applicability of a novel advanced manufacturing process called surface structuring by laser remelting (SSLRM) [1, 2] for microfabrication of light guide tooling inserts with potential applications in automotive lighting.

FABRICATION OF LIGHT GUIDE INSERTS

With introduction of novel multibeam LED light sources combined with micro-optical, diffraction and holographic structures and sensors, automotive lighting is significantly expanding its capabilities from conventional signaling and safety awareness towards advanced and intelligent attributes of autonomous and electric vehicles, such as reconfigurable/adaptable styling, sensoring (e.g. lidars), head up displays, communication and other value adding functionalities.

Edge-lit light guide (LG) is one of widely used optical structures for the delivery of incoming light to and for homogeneous illumination of a specific area or surface. In general, LGs can have a free-form curvature design with specifically placed and oriented light-redirecting/scattering micro-optical structures located opposite to the illuminated area. Two types of light redirecting/scattering micro-optical structures can be used – v-grooves [3] and cylindrical dimples [4]. This research is focused only on v-grooves based LGs.

Optical performance of the edge-lit LGs critically depends on optimization of v-groove geometry parameters, such as, depth, included angle, distance between consecutive v-grooves, 3D posture of each v-groove along the LG shape, and several other parameters. Typically, a merit function for multi-parameter optimization will target maximum and uniform illumination of an illuminated surface or specific area. In the case of automotive tooling, design and optimization of LGs becomes even more complicated as tooling inserts have free-form geometry following the car body styling and fuzzy logic optimization is one of the applicable calculation methods [3].

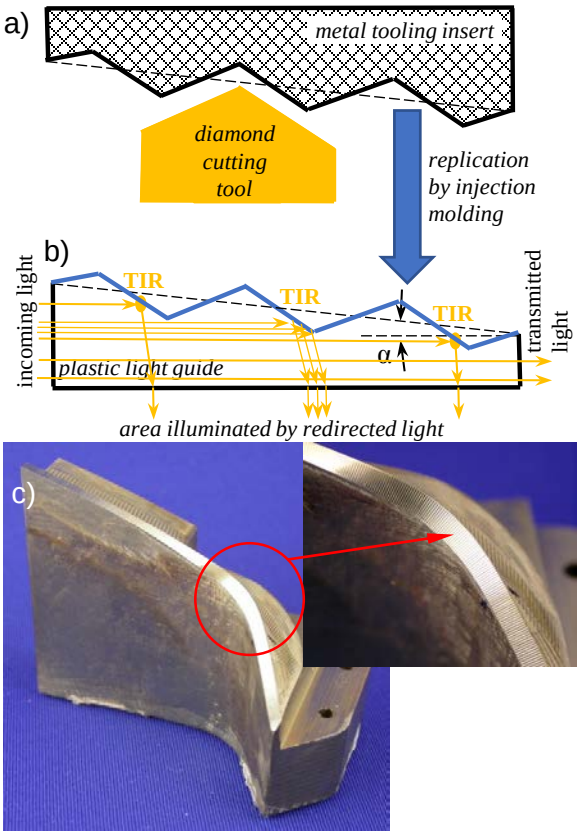

FIGURE 1. Conventional fabrication of LGTIs by SPDC (a), GL optical design with symmetrical v-grooves (b), and free-form LGTI (c).

Fig. 1a shows conventional fabrication by a single point diamond cutting (SPDC) process and typical free-form light guide tooling insert (LGTI). Fabrication of LG functional parts is a two-step process – a) 5-axis SPDC of an LGTI from a non-ferrous material or micromilling an insert from a tooling steel and b) mass-scale replication of LGTIs into plastic functional LGs using injection molding or hot embossing technologies.

Typical free-form LGTI is shown in Fig. 1c. It is hard to admit the reality that there is no conventional knowledge in fabrication of tolling for edge-lit light guides and light pipes as it is a thorough, hard-to-learn, knowledge-based process that requires advanced understanding of spatial geometrical rotation and translation. Typically, such knowledge will be kept as an internal-to-company knowhow.

Specifically for this study, edge-lit LG is designed as a transparent solid body between a top wedged surface having a tilting angle α and bottom illuminated surface (see Fig. 1b). Light redirecting v-grooves are located on the wedged surface and have uniform geometry, symmetrical shape and even distribution along the wedged surface. Illumination of the bottom surface is achieved through redirecting incoming light by a total internal reflection (TIR) phenomenon. These arrangements were made for the design simplification and for most suitable swap of the SPDC with the SSLRM process used in this study in order to demonstrate its applicability and estimate effectiveness of such replacement.

STRUCTURING BY LASER REMELTING

SSLRM process [3, 4] is one of very few novel advanced manufacturing technologies standing between material removal and material addition processes. It was already shown that the process works on a tool steel used for cold forging in automotive applications. [5] and automotive lighting is another most promising application of this technology. During SSLRM, surface geometry is formed by redistributing and relocating workpiece material in a molten state by the moving laser beam. It is a complex, highly non-linear thermo-dynamic process where material rapid melting, reallocation and rapid solidification is controlled by the parameters of the applied continuous wave laser irradiation. For each location of the laser-material interface along laser path trajectory, these three mentioned above physical phenomena form desired surface shape and topography interdependently and concurrently as all of them directly contribute to the actual volume of the molten material.

Fig. 2 shows practical Implementation of the SSLRM process. While laser beam scans the surface with a constant scanning speed v, sinusoidal modulation of the laser power continuously changing the actual volume of molten material and conforming thermal dilatation. In this case, spatial orientation of the solidification interface will follow the sine-shape modulation of the laser power.

In turn, time/space-controlled variations of the laser power directly transform into height, size, and form of the produced surface topography. Since the structure solidifies directly from the melt, its surface is smoothened due to surface tension similar to a laser polished surface. Such unique process performance offers advanced capabilities towards surface topography reconfiguration due to the absence of material removal or addition combined with process simplicity and efficiency that opens a wide window of industrial applications.

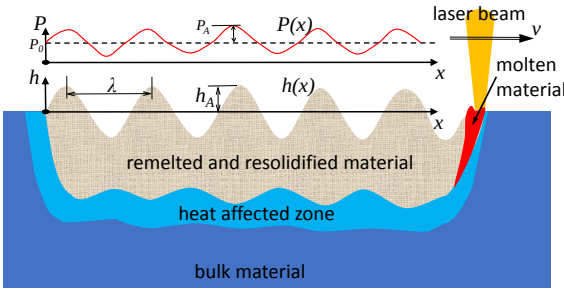

FIGURE 2. Implementation of SSLRM process.

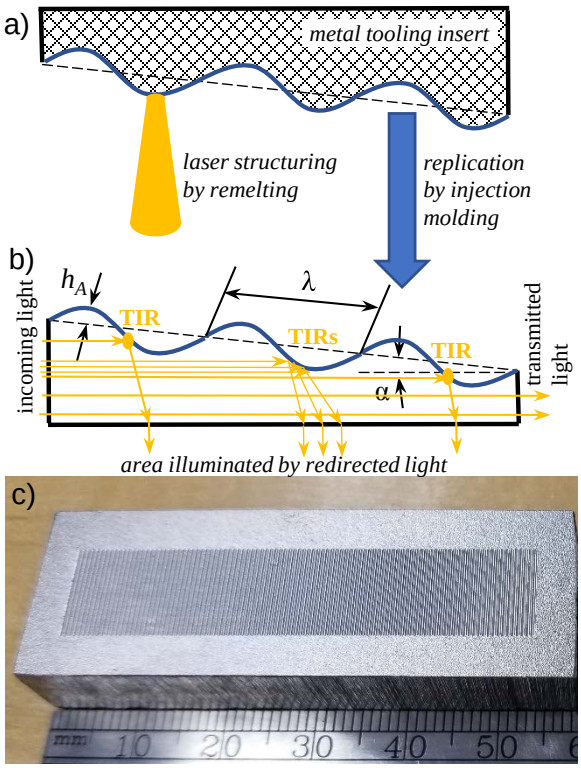

FIGURE 3. Fabrication of LGTIs by SSLRM (a), LG optical design with sine-shape grooves (b), and one of fabricated LGTI (c).

LGTI SSLRM FABRICATION AND LG DESIGN

As SSLRM process has already demonstrated successful and reliable fabrication of sine-shaped structures [1, 2, 5], it was proposed to use these structures instead of conventional v-grooves described earlier with their uniform, symmetrical and evenly distribution along the wedged surface.

Three LGTIs with a period of λ = 500 um and different heights of 25 µm, 40 µm and 55 µm were fabricated from tooling steel 1.2343 using a laser polishing system at Fraunhofer Institute for Laser Technology (Aachen, Germany) (see Fig. 3). Detailed description of the laser polishing system and typical SSLRM process parameters can be found in [6] as process parameter optimization was not the objective of this study. One of the LGTIs fabricated by SSLRM is shown in Fig. 3c.

Replacement of symmetrical v-grooves with sine-shape optical structures is also beneficial from overall optical performance of the functional LGs. Use of sine-shape grooves may redirect incoming incident light rays by TIR with a much wider spread angle as collimated rays are hitting variable within one period sine curve and therefore increasing uniformity and illumination of the bottom illuminated surface. Such comparison can be seen between Fig. 1b and Fig. 3b.

The optical performance of the LG (λ = 500 µm, h_A = 40 µm, α = 5°, made from PMMA plastic) was simulated by Zemax software in terms of ray tracing. The results of the ray tracing and achieved distribution of incoherent irradiance over the bottom illuminated area are shown in Fig. 4. LG optical performance was estimated by two calculated parameters of the light redirection: a) overall light delivery efficiency as a percentage of the incoming light power delivered to the bottom illuminated area and b) overall illumination efficiency as a percentage of the illuminated area with respect to the total bottom area. For this LG, light delivery efficiency of 65.8% was achieved while covering 95.3% of the illuminated area.

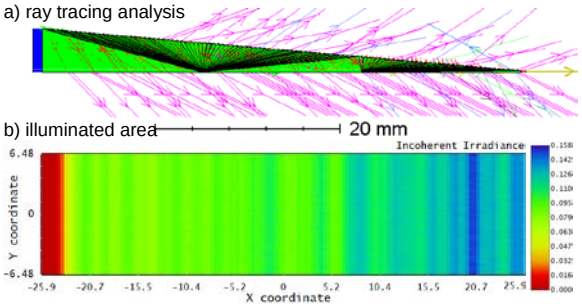

FIGURE 4. Ray tracing analysis (a) and illuminated area (b) of the LG with λ = 500 µm, h_A = 40 µm and α = 5 deg.

FORM GEOMETRY AND SURFACE QUALITY

Surface topographies of all three LGTIs were measured using a white light optical profilometer with a vertical resolution of 1 Å. The surfaces of all samples were scanned with a lateral resolution of 1.29 µm over 12.0 x 2.5 mm area and recorded as a data file for further analysis. Two types of the surface topography analysis were performed. First of all, form geometry was estimated through calculating averaged period, amplitude and their standard deviation of the sine-shape LGs.

Results are presented in Table 1 and 3D surface topographies and averaged cross-section profiles of fabricated LGTIs are shown in Fig. 5.

TABLE 1. Form geometry characteristics of fabricated LGTIs.

# of passes	Period µm	Amplitude µm	Amplitude per pass, µm
4	498.5±3.9	26.1±1.5	6.525
10	498.2±3.8	40.0±2.0	4.000
16	497.8±3.3	55.3±3.1	3.456

It is also necessary to point out that each LGTI sample was fabricated with a different number of processing passes however keeping all other process parameters unchanged. More specific information regarding the effect of a number of processing passes on a form geometry formation and other process parameters can be found in [5, 6]. It is quite evident that SSLRM process is not linear with respect to the number of processing passes. A larger amplitude per pass can be obtained during several first passes (e.g. 6.525 µm during first four passes) where SSLPM is more efficient with respect to the form geometry formation as molten material is moved over the initially flat surface. Further on, efficiency of the SSLRM process becomes less (e.g. 3.455 µm over 16 passes). This is due to that the polishing aspect of remelting gradually takes over. The forced material redistribution caused by the laser power modulation competes with the "natural" material redistribution (polishing) due to surface tension, capillary, etc. This results in a decrease in structuring efficiency (saturation effect).

After the first fabrication step of the form geometry formation, laser micro polishing process using pulsed laser radiation was applied in order to improve surface quality of the fabricated LGTI samples. Therefore, surface quality of fabricated samples was analyzed in the next step. Obtained results are presented in Fig. 6 as a complete spectrum of the areal surface roughness (see Fig. 6a) and areal surface micro-roughness (see Fig. 6b) where surface quality is typically reduced with increasing number of processing passes.

It is also necessary to mention in addition that the created sine-shape grooves can be treated as waviness components in the complete areal surface roughness spectrum (see Fig. 6a). Periods of all fabricated sine-shape grooves lay within the same wavelength range of 330.24-660.48 nm but with increasing amplitudes.

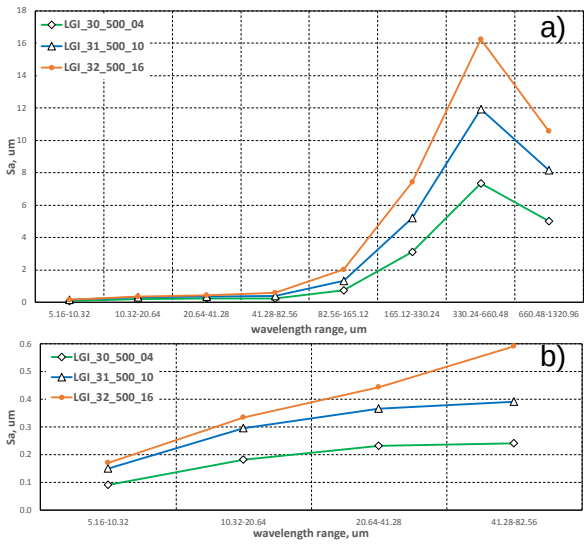

FIGURE 6. Complete areal roughness (a) and areal micro-roughness (b) spectrums of LGTI.

Fabricated LGTIs were replicated into functional plastic LG prototypes using a hot embossing process and a temperature/force-controlled hot press. Results of the replication are shown in Fig. 7 presenting examples of a fabricated plastic LG prototype, its 3D surface topography and cross-section profile with form geometry characteristics. As it was expected, period and amplitude of the sine-shape grooves are in good agreement with the same parameters of LGTIs.

COMPARATIVE OPTICAL PERFORMANCE

In the limited scope of the current study, optical performance of the functional plastic LG prototype with a sine-shape wedge was preliminary estimated by comparing with optical performance of the plastic LG with a flat wedge. Such flat wedge LG does not exhibit light redirection functionality as incoming rays will minimally illuminate the area at its end only. The flat-wedge LG sample was fabricated from PMMA plastics using a single point diamond cutting process achieving areal surface roughness S_a below 20 nm. An optical set-up was assembled integrating a collimated 532 nm light source, 3x beam expander and sample holder for consistent alignment of all LG functional prototypes. Images of the optical face illuminated by the redirected light were captured for both sine-shape wedge and flat wedge LGs. The results presented in Fig. 8 demonstrate a distinct difference in the optical performances. Sine-shape wedge LG has fully illuminated area (Fig. 8b) while flat wedge LG demonstrates only illuminated background surface with no LG illumination (Fig. 8a).

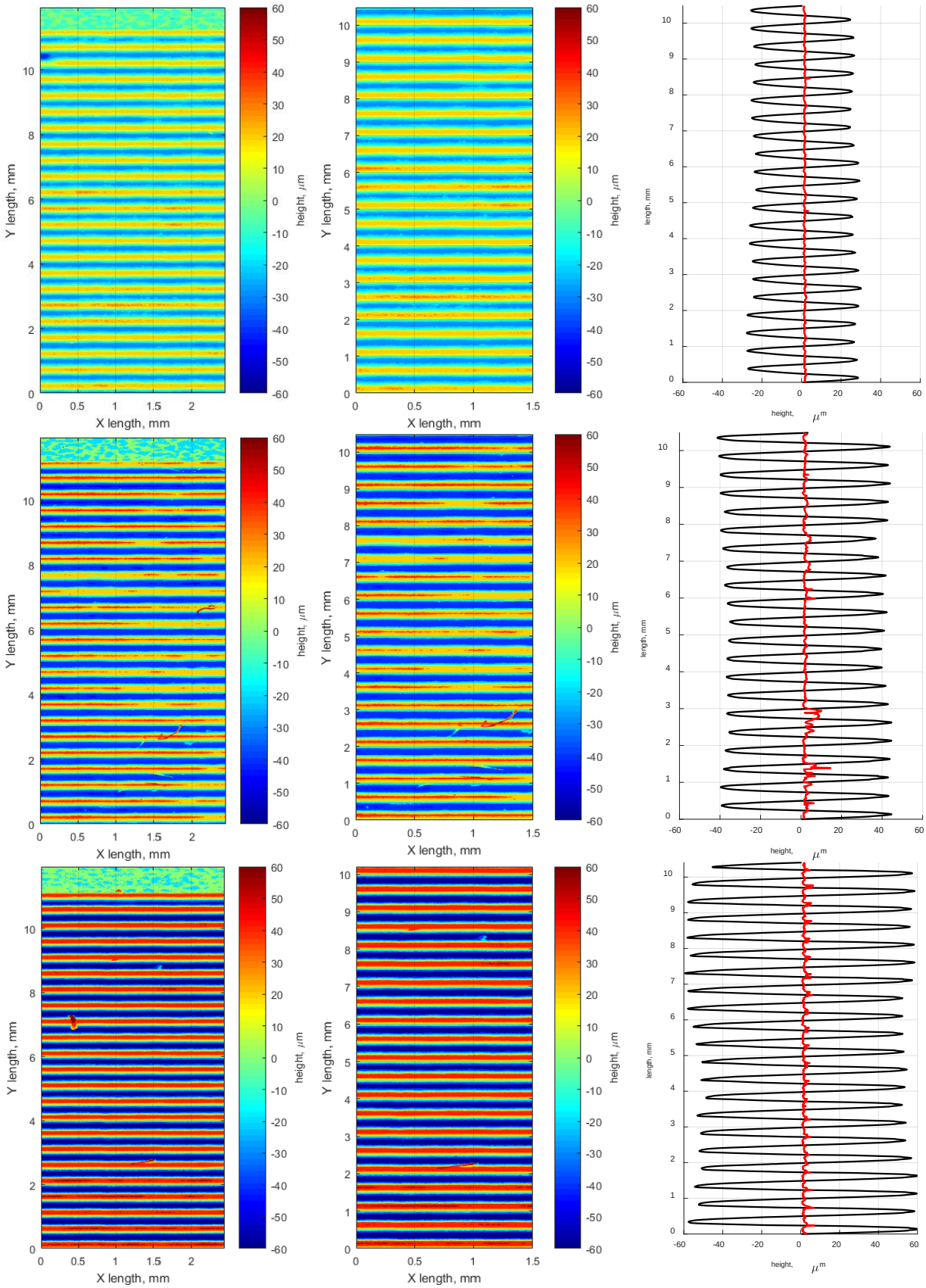

FIGURE 5. 3D surface topographies and averaged cross-section profiles of fabricated LGTIs.

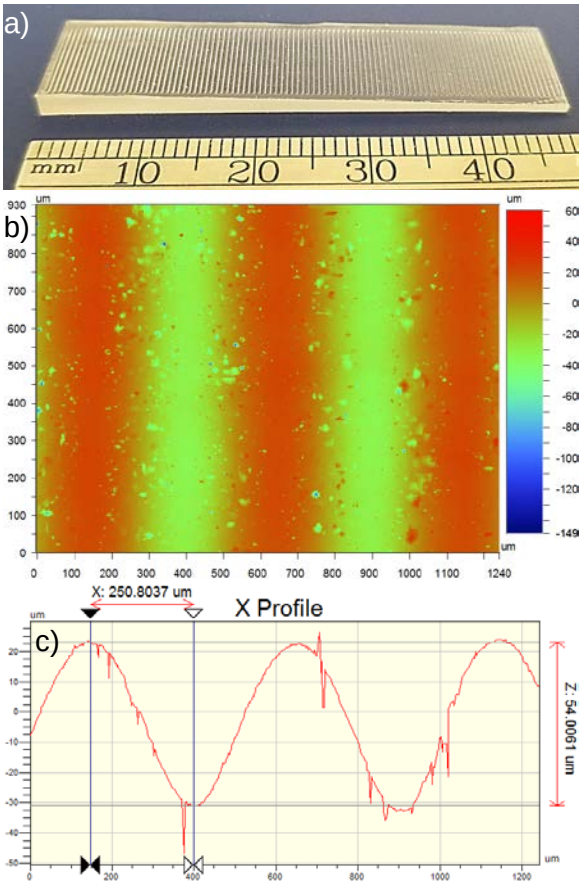

FIGURE 7. Examples of a) fabricated plastic light guide prototype, b) 3D surface topography and c) cross-section profile with its characteristics.

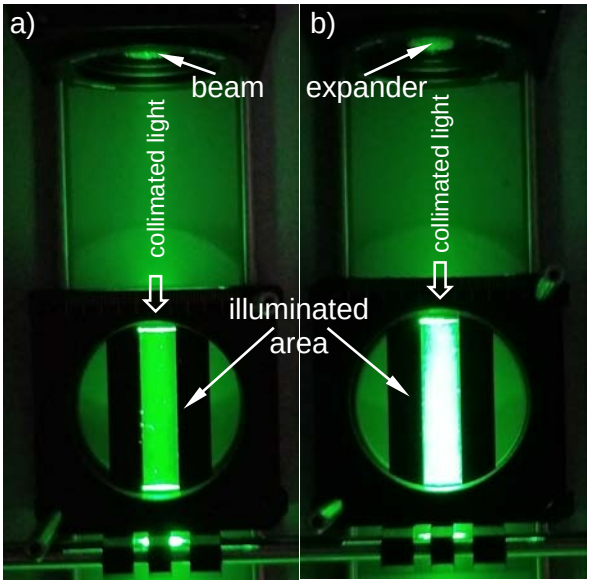

FIGURE 8. Visual comparison of the optical performance of the flat wedge LG (a) and sine-shape wedge LG (b).

SUMMARY, CONCLUSIONS, FUTURE WORK

The main objective of this study was to demonstrate applicability of the SSLRM process for efficient fabrication of edge-lit LGTIs for automotive lighting applications. Several LGTIs were fabricated demonstrating high accuracy and precision in form geometry achieving sine-shape period and amplitudes with deviations <4 μm and <3 μm, respectively, with no optimization applied. Areal surface roughness was achieved ~220 nm that is acceptable by tooling industry for majority of practical applications. LG functional prototypes was replicated in plastic by a hot embossing preserving original form geometry and surface quality characteristics. Optical performance of the plastic sine-shape wedge LG prototype was compared with identical-by-size flat wedge LG sample demonstrating high illumination efficiency. Future work will involve SSLRM process and LG optical performance optimization.

ACKNOWLEDGMENT

The work presented in this study is the result of the collaboration between National Research Council of Canada, RWTH University (Germany), Fraunhofer Institute of Laser Technology (Germany), and Western University (Canada).
* contributed equally to this work

REFERENCES

[1] Temmler A. Laserumschmelzstrukturierung. PhD thesis, RWTH Aachen, Shaker Verlag, Aachen, Germany, 2012, 160 p.
[2] Temmler A., Walochnik M.A., Willenborg E., Wissenbach K. Surface structuring by remelting of titanium alloy Ti6Al4V, J. of Laser Applications. 2015; 27: S29103, 8 p.
[3] Yu J.C., Chen J.H., Liu, S.C. Design of LED edge-lit light bar for automotive taillight applications, Proc. of SPIE, 2013, 8835:88350G
[4] Ronny R.A., Knopf G.K., Bordatchev, E.V. Micromilled optical elements for edge-lit illumination, J. Micro/Nanolith. MEMS MOEMS, 2013, 12(2), paper 023002, 11 p.
[5] Temmler, A., Comiotto, M., Ross, I., Kuepper, M., Liu, D.M., R. Poprawe. Surface structuring by laser remelting of 1.2379 (D2) for cold forging tools in automotive applications. J. Laser Appl., 2019, 31, paper 022017, 12 p.
[6] Temmler A., Küpper, M., Walochnik, M.A., Lanfermann, A., Schmickler, T., Bach, A., Greifenberg, T., Oreshkin, O., Willenborg, E., Wissenbach, K., Poprawe, R. Surface structuring by laser remelting of metals, J. of Laser Applications, 29(1), paper 12015, 12p.

ENABLING BEARING TECHNOLOGIES FOR HIGH-POWER OIL-FREE TURBOMACHINERY

Bugra Ertas
Mechanical Systems
GE Research Center
Niskayuna, NY 12309 USA

ABSTRACT

The following topic will focus on the recent advancements in gas film bearing technology aimed at enabling oil-free operation of high-power turbomachinery. Virtually all turbomachines such as compressors, turbines, and electric machines in the megawatt power range today utilize oil-lubricated bearing systems to support the rotating shaft assembly. To date these bearing systems have provided reliable operation of rotating equipment. However ever-increasing demands in improved power density and efficiency are challenging engineers to consider advanced bearing systems utilizing the working fluid of the machine to lubricate bearings. Using process-fluid lubricated gas bearings versus oil-bearings not only yields improved performance, but also is an enabler for emerging applications on the fringe of turbomachine technology development.

The present work provides an overview of existing gas bearing technologies followed by the challenges associated with implementing these devices into large turbomachinery systems. With these hurdles in mind, the paper reviews recent efforts by researchers to improve these engineering metrics. Finally, the work herein outlines the evolutionary progression of compliant-hybrid gas bearings over the last decade; ultimately requiring the use of additive manufacturing. Concluding remarks focus on the remaining challenges and technology hurdles for realizing oil-free operation in megawatt-power-class turbomachinery.

INTRODUCTION

Virtually all high-power turbomachinery in the megawatt class range utilize oil-lubricated bearings to lubricate the rotating assembly. Oil is a preferred lubricant due to its abundance, hydrodynamic pressure generating capability, and the ability to provide high levels of damping due to the relatively high viscosity when compared to gases. However, implementing an oil-system requires the engineering of complex lubrication circuits, bearing sumps, and ancillary components. The oil needs to be protected from the process fluid of the machine and visa-versa. The concept outlined in this paper replaces oil with the process fluid of the machine to lubricate the bearing. With this approach entire lube system and can be eliminated while greatly simplifying the mechanical design of bearing sumps. Furthermore, process gas lubricated bearing systems can expose new design spaces allowing for novel machine architectures. If done successfully, process fluid lubrication yields benefit in cost, reliability, and performance. A good example comes from implementation of foil bearings in air cycle machines and microturbine generators [1,2]. These types machines have demonstrated remarkable reliability with gas foil bearings but are limited to low power ratings typically <500KW. The two main challenges existing with gas bearings, like foil bearings, for penetration into megawatt class turbomachinery are load capacity and damping.

TECHNOLOGY HURDLES

Existing state-of-the-art gas bearings used in turbomachinery are mainly foil bearings. Foil bearings are a type of hydrodynamic bearing with a flexible and compliant bearing surface (Figure 1). Pressure generation is created with relative speed between the journal and top foil. This pressure generation is responsible for the load carrying capacity and becomes larger with increasing rotor speed. Figure 2 shows a typical representation of how a foil bearing operates in a mission cycle.

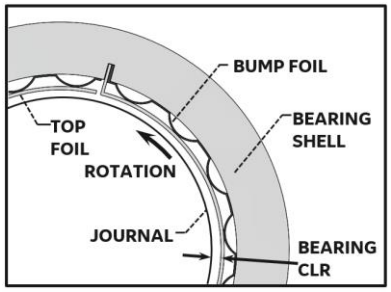

FIGURE 1. Typical Foil Bearing

Initially at 0rpm, since there is no journal speed, the journal is resting on the bearing foil surface. As the journal starts to rotate there is sliding contact and friction between solid surfaces. This regime creates a start-up torque spike. As journal speed increases the bearing transitions through a boundary layer (B.L.) lubrication regime followed by complete hydrodynamic lift-off with a fully developed lubricating film. In result, the foil bearing needs to be able to sustain several start-stop cycles enduring sliding friction between parts. To achieve this, coating needs to be employed. With this approach the foil bearing is limited to lighter rotor weights and therefore lower power applications as the coating technology is the limiting factor.

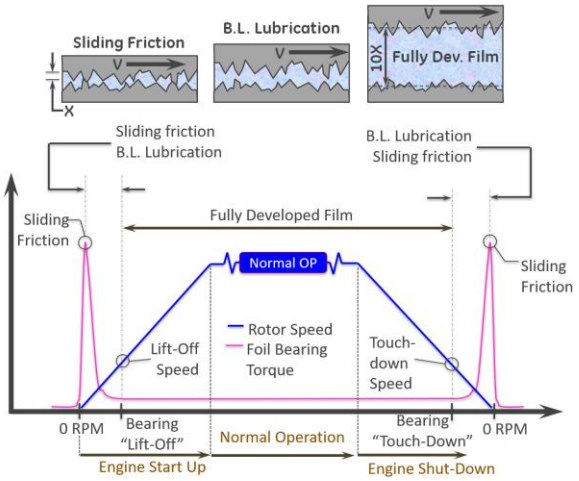

FIGURE 2. Torque-Speed Trend for Foil Bearings Showing Lubricating Regimes

Therefore, the first main technical hurdle for implementing gas lubricated bearings to larger equipment is load capacity. The second hurdle is damping. Damping is a mechanical force element that opposes vibratory velocity of dynamic mechanical systems. Figures 3-4 illustrate how damping influences vibration of rotating systems and how the requirement of damping increases as the stiffness coefficient of the system is increased.

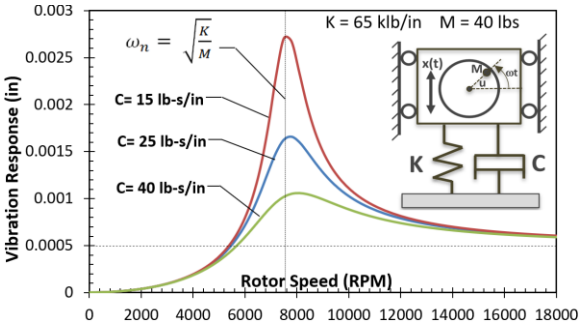

FIGURE 3. Synchronous Response to Rotor Unbalance for Varying Damping Coefficients While Keeping Stiffness Constant

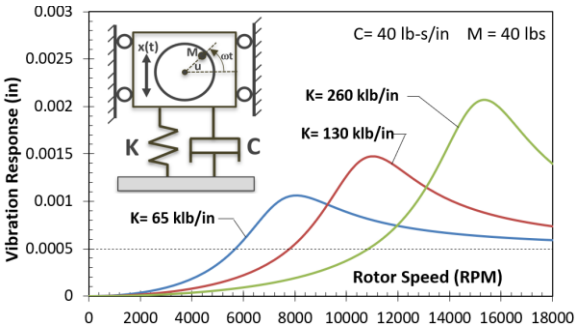

FIGURE 4. Synchronous Response to Rotor Unbalance for Varying Stiffness Coefficients While Keeping Damping Constant

Figure 3 shows a simple mechanical system with a rotating unbalance force as the forced excitation. In this figure damping is varied as stiffness is held constant. As one would expect the vibration level is reduced as the damping coefficient is increased. Figure 4 holds damping constant but varies the stiffness coefficient. In this case note that the vibration increases as the stiffness coefficient becomes larger in magnitude. The demand for damping goes up for the high stiffness case in order to retain the same amplification factor as the lower stiffness case. This simple example illustrates that damping alone is insufficient to define the damping capability of a spring damper system; what is required is the ratio of stiffness to damping. This is famously defined by the damping ratio (eq. 1), which relates the critical damping (eq. 2) to the absolute damping in the system. Where ζ is damping ratio, C is damping, C_c is critical damping, K is stiffness, and M is mass. Note that the critical damping is a function of stiffness.

$$\zeta = \frac{C}{C_c} \qquad (1)$$

$$C_c = 2\sqrt{K \cdot M} \quad (2)$$

In summary, engineering a low stiffness in combination with high damping maximizes the damping ratio.

In the case for gas films found in bearings, the ratio of stiffness to damping is very high and therefore when compared to oil-based bearing systems the damping capability of gas films is significantly compromised. This is where the foil bearing concept takes advantage of the "soft" support to improve equivalent damping of the bearing system.

EVOLUTION OF GAS BEARING SYSTEMS

This section builds on the main two technical challenges highlighted in the previous section and gives a cursory overview of the approach used to evolve gas bearings to mitigate the load capacity and damping challenges. As power rating of the turbomachine increases, the rotor diameters and weight becomes larger. Figure 5 shows a high levels chart illustrating the landscape for hydrodynamic versus hydrostatic bearing systems.

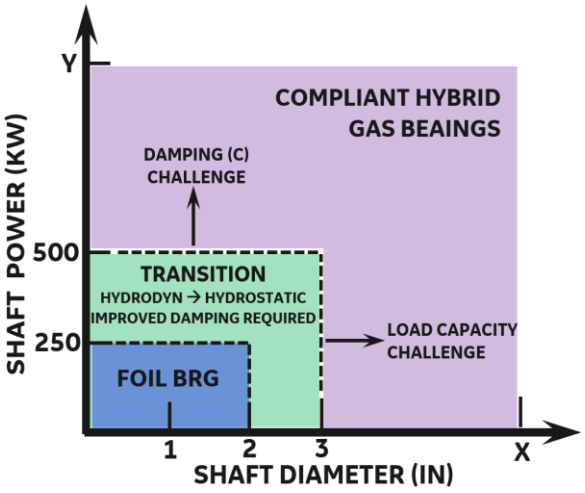

FIGURE 5. Radial Gas Bearing Design Space

As the shaft diameter increase the mass of the rotating assembly also increases. With mass increasing hydrostatics are required to support rotor loads. Hydrostatic pressurization involves using an external pressure source to lift the rotor and can be achieved through several configurations and gas delivery methods. Increased shaft power also implies higher levels of fluid forces between the rotating assembly and stationary casing of the machine. These fluid forces, either from the turbomachinery stages or seals, generate destabilizing dynamic forces. To mitigate high vibration generated from destabilizing forces, one must introduce higher levels of damping. The key to generating high levels of damping in gas bearings resides in utilizing a soft bearing support in series with the gas film. Compared to rigid geometry gas bearings, either hydrodynamic or hydrostatic, soft mounting the gas film on a flexible support that possesses a favorable stiffness to damping ratio generates superior damping capability to the rotating system. Soft-mounting a bearing system is not a new concept as aircraft engine systems utilize flexible bearing supports with rolling element bearings [3]. Soft-mounting the bearing system transforms rotor bending modes to rigid body modes, reduces transmitted dynamic bearing loads, and can significantly reduce rotor vibration magnitudes. Figure 6 illustrates how a soft support would maximize the equivalent damping of the bearing system. The simple model in Figure 6 shows that the ratio of gas film stiffness (K_a) and bearing support stiffness (K_b) have strong influence on the equivalent damping of the overall system (C_{eq}). As the bearing support stiffness (K_b) is reduced, the equivalent damping (C_{eq}) approaches the bearing support damping (C_b).

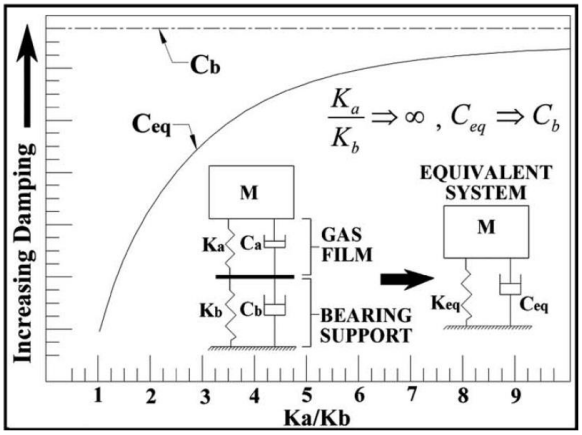

FIGURE 6. Maximizing Equivalent Damping Using Soft Bearing Supports

This bearing and support configuration can allow for high damping even with a relatively low valued gas film damping (C_g) coefficient.

Considering the previously discussed approaches for obtaining higher load capcity and damping, considerable research has been performed on compliant hybrid gas bearings. Figure 7 shows the evolution of compliant hybrid gas bearings over the last decade. The bearing concept involves using hydrostatic pressurization in combination with a flexible

support possessing a robust damper. Initially the generation 1 (Gen1) bearing used a simple square hydrostatic recess to deliver pressurized fluid between the bearing surface and journal. The GEN1 concept [4] further implemented an oil-free metal mesh damper into the bearing support. Although these two novel additions to existing hydrostatic bearings improved load capacity and damping when compared to foil bearings, there were still limitations in supporting edge loading and mitigating vibration response on heavy rotor systems. From this conclusion the development aimed to improve the gas delivery method and the damping element in the bearing support. The GEN2 [5] concept addresses these shortcomings through implemented a distributed gas delivery system using multiple holes or porous media to enhance the edge loading capability of the bearing pad. The GEN 2 design improved the damping capability through the development of hermetic squeeze film dampers rather than having metal mesh dampers in the bearing support. The concept proved to have significantly higher damping levels when compared to friction based damping elements like foils or metal mesh. However, the GEN2 design used modular fluid dampers and resulted in over 500 parts in the assembly; making the design impractical for industrial applications. The GEN3 concepts were developed [6-8], which used additive manufacturing or diffusion bonding to integrate complex functionality into a single piece bearing design. The integral designs, especially the additive approach, yielded a cost effective and compact configuration showing good promise for implementation into high-power turbomachinery. However, key challenges in the wear-couple between the bearing and journal remain.

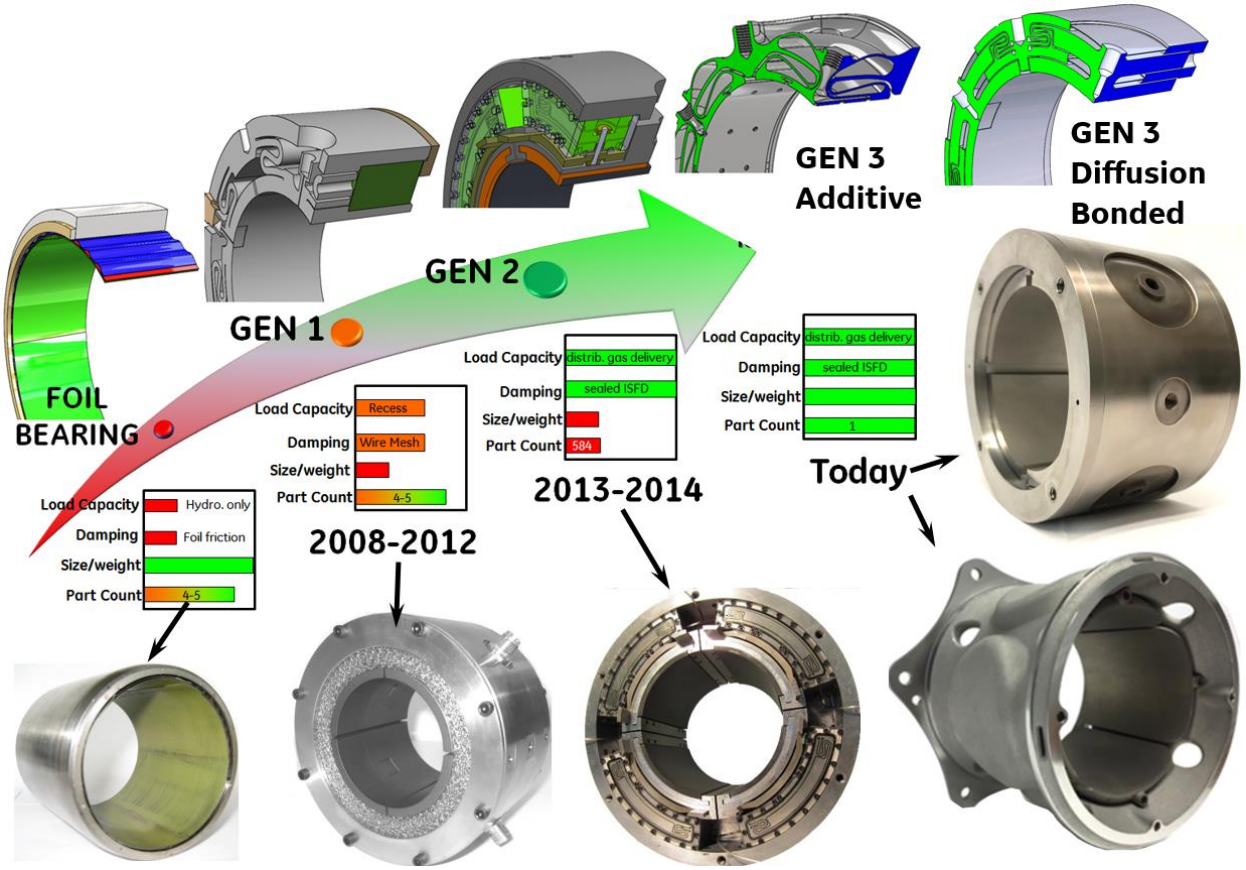

FIGURE 7. Evolution of Compliant Hybrid Gas Bearings

REMAINING CHALLENGES

In addition to the need for higher damping and load capacity for mission critical high-performance turbomachinery, there is a requirement of the gas bearing system to sustain unintended touch-down conditions during off-design points. For example, aircraft engines require the ability of the bearing system to absorb blade-out forces and bearings in centrifugal compressors during surge and stall

must survive loads an order of magnitude higher than the 1G reaction load. Under these circumstances it is most likely that the bearing surface will experience a rub at high surface speeds and high loads. Coating technology or the tribological wear-couple between the rotor and bearing becomes of paramount importance.

One highly promising technology that can be implemented in these max-load off-design cases are porous carbon media bearings. Porous carbon bearings (Figure 8) have a unique crystalline structure that allows for easy slip of parallel planes in the structure due to sliding motion while retaining high compressive stiffness in the normal to the motion but in line with the load. Recent testing of porous carbon media for over-load conditions show superb ability to sustain high loads during solid dry friction contact while at high rotor speed [5,9]. Although porous carbon bearings are utilized in several application today, they still have yet to penetrate the turbomachinery industry. A natural evolution would involve the integration of porous carbon with a GEN3 type compliant hybrid bearing to address the risk of bearing touch down at high speeds and loads.

FIGURE 8. Porous Carbon Gas Bearing

CONCLUSION

The following paper discussed the evolution of gas bearing technology keenly focused on enabling the oil-free operation of high-power turbomachinery. With the recent advancement in load capacity and damping, compliant hybrid gas bearings show great promise in achieving the oil-free turbomachinery milestone. Next step in the development involve developing reliable coatings or wear-couples that allow for the bearing system to sustain rubs at high speeds and loads. Porous carbon bearing systems are potential candidates for this next step in the evolution of gas bearings and demand further research to mature the technology for high-power turbomachinery.

ACKNOWLEDGEMENTS

Thanks to Newway air bearings for graciously allowing the use of example pictures of porous carbon bearings.

REFERENCES

[1] Agrawal, G., 1990, “Foil Gas Bearings for Turbomachinery,” SAE Technical Paper No. 901236.

[2] Lubell, D. R., Wade, J. L., Chauhan, N. S., and Nourse, J. G., 2008, “Identification and Correction of Rotor Instability in an Oil-Free Gas Turbine,” ASME Paper No. GT2008-50305.

[3] Magge, N., 1975, “Philosophy, Design, and Evaluation of Soft-Mounted Engine Rotor Systems,” J. Aircr., **12**(4), pp. 318–324.

[4] Ertas, B. H., 2008, “Compliant Hybrid Journal Bearings Using Integral Wire Mesh Dampers,” ASME J. Eng. Gas Turbines Power, 131(2), p. 022503.

[5] Ertas, B., and Delgado, A., 2018, “Compliant Hybrid Gas Bearing Using Modular Hermetically Sealed Squeeze Film Dampers,” ASME J. Eng. Gas Turbines Power, 141(2), p. 022504.

[6] Mook, T. J., Ertas, B.H., Bellardi, J. J., “Bearing”, US Patent No. 9746029, Aug. 29, 2017.

[7] Ertas, B.H, Mook, J. T., Bellardi, J. J., “Additive Thrust Gas Bearing”, US Patent No. 10036279, July 31st, 2018.

[8] Ertas, B.H., 2019, “Compliant Hybrid Gas Bearing Using Integral Hermetically-Sealed Squeeze Film Dampers”, Proc. Gas Turbine Tech. Conf. Exp. ASME Turbo Expo, Phoenix, AZ, June 17-21, Paper No. GT2019-90865.

[9] San Andres, L., Cable, A., T., Zheng, Y., De Santiago, O., and Devitt, D., 2016, “Assessment of Porous Type Gas Bearings: Measurements of Bearing Performance and Rotor Vibrations,” ASME Paper No. GT2016-57876.

CARBON-GRAPHITE GAS BEARINGS FOR TURBOMACHINERY

Drew Devitt[1], Dr Luis San Andres[2] and Sung-Hwa Jeung
[1]New Way Air Bearings
Aston, Pa. USA
[2]Texas A&M Turbo Lab
College Station, Tx. USA

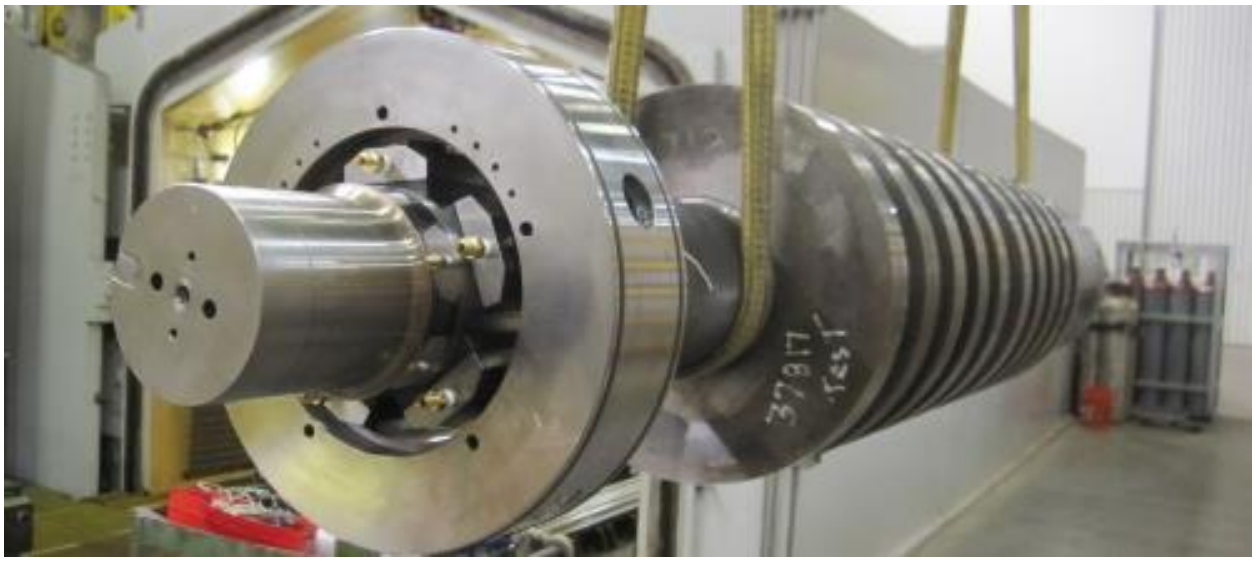

FIGURE 1. Dresser Rand test rotor mounted on New Way Gas Bearings at the TurboCare Balance Bunker in Houston, TX.

INTRODUCTION

Rotors in multi megawatt rotating equipment are almost all supported on hydrodynamic oil bearings. This has been the case for over 100 years. Kingsbury Corp., one of the inventors of tilting pad hydrodynamic bearings, is still a leader in the industry. Users of high power rotating equipment, like the power generation and the oil and gas industries, are conservative. Still there is a drive for smaller, lighter, faster, hotter, shorter, more reliable, efficient, ecological, safer and simpler equipment. It is the oil lubrication that is often the problem in achieving these goals.

Alternative bearing technologies exist; Magnetic bearings have had highly published introductions and successes although few of the high power machines use magnetic bearings. They do not extend the temperature range over oil bearings, are not compact enough for economical retrofits, and are not yet considered simple to maintain.

Aerodynamic bearings have seen wide acceptance in air handling units in commercial and military aircraft. They have also been finding use in blowers for aeration and smaller power generation turbines. Capstone, a micro-turbine manufacturer, has a 1 MW turbine for sale now as their largest offering and it employs aerodynamic bearings. Aerodynamic bearings are compact and simple but have low load capacity and the contact at stop/start cycles becomes reliability threatening with the friction from larger rotors.

This paper explores the possibilities of externally pressurized bearings, also known as aerostatic bearings for the support of multi megawatt rotating equipment. The authors of this paper having experience with porous carbon air bearings in other industries (Semi-Conductor, Metrology, Machine Tool, Medical) employed porous carbon compensation gas bearing technology in these developments.

Aerostatic bearings provide zero friction stop and starts and have load capacity limited only by input pressure. (Authors have demonstrated stable operation in excess of 1000psi loading).

They offer the possibility of operation on process gas for canned or sealess designs at high (carbon oxidizes about 800°C) or cryogenic temperatures.

THE TEST ROTOR

Dresser Rand (DR), a leading manufacturer of large scale industrial compression technology, after being tempted with porous gas bearings by New Way, saw enough promise to challenge the authors with a particular test rotor. The rotor provided by DR had been used in the development of the Datum line of compressors. Weighing 700lbs, it is 2m long with 1.52m in between bearing centers with 100mm journals. Modeled after a 10 stage centrifugal compressor, the stages are solid discs, rather than cut impellers to increase mass and the otherwise 100mm diameter shaft is undercut to 85mm between each stage to increase flexibility. It was used as a sort of worst-case-test for bearings and dampers. The compression work being done by such a rotor is about 30MW and about 800hp is used to cool the bearing oil. Kuzdzal and Hustak [2], who worked at Dresser-Rand, conducted a study using the rotor. The authors were studying squeeze film dampers' ability to control imbalance response and rotordynamic instability.

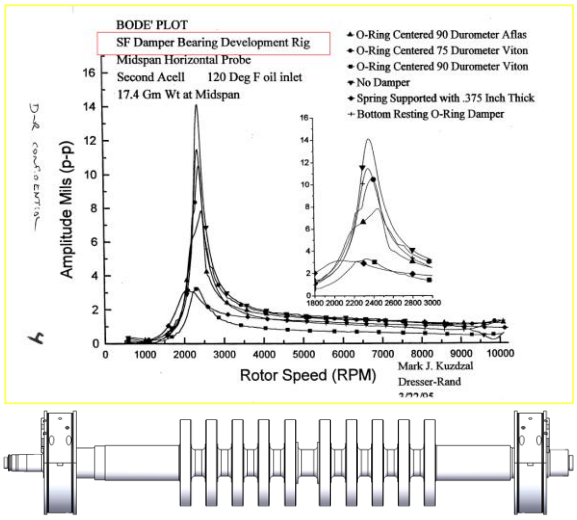

FIGURE 2 Using the same rotor, Kuzdzal and Hustak [1] illustrated the effectiveness of SFDs to reduce vibration amplitudes.

TEST BEARING DEVELOPMENT

The porous-media gas bearing geometry was modeled using the same 5 pad tilting-pad bearing design previously used. This was done in part to prove that direct replicability of the oil bearings with gas bearings is a possibility. The bearings were run on both nitrogen and carbon-dioxide.

The first tests conducted were aimed at characterizing bearing heat generation. The bearing cartridge containing the bearings was about 10 inches in diameter. A radial air bearing was used under the test bearing cartridge to push up with 400lbs, loading the test bearings into the spinning shaft. Two more sets of bearings and cartridges are used to hold the spinning shaft down. The test bearing cartridge is constrained in 5 degrees of freedom, has 400lbs of load yet is still able to rotate about the shaft axis

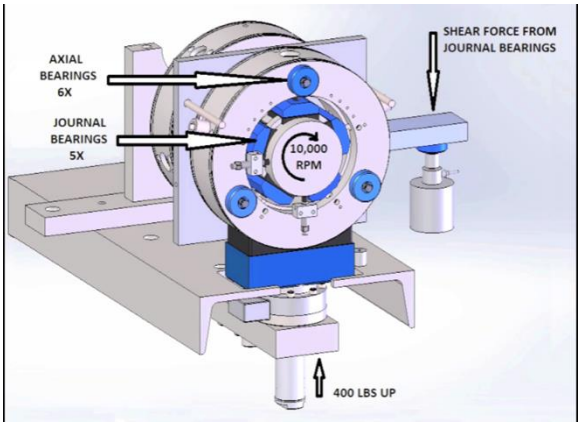

FIGURE 3 The test cartridge is constrained in 5° of freedom with 400lbs of radial load. A force gage can be used to directly measure bearing shear.

The authors believed they could measure the shear force between the test bearings and the spinning shaft directly by attaching an arm to a force gage, rather than looking to temperature probes and estimating losses by measuring secondary effects. Interestingly, with a 1-gram resolution force gage, results were not conclusive. Even at 14,000 RPM, the resulting drag torque was less than the resolution of the gage. The maximum power loss from bearing friction was estimated to be less than 100 watts and actual temperature probes correlated with rises less than 1°C per 15 minutes at 13,000 RPM, under load.

The temperature probes were inserted though the metal backing and down into the carbon less than 3mm from the face. Carbon has high thermal conductivity.

In the actual test with the rotor in the bunker, when supplied with 10 bar nitrogen, the rotor was able to run at 9000 rpm for 15 minutes without generating any measureable temperature rise.

While operating on co2, the bearing temperatures decreased by 2°c under the same conditions.

DYNAMIC LOAD TESTING

The next test was to see how the bearings would handle vibrations from critical speeds and imbalance. Noting from the DR paper that the rotor's first critical speed was 2300 rpm, the authors fabricated imbalance weights to spin between bearing sets creating rotating forces of 200lbs, 400lbs and 800lbs at the critical speed. These imbalance forces are far beyond what would be considered appropriate by the API; however, the authors intended to induce a worst-case scenario to illustrate the usefulness of porous-media air bearings. Using eddy-current probes mounted in the pedestal, the authors were able measure motion of the whole bearing cartage in the damper and the shaft in the bearing cartridge.

As an initial benchmark, the 400lbs imbalance weight was run at 2300 rpm for 6 hours continuously without measurable change in the lateral displacements.

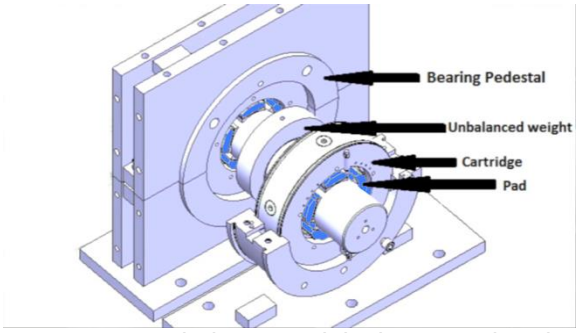

FIGURE 4 Unbalance weight between bearing sets

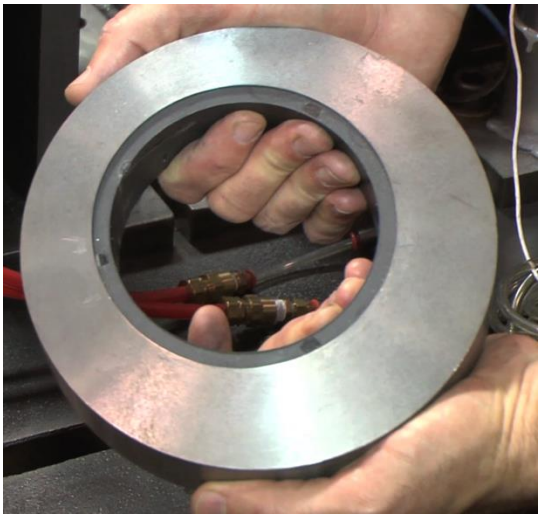

FIGURE 5 Actual unbalance weight spun at 2300 RPM makes 800lbs of synchronous radial load.

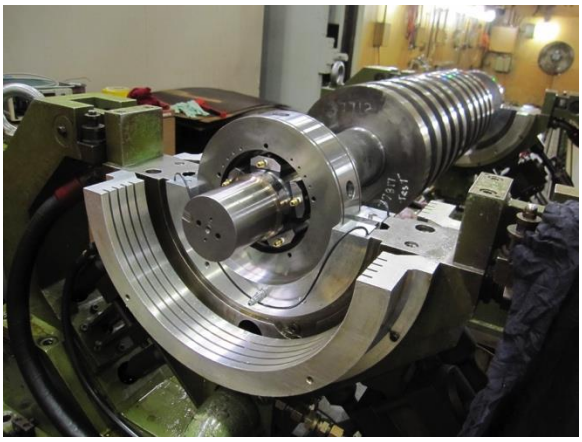

FIGURE 6 DR rotor, supported by New Way Air Bearings in a squeeze film oil dampers custom fit to the TurboCare bunker pedestals.

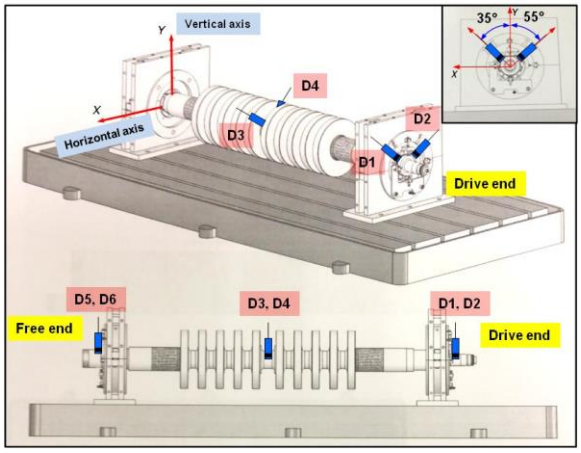

FIGURE 7, DR rotor on New Way Air Bearings with indicated planes of measured displacement.

FIGURE shows the response spectrum of the rotor during run-up and coast-down, measured at the bearing midspan. Note the presence of a critical speed at the mentioned 2300 rpm (38 hz).

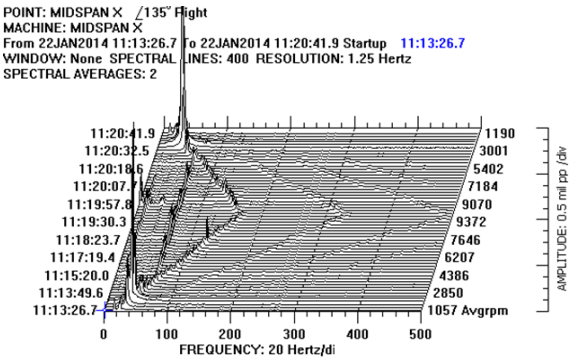

FIGURE 8. Spectrum of measured rotor response at the bearing midspan.

While cycling the actual rotor up and down on the gas bearings at TurboCare, the operators passed through the first bending critical multiple times, each time surviving an amplification factor (af) of 23 times. Additionally the authors were able to run the rotor continuously at 4 times the first critical speed (9200 RPM). The authors believe these are first-time ever achievements for gas bearings.

FIGURE 9 shows the measured rotor response at the bearing cartridges. Note the presence of another critical speed at about 9000 RPM (150 Hz).

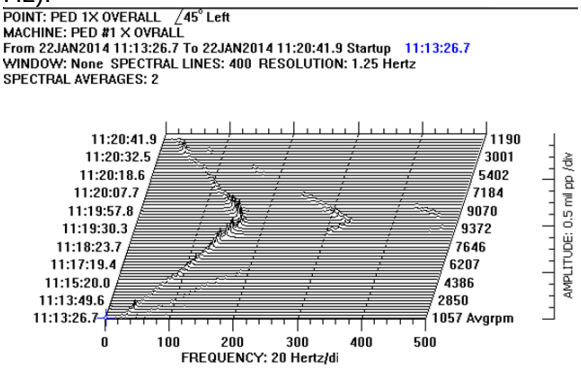

FIGURE 9. Spectrum of measured rotor response at the bearing cartridge.

Unfortunately the challenge from Dresser Rand was to spin the rotor to 10,000 RPM and at or just before the goal, the undriven bearing set failed. Eddy-current probe measurements show that the damper in the bearing cartridges experienced very little motion. The principal of operation of a damper is that they can dissipate energy and absorb large amplitude motion. FIGURE 10 shows the relative motion of the bearing cartridge with respect to the damper. Note that there is little to no motion during both run-up and coast-down. The small motion seen is at the 1st and 2nd critical speeds (2300 and 9200 RPM).

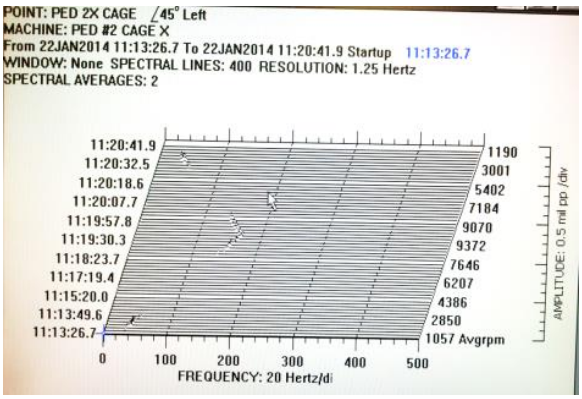

FIGURE 10. Measured relative motion between the bearing cartridge and damper.

Although the crash was rather spectacular and the bearing surfaces were both destroyed there was no metal to metal contact and the rotor journal cleaned up during regrind with less then .02mm of stock removal.

ROTORDYNAMIC MODELING

San Andres [3] assisted New Way with rotordynamic modeling, using the XLTRC² Software, developed at the Texas A&M Turbomachinery Lab.

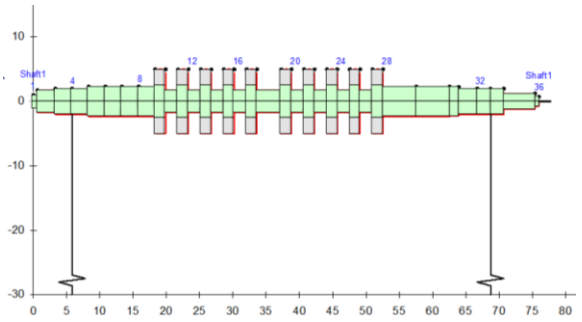

FIGURE 11. Rotor geometry modeled in XLTRC² by San Andres [6].

The code predicts critical speeds of 2600 RPM and 8800 RPM, which agrees well with test results. FIGURE 12 and FIGURE 13 show the predicted mode shapes of the rotor at the two critical speeds. Note that the damping ratio of the 2nd critical is an order of magnitude greater than that of the 1st critical speed.

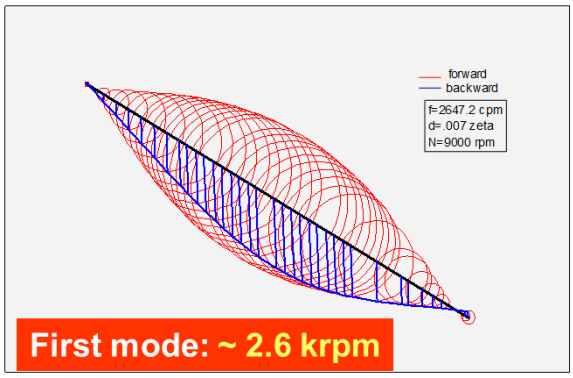

FIGURE 12. Predicted mode shape at the rotor's 1st critical speed, from San Andres [3].

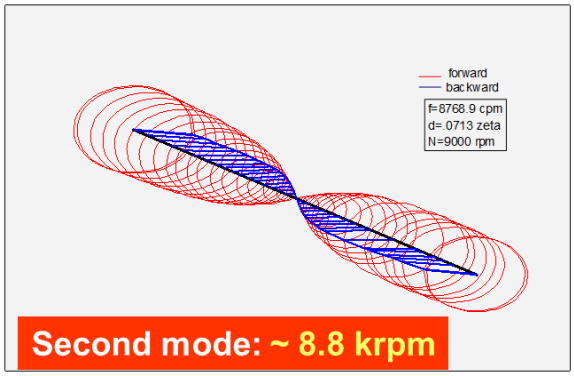

FIGURE 13. Predicted mode shape at the rotor's 2nd critical speed, from San Andres [3].

Predictions for AF also agree well with measurements taken at TurboCare. The author cannot explain why the dampers did not engage or why the measured relative motion is so small. However, a revised report by San Andres [4] shows that locked dampers would have resulted in a well-damped natural frequency at 4300 RPM, in addition to natural frequencies at 2500 and 9400 RPM. However, this revised model does not predict AF as well as initially predicted.

SUMMARY

Although the goal of 10,000 RPM was not achieved, we feel the effort was successful; passing through critical speeds with high amplification factors in relatively large flexible rotors. We will be returning to this effort with other ideas for damping that do not employ oil.

REFERENCES

[1] G. Agrawal, "Foil Air/Gas Bearing Technology - An Overview," in International Gas Turbine and Aeroengine Congress & Exhibition, ASME, 1997.

[2] M. Kuzdzal and J. Hustak, "Squeeze Film Damper Bearing Experimental vs. Analytical Results for Various Damper Configurations," in Proceedings of the Twenty-fifth Turbomachinery Symposium, 1996.

[3] L. San Andres, "Proprietary Report to New Way Air Bearings," College Station, 2014.

[4] L. San Andres, "Proprietary Report to New Way Air Bearings (2)," 2014.

CROSS-AXIS DYNAMIC-COUPLING ANALYSIS FOR 6-DOF MAGNETICALLY-LEVITATED STAGE DESIGN

Vu Nguyen
Center for X-Ray Optics
Lawrence Berkeley National Laboratory
Berkeley, California, U.S.A

Won-jong Kim
Department of Mechanical Engineering
Texas A&M University
College Station, Texas, U.S.A

INTRODUCTION

In multi-axis positioning, single-moving-part stages have only one moving part performing motions in all the possible axes [1, 2]. A key advantage of these stages is the avoidance of cumulative position errors due to mechanical bearings' tolerances. For single-moving-part stages, the mechanical components include 1) a moving platen, 2) the base, 3) actuators, and 4) bearings. Given that each actuator or bearing of the stage is broken down to a mover and a stationary part, in a single-moving-part stage the movers of all the actuators and bearings are rigidly assembled to the moving platen. In most cases, rotational motions, either in-plane (*xy*) or out-of-plane, are realized by two actuators generating parallel forces [1–4]. For multi-axis nano-precision stages with millimeter-order strokes in *xy*, Lorentz coils have been used due to the need for non-contact force generation, and their linear force model facilitates the real-time feedback control [1–4]. Common designs for 6-DOF single-moving-part stages are a square [3], cross [4], and triangle [1], as depicted in Fig. 1. The movers can be either permanent magnets (PMs) or coils. Here, 1 is the base, 2 is the single moving part, and 3 is the actuator.

In motion stages with mechanical bearings, the friction induced by cross-coupling forces normal to the bearing surfaces is a disturbance that degrades the control performance. Efforts on minimizing the parasitic errors in multi-axis positioning, however, were reported mainly for flexures [5, 6]. With the rapid development in semiconductor manufacturing, microscopy, and additive manufacturing, the requirements of motion stages have constantly increased [7, 8]. Together with the nanoscale precision and multi-DOF positioning capability, the required travel ranges for the above applications are exceeding the capability of flexure stages. For 6-DOF single-moving-part stages with magnetic or air bearings, the position error in one axis over the entire travel range of another axis is dependent not only on the reference surfaces of sensors and bearings but also on the loading conditions and control performance. Here, instead of the parasitic errors, it is more relevant to consider the cross-axis perturbation, which is the peak-to-peak (p-p) position fluctuation of one axis (the perturbed axis) when the desired motion command is performed in another axis (the primary axis). Results with cross-axis perturbations were reported in [1, 4, 9, 10].

The main cause of cross-axis perturbations is the off-axis error forces or torques. These errors result from the (static and dynamic) couplings between multiple actuators of the same stage. Although leading to position errors and possibly instability, the problem of dynamic couplings has not been extensively investigated. The focuses of most efforts in this area were mainly on the modeling and control of certain structures [1–3, 9–11]. Besides, why a design configuration was selected was usually not well justified. Maglev and air-bearing stages with a single moving part have been reported with the capability to perform 6-DOF motions [1, 2]. However, challenges still remain in dealing with the off-axis error forces affecting the control performance in multi-DOFs at the scales of nanometers and micro-radians.

The causes of error forces include 1) geometrical errors (perpendicularity, parallelism between the actuators' axes, and straightness of coil turns), 2) dynamic couplings between the axes due to the actuators' structure (PMs' fringing effect, coils' end effect), 3) errors in the coil currents, and 4) errors in the coil fill factor and PMs' remanence. In case there are two actuators that are supposed to produce two equal forces in the same direction, the errors from the current amplifiers result in a difference in these forces, and, thereby, an error torque. In this paper a force error is defined as the difference between the desired force and the actual force generated by an actuator along the same axis. The causes 3) and 4) mentioned above produce this error. An error force is the undesired off-axis force generated in another axis when an actuator produces a desired force in its primary axis, due to the causes of 1) and 2).

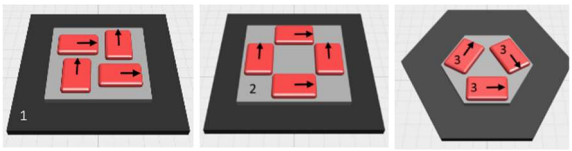

FIGURE 1. Configurations of single-moving-part stages: square, cross, and triangle (left to right).

This paper presents an analysis to quantify the effects of cross-axis couplings and compare those effects between the designs of multi-axis stages. The actuator of interest in this case is of Lorentz-force type, which has been commonly used for 6-DOF single-moving-part stages with a long *xy* stroke [1–4, 9, 11]. With a 6-DOF single-moving-part stage broken into its basic units (each is a Lorentz-force actuator), a bounded off-axis error force is assumed for each actuator. The effect of cross-axis dynamic couplings in the system model used for feedback control is quantified by the norm of the transformation matrix between the closed-loop control efforts and the coil currents. In Fig. 1, the actuator units of the stages are assumed to have the same size and force-generation capability. Each actuator generates two orthogonal forces, one in the horizontal and the other in the vertical direction. The distance from the horizontal axis of symmetry of each actuator to the central vertical axis of the entire moving part, about which the torque is calculated, is the same, l. The off-axis error-force bounds of all the actuators are assumed to be the same. The question of interest is which design among the three shown in Fig. 1 has the least cross-axis coupling. Fig. 2 is a photograph of the setup on which experimental results are obtained to support the analysis presented in this paper.

DYNAMIC COUPLING ANALYSIS

Qualitative Analysis

For a triangular design as in Fig. 3(a) to generate a force in *x*, motor 2 needs to generate a force in *x*, F_{2x}, while motors 1 and 3 need to produce two opposite forces in *y* to balance the torque about the vertical axis generated by F_{2x} [12, 13]. Three motors must be energized, and the currents in the motors 1 and 3 must be calculated based on F_{2x} so that the net torque about the vertical axis is ideally zero. In practice, due to the power amplifiers' nonlinearity and errors in the motor's geometry, errors are present. For the square stage in Fig. 3(b), if a torque needs to be generated about the *x*-axis passing through the mover's geometric center, and, at the same time, a force needs to be produced in *x*, both two motors 1 and 3 must be energized. However, when motors 1 and 3 produce two forces in the opposite directions along *z*, they produce an undesired error torque about the *y*-axis. To cancel this error, other two motors, 2 and 4, must be energized. Totally 4 motors must be energized in this case. With the cross design as in Fig. 3(c), two motors, 2 and 4, are sufficient to actuate the mover along the *x*-axis and, at the same time, generate an out-of-plane torque about this axis. For the square design in Fig. 3(b), the difference between F_{1z} and F_{3z} creates a toque about both *x* and *y*. For the cross layout in Fig. 3(c), the difference between the vertical forces, F_{2z} and F_{4z}, produces a desired toque about *x*. They, however, only generate a negligible error torque about *y* because the ideal acting points of the forces at motors 2 and 4 are aligned in the *y*-axis.

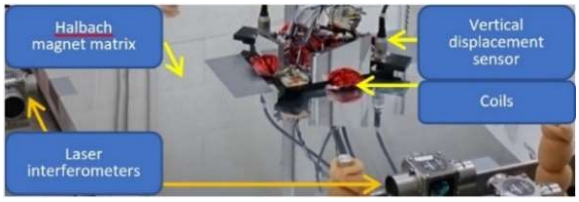

FIGURE 2. Photograph of the 6-DOF maglev stage to support the analysis presented herein.

Quantitative Analysis of 6-DOF Stages Using Halbach Arrays and Lorentz Coils

In this analysis, $\boldsymbol{F_t}$ is the vector consisting of the total Lorentz forces and torques acting on the moving part of a 6-DOF stage as in Figs. 3(b–d).

$$\boldsymbol{F_t} = [F_x\ F_y\ T_z\ T_x\ T_y\ F_z]^{\boldsymbol{T}} \quad (1)$$

$\boldsymbol{F_a}$ is the vector consisting of the force components generated by the individual actuators that constitute the 6-DOF motion system. With the square, cross, and triangular configurations depicted in Figs. 3(b–d), $\boldsymbol{F_a}$ is as follows, respectively.

$$\boldsymbol{F_{a\_square}} = [F_{1x}\ F_{1z}\ F_{2y}\ F_{2z}\ F_{3x}\ F_{3z}\ F_{4y}\ F_{4z}]^T \quad (2)$$

$$\boldsymbol{F_{a\_cross}} = [F_{1y}\ F_{1z}\ F_{2x}\ F_{2z}\ F_{3y}\ F_{3z}\ F_{4x}\ F_{4z}]^T \quad (3)$$

$$\boldsymbol{F_{a\_triangular}} = [F_{1h}\ F_{1z}\ F_{2h}\ F_{2z}\ F_{3h}\ F_{3z}]^T \quad (4)$$

Here, F_{ju} is the Lorentz force component generated by the actuator numbered *j* along the *u*-axis. In case of the triangular design, F_{jh} is the Lorentz force produced by actuator *j* in the *XY* plane. The relation between $\boldsymbol{F_t}$ and $\boldsymbol{F_a}$ is

$$\boldsymbol{F_t} = \boldsymbol{A}\boldsymbol{F_a}. \quad (5)$$

Here, $\boldsymbol{A}$ is the constant-element matrix in Eqs. (6–8). Assumptions for this analysis are 1) the mover's center of mass is its geometric center in the *xy* plane, 2) each actuator generates two independent and orthogonal forces with the acting point at its geometric center seen in the *xy* plane, 3) the gap between the planar coils and the PMs' surface is constant, and 4) for all the actuators the distance to calculate the torque

about the mover's vertical axis of symmetry is the same, l. In Eq. (8), α = π/6 rad for the design in Fig. 3(d) and α = 0 for the one in Fig. 3(a).

$$\boldsymbol{A_{square}} = \begin{bmatrix} 1 & 0 & 0 & 0 & 1 & 0 & 0 & 0 \\ 0 & 0 & 1 & 0 & 0 & 0 & 1 & 0 \\ -l & 0 & -l & 0 & l & 0 & l & 0 \\ 0 & -l & 0 & l & 0 & l & 0 & -l \\ 0 & -l & 0 & -l & 0 & l & 0 & l \\ 0 & 1 & 0 & 1 & 0 & 1 & 0 & 1 \end{bmatrix} \quad (6)$$

$$\boldsymbol{A_{cross}} = \begin{bmatrix} 0 & 0 & 1 & 0 & 0 & 0 & 1 & 0 \\ 1 & 0 & 0 & 0 & 1 & 0 & 0 & 0 \\ l & 0 & -l & 0 & -l & 0 & l & 0 \\ 0 & 0 & 0 & l & 0 & 0 & 0 & -l \\ 0 & -l & 0 & 0 & 0 & l & 0 & 0 \\ 0 & 1 & 0 & 1 & 0 & 1 & 0 & 1 \end{bmatrix} \quad (7)$$

$$\boldsymbol{A_{triang}} = \begin{bmatrix} -\sin\alpha & 0 & -\sin\alpha & 0 & 1 & 0 \\ \cos\alpha & 0 & -\cos\alpha & 0 & 0 & 0 \\ l & 0 & l & 0 & l & 0 \\ 0 & l\sin\alpha & 0 & l\sin\alpha & 0 & -l \\ 0 & -l\cos\alpha & 0 & l\cos\alpha & 0 & 0 \\ 0 & 1 & 0 & 1 & 0 & 1 \end{bmatrix} \quad (8)$$

Due to the sinusoidal variation of the magnetic-flux density in one direction on the horizontal plane of the linear Halbach array, the total Lorentz-force vector produced by the planar Lorentz actuators, each with either 3-phase coils [3, 12] or 2-phase coils [13], can be expressed as

$$\boldsymbol{F_a} = k\boldsymbol{Si}, \quad (9)$$

where ***i*** is the current vector. Here, *k* is a constant depending on the peak magnetization of the magnets, the array's spatial pitch and thickness, the coils' geometry, and the magnet-coil gap [3, 12, 13]. It represents the actuator's force density for levitation and thrust. With the same actuator structure and magnet-coil gap, in this analysis the same constant *k* is assumed for three designs in Figs. 3(b–d). ***S*** is the matrix representing the position-dependent components of the force calculation. For the square and cross designs, ***S*** is a 8 × 8 matrix and ***i*** is a 8 × 1 vector. For the triangular designs ***S*** is 6 × 6 and ***i*** is 6 × 1. The derivations of *k* and ***S*** for a triangular design and a cross one can be found in Chapter IV of [12] and III of [14], respectively. The matrix ***S*** is formed by blocks of 2 × 2 rotational-transformation matrices in its diagonal. ***S*** is, therefore, orthogonal. That is, $\boldsymbol{S}^{-1} = \boldsymbol{S}^{T}$. This is the key advantage of the Lorentz-force actuators using a Halbach array. This allows for the currents to be calculated from the control efforts of the stage's controller without calculating $\boldsymbol{S}^{-1}$ in real time.

To derive a linear model for the 6-DOF planar stage, Eq. (5) and ***B***, the pseudoinverse of the constant-element matrix ***A***, are used. The control effort vector, ***U***, is introduced by $\boldsymbol{F_a} = k\boldsymbol{BU}$, where $\boldsymbol{U} = [u_x\ u_y\ u_{\theta z}\ u_z\ u_{\theta x}\ u_{\theta y}]^T$. Each element of ***U*** is the decoupled control effort in one axis of the stage. Substituting $\boldsymbol{F_a} = k\boldsymbol{BU}$ into $\boldsymbol{F_t} = \boldsymbol{AF_a}$ yields $\boldsymbol{F_t} = k\boldsymbol{U}$. From this and $\boldsymbol{F_t} = \boldsymbol{M\ddot{p}}$ (pure-mass model assumed), where ***M*** is the 6 × 6 mass matrix and ***p*** is the 6 × 1 position vector of the mover, the system model is formed as $\boldsymbol{M\ddot{p}} = k\boldsymbol{U}$.

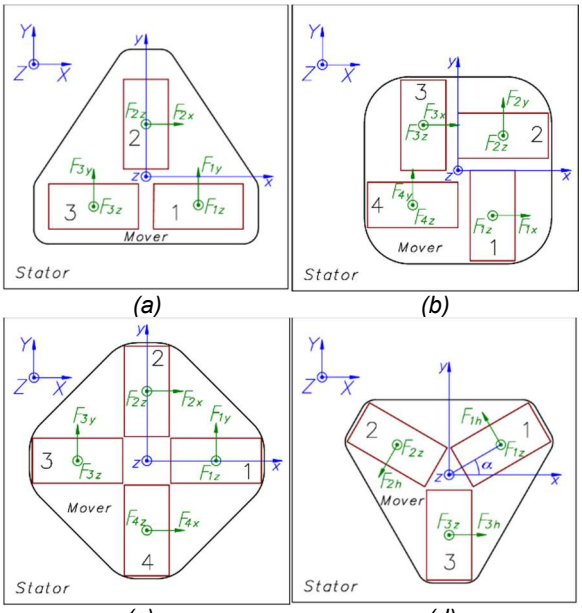

FIGURE 3. Four configurations of stage designs.

With ***C***(*s*) being the 6 × 1 vector of decoupled controllers in the 6 axes, one has $\boldsymbol{U}(s) = \boldsymbol{C}(s)\boldsymbol{E}(s)$, where $\boldsymbol{E}(s)$ represents the Laplace transform of the position-feedback error ***e***(*t*). The control efforts *u* in the vector ***U*** are calculated based on the implemented feedback-controller structure. The coil currents are calculated based on Eq. (9) and $\boldsymbol{F_a} = k\boldsymbol{BU}$. This gives $\boldsymbol{i} = \boldsymbol{S}^T\boldsymbol{BU}$. Because $\boldsymbol{S^T}$ is orthogonal, we have $\|\boldsymbol{S}^T B\|_2 = \|B\|_2$. Therefore, $\|B\|_2$ represents the magnitude of the current vector ***i*** depending on the control effort vector ***U***. In practice, when a cross-axis error force or torque occurs, the corresponding element of the ***A*** matrix in Eqs. (6–8) must be changed to reflect the error. With the cross-axis error forces, the accordingly-varied ***B*** should be the one that yields the accurate values of the coil currents to guarantee the desired performance of the designed controllers. However, practically only the constant-element (and nominal) ***B*** is utilized in real-time control. Therefore, there is an error between the calculated current vector (from the fixed ***B***) and the desired current vector that should be computed by the varied ***B***. With the same cross-axis error-force bound, it is, therefore, worth to estimate the variation range of $\|\boldsymbol{B}\|_2$ so that the variation of the magnitude of the coil current vector can be evaluated. Specifically, the envelope of $\|\boldsymbol{B}_{varied}\|_2/\|\boldsymbol{B}_{nominal}\|_2$ should be estimated and compared between the designs.

Coupling Analysis for Out-of-Plane Dynamics

Assuming that the motor 1 generating a force F_{1x} in *x* has an error force in *z* of $\Delta F_z = \varepsilon_{1xz} F_{1x}$, where $|\varepsilon_{1xz}|$ is bounded by ϵ, the matrices of ***A*** as in Eqs. (6–8) are changed as follows.

$$\boldsymbol{A}_{square\_varried} = \begin{bmatrix} 1 & 0 & 0 & 0 & 1 & 0 & 0 & 0 \\ 0 & 0 & 1 & 0 & 0 & 0 & 1 & 0 \\ -l & 0 & -l & 0 & l & 0 & l & 0 \\ -\varepsilon_{1xz} l & -l & \varepsilon_{2yz} l & l & \varepsilon_{3xz} l & l & -\varepsilon_{4yz} l & -l \\ -\varepsilon_{1xz} l & -l & -\varepsilon_{2yz} l & -l & \varepsilon_{3xz} l & l & \varepsilon_{4yz} l & l \\ \varepsilon_{1xz} & 1 & \varepsilon_{2yz} & 1 & \varepsilon_{3xz} & 1 & \varepsilon_{4yz} & 1 \end{bmatrix} \quad (10)$$

$$\boldsymbol{A}_{cross\_varied} = \begin{bmatrix} 0 & 0 & 1 & 0 & 0 & 0 & 1 & 0 \\ 1 & 0 & 0 & 0 & 1 & 0 & 0 & 0 \\ l & 0 & -l & 0 & -l & 0 & l & 0 \\ 0 & 0 & \varepsilon_{2xz} l & l & 0 & 0 & -\varepsilon_{4xz} l & -l \\ -\varepsilon_{1yz} l & -l & 0 & 0 & \varepsilon_{3yz} l & l & 0 & 0 \\ \varepsilon_{1yz} & 1 & \varepsilon_{2xz} & 1 & \varepsilon_{3yz} & 1 & \varepsilon_{4xz} & 1 \end{bmatrix} \quad (11)$$

$$\boldsymbol{A}_{triang\_varied} = \begin{bmatrix} -\sin\alpha & 0 & -\sin\alpha & 0 & 1 & 0 \\ \cos\alpha & 0 & -\cos\alpha & 0 & 0 & 0 \\ l & 0 & l & 0 & l & 0 \\ \varepsilon_{1hz} l \sin\alpha & l\sin\alpha & \varepsilon_{1hz} l \sin\alpha & l\sin\alpha & -\varepsilon_{3hz} l & -l \\ -\varepsilon_{1hz} l \cos\alpha & -l\cos\alpha & \varepsilon_{2hz} l \cos\alpha & l\cos\alpha & 0 & 0 \\ \varepsilon_{1hz} & 1 & \varepsilon_{2hz} & 1 & \varepsilon_{3hz} & 1 \end{bmatrix} \quad (12)$$

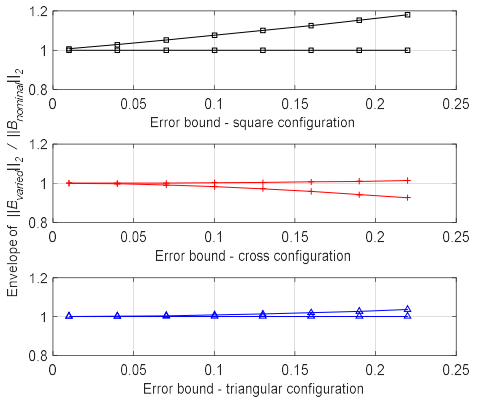
Envelope of $\|B_{varied}\|_2 / \|B_{nominal}\|_2$
Error bound - square configuration
Error bound - cross configuration
Error bound - triangular configuration

FIGURE 4. Envelope of $\|\boldsymbol{B}_{varied}\|_2/\|\boldsymbol{B}_{nominal}\|_2$ for the out-of-plane dynamics.

It is noticed that $1/\|\boldsymbol{B}\|_2$ is the lower bound of $\|\boldsymbol{A}\|_2$, and, therefore, is a continuous function on the open set of the matrix elements [15]. Given the fact that ε_{juv} varies in $[-\epsilon, \epsilon]$, this discussion is not aimed at deriving a rigorous analysis to constrain $\|\boldsymbol{B}\|_2$ but providing an estimate of the envelope of the ratio between the 2-norm of the varied ***B*** (calculated from the varied ***A*** in Eqs. 10–12), and that of the nominal ***B*** calculated from the nominal ***A*** in Eqs. (6–8). This is done by computing the ratio of $\|\boldsymbol{B}_{varied}\|_2/\|\boldsymbol{B}_{nominal}\|_2$ with the elements of ε_{juv} switched between evenly distributed values in $[-\epsilon, \epsilon]$. With l = 0.1 m and $\epsilon \in$ [0.01, 0.22], the envelopes of this ratio for all three designs are plotted in Fig. 4. The triangular configuration has the narrowest envelope and the square configuration has the largest one.

Force-Error Analysis for In-Plane Dynamics

The force error considered here is the difference between the actual force generated by an actuator and the desired force to be generated in the same axis. It can be a static or a dynamic one. The causes of static errors include the coil fill factor, actuator's geometrical errors, and errors in the PMs' magnetizations. The causes of the dynamic errors include the lag in the actuator's response compared with the controller's command, and the actuator saturation. This lag is due to not only the slew rate but also the phase change in the power-electronic dynamics at high frequencies. For the in-plane dynamics (*x*, *y*, and the rotation about the vertical axis), the ***A*** matrix can be reduced from Eqs. (10–12).

$$\boldsymbol{A}_{square\_inplane} = \begin{bmatrix} 1 & 0 & 1 & 0 \\ 0 & 1 & 0 & 1 \\ -l & -l & l & l \end{bmatrix} \quad (13)$$

$$\boldsymbol{A}_{cross\_inplane} = \begin{bmatrix} 0 & 1 & 0 & 1 \\ 1 & 0 & 1 & 0 \\ l & -l & -l & l \end{bmatrix} \quad (14)$$

$$\boldsymbol{A}_{triangular\_inplane} = \begin{bmatrix} -\sin\alpha & -\sin\alpha & 1 \\ \cos\alpha & -\cos\alpha & 0 \\ l & l & l \end{bmatrix} \quad (15)$$

We consider the case when each Lorentz force component in *xy* has a force error, where the actual force component is $F_{1x}(1+\varepsilon_{1x})$. Here F_{1x} is the desired force to be generated by actuator 1 in *x*, and $|\varepsilon_{1x}|$ is bounded by ϵ. The forces generated by the actuators are combined to drive the moving platen in one axis and minimize the position fluctuations in the other axes, all in closed-loop control. A force error at one actuator requires other actuators to respond accordingly to compensate for this error. The ***A*** matrices with the force errors in *x* and *y* for the three design configurations mentioned above are

$$\boldsymbol{A}_{square\_inplane\_varied} = \begin{bmatrix} 1+\varepsilon_{1x} & 0 & 1+\varepsilon_{3x} & 0 \\ 0 & 1+\varepsilon_{2y} & 0 & 1+\varepsilon_{4y} \\ -l(1+\varepsilon_{1x}) & -l(1+\varepsilon_{2y}) & l(1+\varepsilon_{3x}) & l(1+\varepsilon_{4y}) \end{bmatrix}, \quad (16)$$

$$\boldsymbol{A}_{cross\_inplane\_varied} = \begin{bmatrix} 0 & 1+\varepsilon_{2x} & 0 & 1+\varepsilon_{4x} \\ 1+\varepsilon_{1y} & 0 & 1+\varepsilon_{3y} & 0 \\ l(1+\varepsilon_{1y}) & -l(1+\varepsilon_{2x}) & -l(1+\varepsilon_{3y}) & l(1+\varepsilon_{4x}) \end{bmatrix}, \quad (17)$$

$$\boldsymbol{A}_{triangular\_inplane\_varied} = \begin{bmatrix} -(1+\varepsilon_{1h})\sin\alpha & -(1+\varepsilon_{2h})\sin\alpha & 1+\varepsilon_{3h} \\ (1+\varepsilon_{1h})\cos\alpha & -(1+\varepsilon_{2h})\cos\alpha & 0 \\ l(1+\varepsilon_{1h}) & l(1+\varepsilon_{2h}) & l(1+\varepsilon_{3h}) \end{bmatrix}. \quad (18)$$

Fig. 5 gives the envelopes of $\|\boldsymbol{B}\|_2$ for the ***A*** matrices in Eqs. (16–18) in case one actuator of the associated system has a bounded force error specified by $\epsilon \in$ [0.01, 0.22]. For the in-plane dynamics, the envelopes for the square and cross designs are the same and smaller than that of the triangular one. This indicates that the effect of the actuators' force errors on the triangular design is worse than that on the square and cross ones.

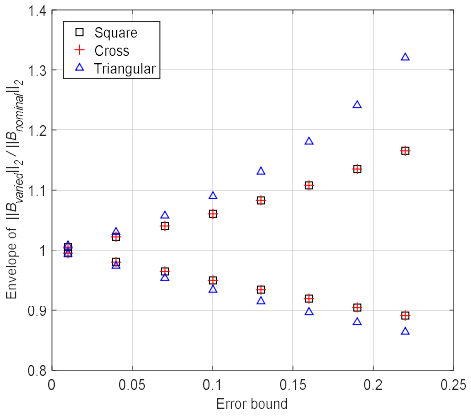

FIGURE 5. Envelope of $\|\boldsymbol{B}_{varied}\|_2/\|\boldsymbol{B}_{nominal}\|_2$ for the in-plane dynamics.

In case a vibration-isolation stage is of interest (no need for high-speed motions in *xy*), this analysis suggests that the triangular one is the choice. If a long-stroke and high-speed stage is needed, where a compact mover is required and the out-of-plane dynamics is not a concern, the square design is the selection. If a long-stroke and high-speed stage is needed, where the mover is magnetically levitated by Lorentz forces, the cross design helps reduce the effects of the off-axis error forces on the out-of-plane dynamics and the *xy* force errors on the in-plane dynamics.

EXPERIMENTAL RESULTS

The Cross-Coupling Quantity

In this work we propose a quantity entitled "cross-coupling quantity" (CCQ) as a measure to compare the levels of cross-axis couplings in multi-axis motion control. The CCQ introduced here is defined for each pair of primary and perturbed axes. It is defined as the product of the transient response's peak time in the primary axis and the ratio between the perturbed axis' p-p fluctuation and primary axis' displacement. The CCQ between the θ_z (perturbed) and θ_y (primary) is $t_p\theta_{z\_pp}/\theta_{y\_d}$, where t_p and θ_{y_d} are, respectively, the peak time and displacement along θ_y. The p-p position fluctuation in θ_z is θ_{z_pp}. The peak time is used to calculate the CCQ because 1) it takes into account the speed and acceleration of the primary axis' motion, 2) the duration of the peak time is the window when the peak fluctuation in the perturbed axis is most likely to occur, and 3) for a given response's plot, the peak time can be estimated without the need of the raw data. The CCQ unit depends on the type of motions in the primary and the perturbed axes. Table 1 provides the unit of the CCQ in all cases. A decrease in the CCQ implies a reduction and, therefore, an improvement in the cross-axis coupling.

TABLE 1. The CCQ units in all the cases, where T and R stand for translational and rotational.

Primary axis	T	T	R	R
Perturbed axis	T	R	T	R
CCQ	s	rad·s / m	m·s / rad	s

Experimental Results Performed on a Cross-Configuration 6-DOF Maglev Planar Stage

This part presents results performed on a cross-configuration moving-coil maglev stage that we designed and built using planar Lorentz coils and a Halbach magnet matrix. Details about the mechanical fabrication, geometries, system modeling, and proportional-integral-derivative controller design for this 6-DOF maglev stage can be found in [14]. Figure 6 plots a transient response with the displacement of 14 mm in *x* and the position perturbations in θ_y and θ_z. The peak time of this position profile is 0.30 s. Table 2 gives the CCQ values between *x* and these two axes.

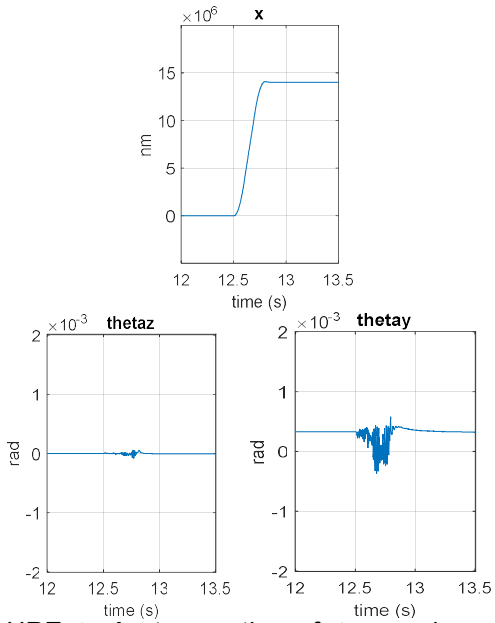

FIGURE 6. A step motion of 14 mm in x and perturbations in θ_z and θ_y.

TABLE 2. The CCQ values between x and other axes in the step response presented in Fig. 6.

Axis	*y* (μm)	θ_z (μrad)	θ_y (μrad)
p-p perturbation	16.5	134.8	945
CCQ	0.0004	0.0029	0.0203
CCQ unit	s	rad·s / m	rad·s / m

Fig. 14 of [9] reports a step response of 7 mm in *x* and *y* with the peak time of 0.1 s, the p-p perturbations are 9.5 mrad in θ_z (rotation about the vertical axis), and 4 mrad in θ_y (out-of-plane rotation). Compared with the CCQ of our stage in Table 2, the CCQ between the primary axis and the out-of-plane rotation in [9] is 2.8 times larger, and that between the primary axis and the in-

plane rotation in [9] is 46.8 times larger, as seen in Table 3. The mechanical design configuration in [9] is a triangular one. The effect of cross-axis couplings on the in-plane dynamics of this triangular stage is of a significantly greater concern compared to that of our cross-configuration design.

TABLE 3. The CCQ values between x and two other axes, θ_z and θ_y in the 7-mm step of [9].

Axis	θ_z (mrad)	θ_y (mrad)
p-p perturbation	9.5	4.0
CCQ	0.1357	0.0571
CCQ unit	rad·s / m	rad·s / m

Fig. 16(c) of [4] presents a translational motion of 30 mm in *y*, the primary axis. The corresponding rms position error in *x* is 8.6 μm, and the peak time is approximately 0.3 s. The CCQ between *y* and *x* is 0.09×10^{-3} s. In our experimental result shown in Figs. 6 and 7, the rms position error in *y* is 2.4 μm, and the CCQ calculated from this response is 0.05×10^{-3} s. Our stage has a better CCQ because we employed a smaller number of coils (8 versus 60 in [4]) and used longer coils with better straightness in regard to minimizing the cross-axis couplings.

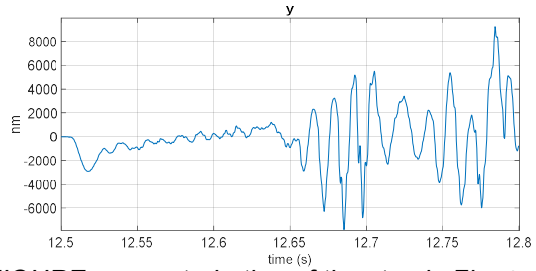

FIGURE 7. y perturbation of the step in Fig. 6.

CONCLUSIONS

In this paper we provide a topological analysis to quantify and compare the effects of cross-axis couplings on multi-axis positioning with single-moving-part motion stages. This analysis is expected to help designers select the right design configuration for their specific multi-DOF motion-control applications. In addition, we introduce the CCQ as a standard measure to compare the levels of cross-axis couplings in multi-axis motion control. The CCQ is an augmentation of the conventional parasitic error, and aimed at comparing the cross-axis perturbations in transient responses of multi-DOF motion stages.

REFERENCES

[1] Verma S, Shakir H, Kim WJ. Novel electromagnetic actuation scheme for multi-axis nanopositioning. IEEE Trans. Mag. 2006;42(8):2052–62.

[2] Fesperman R, Ozturk O, Hocken R, Ruben S, Tsao TC, Phipps J, Lemmons T, Brien J, Caskey G. Multi-scale alignment and positioning system – MAPS. Prec. Eng. 2012;36(4):517–37.

[3] Compter IJC. Electro-dynamic planar motor. Prec. Eng. 2004;28:171–80.

[4] Zhu H, Teo TJ, Pang CK. Design and modeling of a six-degree-of-freedom magnetically levitated positioner using square coils and 1-D Halbach arrays. IEEE Trans. Ind. Elect. 2017;64(1):440–50.

[5] Kenton BJ, Leang KK. Design and control of a three-axis serial-kinematic high-bandwidth nanopositioner. IEEE/ASME Trans. Mech. 2012;17(2):356–69.

[6] Roy NK, Cullinan MA. Design and characterization of a two-axis, flexure-based nanopositioning stage with 50 mm travel and reduced higher order modes. Prec. Eng. 2018; 53:236–47.

[7] Smith ST, Seugling RM. Sensor and actuator considerations for precision, small machines. Prec. Eng. 2006;30(3):245–64.

[8] Cheng H, Chen H, Mooring BW. Accuracy analysis of dynamic-wafer-handling robotic system in semiconductor manufacturing. IEEE Trans. Ind. Elec. 2014;61(3):1402–10.

[9] Chen MY, Lin TB, Hung SK, Fu LC. Design and experiment of a macro–micro planar maglev positioning system. IEEE Trans. Ind. Elect. 2012;59(11):4128–39.

[10] Basovich S, Arogeti SA, Menaker Y, Brand Z. Magnetically levitated six-DOF precision positioning stage with uncertain payload. IEEE/ASME Trans. Mech. 2016;21(2):660–73.

[11] Jansen JW, Lierop vCMM, Lomonova E A, Vandenput AJA. Magnetically levitated planar actuator with moving magnets. IEEE Trans. Ind. App. 2008;44(4):1108–15.

[12] Hu T. Design and Control of a 6-Degree-of-Freedom Levitated Positioner with High Precision. Ph.D. thesis, Texas A&M University, College Station, TX, May 2005.

[13] Nguyen VH, Kim WJ. Design and control of a compact lightweight planar positioner moving over a concentrated-field magnet matrix. IEEE/ASME Trans. Mech. 2013;18(3):1090–99.

[14] Nguyen VH. Universal Framework for Linear Motors and Multi-Axis Stages with Magnetic Levitation. Ph.D. thesis, Texas A&M University, College Station, TX, Dec. 2015.

[15] Grcar J F. A matrix lower bound. Linear Algebra and its Applications 2010; 433(1):203–20.

A study of Micro-Mechanical Logic Elements

Frederick Sun[1], Robert M. Panas[1], Jonathan B. Hopkins[2], and Andrew J. Pascall[1]
[1]Lawrence Livermore National Laboratory (LLNL), Livermore, CA, USA
[2]Department of Mechanical and Aerospace Engineering, University of California Los Angeles, Los Angeles, CA, USA

INSTRUCTION

In this paper, the authors investigate several design of micro-mechanical logic elements, providing fundamental building blocks to micro-mechanical logic computation. Mechanical computation offers a variety of advantages over traditional semiconductor electronics. Data processing and storage based on pure mechanical force and displacement can offer benefits such as low energy consumption, mechanical interaction with its surroundings, and survive under harsh environment such as intense radiation where semiconductors are prone to failure. In applications such as sensors under hazardous conditions, mechanical logic show promise with their resistance to harsh environment with low maintenance requirements. However due to manufacturing capabilities, mechanical logic elements and systems had been large and bulky in the past, limiting its practicality. Recent advancement in 3D micro-additive manufacturing technology have provided fabrication techniques which enables the construction of complex micro-structures, and thereby allowing the manufacturing of micro-mechanical logic elements.

The proposed micromechanical logic elements in this paper utilize bi-stable micro-flexures to perform digital computations, the on and off state of a digital system is represented with the two different stable equilibrium state of the bi-stable mechanism. While there exist prior designs [1] that utilize similar concepts, the designs in this paper achieved improved stability, reliability, and signal propagation properties.

Four micromechanical logic element designs are presented in this paper. The first is a fundamental bi-stable switch, the remainder three are various design of AND gates.

BI-STABLE GATE DESIGN

Figure 1.A shows the design of a bi-stable switch. On each symmetric side of the switch there are two sets of parallel guide flexures, labeled 1 and 2, implemented in the form of blade flexures parallel with each other. The design requires flexure set 1 should be significantly longer such that it is more compliant then flexure set 2. Two intermediate stages connect the sets of parallel guide flexures. A final stage is in the center, in which its location will represents the 0 and 1 digital. The hashed lines on the sides indicate the location where the switch is held fixed to the ground.

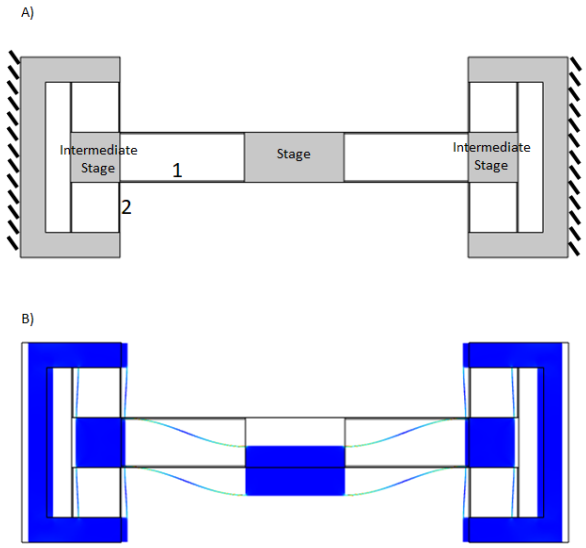

FIGURE 1. A) Model of the design of a bi-stable micro-mechanical switch, B) Simulation of a loaded bi-stable micro-mechanical switch

The bi-stable switch is operated by first loading the sides, which will result in the center stage snapping to one of the stable equilibrium states as shown in Figure 1.B. A digital state can then be defined in the setup. In this paper the downward stable equilibrium position is defined as 0, and the upward stable equilibrium position is defined as 1. The CAD model construction and simulation of the center stage equilibrium position were performed in COMSOL Multiphysics. The loading prescribed on the side of the switch can be achieved by printing the switch on a strained substrate, and then

releasing the substrate after completion of the print, the substrate will then contract to pinch in the sides of the switch.

In the design shown in Figure 1, the longer of the two sets of parallel guide flexures provided the motion range of the 0 and 1 state, and the shorter of the two sets provided the stiffness that drives the stage into one of the equilibrium states. Unlike prior designs [1] that utilizes buckling, the proposed switch in achieved a bi-stabile configuration by arranging the two sets of parallel guide flexures in a manner such that their elastic potential energy forms an energy trap at the two stable equilibrium points. The design avoids buckling of the flexure elements, and thereby reduces the stress and minimizes damage on the flexure elements over numerous cycles of continuous operation.

Note that the loading on the side is difficult to control and may result in the elastic potential energy barrier to be too large or too small, a potential energy barrier too small can be popped through by uncontrolled perturbations, and a barrier too large can cause the flexure elements to buckle before switching takes place, therefore another benefit of the design proposed in Figure 1 is that it allows tuning of the potential energy barrier by adjusting the length of flexure set 2 to match the characteristics of the initial loading on the switch, and in turn improve the reliability of a signal propagating from one switch to the next.

AND GATE DESIGNS

AND Gate Design #1

Figure 2 shows the first of the three AND gate designs. The design is the simplest of the three with the ease of fabrication placed as one of the main objectives. The design comprises of the bi-stable switch shown in Figure 1 as the output, two input stages, and two bent blade flexures connecting the input to the output. The input stages can be connected directly to an input transducer or attached to bi-stable switches oriented 90 degrees to the output switch, with the flexures pointing out of the page. The input stages in Figure 2 are assumed to only have an allowable motion in the vertical direction. Figure 2.B shows the AND gate snapping to the downward position under initial loading. Figure 2.C shows the output stage remains stationary when one of the inputs is displaced upwards. Figure 2.D shows the output stage is popped to

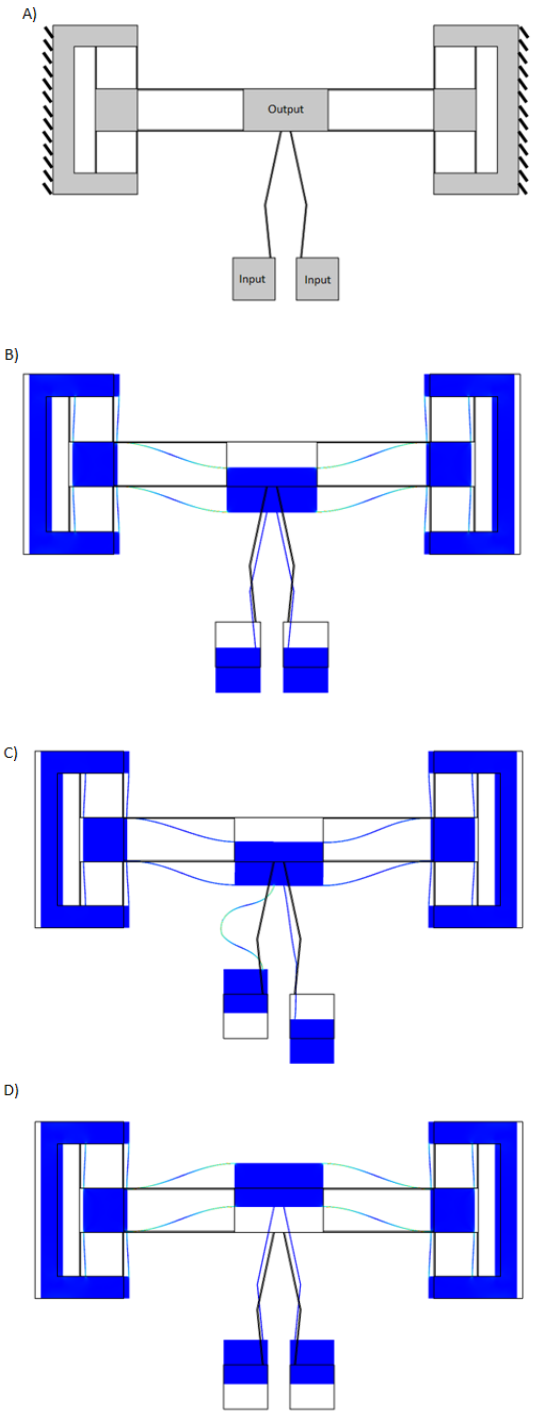

FIGURE 2. A) Design of a micro-mechanical AND gate with single bent blade connection, B) Simulation of said AND gate while initial-loaded C) Simulation of said micro-mechanical AND gate with one input in the up position, D) Simulation of said micro-mechanical AND gate with both inputs in the up position

the upward position when both inputs are displaced upwards. The design successfully achieves its function as an AND gate.

The bent blades in Figure 2 offers a simple solution to keep the output stage in the down position when only one of the input stages is displaced to the up position. The bent blades can undergo large amount of compression as shown in Figure 2.C but has limited motion range while undergoing tension, therefore when only one of the inputs is switched from down position to the up position, the bent blade connecting the input in the down position undergoes tension and keeps the output stage in equilibrium without relying on the stiffness in the bi-stable switch element. By not relying on the stiffness of the bi-stable switch to maintain the output stage's position, the design is advantageous since it will not diminish the residual elastic potential energy stored in the switch, which is needed to activate the next switch in a potential long chain of bi-stable switches in a complex micro-mechanical logic circuit.

AND Gate Design #2

Figure 3 shows the second of the three AND gate designs. The design is similar in topology to the first design except the single bent blade is replaced by two sets of parallel guide flexures connected in series and aligned almost in a straight line. Each set of the parallel guide flexures comprises of two blade flexures arranged to be parallel with each other. This design traded the simplicity in the first design for stiffness between the output and the input when a load is applied on the output. Figure 3.B through Figure 3.D shows the simulation results of the design in configurations at initial-loaded, at one input switched from down to up, and at both inputs switched from down to up respectively. The design successfully achieves its function as an AND gate.

The design achieves its AND gate function in a similar fashion as with the first design. The allowable motion range in the connecting flexures are asymmetrical, permitting a large range under compression but only a small range under tension. When one of the inputs push the output up, the other input exerts a force holding the output stage in place. The output stage is only allowed to move up when both inputs are in the up position.

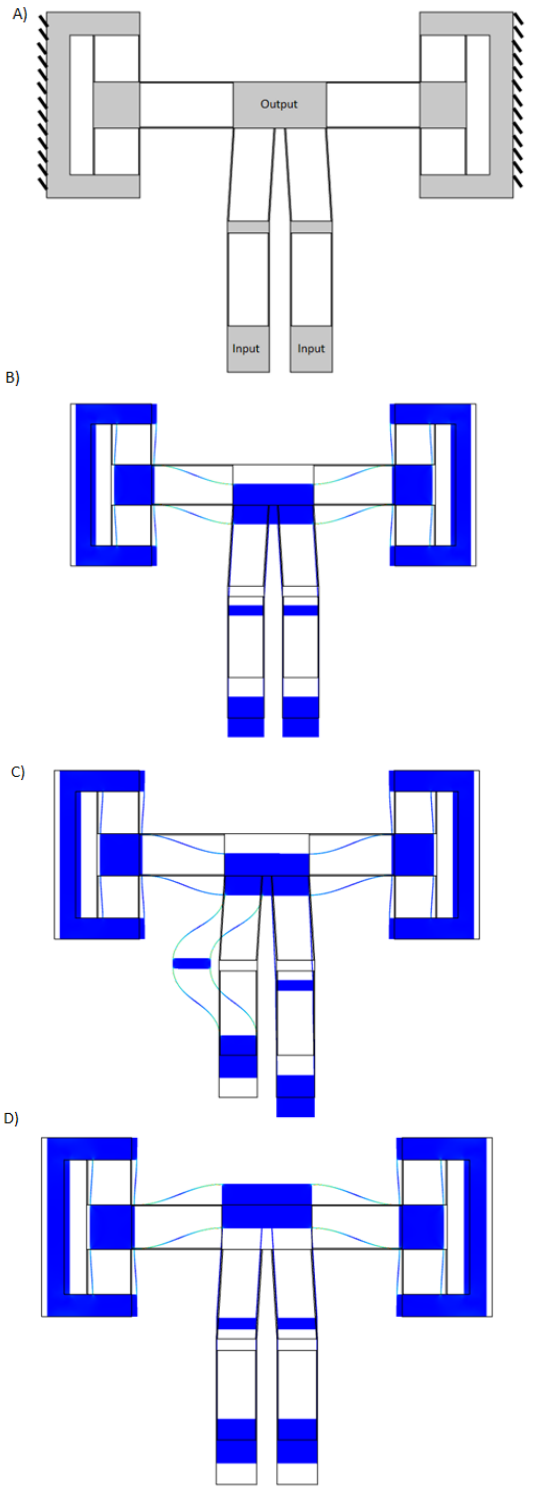

FIGURE 3. A) Design of a micro-mechanical AND gate with parallel guide flexure connection, B) Simulation of said AND gate while initial-loaded C) Simulation of said micro-mechanical AND gate with one input in the up position, D) Simulation of said micro-mechanical AND gate with both inputs in the up position

Due to the blade flexures of the two parallel guide flexures are aligned to be almost on the same line, the stiffness of the serial connection flexure system is high at the first instance when input load is applied, then rapidly drops off when finite displacement takes place. The design allows backward propagation of signals, such that if the output tab is forced to switch from up to down there is enough stiffness in the flexure to displace the input tabs, enabling the mechanical digital signals to travel in both directions.

AND Gate Design #3

Figure 4 shows the last of the three AND gate designs. The parallel guide flexures connecting the input and output stages to the fixed frame in this design is an alternative approach to achieve a bi-stable mechanism without the buckling of individual flexure elements, it serves the same function as with designs in Figure 1, 2, and 3. An additional intermediate stage is introduced between the input and output tabs as shown in Figure 1.A. The input and intermediate stages are connected by rotational pivot flexures, implemented in the form of two blade flexures angled with each other and intersecting at the axis of rotation. The intermediate and output stages are connected by two rotational pivot flexures stacked on top of one another and implemented as two sets of intersecting blade flexures.

Even though the design has a significantly different appearance from the previous two the core principles remain the same, the sides of the switch is loaded before operation for the switches to converge to one of the stable equilibrium positions, as shown in Figure 4.B, then when only one input is displaced from down to up the output remains in the down position, as shown in Figure 4.C, and only when both inputs are in the up position the output moves up, as shown in Figure 4.D, fulfilling the function of an AND gate.

The design in Figure 4 achieves the AND gate function by eliminating permissible motion in the upward direction for the output stage if one of the input tabs are being held in the down position. When only one of the input tabs is pushed up, the intermediate stage rotates about the axis of the rotational pivot flexure on the input tab that is being held down and the output tab is slightly pulled down instead of going up. The output tab stays down due to kinematic

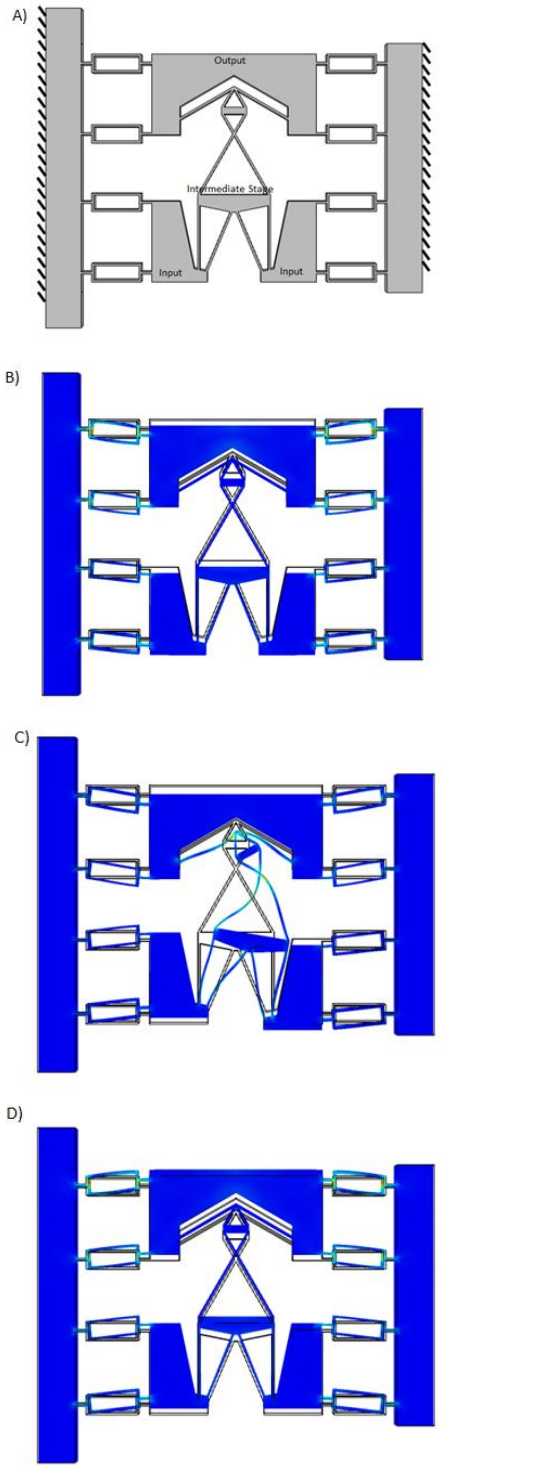

FIGURE 4. A) Design of a micro-mechanical AND gate with rotational pivot flexure and intermediate stage, B) Simulation of said AND gate while initial-loaded C) Simulation of said micro-mechanical AND gate with one input in the up position, D) Simulation of said micro-mechanical AND gate with both inputs in the up position

which is independent of material properties instead of a force balance that may require extensive tuning.

The connection between the input and output tabs are also significantly more rigid in the design in Figure 4 as there is permissible motion in the vertical direction if the output is being forced down.

FUTURE WORKS

In this paper the authors have investigated several micro-mechanical logic elements, each with their own merit. Future goals include refining the merits of the designs into a final design to be deployed in a complex micro-mechanical logic circuit.

ACKNOWLEDGEMENT

This work was performed under the auspices of the U.S. Department of Energy by Lawrence Livermore National Laboratory under Contract DE-AC52-07NA27344. LLNL-PROC-781723

REFERENCES

[1] Song, Y., Panas, R.M., Chizari, S., Shaw, L.A., Mancini, J.A., Hopkins, J.B., Pascall, A.J., 2019, “Additively Manufacturable Micro-Mechanical Logic Gates,” Nature Communications, 10: 882 (6 pages)

DESIGN OF A CAPACITIVE-SENSOR-ARRAY-BASED REAL-TIME MIRROR PROFILER FOR ELLIPTICALLY DYNAMIC BENT MIRROR FOR HARD X-RAY ZOOM OPTICS

D. Shu, J. Anton, S. Kearney, R. Harder, X. Shi, T. Mooney, S. Mashrafi, J. Qian, B. Shi, and L. Assoufid

Advanced Photon Source, Argonne National Laboratory, Argonne, IL 60439, U.S.A.

Abstract

A dynamic mirror bender APS Z7-5004 to perform initial test for hard x-ray zoom optics [1,2] has been designed and constructed as a part of the Argonne National Laboratory (ANL) Laboratory-Directed Research and Development (LDRD) project at the Advanced Photon Source (APS). Using a compact laminar overconstrained flexure bending mechanism [3-6] with capacitive-sensors, the shape of this 300-mm-long elliptical mirror is designed to be tunable between curvatures with radii of ~0.525 and ~74 km. To ensure bender's positioning reproducibility and to monitor the mirror's surface profile, a capacitive-sensor-array-based real-time mirror profiler is applied to the mirror bender [7]. The mechanical design and preliminary test of the real-time mirror bender are presented in this paper.

INTRODUCTION

The Advanced Photon Source (APS) at Argonne National Laboratory (ANL) is a national user facility for synchrotron radiation research. The APS Upgrade's massive increase in coherence will particularly benefit several specific types of x-ray science techniques, especially for X-ray coherent imaging and X-ray nanoprobe applications. Since the X-ray zoom optics system will enable the capability of delivering full coherent flux into a range of spot sizes, it will not only satisfy the needs of a broad user community interested in high-resolution coherent imaging, microdiffraction, or spectroscopy using focused beams, but also will enable a longer working distance relative to spot size in the final optics to develop sufficient coherence lengths for x-ray optics with high numerical aperture.

A proof-of-principle prototype of one dimensional hard X-ray zoom optics has been designed and constructed as a part of the ANL LDRD project at the APS. As shown in Figure 1, the one dimensional hard X-ray zoom optics prototype includes a pair of adaptive deformable focusing mirrors. The first mirror using laminar flexure bending mechanism provides the intermediate focus while the second commercial bimorph mirror provides the desired variable focal spot size at a fixed focal plane. Both mirrors are equipped with in situ optical surface measurement profilers, and combined with an in situ x-ray wavefront sensor in a closed-loop control system, for rapid wavefront monitoring and optimization [8].

In this paper, the mechanical design and preliminary test of the dynamic mirror bender for the 300-mm-long first mirror of the one dimensional hard X-ray zoom optics prototype, including its capacitive-sensor-array-based real-time mirror profiler, are presented.

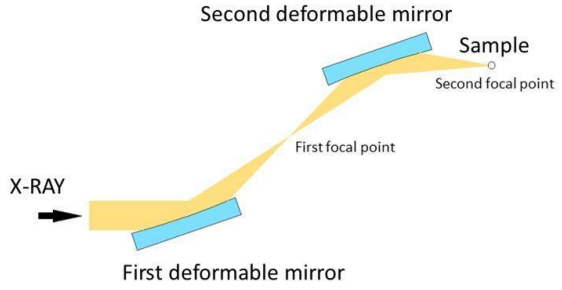

Figure 1. Schematic diagram of the one dimensional hard X-ray zoom optics prototype including a pair of adaptive deformable focusing mirrors.

DESIGN OF LAMINAR FLEXURE BENDING MECHANISM FOR 300-MM-LONG X-RAY DEFORMABLE MIRROR

The mechanical design of the bending mechanism for the 300-mm-long first mirror is similar to the APS Z7-5005 (for 160-mm-long mirror) and Z7-5006 (for 90-mm-long mirror) miniature dynamic mirror benders [9]. The APS Z7-5004 mirror bender for 300-mm-long mirror consists of an Invar base, a pair of laminar

flexure mechanism modules, a pair of bending arms, and two Newport™ Picomotor™ 8301 linear actuators for bending arms as shown in Figure 2.

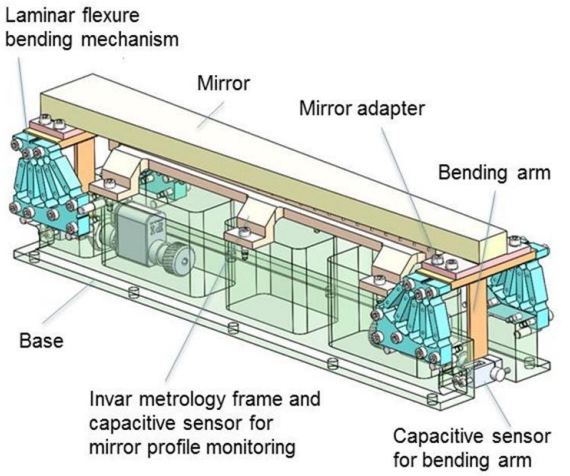

Figure 2. 3-D model of the Z7-5004 dynamic mirror bender for the 300-mm-long x-ray mirror with Newport™ Picomotor™ 8301 linear actuators. The position of each bending arm is measured by a Lion Precision™ C5R capacitive sensor C5R with CPL290 driver. The sensor is set in a near gap of 125 micron to perform within the range of 500 micron with 1.5 nm resolution @ 100 Hz bandwidth.

The laminar flexure bending mechanism module is a solid laminar bonded complex structure as shown in Figure 3 (Left). Constructed with stacks of thin metal weak-link sheets which are manufactured using photochemical machining processes with lithography techniques [3,4], it is a tip-tilting flexure mechanism with ultrahigh positioning sensitivity and stability.

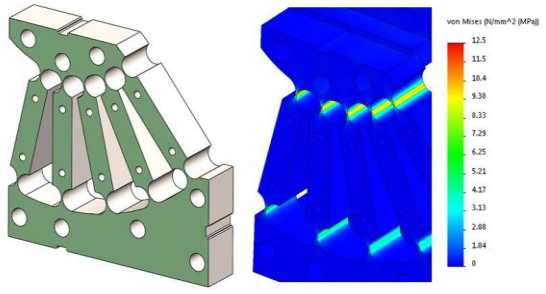

Figure 3. Left: 3-D model of the laminar flexure bending mechanism module. Right: Finite element analysis (FEA) results for the Z7-5004 laminar flexure bending mechanism with 1 N·m maximum bending moment to each bending arm.

Using two Newport™ Picomotor™ 8301 actuators, the Z7-5004 miniature dynamic mirror bender can provide more than 1.3 N·m maximum bending moment to each bending arm. With the maximum bending condition, the maximum Von-Mises stress on the 8-mm-thick weak-link modules reaches ~15 MPa, which is much less than 10% of the material yield stress for Invar 36.

DESIGN OF CAPACITIVE-SENSOR-ARRAY-BASED REAL-TIME MIRROR PROFILER PROTOTYPE

To further monitor and control the mirror bending condition, Invar frame with an array of capacitive sensors (probe model C3R with CPL290 readout electronics from Lion Precision™) are designed as optional metrology attachments for the compact mirror benders.

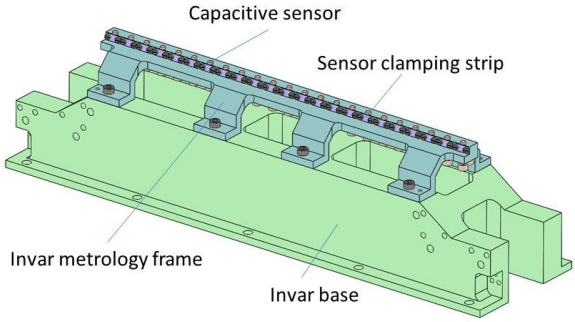

Figure 4. 3-D model of the Z7-5004 capacitive-sensor-array-based real-time mirror profiler.

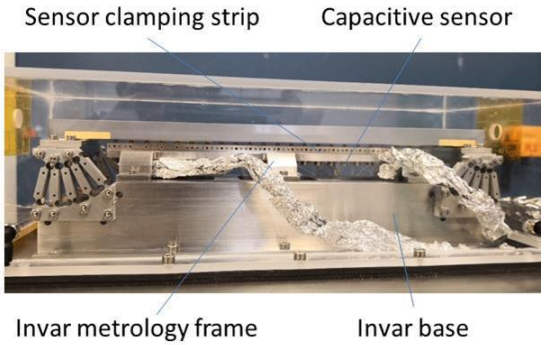

Figure 5. Photograph of the capacitive-sensor-array-based real-time mirror profiler mounted on the Z7-5004 mirror bender base as an optional attachment.

As shown in Figure 4 and 5, the real-time mirror profiler is mounted on the mirror bender base as an optional attachment. It consists of an Invar metrology frame, an array of capacitive sensors, and sensor clamping strips.
Since the silicon mirror is not a perfect electric conductor, to prepare the displacement

measurement on the back of the mirror, a thin layer of gold is coated on the mirror back to perform a well-grounded surface for the capacitive sensors array. FEA study showed that, for a mirror with even thickness, the profile of the mirror back is very similar to the mirror optical surface within the dynamic bending radius of curvature of 0.5 – 74 km.

PRELIMINARY TEST OF THE CAPACITIVE-SENSOR-ARRAY BASED REAL-TIME MIRROR PROFILER

Preliminary mechanical test for the capacitive-sensor-array based real-time mirror profiler was performed in April 2019 with an APS Z7-5004 mirror bender for 300-mm-long mirror as shown in Figure 6. Figure 7 shows the bender's bending arm positions readout from a pair of capacitive sensors during the test.

Figure 6. Photograph of the mechanical test for the capacitive-sensor-array based real-time mirror profiler.

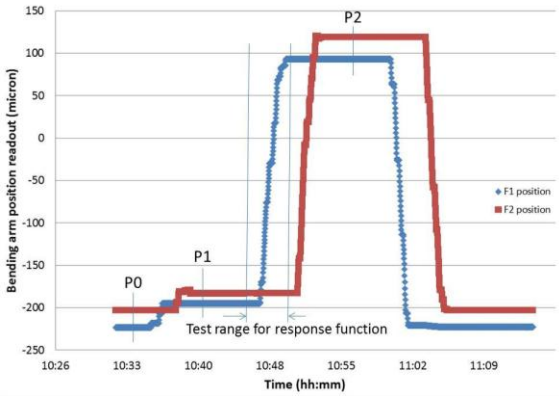

Figure 7. Mirror bender's bending arm positions readout from a pair of capacitive sensors during the preliminary mechanical test for the capacitive-sensor-array based real-time mirror profiler.

The mirror profiles readouts from the capacitive-sensor-array based real-time mirror profiler have been compared with the measurement results from a Long Trace Profiler (LTP). Figure 8 shows a photograph of the LTP test setup for the APS Z7-5004 mirror bender with real-time mirror profiler. Capacitive sensor readings are repeatable, and reasonably agreed with LTP measurement results in the two testing mirror profiles P1 and P2. The capacitive sensor readings can be further calibrated with LTP measurement as shown in Figure 9.

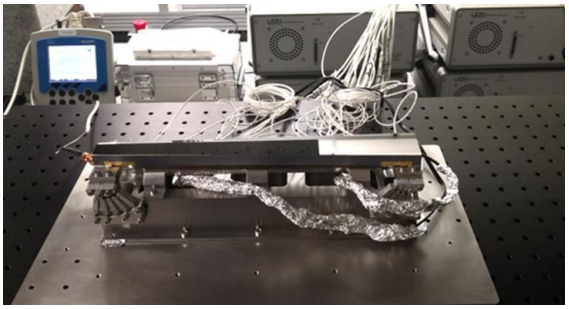

Figure 8. Photograph of the LTP test setup for the APS Z7-5004 mirror bender with real-time mirror profiler.

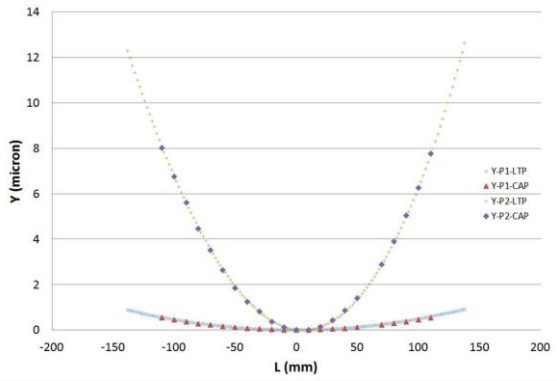

Figure 9. Comparison of the mirror profiles readouts from the capacitive-sensor-array based real-time mirror profiler to the measurement results from a Long Trace Profiler (LTP) with the two testing mirror profiles P1 and P2. The capacitive sensor readings are calibrated with LTP measurement for P2 profile.

Figure 10 shows the capacitive sensor response function with the narrow-side mirror bending arm F2 is staying at the P1 position while the wide-side mirror bending arm F1 is changing from P1 position to P2 position.

SUMMARY

A capacitive-sensor-array based real-time mirror profiler has been designed and constructed with

300-mm-long elliptically dynamic bent mirror for the one dimensional hard X-ray zoom optics prototype at the APS. Table 1 summarized the design specifications of the APS Z7-5004 dynamic mirror bender for the 300-mm-long X-ray mirror with capacitive-sensor-array-based real-time mirror profiler as an attachment. This mirror bender is a test bed to optimize the future design with minimum number of capacitive sensors to be used for the in situ metrology array.

Preliminary test of the real-time mirror profiler showed that it is feasible to build a real-time mirror profiler with an array of capacitive sensors to measure the mirror back surface, as long as the mirror has an even thickness and the back of the mirror has a well-grounded metal coated surface. During the bending drivers tests with drivers positioning repeated in micron level for P2 profile, the real-time mirror profiler demonstrated good readout reproducibility from the capacitive sensors array in the range of few nanometers.

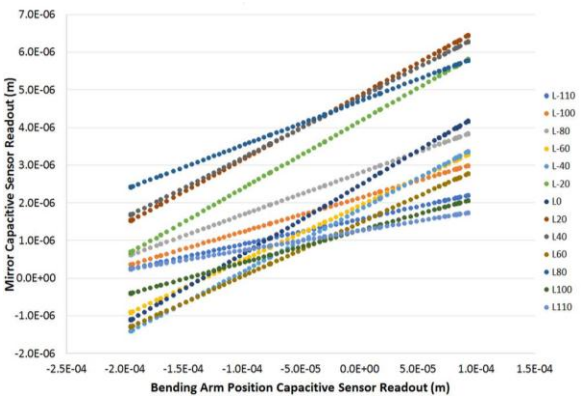

Figure 10, Response function test with the capacitive sensorarray. During the test, the wide-side mirror bending arm F1 is staying at the P1 position while the narrow-side mirror bending arm F2 is changing from P1 position to P2 position.

The first X-ray testing and characterization was performed in April 12-18, 2019 at the APS X-ray optics test beamline 1-BM. The X-ray tests are including measurements of the mirror response function with grating interferometry, and measurement of the focal spot and intensity distribution and profile at the focal plane and off focus across a broad range of mirror shape parameters. The X-ray test results will be published in separate papers, as well as the detailed results from FEA studies for the APS Z7-5004 dynamic mirror bender.

ACKNOWLEDGEMENTS

The authors would like to thank M. Wojcik, and K. Lang from the Argonne National Laboratory for their help in the LTP and X-ray test. Work supported by the U.S. Department of Energy, Office of Science, under Contract No. DE-AC02-06CH11357.

Table 1. Design specifications of the APS Z7-5004 dynamic mirror bender with capacitive-sensor-array based real-time mirror profiler

Overall dimensions (mm)	300 (L) x 82 (W) x 85 (H)
Normal load capacity (kg)	0.5
Bender driver type	Newport™ PicoMotor 8301 UHV
Bender capacitive sensor	Lion Precision™ C5R with CPL290
Bender axial load capacity (N)	20
Bender closed-loop travel range (micron)	500
Bender min. incremental (nm)	20
Manual adjustment option	Yes
Tunable bending moment (N.m)	0.1 - 1
Capacitive sensor array	Lion Precision™ C3R with CPL290
Capacitive sensor array resolution	1 nm @ 1kHz

REFERENCES

[1] Kimura, T. Kimura, S. Matsuyama, K. Yamauchi, Y. Nishino, Opt. Express, 21(8), 9267(2013)http://doi.org/10.1364/OE.21.009267

[2] Kirkpartrick, P. and Baez, A. V. Formation of Optical Images by X-Rays. JOSA. 1948; 38(9): 766-773.

[3] U.S. Patent granted No. 6,607,840, D. Shu, T. S. Toellner, and E. E. Alp, 2003.

[4] U.S. Patent granted No. 6,984,335, D. Shu, T. S. Toellner, and E. E. Alp, 2006.

[5] D. Shu, T. S. Toellner, E. E. Alp, J. Maser, J. Ilavsky, S. D. Shastri, P. L. Lee, S. Narayanan, and G. G. Long, AIP CP879, 1073-1076 (2007)

[6] D. Shu, A. Li, S. P. Kearney, C. Mao, J. Anton, and Y. Pan, Proceedings of MEDSI 2016, Barcelona, Spain.

[7] D. Shu, , J. Anton, S. P. Kearney, R. Harder, X. Shi, T. Mooney, and L. Assoufid, XOPT, Yokohama, Japan, 2019

[8] S. Kearney, L. Assoufid, W. Grizolli, T. Kolodziej, K. Lang, A. Macrander, Y. Shvyd'ko, X. Shi, D. Shu, and M. Wojcik, Proceedings of MEDSI-2018, Paris, France.

[9] D. Shu, A. Li, S. P. Kearney, C. Mao, J. Anton, S. Yan, D. Liang, and Y. Pan, Proceedings of 2017 ASPE Annual Meeting, Charlotte, NC, USA

The submitted manuscript has been created by UChicago Argonne, LLC, Operator of Argonne National Laboratory ("Argonne"). Argonne, a U.S. Department of Energy Office of Science laboratory, is operated under Contract No. DE-AC02-06CH11357. The U.S. Government retains for itself, and others acting on its behalf, a paid-up nonexclusive, irrevocable worldwide license in said article to reproduce, prepare derivative works, distribute copies to the public, and perform publicly and display publicly, by or on behalf of the Government.

SENSING AND COMMUTATION OF A SPHERICAL PERMANENT MAGNETIC DIPOLE ACTUATOR

Tyler T. Hamer[1], Joshua Chabot[2], and David L. Trumper[1]
[1]Department of Mechanical Engineering
Massachusetts Institute of Technology
Cambridge, MA, USA
[2]MIT Lincoln Laboratory
Lexington, MA, USA

INTRODUCTION

Spacecraft attitude control systems (ACS) utilize multiple actuators, such as reaction wheels, control moment gyroscopes (CMGs), or thrusters, to rotate the spacecraft in 3 degrees of freedom (DoF). An ACS's quality is commonly judged on SWaP (Size, Weight, and Power), torque generation, momentum storage, pointing stability, and reliability. Reaction wheels are inefficient at generating torque and storing momentum while CMGs typically have large footprints. Additionally both reaction wheels and CMGs rely on mechanical bearings, which can introduce pointing jitter and are a common point of failure. Thrusters use propellant, a finite resource, thus limiting mission duration.

Reaction spheres can rotate a spacecraft about an arbitrary axis, reducing the ACS from three or more single-axis actuators down to a single multi-axis actuator. Reaction spheres rotate the spacecraft either with an equal-and-opposite torque about their axis of rotation when accelerated about that axis, similar to reaction wheels, or with a gyroscopic torque used to reorient their axis of rotation, similar to CMGs. When operated similar to CMGs, reaction spheres generate higher torque per unit of power than reaction wheels. Lastly, reaction spheres can be magnetically levitated, eliminating the need for mechanical bearings, resulting in increased pointing accuracy, momentum storage, and ACS life.

While NASA first proposed reaction spheres over a half century ago, limitations with previous designs have kept the technology from commercialization [1]. Recently, reaction spheres with a dipole permanent magnet as the rotor have appeared promising due to their mechanical simplicity and simple modeling despite being unable to generate torque about their rotor's axis of magnetization [2, 3]. In fact, a prototype reaction sphere with a dipole permanent magnet as the rotor was modeled, designed, and vertically suspended [4]. This paper continues the work from [4] on the permanent magnetic dipole reaction sphere bench-level prototype depicted in Figure 1 by presenting the sensing and commutation of the bench-level prototype for multi-DoF suspension and rotation.

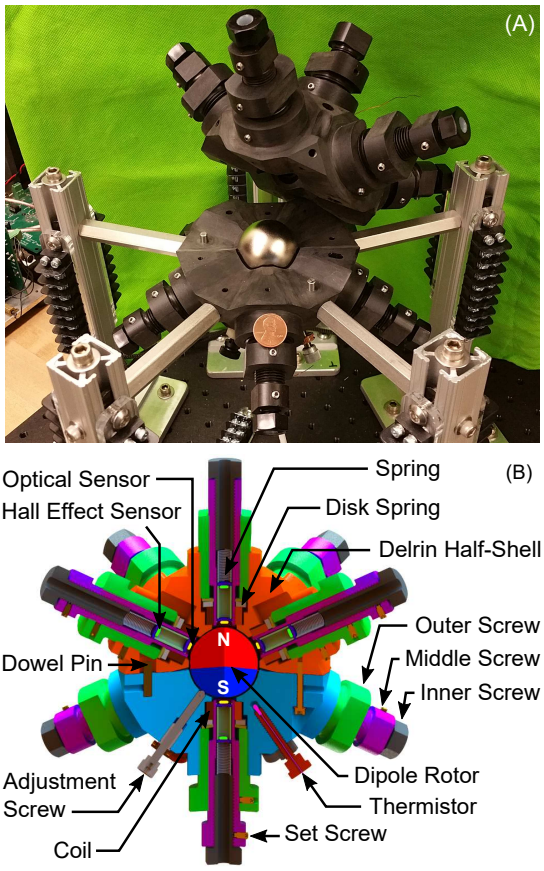

FIGURE 1. Permanent magnetic dipole reaction sphere (a) bench-level prototype with (b) label cross section. [4]

DISTRIBUTION STATEMENT A. Approved for public release. Distribution is unlimited.
This material is based upon work supported under Air Force Contract No. FA8702-15-D-0001. Any opinions, findings, conclusions or recommendations expressed in this material are those of the author(s) and do not necessarily reflect the views of the U.S. Air Force.

BENCH-LEVEL PROTOTYPE

The bench-level prototype for the permanent magnetic dipole reaction sphere is depicted in Figure 1 along with a labeled crossed section. The rotor is a 38.1 mm (1.5 in) diameter, spherical NdFeB (Grade 42) permanent magnet (K&J Magnetics SX8). Two symmetric Delrin half-shells mate together to form the dodecahedron stator surrounding the rotor. A radial array of 12 equidistant cylindrical coils, one centered on each face of the dodecahedron stator, suspend and rotate the rotor. When the rotor is centered within the stator's spherical pocket, the prototype has a 1 mm mechanical air gap and a 2 mm magnetic air gap, allowing the rotor to translate up to ± 1 mm in 3 DoF.

A radial array of 12 equidistant Hall effect sensors (Allegro A1308KUA-1-T), each placed coaxially within a coil, measure the radial component of the rotor's external magnetic flux density with a noise-limited standard deviation of 48 μT. A least squares fit of these 12 radial magnetic flux density measurements reconstructs the direction of the rotor's axis of magnetization with a standard deviation of 190 μrad.

A radial array of 12 equidistant reflective optical sensors (Fairchild QRE1113GR), each also placed coaxially within a coil, measure their normal distances from the rotor's surface with a noise-limited standard deviation of 0.24 μm. Each optical sensor and its diametrically opposed optical sensor's measurements are subtracted to form a differential measurement of the position of the rotor's center along the axis of their coil pair. A least squares fit of these 6 differential measurements reconstructs the position of the rotor's center with a standard deviation of 0.05 μm.

The measured direction of the rotor's axis of magnetization is used to construct the commutation law for the current through each coil for a desired torque and force on the rotor. Desired torque is created from following reference angular velocities using three single-DoF controllers with the direction of the rotor's axis of magnetization as feedback. Desired force is created to keep the rotor centered in the stator using three single-DoF controllers with the position of the rotor's center as feedback.

COMMUTATION

Current driven through each coil applies a torque and force to the dipole rotor due to the interaction of each current with the rotor's external magnetic field. Given the rotor is a magnetic dipole, approximating each coil as a magnetic dipole as well, allows the torque ${}^{\mathrm{c}}\boldsymbol{T}_{\mathrm{r}}$ and force ${}^{\mathrm{c}}\boldsymbol{F}_{\mathrm{r}}$ applied to the rotor by a single coil to be well approximated by the interaction of two magnetic dipoles:

$$ {}^{\mathrm{c}}\boldsymbol{T}_{\mathrm{r}} = -\left(\boldsymbol{m}_{\mathrm{c}} \times \boldsymbol{B}_{\mathrm{r}}\right) \tag{1a} $$

$$ {}^{\mathrm{c}}\boldsymbol{F}_{\mathrm{r}} = -\bigtriangledown\left(\boldsymbol{m}_{\mathrm{c}} \cdot \boldsymbol{B}_{\mathrm{r}}\right), \tag{1b} $$

where $\boldsymbol{B}_{\mathrm{r}}$ is the external magnetic flux density of the rotor and and $\boldsymbol{m}_{\mathrm{c}}$ is the approximated magnetic dipole moment of the coil. Such an approximation previously yielded a force prediction within 3% of experimental values [4].

Solutions to Equation (1) for single coil torque and force take scaled forms of the governing equations for simple brushed DC motors and voice coils respectively, when the rotor's center lies along that coil's axis (${}^{\mathrm{r}}\boldsymbol{r}_{\mathrm{c}}/\left|{}^{\mathrm{r}}\boldsymbol{r}_{\mathrm{c}}\right| = \boldsymbol{n}_{\mathrm{c}}$) [4]:

$$ {}^{\mathrm{c}}\boldsymbol{T}_{\mathrm{r}} = K_{\mathrm{T}} i_{\mathrm{c}} (\boldsymbol{n}_{\mathrm{c}} \times \boldsymbol{n}_{\mathrm{r}}) \tag{2a} $$

$$ {}^{\mathrm{c}}\boldsymbol{F}_{\mathrm{r}} = \frac{1}{2} K_{\mathrm{F}} i_{\mathrm{c}} [3(\boldsymbol{n}_{\mathrm{r}} \cdot \boldsymbol{n}_{\mathrm{c}})\boldsymbol{n}_{c} - \boldsymbol{n}_{\mathrm{r}}], \tag{2b} $$

where K_{T} and K_{F} are the reaction sphere's respective single coil torque-and force-constants, i_{c} is the current applied to the coil, ${}^{\mathrm{r}}\boldsymbol{r}_{\mathrm{c}}$ is the position of the coil's approximated dipole with respect to the rotor's center, and $\boldsymbol{n}_{\mathrm{c}}$ and $\boldsymbol{n}_{\mathrm{r}}$ are unit vectors pointing along the coil's axis and the rotor's axis of magnetization respectively. The vector components of Equation (2) scale and distribute the torque and force magnitude across the reaction sphere's degrees of freedom (DoF). In particular, the torque vector cannot have a component along the rotor's axis of magnetization and is always perpendicular to the force vector. The force vector points along a linear combination of the rotor's axis of magnetization and the coil's axis.

Superimposing the torque and force from each coil yields the overall torque ${}^{\mathrm{c_{tot}}}\boldsymbol{T}_{\mathrm{r}}$ and force ${}^{\mathrm{c_{tot}}}\boldsymbol{F}_{\mathrm{r}}$ on the rotor. For a rotor centered within a radial array of identical, equidistant surrounding coils (thus the rotor's center lies along each coil's axis), these are [4]

$$ {}^{\mathrm{c_{tot}}}\boldsymbol{T}_{\mathrm{r}} = \sum_{a=1}^{b} {}^{\mathrm{c}_a}\boldsymbol{T}_{\mathrm{r}} = K_{\mathrm{T}} \sum_{a=1}^{b} i_{\mathrm{c}_a} \left(\boldsymbol{n}_{\mathrm{c}_a} \times \boldsymbol{n}_{\mathrm{r}}\right) \tag{3a} $$

$$ {}^{\mathrm{c_{tot}}}\boldsymbol{F}_{\mathrm{r}} = \sum_{a=1}^{b} {}^{\mathrm{c}_a}\boldsymbol{F}_{\mathrm{r}} = \frac{1}{2} K_{\mathrm{F}} \sum_{a=1}^{b} i_{\mathrm{c}_a} \left[3\left(\boldsymbol{n}_{\mathrm{r}} \cdot \boldsymbol{n}_{\mathrm{c}_a}\right) \boldsymbol{n}_{\mathrm{c}_a} - \boldsymbol{n}_{\mathrm{r}}\right], \tag{3b} $$

where $b = 12$ as 12 coils, one centered on each face of the dodecahedron stator, drive the rotor in the bench-level prototype.

As commonly done with multi-coil actuators, expressing Equation (3) in matrix form allows the construction of a commutation law to determine the amount of current applied to each coil for a desired torque and force on the rotor:

$$\begin{bmatrix} {}^{\mathrm{c_{tot}}}\boldsymbol{T}_{\mathrm{r}} \\ {}^{\mathrm{c_{tot}}}\boldsymbol{F}_{\mathrm{r}} \end{bmatrix} = \begin{bmatrix} K_{\mathrm{T}}\mathbb{N}_{\mathrm{T}} \\ \frac{1}{2}K_{\mathrm{F}}\mathbb{N}_{\mathrm{F}} \end{bmatrix} \boldsymbol{i}_{\mathrm{c}}, \tag{4}$$

where $\boldsymbol{i}_{\mathrm{c}}$ is the $b \times 1$ current vector and respectively, $\mathbb{N}_{\mathrm{T}}$ and $\mathbb{N}_{\mathrm{F}}$ are $3 \times b$ normalized torque and force matrices given by

$$\mathbb{N}_{\mathrm{T}} = \begin{bmatrix} (\boldsymbol{n}_{\mathrm{c}_1} \times \boldsymbol{n}_{\mathrm{r}}) & \cdots & (\boldsymbol{n}_{\mathrm{c}_b} \times \boldsymbol{n}_{\mathrm{r}}) \end{bmatrix} \tag{5a}$$

$$\mathbb{N}_{\mathrm{F}} = \begin{bmatrix} 3\left(\boldsymbol{n}_{\mathrm{r}} \cdot \boldsymbol{n}_{\mathrm{c}_1}\right)\boldsymbol{n}_{\mathrm{c}_1} - \boldsymbol{n}_{\mathrm{r}} & \cdots & 3\left(\boldsymbol{n}_{\mathrm{r}} \cdot \boldsymbol{n}_{\mathrm{c}_b}\right)\boldsymbol{n}_{\mathrm{c}_b} - \boldsymbol{n}_{\mathrm{r}} \end{bmatrix}. \tag{5b}$$

Each column of the normalized torque matrix lies orthogonal to the rotor's axis of magnetization and its corresponding coil's axis, whereas each column of the normalized force matrix lies along a linear combination of rotor's axis of magnetization and its corresponding coil's axis. As a result, the normalized torque and force matrices are mutually orthogonal ($\mathbb{N}_{\mathrm{T}}\mathbb{N}_{\mathrm{F}}^{\mathsf{T}} = \mathbb{N}_{\mathrm{F}}\mathbb{N}_{\mathrm{T}}^{\mathsf{T}} = \mathbb{0}$). This orthogonality arises from the symmetry of the rotor's magnetic field and the coils' layout. Further this orthogonality decouples the torque and force due to the applied current, allowing torque and force to be controlled independently.

Applying right Moore-Penrose pseudoinverses since $\mathbb{N}_{\mathrm{T}}$ and $\mathbb{N}_{\mathrm{F}}$ have more columns than rows, the commutation law is

$$\boldsymbol{i}_{\mathrm{c}} = \left(K_{\mathrm{T}}{}^{-1}\mathbb{N}_{\mathrm{T}}^{+}\right){}^{\mathrm{c_{tot}}}\boldsymbol{T}_{\mathrm{r}} + \left(2K_{\mathrm{F}}{}^{-1}\mathbb{N}_{\mathrm{F}}^{+}\right){}^{\mathrm{c_{tot}}}\boldsymbol{F}_{\mathrm{r}}, \tag{6}$$

where

$$\mathbb{N}_{\mathrm{T}}^{+} = \mathbb{N}_{\mathrm{T}}^{\mathsf{T}}(\mathbb{N}_{\mathrm{T}}\mathbb{N}_{\mathrm{T}}^{\mathsf{T}})^{-1} \tag{7a}$$

$$\mathbb{N}_{\mathrm{F}}^{+} = \mathbb{N}_{\mathrm{F}}^{\mathsf{T}}(\mathbb{N}_{\mathrm{F}}\mathbb{N}_{\mathrm{F}}^{\mathsf{T}})^{-1}. \tag{7b}$$

The rank of $\mathbb{N}_{\mathrm{F}}$ and $\mathbb{N}_{\mathrm{F}}\mathbb{N}_{\mathrm{F}}^{\mathsf{T}}$ is three (full rank) whereas the rank of $\mathbb{N}_{\mathrm{T}}$ and $\mathbb{N}_{\mathrm{T}}\mathbb{N}_{\mathrm{T}}^{\mathsf{T}}$ is only two (rank deficient). Thus the right pseudoinverse is only guaranteed to exist for $\mathbb{N}_{\mathrm{F}}$. While the right pseudoinverse can be taken of $\mathbb{N}_{\mathrm{T}}$, this pseudoinverse will not produce currents for any component of the input torque along the rotor's axis of the magnetization. Thus all torque trajectories must not include a component along the rotor's axis of magnetization. Additionally, Equation (6) is the least squares solution to Equation (4). Hence the resulting coil currents minimizes the L^2-norm and in turn the total power dissipated by the coils collectively [5]. Lastly, as $\mathbb{N}_{\mathrm{T}}$ and $\mathbb{N}_{\mathrm{F}}$ are functions of $\boldsymbol{n}_{\mathrm{r}}$ which changes overtime. Thus the direction of the rotor's axis of magnetization must be measured or estimated in real-time. With the direction of the rotor's axis of magnetization known, $\mathbb{N}_{\mathrm{T}}$, $\mathbb{N}_{\mathrm{F}}$, and their pseudoinverses are then computed or found via lookup table in real-time.

ORIENTATION SENSING

The rotor's actual and each coil's approximated external magnetic flux densities are the magnetic flux density of a dipole $\boldsymbol{B}_{\mathrm{dipole}}$:

$$\boldsymbol{B}_{\mathrm{dipole}}(\boldsymbol{r}) = \frac{\mu_0}{4\pi}\left[\frac{3\boldsymbol{r}\left(\boldsymbol{m}_{\mathrm{dipole}} \cdot \boldsymbol{r}\right)}{|\boldsymbol{r}|^5} - \frac{\boldsymbol{m}_{\mathrm{dipole}}}{|\boldsymbol{r}|^3}\right], \tag{8}$$

where μ_0 is the permeability of free space. $\boldsymbol{m}_{\mathrm{dipole}}$ is the magnetic dipole moment while $\boldsymbol{r}$ is the position of the point of interest with respect to the center of that dipole moment. For a rotor centered within a radial array of equidistant surrounding coils, the radial component of the rotor's external magnetic flux density lies along the axis of each coil.

A radial array of equidistant Hall effect sensors measure the magnetic flux density normal to their surfaces. As each Hall effect sensor lies co-axially along a coil in the bench-level prototype, the magnetic flux density normal to each Hall effect sensor's surface lies along the axis of that sensor's corresponding coil. Thus the magnetic flux density B_{H_i} measured by ith Hall effect sensor along the ith coil consists of the radial component of the centered rotor's external magnetic flux density $\boldsymbol{B}_{\mathrm{r}}$ and contributions from each coil's external magnetic flux density $\boldsymbol{B}_{\mathrm{c}_a}$:

$$B_{\mathrm{H}_i} = \left(\boldsymbol{B}_{\mathrm{r}} \cdot \boldsymbol{n}_{\mathrm{c}_i}\right) + \sum_{a=1}^{b}\left(\boldsymbol{B}_{\mathrm{c}_a} \cdot \boldsymbol{n}_{\mathrm{c}_i}\right). \tag{9}$$

The external magnetic flux density of a centered rotor can be written as

$$\boldsymbol{B}_{\mathrm{r}} = \tfrac{1}{2}\left|\boldsymbol{B}_{\mathrm{r}}\right|\left[3\left(\boldsymbol{n}_{\mathrm{r}} \cdot \boldsymbol{n}_{\mathrm{c}_i}\right)\boldsymbol{n}_{\mathrm{c}_i} - \boldsymbol{n}_{\mathrm{r}}\right], \tag{10}$$

whose magnitude $|\boldsymbol{B}_{\mathrm{r}}|$ is given by

$$\frac{1}{2}\left|\boldsymbol{B}_{\mathrm{r}}\right| = \frac{\mu_0}{4\pi}\frac{|\boldsymbol{m}_{\mathrm{r}}|}{|\boldsymbol{r}|^3}, \tag{11}$$

where $\boldsymbol{m}_{\mathrm{r}}$ is the rotor's magnetic dipole moment. Thus, the radial component of the rotor's external magnetic flux density is

$$\left(\boldsymbol{B}_{\mathrm{r}} \cdot \boldsymbol{n}_{\mathrm{c}_i}\right) = \left|\boldsymbol{B}_{\mathrm{r}}\right|\left(\boldsymbol{n}_{\mathrm{r}} \cdot \boldsymbol{n}_{\mathrm{c}_i}\right). \tag{12}$$

Additionally, as each coil current is directly controlled, each coil's magnetic flux density can be calculated in real-time and calibrated out.

Acknowledging this calibration and Equation (12), Equation (9) can be rewritten as:

$$\widetilde{B}_{\mathrm{H}_i} = B_{\mathrm{H}_i} - \sum_{a=1}^{b} \left(\boldsymbol{B}_{\mathrm{c}_a} \cdot \boldsymbol{n}_{\mathrm{c}_i} \right) = |\boldsymbol{B}_{\mathrm{r}}| \left(\boldsymbol{n}_{\mathrm{r}} \cdot \boldsymbol{n}_{\mathrm{c}_i} \right), \quad (13)$$

where $\widetilde{B}_{\mathrm{H}_i}$ is the component of the ith measured magnetic flux density purely due to the centered rotor's external magnetic field. Again $b = 12$ as there are 12 Hall effect sensors, one along each of the 12 coils in the bench-level prototype.

By expressing Equation (13) in matrix form, an inverse can be constructed to determine the direction of the rotor's axis of magnetization from the measured magnetic flux densities like with 2 pole brushless DC motors:

$$\widetilde{\boldsymbol{B}}_{\mathrm{H}} = |\boldsymbol{B}_{\mathrm{r}}| \begin{bmatrix} \boldsymbol{n}_{\mathrm{c}_1} \cdot \boldsymbol{n}_{\mathrm{r}} \\ \vdots \\ \boldsymbol{n}_{\mathrm{c}_b} \cdot \boldsymbol{n}_{\mathrm{r}} \end{bmatrix} = |\boldsymbol{B}_{\mathrm{r}}| \, \mathbb{N}_{\mathrm{c}}{}^{\mathsf{T}} \boldsymbol{n}_{\mathrm{r}} \quad (14)$$

where $\widetilde{\boldsymbol{B}}_{\mathrm{H}}$ is a $b \times 1$ column vector containing the calibrated magnetic flux densities measured by each Hall effect sensor. $\mathbb{N}_{\mathrm{c}}$ is the $3 \times b$ coil matrix whose columns are the directions of each coil's axis:

$$\mathbb{N}_{\mathrm{c}} = \begin{bmatrix} \boldsymbol{n}_{\mathrm{c}_1} & \cdots & \boldsymbol{n}_{\mathrm{c}_b} \end{bmatrix}. \quad (15)$$

Applying the left Moore-Penrose pseudoinverse as $\mathbb{N}_{\mathrm{c}}{}^{\mathsf{T}}$ has more rows than columns, the measured direction of the rotor's axis of magnetization is

$$\boldsymbol{n}_{\mathrm{r}} = |\boldsymbol{B}_{\mathrm{r}}|^{-1} \left(\mathbb{N}_{\mathrm{c}}{}^{\mathsf{T}} \right)^{+} \widetilde{\boldsymbol{B}}_{\mathrm{H}}, \quad (16)$$

where

$$\left(\mathbb{N}_{\mathrm{c}}{}^{\mathsf{T}} \right)^{+} = (\mathbb{N}_{\mathrm{c}} \mathbb{N}_{\mathrm{c}}{}^{\mathsf{T}})^{-1} \mathbb{N}_{\mathrm{c}}. \quad (17)$$

The rank of $\mathbb{N}_{\mathrm{c}}$ and $\mathbb{N}_{\mathrm{c}} \mathbb{N}_{\mathrm{c}}{}^{\mathsf{T}}$ is three (full rank) so the left pseudoinverse is always guaranteed to exist. Further, unlike $\mathbb{N}_{\mathrm{T}}$ and $\mathbb{N}_{\mathrm{F}}$ which can change with time, $\mathbb{N}_{\mathrm{c}}$ is fixed with respect to time as the coil's positions are fixed. Thus $\mathbb{N}_{\mathrm{c}}$ and its pseudoinverse can be precomputed, reducing computation in the control loop.

POSITION SENSING

A radial array of equidistant optical sensors measures their normal distances from the rotor's surface. As with the Hall effect sensors, each optical sensor lies co-axially along a coil in the bench-level prototype. Due to the symmetry of the prototype's coil arrangement, each optical sensor is diametrically opposed to another optical sensor ($\boldsymbol{n}_{\mathrm{c}_{b+1-a}} = -\boldsymbol{n}_{\mathrm{c}_a}$), allowing for differential measurement of the position of the rotor's center along the axis of that coil pair. The rotor's center position δ_{p_a} along the ath coil pair's axis is

$$\delta_{\mathrm{p}_a} = \tfrac{1}{2} \left(\delta_a - \delta_{b+1-a} \right), \quad (18)$$

where δ_a and δ_{b+1-a} are the normal distance the rotor's surface is from the ath optical sensor and its diametrically opposed optical sensor. As the rotor is spherical, both motion along and orthogonal to the ath coil pair's axis changes δ_a and δ_{b+1-a}. However, motion along the axis is differential mode while motion orthogonal to the axis is common mode and thus rejected in the calculation of δ_{p_a}. $a = 1, 2, \ldots, b/2$ where again $b = 12$ as there are 12 optical sensors (6 optical sensor pairs), one along each of the 12 coils in the bench-level prototype.

By expressing Equation (18) in matrix form, an inverse can be constructed to determine the position of the rotor's center from the measured normal distances between the optical sensors and the rotor's surface:

$$\boldsymbol{\delta}_{\mathrm{p}} = \begin{bmatrix} \boldsymbol{n}_{\mathrm{c}_1} \cdot \boldsymbol{r}_{\mathrm{r}} \\ \vdots \\ \boldsymbol{n}_{\mathrm{c}_{b/2}} \cdot \boldsymbol{r}_{\mathrm{r}} \end{bmatrix} = \mathbb{N}_{\mathrm{p}}{}^{\mathsf{T}} \boldsymbol{r}_{\mathrm{r}}, \quad (19)$$

where $\boldsymbol{\delta}_{\mathrm{p}}$ is a $b/2 \times 1$ column vector containing the position of the rotor's center along each coil pair's axis measured by each pair of optical sensors. $\mathbb{N}_{\mathrm{p}}$ is the $3 \times b/2$ coil pair matrix whose columns are the direction of each coil pair's axis:

$$\mathbb{N}_{\mathrm{p}} = \begin{bmatrix} \boldsymbol{n}_{\mathrm{c}_1} & \cdots & \boldsymbol{n}_{\mathrm{c}_{b/2}} \end{bmatrix}. \quad (20)$$

Applying the left Moore-Penrose pseudoinverse as $\mathbb{N}_{\mathrm{p}}{}^{\mathsf{T}}$ has more rows than columns like with determining the direction of the rotor's axis of magnetization, the measured position of the rotor's center is

$$\boldsymbol{r}_{\mathrm{r}} = \left(\mathbb{N}_{\mathrm{p}}{}^{\mathsf{T}} \right)^{+} \boldsymbol{\delta}_{\mathrm{p}} \quad (21)$$

where

$$\left(\mathbb{N}_{\mathrm{p}}{}^{\mathsf{T}} \right)^{+} = (\mathbb{N}_{\mathrm{p}} \mathbb{N}_{\mathrm{p}}{}^{\mathsf{T}})^{-1} \mathbb{N}_{\mathrm{p}}. \quad (22)$$

The rank of $\mathbb{N}_{\mathrm{p}}$ and $\mathbb{N}_{\mathrm{p}} \mathbb{N}_{\mathrm{p}}{}^{\mathsf{T}}$ is three (full rank) so the right pseudoinverse is always guaranteed to exist. Since the coil's positions are fixed, $\mathbb{N}_{\mathrm{p}}$ is fixed with respect to time like $\mathbb{N}_{\mathrm{c}}$. Thus $\mathbb{N}_{\mathrm{p}}$ and its pseudoinverse can also be precomputed, reducing computation in the control loop.

CONTROL

The commutation law determines the desired current needed in each coil to apply any desired torque not about the axis of magnetization and any force to

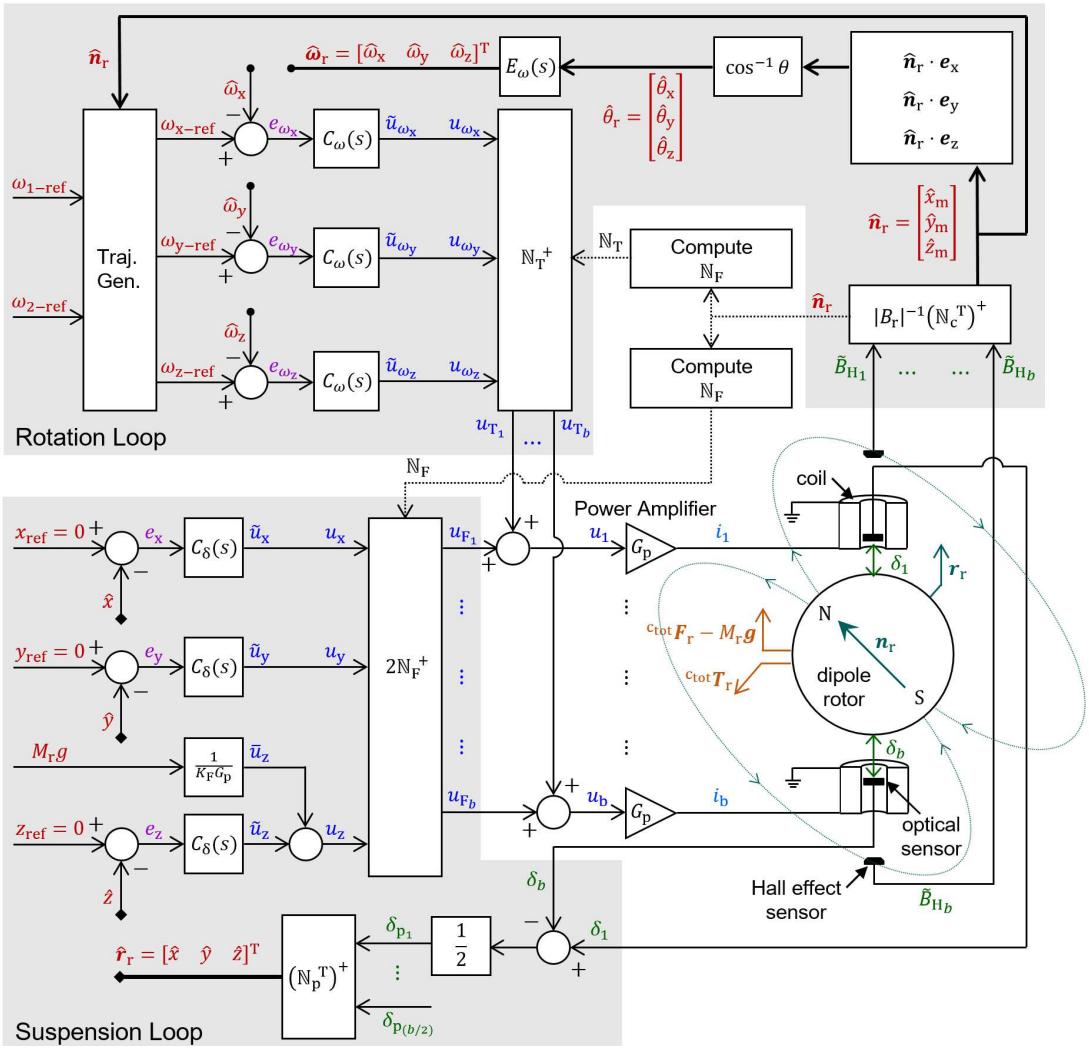

FIGURE 2. Block diagram for 2 DoF rotation and 3 DoF suspension of the dipole rotor. $C_\omega(s)$ are identical single-DoF controllers for rotation while $C_\delta(s)$ are identical single-DoF controllers for translation. $E_\omega(s)$ is the rotor angular velocity estimator. $\mathbb{N}_T^+$ and $\mathbb{N}_F^+$ are pseudoinverses calculated in real-time to commutate the current for desired torque and force, respectively, whereas $(\mathbb{N}_c^T)^+$ and $(\mathbb{N}_p^T)^+$ are precalculated pseudoinverses to determine the orientation of the rotor's axis of magnetization and the position of the rotor's center respectively. The trajectory generator converts rotation about the two axes orthogonal to the rotor's axis of magnetization to rotation about $\boldsymbol{e}_x$, $\boldsymbol{e}_y$, and $\boldsymbol{e}_z$. The trajectory generation to convert ω_{1-ref} and ω_{2-ref} is simply acknowledged so torque along the rotor's axis of magnetization is not commanded, but is not discussed in further detail.

the rotor. As a result, each DoF in rotation and suspension are decoupled, not just rotation and suspension in general. Thus, the rotor's rotation about the two axes perpendicular to its axis of magnetization $\boldsymbol{e}_1$ and $\boldsymbol{e}_2$ and the rotor's suspension in along the $\boldsymbol{e}_x$, $\boldsymbol{e}_y$, and $\boldsymbol{e}_z$ directions can be independently controlled by simple single-DoF controllers as shown in Figure 2.

To design a controller for rotation of the rotor about $\boldsymbol{e}_x$, $\boldsymbol{e}_y$, or $\boldsymbol{e}_z$, the rotor can be represented as a free mass. Angular velocity of the free mass with respect to a torque input is a first order system. As no additional phase is needed when closing the loop on a first order system, the simplest controller to control the rotor's rotation about a single axis is a proportional controller:

$$C_\omega(s) = K_{p\text{-}\omega}. \tag{23}$$

To design a controller for suspension of the rotor along $\boldsymbol{e}_x$, $\boldsymbol{e}_y$, or $\boldsymbol{e}_z$, the rotor can again be represented as a free mass [4]. However, position of the free mass with respect to a force input is an unstable second order system. As additional phase is needed when closing the loop on unstable second

order systems, the simplest controller to control the rotor's position along a single axis is a lead compensator:

$$C_\delta(s) = K_{\text{p-}\delta}\frac{\alpha\tau_\text{d}s+1}{\tau_\text{d}s+1}. \quad (24)$$

Previously, the values $K_{\text{p-}\delta}$ = 14.8, α = 3, and τ_d = 0.0015 sec were found to yield a crossover $\omega_{\text{c-}\delta}$ = 60 Hz with a phase margin of $\phi_{\text{M-}\delta}$ = 25 ° for vertical suspensions of the rotor with a single coil [4].

For feedback, each single-DoF suspension controller uses its respective component of the position of the rotor's center measured by the optical sensors. However, each single-DoF rotation controller needs rotation of the rotor about $\boldsymbol{e}_\text{x}$, $\boldsymbol{e}_\text{y}$, or $\boldsymbol{e}_\text{z}$ for feedback, which is not measured by the Hall effect sensors. To determine the rotor's rotation about $\boldsymbol{e}_\text{x}$ for example, the rotor's axis of magnetization is projected into a plane orthogonal to $\boldsymbol{e}_\text{x}$. Then the angle between the projection and one of the other directions, $\boldsymbol{e}_\text{y}$, or $\boldsymbol{e}_\text{z}$, is calculated. The same method is applied to find the rotor's rotation about $\boldsymbol{e}_\text{y}$, or $\boldsymbol{e}_\text{z}$. From these calculated angles, a simple estimator $E_\omega(s)$ determines rotation about those axes:

$$E_\omega(s) = \frac{K_\text{d}s}{\tau_\text{lp}s+1}. \quad (25)$$

For suspension, translation along all 3 DoF can be instantaneously controlled. However for rotation, only rotation about the 2 DoF perpendicular to the rotor's axis of magnetization can be instantaneously controlled as torque cannot be generated about the axis of magnetization. Thus trajectory generation is needed before the rotational controllers. Such trajectory generation would direct the rotor into new orientations when desired rotation is not feasible. For example, to rotate about $\boldsymbol{e}_\text{x}$ when the rotor's axis of magnetization points along $\boldsymbol{e}_\text{x}$, the rotor can be first rotated 90° such that the axis of magnetization now points along $\boldsymbol{e}_\text{y}$ or $\boldsymbol{e}_\text{z}$ and then rotation about $\boldsymbol{e}_\text{x}$ could be commanded. Such trajectory generation will not allow a spacecraft to instantaneously rotate in 3 DoF, but will allow a spacecraft to achieve rotation in 3 DoF over time as is practically needed. This trajectory generation is simply acknowledged in this paper and is not discussed in further detail.

CONCLUSION

Compared to reaction wheels, control moment gyroscopes (CMGs), and thrusters, reaction spheres have the potential to reduce SWaP (Space, Weight, and Power) and improve torque generation, momentum storage, pointing stability, and reliability of a spacecraft's attitude control system (ACS). This paper continues the work from [4] on a permanent magnetic dipole reaction sphere. Specifically, commutation and sensing of the reaction sphere for multi-DoF suspension and rotation were presented.

First, torque and force on the dipole rotor by the bench-level prototype's coils were shown to be decoupled due to symmetry in the coils' layout. This decoupling allowed a commutation law for the coils to be constructed from two pseudoinverses. As the original matrices for the pseudoinverses are dependent on the rotor's orientation, these original matrics and their pseudoinverse must be calculated in real-time. Afterwards, orientation of the rotor's axis of magnetization was found via a pseudoinverse from the measured rotor's radial external magnetic flux density by the surrounding Hall effect sensors. Likewise, position of the rotor's center was found via a pseudoinverse from differential measurements of the position of the rotor's center along pairs of diametrically opposed optical sensors. Unlike for commutation, the sensing pseudoinverses can be precomputed. Lastly, the commutation law enables rotation and suspension of the rotor to be controlled by multiple single-DoF control loops.

REFERENCES

[1] Zhu L, Guo J, Gill E. Review of reaction spheres for spacecraft attitude control. Progress in Aerospace Sciences. 2017 May;91:67–86.

[2] Wang J, Jewell GW, Howe D. Analysis, design and control of a novel spherical permanent-magnet actuator. IEE Proceedings - Electric Power Applications. 1998 January;145(1):61–71.

[3] Chabot J. A Spherical Magnetic Dipole Actuator for Spacecraft Attitude Control [Master's Thesis]. Aerospace Engineering Sciences, University of Colorado; 2015.

[4] Hamer TT, Noh M, Zhou L, Chabot J, Trumper DL. A Magnetically Suspended, Spherical Permanent Magnetic Dipole Actuator. In: Proceedings of The Thirty-Third Annual Meeting of the American Society for Precision Engineering. American Society for Precision Engineering. Raleigh, NC, USA: ASPE; 2018. p. 70–75.

[5] Rossini L, Chételat O, Onillon E, Perriard Y. Force and torque analytical models of a reaction sphere actuator based on spherical harmonic rotation and decomposition. IEEE/ASME Transactions on Mechatronics. 2012;18(3):1006–1018.

FINITE ELEMENT MODEL FOR PRE-MAGNETIZED LINEAR HYSTERESIS MOTORS

Lei Zhou[1], **David L. Trumper**[2]
[1] **Mitsubishi Electric Research Laboratories, Cambridge, MA, USA**
[2] **Massachusetts Institute of Technology, Cambridge, MA, USA**

INTRODUCTION

Hysteresis motors are electric machine that utilize the secondary material's magnetic hysteresis effect for thrust generation [1], and these motors have advantages of rugged construction, vibration-free operation, constant thrust in transient, and self-starting [2]. Typical applications for these motors include synchronous clocks, tape drives, pumps, and centrifuges [3–5]. Another distinct feature of hysteresis motors is that their secondaries can be made of a monolithic piece of magnetically semi-hard alloy, which typically has high strength and stiffness. This fact makes the hysteresis motors attractive to many precision devices for special applications, such as in-vacuum operation [6], high-temperature/high-speed drives [7], and space devices [8].

Comparing with many other motor types, the major drawback of hysteresis motors is that their thrust force/torque generation capability is relatively low. Pre-magnetization is an effective method to improve the performance of hysteresis motors in synchronous operation. The pre-magnetization is achieved by magnetizing the hysteresis secondary with an impulse of strong external field generated by the stator before the motor's normal operation, and then operate the motor at a lower stator excitation amplitude. Recent reference [9] studied the effect of pre-magnetization for a rotary hysteresis motor, and data show that pre-magnetization has a very positive effect to the motor's torque generation capability and efficiency. However, to our knowledge, the modeling of the pre-magnetization for hysteresis motors has not been studied in literature.

Aiming at providing a design tool for pre-magnetized hysteresis motors for various applications, this work presents a finite-element-based model for pre-magnetized linear hysteresis motors. Here, the pre-magnetized hysteresis secondary is modeled as an array of permanent magnets, where the magnetization status of each magnet is determined by the field during the pre-magnetization process. Experiments with a linear hysteresis motor is compared with the modeled data. Good agreement between the model and measurement validates the modeling process.

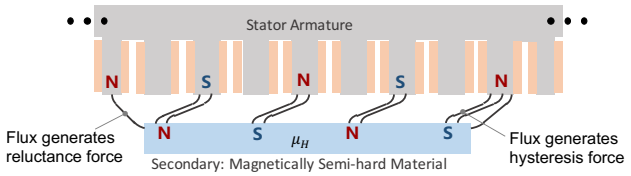

FIGURE 1. Diagram of magnetic flux in a two-phase linear hysteresis motor showing the generation of hysteresis and reluctance thrust forces.

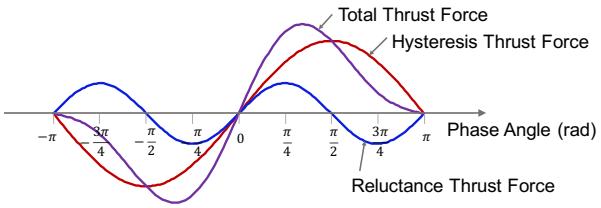

FIGURE 2. Thrust force and phase angle relationships in hysteresis-reluctance hybrid motors.

LINEAR HYSTERESIS MOTOR OPERATING PRINCIPLE

Fig. 1 shows a diagram of the air gap magnetic fluxes in a linear hysteresis motor. The motor's stator is a general multi-phase stator for linear AC motors. The secondary is made of magnetically semi-hard alloy. When the motor windings are excited, the induced magnetization in the secondary lags behind the external field due to the magnetic hysteresis effect of the secondary material, thereby generating thrust force [1].

In a linear hysteresis motor, aside from the hysteresis thrust force, there is an additional reluctance thrust force generated due to the end effects. As shown in Fig. 1, the air gap fluxes due to the secondary magnetization generate hysteresis thrust force, and the fluxes at the front and back edges of the secondary generate reluctance thrust forces. As a result, the force generation in a linear hysteresis motor resembles that of a interior permanent magnet synchronous motor, where two mechanisms of thrust force generation are co-existing. Fig. 2 shows a diagram of the thrust force and phase relationship of linear hysteresis motor in synchronous operation. Here, both

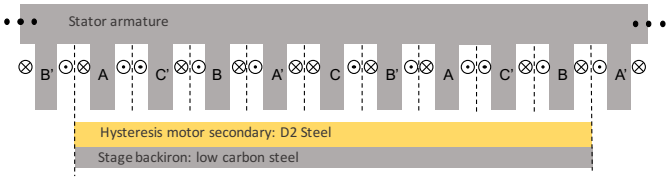

FIGURE 3. Diagram of linear hysteresis motor winding configuration.

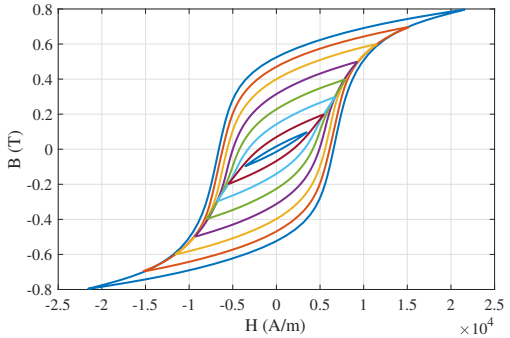

FIGURE 4. Measured hysteresis property of D2 tool steel under different excitation amplitude. Horizontal axis: field intensity (H-field). Vertical axis: flux density (B-field). Measurement taken by Dr. Gereon Goldbeck at the Johannes Kepler University in Linz, Austria.

hysteresis thrust force and reluctance thrust force are sinusoidal with respect to the horizontal axis, which is the phase difference between the stator excitation and the secondary's field. The hysteresis thrust force has a wavelength of 2π, while the reluctance force's wavelength is π. The summation of two thrust forces makes the phase of the peak total thrust force shifts to the center.

LINEAR HYSTERESIS MOTOR DESIGN

Fig. 3 shows a diagram of the linear hysteresis motor studied in this work. The stator uses a three-phase equivalent of six-phase lumped winding, where each coil has 151 turns. The secondary of the motor is made of hardened D2 tool steel. Fig. 4 shows the measured B-H curve of the secondary material under different B-field amplitude. Reference [10] introduces the hysteresis measurement setup being used. The length of the secondary equals 9 stator tooth pitch, which is 1.5 times of the wavelength of motor stator winding. The geometric parameters of the linear hysteresis motor are shown in Table 1.

The hysteresis motor secondary is pre-magnetized to improve the motors' thrust force generation capability. The pre-magnetization is done by setting the air gap length to zero, i.e., making the secondary in full contact with the motor stator, and then excite the motor stator with a DC three-phase current of an increasing current amplitude up to 5 A. When the pre-magnetizing field generated by the stator is removed, the magnetization inside the motor secondary does not fully vanish due to the material's magnetic hysteresis. When the motor is operating, we energize the motor stators at a lower current amplitude compared to the pre-magnetizing current (around 2 A), and the motor air gap length is set to 1.5 mm. Under this condition, the motor's operation does not significantly change the magnetization status of the secondary. As a result, the pre-magnetized linear hysteresis motor's characteristic resembles that of a weak linear permanent magnet motor with relatively high secondary permeability.

TABLE 1. Prameters of linear hysteresis motors.

Parameter Description	Value
Hysteresis secondary length	192 mm
Hysteresis secondary width	40 mm
Hysteresis secondary thickness	9.5 mm
Hysteresis secondary skew length	18.8 mm
Stator length	650 mm
Stage width	40 mm
Stage height	45 mm
Slot pitch	18.8 mm
Slot width	10.3 mm
Tooth width	8.5 mm
Slot depth	26 mm

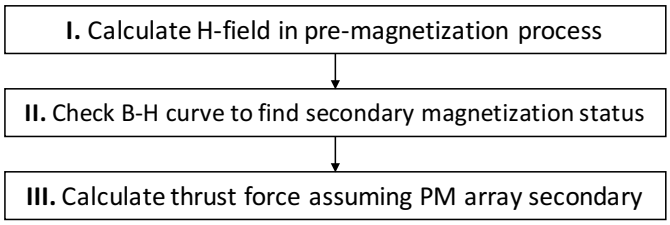
I. Calculate H-field in pre-magnetization process
II. Check B-H curve to find secondary magnetization status
III. Calculate thrust force assuming PM array secondary

FIGURE 5. Modeling process of pre-magnetized linear hysteresis motors.

MODELING FOR PRE-MAGNETIZED LINEAR HYSTERESIS MOTOR

Fig. 5 summarizes the modeling process of the pre-magnetized linear hysteresis motor. There are three steps in this model. In the first step, we calculate the field intensity (H-field) inside the secondary during the pre-magnetization process using a finite element simulation. In the second step, we check the measured hysteresis data of the secondary material, and use the calculated pre-magnetizing H-field to determine the material property of the secondary after pre-magnetization. Finally, we model the magnetized hysteresis secondary as an array of permanent magnets, where the magnets' material property is determined in the previous steps, and calcu-

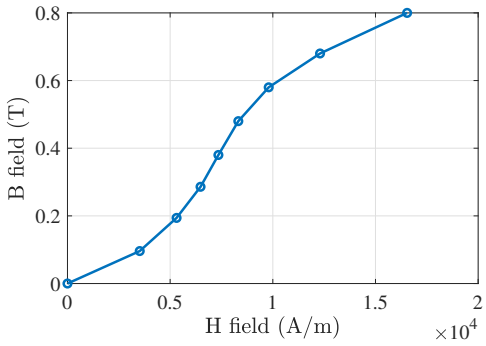

FIGURE 6. Nonlinear B-H curve of secondary material during pre-magnetization simulation. Also known as the "virgin magnetization curve" of the material.

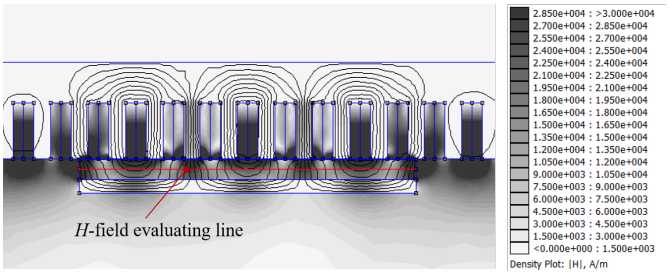

FIGURE 7. Magnetic field intensity (H-field) in the pre-magnetization process simulated with FEMM. Here magnetostatic simulation is used. The air gap length is zero, and current amplitude equals 5 A.

late the thrust force generation of the linear motor. Below we discuss the detailed modeling process in each step.

Step I: Pre-magnetizing field calculation

We first calculate the field intensity (H-field) inside the secondary generated by the stator in the pre-magnetization process. Here the finite element package FEMM [11] is used. In this simulation, the motor air gap length is set to zero, and the peak current amplitude in the stator windings is 5 A. The frequency of the simulation is set to zero. Fig. 6 shows the B-H property of the secondary material used in this simulation, which is achieved by collecting the maximum points in each measured B-H loop of the hardened D2 tool steel in Fig. 4. The data in Fig. 6 is also often referred to as the "virgin magnetization curve" of a hysteresis material, which represents the B-H status of the hysteresis material when it is first being magnetized.

Fig. 7 shows the simulated field plot of H-field distribution in the linear hysteresis motor during the pre-magnetization process. Here the H-field evaluating line is defined as a horizontal line in the secondary through the middle of its thickness, as shown by the red line in

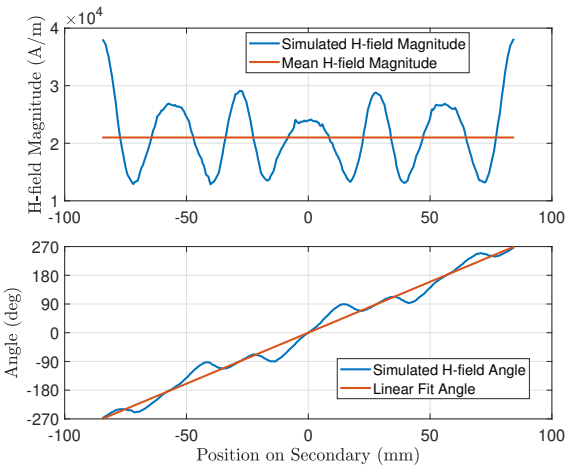

FIGURE 8. Simulated field intensity magnitude and angle in secondary along mid line during the pre-magnetization process.

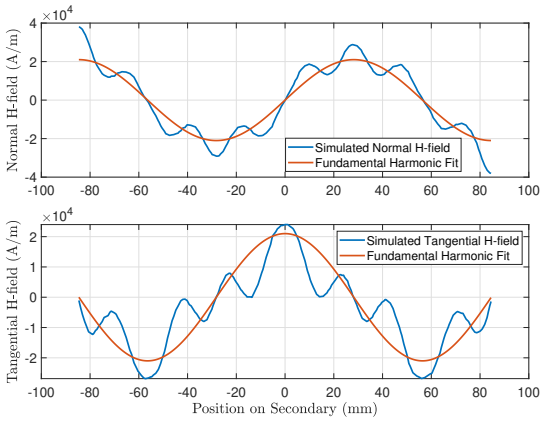

FIGURE 9. Normal and tangential components of field intensity during the pre-magnetization in secondary along mid line simulated by FEMM. Blue: simulated data. Orange: fundamental harmonic fit data calculated from magnitude $|H| = 2.1 \times 10^4$ A/m and angle $\theta = 2\pi y_r/\lambda_m$ rad.

Fig. 7. Fig. 8 shows the magnitude and angle of the simulated H-field along the H-field evaluating line. The average of the H-field magnitude and the linear fit for the angle are also plotted with orange lines in Fig. 8. Here, the average H-field magnitude is $|H| = 2.1 \times 10^4$ A/m, and the fitted angle is $\theta = 2\pi y_r/\lambda_m$ rad, where $\lambda_m = 112$ mm is the wavelength of the motor magneto-motive force (MMF). Fig. 9 shows the normal (vertical) and tangential (horizontal) components of the simulated H-field. The fundamental harmonic fit of the H-field components calculated from the average magnitude and the fitted phase

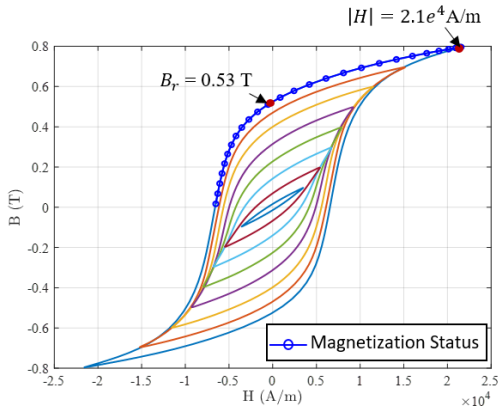

FIGURE 10. Measured B-H curve of the D2 tool steel. The material's magnetization status curve after pre-magnetization is highlighted in blue circles.

are also plotted in Fig. 9. It can be seen that the two components of the simulated H-field are in general matching well with their fundamental harmonic fits except the tooth harmonic field.

Step II: Checking B-H curve for magnetization status

In the second step, we check the measured B-H curve of the hysteresis secondary material (shown again in Fig. 10) to find its magnetic property after pre-magnetization. Checking the data in Fig. 10 with $|H| = 2.1 \times 10^4$ A/m, one can find that the magnetization status of the material after pre-magnetization can be represented by the outmost loop in Fig. 10, specifically the region highlighted with blue circles. When the external pre-magnetizing field generated by the stator is removed, the magnetization of the material is $B_r = 0.53$ T, which is the remanence of the material.

Step III: Thrust force calculation.

In the last step, we model the hysteresis secondary as a permanent magnet array, and calculate the thrust force of the motor using finite element method. Here, the material property of the magnets is set with the magnetization status curve in Fig. 10. Note that unlike typical rare-earth magnets, this B-H curve is nonlinear. When an alternating external field is generated by the stator, such material can exhibit hysteresis when they are demagnetized. That is, when an external H-field pushes the material's magnetization status to a lower point in the demagnetization curve, the flux density level does not recover to the previous magnitude when the external H-field changes direction. Instead, the magnetization status follows a minor hysteresis loop, thereby generating secondary loss. In our model for pre-magnetized linear hysteresis motors, such material nonlinearity is not captured. This is acceptable here for two reasons. First, the H-field magnitude generated by the stator when the motor is operating is significantly smaller than the field during the pre-magnetization phase. This allows us to approximate the B-H curve of the material in the operating range with a linear curve without significant loss of accuracy. Second, the modeled linear hysteresis motor is operated synchronously, where the fundamental harmonic of the external magnetic field does not slip with respect to the secondary material, and only has a phase difference with respect to the secondary material when the stage is accelerating or decelerating. This fact further reduces the magnitude of the external H-field variation range in the material.

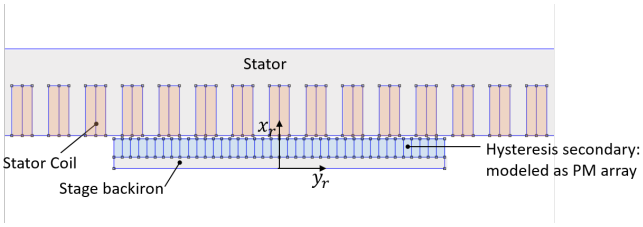

FIGURE 11. Finite element model for linear hysteresis motor thrust force calculation in FEMM. Here the pre-magnetized hysteresis secondary is modeled as a permanent magnet array of 40 segments. The material of all segments are the same, while the direction of the magnetization is determined by the H-field during pre-magnetization, i.e. $\theta = 2\pi y_r/\lambda_m$ rad.

The calculation of the thrust force also uses FEMM. Fig. 11 shows a diagram of the finite element model for the linear hysteresis motor. Here, the hysteresis secondary is modeled as an array of permanent magnets comprising 40 segments. The material of all segments are the same. The magnetization direction of the secondary segments is determined $\theta = 2\pi y_r/\lambda_m$ rad, where y_r is the position of the center point of a certain segment in the secondary coordinate. The segment's material property is set by the magnetization status curve as shown by the highlighted line in Fig. 10. Note that this model ignores the tooth harmonic of the secondary magnetization. Note that this simulation will include both hysteresis and reluctance thrust force generation, since the secondary material has magnetization for hysteresis thrust force generation, and has relatively high permeability for reluctance force generation.

We then calculate the thrust force generated by reluctance force only to separate the reluctance effect and the hysteresis effect. In this simulation, the coercivity of the secondary material is set to zero. The material's property is assumed to be linear, and its permeability is set to the slope of the nonlinear B-H curve around the remanence point B_r, which is $\mu_H = 29\mu_0$. Fig. 12 shows the simulated thrust force decomposition in a pre-magnetized lin-

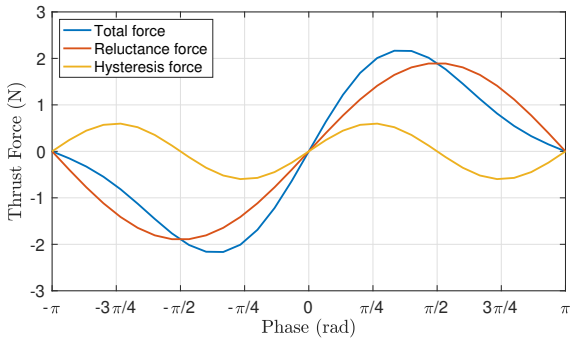

FIGURE 12. Simulated thrust force generation in pre-magnetized linear hysteresis motor with respect to phase of motor stator excitation. Stator current amplitude is 2 A.

ear hysteresis motor using our model. The stator current amplitude in simulation is set to 2 A. The hysteresis thrust force (orange curve) is estimated by subtracting the simulated reluctance thrust force from the simulated total thrust force. It can be seen that this simulated reluctance force demonstrates two periods between $-\pi$ and π, and the estimated hysteresis thrust force is sinusoidal with respect to the phase of excitation, and its peaks are at $\pm\pi/2$. These observations match our prediction in Fig. 2 in the previous section.

EXPERIMENTAL VALIDATIONS

The proposed model is validated via tests using a magnetically-levitated linear stage driven by linear hysteresis motors. Fig. 13 shows the photos of the linear stage prototype, hysteresis secondary, and stator. The detailed design, building, and testing for this linear stage is presented in [6]. The motor's design parameters are shown in Table 1. Note that our linear stage uses a two-sided motor configuration. The force measurement is the total thrust force of the linear stage, which is generated by two linear hysteresis motors on both sides.

First the linear stage's secondaries are pre-magnetized. The pre-magnetization process uses zero air gap and a current amplitude of 5 A. The hysteresis secondaries on both sides of the stage are magnetized symmetrically. We then measure the linear stage's thrust force with respect to the phase difference between the stator excitation and the secondary magnetization under different stator current amplitude. Note that the stage's position does not move during the measurement. Fig. 14 shows the measured thrust force and the simulated force using the finite element model plotted together. Note that the simulated data was multiplied by two to model the double-sided linear motor. Fig. 14 shows that the simulation results and the measurements are agreeing well. This comparison validates the model for pre-magnetized linear hysteresis motors.

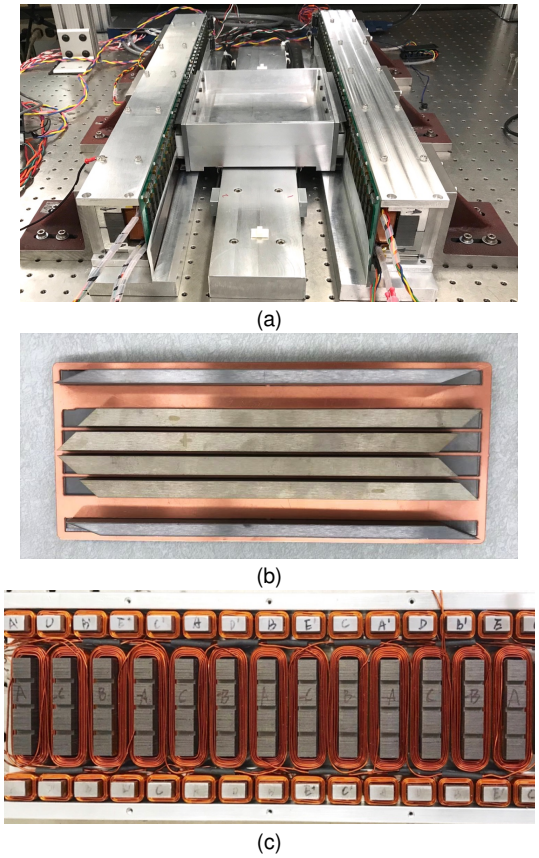

FIGURE 13. Photos of the magnetically-levitated linear stage driven by linear hysteresis motors [6]. (a) Full stage prototype. (b) Motor secondary on the moving stage. (c) Stator.

CONCLUSIONS AND FUTURE WORK

In this paper, a finite-element-based modeling process for pre-magnetized linear hysteresis motors is presented. In this model, the pre-magnetized hysteresis secondary is modeled as a permanent magnet array, where the magnets' material property is determined by the field calculation in the pre-magnetization process. The model is compared with experimental measurements on a hysteresis-motor-driven magnetically-levitated linear stage. Good agreement between the simulation and measurements validates the modeling process. This method can be extended to the modeling for other devices using hysteresis alloy, such as hysteresis clutches and relays.

In this work, hysteresis secondary is modeled under the assumption that the motor's operation does not change the secondary's magnetization status. Future work should consider the modeling for pre-magnetized hysteresis materials with the minor hysteresis loops considered, which can capture the magnetization status of the material under large external fields with improved ac-

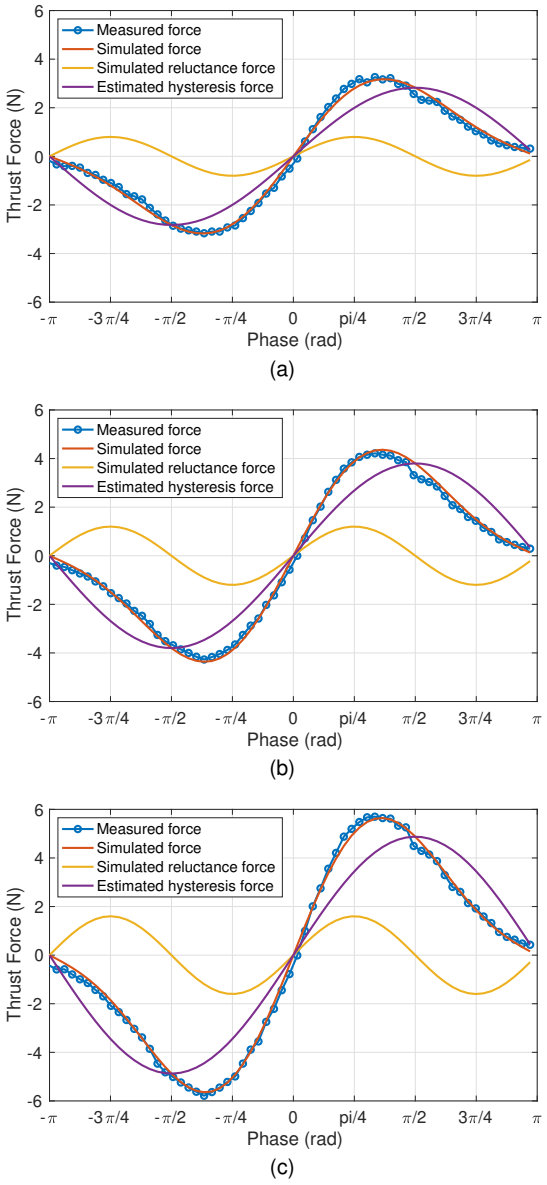

FIGURE 14. Comparison between measured and simulated thrust forces of the linear stage under different current amplitudes. (a) Current amplitude 1.5 A. (b) Current amplitude 2 A. (c) Current amplitude 2.5 A.

curacy.

ACKNOWLEDGMENT

The authors thank ASML for supporting this work. We thank Dr. Ruvinda Gunawardana and Dr. Minkyu Kim at ASML for valuable discussions throughout the project.

We thank Dr. Wolfgang Gruber and Gereon Goldbeck at JKU, Linz, Austria for their help with the hysteresis property measurements.

REFERENCES

[1] Teare BR. Theory of hysteresis-motor torque. Electrical Engineering. 1940;59(12):907–912.

[2] Rahman MA, Osheiba AM. Steady-state performance analysis of polyphase hysteresis-reluctance motors. IEEE Trans on Industry applications. 1985;(3):659–663.

[3] Brown JJR, Hartke DH. Magnetic tape timing system; 1962. US Patent 3,070,800.

[4] Noh M, Gruber W, Trumper DL. Hysteresis bearingless slice motors with homopolar flux-biasing. IEEE/ASME Trans on mechatronics. 2017;22(5):2308–2318.

[5] Mundt J, Kasper H, Pritsch E. Method for optimizing the power input of a plurality of hysteresis motors connected in parallel; 1984. US Patent 4,447,788.

[6] Zhou L, Trumper D. Magnetically levitated linear stage for in-vacuum transportation tasks. In: 33 Annual Conference of American Society of Precision Engineering. ASPE; 2018. p. 1–6.

[7] Galluzzi R, Tonoli A, Amati N. Magnetic hysteresis machines for next-generation electric turbochargers. In: 2017 International Conference of Electrical and Electronic Technologies for Automotive. IEEE; 2017. p. 1–5.

[8] Zhou L, Nejad MI, Trumper DL. One-axis hysteresis motor driven magnetically suspended reaction sphere. Mechatronics. 2017;42:69–80.

[9] Galluzzi R, Amati N, Tonoli A. Modeling, Design and Validation of Magnetic Hysteresis Motors. IEEE Transactions on Industrial Electronics. 2019;.

[10] Cossale M, Kitzberger M, Goldbeck G, Bramerdorfer G, Andessner D, Amrhein W. Investigation and Modeling of Local Degradation in Soft Magnetic Materials. In: 2018 IEEE Energy Conversion Congress and Exposition (ECCE). IEEE; 2018. p. 5365–5370.

[11] Meeker D. Finite element method magnetics. FEMM. 2010;4:32.

FRICTION ISOLATED ROTARY SYSTEM FOR HIGH-PRECISION ROLL-TO-ROLL MANUFACTURING

Dongwoo Kang[1], Xin Dong[2], Hyunchang Kim[1], Pyungwon Park[1], and Chinedum E. Okwudire[2]
[1]Department of Printed Electronics
Korea Institute of Machinery and Materials
Yuseong-gu, Daejeon, Korea
[2]Department of Mechanical Engineering
University of Michigan
Ann Arbor, MI, USA

OVERVIEW

This paper presents a rotary system for high-precision roll-to-roll manufacturing process. Friction isolator (FI), a robust mechatronics approach proposed in [1, 2], is implemented in the system to mitigate the undesirable effects of friction. Frequency- and time-domain simulation analysis demonstrates that the rotary system with FI achieves significantly improved attenuation of frictional disturbance, compared to the case without it. A rotary FI is designed to minimize the adverse effects of bearing friction without overly sacrificing the high rigidity of the machine. A precision rotary system is then built using the designed FI prototype and ongoing work is focused on experimentally validating the tracking performance of the rotary system during continuous roll-to-roll manufacturing.

BACKGROUND AND MOTIVATION

Roll-to-roll manufacturing processes, that pattern and coat electronic functional materials on plastic films, are considered as low-cost and high throughput technologies to manufacture flexible and large-area thin film electronics, such as organic photovoltaics, thin film transistors, light-emitting diodes and fuel cells [3]. In a typical roll-to-roll manufacturing system (see Figure 1), processes are carried out by transporting the plastic film continuously from unwinder to winder. For this purpose, the processing roller is generally controlled to move at constant velocity (CV) while tension of the plastic film is controlled by the unwinder and winder. Therefore, precision (i.e., tracking performance) of the processing roller during CV motion is crucial to the performance of roll-to-roll system because the resulting position error directly affects the quality of the manufactured products. For example, the directional coating uniformity and patterning error of the machine will be degraded by the velocity ripple and position error of the processing roller during coating processes [4] and patterning processes [5], respectively.

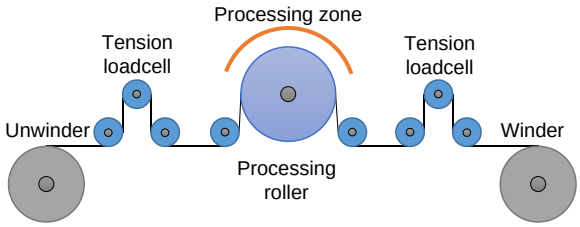

FIGURE 1. Schematic of a typical roll-to-roll manufacturing system.

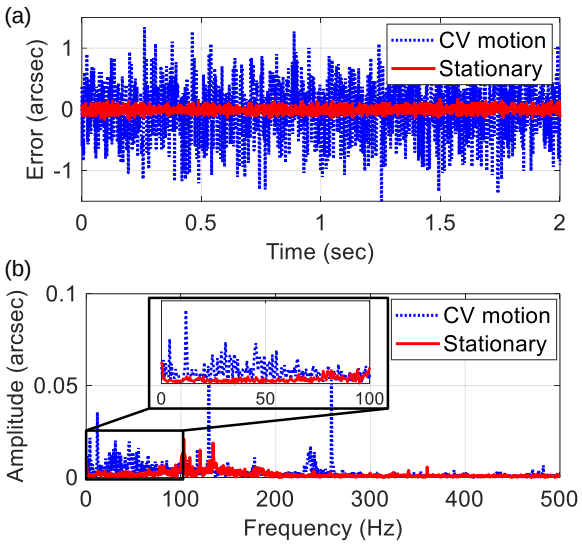

FIGURE 2. (a) Typical position errors of the rotary system guided by ball bearings; (b) frequency spectra of the error signals.

Friction forces due to the guiding ball bearings are major disturbances that affect the precision of the processing roller [6]. It is well known that

nonlinear friction behavior near zero velocity region significantly jeopardizes motion accuracy [1, 2, 7]. During CV motions, variation of friction occurs as the balls roll inside the bearing groove [6], severely hampering the tracking performance of the system. Figure 2 (a) shows the typical motion errors of the processing roller while it is stationary (i.e., in-position) and moving at a CV of 12 rpm. The feedback controller is tuned to have a closed loop bandwidth of 100 Hz which is much higher than the dominant frequency of the rotary motion (0.2 Hz). As shown in the frequency spectra of the position error signals (see Figure 2 (b)), the dominant peaks at low frequency region (< 10 Hz) are caused by the force ripple of the motor [8], which can be compensated by repetitive control; the remaining broad-band frequency components (10 – 100 Hz) with large amplitudes are mainly due to frictional disturbance from the rotary ball bearings.

To address the undesirable effects of friction on the precision and speed of motion stages, friction isolator (FI), a robust and cost-effective mechatronics approach (also known as compliant joint method), has been proposed by Dong et al. in [1]. They have demonstrated that FI significantly reduces the settling times and quadrant glitches of linear motion stages during point-to-point motions and circular motions. [1, 2]. However, the influence of FI on the tracking performance of servo systems during CV motions has not been explored; also, its applicability to rotary motions has not been demonstrated. Therefore, this paper focuses on investigating the benefits of FI on mitigating the effects of frictional variations on the precision of continuous roll-to-roll manufacturing system, in particular, the processing roller. The concept of friction isolated rotary system is described and its superior performance is demonstrated in simulations. The design of a prototype rotary system with FI is then outlined for experimental validations.

FRICTION ISOLATED ROTARY SYSTEM

Figure 3 shows the schematic of the proposed rotary system with friction isolator (FI). The processing roller, of inertia I_p is connected to the rotary bearings of inertia I_a using two FIs with rotational stiffness k and damping c. The inner rings of the ball bearings are connected to the FIs and the outer rings are fixed to the ground. The viscous friction coefficient between sliding surfaces of the bearings is denoted by c_f. T_a, T_p and T_f are respectively the driving torque of the motor, process induced disturbance torque and frictional disturbance torque of the ball bearing.

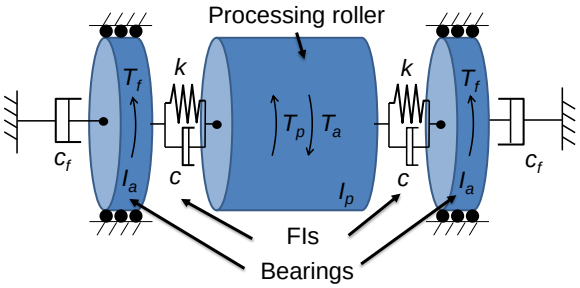

FIGURE 3. Schematic of a rotary system equipped with FIs.

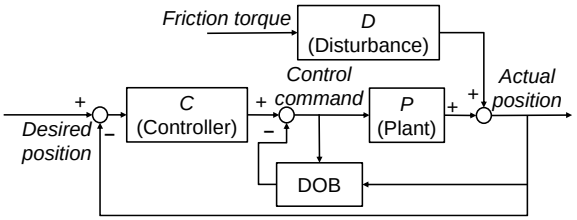

FIGURE 4. Control block diagram with feedback controller and DOB.

An industrial standard PID controller is used to control the motion of the processing roller; it is tuned to 100 Hz closed loop bandwidth. Since the feedback controller has limited ability in rejecting disturbances, an inverse-model-based disturbance observer (DOB) [2, 9] is implemented to further attenuate the low frequency disturbances due to frictional variations; it is tuned to 80 Hz bandwidth. The effectiveness of FI can be shown by calculating the open loop disturbance transfer function, D, as

$$D_R = 2G_{p,R} \quad (1)$$

$$D_{FI} = 2G_{p,FI}(cs + k) / [I_a s^2 + (c + c_f)s + k] \quad (2)$$

where s is the Laplace variable, G_p is the plant dynamics and subscripts R and FI denote the cases without and with FI. They are given by

$$G_{p,R} = 1 / [(I_p + 2I_a)s^2 + 2c_f s] \quad (3)$$

$$G_{p,FI} = [I_a s^2 + (c + c_f)s + k] / \{I_p I_a s^4 + [c(I_p + 2I_a) + c_f I_p]s^3 + [k(I_p + 2I_a) + 2cc_f]s^2 + 2kc_f s]\} \quad (4)$$

Note that in the rigid case (i.e., without FI), the processing roller is rigidly connected to the bearings. It is clearly shown that the undesirable effects of frictional disturbances are low-pass filtered by the dynamics of FI. To further illustrate the effects of stiffness and damping parameters on the performance of FI, the closed loop transfer

function from frictional disturbance to roller position (including the DOB) is obtained as [9],

$$G_d = DG_n(1 - Q) / [Q(G_p - G_n) + G_n(1 + CG_p)] \quad (5)$$

where C is the feedback (PID) controller, Q is a low-pass filter to guarantee stability and G_n is the nominal plant model that describes the low-frequency characteristics of the conventional rotary system (dominated by rigid body dynamics)

$$C = K_p + K_d s / (T_f s + 1) + K_i / s \quad (6)$$

$$Q = (2\pi f_Q)^2 / (s + 2\pi f_Q)^2 \quad (7)$$

$$G_n = 1 / [(I_p + 2I_a)s^2 + 2c_f s] \quad (8)$$

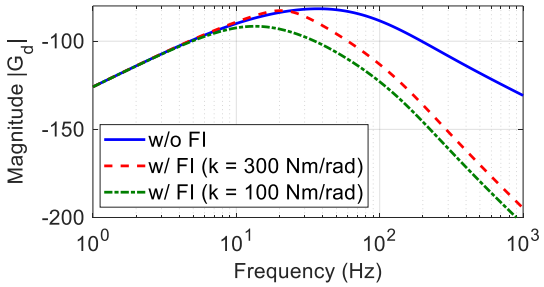

FIGURE 5. Magnitudes of $G_{d,R}$ and $G_{d,FI}$ with different stiffness for FI; c_f = 2 Nms/rad is used.

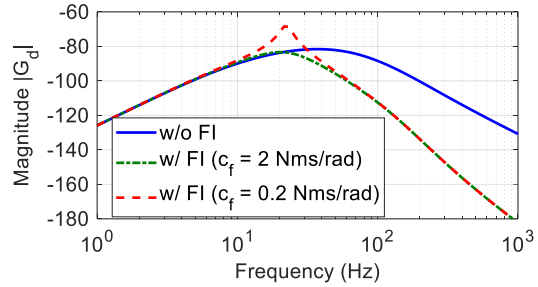

FIGURE 6. Effects of viscous damping c_f on the performance of FI; k = 300 Nm/rad is used.

TABLE 1. Parameters of the rotary system.

Parameters	Value
I_p	0.15 kgm^2
I_a	0.015 kgm^2
K_p	1.54 × 10^4 N$_{rms}$/rad
K_d	81.62 N$_{rms}$s/rad
K_i	6.16 × 10^5 N$_{rms}$/rads
T_f	0.0005884 s
f_Q	80 Hz

Figure 5 compares the magnitudes of $G_{d,R}$ and $G_{d,FI}$ using different stiffness k for FI. Note that a modal damping of 0.1% is introduced to account for the damping of FI (i.e., c) and the remaining parameters are summarized in Table 1. Observe that the frictional disturbance in the high frequency region is effectively suppressed by the FI, thanks to its low-pass filtering effects. The benefits of FI become more dominant when the stiffness is reduced since the magnitude of $G_{d,FI}$ quickly rolls off after the resonance peak. In other words, a lower stiffness FI leads to better suppression of frictional disturbance.

Figure 6 shows the effects of viscous friction on the performance of FI. Since the FI design often has limited damping [2], the resonance peak has very large amplitude if the frictional damping is small. This poses significant challenge since the dominant resonance can be easily excited (e.g., by friction variation), generating large position errors. Therefore, a high viscous damping coefficient of the bearing is needed in order to attenuate the resonance peak and achieve the desired performance of FI.

DESIGN OF ROTARY SYSTEM WITH FI

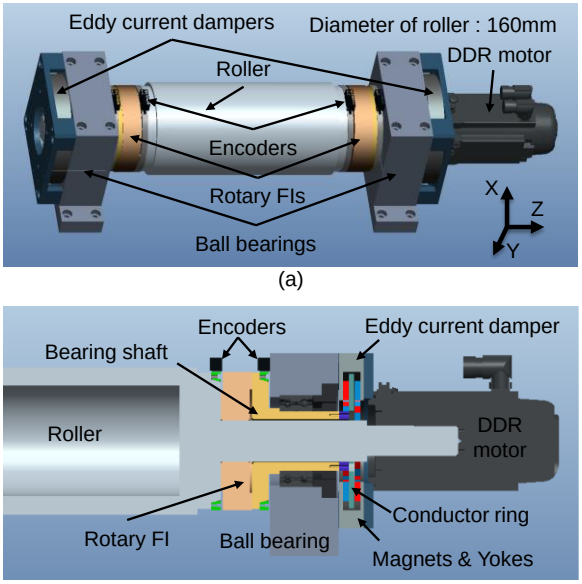

FIGURE 7. (a) CAD model and (b) cross-section view of the friction isolated rotary system.

Figure 7 shows the CAD model of the proposed friction isolated rotary system. The processing roller is guided by two angular contact ball bearings (NSK, 7013A). It is driven by a direct drive motor (Kollmorgen, C042A). To augment the bearing friction, c_f, an eddy current damper is implemented at the interface between the ball bearings and the ground.

The FIs are used to connect the processing roller to the rotary bearings. Figure 8 shows the schematics of the proposed FI design. Symmetric cartwheel flexure (SCF) mechanism [10, 11] with 4 leaf springs are adopted in the design; the center platform of the flexure is connected to the ball bearing and the outer platform is connected to the processing roller. To achieve the desired attenuation of frictional disturbance, the FI should have minimal stiffness k in the motion direction; in the meantime, the FI must maintain high stiffness in the off-motion directions (e.g., radial directions), so as not to overly sacrifice the rigidity of the ball bearing. Therefore, the parameters of the SCF mechanism, specifically, leaf length l, leaf thickness t, leaf width b, inner platform radius r_i and viscous damping coefficient c_f, are optimized to maximize the stiffness ratios between off-motion directions and motion direction while satisfying other design constraints (e.g., maximum stress, dimension).

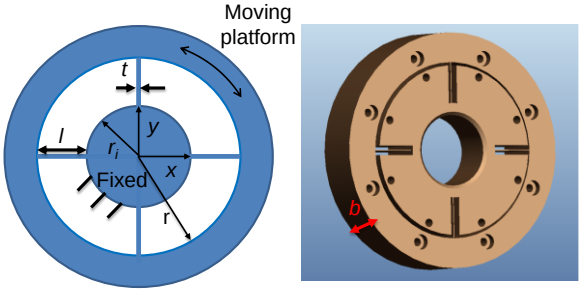

FIGURE 8. (a) Schematic and (b) CAD drawing of symmetric cartwheel flexure (SCF) design [10].

To achieve the desired viscous damping, a rotary eddy current mechanism is designed. The permanent magnets of the proposed damper is arranged in circumferential direction, which is similar to that of a doubled-sided linear motor. The rotating disc is placed between the upper and lower magnetic arrays and viscous damping torque is achieved due to the interaction of eddy current and magnetic field. Figure 9 shows an example of the simulated eddy current density and magnetic field (using ANSYS) when the disc is rotating at 1 rpm. The resulting damping torque can be calculated by volume integration of the rotating disc as

$$T_{damp} = \int r_v \times (J \times B)\, d\tau \qquad (9)$$

where r_v is the radial location of the infinitesimal element used in volume integration, J is the current density, B is the magnetic field, and $d\tau$ is the volume of the infinitesimal element. With an outer radius of 95 mm and a thickness of 27 mm, the desired viscous damping coefficient of 1.2 Nms/rad is achieved.

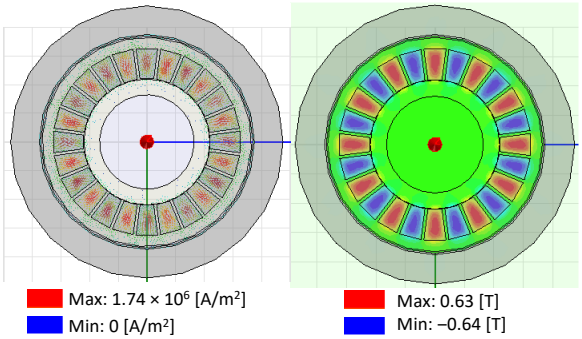

FIGURE 9. Simulated eddy current density (left) and magnetic field (right) using ANSYS.

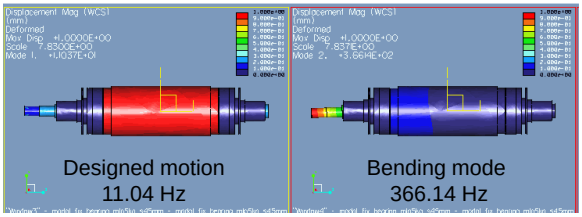

FIGURE 10. Simulated resonance modes of the designed rotary system with FI.

Figure 10 shows the simulated resonance modes of the rotary system assembly with FI. Note that the lowest uncontrollable mode is 366.14 Hz which is much higher than our desired closed loop bandwidth, i.e., 100 Hz.

SIMULATION ANALYSIS

The performance of the proposed rotary system with FI is compared with the conventional system (no FI) in simulation. Table 2 summarizes the parameters obtained from the designed SCF; note that viscous coefficient (i.e., c_f) of the case without eddy current damper is contributed by the viscous friction from the ball bearing. Figure 11 shows the simulated tracking performance of the designed rotary system when the processing roller is moving at 10 rpm CV. To replicate the practical scenario when friction variation occurs, normally distributed disturbance force with 0.15 Nm standard deviation (i.e., RMS value) is introduced in the simulation. The case without FI has an RMS error of 1.41 μrad during the CV motion. In the absence of the eddy current damper, the system with FI suffers from significant vibrations around the resonance frequency, leading to an increased RMS error to 2.62 μrad. Using the FI with the designed eddy current damper, the system achieves 36%

reduction of the RMS error (0.91 μrad), when compared to the no FI case.

Table 2. Parameters used in simulations.

Parameters	Value
I_p	0.1401 kgm^2
I_a	0.01491 kgm^2
k	324.85 Nm/rad
c	0 Nms/rad
c_f (w/o damper)	0.2 Nms/rad
c_f (w/ damper)	1.4 Nms/rad

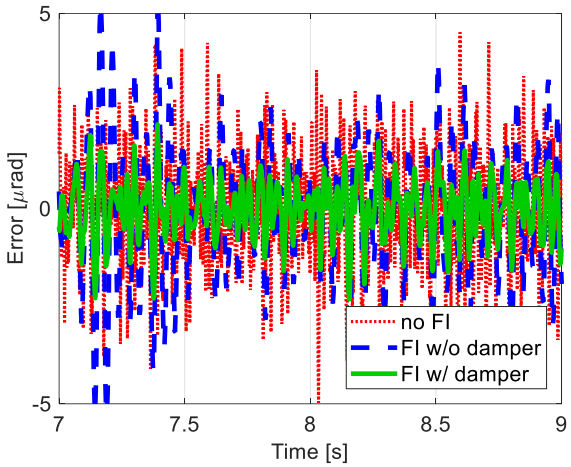

FIGURE 11. Simulated tracking error of the proposed rotary system during 10 rpm CV motion.

CONCLUSIONS AND FUTURE WORK

In this paper, a novel rotary system for achieving high precision continuous roll-to-roll manufacturing has been presented. The proposed system integrates friction isolator (FI), a mechanical component, to mitigate the undesirable effects of friction on the tracking performance of the processing roller. It has been demonstrated through frequency domain analysis that FI improves the disturbance rejection ability of the system by low-pass-filtering the frictional disturbance from the supporting bearings. A rotary FI prototype has then been designed with symmetric cartwheel flexure mechanism; its parameters have been optimized to achieve lowest stiffness in the motion direction (for better disturbance suppression) while maintaining high stiffness in off-motion directions so as not to unduly sacrifice the rigidity of the machine. An eddy current damper has been designed to provide additional viscous damping that is critical for attenuating the vibrations due to FI. It has been demonstrated in simulation that the proposed FI achieves 36% reductions in RMS tracking error during a CV motion of 1 rpm, compared to the case without it.

A rotary system that equipped with the FI prototype has been designed and manufactured – see Figure 12. The direct drive motor is powered using a PWM amplifier (Kollmorgen, AKD-B00606). The angular position of the processing roller is measured using a ring encoder (Renishaw, Encoder head – RGH20Y, Ring scale – PESR20USA150) that is mounted on the side surface of the roller; it has an angular resolution of 1.33 μrad. The feedback controller is implemented using a real-time control board (dSPACE, DS1005). Ongoing work focuses on experimentally validating the performance of the proposed system; tracking error of the processing roller will be evaluated during continuous roll-to-roll manufacturing process, i.e., constant velocity motion. The results of the experiments will be presented at the ASPE annual meeting.

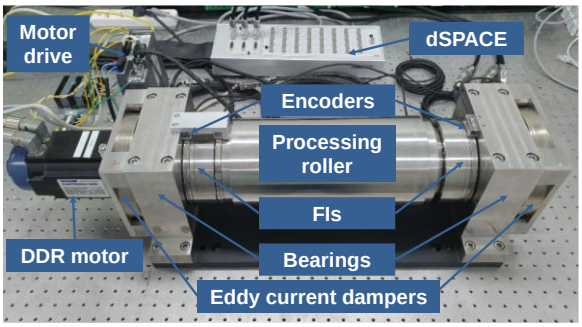

FIGURE 12. In-house built rotary system prototype equipped with the designed FI.

ACKNOWLEDGEMENTS

This work is funded by Korea Institute of Machinery and Materials (KIMM) through the Government-funded Research Program (Grant NK217D): Development of Roll-to-Roll Hybrid Manufacturing System for Flexible Electronic Devices and by National Science Foundation (NSF) Award (CMMI #1855390): Towards a Fundamental Understanding of a Simple, Effective and Robust Approach for Mitigating Friction in Nanopositioning Stages.

REFERENCES

[1] Dong X, Liu X, Yoon D, Okwudire CE. Simple and robust feedforward compensation of quadrant glitches using a compliant joint. CIRP Ann.-Manuf. Techn. 2017; 66: 353-356.

[2] Dong X, Okwudire CE. An experimental investigation of the effects of the compliant joint method on feedback compensation of

pre-sliding/pre-rolling friction. Precis. Eng. 2018; 54: 81-90.
[3] Søndergaard RR, Hösel M, Krebs FC. Roll-to-Roll Fabrication of Large Area Functional Organic Materials. J. Polym. Sci. B. 2013; 51: 16-34.
[4] Choi Y, Lee S, Jo J. High-Precision Slot-Die Coating Machine for Thin Films of Flexible Display. J. Korean Soc. Precis. Eng. 2014; 31: 491-495.
[5] Kim H, Lee E, Choi Y, Kwon S, Lee S, Jo J, Lee T, Kang D. Development of a precision reverse offset printing system. Rev. Sci. Instrum. 2016; 87: 015102.
[6] Fujita T, Matsubara A, Yamazaki K. Experimental characterization of disturbance force in a linear drive system with high-precision rolling guideways. Int. J. Mach. Tool Manu. 2011; 51: 104-111.
[7] Dong X, Yoon D, Okwudire CE. A novel approach for mitigating the effects of pre-rolling/pre-sliding friction on the settling time of rolling bearing nanopositioning stages using high frequency vibration. Precis. Eng. 2017; 47: 375-388.
[8] Bascetta L, Rocco P, Magnani G. Force Ripple Compensation in Linear Motors Based on Closed-Loop Position-Dependent Identification. IEEE-ASME T. Mech. 2010; 15: 349-359.
[9] Schrijver E, Dijk JV. Disturbance Observers for Rigid Mechanical Systems: Equivalence, Stability and Design. J DYN SYST-T ASME 2002; 124: 539-548.
[10] Kim K, Ahn D, Gweon D. Optimal Design of A 1-Rotational DOF Flexure joint for a 3-DOF H-type Stage. Mechatronics 2012; 22: 24-32.
[11] Kang D, Gweon D. Analysis and Design of a Cartwheel-type flexure hinge. Precis. Eng. 2013; 37: 33-43.

LEARNING BASED PRE-COMPENSATION OF PRE-SLIDING FRICTION AND SERVO TRACKING ERRORS FOR PRECISION MOTION CONTROL

Alper Dumanli, Burak Sencer
School of Mechanical, Industrial and Manufacturing Engineering
Oregon State University
Corvallis, Oregon, USA

INTRODUCTION

Accuracy of high-precision manufacturing equipment, such as precision machine tools and photolithography systems, rely heavily on dynamic behavior of their motion generation mechanisms (e.g. feed drives) [1]. Feed drives suffer from various positioning error sources, which deteriorate their dynamic accuracy and cause decreased product quality. Firstly, as the axes of a machine tool accelerate and decelerate, inertial and viscous friction forces are countered by the closed loop servo-control system of feed drives. The lagging response of the closed loop system to these forces inevitably create motion tracking errors [1]. Secondly, as each axis comes to a full-stop and changes its direction of motion, nonlinear friction forces induced by pre-motion (pre-sliding and/or pre-rolling) friction regime act as external disturbances on the feed drive control system [2], which further deteriorate positioning errors. Circumventing adverse effects of dynamic errors has been the everlasting interest of precision engineering community.

First strategy to mitigate the effects of these dynamic error sources is to use advanced feedback (FB) control structures. For example, in [3] and [5], FB controllers are designed as high-order linear controllers to robustly extend the bandwidth of the closed loop control system beyond vibrational dynamics of feed drives. Or, additional nonlinear and parameter-adaptive components can be added to the FB controller in order to improve closed loop dynamic behavior [1], [3], [4]. Despite being effective, these strategies require control engineering expertise to design and implement, since they may lead to closed loop stability issues. Second strategy is to enhance conventional FB controllers' performance by additional feedforward (FF) controllers. A typical feedforward controller utilizes an inverse model of system dynamics to widen the tracking bandwidth [5]. In order to obtain inverse models for FF control, dynamic behavior of the system must be modeled accurately. This makes FF controllers prone to variations in the system dynamics. Performance of linear FF controllers can be improved through data-based parameter tuning by the use of iterative learning controllers (ILC) [8]. The third strategy seeks to mitigate lack of robustness in feedforward control by providing optimal reference trajectories. In [6], acceleration profiles are generated optimally in order to avoid vibrations, and in [7], trajectories are pre-compensated for the servo-lag for improved multi-axis contouring performance.

In this paper, benefits of feedforward control and optimal trajectory generation are combined, and a novel learning-based trajectory pre-compensation method is presented. In the proposed method, a trajectory pre-compensation filter is utilized to modify reference trajectories in order to eliminate feed drive servo tracking errors. Optimal pre-compensation filter parameters are obtained through machine-in-the-loop (online) convex optimization.

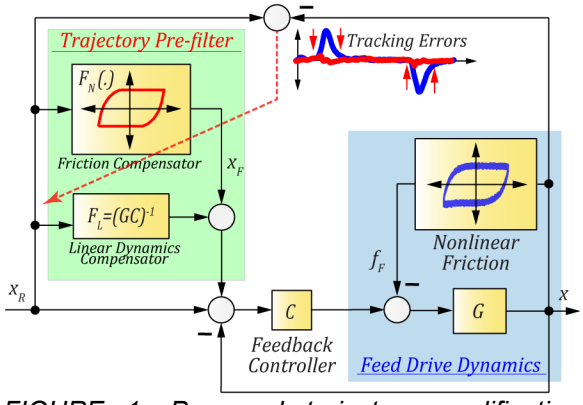

FIGURE 1: Proposed trajectory modification strategy.

An overview of the proposed approach is illustrated in Fig. 1. As shown, two

compensation filters (F_L and F_N) are used to modify the reference trajectory x_R. The modified trajectory $x_M=x_R+F_Lx_R+F_N(x_R)$ is then sent to the closed-loop controlled feed drive system in order to ensure that the original reference trajectory x_R and the actual feed drive position x are as close as possible ($x_R \approx x$). The filter F_L is a linear filter, and it is used for cancelling the linear feed drive dynamics such as inertia and viscous friction effects. F_N, on the other hand, is a nonlinear filter, and it compensates for nonlinear friction forces that arise when the feed drive goes through pre-sliding regime.

ITERATIVE TRAJECTORY COMPENSATION FOR ACCURATE ELIMINATION OF INERTIA AND VISCOUS FRICTION INDUCED ERRORS

Conventional feedback control systems for precision machine tools are typically designed as Cascade P-PI Controllers, which are tuned deliberately to avoid excitation of structural resonances. This results in closed loop behavior which is dominated by rigid body dynamics, inducing large servo errors during acceleration and deceleration segments of the reference trajectory. In order to compensate for the closed loop dynamics (G_{CL}), the linear pre-compensator (F_L) for each axis can be designed as:

$$\frac{x}{x_R} = \left(1+F_L\right)\left(\frac{GC}{1+GC}\right) \cong 1 \qquad \text{with: } F_L = \frac{ms^3+bs^2}{K_Ds^2+K_Ps+K_I} \tag{1}$$

where x is the displacement of a single axis, and m and b are the inertia and viscous friction coefficient of the feed drive moving along that axis. K_D, K_P and K_I are the PID-equivalent coefficients of the FB P-PI controller. Since every P-PI controller can be written and analyzed as a PID controller, PID formulation is used here for notational brevity. This fixed structure of F_L ensures that rigid body dynamics is compensated by its numerator and controller dynamics is compensated by its denominator.

To obtain effective error elimination using F_L, its parameters must be identified accurately. This paper proposes a two-stage online optimization strategy to identify F_L. At first, parameters of F_L are obtained by utilizing least-squares (LS) regression. The strategy is as follows. The machine is moved with a simple point-to-point (P2P) command trajectory, and position tracking error caused by linear servo-dynamics (e_L) is recorded, The error dynamics can be represented in Laplace and time domains as:

$$\frac{e_L}{x_R} = \frac{1}{1+GC} = \frac{ms^3+bs^2}{ms^3+\left(K_D+b\right)s^2+K_Ps+K_I}$$

$$e_L = x_R - \frac{1}{m}\left(\begin{array}{l}\left(K_D+b\right)\int_0^t e_L d\tau + K_P\int_0^t\int e_L d\tau \\ \cdots + K_P\int_0^t\int\int e_L d\tau - b\int_0^t x_R d\tau\end{array}\right) \tag{2}$$

Then, the following optimization problem is solved to obtain an initial estimate of the pre-compensator parameters:

$$\min_{\boldsymbol{\theta}} \frac{1}{2}\left\|\boldsymbol{\Phi\theta}-\boldsymbol{\gamma}\right\|_2^2 \quad \text{subject to: } \boldsymbol{\theta} \geq 0 \tag{3}$$

with:

$$\boldsymbol{\gamma} = \begin{bmatrix} x_R(0)-e_L(0) \\ x_R(T_s)-e_L(T_s) \\ \vdots \\ x_R(MT_s)-e_L(MT_s) \end{bmatrix}, \boldsymbol{\theta} = \begin{bmatrix}\theta_1\\ \theta_2\\ \theta_3\\ \theta_4\end{bmatrix} = \begin{bmatrix}K_D+b\\ K_P\\ K_I\\ b\end{bmatrix}\frac{1}{m}$$

$$\boldsymbol{\Phi} = \begin{bmatrix} e_i(0) & e_{ii}(0) & e_{iii}(0) & -x_{Ri}(0) \\ e_i(T_s) & e_{ii}(T_s) & e_{iii}(T_s) & -x_{Ri}(T_s) \\ \vdots & \vdots & \vdots & \vdots \\ e_i(MT_s) & e_{ii}(MT_s) & e_{iii}(MT_s) & -x_{Ri}(MT_s) \end{bmatrix}$$

where e_i, e_{ii}, e_{iii} are integrated error profiles through Tustin discretization.

The trajectory (x_R) used in this optimization problem contains multiple acceleration and deceleration segments, and it is shown in Fig. 2.

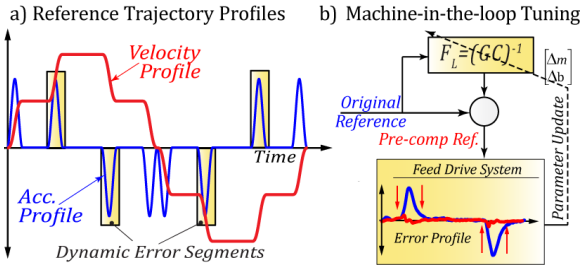

FIGURE 2: Machine-in-the-loop tuning of trajectory pre-filter F_L.

At the very beginning of the trajectory, tracking errors are influenced by both feed drive dynamics (inertia and viscous friction) and non-linear friction forces (due to pre-sliding friction regime). Additionally, the same influence of the non-linear friction forces are also apparent in the error profile around the acceleration segment where the trajectory changes its direction

(velocity reversal) and at the last deceleration segment of the trajectory. However, in the optimization problem postulated by Eq. (3), linear feed drive dynamics (*m, b, K_P, K_D* and *K_I*) is considered as the only error source. In order to ensure that the influence of nonlinear friction does not affect the solution accuracy of Eq. (3), only the acc/dec segments where linear dynamics are dominant are included in e_L. These segments are marked by yellow and named as "Dynamic Error Segments" in Fig. 2.

The solution provided by Eq. (3) is used to construct an initial estimate of F_L, and it provides significant reduction in tracking errors. However, it tries to minimize the estimation error between actual and modeled axis position. In other words, it tries to fit closed loop dynamics. The main objective of the proposed trajectory pre-filtering approach is to minimize the tracking errors themselves. In order to introduce this objective to the optimization procedure, identified pre-filter parameters are refined by solving the following optimization problem:

$$\min_{m,\,b}\left(J_L = \frac{1}{2}\left\|\mathbf{e}_L\right\|_2^2 = \frac{1}{2}\mathbf{e}_L^T\mathbf{e}_L\right), \quad \text{subject to: } m \geq 0,\ b \geq 0 \tag{4}$$

where $\mathbf{e}_L$ is the vector of recorded tracking errors, and therefore the optimization problem directly aims to minimize tracking errors. Eq. (4) is solved iteratively, where the machine is commanded the trajectory x_R (see Fig. 2.a) at each iteration, and the pre-filter parameters *m* and *b* are updated to steer the objective function to an optimum. Notice that in this optimization stage, only estimated inertia (*m*) and viscous friction (*b*) of the drive are updated. The reason for this is twofold: **(1)** Feed drive dynamics (*m* and *b*) may vary over time (e.g. in machining applications, inertia of the workpiece decreases during cutting). By solving Eq. (4) iteratively, these variations can be easily captured. On the other hand, parameters of the closed loop control system on a conventional feed drive are typically invariant. **(2)** Only updating *m* and *b* ensures that Eq. (4) postulates a convex optimization problem. Therefore, its solution is guaranteed to be a global optimum.

Eq. (4) is solved by updating the pre-filter parameters utilizing the data-based gradient (∇J_L) and Hessian ($\nabla^2 J_L$) of the optimization objective with respect to the optimization variables, which can be written in terms of the tracking error vector $\mathbf{e}_L$ as:

$$\nabla J_L = \mathbf{e}_L^T \nabla \mathbf{e}_L, \quad \nabla^2 J_L = \nabla \mathbf{e}_L^T \nabla \mathbf{e}_L, \quad \nabla = \begin{bmatrix} \dfrac{\partial}{\partial m} \\ \dfrac{\partial}{\partial b} \end{bmatrix} \tag{5}$$

As seen, in order to calculate ∇J_L and the $\nabla^2 J_L$, gradient of the tracking error vector ($\nabla \mathbf{e}_L$) is required, which can be obtained as follows:

$$e_L = x_R - x = \left(\frac{1 - F_L GC}{1 + GC}\right) x_R$$

$$\nabla e_L = \begin{bmatrix} \dfrac{\partial e_L}{\partial m} \\ \dfrac{\partial e_L}{\partial b} \end{bmatrix} = -\nabla F_L \underbrace{\left(\frac{GC}{1 + GC}\right) x_R}_{x} \tag{6}$$

$$\text{where } \nabla F_L = \begin{bmatrix} s^3 \\ s^2 \end{bmatrix} \frac{1}{K_D s^2 + K_P s + K_I}$$

Utilizing $\nabla \mathbf{e}_L$ obtained from Eq. (6) and recorded tracking errors ($\mathbf{e}_L$), the pre-filter parameters are updated with Newton's Method as:

$$\begin{bmatrix} m \\ b \end{bmatrix}^{k+1} = \begin{bmatrix} m \\ b \end{bmatrix}^{k} - \alpha \left(\nabla^2 J_L\right)^{-1} \left(\nabla J_L\right) \tag{7}$$

where α is the learning coefficient. This parameter update strategy ensures that F_L steers the tracking errors to a global minimum safely as long as the inequality constraints in Eq. (4) are not violated. In case of constraint violation, the update law given by Eq. (7) is modified using Primal-Dual Interior Point Algorithm, details of which can be found in [9]. The influence of α in Eq. (7) on convergence performance can be analyzed using discrete systems theory as described in [8], and it can be concluded that a reliable range for α is $0<\alpha<1$.

Experimental Verification

Effectiveness of the proposed dynamic compensation algorithm is validated on a 3-Axis CNC Machining Center shown in Fig. 3.a. *X* and *Y* axes are controlled by hand-tuned Cascade P-PI controllers. Using a single G-code consisting several linear interpolation commands (G01), X axis is moved back and forth at 50 and 100 mm/sec. The reference trajectory and error profiles are recorded at 10 kHz. As seen by Fig. 3.c, error peaks occur around acceleration and deceleration segments of the trajectory.

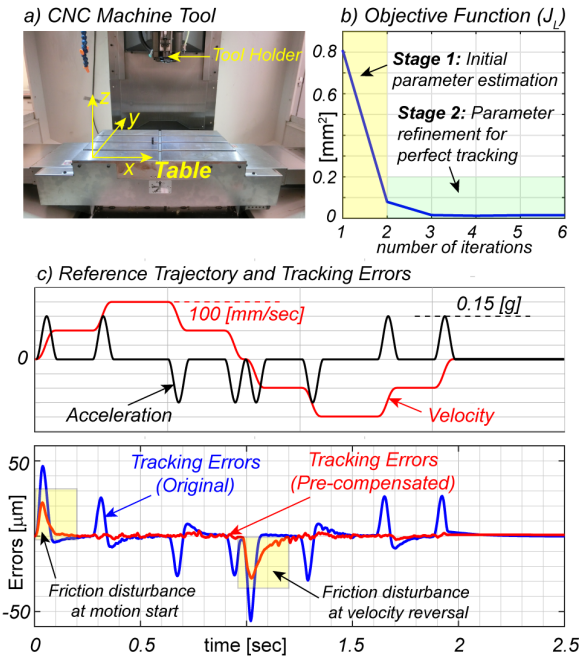

FIGURE 3: Experimental validation of servo dynamics compensation.

Utilizing Eqs. (3) and (7), the linear pre-filter F_L is iteratively tuned (trained) with α=0.75 by repeatedly moving the machine with the trajectory shown in Fig. 3.c. Fig. 3.b shows the convergence performance of this tuning process. As seen, after 6 iterations, error peaks are significantly reduced and reliable convergence is observed. Notice that at the beginning of the trajectory, and also at the instant where the machine comes to a full stop and changes its motion direction (velocity reversal), 20-30 µm error peaks are observed. These peaks are due to pre-sliding regime friction forces, and these segments are deliberately avoided in tuning F_L (see Fig. 2) in order to guarantee that nonlinear friction forces do not interfere with the optimality of F_L.

Once the linear pre-compensator F_L is optimized, it can be applied to any arbitrary trajectory to minimize the errors induced by feed drive dynamics. An example on a circular toolpath is provided in the following section.

ITERATIVE TRAJECTORY COMPENSATION FOR ELIMINATION OF PRE-SLIDING FRICTION INDUCED ERRORS

Nonlinear friction forces, as well, pose a major limitation on achievable accuracy of precision machine tools. For example, in Fig. 3.c, even though linear feed drive dynamics are compensated by F_L, large error peaks are observed in the vicinity of velocity reversals, which are induced by pre-sliding regime friction forces. Nonlinear pre-compensator F_N is designed in this section to eliminate the errors caused by these nonlinear friction forces.

Since the tracking errors caused by linear feed dynamics are pre-compensated by F_L, nonlinear friction induced errors can be written as:

$$e = f_F \underbrace{\left(\frac{G}{1+GC}\right)}_{D(s)} - x_F \underbrace{\left(\frac{GC}{1+GC}\right)}_{G_{CL}(s)} = \left(\frac{f_F}{C} - x_F\right)\underbrace{\left(\frac{GC}{1+GC}\right)}_{G_{CL}(s)} \quad (8)$$

where x_F is the pre-compensation signal generated by the nonlinear pre-compensator $F_N(.)$ (see Fig. 1). $D(s)$ and $G_{CL}(s)$ denote disturbance and tracking transfer functions of the feed drive respectively. f_F is the nonlinear pre-sliding friction force acting on the feed drive as an external disturbance. Notice that, by designing x_F as an estimate of nonlinear friction force filtered by the inverse controller dynamics $C^{-1}(s)$, friction induced errors can be completely eliminated. Thus, nonlinear friction pre-compensator $F_N(.)$ is designed as:

$$x_F = f_{GMS} C^{-1}(s) \quad (9)$$

Calculation of x_F signal requires the knowledge of $C(s)$, which is already identified in the previous section, and also an accurate estimation of pre-sliding friction (f_{GMS}), which is constructed using Generalized Maxwell Slip (GMS) friction model as described in the following.

GMS is widely used in modeling pre-sliding regime friction in precision engineering applications. However, due to hysteretic stick/slip discontinuity, it is a highly nonlinear model. For this reason, identifying parameters of a GMS model is challenging in practice, and its parameters are either tuned manually or identified using non-convex optimization methods [10]. In this paper, a novel reformulation of the GMS model is presented in order to iteratively tune its parameters using convex optimization methods. In this reformulation, stick/slip conditions are defined based on displacements, and the estimated friction force f_{GMS} is written as:

$$f_{GMS} = \sum_{i=1}^{K} k_i z_i$$
$$\frac{dz_i}{dt} = \begin{cases} \dot{x}_R = v_R, & \text{if stick } \left(i.e.\ z_i \le |P_i/2|\right) \\ 0, & \text{if slip } \left(i.e.\ z_i > |P_i/2|\right) \end{cases} \quad (10)$$

where K is the number of Maxwell Slip (MS) blocks, and k_i is the stiffness of the i^{th} MS block while it is sticking. As blocks undergo micro-translation (z_i), each block either sticks or slips. An MS block only slips when it exceeds its break-away (stick) distance, which determines whether the block is sticking or slipping at a given time. Note that in conventional GMS formulation, stick/slip conditions are determined by forces on MS blocks instead [2]. Stick distances of feed drives typically lie in the range of 10~100 μm [2], which can be determined by a simple tracking experiment. Stick distances can then be distributed evenly among the MS blocks to satisfy $P_1<P_2<\ldots<P_K=P$, where P is the measured break-away distance of the feed drive. Since P is easily measured, the only unknowns in this GMS formulation are the spring coefficients of each MS block (k_i), which are identified iteratively in order to minimize the tracking errors. In order to achieve this, first, it is shown that f_{GMS} is a linear function of each k_i by putting it in vector-matrix form as:

$$\frac{d}{dt}\mathbf{f}_{GMS} = \mathbf{A}\mathbf{k}, \quad \text{where } \mathbf{A} = \begin{bmatrix} \dot{\mathbf{z}}_1 & \dot{\mathbf{z}}_2 & \cdots & \dot{\mathbf{z}}_K \end{bmatrix} \quad (11)$$

where $\mathbf{k}=[k_1 \ldots k_K]^T$ is the vector of spring coefficients. **A** is the *spring activation matrix*. Each column of **A** contains velocities (dz_i/dt) of each MS block. For instance, first MS block starts sticking after a velocity reversal ($t=0$) until its displacement z_1 reaches P_1. The second block starts sticking at the same instant ($t=0$), but it sticks slightly longer, until $z_2=P_2$. **A** is a function of the reference trajectory v_R, and therefore it is "velocity reversal dependent". Structure of **A** and its role in the presented GMS reformulation is illustrated by Fig. 4.

In order to obtain optimal spring coefficients of the GMS friction model, an optimization problem is postulated, where the tracking errors are minimized as:

$$\min_{\mathbf{k}} \left(J_N = \frac{1}{2}\|\mathbf{e}_v\|_2^2 = \frac{1}{2}\mathbf{e}_v^T\mathbf{e}_v \right), \quad \text{subject to: } \mathbf{k} \ge 0 \quad (12)$$

where $\mathbf{e}_v$ is the tracking error vector recorded in the vicinity of a velocity reversal. Eq. (12) depicts a convex optimization problem with a quadratic objective, and therefore both the gradient and Hessian of the objective function can be written as functions of the error gradient $\nabla\mathbf{e}_L$ (see Eq. (5)), which can be derived as:

$$e = \left(f_F - f_{GMS}\right)\frac{1}{C}\left(\frac{GC}{1+GC}\right)$$
$$\nabla e = -\nabla f_{GMS}\,\frac{1}{C}\left(\frac{GC}{1+GC}\right)$$
$$\text{where: } \nabla\mathbf{f}_{GMS} = \int_{t=0}^{MT_s} \mathbf{A}dt \quad (13)$$
$$\nabla = \begin{bmatrix} \frac{\partial}{\partial k_1} & \cdots & \frac{\partial}{\partial k_K} \end{bmatrix}^T$$

where ∇f_{GMS} is the gradient of the friction estimate with respect to **k**, and $\nabla\mathbf{f}_{GMS}$ is its discretized vector containing M samples.

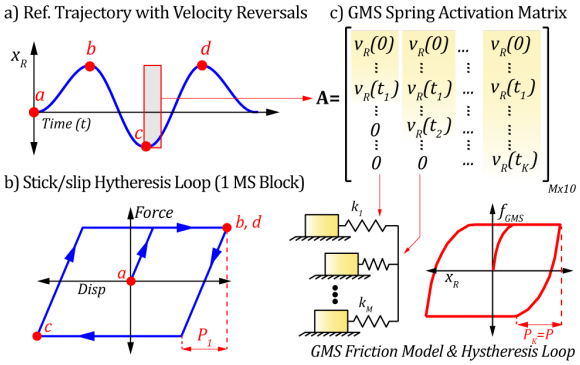

FIGURE 4: Modified GMS Model and the Spring Activation Matrix (**A**).

As shown, proposed formulation of GMS model (Eqs. (10) and (11)) allows us to define friction induced error gradient explicitly as a function of the reference trajectory. Machine-in-the-loop iterations are used to safely optimize (train) the friction pre-compensator parameters $F_N=C^{-1}f_{GMS}$ using second order Newton's iterations as:

$$\mathbf{k}^{k+1} = \mathbf{k}^k - \alpha\left(\nabla^2 J_N\right)^{-1}\left(\nabla J_N\right) \quad (14)$$

Similar to Eq. (7), this update scheme guides the parameters of the GMS model to a global optimum as long as the inequality constraints in Eq. (12) are not violated. In case of constraint violation, update scheme given in Eq. (14) is modified using Primal-Dual Interior Point Algorithm [9].

Experimental Verification

Effectiveness of the nonlinear trajectory pre-filtering technique is validated on the same feed drive system (see Fig. 3.a). A circular toolpath is planned with a federate of 80 mm/sec as shown in Figs. 5.a and 5.c. The linear F_L filter (tuned previously) is used to compensate for the servo dynamics. As a result, large quadrant glitches

occur around velocity reversals due to friction disturbances acting against the motion, and they are visible on the error profile shown in Fig. 5.e. Friction compensator pre-filter F_N is optimized (trained) iteratively based on Eq. (14) 5.c. 10 MS blocks are used to capture the pre-sliding friction regime of the feed drive. As shown in Fig. 5.b, after 9th iteration, stick-slip hysteresis curve is automatically identified, and reference trajectory is modified to perfectly cancel quadrant glitches as shown in Fig 5.e. Contour errors are reduced down to 2 μm. By combining both linear and servo dynamics and the friction pre-compensator filters, near-perfect tracking is achieved. Once trained (optimized), the trajectory compensation filters can be used for any arbitrary trajectory to eliminate friction induced errors and enhance multi-axis contouring performance.

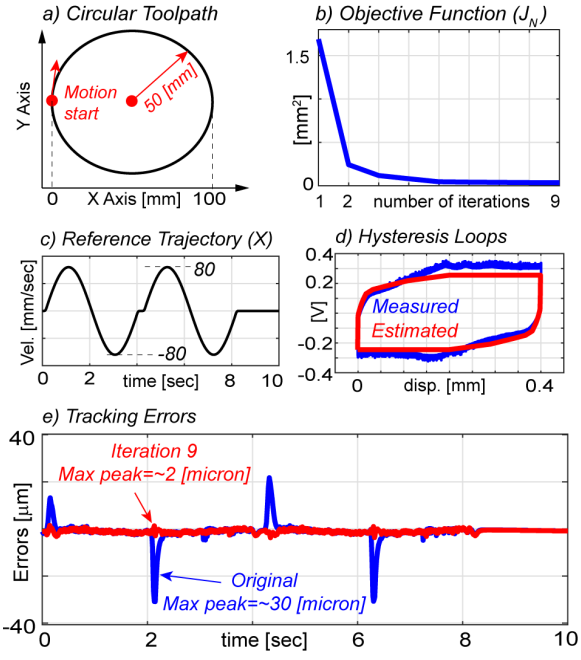

FIGURE 5: Experimental validation of pre-sliding hysteresis stick/slip pre-compensation.

CONCLUSIONS

A novel tracking error pre-compensation scheme is proposed, which greatly improves dynamic accuracy of machine tools compensating for the closed-loop servo and stick/slip (pre-sliding) friction induced errors by modifying reference trajectory. Proposed scheme does not need any prior knowledge of feed-drive dynamics, nor does it require complicated open-loop identification experiments. It is implemented by a digital pre-filter whose parameters are optimally tuned automatically. It requires no expertise. Safe and reliable auto-tuning is achieved by formulating the tuning problem based on iterative learning and convex optimization. Overall, proposed technique can improve dynamic accuracy of newer and older machines equipped with a modern NC system.

REFERENCES

[1] Altintas Y, Verl A, Brecher C, Uriarte L, Pritschow G. Machine Tool Feed Drives. Annals of the CIRP. 2011; 60:779-796.

[2] Jamaludin Z, Van Brussel H. Pipeleers G, Swevers J. Accurate motion control of xy high-speed linear drives using friction model feedforward and cutting forces estimation. Annals of the CIRP. 2008; 57(1):403-406.

[3] Erkorkmaz K, Kamalzadeh A. High bandwidth control of ball screw drives. Annals of the CIRP. 2006; 55(1):393-398.

[4] Van Brussel H, Van den Braembussche P. Robust control of feed drives with linear motors. Annals of the CIRP. 1998; 47(1):325-328.

[5] Dumanli A, Sencer B. Optimal high-bandwidth control of ball-screw drives with acceleration and jerk feedback. Precision Engineering. 2018; 54:254-268.

[6] Sencer B, Dumanli A. Spline interpolation with optimal frequency spectrum for vibration avoidance. Annals of the CIRP. 2018; 67(1):377-380.

[7] Altintas Y, Khoshdarregi MR. Contour Error Control of CNC Machine Tools with Vibration Avoidance. Annals of the CIRP. 2012; 61(1):335–338.

[8] Boeren, F, Bareja A, Kok T, Oomen T. Frequency-Domain ILC Approach for Repeating and Varying Tasks: Application to Semiconductor Bonding Equipment. IEEE/ASME Transactions on Mechatronics. 2016; 21(6):2716-2727.

[9] Meulen SH, Tousain RL, Bosgra OH. Fixed Structure Feedforward Controller Design Exploiting Iterative Trials: Application to a Wafer Stage and a Desktop Printer. J. Dyn. Sys., Meas., Control. 2008; 130(5):051006.

[10] Boyd S, Vandenberghe L. Convex optimization. Cambridge Univ. press. 2004.

[11] Amthor A, Zschaeck S, Ament C. High Precision Control Using an Adaptive Friction Comp. Approach. IEEE Transactions on Automatic Control. 2010; 55(1):274-278.

DEEP LEARNING-BASED PRECISION CONTROL FOR SIX-AXIS COMPLIANT NANOPOSITIONER

[1]Xiangbo Liu, [1]Chenglin Li, [2]Hongsheng Li, [2]Xiaogang Wang, and [1]Shih-Chi Chen[*]
[1]Department of Mechanical and Automation Engineering
The Chinese University of Hong Kong
[2]Department of Electronic Engineering
The Chinese University of Hong Kong
Shatin, N.T., Hong Kong SAR, China
[*]Email: scchen@mae.cuhk.edu.hk

In this work, we present a new control method for compliant mechanisms based on deep learning models that achieve 100 nm precision in multiple axes with low-lost strain sensor arrays. In our setup, the strain sensor array is applied to the flexing components on a custom-designed compliant six-axis nanopositioner such that it simultaneously measures the mechanical strain (i.e., displacement) and mode shapes for real-time control, i.e., the deep model can learn, predict, and control the motion of the nanopositioner as a time sequence or 2-D images. During the training stage, capacitance sensors are used as references to minimize position errors; the number and location of sensor arrays can be optimized via the deep learning model. In the experiments, we demonstrate that the deep model developed based on the reinforcement learning method [1] can fully replace the classical PID control, realizing 100 nm precision without tuning any control parameters.

INTRODUCTION

Conventionally, precision motion stages and positioners achieve submicron or nanometer level precision by exploiting the precision engineering principle that calls for high repeatability components, e.g., air bearing or flexures, and high resolution sensors and actuators in combination with adequate control methods [2]. However, these solutions are usually of high cost with limited range of applications. To address the issue, we propose a deep learning-based control platform that uses low-cost strain sensor arrays to replace the capacitance probes on a six-axis nanomanipulator, with potentially improved performance and capability, i.e., monitoring the mode shapes and systems dynamics with real-time control.

Deep learning has achieved great success in many fields including speech recognition and synthesis, computer vision, and natural language. Recently, researchers have started to explore integrating deep learning and reinforcement learning into the perception and the control of robots [3], where robots learn by interacting with the environment, leading to promising results. Yet, there is still much room to improve for many industrial applications, e.g., control of precision machines. Generally, deep learning is a powerful tool for treating regression and classification problems based on big data. In our work, given the high repeatability (i.e., nanometer level) of the compliant nanopositioner and high dimensions of the signals, deep learning can be implemented to improve the system performance.

WORKING PRINCIPLE

Figure 1 presents the working principle of the deep learning-based control, realized via low-cost strain sensors installed on the flexing components of a compliant mechanism. Here we use the HexFlex, i.e., a six-axis planar compliant mechanism [4], to illustrate how strain sensors are distributed on the structure.

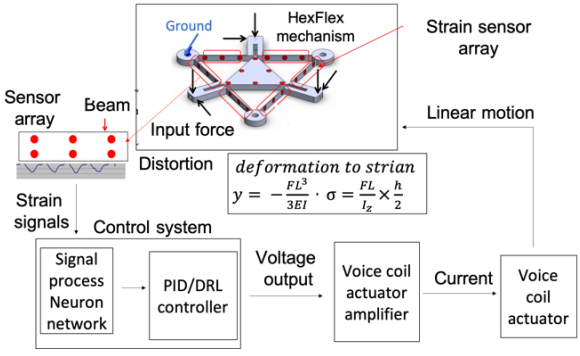

FIGURE 1. Principle of deep-learning-based control for a compliant nanopositioner. The red

dots on the HexFlex mechanism show the initial positions of the strain sensors. DRL: Deep reinforcement learning.

First, strain sensors are uniformly applied to the non-rigid structures on the HexFlex mechanism, where each strain sensor serves a pixel in a 2-D image. The strain sensors should be sufficiently dense to capture basic motions and mode shapes of a structure, e.g., bending and torsion of a double-clamped beam. Knowledge of beam theory can be applied to select high-stress locations and to avoid nodal points in resonant modes. Alternatively, the redundant sensors can also be removed by training the deep learning model. As the motion of the six-axis stage is generated by the deformation of its flexing components, e.g., beam or plates, the measured mechanical strains will have complex yet deterministic relationships with the stage motion. This means that the strain signals can provide the multi-axis motion information and serve as feedback signals to the deep learning-based controller.

Regarding the deep learning model, instead of using a typical deep neural network to predict compensation of position errors in a single step, we have developed a physics-guided deep model that drives the actuators in multiple steps to generate smooth and accurate motion. As the target position error is only measured at the last stage during training, reinforcement learning is used to train the neural networks in the intermediate stages through the design of reward functions, so that the neural networks can predict proper control given input from the strain sensors only at the testing stage. At the training stage, high-precision capacitance sensors are used to detect the positions of the nanopositioner, which are used in the reward functions of intermediate stages in reinforcement learning. As analytic models cannot capture all physical phenomena (e.g., non-ideal boundary conditions, manufacturing errors, thermal errors etc.), the deep learning model can evolve to fill the gap between the engineering model and reference data. Lastly, the collected dataset is used to coach the deep model so that it precisely predicts the position and dynamic behavior of the system. At the testing stage, capacitance sensors are removed and only the strain sensor array is used to predict control.

COMPLIANT SIX-AXIS NANOPOSITIONER

Figure 2 presents the custom-designed parallel six-axis nanopositioner, driven by six voice coil actuators (VCA) (NCC15-24-090-1X, H2W) located below the flexure stage. As shown in Fig. 3A and 3B, this compact configuration is achieved by combining and arranging the flexible beams in unique ways that enable improved dynamic performance [5]. The width of each beam is selected to be 10 mm wide to provide room for strain sensors. Six capacitance probes (C8/CPL190, Lion Precision, resolution = 20 nm) are used to monitor and record motions of the nanopositioner for calibration and training. The performance of the parallel six-axis nanopositioner is summarized in Table 1.

TABLE 1. Performance of the parallel six-axis nanopositioner

	Bandwidth	Range	Resolution
X	121 Hz	±80 μm	30 nm
Y	126 Hz	±60 μm	25 nm
Z	118 Hz	±70 μm	40 nm
θ_X	246 Hz	±900 μrad	1.5 μrad
θ_Y	216 Hz	±1700 μrad	1.4 μrad
θ_Z	188 Hz	±600 μrad	1.0 μrad

STRAIN SENSORS

We install the strain sensors at the high strain locations to increase the system sensitivity and resolution, as shown in Fig. 3B, as in the concept validation stage the nanopositioner is operated at low speeds. Strain sensors are governed by equations (1) and (2):

$$V = U\frac{\Delta R}{4R} \quad (1)$$

$$GF = \frac{\Delta R/R}{\varepsilon} \quad (2)$$

where U = 2.0 V is the Wheatstone bridge active voltage, determined by the data acquisition board (DAQ); GF is the gauge factor; and R is the base resistance of strain sensors, ε is the surface strain. According to Eq. (1) and (2), the larger the GF, the higher the voltage (V). Based on the analysis, self-temperature compensated semiconductor strain sensors (KSN series, KYOWA) are selected for our experiments with GF = 120; R = 120 Ωm. By combining Eq. (1) and (2), the relationship between the mechanical strain and displacement (d) can be derived, as expressed in Eq. (3).

$$d = \frac{2L^2\varepsilon}{3h} \quad (3)$$

According to the system design, L = 24 mm. The DAQ board (NI9235) has a minimum measurable voltage of V_0 ~ 10^{-7} V. Accordingly, from Eq. (3), the theoretical minimum detectable displacement of each strain sensor is calculated to be d_{min} ~ 5 nm. This shows nanometer level precision control can be achieved with low-cost strain sensors with proper control strategy. In the calibration experiments, we have experimentally confirm the strain sensors have a resolution of 100 nm, limited by electronic noises.

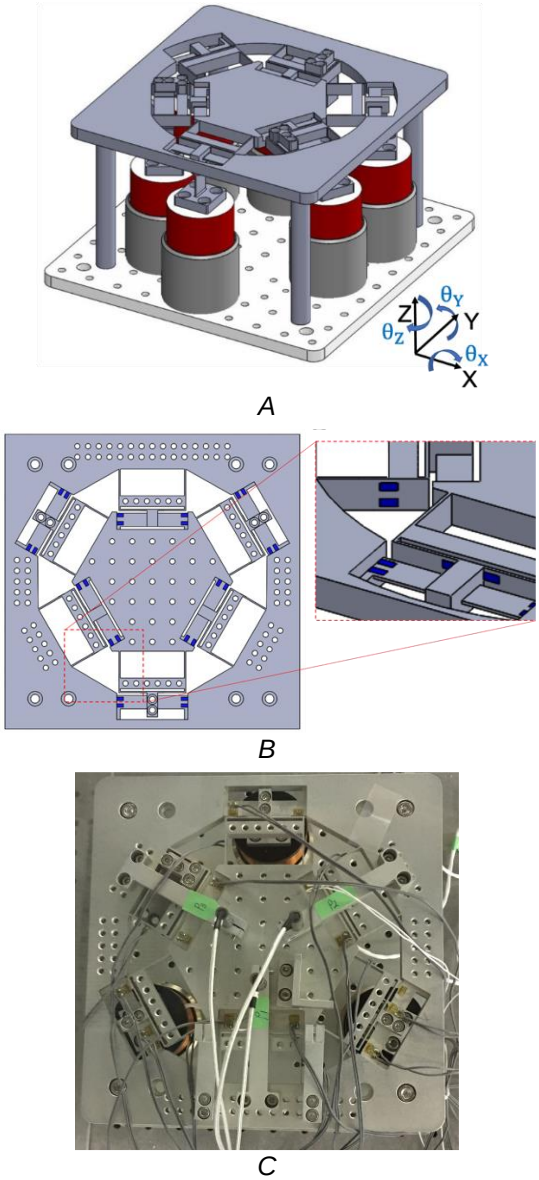

A

B

C

FIGURE 2. Parallel six-axis nanopositioner. A. CAD model; B. Location of strains sensors; C. Completed stage.

EXPERIMENTS

In this section, we devise and perform positioning experiments to validate the deep learning-based control method can achieve 100 nm level precision. All net models in this work are developed on the pytorch-gpu. Data acquisition programs are developed on the LabVIEW 2018-pro with the Enthought Python Integration Toolkit.

DESIGN AND TRAINING OF CNN MODEL

As shown in Fig. 1, the stage displacement (or beam deformation) and mechanical strain have a linear relationship based on the beam theory. Considering this linear relationship and the non-linear nature of the strain sensors, we have developed a convolutional neural network (CNN) as illustrated in Fig. 3, where the linear and nonlinear layers correspond to the aforementioned two cases; and each fully connected layer contains 12,000 neurons.

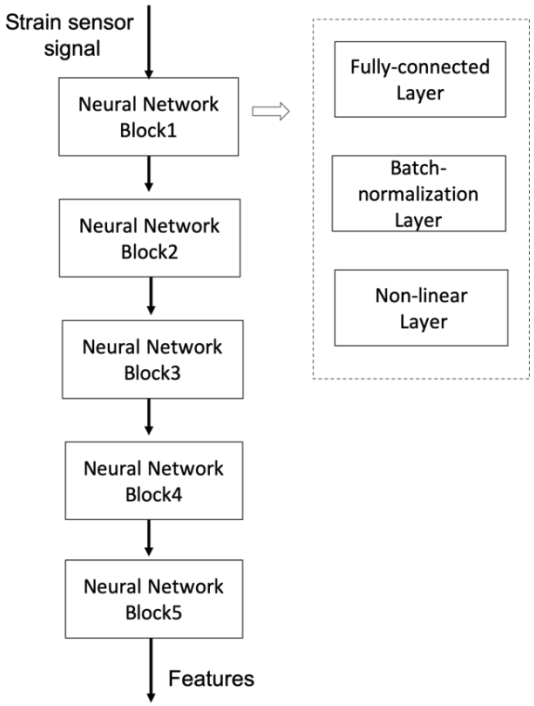

FIGURE 3. Structure of the deep learning model with 12,000 neurons in each fully-connected layer.

To train the deep learning model, the nanopositioner is commanded to perform designed positioning tasks with a variety of ranges (0 -15 µm) with a minimum step size of 50 nm. During the training process, capacitance probes are used as the reference data; and via the probes, the PID control is implemented to achieve a precision of 10 nm. During each

positioning task, the DAQ records signals from the strain sensors for 2 seconds at a rate of 1 kHz.

STATIC POSITION CONTROL

For validation, 90% of the data from the strain sensor are used to train the deep model; the model is then used to predict the stage motion and compare with the rest 10% data. After 200 epochs trained, the test error is ~200 nm. The required training time is less than 1 hour. The test results along the θ_X, θ_Y, Z axes are presented in Fig. 4A, 4B, and 4C respectively. From Fig. 4, one can confirm that the deep learning model can achieve precision static displacement control.

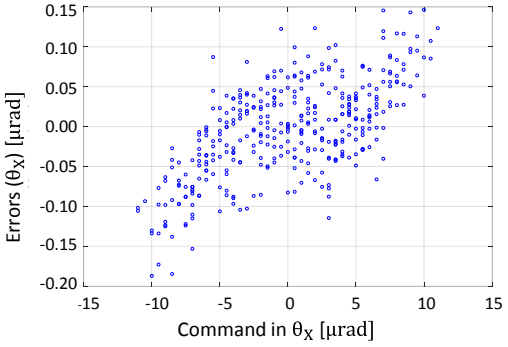

A

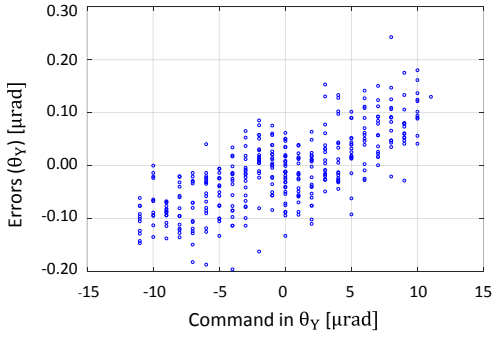

B

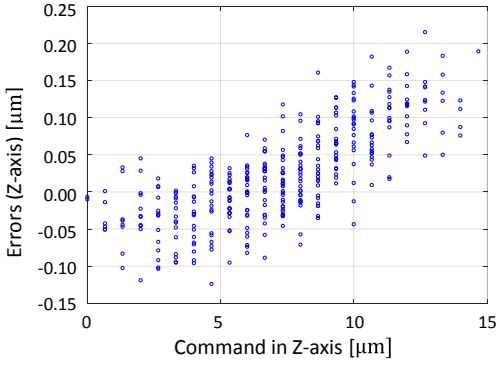

C

FIGURE 4. Positioning errors in A. θ_X; B. θ_Y; and C. Z-axis

DYNAMIC POSITIONING

In this section, we present the development of a deep reinforcement learning (DRL) model, shown in Fig. 5, for dynamic position control, where the optimal control strategy is "self-learned" through training.

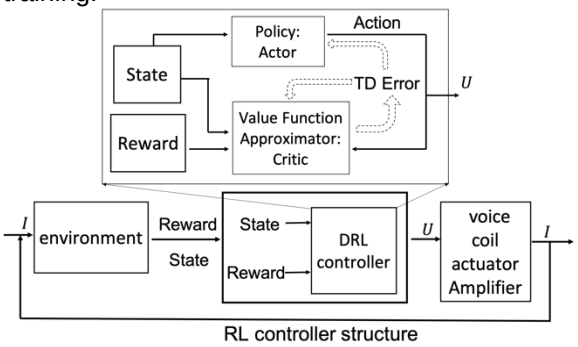

FIGURE 5. Deep reinforcement learning (DRL) controller for the parallel six-axis nanopositioner. Displacement $\tilde{P} = [\tilde{p}_1, \tilde{p}_2, \tilde{p}_3, \tilde{p}_4, \tilde{p}_5, \tilde{p}_6]$; U = Output actions.

The basic deep reinforcement learning (DRL) problem can be considered as a Markov decision process (MDP), whose aim is to find an action strategy to maximize the specified rewards. Considering the control system as a simple environment, the controller functions as an agent that interacts with the environment by sending and receiving inputs/feedback to/from the system. Based on the characteristics of the system including speed, overshoot and stability, we can define rewards to the agent. The controller self-optimization is also a DRL problem that has a continuous action space.

In Fig. 5, system state is represented by the displacement $\tilde{P}$, the first-order derivative $\dot{\tilde{P}}$, the target position P^* and the input voltage $\tilde{U}$. The displacement in each axis are measured by the capacitance sensors whose output is expressed as $[\tilde{p}_1, \tilde{p}_2, \tilde{p}_3, \tilde{p}_4, \tilde{p}_5, \tilde{p}_6]$. The output action is the output voltage U, which is used to control the VCAs. Output voltages have a continuous value from -2.5 V to 2.5 V. To address the issue, we use deep deterministic policy gradient (DDPG) algorithm [6] as our DRL model. The DDPG algorithm is known for its effectiveness for continuous-action-space systems. The DRL model consists of two networks, i.e., critic and actor network. The actor network receives the current state as the input and outputs an action. With this predicted action, the real environment then returns the next state and rewards the DRL model. Meanwhile, the critic network receives

both the current state and predicted action as the input, and outputs a Q value which judges the selected action that corresponds to current state. With the predictions and feedback, the two networks are updated. In our controller, the actor network consists of an input layer with 24 neurons; three hidden fully-connected layers with 300 neurons in each layer; and an output layer with six neurons, generating the predicted actions. The critic network consists of an input layer with 30 neurons, 5 hidden fully-connected layers with 300 neurons in each layer; and an output layer with one neuron, generating Q-values that reveal the performance of the selected actions.

The state space and action space are complex, and requires a lot of time to learn from a randomly initialized model. To shorten the learning time and avoid unnecessary damages to the real systems, we pre-train the DRL model in a virtual environment before applying it to the real system. First, we build the virtual environment by simulating the real environment with neural networks. According to control theory, we know that the next system state is determined by the current velocity, position and input voltage. So, a neural network can be designed to model this relationship. The input of the network consists of the current position, velocity and input voltage; and the output is the next position. The parameters of this network are updated using the collected real system data. With the trained virtual environment network, we can pre-train the DRL controller.

To pre-train the controller, the required training data are automatically collected over 50 hours by randomly setting the target positions from 0 – 25 µm, while the PID controller drives the nanopositioner to the target positions. During the time, the DAQ records the reference positions from the capacitance probes and the voltage output from the PID controller. First, the actor network and critic network are initialized randomly. Then, by using the collected data, the virtual environment model is trained. Under the virtual environment, we pre-train the controller to function as the PID controller. The pre-training step can help rapidly optimize the model for real operation. This is particular efficient for systems with a large state space. After pre-training, we replace the simulated virtual environment with the parallel nanopositioner. Lastly, the controller is trained with the dynamic system.

Figure 6 presents the three-axis positioning results based on the DRL model. In the experiment, the stage is commanded to move to the 0 rad, 0 rad, and 5 µm positions in the θ_X, θ_Y, Z axes respectively, where the initial positions in each axis are randomly selected. The results show that the stage moves to the target position with less than 100 nm translational errors and 10 µrad angular errors within 5 seconds, which achieves our target precision. The DRL controller model used in this test is trained for 2000 epochs with a pre-training time of 2 hours. (The total training time can be substantially reduced by pre-training.) With more training time and data, the controller can be further improved both in terms of speed and precision.

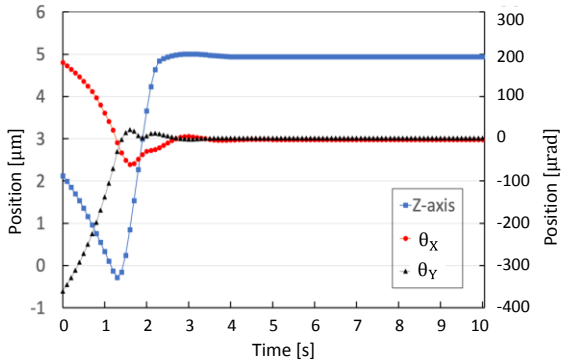

FIGURE 6. Positioning experiments along the θ_X, θ_Y, and Z axes based on the DRL controller.

CONCLUSION

We have presented a new deep-learning based control method to a custom-designed parallel six-axis nanopositioner, achieving a static and dynamic positioning accuracy of 200 nm and 100 nm respectively. The deep model is realized by applying an array of low-cost strain sensors to the nanopositioner. The training of the deep model is performed automatically, where the reference signals are obtained from six capacitance sensors. The experimental results can be further improved with more training time and training data. The new control method can be easily applied to other precision machines to improve performance with reduced cost.

ACKNOWLEDGMENT

This work is supported by the HKSAR Innovation and Technology Commission (ITC) Innovation and Technology Fund (ITF), ITS/077/17FP: Deep Learning for Next-generation Precision Machine Tools and Manufacturing.

REFERENCES

[1] Kaelbling LP, Littman ML, Moore AW. Reinforcement learning: A survey. Journal of Artificial Intelligence Research. 1996; 4: 237-285.

[2] Slocum AH. Precision Machine Design, Society of Manufacturing Engineers. 1992.

[3] Levine S, Finn C, Darrell T, Abbeel P. End-to-end Training of Deep Visuomotor Policies. Journal of Machine Learning Research. 2016; 17: 1 - 40.

[4] Culpepper ML, Anderson G. Design of a Low-cost Nano-manipulator which Utilizes a Monolithic, Spatial Compliant Mechanism. Precision Engineering. 2004; 28(4): 469 - 482.

[5] Li C, Liu X, Chen S. Design of a Six-axis Parallel Nanopositioner using Decoupled Flexural Legs. Proc. of the Annual Meeting of the ASPE, Pittsburgh, PA, USA, Oct. 2019.

[6] LILLICRAP, Timothy P., et al. Continuous control with deep reinforcement learning. arXiv preprint arXiv:1509.02971, 2015.

INTELLIGENT SYSTEMS FOR OPTICAL FORM MEASUREMENT: AUTOMATED ASSESSMENT OF POSE AND COVERAGE

Sofia Catalucci[1], Nicola Senin[1,2], Samanta Piano[1], Richard Leach[1]
[1]Manufacturing Metrology Team, Faculty of Engineering
University of Nottingham
Nottingham, United Kingdom
[2]Department of Engineering
University of Perugia
Perugia, Italy

INTRODUCTION

This work addresses the development of intelligent and adaptive optical form measurement systems for quality inspection of additively manufactured complex parts. The ultimate objective is to obtain smart optical measurement systems capable of automatically reconfiguring themselves while inspecting new geometries, and capable of assessing whether completed measurements are sufficient, or further measurements should be performed. Intelligent behaviour is achieved through automated self-assessment of measurement performance, while the measurement itself is being executed [1]. The decisional process is supported by multiple sources of information [2], namely: knowledge of part specifications (CAD model, dimensional and geometric tolerances, materials); knowledge of the manufacturing process and the material, leading to predictability of likely types of form error; knowledge of the measurement instrument itself (metrological performance and behaviour), and how it is expected to interact with any specific material and part geometry. The optical measurement technologies covered by the project produce point clouds: the work presented in this paper focuses on algorithmic processing of point clouds, and deals with the following, specific challenges: a) automated point cloud localisation within the part geometry, i.e. identifying what surfaces have been captured by any given point cloud, acquired from a part of unknown position and orientation; b) automated assessment of coverage and sampling density for the exposed surfaces, including recognition of critical regions (i.e. poorly represented by the point cloud), in order to support automated planning for further measurements.

TEST SET UP

The experimental set-up is based on a combination of a commercial measurement fringe projection system (blue-light technology GOM Atos Core 300), shown in Figure 1, and the point cloud processing commercial software Polyworks Inspector by Innovmetric. Automation is achieved by interfacing Polyworks with MATLAB, via scripting.

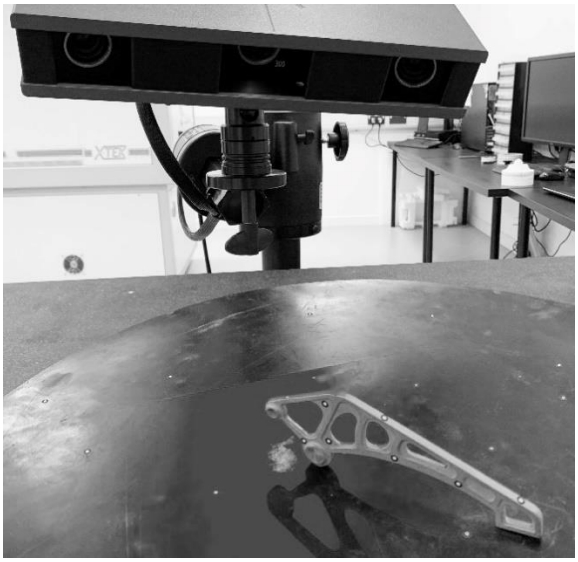

FIGURE 1. The optical measurement system while measuring one of the test parts.

Test cases

The selected test measurement parts are shown in Figure 2. Sample A (Figure 2a) was fabricated by selective laser sintering (SLS) using Nylon 12, with size of a rectangular enclosing envelope (50 × 50 × 28) mm; sample B (Figure 2b) was fabricated by laser powder bed fusion (LPBF) using stainless steel 316L, with dimensions of (125 × 45 × 8) mm.

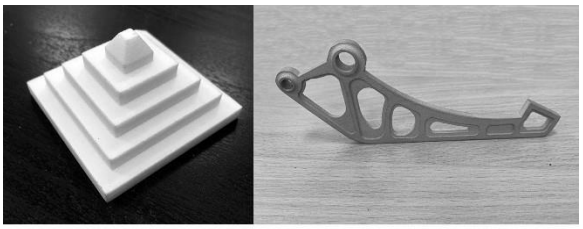

a) b)

FIGURE 2. Test parts; a) Nylon 12 pyramid sample (50 × 50 × 28) mm fabricated by SLS; b) stainless steel 316L automotive sample (125 × 45 × 8) mm fabricated by LPBF.

The nominal geometries of the test parts are available as triangle meshes. Example results of single measurements on the test parts with unknown pose are shown in Figure 3a for sample A and Figure 3b for sample B.

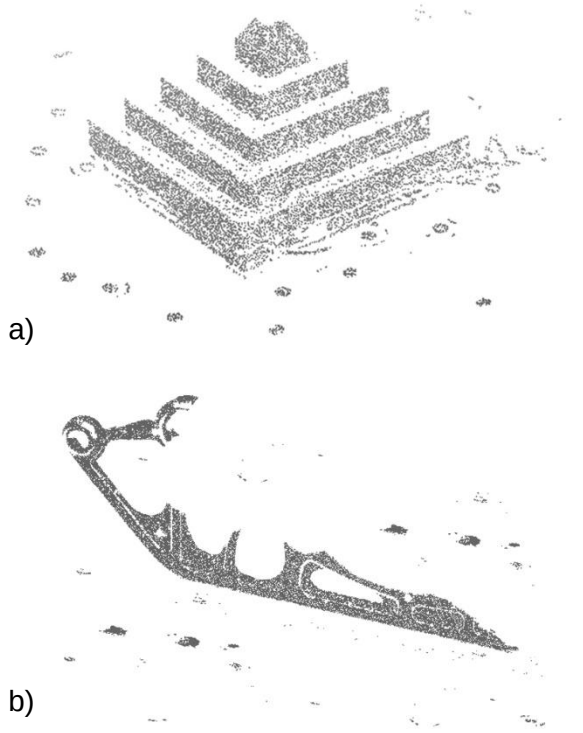

a)

b)

FIGURE 3. Example measurements: a) sample A; b) sample B.

As sample A has four nominally identical sides, pose estimation only pertains to the accurate identification of the angular orientation of the visible corner in the point cloud.

DATA PROCESSING METHOD

The first data processing step consists of detecting the pose by identification and best-matching of landmark features present on both the measured point cloud and the nominal reference geometry (triangle mesh). In the second step, once the point cloud has been aligned to the mesh, the degree of coverage can be assessed by identifying the surfaces that have not been reached by the measurement instrument. For the covered surfaces, the density and spatial distribution of the measured points can be computed by inspecting the positions of the points falling within each triangle of the mesh.

STEP 1: ALIGNMENT

Alignment, also referred to as registration, consists of a coarse phase and a fine phase.

Coarse registration

Coarse registration is based on the identification and matching of common landmarks both in the measured point cloud and in the triangle mesh. Landmarks can be identified through computation of local feature descriptors [3-5]. In this work, local curvatures are used.

Surface normal vectors are identified both on the point cloud and in the triangle mesh, by using principal component analysis [6] on local subsets of neighbouring points selected via the *k*-nearest neighbour algorithm [7]. The principal curvatures $k1$ and $k2$ are then computed [8]. From the principal curvatures, the Gaussian curvature *K* and mean curvature *H* are computed as follows:

$$K = k1 \cdot k2, \quad (1)$$

$$H = \frac{(k1 + k2)}{2}. \quad (2)$$

Example results for curvature are shown in Figures 4 to 7.

The next step involves the identification of clusters of points with similar curvature values: a first *k*-means clustering process [9] was used to identify *k*-classes of curvature values (*k* = 5). The highest-curvature class was then isolated; the resulting points were subjected to another clustering process, this time aimed at isolating spatially distant subsets of points with high-curvature values. The second clustering was, therefore, hierarchical and based on Euclidean distances between points (Figures 8 to 11).

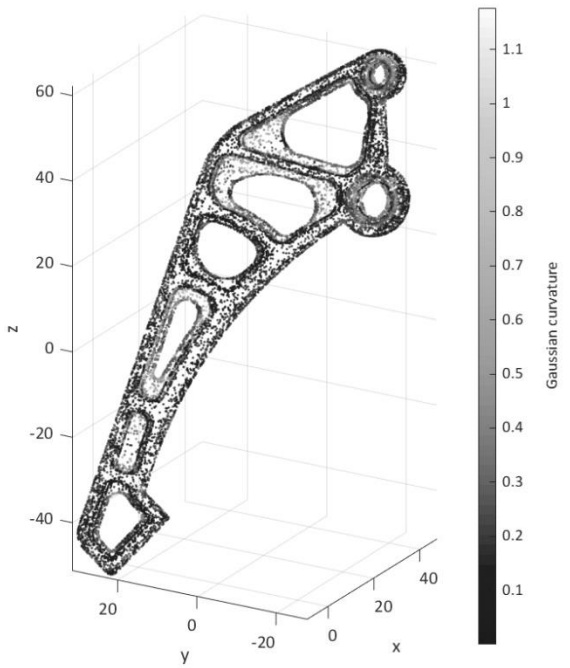

FIGURE 4. Gaussian curvature K estimation on extracted vertices of the triangle mesh (sample B).

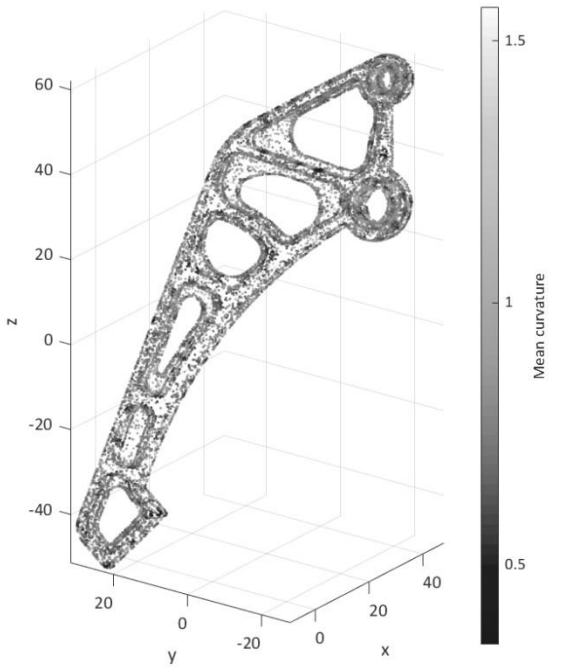

FIGURE 5. Mean curvature H estimation on extracted vertices of the triangle mesh (sample B).

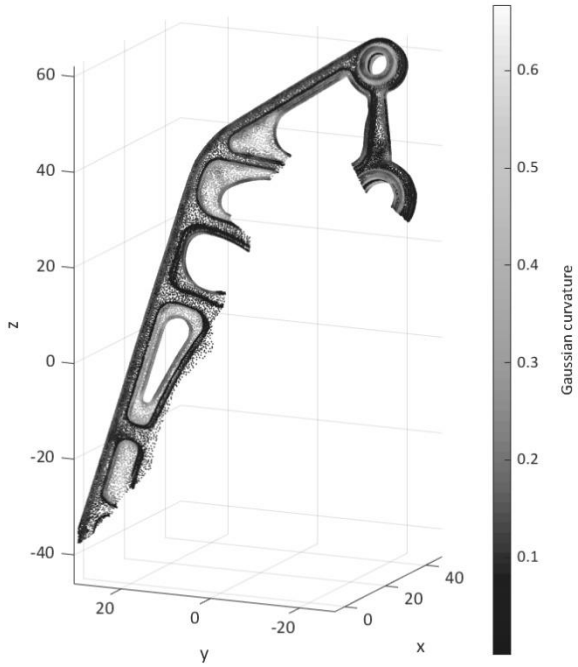

FIGURE 6. Gaussian curvature K estimation on point cloud dataset (sample B).

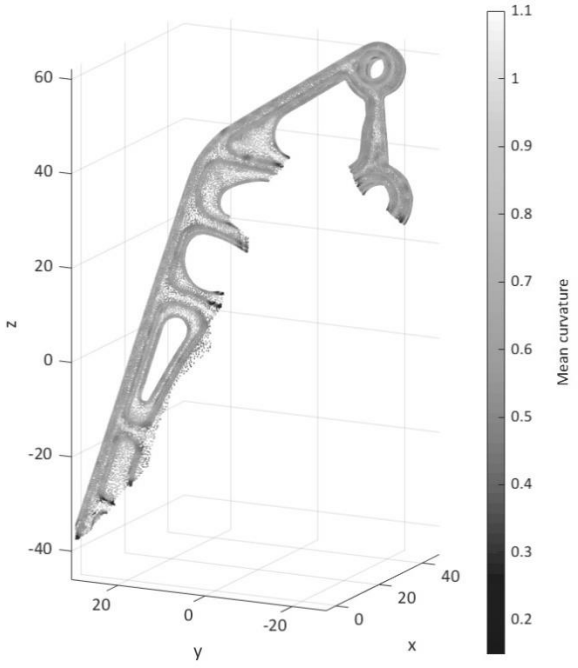

FIGURE 7. Mean curvature H estimation on point cloud dataset (sample B).

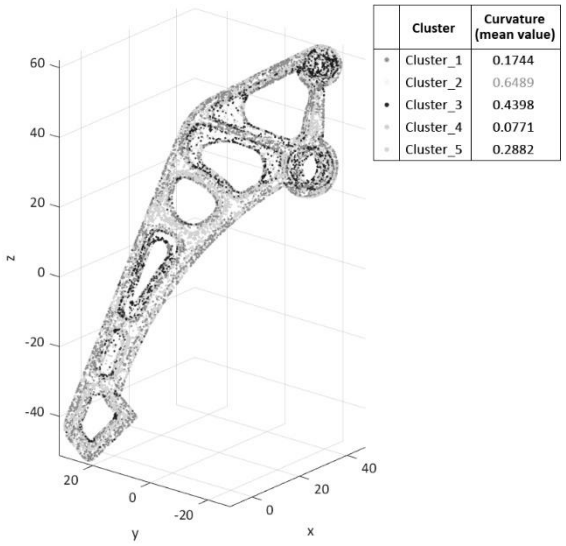

FIGURE 8. k-means clustering on K curvature. Cluster 2 refers to the extracted vertices of the triangle mesh with the highest curvature values (sample B).

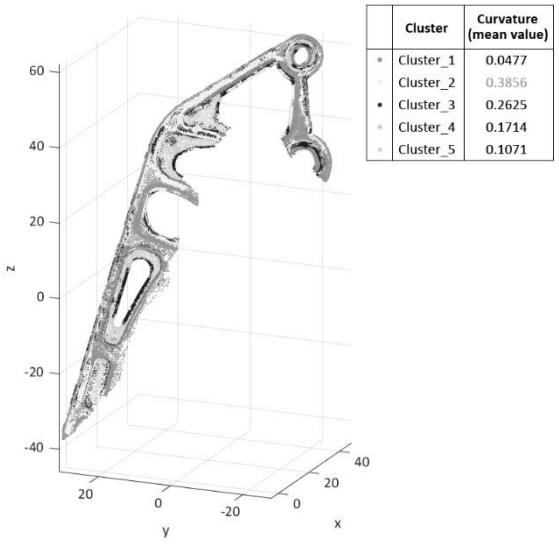

FIGURE 10. k-means clustering on K curvature. Cluster 2 refers to the points with the highest curvature values (sample B).

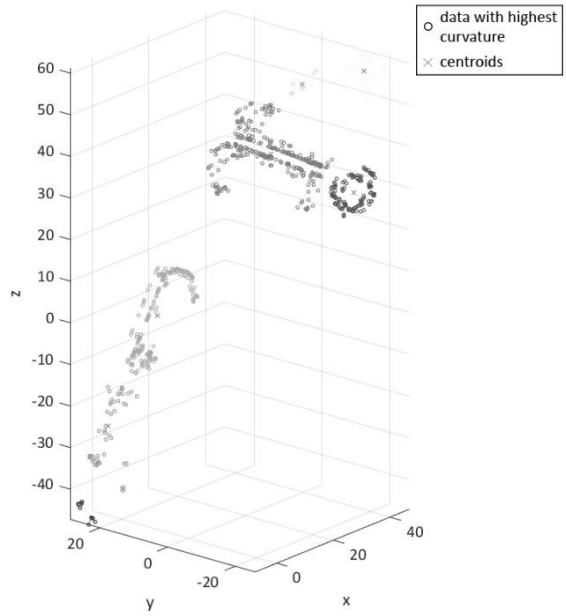

FIGURE 9. Hierarchical clustering and centroids computation of clustered extracted vertices of the triangle mesh (sample B). The points taken into account are the ones with the highest curvature values.

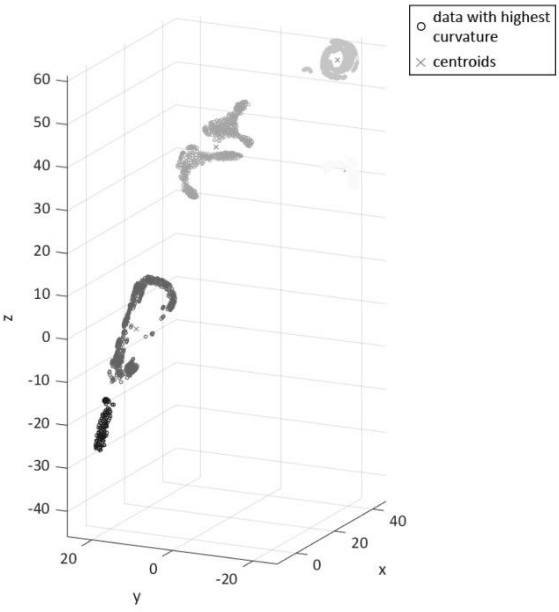

FIGURE 11. Hierarchical clustering and centroids computation of clustered point cloud (sample B). The points taken into account are the ones with the highest curvature values.

The identified common landmarks in both datasets, described by high curvature values, are then best-matched, using Random sample consensus (RANSAC) [10,11]: at each iteration, good matches were considered those resulting in a spatial alignment which minimises the sum of squared distances between matched points, using the Procrustes algorithm [12].

Fine registration

Fine registration is based on a best-fit algorithm [15], which iteratively minimises the distances from the measured dataset to the reference entity, revising the transformation based on a rigid transformation (translation and rotation) until the variation of the squared error is minimised. The “registration error function” is defined as the sum of squared Euclidean distances between each point in the cloud and its closest neighbour located on the triangular facets [13].

COVERAGE ASSESSMENT

After the fine registration process is completed, each triangular facet belonging to the original mesh will have a certain number of measured points associated with it. Coverage expresses how comprehensively each triangle is represented by the associated measured points. To assess coverage, the number of points falling within each triangle is considered in relation to the area of the triangle with the purpose to obtain a measure of spatial sampling density, i.e. number of points per unit area. Sampling density is computed on all the triangles (Figure 12). Then, a percentage of the maximum density is set as threshold to discriminate between adequately and inadequately covered triangles (simply referred to as "uncovered"). Finally, a coverage ratio can be defined as the percentage of triangles with adequate coverage over the total number of triangles in the mesh. Additionally, the ratio between the total area occupied by triangles classified as covered, and the total area of all the triangles in the mesh, can be computed, and is referred to as "covered area ratio".

Example results of coverage computation are shown in Figures 13 to 14, where the threshold has been set to 75% of the maximum sampling density per triangle. The areal coverage is either estimated based on the number of triangular facets associated with measured points over the total number of triangles, and the sum of the covered area over the total area of the object (Table 1).

FIGURE 12. Triangle facets; colouring proportional to sampling density (sample B).

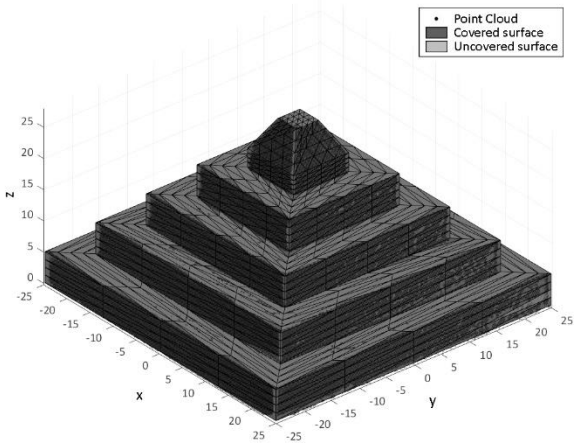

FIGURE 13. Covered and uncovered triangles for sample A (threshold on sampling density at 75%).

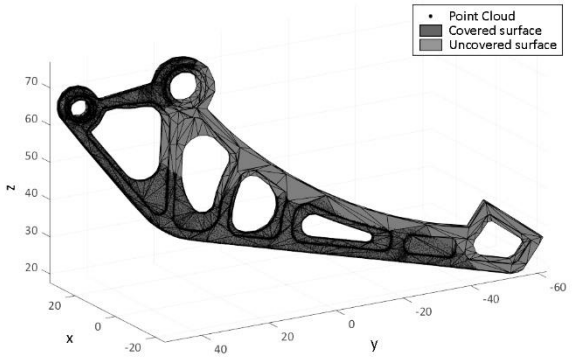

FIGURE 14. Covered and uncovered triangles for sample B (threshold on sampling density at 75%).

TABLE 1. Coverage ratio results.

	No. of triangles in the mesh	Coverage ratio (% covered triangles)	Covered area ratio (% covered area)
Sample A	1344	22%	32%
Sample B	1785	39%	42%

CONCLUSIONS AND FUTURE WORK

In this paper, preliminary results from the early stage development of an intelligent system for complex shape measuring have been presented. Methods and algorithms for the automatic assessment of part pose and measurement coverage have been introduced and discussed with the support of two test cases. The prototype implementation is realised using a combination of commercial measurement hardware and software, and custom software modules developed in-house.

Future work will address: 1) the estimation of uncertainty associated with alignment and assessment of coverage. Alignment in particular may be affected by problems of geometric stability (e.g. see [14] for ICP); 2) the differentiation of part surfaces depending on functional relevance, so that assessment of coverage quality can be weighed; 3) the implementation of feedback mechanisms based on the results of pose and coverage estimation, to automate planning for further measurement actions.

ACKNOWLEDGEMENTS

The authors would like to acknowledge Patrick Bointon of the Manufacturing Metrology Team, Leonidas Gargalis and Joe White of the Centre for Additive Manufacturing, University of Nottingham, for their assistance in designing and producing the test cases. We also acknowledge funding from EPRSC project EP/M008983/1.

REFERENCES

[1] Stavroulakis P, Chen S, Derlome C, Bointon P, Tzimiropoulos G, Leach R K. Rapid calibration tracking of extrinsic projector parameters in fringe projection using machine learning. Opt. Lasers Eng. 2019; 114: 7-14.

[2] Senin N, Leach R K. Information-rich surface metrology. Proc. CIRP. 2018; 75: 19-26.

[3] Hana X F, Jin J S, Xie J, Wang M J, Jiang W. A comprehensive review of 3D point cloud descriptors. 2018; arXiv:1802.02297.

[4] Tombari F, Salti S, Di Stefano L. Unique signatures of histograms for local surface description. European conference on computer vision. Springer; 2010. 356-369.

[5] Bellekens B, Spruyt V, Berkvens R, Penne R, Weyn M. A benchmark survey of rigid 3d point cloud registration algorithms. Inter. Journ. Adv. Intell. Sysm. 2015.

[6] Chung D, Lee Y DS. Registration of multiple-range views using the reverse-calibration technique. Pattern Recogn. 1998; 31: 457-464.

[7] Friedman J H, Bentely J, Finkel R A. An Algorithm for Finding Best Matches in Logarithmic Expected Time. ACM Transactions on Mathematical Software. 1977; 3: 209-226.

[8] Merigot Q, Ovsjanikov M, Guibas L J. Voronoi-based curvature and feature estimation from point clouds. Visualization and Computer Graphics, IEEE Transactions on. 2011; 17: 743-756.

[9] Ding C, He X. K-means clustering via Principal Component Analysis. Proceedings of International Conference on Machine Learning. 2004. 225-232.

[10] Moretti M, Gambucci G, Leach R K, Senin N. Assessment of surface topography modifications through feature-based registration of areal topography data. Surf. Topogr. Metrol. Prop. 2019; 7.

[11] Fishler M A, Bolles R C. Random sample consensus: A paradigm for model fitting with applications to image analysis and automated cartography. Commun. ACM. 1981; 24: 381-95.

[12] Kendall D G. A survey of the statistical theory of shape. Statistical Science. 1989; 4: 87-99.

[13] Besl P, McKay N. A method for registration of 3-D shapes. IEEE TPAMI. 1992; 14: 239-256.

[14] Gelfand N, Ikemoto L, Rusinkiewicz S, Levoy M. Geometrically stable sampling for the ICP algorithm. Proceedings of International Conference on 3-D Digital Imaging and Modeling, 3DIM. 2003.

KINEMATIC ERROR ANALYSIS OF STAGE TRACKING USING STEREO VISION

Mohammed A. Isa[1], Danny Sims-Waterhouse[1], Samanta Piano[1], and Richard Leach[1]
[1]Manufacturing Metrology Team
Faculty of Engineering, University of Nottingham
Nottingham, UK

INSTRUCTION

Advanced manufacturing techniques, such as additive manufacturing, are shaping the very nature of present-day industry and continue to redirect future research and developments. Simultaneously, 3D measurement is being integrated into manufacturing processes beyond quality control. 3D measurements are required for in-line and in-process applications to enhance condition monitoring, processing decisions, machine control and real-time corrections [1]. Subject to these demands, the preference for fast, portable and flexible solutions applicable to complex geometries in metrology is dominating. With additive manufacturing having form accuracy in the order of tens to hundreds of micrometres [2], feasible optical 3D measurement methods, such as photogrammetry and fringe projection, become viable options for quality assessment. However, the use of these methods requires testing to ascertain the limits of their capability and reliability.

Photogrammetry provides compact 3D measurement solutions that are integrable and suitable for in-situ applications [3]. Common photogrammetric solutions involve space triangulation and multi-vision imaging. Multi-vision systems use one or more additional camera viewpoints. As the basis of multi-vision systems, stereo vision uses one additional camera to establish triangulation of detected image points with a 3D scene. In principle, more cameras provide further triangulation constraints of a scene which can increase accuracy [4].

To relate image distances to metric scales of objects, either known dimensions in the acquired images or known relative camera positions are used. In most commercial products, there is a requirement to use markers or feature-based gauges [5] for higher accuracy in photogrammetry. Marker-less methods, such as the structure from motion method, lack the necessary accuracy and are, therefore, limited to preliminary measurements and collision avoidance in industrial applications [6]. As an initial step to improve their accuracy, it is essential to evaluate of the performance of the multi-imaging systems used in these photogrammetric methods.

This paper is focused on evaluating the performance of a stereo vision system in measuring the kinematic error of a translation stage. To accomplish this, motion of a linear stage is measured using both stereo vision and laser interferometry. The laser interferometer measurements provide a traceable benchmark for the performance evaluation of the stereo vision system. The main contribution to the overall kinematic error of a motion system usually comes from quasi-static sources [7]. Quasi-static errors are time-invariant and include geometric errors, misalignment and other errors due to manufacturing defects. Errors in the stage degrees of freedom are measured and analysed in the following sections.

EXPERIMENTAL SETUP

The kinematics of a motorised single-axis linear stage, with 100 mm traveling range, have been studied by measuring its linear and angular degrees of freedom. The moving plate of the linear stage was aligned to a linear rail using tight guiding wheels, that were collectively driven by a lead screw mechanism. A maximum load of 115 N and a positioning accuracy of 26 μm are specified by the stage's manufacturer. An optical target (a checkerboard pattern 48 mm × 44 mm) was used as a stage tracking target. The optical target and a retroreflector were mounted on the stage to provide positional feedback to the stereo system and the interferometer respectively.

The stereo vision system is composed of two CMOS machine vision cameras with sensors of 1.85 μm pixel size and 12.2 megapixel resolution.

Two imaging lenses with 16 mm focal length were fitted to the cameras. The cameras were mounted together on a stereo-camera rig with an adjustable baseline length and angle. Using the baseline length of 174.497 mm, the field of view and focus length of the cameras were set to cover the travel distance of the stage. Zhang's method [8] was used to determine the cameras' intrinsic parameters and their relative position.

A Renishaw 80XL laser interferometer system was used to validate the stereo vision measurements of the linear and angular degrees of freedom of the stage. To ensure accurate measurement in varying environmental conditions, the interferometer system is coupled with environment sensors for wavelength compensation. The interferometer is certified by the manufacturer to provide linear measurements with ±0.2 μm accuracy within the 100 mm working range of this application. For angular measurements in the same working range, the laser interferometer's accuracy specification is of the order of 1 μrad. Figure 1 shows the optical setup of the beam splitters and reflectors used in the linear and angular measurements. The optoelectronic detector of the interferometry setup uses the path difference between the measurement and reference beams to determine the linear (or angular) displacement of the moving reflector.

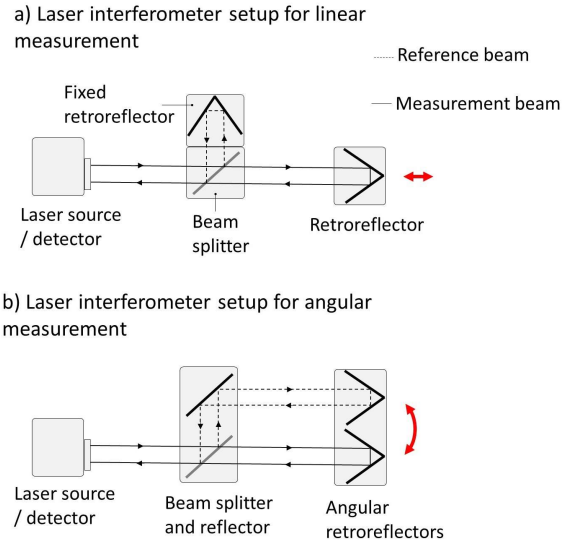

FIGURE 1. Optical setup for linear and angular displacement measurement.

KINEMATIC ERROR EVALUATION

Mechanical systems can be described as ideal kinematic chains of rigid bodies, however, due to imperfections in structural components and the relationship between them, there are kinematic errors in the moving components [9]. In the case of a linear stage, the kinematic error is the deviation in the position and orientation of the stage from the ideal prismatic kinematics.

For an arbitrary motion system, Eman et. al. [10] developed a generalised error model to take into account kinematic error of moving systems. The relationship between entities of a motion system is described using homogeneous transformation matrices. In a similar way, the kinematic error is expressed in terms of homogeneous error matrix $\delta\mathrm{T}$. The error matrix describes the change in the transformation matrix caused by the kinematic error. Moreover, the components of the error matrix are related to the six degrees of freedom of motion—three linear components $[\delta_x, \delta_y, \delta_z]^T$ and three angular components $[\epsilon_x, \epsilon_y, \epsilon_z]^T$. Figure 2 shows the error components in a Cartesian coordinate system affixed to a linear stage.

For the linear stage, illustrated in Figure 2, the error matrix $(\delta\mathrm{T})$ of the moving stage is given in the equation

$$\delta\mathrm{T} = \begin{bmatrix} 0 & -\epsilon_z & \epsilon_y & \delta_x \\ \epsilon_z & 0 & -\epsilon_x & \delta_y \\ -\epsilon_y & \epsilon_x & 0 & \delta_z \\ 0 & 0 & 0 & 0 \end{bmatrix}. \quad (1)$$

It is worth noting that the error components in Equation (1) depend on the active joint variable (variable of the major displacement) and are obtained from first order estimation [10].

The chosen reference coordinates, and the stereo camera configurations, are shown in Figure 2. From the reference stereo vision frame C, image pairs are captured in sequence $\mathrm{i} = 1,2,\ldots 10$ as the stage is displaced, moving from the starting position O. The average displacement of the stage evaluated at the i^{th} stereo images is defined as ${}^{\mathrm{C}}\mathrm{r}_{\mathrm{i}}$ in frame C. Similarly, ${}^{\mathrm{C}}\mathrm{T}_{\mathrm{P}_{\mathrm{i}}}$ is defined as the homogeneous transformation matrix of frame P_{i} with respect to C. Frame P_{i} is attached to the optical target at the i^{th} imaging instance as illustrated in Figure 2. The displacement ${}^{\mathrm{C}}\mathrm{r}_{\mathrm{i}}$ is found using stereo triangulation of the detected pixel locations that correspond to the optical target points. In addition, the rotation part of the matrix ${}^{\mathrm{C}}\mathrm{T}_{\mathrm{P}_{\mathrm{i}}}$ is found by extracting the horizontal and vertical

vectors formed by the points on the target, where twelve horizontal and eleven vertical points are aligned in the xy plane of frame P_i.

The motion direction is estimated by principal component analysis of the detected displacement points along the range of the stage. A stage reference frame, S_i is defined such that its x-direction coincides with the motion direction of the linear stage at the i^{th} imaging instance. While the frames P_i and S_i are rigidly attached to the moving stage, the reference frame O is defined to be fixed in space and coincident with S_1 at the initial stage position $(i = 1)$ serving as a global reference point.

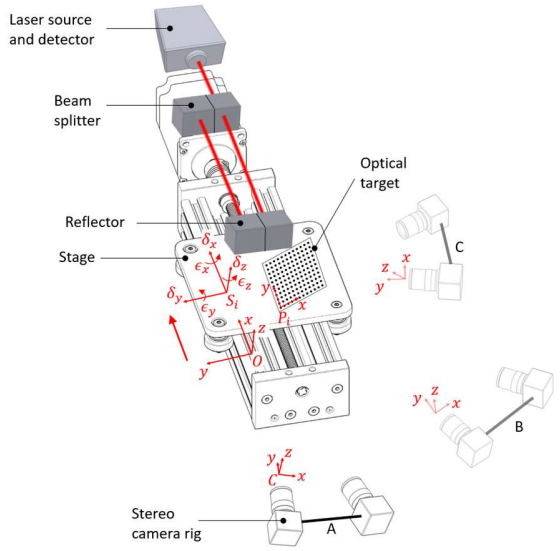

FIGURE 2. Illustration of the setup showing stereo configurations (A, B and C) and the designated reference frames. Stage error components are shown at the stage frame S_i with the optical target frame P_i also fixed to the stage.

The linear displacement error, denoting the δ_x error component of the stereo vision system, is evaluated by subtracting the linear laser interferometry reading (x_{LI}) from $|{}^{C}r_i - {}^{C}r_1|$, $\delta_x = |{}^{C}r_i - {}^{C}r_1| - x_{LI}$. By using ${}^{C}r_i$, and ${}^{C}T_O$, it is possible to estimate the straightness error components, δ_y and δ_z. The values of the straightness components are computed by transformation of the detected points from C to O coordinate frame,

$$\begin{bmatrix} x_{LI} + \delta_x \\ \delta_y \\ \delta_z \\ 1 \end{bmatrix} = {}^{C}T_O^{T} \cdot \begin{bmatrix} {}^{C}r_i \\ 1 \end{bmatrix}, \quad (2)$$

where the first component on the left-hand side provides an alternative way of evaluating δ_x from interferometer measurement x_{LI}. The values of δ_y and δ_z in Equation (2) represent the effective straightness of the stage motion as deviation from the fitted motion axis x in frame O.
The angular error components are evaluated from the difference in rotation between S_i and O, ${}^{O}R_{S_i}$, given by

$${}^{O}R_{S_i} = {}^{C}R_O^{T} \cdot {}^{C}R_{S_i}. \quad (3)$$

The rotation matrices ${}^{C}R_O$ and ${}^{C}R_{S_i}$ in Equation (3) are the relative rotations of frames O and S_i respectively, from the frame C. From entries of the matrix ${}^{O}R_{S_i}$, the Euler angles [11],

$$\begin{bmatrix} \epsilon_z \\ \epsilon_y \\ \epsilon_x \end{bmatrix} = \begin{bmatrix} \operatorname{atan}\left(\frac{{}^{O}R_{S_i}(2,1)}{{}^{O}R_{S_i}(1,1)}\right) \\ \operatorname{atan}\left(-\frac{{}^{O}R_{S_i}(3,1)}{\sqrt{{}^{O}R_{S_i}(3,2)^2 + {}^{O}R_{S_i}(3,3)^2}}\right) \\ \operatorname{atan}\left(\frac{{}^{O}R_{S_i}(3,2)}{{}^{O}R_{S_i}(3,3)}\right) \end{bmatrix}, \quad (4)$$

are directly computed to give the yaw, pitch and roll error components. The matrix element ${}^{O}R_{S_i}(n, m)$ denotes the n^{th} row and m^{th} column of a matrix ${}^{O}R_{S_i}$, as applied in Equation (4).

RESULTS

The calculated error components are analysed in this section. The experiment was repeated five times to determine measurement repeatability and reliability. Moreover, the experiment is also repeated in three different configurations of the stereo vision system, as shown in Figure 2.

Verification of stereo vision measurements

The accuracy of the stereo vision system in measuring the linear displacement of the stage is analysed. In each configuration of the stereo system, images containing the optical targets are captured while the laser interferometer readings are recorded at ten different positions of the stage.

Figure 3 shows the linear displacement error and the estimation of straightness with the extremes of the repeated measurements shown as error bars. The results are evaluated in configuration A, as illustrated in Figure 2. The linear error is less than 15 μm and varies by a maximum value of 5 μm. The straightness error in z-direction is a little higher than the error in y-direction. While the z straightness error might be affected by Abbe

offset error (<2 μm), it is quite feasible for the stage to have non-uniform straightness in the two directions.

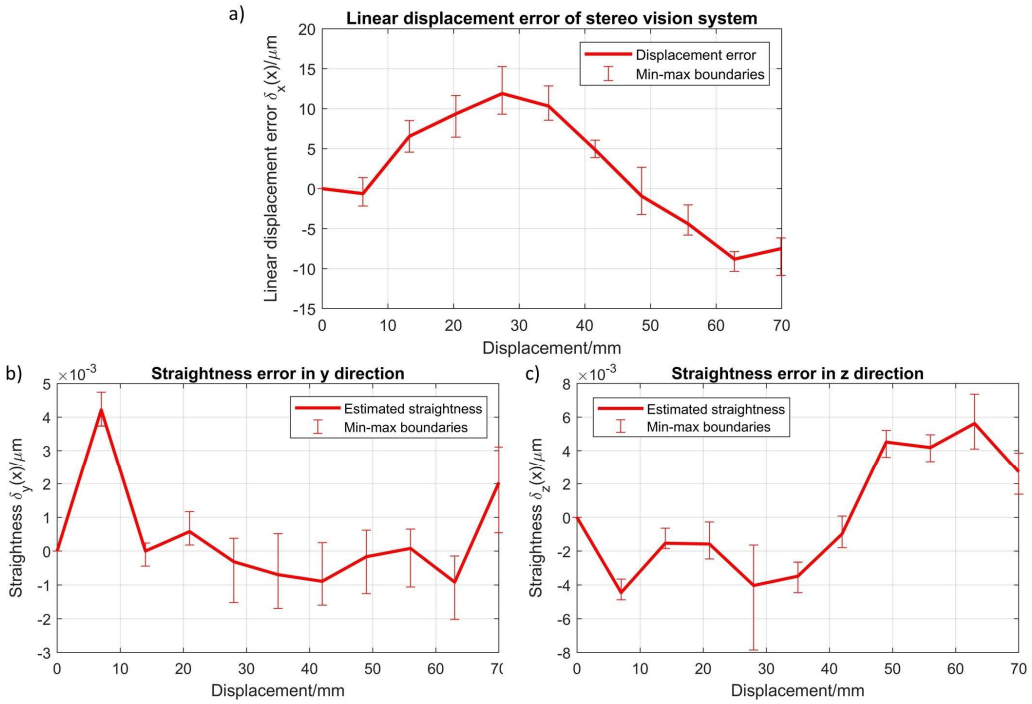

FIGURE 3. Linear measurement results of (a) linear displacement error and straightness errors in (b) and (c). All the results are obtained in configuration A. The displacement error is measured from laser interterferometer while the straightness errors are estimated by the deviations from a fitted line of motion.

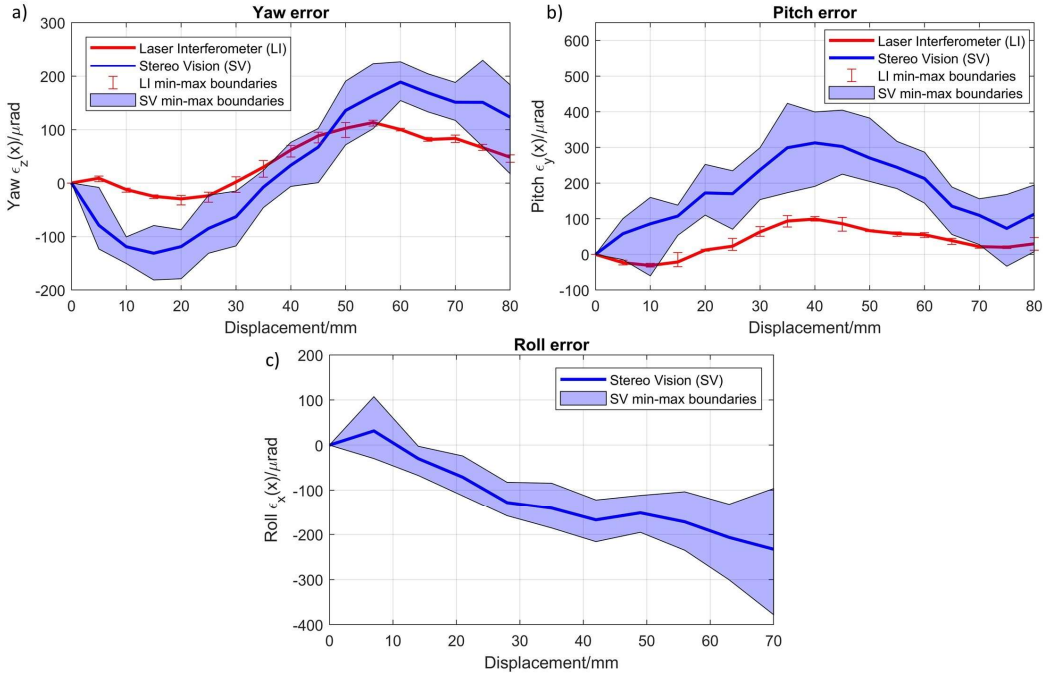

FIGURE 4. Angular measurement results showing error in (a) yaw, (b) pitch and (c) roll in configuration A measured by laser interferometer (LI) and stereo vision (SV).

Figure 4 shows the mean laser interferometer measurements with error bars showing the extreme readings of angular experiments. The corresponding angular displacements computed from the stereo vision are also shown in the same figures. Variations in the displacement measurements of the stereo vision system are indicated by the envelope plots, which indicate the minimum and maximum results across the five experiments. Measurement results in Figure 4 were obtained from configuration A, however, the following observations are also valid for the other stereo vision configurations. A small angular displacement of less than 100 μrad in yaw and pitch was observed by the interferometer. The yaw and pitch angles of the stereo vision measurement in Figure 4a) and b) were significantly overestimated when compared to the laser interferometer readings. The estimated roll values in Figure 4c) remain unverified because the angular setup of the laser interferometer could not be used for roll measurements. The spread of the stereo vision measurements is, on average, up to five times wider than the spread in the laser interferometer results.

Scene invariance of measurements

For the measurement of the stereo system to be extended to other applications, it is required to ensure the scene invariance of the measurement. The internal parameters of the camera should be consistent in measurement within the field of view of interest. Figure 5 and Figure 6 show the compared linear and angular results for the three different configurations. In general, the angular measurements are less consistent. However, it is noteworthy that angular distortions of less than 100 μrad result in small variations of the target image points that challenge the image resolution of the camera at the distance of 250mm to 350 mm.

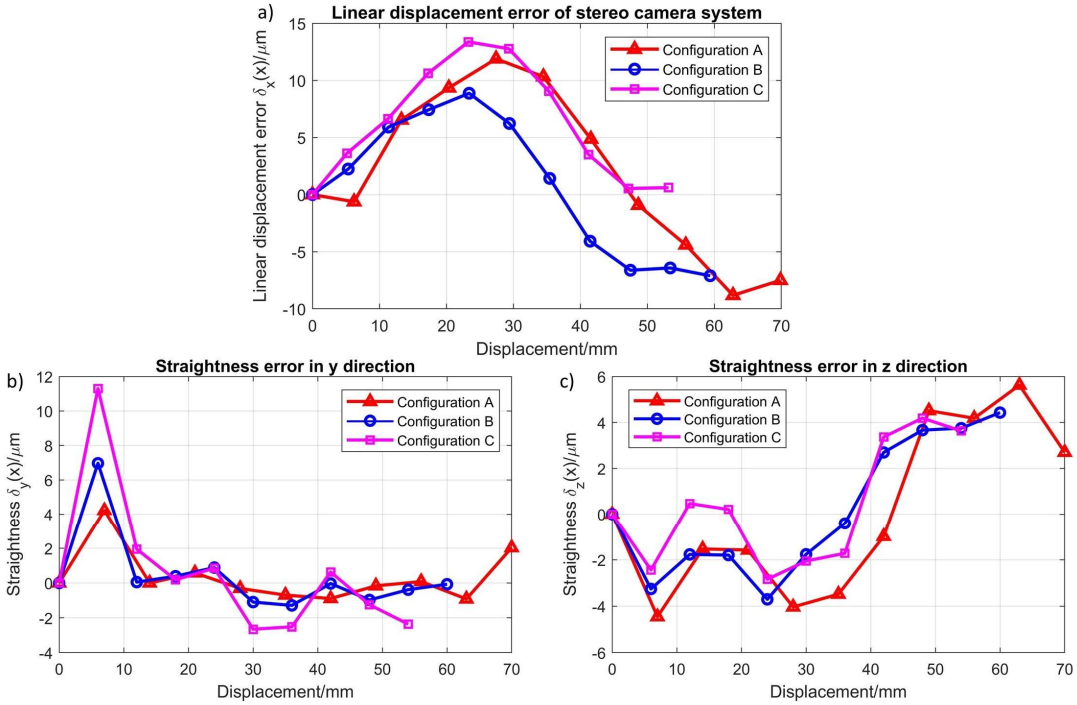

FIGURE 5. Comparison of average linear measurements in three configurations A, B, and C. Error in (a) linear displacement, (b) y-directional straightness and (c) z-directional straightness are shown.

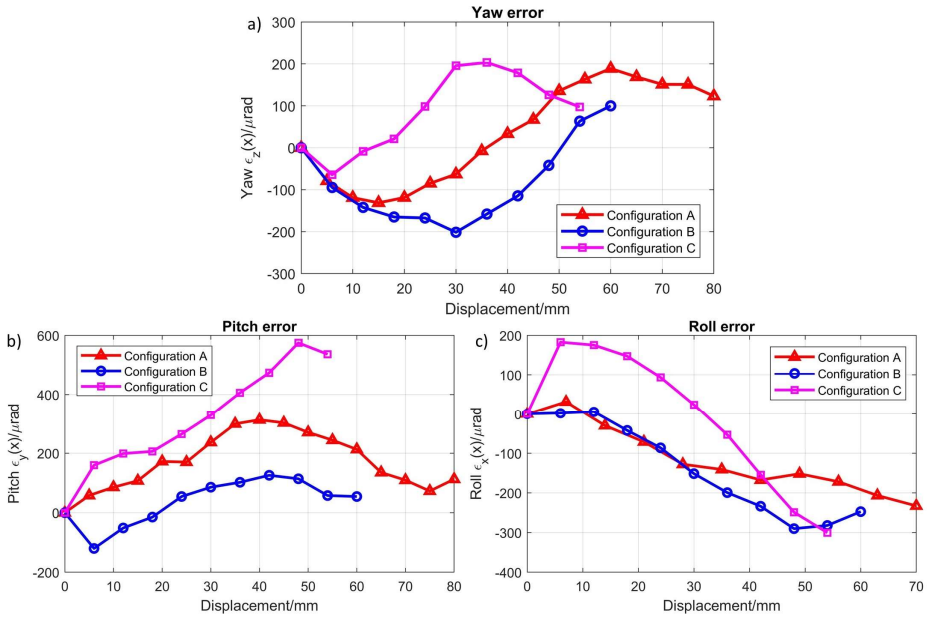

FIGURE 6. Comparison of average angular measurements in three configurations A, B, and C. Error in (a) yaw, (b) pitch and (c) roll are given.

CONCLUSION

By comparison of the overall kinematical accuracy of a linear stage with a laser interferometer, the achievable accuracy of a stereo vision system has been studied. This work will be extended to the complete generation of error model of stereo vision, generation of a 3D map of errors and design of an error compensation model. The work provides an alternative way of measuring kinematic error of mechanical systems using stereo vision system.

REFERENCES

[1] Gao W, Haitjema H, Fang FZ, Leach RK, Cheung CF, Savio E, Linaries, J M. On-machine and in-process surface metrology for precision manufacturing CIRP Annals - Manufacturing Technology 2019.

[2] Leach RK, Bourell D, Carmignato S, Donmez A, Senin N, Dewulf W. Geometrical metrology for metal additive manufacturing. CIRP Ann. 2019.

[3] Goda I, Hostis GL, Guerlain P. In-situ non-contact 3D optical deformation measurement of large capacity composite tank based on close-range photogrammetry. Opt. Lasers Eng. 2019;119:37–55.

[4] Möller C, Christian H, Hasmukhbhai N. Enhanced absolute accuracy of an industrial milling robot using stereo camera system. Procedia Technol. 2016;26:389–98.

[5] Cuesta E, Alvarez BJ, Martinez-Pellitero S, Barreiro J, Patiño H. Metrological evaluation of laser scanner integrated with measuring arm using optical feature-based gauge. Opt. Lasers Eng. 2019;121:120–132.

[6] Bösemann W. Industrial photogrammetry - Accepted metrology tool or exotic niche. Int Arch Photogramm. Remote Sens. Spat. Inf. Sci. - ISPRS Arch. 2016;41:15–24.

[7] Echerfaoui Y, Ouafi A El, Chebak A. Laser interferometer based measurement for positioning error compensation in Cartesian multi-axis systems. J. Anal. Sci. Methods Instrum. 2017;07:75–92.

[8] Zhang Z. A flexible new technique for camera calibration. IEEE Trans. Pattern Anal. Mach. Intell. 2000;22:1330–4.

[9] Zheng Y, Duan J. A geometric and kinematic error model and compensation of a 6-axis motorized optical fiber alignment stage. Adv. Mech. Eng. 2015;7:1–12.

[10] Eman KF, Wu BT, F. DM. Generalised geometric error model for multi-axis machines [J]. Ann. CIRP, 1987, V 1987;36:253–6.

[11] Slabaugh GG. Computing Euler angles from a rotation matrix. Tech. Rep. City Univ. London 1999;6:1–6.

RETRACE ERROR CALIBRATION ALGORITHM FOR NON-NULL INTERFEROMETRIC TESTING

Martin Tangari Larrategui[1,2], Yanqi Zhang[2], Andrew D. Rocha[2], Thomas G. Brown[1], Jonathan D. Ellis[2]
[1]The Institute of Optics
University of Rochester, Rochester, NY, USA
[2]James C. Wyant College of Optical Sciences
University of Arizona, Tucson, AZ, USA

INTRODUCTION

We present an extension to an existing retrace error calibration method for interferometric surface figure testing. Our proposed method is more suitable for non-null testing, where the retrace errors become more significant and their correction essential.

Surface figure quality is commonly specified to fractions of a system operating wavelength. The error contribution of the metrology tool can only account for a small fraction of this error budget. A popular technique to perform such an accurate measurement is null interferometry [1].

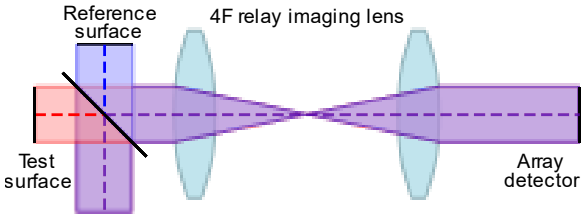

FIGURE 1. Diagram of a null interferometer. The imaging lens maps both test and reference surfaces to an array detector.

In a common path measurement, rays reflecting from the reference and test surfaces trace the same nominal path through the imaging lens. Since the aberrations in the imaging lens are common to both paths, these cancel when the beams are recombined in the array detector. Retrace errors are therefore negligible. The measured irradiance is given by

$$I = \left(E^{i(2\phi_T+\phi_E)} + E^{i(2\phi_R+\phi_E)}\right)\left(E^{-i(2\phi_T+\phi_E)} + E^{-i(2\phi_R+\phi_E)}\right) \quad (1)$$
$$= 2E\left(1+\cos\left(2\phi_T - 2\phi_R\right)\right) = 2E\left(1+\cos\left(2\Delta\phi\right)\right),$$

where I is the measured irradiance, E is the electric field amplitude and ϕ_T, ϕ_R and ϕ_E are the test, reference, and aberration errors phase components respectively and $\Delta\phi$ is the phase difference between the test and reference beams. The phase difference in the measurement can be extracted by measuring the irradiance at three or more reference surface positions and applying an appropriate phase stepping algorithm [1].

NON-NULL INTERFEROMETRY

In an effort to reduce the footprint and improve the performance of optical systems, designers have lately favored non-spherical and non-symmetric surfaces such as aspheres and freeforms [2]. Diamond turning and milling allowed for the manufacturing of theses surfaces for a range of materials [3]. Non-null interferometric techniques that extend the dynamic range beyond the monochromatic Nyquist limit were created to measure these surfaces. These include Grievenkamp's non-null interferometry [4] and Wyant's multiple-wavelength phase stepping interferometry [5].

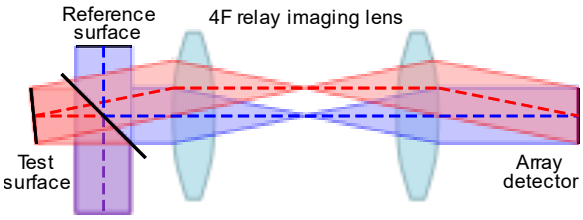

FIGURE 2. Diagram of a non-null interferometer. The lens HFOV must be larger than twice the test surface maximum slope departure from flat to prevent vignetting.

In this case, rays reflecting from the reference and test surfaces trace different nominal paths across the imaging lens. The aberrations are no longer common to both paths, leading to long range retrace errors. If uncorrected, retrace errors are indistinguishable from manufacturing errors. Retrace errors can be mathematically represented by an additional phase error using

$$I = \left(E^{i(2\phi_T+\phi_{ET})} + E^{i(2\phi_R+\phi_{ER})}\right)\left(E^{-i(2\phi_T+\phi_{ET})} + E^{-i(2\phi_R+\phi_{ER})}\right) \quad (2)$$
$$= 2E\left(1+\cos\left(2\Delta\phi + \Delta\phi_E\right)\right),$$

where ϕ_{ET} and ϕ_{ER} are the phase errors in the test and reference beams respectively and $\Delta\phi_E$ is their difference.

IMAGING LENS

An afocal relay imaging lens was designed from Edmund Optics stock singlets to illustrate the existing and proposed calibration methods. It consists of a pair of Cooke triplets with an 11 mm diameter entrance pupil, a 2.86° HFOV and a maximum wavefront error RMS of 0.02 waves across the field for a 0.604 µm wavelength. The imaging lens is shown in Figure 3.

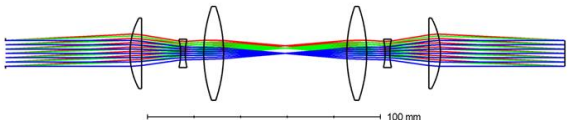

FIGURE 3. Optical model of the 1:1 relay imaging lens. The test and reference surfaces are modelled as the aperture stop/entrance pupil, which are imaged to the detector (exit pupil) [6].

Simulated measurements were performed in FRED with a 12 mm aperture monochromatic extended source (101 beams across the aperture along the X- and Y-directions) and a 2400x2400 pixel array detector (5 µm pixel pitch). An 11 mm pupil was applied in post processing.

TEST SURFACE

A concave spherical test surface was selected to evaluate the performance of the correction algorithm. Its diameter is 11 mm and its radius of curvature is 250 mm (R/22.7). The radius was selected to constraint the maximum slope departure to 1.43° (half of the HFOV of the imaging lens).

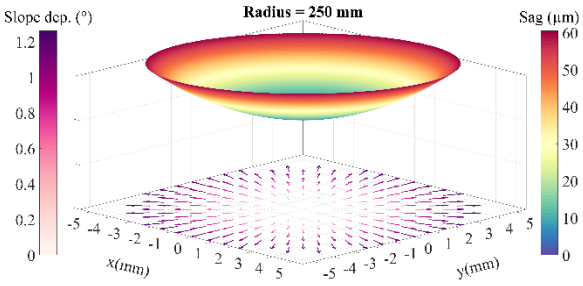

FIGURE 4. Spherical test surface used to evaluate the performance of the different calibration methods. The figure shows the surface sag and the magnitude and direction of its slope departure from flat.

LINEAR CORRECTION METHOD

A calibration method was patented by Dörband and Frank [7] and published in the literature by Dörband, Müller, and Gross [8]. Their algorithm assumes long range retrace errors to be linearly dependent on the slope departure of the test surface. Under this assumption, retrace errors can be corrected by first performing calibration error measurements on two planar surfaces tilted by the maximum interferometer acceptance angle along two orthogonal directions ($\alpha_x = \alpha_y = \alpha_{MAX}$, half the imaging lens HFOV). For unity magnification, the calibration to be applied at each (x, y) pupil point is given by [7,8],

$$C(x,y) = \frac{E_C(x,y,\alpha_x,\alpha_y)\Big|_{\substack{\alpha_x=\alpha_{MAX}\\ \alpha_y=0}}}{\alpha_{MAX}} \arctan\left(\frac{\partial Z(x,y)}{\partial x}\right) + \frac{E_C(x,y,\alpha_x,\alpha_y)\Big|_{\substack{\alpha_x=0\\ \alpha_y=\alpha_{MAX}}}}{\alpha_{MAX}} \arctan\left(\frac{\partial Z(x,y)}{\partial y}\right), \quad (3)$$

where $E_C(x, y, \alpha_x, \alpha_y)$ is the surface measurement error (measurement minus the input surface for the calibration surface) at the two extrema angles as shown in Figure 5.

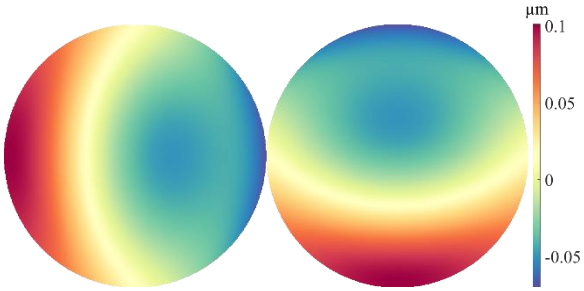

FIGURE 5. Measurement error phase maps for the maximum -X and -Y directions tilt calibration surfaces. These are the only inputs of the linear retrace error correction method [7,8].

HIGHER ORDER CORRECTION METHOD

In our previous work, we extended Dörband's method to quadratic order [9]. In this paper, we present an extension to any higher order in a more concise mathematical formulation. Equation 3 can be rewritten as

$$C(x,y) = E_{\alpha_x}(x,y)\left(\frac{1}{\alpha_{MAX}} \arctan\left(\frac{\partial Z(x,y)}{\partial x}\right)\right) + E_{\alpha_y}(x,y)\left(\frac{1}{\alpha_{MAX}} \arctan\left(\frac{\partial Z(x,y)}{\partial y}\right)\right), \quad (4)$$

where $E_{\alpha x}$ and $E_{\alpha y}$ are the linear error coefficient matrices based on the calibration error measurements. If the minimum two orthogonal calibration measurements are performed, these correspond to the two error matrices shown in Figure 4. If *n* measurements are performed, the error coefficient matrices can be calculated through solving an overdetermined linear system given by

$$\begin{bmatrix} \left(\frac{\alpha_{x_1}}{\alpha_{MAX}}\right) & \left(\frac{\alpha_{y_1}}{\alpha_{MAX}}\right) \\ \vdots & \vdots \\ \left(\frac{\alpha_{x_n}}{\alpha_{MAX}}\right) & \left(\frac{\alpha_{y_n}}{\alpha_{MAX}}\right) \end{bmatrix} \begin{bmatrix} E_{\alpha_x}(x,y) \\ E_{\alpha_y}(x,y) \end{bmatrix} = \begin{bmatrix} E_1(x,y) \\ \vdots \\ E_n(x,y) \end{bmatrix}, \quad (5)$$

where α_{xi} and α_{yi} are the *X*- and *Y*- direction tilt angles of the planar calibration surface and $E_i(x,y)$ is the error matrix for that tilt. The scalar coefficients in the *n x 2* matrix of Equation 5 must be multiplied by *m x m* identity matrices for the equation to be dimensionally consistent. Sparse matrices can be used in practice for computational efficiency.

Under this new formulation of Equations 4 and 5, it is trivial to extend the calibration algorithm to any arbitrary order. For instance, up to third order, Equations 4 and 5 become Equations 6 and 7.

$$\begin{aligned} C(x,y) = {} & E_{\alpha_x}(x,y)\left(\frac{1}{\alpha_{MAX}}\arctan\left(\frac{\partial Z(x,y)}{\partial x}\right)\right) + E_{\alpha_y}(x,y)\left(\frac{1}{\alpha_{MAX}}\arctan\left(\frac{\partial Z(x,y)}{\partial y}\right)\right) \\ & + E_{\alpha_x{}^2}(x,y)\left(\frac{1}{\alpha_{MAX}}\arctan\left(\frac{\partial Z(x,y)}{\partial x}\right)\right)^2 + E_{\alpha_x\alpha_y}(x,y)\left(\frac{1}{\alpha_{MAX}{}^2}\arctan\left(\frac{\partial Z(x,y)}{\partial x}\right)\arctan\left(\frac{\partial Z(x,y)}{\partial y}\right)\right) + E_{\alpha_y{}^2}(x,y)\left(\frac{1}{\alpha_{MAX}}\arctan\left(\frac{\partial Z(x,y)}{\partial y}\right)\right)^2 \\ & + E_{\alpha_x{}^3}(x,y)\left(\frac{1}{\alpha_{MAX}}\arctan\left(\frac{\partial Z(x,y)}{\partial x}\right)\right)^3 + E_{\alpha_x{}^2\alpha_y}(x,y)\left(\frac{1}{\alpha_{MAX}{}^3}\left(\arctan\left(\frac{\partial Z(x,y)}{\partial x}\right)\right)^2\arctan\left(\frac{\partial Z(x,y)}{\partial y}\right)\right) \\ & + E_{\alpha_x\alpha_y{}^2}(x,y)\left(\frac{1}{\alpha_{MAX}{}^3}\arctan\left(\frac{\partial Z(x,y)}{\partial x}\right)\left(\arctan\left(\frac{\partial Z(x,y)}{\partial y}\right)\right)^2\right) + E_{\alpha_y{}^3}(x,y)\left(\frac{1}{\alpha_{MAX}}\arctan\left(\frac{\partial Z(x,y)}{\partial y}\right)\right)^3 \end{aligned} \quad (6)$$

$$\begin{bmatrix} \left(\frac{\alpha_{x_1}}{\alpha_{MAX}}\right) & \left(\frac{\alpha_{y_1}}{\alpha_{MAX}}\right) & \left(\frac{\alpha_{x_1}}{\alpha_{MAX}}\right)^2 & \left(\frac{\alpha_{x_1}\alpha_{y_1}}{\alpha_{MAX}{}^2}\right) & \left(\frac{\alpha_{y_1}}{\alpha_{MAX}}\right)^2 & \left(\frac{\alpha_{x_1}}{\alpha_{MAX}}\right)^3 & \left(\frac{\alpha_{x_1}{}^2\alpha_{y_1}}{\alpha_{MAX}{}^3}\right) & \left(\frac{\alpha_{x_1}\alpha_{y_1}{}^2}{\alpha_{MAX}{}^3}\right) & \left(\frac{\alpha_{y_1}}{\alpha_{MAX}}\right)^3 \\ \vdots & \vdots & \vdots & \vdots & \vdots & \vdots & \vdots & \vdots & \vdots \\ \left(\frac{\alpha_{x_n}}{\alpha_{MAX}}\right) & \left(\frac{\alpha_{y_n}}{\alpha_{MAX}}\right) & \left(\frac{\alpha_{x_n}}{\alpha_{MAX}}\right)^2 & \left(\frac{\alpha_{x_n}\alpha_{y_n}}{\alpha_{MAX}{}^2}\right) & \left(\frac{\alpha_{y_n}}{\alpha_{MAX}}\right)^2 & \left(\frac{\alpha_{x_n}}{\alpha_{MAX}}\right)^3 & \left(\frac{\alpha_{x_n}{}^2\alpha_{y_n}}{\alpha_{MAX}{}^2}\right) & \left(\frac{\alpha_{x_n}\alpha_{y_n}{}^2}{\alpha_{MAX}{}^2}\right) & \left(\frac{\alpha_{y_n}}{\alpha_{MAX}}\right)^3 \end{bmatrix} \begin{bmatrix} E_{\alpha_x}(x,y) \\ E_{\alpha_y}(x,y) \\ E_{\alpha_x{}^2}(x,y) \\ E_{\alpha_x\alpha_y}(x,y) \\ E_{\alpha_y{}^2}(x,y) \\ E_{\alpha_x{}^3}(x,y) \\ E_{\alpha_x{}^2\alpha_y}(x,y) \\ E_{\alpha_x\alpha_y{}^2}(x,y) \\ E_{\alpha_y{}^3}(x,y) \end{bmatrix} = \begin{bmatrix} E_1(x,y) \\ \vdots \\ E_n(x,y) \end{bmatrix} \quad (7)$$

CALIBRATION SURFACE SELECTION

The minimum number of calibration measurements is determined by the number of error coefficient matrices for the selected order of the calibration algorithm: two for linear, five for quadratic, nine for cubic and so on. The α_x and α_y tilt angles of the calibration surfaces can, in general, be arbitrary as long as two conditions are satisfied. Since aberrations are proportional to the filed of view and usually largest at the edge of the field, it is important to sample angles satisfying:

$$\sqrt{\alpha_x{}^2 + \alpha_y{}^2} \approx \frac{1}{2}HFOV. \quad (8)$$

For instance, the quadratic order error coefficient matrices can be calculated with only five calibration error measurements (equally spaced every 72° along the edge of the field) as opposed to the eight measurements presented in our previous work [9].

Secondly, calibration surfaces tilted less than half the lens HFOV must be used for third and higher order corrections. Equation 7 shows that since the tilt angles are normalized, the columns of the

coefficient matrix become linearly dependent when only points on the edge of the field are used. In this case, the system is underdetermined and has no solution. This condition can be more easily visualized by parametrizing the tilt angle by

$$\frac{\alpha_x}{\alpha_{MAX}} = \cos(\theta) \quad \text{and} \quad \frac{\alpha_y}{\alpha_{MAX}} = \sin(\theta). \qquad (9)$$

For completeness, 317 tilted calibrations surfaces were used corresponding to 21 equally spaced tilts in both the *X*- and *Y*- directions. The corresponding calibration surface measurements and their errors are shown in Figures 6 and 7.

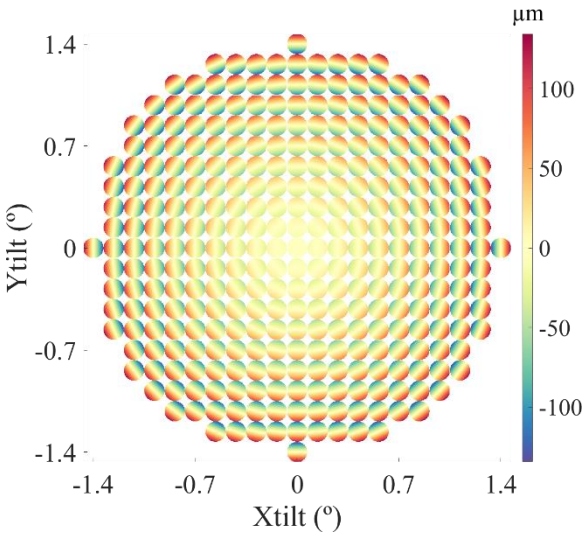

FIGURE 6. Measurement phase maps for a 21 by 21 array of tilted calibration surfaces. The full field of view is sampled at 0.14° intervals. Towards the edge of the field, the sag departure exceeds 250 µm.

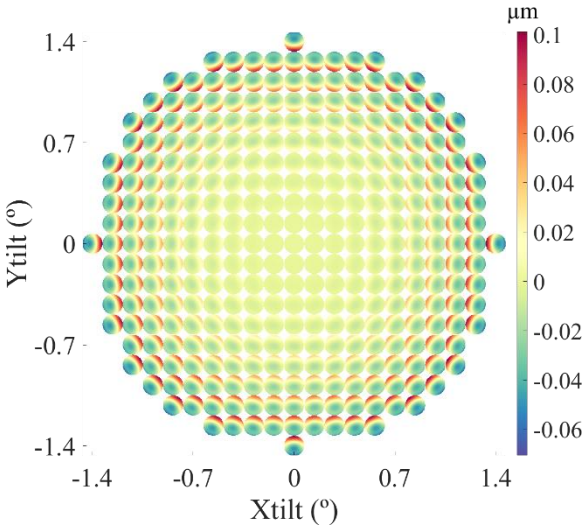

FIGURE 7. Measurement error phase maps for the 21 by 21 array of tilted calibration surfaces shown in Figure 6.

RESULTS

The error coefficient matrices up to eighth order were calculated using Equation 7 and the data of Figure 7. The results for first through fourth order are shown in Figure 8.

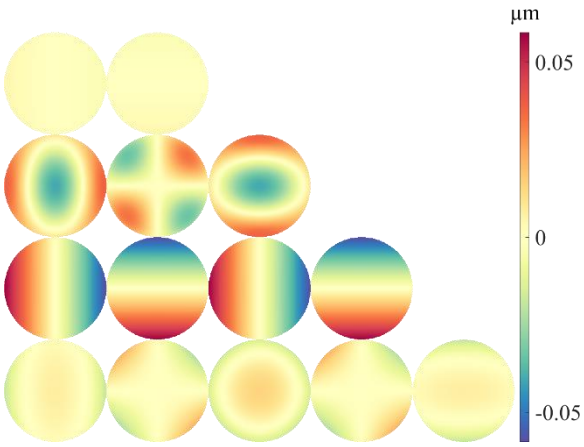

FIGURE 8. Error coefficient matrices arranged in rows by increasing order. First order (linear) in the first row through fourth order in the last row. For this lens, second (quadratic) and third order have the largest error components.

The error correction matrices were multiplied with the measured test surface derivatives and their powers as indicated in equation 6. The resulting calibration matrix was then subtracted from the test surface measurement. The results are summarized in Figure 9.

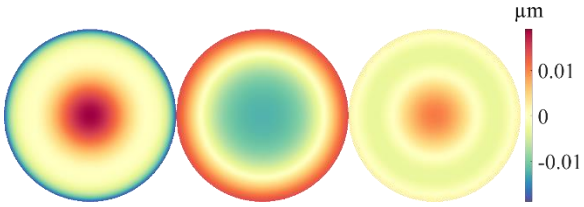

FIGURE 9. Correction algorithm results showing from left to right: the error before correction (0.038 µm PV, 0.008 µm RMS), the error after quadratic correction (0.027 µm PV, 0.009 µm RMS) [9], and the error after the higher order correction (0.014 µm PV, 0.003 µm RMS) proposed in this paper.

As shown in Figure 9, the quadratic error correction reduced the PV error by 29.6% and increased the RMS error by 9.5%. The proposed

higher order correction reduced the PV error by 63.5% and reduced the RMS error by 56.9%.

CONCLUSIONS

Calibrating for retrace errors is essential to achieve high accuracy results in non-null interferometric surface figure testing. The method presented in this paper can be easily applied to any interferometer and requires no *a priori* knowledge of the imaging system. The proposed method was shown to successfully reduce measurement errors caused by imaging lens aberrations for large slope departures. Other errors such as environmental effects, system vibration, speckle, etc. can be corrected applying null interferometry techniques and were therefore not included in this work.

Future work includes applying this method to an interferometer with the proposed lens and a commercial interferometer. This can be easily done with a flat mirror on a closed-loop controlled tip and tilt stage as a calibration surface.

ACKNOWLEDGEMENTS

We would like to thank the NSF and the NSF I/UCRC Center for Freeform Optics for their support under contracts CMMI 1653510 and IIP 1822049.

REFERENCES

[1] Malacara D. Optical Shop Testing. New Jersey: John Wiley & Sons, Inc.; 2007.

[2] Thompson K.P., Rolland J.P. Freeform optical surfaces: A revolution in imaging optical design. Opt. Photon. News. 2012 Jun; 23(6): 30-5.

[3] Blalock T., Medicus K., DeGroote Nelson J. Fabrication of freeform optics. Proc. SPIE. 2015 Aug; 9575.

[4] Lowman A.E., Greivenkamp J. E. Modeling an interferometer for non-null testing of aspheres. Proc. SPIE. 1995 Sep; 2536.

[5] Cheng Y-Y., Wyant J.C. Multiple-wavelength phase-shifting interferometry. Appl. Opt. 1985 Mar; 24(6): 804-7.

[6] Murphy P.E., Brown T.G., Moore D.T. Interference imaging for aspheric surface testing. Appl. Opt. 2000 May; 39(13): 2122-9.

[7] Dörband B., Frank R. Method and an apparatus for measuring a deviation of an optical test surface from a target shape. U.S. Patent No. 8269981 B1. 2012 Sep 18.

[8] Dörband B., Müller H. Gross H. Testing the Geometry of Optical Components in Handbook of optical systems: Volume 5: Metrology of optical components and systems. Darmstadt: WILEY-VCH Verlag GmbH; 2012. p. 745-7.

[9] Tangari Larrategui M., Zhang Y., Rocha A.D., Brown T.G., Ellis J.D. Quadratic extension to retrace error calibration algorithm for non-null interferometric surface figure testing of nominally flat reflective surfaces. Proc. OSA. 2019 Jun; JW3A.7.

Dual-mode multi-wavelength snapshot interferometric system for on-machine metrology

Xiaobo Tian[1], Daodang Wang[1,2], Alexander Sohn[3], Oliver J. Spires[1], and Rongguang Liang[1]

[1]James C. Wyant College of Optical Sciences
University of Arizona
Tucson, Arizona, USA
[2]College of Metrology and Measurement Engineering
China Jiliang University
Hangzhou, Zhejiang, China
[3] Facebook Reality Labs
Seattle, Washington, USA

INTRODUCTION

This paper describes a dual-mode multi-wavelength snapshot interferometric system (DMSIS) for on-machine metrology. Typically, commercial measurement tools are designed for off-line metrology and not suitable for on-machine metrology. It is usually necessary to remove the part from the machine for off-line metrology and then remount it back to the machine if the part is not fabricated to the specification, increasing the fabrication time and introducing extra errors. The reported compact DMSIS uses pixelated polarization camera [1] to capture four phase-shifted interferograms in a single shot, meeting the fundamental requirements for on-machine metrology: compact, fast, accurate, and less sensitive to environment.

In past few years, we have developed dual-mode snapshot interferometric systems for on-machine metrology in single wavelength [2,3]. One limitation of single wavelength phase shifting interferometer is that the phase difference between two adjacent points must be less than π, limiting the measurement range. In this paper, multi-wavelength approach is applied to address this limitation [4]. Using pixelated color polarization camera, DMSIS integrates a multi-wavelength laser interferometer for measuring optical surface shape with large slopes and a low-coherence interference microscope for measuring surface roughness. Since only one measurement is needed for measuring surface shape or surface structure and roughness, the system is fast and less sensitive to environment. With multi-wavelength interferometric method, the dynamic range of the system is increased significantly. DMSIS has been prototyped and tested on a Moore Nanotech 350FG diamond turning machine (DTM).

SYSTEM LAYOUT

DMSIS is based on a Linnik interferometer configuration as shown in Fig. 1. Three lasers operating at 632.8 nm, 543 nm and 488 nm provide multi-wavelength illumination for red (R), green (G) and blue channels for measuring surface shape. The RGB laser beams are coupled into a single-mode fiber and collimated by a collimator. A red light emitting diode (LED) with a center wavelength of 630 nm is coupled into a multimode fiber for measuring surface structure and roughness. Interferometer mode and interference microscope mode can be switched by changing the illumination fibers. A dichroic beamsplitter can be added to combine coherent and incoherent illumination so that the measurement mode can be switched quietly. A beam expander (BE) is added after collimator. A polarizer (P) is placed between a folding mirror and a non-polarizing beam splitter (BS), adjusting the relative intensities of the test arm and reference arm for better fringe contrast. After passing through the polarizer, BS and polarizing beam splitter (PBS), the linear polarized light is divided into two beams with orthogonal polarization. Two identical long working distance microscope objectives (MO1 and MO2, Edmund M Plan Apo 10X) with NA 0.28 are used for matching the optical paths, forming a Linnik interferometric system. An achromatic zero order quarter wave plate (QWP) with its fast axis at 45°

is placed in front of the camera and transforms the two orthogonal linear polarized beams to opposite circular polarized beams. A pixelated color polarization camera (PCam) is used to capture phase-shifted interferograms in RGB channels simultaneously. In PCam, a Sony's polarization image sensor is adopted, in which a micro-polarizer array with four linear polarizers at 0°, 45°, 90°, and 135° is placed next to RGB Bayer filter. The combination of micro-polarizer array and RGB Bayer filter in the PCam forms a 4 × 4 superpixel (Figure 2), which consists of the 0°, 45°, 90°, and 135° linear polarization in RGB channels

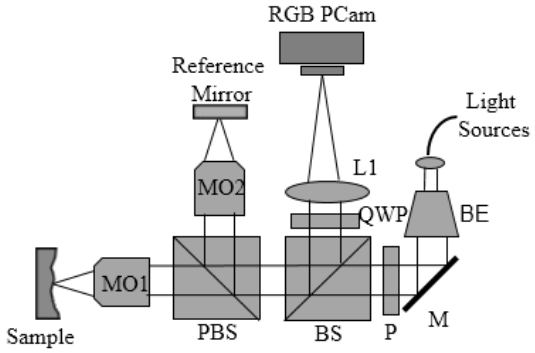

FIGURE 1. Dual-mode multi-wavelength snapshot interferometric system. QWP: quarter wave plate; P: polarizer; BS: non-polarizing beam splitter; PBS: polarizing beam splitter; BE: beam expander; L1: image lenses; M: mirror; MO1 - MO2: microscope objectives; and PCam: pixelated polarization camera

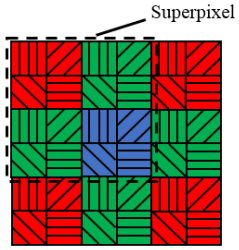

FIGURE 2. Schematic pixel layout for 6x6 weighted average calculation.

OPERATING PRINCIPLE

With extracted phase-shifted interferograms in RGB channels, the phase distribution related to the surface under test at each wavelength can be calculated with a four-step phase shifting algorithm. Due to the imperfect performance of micro-polarizer array and RGB Bayer layer in PCam, the error sources including the field of view (FOV) error and crosstalk among RGB signals. Photon response nonuniformity (PRNU) and micro-polarizer orientation misalignment (POMA) can introduce additional measurement errors as well. The PCam should be calculated before taking measurement [4, 5]. In order to reduce the error caused by PCam, the phase is calculated by a weighted average in a 6 x 6 grid, as shown in Fig. 2.

The weighted average is a linear combination of neighboring pixels, which has the same format of linear interpolation of $I_{0°}$, $I_{45°}$, $I_{90°}$ and $I_{135°}$ polarization state in each pixel. Thus a linear-spline interpolation can also be used to recover the missing intensity of each pixel as $I=[I_{R0}\ I_{R1}\ I_{R2}\ I_{R3}\ I_{G0}\ I_{G1}\ I_{G2}\ I_{G3}\ I_{B0}\ I_{B1}\ I_{B2}\ I_{B3}]^T$, where R, G and B are the input light at red, green and blue channels, 0, 1, 2 and 3 are corresponding to 0°, 45°, 90° and 135° linear polarization states. The surface phase information in RGB channel can be calculated as:

$$\tan(\phi_R)=\frac{I_{R3}-I_{R1}}{I_{R0}-I_{R2}}$$
$$\tan(\phi_G)=\frac{I_{G3}-I_{G1}}{I_{G0}-I_{G2}} \quad (1)$$
$$\tan(\phi_B)=\frac{I_{B3}-I_{B1}}{I_{B0}-I_{B2}}$$

In surface structure and roughness measurement, once two phases ϕ_1 and ϕ_2 are obtained for two wavelengths λ_1 and λ_2, the measurable surface height H can be expanded from $\lambda_1/4$ to $\Lambda_{12}/4$ where $\Lambda_{12}=\lambda_1\lambda_2/|\lambda_1-\lambda_2|$ is the equivalent wavelength. The equivalent phase $\Phi=\phi_1-\phi_2$ is related to the surface height as [6]

$$H_{12}=\frac{\Lambda_{12}}{2}\cdot\frac{\Phi}{2\pi} \quad (2)$$

However, the phase error is also increased by a factor of Λ_{12}/λ_1 in this method. To avoid this induced phase error, the fringe order method is used [7]. Using the step height measured by the equivalent wavelength, the fringe order N_1 of λ_1 is determined. Then the step height H_1 is calculated:

$$H_1=\frac{\lambda_1}{2}\left(\frac{\phi_1}{2\pi}+N_1\right) \quad (3)$$

$$N_1=round\left(\frac{2H_{12}}{\lambda_1}\right) \quad (4)$$

where *round* is the nearest integer. By using the fringe order method, a high precision and long measurement range can be achieved. In order to

get correct fringe order N_1, the phase noise in ϕ_1 must be smaller than $\lambda_1/(4\Lambda_{12})$.

For the case of three wavelengths, three phases ϕ_1, ϕ_2 and ϕ_3 are obtained. The equivalent wavelength for λ_1 and λ_2 is $\Lambda_{12} = \lambda_1\lambda_2 / |\lambda_1 - \lambda_2|$, for λ_2 and λ_3 is $\Lambda_{23} = \lambda_2\lambda_3 / |\lambda_2 - \lambda_3|$. Then a longer equivalent wavelength is obtained by $\Lambda_{12-23} = \Lambda_{12}\Lambda_{23} / |\Lambda_{12} - \Lambda_{23}|$, with step height:

$$H_{12-23} = \frac{\Lambda_{12-23}}{2} \cdot \frac{(\phi_1 - \phi_2) - (\phi_2 - \phi_3)}{2\pi} \qquad (5)$$

Instead of calculating the fringe order of λ_1 directly, we first calculate the fringe order of Λ_{12} based on $H_{12\text{-}23}$ and then calculate H_{12}, from which the final step height H_1 is obtained. The maximum phase noise limit is significantly increased from $\lambda_1/(4\Lambda_{12\text{-}23})$ to $\lambda_1/(4\Lambda_{12})$ or $\Lambda_{12}/(4\Lambda_{12\text{-}23})$.

EXPERIMENT

Optical surfaces were diamond turned and tested with DMSIS mounted on the Z-axis slide of the DTM. The on-machine measurement results were compared with the off-line measurement results from a Zygo NewView 8300 optical surface profiler and Zygo Verifire laser interferometer. Figure 3 shows the measured surface roughness of a diamond turned copper concave surface. The radius of curvature is 50 mm. The measurement area is about 800 μm x 800 μm. Tip, tilt and power terms of Zernike polynomial were removed in the surface roughness measurement. The surface root mean square (RMS) of the copper surface is 10.36 nm in off-line (Fig. 3(a)) and 10.62 nm in DMSIS (Fig. 3(b)). Figure 3(c) shows one of the interferograms captured by the system. The measurement result from DMSIS shows a good agreement with off-line measurement as shown in Fig. 3(d). On-machine RMS surface roughness from DMSIS is slightly larger than the off-line measurement Zygo Newview8300, the possible cause could be the fact that the red LED with narrow bandwidth is used in DMSIS and white LED is used in Zygo NewView 8300.

In interferometer mode, the microscope objective in reference arm (MO2) is removed, forming a multi-wavelength laser interferometer. Figure 4 shows the comparison of the measured surface shape of the same diamond turned copper surfaces with 50 mm radius of curvature and 25 mm diameter. The peak-to-valley (PV) of the copper surface is 634.3 nm in off-line (Zygo Verifire laser interferometer) and 657.1 nm in DMSIS, while RMS is 115.2 nm in off-line and 116.5 nm in DMSIS respectively.

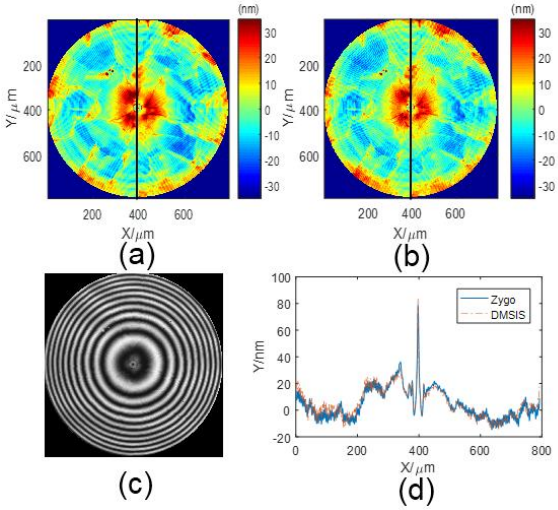

FIGURE 3. Surface roughness measurement of a diamond turned copper surface: (a) off-line measurement, (b) DMSIS measurement, (c) interferogram in DMSIS, and (d) line profile comparison.

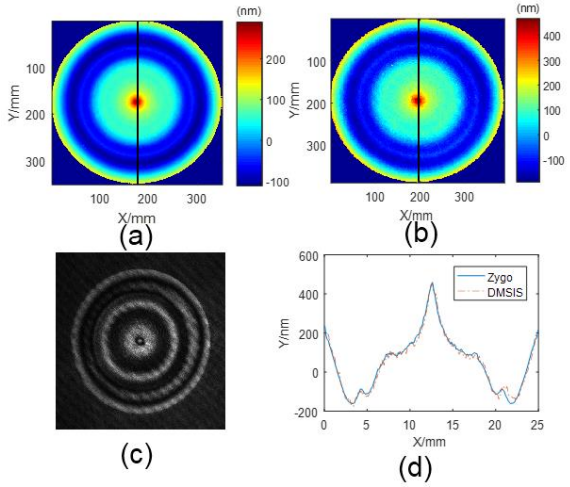

FIGURE 4. Surface shape measurement of a diamond turned copper surface: (a) off-line measurement, (b) DMSIS measurement, (c) interferogram in DMSIS, and (d) line profile comparison.

To demonstrate the feasibility for testing the surfaces with larger slopes, the measurement of a freeform mirror with conic constant K_x=-2 and radius R_x=23.5 mm in x direction, K_y=-1 and R_y=26 mm in y direction was carried out. According to Fig. 5(a), the fringes in the outer region are very dense, and the actual sag difference of test surface between consecutive sampling pixels in the outer region exceeds the measurable range λ/4 at R, G and B wavelengths. Figure 5(b) is the reconstructed surface map with multi-wavelength method, in which the maximum measurable actual sag difference of the test surface between consecutive sampling pixels is extended to $\Lambda_{RG\text{-}GB/4}$=4.6482 μm. The measured PV and RMS values are 39.4340 μm and 7.9615 μm, respectively. It should be noted that the retrace error is included in the reconstructed surface map, and it can be calibrated by ray tracing the testing system model

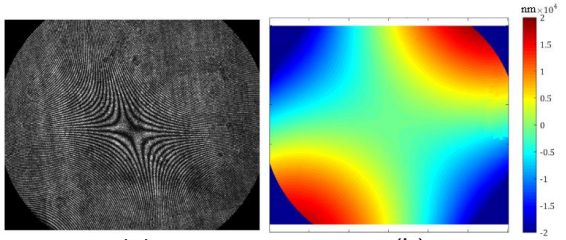

FIGURE 5. Surface shape measurement of a diamond turned copper freeform surface: (a) interferogram in R channel (b) surface map of freeform surface with multi-wavelength method.

CONCLUTION

In this paper, we present a compact, dual-mode multi-wavelength snapshot interferometric system for on-machine metrology to measure surface shape with large slope and surface roughness. Its unique dual-mode and snapshot features are particularly suitable for on-machine metrology. The measurement results demonstrate the DMSIS is a feasible system for on-machine metrology. Since it is a reasonably compact system using a commercial microscope objective as the transmission sphere, the measurement range for a convex surface is limited by the working distance of the objective. A custom objective can be developed to address this issue.

REFERENCES

[1] J Millerd, J Wyant, U.S. Patent No. 7,230,718, 2007.
[2] D Wang, R Liang, Optics Letter, 41(1), 41-44, 2016.
[3] X Tian, Y Zhang, A Sohn, O Spires, R Liang, Optical Engineering 58(4), 044104, 2019
[4] X Tian, X Tu, J Zhang, O Spires, N Brock, S Pau, R Liang, Optics Express 26(14), 18279-18291, 2018
[5] Z Chen, X Wang, R Liang, Applied Optics 54, 995, 2015.
[6] Y Cheng, J Wyant, Applied Optics 23(24), 4539-4543, 1984.
[7] K Creath, Applied Optics 26(14), 2810-2816, 1987.

DESIGN OF THE QEMMS KIBBLE BALANCE

Rafael Marangoni[1], Darine Haddad[1], Frank Seifert[1,2], Leon Chao[1], David Newell[1] and Stephan Schlamminger[1]
[1]Fundamental Electrical Measurements Group
National Institute of Standards and Technology
Gaithersburg, MD, United States of America
[2]Joint Quantum Institute
University of Maryland
College Park, MD, United States of America

INTRODUCTION

The Quantum Electro-Mechanical Metrology Suite (QEMMS) is being designed at the National Institute of Standards and Technology. It provides measurements of the three mechanical standards of time, length and mass and three quantum standards of voltage, resistance, and current, all traceable to the International System of Units (SI). The system features a Kibble balance, a programmable Josephson voltage standard and a graphene based quantum Hall resistance standard. The QEMMS Kibble balance will be used to measure masses with nominal values up to 100 g with relative uncertainties lower than 2×10^{-8}.

In a Kibble balance, the weight of a mass is compared to the force generated by an electromagnetic actuator [1,2]. The actuator is composed by a coil inside a permanent magnet system. When a current I flows in the coil, a force proportional to the gradient of the magnetic flux Φ through the coil is produced. The electric current in the coil is adjusted in a way to compensate the weight of the mass m, which must be determined:

$$mg = -\frac{\partial\Phi}{\partial z}I \qquad (1)$$

where g represents the local free fall acceleration and z represents the position of the coil inside the permanent magnet system. This phase of the measurement is known as the weighing mode.

In a separate experiment, the coil is moved with constant velocity v and, due to the faraday law of induction, an electrical voltage u is induced such that:

$$u = -\frac{\partial\Phi}{\partial z}v \qquad (2)$$

This phase of the measurement is known as velocity mode. By combining expressions (1) and (2) the following equation for the mass measurement can be obtained:

$$m = \frac{Iu}{gv} \qquad (3)$$

The electric current I is normally determined by measuring the voltage drop on a reference resistor, the voltage u is measured by using a Josephson voltage standard, the local free fall acceleration g is measured by using an absolute gravimeter and the velocity v is measured by using a laser interferometer.

BALANCE DESIGN

The mechanism is a fundamental part of the balance design. In a Kibble balance, it has basically two functions: provide a force comparison system during weighing mode and provide a moving system during velocity mode. In some balances, both functions are performed by the same mechanism and, in other cases, there are two different mechanisms dedicated to each function. For instance, the Kibble balance of the National Institute of Standards and Technology NIST-4, uses a wheel with a knife edge for realizing the motion during the velocity mode and also for measuring the forces during weighing mode. The Kibble balance of the Laboratoire National de Métrologie et d'Essais (LNE) uses two different mechanisms for velocity and weighing modes: A compliant mechanism is used to move the whole weighing system during the velocity mode. The weighing system is composed of a beam balance suspended by flexure strips. There are different requirements for the moving and weighing mechanisms. During the velocity mode, it is desired to have a linear motion with predetermined velocity, direction and range of motion. In this case, positioning precision is more important. During the weighing mode, it is desired to have a mechanism capable of measuring forces with low uncertainty.

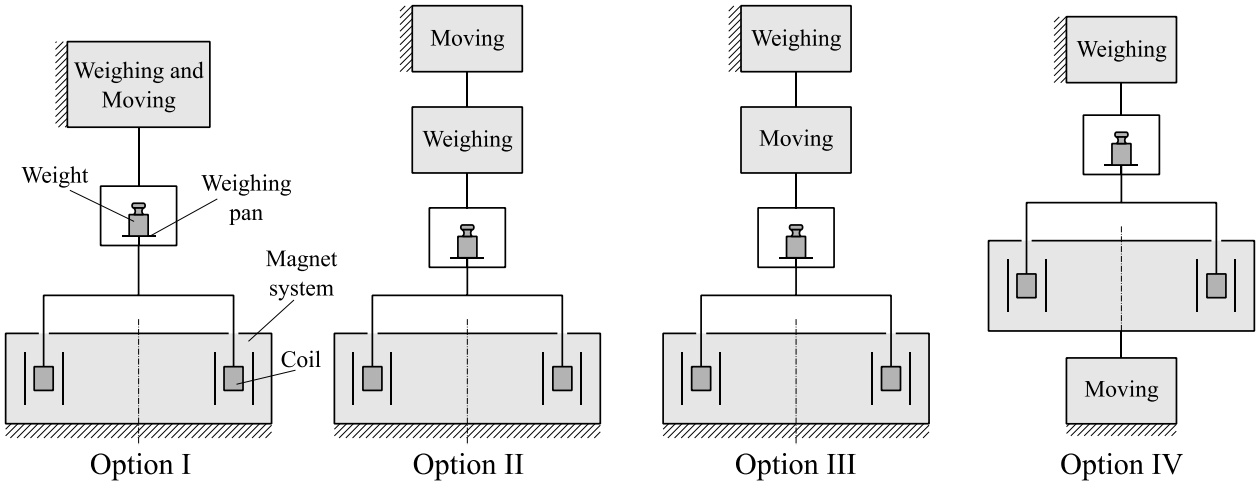

Figure 1: Different options for the balance design considering the location of weighing and moving mechanisms. For option I both mechanisms are integrated and fixed, for option II the moving mechanism is fixed and the weighing mechanism is moveable, for the option III the weighing mechanism is fixed and the moving mechanism is moveable and for option IV both weighing and moving mechanisms are fixed. In the last case, the moving mechanism is attached to a moveable magnet system.

Mechanism nonlinearities related to hysteresis must be avoided in this case.

There are several options for the balance mechanism available in the literature. The National Metrology Institutes of Canada, China, France, Germany, New Zealand, South Korea, Switzerland, United Kingdom, United States of America and Turkey work on the development of Kibble balances that use different designs. Figure 1 shows the basic structures of the designs. All designs are basically composed by a weighing system, a moving system, a load pan and a permanent magnet system with a coil. For the Kibble balances of the National Institute of Standards and Technology (NIST, USA), the National Research Council (NRC, Canada), the National Physical Laboratory (NPL, United Kingdom), the Physikalisch-Technische Bundesanstalt (PTB, Germany) and the Measurement Standards Laboratory (MSL, New Zealand), the weighing and moving mechanisms of the balance are integrated. The NIST and NRC Kibble balances use a knife edge for performing both weighing and moving tasks, the NPL and the PTB balances use flexure hinges and the MSL balance uses a piston mechanism for both tasks. The Kibble balances of the Korea Research Institute of Standards and Science (KRISS, South Korea), the LNE and the Federal Institute of Metrology (METAS, Switzerland) use a fixed moving mechanism and a moveable weighing mechanism (option II). The KRISS and METAS balances are based on commercial weighing cells while the LNE balance uses a beam balance supported by flexure strips. The moving mechanisms of the LNE and METAS balances are based on compliant mechanisms with flexures and the KRISS balance uses a piston guide to move the weighing cell and the coil. The Kibble balances of the Bureau International des Poids et Mesures (BIPM, in France) and the National Institute of Metrology (NIM, China) use a fixed commercial weighing cell as weighing mechanism. The BIPM balance uses an electrostatic motor to move the coil and the NIM balance uses a piezoelectric ceramic actuator. The Kibble balance of the Ulusal Metroloji Enstitüsü (UME,

Table 1: Different mechanisms for the Kibble balance with respective type, weighing system and moving system. The abbreviations used are weighing cell (WC), piston mechanism (PM), knife edge (KE), flexures (FL), electrostatic motor (EM), piston guide (PG) and piezoelectric ceramic (PC).

Laboratory	Type	Weighing System	Moving System
BIPM	III	WC	EM
KRISS	II	WC	PG
LNE	II	FL	FL
METAS	II	WC	FL
MSL	I	PM	PM
NIM	III	WC	PC
NIST	I	KE	KE
NPL	I	FL	FL
NRC	I	KE	KE
PTB	I	FL	FL
UME	IV	WC	PM

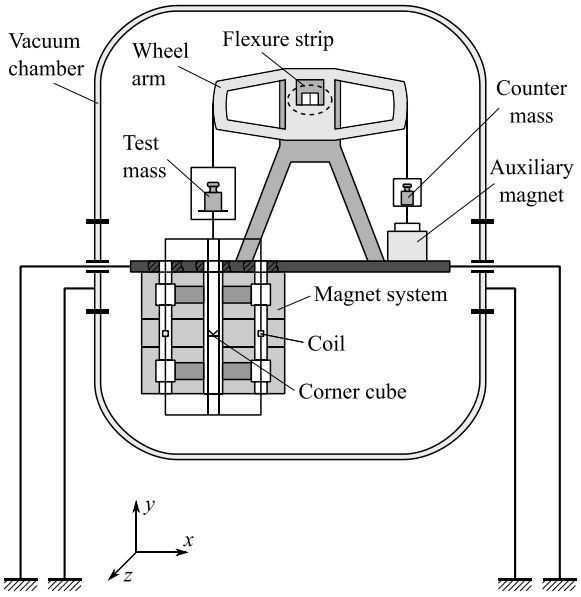

Figure 2: Preliminary design for the QEMMS Kibble balance.

Turkey) uses a fixed commercial weighing cell for the force measurement and a moving mechanism based on a piston mechanism to move the magnet system (option IV).

The Kibble balances of the National Metrology Institutes and the BIPM are listed in Table 1, together with the respective option types, weighing mechanisms and moving mechanisms.

An advantage of having both moving and weighing mechanisms integrated (option I), is the simple design of the balance. The Kibble balances used by the NIST and NRC for the measurement of the Planck constant before the last revision of the SI are of option type I. The mechanisms of both balances are based on knife edges, that have a great performance for mass measurement in the range of 1 kg. For measuring masses in the range of 100 g and lower, systems based on flexure hinges are normally used in commercial weighing cells to provide higher resolution.

Single flexure strips are being considered for realizing both weighing and moving mechanisms of the QEMMS Kibble balance. Flexure strips have been used in mass comparators since more than 30 years and exhibit a great performance. Figure 2 shows the planned design for the QEMMS Kibble balance. It is composed by a wheel arm supported by the flexure strip. This design is similar to the principle used in the NIST-4. The vacuum chamber and the balance structure are decoupled to avoid error influences caused by

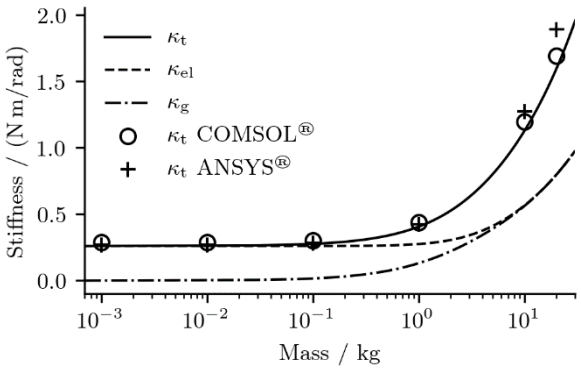

Figure 3: Results of analytic model and finite element analysis for single flexure strip.

vibrations in the chamber. The magnet system, which is described with more details later in this paper, is composed by two permanent magnets.

In the balance design, some components require special attention when specifying the manufacturing tolerances with the objective to reach the desired uncertainty for the mass measurement. These are the flexure strip, the wheel arm and the magnet system. The flexure strip should be ideally made of a single crystal material to avoid error influences caused by crystal defects. The surface quality and geometrical tolerances must be specified in way to obtain a precise motion in the velocity mode. The design tolerances for the wheel arm and band also have to be specified in a way to avoid parasitic motions of the coil during velocity mode. The magnet system must generate a uniform magnetic field stable in time. For this reason, the components of the magnet system must be machined precisely, and a very stable magnetic material must be used for the permanent magnets.

FLEXURE STRIP

The biggest challenge in using flexure strips in a Kibble balance is the possible hysteresis caused by the high deflections during the velocity mode. The hysteresis effect caused by anelasticity in flexure strips is analyzed in [3]. In this paper, the basic equations for modelling flexure strips are described. For instance, the torsional stiffness in the ***z*** direction is given by the following expression:

$$\kappa_t = \frac{W}{\alpha}\coth \alpha L \tag{4}$$

where W represents the load force and L is the flexure length. The quantities α and H are given by the following expressions:

$$\alpha^2 = \frac{W}{EH} \tag{5}$$

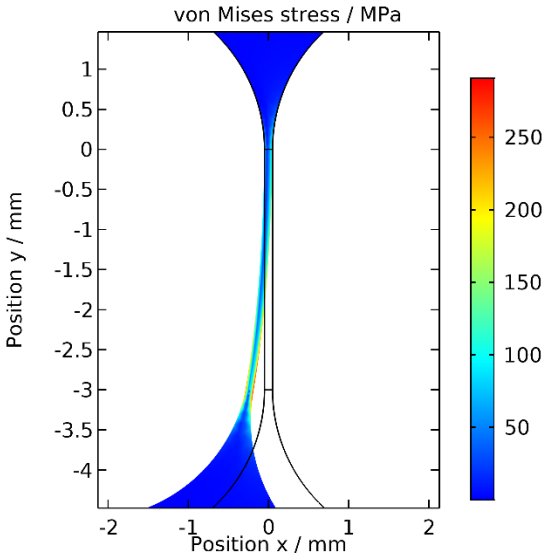

Figure 4: Finite element analysis for a single flexure strip. This flexure can be used to support the beam balance during weighing mode and realize the motion during velocity mode. Deformation exagerated by a factor of 2.

$$H = \frac{bt^3}{12} \tag{6}$$

with the Young modulus given by E, the flexure thickness given by t and flexure width given by b. Equation (4) represents the total stiffness in the flexure, which is given by the sum of the elastic and gravitational terms. These terms are respectively:

$$\kappa_{\mathrm{el}} = \frac{W}{2\alpha}\left(\coth \alpha L + \frac{\alpha L}{\sinh^2 \alpha L}\right) \tag{7}$$

$$\kappa_{\mathrm{g}} = \frac{W}{2\alpha}\left(\coth \alpha L - \frac{\alpha L}{\sinh^2 \alpha L}\right) \tag{8}$$

The gravitational term represents the contributions to the stiffness related to the gravitational potential energy. For load masses smaller than 100 g, this component is almost zero. For higher masses, this component increases and becomes as significative as the elastic stiffness term. The elastic term is caused by the elasticity of the flexure material and is related to the elastic potential energy.

Figure 3 shows results obtained with the equations (4), (7) and (8) together with simulation results of finite element analysis software. In this plot, the torsional stiffness in *z* direction is shown as a function of the load mass in the flexure. For masses lower than 1 kg, the elastic term of the stiffness is dominant. For higher masses, the gravity term becomes as significant as the elastic

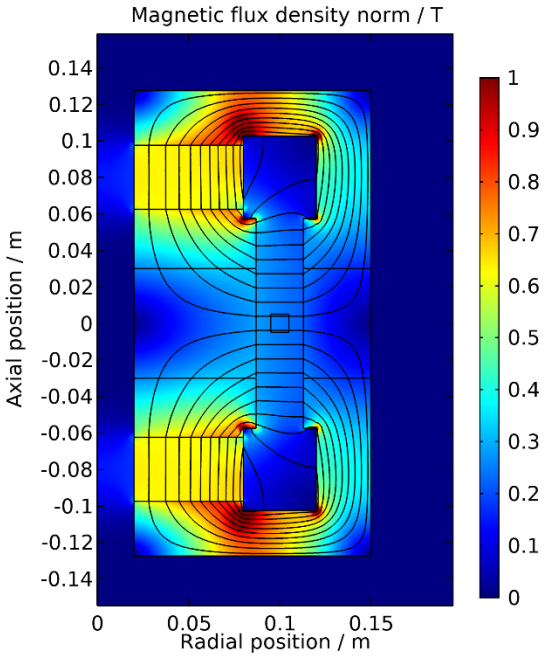

Figure 5: Finite element analysis for the permanent magnet system used in the QEMMS Kibble balance.

term. There is also a relatively good agreement between the results from analytic model and simulation.

During the design of the flexure strip for the QEMMS Kibble balance, some basic requirements must be considered. That includes a resolution of 0.2 µg for the mechanism, an amplitude of motion of ±2.5 cm for the coil in *y* direction and a load of 5 kg in the flexure. During operation, the stresses must remain lower than the material yield strength in order avoid plastic deformations and the residual motions must be minimized for the velocity mode. Figure 4 shows a result of finite element analysis for a monolithic flexure strip made of Beryllium Copper. The width and thickness used for the simulation are 20 mm and 100 µm, respectively. The stresses in the flexure for the maximal deflection are lower than 300 MPa. The yield strength for the alloy used in the flexure is expected to be at least 1200 MPa. In this case, the maximal stresses are about 25% of the yield strength.

MAGNET SYSTEM

The magnet system is responsible for generating the magnetic flux in the region where the coil is located. Figure 2 shows the magnet system in the balance. In order to obtain measurements within the required uncertainty, it is necessary to keep

the magnetic flux stable in time and minimize the back action of the coil current in the magnet. This back action is the influence of the coil current in the magnetic flux generated by the permanent magnet system. In the coil region, a radial magnetic field with small gradient in *y* direction is also necessary.

For the QEMMS, a magnet system like the one of the NIST-4 Kibble balance [2] will be used. This design is similar to the magnet of the BIPM Kibble balance [4]. It is composed by two permanent magnets with opposite magnetization directions and a yoke made of soft steel. A simulation result showing the magnetic flux density in the magnet is present in Figure 5. The radial flux density in the air gap is about 0.24 T and the air gap width is 2.6 cm.

There are basically two main advantages of the magnet system when compared to the NIST-4 magnet: the reduction of the forces necessary to split the magnet and access the coil, and the lighter design. The split forces for the new magnet are almost 20 times smaller and the system is about 8 times lighter than the NIST-4 magnet. In this way, it is possible to integrate the magnet splitter in the balance and simplify the operation.

CONCLUSIONS

The main design aspects of the QEMMS Kibble balance were described, including the mechanisms for both velocity and weighing mode and the permanent magnet system. The most important requirements for these systems are described and a short performance evaluation is provided.

DISCLAIMER

This article is authored by employees of the U.S. federal government and is not subject to copyright. Commercial equipment and materials are identified in order to adequately specify certain procedures. In no case does such identification imply recommendation or endorsement by the National Institute of Standards and Technology, nor does it imply that the materials or equipment identified are necessarily the best available for the purpose.

REFERENCES

[1] Robinson I A, Schlamminger S. The watt or Kibble balance: a technique for implementing the new SI definition of the unit of mass. Metrologia 53, A46-A74, 2016.

[2] Haddad D, Seifert F, Chao L S, Possolo A, Newell D B, Pratt J R, Williams C J, Schlamminger S. Measurement of the Planck constant at the National Institute of Standards and Technology from 2015 to 2017. Metrologia 54, 633-641, 2017.

[3] Speake C C. Anelasticity in flexure strips revisited. Metrologia 55, 114-119, 2018.

[4] Li S, Bielsa F, Stock M, Kiss A, Fang H. A permanent magnet system for Kibble balances. Metrologia 54, 775-783, 2017.

EFFICIENT INTERPOLATOR WITH MINIMAL FEEDRATE FLUCTUATION FOR PARAMETRIC TOOLPATH

Jiali Jiang[1], Fuyan Lin[1], Yong Zhang[2], Hui Zhang[2], Peiqing Ye[2]

[1] Department of Mechanical Electronic & Information Engineering
China University of Mining & Technology
Beijing, China
[2]Department of Mechanical Engineering
Tsinghua University
Beijing, China

INTRODUCTION

With the development of CAD/CAM technology, traditional linear and circular interpolation cannot meet the requirements of modern CNC machining in grinding apparatus, aviation and other fields. In order to process complex surfaces, parametric toolpath has played an important role in altering the traditional interpolation methods of small straight-line segment approximating parametric curves [1].

There are several methods proposed for spline interpolation. Traditionally, Taylor expansion method is the most widely applied in interpolation, which could obtain the next interpolation parameter and then calculate the actual interpolation points. However, because of the non-linear correspondence between the curve arc length and the parameters, there is deviation during parameters calculation by means of Taylor formula according to the chain derivation as follows:

$$\dot{s} = \frac{ds}{dt} = \| \mathrm{r}'(u) \| \cdot \frac{d\hat{u}}{ds_d} \cdot \frac{ds_d}{dt} = \| \mathrm{r}'(u) \| \cdot \frac{d\hat{u}}{ds_d} \cdot \dot{s}_d \quad (1)$$

Where s is arc length of the curve, $\dot{s}$ is the actual feedrate value at the moment, and $\hat{u}$ is the curve parameter estimated from the numerical method. Because of the existing nonlinear mapping, $\| \mathrm{r}'(u) \| \cdot (d\hat{u} / ds_d)$ is not equal to one. Besides, in the Eq. (1), s_d is the arc length determined by expected feedrate at the moment, which means $s_d = v_k^* T_s$. When the curve is interpolated, there exists the problem of replacing arc length with chord length. Meanwhile, it is inevitable to find the deviation between expected feedrate and actual feedrate, which could bring the feedrate fluctuation. As shown in the Figure 1 [2].

Due to the reason above, the actual feedrate could be calculated by the arc length and the interpolation period $v_k = \left| \mathrm{r}(u_{k+1}) - \mathrm{r}(u_k) \right| / T_s$.

$$\varepsilon = \frac{\left| v_k^* - v_k \right|}{v_k^*} \times 100\% \quad (2)$$

For minimal feedrate fluctuation, it only needs to find u_{k+1} to establish $f(u) = 0$ in Eq. (3). However, the theoretical solution of the formula is much complex.

$$f(u) = \left\| \mathrm{r}(u) - \mathrm{r}(u_k) \right\| / v_k^* - T_s = 0 \quad (3)$$

The Newton iterative method (CTA) is adopted in most common numerical methods. The iteration process is given as Eq. (4). And the initial value of iteration can use the curve parameter obtained from the traditional Taylor formula.

$$\begin{aligned} &do: \\ &t_i = t_{i-1} - \frac{f(t_{i-1})}{f'(t_{i-1})}, i = 1,2,3\cdots \\ &v_i = \left\| \mathrm{r}(t_i) - \mathrm{r}(u_k) \right\| / T_s \\ &until: \left| \frac{v_k^* - v_i}{v_k^*} \right| \le \varepsilon \\ &then: u_{k+1} = t_i \end{aligned} \quad (4)$$

Where t_i is the parameter obtained at the i th iteration for calculating the curve parameter u_{k+1}, v_i is the estimated feedrate at the i th iteration. ε is the upper bound of the given feedrate fluctuation. If using a constant M to replace $f'(t_{i-1})$, simple Newton iterative method (SCTA) avoids the derivative calculation, but its convergence property is related to the selection of constant M. In addition, it could only ensure linear convergence and not improve calculating efficiency [3].

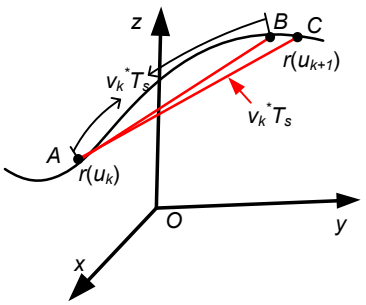

Figure 1. Replacing arc length with chord length

STEFFENSEN-ITERATIVE-ACCELERATOR INTERPOLATOR

In order to get higher efficiency, the convergence order needs to be increased on the basis of ensuring the accuracy. Therefore, the Aitken accelerated iteration algorithm is introduced. If x_k is the predicted value of x^*, x_k is corrected by iterative formula for the first time as follows:

$$x_{k+1} = f(x_k) \tag{5}$$

If $f'(\zeta)$ varies little in the interval, the estimated value is L. ξ is between x_k and x^* by the mean value theorem.

$$x_{k+1} - x^* = f'(\xi)(x_k - x^*) \approx L(x_k - x^*) \tag{6}$$

x_k is corrected again as follows:

$$\begin{aligned} x_{k+2} &= f(x_{k+1}) \\ x_{k+2} - x^* &\approx L(x_{k+1} - x^*) \end{aligned} \tag{7}$$

Generally, the right side of the equation is regarded as the new approximate value of x^*, which could be written as $\bar{x}_{k+1}$, so we can derive Aitken accelerated iteration expression.

$$\bar{x}_{k+1} = x_k - \frac{(x_{k+1} - x_k)^2}{x_{k+2} - 2x_{k+1} + x_k} \tag{8}$$

Steffensen Iterative Accelerator (SIA) could be defined with fixed point iteration on the basis of the Aitken iteration accelerator in Eq. (9).

$$x_{k+1} = x_k - \frac{f^2(x_k)}{f(x_k + f(x_k)) - f(x_k)} \tag{9}$$

The interpolation result of the first-order Taylor formula could be utilized as the iteration initial value of SIA method. Furthermore, the second order convergence of SIA method is demonstrated:

$f(x_k)$ is developed through the Taylor formula of Peano remainder as follows:

$$f(x_k) = f'(x^*)e_k + 0.5f''(x^*)e_k^2 + o(e_k^2) \tag{10}$$

$f(x_k + f(x_k))$ is developed through the Taylor formula of Peano remainder:

$$\begin{aligned} f(x_k + f(x_k)) &= f'(x^*)[e_k + f(x_k)] \\ &+0.5f''(x^*)[e_k + f(x_k)]^2 + o(e_k^2) \end{aligned} \tag{11}$$

Then Eq. (11) minus Eq. (10) as follows:

$$\begin{aligned} f(x_k + f(x_k)) - f(x_k) &= f'^2(x^*)e_k \\ &+0.5(3 + f'(x^*))f'(x^*)f''(x^*)e_k^2 + o(e_k^2) \end{aligned} \tag{12}$$

Supposed that the first-order and second-order derivative of $f(x^*)$ are written as f', f'' respectively, Eq. (12) could transform Eq. (13).

$$\begin{aligned} &\frac{f(x_k + f(x_k)) - f(x_k)}{f(x_k)} = \\ &\frac{f'^2 + 0.5(3 + f')f'f''e_k^2}{f'(x^*) + 0.5f''e_k} + o(e_k) \end{aligned} \tag{13}$$

In order to prove the second-order convergence of $f(x)$, we only need to guarantee that Eq. (14) has boundary.

$$\lim_{k\to\infty} \frac{x_{k+1} - x^*}{(x_k - x^*)^2} = \lim_{k\to\infty} \frac{e_{k+1}}{e_k^2} \tag{14}$$

After analyzing above, e_{k+1} could be written as follows:

$$\begin{aligned} e_{k+1} &= x_{k+1} - x^* \\ &= x_{k+1} - x_k + x_k - x^* \\ &= \frac{0.5(1 + f'(x^*))f'(x^*)f''(x^*)e_k^2 + o(e_k^2)}{f'(x^*) + 0.5f''(x^*)e_k} \\ &= \frac{f'^2(x^*) + 0.5(3 + f'(x^*))f''(x^*)e_k}{f'(x^*) + 0.5f''(x^*)e_k} + o(e_k) \end{aligned} \tag{15}$$

When $k \to \infty$, we substitute Eq. (14) and Eq. (15) into Eq. (16) as follows:

$$\lim_{k\to\infty} \frac{x_{k+1} - x^*}{(x_k - x^*)^2} = \lim_{k\to\infty} \frac{e_{k+1}}{e_k^2} \tag{16}$$

There is an upper boundary in Eq. (16), so SIA method could ensure the second-order convergence at least.

Combined with curve interpolation process, the SIA method with minimal feedrate fluctuation is presented. As shown in Eq. (17):

$$\begin{aligned} &y_i = f(t_{i-1}), z_i = f(y_i + t_{i-1}) \\ &t_i = t_{i-1} - \frac{y_i^2}{z_i - y_i} \\ &v_i = \frac{\|r(t_i) - r(u_k)\|}{T} \\ &until: \frac{|v_i - v^*|}{v^*} \le \varepsilon, \ then: u_{k+1} = t_i \end{aligned} \tag{17}$$

SIMULATION VALIDATIONS

It is from the previous demonstration that the interpolation on the basis of SIA method is equipped with the second-order convergence. Besides, there is no curve derivation calculation during the process, which could converge to the expected value faster.

In this section, we make comparison among SIA method, Newton iterative method, simple Newton iterative method, the second-order Taylor formula method and the first-order Taylor formula method. A cat-shaped in Fig. 2 (a) formed from third-degree B-spline curves is utilized to test the interpolation accuracy and efficiency. Figure 2 (b) is the feedrate profile calculated from interpolation points.

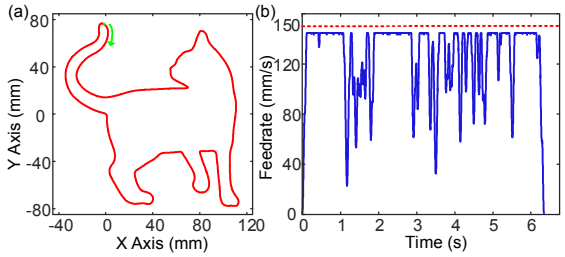

Figure 2. Parametric toolpath for simulations and feedrate fluctuation

The feedrate fluctuation in Fig. 3 is calculated from Eq. (2) by means of the traditional Taylor formula. Figure 3(a) shows that the first-order Taylor interpolation could lead to apparent feedrate fluctuation and worse machining accuracy. Furthermore, when Taylor formula is used to calculate arc length, the more curved the trajectory is, the bigger truncation error is. As a result, the feedrate fluctuation becomes more and more apparent. Compared with the first-order Taylor interpolation, the second-order Taylor interpolation could reduce feedrate fluctuation evidently in the Fig. 3(b). Nevertheless, the feedrate fluctuation of the large curvature is still not satisfied, which causes that desired machining results are difficult to achieve.

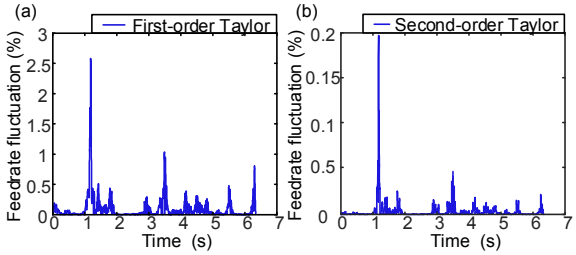

Figure 3. Feedrate fluctuation comparison of Taylor interpolation methods

In order to test performance of algorithms, the constraint value of the feedrate fluctuation is set as $\varepsilon = 0.0001\,\%$. The feedrate fluctuation curves are obtained from SIA method, CTA method and SCTA method in Fig. 4. We could discover that the feedrate fluctuation value of all interpolation points meets anticipated restraint.

In contrast to the SIA method, we should pay attention to the calculation efficiency of the five methods mentioned in this section. When computational load is reduced, hard real-time task of interpolation is executed easily in motion control system. The relative calculation efficiency of the other four interpolation methods is defined as Eq. (18), where t_i^{SIA} is the time spent on the ith interpolation point calculation.

$$\eta = \frac{t_i - t_i^{SIA}}{t_i^{SIA}} \times 100\% \tag{18}$$

Time consumed by CTA method is related to SIA method at each interpolation points as shown in Fig. 5 (a). We could find that the average time spent by CTA method is 1.48 times consuming of SIA method. Because convergence rate of SIA method is faster than the equivalent of CTA on each interpolation points. In Fig. 5 (b) SCTA method is worse than SIA method in terms of calculation efficiency. The average time of each point is 1.39 times longer than SIA method. When constant M is selected inappropriately, convergence rate will be reduced.

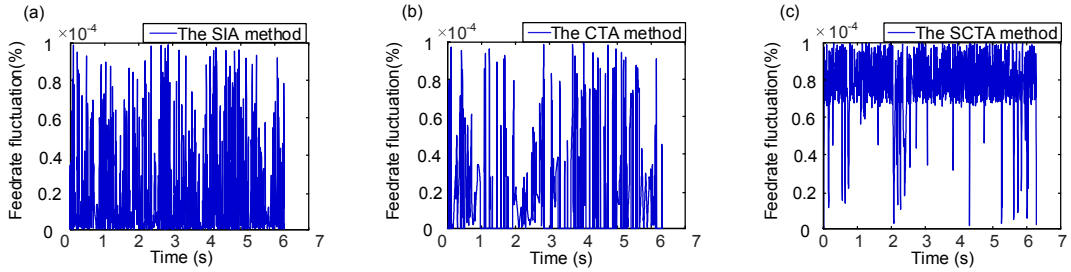

Figure 4. Feedrate fluctuation comparison of feedback interpolation methods

In order to show iteration step from one interpolation point to the next point, Fig. 5 (c) and Fig. 5 (d) compared SIA method with CTA method and SCTA method respectively. Iteration step is one of factors affecting efficiency, the calculation time of each step is also an important factor. In Fig. 5 (c), the initial value of CTA is closer to the actual value, so the iteration steps is less than SIA steps but every iteration period needs to calculate derivative in CTA method. In Fig. 5 (d), there is not derivative calculation in SIA method and SCTA method, therefore, step is a main factor, iteration step of SIA method is less than SCTA method's significantly.

Similarly, we would compare SIA method with two typical Taylor interpolation methods. On the one hand, as shown in Fig. 6 (a), the first-order Taylor interpolation method only calculates the first-order derivative. However, the apparent feedrate fluctuation is not allowed in the actual machining. On the other hand, as shown in Fig. 6 (b), the second-order Taylor interpolation method needs more complicated calculation with second-order derivative. Therefore, comparing with SIA method, the calculation efficiency of the second-order Taylor interpolation method just rises by 0.75%, which is not extremely obvious. Moreover, the average time of each point is shorter 0.99 times. But there is strict limit of feedrate fluctuation by means of SIA method.

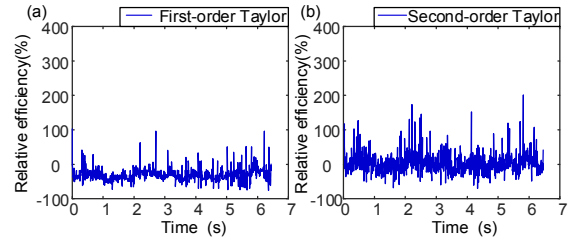

Figure 6. Relative calculation efficiency of Taylor interpolation methods

CONCLUSION

In this paper, a feedrate feedback interpolation algorithm based on Steffensen iterative acceleration is presented. The parametric toolpath interpolation is optimally designed to guarantee the minimal feedrate fluctuation, and rapid convergence and the second-order convergence is proved theoretically. Compared with previous interpolation methods in literature, the proposed method has the following advantages:

(1) The minimal feedrate fluctuation is constrained rigorously in parametric toolpath interpolation process. (2) While improving the convergence speed, the strict convergence is ensured. (3) The algorithm avoids the derivative computation, so computational load is reduced and hard real-time task of interpolation is executed easily in motion control system. Eventually, the proposed method is validated by simulations and compared with Taylor expansion method, Newton iterative method and simple Newton iterative method in feedrate fluctuation and computational efficiency respectively. In conclusion, this interpolator is suitable for the CNC machine tool with high feedrate and high precision.

REFERENCES

[1] Cheng C W, Tsai M C. Feedrate control for non-uniform rational B-spine motion command generation, Proceeding of the Institution of Mechanical Engineers, Part B: Journal of Engineering Manufacture, 2006; 220(11): 1855-1861.

[2] Huan Zhao, LiMin Zhu. A parametric interpolator with minimal feed fluctuation for CNC machine tools using arc-length compensation and feedback correction. International Journal of Machine Tools & Manufacture, 2013; 75: 1-8.

[3] Michele Heng, Kaan Erkorkmaz. Design of a NURBS interpolator with minimal feed fluctuation and continuous feed modulation capability. International Journal of Machine Tools & Manufacture, 2010; 50: 281-293.

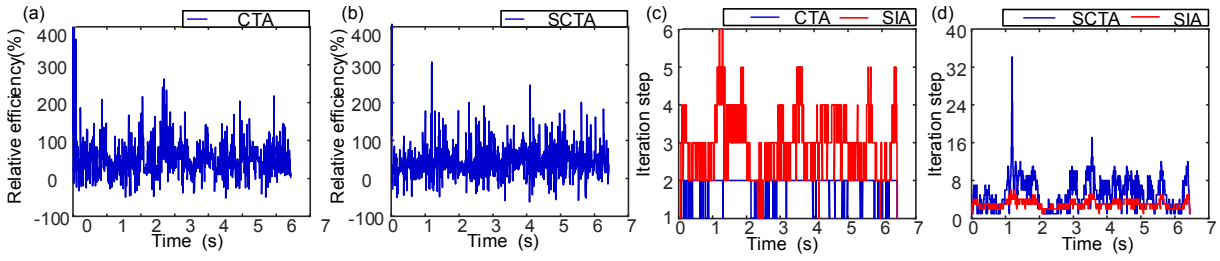

Figure 5. Relative calculation efficiency and iteration step of CTA method and SCTA method

.

Ultra-Precision Angle Sensors and Multi-Axis Closed-Loop Control

Edward Dowski, Jr, Gregory Johnson, Nelson Claytor
Ascentia Imaging, Inc., 3133 Indian Road, Boulder, Colorado 80303

INTRODUCTION

The concept of six degree-of-freedom closed-loop control for general positioning is often difficult to implement due to the lack of real-time independent measurements of position and orientation or at a cost that a broad application can tolerate. With real-time, ultra-precise and low-cost error measurements, a new class of multi-axis positioning systems can dynamically respond to changes in applied forces, wear, environment, etc.

We are proposing a new class of general positioning enabled by low-cost and ultra-precise angle measurement sensors that have been developed for commercial, industrial and military applications. These angle measurement sensors measure the angle between the sensor (or receiver / Rx) and remote targets (or transmitters / Tx) to arc-second precision. By measuring the angles to multiple Tx's or with multiple Rx's six degree-of-freedom position and orientation measurements can be made. The Rx's are composed of molded precision optical modules, specialized coding masks, analog optical detectors and digital processing. The Tx's are simple off-the-shelf LEDs or laser diodes, possibly including retro-reflectors. The actual precision of these sensors is essentially user-defined through signal strength or signal-to-noise-ratio or SNR. We call the general technology "Angle Coding" and the particular products Accu-Arc sensors.

Ultra-precise angular sensors can be used in a wide range of applications including:

- Navigation/localization of autonomous vehicles or handheld tools in controlled environments
- Localization of distant targets/tools relative to a fixed reference system
- Ultra-precise measurement/localization of distant objects via laser scanning
- High-speed, ultra-precise and low-cost closed-loop control of positioning systems. Angular positioning systems for example can be configured to reach angular precision of micro radians or tenths of arc seconds with kHz bandwidths.

Some characteristics of our Accu-Arc receivers are shown in Figure 1. The nominal Rx contains an optical module, analog and digital processing electronics and fits within a roughly 4.5 cm cube. The volume of the optics module is only about 1 cm^3 and so significantly more compact packaging is possible. The nominal angular precision can be about 4 arc seconds, depending on system SNR. The FOV is +/- 20 degrees. The nominal system update rate is 100 Hz although much higher speeds are possible. Targets (or Tx's) consist of 950nm modulated LEDs, laser diodes or reflected modulated light from laser scanning systems or retro-reflectors. Sixteen independent targets can be simultaneously measured.

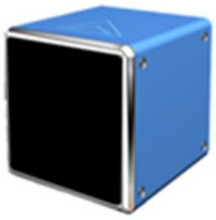

Angular Precision	≥ 4 arc seconds (nominal)
Field of View	± 20 degrees
Update Rate	≤ 100 Hz
Number of Targets	≤ 16
Illumination Wavelength	950 nm

FIGURE 1: Nominal Accu-Arc receiver or Rx.

An example of measured angular precision is shown in Figure 2. The measurement was via a back-and-forth motion of +/- 180 arc seconds (or +/- 0.05 degrees) with a 100 Hz update rate. With a nominal configuration a particular Accu-Arc system can achieve an angular precision of about 4 arc seconds (20 μ radians) or better (depending on the SNR). With other configurations for applications requiring much higher precision, 0.1 arc second (0.5 μ radians) precision can be enabled.

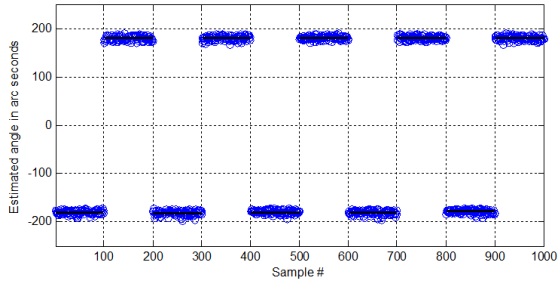

FIGURE 2: Example measured precision can be about 4 arc seconds (20 μ radians) for a nominal configuration with an update rate of 100 Hz. The black lines in Figure 2 represent the mean value of each section of estimates.

Angle Coding and Accu-Arc sensors are possible today because of a relatively recent convergence of ultra-precision optical array design, fabrication and assembly and advanced remote sensing theory and optimization. The Ascentia Imaging team pioneered many aspects of ultra-precision optical design, fabrication and assembly, including the development of wafer scale optics and cameras for the cell phone industry. The application of advanced radar techniques to what can be loosely called "cameras" was also pioneered by the Ascentia Imaging team, beginning in 1995.

SENSOR OPTICS AND DSP

Figures 3 and 4 describe the interior components of an Accu-Arc receiver. The major optical components from Figure 3 are the custom visible-block color filter, the 16 channel two-lens optical module, the light-absorbing lithographic intensity and optical NIR absorbing wedge masks and a 16-channel analog detector and trans-impedance amplifier board. Figure 4 shows the entire system assembled with the addition of an ADC board, processor board and I/O hardware.

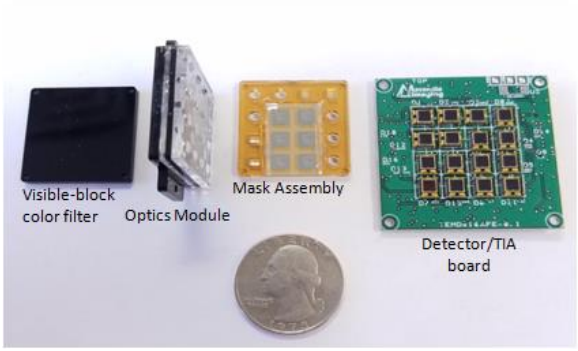

FIGURE 3: Optical assembly including analog single-pixel detectors.

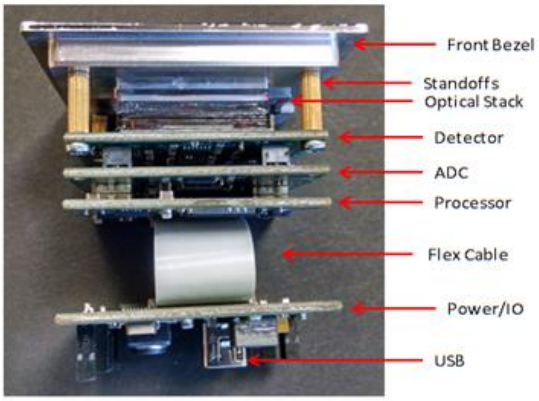

FIGURE 4: Optics with analog and digital electronics.

A summary of characteristics of the optical components include:

- Visible-block color filter: Custom dye formulation that acts as a high-pass optical color filter with cutoff at about 900nm. As the silicon detector has a steep cutoff at about 1000 nm, the combined color filter/detector has about a 100nm pass band.
- 16 channel optical module: 4x4 optical modules includes a first and second aspheric lens arrays and two spacers. Each optical channel is identical in the module and is designed so that the image of a point (or PSF) is a specialized form that acts with a lithographic intensity grating (as part of the mask assembly) positioned near the classical image plane to form sinusoidal intensity responses vs angle to a Tx. The aperture arrays, lens arrays, and spacers are all injection molded, and have molded self-aligning features that allow each component in each channel to be centered and spaced to better than 5μm relative to its

desired position. Both lens arrays and the color filter are AR coated.

- Mask assembly: Consists of a series of molded optical NIR optical absorbing "wedges" that act to form essentially linear intensity responses in NIR illumination vs angle to a Tx, and a series of NIR opaque lithographic gratings (seen as grey objects in the mask assembly in Figure 3). Since the alignment requirements for the lithographic gratings are even tighter than those for the other optical components, the gratings are actively aligned during the assembly process.
- 16 channel detector/TIA board: Single-pixel photon detectors, one for each of 16 optical channels, act to count the number of photons that are received through the optics after the intensity masks. Trans-impedance amplifiers, with gains of about 1M, act to maximize received SNR for weak Tx signals in the presence of strong interferers, like the sun, or at a maximum range. Negative DC feedback circuitry acts to prevent strong signals from circuitry bias or having the sun directly in the FOV of the Rx from saturating the ADC.

The unique nature of sensing angle-dependent intensity values enables sixteen orthogonal measurements that define a particular sensed angle. By comparing the measured values to calibration values, the measurements can then be used to estimate angle.

A conceptual view of the Accu-Arc Rx of Figure 4 is described in Figure 5. This view represents a slice through the 4x4 optical/digital structures. The completely custom analog optical front end consists of the visible-block color filter (CF), the lens arrays (L1 and L2), the spacer arrays (S1 and S2) and the mask assembly (Ma). The analog detector board (D/TIA) has a high-gain trans-impedance amplifier which prepares the analog signals for sampling. The digital section consists of off-the-shelf electrical components configured to convert the analog output from the D/TIA into digital form (A/D) and then process the resulting 16 channel digital stream into angle estimates.

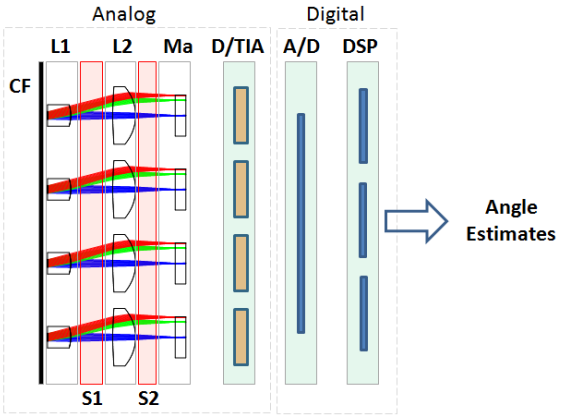

FIGURE 5: Layout of optical module and electronics.

The three sets of rays (colored blue, green and red) traced through the optics of Figure 5 represent the ray paths for three Tx's positioned boresight to the sensor, 14 degrees to the sensor and 20 degrees to the sensor. The two-lens system is designed so that the rays intersect the mask assembly close to perpendicular and with a specially designed form (or PSF) so that the response measured at the output of the detector/ TIA is sinusoidal with angle.

Figure 6 shows example normalized intensity responses vs angle of three channels of the Accu-Arc system. The mask assembly acts to make the output of each optical channel unique and orthogonal to each other as a function of angle to a Tx. The signals from what we call low frequency (LF) channels vary essentially linearly with angle. The signals from what we call high frequency (HF) channels vary sinusoidally with angle. The HF signals are purposely designed so that pairs of resulting signals from different optical channels are shifted 90 degrees relative to each other. Because of the specialized optics, signals from the two high frequency channels closely follow a cosine and sine form. Or, pairs of high frequency channels are orthogonal to each other in Tx angle space. This is a fundamental characteristic of Accu-Arc systems that directly leads to ultra-precise angular estimation.

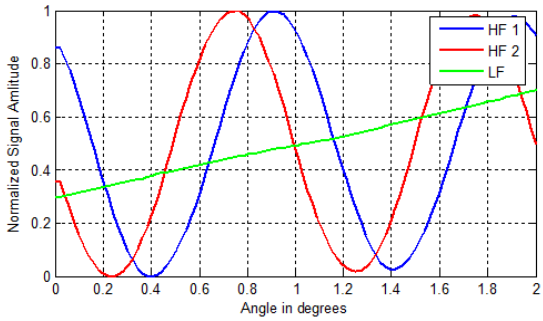

FIGURE 6: Normalized signals vs angular position on a Tx.

The HF channels in Figure 6 can be seen to have a much higher sensitivity vs angle than the LF channel. The HF channels in effect are responsible for high angular estimation precision, but with angular ambiguity. The LF channels are designed to un-wrap this angular ambiguity. The combination of LF and HF channels then enables high angular estimation precision over a wide FOV.

Another type of representation of the three curves of Figure 6 is shown in Figure 7. Instead of three 2D plots, Figure 7 shows the data plotted in 3 dimensions. Angle is now represented as position along a curve.

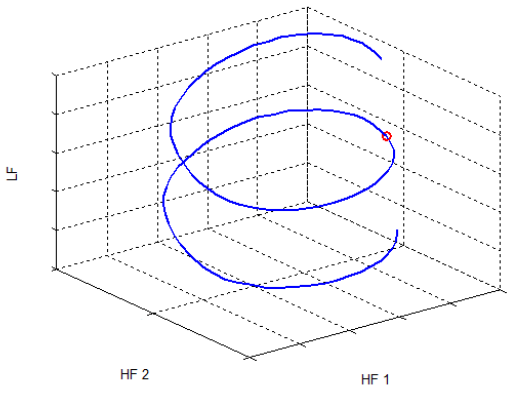

FIGURE 7: The curves of Figure 6 represented as a 3D plot.

Notice that the overall shape of this curve can generally be described as a “spiral” through 3 dimensions. There are two such spirals for 2D angular measurements. Any valid data from the 3 channels of Figure 6, over the same angular range, has to lie somewhere along this curve. The red circle of Figure 7, for example, represents the data of Figure 6 from the 1 degree point on the horizontal axis. Any invalid data, possibly due to reflections, dirt, dust, rain and snow, blocked apertures, other obstructions, etc. must lie significantly off this curve. This type of multi-channel configuration enables very fast and very precise digital detection and estimation.

MULTI-AXIS CLOSED-LOOP POSITIONING CONTROL

We are proposing that use of low-cost and precise angle sensors can enable a new class of close-loop control. In some cases, the main new aspect can be precision control with widespread affordability. Figure 8 describes a general layout of closed-loop positioning control.

With the actual position/orientation, a position/orientation error can be formed and the system commanded to reduce the error. With closed-loop control error reduction, or precision and accuracy, can then become an issue of degree-of-freedom position/orientation control and mechanical and electrical bandwidth rather than of positioning system mechanical stiffness.

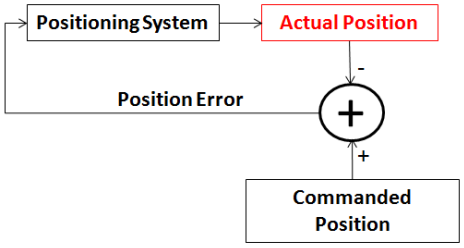

FIGURE 8: General layout of closed-loop position control. Actual position, with 6 degrees of freedom, can be available through Accu-Arc angle-measurement sensors.

Consider two rotation stages configured in a 2-axis gimbal positioning system, for a simple example (see Figure 9). This type of system can position an object via rotation in both the azimuth plane (or horizontal rotation) and elevation plane (or vertical rotation). Even if the single-degree of freedom of rotation is perfect for each stage, the actual precise 3D (or 6D) position/orientation of the mounted object is unknown and very likely far from that intended, if measured on a fine-enough scale. Even with open-loop calibration, the actual position/orientation is affected by mounting fixture(s) of the object, force and/or weight being applied to the stages, the speed and velocity of motion, environmental conditions etc.

How does even this simple 2-axis positioning system become more accurate, more precise and/or more affordable than commonly available today? Or, how can mechanical cost and complexity that translates into system stiffness be transferred to the relatively small cost and complexity of modern optics and electronics, while also increasing system performance? Modern Accu-Arc angle-measurement sensors offer one method of achieving next-generation precision positioning.

Figure 9 describes a conceptual and simplified 2-axis example gimbal system. This system has a fixture mounted near the 2D center of rotation. Mounted at a distance d from the center of rotation are two or more sets of LEDs or retroreflectors. Remote Accu-Arc angle-measurement sensors are mounted a distance R from the LEDs. The sets of LEDs enable 6DOF position and orientation estimates from the Rx's.

The sensors form a metrology frame that can be used to close the loop on the position of the axes relative to that metrology frame, significantly increasing the accuracy of positioning and orientation [1]. Because the metrology frame is stiff and provides a reference for the directly measured positions of the axes, the axes themselves do not require precise calibration, and do not require extreme stiffness to maintain that calibration. What can the measured angular precision of the object be with such a system layout?

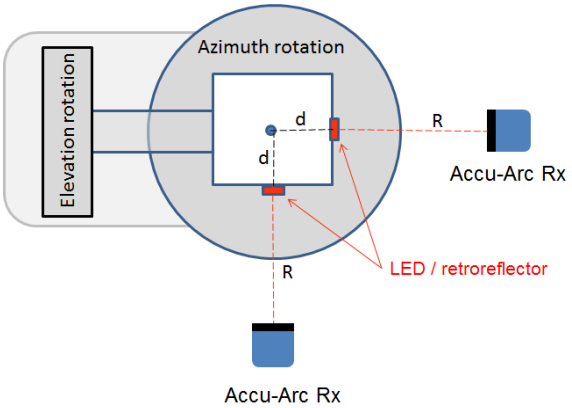

FIGURE 9: Example 2-axis gimbal positioning system.

Estimation theory and the Cramer-Rao Bound / Fisher Information [2] allows an understanding of the potential precision available to the commanded positioning of the rotational axes of Figure 9. These are the same theoretical estimation tools that are used to design Angle Coding systems.

If the standard deviation of the Accu-Arc Rx's angular measurements is $\sigma_{\text{Accu-Arc}}$, then the measured standard deviation of the commanded angle can be:

$$\sigma_{\text{axes}} \leq \frac{R}{d} \times \sigma_{\text{Accu-Arc}}$$

Or, the angular measurement precision of the axes of the system of Figure 9 can be linearly related to the angular precision of the Accu-Arc Rx's that are remotely measuring the angle to the LEDs or retroreflectors. The potential angular extent of the positioning axes of Figure 9 is (R/d) times the FOV of the Accu-Arc Rx. System design then entails the balancing of the physical dimensions (R/d), the update rate (Hz to khz), and geometry to suit the application. The nominal FOV, from Figure 1, is about +/- 20 degrees. Use of multiple Rx's can increase the FOV and thus angular extent.

There are a large number of possible configurations for even two-axis gimbal systems, often application-specific configurations, beyond that of Figure 9. LEDs/retroreflectors can be distributed throughout the system for ease of use as well as accurate position / alignment / orientation measurement. More than two Rx's can be used to enable larger motion of the stages along with compact form factors of the entire system. As the distance R for compact systems can be 1m or less, standard LED's and/or retroreflectors with laser diode sources can enable a broad range of SNR's and therefore very high potential precision for the novel Accu-Arc configurations. Variations in Accu-Arc Rx's such as simultaneous sampling of different Rx's and kHz update rates are possible.

CONCLUSIONS

Multi-axis closed-loop control with low-cost precision sensing has the potential to increase the performance and affordability of future positioning systems. With remote real-time position and orientation measurements the entire control system can be centered on mechanical and electrical bandwidth and less on classical calibrated open-loop control that relies on static calibration and stiffness in independent

axes. Accu-Arc angle measurement sensors can possibly enable such future systems.

REFERENCES

[1] Shawn P. Moylan, Bradley Damazo, and M. Alkan Donmez. Implementation of a Metrology Frame to Improve Positioning of Micro/Meso-Scale Machine Tools, 2009 Transactions of the North American Manufacturing Research Conference, 2009; 37: 573-580.

[2] Louis L. Scharf, Cédric Demeure. Statistical Signal Processing: Detection, Estimation, and Time Series Analysis. Addison-Wesley Publishing Company. New York: 1991

PRACTICAL FEEDFORWARD TECHNIQUES FOR ACCURATE DESKTOP 3D PRINTING

Alper Dumanli, Tucker Shannon, Shingo Tajima, Burak Sencer
School of Mechanical, Industrial and Manufacturing Engineering
Oregon State University
Corvallis, Oregon, USA

INTRODUCTION

The focus of modern manufacturing has been shifted from traditional subtractive, milling, turning, drilling processes, towards layer by layer additive (AM) techniques. Current rapid prototyping market is mostly dominated by low cost hobbyist applications that are geared towards production of polymer components. Amongst other polymer AM techniques, Fused Filament Fabrication (FFF) has been the most popular polymer printing method [1]. It can be easily implemented on cheap desktop printing platforms. In FFF, molten thermoplastic filament is fed through a printing head (nozzle) onto a movable printing stage. The stage (printing platform) is typically driven by low cost stepper motors. Similarly, the deposition is also controlled in an open-loop fashion through extruder feeder motor [1]. Quality and accuracy of the printed parts are greatly influenced by 1) positioning accuracy of the printing platform and 2) the deposition quality of the printing head/nozzle (feeder) system. This paper presents practical techniques to enhance quality of FFF desktop 3D printing by improving positioning accuracy of the motion platform and the feeder system.

Unwanted vibrations deteriorate positioning accuracy of modern motion systems. Similar effect is observed on cheap AM machines as well [2]. Motion of the printing platform is planned by conventional G-Code syntax [3]. As the platform accelerates during the printing process, it induces inertial vibrations to the flexible structure of the printer. These unwanted vibrations, in return, deteriorate part quality by creating surface waviness on the printed parts [4]. Notice that, since stepper motor systems are operated in open-loop, these vibrations cannot be dampened actively [2]. One way to avoid them is by modifying frequency spectrum of the acceleration/deceleration profiles of the reference trajectory.

On the other hand, the filament extrusion system is responsible for depositing desired amount of molten material. For accurate printing, material deposition rate should be synchronized with the feedrate, i.e. the tangential velocity of the motion stage. Once this synchronization is disturbed, excessive or insufficient material deposition is observed, which results in non-uniform print surface [3].

In this paper, two feedforward control methods are presented to avoid the adverse effects of structural vibrations and uneven material deposition. Firstly, a digital filter is designed to command filament deposition in synch with the printing velocity. Secondly, an FIR-based trajectory generation technique is implemented to generate smooth velocity profiles for the motion stage, which avoids exciting lightly damped structural modes of the 3D printer structure for accurate stage motion.

ACCURATE SYNCHRONIZATION OF MATERIAL DEPOSITION RATE

In FFF, the filament is fed through a heating chamber by a pinch wheel mechanism [1] driven by a stepper-motor, which is called the *Extruder Stepper Motor*. The filament is heated up to its melting temperature and extruded through a conical nozzle, and material is deposited onto the printing platform. Fig. 1 depicts a commercial printing head module system with its components. In order to deposit even polymer layers, material extrusion (deposition) rate must be synchronized with the velocity of the printing platform. For instance, constant deposition rate is required when the printing platform is moving at a constant speed (feed). On the other hand, when the printing platform undergoes acceleration/deceleration, the material deposition rate should also be modulated accordingly so that the material deposited on a unit area is kept unchanged.

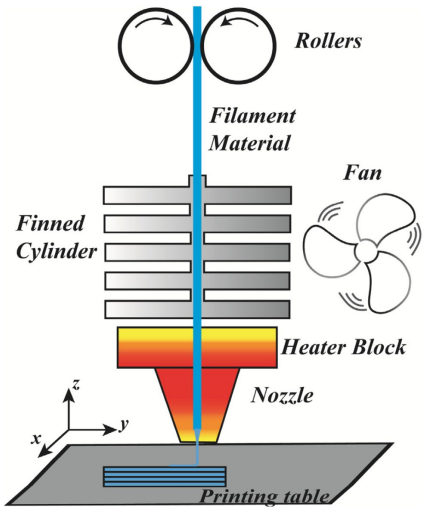

FIGURE 1: Illustration of a commercial printing head [3].

A practical way to synchronize the deposition rate with the stage motion is to command the extruder stepper motor speed linearly with the printing feedrate [3]:

$$v_E = \alpha v_T \tag{1}$$

where v_E and v_T are the extruder stepper motor speed and printing platform speed. α is simply the speed ratio between v_E and v_T that needs to be identified experimentally to attain desired layer width. On the other hand, the deposition rate (e_{des}) is a function of the extruder stepper motor speed v_E :

$$e_{des} = \beta v_E \tag{2}$$

where β is the geometric conversion ratio between angular displacement of the extruder stepper motor and the translational displacement of the filament while exiting the nozzle.

Notice that, above expressions (Eqs. (1) and (2)) are related to deposition rate through their geometric relationship, which is valid only at steady state operation. The dynamics of extrusion considering the thermomechanical and fluidic behavior of the liquefier [5] must be taken into account for accurate deposition rate control when the stage velocity changes rapidly. The dynamics between desired $e_{des}(t)$ and actual deposition rates $e(t)$ can be modeled by a first order delayed differential equation [5, 6] as:

$$e(t) + \tau \frac{de(t)}{dt} = e_{des}(t - \lambda)$$
$$\Downarrow \tag{3}$$
$$H(s) = \frac{E(s)}{E_{des}(s)} = \frac{1}{\tau s + 1}\exp(-\lambda s)$$

where $E(s)$ and $E_{des}(s)$ are the Laplace (s) domain representations of the actual and desired extrusion rates, respectively. τ is the *Extruder Time Constant* (ETC) representing the resistance to abrupt changes in the stepper motor displacements due to material properties of the filament such as viscosity and thermal conductivity [5, 6]. Finally, λ is the time delay between the initial displacement of the stepper motor and the extruded material. As a result of the dynamic behavior governed by $H(s)$, the deposited material resists to sudden changes in the extruder stepper motor displacement inputs. This poses a limitation on synchronization between actual extrusion rate and stage velocity, and therefore it restricts the achievable print quality. Specifically, the first order delayed dynamics between actual and desired deposition rated induces over and under deposition whenever the stage accelerates and decelerates. This can be best observed during printing of sharp corner. An example is shown in Fig 2. When the printing platform accelerates, layer deposition cannot start instantly, and thus under-extrusion occurs. Similarly, during cornering section (halfway through the motion) and at the end of the motion over-extrusion is observed.

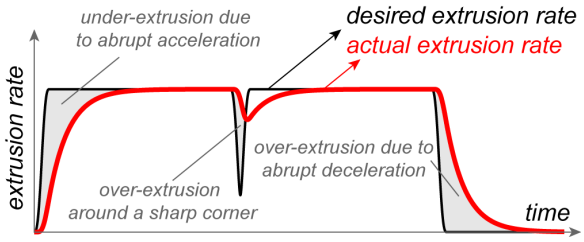

FIGURE 2: Extrusion dynamics on a sample cornering motion.

In order to mitigate adverse effects of excessive (over-deposition) or insufficient material (under) deposition, a feedforward (FF) filter is designed in this work to synchronize the actual deposition rate with the stage speed. The deposition FF filter is selected as $H^{-1}(s)$ from Eq. (3),

$$e_M(t) = e_{des}(t+\lambda_e) + \tau_e \frac{d}{dt}\left(e_{des}(t+\lambda_e)\right)$$
$$\Downarrow \qquad (4)$$
$$\frac{E_M(s)}{E_{des}(s)} = F(s) = \exp(\lambda_e s)(1+\tau_e s)$$

where $e_M(t)$ is the modified extrusion rate command. τ_e and λ_e are parameters of $H(s)$ from Eq. (3). Incorporating the deposition FF filter, the extrusion dynamics becomes:

$$\begin{aligned} E(s) &= E_{des}(s)F(s)H(s) \\ &= E_{des}(s)\frac{\tau_e s+1}{\tau s+1}\exp(-\lambda s)\exp(\lambda_e s) \\ &\simeq E_{des}(s) \end{aligned} \qquad (5)$$

Notice that filter the parameters τ_e and λ_e need to be tuned. In this work, this is achieved by a single printing experiment and described in the following section.

ON-THE-FLY TUNING OF DEPOSITION FILTER

A commercial Desktop 3D Printer (HICTOP Prusa i3) shown in Fig. 3 is used in experimental validation. Extrusion dynamics is first observed by printing a thin wall structure shown in Fig. 4.

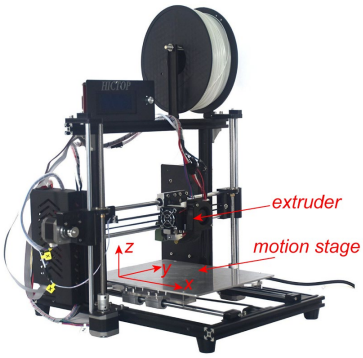

FIGURE 3: Commercial 3D Printer used in experiments.

Thickness of the structure is set equal to the extruder nozzle diameter (0.4 [mm]). 20 consecutive layers at a feedrate of 80 [mm/sec] are used for printing the structure up to the height of 4[mm]. Fig. 6.a shows the actual print quality when the existing setting of the printer used, which only uses steady-state based synchronization of deposition rate with the printing feedrate. The parameters of Eqs. (1) and (2) are identified as $\alpha\beta=0.0313$. Fig. 6.a indicates that, at the beginning of each layer, under-extrusion is dominant.

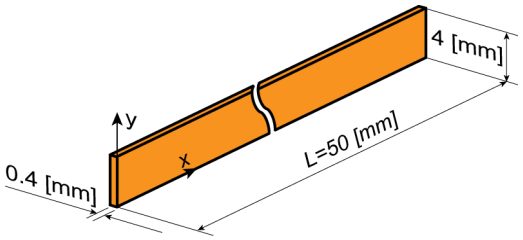

FIGURE 4: Thin walled print structure.

This is caused by the lag of the actual extrusion rate with respect to the axis velocity which changes rapidly due to initial tangential acceleration of the printing platform. The length of the inconsistent print (L_{inc}) in Fig. 6.a is measured to be 9.89[mm], which corresponds to the transient response of $H(s)$ to the extruder stepper motor velocity profile. The 1st order dynamics of the extruder dynamics is identified experimentally as follows.

The transient feedrate profile is considered in two phases (see Fig. 5):

i) Constant acceleration (trapezoidal velocity) phase
ii) Constant velocity (zero acceleration) phase.

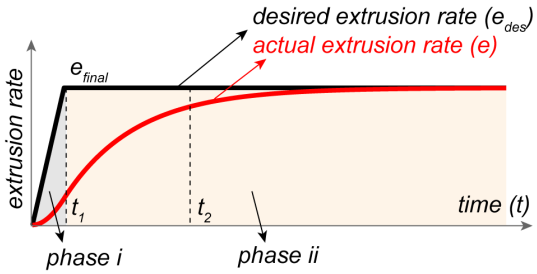

FIGURE 5: Extrusion dynamics identification.

For both phases, actual extrusion rate (e) can be determined analytically. First, the extrusion rate at the end of phase i ($t=t_1$) is derived in terms of τ utilizing the ramp response of $H(s)$ as:

$$e(t_1) = \frac{\tau e_{final}}{t_1}\left(\frac{t_1}{\tau} - 1 + \exp\left(-\frac{t_1}{\tau}\right)\right) \qquad (6)$$

where e_{final} is the constant extrusion rate that corresponds to the constant tangential velocity portion of the motion stage trajectory. λ is taken as $\lambda=0$ since $\tau>>\lambda$ holds in practice [5, 6]. The estimation of the actual extrusion rate at the end of phase i, $e(t_1)$, is substituted in the solution of the following differential equation at the instant where actual extrusion rate gets significantly close to the desired extrusion rate ($t=t_2$) as:

$$\tau \frac{d}{dt} e'(t') + e'(t') = e_{final} \qquad (7)$$
$$\text{with:} \quad e'(0) = e(t_1) \quad \text{and} \quad t' = t - t_1$$

where *e'* is simply the time shifted extrusion rate (*e*) in order initialize the Eq. (7) at $t=t_1$, and *t'* is the free time variable which is offset by t_1 amount. Since the tangential velocity reference sent to the motion stage is known, the instant where the stage travels L_{inc} amount (t_2) is known as well. By assuming the actual extrusion rate reaches to 90% of the desired extrusion rate at $t=t_2$ (see Fig. 5), the estimated ETC (τ_e) is obtained by analytically solving Eq. (7) at $t=t_2$ as:

$$0 = 0.9 - \left(1 - \exp\left(-\frac{t_2 - t_1}{\tau_e}\right)\right) \qquad (8)$$
$$\cdots - \frac{1}{t_1}\left(\frac{t_1}{\tau_e} - 1 + \exp\left(-\frac{t_1}{\tau_e}\right)\right)\exp\left(-\frac{t_2 - t_1}{\tau_e}\right)$$

As seen, τ_e is the only unknown in Eq. (8), and therefore it can be efficiently determined using widely available root finding algorithms. By solving Eq. (8), τ_e is determined as $\tau_e=0.06$ [sec], and the thin walled identification part shown in Fig. 4 is reprinted utilizing the extruder dynamics compensation filter *F(s)*. The resulting part is shown in Fig 6.b.

a) Without extrusion dynamics compensation

b) With extrusion dynamics compensation

FIGURE 6: Thin walled rectangular print without(a) and with(b) extrusion dynamics compensation.

REAL-TIME TRAJECTORY GENERATION FOR VIBRATION AVOIDANCE

As the stage moves at high acceleration, it generates inertial forces that are sustained by the clumsy structure of desktop 3D printer. If frequency spectrum of those forces contain energy in the vicinity of structural resonances, they may easily induce forced vibrations when the print stage alters its velocity. Notice that frequency spectrum of those inertial forces is dictated by the reference trajectory itself. Hence, notch or input shaper filters [7] are used in practice to shape the frequency spectrum of reference motion commands. Although these techniques are effective in erasing the spectral energy around resonances, they induce delay to the motion [8] and induce large contouring errors that manifest themselves as printing errors. In this work a simple consolidated Finite Impulse Response (FIR) filtering based trajectory generation scheme [9] is adapted on the 3D printer to showcase its ability on improving the printing quality and speed.

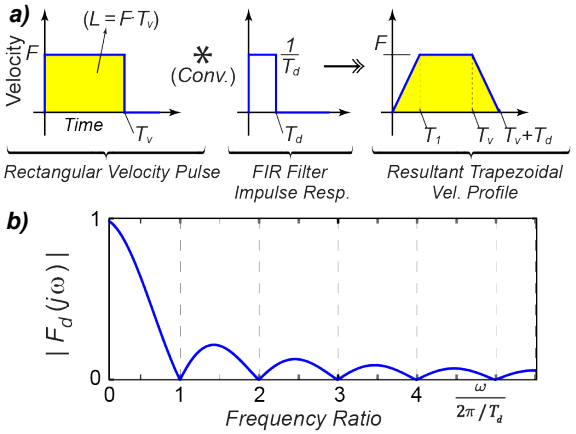

FIGURE 7: FIR based reference trajectory generation

The FIR based trajectory generation bases on filtering of a rectangular velocity pulse through set of *1st* order FIR filters whose transfer function F_d(s) is given by

$$F_d(s) = \frac{1 - e^{-sT_d}}{sT_d} \qquad (9)$$

where T_d is delay of the FIR filter. Fig. 7 depicts generation of a simple trapezoidal velocity profile by filtering a pulse velocity command. When a velocity pulse with at length of T_v is convolved with a *1st* order FIR filter, the pulse velocity command is converted into a trapezoidal profile. Duration of the profile is elongated by the delay of the filter $T_{total} = T_v + T_d$. On the other hand, frequency spectrum of a *1st* order FIR filter is shown in Fig. 7.b. Note that FIR filter introduces narrow notches at integer multiples of filter delay, $2\pi k/T_d, k = 1,...N$. As a result, when the pulse velocity command is filtered, its overall frequency spectrum is shaped. By simply matching filter delay with natural period of machine's lightly damped structural modes, $\omega_n = 2\pi k / T_d$ any unwanted vibrations could be avoided [9]. Furthermore, addition of more filters

serially generates smoother velocity profiles, which helps to cancel multiple resonances in the system and gain robustness against parameter variations [9]. In practice, two FIR filters are used to generate jerk limited trajectory (trapezoidal acceleration), so that it can be accurately followed by band limited drives of the 3D-printer.

The filter delay may lead to large contouring errors during printing of complex components. Contour errors are induced at regions when the feed direction is altered. For instance, they are most visible at sharp corners of the part, and they can be controlled by the printing feedrate/speed [3]. Larger printing feeds induce larger contour errors [3]. In this work, these contour errors at sharp corners are confined analytically by calculating the fastest cornering feedrate.

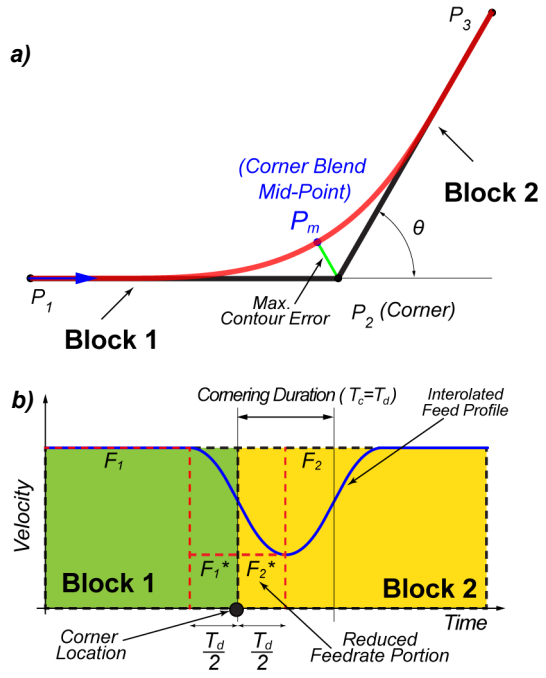

FIGURE 8: Illustration of the smooth trajectory around a corner.

Fig. 8 summarizes the approach. In Fig. 8.a two consecutive linear printing segments are shown. Notice that those segments create a sharp corner at which the feed direction is altered. The velocity(feed) pulses are shown in Fig. 8.b. If consecutive feedrates are identical F1=F2, the largest contour error due to FIR filtering occurs in the middle of the trajectory. In this technique, the feedrate at the corner is reduced down to F1*=F2* as shown in Fig. 8.b to confine the maximum contour error. By considering the geometry and the filter dynamics the reduced feedrate around block junctions can be calculated analytically as:

$$F_1^* = F_2^* = \frac{\varepsilon_{\max}}{\left(\frac{3T_1^2 + T_2^2}{24T_1}\right)\sqrt{2-2\cos(\theta)}} \qquad (10)$$

where T_1 and T_2 (considering 2 FIR Filters) are the delays of the filters and θ is the cornering angle formed by the linear blocks.

EXPERIMENTAL VALIDATION OF PROPOSED TECHNIQUES

The effectiveness of the proposed methods is demonstrated by printing a sample part with a hollow square prism geometry shown in Fig 9.b. The G-Code that is used in the printing process is generated using an open source 3D slicing software (Ultimaker Cura).

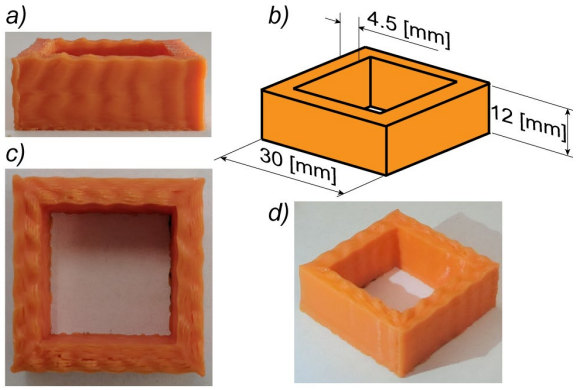

FIGURE 9: Hollow square prism geometry for experimental validation and its print using the default commercial G-code parser. a) Side view b) CAD drawing c) Top view d) Isometric view.

This G-code is first processed by the on-board G-code parser, which is a part of the commercial 3D printer, and the resulted trajectory is sent to the 3D Printer for printing. The maximum velocity and acceleration of the trajectory are set to 150 [mm/sec] and 1 [g] respectively. The resulting print is shown in Fig. 9. There are two main defects of this resulting print, which showcase the limitations of the commercially available trajectory generator:

1) Rapid variations in axis-acceleration excites the structural dynamics of the printer, causing vibration marks on the sides of the printed part (see Fig. 9.a).

2) Around the corners of the part, where the tangential velocity abruptly decreases and increases again, over-extrusion creates unwanted material accumulation (see Fig. 9.c).

Firstly, in an effort to eliminate the effects of vibration, the FIR-based smooth trajectory approach presented in the previous section is implemented. 2 FIR filters are utilized to generate a jerk limited trajectory with time constants (delays) selected as 0.0294 [sec] and 0.0385 [sec]. Filter delays are tuned on the fly by trial-and-error to attenuate vibrations from resonances of the x and y axes of the motion stage. The feedrate around the corners is adjusted by Eq.(10) to confine cornering errors up to 0.45 [mm], which is slightly larger than the extruder's diameter. The resulting part is shown in Fig. 10.a. As observed, vibration-induced surface waviness on the sides of the part is completely eliminated and a smoother surface finish is achieved.

Prints with Smooth Trajectory

a) w/o Extrusion Dynamics Compensation

b) w/ Extrusion Dynamics Compensation

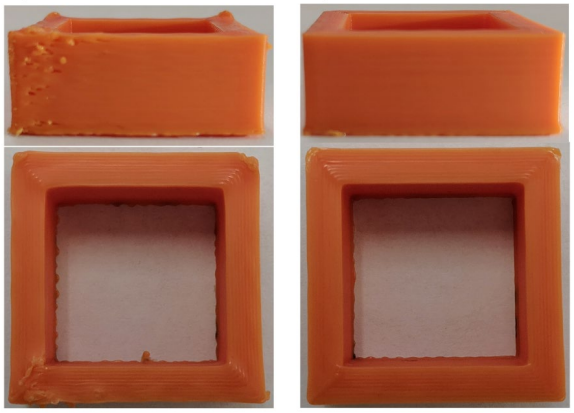

FIGURE 10: 3D printed models using FIR-based smooth trajectory without(a) and with(b) synchronized extrusion rate.

Eliminating the vibration induced errors showcases the second error source, which is due to the ill-synchronized deposition rate. These errors are visible around the corners of the part (See Fig 10.a). In order to eliminate them, the extrusion dynamics compensation filter *F(s)* (see Eq. (4)) is employed and commands to the extrusion stepper motors are modulated. The resulting part is shown in Fig 10.b. The material build-up around the corners are eliminated and combined with vibration-less motion, high-quality part printing is achieved.

CONCLUSIONS

Two practical feedforward method is proposed in order to improve accuracy of Fused Filament Fabrication-based Desktop 3D Printers. First, a dynamic compensation filter is proposed to eliminate excessive or insufficient material deposition. Extrusion dynamics is identified using a simple thin wall printing test. Next, a smooth trajectory generation algorithm is proposed in order to avoid structural vibrations in high speed 3D printing. It is validated that proposed techniques can easily be implemented on commercial desktop 3D printers and it can significantly aid to faster and more accurate printing of polymer components.

REFERENCES

[1] Go J, Schiffres SN, Stevens AG, Hart AJ. Rate limits of additive manufacturing by fused filament fabrication and guidelines for high-throughput system design. Additive Manufacturing. 2017; 16: 1-11.

[2] Go J, Hart AJ. Fast Desktop-Scale Extrusion Additive Manufacturing. Additive Manufacturing. 2017; 18: 276-284.

[3] Ertay DS, Yuen A, Altintas Y. Synchronized material deposition rate control with path velocity on fused filament fabrication machines. Additive Manufacturing. 2018; 19: 205-213.

[4] Duan M, Yoon D, Okwudire CE. A limited-preview filtered B-spline approach to tracking control – With application to vibration-induced error compensation of a 3D printer. Mechatronics. 2018; 56: 287-296.

[5] Bellini A, Guceri S, Bertoldi M. Liquefier Dynamics in Fused Deposition. Journal of ASME Manufacturing Science and Engineering. 2004; 126: 237-246.

[6] Hoelze DJ, Alleyne AG, Wagoner Johnson AJ. Iterative Learning Control for Robotic Deposition Using Machine Vision. American Control Conference. 2008; 4541-4547.

[7] Altintas Y, Khoshdarregi MR. Contour Error Control of CNC Machine Tools with Vibration Avoidance. Annals of the CIRP. 2012; 61:335-338.

[8] Sencer B, Dumanli A, Yamada Y. Spline interpolation with optimal frequency spectrum for vibration avoidance. Annals of the CIRP. 2018; 67:377-380.

[9] Tajima S, Sencer B, Shamoto E. Accurate interpolation of machining tool-paths based on FIR filtering. Precision Engineering. 2018; 52:332-344.

DESIGN OF A 5-AXIS MANIPULATOR FOR THE AUTOMATIC LAPPING PROCESS

Sangki Park[1], Daegwon Koh[1], Jaeyoon Shim[1], Jong-Jae Kim[1] and Sun-Kyu Lee[1]
[1]School of Mechanical Engineering
Gwangju Institute of Science and Technology (GIST)
Gwangju, Republic of Korea

INTRODUCTION

Surface finishing is a crucial process for the final products of molds or 3D printed products. Depending on the finishing results, the quality such as machining accuracy and surface roughness is determined, and in special cases, this quality also affects the performance of products. Up to date, most surface finishing operations have been regarded as manned work, which requires a long process time and high cost. However, as the demand for high quality large-sized molds products increases, an automation of surface finishing has attracted globally attention. At the same time, labor issues such as recruitment of highly skilled worker and industrial diseases are also emerging.

To solve these problems, research for automation of surface finishing has been explored by applying either machine tools or industrial robots. Researches using 3-axis or 5-axis CNC machine have been carried out. However, the work surface is limited due to the constraint on the size of the workspace. In addition, from a structural point of view, the tool can't reach a certain geometry condition, and from control point of view, the operator is not able to manage the process without accurate tool path information.

In recent years, due to the various advantages of industrial robots, robotic machining and finishing researches are actively being announced. Robotic finishing can be categorized into two techniques; control approach using end-effector and robot itself. In the first approach, the robot follows the nominal path and the end-effector controls the contact force passively or actively. This approach is suitable for polishing that keeps a low constant force, while grinding and lapping with higher material removal rate and higher force variation require a heavier loading system. The second approach is to control the torque of each robot axis according to the force command considering the robot dynamics. This approach is less applicable compared to the first approach due to the limitation of the controller accessibility of the industrial robot and the difficulty in implementing the robot force control. However, force control is possible even with a robot alone, and above all, even lapping or grinding associating with higher load variation can't depend on end-effector force control approach which has been mainly applied for polishing. This approach determines the behavior of the robot according to the intention of the researcher, so that feed-forward torque control and compliance control can be employed in accordance with the application.

In this study, a lapping machine consisting of a newly designed parallelogram type 5-axis manipulator and the 3-axis gantry machine is proposed to expand the workspace as well as to provide high stiffness of the manipulator. The lapping operation was performed by adopting a feed-forward torque control to remove the milling tool marks with uniform normal force. The experiment was conducted by considering the tool compliance.

LAPPING MACHINE

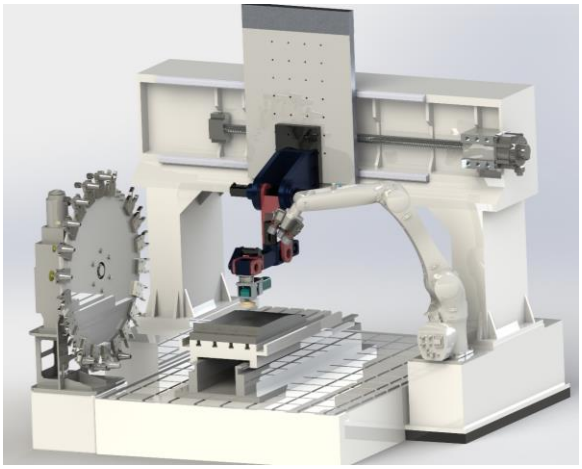

FIGURE 1. Automatic lapping machine with the parallelogram type 5-axis manipulator

A lapping machine was developed by consisting of conventional gantry, slide table and a 5-axis manipulator. A rotating wheel (e.g. Electro-spindle or pneumatic-spindle) is mounted at the end-effector for intending the surface lapping operation. The possible workspace of end-effector is 200 mm × 250 mm ×300 mm in x, y, z-direction. The manipulator is controlled to provide not only the precise cutting depth but the precise force accompanying with the wheel posture normal to the work surface, and covering the small work range. For a large work surface, slide table and gantry move for positioning the local work area with keeping both the wheel posture and the rigidity. To secure the joint rigidity, angular ball bearings are assembled at both ends of the connecting pins.

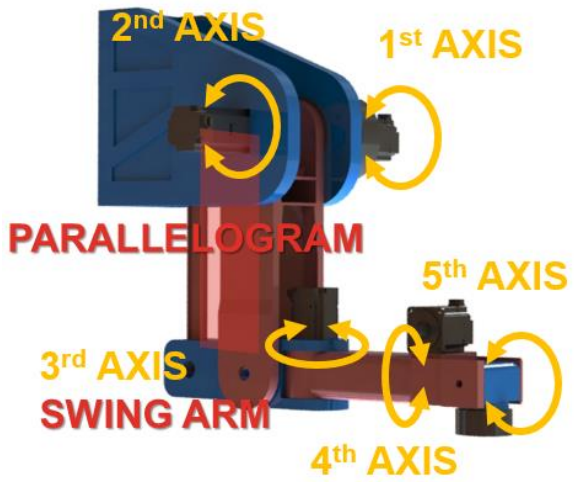

FIGURE 2. Designed parallelogram type 5-axis manipulator

TABLE 1. Specification of 5-axis manipulator

Link No.	1	2	3	4	5
Mass (kg)	5.64	6.55	4.05	2.04	1.19
Power (kW)	0.6	0.6	0.4	0.2	0.2
Gear ratio	120	120	100	101	100
Joint stiffness (10^4Nm/rad)	6.7	6.7	1.3	0.7	0.7

And, the 5-axis manipulator has two remarkable features compared to the general 6-axis articulated manipulator. First, the parallelogram mechanism is adopted to locate the center of mass near the base of manipulator since the total load of manipulator can be reduced and can affect the performance of the actuator. Moreover, the parallelogram mechanism is kinematically and dynamically decoupled, i.e. the loads (e.g. link weight, disturbance) of the first and second axes can be separated.

Second, a swing arm mechanism is adopted to improve dynamic motion in planar operations. The most frequent motion in the manual lapping or polishing operation is to wipe the object. Hence, the third axis acts as a base axis in the general 6-axis articulated manipulator, making it agile and flexible swing motion the local workspace.

COMPLIANCE

The driving torque of manipulator can be given by kinetic and potential energy functions of system. And, the deflection of each joint caused by flexibility of reducer is relative to the driving torque. The equation of motion [1] is given by,

$$M(q)\ddot{q} + C(q,\dot{q})\dot{q} + g(q) = \tau + J^T(q) f \quad (1)$$

$$\tau = J^T f - g = k_q \Delta q \quad (2)$$

Where $\boldsymbol{M}$ is the moment of inertia matrix, $\boldsymbol{C}$ is the Coriolis and centrifugal force matrix, $\boldsymbol{g}$ is the gravity vector, $\boldsymbol{\tau}$ is the driving torque vector of manipulator, and $\boldsymbol{f}$ is the external force vector with the Jacobian of robot manipulator. $\boldsymbol{k_q}$ is the joint stiffness, and $\boldsymbol{\Delta q}$ is the deflection of joint.

$$\tau_{i+1} - \tau_i = J^T(f_{i+1} - f_i) = k_q(\Delta q_{i+1} - \Delta q_i) \quad (3)$$

$$K_X = J^{-T} K_q J^{-1} \quad (4)$$

$$\frac{1}{k} = \frac{1}{k_z} + \frac{1}{k_{tool}} \quad (5)$$

Eq. (2) is the calculation of the deflection, and eq. (3) is the calculation of the compliance. $\boldsymbol{K_X}$ is the Cartesian space stiffness matrix. The z-axis translational stiffness of the manipulator $\boldsymbol{k_z}$ is mainly influenced by the rotational stiffness matrix of each joint $\boldsymbol{K_q}$. Through the measurement of deflection and reaction force of end-effector as shown in eq. (4), all of the equations can be determined in terms of compliance. The overall compliance is divided into manipulator and tool. The compliant tool is recommended for the tool marks removal by adopting force control not to hurt the original pre-machined shape. The overall compliances of each case by grit size of abrasive tool are listed in Table 2.

TABLE 2. Overall compliances

Case	w/o tool	#24	#400
Compliance (μm/N)	7.7	12.2	108.9

FEED-FORWARD TORQUE CONTROL

Feed-forward torque control method is adopted to keep the constant reaction force on the constrained surface (i.e. original pre-machined surface). In this case, both position and force are controlled simultaneously, in accordance with the estimated driving torque of each joint by force control rules. Feed-forward torque control has the advantage to accomplish force control without time delay, where the force error is not influenced by the dynamical motion along the surface in non-constrained direction.

$$g_i = \sum_{j=1}^{n} (-m_j A_{ji} r_j^j) \quad (6)$$

$$A_{ji} = \frac{\partial T_0^i}{\partial q_j} = T_0^{j-1} Q T_{j-1}^i \quad (7)$$

Eq. (6) and (7) show how to calculate gravity vector based on Euler-Lagrangian formulation. ***r*** is the length of center of gravity, ***T*** is the homogeneous transformation matrix and ***Q*** is the derivative matrix.

$$g_i = \sum_{j=1}^{1} (-m_j g A_{ji} r_j^j) \ (i=1),$$

$$g_i = \sum_{j=2}^{5} (-m_j g A_{ji} r_j^j) \ (2 \le i \le 5) \quad (8)$$

$$\tau_2 = g_2 - J^T f \quad (9)$$

Eq. (8) shows the characteristic of parallelogram mechanism, where $\boldsymbol{g_i}$ is the gravitational force of joint ***i***. The decoupling of joint 1 and 2 reduces the cumulative effect of control load and positioning error. In addition, the structure of 5-axis manipulator indicates that the joint 2 is optimal for responding to the reaction force in the plane utilizing its weight. Hence, only joint 2 adopts proposed feed-forward torque control rule in Eq. (9) to utilize a 'Deadweight' force effectively, and the others follow conventional motion control rule.

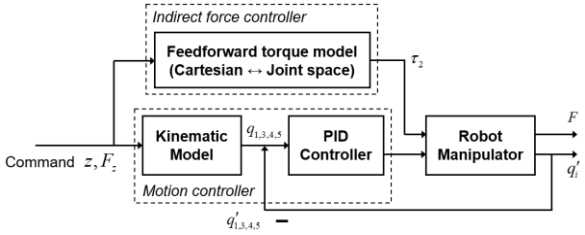

FIGURE 3. Block diagram of feed-forward torque control

EXPERIMENT

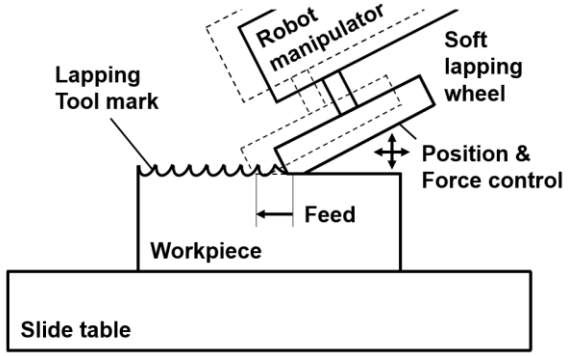

FIGURE 4. Tool mark removal with feed-forward torque control

Fig. 4 describes how to accomplish the lapping process for tool mark removal as well as surface roughness improvement by using proposed feed-forward torque control.

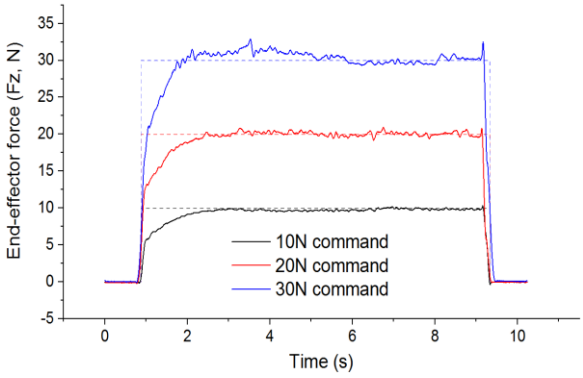

FIGURE 5. Comparison of normal force without lapping

As shown in Fig. 5, the proposed feed-forward torque control follows the commanded force adequately. These results indicate that it can keep uniform machining force without using the

force sensor. Since this method doesn't converge the force feedback value as in the conventional direct force control, it has bot the variation caused by tracking error.

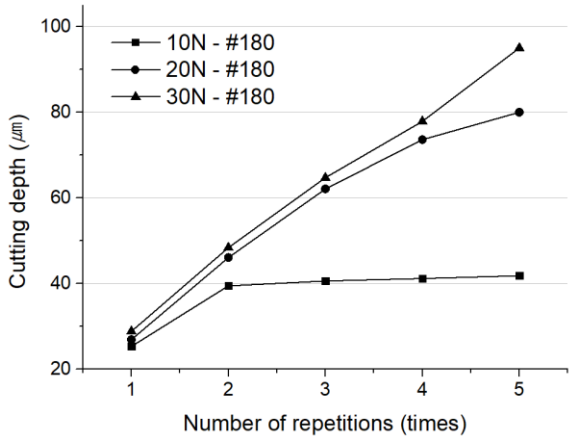

FIGURE 6. Comparison of cutting depth and surface roughness according to normal force change (Feed rate : 5mm/s, tool : #180)

It was demonstrated that the rougher tool (#180) should be used to remove the tool marks rather than softer tool (#400). However, the cutting depth increases drastically by increasing the control force with #180 tool as depicted in Fig. 6. It should be noted that the tool is so relatively rigid that the cutting volume rapidly increases and the original surface geometry can be hurt by the number of repetitions and control force change.

FIGURE 7. Tool mark removal result ((a) Before : face mill, (b) After : #180)

Fig. 7 compares the surface roughness before and after lapping process using #180 compliant tools. Tool marks due to the face milling with an amplitude of about 6 μm are completely removed and surface roughness Rz is decreased from 6.1 μm to 1.2 μm, but the lapping mark generated. Typically, the lapping is repetitive and sequential to the abrasive tool, burnishing and polishing process is followed to remove scratches caused by lapping tool.

CONCLUSION

In this study, a lapping machine consisting of a newly designed parallelogram type 5-axis manipulator associating the 3-axis gantry machine is proposed to expand the large work space as well as to provide high stiffness of the manipulator. Feed-forward torque control was performed by the joint 2 of manipulator. Consequently, the proposed machine and control method produces the surface roughness of 1.2 μm in tool marks removal by using #180 tool.

From the results, the proposed manipulator and control method has potential to be applied toward unmanned lapping system for large workpiece.

ACKNOWLEDGEMENT

This work was supported by the Technology Innovation Program (10053248, Development of Manufacturing System for CFRP) funded by the Ministry of Trade, Industry & Energy (MOTIE, Korea), National Research Foundation of Korea (NRF) granted by the Korea government (MSIT) (Grant No. 2018R1D1A1B07049492), and Institute of Integrated Technology (IIT) Research Project through a grant provided by GIST in 2019.

REFERENCES

[1] Richard M. Murray, Zexiang Li, S. Shankar Sastry. A Mathematical Introduction to Robotic Manipulation. CRC Press. 1994.

[2] Toshiro K. Doi, Osamu Ohnishi, Eckart Uhlmann, Arne Dethlefs. Handbook of Ceramics Grinding and Polishing (Second Edition) Chapter 6 – Lapping and Polishing. CRC Press. William Andrew Publishing. 2015; 263-325.

[3] Fengjie Tian, Chong Lv, Zhenguo Li, Guangbao Liu. Modeling and control of robotic automatic polishing for curved surfaces. CIRP Journal of Manufacturing Science and Technology. 2016; 14: 55-64.

LEVITATION HEIGHT CONTROL OF LEVITATION ACTUATOR USING PROPORTIONAL CONTROL

Ayaka Nakazato[1], Akihiro Torii[1], Kae Doki[1] and Suguru Mototani[1]
[1]Department or Electrical Engineering and Electronics
Aichi Institute of Technology
Toyota, Aichi, Japan

INTRODUCTION

Precision production has been focused in manufacturing because of the widespread applications of the miniature products. A lot of machines, such as cutting, grinding, etching, etc. are used in a factory, causing problems of space in the factory. A desktop size production system is one solution for space saving. Small-scale actuators for positioning and manufacturing are required in the system. Piezoelectric elements (piezos) are widely used in a compact production system. They are applied to various engineering problems for precision stages, robots and appliances in which their minute deformations are employed.

Some applications use the piezos for minute movements of less than 10 μm and wide range of greater than 10 mm. An xyθ actuators using the piezos has been developed [1]. By using the piezos, a general-purpose and compact-size moving mechanism can be realized. In addition to the translational and rotational motion, a levitation function using the piezo is added to eliminate friction.

The microrobot composed of three levitation mechanisms and two horizontal piezos has been proposed [2]. The microrobot moved by the principle of an inchworm. It was necessary to control the levitation height individually to prevent the trouble of the motion. In the conventional levitation actuator, the piezo was fixed by using adhesive between a counterweight and a metal plate [3]. The fixed condition of the adhesive affected the levitation characteristics such as the levitation height and the levitation frequency. For this reason, we developed a levitation actuator using hinges [4].

In this paper, the levitation height control of the levitation actuator is described. The levitation actuator using a hinge is constructed. The levitation height is controlled with a closed-loop feedback. The drive frequency is controlled to maintain the levitation height.

LEVITATION ACTUATOR

Levitation principle

Figure 1 shows the operating principle of the levitation actuator. By applying a sinusoidal voltage at an appropriate frequency to the piezo of the levitation actuator, the piezo extends and contracts quickly. At the same time, the plate vibrates at high speed. Since the plate vibrates at high speed, an air gap is formed between the plate and the floor surface. As a result, the air film generated by the squeeze film effect is formed, and the actuator can levitate. We can realize non-contact mechanism, and eliminate the friction.

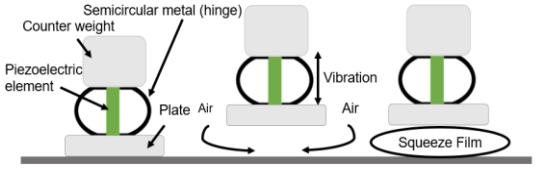

Figure 1 Principle of levitation. Vertical vibration of piezoelectric element forms squeeze film underneath plate.

Construction

The levitation actuator used in the measurement is shown in Figure 2. The plate is 30 mm in diameter, 3 mm in thick and 5.7 g in weight. The counter weight is 20 mm in diameter, 15 mm in height, and 34.9 g in weight. A stacked-type piezo (NEC-Tokin, AD0505D16, 20 mm long) is used. The piezo is sandwiched between semicircular metals with an outer diameter of 21 mm and is fixed in its longitudinal direction. The semicircular metals are fixed between the weight and the plate. The total weight is 63.6 g, and the total length is 43 mm. The semicircular metals are fixed between the weight and the plate. The weight, semicircular metals, and plate are fixed with screws. A torque screwdriver is used to maintain a predetermined tightening torque 18 cNm.

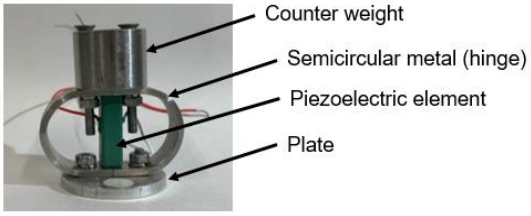

Figure 2 Developed levitation actuator with hinge. Counter weight, semicircular metal, and plate are screwed.

LEVITATION HEIGHT CONTROL

Frequency control using VCF

The levitation height is controlled by changing the drive frequency. A variable control frequency (VCF) function of a function generator (FG-163, NF Corporation) is used to vary the frequency according to the input voltage of the VCF terminal.

The output frequency is investigated by applying a voltage using a stabilized power supply. A voltage from 0.0 V to 5.0 V is input to the VCF terminal. The relationship of the input voltage to the VCF terminal and the output frequency is shown in Figure 3. The output frequency varies linearly from 1.0 kHz to 11.0 kHz.

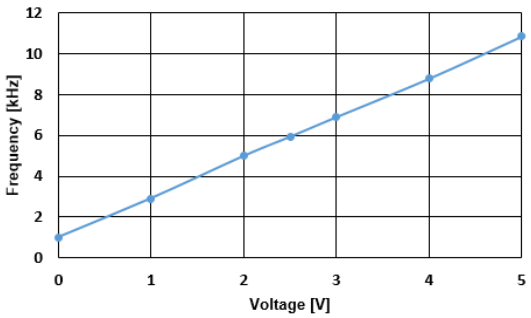

Figure 3 Dependence of input voltage to VCF terminal and output frequency of function generator.

Levitation height control

The control block diagram for the levitation height control is shown in Figure 4. The levitation height of the plate of the levitation actuator is measured by a laser displacement meter (LK-H052, Keyence). The five measurement data are averaged by Arduino, which outputs the averaged signal to the VCF terminal of the frequency generator every five measurements. The averaged signal inputting to the VCF terminal holds for five measurements. In order to prevent hunting, a dead band block is introduced. The block outputs the change Δu which is accumulated by the block followed. The resolution of a minute variation Δu is defined as 5/255 (=0.02) V due to the 8-bit output resolution of Arduino. The blocks in the broken line are implemented in Arduino.

The measured levitation height is acquired every 38 ms and five data are averaged. One control cycle is approximately 230 ms including calculation time in Arduino. Due to the dead band of the controller, the levitation height of the actuator ranges from 20 μm to 25 μm.

The function generator generates the sine wave with the amplitude of 2 V peak-to-peak and the frequency determined by the VCF signal. The sine wave is applied to the levitation actuator through an amplifier (HSA 4052, NF corporation). The voltage applied to the actuator is 40 V peak-to-peak.

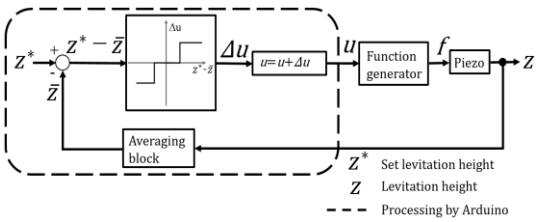

Figure 4 The block diagram of the control system. The dead band block is introduced and the drive frequency depends on the summation of the block output.

Experimental results

Figure 5 shows the measurement results of the levitation height control. The drive frequency, the levitation height, and the average height are measured. During 0 ms to approximately 10 ms, no levitation is observed except in the vicinity of 6 ms. The levitation height increases as the frequency increases after 10 ms. After the levitation actuator reached the reference height, 20 μm to 25 μm, the levitation height is controlled. The drive frequency is lowered when the levitation height exceeds the reference height, and the drive frequency is heightened when the

levitation height descends the reference height. After 20 s, the frequency continues changing around 3.4 kHz to make the levitation height constant.

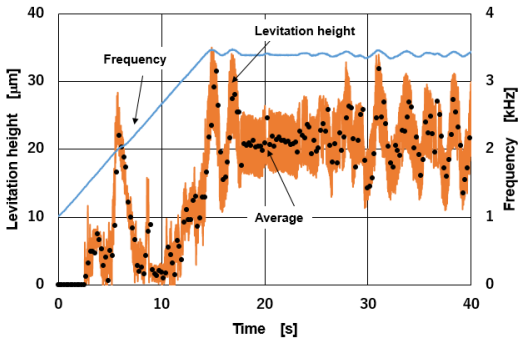

Figure 5 Experimental result. Drive frequency rises slowly and the levitation is stable in approximately 15 ms.

PROPORTIONAL CONTROL FOR LEVITATION HEIGHT CONTROL

The control method described in the previous chapter, the levitation height could be controlled by using the drive frequency control. The levitation height however fluctuated and the rising was slow. The reason is that the amount of frequency change which corresponds to Δu determined by the dead band control block is constant. Therefore, the proportional (P) control is introduced to the levitation height control.

Levitation height control using P control

The control block diagram for the levitation height control using P control is shown in Figure 6. The dead band block is replaced. The gain Kp in the P control is introduced. The averaging block calculates five levitation heights measured by the laser displacement meter, outputs the height averaged, and hold the data till next timing, similar with the previous chapter.

One levitation height measurement costs 38 ms, five measurements 190 ms, and 230 ms in total including the processing time of Arduino. The reference levitation height is from 5 μm to 10 μm. The proportional gain Kp varies from Kp=0.5 to Kp=2.0.

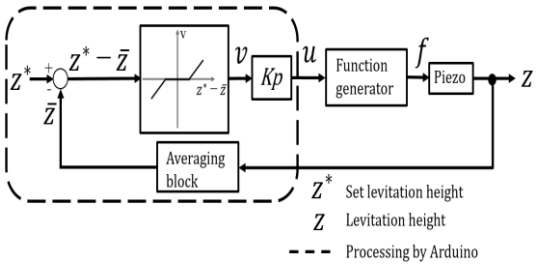

Figure 6 The block diagram of the control system using proportional control with dead band.

Experimental results using proportional control

Figure 7 shows the measurement results. The time derivative of the frequency df/dt is used to evaluate the response of the control.

When Kp equals 0.5 as shown in Figure 7(a), the time derivative of the drive frequency df/dt equals 0.33 kHz/s, and the frequency used for the levitation is approximately 2.3 kHz. The control is unstable. The levitation height rapidly increases and decreases when the input frequency is approximately 2.5 kHz.

When Kp equals 1.0 as shown in Figure 7(b), the derivative df/dt equals 0.70 kHz/s, and the frequency used for the levitation is approximately 2.7 kHz. The levitation actuator is levitated within the reference height in 5 s.

When Kp equals 1.5 as shown in Figure 7(c), the derivative df/dt equals 1.05 kHz/s, and the frequency used for the levitation is approximately 4.4 kHz. The levitation height fluctuates until 6 s. The levitation however is stable after 6 s.

When Kp equals 2.0 as shown in Figure 7(d), the derivative df/dt equals 1.34 kHz/s, and the frequency is approximately 4.2 kHz. The levitation height fluctuates.

The rise time when the actuator reaches the reference height shown in Figure 7 is shorter than that shown in Figure 5. The advantage of the P control was indicated. Figure 7 implied that the frequency response of the closed-loop control system had a sharp resonant peak frequency between 1 kHz and 4.4 kHz. Feedback gain Kp and averaging calculation will be carefully tuned to prevent hunting phenomena observed in Figure 7.

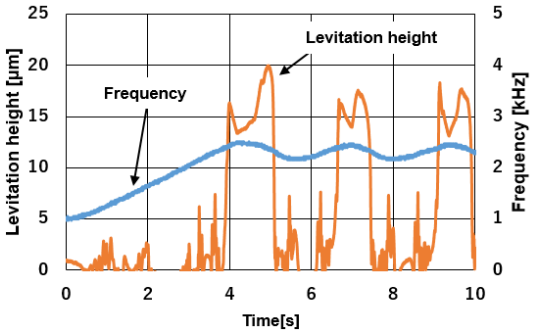

(a) Kp=0.5

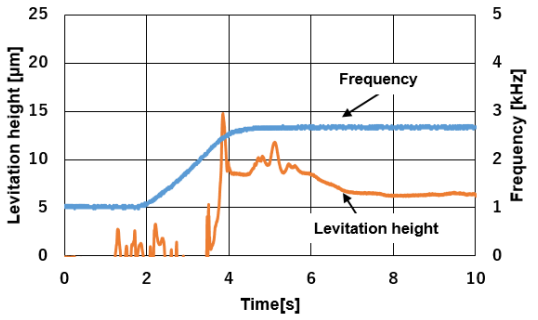

(b) Kp=1.0

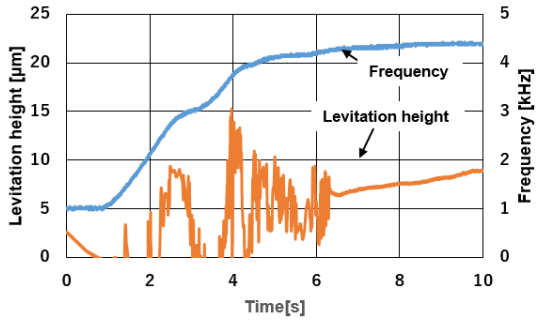

(c) Kp=1.5

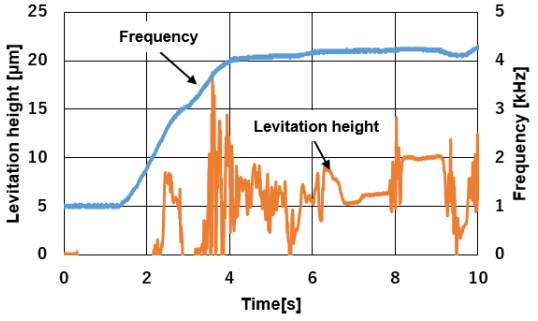

(d) Kp=2.0

Figure 7 Experimental results. The frequency used for the levitation differs according to the constant Kp.

SUMMARY

The levitation height of a levitation actuator was controlled using the proportional feedback control. A dead band was introduced in the feedback control. After averaging of the levitation height measured, the drive frequency was controlled by the use of voltage control frequency function of the function generator. A stable levitation was realized using an appropriate feedback constant. The levitation height however fluctuated with inappropriate feedback constant. In future, the averaging calculation, the width of the dead band, and the feedback constant are tuned.

REFERENCES

[1] Jean-Charles Pelletier, Hisayuki Aoyama, Yuuka Irie and Nadine Piat, “Development of a Micro-manipulator for Bio-Targets Using Micro-Flows”, J. of Robotics and Mechatronics, Vol. 30, No. 4, pp. 638-649, 2018

[2] A. Torii, S. Kengaku, T. Yamada, A. Ueda, “An Inchworm-type Microactuator Using Levitation Mechanisms”, european society for precision engineering and nanotechnology, Vol. 2, pp. 85-88, 2011

[3] Shori Sone, Akihiro Torii, Kae Doki, “Motion estimation of a levitation mechanisms using piezoelectric element”, Micro-Nano Mechatronics and Human Science (MHS2013), P1-5, pp. 25-30, 2013

[4] Ayaka Nakazato, Akihiro Torii, Kae Doki, Suguru Mototani, “INVESTIGATION OF ASSEMBLY OF A LEVITATION ACTUATOR”, Proceedings of the 33rd ASPE Annual meeting, 2018

ROTATION OF AN INCHWORM USING PIEZOELECTRIC ELEMENTS AND ELECTROMAGNETS

Hiroaki Miyake[1], Akihiro Torii[1],
Suguru Mototani[1] and Kae Doki[1]
Department of Electrical Engineering and Electronics
[1] Aichi Institute of Technology
Aichi, Japan

INTRODUCTION

In recent years, various devices such as mobile phones and home appliances have been miniaturized and improved in performance. Although many components use these precision products, the production equipment uses a lot of energy and space. If an actuator capable of multi-degree-of-freedom (DOF) operation is used in the production system, the number of actuators, installation space, and energy consumption can be reduced compared to the conventional large-scale production equipment. Therefore, micro robots with piezoelectric elements were studied in order to realize cost saving and energy efficient manufacturing [1,2,3]. The robot was developed for precise and omni-directional microscope processing [4].

In our laboratory, we have developed a micro mobile inchworm that can operate with multiple degrees of freedom by combining the adhesion of three electromagnets with the floor surface and the expansion and contraction of three piezoelectric elements [5]. The purpose of the development of the inchworm is to realize a multi-DOF precision positioning system. In our previous study, the position and orientation of the inchworm were measured, and it was possible to correct the error while moving [6]. However, the speed of the inchworm was so slow that the inchworm was not adapted to high speed application. The transient phenomena of the electromagnet controlled by a square wave impeded the high speed operation of the inchworm. The electromagnets are therefore controlled by sinusoidal current so that the inchworm are adapted to high speed operation [7].

The inchworm moves linearly and rotationally and its operating speed increased with frequency. The phase difference between the electromagnetic force and the deformation of the piezoelectric element, however, prevented the movement of the inchworm. In consideration of these effects, the motion of the inchworm required improvement.

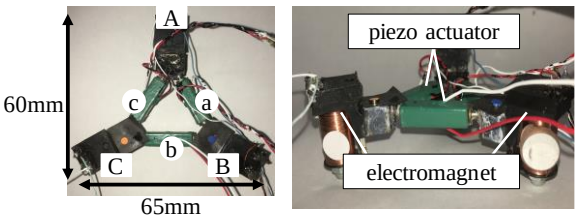

(a) Top view (b) Side view

FIGURE 1. Photo of inchworm

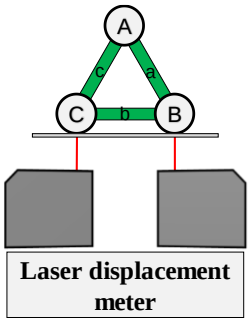

FIGURE 2. Measurement method using a laser displacement meter

In this study, we propose a new operation signal, and show the displacement in the θ-axis direction. Furthermore, the rotation of the inchworm and its distribution are clarified.

INCHWORM

Figure 1 shows the photo of the inchworm. The inchworm has three piezoelectric elements consisting the sides of a triangle, and electromagnets attached to a connection point of the piezoelectric elements. Three electromagnets are electromagnet-A, -B and -C, and the piezoelectric elements are piezo-a, -b and -c. The electromagnet is in contact with a metal floor. The piezoelectric element used is AD0505D16F manufactured by NEC Tokin Co., and extends 17.4 μm with respect to an applied voltage of 150 VDC. The electromagnet has an internal

resistance of 300 Ω and an inductance of 800 mH. The inchworm is 65 mm wide, 28 mm high, and the weight is 80 g. The size depends on the length (20 mm) of the piezoelectric element, and the height depends on the length (25 mm) of the core of the electromagnet. A hemispherical metal is attached to the bottom of the electromagnet.

The position of the inchworm is measured with a laser displacement meters, and the measurement method and measurement points are shown in Figure 2. The laser displacement meter is LK-G30A manufactured by Keyence Co. The repeatability is 0.02 µm.

The inchworm moves according to the principle of an inchworm. As an example, the movement in the θ-axis direction is described. Figure 3 shows the driving principle of the inchworm in the θ-axis direction. Electromagnet-A, B, C are excited by sinusoidal waves, and attraction forces of the electromagnets are generated. Piezo-a, b, c are driven by rectangular waves, and the piezo-a, b, c deform. The inchworm moves by synchronizing the adhesion of the three electromagnets to the floor and the expansion and contraction of the three piezoelectric elements. As shown in Figure 3, by repeating steps 1 to 3 as one cycle, the non-excited electromagnet moves and the inchworm can move in the θ direction.

The inchworm moved using the operating cycle shown in Figure 3. The positions of Electromagnet-B and -C were measured for 55 s. Figure 4 shows the measurement results. The position of the Electromagnet-C was 600 µm, and the position of the Electromagnet-B was −80 µm.

As shown in Figure 4, the inchworm did not rotate by the use of the control signal shown in Figure 3. Therefore, a new control signal which enables the inchworm rotate is required.

NEW ROTATIONAL DISPLACEMENT CONTROL

Figure 5 shows a new control signals of the proposed method. The inchworm rotates in the clockwise direction around Element-B at the

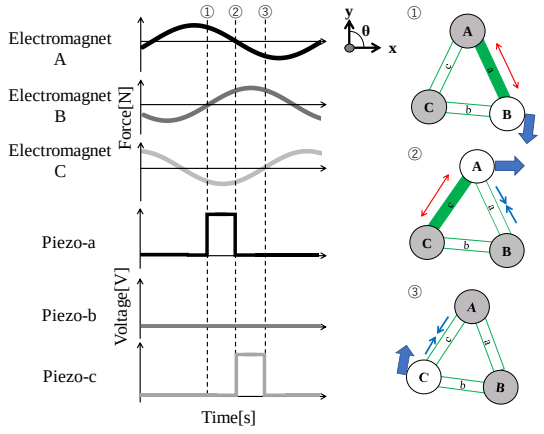

FIGURE 3. Control signal and schematic diagram of the conventional method

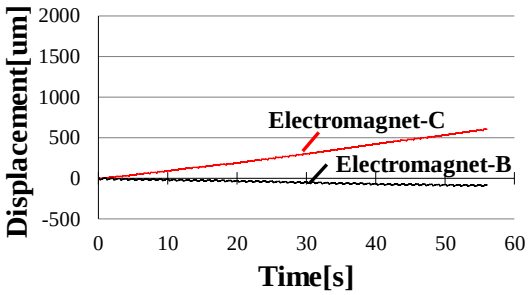

FIGURE 4. Position displacement by conventional method

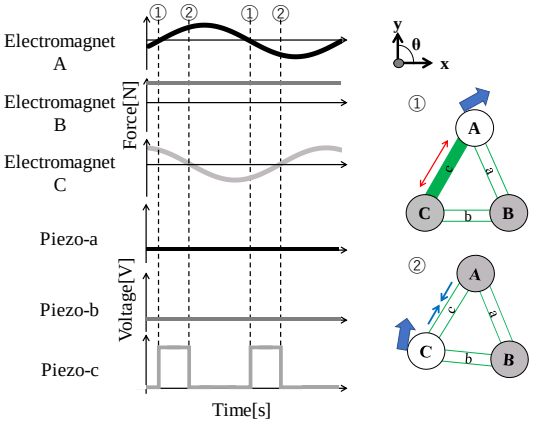

FIGURE 5. Control signal and schematic diagram of the proposed method

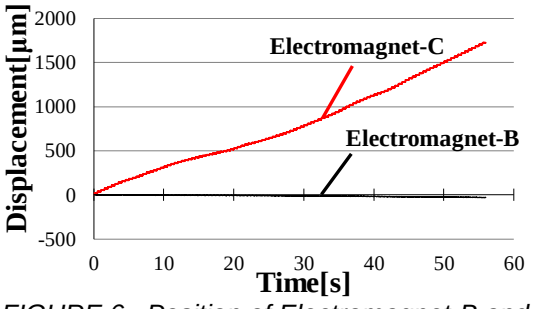

FIGURE 6. Position of Electromagnet-B and -C in the clockwise rotation around Electromagnet-B

center of rotation by the control signal shown in Figure 5. While Electromagnet-B is being excited, Electromagnet-A and –C moves sequentially by the deformation of Piezo-C The measurement results for 55 s are shown in Figure 6. The position of the Electromagnet-C was 1725 µm, and the position of the Electromagnet-B was −30 µm. The displacement of Electromagnet-B in y-direction is much smaller than that of Electromagnet-C. Therefore, the inchworm rotates around Electromagnet-B as the center of rotation.

The experiments of θ displacement around Electromagnet-A and -B both in the clockwise direction are conducted. Similar control signals as shown in Figure 5 are used. Figure 7 shows the displacement of Electromagnet-B and -C when the inchworm rotates around Electromagnet-A in the clockwise direction. Since the negative displacement of Electromagnet-B and the positive displacement of Electromagnet–C were symmetry with respect to the horizontal axis, the inchworm rotated around Electromagnet-A in the clockwise direction. Figure 8 shows the experimental results when the inchworm rotates around Electromagnet-C in the clockwise direction. Since the position of Electromagnet-C did not change and Electromagnet-B moved in the negative direction, it was confirmed that the inchworm rotated around Electromagnet-C.

ROTATION ANGLE

Figure 9 shows the method for measuring the rotation angle. The displacement of the Electromagnet-B is Y_B, the displacement of the Electromagnet-C is Y_C, and the length between Electromagnet-B and -C is D (6 cm). The rotation angle θ is expressed by Equation (1).

$$\theta = \sin^{-1}\left(\frac{Y_C - Y_B}{D}\right) \qquad (1)$$

When moving in the θ direction by the conventional method, the position of the center of rotation is O. The point O is a midpoint between Electromagnet-B and Electromagnet-C in Figure 9. On the other hand, the center of rotation is Electromagnet-B in the proposed method. Figure 10 plots the angle of rotation of the inchworm as a function of time. The rotation angle centered on O was 0.7 degrees after 55 s, and the rotation angle centered on Electromagnet-B was 1.7 degrees. Therefore, the rotation angle obtained by the proposed signal was about two times

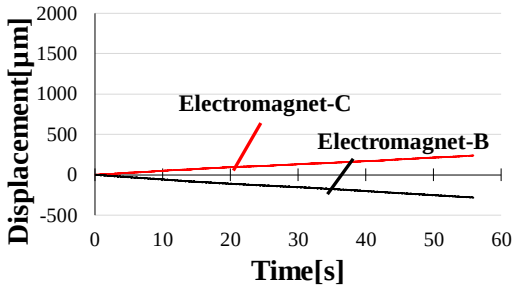

FIGURE 7. Position of Electromagnet-B and –C in the clockwise rotation around Electromagnet-A

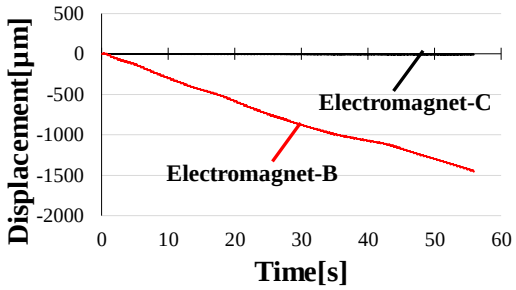

FIGURE 8. Position of Electromagnet-B and –C in the clockwise rotation around Electromagnet-C

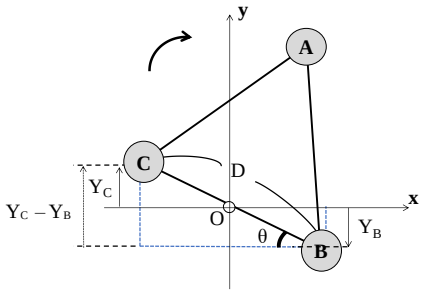

FIGURE 9. Angle measurement method

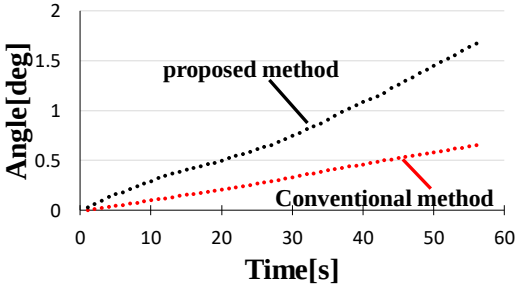

Figure 10. Comparison of rotation angle

larger than that obtained by the conventional signal.

Figure 11 shows a histogram of the rotation angle θ in one cycle. The average of the conventional method was 11.9×10^{-3} deg and the standard deviation was 0.3×10^{-3} deg. The average of the proposed method is 29.9×10^{-3} deg and the standard deviation is 7.9×10^{-3} deg. From this result, the variation of the proposed method was larger than that of the conventional method.

SUMMARY

In this paper, we clarify the performance of inchworm movement in the θ-direction using the proposed operation cycle. From the experiment, the inchworm rotated around the electromagnet consisting the inchworm. The large rotation angle was obtained compared with the conventional method. Although the rotation angle for each period was large, the large distribution was induced. In the future, we will investigate the method that reduces the distribution of one-step rotation by using the proposed method.

REFERENCES

1. Sahai R, Avadhanula S, Groff R, Steltz E, Wood R, Fearing RS. Towards a 3 g crawling robot through the integration of microrobot technologies. IEEE international conference on robotics and automation. 2006. p. 296–302.
2. Fatikow S, Seyfried J, Fahlbusch S, Buerkle A, Schmoeckel F. A flexible microrobot-based micro assembly station. Journal of Intelligent and Robotic Systems 2000;27:135–69.
3. Fuchiwaki O, Kawai T, Ohta A, Misaki D, Aoyama H. Development of a positioning and compensation device for a versatile micro robot. In: Proceedings of IEEE international conference on intelligent robots and systems (IROS 2008). 2008. p. 83–8.
4. Ohmi Fuchiwaki, “Insect-sized holonomic robots for precise, omnidirectional, and flexible”, Precision Engineering 37 (2013) 88-106
5. Akihiro Torii, Masaaki Banno, Akiteru Ueda, and Kae Doki, “A study on the small-size self-propelled stewart-platform”, IEEJ Trans. EIS, Vol. 130, No. 4, pp. 660-667(2010) (in Japanese)
6. Yushi Takaki, Akihiro Torii, Ayaka Nakazato, Suguru Mototani and Kae Doki, “Improvement of The Trajectory of an Inchworm with A Low Cost Camera”, Proceedings of the 33rd ASPE Annual meeting, Poster Session 1, Micro and Nano Technologies 4, 2018
7. Hiroaki Miyake, Akihiro Torii, Yushi Takaki, Kae Doki, Suguru Mototani “Moving velocity of inchworm using alternating current”, "Electromagnetic Force Dynamics" Symposium (SEAD31), No.19-6, 2019 (in Japanese)

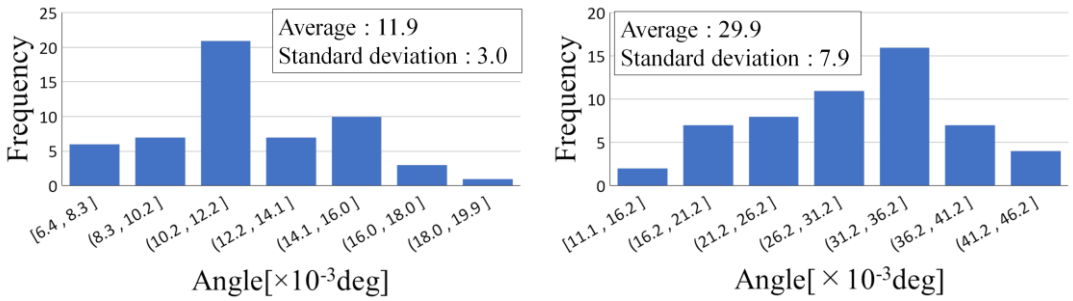

(a) Rotation angle per cycle in the conventional method

(b) Rotation angle per cycle in the proposed method

Figure 11. Comparison of distribution in rotation angle per cycle

INFLUENCE OF PREPARATION PROCESS ON SURFACE TOPOGRAPHY AND NANOTRIBOLOGICAL PROPERTIES OF MOLECULAR FILMS ON DLC SUBSTRATE

Shusen Guo[1], Tao Sun[1,*], Yongzhi Cao[1,*], Le Gu[1], Chuanwei Zhang[1], Zhiqiang Xu[2], and Hongchuan Li[2]
[1]School of Mechatronics Engineering
Harbin Institute of Technology
Harbin, Heilongjiang, China
[2]Beijing Institute of Aerospace Control Devices
Beijing, Beijing, China

INTRODUCTION

Molecular films are commonly used to decrease the friction coefficient and surface wear rate [1]. In tribology, this regime is known as the boundary lubrication (BL), where the hydrodynamic lubrication cannot be achieved. In this regime, molecular films can avoid direct contacts between sliding interfaces, and the shear stress of boundary films is obviously lower than that of bare solid surfaces. The boundary lubrication phenomena frequently occur in the practical machinery, such as the start-stop process of moving parts and the mechanical devices operated under overload situations. Thus, there is an urgent need for revealing the lubrication mechanisms of molecular films and employing it in the practical applications.

The distribution and thickness of molecular films have a significant influence on the lubrication performance. These film properties are determined by the preparation process. Based on the formation mechanism of molecular films, the physisorbed films can be prepared with Langmuir-Blodgett method. The chemisorbed films can be prepared by immersing substrates in lubricant solutions, and the rinse of surface monolayers with solvent is needed to remove the excess lubricant molecules from the substrate [2, 3]. For the experimental measurements, the atomic force microscope (AFM) is a suitable technique to investigate the structural and frictional properties of monolayers [4, 5]. During the measurement, the AFM tip sliding across sample surfaces can simulate the frictional process between a single asperity and the counterpart surface. This is one distinct advantage suitable for studying the nanotribological behavior of molecular films. In order to employ molecular films in practical applications, detailed studies are needed to investigate the effect of preparation process on film properties and reveal the lubrication mechanism of molecular films.

The focus of this paper is to study the influence of preparation process on film properties, such as the distribution and thickness of molecular films. The AFM combined with scanning electron microscope (SEM) is employed to characterize the surface topography and frictional behavior of molecular films. And the lubrication mechanism of surface monolayers is analyzed.

EXPERIMENTAL TECHNIQUE

Materials

To prepare the substrates, silicon wafers were first cut into 25 mm × 25 mm pieces and ultrasonically cleaned with water and ethanol. Then, the clean silicon wafers were coated with amorphous diamond-like carbon (DLC) film, which serves as a tribochemical layer providing low friction and good wear resistance. During the coating process, the frictional properties of DLC film can be adjusted by controlling the additive. The Ti-DLC film appears great ability in reducing friction coefficient, which is employed in this study [6]. The lubricant used herein is HM-900, which is mainly composed of potassium stearate ($CH_3(CH_2)_{16}COOK$) molecules. Numerous experimental studies have revealed that the straight-chain (saturated) carboxylate salts can be used as an effective boundary lubricant [7, 8].

Monolayers Preparation

Prior to the monolayers preparation, DLC films were ultrasonically cleaned with ethanol for 15 minutes, ultrasonically cleaned with acetone for another 15 minutes and finally dried using compressed air. Then, surface monolayers were

prepared on DLC substrates by liquid phase deposition. The lubricant solution of 0.75% (wt) was prepared by dissolving lubricant powders in ethanol. To facilitate the powder dissolving, the solution was agitated for 5 minutes and maintained at 75 °C for one hour. Then, the clean DLC substrates were immersed in lubricant solution for one hour at 75 °C. The surface monolayers were formed spontaneously during the immersion process. In order to complete the monolayer preparation and investigate the effect of preparation process on film properties, the resulting substrates were gently smeared with degreasing cloth and then rinsed with fresh ethanol solvent to remove the excess lubricants from the substrate surface. Figure 1 shows the preparation process of surface monolayers and each characterization during the whole process.

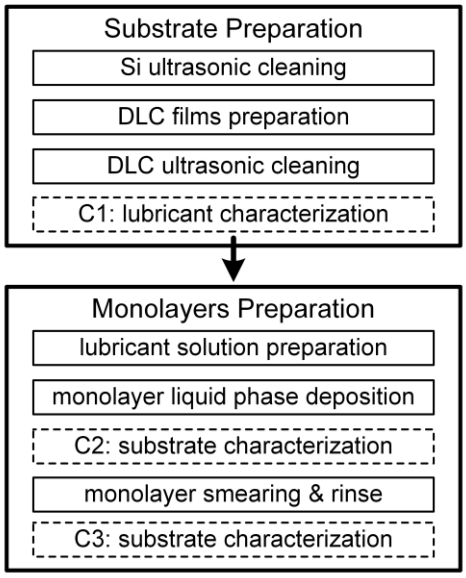

FIGURE 1. Block diagram of monolayer preparation process and the three characterizations during the whole process.

Monolayers Characterization

In this paper, the SEM and AFM were employed to characterize the surface topography and nanotribological properties of molecular films. The SEM can investigate the surface topography under macro-, micro- and nano-scale. The AFM is more suitable for the surface characterization under nanoscale. Furthermore, the AFM employs a sharp tip, with a tip radius of 20 nm, to obtain the high-resolution imaging of surfaces and also the surface height information. However, the observed region of AFM is much smaller when compared with SEM. Therefore, we combined the SEM and AFM to characterize the surface topography of molecular films.

For the investigation of frictional behavior, the AFM contact mode was used. All the measurements were carried out in a scan direction perpendicular to the cantilever long axis. Surface topography and surface friction can be imaged simultaneously. During the measurement, the frictional force acting on the cantilever would generate torsion signal (volt) in position sensitive detector (PSD), and the calibration constant should be computed to convert voltage signal to frictional force. Therefore, an improved wedge calibration method introduced by Varenberg et al. [9] was employed to obtain the calibration constant, as shown in Figure 2.

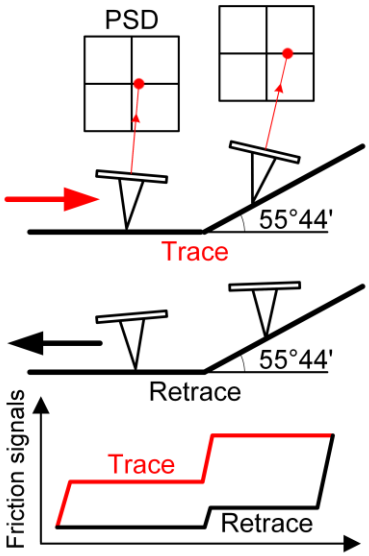

FIGURE 2. Schematic of the wedge calibration method proposed by Varenberg, the red dot in figure represents the reflected laser dot from the vertex of cantilever.

RESULTS AND DISCUSSION

The lubricant powders before dissolving were observed with SEM, as shown in Figure 3. The sample was prepared by uniformly distributing lubricant powders over the conductive adhesive tape, and the excess powders were removed by the compressed air. Prior to the observation, Au sputtering was conducted to improve the sample conductivity. It can be observed that there exists layered structures in the lubricant powder, and because of the interlayer bonding forces, it facilitates the formation of lubricant powders. During the powder dissolving, the solution maintains at a high temperature of 75 °C, and

the solvent ethanol interacts with the lubricant molecules, which facilitates the dissolving process.

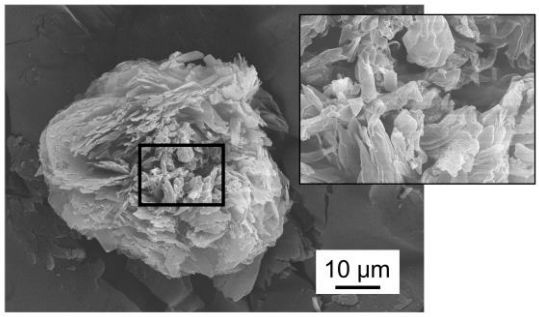

FIGURE 3. Representative SEM images of a lubricant powder over conductive adhesive tape and local high-magnification image.

Figure 4 shows representative SEM images of molecular films from a top view and a 45° tilt angle side view. It can be observed that after the liquid phase deposition, adsorptive monolayers are randomly and densely distributed over the DLC substrate, and the film thickness is irregular. It should be noted that the AFM is not a suitable method to characterize the sample with dramatic height change, and thus the SEM was employed herein. Furthermore, the excess and irregular monolayers are detrimental to the controllability of lubrication performance. Therefore, the smearing and rinsing process of monolayers is needed to remove the excess lubricants from the substrate surface.

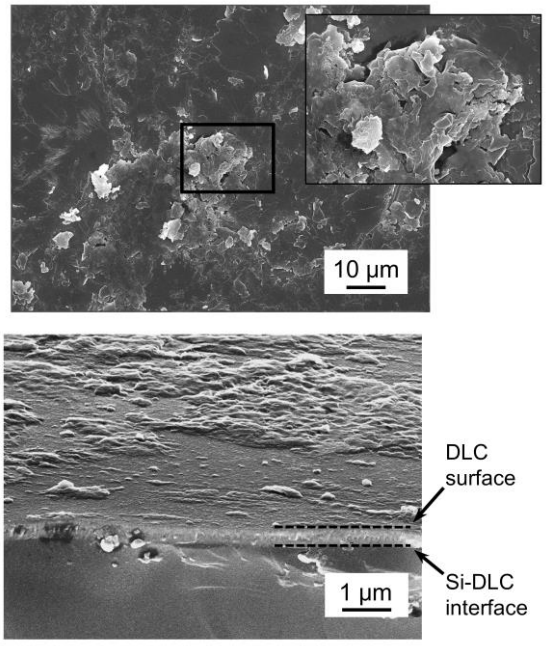

FIGURE 4. Representative SEM images of surface monolayers after liquid phase deposition from a top view and a 45° tilt angle side view, two dashed lines in Figure indicate the Si-DLC interface and DLC surface, respectively.

Figure 5 shows representative SEM images of substrate monolayers after the smearing and rinsing from a 45° tilt angle side view, it can be observed that numerous lubricant molecules have been removed during this process. Some island-like monolayers are formed on the DLC substrate, and the distribution of monolayers is not continuous. As shown in the high-magnification image, there exists evenly distributed carbon clusters generated during the DLC preparation. However, the gray scale plot is difficult to distinguish the surface monolayers and DLC surface.

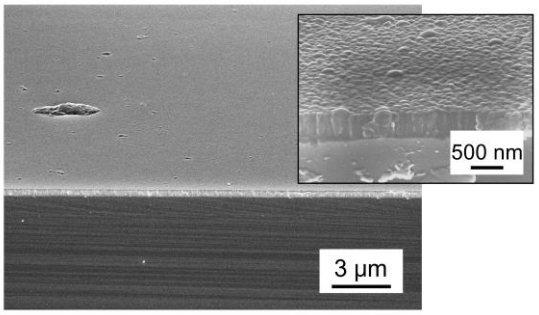

FIGURE 5. Representative SEM images of surface monolayers after the smearing and rinsing process, observed with two magnifications to show both the surface monolayers (low) and DLC topography (high).

The maximum magnification of SEM is limited by the conductivity of samples. Also, the monolayer thickness and frictional force cannot be obtained through SEM. Thus, the AFM was employed as an important complementary method to investigate the monolayer topography and frictional behavior.

Considering the limited range of AFM imaging, measurements of molecular films were carried out multiple times over different positions. The representative surface topography of molecular films and corresponding surface friction were shown in Figure 6 and Figure 7, respectively. The typical film thickness is in the range of 20-30 nm. And the friction of monolayers is significantly lower than that of DLC substrate. Furthermore, the friction change on monolayers is much more stable. Whereas the friction over DLC surfaces changes dramatically. It can be inferred that monolayers can not only reduce the friction during sliding, but also make the change

of frictional force not obvious, which is beneficial to the surface lubrication.

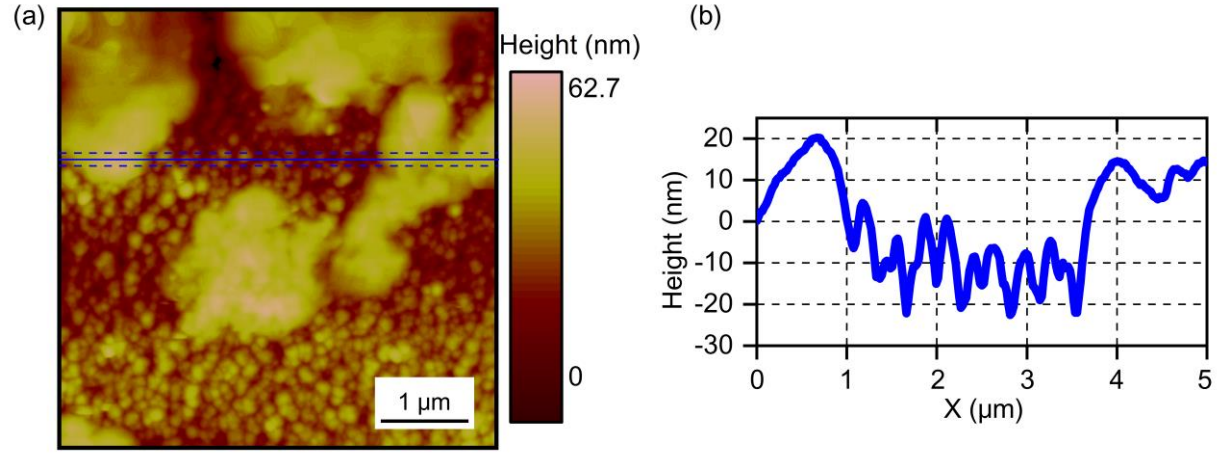

FIGURE 6. (a) The representative AFM image of surface monolayers after the smearing and rinsing process. (b) The cross-section line profile of corresponding AFM image.

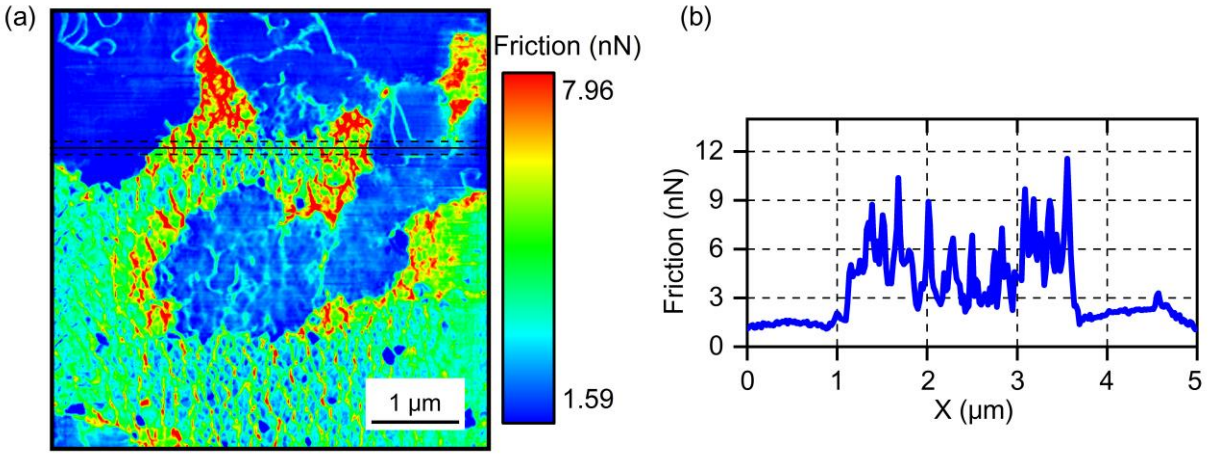

FIGURE 7. (a) Corresponding AFM image of surface friction after the smearing and rinsing process. (b) The cross-section line profile of corresponding AFM image.

CONCLUSIONS

Through the above analysis, it can be observed that after the liquid phase deposition, numerous lubricant molecules adsorb on the DLC surfaces. Under this case, the monolayers distribution is irregular and dense. Therefore, the smearing and rinsing process is needed to remove the excess molecules. After the smearing and rinsing, the molecules have been removed and the film thickness is reduced. Through the AFM characterization, it can be found that the film thickness is in the range of 20-30 nm. Furthermore, the friction on monolayers is much lower and much more stable.

ACKNOWLEDGEMENT

This work was supported by the Joint Funds Key Project of the National Natural Science Foundation of China (No.U1537214), National Natural Science Foundation of China (No. 21573054), State key laboratory of precision measuring technology and instruments (Tianjin University No. PILAB1701) and the State Key Program of National Natural Science of China (No. 51535003).

REFERENCES

[1] Bhushan B, Kasai T, Kulik G, Barbieri L, Hoffmann P. AFM Study of Perfluoroalkylsilane and Alkylsilane Self-assembled Monolayers for Anti-stiction in MEMS/NEMS. Ultramicroscopy. 2005; 105: 176-188.

[2] Ulman A. Formation and Structure of Self-Assembled Monolayers. Chemical Reviews. 1996; 96: 1533-1544.

[3] Miyashita T. Recent Studies on Functional Ultrathin Polymer Films Prepared by the Langmuir-Blodgett Technique. Progress in Polymer Science. 1993; 18: 263-294.
[4] Liu H, Bhushan B, Eck W, Kueller A. Investigation of Nanotribological Properties of Self-assembled Monolayers with Alkyl and Biphenyl Spacer Chains (invited). Ultramicroscopy. 2002; 91: 185-202.
[5] Ren S, Yang S, Zhao Y. Micro- and Macro-Tribological Study on a Self-Assembled Dual-Layer Film. Langmuir. 2003; 19: 2763-2767.
[6] Cui J, Qiang L, Zhang B, Ling X, Yang T, Zhang J. Mechanical and Tribological Properties of Ti-DLC Films with Different Ti Content by Magnetron Sputtering Technique. Applied Surface Science. 2012; 258: 5025-5030.
[7] Tao Y. Structural Comparison of Self-assembled Monolayers of N-alkanoic Acids on the Surfaces of Silver, Copper, and Aluminum. Journal of the American Chemical Society. 1993; 115: 4350-4358.
[8] Lim M, Feng K, Chen X, Wu N, Raman A, Nightingale J, Gawalt E, Korakakis D, Hornak L, Timperman A. Adsorption and Desorption of Stearic Acid Self-Assembled Monolayers on Aluminum Oxide. Langmuir. 2007; 23: 2444-2452.
[9] Varenberg M, Etsion I, Halperin G. An Improved Wedge Calibration Method for Lateral Force in Atomic Force Microscopy. Review of Scientific Instruments. 2003; 74: 3362-3367.

TOOL EDGE GEOMETRY FROM STRUCTURED LIGHT SCANNING

Timothy No and Tony L. Schmitz
Department of Mechanical, Aerospace, and Biomedical Engineering
University of Tennessee, Knoxville, TN, USA

INTRODUCTION

Structured light scanners are used to generate three-dimensional models of physical objects. These models can be measured and inspected for reverse engineering or quality control applications. Cutting tools, such as endmills or drills, can be scanned and measured to obtain tool specific geometry. For example, the edge profile for each tooth of a serrated endmill was measured and used to predict cutting forces and stability [1]. The objective of this paper is to demonstrate the capability of measuring the rake and relief profiles for a scanned endmill.

Keywords: 3D scanning, endmill, rake angle, relief angle

EXPERIMENTAL SETUP

The tool surface was prepared prior to scanning. An airbrush was used to spray the fluted end with a titanium dioxide coating, providing the surface with both a light color and diffuse reflection for optimal scanning (Fig. 1). Reference markers placed along the shank of the tool enabled multiple scans to be stitched together to create the final point cloud/3D model. Figures 2-3 display the scanning system and final 3D tool scan. The overall size of the scanned tool is displayed in Fig. 4. The GOM ATOS Capsule scanner and GOM Inspect software was used for this research.

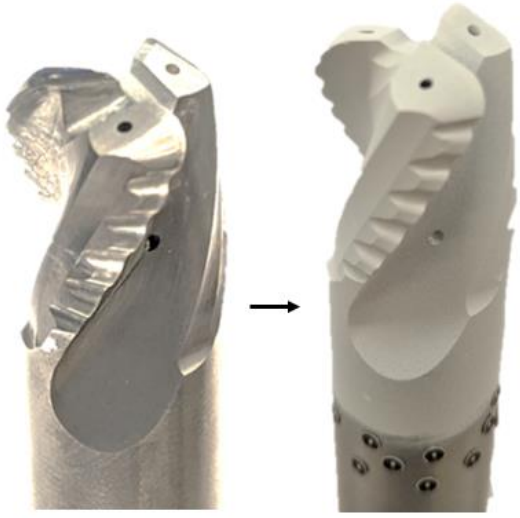

Figure 1. Tool prepared for scanning. Uncoated (left) and coated with reference markers (right).

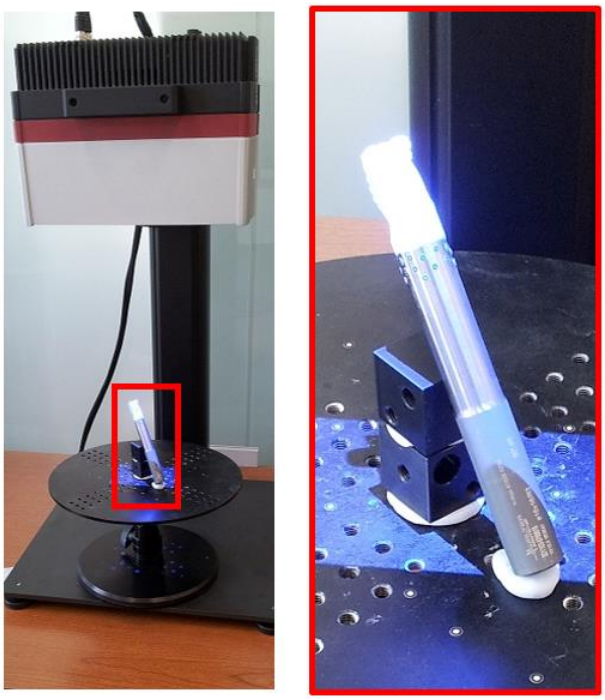

Figure 2. Setup on the GOM scanner.

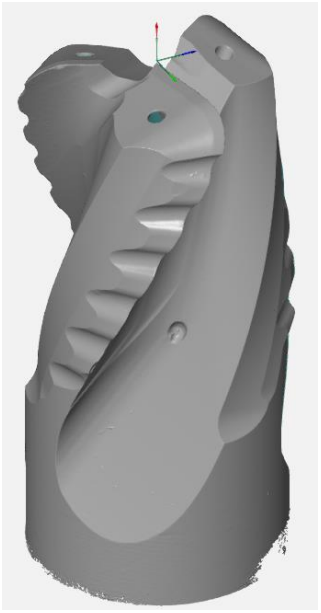

Figure 3. Scanned 3D model.

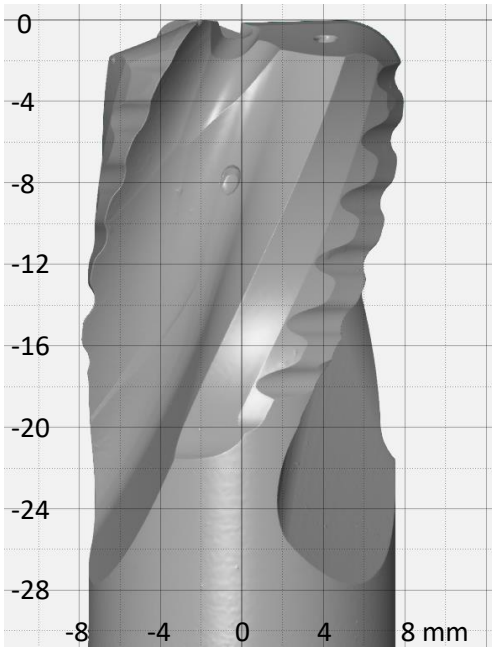

Figure 4. Scale for scanned endmill. The vertical axis is the z-axis.

DATA ANALYSIS

In order to perform geometric measurements, a coordinate system must be established on the tool. A cylinder was fit to the tool shank and a plane was created from the fluted end's extreme points. The intersection of the cylinder's axis and the plane was set as the origin of the coordinate system. Planar cross-sections were created along the z-axis of the tool. Each section contained the rake and relief profiles of each tooth at the corresponding axial location (Fig. 5). A simplified example of rake and relief angles is displayed in Fig. 6.

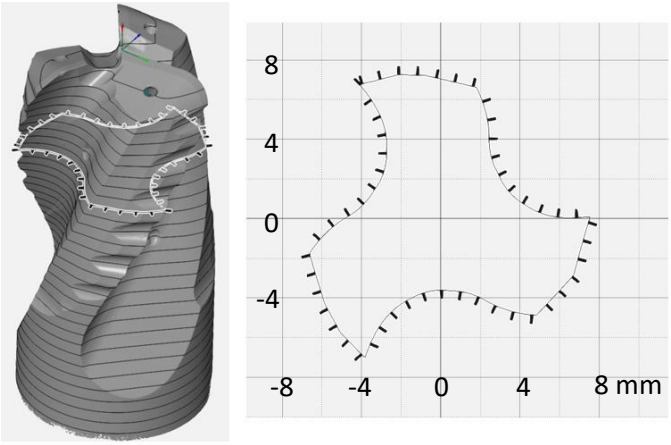

Figure 5. Planar cross-sections of 3D model (left) and z = -10 mm section (right).

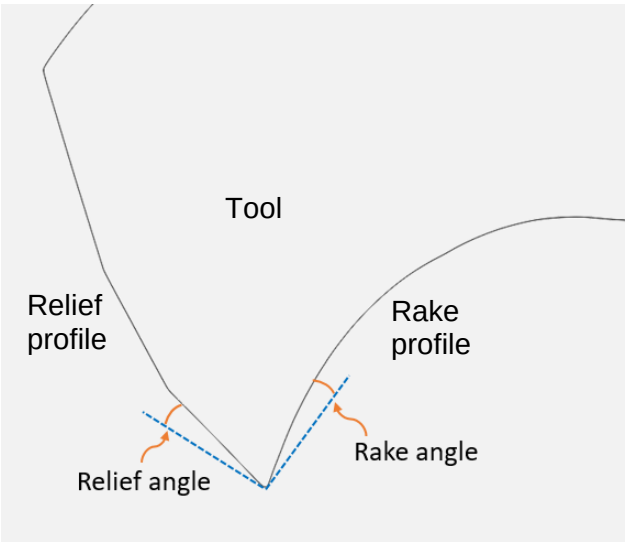

Figure 6. Example of rake and relief angles.

To calculate the rake and relief angles, equidistant points were placed along the rake and relief profiles (Fig. 7). The spacing between each point was 0.025 mm. Each point had an x,y,z coordinate and unit normal vector. A reference vector was created by connecting the origin of the section to the center of a best-fit circle at the tooth tip, where the rake and relief profiles meet (Fig. 8). To measure the rake angles, the unit normal vectors along the rake profile were rotated 90 deg clockwise to become unit tangent vectors. The rake angle was the angle between the tangent vector and reference vector. The same method was used to calculate the relief angles except the reference vector was now perpendicular (rotated 90 deg) to the original.

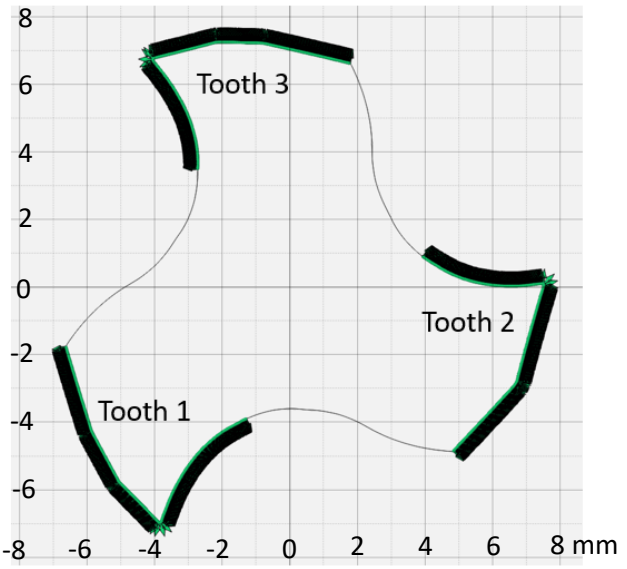

Figure 7. Rake and relief points for each tooth of the z = -10 mm section.

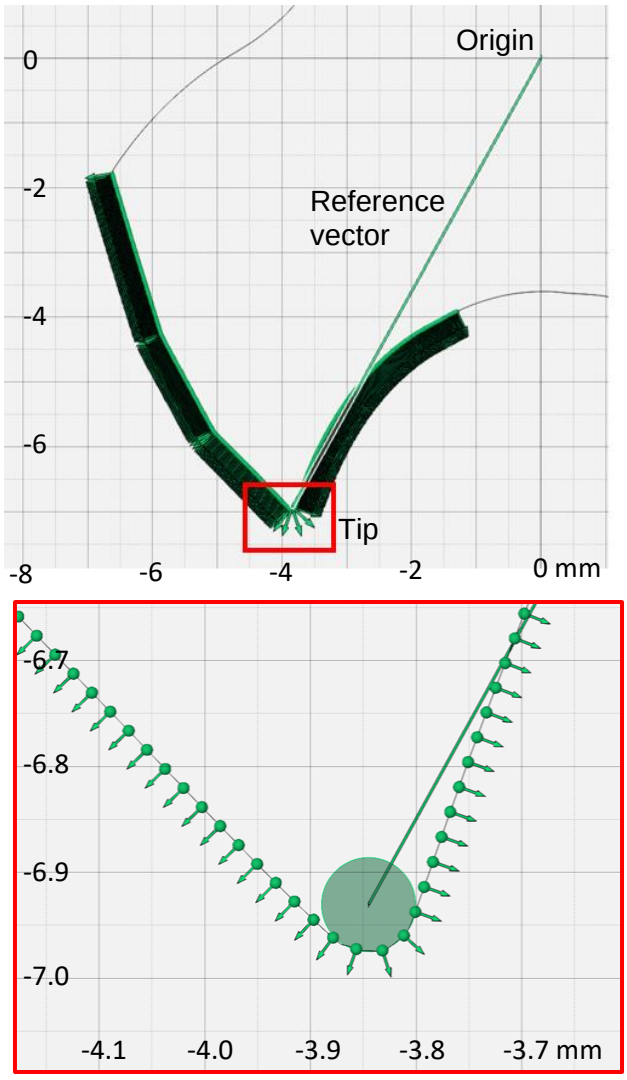

Figure 8. Reference vector (top) and tip details (bottom) for tooth 1 of the z = -10 mm section.

RESULTS

The rake and relief angles were plotted with respect to point distance, which is the distance traversed along the rake or relief profile from tip to point. A point at the tip was selected as the zero point so the distance of each subsequent point, moving away from the tip, could be calculated based on the equidistant point spacing. The rake and relief plots for tooth 1 are shown in Figs. 9 and 10. The rake angle is positive at the tip but flattens out and becomes negative as it moves further along the rake profile. The rake angle transitions linearly from positive to negative, which indicates that the rake profile is curvilinear. The relief angle plot shows three angles corresponding to the three flat sections along the relief profile.

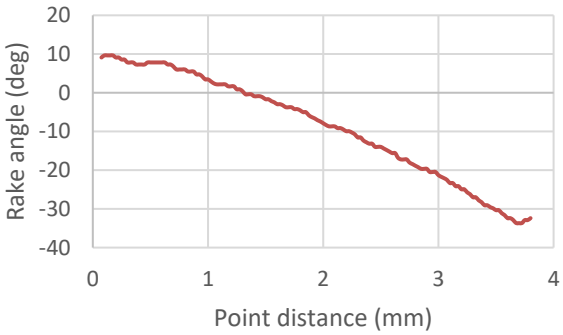

Figure 9. Rake angle measurements for tooth 1 of the z = -10 mm section.

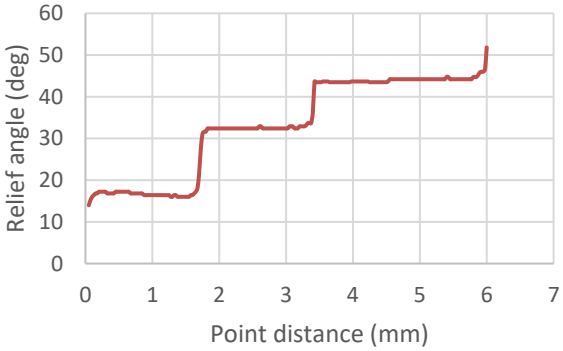

Figure 10. Relief angle measurements for tooth 1 of the z = -10 mm section.

The rake and relief angles were calculated for tooth 2 and tooth 3; the combined plots for all three teeth are shown in Figs. 11 and 12. The same trend can be seen in the combined rake angle plot; however, tooth 2 transitions from positive to negative slightly earlier than the other two teeth. Tooth 2 also differs in the combined relief angle plot (two vs. three angles).

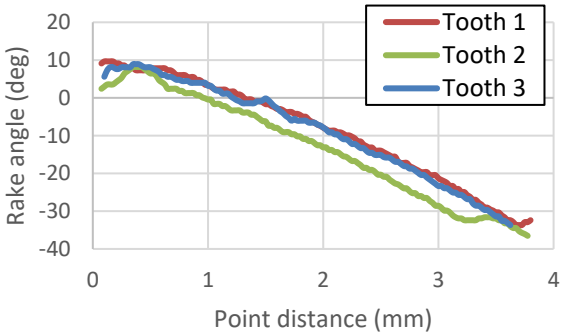

Figure 11. Rake angle measurements for all three teeth of the z = -10 mm section.

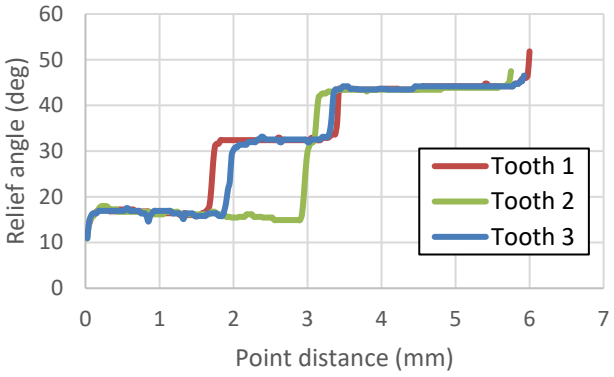

Figure 12. Relief angle measurements for all three teeth of the z = -10 mm section.

The previous plots compare the rake and relief angles of the three teeth at one z-section (-10 mm). The next set of plots compares one tooth (tooth 1) at multiple z-sections (Figs. 13 and 14).

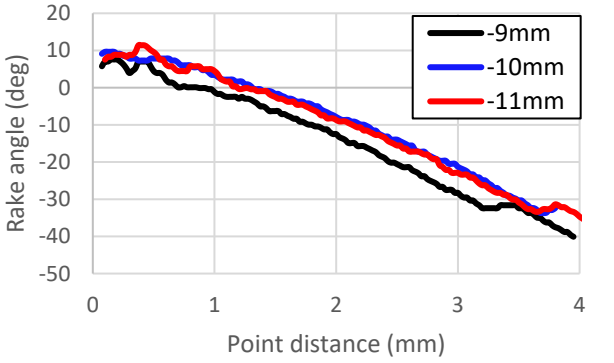

Figure 13. Rake angle measurements for multiple z-sections of tooth 1.

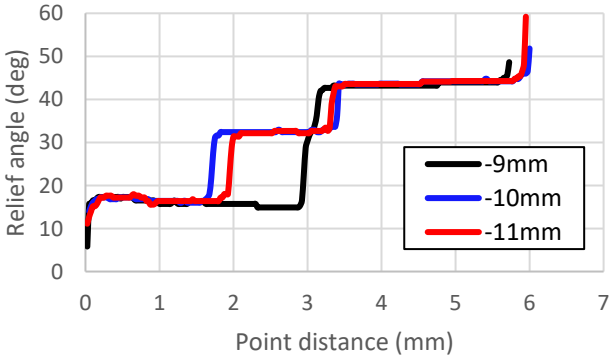

Figure 14. Relief angle measurements for multiple z-sections of tooth.

As seen in the previous figures, the rake and relief angle plots comparing multiple teeth of one section and multiple sections of one tooth are nearly identical. This is not a coincidence, but due to the design of the serrated cutting edges.

Figure 4 shows that the serration pattern along a single tooth repeats approximately every -3 mm (z). The serrated edge can be thought of as a wave with peaks and troughs. Any three consecutive, -1 mm z-sections along the serrated edge of a tooth have two peaks and one trough. The relief angles on a peak section have three distinct angles, while a trough section has only two. The rake angles have roughly the same profile, but the trough section has a shorter tip and transitions sooner from a positive to negative angle (e.g., Fig. 11: Tooth 2, z = -10 mm).

This pattern of two peaks and one trough repeats for the three teeth of one section due to the offset of the serrations between each tooth. For a given section, if a tooth is in a trough, then the other two teeth will be on a peak. Another way to visualize this is by looking at a planar view of multiple sections together. Figures 15 and 16 show the same z-sections, but now labeled A (-9 mm), B (-10 mm), and C (-11 mm). The three teeth are labeled as well.

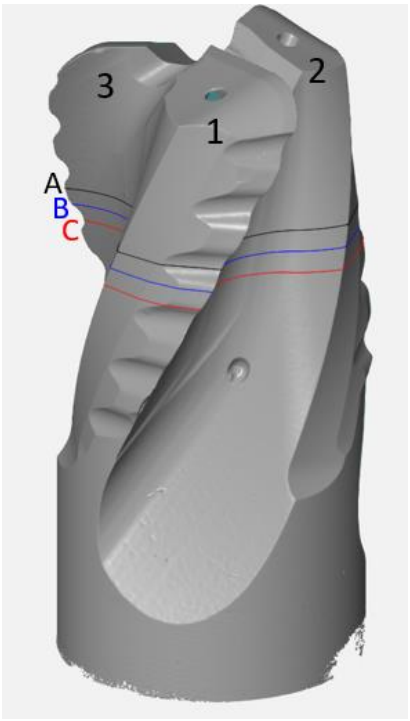

Figure 15. 3D view of consecutive z-sections.

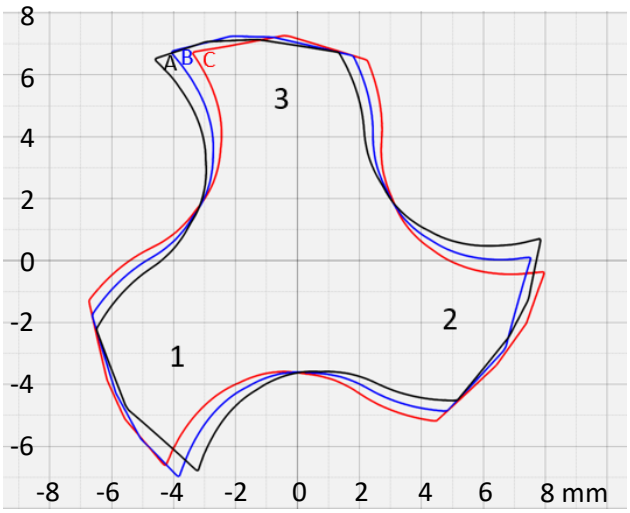

Figure 16. Top view of consecutive z-sections.

The shorter teeth in the trough sections were quantified by measuring the radius (distance from center to the tip) for each tooth; see Table 1. The measured values along a section or tooth follow the serration pattern.

Table 1. Radii measurements (all dimensions in mm) for section comparison.

		Tooth		
		1	2	3
Section	A	7.512	7.853	7.959
	B	7.957	7.512	7.862
	C	7.870	7.955	7.508

CONCLUSIONS

This paper demonstrates the capability of using structured light scanning for tool edge geometry measurements, specifically rake and relief angles. Once a coordinate reference frame was established, planar cross-sections were created, revealing the rake and relief profiles along the axis of the tool. Data points along each profile were extracted to calculate the rake and relief angles. The measurements show the serration pattern designed along and between each tooth for the selected non-standard edge geometry endmill.

REFERENCES

[1] No, T., Gomez, M., Copenhaver, R., Uribe Perez, J., Tyler, C., and Schmitz, T., 2019, Scanning and Modeling for Non-standard Edge Geometry Endmills, Procedia Manufacturing, 34: 305-315.

COMPRESSIVE SENSING FOR FAST 3-D TWO-PHOTON MICROSCOPY

Chenyang Wen, Mindan Ren, and Shih-Chi Chen*
Department of Mechanical and Automation Engineering
The Chinese University of Hong Kong
Shatin, N.T., Hong Kong SAR, China
*Email: scchen@mae.cuhk.edu.hk

In this paper, we present a multi-focus compressive sensing (CS) method for 3-D and random-access two-photon excitation (TPE) microscopy based on a digital micromirror device (DMD). Through CS, the imaging speed of the DMD-based TPE microscope [1] has been improved by a factor of 4 without sacrificing the resolution. Simulation and imaging experiments have been performed to verify the predicted performance enhancement and to identify the optimal processing parameters of the system, including number of laser foci and sampling rate.

INSTRUCTIONS

TPE microscopy is one of the most widely used fluorescent imaging technique that has the advantages of optical sectioning, high-resolution, and deep tissue penetration etc. In the past two decades, TPE microscopy has enabled and led to numerous discoveries in physiology, neurobiology, and embryology etc. [2,3]. Conventionally, a 2-D optical cross-section in a TPE system is obtained by raster-scanning the laser focus across the imaging plane via a pair of galvanometric scanners. Next, a point detector, e.g., photomultiplier tube (PMT), sequentially collects the emission from each excited point in space to form a 2-D image. A 3-D image can be generated by scanning the sample or laser focus axially via an additional scanner, e.g., translational stage or electrically tunable lens [4]. As the scanning speed increases, imaging quality, e.g., signal-to-noise ratio (SNR), is usually compromised by the decreasing pixel dwell time.

To address the issue, here we present a CS-based 3-D random-access TPE microscope, where multiple laser foci are simultaneously generated to form arbitrarily structured illumination patterns by using a DMD and binary holography, leading to a 4x speed enhancement without sacrificing the resolution. The DMD generated 1 - 30 laser foci (limited by total laser power) can be positioned to any selected points in space by the designed holograms [1,5]. By switching the holograms stored in the DMD memory, the laser foci can scan the planned trajectories at the DMD pattern rate (22.7 kHz). As such, the recorded intensity information can be used to reconstruct 3-D images of a sample via CS algorithms.

SYSTEM CONFIGURATION

Figure 1 presents the optical configuration of the CS-based 3-D random-access TPE microscope, where the laser source is an 80 MHz Ti:sapphire femtosecond laser (Chameleon Ultra II, Coherent) with a pulse width and central wavelength of 200 fs and 800 nm respectively. First, a polarizing beam splitter (PBS) and half-wave plate (HWP) are used to control the laser power. A DMD (DLP 4100, 0.7'' XGA, Texas Instruments) modulates the wavefront of the incoming laser beam to achieve multi-focus random-access scanning via the designed binary holograms. Lastly, the generated laser foci are focused via an infinity-corrected objective lens (25X CFI Apo LWD N.A. 1.10, Nikon). To compensate the angular dispersion introduced by the DMD, a blazed transmission grating (1200 lines/mm, Lightsmyth) and a 4-f system (L1, L2) are introduced to compensate the angular dispersion. Notably, the DMD chip is in conjugation with the back aperture of the objective lens; and a spatial filter (SF) collects the 1st order diffraction beam, which contains the encoded wavefront information. The emissions from the sample are directed to a PMT (R10699 and C7950, Hamamatsu) via a long-pass dichroic mirror (DM).

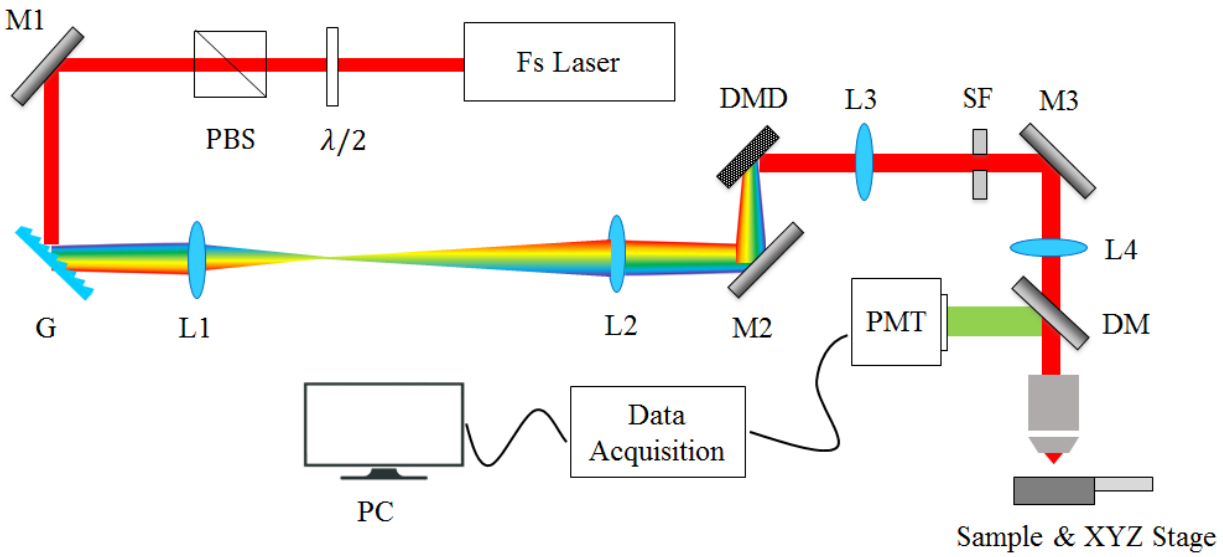

FIGURE 1. Optical configuration of the DMD-based TPE. Laser foci are scanned by the DMD multi-focus scanner; M1 - M3, high-reflectivity mirrors; L1 - L4, lenses (f_{L1}, f_{L2}, f_{L3}, f_{L4} =100, 250, 200 and 200 mm, respectively).

BINARY HOLOGRAM

First, we describe the generation and optimization of holograms for single- and multi-focus 3-D scanning [6] and weighted Gerchberg-Saxton [7,8] algorithm. For single focus scanning, the required phase $\phi(x,y)$ can be calculated by superposing spherical and tilted wavefronts as expressed in Eq. (1).

$$\phi(x,y) = \frac{\pi \Delta z M_{obj}^2 (x^2+y^2)}{\lambda f_{L3}^2} + \frac{2\pi M_{obj}}{\lambda f_{L3}} (x\Delta x + y\Delta y) \quad \textbf{(1)}$$

where Δx, Δy, Δz are the desired displacements of the laser focus in x, y, z axes respectively. λ is the wavelength; and M_{obj} is the magnification of the objective lens. As the DMD consists of millions of micromirrors and each mirror has two stable states at ±12°, it can be used as a programmable binary grating. According to Lee holography, any calculated phase $\phi(x,y)$ from Eq. (1) can be converted into binary patterns by Eq. (2):

$$H(i,j) = \begin{cases} 1, & -\frac{q}{2} \le \frac{x}{T} + \frac{\phi(x,y)}{2\pi} + k \le \frac{q}{2} \\ 0, & otherwise \end{cases} \quad \textbf{(2)}$$

where $H(i,j) \in \{0,1\}$ $(1 \le i \le m;\ 1 \le j \le n;\ i,j \in N)$ represents the pixels on the DMD; 1 and 0 refer to the "on" and "off" states respectively; m and n represent the number of rows and columns respectively; x = i·d and y = j·d; d is the DMD pixel size; T is the grating period of the hologram; k is an integer; and q is a constant that determines the widths of the fringes.

For multi-foci scanning, weighted Gerchberg-Saxton algorithm is adopted to ensure the generated laser foci have highly uniform intensity distribution. Specifically, two coefficients w_t and θ_t are introduced to the phase equation for adjusting the weight and phase of the t^{th} focus. The algorithm starts by assigning the target foci with equal intensities and random phases, i.e., let w_t = 1 and θ_t to random numbers. The optimal solution can be found through iterations. In each iteration, the phase $\phi'(x,y)$ of the weighted complex hologram can be obtained by Eq. (3),

$$\phi'(x,y) = arg\left[\sum_t w_t e^{i(\phi_t(x,y)+\theta_t)}\right] \quad \textbf{(3)}$$

where $\phi_t(x,y)$ is the phase of the t^{th} focus obtained by Eq. (1). The intensity of the t^{th} focus (I_t) can be estimated by $I_t = |V_t|^2$, where V_t is expressed in Eq. (4). Note that $H(i,j)$ in Eq. (4) is obtained by substituting the results in Eq. (3) into Eq. (2). To perform the iteration, w_t and θ_t are updated using Eq. (5) and (6).

$$V_t = \sum_{i=1}^{m} \sum_{j=1}^{n} H(i,j) e^{i(-\phi_t(i\cdot d, j\cdot d))} \quad \textbf{(4)}$$

$$w_t = w_t \frac{\langle |V_t| \rangle}{|V_t|} \quad \textbf{(5)}$$

$$\theta_t = arg(V_t) \quad \textbf{(6)}$$

where the angled brackets denote the average of all foci. At each iteration, w_t is optimized to reduce the deviations of $|V_t|$. The algorithm will typically converge within 15 iterations, generating laser foci of uniform intensity (i.e., >99% intensity uniformity).

MULTI-FOCUS COMPRESSIVE SENSING

CS is a signal processing technique for acquiring and reconstructing sparse signals by using significantly lower data points than required by the Nyquist rate. In this section, we describe how CS algorithms are applied in the DMD TPE microscope to enhance the imaging speed. During a measurement, the specimen is first illuminated with a selected number of laser foci that are randomly distributed in space. Next, the combined emissions ar collected by the PMT, i.e., point detector. After *M* measurements, the signals from the PMT can be described by an underdetermined equation, as expressed in Eq. (7),

$$b = Ax \quad \textbf{(7)}$$

where *x* is a vectorized image (*N* ×1). *A* is the measurement matrix of size $M \times N$ ($M < N$). Each row in *A* represents a measurement, where the total number of "1" in each row equals to the number of laser foci used in that measurement. The image can be reconstructed by solving the optimization problem, as expressed in Eq. (8),

$$\min_{x} \|\nabla x\|_1 + \tau \|Fx\|_1 \quad s.t. b = Ax \quad \textbf{(8)}$$

where ∇ represents a 2-D total variation (TV) operator to preserve the sharp features of the image and to denoise; *F* represents discrete cosine transform; *τ* is a weighting parameter to balance the two regularizers. The optimization problem can be solved by applying the alternating direction method of multipliers algorithm, which has been widely used for solving l1-regularized optimization problems [9]. Next, we apply the one-step gradient descent algorithm, derived based on the nonmonotone line search technique, to expedite the image reconstruction process [10].

EXPERIMENTAL RESULTS

We first perform simulated experiments to verify the CS-based multi-focus imaging scheme on the Shepp-Logan phantom with different numbers of foci; the results are presented in Fig.2. Figure 2(a) presents the raw image of the Shepp-Logan phantom; Figure 2(b) - 2(i) present the under-sampled images and reconstructed images using 1, 2, 3, 5, 10, 20, and 30 laser foci respectively. In the experiment, the size of the image is set to 100×100 pixels and sampling rate is fixed at 30%, i.e., speed enhancement ~ 3.33. The size of each laser focus and the minimum step size are set as one pixel. From the results in Fig. 2, it can be clearly observed that (1) the image quality and sharpness increase with increasing number of laser foci; and (2) the CS reconstructed images show superior resolution and details than the under-sampled image and become comparable to the raw image if sufficient laser foci (>5) are used. (Note that the sampling rate is kept constant when varying the number of foci.)

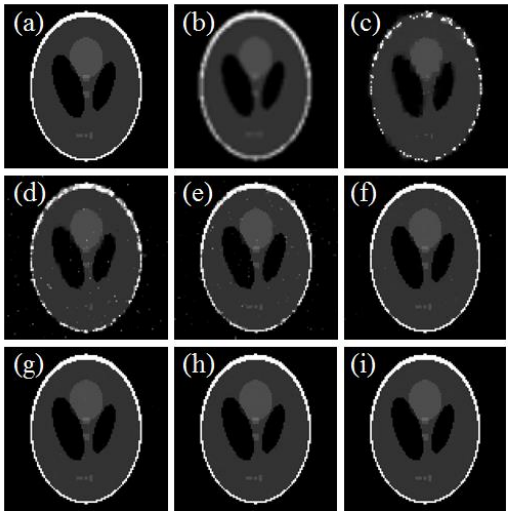

FIGURE 2. Simulated imaging experiments based on Shepp-Logan phantom. (a) Raw image; (b) uniformly under-sampled image; (c)-(i) reconstructed images with 1, 2, 3, 5,10, 20, and 30 laser foci respectively.

To quantify the image reconstruction errors, relative error (RE) analysis is used, i.e., $\|x - \overline{x}\|_2 / \|x\|_2$, where $\overline{x}$ represents the reconstructed images. Figure 3 presents the calculated RE values for 1 - 30 foci with a 30% sampling rate. The results agree with our observation from Fig. 2 that the image reconstruction errors decrease rapidly with increasing laser foci and gradually saturate when the number of foci approaches 5.

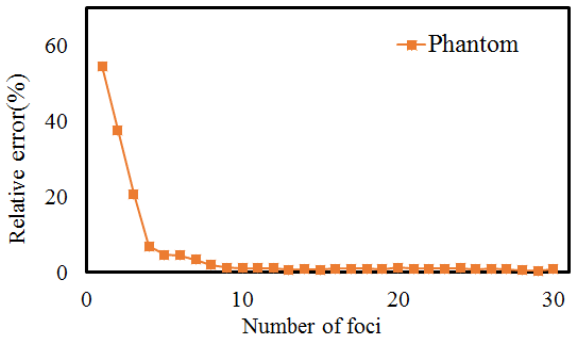

FIGURE 3. Relative error (RE) analysis of multi-focus CS imaging using 1 - 30 laser foci.

Before the CS imaging experiments, we first experimentally verify laser foci of arbitrary 2-D patterns and uniform intensity can be generated by the DMD. This is done by replacing the PMT with a CCD camera to image a glass slide containing a thin layer of Rhodamine B. In the experiment, 16 laser foci are randomly generated on the sample. The results are shown in Fig. 4, where one may observe that the generated 16 foci have good intensity distribution.

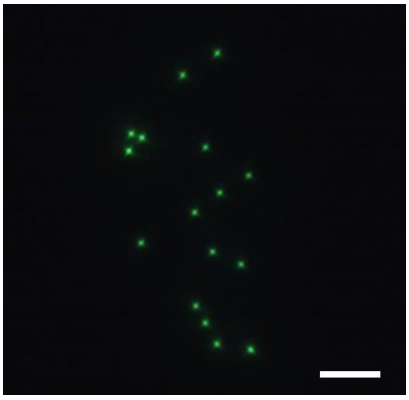

FIGURE 4. Fluorescence of Rhodamine B slide excited by 16 randomly located laser foci, optimized by the weighted Gerchberg-Saxton algorithm. (scale bar = 20 μm)

Lastly, we perform imaging experiments on pollen samples to demonstrate (1) the 3-D imaging capability, i.e., optical cross-sections on an arbitrarily selected inclined plane in space; and (2) the speed enhancement. Figures 5(a) and 5(b) present the imaging results of a pollen grain, obtained via raster-scanning (single-focus) and CS-based multi-focus scanning (25% sampling rate and 5 foci), where each image consists of 100 × 100 pixels. From Fig. 5, one may find that the two images show indistinguishable resolution and quality. As the holograms in the DMD update at 22.7 kHz DMD, the total imaging time for Fig. 5(a) and 5(b) is 0.44 second 0.11 second (~9.1 frames per second) respectively, indicating the CS-based DMD imaging scheme can improve the imaging speed by a factor of 4 without compromising the image quality and resolution on suitable (i.e. sparse) specimens.

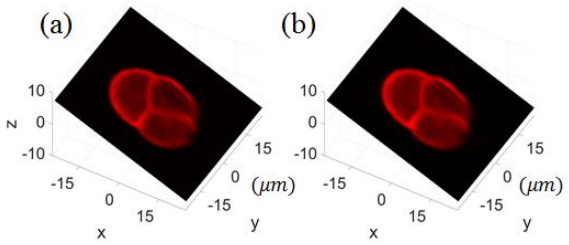

FIGURE 5. Cross-sectional TPE images of a pollen grain on an inclined plane obtained from (a) raster scanning; and (b) CS multi-focus scanning with a 25% sampling rate.

CONCLUSION

In conclusion, we have presented a new CS-based 3D random-access TPE microscope based on binary holography, achieving substantially improved imaging rate (~4 times). Simulation have been performed to identify the optimal CS processing parameters including the number of randomly generated laser foci (5-10) and sampling rate (~30%). Next, fluorescent imaging experiments on pollen samples are performed to demonstrate the capabilities of fast 3-D imaging on arbitrarily defined planes, achieving an imaging speed of 9.1 fps with CS algorithm. The new CS-based DMD imaging platform may find important applications in bio-imaging and optogenetics for studying fast dynamic events and simultaneously investigating multiple regions of interests in vivo.

ACKNOWLEDGMENT

This work is supported by the HKSAR Research Grants Council (RGC), General Research Fund (GRF), (CUHK 14206517 & 14209081).

REFERENCES

[1] Geng Q, Gu C, Cheng J, Chen S. Digital Micromirror Device-based Two-photon Microscopy for Three-dimensional and Random-access Imaging. Optica. 2017; 4: 674-677.

[2] So PTC, Kim K, Buehler C, Masters BR, Hsu L, Dong C-Y. Excitation Microscopy. Methods in Cellular Imaging. 2013: 147.

[3] Helmchen F, Denk W. Deep Tissue Two-photon Microscopy. Nature Methods. 2005; 2: 932.

[4] Sancataldo G, Silvestri L, Mascaro ALA, Sacconi L, Pavone FS. Advanced Fluorescence Microscopy for in vivo Imaging of Neuronal Activity. Optica. 2019; 6:758-765.

[5] Geng Q, Wang D, Chen P, Chen S. Ultrafast Multi-focus 3-D Nano-fabrication based on Two-photon Polymerization. Nature Communications. 2019; 10: 2179.
[6] Lee WH. Binary Synthetic Holograms. Applied Optics. 1974; 13: 1677-1682.
[7] Stuart D, Barter O, Kuhn A. Fast Algorithms for Generating Binary Holograms. arXiv preprint arXiv:1409.1841. 2014.
[8] Vizsnyiczai G, Kelemen L, Ormos P. Holographic Multi-Focus 3D Two-Photon Polymerization with Real-Time Calculated Holograms. Optics Express. 2014; 22: 24217-24223.
[9] Boyd S, Parikh N, Chu E, Peleato B, Eckstein J. Distributed Optimization and Statistical Learning via the Alternating Direction Method of Multipliers. Foundations and Trends® in Machine learning. 2011; 3: 1-122.
[10] Li C, Yin W, Jiang H, Zhang Y. An Efficient Augmented Lagrangian Method with Applications to Total Variation Minimization. Computational Optimization and Applications. 2013; 56: 507-530.

REVERSE TASK IN SURFACE METROLOGY - SIMULATION OF INITIAL ONE-PROCESS PROFILE BASED ON RESULTED TWO-PROCESS PROFILE

Pawel Pawlus[1] and Rafal Reizer[2]
[1] Faculty of Mechanical Engineering and Aeronautics
Rzeszow University of Technology
Rzeszow, Poland
[2] Faculty of Mathematics and Natural Sciences
University of Rzeszow
Rzeszow, Poland

INTRODUCTION

Most surfaces have an approximately Gaussian ordinate distribution. They are one-process surfaces because they contain traces of only one process. Two-process surfaces having traces of two processes are created from the one-process texture in a low wear process (wear within the limit of the original surface topography). This type of surface consists of smooth wear-resistance plateau parts with deep valleys working as reservoirs for lubricant and traps for debris. This structure connects in an ideal way good sliding properties of a smooth surface with a great ability to maintain oil of a porous structure. Two-process textures seem to be more functionally important than one-process topographies.

Therefore attempts were made in order to obtain two-process surface during machining. This surface should resemble a texture created during running-in. In this case, a duration of running-in and wear decreased. From this reason two-process textures were created. A plateau-honed cylinder surface is the practical example of such structures. It consists two random portions – a plateau smooth part and a valley rough part. Because of excellent functional properties of such surfaces many other two-process surfaces were created – random, deterministic or random-deterministic. They are called textured surfaces. Surface texturing is an option of surface engineering depending on creating dimples (cavities, oil pockets) on sliding surfaces. Surface texturing leads to minimize the frictional resistance in mixed and fluid lubrications, the tendency to seizure and wear.

The one-process surface is well described and modelled. Typically the contact of surfaces of Gaussian ordinate distribution was analysed. The analysis of the measured one-process texture is simple. There is no problem with a digital filtration. A typical Gaussian filter can be used. Some problems aroused for two-process texture. The application of the Gaussian filter causes profile distortions near the deep valleys. It is necessary to increase the cut-of or use different filters, like double Gaussian filter (ISO 13565-1) or robust. The one process random profile can be easily described by only two parameters: height and horizontal. This profile can be completely described by the standard deviation of roughness height – the Rq parameter, and a correlation length – the distance, at which the autocorrelation function slowly decays to 0.1 value [1]. Figure 1 presents the random one-process profile and its autocorrelation function.

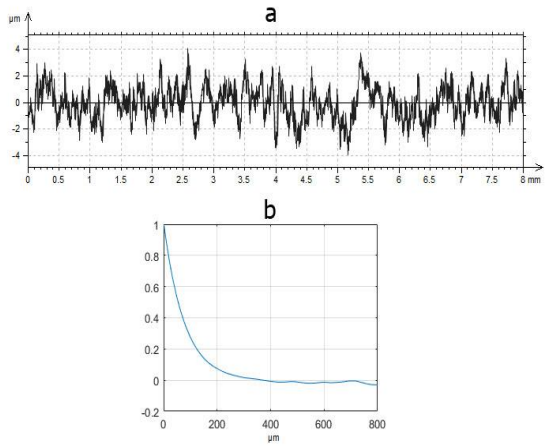

FIGURE 1. One-process random profile (a) and its autocorrelation function (b).

Randomly generating surfaces offer some advantages. Simulation of surfaces created in manufacturing or wear led to a decrease in cost and time of experimental research. The modeled

surfaces can be used in problems of contact, friction and wear.
One-process profile can be computer generated based on the Pq parameter (standard deviation of roughness height) and correlation length using ARMA or FFT [1] methods.
Description of the two-process profile is more complicated compared to that of the one-process roughness. These profiles cannot be described only by two parameters. Therefore the special standards dedicated for two-process surfaces came into existence. The first of them ISO 13565-2 (Rk group) is based on profile division into 3 parts: peak, core and valleys. Therefore there are 5 parameters describing material ratio curve of two-process profile. They are: the core roughness height Pk, the reduced peak height Ppk, the reduced valley depth Pvk and two material ratios at transitions points from the peak part to the core part and from the core portion to the valley portion. The second standard ISO 13565-3 divides profile into 2 parts: peak (plateau) and valley. However both these standard do not include horizontal parameters.

FORMULATION OF THE PROBLEM

The standard ISO 13565-3 is the base of modeling two-process profile. The parameters describing two-process surface can be calculated from the probability plot of a material ratio curve. Two-process profile is represented by two straight lines describing peak (plateau) and valley portions. The slope of these lines are the standard deviation of plateau (Ppq) and of valley (Pvq), respectively [3]. This standard also includes material ratio at the transition point Pmq (Figure 2).

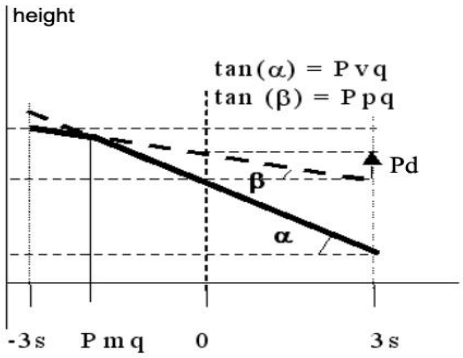

FIGURE 2. Graphical interpretation of the probability parameters.

In simulation procedure two profiles of Gaussian ordinate distributions were superimposed for a given distance between their mean lines Pd shown in Figure 2. This distance relates to the parameters Ppq, Pvq and Pmq by the following equation [4]:

$$Pd = Pmq(Ppq - Pvq) \qquad (1)$$

From these two profiles the smaller ordinates are selected. Figure 3 presents the example of computer creation of two-process profile.
However this procedure do not allow to predict horizontal parameters (correlation lengths) of two profiles (plateau and valley) of two-process surface. Due to it, there is a problem with obtaining the correct autocorrelation length of the two-process profile. The iterative procedure of selecting correlations length of two Gaussian profiles is one of solutions [5, 6]. However after its application the correlation length of two-process profile can be similar to that of the measured profile, however we don't know if the correlation lengths of plateau and valley parts are correct.

a

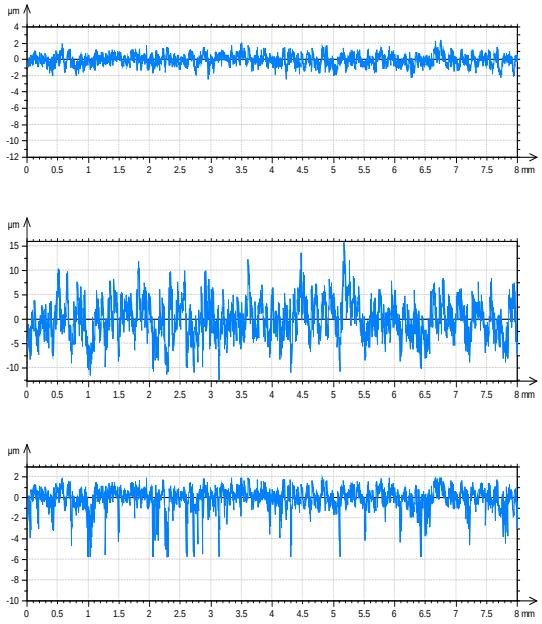

FIGURE 3. Computer creation of two-process profile: plateau profile (a), valley profile (b), two-process profile (c).

The proper estimation of the correlation length of the valley profile is more important from that of the plateau profile. This is because the valley profile really exists. It can be profile after finish honing during plateau honing operation and profile before wear.
There is the following reverse problem: how to simulate the valley profile (Figure 3b) when the

two-process profile is known (Figure 3c). As mentioned above, each Gaussian profile can be described by the standard deviation of height (the Pq parameter) and the correlation length. There is no problem with estimation the Pq parameter of the valley profile. It is equal (similar due to some errors) to the Pvq parameter of the two-process profile. This parameter can be estimated from the probability plot of the material ratio curve (Figure 2).

The correct modeling of the valley profile is a problem of huge importance. In some cases we cannot measure surface after machining, only after a low wear. It is necessary to obtain information about the shape of the one-process profile after machining in order to know how roughness of machined surface affects tribological properties of sliding element. Similar information is important also in a study of machining process like plateau honing. The question is: how the initial surface roughness affect surface obtained after the second process?

SOLUTION OF PROBLEM

In the first step it is necessary to extract profile details of the valley portions – Figure 4.

It is known that the part of the profile under the solid red line originates from the valley profile (Figure 4b). Therefore the two-process profile was truncated and lower part was analysed. In this case the truncation level is the ordinate of crossing approximate straight line characterizing the valley parts with the vertical axis (in a profile study, it is a little larger than 3s). However sometimes, for a profile characterized by the high transition point Rmq, the valley part could contain only individual non-statistical valleys. In this case the truncation level can lie upper (see dotted line in Figure 4). However, one should know that near the transition point there can be a mixture between points originated from the plateau and valley portions which could be a source ed to some errors. So the selection of the truncation level should be treated with a great care.

Then one should know how the autocorrelation functions of one-process profiles after the same kind of machining are changing with the truncation of the profile height. It was found that after truncation the correlation length decreased. This was connected with a reduction in the width of deep valleys affecting the correlation length and the spectrum [7]. Since for one-process texture the profile probability plot has the shape of one straight line, one should know how its correlation length changes for the given material ratios.

a

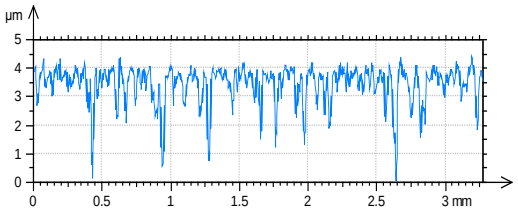

b

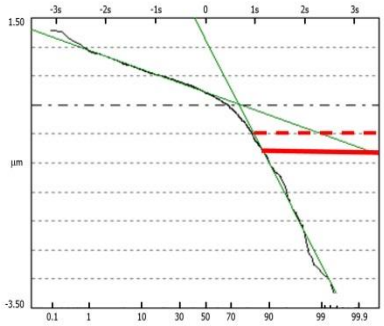

c

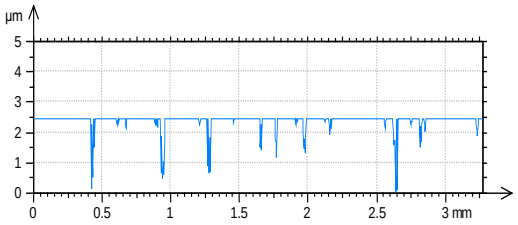

FIGURE 4. Two-process cylinder profile (a), its probability plot (b), truncated profile containing the valley part (c).

This analysis should be made for many surfaces after the same treatment. It was found that different changes were obtained after analysis of surfaces after various kind of machining, like polishing, lapping, grinding or vapour blasting. For example Figure 5a presents the average graph obtained for one-process surfaces after finish honing of more than 20 cylinders by various methods including different kinds of stones (diamond and ceramic). It is important that the shapes of the ordinate distributions of these textures should be approximately symmetric (the skewness Psk should be near 0, the emptiness coefficient Pp/Pt near 0.5), without spikes or individual valleys. Then reciprocal MF of correlation lengths for the given material ratios should be calculated. After truncation of two-process profile for the given material ratio the correlation length should be

calculated. The correlation length of one-process profile is equal to the obtained correlation length of truncated two-process profiles multiplied by the MF factor obtained from Figure 5b. The material ratios of truncated profiles were restricted to the range: 50-98%.
Probabilistic plot of material ratio curve was earlier used for study of the stage of the wear process [8].

a

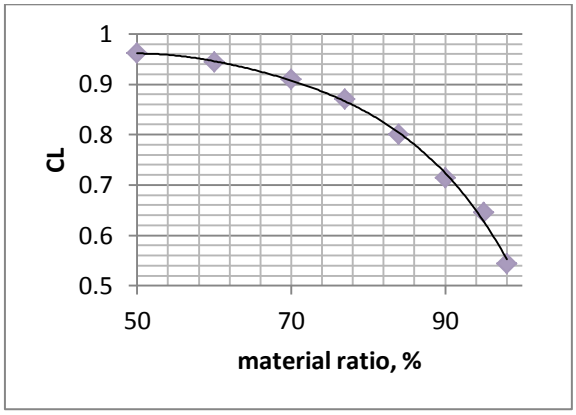

b

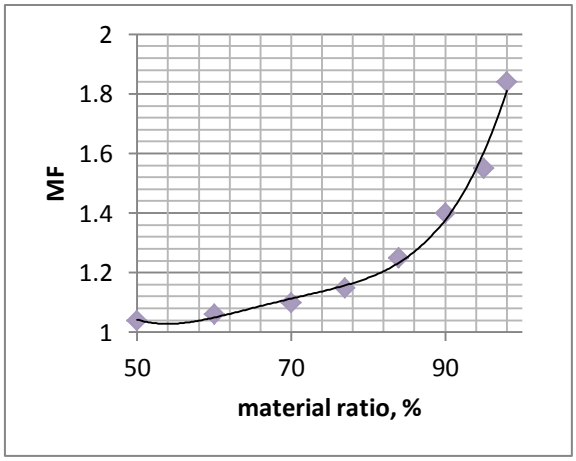

FIGURE 5. Correlation length CL of truncated one-process profile after honing (a), magnification factor MF (b) versus material ratio.

After determination of the curve presenting the multiplication factor versus the material ratio (Figure 5b) on the basis of series of profiles after the same kind of machining, there are the following steps in the procedure of simulation of the profile of the base one-process surface:

- determination of the profile probability plot,
- determination the Pq parameter of the one-process profile as the Pvq parameter of two-process profile,
- truncation of the two-process profile,
- determination of the autocorrelation function of the truncated two-process profile for the given material ratio,
- calculation of the correlation length of the truncated profile,
- determination of magnification factor MF (Figure 5b),
- calculation of the correlation length of one-process valley profile by magnification of the correlation length of truncated two-process profile by the MF factor,
- modeling the profile using for example FFT method [2].

There are some limitations of its method usage. The first of them is mentioned above necessity to exclude profile details related to individual non-statistical grooves and mixture of two processes. Therefore the determination of the truncation level should be treated with a great care. The analysis of probability plot of material ratio curve can be helpful. We also must be sure that the valley part had not been changed during wear of machining. Therefore conditions of wear and machining processes should be taken into consideration. During wear sometimes plastic deformation, not only wear removal can take place.

This method can be also used in the 3D (areal) analysis. It this case the correlation lengths in perpendicular directions must be estimated for several representative profiles.

This method can be also used for estimation of the correlation length of the upper plateau profile. However this task is not such important as the analysis of valley profile, since the plateau profile does not really exist.

This approach can be also helpful in simulation of two-process 2D profiles and 3D surfaces. The known correlation length of two-process profile can be also helpful in simulation process.

VALIDATION OF METHOD

This method was validated for two groups of cylinder liner surfaces. Cylinder liners from the first were made from grey cast iron. They were only finish honed by diamond or ceramics tools. Therefore they had one-process random textures. These cylinders were subjected to tribological test using OPTIMOL SRV tester. They co-acted with a detail of piston ring in lubricated condition. During this test a low wear took place. Before and after tests topographies of cylinder liner were measured in very similar places (the mechanical and the digital relocations were used) by a white light interferometer Talysurf CCI Lite of 0.01 nm

vertical resolution – Figure 6. The initial measuring area 3.3 mm x 3.3 mm contained 1024 x 1024 points. During the analysis the form was removed by the polynomial of the 2-nd level, digital filtration was not used. Spikes were eliminated by truncation. From the cylinders, axial profiles were selected. For each profile after operating, the procedure described above was made for at least three truncation levels starting from the upper level resulting from the probability plot of the material ratio curve (Figure 4b). The lowest level typically corresponded to material ratio of 98% - however this level depended on the shape of the material ratio curve. For one-process cylinder liner surfaces after finish honing the correlation length was computed. The average correlation length obtained from truncated cylinder liner profile after operating were compared with that from honed cylinder profile. About 20 different surface textures were analysed. It was found that during operating only the wear removal took place, without the plastic deformation.

a

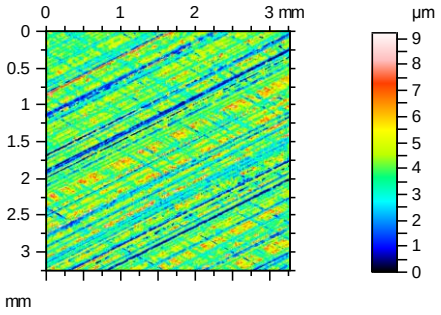

b

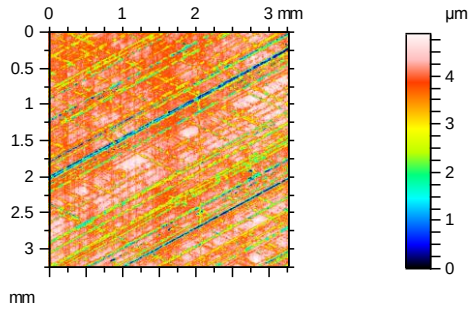

FIGURE 6. Surface of cylinder liner after finish honing (a) and after tribological test (b).

It was found that the average error was 6.5%, while maximum error was 12%. Figure 7 presents example of one-process, two-process and modeled one-process profile. One-process profile was simulated using FFT method [2].

a

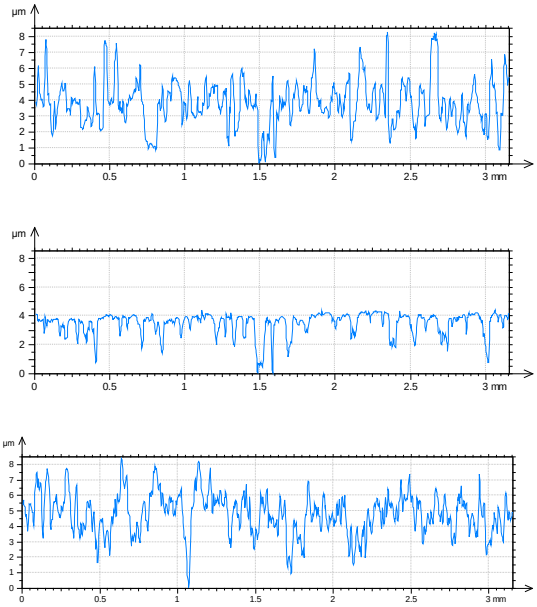

b

c

FIGURE 7. One-process cylinder liner profile after finish honing (a), after tribological test (b), simulated one-process profile (c).

Similar tests were carried out for finish honed (one-process) and plateau honed (two-process) surfaces of cylinder liners from grey cast iron. Differently to experiment mentioned above, it was not possible to measure cylinder liners exactly in the same place after finish and plateau honing. Therefore from one surface (also measured by the white light interferometer) three axial profiles were selected. The test procedure was similar to mentioned above, however the average value of three correlation lengths from one-process cylinder profiles (after finish honing) were compared with average value of estimated correlation length obtained on the basis of measurement of three two-process profiles after plateau honing. It this study, about 20 different surface topographies were analysed. It was found that the mean error was 5.8%, however maximum error was 15%. Figure 8 shows example of one-process, two-process and simulated one-process profile.

One can see that application of this method assured comparatively good results in both analysed cases. We focused mainly on estimation of the correlation length. Although the standard deviation of the roughness height can be estimated from the probability plot of the material ratio curve of two-process surfaces (Figure 4b) there can be errors connected with its estimation. For example roughness

probability plot of one-process surface has sometimes a deviation of the linear shape. However these errors were analysed elsewhere.

a

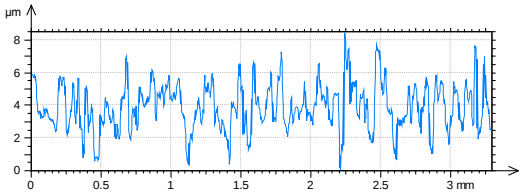

b

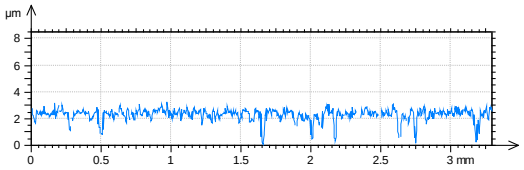

c

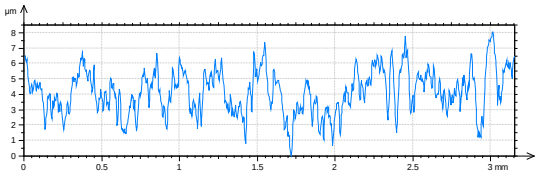

FIGURE 8. One-process cylinder liner profile after finish honing (a), after plateau honing (b), simulated one-process profile (c).

CONCLUSIONS

The method of simulation of one-process profile on the basis of two-process profile was developed. One-process profile is characterized by the standard deviation of the profile height and the correlation length. In simulation probability plot of two-process profile is helpful. After analysis of this plot, the height of one-process profile can be directly estimated. The correlation length can be achieved based on truncation of two-process profile. In procedure of correlation length estimation information about autocorrelation function shapes of many profiles after the same kind of machining is needed.

The proposed procedure was validated for two groups of surfaces. It was found that the average error of the correlation length of one-process profile estimation was not higher than 7%, while maximum error was not larger than14%.

This method can be easily extended to simulate the base one-process surface of 3D (areal) surface topography. It will be helpful in two-process surface modeling.

REFERENCES

[1] Whitehouse D.J., Archard J.F. The properties of random surface of significance in their contact. Proc. R. Soc. 1970; A 316: 97-121.

[2] Wu J.-J.: Simulation of rough surfaces with FFT. Tribology International. 2000; 33: 47-58.

[3] Malburg M.C., Raja J. Characterization of surface texture generated by plateau-honing process. CIRP Annals. 1993; 42: 637-640.

[4] Pawlus P. Simulation of stratified surface topographies. Wear. 2008; 264: 457-463.

[5] Reizer R., Pawlus P. Modeling of plateau honed surface topography. Proceedings of the Institution of Mechanical Engineers, Part B: Journal of Engineering Manufacture. 2012; 226: 1564-1578.

[6] Hu S., Brunetiere N., Huang W., Liu X., Wang Y. Bi-Gaussian surface identification and reconstruction with revised autocorrelation functions. Tribology International. 2017; 110: 185-194.

[7] Pawlus P., Chetwynd D.G. Efficient characterization of surface topography in cylinder bores. Precision Engineering. 1996; 19: 164-174.

[8] Pawlus P., Grabon W. The method of truncation parameters measurement from material ratio curve. Precision Engineering. 2008; 32: 342-347.

A MULTI-SCOPIC 3D PRECISION MEASUREMENT SYSTEM FOR DEEP BLIND HOLES

Da Li[1], and Benny Cheung[1]
[1] State Key Laboratory of Ultra-precision Machining Technology, Department of Industrial and Systems Engineering, The Hong Kong Polytechnic University, Hung Hom, Kowloon, Kong Kong.

INTRODUCTION

Three-dimensional (3D) micro-structured surfaces have been widely used in the development of various products in different industrial fields to realize specially designed optical and mechanical functions, especially in PCB, semiconductor or LED industry, etc. However, the complexity of 3D-structured surfaces imposes considerable challenges for the control of the manufacturing process and quality assurance (QA), which makes 3D measurement to be indispensable. These related industries usually have extreme large production thoughput which requires the QA process to be high efficiency or even possibility to be performed real-time and in-process based on 3D measurement.

In the past decades, many high-precision coordinate measuring instruments have been developed [1] to perform 3D measurement. However, most of them are based on touch probe coordinate measurement principle with the use of the contact probe or non-contact optical probe. Contact-type CMM can provide high accurate measurement for various types of freeform surfaces, but the possible scratch marks caused by the contact between the probe and the measured surface is undesirable and unavoidable. Moreover, the measuring efficiency is rather low for mass production. In this sense, optical techniques [2] are widely used to develop a non-contact probe, such as light scattering techniques [3], fiber interferometry [4] and optical slope sensors [5], to measure the surface. They are reported as being capable of performing fast measurement of surface roughness and micro structures with nanometric accuracy. However, it is difficult to overcome the rigorous measurement requirements such as various surface structures, surface roughness or material, etc.

Multi-scopic technologies provide object space information with multi-perspectives through the use of microlens array (MLA), which is an emerging technology for the measurement of 3D micro-structured surfaces [6]. The multi-scopic 3D technology not only provides a compact system design but also allows the acquisition of snapshot data for high accurate reconstruction of 3D micro-structured surfaces under a shop floor environment.

Moreover, the conventional multi-scopic-based 3D reconstruction method encountered various limitations, such as heavy computation requirement [7], information loss [8], reduction of measuring resolution [9] or limited systematic compatibility [10]. Previous research study by the authors proposed a method in which the measured data are directly extracted based on disparity information (DEDI) of the captured images and processed through statistical analysis in order to have a precise match [11]. The precision and efficiency of this DEDI 3D information extraction algorithm are ensured to provide accurate final 3D measuring results.

In this paper, a multi-scopic measurement system is developed for the measurement of deep blind hole in PCB industry. It is interesting to note that holes are basic structure for PCB manufacture and the key dimensions of the hole includes lateral direction and depth information, which make 3D measurement to be a preferred solution. Since the quantity of holes on single board is very large and the nature of mass production, measuring efficiency is another key requirement. The developed multi-scopic 3D measurement technology is able to meet the demands of the user according to its fundamental theory. Experimental system is developed and fine-tuned accordingly for the measurement process of deep blind holes, which is the interim component during the PCB manufacturing process. Cross verification from ultra-precision offline metrology system shows that the measurement result from the proposed system achieve sub-micron accuracy.

MULTI_SCOPIC 3D MEASUREMENT SYSTEM

The multi-scopic 3D measurement method is a novel theory which has been proposed recently [8]. The raw 3D information of the to-be-measured surface is acquired in a single snapshot through a CCD camera and a micro

lens array (MLA). The 3D digital model of the to-be-measured surface with the measuring data is precisely reconstructed through a system-associated DEDI method [11]. The multi-scopic-based 3D metrology system is capable of performing the in-situ measuring process of micro-structured surfaces, with sub-micrometer measuring repeatability under different measuring environments.

The basic principle of the multi-scopic metrology theory is shown in Fig. 1. It is divided into two processes which include a recording process and reconstruction process, respectively. Since the spatial positions of the elemental lenses vary, the acquisition of elemental images (EIs) have subtle differences which are referred to be disparities. These image points from different EIs which originate from a single object point are called corresponding points. The disparity of a certain point of the target that is located at a certain depth is quantitatively expressed by the parameters of the system setup and the variable of its depth information. The 3D information of the object space is retained in these disparities which are the carriers of the 3D information of the target that can be transferred to the reconstruction process. The disparity information can be represented by the number of pixels times single pixel size which are determined by the basic theory of machine vision-based measurement systems.

$$\frac{\Delta D^{(m,n)}}{(m,n)\times D_{EI}} = \frac{g}{SD} \tag{1}$$

where $\Delta D^{(m,n)}$ is the disparity information; D_{EI} is the diameter of the EIs; m and n are the coordinate information of the elemental lens counting from the central one; g is the distance between the EIs and the MLA according to the system setup; and SD is short for the shooting distance which represents the depth information of the target point. The number of pixels and the to-be-measured value of the targets can be established in both the lateral and axial directions. The measured value along the lateral direction can be expressed as:

$$\frac{D_{sEI}}{D_l} \approx \frac{N_p \times p}{D_l} \cdot \frac{g}{SD} \tag{2}$$

A quantitative relationship between where D_{sEI} D_{sEI} is the distance between two image points in a single EI as shown in the distance of two focused EI points of the red circle point and the blue square point in the n^{th} EI as shown in Fig. 1; SD is the depth information of the plane which is determined by the known disparity information; g is the distance between the EIs and the MLA according to the system setup, and D_l is the measured value of two target points as shown in the measured value between the two reconstructed image points (circle point and square point) in Fig. 1.

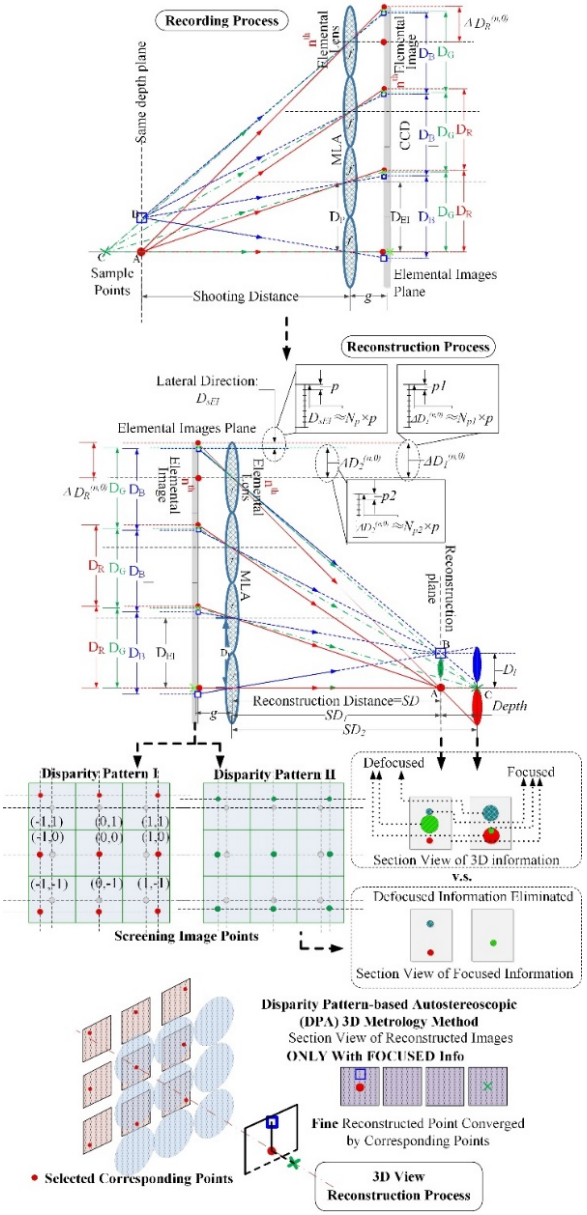

FIGURE 1. Basic science of the multi-scopic 3D measurement method

For the axial direction, the circle point A and the cross point C are used as a simple illustration. The distance between two depth planes, which is

the measured value in the axial direction, is determined by Eq. (2) as follows:

$$SD_2 - SD_1 = gn\left(\frac{D_{EI}}{\Delta D_2^{(n,0)}} - \frac{D_{EI}}{\Delta D_1^{(n,0)}}\right) \approx gn\left(\frac{D_{EI}}{N_{p2} \times p} - \frac{D_{EI}}{N_{p1} \times p}\right) \quad (3)$$

where SD_1 and SD_2 are the abstract axial positions of two depth planes, which are shown in Fig. 1 as the depth plane of the circle point and cross point, n is the n^{th} EI; $\Delta D_1^{(n,0)}$ and $\Delta D_2^{(n,0)}$ are the disparity information of different depth information in the n^{th} EI which are shown as the disparity information of the circle point and cross point between the n^{th} EI and the central EI as shown in Fig. 1; g is also the distance between the EIs and the MLA according to the system setup, and the depth is the measured value between two depth planes in the axial direction.

The quantitative relationship in Eq. (2) and Eq. (3) satisfies the fundamental theory of the indirect metrology system. This is the theoretical foundation of the multi-scopic-based 3D measuring method. After obtaining the elemental images with 3D information recorded during the recording process, the disparity information is confirmed and extracted through a precision matching process of the corresponding points among the EIs so as to represent different depth information. Since every depth plane has its own focused information, which is represented by the corresponding points, the defocused information on every depth plane is eliminated as shown in Fig. 1. As a result, the 3D scene with lateral and axial digital information is fully reconstructed.

Based on the reversibility of the optic rays, the two processes become symmetrical by using the same micro-lens array (MLA) and system setup, which infers that the object space is precisely reconstructed with a scale that is not changed as shown in Fig. 1. This nature of multi-scopic theory is the foundation of the multi-scopic-based measurement method.

EXPERIMENTAL WORK

Based on the theory of multi-scopic 3D measurement method. A measurement system is developed for measuring deep blind hole with application in PCB industry. Fig. 2 shows the schematic diagram of the multi-scopic 3D measurement system which is composed of a CCD carmera working on visible spectrum, a microlens array with the scale of 20×20, LED white light source, and long working distance 10X objective lens from Mitutoyo.

An MLA is incorporated to a traditional microscope imaging system to provide multiple perspectives of the object scene. A 10X Mitutoyo long working distance objective lens is used as the main lens of the whole system. Axial illumination is also imported to the system through optical fibers and LED light source due to the 3D features of the micro-structured surface to be measured. The deep blind hole in PCB industry usually has a depth-to-diameter ratio which is equal to 1 or even smaller than 1. This provides great challenges to many 3D measurement methods and illumination style. Traditional side illumination is not applicable in this case because the micro-structure is deep which makes very little light transmit into the bottom of the structure.

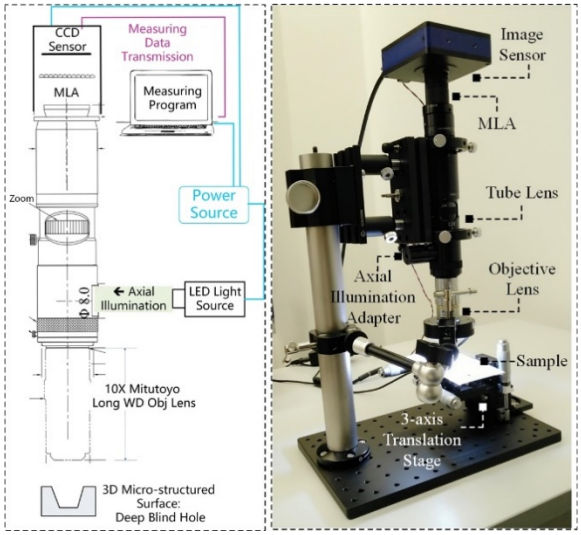

FIGURE 2. Schematic design and setup of the multi-scopic 3D measurement system for deep blind hole

Fig. 2 also shows the experimental setup of the proposed multi-scopic 3D measurement system. The raw 3D information of the target surfaces is acquired in a single snapshot through a CCD camera and a micro lens array (MLA). The 3D digital model of the target surface with the measuring data is precisely reconstructed through a system-associated direct extraction of disparity information (DEDI) method because the error is eliminated by statistical analysis used in the method.

Multiple measurements were conducted on a machined micro-structure of deep blind hole. As a kind of micro-structure which brings a lot of challenges to various measuring devices, the deep blind hole structure can be clearly reconstructed from the top to the bottom with the

depth information through the proposed metrology system and associated data processing method as shown in Fig 3. An ultra-precision off-line measurement system Talysurf CCI is introduced to measure the same targeted blind hole of the sample in order to provide reference measuring data.

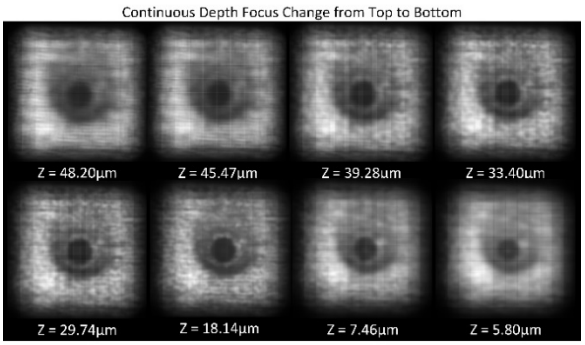

FIGURE 3. Reconstructed images of different depths of the deep blind hole

Table.1 shows the measurement results. The bias denotes the difference between the mean value of measuring data and reference value. Max. Abs. Err denotes the max absolute error comparing to the reference values during the repeat experiments. It is found that the system is capable of measuring deep blind hole surfaces with sub-micrometer measuring repeatability, comparing with the reference measurement data from Talysurf CCI as shown in Fig. 4.

TABLE 1. Summary of measurement results

Item	Dimension	Bias *(μm)*	Standard Deviation *(μm)*	Max. Abs. Err. *(μm)*
Sample 1	Top Radius	0.47	0.60	1.10
	Bottom Radius	0.23	0.50	1.13
	Depth	0.68	0.43	0.98
Sample 2	Top Radius	0.51	0.89	1.02
	Bottom Radius	0.35	0.63	0.81
	Depth	0.41	0.29	0.85

CONCLUSION

A 3D precision measurement system is developed for measuring deep blind holes with applications for PCB industry. The system is built based on multi-scopic measurement technology. Experimental studies not only verify the technical feasibilities in terms of accuracy and repeatability but also proved that the proposed system as a promising method for practical industrial metrology.

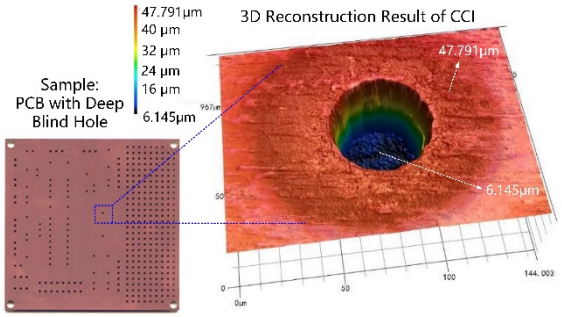

FIGURE 4. Sample and reference measuring data provided by Talysurf CCI.

ACKNOWLEDGEMENT

The work described in this paper was supported by a grant from the Research Grants Council of the Government of the Hong Kong Special Administrative Region, China. (Project Code: 15202315).

REFERENCES

[1] Hansen, H.N., Carneiro, K., Haitjema, H., Chiffre D.L., 2006, Dimensional Micro and Nano Metrology, Annals of the CIRP, 55/2:721–743.

[2] Hocken, R.J., Chakraborty N., Brown, C., 2005, Optical Metrology of Surfaces, Annals of CIRP, 54/2: 169-183.

[3] Taguchi, A., Miyoshi, T., Takaya, Y., Takahashi, S., 2004, Optical 3D profilometer for in-process measurement of microsurface based on phase retrieval technique, Precision Engineering, 28: 152-163.

[4] Jiang, X., 2011, In situ real-time measurement for micro-structured surfaces, Annals of the CIRP, 60(1): 563-566.

[5] Gao, W., Tano, M., Sato, S., Kiyono, S.,2006, On-machine Measurement of a Cylindrical Surface with Sinusoidal Micro-structures by an Optical Slope Sensor, Precision Engineering, 30: 274-279.

[6] Li, D, Cheung C.F., Ren M.J., Zhou, L., Zhao, X., 2014, Autosteoreoscopy-based three-dimensional on-machine measuring system for micro-structured surfaces, Optics Express, 22: 25635-25650

[7] Hong, S.-H., Jang J.-S., Javidi B., 2004, Three-dimensional volumetric object reconstruction using computational integral imaging, Optical Express, 12: 483-491

[8] Shin, D.-H, Yoo, H., 2009, Computational integral imaging reconstruction method of 3D images using pixel-to-pixel mapping and image interpolation, Optics Communications, 282: 2760-2767.
[9] Cho, M., Javidi B., 2009, Computational Reconstruction of Three-Dimensional Integral Imaging by Rearrangement of Elemental Image Pixels, Journal of Display Technology, 5: 61-65.
[10] Lee J.-J., Lee, Lee, B,-G., Yoo, H., 2011, Depth extraction of three-dimensional objects using block matching for slice images in synthetic aperture integral imaging, Apply optics, 50: 5624-5629
[11] Da Li, Chi Fai Cheung, MingJun Ren, David Whitehouse, and Xing Zhao, "Disparity pattern-based autostereoscopic 3D metrology system for in situ measurement of microstructured surfaces," Opt. Lett. 40, 5271-5274 (2015)

Methods of optically profiling surfaces

Kumar Arumugam, Alex Caviness, Tara Newman, Farzaneh Shabahang, Tsing-Hua Her, and Stuart T Smith
University of North Carolina at Charlotte
Charlotte, North Carolina, USA

INTRODUCTION

This study revisits known methods for determining surface topography on engineering surfaces using optical reflection. Specifically examined are methods that illuminate a localized region and measure the subsequent reflection. Figure 1 shows the three methods that are being studied.

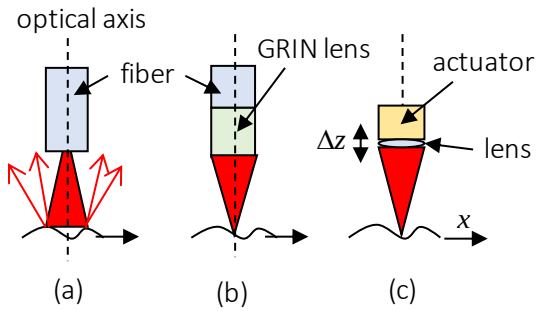

Figure 1: (a) An External cavity Fiber Fabry-Perot Interferometer (EFFPI) with a bare fiber tip emitting a diverging beam (b) EFFPI with a Gradient Refractive INdex lens attached to the tip of fiber emitting a converging beam (c) piezo-electrically actuated lens in a focus detecting probe

Two of these techniques use fiber Fabry-Perot interferometry [1,2] and frequency modulation of the laser source to determine surface height variation. The major difference between these two methods is one uses a bare fiber tip (resulting in divergence of the beam) while the other has a focused beam. The former has the benefit of greater range but is limited by the expanding spot size (i.e. lateral resolution of surface topography measurement) with fiber-surface separation. The latter has the benefit of a smaller spot size and greater working distance, but the range is limited by Rayleigh length.

The other method, a variant of a monochromatic confocal probe, oscillates the focal point along the optical axis to determine surface topography. The surface is profiled using focus detection where the focus of a single wavelength of light is dependent on the distance between the probe and the surface. Thus, the profile of the surface can be measured by the change in probe base to focal point distance as the probe is moved across the surface perpendicular to the optical axis. This has the advantages of eliminating the need for coherent light and being absolute relative to lens position.

The goal of this initiative is to explore the limits of surface topographies that can be reliably measured by the aforementioned methods. Specific attention would be given to surface slope, amplitude, material, and spatial frequencies.

Fabry-Perot interferometry using a bare fiber end

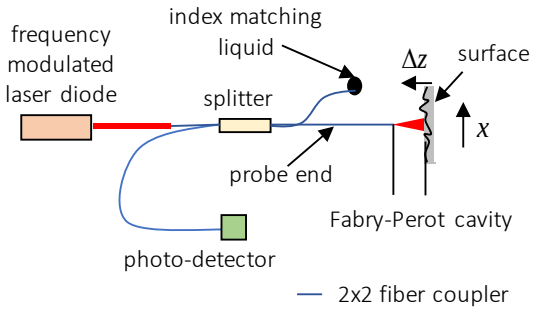

Figure 2: Schematic of external cavity Fiber Fabry-Perot interferometer to measure surface deviations

Figure 2 shows a schematic of the experimental setup which uses a frequency modulated infra-red laser source (Thorlabs TLK-1050M) coupled to a 2X2 fiber coupler - single mode (TW1064R5A2A). one of the exiting ends is immersed in a black container with a refractive index matching liquid. This avoids back reflection from the face of the fiber by allowing the light to transmit through the liquid and absorb by the black surface of the container. Another end is the probe end emitting a diverging beam, and is positioned in front of the surface forming a Fabry-Perot cavity.

Figure 3 shows the probe end made of glass transmitting a beam of light, which is 96 % of light from the splitter (see Figure 2). 4 % of light from the splitter reflects from the face of the fiber and goes back in to the fiber. Depending on the reflectivity (r_m) of the surface being measured, $0.96r_m$ of light reflects from the surface. About $0.92r_m$ of this light transmits in to the fiber, and $0.038r_m$ reflects from the face of the fiber. All these light paths interfere among each other, both in the Fabry-Perot cavity and inside the fiber, and reaches the photodetector (Thorlabs D400FC)

A sinusoidal intensity variation at the photodetector (temporal fringes) is observed, as the surface is scanned perpendicular to optical axis. This is due to the phase change ($\Delta\phi$) in the reflected light from the surface, caused by its surface deviations along x axis.

Frequency modulation at f_m = 400 Hz creates harmonics that contains this phase information. The output of the photodetector is connected to a lock-in amplifier (Ametek DSP 7270) to extract and output the amplitudes of the harmonics. Computing the inverse tangent of these amplitudes (I_{1f_m}, I_{2f_m}) yields the phase change ($\Delta\phi$),

$$\Delta\phi = \tan^{-1}\left(\frac{I_{2f_m}}{I_{f_m}}\right) \qquad (1)$$

surface deviation (Δz) is computed from the phase difference using

$$\Delta z = \frac{\lambda_0}{4\pi}\left(\Delta\phi + 2\pi n\right) \qquad (2)$$

where, $\lambda_0 = 1050\,\text{nm}$ is the fundamental wavelength of laser, and n is the number of rotations of quadrature produced by plotting I_{1f_m} vs. I_{2f_m} [2].

Figure 4 shows the experimental facility with tilt alignment and working distance adjustment mechanisms. A capacitance probe is used to align the surface perpendicular to the probe. Also, to achieve a reasonably small spot size, a micrometer is used to bring the probe tip close to the surface to about 0.25 mm. The spot size increases with the gap between probe tip and surface, since the beam diverges from the probe tip to surface.

Equation (3) estimates the spot radius, w at distance, z = 0.25 mm to be 84 µm.

$$w(z) = w_0\sqrt{1+\left(\frac{z}{z_R}\right)^2} \qquad (3)$$

where, Rayleigh length, $z_R = \frac{\pi w_0^{\,2}}{\lambda_0}$, and

w_0 = 4 µm is the spot radius at the face of fiber. This is assumed to be equal to the radius of the core of a single mode fiber.

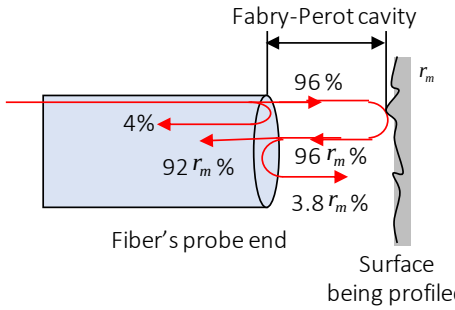

Figure 3: Schematic showing the reflected and transmitted light from the face of the fiber and the surface, whose deviations are measured

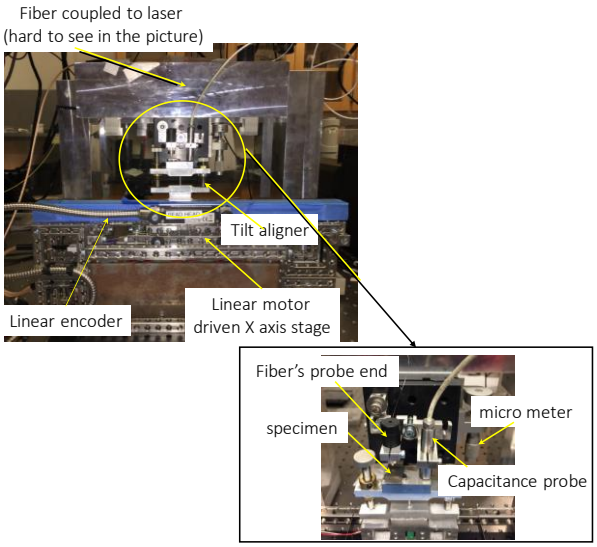

Figure 4: picture of the experimental facility, and inset showing the surface of interest, a rod flexure and a capacitance probe for tilt adjustment

Results

Two sinusoidal surfaces manufactured by Rubert & co. Ltd. are used to study surface deviations. A Coherent Scanning Interferometer (CSI, Zygo Nexview, 20X obj.) is also used to image an area of 418 μm^2 of the surface, S-filtered with a cut-off of 2 µm, and provides the surface parameters for this study [3].

Figure 5 (a) and (b) shows the CSI image of sinusoidal surface A, and its measured profile using the bare fiber interferometer respectively. The black line in Figure 5 (b) represents the back and forth motion of the surface in x axis about a distance of 250 µm in 40 s. The yellow curve in Figure 5(b) represents the height of surface deviations measured. About three peaks are observed for the travel range of 250 µm in both CSI image and measured profile. The measured peak to valley height is Pt = 1.1 µm.

It is noted that in the shown result, tilt of the specimen is not removed, and the sampling length 250 µm does not follow ISO 4288 suggestion of 4 mm [4].

Figure 6 (a) and (b) shows the CSI image of sinusoidal surface B, and its measured profile using the bare fiber interferometer respectively. About five peaks are observed for the travel range of 250 µm in both CSI image and measured profile. However, the measured peak to valley height using the profiler is Pt = 0.8 µm, as opposed to Pt = 1.5 µm measured using CSI. This could be due to the spot size limitation of 84 µm.

Also, the inset in Figure 6 (b) shows horn-like artifacts on the peaks of the sinusoids. This is speculated to be the error in phase unwrapping algorithm, and has to be rectified in the future work. Limits of measurable amplitude and lateral resolution would also be studied. It is noticed that to measure a span of 250 µm it takes 40 s. This low bandwidth is due to the maximum achievable frequency modulation (f_m) of the laser being limited to 400 Hz, as the laser source (Thorlabs TLK-1050M) used in the experiment utilizes mechanical modulation hits its resonance above 400 Hz. Future work would use a different technique to attain a faster modulation frequency with up to 300 kHz being used in other interferomtric measurements [5].

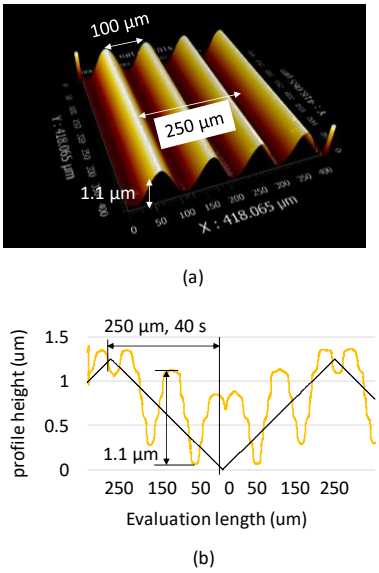

Figure 5: (a) CSI image of a sinusoidal surface A, Rubert 531, RSm = 100 µm, Pt = 1.0 µm, Sq = 0.35 µm, Sz = 1.1 µm, Sdq = 22 µm/mm, (b) measured profile of the surface with the bare fiber Fabry-Perot interferometer

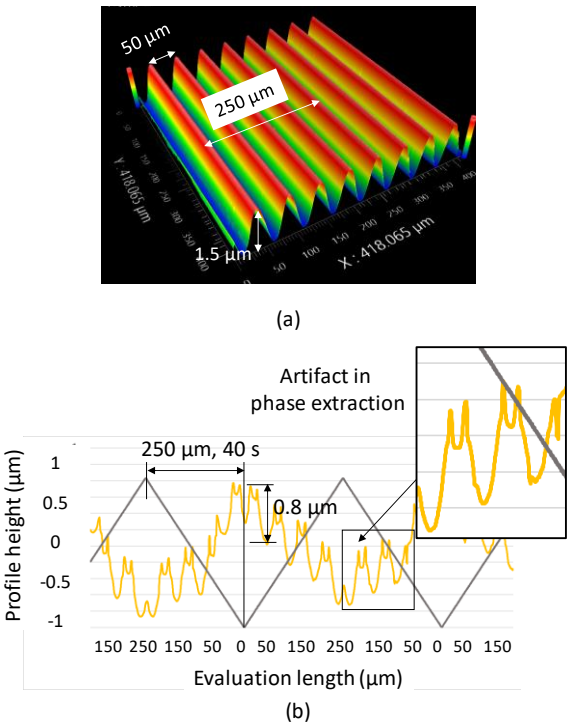

Figure 6: (a) CSI image of a sinusoidal surface B, Rubert 528, RSm = 50 µm, Pt = 1.5 µm, Sq = 0.57 µm, Sz = 1.7 µm, Sdq = 75.4 µm/mm, (b) measured profile of the surface with the bare fiber Fabry-Perot interferometer

Improvements to Fabry-Perot interferometry using a GRIN lens attached to fiber tip

Figure 7 shows the schematic of an improved experimental facility that uses a synchronous frequency modulator [5] to oscillate an acousto-optic modulator (AOM-602 407301, IntraAction Corp.) with a carrier frequency of f_0 = 60 MHz and, for this experiment, a modulated frequency f_m = 40 kHz. This would improve the speed at which the surface can be traversed perpendicular to the optical axis.

Current through the laser diode (VLM-650) is controlled to be constant using a laser diode driver (Thorlabs EK1101) with the feedback from the photodetector (BPX61). The facility also uses a GRIN lens (Agiltron OCTC-031000132) attached to a single mode fiber to improve the spatial resolution of surface deviation measurements. The experiments using the facility shown in Figure 8 is currently being performed.

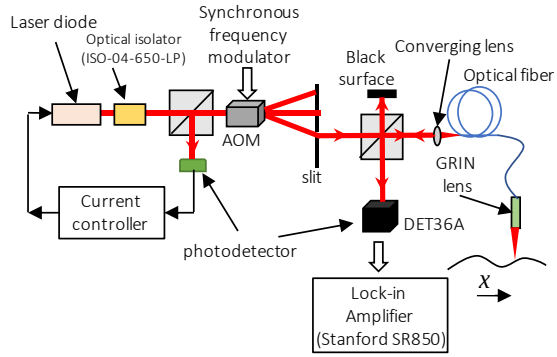

Figure 7: Schematic of external cavity Fiber Fabry-Perot interferometer to measure surface deviations

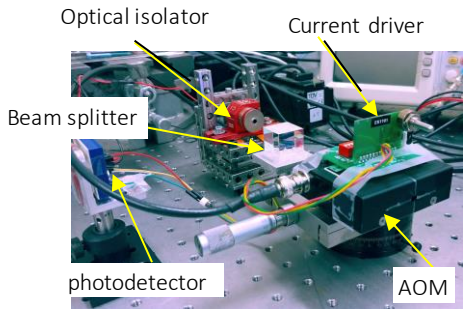

(a)

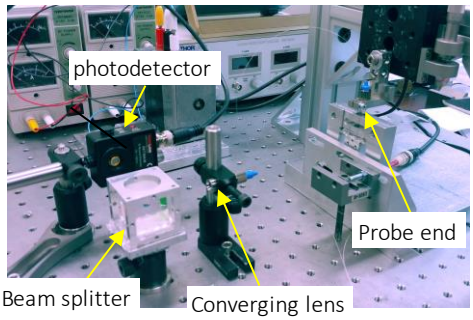

(b)

Figure 8: Picture of the experimental facility showing (a) left half of the schematic, Figure 9, (b) right half of the schematic

Focus detecting probe

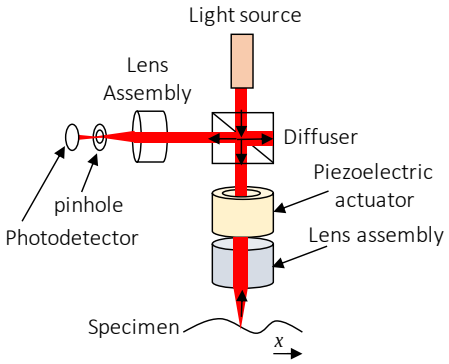

Figure 9: Schematic of the focus-based detector

Figure 9 shows the schematic of a compact monochromatic confocal probe [6]. The light source used is a micro light emitting diode (LTST-C191KRKT) emitting a single frequency beam of red light which goes through a 50/50 beam splitter. The orthogonal output of the beam splitter is not needed and is diffused to limit back reflection. The other output goes through a microscope objective lens assembly attached to a lead zirconate titanate (PZT) piezoelectric actuator where the focal point oscillates vertically and spans the surface of the workpiece and is reflected back through the lens assembly.

When the beam re-enters the beam splitter, it is reflected through a lens assembly and a pinhole that focus the light on the photodetector (BPX61). The photodetector reads the luminous intensity of the beam which peaks whenever the distance from the objective to the workpiece is such that the light focusses on the workpiece surface. This focal distance is a constant relative to the lens that provides the location of the surface to be determined. To find the focus, the lens assembly

is modulated 10 µm with the PZT actuator. The probe can then be actuated across the surface of the workplace to create a surface profile. Constructing an experimental facility for this focus-based probe is an ongoing effort.

Conclusion

Working principles of two interferometric and one focus-based probes for measuring surface deviations are discussed. Experimental facilities have been constructed and are being improved for testing each of these methods. Preliminary results indicate that the bare fiber tip method can measure a periodic surface with amplitudes up to 1.5 µm and lateral periods down to 50 µm. The limits of both amplitude and lateral resolution are being evaluated.

Acknowledgement

We would like to thank the Center for Precision Metrology, UNC Charlotte for providing the necessary fund for the above-mentioned work.

References

[1] P. Wilkinson and J. Pratt, Analytical method for low finesse, external cavity, fiber Fabry-Perot interferometers including multiple reflections and angular misalignment, Applied optics, 2011; Vol 11, No. 53, p. 4671 – 4680

[2] B. Nowakowski, Development of a miniature, multi-channel, extended range Fabry-Perot Fiber-optic laser interferometer system for low frequency SI-traceable displacement measurement Proc. EuSPEn, 15, 157-158

[3] ISO 25178-2 Geometrical product specifications (GPS) – Surface texture: Areal – Part2: Terms, definitions and surface texture parameters, International Organization for Standardization, Geneva 2012

[4] ISO 4288 Geometrical product specifications (GPS) – Surface texture: Profile method – Rules and procedures for the assessment of surface texture, International Organization for Standardization, Geneva 1996

[5] M. Arablu, Synchronous radio-frequency FM signal generator using direct digital synthesizers, Rev. Sci. Instru., 2018, 89, 045009-2 to 8

[6] R. Brodmann, W. Smilga, Evaluation Of A Commercial Microtopography Sensor, Proc. SPIE 0802, In-Process Optical Metrology for Precision Machining, 1987; doi: 10.1117/12.967117

Modeling approach for characterization of decomposition behavior in powder injection molding process

J.S. Han[1], J.Y. Jeong[1,2], D.S. Choi[1], T.J. Je[1,2], S.J. Park[3]
[1]Department or Nano-Manufacturing Technology
Korea Institute of Machinery and Materials (KIMM)
[2]Department of Nano Mechatronics
University of Science and Technology (UST)
[3]Department of Mechanical Engineering
Pohang University of Science and Technology (POSTECH)

INTRODUCTION

Powder injection molding (PIM) process is one of the promising bottom up manufacturing technology which enable to fabricate near-net-shape metal and ceramic structure without conducting post-processing. Conventional PIM process consists four main steps; mixing, injection molding, debinding and sintering. To obtain sustainable manufacturing process, there has many of researches related with process development and optimization based on theory, experiments, and numerical simulation [1-3].

Experimental condition-based optimization process is usually considered as an intuitive technique to achieve best processing condition. However, it usually requires lots of processing time and cost. To develop material and process effectively, numerical model-based optimization process is needed to be developed.

Master curve modeling is one of the powerful tool to characterize material behavior regardless of processing conditions. For material development and process optimization, master curve is widely used [4]. Especially for decomposition behavior in debinding process well-matched with this master curve model.

Several research works have been conducted by using MDC model to analyze decomposition behavior [5-6]. However, for PZT ceramics, there has not many reported researches because of its special characteristics.

To characterize material behavior during thermal debinding of PIM process, decomposition behavior of PZT ceramics were modeled based on thermal gravity analysis (TGA). Derived modelling based master curve matched well with the experimental based TGA results.

THEORY

Based on master curve analysis, experimental term and weight fraction term can be separated and the representative decomposition curve can be plotted regardless of heating cycles. Detailed expressions are described as follows. The thermal degradation of polymeric binders can be described by first-order reaction kinetics as shown in Equation 1:

$$\frac{d\alpha}{dt} = -K\alpha \tag{1}$$

where α is the remaining weight fraction of binder, t is the time, and K is the constant for thermal degradation of binder, which can be also expressed using the Arrhenius equation in Equation 2:

$$K = k_0 \exp\left(-\frac{Q}{RT}\right) \tag{2}$$

here, k_0 is the specific rate constant, Q is the apparent activation energy for thermal degradation of binder, R is the gas constant and T is the absolute temperature.

As combining Equation (1) and Equation (2), Equation (3) can be achieved:

$$-\int_1^{\alpha}\frac{d\alpha}{\alpha} = -\ln\alpha = \int_0^t k_0 \exp\left(-\frac{Q}{RT}\right)dt = k_0\Theta \tag{3}$$

where Θ is defined as work of decomposition which related to the temperature and activation energy for a specific feedstock system. The formula of it can be described in form of Equation (4).

$$\Theta(t,T;Q) \equiv \int_0^t \exp\left(-\frac{Q}{RT}\right)dt \quad (4)$$

and from Equation (3), the remaning weight fraction of binder can be expressed using the work of decomposition Θ as shown in Equation (5).

$$\alpha(\Theta,k_0) = \exp(-k_0\Theta) \quad (5)$$

To calculate work of decomposition, apparent activation energy needs to be determined. In this work, Kissinger [7] method was used to calculated apparent activation energy. The Kissinger method uses the temperature $T_{\max}$ where the maximum rate of weight loss occurs as seen in Eq. (5) and under the condition of a constant heating rate r, Eq. (6) can be expressed as Eq. (7). Thus, from Eq. (7), we can derive the activation energy as plotting the relations between $\ln[r/(T_{\max})^2]$ and $-1/RT_{\max}$.

$$\frac{d}{dt}\left(-\frac{d\alpha}{dt}\right) = 0 \quad \text{and} \quad T = T_{\max} \quad (6)$$

$$\frac{rQ}{RT_{\max}^2} = k_0 \exp\left(-\frac{Q}{RT_{\max}}\right) \quad \text{at } T = T_{\max} \quad (7)$$

By using derived apparent activation energy, experimental results can be plotted using Equation (4) and weight fraction results can be plotted using Equation (5). Using MDC which means of Equation (5), experimental results can be merged into one representative curve.

RESULTS AND DISCUSSION

PZT ceramics powder was used in this research. Figure 1 shows SEM image of powder morphology. Mean particle size was around 520nm and pycnometer density was 7.98 (10^3kg/m^3).

For a binder system, a mixture of paraffin wax (PW), polypropylene (PP), polyethylene (PE) and stearic acid (SA) was used. PP and PE were designed for the primary binder which strengthens the primary products and PW was designed for the secondary binder, which enhances the rheological property of the feedstock. SA was used as the surfactant.

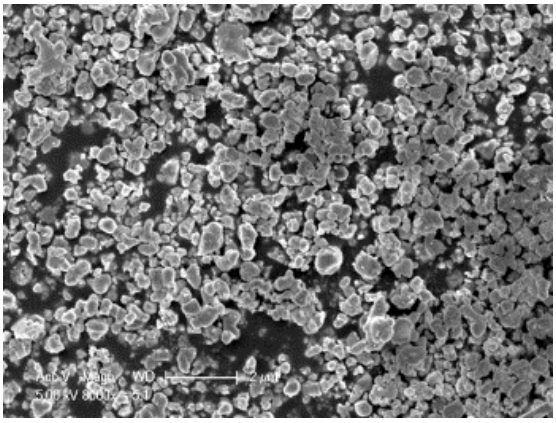

FIGURE 1. Shape morphology of powder [8]

For thermal debinding, thermal gravimetric analysis (TGA) was conducted to optimized heating cycle. Figure 1 shows the tendency of weight percent of binder loss in feedstock. As temperature increases, each binder was decomposed in a step wise manner and complete loss of binders were observed at 500 °C.

Figure 2 shows activation energies acquired by Kissinger method and Figure 3 shows constructed master curve for PZT feedstock. Constructed curve matched well with the experimental data. This master curve can be used for following applications. Firstly, it can be used for the process parameter optimization. Based on constructed master curve, process parameters can be optimized under constructed processing constraints. Secondly it can be used to compare thermal degradation property of feedstock. It can be used as a powerful tool to characterize polymeric binder system.

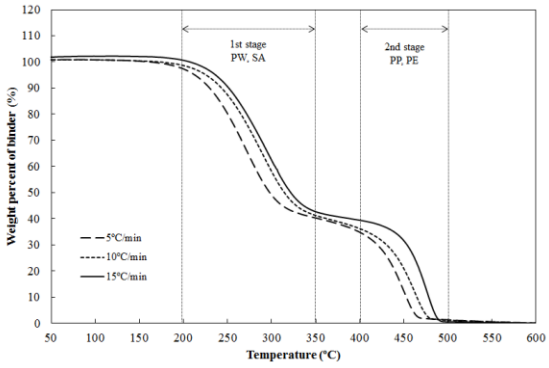

FIGURE 1. Thermal gravity analysis (TGA) results with respect to different heating rates [8]

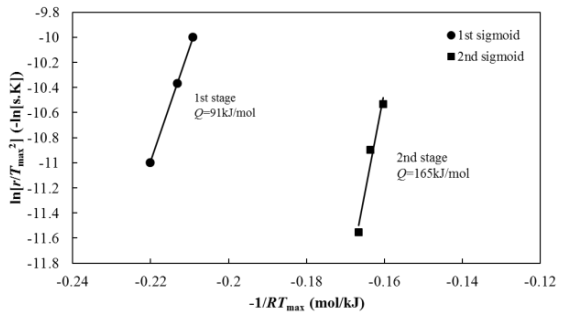

FIGURE 2. Apparent activation of PZT feedstock [8]

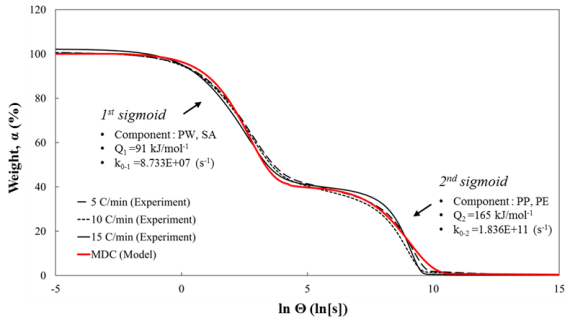

FIGURE 3. Constructed master decomposition curve for PMN-PZT feedstock

CONCLUSION

Master decomposition curve was derived based on thermal gravity analysis of PZT ceramics. Constructed curve matched well with the experimental results. Process optimization and material development will be conducted based on characterization process of master curve approach.

REFERENCES

[1] Piotter V, Bauer R, Knitter R, Mueller M, Muller T, Plewa K. Powder injection moulding of metallic and ceramic micro parts. Microsystem Technology. 2011; 17: 251-263

[2] German RM and Bose A. Injection Molding of Metals and Ceramics. Metal Power Industries Federation, New Jersey: 1997.

[3] Park SJ, Wu Y, Heaney DF, Zou X, Gai G, German RM. Rheological and thermal debinding behaviors in titanium powder injection molding. Metallurgical and Materials Transactions A. 2009; 40A: 215-222

[4] Aggarwal G, Park SJ, Smid I, German RM. Master decomposition curve for binders used in powder injection molding. Metallurgical and Materials Transactions A. 2007; 38A: 606-614'

[5] Sunder V, Enneti, R, Park SJ, German RM. Master decomposition curve analysis of ethylene vinyl acetate pyrolysis: influence of metal powders. Powder Metallurgy. 2008; 51: 368-375

[6] Ennti R, Shivashankar TS, Park SJ, German RM, Sundar V. Master debinding curves for solvent extraction of binders in powder injection molding. Powder Technology. 2012; 228:14-17

[7] Kissinger HE. Reaction kinetics in differe ntial thermal analysis. Anal Chem 1957; 29: 1702-1706

[8] Han JS, Oh KH, Moon WK, Kim K, Joh C, Seo HS, Bollina R, Park SJ. Bio-inspired piezoelectric artificial hair cell sensor fabricated by powder injection molding. Smart materials and structures. 2015; 24: 1-13

Acknowledgement

This work was funded by Korea Institute of Machinery and Materials (NK 218D) and the work was also supported by the Technology Innovation Program (20003945, Development of Core manufacturing technology of 4-axes ultra precision machining system and lens module for next-generation mobile lens having about 100nm shape accuracy) funded By the Ministry of Trade, Industry & Energy(MOTIE, Korea).

YSZ FOREST STRUCTURED FILM USING CENTRIFUGAL MOLDING METHOD FOR SOFC PERFORMANCE IMPROVEMENT

Toshihide Okamura[1], Keisuke Nagato[1], Morio Tomizawa[1], and Masayuki Nakao[1]
[1] Department of Mechanical Engineering,
The University of Tokyo,
Bunkyo-ku, Tokyo, Japan

INTRODUCTION

Hydrogen is expected to be used as a new energy source to address the current problems of energy faced around the world. Solid oxide fuel cells (SOFCs) are forerunners in devices that generate electricity from hydrogen. FIGURE 1 shows a schematic of a conventional SOFC anode and the anode proposed in this paper. Oxide ions generated at the cathode move in the electrolyte (yttria stabilized zirconia, YSZ) and react at the three-phase boundaries (TPBs) of the pore, YSZ, and Ni at the anode.

As the anode layer of conventional SOFCs is produced via screen printing a mixed paste of YSZ and Ni particles, the transport paths of oxide ions and electrons are random, as shown in FIGURE 1 (a). Thus, the transport efficiency is poor, and the loss or the polarization resistance is high. Therefore, it may be possible to improve the performance of SOFCs by efficiently transporting oxide ions using a fine pillar structure, in which YSZ and Ni particles are arranged in a column, as shown in FIGURE 1 (b) [1].

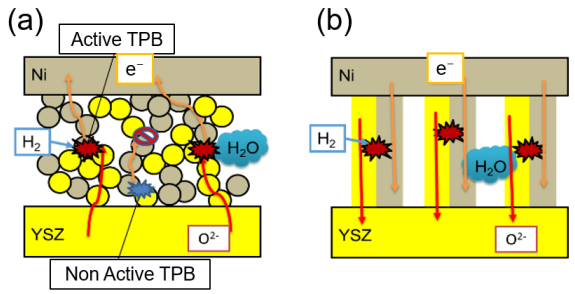

FIGURE 1. Schematic of anode (a) Conventional, (b) Proposed.

Laser processing has been proposed as a method to fabricate a fine YSZ pillar structure, but the scale of the fine structure depends on the spot diameter of the laser, which is limited to several tens of μm [2]. Therefore, in this study, a YSZ microstructure is prepared from particles using powder molding. We previously developed a powder molding method using centrifugal-force-based isostatic pressing (centrifugal molding method) to pack YSZ powder into micropores and prepare a YSZ "forest" structure [3]. However, in the previous study, we could not demold the YSZ forest structure, and the influence of centrifugal force and pressure on pillar structure formation was not clarified. Using the discrete element method (DEM), the behavior of particles in powder packing is analyzed by approximating a spring-mass damper system [4, 5, 6]. However, in the case of nanoscale particles, the effects of van der Waals force, electrostatic force, liquid crosslinking force, etc. become enhanced, and actual particle behavior may differ from that observed in simulations. Thus, it is necessary to conduct powder molding experimentally. In this study, the mold release of the microstructure, which we did not reach in the previous research, was carried out, and we investigated the influence of the centrifugal force and pressure on pillar structure formation. Then we investigated the influence of pillar structure on anode performance.

EXPERIMENTAL

Experiment 1

To construct a micro pillar structure, we packed YSZ nanoparticles (TZ-8Y, Tosoh Co.) into micropores. The procedure of the centrifugal molding method is shown in FIGURE 2. In previous study, anodized aluminum (alumina) films have been used as molds with micropores, but in this case, the alumina was degenerated following the sintering of YSZ powder, and there was a problem in that the YSZ microstructure could not be demolded. Thus, in this study, mold release was simultaneously performed with sintering by using a material that could be burnt out under a high-temperature atmosphere for a mold with micropores (FIGURE 2 (f)). Acrylic polymer (PMMA) was used as this material, and thermal nanoimprinting was used to transcribe micropores to PMMA. The PMMA surface after thermal nanoimprinting is shown in FIGURE 3. The micropore parameters of PMMA after thermal nanoimprinting are shown in FIGURE 2(a). Next, YSZ paste was coated on the PMMA

surface (FIGURE 2(b)). This paste was prepared by mixing YSZ particles (40 nm), solvent (terpineol), and dispersant (details unknown, Kyocera Co.). The volume fraction of the YSZ particles was adjusted to 33%. Next, the paste and the PMMA were centrifuged together for 5 min (FIGURE 2(c)), and then the solvent was evaporated (FIGURE 2(d)). The centrifugal acceleration was 1.25×10^4 m/s^2 (1250 G) and 2.50×10^4 m/s^2 (2500 G). The solvent was evaporated at 80 °C for 30 min (FIGURE 2(d)).

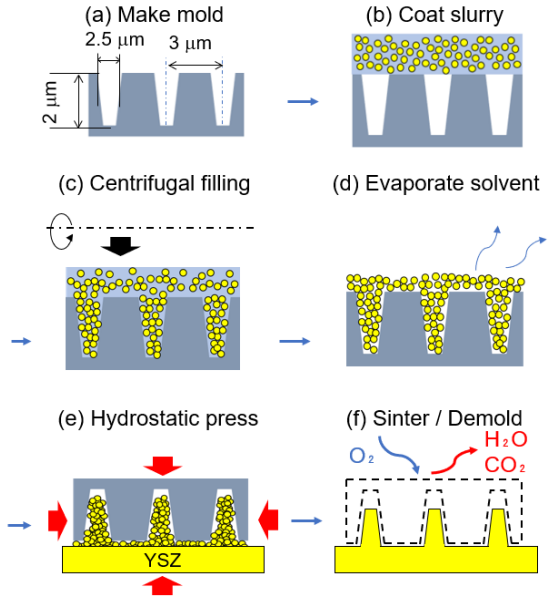

FIGURE 2. Schematic of molding a YSZ forest structure.

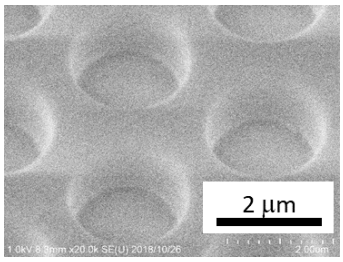

FIGURE 3. PMMA surface after thermal nanoimprinting.

After centrifugal filling, YSZ paste (50% volume fraction) was screen printed with a thickness of 50 μm on the surface of bulk YSZ (diameter 14 mm, thickness 0.2 mm, both-side mirror finish, Nippon Fine Ceramics Co.) to construct a buffer layer. This process was conducted to stabilize the bonds between PMMA and the YSZ bulk. Before the buffer layer was dried, the packed sample (PMMA) was attached to the YSZ bulk. Pressures of 0, 50, 100, 150, and 200 MPa were applied using cold isostatic pressing (CIP, Sansho Industries Co.) (FIGURE 2(e)). Then, in an electric furnace, the temperature was raised to 1400 °C at 4.7 K / min, and sintering, as well as simultaneous mold release, was performed at 1400 °C for 3 h (FIGURE 2(f)).

After sintering, the surface of the sample was observed by a cross-sectional scanning electron microscope (SEM, SU8010, Hitachi High-Technologies Co), and the heights of the YSZ pillars were measured by a laser microscope (OLS4100 OLYMPUS Co.).

Experiment 2

After demolding, a mixed paste of YSZ and NiO was screen printed on the surface of a sample that was centrifugally molded at 2500 G and pressurized at 200 MPa. Then, the sample was sintered at 1400 °C for 3 hours to prepare an anode with a YSZ pillar structure. The mixed paste had a volume fraction of 33%, and the mass ratio of YSZ to NiO was 2:1. This was adjusted such that the volume ratio of Ni and YSZ was 1:1 after NiO was reduced to Ni. The same procedure was repeated on the back side of YSZ to form a symmetric cell. In addition, cells without a YSZ forest structure were prepared similarly, and the performance of both the cells was evaluated.

RESULTS and DISCUSSION 1

TABLE 1 shows SEM images of the surface of samples centrifuged at 0, 2500 G and pressurized at 0, 100, and 200 MPa. When a centrifugal force and pressure were applied, a pillar structure could be confirmed (TABLE 1(a), (b)). When only a centrifugal force (and no pressure) was applied, a distorted pillar structure could be observed (TABLE 1(c)). When only pressure (and no centrifugal force) was applied, a conical pillar structure was observed (TABLE 1(d), (e)). A pillar structure could not be observed when both the centrifugal force and pressure were not applied (TABLE 1(f)). In addition, there was no significant difference in the shape of the pillar structure of the sample that was centrifugally molded at 1250 G compared to that molded at 2500 G.

The YSZ pillar structure was observed with a laser microscope, and the height of the pillar structure was measured. The relationship between pressure and pillar height for each centrifugal acceleration is shown in FIGURE 4. As can be seen from FIGURE 4, at pressures of 50 MPa or less, the height of the pillars increased as the centrifugal force increased. In addition, the height of the pillars did not change significantly

when the applied pressure was 100 MPa or more for the sample that was centrifugally filled at 1250 G and the one that was not subjected to centrifugal filling. In contrast, the samples centrifugally filled at 2500 G did not exhibit a large change in pillar height regardless of the pressure. In addition, as the pillars of the sample obtained by centrifugal filling at 2500 G and pressing at 200 MPa had a height of approximately 1.1 μm, a dimeter of 1.6 μm, and a pitch of 2.5 μm. If the micropores were sufficiently filled with powder during centrifugal filling, the shrinkage due to sintering was approximately 78%.

TABLE 1. Surface of YSZ after sintering at 1400 °C.

Centrifugal acceleration (m/s^2)	Pressure (MPa)		
	200	100	0
2.5×10^4	(a) 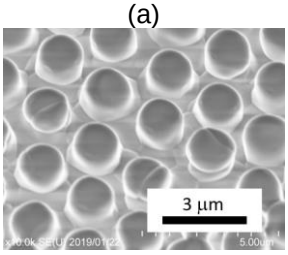	(b) 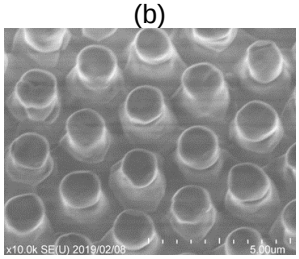	(c) 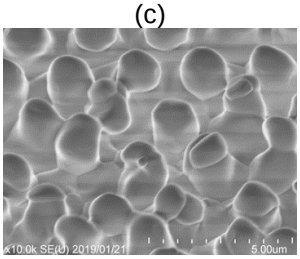
0	(d) 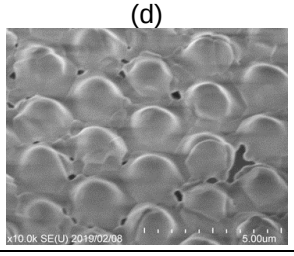	(e) 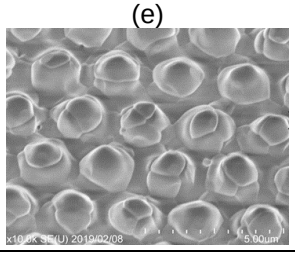	(f) 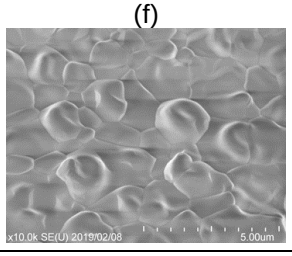

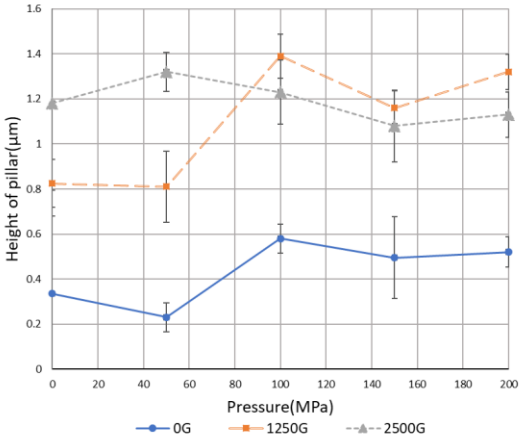

FIGURE 4. Effects of pressure and centrifugal force on height of YSZ pillar.

When no centrifugal force was applied, the paste was considered to be slightly filled into the micropores by the capillary force, as it had a conical pillar structure (FIGURE 5). Moreover, a more homogeneous pillar structure was obtained by applying pressure at any centrifugal force. The reason for this is considered to be that the adhesion between the powders filled in micropores was enhanced by the application of pressure, and then the particles became less affected by the deformation of PMMA during sintering (FIGURE 6).

While samples molded at 1250 G formed pillars of increased heights when a pressure of 100 MPa or more was applied, the height of pillars of samples molded at 2500 G did not significantly change with any pressure. It is considered that YSZ particles were densely embedded in micropores to a certain degree during centrifugal filling.

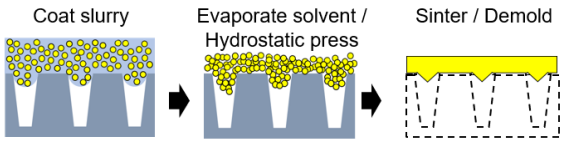

FIGURE 5. Schematic of forming conical pillars.

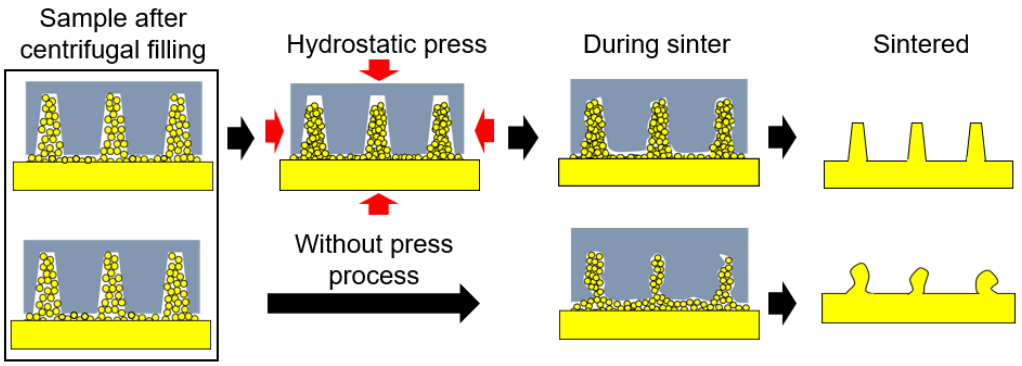

FIGURE 6. Differences in pillar shapes depending on the presence or absence of applied pressure.

RESULTS and DISCUSSION 2

FIGURE 7 shows the performance evaluation results of cells with and without a forest structure. As can be seen from FIGURE 7, the polarization resistance decreased by approximately 25% when a forest structure was fabricated at the SOFC anode.

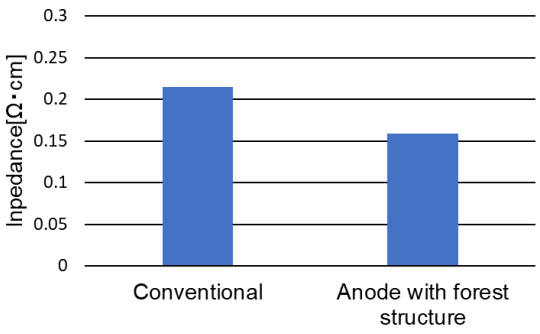

FIGURE 7. Difference in impedance of cells with and without a forest structure.

The polarization resistance was decreased owing to the formation of a forest structure because of the increase in the transport efficiency of oxide ions and the increase in the surface area of the reaction.

CONCLUSIONS

For the YSZ powder and micropores of a certain aspect ratio used in this study, it can be said that a centrifugal acceleration of 2500 G or more is sufficient. Furthermore, it was found that a homogeneous YSZ pillar structure could be fabricated by applying a pressure of 100 MPa or more after centrifugal filling.

In addition, the polarization resistance decreased by approximately 25% in cells with a forest structure compared to those without the forest structure; this indicates that the aspect ratio used in this experiment could effectively improve the transport efficiency or increase the surface area of the reaction.

In this study, only a YSZ pillar structure was fabricated, and parameters such as the aspect ratio of the pillar structure and the pitch of the pillars were not changed. Therefore, it is unclear whether the improvement in performance can be attributed to the improvement in the transport efficiency of oxide ions or the increase in the surface area of YSZ and Ni. The performance improvement mechanism of SOFCs can be understood and optimal values of these parameters can be obtained by a detailed analysis of these parameters and by conducting a three-dimensional structural analysis of the fabricated cells.

REFERENCES

[1] Bidrawn F, Küngas R, Vohs J M, Gorte R J. Modeling impedance response of SOFC cathodes prepared by infiltration. Journal of The Electrochemical Society. 2011; 158: 514-525.

[2] Shimura T, Nagato K, Shikazono N. Evaluation of electrochemical performance of solid-oxide fuel cell anode with pillar-based electrolyte structures. International Journal of Hydrogen Energy. 2019; 44: 12043-12056.

[3] Sakai A, Nagato K, Nakao M. Infiltration of YSZ nanoparticles into microholes by centrifugation. Micro Nano Engineering. 2017; 19: 18-22.

[4] Ketterhagen W R, am Ende M T, Hancock B C. Process modeling in the pharmaceutical industry using the discrete element method. Journal of Pharmaceutical Sciences. 2009; 98: 442-470.

[5] Nguyen H T, Cosson B, Lacrampe M F, Krawczak P. Numerical simulation on the

flow and heat transfer of polymer powder in rotational molding. International Journal of Material Forming. 2015; 8: 423-438.
[6] Park S J, Ahn S, Kang T G, Chung S T, Kwon Y S, Chung S H, German R M. A review of computer simulations in powder injection molding. International Journal of Powder Metallurgy. 2010; 46: 37-46.

TOWARDS EMBEDDED HIGH-SPEED CONTROL FOR DYNAMIC TIP-BASED NANOMETROLOGY IN ROLL-TO-ROLL MANUFACTURING

Liam G. Connolly and Michael Cullinan
Walker Department of Mechanical Engineering
The University of Texas at Austin
Austin, Texas, USA

ABSTACT
This paper presents the design of an embedded system to control the positioning of a measurement gantry with nanometer scale precision. The proposed system must acquire stage position data from an interferometric measurement system, perform control calculations at a high speed (>5 kHz), and regulate the position and velocity of the measurement gantry structure. The aim of this control system is to enable atomic force microscope (AFM) data collection from a flexible substrate without the halting of web movement in a typical roll-to-roll (R2R) manufacturing layout. As the economies of scale for R2R manufacturing of nanofeatured products are largely derived from fast processing, the ability to collect nanometrology data without altering the continuous nature of a given R2R process can be advantageous in concert with process control techniques. As such, the control system must operate in an uncertain physical environment with a variety of unpredictable sources of mechanical vibrations and imperfect temperature and humidity control – making adequate rejection of both stage and measurement disturbances critical to nominal system operation. A field programmable gate array (FPGA) based controller hardware implementation is chosen for its adaptability and high-speed, parallelized computational capabilities. Measurement feedback is provided by a fiber based interferometric sensor system. Candidate controller architectures are explored to determine the most suitable path forward for final implementation of a control system which can meet these requirements.

INTRODUCTION
Interest in applications of R2R manufacturing of nanofeatured coatings, films, sensors, and other electronic devices has significantly increased in recent years due to the promise of higher speed, larger area processing in lowering the cost of products which would have traditionally be

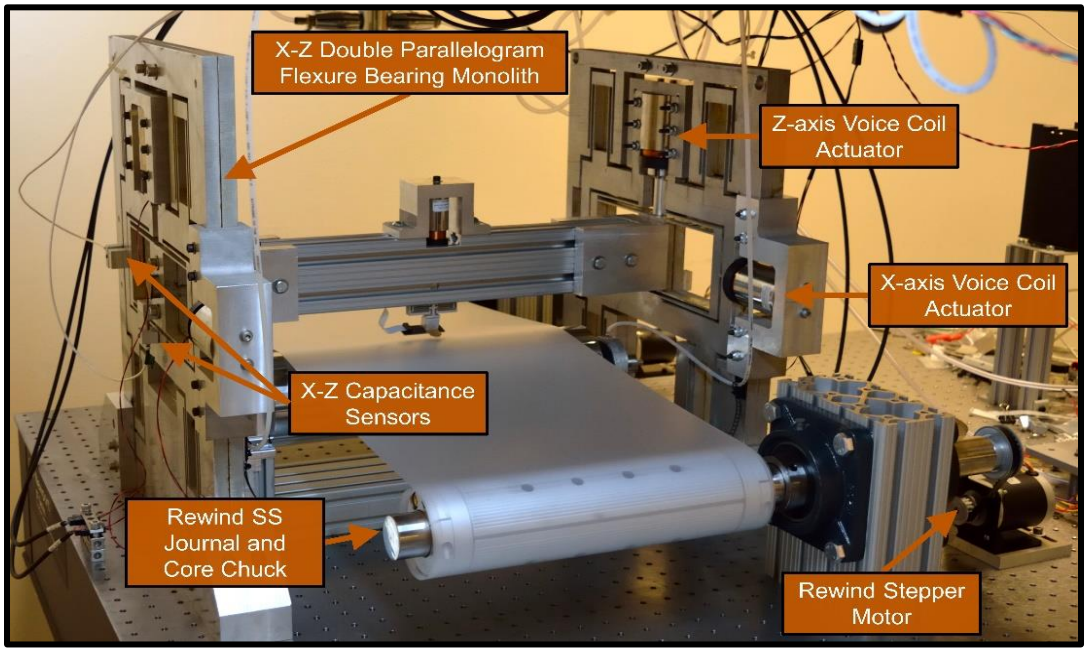
X-Z Double Parallelogram Flexure Bearing Monolith
Z-axis Voice Coil Actuator
X-axis Voice Coil Actuator
X-Z Capacitance Sensors
Rewind SS Journal and Core Chuck
Rewind Stepper Motor

FIGURE 1. Nanometrology System Overview

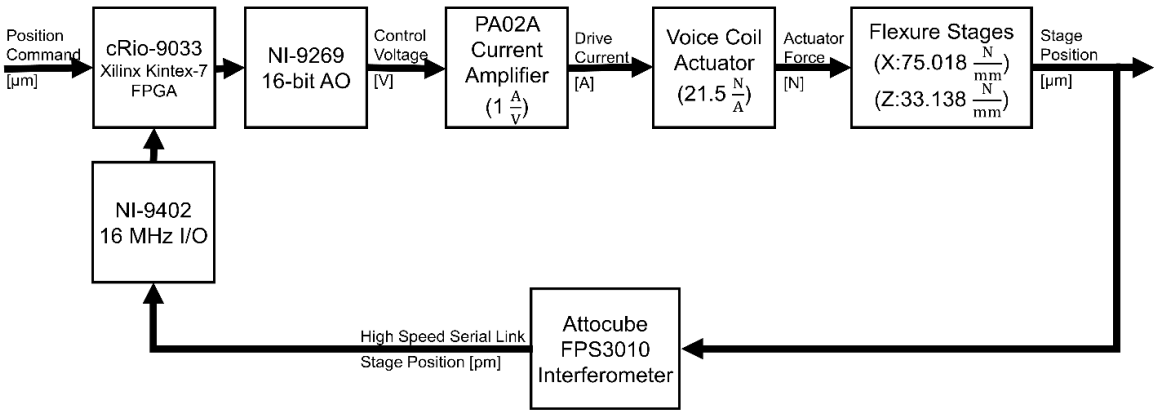

FIGURE 2. General Experiment Hardware Setup

manufactured with silicon wafer substrates [1]–[4].

However, in moving from wafer-based fabrication to step-and-repeat R2R manufacturing to continuous R2R manufacturing, new methodologies for conducting nanoscale metrology in order to provide adequate data for process feedback must be investigated [5]. Previous work demonstrates the application of a novel and inexpensive micro-electro-mechanical system (MEMS) based single chip AFM (sc-AFM, ICSPI Corp.) to step-and-repeat manufacturing [6]. In applying tip-based measurement to this continuous manufacturing quandary, a new strategy for topography measurement without web stoppage must be devised. Such a system schema where the web-direction axis of the two-axis positioning system shown in Fig. 1 tracks web velocity while the other, vertical positioning axis tracks the curvature of the roller on which measurement is occurring such that the relative velocity between web and sc-AFM is effectively zero. This operational mode would enable quasi-real-time acquisition of nanoscale topography data for process feedback.

EXPERIMENTAL APPARATEUS

The system setup used to implement the final control algorithm and perform the positioning of the sc-AFM is detailed in Fig. 2. An FPGA based National Instruments compact-RIO controller is chosen for its robust nature and cost effective, flexible implementation for a variety of digital and analog I/O channels. A current amplifier (Apex Microtechnology PA02A) is used to transduce the voltage signal from the controller to a drive current to the voice coil actuators (MotiCont LVC M-051-054-02). This actuator is rigidly connected to a custom double parallelogram module flexure stage [6]. Feedback of the stage position signal is accomplished through a high speed serial link (HSSL) from the interferometric sensor (Attocube FPS3010) to the FPGA [7]. HSSL is chosen over the more common quadrature ("A-quad-B") signal system due to its ability to report absolute position and resistance to loss of sync or other communication channel aberrations which might cause loss of position with a quadrature signal. The HSSL clock period is chosen to give a minimum 50 kHz sampling rate without resolution loss given the 16 MHz switching frequency of the digital I/O channels and a 48-bit data-word.

SYSTEM IDENTIFICATION AND MODELING

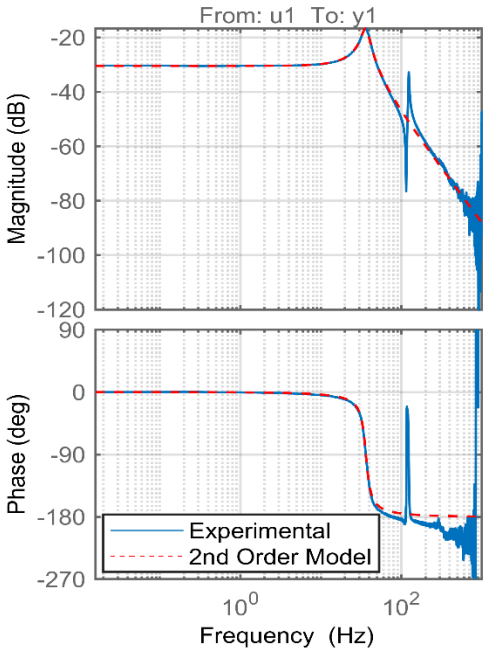

FIGURE 3: Bode response and 2nd order model of single monolith flexure bearing Z stage.

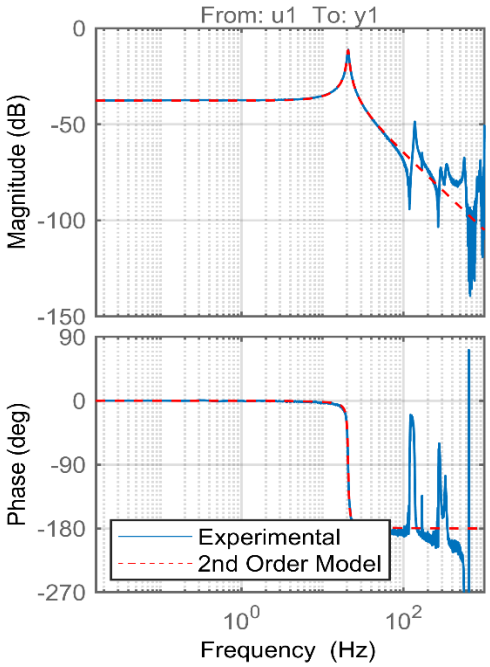

FIGURE 4: Bode response and 2nd order model of single monolith flexure bearing X stage.

To best guide design of the desired control system, a frequency response function (FRF) is derived from experimental input-output data. In order to capture the stage dynamics present, a 1 kHz gaussian white noise signal is applied to the current driver and stage position output measured [8], [9]. From these FRFs, a 2nd order transfer function model is fit to the data to derive system coefficients for stiffness and damping ratio. The results of the system identification can be seen in Figs. 3 and 4, where the X-axis is the web-direction positioner and the Z-axis the vertical positioner.

With accurate, as-fabricated measures of flexure stiffness, damping ratio, and equivalent mass without payload from the 2nd order model, the coupling between each flexure bearing monolith due to the connecting AFM gantry, is then modeled in the 4th order system represented in Fig. 5 where y_i is monolith stage position, k_i flexure bearing stiffness, b_i damping coefficient, and f_i force actuator input. In this model each monoliths stage output position is related to the input force from the voice coil actuators [10]. The resulting transfer function which models this cross-stage coupling behavior, G, is then used to drive controller design as outlined in Eq. 1.

$$\begin{bmatrix} y_1 \\ y_2 \end{bmatrix} = \begin{bmatrix} G_{11} & G_{12} \\ G_{21} & G_{22} \end{bmatrix} \begin{bmatrix} f_1 \\ f_2 \end{bmatrix} = \boldsymbol{G} \begin{bmatrix} f_1 \\ f_2 \end{bmatrix} \qquad (1)$$

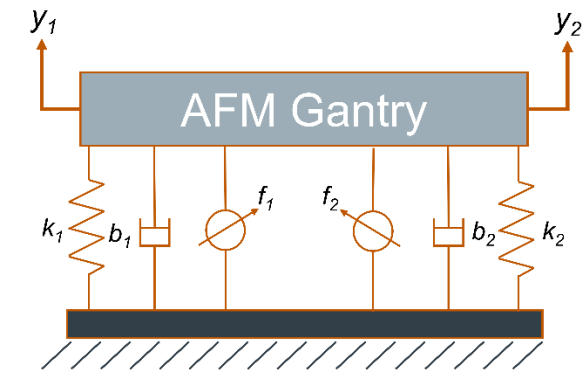

FIGURE 5: Schematic of 4th order coupled flexure-gantry dynamic system.

MODEL BASED CONTROL DESIGN

As a means of testing a variety of control designs without the overhead of custom LabVIEW FPGA programming for each controller implementation, a linear simulation framework is utilized to evaluate various candidate designs.

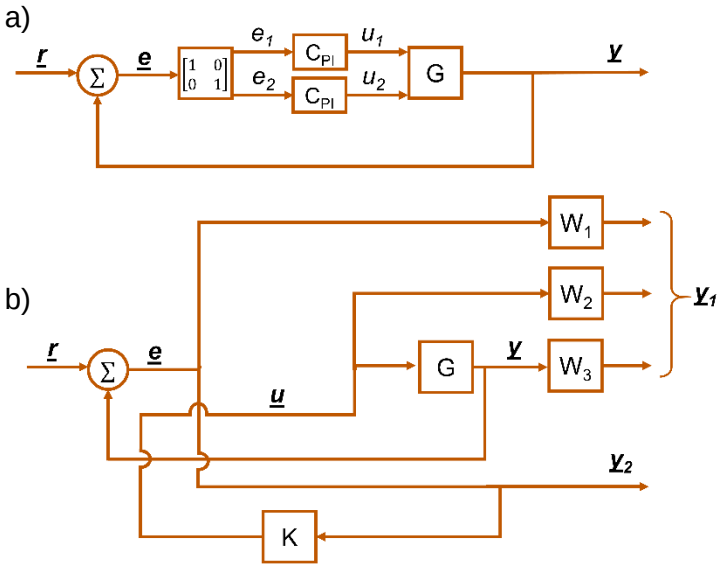

FIGURE 6: a) Decoupled PI control of MIMO dynamic system G. b) Control diagram of H∞ stabilized controller K of system G.

Proportional-Integral Control

Proportional-Integral (PI) control has been a cornerstone of controller design for decades due to its ease of implementation, and performance relative to the complexity of design and gain tuning. In the multiple-input-multiple-output (MIMO) implementation of this architecture a decoupling gain matrix equal to the identity matrix with size equal to the number of control inputs is used to implement parallel PI controllers to

control the system. For evaluation of PI control in this system, PI gains were chosen to achieve a 10 dB gain margin [11]. A block diagram of this controller is shown in Fig. 6A.

Robust Control: H Infinity Design

Robust control design has been shown to improve performance in applications with measurement uncertainty, hard limits on actuator slew rate and maximum output, and where physical disturbances make precise control difficult. Through the incorporation of objectives such as bandwidth, resolution, disturbance and measurement noise rejection or attenuation, and real-world control effort, an optimal controller can be implemented without tedious online gain calculation, infeasible with current hardware, which will also improve overall system performance. In this paradigm *K* is the optimized controller which minimizes the H∞ norm of the closed loop transfer function shown in Eq. 2 where S and T are the sensitivity and complementary sensitivity functions and R is a measure of control effort [12], [13].

$$\boldsymbol{T} = \begin{bmatrix} W_1 S \\ W_2 R \\ W_3 T \end{bmatrix} \quad (2)$$

$$\boldsymbol{S} = (1 + GK)^{-1} \quad (3)$$

$$\boldsymbol{R} = K(1 + GK)^{-1} \quad (4)$$

$$\boldsymbol{T} = GK(1 + GK)^{-1} \quad (5)$$

As such the inverse of W_1 and W_3 influences the control bandwidth and disturbance attenuation respectively. W_1 is typically modeled after a low pass and W_2 a high pass filter in order to provide good tracking performance and robustness. In the loop-shaping method, these weights are chosen algorithmically in order to optimize T such that it matches a closed loop behavior goal in the frequency space: high bandwidth in the desired region and suppressed coupling behavior. The block diagram of this controller is shown in Fig. 6B, where K is the resulting 14th order stabilizing controller.

Controller Simulation Results

The bode response of the modeled open loop system G, decoupled PI controller, and resultant

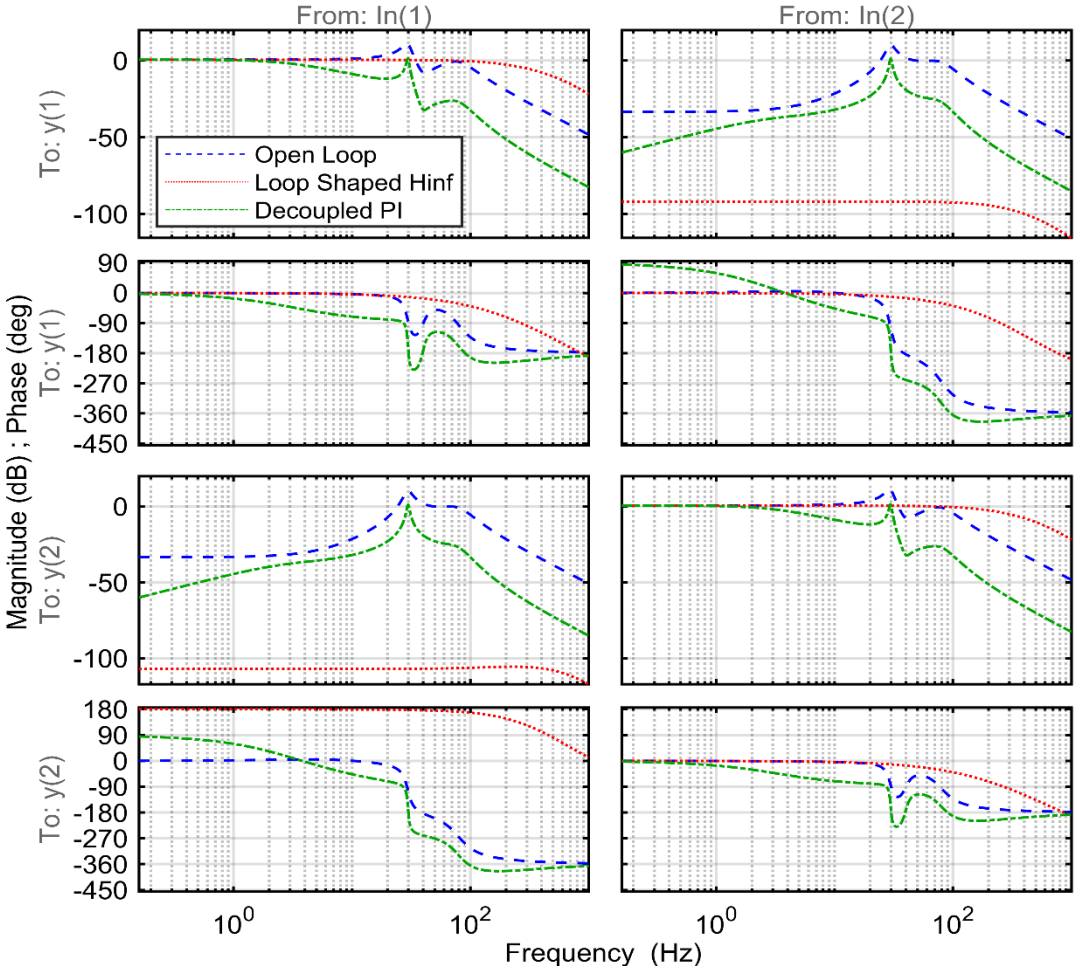

FIGURE 7: Bode response of two-input-two-output open loop model and closed loop systems.

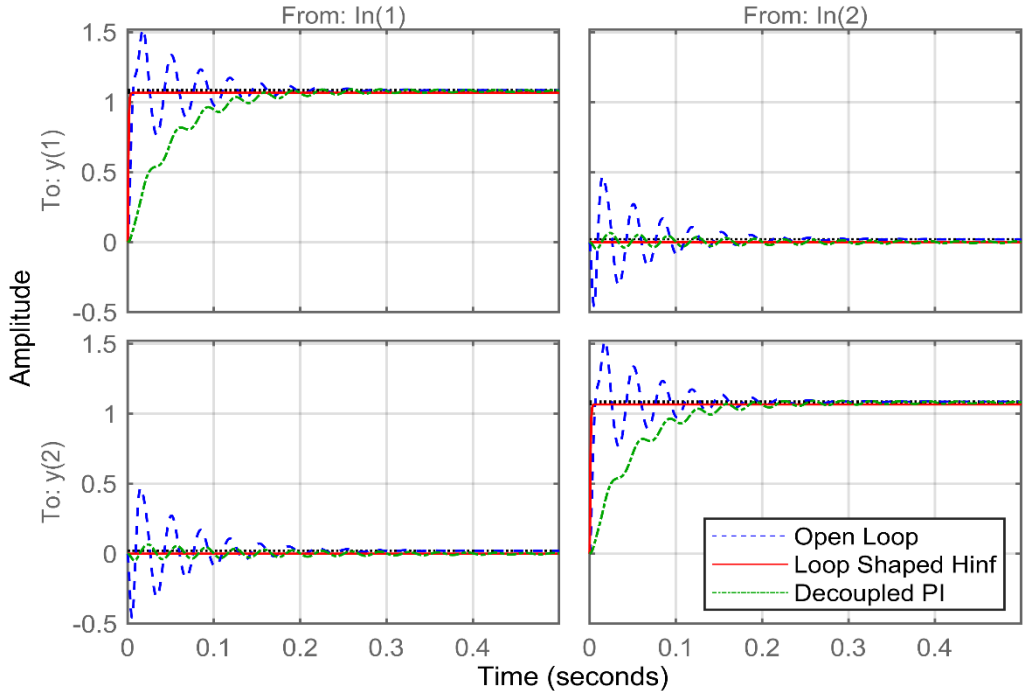

FIGURE 8: Step input response of 2-input 2-output open loop model and closed loop systems.

H∞ synthesized closed loop controller are shown in Fig. 7. From this frequency response it is clear that both the tracking bandwidth and cross coupling suppression of the H∞ controller are superior to the open loop system and decoupled PI controller. The transient behavior of all three systems is further evaluated with a step inputs to the stage input voice coil actuators, as shown in Fig. 8. The rise and settling time of the H∞ controller to both position commands and coupling disturbances are significantly lower than either the open loop system or the PI control scheme.

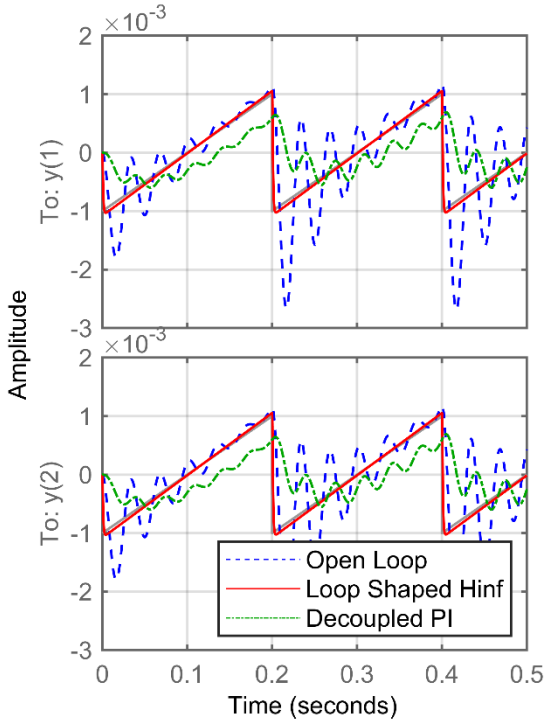

FIGURE 9: Reference tracking performance of a 5 Hz sawtooth wave command to both inputs of the open loop model and closed loop systems.

Lastly, higher frequency tracking behavior of the three systems is tested in Fig. 9. with a 5 Hz sawtooth wave position command input to both stages simultaneously. The results of this simulation demonstrate the significant gap in controller bandwidth and reference tracking performance between the proposed PI and H∞ closed loop systems.

FUTURE WORK

While the H∞ synthesis scheme aims to design a more robust control system, a large part of the final performance depends upon accurate modeling of the real-world sensor noise, input and output disturbances, uncertainty in physical quantities, and actuator constraints in the system used to optimize the controller *K*. To verify accuracy of the initial system model *G*, a white noise system identification will be carried out to estimate an experimental transfer function for the coupled system to be used for final controller

synthesis. Moreover, uncertainty, quantization, and noise models will also be experimentally validated. Once confirmed to accurately portray machine conditions, an order reduction and fixed-point mathematics error study will be carried out in order to guide FPGA implementation of the final closed loop control system within the resource constraints of the chosen FPGA controller. Finally, when the AFM gantry nanopositioner control performance has been evaluated and deemed sufficiently precise and robust for operation during an AFM scan without degradation of measurement quality, velocity regulation of the web system will be added to the MIMO control architecture in order to enable the primary system goal of moving-web collection of nanometrology data.

REFERENCES

[1] H. Lan, “Large-Area Nanoimprint Lithography and Applications,” *Micro/Nanolithography - A Heuristic Asp. Endur. Technol.*, 2018.

[2] A. C. O’Connor, T. J. Beaulieu, and G. D. Rothrock, “Economic Analysis of Technology Infrastructure Needs for Advanced Manufacturing: Roll-to-Roll Manufacturing,” 2016.

[3] S. Ahn *et al.*, “Roll-to-roll nanopatterning using jet and flash imprint lithography,” 2012, vol. 8323, no., pp. 83231L-8323–7.

[4] A. Nathan *et al.*, “Flexible electronics: The next ubiquitous platform,” *Proc. IEEE*, vol. 100, no. SPL CONTENT, pp. 1486–1517, 2012.

[5] T.-F. Yao, L. G. Connolly, and M. Cullinan, “Expanded area metrology for tip-based wafer inspection in the nanomanufacturing of electronic devices,” *J. Micro/Nanolithography, MEMS, MOEMS*, vol. 18, no. 03, p. 1, Sep. 2019.

[6] L. G. Connolly, T.-F. Yao, A. Chang, and M. Cullinan, “A tip-based metrology framework for real-time process feedback of roll-to-roll fabricated nanopatterned structures,” *Precis. Eng.*, Apr. 2019.

[7] N. Inami, Y. Takeichi, and K. Ono, “Real-time motion control and data acquisition system for scanning X-ray microscopy using programmable hardware,” *J. Phys. Conf. Ser.*, vol. 502, no. 1, 2014.

[8] “New Ways of Estimating Frequency Response Functions.,” *S V Sound Vib.*, vol. 18, no. 11, pp. 34–38, 1984.

[9] N. K. Roy and M. A. Cullinan, “Fast Trajectory Tracking of a Flexure-Based, Multiaxis Nanopositioner With 50-mm Travel,” *IEEE/ASME Trans. Mechatronics*, vol. 23, no. 6, pp. 2805–2813, Dec. 2018.

[10] X. Zhou, D. Wang, J. Wang, and S. C. Chen, “Precision design and control of a flexure-based roll-to-roll printing system,” *Precis. Eng.*, vol. 45, pp. 332–341, 2015.

[11] S. Salapaka, A. Sebastian, J. P. Cleveland, and M. V. Salapaka, “High bandwidth nano-positioner: A robust control approach,” *Rev. Sci. Instrum.*, vol. 73, no. 9, p. 3232, 2002.

[12] R. Y. Chiang and M. G. Safonov, “H∞ synthesis using a bilinear pole shifting transform,” *J. Guid. Control. Dyn.*, 1992.

[13] K. Glover and D. Mcfarlane, “Robust Stabilization of Normalized Coprime Factor Plant Descriptions with H∞-Bounded Uncertainty,” *IEEE Trans. Automat. Contr.*, 1989.

MEMS DYNAMIC MECHANICAL ANALYZER FOR *IN SITU* VISCOELASTIC CHARACTERIZATION OF 3D PRINTED MICROSTRUCTURES

David R. Cayll[1], Ian S. Ladner[1], Joon Hyong Cho[1], Sourabh Saha[2], and Michael A. Cullinan[1]

[1]Department of Mechanical Engineering
University of Texas at Austin
Austin, Texas, United States of America
[2]Materials Engineering Division
Lawrence Livermore National Laboratory
Livermore, California, United States of America

ABSTRACT

Microscale 3D printing opens many applications in rapid prototyping useful in photonics, bioengineering, and nano/microstructured metamaterials applications. However, in order to optimize designs, a full characterization of the size and strain rate dependent material properties must be done. This work presents the design, fabrication, calibration, and testing of a MEMS dynamic mechanical analyzer for in situ viscoelastic characterization of two photon lithographically printed structures. The load cell in this work has a displacement resolution of 1.5 nm and a load resolution of 149 nN. This system is capable of sinusoidally driving tensile tests from 0.001 Hz to 10 Hz and incorporates temperature control of $\pm$1°C up to 47°C.

INTRODUCTION

Two photon lithography (TPL) is a 3D printing technique that has been demonstrated to write sub-diffraction limited features over a millimeter scale area. This is due to the energy requirements in the polymerization process of the resist. As the name suggests, two photon absorption is required to cure the polymer, and that only occurs at laser focus, therefore, sub-diffraction limited feature sizes are achievable[1].

At the smallest scales that TPL can achieve, there are many factors that can affect properties of the polymerized material such as write speed, UV post cure, and treatment with radicals [2]. Ladner et. al. showed that TPL printing single volumetric pixels, or voxels, directly onto MEMS tensile testers provides a reliable platform for testing static material properties.

However, properties of polymers can change drastically depending on strain rate as well. Depending on this rate, the polymer could be in a rubbery or glassy regime with vastly different properties. The transition between the two regimes can be characterized experimentally through dynamic mechanical analysis (DMA). DMA tools allow for temperature and frequency controlled tests all while measuring tensile stress and strain of the material while staying in the linear elastic regime.

DEVICE DESIGN AND FABRICATION

The MEMS tensile tester shown as fabricated in Figure 1 consists of five main components: the load sensor, TPL print stage, displacement sensor, linear thermal actuator, and two sets of folded flexure bearings. Both the load and displacement sensors are differential capacitive sensors with functional requirements quoted in table 1.

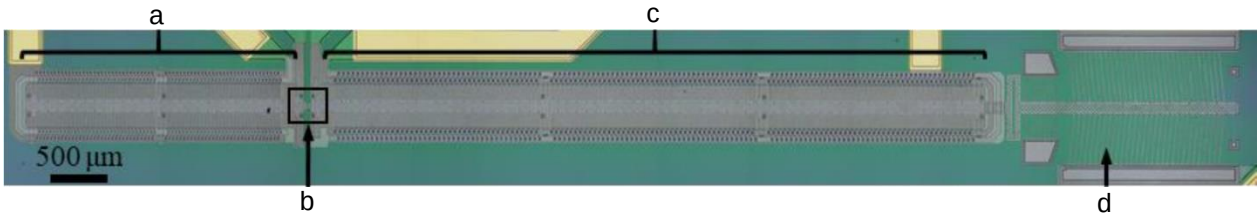

FIGURE 1. As-fabricated MEMS tensile tester. 1a) Load sensor 1b) TPL print stage 1c) Displacement sensor 1d) Thermal actuator. Folded flexure bearings appear every ~1000 um along the two stages.

TABLE 1. Functional Requirements for tensile tester stage and sensor design.

	Load Sensor	Disp. Sensor
Resolution	75 nN	0.625 nm
Range	250 uN	1.5 µm
Stiffness	140 N/m	28.3 kN/m

The Chevron beam style thermal actuator is heated using DC current causing the individual beams expand to impart linear stage displacement. This movement is guided by the folded flexure bearings. The lumped mechanical model in Figure 2 and the force balance in equations 1-3 show that the displacement-controlled tests assumption is valid. For the tool to be displacement controlled as opposed to force controlled, i.e. ≤1% Δx_s error, the stiffness of the displacement stage flexures and actuator together must be over two orders of magnitude higher than the load stage flexure.

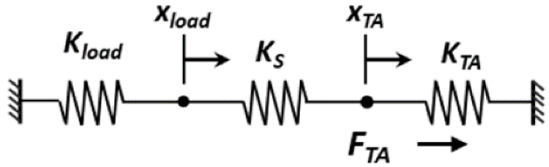

FIGURE 2: Lumped mechanical model.

$$x_{load} + x_s = x_{TA} \quad (1)$$

$$K_{load}x_{load} = K_s x_s \quad (2)$$

$$K_s x_s + K_{TA}x_{TA} = F_{TA} \quad (3)$$

Stiction

In order to be integrated into the TPL printing process, the MEMS device must survive immersion into and removal from the PGMEA developer used to remove uncured resist. The major failure mode when being transferred between solutions is stiction. Stiction is when any suspended structure, in this case the stage and capacitive sensors, is pulled towards another surface and becomes adhered. In order to protect against this failure mode, the surface area between the two surfaces must be minimized, so that the stiffness of the members can overcome the capillary force. Equations 4-5 show the critical length of the capacitive fingers to eliminate stiction. Stiction can be due to capillary forces, eqn. 4, as well as surface-to-surface adhesion due to peeling forces, eqn. 5 [3].

$$L_{crit,EC} = \sqrt[4]{\frac{2Eg^2h^3}{9\gamma_l \cos\theta_c(1+h/b)}} \quad (4)$$

$$L_{crit,P} = \sqrt[4]{\frac{3Eg^2h^3}{8\gamma_s}} \quad (5)$$

where g is vertical gap between the suspended beam and the substrate, h is beam height, L is beam length, b is beam width, γ_l is liquid surface tension, θ_c is liquid contact angle, and γ_s is the solid surface tension.

In order to hold enough capacitive fingers for the required sensitivity, the stage must be larger than the L_{crit} from eqns. 4-5. To mitigate stiction, release dimples were used to decrease contacting surface area significantly so that the spring force from the flexures can overcome the capillary and peel forces.

Capacitive Sensors

In order to gather reliable stress strain data out of the DMA, positions of both stages need to be sampled at a high rate in real time so that phase data can be extracted. Figure 3 shows a schematic of the capacitive sensors. Capacitors C_1 and C_2 are the differential pair to be measured.

Eq. 6 describes the linear relationship between

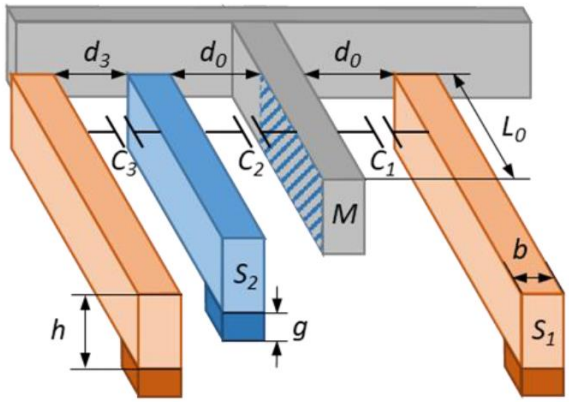

FIGURE 3. Differential Capacitive displacement sensor unit cell.

gap distance, Δd and change in capacitance, ΔC. To measure displacements of 0.625 nm stated in the functional requirements in Table 2, the sensors must be able to measure a 0.1 fF change in capacitance.

$$\Delta C = 2n\varepsilon l_o h \frac{1+2(C_3/C_0)}{d_0^2}\Delta d \quad (6)$$

Capacitance Measurement Circuit

In order to measure the 0.1 fF change in capacitance that the differential capacitors were designed for, a commercial capacitance measurement IC, the MS3110 from Irvine Sensors was selected. However, the parasitic capacitance in the circuit caused the IC output to saturate, and it was ultimately unusable. Instead,

the charge integration circuit shown in Figure 4 was implemented to overcome charge saturation in the IC.

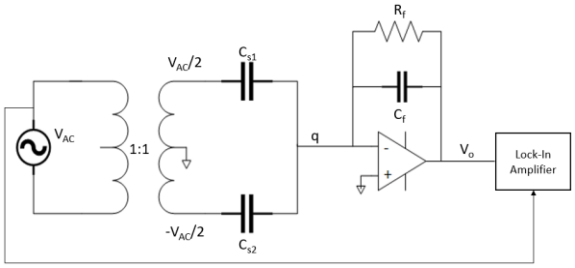

FIGURE 4. Lock in Amplifier Capacitance Measurement Circuit.

This circuit uses an LT1793 op-amp with very low noise and high input impedance as a charge integrator. The Zurich Instruments UHF lock-in amplifier (LIA) with built-in digital signal processing and logging capabilities was used to measure the magnitude of output voltage, V_O, at the reference frequency V_{AC}. Using the lock-in amplifier for this measurement demodulates the output signal and passes it through a low pass filter so the signal at frequency f_{AC} is sufficiently low noise. Equations 7-8 describe the relationship between charge, change in capacitance, and output voltage in the circuit in Figure 4.

$$q = \frac{1}{2}(C_1 - C_2)V_{AC} \quad (7)$$

$$V_O = \frac{1}{C_f}q \quad (8)$$

Charge accumulated on the common terminal, 'M' from Figure 3, of the capacitors C_1 and C_2, is directly proportional to the magnitude of change in capacitance between the two capacitors. The frequency of V_{AC} was set at 500 kHz to stay below the bandwidth of the op-amp as well as above the amplifier's high pass filter cutoff frequency. C_f was minimized to maximize the gain of the amplifier, and R_f was used to tune the cutoff frequency of the amplifier.

In order to further reduce noise further, a low pass filter was implemented that utilized the digital processing capabilities of the UHF LIA. This filter was used to filter the V_O signal so that a sine wave could be fit in the time domain to extract the valuable phase information from our DMA test.

The bandwidth of this DMA system will be limited by the settling time of the thermal actuator. A model proposed by Hickey et. al [4] was used to approximate the second order transfer function of the thermal actuator. The time constant of the system was 0.791 ms, therefore in order to safely assume the signal input stays in phase with the displacement, a limit of 10 Hz is placed on the actuator. This is not an issue as many materials are tested in the 0.01-10 Hz range, and there are ways to increase the range with modulating temperature as well.

SENSOR CALIBRATION

Digital Image correlation (DIC) has been used to characterize this system in quasi-static tests down to an in-plane resolution of 1.59 nm for the displacement sensor, and 0.92 nm [5]. To achieve subpixel resolutions, there is a major trade off with image collection time. Each datapoint collected in quasi-static mode took 7 seconds and is inadequate for testing strain rate dependent properties since the smallest discernable frequency would be 0.07Hz.

Displacement Sensor

The MEMS tensile tester was designed as a strain-controlled device; therefore, the force imparted by the load stage will not affect the location of the displacement stage. This allows the location of the displacement stage to be found deterministically using equation 9. [5].

$$d = \left(\frac{V}{3.49}\right)^2 \quad (9)$$

Load Sensor

To calibrate the LIA circuit, a tensile testing MEMS with connected stages was actuated with the thermal actuator, and the sensor response was logged. Figure 5 shows the linear response between actuated distance and LIA circuit output voltage. Since this tool will always be actuated with a sine wave, the sensor was calibrated with a sine wave. The amplitude of actuation voltage was determined using equation 8, and 15 periods of response were recorded. This data was then curve fit, and the error bars shown in Figure 5 are the RMSE of the curve fit at each point. The standard deviation of the position averaged across the full range is 1.5 nm.

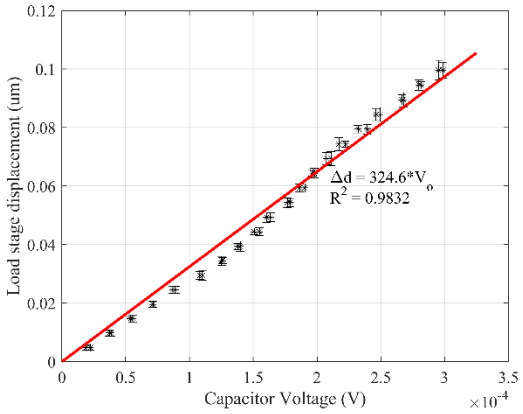

FIGURE 5. LIA charge integrator output calibration curve.

The curve fit method was used over FFT because the error is easily quantifiable and data fidelity can be found using the coefficient of determination, R^2. An example of this curve fit of the connected stage calibration device at 50 nm of displacement and 0.1 Hz is shown in Figure 6.

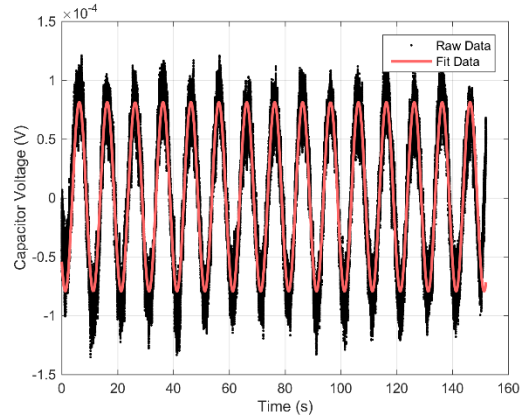

FIGURE 6. Load stage capacitive sensor voltage output, V_O, and raw sensor data with best fit line vs Time. RMSE = 1.65e-5; R^2 = 0.919.

Using the relationship in equation 7-8, the smallest change in capacitance sensed by the load sensor can be determined with the RMSE data presented in Figure 6. Using a 95% confidence interval, a 2σ deviation from the fit line is the smallest measurable displacement and can therefore be used to characterize the resolution of the sensor. The ΔC found is 0.04 fF. However, when the calibration curve in Figure 5 is used to determine the displacement for the given RMSE capacitor voltage, actual displacement measured is 1.5 nm. This is about twice as large as what is expected using equation 6. This can be attributed to the difficulties in manufacturing, namely the multi-layered polysilicon body layer that may hold unwanted charge between layers, as well as high roughness sidewalls of the same polysilicon body layer.

As designed, the load sensor stage has a stiffness approximately equal to the stiffness of the TPL printed voxel. This allows the load stage and TPL printed voxel to displace about the same amount while under test which allows for the optimal sensing accuracy along with measurement range.

The last part of the load cell that must be characterized is the stiffness of the linear flexures. These provide the restoring force that will allow us to measure the force on the TPL part between the stages. The manufacturing difficulties described above also impacted the stiffness of the device under test. Using SEM images along with finite element modeling, the kerf, or over etching, was quantified. The device used for the example test in Figure 7 has a stiffness of 99.47 $\pm$ 5.47 N/m [5].

PRELIMINARY RESULTS

An important viscoelastic property is loss factor, or *tan(δ).* This loss factor describes how much energy is dissipated in the form of heat while the material is being strained. A rubbery polymer is expected to have a higher loss factor than a glassier polymer. This behavior can be seen in Figure 7. As frequency increases, so does the loss factor. The loss factor is the ratio of complex modulus, *E''* over the real modulus, *E'*. At the glass transition, there is a peak in the loss factor. Figure 7 is taken at room temperature, however, if data is taken at higher temperatures, the time-temperature correspondence principle states that tests at higher temperatures are roughly equivalent to tests at higher frequencies[6]. In order to get a full picture of this polymer, tests at higher and lower temperatures are necessary since it is time consuming to run tests at lower frequencies and higher frequency tests run into transducer and datalogging bandwidth issues.

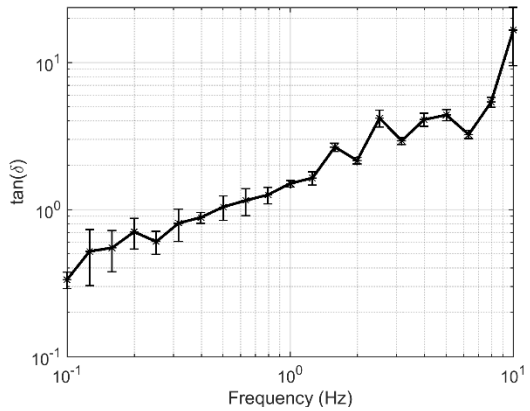

FIGURE 7. Loss factor, tan(δ), of a 3D printed TPL voxel.

CONCLUSION

A microscale dynamic mechanical analyzer has been presented to characterize the viscoelastic properties of two photon lithography printed parts. Dynamic tests will be performed within the linear elastic regime of the polymer. Successful calibration of the device shows that the capacitive sensor used to measure force has a displacement resolution of 1.5 nm, which corresponds to a force resolution of 149 nN. These resolutions are about half of the desired resolutions but allows high sample rates necessary for DMA testing. Future work includes temperature dependent tests to further characterize the materials along with complex modulus measurements.

ACKNOWLEDGEMENTS

Thank you to LLNL for providing 3D printed structures for testing and Jason Gorman at NIST for assisting with the capacitive sensor readout circuit design. This work was performed under the auspices of the U.S. Department of Energy by Lawrence Livermore National Laboratory under Contract DE-AC52-07NA27344 and by the University of Texas at Austin under Subcontracts B617787, B621043, and B626195. Funding was available from LLNL's LDRD project 16-ERD-047. LLNL-ABS-782467-DRAFT

The work was partly done at the Texas Nanofabrication Facility supported by NSF grant NNCI-1542159

REFERENCES

[1] L. J. Jiang, J. H. Campbell, Y. F. Lu, T. Bernat, and N. Petta, "Direct writing target structures by two-photon polymerization," *Fusion Sci. Technol.*, vol. 70, no. 2, pp. 295–309, 2016.

[2] S. K. S. Ian S. Ladner, Michael A. Cullinan, "Processing-dependent tensile behavior of polymer nanowires fabricated via two-photon lithography," *RSC Adv. (under Rev.*, 2019.

[3] C. H. Mastrangelo, "Suppression of stiction in MEMS," *Mater. Res. Soc. Symp. - Proc.*, pp. 105–116, 2000.

[4] R. Hickey, D. Sameoto, T. Hubbard, and M. Kujath, "Time and frequency response of two-arm micromachined thermal actuators," *J. Micromechanics Microengineering*, vol. 13, no. 1, pp. 40–46, 2003.

[5] I. S. Ladner, "Mechanical Characterization of Two-Photon Polymerization Submicron Features," (Doctoral Disseration). University of Texas at Austin, 2018.

[6] W. J. Shaw, Montgomery T., Macknight, *Introduction to Polymer Viscoelasticity*, 3rd ed. Hoboken: John Wiley & Sons Inc, 2005.

High speed Stimulated Raman scattering microscope with shot noise limited detection

Haozheng Li[1], Ping Wang[1]

[1]*Britton Chance Center for Biomedical Photonics, Wuhan National Laboratory for Optoelectronics-Huazhong University of Science and Technology, Wuhan, Hubei 430074, China*

High speed label-free imaging with molecular specification is highly desired for biomedical and material sciences. Spontaneous Raman microscopy is able to provide vibrational identification of chemical bonds, but often hindered by low sensitivity. Nonlinear stimulated Raman scattering (SRS) microscopy is a novel label-free imaging method with significantly gained signal and image contrast. Moreover, SRS microscopy offers background-free chemical imaging with readily interpretable spectra, and high spatial and temporal resolution. By precise and fast mechanical control, we report high speed SRS monitoring and imaging of chemical reactions in situ. Especially for 3D micro-printing, photoetching and biocompatible hydrogels, high speed and submicron resolution SRS microscopy provides molecular and non-invasive tool for compositional imaging during chemical reaction.

PARALLEL POSITIONING DEVICE FOR X-RAY DIFFRACTION LABORATORY USE

Gheorghe O., Norman H. and Johannes D.
R&D
HUBER Positioning & Diffraction GmbH & Co.KG
Rimsting, Bayern, Germany

INTRODUCTION

At present, aside from the continuous interest in natural sciences (e.g., physics, chemistry, and biology) to discover the fundamental principles and rules governing the atomic-scale structure of materials, knowledge on applied materials at the nanoscale are also of premium interest. As the semiconductor industry clearly show the tendency towards the introduction of nanostructures in working devices, nanomaterials are actually in the "micro focus" of investigations of prestigious research institutions worldwide.

However, the "semicon" nanomaterials with improved or modified functionalities need to be prepared and characterized and the data interpreted, by adequate methodologies (e.g., techniques and tools) [1].

X-ray diffraction (XRD) proved to be a reliable technique for investigating the physical and chemical atomic structures behaviours for relative long time [2]. The routes chosen by researchers vary: a) some used the power of synchrotrons or b) accessible, laboratory sources light. Accordingly, new equipment (e.g., machines and instruments) have been (or, are to be) built.

The synchrotron equipment's for XRD are generally based on multi circle machines (diffractometers). A coordinated motion of several circles (rotations) is performed with the specificity of diffraction (laws of physics). Several producers exist, for example [3]. This geometry results in large and heavy-duty machines, working in dedicated large rooms (experimental hutches).

On the contrary, in laboratory X-ray investigations, Dms must fulfil some additional specific requirements regarding adjacent conditions (e.g., source and space). Machines must work in tight spaces with increased manipulated (positioning) precision for beam (optics), samples, and detectors (Dts) to encompass the low power sources and get correct high-resolution diffraction data. Several well-known producers, such as BRUCKER, PANALYTICAL, and RIGAKU exist.

A successful joint collaboration between several academic and research institutions (CRC) aiming to study multifunctional materials and characterize them based on specific properties (ferroelectric, magnetic, semiconducting, and/or isolating) based on a research project is coming to an end (2019) [4]. To continue the investigations, a new dedicated Dm for laboratory use has to be developed and work in a well-known scientific applicative research location (MPG/MSP) [5]. The new machine will work with both, the classical (XRD) and actual modern (e.g., SXRD and GISAXS) X-ray diffraction techniques. It is expected to investigate nanostructures under various atomic aspects, mainly to characterize new oxide heterostructures compounds (surfaces/ interfaces).

Inside, a new device for positioning samples (and, specific instruments) with high precision was included. The positioning device (PD) is based on a parallel kinematic (PK) [6] structure and expected to pose (translation and rotations) a heavy body in all six dof (DoF) with the highest precision by fitting the allocated (limited) space. With a compact (height) and acceptable cost (XY stages), the device comes as an alternative to the more expensive existing (e.g., serial and parallel) products. An overview of the device from kinematic and conceptual design points of view, together with its integration are presented here.

DIFFRACTOMETER

A Diffractometer (Dm) machine must provide a high precision coordinate motion for the sample (S) and the detector (Dt), by taking in to account the X-ray beams (X_i-incident/ X_d-refracted). Moreover, it has to manipulate (e.g., posing and aligning) a sample (and, instruments) toward an incoming X-ray (X_i) beam and to pose the Dt at required distance after the diffracted (scattered) beam (X_d) goes. Then, the obtained spots (pixel image) data are to be transposed to a PC control

unit for interpretation and analysis (reconstruction) of the diffraction pattern.
As mentioned before, different configurations of Dm are available for laboratory use. In most of them, the sample and X-ray source (solid metal anode/Cu) together with the micro focusing optics all move around a horizontally axis to minimizing the positioning sample/source errors, e.g. D8 ADVANCED [7].
However, in the actual proposed Dm intending to work for high performance surface / interface analysis, a fixed type X-ray source located nearby (660mm) of the Dm has been chosen.

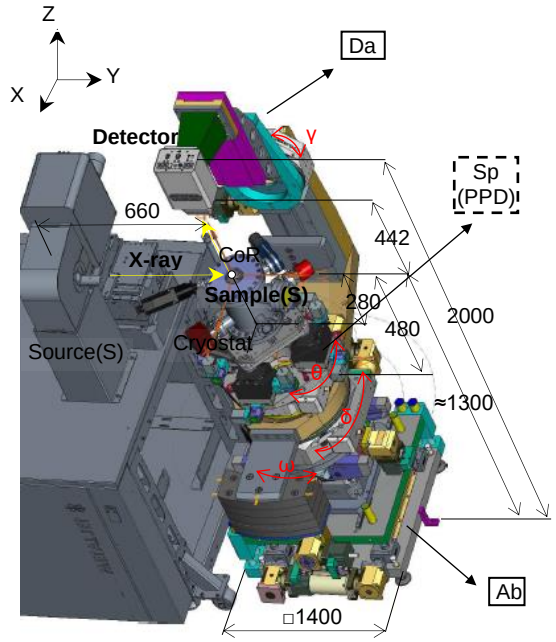

FIGURE 1. X-ray LabDm (Overview)

The liquid-metal technology (METAL JET) [8] already proved to be an actual advanced source. Together with high-quality focusing optics (HELIOS) [9], not shown in the figure, the intensity of the beam is transferred as much as possible to the sample. (In addition, the multilayer Ga mirror proved to deliver the best flux intensity (3x) than actual conventional microfocus/rotating anodes [7]). By this, the entire system (source & optics) is providing the most intense lab X-ray beam, meeting the increasing demands of actual modern diffraction techniques.
HUBER has a long history of successfully developing ultimate X-ray machines (synchrotron). For the newly developed laboratory Dm (LabDm), a modular (4+2) structure working for similar applications has been chosen [3], as reference. Several modifications coming from the specificity of the investigations have been applied, Fig.1.
The kinematic working principle is as follows: The $C_1(\delta)$ circle must provide full rotation precision motion of Dt around the vertical Dm axis (Z). However, because of the adjacent systems (source), the practical angular motion is set to (-10…+190), only. The $C_2(\gamma)$ circle is responsible for the upper part precision positioning motion of Dt around the horizontal axis (X) of Dm. It can be performed inside of 270° range angle. The $C_3(\theta)$ circle is related with sample positioning (Sp) which has to perform full rotations around the same Dm vertical axis. The $C_4(\omega)$ circle performs angular positioning motions around the horizontal axis (X) including all devices above it. This will be performed with a much more limited angle 6° (-1…+5). The $C_5(\chi)$ circle (not shown in Fig.1) will provide the rotation of S around a movable (C_3) horizontal axis (X). It is now included as Rx rotations in the newly designed device. The $C_6(\varphi)$ circle (not shown in Fig.1) will provide the rotation of S around a movable (C_3) second horizontal axis (Y) included as the second rotation (Ry) in a newly designed device, too. C_1 and C_2 are related with Da; C_3, C_5 and C_6 with Sp motions.
An overview of above basic motions (C_1,…,C_4) and related precision is given in Tab. 1.

TABLE 1. LabDm - Motion parameters (Circles)

Circles	Travel	Acc.	Res.	U
$C_1(\delta)$	±180	0.001	0.00025	°
$C_2(\gamma)$	±135			
$C_3(\theta)$	±180			
$C_4(\omega)$	-1 +5			

From structural point of view Dm is comprising several (sub)systems and modules.

Sp system
Sp system must spatially orient (3D) the sample and instruments (e.g., cryostat [10]) at the required physical angles with the highest precision, toward the incoming X-ray beam (X_i, i-incident). In addition, the sample must be translated along the main axis directions. The whole Sp system includes: a) first device for performing large rotation (C_3) and b) multi-axis positioning device (PD) performing small displacements (X,Y,Z,Rx,Ry, Rz) stacked one after the other. They are materialized by a high precision Gonio (G420 / X2W2) and a newly designed high precision PK device.

Dt arm

The diffracted beam (spots) from the irradiated sample must be gathered together and imaged by a Dt. In doing this, the Da system is built as a manipulator comprising two moving parts, connecting through orthogonal joints/rotations (C_1, C_2) materialized by high precision Gonio stages (G430/X2W1, G420/ X2W2) and a manually adjusting distance (±150 mm) stages. The Dt is a reliable, easy-to-use and robust 2D sensitive detector (PILATUS3 R 100K-A) [11] with 4.5 kg.

Inclination Module

As mentioned before, actual modern techniques (SAXRD, GISAS) for the characterization of various surfaces need a small rotation around the X axis (C_4). This is performed, for (Da) and (Sp) with high precision by a heavy load Gonio Segment (5202HL) device.

Ab

All systems and devices above must be supported by a stiff and reliable system, able to perform rough alignment motions (Z, X) regarding the X-ray beam position (Y). An Alignment base (Ab) was built (5103.D40) on a PK principles (1dof) which performs motion along Z axis (± 10 mm) and with additional linear guides on top, the whole Dm along the X axis ((± 50 mm). After the alignment operations, four feet are keeping the system fixed on the laboratory base.

The Dm is including also all the necessary electronics devices–drivers, controllers (SMC 9300) display and the Ethernet links to communicate with a PC, where a SPEC/C PLOT (Linux) software is running. The motorized components include safety stops and zero position points, as reference. Most of the general motions will be realized to be performed inside the required precision, by using special adjustment means (screws, eccentric pins, etc).

PARALLEL POSITIONING DEVICE(PPD)

Parallel mechanisms have been seen for relative long time as alternative to traditional serial ones. Especially, in some applications requiring reduced working space, but increased stiffness, speed and/or precision. They are already succeeded to prove their advantages through a plenty of different structures proposed in the literature. However, some of them from theoretical and not the applicative point of view. Most of them, related with positioning applications are based on HEXAPOD or DELTA.

The precision hexapods, e.g., [12] are already fund their place in synchrotron related positioning tasks, in particular, as for sample (and, instruments) manipulations. Several producers are currently available: PI, SYMETRIE, AEROTECH and NEWPORT. However, the necessity to pack all components (motors, screw, guides, and sensors) in each of the six (6) struts results in a complex structure with an increased height which cannot always be offered by the Dm designers [13]. Moreover, this is the case not only for the standard Diffractometers and the price should also be considered.

From the beginning of PKMs new solutions have been investigated as alternative to hexapods. Concentrating the actuation in fewer than six points was one of the first idea, e.g., [14]. Then, based on the new direct-drive (DD) technology (planar motors) several other proposals have been made, e.g., [15]. Detailed kinematic aspects (including the positional problems/IPP&DPP) has been studied in [16] and the first applicative device realized using XY stages [17]. A redundant mechanism has been introduced [18] as a machine tool device for the first time. Later on, more redundant mechanisms have been proposed in the specific literature. However, only few were proposed for the special application of positioning in an X-ray environment.

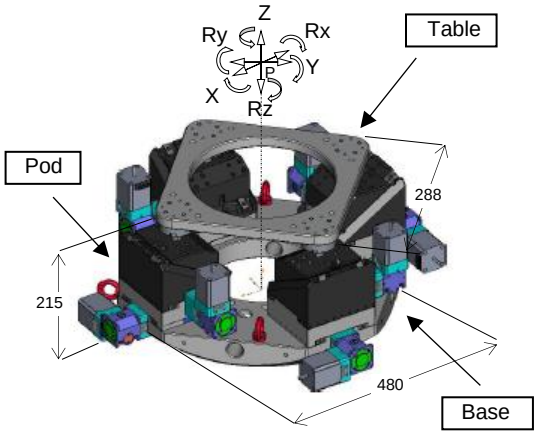

FIGURE 2. PPD

The proposed PPD, Fig. 2 is based on a new redundant parallel kinematic (Rd-PK) concept, called OCTOGLIDE [19]. The PPD has four (4) pillars, each with 2dof belonging to the QUADROPOD family. It offers several advantages such as simplicity(intuitive), decoupling and singularity free motions, all in a compact package with increased power. The first tests performed on a similar structure (prototype),

regarding the accuracy, including the straightness and flatness (required by the surface/interface investigations) has met the expectations [20].
Now, in the same modular design concept but with other commercially available components, the PPD device is powered by high precision XY actuation stages (5102/XE) but guided through high precision spherical rolling joints (SRJ016C/SP [21]). The device is expecting to provide stable and high precision motions of the table along and around the main axes (X,Y,Z, Rx,Ry,Rz) and in the related planes (XY, XZ, etc) by a closed loop control including stepping motors (VEXTA PKP245D [22]), custom gear boxes (2042.20) and linear encoders/scales (RESOLUTE [23]). An overview of the design concept (CAD) is given and the precision parameters are included in Tab.2. The carrying capacity (cryostat) is approx. 50 kg and the distance up to the center of rotation (P) 280 mm mounted through an adapter plate.

TABLE 2. PPD / Positioning parameters

Axis	Stroke(±)	Accuracy	Units
X, Y, Z	25, 25, 14	0,003	mm
Rx,Ry,Rz	5, 5, 6	0,003	°

CONCLUSIONS

A new high precision Dm will soon be manufactured. A specific PPD has been developed to work inside. Based on a redundant parallel kinematic principle (Rd-PK), the design concept was based on precision XY stages as actuators. It is expected to deliver high precision motion in positioning the sample along (and, around) any investigative axis and related planes being a powerful device in a compact package, as an alternative to the actual existent (serial or parallel) devices. Through small modifications, it can be used in other applications, e.g. extreme conditions (vacuum, etc.). Future work will include the working tests and adaptation to extreme conditions.

REFERENCES

[1] Lamberti C., Agostini G., Characterization of Semiconductor Heterostructures and Nanostructures, Elsevier, ISBN: 978-0-444-59551-5, 2 ed., 2013.
[2] Meyerheim L. H, X-ray Diffraction as a Tool to Study Nanostructures, Tutorial, MPRS/ STNS, 21.1.2018.
[3] HUBER Diffraction and Positioning GmbH & Co.KG, www. xhuber.com, 2019.
[4] Collaborative research Center-Functionality of Oxide Interfaces, SFB 762, http:// www. physik.uni-halle.de/sfb762, 2019
[5] Max Planck Institute für Microstructure Physics (MPG/MSP), https://www.mpi-halle. mpg.de/startseite, Aug. 2019.
[6] Merlet J-P., Parallel Robots, ISBN-9781402 041322, Springer, Netherlands, ed. 2, 2006.
[7] D8 Advance, Powder diffraction, Technical Sheet, BRUCKER, 2019.
[8] MetalJet Technology-A brief introduction, EXILLUM, 2019.
[9] HELIOS Optics for METALJET, Technical sheet, INCOATEC, 2019.
[10] Cryostats Systems, CryoVac, http://www. cryovac .de/, 2019.
[11] PILATUS3 R, Technical Specifications and Operating Procedure, V5, DECTRIS, 2016.
[12] Hexapods, Physik Instrumente GmbH(PI), BRO 14D, 2012.
[13] Olea, G., “Precision Hexapod-Preliminary CAD (A work for micro)”, Proc. of EUSPEN 2010, 2: 379-382.
[14] Tahmasebi F. Kinematic Synthesis and Analysis of a Novel Class of Six-DOF Parallel Minimanipulators, ISR 93-1, NSFERC, 1993.
[15] Ben-Horin R and Shoham M. Six-Degrees-of-Freedom Parallel Manipulator with Three Planarly Actuated Links, IEEE/IROS’97, Vol.3, Grenoble, France, 1997.
[16] Olea G. Contributions to the Kinematics, Dynamics and CAD of “A” type Spatial Parallel Mechanisms in Three Points Guided, Ph.D., TU Cluj, Romania, 1998.
[17] Olea G. et al., “Spatial Parallel Mechanism with 2DOF L-L Actuators”, Proc. of ISR 2001, Seoul, Korea, 1129-1134.
[18] Kim J. et al. A New Parallel Mechanism Machine Tool, CIRP Annals, Vol. 48. 337-340,1999.
[19] Olea G. et al. OCTOGLIDE- Table Positioning Device for Diffraction Application, Proc. Of MEDSI2016, Barcelona, Spain, 38-40.
[20] Olea, G. et al. Accuracy of positioning for a table device, Proc. of EUSPEN 2018, Venice, Italy,237-238.
[21] Spherical Rolling Joint, Technical Sheet, HEPHAIST Seiko, Japan, 2019.
[22] General Catalog, ORIENTALMOTOR, 2018/2019.
[23] RESOLUTE absolute optical encoder with BiSS, Data sheet, RENISHAW, 07.2012.

Research on the Modeling of Burr Formation Process in Micro-flat Milling Operation on Ti-6Al-4V

Ni CHEN, Yang WU, Zhenjun LI, Liang LI, Ning HE
National Key Laboratory of Science and Technology on Helicopter Transmission, Nanjing University of Aeronautics and Astronautics, Nanjing 210016, PR China

INTRODUCTION

With the development of aerospace, national defense industry, modern medicine and bioengineering technology, the demands of high accuracy micro-parts and micro-scale features are increasing in nowadays. Micro-milling is widely used in the fabrication of microstructures due to the high material removal rate and a wide range of machinable materials [1]. However, its development has been limited by some factors, the most important of which is burr formation, burr deteriorates the surface quality, increases the surface roughness, and is extremely difficult to remove, so burr minimization and control techniques are becoming the focus of current research.

In order to overcome this problem, many experimental and simulation studies have been conducted by researchers at home and abroad. Gillespie and Blotter [2] studied the mechanisms causing machining burrs and presented four analytical models that predict burr properties, and they indicated that lateral deformation, chip rollover, and material tearing are the three basic mechanisms. Saptaji et al. [3] studied the effect of side edge angle and taper tool angle on the top burrs in micro-milling by detecting the top burr formation of aluminum alloy Al-6061 in micro-milling, they concluded that the interaction of the increasing side edge angle and taper angle leads to the reduction of buss size. The chip formation in micro-end milling of aluminum alloy was investigated by Wang et al. [4] through a 2 dimensional FE simulation method. In this study, the chip velocity, strain rate, contact pressure, cutting force and chip flow can be predicted by the FE simulation. Thepsonthi and Ozel [5, 6] investigated the top burr formation of Ti-alloy Ti-6Al-4V in micro-milling using the process modeling and optimization methods. They found that the integrated toolpath strategy, axial depth of cut and feed rate are the major process parameters which affect the top burr formation and surface roughness. In this paper, 3-dimensional micro-flat end milling with double helix edges operation FEM models on Ti-6Al-4V have been established to obtain a better investigation and understanding of burr formation process. And the formation process of four types of burrs have been explained combined with the simulation results. At last, the effect of cutting parameters on burr size is analyzed by the simulation models.

ESTABLISHMENT OF FEM MODELS AND VALIDATION OF EXPERIMENTS

For better research and understanding of the different buff formation process and effects of cutting parameters on burr size, 3-dimensional FEM models have been constructed. The remainder of this section will give an introduction about several important steps of this establishment.

In this study, the finite element simulation of full slotting micro-milling was carried out on a titanium base alloy, Ti-6Al-4V. And J-C constitutive model, a semi-empirical constitutive model proposed by Johnson and Cook [7] in 1983, was employed in this study to decently describe the mechanical behavior of Ti-6Al-4V. According to this model, the J-C constitutive equation was defined as follows:

$$\sigma_{JC}=[A+B\varepsilon^{n}][1+C\ln\left(\frac{\dot{\varepsilon}}{\dot{\varepsilon}_0}\right)][1-\left(\frac{T-T_r}{T_{melt}-T_r}\right)^{m}] \qquad (1)$$

A set of model parameters which are dependent on workpiece material in this model were determined empirically, and these material constants were also utilized in Umbrello's FEM model [8], in which good predictions of cutting force and chip morphologies were achieved.

The constant shear hypothesis is utilized in this paper to construct the shear friction model. According to that hypothesis, the friction factor for tool and workpiece is assumed to be 0.7, and 0.1 is considered as the friction factor for chip and workpiece. A micro-flat end milling with double helix edges is employed in this

simulation model, of which diameter is 0.1 mm and edge radius is 1 μm.

In order to verify the veracity of FEM models, micro-slot milling experiments of Ti-6Al-4V have been operated on the self-developed three-axis miniatured machine, and the cutting tool employed is a double-edged micro-flat end mill with a 0.2 mm diameter. The morphology of micro slot, machined surface, and burr formation are observed utilizing the scanning electron microscopy (SEM, S4800, Hitachi).

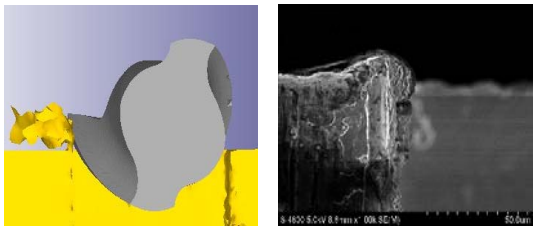

(a) Exit burr (simulation) *(b) Exit burr*

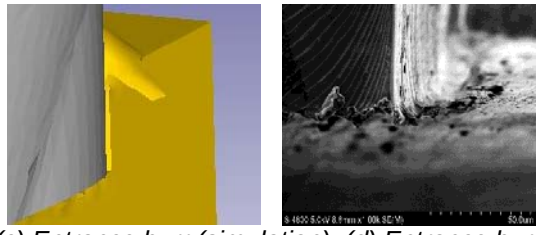

(c) Entrance burr (simulation) (d) Entrance burr

FIGURE 1. Burr morphologies obtained by simulation and experiment.

The results of simulations and experiments are shown in Fig.1. Obviously, the burr morphologies and location are similar in experiments and simulations, the exit burr morphology obtained by experiments and simulations , as shown in Fig.1 (a) and (b), are coincided well. And the entrance burr morphology acquired from the experiments agrees well with that of simulations. Therefore, the finite element models have been preliminary verified.

BURR FORMATION PROCESS

In general, entrance burr occurs at the entrance of a slot. Fig.2 shows the formation process of entrance burr. At the beginning of the cutting operation, the workpiece material is cut off by the cutter due to the tool rotation around the axis, so chips are formed. During the process of feeding and rotation of tool, part of the chips separate from the workpiece, however, the remainder of chips adheres to the surface of cutting edge and rotates with the tool together. When a tool rotation movement ends and the cutting edge cut out from the workpiece, this part of chips are extruded by the tool flank face to stick to the down milling side of the workpiece instead of separation owing to the insufficient tool-chip interaction. Therefore, the entrance burr is generated at the entrance of the micro slot.

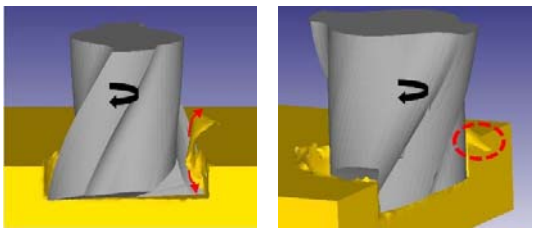

(a) Chip separation *(b) Final entrance burr*

FIGURE 2. Formation process of entrance burr.

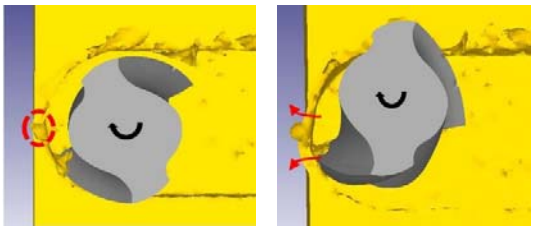

(a) The thin uncut material (b) Squeezing of the material

(c) Thin material deformation (d) Final exit burr

FIGURE 3. Formation process of exit burr.

The exit burr is essentially a chip which is bent rather than sheared resulting in a comparatively large burr. It's usually significant and is one of the most visible burrs. The uncut workpiece material becomes very thin when the tool continues to move close to the end edge of the micro slot, this fraction of material tends to deform easily and even to be squeezed out from the slot as a result of the tool feeding motion, as shown in Fig.3. Because of the squeezing and deformation, what to be cut by the tool is that deformed materials which lead to more difficult guarantees of sufficient tool-workpiece interaction, therefore, these materials fail to be

cut down by the tool thus lead to the failure of chip separation, and this part of materials stick to the exit of the micro slot resulting in the generation of the exit burr.

According to the simulation, burrs also generate at the slot base especially at the down milling side of the slot base. This slot base burr will reduce the surface quality and increase the surface roughness. Fig.4 shows its formation process, according to the simulation, the material which are cut off by the tool forms chip, and chip separates from the workpiece as a result of tearing against the cutting edge of the tool forms chip, and chip separates from the workpiece as a result of tearing against the cutting edge of the tool rather than shearing. Unfortunately, not all of the chips can be pushed out from the workpiece, a small portion of the chip stick to the rake face of the cutter, and roll down to the slot base as the movement of the tool. These chip moves with the cutter and leads to a rougher surface and formation of slot base burr due to the extrusion of the tool bottom face. This sort of burrs are small but massive in amount, like a group of pits, most of them are located on the reverse milling side, as shown in Fig.4

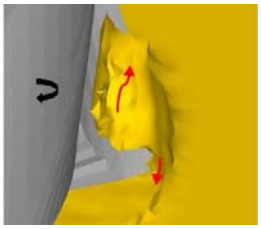

(a) Chip separation

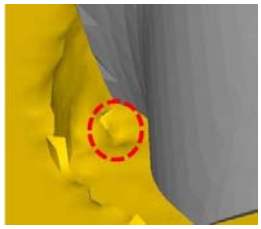

(b) Pits

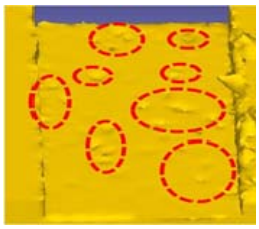

(c) Final slot base burr

FIGURE 4. Formation process of slot base burr.

Top burr is also one of the most significant burrs and can be usually observed at the top of the slot especially the top of the down milling side of the slot. The formation process of the top burr can be attributed to the interaction of several causes depending on the simulation results. First of all, the chip which were previously formed flows upwards along the rake face of the cutter, it tends to curl and overturn because of the rotation of the tool, and it will tear along the cutting edge when it's under the large enough tensile stress, however, not all of the chip is pushed out from the workpiece by the extrusion of the flank face, the connecting material between the workpiece and chip stays on the top of the slot instead of being taken away. Then, this part of material is pushed outwards to form the initial top burr by the tool cutting edge during the following tool rotation. What's more, the above action such as the chip's curl and overturn, the chip separation and the pushing outwards of the connecting material continue over and over again as the movement of the cutter tool, the initial top burr accumulates to form into the final top burr.

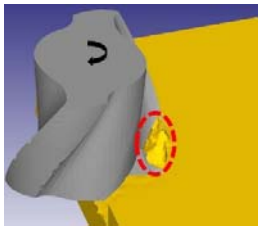

(a) Chip formation

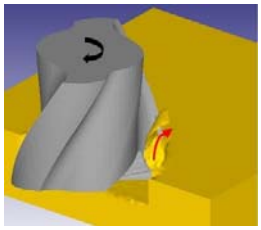

(b) Chip curl

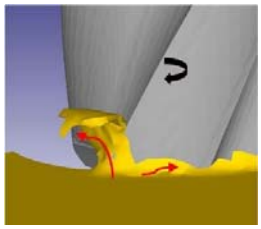

(c) Chip separation

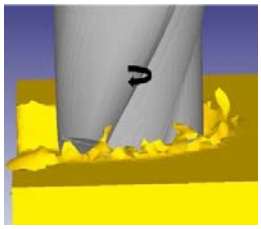

(d) Final top burr

FIGURE 5. Formation process of top burr.

EFFECTS OF CUTTING PARAMETERS ON BURR SIZE

In this section, several single factor simulation models have been established to study the effects of cutting parameters on entrance and exit burr size, Fig.6 through Fig.8 show the effects of different cutting parameters on the length and width of the entrance and exit burr. As shown in Fig.6, Fig.7 and Fig.8, the burr length varies obviously with the change of cutting parameters ,but the burr width do not alter significantly by the cutting parameters. As shown in Fig.6, the effects of depth of cut on entrance and exit burr size have been studied by several FEM models in which a_p varies from 0.5 to 2.0 μm, while the other cutting parameters (f_r ,2 mm/sec; *n*, 30000 r/min), and the cutting

tool keeps the exactly same. the burr length increases with the increasing of the depth of cut, and it increases slowly when a_p is less than 10 μm, with the $a_p$continues to increase, the length of burr increases sharply. However , the width of burr is almost same in the value of a_p; Fig.7 shows the effects of feed on burr size, several models with feed rate ranging from 0.5 to 2 mm/sec and sharing the same cutting parameters (a_p, 20 μm; *n*, 30000 r/min) and cutting tools are established, the burr length decreases with the increasing of feed rate, it decreases drastically when f_r is less than 1 mm/sec, with the $f_r$continues to increase, the length of burr decreases slowly. The same thing is that the width of burr almost keeps unchanged and is nearly independent on the feed rate. And the effects of spindle speed on burr size can be seen from the Fig.8, several models with spindle speed ranging from 10,000 to 40,000 rpm and sharing the same cutting parameters (a_p, 20 μm; f_r, 2 mm/sec) and cutting tools are established. its influence is almost same with that of feed rate, the length of burr decreases sharply when spindle speed is less than 20000 r/min, and it decreases slowly when spindle speed continues to increase.

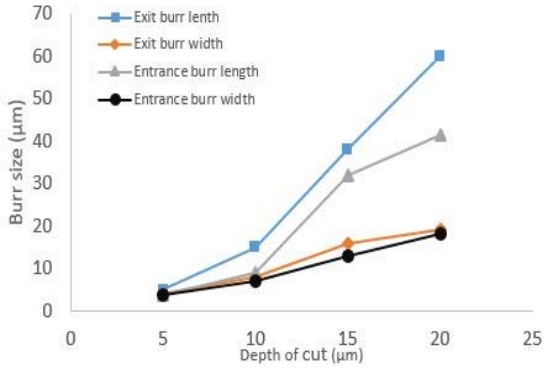

FIGURE 6. Burr size with respect to different a_p.

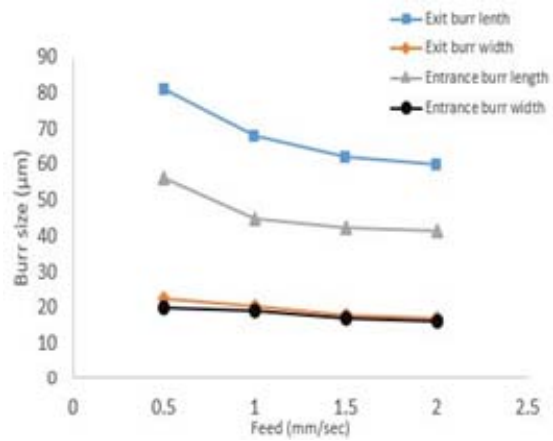

FIGURE 7. Burr size with respect to different f_r.

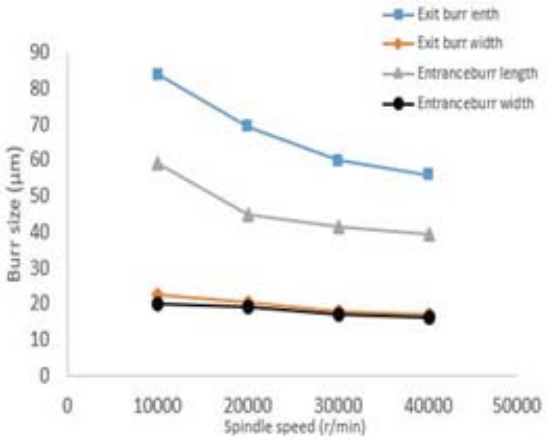

FIGURE 8. Burr size with respect to different n.

SUMMARY

(1) In micro-flat end milling simulation on Ti-6Al-4V, four types of burrs have been detected, they are entrance burr, exit burr, top burr and slot base burr separately. Both of the entrance and exit burr formation process and cause can be attributed to the insufficient engagement of tool and workpiece. The slot base burr is formed because of the extrusion of tool bottom face to the material which comes from the chip separation process and rolls down to the slot base. As for top burr, the interaction of chip separation, chip curl and squeezing of flank face becomes the reason of its formation.

(2) The effects of cutting parameters on entrance and exit burr size are investigated by micro-flat milling simulation, according to the simulation results, a_p is the critical factor effecting the size of entrance and exit burr. The burr length increases sharply when a_p is more than 10 μm and continues to increase. What's

more, the burr width is almost same with the value of a_p and is nearly independent on the other cutting parameters.
(3) The exit burrs are significant bigger than the entrance burrs, and the change of exit burrs with the cutting parameters is more obvious than entrance burr.

ACKNOWLEDGEMENTS
This work is supported by the NSF of Jiangsu Province (No. BK20180435), NSFC of China (No. 51905270)

REFERENCES
[1] Schueler, G. M et al., "Burr formation and surface characteristics in micro-end milling of titanium alloys." *Burrs-analysis, control and removal*. Springer, Berlin, Heidelberg, 2010. 129-138.
[2] Gillespie, La K et al., "The formation and properties of machining burrs." *Journal of Engineering for Industry* 98.1 (1976): 66-74.
[3] Saptaji et al., "Effect of side edge angle and effective rake angle on top burrs in micro-milling." *Precision Engineering*36.3 (2012): 444-450.
[4] Wang et al., "Chip formation analysis in micromilling operation." *The International Journal of Advanced Manufacturing Technology* 45.5-6 (2009): 430.
[5] Thepsonthi et al., "Multi-objective process optimization for micro-end milling of Ti-6Al-4V titanium alloy." *The International Journal of Advanced Manufacturing Technology* 63.9-12 (2012): 903-914.
[6] Tuğrul Özel et al., "An integrated toolpath and process parameter optimization for high-performance micro-milling process of Ti–6Al–4V titanium alloy." *The International Journal of Advanced Manufacturing Technology* 75.1-4 (2014): 57-75.
[7] Johnson, G. R "A constitutive model and data for materials subjected to large strains, high strain rates, and high temperatures." *Proc. 7th Inf. Sympo. Ballistics* (1983): 541-547.
[8] Umbrello et al., "Finite element simulation of conventional and high speed machining of Ti6Al4V alloy." *Journal of materials processing technology* 196.1-3 (2008): 79-87.

Pressure-fed Mechanisms for Nanopositioning Stage Applications

Jaemin Han[1], Gyu Ha Kim[2], Herminso Villarraga-Gómez[3], and Chabum Lee[1]
[1]J. Mike Walker '66 Department of Mechanical Engineering
Texas A & M University
College Station, Texas, USA
[2]TRI-N Co. Ltd,
Daegu, South Korea
[3]Nikon Metrology, Inc.
Brighton, MI, USA

INSTRODUCTION

The basic principles of compliant mechanisms have been known for a few decades, and the design methods and fabrication methods that could be found in the literature have been well documented in the textbooks[1-3]. This development has been driven by the increasing need for nanometer motion accuracies and the efforts achieving high precision in many industrial sectors such as semiconductor industry, precision machine tool industry, precision manufacturing industry, and so on.

Most of the nanopositioning systems adopt some compliant mechanisms and are used in high precision instruments because they can provide nanometer-scale displacement with a total motion range of at least tens of microns. When the actuation force acts on the mechanism, the bearing structures are deformed to produce the desired displacement. In general, compliant mechanisms are monolithically-manufactured and therefore avoid assembly errors. The monolithic construction also implies a relatively easy manufacturing process and a potentially very compact design. The electric discharge machining[4] (accuracy ~2.5 μm), waterjet machining[5] (accuracy ~ 25 μm), micromilling[6] (accuracy ~2 μm) and polymeric/metallic additive manufacturing[7-12] (accuracy 50~200 μm) are the most common manufacturing methods for compliant mechanisms. However, their part accuracy or manufacturing tolerance (width, height, total length, sometimes roughness) realistically increase in most cases due to complex geometry such as hinges and machining compliance issues[13,14] in case of machining the thin slabs. In the case of compliant mechanisms that are typically designed bilateral symmetric, such part accuracy error challenges stiffness or damping design of bilateral symmetric spring structures because it results in motion error and change in the natural frequency of the system. Because the compliant mechanisms are commonly used in the mechanical systems requiring high precision and accuracy such as atomic force microscopy or fast tool servos, such manufacturing error is not acceptable. In addition to the manufacturing tolerance, in many cases, those part accuracy errors can be combined with actuator-compliant mechanism alignment errors or contact errors[15,16], and ultimately it can badly affect positioning performance. For example, the stiffness k of a rectangular cross-section cantilever[16] can be expressed as its geometric parameters $k = (¼)(bh^3/L^3)(E)$. It can be seen from the expression that k is linearly proportional to the base width b and Young's modulus E, and it strongly depends on the third power of the ratio (height/length) or (h/L). Therefore, in designing a flexure, one can grossly "tune" the stiffness by varying the ratio (h/L), or one can "fine tune" the stiffness by varying the base width b. However, it is only valid if there is no manufacturing error. Because the part machining accuracy error may occur 3-dimensionally within the manufacturing tolerance ranges, the variation of the part stiffness is unavoidable.

Many studies for identifying such errors and measuring those effects (e.g., motion error, cross-talk error, positioning accuracy, and resolution error)[2,9,10] have been reported, but those error compensation methods were not well introduced. Most of the studies were stiffness model-based[17,18]. Because those approaches require to update or correct the model according to the input changes or environmental conditions, it cannot be an ultimate solution. Therefore, there is no method to physically correct those errors, providing the convenience of tuning the dynamic parameters of the compliant mechanisms.

In this study, to compensate for such errors, the pressure-fed mechanism through the hollow-type

spring structures was newly proposed. The monolithic compliant mechanisms made of Stainless Steel was fabricated by the metal 3D printing process, and the internal fluidic channels inside of spring structures were designed to apply pneumatic pressure to each channel. The pressure-fed mechanism can correct or compensate for motion error of the compliant mechanism by pneumatically pressurizing the internal channels. Here, by controlling the pneumatic pressure level and flow direction inside of the internal fluidic channels, the linear motion, yaw motion, stiffness, damping, natural frequency, and positioning precision of the compliant mechanism are discussed.

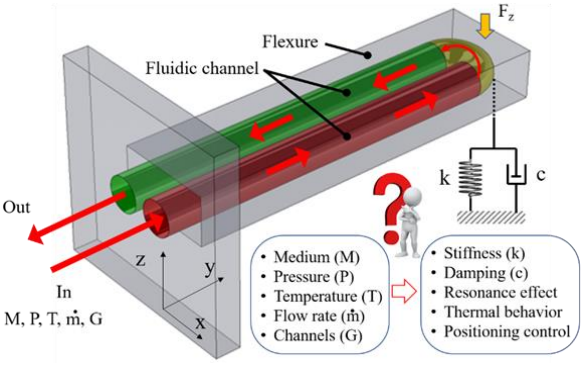

FIGURE 1: A concept of pressure-fed flexure mechanism

In this study, the flexure mechanisms with internal fluidic channels as illustrated in Figure 1 will be fabricated using additive manufacturing (AM) technology to make use of the mechanical design flexibility that can effectively control the material distribution in terms of stiffness, damping and heat spreading of the flexures. By investigating the relationship between the independent variables (medium, pressure, temperature, flow rate, channel configuration) and the dependent variables (stiffness, damping, resonance effect, thermal behavior and positioning control) theoretically and empirically, this study presents about (1) additive manufacturing-based mechanical system design, (2) pressure-fed control approach for solving nonlinear dynamic systems and (3) thermal coupled dynamic modeling of pressure-fed motion systems. As a preliminary study, in this paper, the pressure-fed mechanisms with various fluidic channel geometries were tested under various pressure conditions.

METHOD

Dynamic characteristics of compliant mechanisms are highly dependent on material constitutive properties, geometric compatibility, or force equilibrium conditions. Unlike conventional manufacturing methods such as electric discharge machining, waterjet machining, and micro milling, an additive manufacturing technology that makes use of mechanical design flexibility can effectively control the material distribution (channel size, shape, and placement) in terms of stiffness, damping, and natural frequency. Also, additive manufacturing methods can fundamentally change the current design principles to improve their own performance such as accuracy, precision, repeatability, or removing motion error at a low-cost.

In this study, as shown in Figure 2a, the internal fluidic channels in the spring structures of the compliant mechanism were designed to give the compressed air pressure difference across the internal fluidic channels. The pressure distribution can be monitored from four pressure gauges installed in inlets and outlets. As discussed in Section 1, the stiffness ($k_{X,L}$, $k_{X,R}$) and damping ($c_{X,L}$, $c_{X,R}$) may be different due to additive manufacturing tolerance as seen in

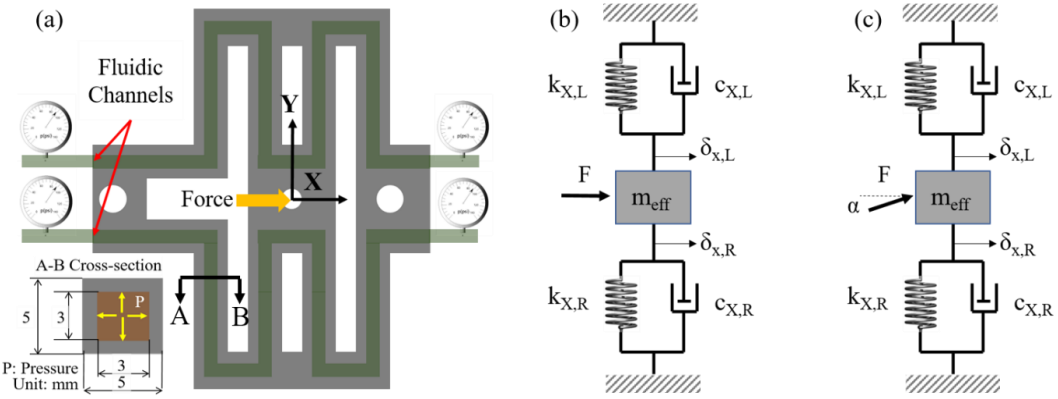

FIGURE 2: Operating principle of the proposed pressure-fed mechanism: (a) schematic description, (b) dynamic model and (c) dynamic model when the force is not applied along the principal direction.

Figure 2b, and the displacement $\delta_{X,L}$ and $\delta_{X,R}$ may be different when the force (F) is applied to the shuttle, which will cause yaw error depending on the two displacement amplitudes. In addition to the stiffness mismatching, the force (F) applied to the shuttle part may not be aligned with the principal direction of the compliant mechanism as seen in Figure 2c. Because the bilateral spring structures are monolithically connected that there are force-displacement interactions between each spring structure, it is difficult to estimate or even measure the dynamic parameters (stiffness and damping) independently. It could be rather convenient or preferred to measure the motion error of compliant mechanisms. The proposed pressure-fed mechanism can independently control bilateral spring structures, and the pressure difference can be in-situ adjusted depending on the linear motion results to make this displacement $\delta_{X,L}$ equal to and the displacement $\delta_{X,R}$. In addition, it can play a role to assist the actuator to push and pull the shuttle.

CHARACTERIZATION

Because the proposed compliant mechanism was additively manufactured (metal power bed), the additive manufacturing Stainless Steel material, here denoted as AM SS, was characterized and compared with the baseline comparison of bulky SS material properties. Three comparison tests were conducted in this study.

The void analysis of two samples above was performed by industrial CT scan that can detect internal features and flaws such as porosity, inclusion or crack displaying this information in 3-dimension. As seen in Figure 3, the void size of the bulky SS sample was uniform approximately 3,000 μm^3, on the other hand, the void size of the AM SS sample was irregularly distributed up to 120,000 μm^3 around the peak count at the volume 15,000 μm^3. It is because the AM SS sample was layer-by-layer printed that there must exist air voids between metal powers. As a result of the void sizes and their distribution of the AM SS sample, it is, however, difficult to draw a conclusion that the additive manufacturing materials and the fabricated parts are not applicable to compliant mechanisms. Although the AM SS material is not homogeneous as good as that of the bulky SS part, it could be attractive to the designers of the compliant mechanisms if it meets its requirements in dynamic aspects.

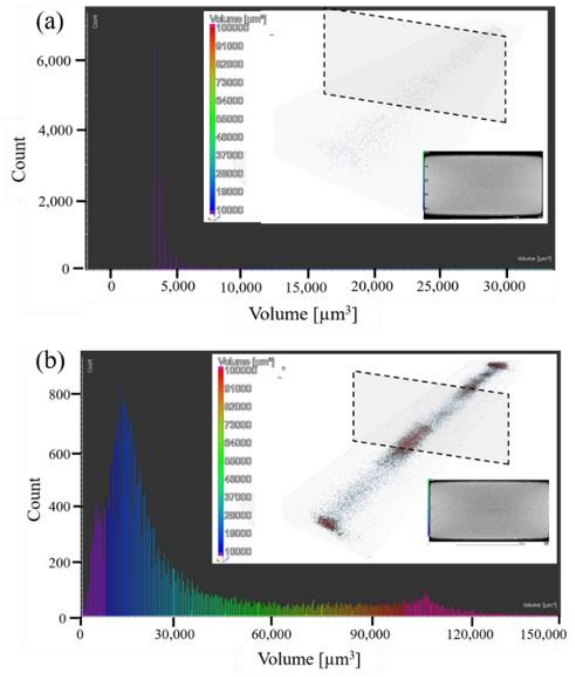

FIGURE 3: Void analysis results of (a) bulky SS and (b) AM SS samples by industrial CT scan.

EXPERIMENTS

The double compound-type compliant mechanism, the so-called nanopositioning stage, was designed with the spring structures (width 5 mm, height 5 mm, length 40 mm) and the internal fluidic channels with the cross-sectional area (3 mm by 3 mm) were created to apply for the pressure (P) distribution along the channels, and then, it was metal 3D printed as seen in Figure 4. The pneumatic lines were connected to the fluidic channels, the pressure gauges were installed in each pneumatic line, and two capacitive sensors (CS) were placed near the measurement target installed on the shuttle. Here two CS placed in the left and right sides were denoted as L_CS and R_CS. The stack-type piezoelectric (PZT) actuator was inserted between the shuttle and ground parts, and was controlled by a PZT driver. From the test run results, two CS showed identical responses to the PZT input voltages under the ambient condition, and the displacement increased as the PZT input voltage increased as shown in Figure 5. In this test, the DC 30V was given to the PZT actuator as an offset voltage.

RESULTS

The PZT actuator was again installed between the shuttle and the ground parts. The binary pulses were applied to the PZT actuator to obtain the step responses of the nanopositioning stage

under the pressure condition and pressure-fed direction while measuring the displacement with two CS. Similar to the previous experiment, two CS were installed to produce the identical displacement information of the nanopositioning stage at the ambient condition (0, 0). This initial condition was set to the reference for the relative comparison of the nanopositioning stage behavior between the ambient condition and pressure-fed conditions. As seen in Figure 6, four difference pressure-fed conditions, (0, 0), (F, 0), (0, F) and (F, F), were tested while moving the stage approximately 40 nm range. The results of (F, 0) and (0, F) conditions showed a similar trend but the displacement directional information. In Figure 6b, the right and left sides of the spring structures moved approximately 50 nm and 30 nm in a negative X direction under the condition (F, 0), on the other hand, the right and left spring structures under the condition (0, F) moved opposite to the case of condition (F, 0) as exact as it was moved. Also, at the condition (F, F) showed, the stage moved approximately 80 nm toward the PZT actuator, and there was no difference in two CS outputs.

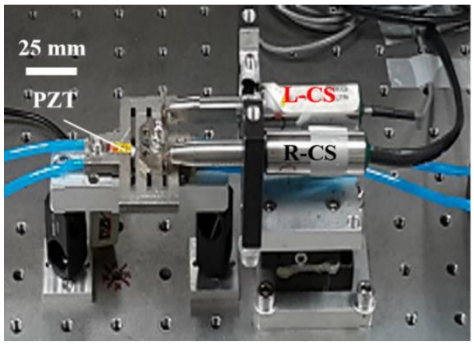

FIGURE 4: Experimental setup.

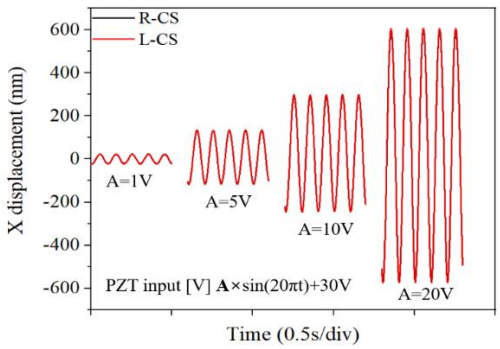

FIGURE 5: Displacement measurement results according to PZT input voltages.

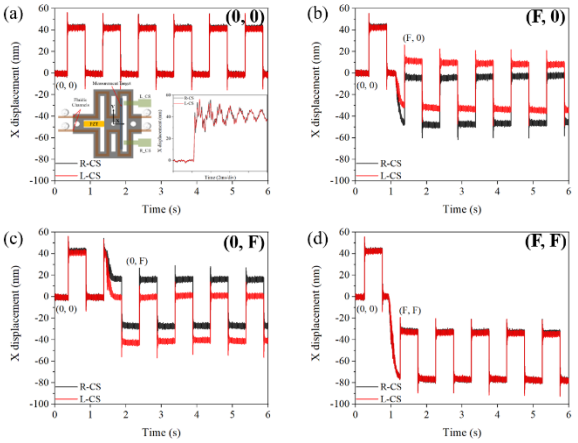

FIGURE 6. Linear displacement results of the step responses according to the pressure-fed conditions.

More interestingly, the angular displacement of the step responses under the pressure-fed conditions was calculated by dividing the difference of two CS outputs (Figure 6) with the distance of two CS. As seen in Figure 7, yaw motion could be bi-directionally controlled approximately up to 0.8 µrad according to the pressure condition and pressure-fed direction. The signal spikes were considered due to the slight difference in two CS sensitivity.

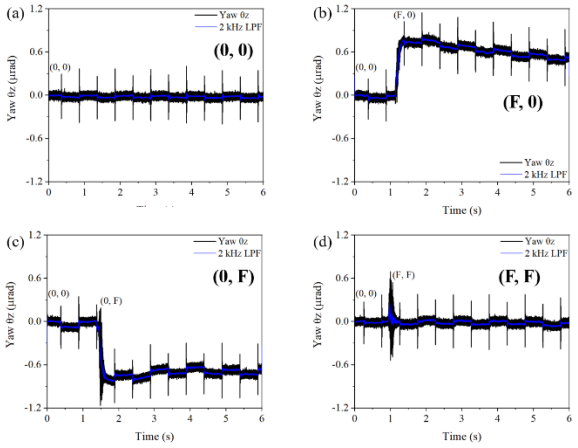

FIGURE 7. Angular displacement results of the step responses according to the pressure-fed conditions.

CONCLUSIONS

The pressure-fed mechanism was experimentally validated with the double compound compliant nanopositioning stag and could be achieved by bi-directionally and independently pressuring the internal fluidic channels of the spring structures.

It showed that the pressure-fed mechanism enables not only to compensate for motion errors of the compliant mechanisms but also to in-situ tune their dynamic behaviors compatible with their applications. According to the shapes and arrangement of the internal fluidic channels, fluid types (air, water, oil, mixed fluids), and pressure conditions, the effectiveness of the pressure-fed mechanism can be maximized. Also, the further development of additive manufacturing processes and materials will accelerate the fundamental approaches to the pressure-fed mechanisms for various dynamic motion systems. For the future work, the pressure-fed mechanism will be tested in the feedback positioning-controlled conditions and at the elevated temperature conditions to test if this mechanism can effectively compensate for thermal effects.

ACKNOWLEDGEMENT

This work was supported by the Texas A&M University and partially the Technology Innovation Program (20000748, Development of 1,000mm/s class laser dicing machine for ultra-thin silicon wafers less than 50 ㎛ using low thermal expansion ceramics) funded By the Ministry of Trade, Industry & Energy(MOTIE, Korea)

REFERENCES

[1] L. Howell, Compliant mechanisms, John Wiley & Sons Inc, 2001.

[2] S. T. Smith, Flexures, Gordon and Breach Science Publishers, ISBN 90-5699-261-9, 2000.

[3] S. Henein, Conception des guidages flexibles, Presses Polytechniques et Universitaires Romandes, ISBN 2-88074-481-4, 2001.

[4] Understanding the wire EDM process, obtained June 24, 2019 from http://www.reliableedm.com/Complete%20EDM%20Handbook/Complete%20EDM%20Handbook_5.pdf

[5] Waterjet machining tolerance, obtained June 24, 2019 from https://waterjets.org/archive/getting-the-most/tips/waterjet-machining-tolerances/.

[6] David J. Guckenberger, Theodorus E. de Groot, Alwin M. D. Wan, David J. Beebe, and Edmond W. K. Young, Micromilling: A method for ultra-rapid prototyping of plastic microfluidic devices, Lab Chip, Vol. 15, No. 11, pp. 2364-2378 (2015).

[7] M. Aliakbari, Additive Manufacturing: State-of-the-Art, Capabilities, and Sample Applications with Cost Analysis, Master of Science Thesis, Department of Industrial Production, KTH, June 2012.

[8] Valmik Bhavar, Prakash Kattire, Vinaykumar Bapuso Patil, S. M. Khot, Kiran Gujar, Rajkumar Raju Singh, A review on power bed fusion technology of metal additive manufacturing, Additive Manufacturing Handbook DOI:10.1201/9781315119105-15 (2017).

[9] Herminso Villarraga Gomez, ChaBum Lee, and Stuart T. Smith, Dimensional metrology with X-ray CT: a comparison with CMM measurements on internal features and compliant structures, Precision Engineering, 51, pp. 291-307 (2018).

[10] ChaBum Lee, Christopher K. Stepanick, Sun-Kyu Lee, and Joshua A. Tarbutton, Cross-coupling effect of large range XY nanopositioning stage fabricated by stereolithography process, Precision Engineering, Vol. 46, pp. 81-87 (2016).

[11] ChaBum Lee, Sun-Kyu Lee and Joshua A Tarbutton, Positioning control effectiveness of optical knife edge displacement sensor-embedded monolithic precision stage, Sens. Actuators A. Vol. 233, pp. 390-396 (2015).

[12] ChaBum Lee and Joshua A Tarbutton, Compliance and control characteristics of an additive manufactured-flexure stage, Rev. Sci. Instrum. 86(4) 045107 (2015).

[13] Nuodi Huang, Chunhui Yin, Liang Liang, Jicai Hu, Shijing Wu, Error compensation for machining of large thin-walled part with sculptured surface based on on-machine measurement, The International Journal of Advanced Manufacturing Technology, Vol. 96, Iss. 9-12, pp. 4345-4352 (2018).

[14] Kolluru K, Axinte D, Becker A, A solution for minimizing vibrations in milling of thin walled casings by applying dampers to workpiece surface. CIRP Ann-Manuf Technol., Vo. 62, No. 1, pp. 415–418 (2013).

[15] Thomas R Hicks and Paul D Atherton, The nanopositioning book, Queensgate Instruments Ltd. 1997.

[16] Herman Soemers, Design principles for precision mechanisms, Enschede, the Netherlands: T-Point Print VoF 2010.

[17] R. Brent Gillespie, Taeyoung Shin. Felix Huang, Brian Trease, Automated Characterization and Compensation for a Compliant Mechanism Haptic Device, IEEE/ASME Transactions on Mechatronics, Vol. 13, Iss. 1, pp. 136-146 (2008).

[18] Margaret Koehler, Allison M. Okamura, Christian Duriez, Stiffness control of deformable robots using finite element modeling, Robotics and Automation Letters IEEE, Vol. 4, No. 2, pp. 469-476 (2019).

MODELING THE DYNAMIC STIFFNESS OF AN AIR BEARING SPINDLE USING FREQUENCY RESPONSE FUNCTIONS

Byron Knapp, Dave Arneson, and Dan Oss
Professional Instruments Company
Hopkins, Minnesota, USA

ABSTRACT

The most demanding machine tool and metrology applications require system models of critical components. Accurate modeling of air bearing spindles for these applications is complicated by the nonlinear behavior of the air films. In this work, a simple model of static and dynamic stiffness is proposed. This approach is justified by experimental determination of the natural frequencies and mode shapes at a variety of inlet pressures. The results show for step-compensated fully preloaded spindle that dynamic tilt stiffness is 30% higher than static while dynamic axial stiffness is 80% higher than static. This proportionate increase in stiffness remains constant at inlet pressures ranging from 0.4 MPa to 0.7 MPa.

BACKGROUND

The air bearing spindle used in this work is shown in Figure 1. It features opposed thrust plates with a stiff shaft connecting them as shown in Figure 2. This spindle exhibits stable operation without pneumatic hammer at pressures above 1.2 MPa (175 PSI). The axial and tilt stiffness of the spindle are provided by the thrust bearings.

FIGURE 1. The Model 4R Blockhead air bearing spindle used in this work.

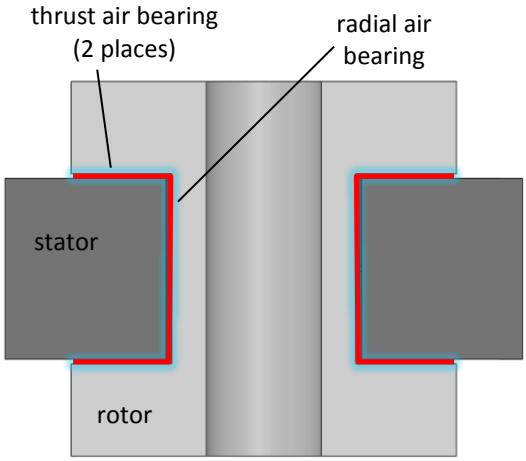

FIGURE 2. Cross-section showing the construction of the 4R Blockhead air bearing.

The thrust bearings are step-compensated with a pressure profile as shown in Figure 3 where P_1 is the recess pressure at $r_1 = 27$ mm, $P_2 = 0.7\ P_1$ is the pressure at the beginning of the step $r_2 = 51$ mm, and the pressure drops to atmosphere P_{atm} at the end of the step $r_3 = 53$ mm. The film thickness at the step is $h_{step} = 5$ µm while the film thickness in the recess is $h_{recess} = 10$ µm.

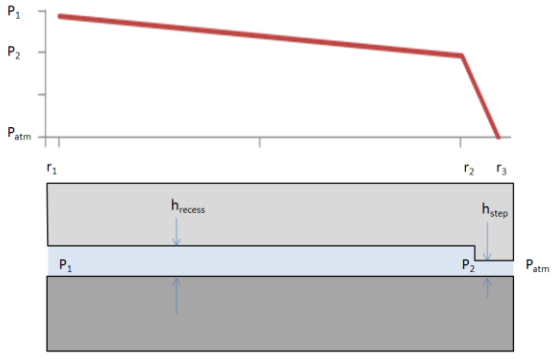

FIGURE 3. Pressure profile of the step-compensated thrust bearing.

In order to predict the axial and tilt dynamics of the spindle, a lumped parameter model is created that includes the static bearing stiffness as well as a frequency dependent squeeze film stiffness [1]. The squeeze film stiffness is zero under static conditions but can contribute significantly to the dynamic stiffness at higher frequencies [2,3]. However, in order to fully characterize the squeeze film, an elaborate experimental scheme is typically required [4].

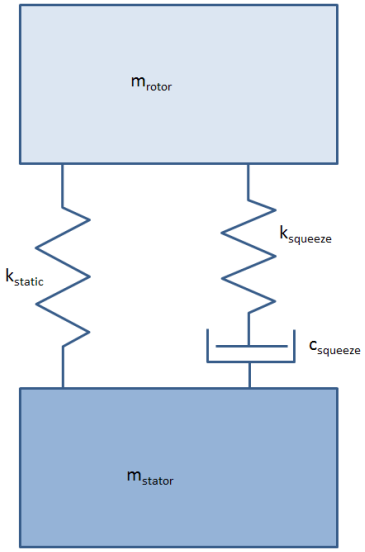

FIGURE 4. Lumped parameter model of the axial air bearing includes the static stiffness and a non-linear squeeze film stiffness.

APPROACH

The novelty of this work is the extraction of the equivalent spring stiffness, $k_{dynamic}$, at the natural frequency using experimental modal analysis. Combined with results of static stiffness testing, Equation 1 is used to determine the $k_{squeeze}$ at the natural frequency.

$$k_{dynamic} = k_{static} + k_{squeeze} \quad (1)$$

$$f_n = \frac{1}{2\pi}\sqrt{\frac{k_{dynamic}\,(m_{rotor}+m_{stator})}{m_{rotor}\,m_{stator}}} \quad (2)$$

Although this approach does not yield the complete definition of the non-linear squeeze film stiffness over the entire frequency range, it does provide valuable information to predict the dynamic response at a critical operating frequency—the natural frequency. This technique was documented by Harold Arneson and Eric Marsh following extensive dynamic testing in Alex Slocum's lab at MIT in 1993.

METHODOLOGY

The experimental apparatus for measuring the static stiffness is shown in Figure 5. To measure axial stiffness, an axial load is applied to the rotor by an air bearing thruster. The area of the piston is precisely controlled to provide a known load given a supplied pressure. Two cartridge type plunger LVDTs (Mitutoyo 519-332) are used to record the axial displacement. Note that two indicators are used to resolve tilting motion that could result from misalignment of the load.

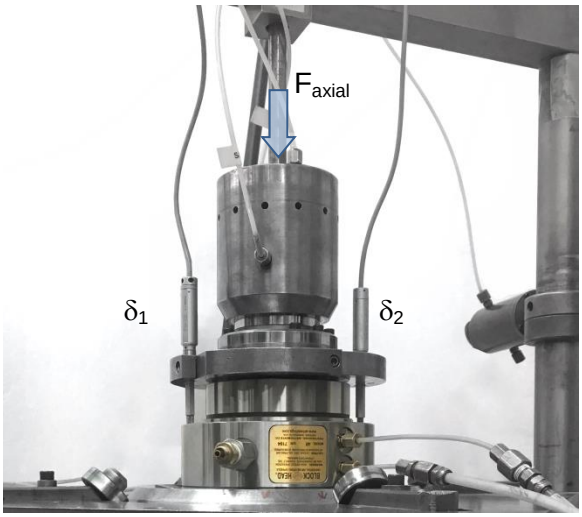

FIGURE 5. Test setup for static stiffness determination in the axial direction.

To measure static tilt stiffness, two pistons apply a moment load while the LVDTs record the tilt displacement as shown in Figure 6.

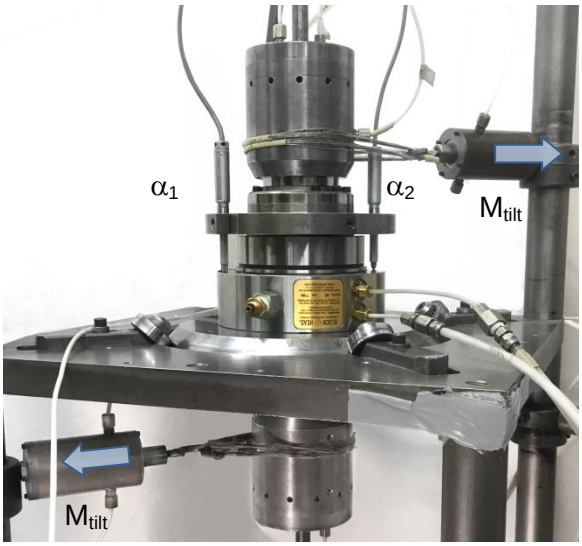

FIGURE 6. Tilt stiffness measurement setup.

FIGURE 7. Experimental modal analysis is used to determine dynamic stiffness.

A roving hammer experimental modal analysis is used to determine natural frequencies and mode shapes as shown in Figure 7. The spindle is supported on compliant foam to minimize boundary condition influences. An impact hammer (Kistler 500 N) excites the structure in the axial direction at 18 different locations on the rotor and stator while an accelerometer (Kister K-Shear 25g) measures the response. A 24-bit dynamic signal analyzer (Data Physics SignalCalc Ace) records excitation and response to calculate the frequency response functions. The static and dynamic stiffness are measured at inlet pressures ranging from 0.4 MPa to 0.7 MPa.

RESULTS

Static stiffness results are shown in Figure 8 and Figure 9 at inlet air pressures of 0.4 MPa through 0.7 MPa. As shown in Table 1, stiffness is approximately linear with air pressure—increasing pressure by 10% results in 10% higher stiffness.

TABLE 1. Summary of static stiffness results.

Inlet Pressure	Axial	Tilt
MPa	k_{static} N/µm	k_{static} Nm/µrad
0.40	269	0.35
0.50	297	0.39
0.55	318	0.42
0.60	336	0.45
0.70	364	0.50

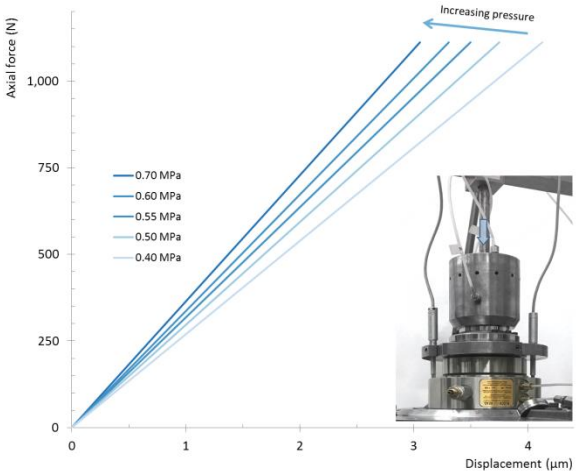

FIGURE 8. Static axial stiffness results at several inlet air pressures.

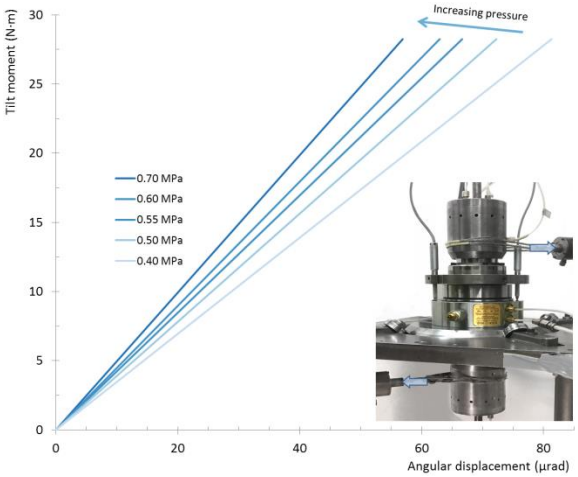

FIGURE 9. Static tilt stiffness results at several inlet air pressures.

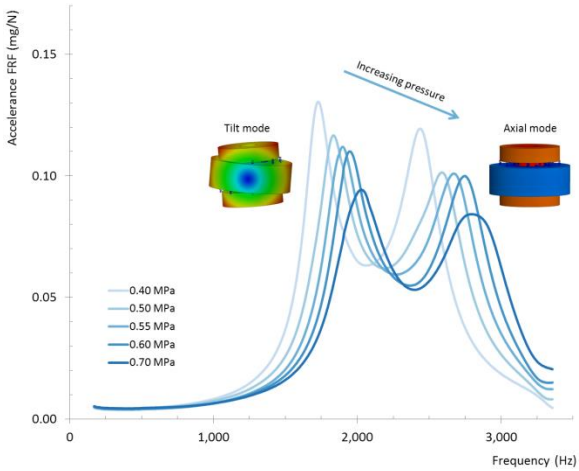

FIGURE 10. Experimental modal analysis is used to determine the dynamic stiffness.

Accelerance frequency response function magnitudes at inlet air pressures of 0.4 MPa through 0.7 MPa are shown in Figure 10. Modal analysis was used to extract the axial and tilt natural frequencies and mode shapes as summarized in Table 2.

TABLE 2. Summary natural frequency and damping ratios extracted from FRFs.

Inlet Pressure	Tilt mode		Axial mode	
MPa	fn Hz	ζ %	fn Hz	ζ %
0.40	1,726	6%	2,440	5%
0.50	1,833	6%	2,588	7%
0.55	1,896	6%	2,675	6%
0.60	1,949	6%	2,733	6%
0.70	2,031	8%	2,800	8%

The mass properties of the spindle are

m_{rotor} = 3.4 kg
J_{rotor} = 0.007 kg m^2
m_{stator} = 5.0 kg
J_{stator} = 0.008 kg m^2

Using these in Equation 1 and Equation 2, dynamic stiffness and squeeze stiffness at the natural frequency is calculated for the lumped parameter model as shown in Table 3.

TABLE 3. Summary dynamic and squeeze stiffness obtained at the natural frequencies.

Inlet Pressure	Tilt mode		Axial mode	
MPa	$k_{dynamic}$ Nm/µrad	$k_{squeeze}$ Nm/µrad	$k_{dynamic}$ N/µm	$k_{squeeze}$ N/µm
0.40	0.45	0.10	479	210
0.50	0.51	0.12	539	242
0.55	0.55	0.13	576	258
0.60	0.58	0.13	601	265
0.70	0.63	0.13	631	267

Due to added stiffness of the squeeze film dynamic tilt stiffness is 30% greater than static tilt stiffness. Similarly, dynamic axial stiffness is 80% greater than static axial stiffness.

CONCLUSIONS

An approach to accurately measuring dynamic stiffness of an air bearing spindle is demonstrated using modal analysis. It is known that additional stiffness under dynamic loading is a result of squeeze film effects. Results demonstrate that for inlet pressures between 0.4 MPa and 0.7 MPa, dynamic tilt stiffness is 30% higher than static tilt stiffness. Dynamic axial stiffness is 80% higher than static axial stiffness over the same range of inlet pressures. These results can be used to accurately model stiffness of the air bearing spindle under static and dynamic conditions.

REFERENCES

[1] Brown GM The dynamic characteristics of a hydrostatic thrust bearing.Int. J. Mach. Tool Des. Res., 1:157-171, 1961.

[2] Gross WA Gas film lubrication. John Wiley and Sons New York, NY: 1962.

[3] Roblee JW and Mote CD Design of externally pressurized gas bearings for stiffness and damping. Tribology International, 23(5):333-345, 1990.

[4] Al-Bender F and Van Brussel H Tilt characteristics of circular centrally fed aerostatic bearings. Tribology International, 25(3):189-197, 1992.

TOOLPATH GENERATION: FREEFORM SURFACE BLENDING AND EXTRAPOLATION

Neil J. Naples and Allen Y. Yi
Department of Integrated System Engineering
The Ohio State University, Columbus, OH, USA

INTRODUCTION

The overall goal of this research is to develop enabling technologies that vastly improve existing toolpath generation techniques for freeform optics manufacturing. These new technologies allow complex optical surfaces of the form $z(x,y)$ or $z(r,\theta)$ to be efficiently machined. To this end, we introduce the concept of surface transitions: a means for transforming from explicit, freeform, optical sag equations that are defined inside arbitrary, closed boundaries into a useful toolpath. Both surface transitions discussed, blending and extrapolation, have their own explicit, continuous, polar sag equations associated with them. Defined outside the boundary of an optical surface, both techniques have the property of adjustable surface continuity so that a toolpaths' smoothness can be manipulated as desired. These two techniques differ mainly in their treatment of boundaries. Whereas extrapolation smoothly extends a surface outside its boundary to infinity, blending smoothly transitions from one non-intersecting boundary to another.

MATHEMATICAL BACKGROUND

The optical surfaces to be extrapolated or blended must be explicit (of the form $z(x,y)$ or $z(r,\theta)$), continuous, well-behaved, differentiable, and must not exhibit vertical slopes – constraints satisfied by most freeform optical prescriptions used today. For calculations to maintain the highest possible precision, the blending and extrapolating surfaces themselves were developed to work directly with this native explicit surface form. Therefore, it is not necessary to parameterize or transform any optical surface before its sag values are computed.

Boundaries

Most toolpaths consist of multiple local regions, each described by a different smooth, closed boundary. A potentially different explicit sag equation describes the global toolpath inside each local region. Therefore, it is crucial to understand how boundaries are defined and evaluated as their application directly affects the form and continuity of a toolpath.

We define discrete coordinates as the most fundamental inputs for boundary construction. These coordinates are usually supplied by an optical engineer, extracted from a CAD model, or defined as the intersection curve between two surfaces – determined by computing where the difference of two surfaces is equal to zero. After Converting to polar coordinates, it is critically important that these discrete coordinates, $(\mathcal{B}_r, \mathcal{B}_\theta)$, trace out a single-valued closed curve – one non-zero radius for every angle.

Evaluating a closed boundary between the discrete coordinates that define it is of paramount importance. Conversion from discrete boundary coordinates to a smooth boundary function is accomplished with a C^2 continuous cubic interpolating spline [1], $\mathcal{S}_r(\theta)$, where $\theta \in [0,\ldots,2\pi]$. Figure 1 shows discrete and continuous versions of an example boundary. As seen in this Figure, C^2 continuous splines exhibit non-zero curvature between discrete boundary coordinates because of the cubic polynomials used in their construction. Additionally, it is clear that boundaries defined in this way can exhibit a great deal of non-convexity.

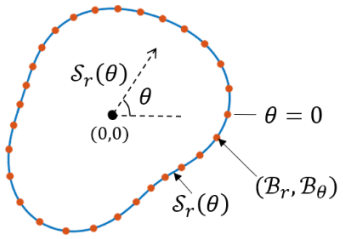

FIGURE 1. Discrete (red) and continuous (blue) boundaries. Input coordinates may be scattered.

Inside/Outside Test

One can now determine if a set of discrete toolpath coordinates lie inside or outside a polar boundary described by the above spline formulation. This is true even if the boundary is not centered on the global toolpath origin, like the boundary of a typical microlens. Illustrated in Figure 2, this calculation is critical for surfaces whose sag equation should not be evaluated outside its defined boundary.

Consider a set of toolpath coordinates, (x_i, y_i), and the boundary from Figure 1 not centered on the toolpath origin. After translating the toolpath origin to the boundary origin and converting its coordinates to polar, the Inside/Outside test in its entirety is

$$\begin{cases} \text{inside}, & r_i \le \mathcal{S}_r(\theta_i) \\ \text{outside}, & \text{otherwise} \end{cases} \quad \forall\, i \in [1, \dots, N_{tp}] \qquad (1)$$

where N_{tp} is the number of coordinates in the toolpath. That is, if the boundary spline has an equal or greater radius than the i^{th} translated toolpath point, the point lies inside the boundary. Otherwise, the point lies outside the boundary.

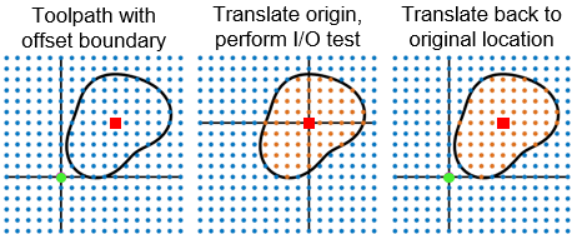

FIGURE 2. Inside/Outside Test. Boundary origin is a red square. Toolpath origin is a green circle. Toolpath coordinates may be scattered.

With the Inside/Outside test applied, calculate sag values by evaluating the explicit optical equation that is defined inside the same polar boundary, as shown in Figure 3.

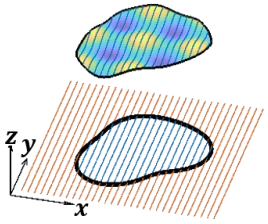

FIGURE 3. Surface described inside closed boundary. Toolpath coordinates may be scattered.

Speaking more generally, the calculations so far represent one half of the necessary framework needed to smoothly describe the entire toolpath for an explicit surface, or array of explicit surfaces, described inside arbitrary boundaries. The other half are the techniques needed to smoothly transition to the rest of the toolpath.

Extrapolating Polynomials

The extension of a 2D function outside its domain is accomplished with polynomial extrapolation. In general, an n^{th} degree extrapolating polynomial, $\mathcal{E}_n(r)$, that extrapolates the curve $z(r)$, beyond the point r_0, is given as

$$\mathcal{E}_n(r) = \sum_{i=0}^{n} \frac{z^{(i)}(r)}{i!}(r - r_0)^i \qquad (2)$$
$$\forall\, r \in (r_0, \infty)$$

for $n \ge 1$ and $z^{(i)}(r)$ being the i^{th} derivative of $z(r)$. By varying the degree of the extrapolating polynomial in Equation 2, continuity at the point of extrapolation is controlled. Assuming n derivatives of $z(r)$ exist, an n^{th} -degree extrapolating polynomial will produce a C^n continuous curve. A curve with linear, quadratic, and cubic extrapolation is shown in Figure 4.

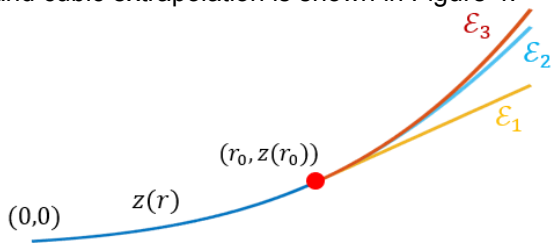

FIGURE 4. 2D curve with three extrapolating polynomials enforcing $C^1 - C^3$ continuity at the point r_0.

Blending Polynomials

The process of constraining a polynomial to interpolate data points with known derivatives is known as Hermite interpolation [2]. An n^{th} degree 2D Hermite blending polynomial, $\mathcal{H}_n(r)$, that blends the two curves, $z_1(r)$ and $z_2(r)$, together between the coordinates r_1 and r_2, with $r_2 > r_1$, is given as

$$\mathcal{H}_n(r) = \sum_{i=0}^{n} C_i r^i \qquad (3)$$
$$\forall\, r \in (r_1, r_2)$$

for odd $n \ge 1$. Additionally, n obeys

$$n = 2d + 1 \qquad (4)$$

where d is the number of derivatives used in the construction of $\mathcal{H}_n(r)$. The $n+1$ polynomial coefficients, C_i, are computed by solving the $(n+1)x(n+1)$ linear system of equations that constrain $z_1(r)$, $z_2(r)$, and their first $(n-1)/2$ derivatives to be equal at the points r_1 and r_2, respectively. For $d = 1$ (cubic, C^1 continuous interpolation) this system looks like

$$\begin{aligned} C_3 r_1^3 + C_2 r_1^2 + C_1 r_1 + C_0 &= z_1(r_1) \\ C_3 r_2^3 + C_2 r_2^2 + C_1 r_2 + C_0 &= z_2(r_2) \\ 3C_3 r_1^2 + 2C_2 r_1 + C_1 &= z_1^{(1)}(r_1) \\ 3C_3 r_2^2 + 2C_2 r_2 + C_1 &= z_2^{(1)}(r_2) \end{aligned} \qquad (5)$$

where varying the degree of the blending polynomial, and thus the equations in the above linear system, controls continuity at r_1 and r_2. Not shown here, it is highly desirable to improve the numerical properties of the above linear system by centering and scaling r_1 and r_2 to have zero mean and unit standard deviation. Assuming d-derivatives of the curve $z_1(r)$ and $z_2(r)$ exist, an n^{th}-degree blending polynomial will produce a $C^{(n-1)/2}$ continuous curve. Two curves joined with cubic, quintic, 7th order, and 9th order blending are shown in Figure 5.

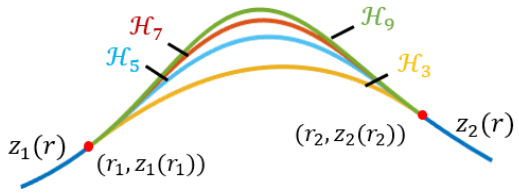

FIGURE 5. 2D curves with four blending polynomials enforcing $C^1 - C^4$ continuity at the points r_1 and r_2.

FREEFORM SURFACE EXTRAPOLATION

Often, the overall boundary of a freeform optical surface is not equal to that of a toolpath. Some optics, higher order polynomials in particular, rapidly diverge beyond their defined boundaries. The point of freeform surface extrapolation, then, is to force a toolpath for a single surface to be smooth and well-behaved everywhere.

We will use the example freeform surface shown in Figure 6 to illustrate the extrapolation process. Since this surface, denoted Z_L, quickly diverges for large xy-inputs, it is defined inside a rectangle with corner radii, which is described by the single valued polar boundary spline $\mathcal{S}_r(\theta)$. The circular boundary of a spiral toolpath, which will bound the final piecewise surface, is also shown in Figure 6. It is this boundary that defines the outer perimeter of the extrapolated surface.

Since $\mathcal{S}_r(\theta)$ describes boundary radius as a function of polar angle, the rz-plane – where θ is constant – defines the location and orientation of a unique 2D extrapolating polynomial for points that lie outside a surfaces' polar boundary. Combining boundary splines and the extrapolating polynomial from Equation 2, it is now possible to generate the n^{th}-degree, explicit, continuous, extrapolating surface, $Z_\mathcal{E}$. Assuming n-derivatives of the freeform optical surface exist and can be computed, $Z_\mathcal{E}$ produces a C^n continuous surface and is given as

$$Z_\mathcal{E}(r,\theta) = \sum_{i=0}^{n} \frac{Z_{L,r}^{(i)}}{i!}\left(r - \mathcal{S}_r(\theta)\right)^i \qquad (6)$$
$$\forall \left[r \in (\mathcal{S}_r(\theta), \infty) \wedge \theta \in [0, 2\pi]\right]$$

where $Z_{L,r}^{(i)}$ is the i^{th} radial derivative of Z_L relative to the center of the boundary. With this formulation, we can see that $Z_\mathcal{E}$ is defined everywhere outside the polar boundary that bounds the freeform optical surface.

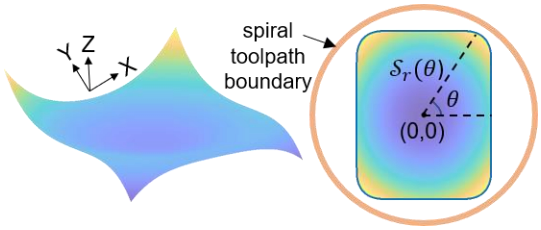

FIGURE 6. Diverging polynomial surface (left) and its optical & toolpath boundaries (right).

The Inside/Outside test is then used to compute toolpath coordinates, evaluating Z_L inside the boundary and $Z_\mathcal{E}$ outside. The top row of Figure 7 shows the example surface and a series of coarsely spaced, radially oriented cubic extrapolating polynomials. When combined in Equation 6, these polynomials generate a C^3 continuous extrapolating surface. The bottom row of Figure 7 shows both spiral and raster line toolpaths applied to the overall surface, illustrating again how the overall surface is continuous and independent of the coordinates input into it.

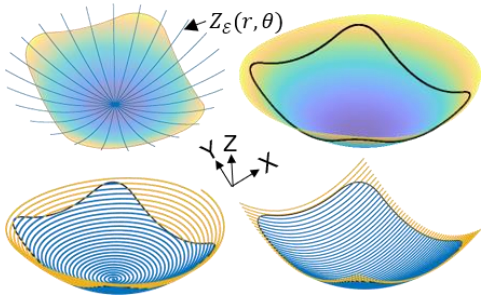

FIGURE 7. Example continuous surface and corresponding toolpaths. Radial extrapolating polynomials (top left), C^3 continuous surface before applying toolpath (top right), spiral toolpath (bottom left), raster line toolpath (bottom right).

Experimental

To experimentally verify that this surface extrapolation technique creates a smooth surface – both outside and at the boundary of an optical surface – two spiral toolpaths exhibiting linear and quartic extrapolation were generated for the

6^{th} degree polynomial seen in Figure 8. These toolpaths are shown in Figure 9, together with the second derivative along the cutting direction of each spiral. It shown that increasing the degree of the extrapolating polynomial, and thus the level of surface continuity, produces a toolpath with smoother accelerations and decreased following error as a machine tool is running.

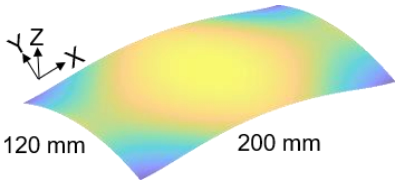

FIGURE 8. 6th degree polynomial defined inside rectangular boundary.

Ten revolutions of each toolpath were evaluated on a Precitech Nanoform X ultraprecision lathe with XZC-axes. Each toolpath was evaluated in the air so all acceleration and following error data was independent of tool force. For each spiral, the X and C-axes moved at a constant velocity due to the constant 1° angular spacing and 5µm radial stepover used, respectively. Therefore, all dynamic motion was constrained and analyzed along the Z-axis.

The linearly extrapolated surface utilized one radial derivative in its construction. Therefore, the acceleration is expected to be fully discontinuous at the rectangular boundary. Verified in Figure 9, discontinuities in calculated and actual acceleration curves are clearly seen. These discontinuities are directly mirrored by a spike in the following error (FE) curve, resulting in a maximum magnitude of 0.962µm. Both acceleration discontinuities and FE spikes are fundamentally due to the C^1 continuous surface construction.

The surface with quartic extrapolation, on the other hand, utilized four radial derivatives in its construction. Also verified in Figure 9, the calculated and actual accelerations are totally smooth – almost sinusoidal. The equally smooth FE has a maximum magnitude of only 0.386µm. The smoothness of this toolpath is fundamentally due to the C^4 continuous surface construction. However, because this quartic surface is a higher order polynomial when compared to a linear surface, it has a larger range of sag values.

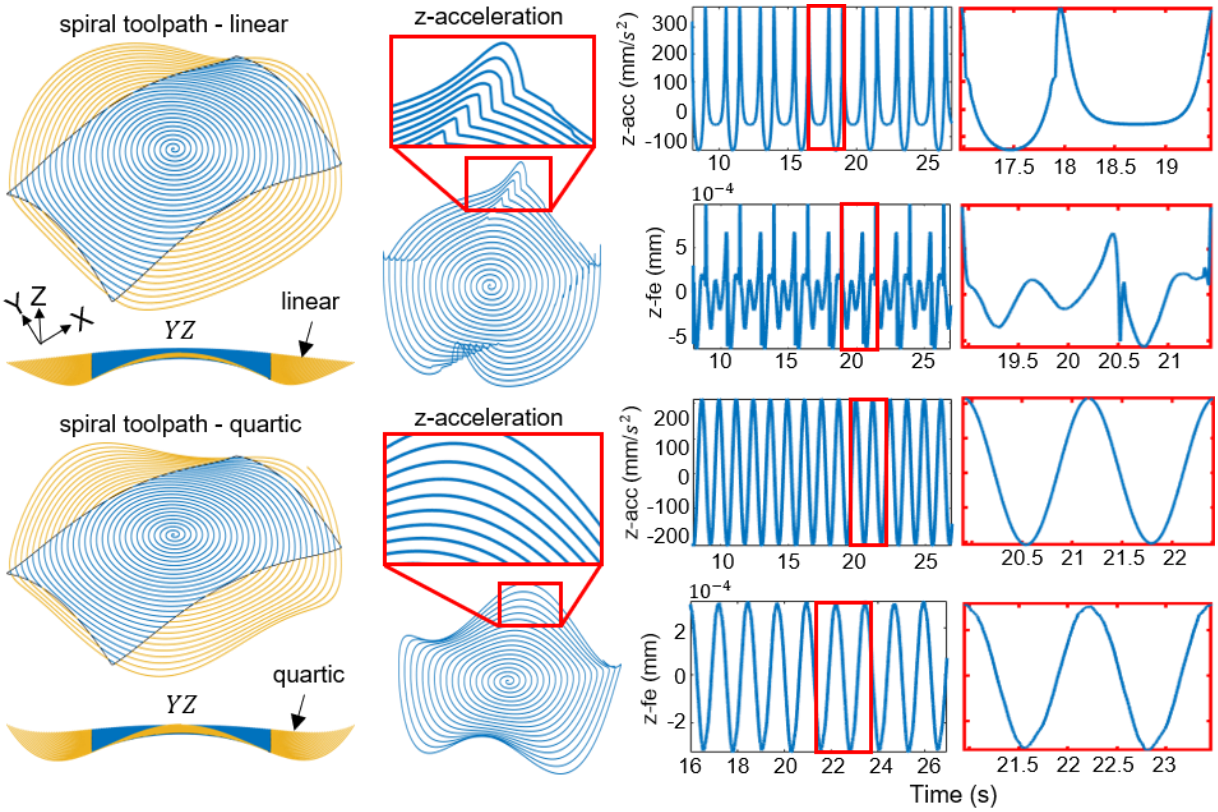

FIGURE 9. Spiral toolpaths exhibiting linear and quartic extrapolation for 6th degree polynomial defined inside rectangular boundary (left column). Stepovers increased for clarity. Computed acceleration (middle column). Acceleration and following error data taken while machine tool was running (right column).

FREEFORM SURFACE BLENDING

The desire to smoothly transition, or blend, between two explicit surfaces is a common situation faced when generating toolpaths. Even though both surfaces may be continuous and well-behaved inside their respective domains, the domains themselves are often different. Using this blending technique, it is possible to smoothly describe an array of surfaces that are blended into a larger base surface – a microlens array for example.

Like extrapolation, the divergent freeform 'lenslet', Z_L, will be used to describe the blending process along with a flat base surface, Z_B. In addition to the polar spline, $\mathcal{S}_r(\theta)$, that bounds Z_L, it is necessary to define a second, larger polar spline, $\mathcal{S}_R(\theta)$, that bounds the blend on the base surface. Illustrated in Figure 10, these two boundaries create a blend 'zone' such that $\mathcal{S}_r(\theta)$ traces out a curve where the blend is at least tangent to the Z_L and $\mathcal{S}_R(\theta)$ creates a curve where the blend is at least tangent to the Z_B.

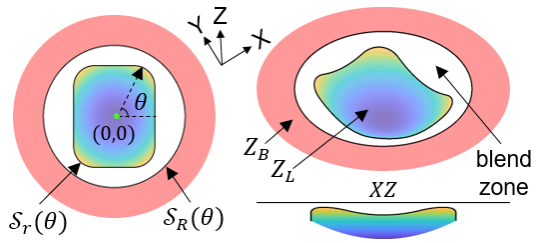

FIGURE 10. Freeform lenslet, flat base surface, and blend zone.

Since $\mathcal{S}_r(\theta)$ and $\mathcal{S}_R(\theta)$ both describe boundary radius as a function of polar angle, the rz-plane – where θ is constant – defines the location and orientation of a unique 2D Hermite blending polynomial for points that lie inside the blend zone defined by both polar splines. Combining boundary splines and the Hermite blending polynomial from Equation 3, it is now possible to generate the n^{th}-degree, explicit, continuous blending surface, $Z_{\mathcal{H}}$. Assuming n-derivatives of the freeform optical surface exist and can be computed, $Z_{\mathcal{H}}$ produces a $C^{(n-1)/2}$ continuous surface and is given as

$$Z_{\mathcal{H}}(r,\theta) = \sum_{i=0}^{n} C_i(\theta) r^i$$
$$\forall \left[r \in \left(\mathcal{S}_r(\theta), \mathcal{S}_R(\theta)\right) \wedge \theta \in [0, 2\pi] \right] \quad (7)$$

where $C_i(\theta)$ are the solutions to the linear system of equations that constrain each Hermite polynomial to be at least tangent to both lenslet and base surface. An example of which, for $n = 1$, is shown in Equations 5. Since the Hermite polynomials are oriented radially, it is necessary to compute radial derivatives of the lenslet and base surface relative to the center of both boundaries.

The Inside/Outside test is then used to compute toolpath coordinates, taking care to evaluate the base surface equation for points that lie outside $\mathcal{S}_R(\theta)$. The top row of Figure 11 shows the example lenslet and base surfaces along with a series of coarsely spaced, radially oriented 5th degree blending polynomials. When combined in Equation 7, these polynomials generate a C^2 continuous blending surface. The bottom row of Figure 11 shows both spiral and raster line toolpaths applied to the overall surface.

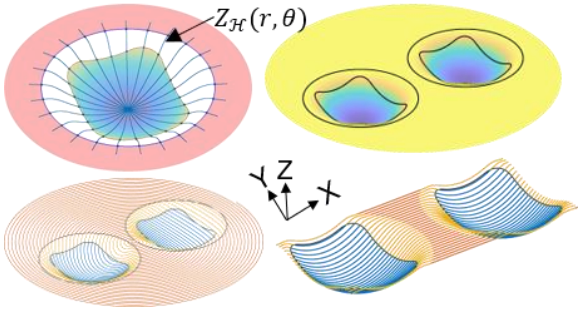

FIGURE 11. Example continuous surface and corresponding toolpaths. Radial blending polynomials (top left), C^2 continuous surface before applying toolpath (top right), spiral toolpath (bottom left), raster line toolpath (bottom right).

Experimental

To illustrate the robustness of the proposed surface generation techniques, the freeform microlens array shown in Figure 12 was machined in brass on a Precitech Nanoform X ultraprecision lathe with a Precitech FTS 5000 Fast Tool Servo. Designed with no exploitable symmetries or simplifications and virtually impossible to model with traditional CAD software, this surface is comprised of an array of explicit freeform – not spherical or aspherical – lenslets superimposed onto an explicit freeform base surface. All lenslets are individually tilted about the X and Y-axes such that they are normal to the base surface at their respective locations. All blend zones are unique and have the same form as the intersection between each respective lenslet and the base surface. Lastly, all lenslet boundary discontinuities were blended with C^3 continuous freeform blends.

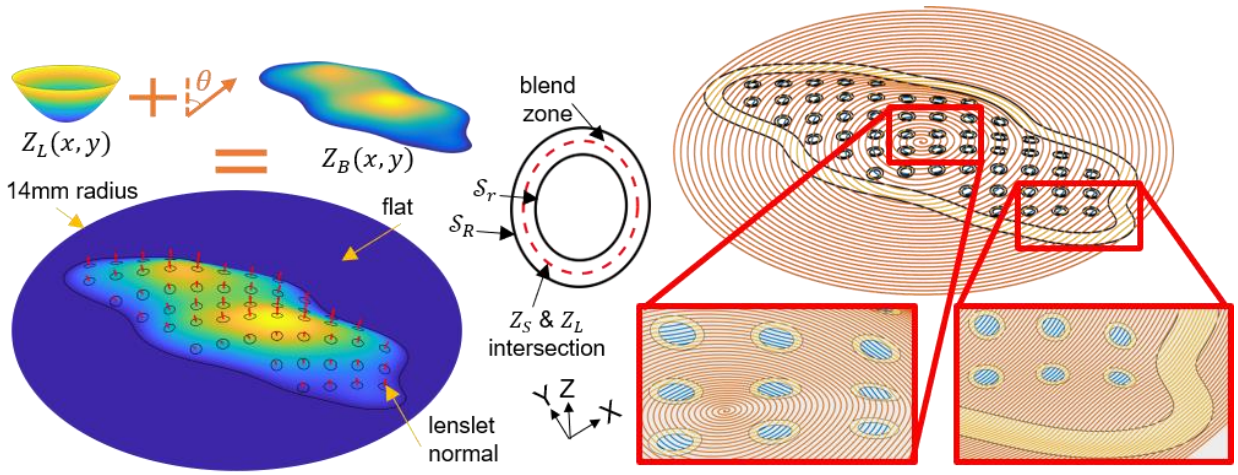

FIGURE 12. Freeform microlens array. Lenslet normals shown in red (left). Sample freeform blend zone (center). Overall C^3 continuous spiral toolpath with increased radial stepovers for clarity (right). Lenslet and base surface sags are is 46μm & 633μm, respectively. All lenslet apertures are freeform, unique, and have radii ranging from 256μm to 310μm.

Figure 13 shows the final brass surface. The overall blended surface exhibits maximum radial and azimuthal slopes of 38.8° and 22.8°, respectively. Therefore, a diamond tool with 200μm radius, 120° sweep, and 25° clearance angle was used. The lenslet surface roughness, measured with a Taylor Hobson CCI non-contact Optical Profiler, is shown in Figure 14.

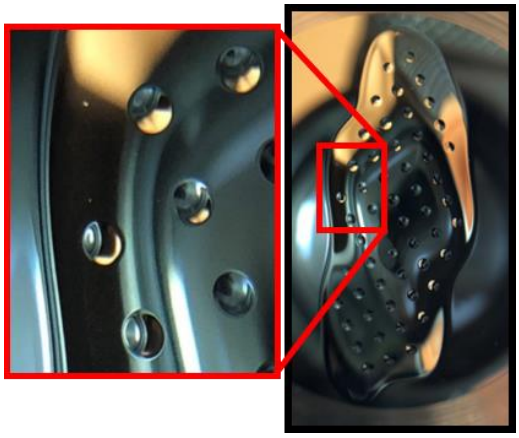

FIGURE 13. Final brass freeform microlens array with C^3 continuous freeform blends.

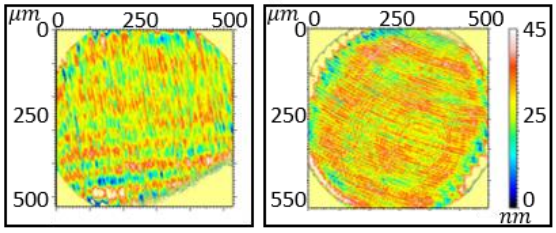

FIGURE 14. Surface roughness. Lenslet near edge: 5.71nm S_a (left). Lenslet near center: 5.43nm S_a (right).

CONCLUSION

This paper briefly introduces the most general surface transition techniques to date for explicitly described freeform optical surfaces that are defined inside arbitrary boundaries. By combining a robust boundary definition, freeform surface extrapolation, and freeform surface blending, key relationships used in the toolpath generation process were described and applied. Designed with a minimum number of assumptions, the proposed surface transitions are described by polynomial curves that emanate radially outside the boundary of an optical surface. It was shown that increasing the degree of the polynomial curves increases overall surface continuity at the expense of increased sag values.

ACKNOLEDDGEMENTS

We would like to thank everyone Ametek Precitech for their support on this research. In particular, we would like to thank Jeff Roblee for his collaboration and guidance.

REFERENCES

[1] C. de Boor, A Practical Guide to Splines, New York: 1978.

[2] R. Hamming, Numerical Methods for Scientists and Engineers, New York: McGraw-Hill, Inc., 1973.

DOUBLE-SIDED POLISHING CONDITIONS TO SUPPRESS EDGE ROLL-OFF OF SILICON WAFER

Sena HARADA[1], Urara SATAKE[1], and Toshiyuki ENOMOTO[1]
[1]Department of Mechanical Engineering, Graduate School of Engineering
Osaka University
Suita, Osaka, Japan

INTRODUCTION

In recent years, demand for high performances and productivities of semiconductor devices has rapidly increased. To improve the performances of the devices, the integration density has been increased, which requires the decrease in the depth of focus margin in lithography process. Therefore, surface flatness of silicon wafers as the base materials for the devices is required to be further improved [1]. In particular, there is strong demand for suppressing deterioration of surface flatness near the outer periphery of a wafer due to edge roll-off (ERO), which occurs in double-sided polishing (DSP) (Figure 1) as the finishing process of the wafer manufacturing. In the previous work [2], we found that ERO can be suppressed by reducing the settlement amount of a wafer into a polishing pad, that is, the deformation of a polishing pad during polishing. Polishing pads made of hard materials undoubtedly have low deformability; however, the use of them leads to deterioration of the surface quality of wafers due to formation of scratches.

In this study, we investigate effects of DSP conditions on the deformation behavior of the polishing pad during polishing. On the basis of the results, we propose DSP conditions that can reduce the deformation of a polishing pad, and hence suppress ERO. The corresponding polishing performances were also evaluated in DSP experiments on silicon wafers.

DEFORMATION BEHAVIOR OF POLISHING PAD DURING DSP [3]

During DSP, the polishing pad is repeatedly loaded by the sliding wafer; that is, the polishing pad is subjected to cyclic loading. The cyclic loading conditions, that is, the combination of the loading periods and the unloading periods, are determined by the DSP conditions. The deformation behavior of the polishing pad during polishing depends on the cyclic loading conditions because of the viscoelasticity of the polishing pad. Thus, we investigate how the deformation behavior of the polishing pad is affected by the cyclic loading conditions.

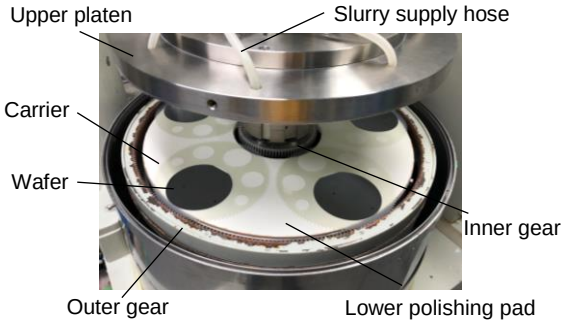

(a) DSP machine

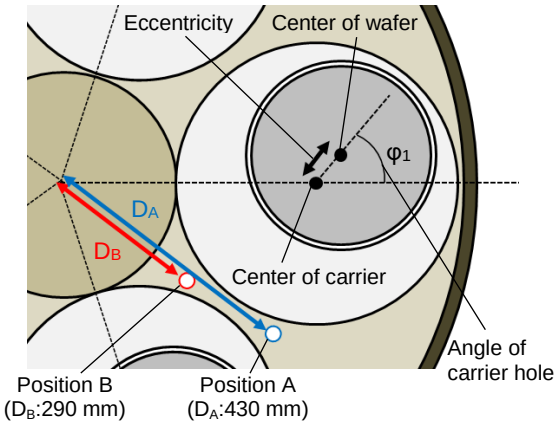

(b) Top view of a lower polishing pad

FIGURE 1. Schematic of DSP process.

CYCLIC LOADING CONDITIONS DURING DSP

In a typical DSP process (Figure 1), several wafers are polished simultaneously and each wafer is placed in the hole of the carrier which rotates while revolving around the center of the polishing pad. The hole is located at the eccentric position of the carrier, hence the wafer moves in both circumferential and radial directions on the polishing pad. Figure 2 shows the cyclic loading conditions at two different positions on the lower polishing pad under DSP conditions listed in Table 1. The loading/unloading cycles of

TABLE 1. DSP conditions.

DSP machine			DSP machine (Hamai Co., Ltd., 9BF)	
-Diameter of inner gear	400 mm		186.2 mm	
-Diameter of carrier	525 mm		232.44 mm	
-Diameter of wafer	300 mm		125 mm	
Eccentricity of carrier hole	88 mm		36.25 mm	
	DSP Conditions A	DSP Conditions B	Proposed Conditions	Reference Conditions
Number of carriers per batch	5	5	5	3
Number of wafers per carrier	1	1	1	1
Initial angle of hole on carrier φ1, φ2, φ3, φ4, φ5 (Figure 1)	0,0,0,0,0 deg	0,0,0,0,0 deg	0,12,24,36,48 deg	0,0,0 deg
Rotation speed of carriers	-2.1 rpm	10.1 rpm	2.5 rpm	-4.1rpm
Orbital speed of carriers	10.7 rpm	5.3 rpm	-4.9 rpm	-5.2 rpm
Rotation speed of upper pad	-5 rpm	-5 rpm	6.6 rpm	4.0 rpm
Rotation speed of lower pad	15 rpm	15 rpm	-20.0 rpm	-12.0 rpm

Conditions A (Figure 2(a)) and C (Figure 2(c)) occur at Position A (Figure 1) under DSP Conditions A and B, respectively. The loading/unloading cycles of Conditions B (Figure 2(b)) and D (Figure 2(d)) occur at Position B (Figure 1) under DSP Conditions A and B, respectively. Because of the above mentioned wafer movement, both the loading period and the unloading period vary with each cycle in every cyclic loading condition. In addition, Conditions B and D, which occur in the inner area on the polishing pad, have fairly long unloading periods.

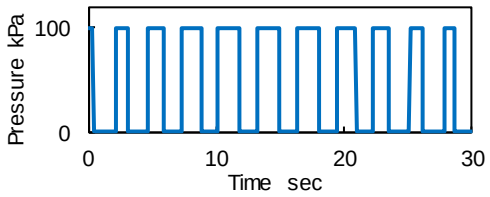

(a) Condition A

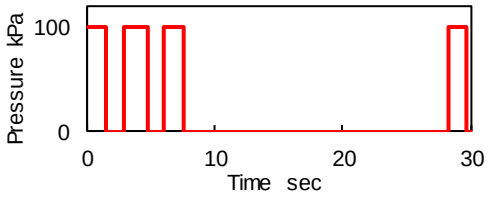

(b) Condition B

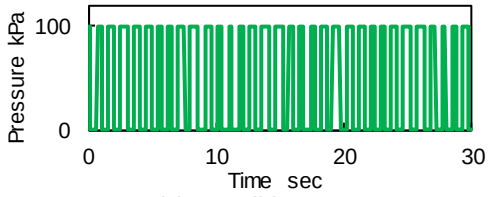

(c) Condition C

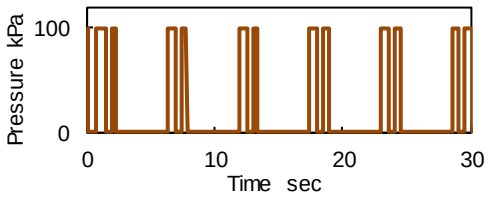

(d) Condition D

FIGURE 2. Cyclic loading conditions.

EFFECT OF CYCLIC LOADING CONDITIONS ON DEFORMABILITY OF POLISHING PAD

To investigate the relation between the cyclic loading conditions and the deformation behavior of the polishing pad, we conducted the repeated indentation creep tests for the commercial nonwoven type polishing pad (Nitta Haas Inc., SUBA 840) under Conditions A and B (Figures 2(a) and (b)). Figure 3(a) shows the measured time-deformation curve in the first cycle of Condition A. The polishing pad deformed instantaneously once subjected to a load, and creep deformation was accumulated over the loading period. The instantaneous elastic deformation disappeared instantaneously once the load was removed, and part of the creep deformation recovered during the unloading period. At the end of the cycle, we observed the residual deformation, which arose from the creep deformation that has not been recovered because of short unloading period. From the measured time-deformation curves (Figures 3(b) and (c)), we found the following features of

deformation behavior of a polishing pad under the repeated loading/unloading cycles:

- The creep deformability of a polishing pad, which is defined as the creep increment during a given loading period, varied every cycle.
- The instantaneous deformability of a polishing pad decreases as the loading/unloading cycle progressed; specifically, the instantaneous elastic deformation in each cycle was directly proportional to the residual deformation in the preceding cycle.

The first feature follows the Boltzmann's superposition principle [4], which describes the response of a viscoelastic material to different loading histories. On the basis of the principle, the creep increment during the loading period is affected by the recovery behavior in every previous cycle. It means that the creep deformability of the polishing pad is effectively reduced when the load is applied soon after the preceding load is removed, that is, when the unloading period is short. On the other hand, the second feature is not observed in the behavior of typical viscoelastic materials. On the basis of the feature, we concluded that the instantaneous deformability of the polishing pad is effectively reduced when the residual deformation is large in the preceding cycle, that is, when the unloading period is relatively short compared to the loading period.

CONSTITUTIVE MODEL OF POLISHING PAD

We established a constitutive model for polishing pads to represent the relation between cyclic loading conditions and a time-deformation curve of a polishing pad. The Schapery's constitutive model [5, 6], which has been widely used to characterize the nonlinear viscoelastic behavior of various materials, was modified on the basis of the above findings. Specifically, the constant term in the Schapery's constitutive equation, which represents the instantaneous elastic deformation, was substituted by a first-degree polynomial function of the residual deformation in the preceding cycle. To verify the proposed constitutive model, the calculated time-deformation curves via the proposed constitutive equation were compared with the measured ones via the repeated indentation creep tests for the commercial nonwoven type polishing pad (Nitta Haas Inc., SUBA 840) under Conditions A–D (Figure 2). Prior to the verification, the material parameters in the proposed constitutive equation were identified via the repeated indentation creep tests under the two different cyclic loading conditions. Figure 4 shows the calculated time-deformation curves via the proposed constitutive model with the identified material parameters and the measured ones from 80 sec to 100 sec. The calculated results were in good agreement with the measured ones under every cyclic loading condition, which confirmed that the proposed constitutive model can evaluate the deformability of a polishing pad under a given DSP conditions.

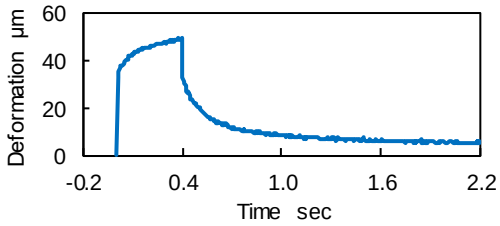

(a) Time-deformation curve in the first cycle under Condition A

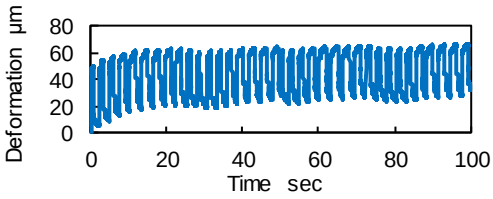

(b) Condition A

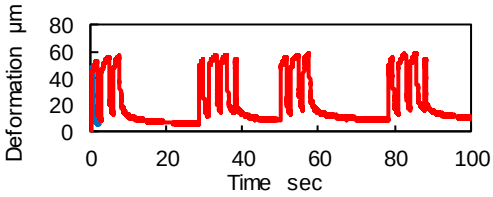

(c) Condition B

FIGURE 3. Measured time-deformation curve of a polishing pad.

DSP CONDITIONS TO SUPPRESS ERO [3]

On the basis of the investigation, we propose the following cyclic loading conditions to reduce the deformation of the polishing pad during polishing, resulting in less ERO:

- The loading period is short, which can reduce the total accumulation of the creep deformation during that loading period.
- The unloading period is short, which can reduce the creep deformability of the polishing pad.
- The unloading period is relatively short compared to the last loading period, which can reduce the instantaneous deformability of the polishing pad.

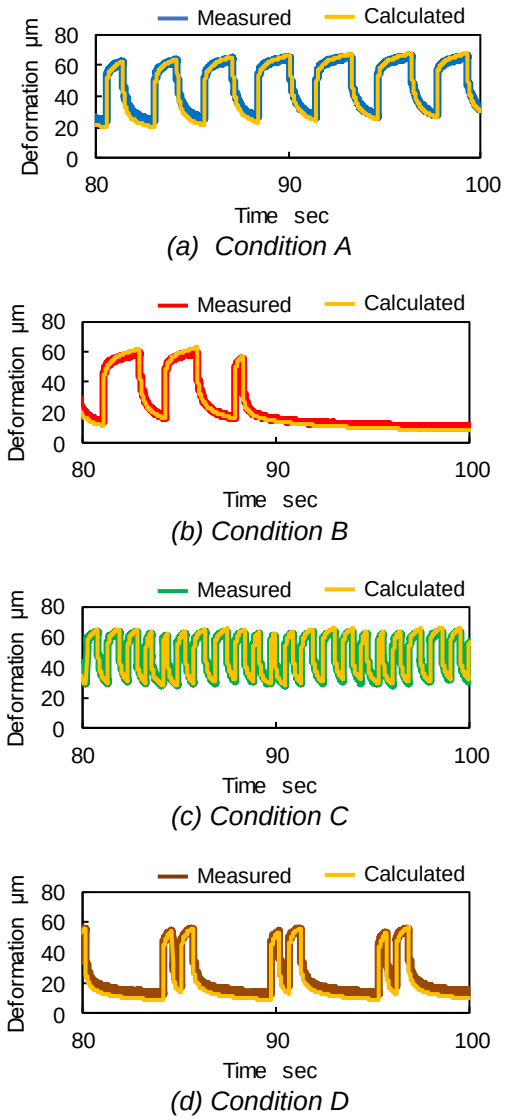

FIGURE 4. Verification of the proposed constitutive equation.

The cyclic loading conditions at each position on the polishing pad is determined by the total number of wafers polished simultaneously, the trajectory of each wafer on the polishing pad, and the sliding speed of each wafer relative to the polishing pad. The above effective cyclic loading conditions can be provided by the following approaches:

- Increase the relative sliding speed of the wafers
- Increase the total number of wafers
- Set the trajectories of the wafers to be close to each other

Both the trajectory and the relative sliding speed of each wafer can be provided as desired by setting the appropriate DSP conditions such as rotation speed of carriers, orbital speed of carriers, rotation speed of polishing pads, and initial arrangement of wafers on a polishing pad, that is, initial angles of the carrier holes (φ shown in Figure 1).

We conducted DSP experiments under the two different DSP conditions (Proposed Conditions, Reference Conditions) listed in Table 1 to verify the effectiveness of the above approaches in reducing ERO. Proposed Conditions were set to reduce the deformation of the lower polishing pad during polishing. Under Proposed Conditions, more wafers are polished simultaneously, and there is the larger difference between the orbital

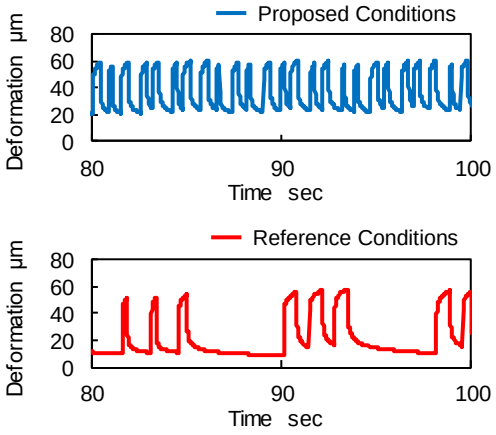

	Instantaneous elastic deformation	Creep deformation
Reference Conditions	32.4 μm	14.4 μm
Proposed Conditions	27.3 μm	9.3 μm

Figure 5. Time-deformation curve of the lower polishing pad under Reference Conditions and Proposed Conditions.

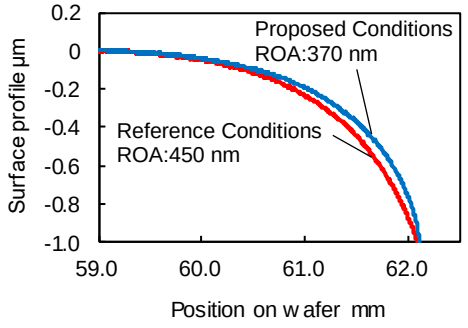

FIGURE 6. Surface profiles near the wafer

speed of the carriers and the rotation speed of the lower polishing pad, leading to larger sliding speed of the wafers relative to the lower polishing pad. In addition, all wafers move along the same path on the lower polishing pad because of the appropriate initial arrangement of the wafers. Figure 5 shows the time-deformation curve from 80 sec to 100 sec at Position B (Figure 1) of the lower polishing pad under Reference Conditions and Proposed Conditions, which were calculated on the basis of the proposed constitutive model for polishing pads. The instantaneous elastic deformation and the creep deformation in the cycle at around 100 sec under Reference Conditions and Proposed Conditions are also shown in Figure 5. These results indicate that Proposed Conditions can effectively reduce the deformation of the lower polishing pad during polishing. Figure 6 shows the profiles of the lower surface near the wafer edge after polishing and roll-off amount (ROA). ROA was defined as the vertical displacement from the level line to the measured wafer profile at a distance of 1 mm from the periphery of the wafer. As shown in the experimental results, Proposed Conditions resulted in less ERO compared to Reference Conditions, which confirmed the effectiveness of the proposed approaches in suppressing ERO.

CONCLUSIONS

To suppress ERO during silicon wafer polishing, we investigated the effects of DSP conditions on the deformation behavior of a polishing pad, which affects ERO. On the basis of the results, we proposed DSP conditions to reduce the deformation of the polishing pad during polishing, resulting in suppression of ERO. DSP experiments confirmed that the proposed DSP conditions can effectively reduce ERO.

REFERENCES

[1] Tönshoff, H.K., Schmieden, W.v., Inasaki, I., König, W., Spur, G. Abrasive Machining of Silicon, Annals of the CIRP. 1990; 39/2:621-635.

[2] Satake, U., Enomoto, T., Obayashi, Y., Sugihara, T. Reducing Edge Roll-Off during Polishing of Substrates. Precision Engineering (Journal of the International Societies for Precision Engineering and Nanotechnology). 2018; 51:97-102.

[3] Satake, U., Harada, S., Enomoto, T. Viscoelastic behavior of polishing pad: Effects on edge roll-off during silicon wafer polishing. submitted to Precision Engineering (Journal of the International Societies for Precision Engineering and Nanotechnology).

[4] R., M., Christensen. Theory of Viscoelasticity. 1971, Academic Press.

[5] R., A., Schapery, On a Thermodynamic Constitutive Theory and Its Application to Various Nonlinear Materials, Thermoinelasticity.1970 :259-285.

[6] R., A., Schapery. Nonlinear Viscoelastic Solids. International Journal of Solids and Structures. 2000; 37:359-366.

Experimental study of the Probe Pre-travel Bending Error

Simi Li [1], Dingwen Yu [1], Long Zeng [2*], and Pingfa Feng [1,2]
[1] Department of Mechanical Engineering
Tsinghua University
Beijing, P.R.China
[2] Tsinghua Shenzhen International Graduate School
Tsinghua University
Shenzhen, P.R.China

1 INSTRUCTIONS

On-machine inspection (OMI) system is being increasingly important in inter-process inspection and verification of dimensional quality of large part or deformation-prone parts. In addition, it is widely applied in automatic workpiece set-up and identification of machine tool's kinematic errors [1]. Touch-trigger probe is the widely applied in OMI systems that the kinematic probe and the gauge strain probe are the most popular ones. The pre-travel errors of both two kinds of probes are anisotropy. Therefore, many researchers have studied the method of modeling of touch-trigger probe pre-travel errors. The bending deflection of the probe stylus caused by different triggering force is a key factor of the pre-travel error anisotropy.In this paper, the probe pre-travel error caused by the bending of the probe stylus (EBBC) is identified.

2 MECHANICAL MODEL FOR THE PROBE STYLUS BENDING

To build the mechanical model for the probe stylus bending, first of all, we need to analyze the bending of the probe stylus installed on the probe in the actual measurement process. Subsequently, based on the assumption that the probe stylus only bending before the probe triggers, a mechanical model of the cantilever beam of the measuring rod is established.

0 shows the measuring process of the touch trigger probe. ω_i is the probe pre-travel error that defined as the distance between the initial contact position P_{ideal} and the position of trigger signal generating P_i. The trigger signal is generated when the trigger force lifts the internal mechanism of the probe. The bending of the probe stylus caused by the trigger force is the main reason for the anisotropy of the probe's pre-travel error.

Generally, the pre-travel error can be calibrated by measuring a reference sphere. According to the known distance of r_{ideal} , the best fitting reference sphere center C by all measurement points and the measurement result P_i, the pre-travel error ω_i can be calculated by

$$\omega_i = r_{ideal} - r_i \quad (1)$$

where r_i is the distance of the CP_i. Additionally, the pre-travel error mainly contains two parts: error caused by stylus bending d_B and error caused by signal transition delay d_S. The later one can be calculated by difference of pre-travel errors in the different velocities.

$$d_B = \frac{P^3}{3EI} \cdot F_h \quad (2)$$

$$d_c = \frac{4P}{\pi D^2 E} \cdot F_v \quad (3)$$

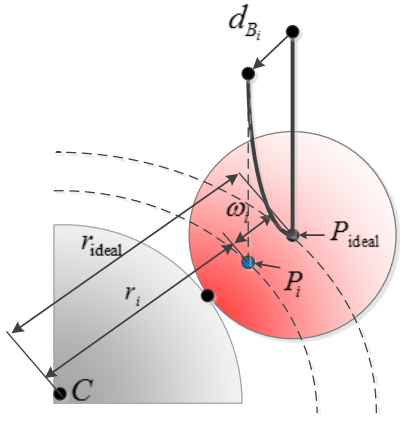

FIGURE 1. Probe error and pre-travel formation process

To study the probe stylus bending deflection, the probe can be assume to be a cantilever beam (as shown in *FIGURE 1*). The angle between the triggering force and the probe stylus is θ, and the triggering force can be divided into bending force F_h and compress force F_v. The bending deflection dB can be calculated by

$$d_B = \frac{P^3}{3EI} \cdot F_h . \quad (4)$$

$$d_c = \frac{4P}{\pi D^2 E} \cdot F_v . \quad (5)$$

*Corresponding auther. Tel: +86 75526035922; E-mail address: zenglong@sz.tsinghua.edu.cn

Where P is the length of probe stylus that is 100mm approximately, D is diameter of the probe stylus that is 3mm approximately and E is the elastic module of the probe stylus. Setting $I = \pi D^4/64$ for a circular cross section.

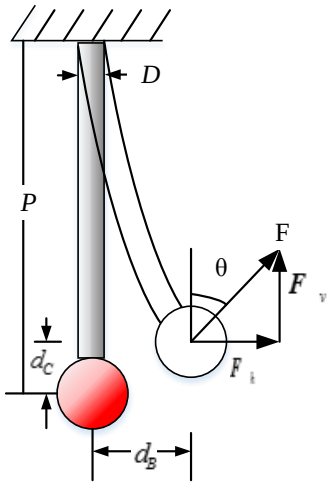

FIGURE 2. The cantilever beam model of the probe stylus

To calculate the deflection of the probe stylus, the triggering forces in different directions and the elastic modules E have to be solved. The triggering force could be measured by using a multi-axis force sensor and the elastic modules E can be solved by cantilever beam bending experiments.

3 PARAMETER COMPUTATION WITH EXPERIMENTS DATA

In order to compute the unknown parameters in the mechanical model above, two experiments are conducted. First, the experiment is conducted to measure the probe triggering force in different directions. Second, an experiment is conducted to measure the corresponding relationship between the contact force and the bending deflection. According to equation (2) and (3), the elastic modules E could be calculated. Based on these two experiments, the bending of probe stylus in different measurement directions can be computed.

3.1 Measurement of the triggering force

To measurement the triggering force in three axis, the measurement setup is shown in *FIGURE 3*. The touch-trigger probe is mounted on the spindle of a three-axis CNC machine tool and the 30mm diameter reference sphere is mounted on the multi-axis force sensor. The probe stylus length are 50mm and 100mm respectively and the measurement speed are 200mm/min, 300 mm/min. The probe approaches the reference sphere in different directions, the OMI system records the trigger position in the workpiece coordinate and the force sensor records three-axis force changing in the whole measurement process. The distribution of measurement points is shown in *FIGURE 4*. To observe the change trend with different polar angles and azimuth angles, there are 37 points distributed on 0°and 180°longitude line and 37 points distributed on the equator line. The polar angles of measurement points on 0° and 180° longitude lines are 0°, 5°,…, 90°. The azimuth angles of measurement points on the equator line are 0°, 10°,…,360°.

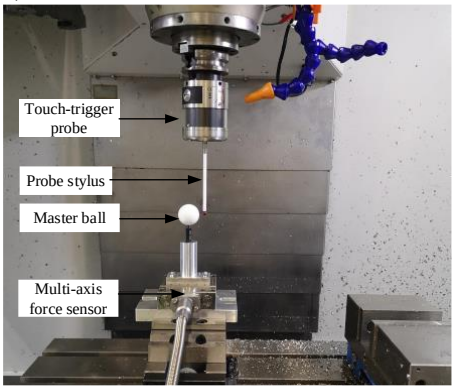

FIGURE 3. Measurement of probe triggering force in different directions

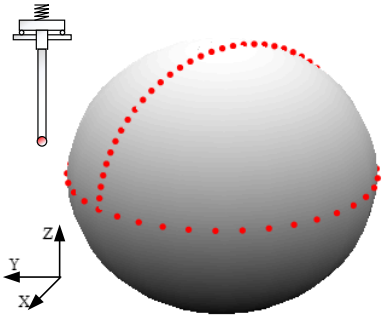

FIGURE 4. Distribution of measurement points

The triggering force measurement results along the longitude line are shown in *FIGURE 5* and that of along the equator line is shown in *FIGURE 6*. According to the measured results, although the measuring force fluctuates slightly at different measuring speeds, it can be considered that it is caused by random errors, so the change of measuring speed will not affect the triggering force. In addition, the length of the probe stylus has a great influence on the triggering force, the X component of the trigger force of the probe installed with a 50 mm stylus is almost twice as large as that installed with a 100 mm stylus. As shown in *FIGURE 5(a)*, although the total triggering force decreases with the increase of the polar angle along the longitude, the component of the triggering force in the X

*Corresponding auther. Tel: +86 75526035922; E-mail address: zenglong@sz.tsinghua.edu.cn

direction increases with the increase of the polar angle. The component of trigger force in Z direction leads to the compression of measuring rod. According to the research by Estler[3], comparing with the bending of the probe stylus, the compression of the probe stylus is relatively small and negligible. Therefore, the deflection of the probe stylus can be calculated according to the component of the trigger force in the X direction. The triggering force in the X direction changing with the polar angle is shown in *FIGURE* 5*(b)*. The triggering force changing with the azimuth angle is shown in *FIGURE 6* that shows a trend of triangular change.

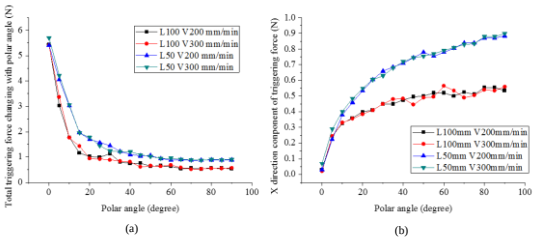

FIGURE 5. Total triggering force and x-direction triggering force of two different length stylus at two velocities

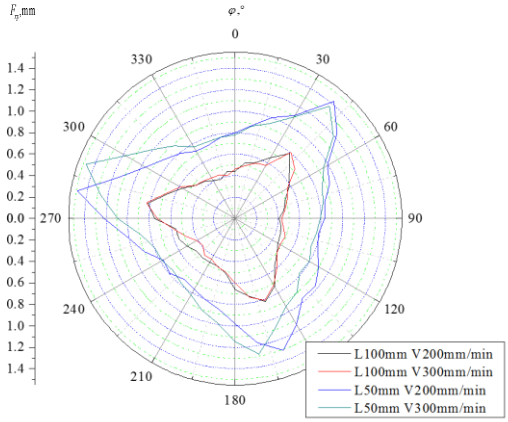

FIGURE 6. Total triggering force changing with azimuth angle of two different length stylus at two velocities

3.2 Identification method for elastic modules

To calculate the bending elastic modules E in equation (2), the bending deflection and the corresponding contact force should be measured simultaneously. The measurement setup is shown in *FIGURE 7*. The probe stylus direct mounted on the machine tool spindle through a tool shank without the touch-trigger probe. In this case, the probe stylus and the spindle construct to be a real cantilever beam. The length of probe styluses are 50 mm and 100 mm respectively and diameter is 3 mm. A rectangle workpiece is mounted on the multi-axis force sensor while the force sensor is mounted on the workbench. The experiment follows four step:

Firstly, adjust the machine tool to the Handwheel control module. Control the probe stylus gradually approached the workpiece that mounted on the force sensor. At the same time observe the force sensor, stop the probe stylus movement when there is force detected.

Secondly, adjust the movement step to 1 μm and gradually away from the workpiece, meanwhile observe the force sensor, stop when the detected force returns to zero.

Thirdly, adjust the machine tool to automatic control module. Control the probe stylus gradually approach to workpiece in a certain speed and detect the three-axis contact force simultaneously. Because of the machine tool backlash, the contact force may be detect after a while.

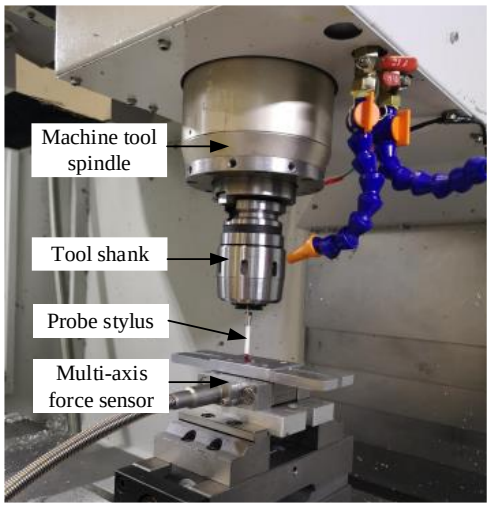

FIGURE 7. Measurement of probe stylus bending and the corresponding force

The bending deflection and corresponding bending force changing trend is shown in *FIGURE 8*. Because in the elastic deformation range, the bending deflection and bending stress of the probe stylus are linear. The elastic module of two styluses are calculated by equation (2), which are 189 Gpa for 100 mm length stylus and 95 Gpa for 50 mm length stylus respectively. Because the pre-travel error of the probe is directly related to the bending deflection of the probe stylus, a longer probe stylus needs a larger modulus of elasticity to ensure that the pre-travel error is not too large.

*Corresponding auther. Tel: +86 75526035922; E-mail address: zenglong@sz.tsinghua.edu.cn

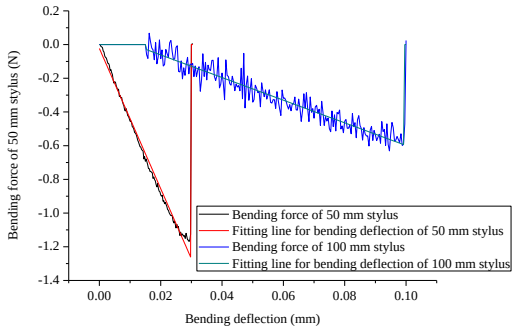
Bending force of 50 mm stylus (N)
Bending deflection (mm)
Bending force of 50 mm stylus
Fitting line for bending deflection of 50 mm stylus
Bending force of 100 mm stylus
Fitting line for bending deflection of 100 mm stylus

FIGURE 8. Measurement of probe stylus bending and the corresponding force

4 VERIFICATION EXPERIMENT

In order to identify the proportion of the pre-travel error caused by the bending of the stylus in the total pre-travel error, a validation experiment was carried out. The pre-travel error and triggering force are measured in the experiment simultaneously and the pre-travel error caused by the bending of the stylus can be calculated by method mentioned above, subsequently, the proportion of that is identified.

The OMI experiment was carried out on a commercial middle size CNC machining center with a workspace of $850\,\mathrm{mm} \times 500\,\mathrm{mm} \times 550\,\mathrm{mm}$. A Renishaw RMP-60 kinematic touch-trigger probe (stylus length: 100mm, ruby diameter: 6mm) was mounted on the machine tool's spindle to calibrate a reference sphere with a diameter of 30mm (shown in *FIGURE 3*). The distribution of measurement points is same as triggering force identification process.

Pre-travel error of probe can be calculated by measuring trigger force and signal transmission error of probe. 0 shows the variation trend of the probe's pre-travel error changing with the azimuth angle. The black line and red line represent the modeling calculation results and experimental calibration results when the measuring speed is 200 mm/min, and the blue line and green line represent the modeling calculation results and experimental calibration results when the measuring speed is 200 mm/min. Increasing speed will increase the error caused by signal transmission, but will not affect the error caused by the bending of the probe stylus. However, to the probe's pre-travel error which varies with the polar angle, the errors of modeling and calibration results are large (as shown in *FIGURE 10*). This is because of the relative sliding between probe and object under test. Therefore, the anisotropy of the probe pre-travel error is mainly caused by the probe stylus bending in different triggering force.

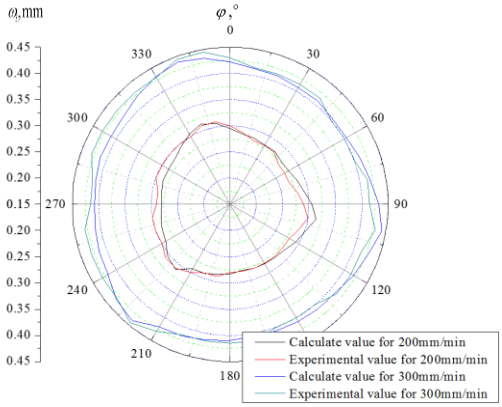

FIGURE 9. Comparison of calculate value and experimental value of pre-travel errors changing with azimuth angle in different velocities

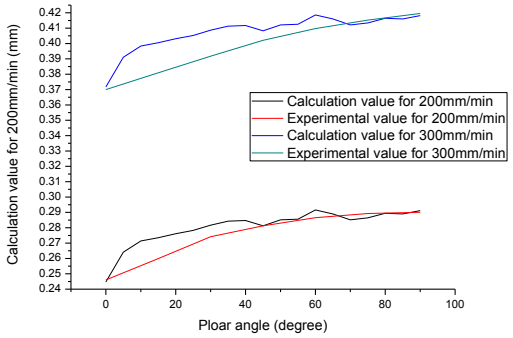
Calculation value for 200mm/min (mm)
Ploar angle (degree)
Calculation value for 200mm/min
Experimental value for 200mm/min
Calculation value for 300mm/min
Experimental value for 300mm/min

FIGURE 10. Comparison of calculate value and experimental value of pre-travel errors changing with polar angle in different velocities

Acknowledgements This paper is supported by Shenzhen Technical Research Project (Grant No.JSGG20180507181638381)
Shenzhen Foundational Research Project (Grant No.JCYJ20180508152128308).
National Defense Basic Scientific Research Program (Grant No. JCKY2018208B014)

REFERENCES

[1] Ibaraki S., Iritani T., and Matsushita T., Calibration of location errors of rotary axes on five-axis machine tools by on-the-machine measurement using a touch-trigger probe. International Journal of Machine Tools and Manufacture, 2012. 58: p. 44-53.
[2] W. Tyler Estler S.D.P., Error compensation for CMM touch trigger probes. 1996: Precision Egnineering

*Corresponding auther. Tel: +86 75526035922; E-mail address: zenglong@sz.tsinghua.edu.cn

LOW COST PLATFORM FOR HYBRID MANUFACTURING OF LIGHT METALS

Justin West, Emma Betters, and Tony Schmitz
Department of Mechanical, Aerospace, and Biomedical Engineering
University of Tennessee, Knoxville, TN

ABSTRACT
Wire arc additive manufacturing (WAAM) uses an electric arc to locally melt and fuse wire to build parts layer by layer. The benefits are a high deposition rate, dense final structures, compatibility with light metals such as aluminum and magnesium, and low cost. In gas metal arc welding (GMAW), wire is fed continuously into the arc where it is melted to form a bead. WAAM parts typically need to be finish machined to achieve the desired final part geometry and surface finish on functional surfaces.

This creates a challenge when moving from an additive machine to a traditional machining center, as it is difficult to align machine axes without reference features. One potential solution is hybrid manufacturing, where the additive process and machining center are coupled. The work coordinate systems for the additive deposition and subtractive machining spindle are set from the same reference, enabling the part to be built and machined in the same setup. This reduces the required overbuild to ensure the part is encompassed by the printed structure and decreases setup time.

In this work, a commercial gas metal arc welder was mounted adjacent to a machine spindle and is triggered using the machine controller. A fixture plate was designed to isolate the machine from the thermal and current input. To develop an understanding of the process, a 5356 aluminum wire alloy was chosen as a less expensive and better understood alternative to more costly light metals, such as magnesium.

Keywords: Hybrid manufacturing, wire arc additive manufacturing, aluminum

INTRODUCTION
The additive manufacturing sector has grown from making small plastic parts to a technology promising flight-ready hardware built from expensive and difficult-to-machine materials, such as titanium and Inconel. Many processes have been developed in the metal additive space, with the main groups being powder bed, blown powder, and wire fed systems. Each of these systems uses an energy source to locally melt metal and build parts layer by layer starting from a build plate.

Additive manufacturing of metallic components dates to 1997, when AeroMet developed a Laser Additive Manufacturing (LAM) system to produce titanium components from powder [1]. Development of additive technology in the following years included the rise of a wide range of powder-based systems including powder fed, powder bed, and blown powder types. Melt energy sources for powder systems include fiber lasers, electron beams, and disk lasers [2]. Wire fed additive systems typically use electron beam, laser, and plasma arc heat sources which are used to locally melt wire into a bead.

Processes that use powder as the filler metal tend to produce parts with a higher resolution, down to a few micrometers, and better surface finish, but sacrifice build rate and part density. They are costly (the typical price for a powder based system in 2012 was $1M [3]) and handling of powders can pose environmental health and safety concerns. Wire fed systems can achieve the highest deposition rates and good final part density, but the resolution is limited by the size of the wire, deposition velocity, and material. In almost all cases, parts need some post processing, usually machining, to meet the required geometry or surface finish requirements.

While it seems more desirable to print parts as close to the final geometry as possible, this often results in a preform that does not contain the final part and is difficult or impossible to machine due to geometry or lack of stiffness. Given that post-machining is already a requirement, it is advantageous to choose an additive process that will give the highest build rates with less emphasis given to surface finish or resolution. For this reason, wire arc additive is the process often selected to produce large preforms in a minimum time frame. Wire is also more readily available, cheaper, and more stable than powdered metal.

For the majority of manufacturing job shops, a $1M investment, for example, in an emerging

technology with significant challenges is difficult to justify, so a low cost, easy to implement solution is an essential first step to familiarize a large share of the workforce with the additive process. This paper outlines the development and use of a commercial gas metal arc welder and a three axis CNC milling machine (two units found in most machine shops) for use in WAAM of aluminum hybrid components.

While development of additive technology in metals has historically been driven by materials which are more cost prohibitive to machine, a 5356 aluminum wire alloy was chosen as a less expensive and better understood alternative to more costly light metals, such as magnesium, to develop an understanding of the process. Future work will be conducted in magnesium alloys due to its high strength to weight ratio.

DESIGN

Equipment selection

The general design goals for this platform were to keep cost, complexity, and machine modifications to a minimum to promote a cost effective and easy to implement system; see Fig. 1. The build materials of interest for this project are aluminum and magnesium alloys. Aluminum was selected as the initial build material as a cost-effective and better understood substitute for magnesium.

A pulse capable Miller 350P gas metal arc welder was chosen as the voltage and wire source. It has a 100% duty cycle at 225 A allowing for continuous operation and a maximum wire feed speed of 800 ipm. The welder has a push/pull style torch, where a small set of rollers feed the wire from the torch end and a slave motor rotates the wire spool. This configuration reduces the strain on the wire and prevents breakage and thinning.

A three axis Haas TM-1 VMC is used as the base for the hybrid platform. It has a maximum table feed rate of 200 ipm, maximum work volume of 30 in × 12 in × 16 in, and a maximum spindle speed of 4000 rpm.

CNC integration

Electrical

A wiring harness was built to divert the trigger circuit from weld torch to the Haas TM-1 controller. The harness connects to the existing machine and torch connectors and links the trigger circuit to a relay in the TM-1 electrical cabinet. The relay allows the gun to be turned on and off using an M code in the machine controller; see Fig. 2.

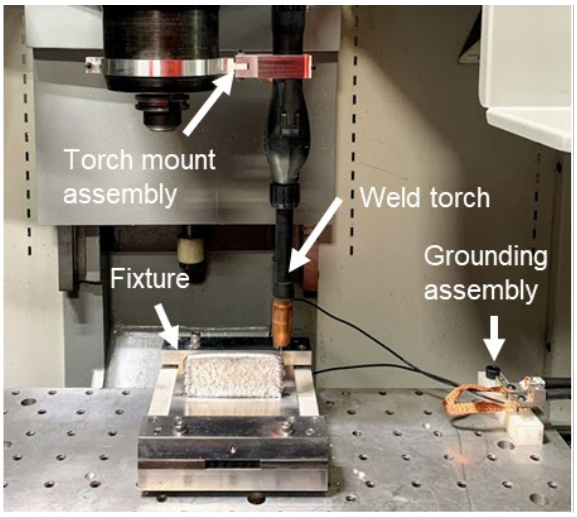

Figure 1: Front view of hybrid setup.

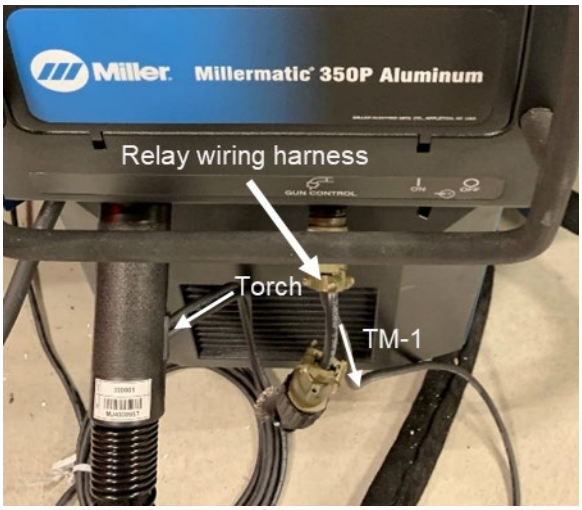

Figure 2: Welder trigger CNC integration cable.

Torch mount

Clamping the torch directly in the spindle would limit the hybrid work volume and require extensive modification to the machine and welder. The torch extension length was chosen to reduce the effects from the heat of the weld zone on the spindle. The clamp is comprised of a semi-permanent spindle ring and torch holder. The spindle ring is installed over the spindle and indicated so that the front of the mounting tab is parallel to the Y (horizontal) axis. The torch is mounted in the torch holder with a slight interference fit and compression from a fastened back plate. Two fasteners are used to connect the spindle ring and torch mount for easy installation and removal. The torch position is nominally perpendicular to the table; however, there is some deviation due to the lack of fine adjustment

in the mount. An empty low projection length tool holder is loaded in the spindle to prevent any spatter or debris from collecting in the taper; see Fig. 3.

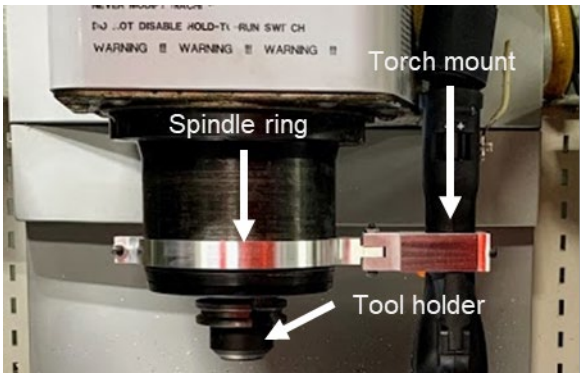

Figure 3: Assembled torch mount.

Fixture

Mechanical

The build fixture is composed of six parts: aluminum jaws, ceramic insulator, titanium spacer, steel base plate, steel spacer, and the grounding assembly. The overall dimensions are 10 in × 10 in × 2.5 in; see Fig. 4. The base plate is bolted directly to the machine table through two countersunk holes located on either side of a center locating bore. A steel spacer with clearance holes for the table bolts is under the base plate. Steel was selected for its low cost, machinability, and higher electrical resistance than aluminum. The build plate is clamped between the aluminum jaws and titanium spacers. Titanium was chosen for its low thermal and electrical conductivity and corrosion resistance at elevated temperatures. The spacers do not run the length of the base plate to reduce contact with the build plate. The spacers, jaws, base plate, and spacer were machined to be flat and parallel to ±0.0015 in. The jaws are located with ground pins that are fixed in the steel base plate and have a RC1 close sliding fit with the jaws. Slots were machined into the jaws to reduce the moment on the locating pins while clamping and allow for plate growth in the Y direction. The clamping force is supplied by two stainless steel fasteners. While building the preform, the fasteners are tightened just enough to bring the jaw into contact with the build plate. This constrains the plate movement and thermal growth in the Z (vertical) direction, but allows it to grow freely in the XY plane. The intent was to limit the build plate distortion by avoiding over constraint of the plate during the build. For builds that require heavy material removal, additional fasteners can be added to directly clamp the build plate to the base plate. A precision bore in the center of the fixture base plate is used to set the work coordinate system of both the machining spindle and weld torch. The bore is a 0.002 in clearance fit for the weld torch nozzle; see Fig. 4.

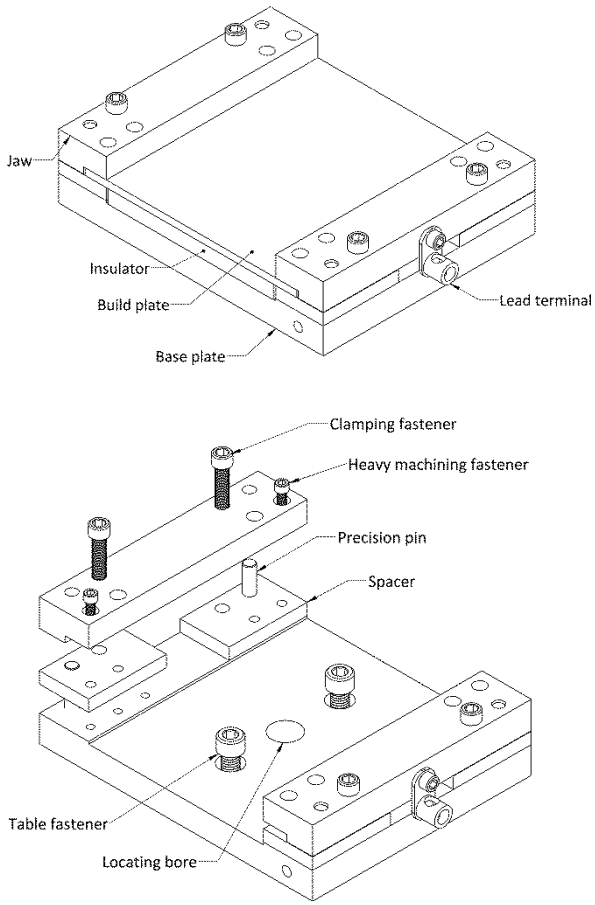

Figure 4: Assembled and exploded view. Build plate and insulator hidden on the exploded view.

Thermal

One of the challenges of coupling an additive process and a machine tool is the heat generation. When the build plate is directly mounted to the machine table, the heat from the build moves from the build area to the table, guide ways, spindle, and base casting. As these components heat up, errors are induced in the machine. Without any isolation from the build process, the machine should be allowed to reach a steady state temperature before finish machining or be compensated for the thermal growth. Since a machine tool takes many hours to return to thermal equilibrium, it is advantageous to isolate the build area from the machine tool. The fixture designed for this

platform uses a high-strength calcium silicate ceramic sheet as a thermal insulator under the build plate to limit the heat transfer to the machine. The conduction pathway is through the contact between the aluminum jaws and the build plate. The jaws dissipate most of the remaining heat, with little energy transferring to the steel base plate through the titanium spacers. The steel base plate rests on a spacer, increasing the surface area for convection and minimizing the area contacting the machine tool table.

Electrical

The welding process requires a path back to the welding unit to complete the circuit. The main copper work lead (sized from the manufacturer recommendation) is bolted directly to the aluminum jaw, creating the lowest impedance path back to the welder. Titanium and steel were used for the spacers and base plate, respectively, in part for their higher electrical resistance. Secondary smaller leads are connected to both ends of the machine table and the steel base plate. The main and secondary leads are connected to a common ground bar, which is connected back to the welder. The secondary leads help prevent erosion of the linear bearings from possible stray eddy currents and provide some protection to the controller in the case of a poorly grounded build plate.

SETUP

Coordinate systems

The torch mounting fixture is installed by aligning the mounting flange of the spindle ring to the Y axis of the machine. The weld gun is secured in the torch mount and the assembly is bolted to the spindle ring with two fasteners. The fixture is bolted to the machine table and aligned to the X axis using a test dial indicator. A probe is loaded into the machine spindle and is used to find the center of the bore. The weld torch is carefully lowered into the center bore to find the center. The tight clearance fit between the bore and weld gun nozzle allows for a repeatable zero (±0.001 in). The machining Z zero is set at the top of the build plate using the machine probe. The additive Z zero is set on the top of the build plate using the end of the contact tube.

Process parameters

The current procedure for determining additive parameters is trial and error with geometries of increasing complexity until a viable final part is produced. This platform does not allow for in process changes to the wire feed speed, so an initial wire feed speed was selected based on the manufacturer recommendation and the table feed rate was varied to establish a relationship with single beads. Using the table feed rate that produced a desirable bead geometry, a wall was printed and the parameters were adjusted to reduce the start and stop defects. The same process was repeated using a fixed table feed and varying the wire feed rate.

Build strategy

For non-linear geometry parts, a continuous spiral build path was chosen to eliminate start and stop defects and maximize the deposition rate. As the build increases in Z height, the table feed is increased to maintain a constant bead geometry by compensating for the additional heat in the part.

RESULTS

A low-cost hybrid system was successfully implemented with no modification required to the off-the-shelf components; see Fig. 5. The benefit of this approach is that it can be applied to most existing machine tools and gas metal arc welders, enabling broader adoption of hybrid techniques without the need for a large capital investment.

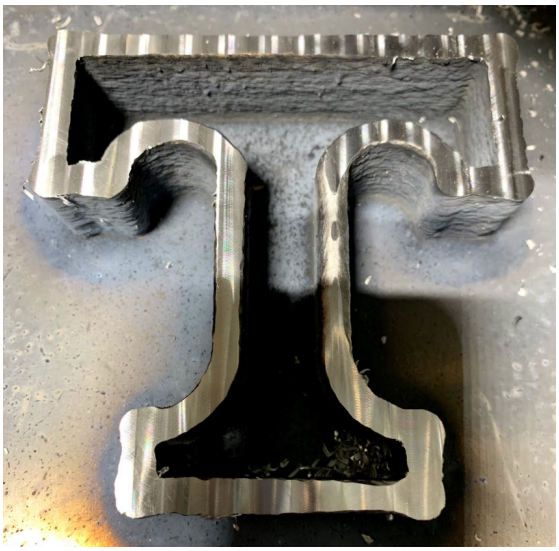

Figure 5: First successful complex shape part and final machining operation on the hybrid platform.

The fixture proved to be a repeatable way to set the work coordinate system (WCS) of the spindle and torch. While the WCS was defined from the same feature, an error in the torch mount design caused some part misalignment that defeated the purpose of the shared coordinate system. The torch was not able to be aligned perpendicular to the table and would shift if

bumped during setup. This resulted in the final parts being shifted by approximately 0.050 in from the machine spindle center. Depending on the final part geometry and overbuild, this level of accuracy may be sufficient.

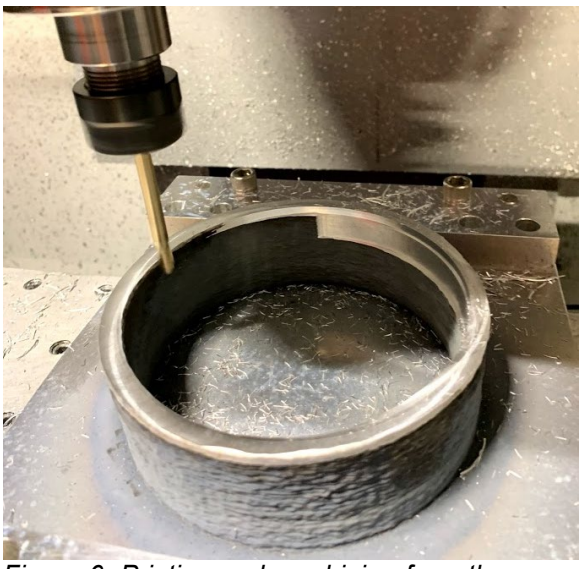

Figure 6: Printing and machining from the same locating feature. Note the part shift and uneven machined surface.

The effect of the build plate clamping condition on final part distortion was tested using identical build geometries, paths, build plate material, and build plate geometry. There was some variation in the wire feed rate for the first five beads between builds. Cylinders were built as a continuous spiral on a room temperature build plate fixture; see Fig. 6. The first build plate had clearance holes (0.266 in) drilled in the corners for the heavy machining fasteners (¼-28). The fasteners were placed in the holes but not tightened. When the plate had cooled, imprints of the threads could be seen in the clearance holes, suggesting the plate grew sufficiently to press into the fasteners. The plates were flat to within 0.005 in before the build. The most part distortion was observed in the first build, with the highest clamping torque and fasteners in place. The lowest distortion was observed in the builds with just enough torque to bring the jaw into contact with the plate and no fasteners in place. The plate distortion was measured by placing the plates on a flat surface and measuring the height of the warped section and subtracting the plate thickness measured at that point. No distortion was noted at the clamped ends. These are preliminary results and more work is needed to test the effect on a larger sample size and on other non-symmetric build geometries; see Fig. 7.

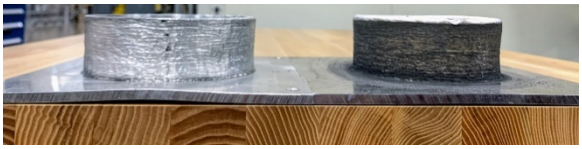

Figure 7: Comparison of two builds with identical build parameters and different clamping conditions.

Table 1: Clamping torque and distortion.

Clamping torque (ft-lb)	Maximum distortion (in)
40	0.106
20	0.086
5	0.024

(Bolt torque ±5%, distortion ±0.005)

FUTURE WORK

A new fixture and torch mounting assembly will be designed to address some of the process issues, including torch perpendicularity, better thermal isolation, and a reduction in the XY plane constraints. The effects of clamping conditions on final part distortion and residual stress is of great interest. It is possible that constraining additive parts purely in the build direction would significantly reduce the residual stresses. A model of the process will be developed to predict bead behavior at varying wire and table feed rates with the goal of controlling bead and part geometry effect in an open loop system. Minimizing the number of sensors and control systems keeps the barrier to entry low and allows for better final part geometry predictions. Magnesium alloys will be tested for their compatibility with the WAAM process.

CONCLUSIONS

The bulk of manufacturing occurs in small job shops that do not have the resources to make large capital investments in an emerging technology. With the approach described here, it is possible to build a hybrid system with a small investment. An easy-to-implement and inexpensive solution allows the technology to spread from machine tool manufacturers and research labs to every corner of the manufacturing sector. Through the implementation of this platform, it was observed that over constraining build plates in additive processes contributes significantly to the final part residual stresses and warping. Implementing a fixturing system that constrains the build plate in the part direction while allowing it to grow in the

planar directions may significantly reduce these residual stresses.

ACKNOWLEDGMENTS
The authors gratefully acknowledge financial support from Department of Defense (Funding Opportunity Announcement W911NF-17-S-0010).

REFERENCES
[1] Wohlers, Terry, and Tim Gornet. "History of additive manufacturing." *Wohlers report* 24.2014 (2014): 118.
[2] Frazier, W.E. J. of Materi Eng and Perform (2014) 23: 1917. https://doi.org/10.1007/s11665-014-0958-z
[3] Thomas, Douglas S. and Stanley W Gilbert. "NIST Special Publication 1176 Costs and Cost Effectiveness of Additive Manufacturing A Literature Review and Discussion." (2014)

APPENDIX A: SETUP DETAILS
A summary of the platform specifications is provided in Table A1.

Table A1: Platform specifications.

Wire alloy	5356 aluminum
Wire diameter	0.047 in
Build plate alloy	5052 aluminum
Build plate thickness	0.25 in
Shielding gas	99.995% argon
Gas flow rate	45 cfh
Wire feed range	200 ipm to 450 ipm
Table feed range	35 ipm to 100 ipm

Development of temperature control system for machine tools

Seiya Kodaka[1], Bima Kawase[1], Jumpei Kusuyama[2] and Yohichi Nakao[2]
[1]Graduate School of Mechanical Engineering
Kanagawa University
Yokohama, Kanagawa, JAPAN
[2]Department of Mechanical Engineering
Kanagawa University
Yokohama, Kanagawa, JAPAN

INTRODUCTION

Recently, requirements of precision machining are becoming increasing for precision components that are used in optical, aircraft and other various industries[1]. In the precision machining, the thermal deformation of machine tool is one of the main cause that deteriorates the machining accuracies. Therefore, minimizing the thermal deformation due to temperature change of the machine tool is in particularly important[2]. For example, the machining error is caused by thermal deformation of built-in motor spindle of the machine tools, specifically, caused by the power losses of the built-in motor and the frictional losses of bearings[3].

Accordingly, temperature control of the machine tool components, especially, spindle, is significantly important to improve machining accuracy. In general, a forced fluid cooling is used for removing generated heat from the machine tool or the specific component. In this case, it is necessary to determine the appropriate cooling conditions to achieve desired machining result, according to the heat generations in the machine tool. It is furthermore desired to control the temperature according to the heat generation change during machining operations. However, effective temperature control technique has not been established yet. In commercialized machine tool, for example, cooling system that supplies cooling fluid to the spindle is used[4]. A practical method easily used is that the temperature of the fluid is controlled according to spindle speeds[5]. However, the spindle temperature is not necessarily determined by only spindle speed.

In addition, there are two limitations in terms of the performances of the conventional chillers. One of them is that the chiller does not have appropriate temperature control resolution. Second, control response of the chiller is not enough if further improvement of the machine tool temperature control is required.

In this study, we propose a new method of fluid temperature control that achieves precise temperature control with improved response. In this proposed method, the temperature of cooling fluid is controlled by mixing fluids that are different temperatures. In this case, the temperature of mixed fluid can be determined by the mixing rate of the flows, that can be made by controlling the flowrates of two fluids. Accordingly, precise control accuracy with better control response are expected. Although the proposed technique is used to control water temperature and component, the proposed technique can be easily applied to various cooling fluids, such as oil and water.

In the rest of this paper, principle and structure of the developed temperature control system are firstly described. Fundamental guidelines for designing the proposed control system are then introduced based on a derived mathematical model. Effectiveness and control performances of this system are evaluated experimentally.

TEMPERATURE CONTROL SYSTEM

BASIC PRINCIPLE

Figure 1 shows the proposed temperature control system. In this system, the temperature of cooling fluid or controlled object such as spindle, depending on the applications, is feedbacked. The control system then controls flowrates of cooling fluids from two supply sources so that the temperature coincides the desired condition.

In this system, cooling fluids are supplied from two reservoirs, where predetermined volumes of waters with different temperatures are accumulated as depicted in Fig. 1. The fluid temperatures in the reservoirs are set so that target temperature of the controlled object can be between the temperatures of the fluids. The higher and lower temperatures of the fluids in the reservoirs are now denoted by T_h and T_l as shown in Fig. 1. For example, it might be easily made to

set T_h to the room temperature. In contrast, the lower temperature T_l can be controlled by a general chiller. In this case, a set of chiller is only needed for the system. As will be presented in experimental results, the proposed control system can achieve more precise control performances than chiller performances, in terms of the response and achievable temperature resolution.

As described, the temperature of supplied cooling fluid is controlled by the mixing two fluids with different temperatures, T_h and T_l, with appropriate flowrate ratio. In this case, temperature of mixed fluid can be directly controlled by not temperature but flowrate control. For example, the flowrate control can be made by flow control valves installed in each supplied channel of the fluids.

Accordingly, precise temperature control with better response is expected. Not only fluid temperature but also the temperature of controlled object can be controlled based on a feedback control technique using the proposed control system.

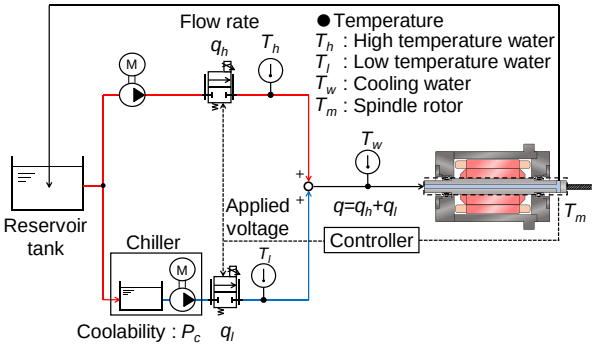

FIGURE 1. Principle of proposed temperature control

BASIC STRUCTURE OF DEVEROPED TEMPERATURE CONTROL SYSTEM

Figure 2 shows the constitution of developed temperature control system. In this system, the pump connected to a reservoir tank supplies fluid of temperature of T_h. In contrast, a chiller pump supplies the fluid of temperature of T_l. Furthermore, the overflowed fluid returns back to the reservoir in the chiller from the reservoir tank. Mixed and temperature controlled fluid is then supplied to the controlled object. The cooling fluid flowing though the controlled object is collected in the reservoir tank. Flowrates of supplied fluids of the temperature, T_h and T_l, are controlled using designed feedback controller so that the desired temperature of the mixed fluid can be made. Flow control valves that can be driven by applied voltages control the flowrates. According to requirements for the temperature control system, the temperature T_h can be chosen to be any temperature by a heater. In the most simple case, T_h is set be room temperature, as described. In the experiments, resistance thermometer sensors were used to measure temperatures of T_h and T_l, and the temperatures of the mixed fluid T_w and controlled object T_m.

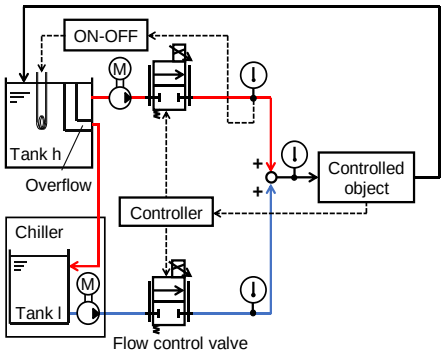

FIGURE 2. Fundamental structure of developed temperature control system

GUIDELINES FOR DESIGNING PROPOSED TEMPERATURE CONTROL SYSTEM

Guidelines for designing proposed temperature control system are introduced based on derived mathematical model. In Fig. 1, the higher side of the temperature fluid (T_h) is supplied by the flowrate (q_h) from the reservoir tank, and the lower side of temperature fluid (T_l) is supplied by the flowrate (q_l) from the chiller. By mixing the flows, the temperature of the mixed fluid can be controlled arbitrarily to be T_w that is between T_h and T_l, as given by Eq. (1).

$$T_w = \frac{q_h T_h + q_l T_l}{q_h + q_l} \tag{1}$$

The cooling fluid temperature (T_w) is determined by the flowrates and temperatures of the supplied fluids. In this study, flowrate of the mixed cooling fluid is constant to be $q = q_h + q_l$, though the condition can change.

Therefore, the relationship of the fluid temperatures of the proposed control system is given by Eq. (2).

$$T_l < T_w < T_h \tag{2}$$

The cooling water of temperature T_w is then supplied to controlled object of temperature T_m. To investigate performances of the developed control system, a component with the heat source

and cooling channel was designed and used for experiments. The designed component imitates a spindle structure equipped with shaft bore-cooling structure.

Cooling capacity by the supplied cooling fluid is defined as P_w. This study assumes that the cooling fluid is supplied to the spindle with shaft bore-cooling structure of the inner diameter (d) and length (l). The cooling capacity (P_w) is given by Eq. (3).

$$P_w = \alpha S\left(T_m - T_w\right) \tag{3}$$

In Eq. (3), α and S denote the heat transfer coefficient and surface area that the heat transfer is made between the inner surfaces and cooling fluid.

Heat transfer coefficient is given by Eq. (4) where λ, d and Nu denote the heat conductivity of water, inner diameter and the Nusselt number, respectively.

$$\alpha = \frac{\lambda Nu}{d} \tag{4}$$

If the flow inside the shaft-bore is turbulent, the Nusselt number is given by Gnielinski equation[6] as Eq. (5).

$$Nu = \frac{(f/2)(Re-1000)Pr}{1+12.7\sqrt{f/2}\left(Pr^{2/3}-1\right)} \tag{5}$$

In Eq. (5), f, Re and Pr denote the friction coefficient of the inner surface, Reynolds number and Prandtl number, respectively.

If the highest cooling performance of the control system is considered, a relationship between the cooling capacity of chiller (P_c) and temperature difference T_h-T_l is given by Eq. (6).

$$P_c = \rho q C_w \left(T_h - T_l\right) \tag{6}$$

Here, ρ, q and C_w are the density, flowrate and specific heat of fluid.

Following Eqns. (2), (3) and (6), cooling value range of this system is given by Eq. (7). when focusing on lower limit of cooling value in Eq. (7), it is determined by temperature difference between high cooling fluid (T_h) and controlled object (T_m). Therefore, the temperature control system can perfume not only cooling but also heating if T_h-T_m is negative value.

$$\begin{aligned} -\alpha S\left(T_h - T_m\right) &< P_w \\ &< \alpha S\frac{P_c}{\rho q C_w} - \alpha S\left(T_h - T_m\right) \end{aligned} \tag{7}$$

In the case of only cooling, by equalizing temperature, T_h and T_l, lower limit of cooling value become Zero.

Maximum cooling capacity (P_{wmax}) of the temperature control system determined by the flowrate and chiller performance given in Eq. (6) can be presented by Eq. (8).

$$P_{wmax} = \alpha S\frac{P_c}{\rho q C_w} \tag{8}$$

TEMPERATURE CONTROL OF COOLING FLUID

Performances of fluid temperature control of the developed temperature control system significantly affects the control performance of the controlled object. Therefore, temperature control accuracy and response of cooling fluid are evaluated experimentally, prior to the temperature control of the control object.

Figure 3 shows the cooling fluid temperature control system. In this experiment, the cooling fluid temperature was controlled by changing the ratio of the flowrates of the different temperature fluids. The control system uses a feedback control, achieving the water temperature of mixed fluid converges to the commanded temperature. In the experimental conditions, the water temperature (T_h) was 20 ℃, in contrast, the water temperature (T_l) was set to 15 ℃. Accordingly, the control system can control the water temperature between 15 ℃ and 20 ℃. Flowrate of cooling fluid (q) was chosen to be 7 L/min.

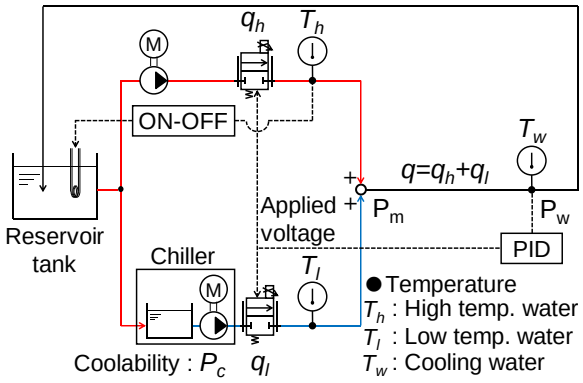

FIGURE 3. Cooling fluid temperature control system

Figure 4 shows the temperature error of the control system. As shown in Fig. 4, the temperature error was about ±0.01 ℃ during three hours experiment.

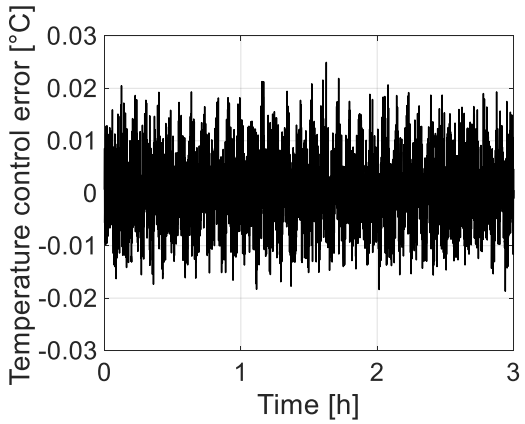

FIGURE 4. Control accuracy of cooling fluid temperature control system

Figure 5 shows a step response of the control system. In the experiment, the desired water temperature changed stepwise from 17.5℃ to 17.4℃. The control response of a conventional chiller was also evaluated. Temperature control error of the chiller and the developed control system are ±0.04 ℃ and ±0.01 ℃. Furthermore, the control responses were evaluated by the settling time as 162.0 seconds and 9.1 seconds, respectively. The results clearly indicate significant improvement in the control performance of the system.

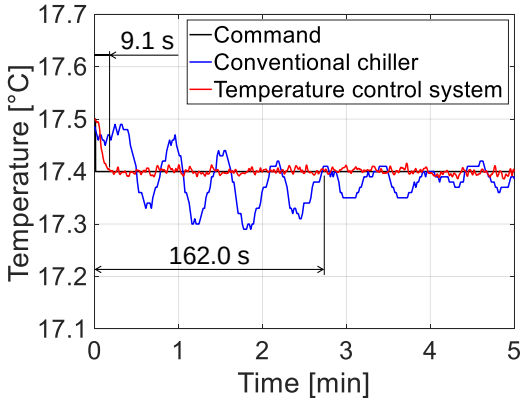

FIGURE 5. Control response of cooling fluid temperature control system and conventional chiller

Figure 6 shows transient response of the fluid temperature by the developed control system. It is considered that the total control delay of 9.1 seconds consists of the dead time of 1.9 seconds, and the first order lag of 7.2 seconds.

A cause of the delay due to dead time is now considered. As presented in Fig. 3, the temperature of mixed fluid was measured by a temperature sensor set at P_w that is downstream from the position of mixing point P_m. Considering the distance between P_m and P_w, and flow velocity, the dead time was estimated to be about 1.3 seconds. Therefore, the main cause of the dead time is due to the delay in the measurement to make feedback signal. The delay will be able to shorten by changing sensor position in the system.

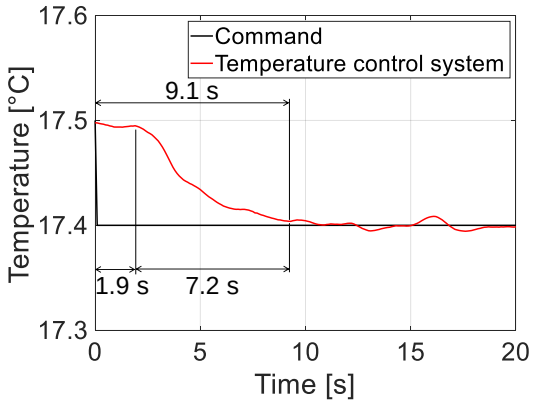

FIGURE 6. Time delay of cooling fluid temperature control system

The main cause of the first order lag in the control response was due to the characteristics of the thermometer that was used in the experiments. The influence of the dynamic characteristics of thermometer can be compensated by designing appropriate filter. Figure 7 shows transient response of the control system with a designed filter to compensate the dynamic characteristics of thermometer though further improvement is needed. Consequently, the time-lag reduces to 1.1 seconds. In total, the resultant delay becomes 3.0 seconds.

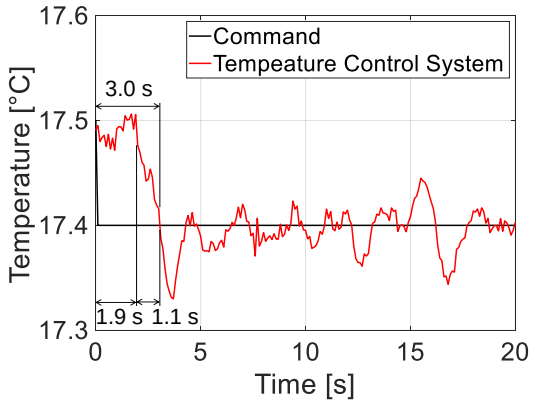

FIGURE 7. Transient response after compensation of delay of thermometer

TEMPERATURE CONTROL OF CONTROLLED OBJECT WITH HEAT SOURCE

The developed temperature control system was applied to control the temperature of a controlled

object with heat source. In Fig. 8, the temperature control system is depicted. In this experiment, a temperature of controlled object with heat source was controlled with different conditions of the heat sources. Basically, control conditions were the same as those described in the previous section. However, in the experiments, the control system was applied to control the temperature of not water but control object with heat generation. Desired control temperature of the controlled object was set to 20 ℃. Magnitude of the heat generation in the controlled object changed stepwise during experiments to examine the control performance.

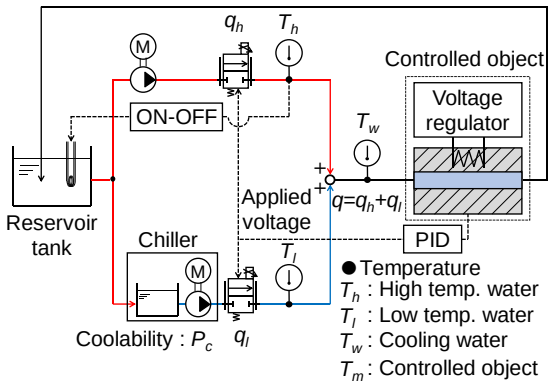

FIGURE 8. Developed temperature control system for controlled object with heat source

Experimental results are depicted in Fig. 9. To present an effectiveness of the developed control system, the experiments were carried out with or without the control system. During the experiments, the magnitude of heat generation changed from 90 W to 120 W at 15 minutes, and from 120 W to 90 W at 60 minutes. As presented in Fig. 9, the temperature of control object changes accordingly due to the heat generation.

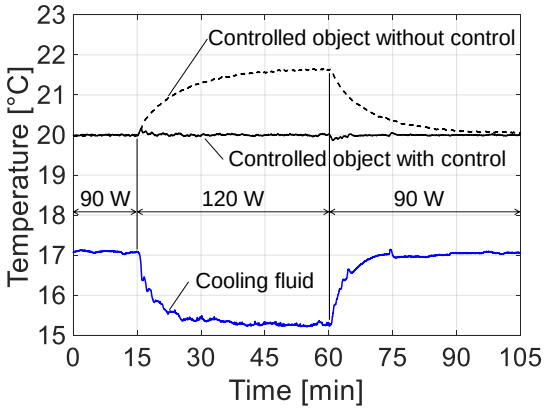

FIGURE 9. Temperature control result of the temperature control system

Temperature changes due to the change in the heat generation are presented in Fig. 10. If the feedback control system was not used, the control error reaches about 1.6 ℃. In contrast, the developed control system reduces the control error about ± 0.03 ℃.

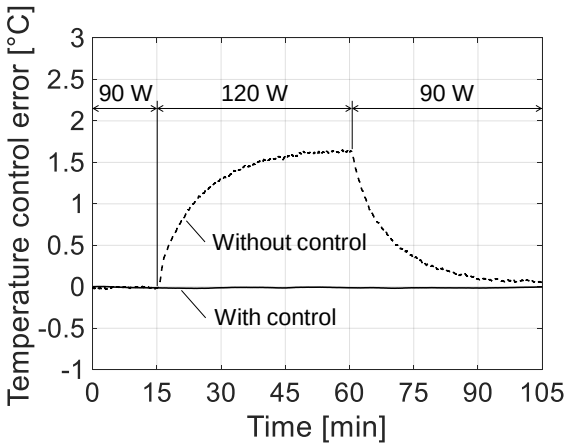

FIGURE 10. Comparison of Control accuracy of with and without control

Figure 11 shows the achievable control accuracy by the temperature control system. It is obvious that the temperature control error for the heated controlled object was about ±0.03 ℃, even the magnitude of heat generation changed from 90 W to 120 W. As presented, when the heating condition changed stepwise, the control error increased temporarily, however, it converged after a transient response of 4 minutes.

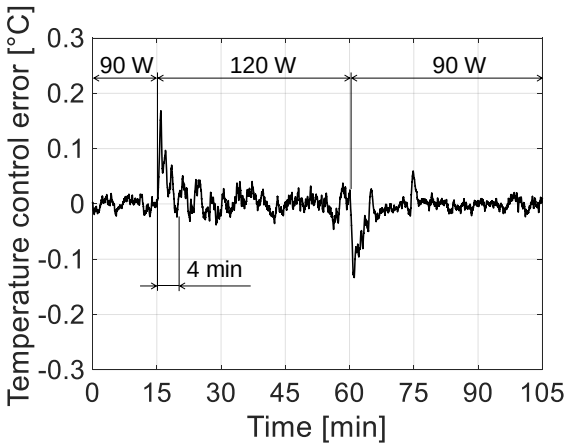

FIGURE 11. Control error by developed temperature control system

CONCLUSIONS

A novel control system that achieves precise temperature control with improved response was proposed aiming at better temperature control of

machine tool or its critical component such as spindle and stage. The effectiveness of the proposed control system was investigated experimentally. Fundamental guidelines for designing the proposed control system were introduced based on derived mathematical model, followed by explanations on the control principle and structure of the developed system. Then, the experimental evaluations yielded the following conclusions.

(1) Control performance of cooling fluid temperature was evaluated. The result showed that control accuracy was about ±0.01 ℃ and control response was about 3.0 seconds.

(2) Performances of the temperature control system for a controlled object with heat source were evaluated. The results showed that the control accuracy for the heated controlled object was about ±0.03 ℃ in the heating conditions of 90 W ~ 120 W.

(3) When the heating condition changed stepwise, the control error increased temporarily. However, the temperature converged after a transient response of 4 minutes.

REFERENCES

[1] Kawai T, Ebihara K, Yamamoto A. 5-axis Ultra Precision Nano Machine Tool by Means of Linear Motor Drive. JSPE. 75. 435. 2006.

[2] J Mayr, J Jedrzejewski, E Uhlmann, M. A. Donmez, W Knapp, F Hartig, K Wendt, T Moriwaki, P Shore, R Schmitt, C Brecher, T Wurz, K Wegener. Thermal issues in machine tools. CIRP Annals. 61. 2. 771-791. 2012.

[3] Y. H. Huang, C. W. Huang, Y. D. Chou, C. C. Ho. An Experimental and Numerical Study of the Thermal Issues of a High-speed Built-in Motor Spindle. Smart Science. 4. 3. 1-7. 2016.

[4] M. A. Donmez, M. H. Hahn, J. A. Soons. A Novel Cooling System to Reduce Thermally-Induced Errors of Machine Tools. CIRP Annals. 56. 1. 521-524. 2007.

[5] Nakayasu K, Akasaka H, Kaneko H, Sato H. Accuracy Improvement of Machine Tool by Machine Temperature Control. JSPE. 2008.

[6] The Japan Society of Mechanical Engineers.JSME data book : heat transfer 5th Edition: 2009.

Finite Element Modeling of Flash Thermography for Sub-Surface Defect Detection in Metals

Kevin A. Patel[1], Harish P. Cherukuri[1], Christopher J. Evans[1], and Angela Davies[1], Samuel Ludwig[1], Letchuman Sripragash[2]
[1]Department of Mechanical Engineering and Engineering Science
UNC Charlotte
Charlotte, NC, USA
[2]Siemens Corporate Technology
Charlotte, NC, USA

INTRODUCTION

The additive manufacturing technique is gaining attention because of its rapid prototyping ability, the ability to manufacture intricate geometries, and flexibility in changing designs. However, it suffers from drawbacks such as dimensional accuracy, surface finish and unfused powder particles. The unfused powder inside the artifact is mainly due to process parameters such as laser speed and laser power. These sorts of defects are responsible for the failure of the part. The goal is to employ a non-destructive testing technique as an in-situ to signify the presence of the defect early in the product development cycle so that manufacturing parameters can be changed to avoid the defect in the successive part.

In this work, the predictive capabilities of Flash Thermography, a non-destructive testing method, is used to detect the presence of defects in metallic parts via the Finite Element Method (FEM). An exact form of 1D heat conduction equation is developed for a square pulse heat source and finite width material [1]. This analytical form helps in understanding the heat diffusion in an artifact when the heat source is in the form of a square pulse. In this paper we explore the thermal signal processing technique "Coefficient maps" (CM) developed by Bin et al. (2018) [2]. The thermograms obtained from numerical results and experimental results are post-processed using the CM technique. Bin et al. showed that CM technique was successful in predicting the presence of the defect in SS-316l using the numerical and experimental results. The thermal properties of the materials play an important role in conducting heat through the material. Hence, to understand the influence of a defect on the temporal variation of the temperature, a defect in the form of a spherical air inclusion is modeled in four different materials, SS-316l, Ti-6Al-4V, Inconel 625, and copper using Abaqus. In order to closely approximate the heat source, the top surface of the artifact is exposed to a heat flux in the form of a square pulse for a few milliseconds. The heat source has been modeled based on the principle that heat diffusion time can be shorter than the flash duration. The change in the temperature of all the nodes on the top surface is recorded for each time-step.

This research focuses on testing the signal processing technique in predicting the presence of the defect at different depths for different materials and analyzing the defect maps to find the material parameter that would have a significant effect in signifying the presence of the defect. The study also shows the applicability and shortcomings of the signal processing technique. A comparison between numerical results and experimental results is presented to extract the vital information regarding the thermal property of the material that would affect the heat conduction process.

THEORY

The most common heat source considered in pulse heating is an optical flash lamp. In flash thermography, the flash is turned on for a few milliseconds to impart enough energy to raise the temperature of the specimen under inspection. All the simulations done in this work are based on a square heat-pulse. Also, in an in-situ measurement, the measurement is taken after melting a few layers of the AM part, so the approximation of semi-infinite material is not appropriate. Hence, for the purpose of modeling, the thickness of the artifact is considered as a finite thickness. The analytical solution for finite width plate with an insulated boundary condition and heat flux of the form of a square pulse is given by equation (1)

$$\Delta T_S^f(0,t) = \frac{Q}{\rho C_p L \tau}\left\{\left(tH(t) - (t-\tau)H(t-\tau)\right) + \sum_{n=1}^{\infty}\frac{2}{\alpha\lambda_n^2}\left[\left(1 - e^{-\alpha\lambda_n^2 t}\right)H(t) - \left(1 - e^{-\alpha\lambda_n^2(t-\tau)}\right)H(t-\tau)\right]\right\} \quad (1)$$

where, Q is the heat energy, τ is the duration of the heat flux, H is the Heaviside function, L is the thickness of the plate, and $\lambda_n = \frac{n\pi}{L}$

The numerical model was validated by comparing the temperature-time profile with the analytical solution for a finite plate of SS-316l (shown in Table 1) with square pulse heat flux. The numerical solution was obtained using ABAQUS Explicit. A plate with dimensions 2 mm × 2 mm × 0.2 mm was given the property of SS-316l with insulated boundary conditions and time step of 10 μs. The heat flux of magnitude 1 MW/m^2 is applied on the top surface for 2 ms as shown in Figure 1.

TABLE 1. Thermal Properties of SS-316l [3]

Material Properties	Thermal Conductivity κ (W/mK)	Density ρ(Kg/m^3)	Specific Heat Capacity C_p (J/KgK)
SS-316l	15	7970	510
Ti64	7.2	4470	560
Inconel 625	9.8	8400	433
Copper	398	8930	385

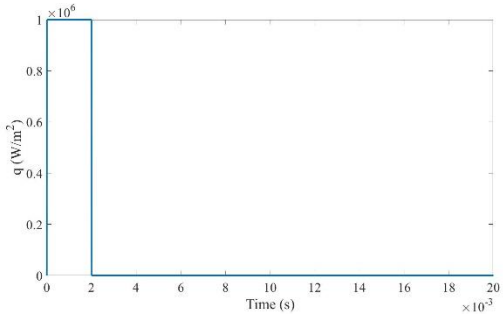

FIGURE 1. Square pulse heat flux.

The analytical and numerical solution plots shown in Figure 2 validates the accuracy of the numerical model. According to the percentage error plot shown along with the temperature-time profile, there is a slight difference in the numerical solution and the analytical solution when the heat flux is applied on the top surface. However,

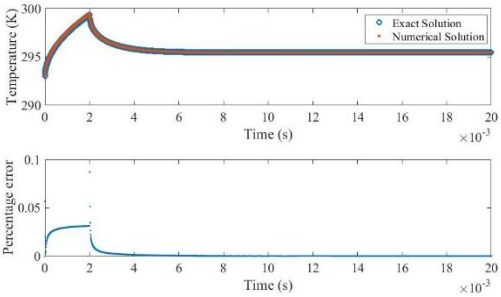

FIGURE 2. Exact and Numerical solution.

they are similar when the heat flux is turned off, and the sample is cooling. The error is because of the mesh size and the time increment used in the numerical analysis. By decreasing the time increment and the mesh size, the percentage error can be further minimized.

INTRODUCTION OF DEFECT IN DIFFERENT MATERIALS

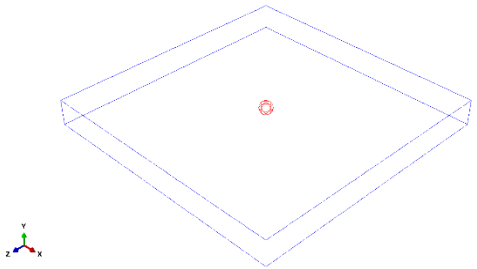

FIGURE 3. Air inclusion in an artifact.

A finite element model is developed in ABAQUS with a single defect, centrally located. With changing the depth of the defect, the change in temperature w.r.t time is extracted for all the nodes and they are converted to logarithmic scale. A linear portion of the logarithmic scale is analyzed and is curve-fitted using 1st order polynomial. The slope (b-map) and intercept (c-map) is calculated for all the surface nodes and a defect map is generated and analyzed to signify the presence of the defect. A spherical defect with a diameter of 100 μm is placed in the artifact. The material properties of the artifact are changed to study the effect of the presence of the defect on the defect maps. For this study the materials considered are mentioned in Table 1. The defect is considered as an air inclusion with the following properties:

TABLE 2. Thermal Properties of Air [3]

Thermal Conductivity κ (W/mK)	Density ρ(Kg/m^3)	Specific Heat Capacity C_p (J/KgK)
0.026	1.177	1005

The red section in Figure 3 represents a defect, i.e., air bubble located centrally in the 2 mm × 2 mm × 0.2 mm block. The heat flux of magnitude 0.1 MW/m^2 is applied on the top surface for 2 ms and the simulation runs for 20 ms. The defect is located 10μm from the top surface. The heat diffusion simulates a 1D heat diffusion model until the heat reaches the defect. As soon as the heat reaches the top surface of a defect, the heat transfer rate is affected, and a hot-spot appears on the top surface which signifies the presence of some discontinuity in the block. The region away from the defect will have a 1D heat diffusion. The temporal variation of the temperature for all the nodes on the top surface is recorded and exported to Matlab for post-processing. The data from first 2 ms is neglected since the heat flux is still on and only the cooling curves are observed to recreate the surface. A logarithm of the change in temperature is calculated and plotted against the logarithm of frame numbers for all the nodes. Then a linear portion of the log scale is curve fitted with a polynomial of the form f(x) =cx+b (c is the slope or c-map and b is the intercept or b-map). These coefficients are obtained for all the nodes, and a surface is passed through them using griddata. If discoloration is observed in the center, it signifies the presence of a defect.

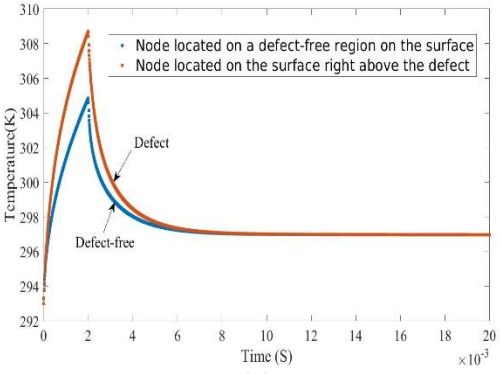

(a)

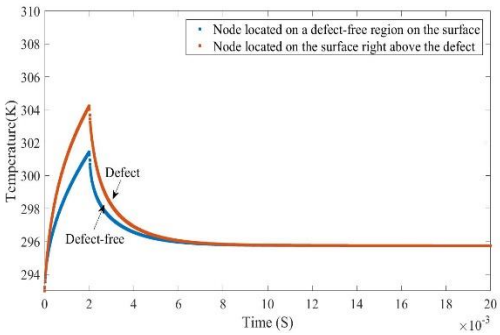

(b)

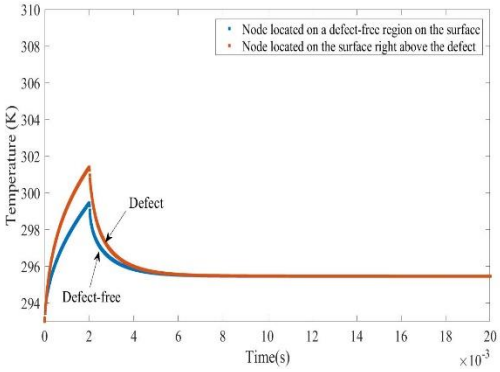

(c)

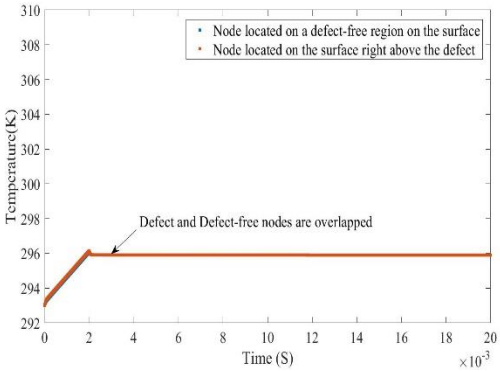
Node located on a defect-free region on the surface
Node located on the surface right above the defect
Defect and Defect-free nodes are overlapped
Temperature(K)
Time (S)
×10^-3
(d)

FIGURE 4. Temporal variation of temperature of (a) Ti-64, (b) Inconel 625, (c) SS-316l, and (d) Copper.

The temperature vs time profile shown in Figure 4 gives a temperature distribution of four different materials – Ti-64, Inconel 625, SS-316l and Copper. The temperature distribution of the defect-free node will follow the 1D heat diffusion model. However, the nodes over the defect will have a higher temperature due to the obstruction in the passage of the heat. The peak temperature is different for all four materials because of the thermal conductivity of the materials. Materials with higher heat capacity have the highest peak temperature and the peak temperature decreases

with decrease in the heat capacity. Copper having the highest thermal conductivity, have the smallest increase in the temperature. Copper conducts the heat at extremely high rate and reaches the equilibrium temperature in very short amount of time due to its thermal conductivity. Even with 10 μs time step, the presence of the defect is not felt in copper. The c-map and b-map failed to show any contrast in the center in the simulation ran for the copper artifact. Hence, in this comparison, the c-map, and b-map of Ti-64, Inconel 625 and SS-316l is shown.

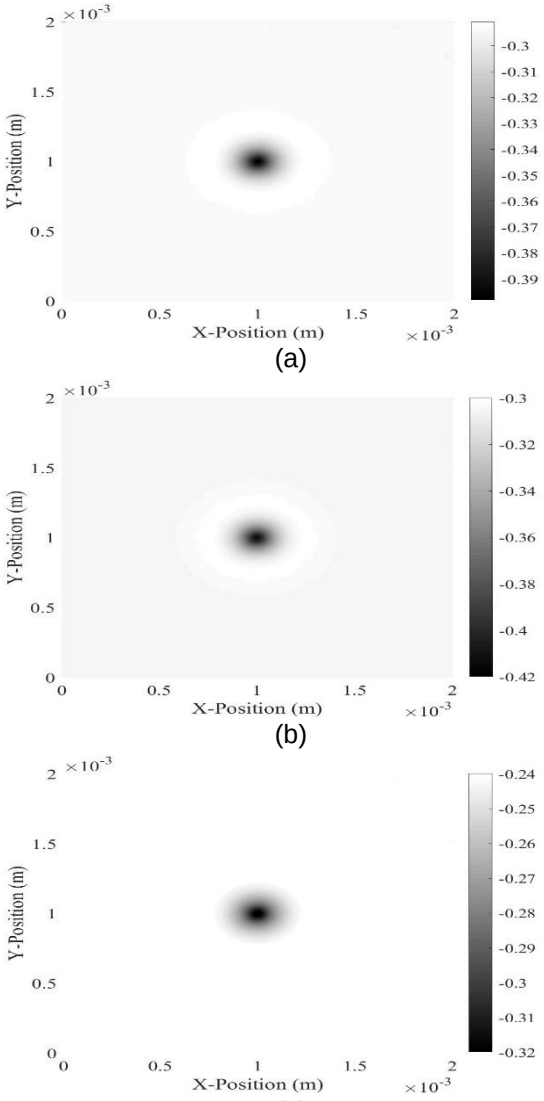

FIGURE 5. c-map for (a) Ti-64, (b) Inconel 625, and (c) SS-316l.

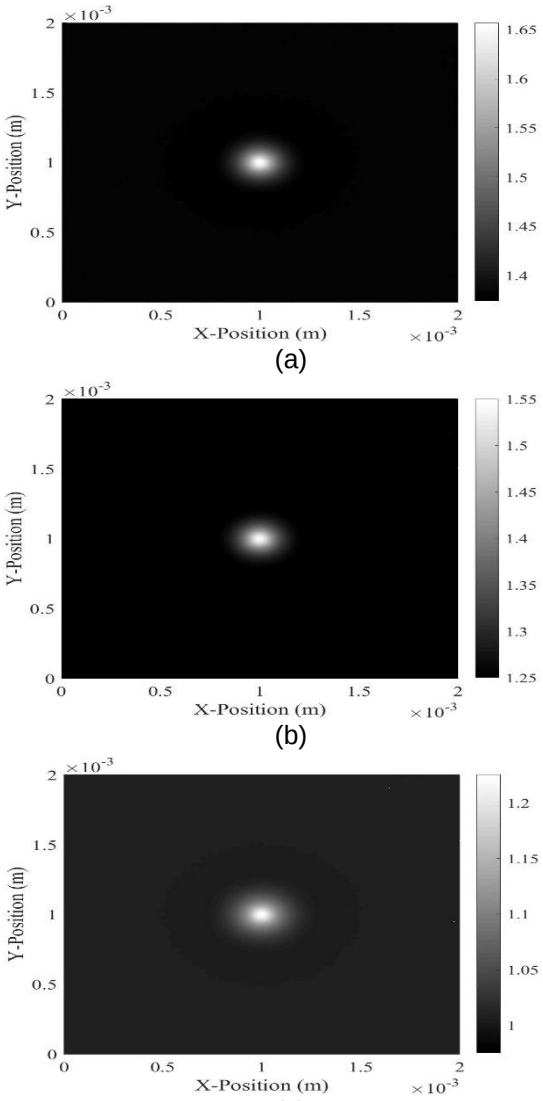

FIGURE 6. b-map for (a) Ti-64, (b) Inconel 625, and (c) SS-316l.

The c-map and b-map shown in Figure 5 and Figure 6 gives a clear indication of the presence of the defect in the center by producing contrast. As the defect is shifted far from the surface, the contrast will begin to fade away. The top surface will fail to show the presence of the defect if the depth of the defect is greater than the width of the defect. The magnitude of the slope and intercept also depend on the amount of data selected to curve-fit the first order polynomial. Since, the numerical simulations for copper artifact did not show the presence of the defect, it was necessary to conduct flash thermography experiment for a copper sample.

FLASH THERMOGRAPHY OF C10100 OFHC COPPER

A flash thermography experiment was conducted on C10100 OHFC copper at Siemens Corporate Technology. The setup is shown in Figure 7. The sample was built with a flat bottom hole defects of varying height and thickness as shown in the Figure 8. Half of the top surface of the sample was sprayed with the high-emissivity black paint to increase the amount of the heat absorption and thermal radiation to reduce the signal-to-noise ratio [1].

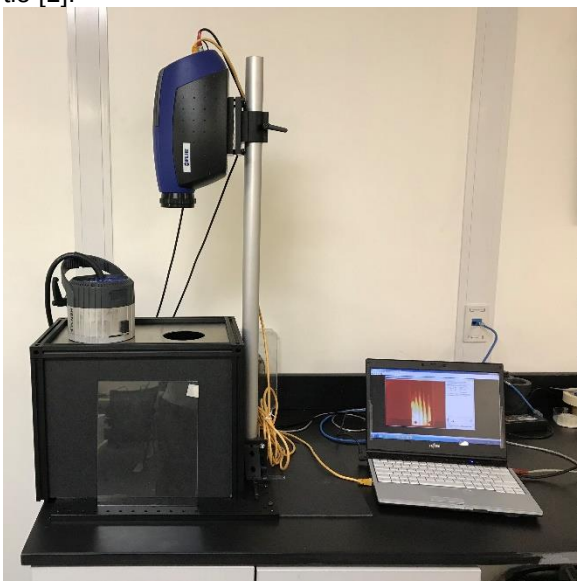

FIGURE 7. Flash thermography setup.

A high energy Xenon flash lamp (Hensel EH pro) is used to heat the top surface of the sample. A thermal camera (FLIR SC5000) with the 328 fps (frames per second) is used to capture the change in temperature of the copper sample after flash heating. The surface area covered by the camera is 45 x 36 mm^2 with 320 x 256 pixels.

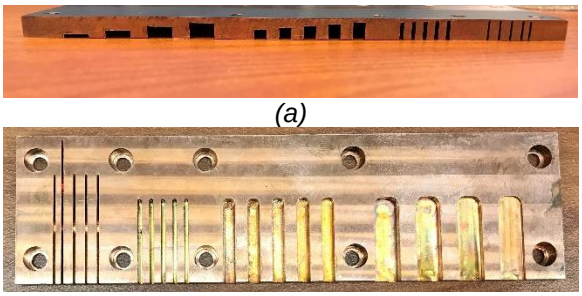

(a)

(b)

FIGURE 8. (a) Front view of the copper sample, and (b) Bottom view of the copper sample.

The copper sample was imparted with the heat energy and the measurements were taken at the interval of 3 ms using thermal camera. Figure 9 shows the raw data obtained from the flash thermography experiment. the milling marks are apparent in the raw data. However, there is no trace of the defect on the top surface. The raw data was processed using coefficient maps algorithm and c-map and b-map were developed as shown in the Figure 10.

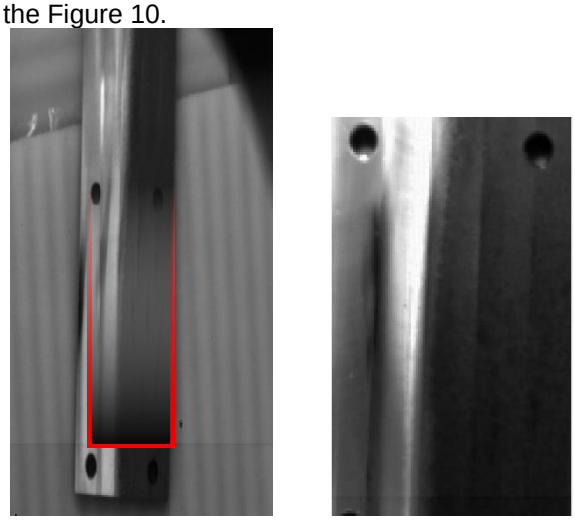

FIGURE 9. Copper sample highlighted with the area of interest.

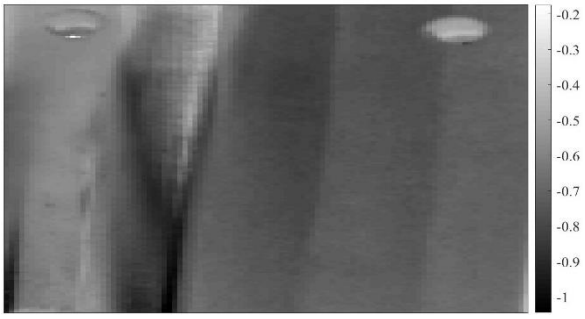

(a)

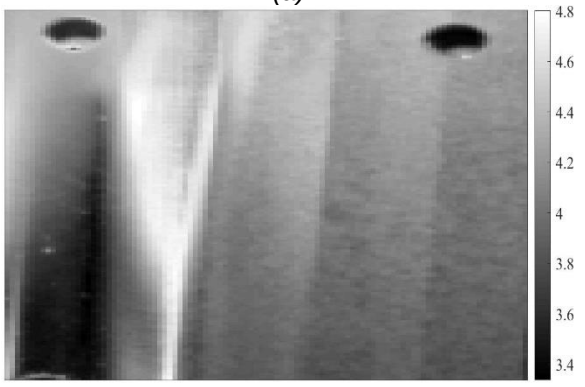

(b)

FIGURE 10. (a) c-map, and (b) b-map for copper sample.

The flat bottom holes are not visible in the defect maps. This result agrees with the numerical results. Copper having high thermal conductivity makes it difficult to capture any sort of discontinuities. To capture the defects for the materials with high thermal conductivity, the frequency of the thermal camera needs to be higher than the current settings and the flash duration has to be much lower depending on the depth of the defect to be detected.

CONCLUSIONS

The coefficient maps signal processing technique is successful in addressing the near surface defects and it also considers the fact that the heat sources are not always well defined. It uses a first order polynomial for curve fitting, hence it is computationally cheap. The slope and intercept changes with the change in the depth of the defect. Materials with lower thermal conductivity have a larger diffusion time compared to materials with higher thermal conductivity. The high thermal conductivity of copper makes it difficult to capture the defect for a thin plate. The material needs to be thick and the defect must be far from the surface. In order to capture near surface defects in copper, the frame rate of the IR camera needs to be extremely high. The experimental results proved that the defect detection is difficult in the materials with higher thermal conductivity. Hence, a camera with a higher fps should be used or other NDT techniques such as X-ray CT should be employed to detect near surface defects. However, this technique can be used as an in-situ in detecting defects such as pores, air inclusion or material inclusion in the additive manufactured part that has lower thermal conductivity.

ACKNOWLEDGEMENT

This work is supported by funding from the University of North Carolina Research Opportunity Initiative.

REFERENCES

[1] Balageas DL, Krapez JC, Cielo P. Pulsed photothermal modeling of layered materials. J Appl Phys 1986;59(2):348–57.

[2] B. Zhang, M. Duemmler, L. Sripragash, O. Adewumi, A. Davies, J. Ziegert, C. Waters, and C. Evans, “Detection of subsurface defect for metal additive manufacturing using flash thermography,” 07 2018.

[3] E. Klar and P. K. Samal, Powder metallurgy stainless steels: processing, microstructures, and properties. ASM international, 2007.

Error motion testing of a bare 4R Blockhead air bearing spindle

Christopher Arneson
Professional Instruments Company
Hopkins, Minnesota, USA

ABSTRACT
Before making the investment into an ultra precision air bearing spindle, a customer may want to know more about the spindle than just the specified accuracy.
Typically, a spindle needs to be motorized in order to test its accuracy. Motorizing the bearing provides the spindle with an encoder and motion control, and is a costly process. This becomes an issue when a customer is looking to purchase a bare bearing. Here at PICo, we can sidestep the time intensive motor installation by attaching a bare air bearing to a spindle that has already been motorized.

Figure 1. Bare 4R Blockhead air bearing spindle.

INTRODUCTION
Blockheads are rated to 1 microinch accuracy for both radial and axial motion. Previously this was determined by centering a 1 microinch test ball on a Blockhead with a 1/2 microinch per gradation Mikrokator. Strict geometries and tight gaps ensure that Blockhead spindles are inherently accurate. Recent advancements in capacitive probe technology have made it possible to perform higher resolution error motion tests on precision air bearing spindles. Collaboration with Dr. Eric Marsh at Penn State University has allowed us to test spindles down to single digit nanometers. Error motion testing is routinely performed on the ISO 5.5 spindle produced, but only per customer request on a 4 inch Blockhead.

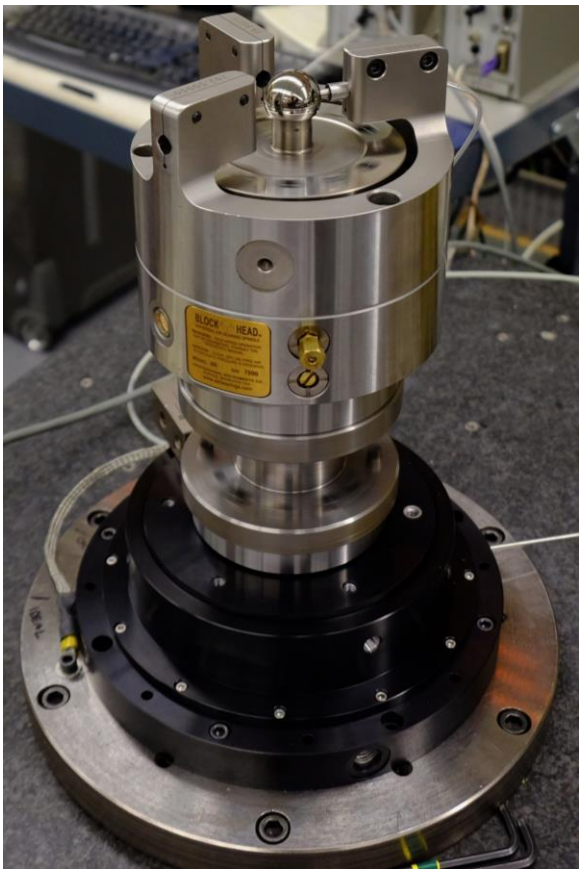

Figure 2. Setup for error motion test on a bare 4R Blockhead air bearing. Base bearing is an ISO 5.5 spindle. Radial probe mount attaches to stator of 4R Blockhead.

HARDWARE
Error motion testing down to the single nanometer level requires hardware and fixturing that provides stiffness to ensure accurate results. This is achieved by utilizing short and stiff

hardware attachments. When the spindle is rotating during error motion testing, imbalances and bending can look like spindle errors. The artifact used for testing spindle error motion is a flange mounted monolithic 440 stainless steel 1 inch diameter test ball. This design was chosen to reduce any non-uniform bending of the artifact and the flange mount is chosen over tapers or collets to eliminate rocking during rotation [2]. The artifact is placed coaxially onto the bearing rotation surface. Attaching the bespoke probe mounts shown in Figure 2 and Figure 3 directly to the 4R's stator ensures that the measurement loop is limited to the Blockhead and that the error motion of the base ISO 5.5 spindle does not contribute to the 4R Blockhead error motion.

Figure 3. Hardware for axial error motion test. Axial probe mount attaches to stator of 4R Blockhead.

METHODOLOGY

Using error separation techniques whilst testing error motion is important because two-lobe errors tend to be the largest spindle and test ball errors. Two-lobe errors in the ball and in the spindle can cancel each other, and may not accurately represent the true spindle error [2].

A bare 4R Blockhead spindle is attached to a motorized ISO 5.5 spindle, the encoder for which triggers data collection for the error motion test. This quickly and easily introduces motion control into the test without spending time motorizing the customer's spindle. It is important to note that the base bearing does not contribute any error to the spindle being tested, since the measurement loop is from the stator of the test spindle to its rotor.

Tested at 500 rpm with a 5nm test ball, a Lion Precision capacitive probe, and analyzed with Lion's Spindle Error Analyzer (SEA) software, three separate radial tests and one axial test are performed.

For the three radial tests the capacitive probe is positioned at the asymmetric angles determined by Professor Marsh, 0°, 99.84375°, 202.5°. The ball error is separated from the spindle error motion using software designed by Dr. Marsh. The three measurements are represented mathematically as the combined contribution of the artifact form error R, including a phase shift due to sensor location, and the x(θ) and y(θ) components of the spindle error [1]. R, x(θ), and y(θ) are solved for using equations 1-3 using Marsh's methods.

$$m_A(\theta) = R(\theta) + x(\theta) \quad (1)$$

$$m_B(\theta) = R(\theta - \phi) + x(\theta)\cos\phi + y(\theta)\sin\phi \quad (2)$$

$$m_C(\theta) = R(\theta - \psi) + x(\theta)\cos\psi + y(\theta)\sin\psi \quad (3)$$

Axial error motion requires one test at the center of the axis of rotation of the spindle, mentioned and referenced in Figure 3.

RESULTS

Blockhead spindles are rated to 1 microinch (25 nanometers) total radial and axial error motions. Having a large two lobe error in the radial polar plot would indicate that there is misalignment between the thrust plates and the shaft of the spindle. Figure 4 shows that the two lobe error is low and the total error motions are 9.14 nm. The total axial error motions, shown in Figure 5 are 4.25 nm with the fundamental component totaling 2.1 nm. Having low fundamental error motion is critical for applications such as ultra-precision diamond turning. These results not only indicate that this spindle performs beyond the rated specification, but also proves the robustness and reliability of the testing hardware. Robust and intentionally designed spindle testing hardware is critical to reliably test spindles at the single digit nanometer level.

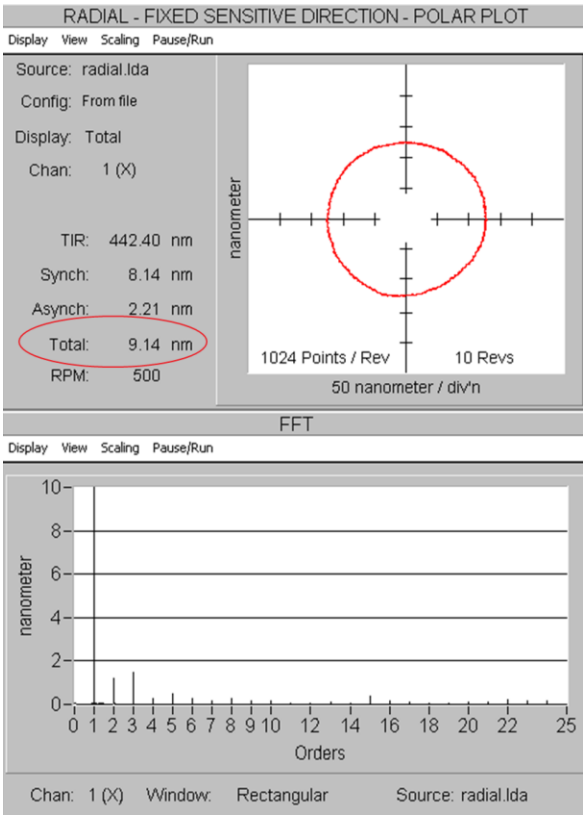

Figure 4. Radial error motion test results

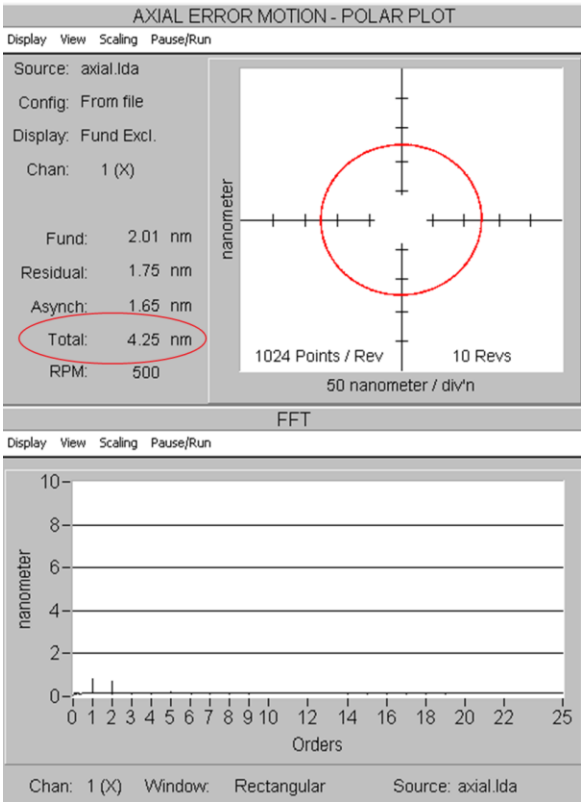

Figure 5. Axial error motion test results

CONCLUSION

Specified to 1 microinch, this 4R Blockhead generously passes its required accuracy with an axial error motion of 4.25 nm and a radial error motion of 9.14 nm. Using stiff fixturing and short measurement loops we can accurately test our bearings to single digit nanometers. Being able to use a spindle that has already been motorized to drive a bare bearing for an error motion test is a novel way to verify the accuracy of a bare bearing while helping to reduce the cost for the customer.

REFERENCES

[1] Marsh E 2010 Precision Spindle Metrology Second Edition (Lancaster, PA: Destech Publications, Inc)

[2] Arneson D 2018 Using error separation to test ultra high accuracy spindles. ASPE 2018. Las Vegas, NV, USA.

[3] 2010 ASME b89.3.4-2010. Axes of Rotation: Methods for Specifying and Testing (New York: ASME)

Modelling of Powder Spreading to Optimize Compaction Consistency

Alexander Groen[1], Mihaela Vlasea[1], and Kaan Erkorkmaz[1]
[1]Mechanical and Mechatronics Engineering
University of Waterloo
Waterloo, Ontario, Canada

INTRODUCTION

Additive Manufacturing (AM) has recently been the target of increasing research efforts because of the complementary advantages over traditional machining processes. AM allows for increased design freedom and enables parts with complex internal structures or consolidated assemblies [1]. AM typically works by the principle of layer by layer build-up of material before arriving at the final part. Most of the popular AM technologies involve a focused heating source to achieve selective material melting and solidification to arrive at the final part. A sub-group of AM methods use a powder bed, where powder is spread by a roller, a rake, or a re-coater blade, to create the next layer. The characteristics of the final part are partially inherited from the powder bed properties, which makes regulating the powder bed an important step in optimizing the process. This research is focused on analyzing and improving the properties of the powder bed, especially density.

The AM method explored in this research is called binder jetting additive manufacturing (BJ-AM). In contrast to the other technologies, BJ-AM uses a liquid "glue" (binder) to temporarily strengthen patterns in a loose powder bed. The powder layer is then either heated or left intact for a period of time to cure the binder and achieve "green" strength parts which are strong enough to maintain shape such that sintering can take place afterwards to realize dense parts. BJ-AM is especially well suited to research on improving the powder bed density because the green part is essentially made of loose powder. A diagram of the binder jetting process is shown in *FIGURE 1*.

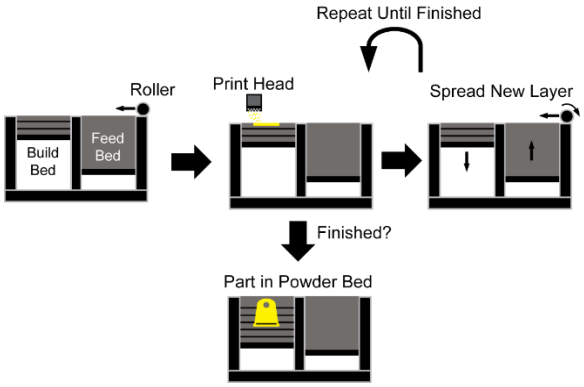

FIGURE 1. Binder jetting process

BINDER JETTING DIFFERENCES

BJ-AM has several advantages and disadvantages which distinguishes it from other AM methods because of the underlying operating principle. BJ-AM has the advantage of working with a wide range of metal alloys, including materials that have high thermal conductivity, which are difficult to use in other methods because they disperse local heating, such as copper [2]. Additionally, BJ-AM uses sintering to create the final parts which should avoid anisotropic defects and stress gradients which are sometimes the result of intense local heating used in other AM methods [3]. Furthermore, a large literature base for powder metallurgy should apply to BJ-AM, where green parts undergo sintering treatments to achieve densification.

Powder Bed Density

The critical disadvantage preventing the adoption of BJ-AM is that it is challenging to achieve full density parts [4]. Parts created with BJ-AM often have severe porosity, where the packing green density can be less than 70%. A high green density is preferred, to minimize part shrinkage, part distortion and anisotropy during densification sintering. Often times, a final density of >90% is desirable, similar to powder metallurgy targets, specifically in the automotive industry. Several works have achieved full density (>99%) in sintered parts using binder jetting through the use of sintering additives and bimodal particle size distributions; these techniques were adopted

from conventional powder metallurgy sintering due to the similarities between the methods [4]. Current efforts to improve binder jetting green part density have been developed through iterations of experiments, while adjusting parameters such as layer thickness, binder saturation level, heater power, drying time and roll speed [5].

Further analysis of parts created from BJ-AM have revealed another serious issue which is the cyclic variation of density, believed to be attributed largely by the powder spreading [6]. Traditional powder metallurgy uses a similar sintering process to BJ-AM but completely different powder delivery, which indicates that the large difference in part quality is due to poor powder spreading parameters. Moreover, a common strategy used in powder metallurgy to achieve high densities are bimodal diameter distributions which increases the theoretical packing ratio from 74% to 93% for spherical particles [7]. However, experiments have shown that in some cases, especially for micro sized particles, using a bimodal diameter distribution can actually reduce the packing ratio which is theorized to be caused from cohesive forces between the particles [7]. It is well known that exposing powder to vibration can improve the flowability and random packing density but experiments have shown that there are critical vibration parameters where increasing the energy input results in lower density; also thought to be from particle size segregation [8]. The results of powder spreading used in BJ-AM resemble high energy vibrations causing inconsistent density, especially around the edges, due to particle segregation in the spread layers.

RESEARCH METHOD

The goal of this research is to develop a model for powder spreading; this model can be then deployed to select process parameters to achieve optimized consistency in density throughout the bed with minimal experimental iterations.

The common process parameters used for influencing the quality of powder spreading in binder jetting are layer thickness, powder volume ahead of the roller, roller rotation speed and roller travel speed. Additional parameters could include variable compaction force delivered via other mechanisms, or bed vibration, which are out of scope for the present work.

Achieving the stated goal requires a combination of model development from simulations, followed by validation through experiments.

Simulations

The planned approach for predicting powder spreading behavior is to use numerical simulations, inspired by other works [7], [9].

Discrete Element Method

Modelling the dynamics of powder is challenging because the particle level dynamics are dictated by a nonlinear contact problem between potentially non-spherical particles, which may impose torques on each other or lock in certain orientations. Additionally, micro-scale dynamics including columbic charge forces, Van der Waals cohesive forces, surface roughness effects, and rolling torques dominate the particle-to-particle interactions; gravity and bulk pressure determine the macro-scale properties without a straightforward relationship. With certain powder delivery conditions, such as compacting found in powder metallurgy, the micro-scale dynamics can be safely neglected, since the bulk pressure will result in strong contact forces that dominate the behavior. In contrast, in loose powder spreading used in BJ-AM, the micro dynamics are believed to determine the bulk behavior since much lower densities are found.

Current efforts in simulating the powder behavior are based on molecular dynamics and a derivative specifically for granular material called the Discrete Element Method (DEM) introduced by Cundall and Strack [10]. Molecular dynamics works by resolving Newton's equation of motion for the entire assembly of particles. The DEM is slightly different, since it tries to describe particles with radii where torque and angular momentum must be considered; the specifics of the implementation are not required for this work but can be found at [10]. A 2D representation of particles in DEM is shown in *FIGURE 2*.

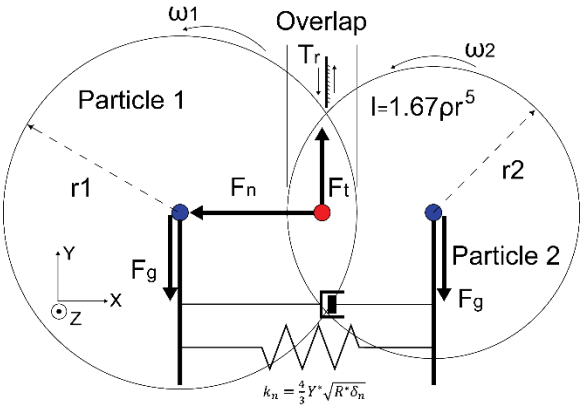

FIGURE 2. Discrete Element Method atom interaction

The DEM works by first determining all of the contact pairs for a given state of the simulation which involves a list of spheres at 3D positions. For a sphere, determining 3D contact is simple, since a pair of spheres are in contact if the distance between the centers is less than the sum of the radii; ray tracing or other involved contact detection is required for mesh faces. Once a list of all the contact pairs has been made, then the interactions are determined for each pair, which can include repulsive force, cohesive force, rolling friction, sliding friction, heat transfer. The Hertzian model for the contact of two elastic spheres is given as (with extra damping term):

$$F^n = \frac{4\sqrt{R_{ij}^{eff}}}{3}\left(\frac{1-v_i^2}{Y_i}+\frac{1-v_j^2}{Y_j}\right)^{-1}\left(\xi^{3/2}+\frac{A_i+A_j}{2}\dot{\xi}\sqrt{\xi}\right)$$

The results obtained from the above model show significantly better agreement with experimental results, specifically for dynamic behavior, when compared to the linear spring-dashpot model [11].

The DEM is typically used to simulate processes involving soft particles such as soil compaction, pharmaceutical tablet pressing, and grain flow into silos. These problems are suitable for the DEM because large networks of overlapping particles can be formed and predictions of actual bulk behavior can be made. A distinct advantage of the DEM over other methods, such as finite element methods, is that particles are not bound to a location which allows for phenomena like segregation from percolation as seen in experiments involving particles [10]. With the added complexity comes some issues that are specifically troublesome for additive manufacturing. Since the DEM uses an explicit integration scheme to arrive at particle positions it, means that a sufficiently small timestep is required to capture wave propagation occurring at less than the natural frequency of an element [12].

In additive manufacturing, the particles are low mass and stiff because they are tiny metal objects meaning that the natural frequency of a simulation element can be very high. Consequently, simulations can destabilize easily and require a small enough timestep such that several days are required for the simulation to complete. Another issue in DEM simulations is that damping in powder does not clearly link to macroscopic properties and must be determined by comparing experimental results to analogous simulation results [11]. Combining these issues suggests that any meaningful results require long calibration simulation for damping before the desired analysis simulations can begin, assuming that all of the required factors are taken into account in the simulation which might not be the case if the powder humidity is ignored.

The DEM has been applied to powder spreading for AM processes, although less often targeted towards BJ-AM. Many of these simulations have used a minimalistic model to reduce computational requirements where only particle to particle repulsion forces are considered and other changes are made such as reduced stiffness to increase the required timestep [13]. Recently, it has been suggested that for particles used in AM the cohesive forces dominate gravity by orders of magnitude meaning that the bulk behavior predicted in simplified simulations may not be accurate when extrapolated to useful processes [7].

Powder Rheometry

An equipment that is used to determine the flowability properties of powder is called a powder rheometer. Recently, there has been an increase in the usage of powder rheometers for other industries where the flowability information is useful for duct or hopper design.

In this work, a Freeman FT4 Powder Rheometer® will be used to obtain force and torque measurements on a blade passing through powder under three predefined test conditions known as the dynamic test, compaction test, and wall shear test. Each test involves a different blade shape interacting with

the powder under different flow and compaction conditions at different velocities.

Specifically, for the dynamic test, a stainless steel blade with 23.5mm diameter is used within a 25mm diameter and 25mL volume glass cylinder. A visualization of the blade is shown in *FIGURE 3*.

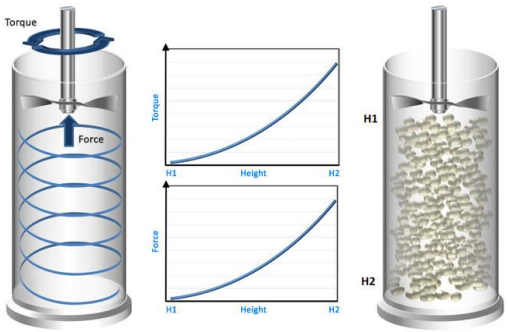

FIGURE 3. Freeman FT4 powder rheometer® dynamic methodology

Other research using the FT4 mainly focus on the flow energy required for the blade to enter the powder [14]. Flow energy is calculated by integrating the force and torque measurements so the value is inherently resistant to noise or spikes in the torque. This research is using the force and torque measurements directly because of the emphasis on eventually using the model for closed-loop control of powder spreading and compaction in powder bed additive manufacturing, with a direct application in BJ-AM.

The powder used in this study is Ti-6Al-4V due to the relatively large particle size ranging from 45µm to 105µm diameter for ease of simulation. Additionally, Ti-6Al-4V has been used in other BJ-AM research [15]. A simulation of the FT4 will be run using powder with initial properties acquired from literature to obtain a simulated force and torque curve for the same conditions. A damped least squares method will be used for calibrating the simulation to match the experimental values as shown in [16].

Levenberg-Marquardt method

As previously mentioned, there is no clear link between the macroscopic (measurable) powder properties and the microscopic (simulation) parameters. Therefore, a calibration procedure is required to get meaningful information from a DEM simulation.

The Levenberg-Marquardt method is a damped least squares method. In essence, a damping factor is added to the sensitivity matrix to avoid instability from a near singular matrix inversion. A flowchart of the simulation algorithm is shown in *FIGURE 4*.

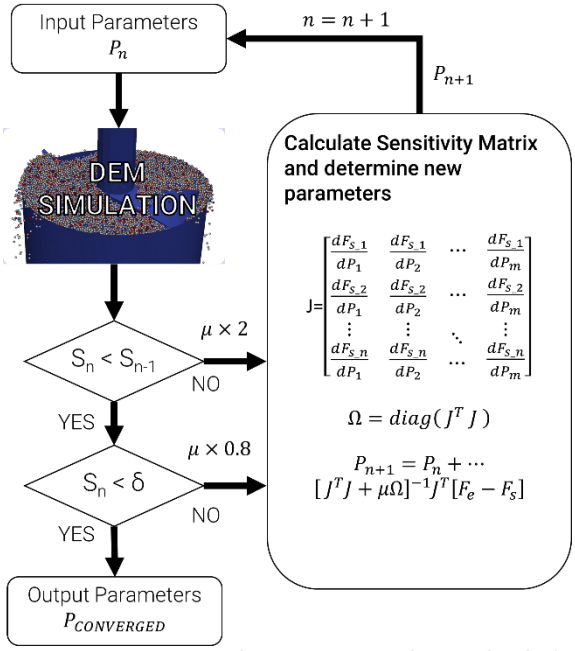
Input Parameters
P_n
$n = n + 1$
P_{n+1}
DEM SIMULATION
Calculate Sensitivity Matrix and determine new parameters
$J=\begin{bmatrix} \frac{dF_{S\_1}}{dP_1} & \frac{dF_{S\_1}}{dP_2} & \cdots & \frac{dF_{S\_1}}{dP_m} \\ \frac{dF_{S\_2}}{dP_1} & \frac{dF_{S\_2}}{dP_2} & \cdots & \frac{dF_{S\_2}}{dP_m} \\ \vdots & \vdots & \ddots & \vdots \\ \frac{dF_{S\_n}}{dP_1} & \frac{dF_{S\_n}}{dP_2} & \cdots & \frac{dF_{S\_n}}{dP_m} \end{bmatrix}$
$\Omega = diag(J^T J)$
$P_{n+1} = P_n + \cdots$
$[J^T J + \mu\Omega]^{-1} J^T [F_e - F_s]$
$S_n < S_{n-1}$
$\mu \times 2$
NO
YES
$S_n < \delta$
$\mu \times 0.8$
NO
YES
Output Parameters
$P_{CONVERGED}$

FIGURE 4. Levenberg-Marquardt method for DEM calibration

The damping factor (µ) initially starts as a large value and is slowly reduced as the results begin to converge. After the first run, the previous least squares error is compared to the current least squares error. If the least squares error is found to decrease then the new parameters are accepted and another iteration occurs. In contrast, if the least squares error increases then the damping factor is increased and the simulation is run again. The procedure is repeated until the least squares error is within a stopping criteria denoted as δ. The convergence of the algorithm must be monitored because it is possible for the least squares error to reach a steady state value that is above the stopping criteria depending on issues with the actual DEM model. If the error is found to be quite large after this procedure then the DEM model needs to be revisited and other details like non-spherical particles may need to be investigated.

To validate the results of the model calibration, a simulation of powder spreading will be performed and the simulated particle arrangement will be compared to “green” particle space organization

obtained in the BJ-AM parts. The particle arrangement in the simulation can be easily observed since the position and size of each particle is tracked. For the “green” particle space organization in BJ-AM parts, a computerized tomography (CT) scan will be used to determine particle arrangement and image processing will also be used to extract meaningful information such as packing density. If the simulation accuracy is found to be poor then adjustments will be made and the previous calibration procedure will be repeated.

Following a validated calibration, the simulation will be used to determine ideal process parameters for roller rotation and travel speed. Further experiments will be run to investigate how well the simulation can be used for predicting process parameters.

EARLY RESULTS AND CONCLUSIONS

Research is still in its early stages and the DEM simulation is being calibrated to match the measurements. The current plots are shown in *FIGURE 5* and *FIGURE 6*.

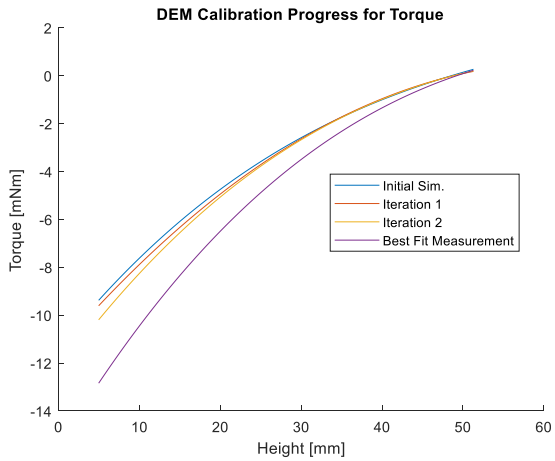

FIGURE 5. DEM Calibration (Torque)

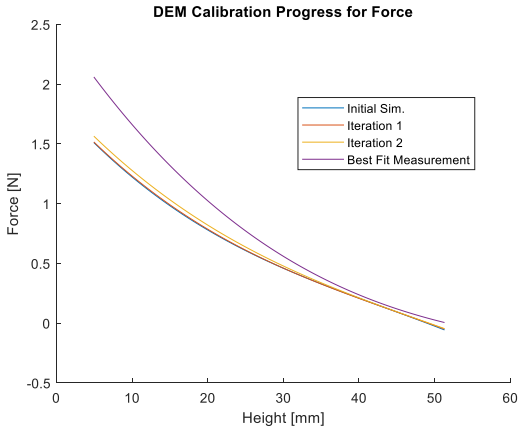

FIGURE 6. DEM Calibration (Force)

The trend in the result resembles the findings in [17]. The simulation closely matches the experimental results for the greater height, where the powder is less packed, but diverges for the closely packed powder at the low height. Future work will involve modifying the simulation code to resolve this issue. The current simulation parameters used are the Young’s modulus (Y), density (ρ), coefficient of restitution (ε), coefficient of friction (μ) and are compared by the least squares error (E). The values of the simulation parameters are shown in *TABLE 1*.

TABLE 1. Simulation Parameters

	Y	ρ	ε	μ	E
Initial	104000	4.43	0.800	0.185	2.9
1	104830	4.46	0.802	0.186	2.4
2	107410	4.59	0.803	0.189	1.8

The calibration process shows clear improvement in the error and further iterations will be run to achieve the minimal error.

REFERENCES

[1] W. Gao *et al.*, “The status, challenges, and future of additive manufacturing in engineering,” *Comput.-Aided Des.*, vol. 69, pp. 65–89, Dec. 2015.

[2] Y. Bai and C. B. Williams, “An exploration of binder jetting of copper,” *Rapid Prototyp. J.*, vol. 21, no. 2, pp. 177–185, Mar. 2015.

[3] I. Rishmawi, M. Salarian, and M. Vlasea, “Tailoring green and sintered density of pure iron parts using binder jetting additive manufacturing,” *Addit. Manuf.*, vol. 24, pp. 508–520, Dec. 2018.

[4] T. Do, P. Kwon, and C. S. Shin, “Process development toward full-density stainless steel parts with binder jetting printing,” *Int. J. Mach. Tools Manuf.*, vol. 121, pp. 50–60, Oct. 2017.

[5] H. Chen and Y. F. Zhao, “Process parameters optimization for improving surface quality and manufacturing accuracy of binder jetting additive manufacturing process,” *Rapid Prototyp. J.*, vol. 22, no. 3, pp. 527–538, Apr. 2016.

[6] E. Wheat, M. Vlasea, J. Hinebaugh, and C. Metcalfe, “Sinter structure analysis of titanium structures fabricated via binder jetting additive manufacturing,” *Mater. Des.*, vol. 156, pp. 167–183, Oct. 2018.

[7] C. Meier, R. Weissbach, J. Weinberg, W. A. Wall, and A. J. Hart, “Critical influences of particle size and adhesion on the powder layer uniformity in metal additive manufacturing,” *J. Mater. Process. Technol.*, vol. 266, pp. 484–501, Apr. 2019.

[8] X. An, C. Li, and Q. Qian, “Experimental study on the 3D vibrated packing densification of binary sphere mixtures,” *Particuology*, vol. 27, pp. 110–114, Aug. 2016.

[9] S. Haeri, “Optimisation of blade type spreaders for powder bed preparation in Additive Manufacturing using DEM simulations,” *Powder Technol.*, vol. 321, pp. 94–104, Nov. 2017.

[10] C. Kloss, C. Goniva, A. Hager, S. Amberger, and S. Pirker, “Models, algorithms and validation for opensource DEM and CFD-DEM,” *Prog. Comput. Fluid Dyn. Int. J.*, vol. 12, no. 2/3, p. 140, 2012.

[11] T. Pöschel and T. Schwager, *Computational granular dynamics: models and algorithms*. Berlin ; New York: Springer-Verlag, 2005.

[12] C. O’Sullivan and J. D. Bray, “Selecting a suitable time step for discrete element simulations that use the central difference time integration scheme,” *Eng. Comput.*, vol. 21, no. 2/3/4, pp. 278–303, Mar. 2004.

[13] W. Zhang, A. Mehta, P. S. Desai, and C. F. H. Iii, “MACHINE LEARNING ENABLED POWDER SPREADING PROCESS MAP FOR METAL ADDITIVE MANUFACTURING (AM),” p. 15.

[14] V. Vivacqua, A. López, R. Hammond, and M. Ghadiri, “DEM analysis of the effect of particle shape, cohesion and strain rate on powder rheometry,” *Powder Technol.*, vol. 342, pp. 653–663, Jan. 2019.

[15] E. Stevens, S. Schloder, E. Bono, D. Schmidt, and M. Chmielus, “Density variation in binder jetting 3D-printed and sintered Ti-6Al-4V,” *Addit. Manuf.*, vol. 22, pp. 746–752, Aug. 2018.

[16] B. Cheng, B. Lane, J. Whiting, and K. Chou, “A Combined Experimental-Numerical Method to Evaluate Powder Thermal Properties in Laser Powder Bed Fusion,” *J. Manuf. Sci. Eng.*, vol. 140, no. 11, p. 111008, Aug. 2018.

[17] P. S. Desai, A. Mehta, P. S. M. Dougherty, and C. F. Higgs, “A rheometry based calibration of a first-order DEM model to generate virtual avatars of metal Additive Manufacturing (AM) powders,” *Powder Technol.*, vol. 342, pp. 441–456, Jan. 2019.

Design and Features Of
The 4 Inch Blockhead Air Bearing Spindle

Samuel O. Arneson, David A. Arneson, Daniel D. Oss, Melvin J. Liebers
Professional Instruments Company
Hopkins, Minnesota, USA

ABSTRACT
The Blockhead air bearing has been a crucial component to various precision manufacturing and metrology applications for over 50 years. Initially described as “The Tooling Block”, the Blockhead was designed to be a useful, everyday precision tool to be used in whatever job was being worked on at the time. The compact and universal nature of the Blockhead air bearings enable them to be used in a variety of applications. This paper will describe the design and features of the Blockhead air bearing.

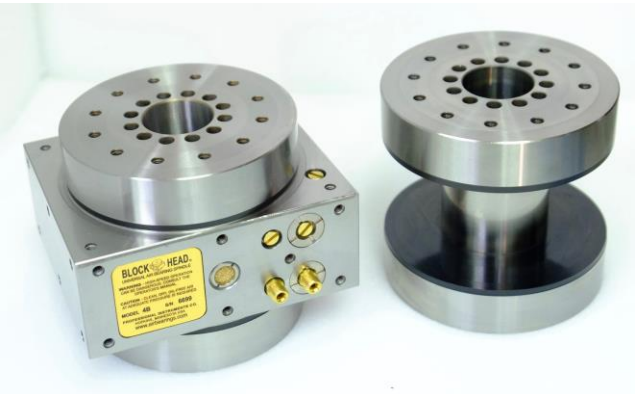

Figure 1: 4B and bare rotor

BACKGROUND
In 1960, Ted and Harold Arneson began work with Professor Arnold Nordsieck at the University of Illinois to fabricate hollow hemispherical gyroscope rotors. This project required spindles much more accurate than Professional Instruments had at the time and led Harold to develop the “Zeron”, a dual-hemisphere air bearing spindle [1]. While the Zeron was useful for the gyroscope project, it required a long shaft which limited the stiffness of the spindle and meant the spindle was cumbersome to manufacture and use. Ted and Harold continued to develop air bearings with the goal of having a spindle that could be freely transferred between different machines or used independently as a roundness tester. Ultimately, they settled on the Blockhead design and sold S/N 2 in 1967 to the Goddard Space Flight Center. S/N 1 is still in use today as the workhead in a Heald 273A internal grinder.

WHY AIR BEARINGS?
Air bearings possess unique characteristics that are important in machine tool design. The following is a partial list of these important characteristics [2]:

1. Hydrostatic spindles maintain a fixed axis of rotation whether stopped or in motion.
2. True circular rotation less than a micro-inch are readily obtainable
3. Absence of mechanical friction permits for accurate centering of workpieces and allows low powered, cool running drives thereby eliminating deflections due to driving means.
4. The high thermal stability of air bearings reduces errors due to spindle heating.
5. Bearing stiffness on the order of several million pounds per inch is achievable, allowing maximum machine tool rigidity to be realized.

BLOCKHEAD SPECIFICATION AND DESIGN

Blockhead air bearing spindles possess high rotational accuracy with extremely high stiffness and reasonable load capacities. This unique combination makes it possible for direct machining of optical tolerances and finishes.

4 Inch Blockhead Air Bearing (100 PSI)		
Load Capacity		
	Ultimate	Working
Radial	65 lb	34 lb
Axial	270 lb	135 lb
Tilt	270 lb-in	135 lb-in
Stiffness		
Radial	0.45 lb/µin	
Axial	1.3 lb/µin	
Tilt	2.6 lb-in/µrad	
Synchronous Error Motion		
Radial	1 µin	
Axial	1 µin	
Tilt	0.1 µrad	

Every Blockhead is tested in house using a bespoke load tester that ensures each spindle was manufactured and assembled correctly.

The Blockhead design is symmetric, featuring two opposed thrust bearings connected by a compact shaft which also serves as a journal bearing. This design is advantageous because when a tilt load is applied to the spindle, as in Figure 3, a restoring force is generated by increased pressures from the decreased clearances in regions P5 and P7 and the decreased pressures from the corresponding regions of increased clearance. This structure allows for a greater load capacity than would otherwise be obtained [3].

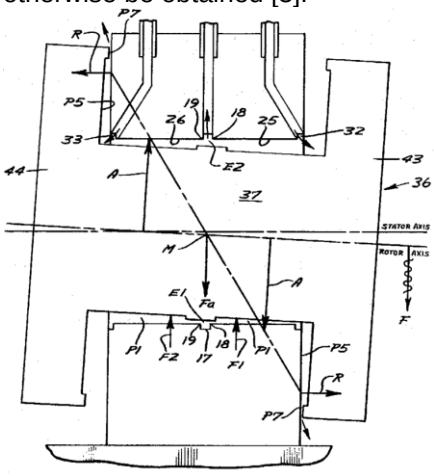

Figure 2: Diagram of Blockhead structure and response to applied load

In addition to the high precision of the Blockhead, they are also robust. When setup correctly with a proper air supply Blockhead spindles can last years with minimal maintenance even in flood coolant conditions.

FORM FACTOR

The Blockhead's characteristic appearance came from Ted's and Harold's desire to have a spindle that they could swap from machine to machine as one might use a set of 1-2-3 blocks. A small footprint was desired so the spindle could fit into most machines, see figure 3. As the spindle became more compact and the shaft became short and stiff to handle radial loads, while the large diameter opposed thrust surfaces handle the axial and tilt loads. The compact size combined with a relatively large projected bearing surface area means that Blockhead air bearing spindles have high volumetric efficiency.

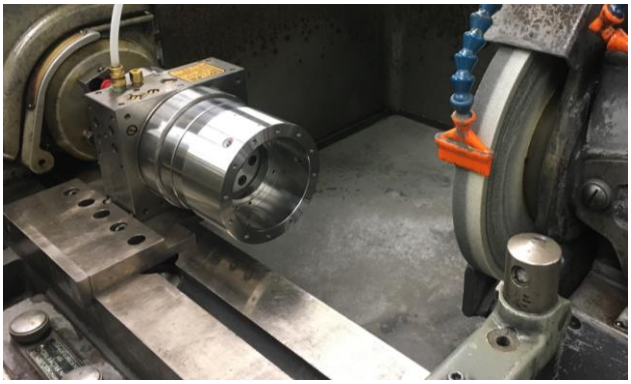

Figure 3: Blockhead installed to an existing grinder

The thrust plates are manufactured with a coating as a safety feature in the event of a crash. This sacrificial coating prevents the bearing from violently seizing during a crash and instead allows the spindle to slowly come to a stop. The stator also provides a generous number of tapped contingency holes to facilitate nearly any mounting orientation.

APPLICATIONS

The Blockhead is often referred to as the "Universal Workhead" and retrofitting existing machines with a Blockhead spindle is one of the most common uses for the spindle. Replacing the existing workhead on a conventional machine with a Blockhead can improve the accuracy in many operations by a factor of five to ten. In particular, Blockheads are regularly added to surface grinders in order to achieve

sub-micron flatness and parallelism. The spindle can be simply mounted onto the magnetic chuck and driven with a belt motor.

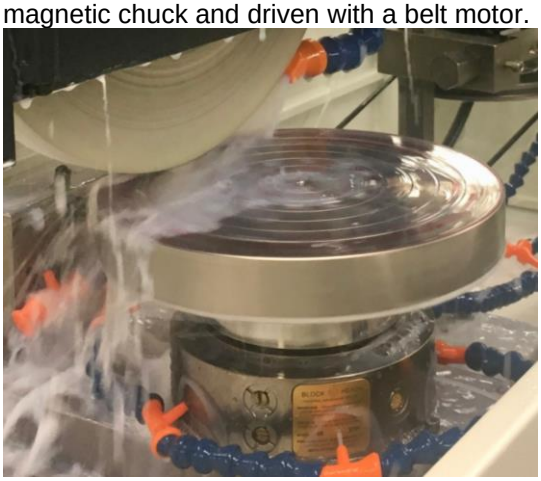

Figure 4: Blockhead mounted in a conventional surface grinder

The Blockhead was instrumental in the early development of hard disk drives. Servo tracks for disk drives were originally manufactured on ball bearing spindles. While effective for many processes, ball bearings have mechanical limitations when it comes to very fine control of rotational and positioning movement. To account for this error the individual data tracks needed to be spaced further apart to prevent fatal errors in the read/write capabilities of the disk drives. The need for higher track density pushed the industry towards more accurate spindles. The Blockhead spindle was ideal because it possessed both the accuracy required and had adequate load capacity to support the massive 14" hard disks at the time.

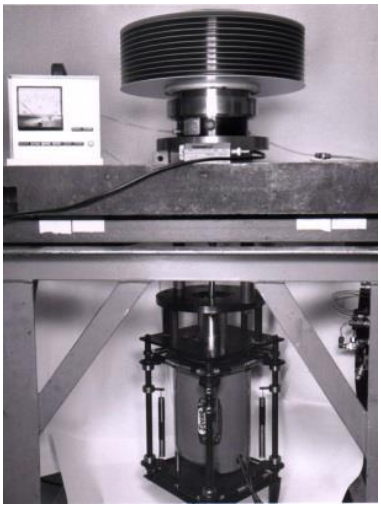

Figure 4: Blockhead supporting the IBM removable disk pack

CONCLUSION

The Blockhead is a fundamental mechanism of pure rotation. The high accuracy and precision of the spindle along with the reasonable load capacity and speed capabilities provide a uniquely universal solution to any rotational application. The compact and thoughtful design of the spindle makes the Blockhead simple to implement into many existing machines.

REFERENCES

[1] Arneson C et al. History of the Blockhead spindle. ASPE 2018.

[2] Arneson H. Operational Experience with Air Bearing Machine Tools. American Society of Mechanical Engineers 1966 Winter Meeting. Nov 27 – Dec 1, 1966.

[3] Arneson HEG, 1969 US Patent No. 3472565

[4] Liebers M et al. Testing the Earliest Sub-Microinch Spindles. ASPE 2015

Addressing Precision Challenges To Fabricate 3D Parts Using Microscale Selective Laser Sintering

Dipankar Behera[1], Nilabh K. Roy[1], and Michael A. Cullinan[1]
[1]Department of Mechanical Engineering
The University of Texas at Austin
Austin, TX, United States of America

ABSTRACT
This paper discusses the different precision engineering challenges which are being addressed to develop 3D parts using a microscale additive manufacturing technology. It highlights the major components of the microscale selective laser sintering (µ-SLS) tool, discusses the different fundamental challenges and outlines the approaches taken to address them and other potential improvements. The paper also presents some examples of the 2.5D/3D parts fabricated using the µ-SLS process.

INTRODUCTION
The rapid growth of additive manufacturing processes in aerospace, energy, and medical sectors is driven by the development of novel materials, architectures and designs for these tools. From a technical and economic perspective, there is a constant demand to improve the scalability of these tools in a production environment. However, the commercially available AM tools have resolutions to the order of 100s of microns which is larger than the required feature sizes in several microscale applications, primarily in the semiconductor industry[1]. With a gradual shift towards compact high-density integrated chips, and 3D stacked chips, it is important to improve the design and manufacturing of the global-level interconnects connecting the different modules in a chip. Microscale AM provides an alternative to complex and expensive subtractive manufacturing processes to fabricate microscale electronic structures for better chip packaging and integration.

The Selective Laser Sintering process (SLS) is a commercially successful layer-by-layer additive manufacturing process for rapid prototyping and production-scale fabrication of 3D macroscale parts with a wide array of capabilities for the process in aerospace, energy, and medical implants sectors. However, the feature size resolution limit for most AM tools exists because of their large laser focus size, their use of powders with ~100 µm particle sizes, and their poor control over thermal and oxidation effects which can result in part porosity and rough surface finishes at the microscale. The Microscale Selective Laser Sintering (µ-SLS) process overcomes many of these limitations through the use of precise focusing optics, nanoparticle (NP) inks, and short exposure times to be able to produce sub-10 µm metallic parts with true-3D structures. In the µ-SLS process, a slot die coating system is used to coat a layer of nanoparticle ink on to a substrate where it is heated and dried to form a uniform layer of NPs. The substrate is then moved to the optical subsystem where a DMD micromirror array is used to project a CW/QCW 808nm diode laser through a set of focusing objectives to the nanoparticles on the substrate in order to sinter them into the desired pattern. This optical setup has a minimum achievable feature size resolution of ~1 µm and is able to pattern up to ~2 million spots simultaneously. Once the NPs in the first

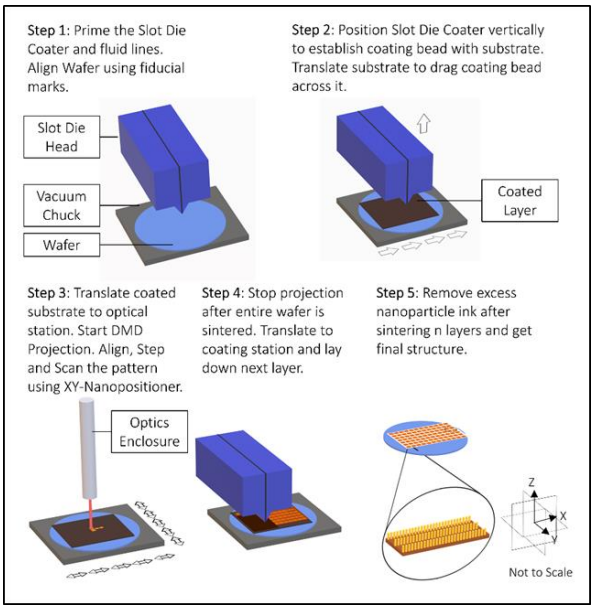
Step 1: Prime the Slot Die Coater and fluid lines. Align Wafer using fiducial marks.
Step 2: Position Slot Die Coater vertically to establish coating bead with substrate. Translate substrate to drag coating bead across it.
Slot Die Head
Vacuum Chuck
Wafer
Coated Layer
Step 3: Translate coated substrate to optical station. Start DMD Projection. Align, Step and Scan the pattern using XY-Nanopositioner.
Step 4: Stop projection after entire wafer is sintered. Translate to coating station and lay down next layer.
Step 5: Remove excess nanoparticle ink after sintering n layers and get final structure.
Optics Enclosure
Z
X
Y
Not to Scale

FIGURE 1. Process schematic of the µ-SLS tool

layer have been sintered, the substrate is brought back to the coating subsystem where a new layer of NPs is coated on top of the sintered layer and this process is repeated until the full 3D part has been built up. Finally, the excess NPs are washed away and the part is annealed to improve its electrical and mechanical properties. This process is outlined in Figure 1 and a more detailed overview of the different subsystems of the µ-SLS development tool can be found in [1]. Further details on the performance of the subsystems can be found in the previous works by the authors[1–3].

IDENTIFYING POTENTIAL CHALLENGES

The overall scalability of the µ-SLS process for high volume manufacturing is evaluated on the following criteria : a) Range of materials that can be processed b) Feature-size resolution that can be achieved c) True-3D fabrication capability d) Volumetric throughput including post-processing steps. The following sections discuss the current state-of-the-art for the system along with the details on the performance of the system. The baseline assumption while identifying these fundamental challenges is that the limitations associated with better accuracy positioners and sensing units may be addressed easily.

MATERIALS CHALLENGES

Most commercially available thermal sintering tools are limited in feature size resolution due to the large particle sizes being used which are typically in the hundreds of micron range[1,4]. To fabricate microscale parts with sub-10 µm features, finer powders in the form of nanoparticles with narrow size distributions are required. However, as the particles are scaled down to the nanoscale, agglomeration of the particles becomes a significant issue due to enhanced van der Waals forces at these scales[5,6]. To reduce this agglomeration problem, the µ-SLS process uses NP inks that use surfactant coatings, which are burned off during the sintering step, to prevent agglomeration of the particles during the coating step. Initial studies of the µ-SLS process have mainly used Cu and Ag nanoparticle (NP) inks to fabricate high complex 2.5D parts and demonstrate the capability to produce 3D microparts[1] though the current iteration of µ-SLS tool can process almost any metallic and polymeric materials that can be suspended in NP inks.

One of the key materials challenges for µ-SLS is the sintering of ceramic materials. This is because nanoceramics often suffer from inhomogeneous particle agglomeration, early onset of sintering due to lower activation energy compared to micron-scale ceramic particles, and a wider distribution of particles due to ineffective nanoparticle separation techniques as compared with metal and polymer NPs[7]. While lower activation energy can be perceived as an advantageous proposition to lowering the sintering energy, when coupled with uneven distribution and packing of these nanoparticles, it becomes difficult to control grain growth. The highly activated behavior of ceramic nanoparticles as compared to its micron-sized counterparts makes these issues highly prevalent in nanoceramics processing. Controlling sintering schedules, introducing grain growth suppressants, driving sintering through isostatic pressing, and coupling densification and superplastic deformation techniques (like forging) at high temperatures are some strategies used to mitigate the problems associated with nanoceramic sintering. However, these approaches are slow for integration into the production environment. Therefore, major challenges still exist in producing ceramic parts using µ-SLS.

FEATURE SIZE RESOLUTION CHALLENGES

Parts with minimum feature size of ~10 microns have been fabricated using the µ-SLS process. The lateral resolution of the µ-SLS process is limited by the heat diffusion away from the laser focal spot when the exposure durations are high. This thermal diffusion creates heat-affected zones (HAZs) around the intended part which results in poor control over net-shaped features and unacceptable surface roughness. The vertical resolution of the process is affected by slot die coated layer thickness and the laser thermal penetration depth which varies with the composition of the NP bed as well as the laser wavelength and intensity.

TRUE-3D FABRICATION CHALLENGES

The µ-SLS process can currently produce multilayer 2.5D structures on a 50 mm wafer. In principal, there should be few limitations to the types of structures and overhangs that µ-SLS can produce since unsintered NPs in the µ-SLS bed act as supports during the build process. In fact, the only major limitation should be the fabrication of closed structures such as hollow spheres

where the unsintered NPs can't be removed from the inside of the part during post processing.

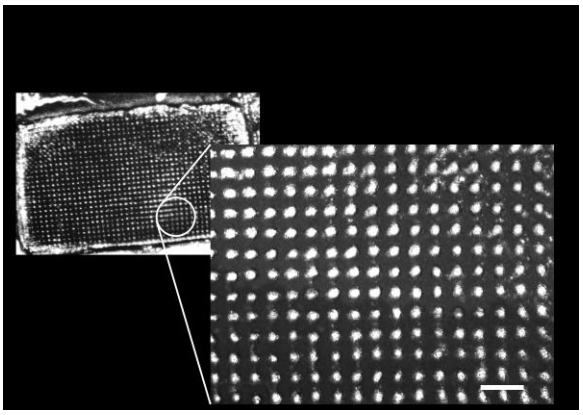

FIGURE 2. (scale bar 100 µm) An optical microscope image showing the full areal scale (2.3 mm X 1.2 mm) array sintered on a 1 µm thick Ag NP ink layer. (inset) Enlarged image of an array of 20 µm diameter circles with 40 µm pitch

However, there are some practical challenges in fabricating true-3D structures with µ-SLS that must be overcome, such as avoiding residual thermal stresses that can warp the part and improving control over interlayer fusion, in order to reach the full potential of µ-SLS to fabricate 3D parts.

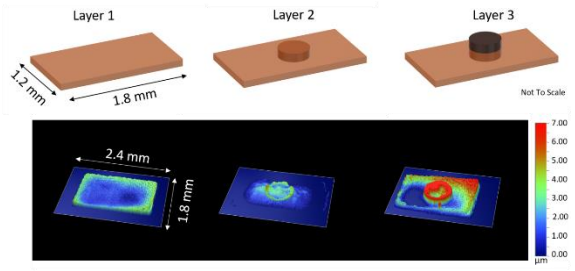

FIGURE 3. Visualization of the layer-by-layer (LbL) fabrication. The first layer is a 1.8 mm by 1.2 mm rectangular structure. A 500 µm circle is sintered on top of the first layer as part of the second and third layer. Optical topographic images showing the LbL progression of the µ-SLS process.

VOLUMETRIC THROUGHPUT CHALLENGES

The volumetric fabrication throughput of the µ-SLS process is currently ~63 mm^3/hr. Features of the µ-SLS system that can possibly limit the throughput of the process are the coating speed, the nanopositioner alignment and settling times, the sintering exposure time, and the inherent scalability tradeoffs between resolution and throughput. The current throughput budget of the µ-SLS process is primarily determined by the efficiency of the sintering process and speed of the slot die coating mechanism. The current sintering time of the µ-SLS system is 100 ms per exposure which includes a 50 ms laser exposure time and a 50 ms stepping time. The exposure time can likely be decreased by increasing the exposure power and the stepping time can be improved by reducing the settling time of the nanopositioning stages. A coating speed of 1 mm/s is currently used for the slot die coating process to ensure uniform coating layers but this coating time can also likely be significantly improved by optimizing the coating process.

POTENTIAL APPROACHES TO ADDRESSING SCALABILITY CHALLENGES

A potential approach which can be integrated with the µ-SLS process to improve consolidation of semiconductor nanoceramics and achieve higher densification rates is using a field-assisted laser flash sintering (FS) technique. In conventional FS techniques, an electric field (1-1000 V/cm) is applied directly to the green part causing effective rapid sintering. While the most widely accepted explanation of the fundamental physical phenomenon behind FS is Joule-heating runaway, researchers are still trying confirm that hypothesis with strong experimental evidence covering a range of ceramic materials[7,8]. Hagen et al [9]demonstrated the idea of Laser Flash Sintering (LFS) of nanoceramics in a layer-by-layer manner by simultaneously using a galvanometric laser scanner while applying pulsed electric field to a substrate to initiate the necking between the particles. The laser facilitates the formation of necks between the selective exposed nanoparticles at significantly lower temperatures and times, eliminating thermal shocks. LFS could potentially be used in conjunction with the µ-SLS process in the future without major modifications to the process in order to improve its ability to fabricate ceramic parts.

The thermal stresses in sintered parts can be reduced by decreasing the thermal gradient across the bed through uniform heating these particles. A conventional hot plate drying technique is used to partially dry the NP layers in the µ-SLS process, but the drying has been found to be too long and non-uniform as the varying energy exposure densities dries each section of the sample differently. To achieve a precise partial drying of the layers by vaporizing the solvents in these NP layers, a uniform energy

exposure density on the surface could be maintained using an infrared emitter. This would allow each layer to be more uniformly heated and dried would should help to reduce the thermal gradients in the fabrication process and thus reduce the thermal stresses in the final part produced resulting in more accurate 3D builds.

Another approach to improve 3D feature control in µ-SLS is through advanced process control including process monitoring and in-situ metrology techniques coupled with closed loop feedback. However, the extremely wide parameter space for optimizing µ-SLS and a dearth of effective models of the µ-SLS process have limited our ability to do advance process control in µ-SLS. Integrating vision, temporal, and thermal metrology systems that can detect material and process abnormalities into the µ-SLS process could help improve our understanding of the µ-SLS process and allow us to more accurately fabricate 3D structures using µ-SLS. A very high process area to spatial feature size ratio (approximately five orders of magnitude) for the µ-SLS process presents significant challenges in yielding useful in-situ optical or thermal information as there's a trade-off between field-of-view and resolution of these measurement techniques. In addition, to make optimal use of in-situ metrology, advanced models of the nanoscale laser-material interactions need to be developed to understand the underlying physics behind the process. In summary, the 3D part production capability of the µ-SLS process can be improved by reducing thermal gradients during sintering and employing advanced process control techniques to monitor part fabrication. However, completely closed hollow structures with thin walls would be almost impossible to produce, given the process design constraints.

The HAZs in µ-SLS can be reduced by reducing the laser exposure duration and increasing the laser power to limit the heat transfer away from the laser spot. Previous results have shown that the use of nano and femtosecond lasers significantly reduces the HAZs but produce much narrower processing windows for nanoparticle sintering due to the very small difference in the sintering and melting exposure thresholds[10]. The HAZs and feature size resolution of µ-SLS can be further improved by using optical proximity correction algorithms, like the ones commonly used in nanolithography, to account for image distortions caused by heat or light spreading from the intended feature exposure area[11].

The optical penetration depth, which determines the vertical resolution of the µ-SLS process, is dependent on the laser wavelength, the laser dwell time, and the thermal diffusivity of the substrate. This entails that understanding the nanoscale transport mechanisms in µ-SLS and using them to create accurate nanoparticle sintering models is critical in achieving high resolution, true-3D parts for µ-SLS[12]. Typical laser penetration depths range from a few hundred nanometers to tens of micrometers depending on the laser wavelength and exact NP composition for metal nanoparticles in the visible spectrum[10,13]. Therefore, the likely limit of the resolution of µ-SLS in the vertical direction is a few hundred nanometers if accurate opto-thermal models of the µ-SLS process can be created and used to optimize the build process.

Currently, a 50 mm wafer can be sintered using the µ-SLS process in ~140 seconds. Of these 140 seconds, the travel time between coating station and optical station, which includes the NP ink deposition and partial ink drying as well as the homing of the stage under the optical subsystem, takes ~60 seconds. Over 90% of this budget is allocated to the coating time which depends on the flow rate inside slot die coater, layer thickness resolution and material rheological properties (specifically, Ca number). The coating time can be experimentally optimized by identifying a coating window for a range of Ca numbers, coating speeds and bed thickness, with the objective of achieving a uniform coating with minimal variation along the direction of coating. Recent results have shown that uniform coatings can be produced with NP inks at ~15 mm/s coating speeds and the drying time could be reduced to ~2 seconds which would reduce the coating and travel time between the coating and optical substations to ~10s.

The total time currently needed to sinter one complete NP layer on the wafer is ~80 seconds, where the timescales are set by the sintering exposure duration and the settling time of the nanopositioning stages. This can be reduced by using higher power lasers which can achieve the similar densification quality at shorter exposure durations. The settling time of the nanopositioner steps can be improved by applying better control strategies to reduce the overshoot during tracking. It is estimated that both the exposure

time and the settling times of the stages could be reduced to ~10 ms which would reduce the overall sintering time to ~16 seconds. With these assumptions the potential volumetric throughput of the µ-SLS system could be increased to ~340 mm^3/hr, for a single layer deposition of 1 µm vertical resolution. Therefore, the overall fabrication time for a 10:1 aspect ratio structure with a vertical and lateral resolution of 1µm could be reduced to a build time of less than 10 minutes including the excess material removal and post-processing steps using the optimized µ-SLS process parameters. Further improvements in the volumetric throughput could be achieved by increasing the layer thickness though this would reduce the vertical resolution proportionally.

CONCLUSIONS AND FUTURE WORK

The paper identifies fundamental development challenges which must be addressed to improve the scalability of the µ-SLS process. While the suggested improvements for the process are under continuous testing and development, in a more general sense, from a precision engineering standpoint, the challenges associated with the process can be solved using a combination of innovative design principles and best practices in the semiconductor industry. However, the potential market for the microscale AM technologies is not just limited to the semiconductor industry. The true-3D fabrication of pure metallic structures would be influential for the medical devices sector as well as for novel sensor design. The electrical and mechanical characterization of these 3D parts is critical for furthering the design space for a variety of microproducts.

REFERENCES

1. Roy, N. K., Behera, D., Dibua, O. G., Foong, C. S. & Cullinan, M. Experimental Study of the Subsystems in a Microscale Additive Manufacturing Experimental Study of the Subsystems in a Microscale Additive Manufacturing Process. *JOM* (2018). doi:10.1007/s11837-018-3223-3
2. Roy, N. K., Behera, D., Dibua, O. G., Foong, C. S. & Cullinan, M. A. Single shot, large area metal sintering with micrometer level resolution. *Opt. Express* **26**, 25534 (2018).
3. Roy, N., Foong, C. & Cullinan, M. Design of a Micro-scale Selective Laser Sintering System. in *Proceedings of Solid Freeform Fabrication (SFF) Symposium, Austin, TX* (2016). doi:10.1115/MSEC2016-8569
4. Roy, N. K., Foong, C. S. & Cullinan, M. A. Effect of size, morphology , and synthesis method on the thermal and sintering properties of copper nanoparticles for use in microscale additive manufacturing processes. *Addit. Manuf.* **21**, 17–29 (2018).
5. Volkman, S. K. *et al.* Mechanistic Studies on Sintering of Silver Nanoparticles. (2011). doi:10.1021/cm202561u
6. Nanda, K. K., Maisels, A., Kruis, F. E., Fissan, H. & Stappert, S. Higher Surface Energy of Free Nanoparticles. 1–4 (2003). doi:10.1103/PhysRevLett.91.106102
7. Lu, K. Sintering of nanoceramics. *Int. Mater. Rev.* **53**, 21–39 (2008).
8. Ze, M., Shomrat, N. & Tsur, Y. Recent Advances in Mechanism Research and Methods for Electric-Field-Assisted Sintering of Ceramics. **1706369**, 1–8 (2018).
9. Hagen, D., Kovar, D. & Beaman, J. J. Effects of Electric Field on Selective Laser Sintering of Yttria-Stabilized Zirconia Ceramic Powder. 909–913 (2018).
10. Roy, N. K. *et al.* A Comprehensive Study of the Sintering of Copper Nanoparticles Using Femtosecond, Nanosecond, and Continuous Wave Lasers. *J. Micro Nano-Manufacturing* **6**, 010903 (2017).
11. Capodieci, L. From optical proximity correction to lithography-driven physical design (1996-2006): 10 years of resolution enhancement technology and the roadmap enablers for the next decade. in *SPIE 31st International Symoposium on Advanced Lithography - Optical Microlithography XIX* **6154**, 615401 (2006).
12. Dibua, O. G., Yuksel, A., Roy, N. K., Foong, C. S. & Cullinan, M. Nanoparticle Sintering Model : Simulation and Calibration Against Experimental Data. *ASME J. Micro-and Nano-manufacturing* **6**, (2019).
13. Theodorakos, I., Zergioti, I., Karnakis, D., Geremia, R. & Zacharatos, F. Selective laser sintering of Ag nanoparticles ink for applications in flexible electronics. *Appl. Surf. Sci.* **336**, 157–162 (2014).

High speed Micro laser assisted machining of single crystal germanium

Hossein Shahinian[1], Jayesh Navare[1], Charan Bodlapati[1], Dmytro Zaytsev[1], Di Kang[1],Hossein Mohammadi[1], Megan Arlt[1], Deepak Ravindra[1]
[1]Micro-LAM , Inc
5960 S Sprinkle Rd
Portage, Michigan, USA

INTRODUCTION

Single crystal Ge is widely used in infrared (IR) optical systems that operate within a wavelength of 3 μm - 5 μm. Ge provides an excellent opportunity for production of diamond turned freeform, aspherical, and diffractive lenses, due to the ability of production of optically smooth surfaces made from Ge using ultraprecision machining processes [1, 2]. Indeed, high volume production of Ge lenses is a common industry practice.

SPDT of Ge has always been of great interest to the research communities involved in ultraprecision machining of brittle materials. Landmark works by Blake and Scattergood [3] and Blackley and Scattergood [4] have provided significant insights in the cutting mechanics of Ge, as well as understanding the ductile regime machining of such brittle material. As outlined by those articles, for certain cutting conditions and tool geometries, pit free, specular surfaces with minimal tool wear [5] is feasible.

One of the key aspects of the tooling geometry in ductile material removal (DMR) of Ge, is the existence of a negative rake angle on the diamond cutting tool. As investigated by several researchers, higher negative rakes promote the DMR manifested in reduction of pits and defect zones on the surface of the workpiece [6, 7].

In this article, we report on SPDT of Ge using the Micro-LAM (aka μ-LAM) process. In previous work, the enhancements of the μ-LAM process to conventional SPDT has been published on materials such as Si and WC [8-10]. The goal of this study is to investigate the effect of tool rake-angle in production of defect free surfaces using the μ-LAM process.

MICRO-LAM PROCESS

The μ-LAM process uses the emission of a laser beam during SPDT of optical components. The laser beam, generated using a Nd:YAG lasing medium, has a wavelength of 1064 nm. Through series of optical elements, the beam is guided towards the cutting medium, made from single crystal diamond. The diamond stone is made such that the laser beam can enter the medium with minimal scattering from the back end of the cutting bit, see FIGURE 1. The laser beam is aligned precisely and the exitance of the beam occurs directly at the cutting edge. As illustrated in FIGURE 1 the exited laser beam is then absorbed by the workpiece material, causing a very localized heated zone during the cutting. It is speculated that this heated zone exhibits thermal softening, thus promoting a more ductile regime of material removal.

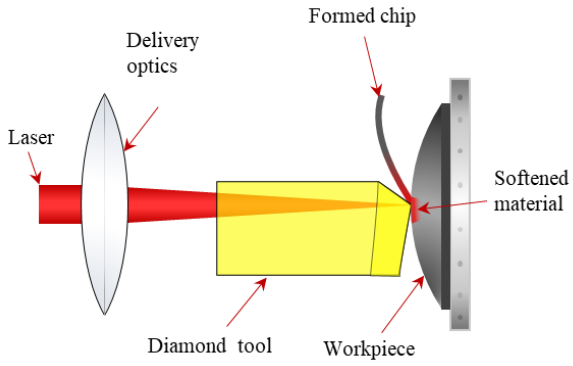

FIGURE 1. μ-LAM process in princple

To accommodate the optics responsible for the delivery of the laser beam at the cutting edge of the tool a custom-made tool post, the Optimus T+1 was designed. Depicted in FIGURE 2, the Optimus T+1 tool post, uses linear slideways for allowing the vertical motion of the tool nose. The tool is affixed a special nose that allows for the accommodation of a shank with a proper opening for the laser beam travelling towards the diamond stone, see FIGURE 2. The diamond tooling uses a specialized design that not only allows the transmission of the laser beam through the diamond medium, it can also be used such that the beam is biased more towards the rake or flank face, depending on the

application of the tool. FIGURE 3 illustrates an instance of the diamond tool used for cutting materials with the µ-LAM process.

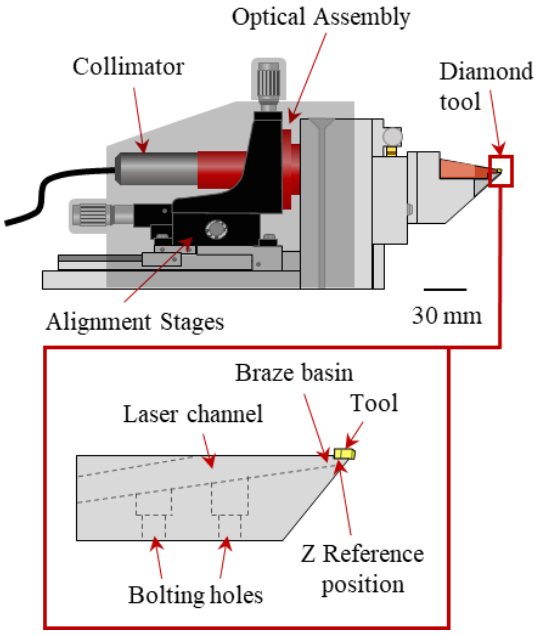

FIGURE 2. Optimus T+1 tool post and special tooling

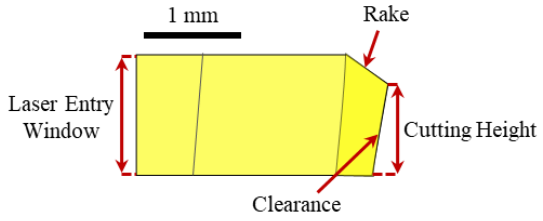

FIGURE 3. Single crystal laser transmissive tool

In the following sections details on the experimental test bed, tools, and laser alignment procedures are enumerated. However, a much more detailed account can be found in [8].

EQUIPMENT AND HARDWARE

Experimental test bed

The machining trials were conducted on a 2-axis ultraprecision Precitech 250 machine. The Optimus T+1 was mounted on the tool table using a T-nut and a 5/16-18 bolt. The laser control module (see FIGURE 4) was activated and the beam was transferred to the OptimusT+1 via an optical fiber. As seen in FIGURE 4, the sample was held on the spindle via a vacuum chuck. In addition to the 1064 nm laser, the module generated a red beam laser concentric with the 1064 nm beam for alignment purposes. This laser had a very low power (<1 mW), providing for a safe and easy laser alignment.

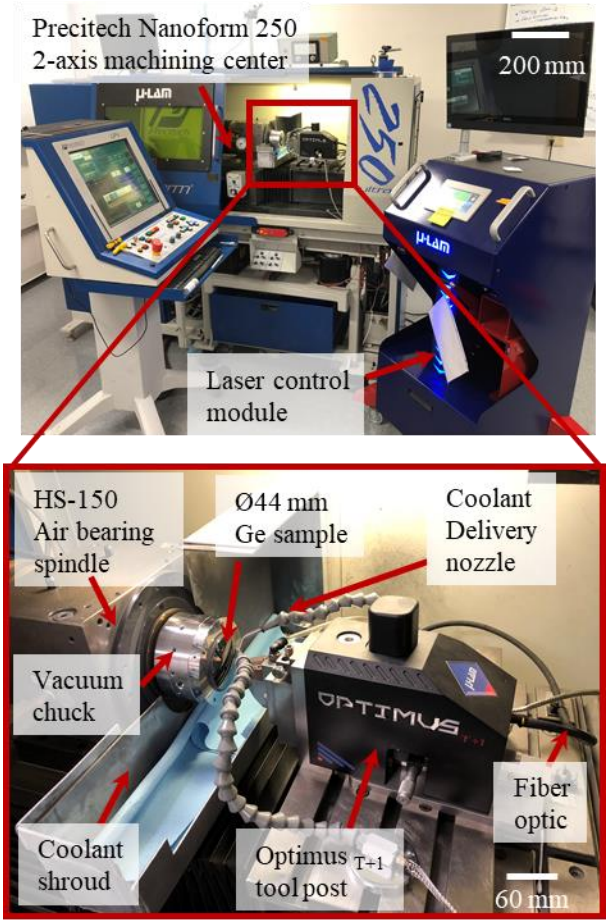

FIGURE 4. Experimental test bed

Laser calibration procedure

The laser spot size at the cutting edge of the tool was calibrated before the inception of the experiments. The calibration setup is depicted in FIGURE 5. A calibration artifact, representing the cutting edge of the tool, was placed on the Optimus T+1 nose. A magnifying lens imaging the face of the artifact on a 320 × 320 pixels detector, was used as the imaging camera. This imaging system was attached to a set of metal bars, that enabled the placement of the camera in front of the artifact, such that the top edge of the artifact was on the focal plane of the imaging system, see FIGURE 5. The guide beam was then activated to measure the laser spot size on

the detector. This spot size was adjusted by displacing the optical assembly using a z-axis micrometer.

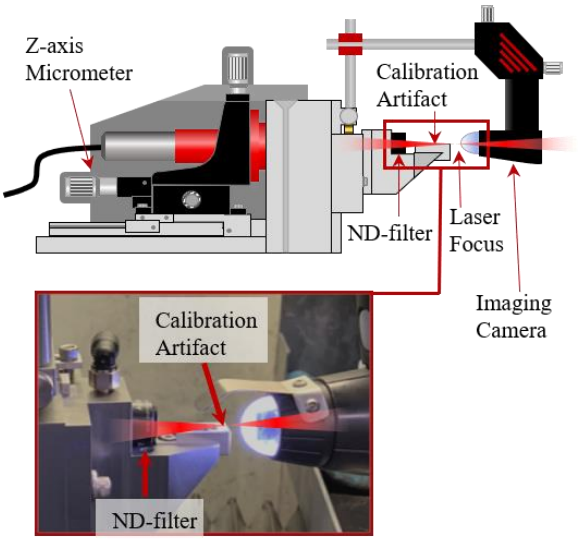

FIGURE 5. Calibration hardware and procedure

Laser alignment

Vertical, and horizontal alignment of the the laser spot with respect to the tool cutting edge, was done by using a custom made instrument as depicted in FIGURE 6(a).

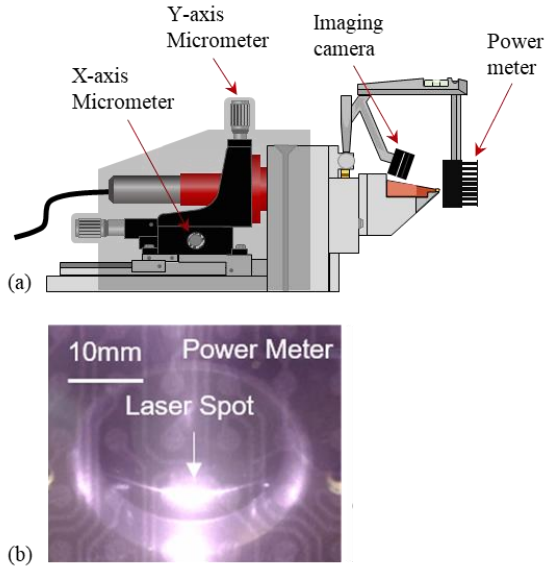

FIGURE 6. Laser lateral alignment hardware and procedure

The instrument uses an imaging camera that captures the aperture of a thermopile sensor (power meter). The lateral position of the laser beam was ensured by visually centralizing the elliptical arc formed by the tool flank face bending the laser beam, see FIGURE 6(b). The position adjustment was done using the X-axis micrometer.

For vertical alignment of the laser beam, laser power measured by the thermopile sensor, was measured and set such that 50% of the power was exiting the flank face, i.e. the total power of the elliptical arc. This was realized by vertically moving the arc using the Y-axis micrometer.

Metrology

The form measurements were done using a Taylor Hobson LuphoScan® 260 HD. This instrument is a multi-wavelength scanning interferometer.

The surface finish of the samples was measured using a Zygo ZeGage Pro HR, a scanning white light interferometer (SWLI).

Table 1. Supporting metrology information

Hardware	Data type and analysis
LuphoScan 260-420 HD	Form measurements Piston, tilt, power removed Total points measured ≈ 10^6 Metrics used: PV (peak-to-valley) – RMS
Zygo ZeGage HR	Roughness measurements 4th order Chebyshev removed High-pass filter with λ = 80 μm Detector size = 1024 × 1024 pixels Metric used: RMS

Diamond Cutting Tools

Three cutting tools, manufactured by K&Y diamond, were used. The tools were made of single crystal diamond material, and all had a nose radius of 1 mm. Table 2 lists all the used tools.

Table 2. Tool information

Tool	Rake angle (°)	Nose radius (mm)	Primary clearance (°)
1	-25	1.0	10
2	-45	1.0	10
3	-65	1.0	10

Test Sample

The sample was a piece of concave Ge with radius of curvature (ROC) of 45 mm and diameter of 44 mm. The sample had a crystal orientation of <111> on the plane perpendicular to the cutting direction.

Diamond turning conditions

For the turning experiments, the air bearing spindle was rotated with a spindle speed of 5000 RPM. The tool was horizontally rotated as much as 10°, with respect to the workpiece. This ensured a symmetric cutting zone on the tool nose. The laser power measured outside the tool was set to be around 7.5 W. Odorless mineral spirits was used as the coolant of the process. To achieve near-net-shape of the final part, the tool was concentered with the spindle by adjusting the height of the cutting edge. A convex witness brass sample with ROC 10 mm, and ∅18 mm was cut and the center feature due to the height misalignment was minimized to a diameter of less than 1 µm.

RESULTS

The three tools listed in Table 2 were used to machine the Ge sample with machining conditions detailed in the previous section.

Maximum linear feed vs rake angle

To determine the maximum linear feed rate of each tool of Table 2, cutting trials were started at a linear feed of 3 mm/min. The linear feed was incrementally increased at the following pass by 1 mm/min. The increase to the feed was applied up to when brittle fracture trefoil zones were appeared on the part. FIGURE 7(a), (b) show two surfaces without and with clear defect/fracture zones, respectively.

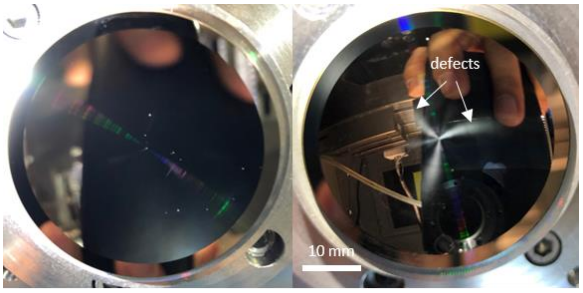

FIGURE 7. Ge sample; (a) with no fracture zones (b) with fracture zones and defects present

Upon the appearance of the brittle fracture zones, 4 passes with the same conditions were taken to ensure the repeatability of producing surfaces with the brittle fracture zones. The linear feed was then reduced as much as 1 mm/min and 10 more passes with the lowered feed was taken. If the surface of the sample was clear of any fracture zones, that feed was considered as maximum feed.

FIGURE 8 shows the maximum linear feeds obtained for the three tools with different rake angles. As evident by the result the maximum feed of which clear and defect free surfaces were achievable by the tools, increased as the rake angle was more negative.

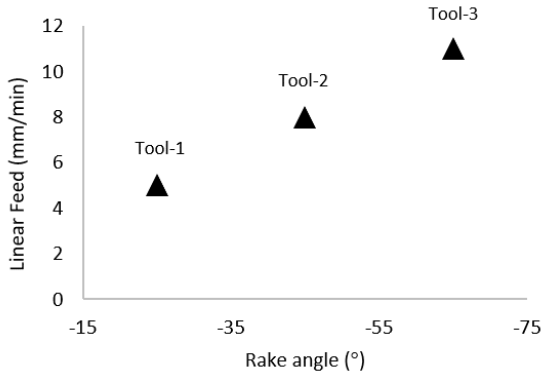

FIGURE 8. Maximum linear feed vs rake angle

This result is in agreement with that reported in [3]. The defects on the surface were imaged using a JSM-IT500HR scanning electron microscope, shown in FIGURE 9. As evident by the images, the defects suggest the occurrence of brittle fracture on the surface.

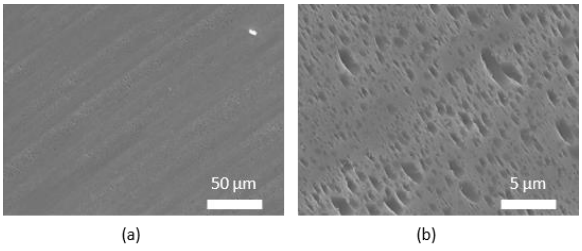

FIGURE 9. SEM imaging of the trefoil fractured zones (a) 1000× zoom and (b) 5000× zoom

Form and roughness measurements

The opportunity to machine fracture free Ge surface with higher feeds and speeds, is a great prospect for enhancement of throughput of

optical shops. Thus, tool-3 was used to machine the surface of the sample for 100 consecutive passes. Form and finish measurements at 10 pass intervals were taken.

Over the 10 measurements the PV of the form error was evaluated as 243 nm ± 125 nm, and RMS value of 51 nm ± 26 nm.

The roughness measurements taken with Zygo Zegage and a 20× Mirau objective had an RMS value of 0.73 nm ± 0.51 nm.

FIGURE 10 depicts a sample form and roughness measurement taken at the 75th pass using tool-3. These results suggest a highly repeatable process, with no excessive tool wear introduced.

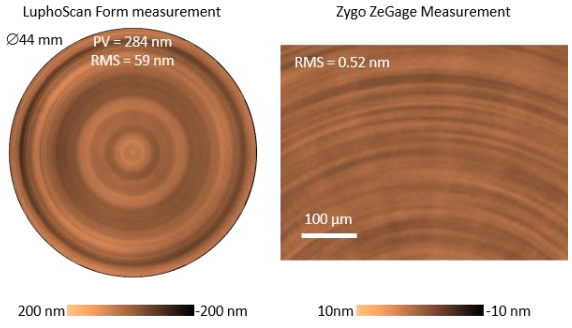

FIGURE 10. Form and surface finish measurement of the Ge sample machined with tool 3 after 75 passes

DISCUSSION

The results reported in the previous section, clearly demonstrated the effect of the negative rake angle on promoting DMR of single crystal Ge. It was seen that with a larger negative rake angle, the tool feed can be higher without inducing brittle fracture on the surface. Based on previous studies [3, 4], this was expected. It is speculated that the significant hydrostatic pressure applied by the -65° rake is enabling the fracture free surface with higher linear feeds.

In addition, extended testing on the sample showed that the form and finish achieved by tool-3 is well within common specs for infrared optical systems, taken after several number of passes. Initial results have demonstrated over 100 Km length of fracture free machined surfaces. It is believed that the IR laser beam used during the µ-LAM process is crucial in extending the tool life sufficiently so as to enable the process in getting a reasonable number of parts per tool.

CONCLUSION

The ability to SPDT single crystal Ge using the µ-LAM process was demonstrated. It was further showed that with special tooling design, higher than common tool feeds is achievable. Such high feeds did not introduce in complexity in producing a part with acceptable form and finish for IR applications. Future studies will be pursued in understanding the phase transformation of the Ge material under high compressive stresses as well as the effect of the laser beam on such transformations.

REFERENCES

1. Dutterer, B.S., et al., *Diamond milling of an Alvarez lens in germanium.* Precision Engineering, 2014. **38**(2): p. 398-408.

2. Yan, J., et al., *Micro grooving on single-crystal germanium for infrared Fresnel lenses.* Journal of micromechanics and microengineering, 2005. **15**(10): p. 1925.

3. Blake, P.N. and R.O. Scattergood, *Ductile-regime machining of germanium and silicon.* Journal of the American ceramic society, 1990. **73**(4): p. 949-957.

4. Blackley, W. and R. Scattergood, *Ductile-regime machining model for diamond turning of brittle materials.* Precision engineering, 1991. **13**(2): p. 95-103.

5. Paul, E., et al., *Chemical aspects of tool wear in single point diamond turning.* Precision Engineering, 1996. **18**(1): p. 4-19.

6. Lai, M., et al., *Effects of crystallographic orientation and negative rake angle on the brittle-ductile transition and subsurface deformation in machining of monocrystalline germanium.* Precision Engineering, 2019. **56**: p. 164-171.

7. Korytár, D., et al., *Cross-sectional TEM study of subsurface damage in SPDT machining of germanium optics.* Applied optics, 2018. **57**(8): p. 1940-1943.

8. Shahinian, H., et al., *Microlaser assisted diamond turning of precision silicon optics.* Optical Engineering, 2019. **58**(9): p. 092607.

9. Shahinian, H., et al. *Micro Laser Assisted Machining (μ-LAM) of Precision Optics*. in *Optical Fabrication and Testing*. 2019. Optical Society of America.

10. Kang, D., et al. *Observations on Ductile Laser Assisted Diamond Turning of Tungsten Carbide*. in *Optical Fabrication and Testing*. 2019. Optical Society of America.

ONE-SIDE CUTTING STRATEGY FOR ULTRAPRECISE SINGLE POINT CUTTING OF V-GROOVES CASE 2: CONSTANT CUTTING AREA

Delfim Joao[1,2,*], Nicolas Milliken[2,1*], O. Remus Tutunea-Fatan[1,2,], and Evgueni V. Bordatchev [2,1,**]**
[1]Western University
London, Ontario, Canada
[2]National Research Council of Canada
London, Ontario, Canada

INTRODUCTION

V-grooves represent one of the important microstructures that have found numerous applications in mechanical, electronic, photonic, and optical components. Their capability to enhance surfaces with numerous types of additional functionalities tends to be the primary reason behind their wide use.

The manufacturing process of these microstructures is normally divided in two main groups essentially involving rotational and non-rational cutting tools, respectively [1, 2]. Past studies involving rotational cutting tools noted that although this machining approach can yield very good results in terms of shape accuracy and surface quality, long slopes tend to be commonly generated at the flat ends of the microgrooves [3]. By contrast, the grooves produced with non-rotational tools revealed that the aforementioned characteristic slopes tend to have a shorter length. This slope reduction is primarily influenced by the tighter control of the tool/workpiece angle both at entrance and exit [3]. Furthermore, the cutting performed with non-rotational tools remains more versatile in a sense that it enables generation of microgrooves with a broad range of curvatures [3].

Common microgroove fabrication procedures involving rotational tools include: flycutting [4], raster milling [5], as well as precision grinding [6]. Although each fabrication method has its own advantages and disadvantages, it can be noted here that – in general terms – they are all capable of producing structures with a nanometric surface finish and submicron form accuracy.

The surveyed literature reveals that ultraprecise single point cutting (USPC) is one of the most used microgroove manufacturing technologies involving non-rotational cutting tools. In addition to the aforementioned benefit associated with the involvement of non-rotational tools USPC enables the generation of extremely accurate structures characterized by an ultraprecise surface finish [7].

MACHINE SETUP AND PROCESS KINEMATICS

The tool used in this study consists of a monocrystalline diamond insert and its triangular holder (*FIGURE 1*). The diamond insert has a set rake angle of 0°, whereas the clearance angle was prescribed at 10°.

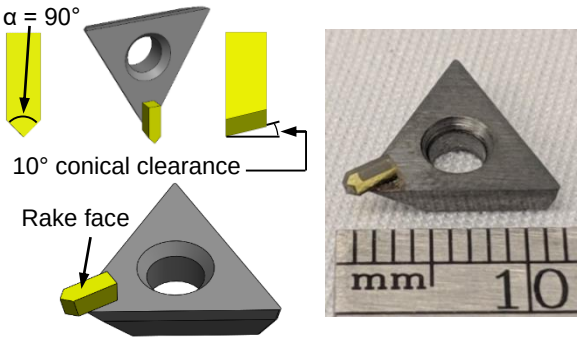

FIGURE 1. V-shaped monocrystalline diamond single point cutting tool

In addition to these two parameters, the tool is also characterized an included angle of 90° that has a direct effect on the geometry of the V-groove. In this case, the tool enables the generation of a symmetric V-groove profile.

Even though the cutting strategies are different in nature, the experimental setup used in this study is identical to the one reported in the past [8].

The inherent cutting kinematics of the current strategy constituted the primary rationale behind the terminology used to describe the current

cutting strategy. According to this approach, points P_1, P_2, P_3 and P_4 denoting the successive cutting passes on the workpiece (*FIGURE 2c*) are all located on one side the profile to be cut. As such, this strategy was termed “one-side”.

The complete cutting kinematics of the strategy involves the tool moving in all three axes (*X*, *Y* and *Z*), whereas its main motion remains contained in the *YZ* plane. The tool follows a repeated sequence of down-across-up in the *YZ* plane before transitioning to the following cutting pass, essentially by moving to a different *X*-axis position (*FIGURE 2b*).

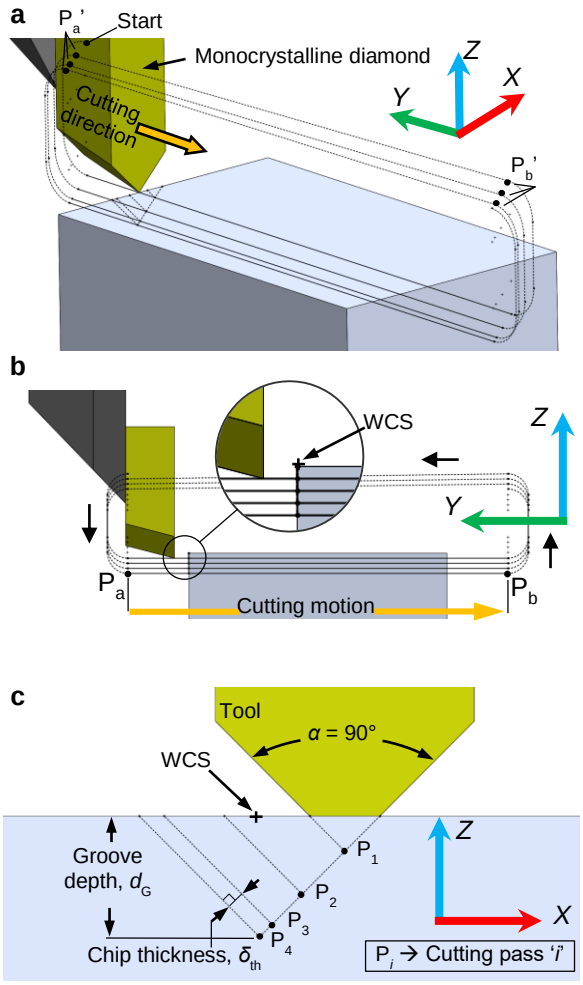

FIGURE 2. Cutting kinematics: (a) isometric view; (b) side view along +X direction; (c) front view along +Y direction.

Cutting/material removal occurs when the tool travels in the negative *Y*-direction, i.e., from P_a to P_b (*FIGURE 2b*). This is followed by the upward ancillary/non-cutting motion that prepares the tool for its transition to the next cutting pass. The transition occurs from P_b’ to P_a’ as depicted in *FIGURE 2a*. After transitioning to the beginning of a new cutting cycle, the tool steps further down by means of second non-cutting downward motion. During the “across” motion the tool tip is always aligned with the bottom of the groove that will be cut (*FIGURE 2c*).

According to the one-side constant-area strategy that represents the main focus of the current study, the distance between points P_1, P_2,…P_N and associated chip thickness (δ_i) cannot be constant since it is determined by the preset ‘constant cutting area’ constraint. More specifically, by starting with a minimal final chip thickness ($\delta_{min} = \delta_N$), the developed post-processor has generated all intermediate cutting passes from the last to the first (i.e., P_N to P_1), which in turns results in a gradually increasing chip thickness (δ_i).

ONE-SIDE CUTTING STRATEGY WITH CONSTANT AREA

The current strategy employs cutting with a constant cutting area. However, the first cut typically has a cutting area less than or equal to the desired ‘constant area’ parameter. This is mainly caused by a combination between the small chip thickness and workpiece surface tolerance that prevent the accurate setting of the *Z*-height of the tool tip. The main parameter of the analytical formulation is constituted by the area to be maintained throughout all passes. This value is heavily dependent on the desired final chip thickness (δ_N). Subsequently, the position of the cutting tip for each cutting pass can be determined by means of the preset constant cutting area.

The typical geometry of the V-groove is characterized by the cutting depth (d_i) and the groove included angle (α) as shown in *FIGURE 3*. In order to determine the constant area of material being removed (A_i), trigonometric relationships involving cutting depth (d_i) and groove included angle (α) were used to generate Eqs. 1-7.

To minimize complexity, the analytical calculations of the constant cutting area and variable depth-of-cut have been initialized from the bottom of the V-groove profile. The chip thickness of the last cutting pass (δ_N) enables determination of the second last depth-of-cut (d_{N-1}), subtracting the last change in depth, Δd_N,

from the final depth of the groove ($d_{Groove}=d_N$), as indicated in Eqs. 1-2.

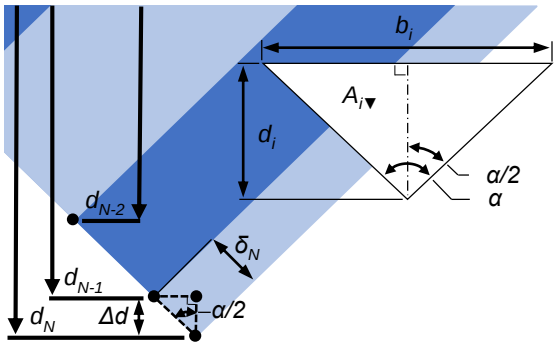

FIGURE 3. Geometric parameters associated with a symmetrical V-groove characterized by an included angle α.

$$\Delta d_i = \delta_i / \sin(\alpha / 2) \quad (1)$$

$$d_i = d_{i+1} - \Delta d_{i+1} \; i = 1,2,3\ldots(N\text{-}1) \quad (2)$$

In addition, the base of a full depth triangle illustrated in Eq. 3 can be combined with Eq. 1 to calculate the full area of a triangle as shown in Eq. 4. After that, the constant cutting area is obtained by subtracting the full depth triangle area of the current profile ($A_{▼}$) from the area of associated with the previous depth of cut ($A_{▼(N-1)}$) and similar iterative formulations can be used after that.

$$b_i = 2d_i \tan(\alpha / 2) \quad (3)$$

$$A_{▼i} = b_i d_i / 2 = d_i^2 \tan(\alpha / 2) \quad (4)$$

$$A_{const} = A_i = A_{▼i} - A_{▼(i-1)}, \; i = 2, 3\ldots N \quad (5)$$

$$A_{▼(i-1)} = A_{▼i} - A_{const} \quad (6)$$

The formulas above will ensure that the cut performed as $d_{(N-1)}$ will be characterized by the same A_{const}. The following depth of cut ($d_{(N-2)}$) is determined by Eq. 7.

$$d_i = \sqrt{A_{▼i} / \tan(\alpha / 2)} \quad (7)$$

Based on these calculations, the analytical dependence of cutting area on cutting pass/depth is illustrated in *FIGURE 4*. As shown in the graph, the very first cut/pass remains the only one characterized by a cutting area equal or less than A_{const}.

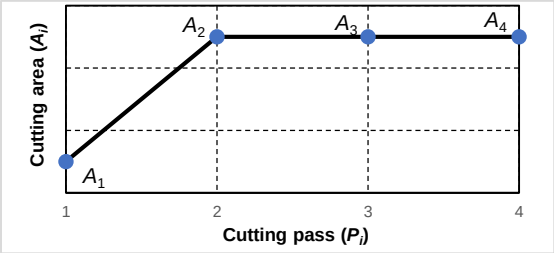

FIGURE 4. Dependence between cutting area and cutting pass

EXPERIMENTAL RESULTS

TABLE 1 summarizes the experimental parameters used in the current study. Cutting trials were performed on an aluminum 6061 block.

TABLE 1. Summary of experimental conditions

Feed rate (mm/min)	500
Last chip thickness (μm)	2
Coolant	Isoparaffin mist

The previously developed LabVIEW-based data acquisition system [8] was used to record cutting force data. *FIGURE 5* depicts an overview of the results obtained. The components of the force (F_X, F_Y, F_Z) were measured for an entire cycle of a V-groove fabrication. Following the processing of the data, a low pass filter with a 10 Hz cut-off frequency was used to remove high-frequency noise from the raw data. This step yielded the filtered raw data of all cutting forces presented in *FIGURE 5a*. The analysis presented here is focused on F_Y (cutting force component along the feed direction) since this represents the main contributor to the 3D cutting force magnitude and surface quality formation. Each pulse in the cutting force signal (*FIGURE 5a*) represents a single cut across the workpiece.

The next step in data processing was focused on the elimination of the visible data drift that was likely introduced by the employed measurement system. This was done by subtracting the linear trend determined from data regions associated with time intervals in which the tool was disengaged from the workpiece. After drift slope of the signal was determined, it was subtracted from the raw measurement and all cutting force components returned the horizontally levelled position in which all non-engaged tool positions

have translated in null components of the cutting force (*FIGURE 5b*).

A more careful analysis of the data presented reveals signal fluctuations on each pulse of the cutting force (*FIGURE 5c*). Although the of the causes of the fluctuations remain unknown at this time, it can be speculated that this might be a consequence of the initial impact between tool and workpiece, possibly translated into a damped vibratory response. The average values for each component of the cutting force are presented in *FIGURE 5d*. As expected, F_X was measured at a negligible value. F_Z, however, is not negligible and seems to be maintained fairy at a constant value. As previously mentioned, F_Y constitutes the largest contributor to the axial cutting force and its magnitude remained quasi-constant throughout the entire V-groove fabrication process.

However, F_Y seems to slowly decay with each cutting pass, possibly due to the gradual decrease of the cutting depth. This downward trend of F_Y might imply that V-groove cutting force is not only dependent on the area of material removed (as implied by the 'classical' material removal rate theory), but also on the chip thickness/cutting depth. Evidently, since the decreasing trend of F_Y is relatively minor, it can be safely assumed that the area of material removed remains the most important contributor to the magnitude of the axial force. The relative influence of the two variables on F_Y can be represented analytically as:

$$F_Y = C_A A_i + C_\delta \delta_i, C_A \gg C_\delta \quad (8)$$

where C_A and C_δ are proportionality coefficients. Although a clear reason behind the interdependence between chip thickness and axial force is not known at this time, it could be perhaps contemplated here that cutting depth-related differences in shear plane formation as well as the altered dynamics of the cutting chip formation might play a role.

In addition to the cutting force results, the surface of the micro groove was assessed by means of an optical profilometer. In order to accurately measure the surface generated, the workpiece had to be tilted by 45° as illustrated in *FIGURE 6a*. This allowed the measured surface to be become normal to the microscope's main measurement direction.

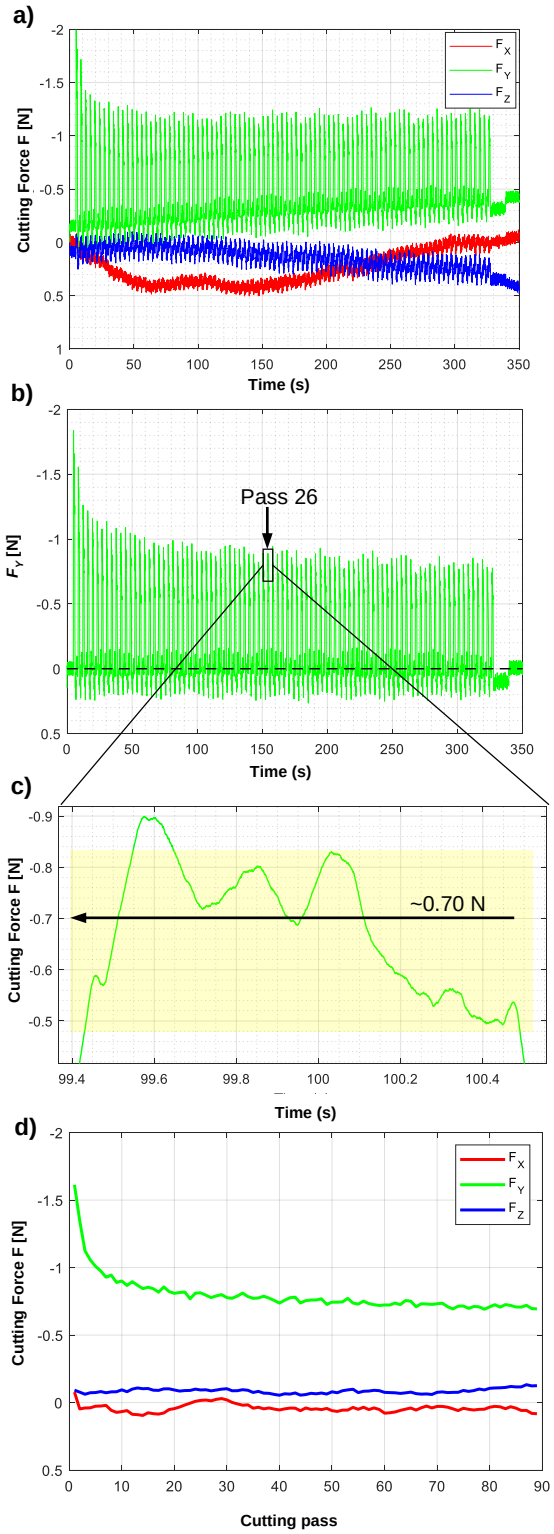

FIGURE 5. Cutting force measurements: (a) raw data; (b) F_Y with measurement drift corrected; (c) sample of average F_Y calculation; (d) average cutting force components.

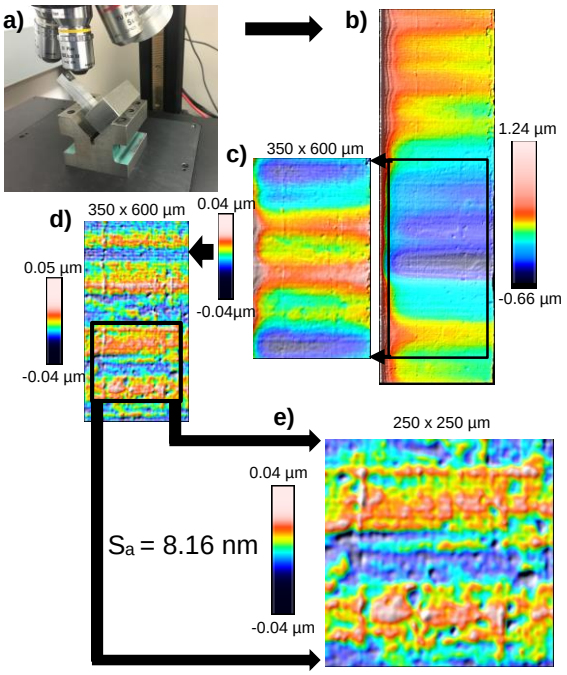

FIGURE 6. Surface quality assessment: (a) tilted workpiece; (b) raw data; (c) data with planar tilt removed; (d) surface roughness obtained by filtering out waviness; e) sample of V-groove surface topography for 2µm chip thickness

FIGURE 6b illustrates the raw data measurement of the surface topography. The effect of the still remaining inclination is visible in the raw data, and it is caused by an out-of-normal condition between the V-groove facet and the measurement direction. This was subsequently corrected through a planar form removal technique (*FIGURE 6c*). Finally, the surface quality data was further filtered with a cutoff wavelength of 80µm (ISO 16610-61) in order to eliminate surface waviness and retain only its roughness (*FIGURE 6d*). The final topographic data is shown in *FIGURE 6e* and the resulting 8.16 nm roughness reveals that the cutting strategy presented here is capable of producing ultraprecise surfaces.

The form accuracy of the fabricated V-Groove profiles was measured by mean of an optical microscope. *FIGURE 7a* illustrates the results of a typical measurement performed on a single profile yielding an included angle of 89.96° that is minimally deviating with respect to the nominal 90° value. Additional angular measurements performed on two profiles are depicted in *FIGURE 6b*. These measurements not only imply the accuracy of the proposed strategy (that is capable to generate near-perfect included V-groove angles), but is also capable to maintain a precise alignment of the profiles. This latter idea is verified by the fact that flank groove line 1 is positioned at 45.02° with respect to the horizontal line connecting two adjacent apices.

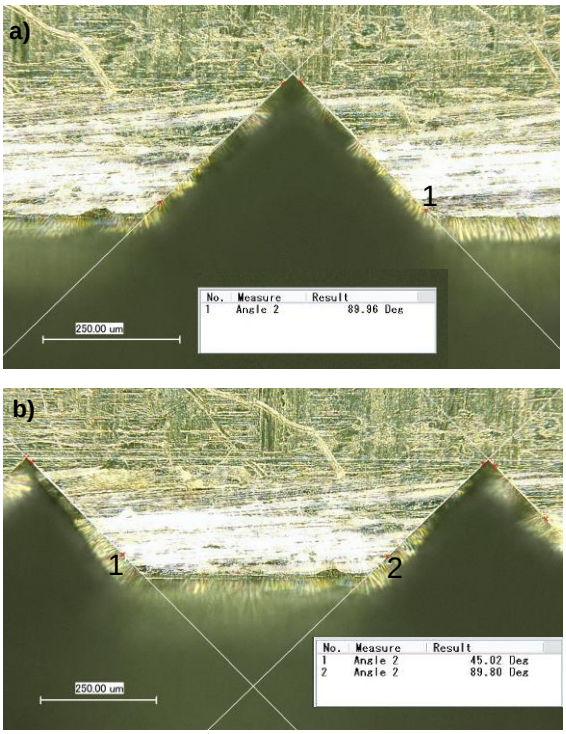

FIGURE 7. Profile accuracy: (a) included angle; (b) orientation of the flank profile

SUMMARY AND CONCLUSIONS

The current study presents a cutting strategy to be used during V-groove fabrication through ultraprecise single point cutting. The profile of the groove is produced by maintaining a constant cutting area. The experimental results suggest that a correlation between the amount of material removed in each pass and the magnitude of F_Y exists. However, while from a theoretical standpoint it is reasonable to predict that F_Y will remain constant since it is directly proportional with the amount of material removed (of a preset constant cutting area), a certain amount of decay in the magnitude of F_Y was noticeable. This might suggest that the gradually decreasing chip thickness also plays an unforeseen but possibly important role on the cutting force magnitude. In addition, surface topography measurements have confirmed that the proposed strategy can produce ultraprecise surfaces.

The analysis presented in the current study sets the foundation for further development of future

and more efficient cutting strategies to be used in ultraprecise single point cutting of V-grooves. Furthermore, simulation models of the cutting mechanics will be developed and then validated against the experimentally acquired results.

ACKNOWLEDGEMENTS

The work presented in this study is the result of the collaboration between Western University (London, Ontario) and National Research Council of Canada (London, Ontario). Partial financial support was also provided by Natural Sciences and Engineering Research Council (NSERC) of Canada.

REFERENCES

[1] Flucke, C., R. Gläbe, and E. Brinksmeier. *Diamond Micro Chiselling–Cutting of Prismatic Micro Optic Arrays*. in *Proceedings of the 7th euspen International Conference, Bremen*. 2007.

[2] Suzuki, H., et al., *Precision cutting of aspherical ceramic molds with micro PCD milling tool.* CIRP annals, 2007. **56**(1): p. 131-134.

[3] Moriya, T., et al., *Creation of V-shaped microgrooves with flat-ends by 6-axis control ultraprecision machining.* CIRP Annals, 2010. **59**(1): p. 61-66.

[4] Fang, F. and Y. Liu, *On minimum exit-burr in micro cutting.* Journal of Micromechanics and Microengineering, 2004. **14**(7): p. 984.

[5] Wang, S., et al., *A study of the fabrication of v-groove structure in ultra-precision milling.* International Journal of Computer Integrated Manufacturing, 2014. **27**(11): p. 986-996.

[6] Wang, S., et al., *Development of a precision grinding machine system for the fabrication of micro V-grooves array.* The International Journal of Advanced Manufacturing Technology, 2018. **97**(5-8): p. 2141-2150.

[7] BIDDUT, A.Q., *Micro-grooving on electroless nickel plated die materials*. 2006.

[8] D. Joao et al., "Axial strategy for ultraprecise single point cutting of V-grooves. Case 1: Constant chip thickness," Procedia Manuf., 2019; in press

MACHINE LEARNING APPROACH PREDICTION OF STRESS-STRAIN CURVES FOR LOW-TEMPERATURE ANNEALED CARBON STEELS

Reona Ito[1], Keisuke Nagato[2], Takayoshi Niho[2] and Masayuki Nakao[2]
[1]Department of Technology Management for Innovation,
The University of Tokyo,
Bunkyo-ku, Tokyo, Japan
[2]Department of Mechanical Engineering,
The University of Tokyo,
Bunkyo-ku, Tokyo, Japan

INTRODUCTION

The mechanical properties of carbon steel, one of the common industrial materials, are determined by the morphology of its microstructure. Therefore, research is being conducted to predict the mechanical properties from the microstructures of materials such as grain size and form of phase in the materials [1,2]. As a popular example of predicting mechanical properties from the microstructure of materials, the Hall–Petch relation [3] has been proposed that can predict the yield stress of materials from the grain size.

However, it is known that mechanical properties of alloys containing multiple elements undergo complex transformation of their microstructures through processes such as heat treatments and other processing methods. Thus, in empirical ways, limits would appear for creating a prediction model that considers the complexity of transformations in microstructures caused by processing of materials. To overcome limitations arising from the complexity, it has been proposed that the mechanical properties of materials can be predicted using the machine learning approach methods that configures artificial neural networks (ANN). This method can create prediction models by training based on complex input information in the microstructures of the materials.

Setti [4] reported an accurate prediction of the stress-strain curves of titanium alloys, which are composed of different phases, by the machine learning approach. Using a similar approach, Adachi [5] predicted the stress-strain curve of ferrite-martensite dual phase (DP) steels by training the ANN with an input value of material genomes, such as volume fraction and micro-hardness of the ferrite phase. In those researches, the method for prediction of the stress-strain curves by the ANN mainly uses information of the microstructures in materials for training. Since the information of the microstructures in the material is complicated and has randomness, the mechanical properties should be predicted using the information or parameters at the process performed on the materials that are more accessible and have reliable data compared with the microstructural parameters.

In this research, we focused on the method to predict the stress-strain curves by the ANN-based machine learning approach using information of heat treatment processes for training.

METHOD

Data Acquisition for Machine Learning

The material used in this paper is 1045 AISI, common medium carbon steels. The specimens are cylinder-shaped with a diameter of 8 mm and a height of 12 mm. We conducted low-temperature annealing, which is usually implemented to make the material soft and remove the residual stress in the material. *FIGURE 1* shows a diagram of the heat treatment. In order to prevent significant oxidization of the material, all heat treatment processes were conducted in a vacuumed electric furnace. The temperature inside of the furnace was raised to T in 20 min regardless of the target temperature T. After the furnace temperature reached T, it was kept at T for time t and was cooled until the temperature in the furnace reached 400 °C at 1 °C per minute of the cooling rate. The furnace was turned off when the temperature reached 400 °C or less, and was air cooled to room temperature RT (approximately 20°C). Each value of the target temperature T and holding time t in the heat treatment conducted in this experiment are shown in the *TABLE 1*. The minimum value of T was set to 450 °C, which is sufficiently above the recrystallization temperature of 1045 AISI, and the maximum value was set to 750 °C. In the range of 450–750 °C, 550 °C, and 650 °C were

also selected for the heat treatment parameter *T*. The holding time *t* was set to three patterns of 30 min, 60 min, and 120 min.

Four types of heat treatments—A, B, C, D—shown in *TABLE 1* were implemented on the specimens in this experiment. After the specimens had been heat-treated, they were compressed by THERMECMASTOR Z (Fuji Electronic Industrial Co., LTD) to obtain the stress-strain curves for machine learning. The strain rate during the compression test was fixed at 0.001.

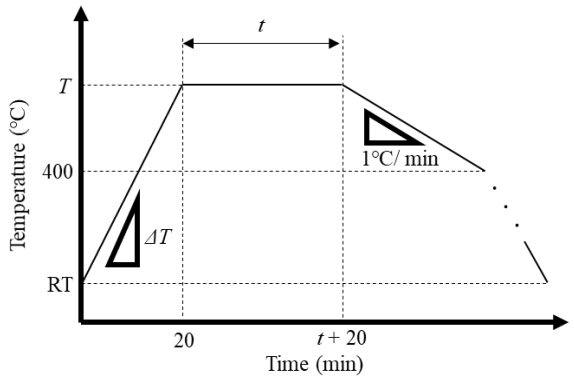

FIGURE 1. Process of heat treatment.

TABLE 1. Specific condition of heat treatment.

		t (min)		
		30	60	120
T (°C)	450	A	-	-
	550	-	B	-
	650	-	-	C
	750	D	-	-

Artificial Neural Network

The ANN used in this experiment was coded with Python 3.6 environment using *Tensorflow*, an open-source software library for machine learning [6]. The network's main structure was roughly divided into three parts, an input layer, hidden layers, and an output layer.

Four feature values, which had been inputted into an input layer, are shown in *FIGURE 2*: the strain value, target temperature *T* (°C), holding time *t* (min), and heating rate ΔT

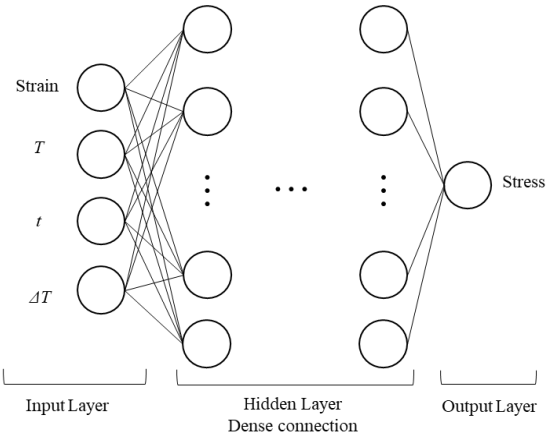

FIGURE 2. Schematic of the artificial neural network.

TABLE 2. Network number and number of nodes for each network.

Network No.	Number of Nodes 1st Hidden Layer	Number of Nodes 2nd Hidden Layer
1	100	-
2	500	-
3	1000	-
4	100	100
5	500	500
6	1000	1000

(°C/min), which are the parameters during the heat treatment process. Owing to the large difference in numerical size depending on the types of feature values (e.g., largest value of stress compared with that of strain), normalization of feature values had been subjected to each feature value such that the minimum value in each feature value is 0 and the maximum value is 1 before inputting them into an input layer. Further, 80% of the total dataset was used as the training data and the rest as validation data for the trained model to check the generalization performance. Batch training [7] was performed in the step of training and the size of the batch was set to 100. *TABLE 2* shows the number of hidden layers and nodes for each layer. The number of nodes in a single hidden layer was examined in three patterns of 100, 500, and 1000, and the number of layers in two patterns of 1 or 2 layers. A total of six patterns of networks (Network No. 1–6 in *TABLE 2*) were implemented in this experiment. Each node was densely connected (a single node is connected to all nodes in the next layer), and the type of activation function applied at all edges (connections of

nodes) was a rectified linear unit (ReLU). In addition, the *Dropout* algorithm [8] was used as the regularization method to prevent overfitting, and the value of the dropout-rate (one of the hyper-parameters in the dropout algorithm) for the nodes in the networks was fixed to 20%.

Mean squared error (MSE) was used for the objective function to optimize the ANN, and *Adam* [9] was selected as the optimization method for training. In the case of using Adam for an optimizer, it is necessary to set the learning rate. In this experiment, the learning rate was set to a constant value of 0.001. Moreover, the number of epochs for training was fixed with a constant parameter of 100.

Three stress-strain curves heat-treated with conditions A, C, and D, listed in *TABLE 1,* were used for training the ANN to predict the stress-strain curve that was subjected to the heat treatment B. To check the prediction accuracy of the trained model, a predicted curve was compared with an actual stress-strain curve obtained from the experiment.

RESULT AND DISCUSSION

Microstructures of specimens (5% nital-etched), which were heat-treated with conditions A and D observed with an optical microscope are shown in *FIGURES 3(a)***,** *(b)*. The microstructure of the specimen that was heat-treated in condition A (45 °C in 30 min, *FIGURE 3(a)*) is composed of a ferrite phase and a pearlite phase which ferrite and cementite phase are formed in stripes (enclosed in a square). On the other hand, the microstructure in a specimen heat-treated under condition D (750 °C in 30 min, *FIGURE 3(b)*) has a larger amount of ferrite phase compared with that under condition A. Moreover, most parts are assumed to be in the pearlite phase before the heat treatment are filled with the ferrite phase leaving the cementite phase clearly. Thereby, although the heat treatment did not perform clear phase transformations since the holding temperature *T* during the heat treatment did not exceed the α-γ phase transformation temperature of AISI1045 (greater than 750 °C), it is clear that the phase morphology in materials had been dramatically and intricately changed due to the heat treatment.

FIGURE 4 shows the stress-strain curves used for training the ANN obtained from the compression test. According to *FIGURE 4*, no obvious similarity was found in the curves. This implies that the profile of the stress-strain curves varied depending on each heat treatment condition. The three curves in *FIGURE 4* are adopted to train the six networks shown in *TABLE 2*.

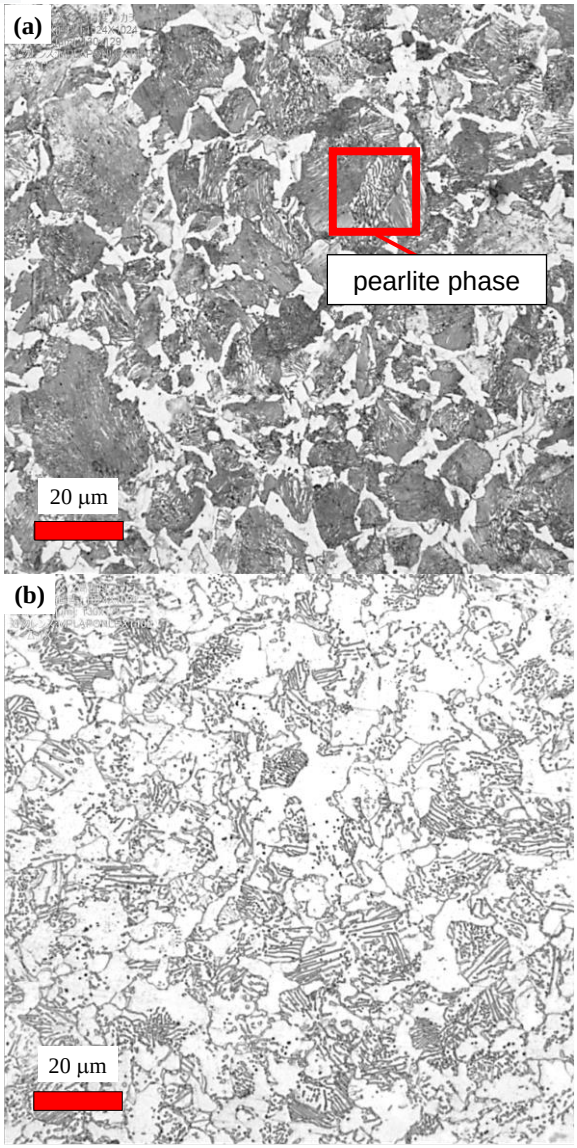

FIGURES 3. Microstructure of AISI1045 heat-treated at (a) 450 °C *in 30 min; (b) 750* °C *in 30 min.*

Moreover, the stress-strain curves heat-treated in condition B predicted by Network Nos. 1, 3, 5, and 6 are shown in *FIGURE 5(a)–(d)*. The stress-strain curve procured by the compression experiment are also shown in *FIGURE 5(a)–(d)*. The predicted curves by the single hidden layer networks with 100 and 1000 nodes (*FIGURE 5(a)* and *(b), respectively*) have large gaps between the curves obtained from the compression test.

According to *FIGURE 5(c)***,** the 500 nodes with the two hidden layer network structure are expected to be closest to the experimental curve. The learning curves of Network No. 5 are shown

in *FIGURE 6*, and it shows that the network had been trained enough without overfitting. Network Nos. 1 and 3 have single hidden layers, and it is speculated that these networks do not have enough complexity to describe the complicated transformation of mechanical properties through heat treatment. Moreover, despite the high complexity of Network No. 6, we can see the gaps between the predicted curve and an experimental curve. This may be caused by the over-fitting of the network.

The curve predicted by the trained Network No. 5 shown in the *FIGURE 5(c)* has a close profile compared with the experimental curve. However, the prediction accuracy after the strain value of 0.2 appears to be deteriorated. The cause of low prediction accuracy was assumed to be the unstable behaviors due to the contaminated training data owing to the formation of voids in the material at a large deformation.

Inoue [10] reported that the fraction of cementite in the pearlite phase causes voids in the material. As shown in *FIGURE 3(a)* and *(b)*, the annealed specimens have microstructures of ferrite and pearlite phases, and as the amount of strain increases, voids occur, and unstable fracture behaviors were introduced into the training data. Thus, the prediction accuracy of the stress-strain curve fell in the high strain range (0.2~).

As a result, it is possible to predict the stress-strain curves by using only the parameters of the heat treatment by machine learning, even for materials whose phase morphology changes complexly, as shown in *FIGURE 3*.

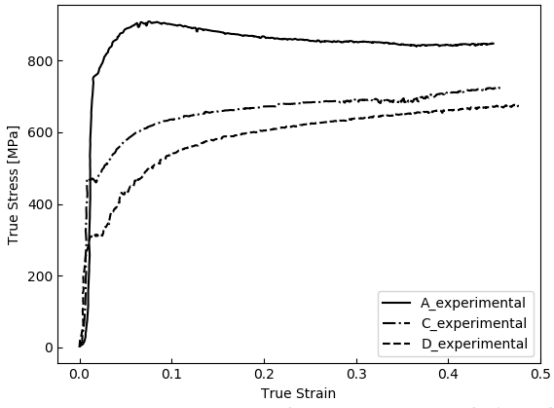

FIGURE 4. Stress-strain curves used for the training of the neural network obtained from the compression experiments for each heat treatment conditions.

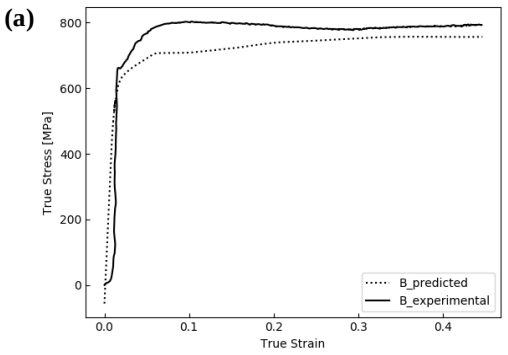

Network No.1 (100)

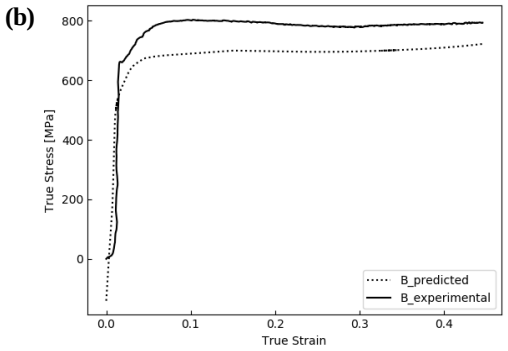

Network No.3 (1000)

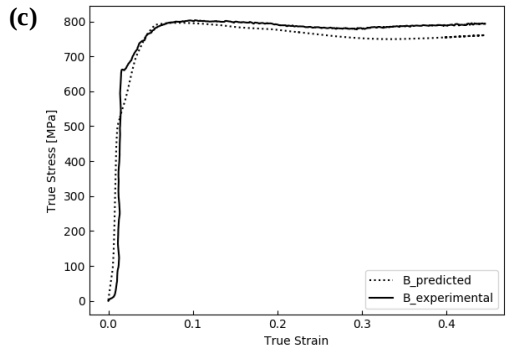

Network No.5 (500-500)

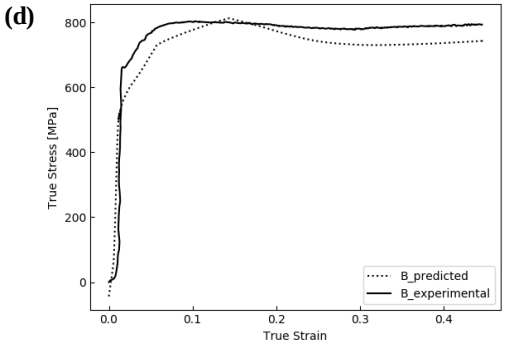

Network No.6 (1000-1000)

FIGURES 5. Predicted stress-strain curves by the trained model and experimental stress-strain curves at (a) Network No. 1, (b) Network No. 3, (c) Network No. 5, (d) Network No. 6.

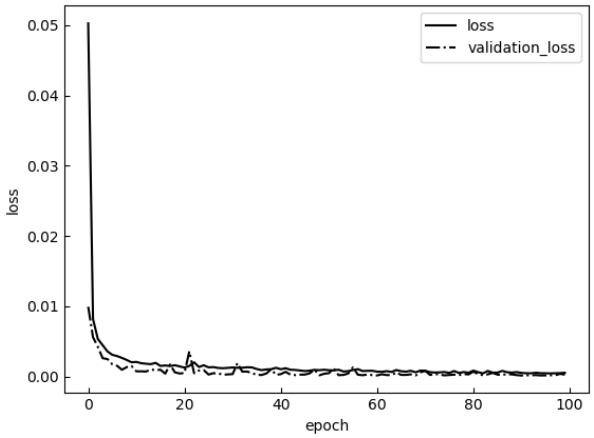

FIGURE 6. Value of MSE (loss) and validation loss vs number of epochs at Network No. 5 (500-500).

CONCLUSION

A compression test was performed on medium carbon steel AISI1045 subjected to four types of heat treatments.

Heat treatment was performed at different holding times from 450 °C (above recrystallization temperature) to 750 °C (below the α-γ phase transformation temperature). The microstructure of the heat-treated material was observed with an optical microscope, and it was found that although the phase transformation did not occur, the morphology of the ferrite phase and pearlite phase was significantly transformed.

Artificial neural networks (ANN) were trained by the data of three stress-strain curves (450 °C in 30 min, 650 °C in 120 min, 750 °C in 30 min) obtained by the compression tests. Using the trained ANN model, the stress-strain curve of the heat-treated carbon steel (550 °C in 60 minutes) was predicted by inputting the strain value, holding temperature, holding time, and temperature rising rate into the trained network. Finally, the network outputted the value of the stress.

The ANN trained in this research had six types and they were compared an accuracy of a prediction of stress-strain curve.

As a result, we found out that the network structure of the two hidden layers with 500 nodes for each layer predicted the closest stress-strain curve to an experimental curve, and it is possible to predict the stress-strain curve by only utilizing the heat treatment parameters by machine learning.

However, the prediction accuracy deteriorated after the strain value reached 0.2. This poor accuracy at the large deformation range was considered as a result from unstable behavior in the material caused by the voids, which formed due to the fracture of cementite in the pearlite phase.

The structure of the network that most accurately predicts the stress-strain curve depends on the dataset. Therefore, when the dataset is changed, the optimal model for predicting the stress-strain curve is different from that obtained in this study. This means that there is a limit to the types of stress-strain curves that can be predicted using the dataset used in this study. In the future, it is required to increase the variation of the stress-strain curves that can be predicted by designing the structure of the dataset.

REFERENCES

[1] Tekkaya A, Allwood J, Bariani P, Bruschi S, Cao J, Gramlich S, Groche P, Hirt G, Ishikawa T, Lobbe C, Lueg-Althoff J, Merklein M, Misiolek W, Pietrzyk M, Shivpuri R, Yanagimoto J. Metal Forming Beyond Shaping: Predicting and Setting Product Properties. CIRP Annals – Manufacturing Technology. 2015; 64: 629-653.

[2] Umemoto M. Relationships Between Microstructure and Mechanical Properties in Steels. Tetsu-to-Hagane. 1995; 81(3): 157-166.

[3] Hansen N. Hall-Petch Relation and Boundary Strengthening. Scripta Materialia. 2004; 51: 801-806.

[4] Setti S, Rao R. Artificial Neural Network Approach for Prediction of Stress-Strain Curve of near β Titanium Alloy. Rare Metals. 2014; 33: 249-257.

[5] High Dimensional Microstructure Data-driven Prediction of Stress-Strain Curve of DP Steels by Primary Artificial Intelligence. Tetsu-to-Hagane. 2016; 102(1): 47-55.

[6] Pedregosa F, Varoquaux G, Gramfort A, Michel V, Thirion B, Grisel O, Blondel M, Prettenhofer P, Weiss R, Dubourg V, Vanderplas J, Passos A, Cournapeau D. Scikit-learn: Machine Learning in Python. Journal of Machine Learning Research. 2011; 12: 2825-2830.

[7] Bishop C. Pattern Recognition and Machine Learning. Springer. New York: 2006.

[8] Srivastava N, Hinton G, Krizhevky A, Sutskever I, Salakhutdinov R. Dropout: A Simple Way to Prevent Neural Networks from Overfitting. Journal of Machine Learning Research. 2014; 15: 1929-1958.

[9] Kingma D, Ba J. ADAM: A Method for Stochastic Optimization. International Conference on Learning Representative. 2015.
[10] Inoue T, Kinoshita S. Strain Partitioning and Void Formation in Ferrite-Pearlite Steels Deformed in Tension. Tetsu-to-Hagane. 1976; 62(1): 90-99.

Study on laser-induced oxidation of Ti6Al4V alloy under two different reactive atmospheres

Wei Zhao[1], Guolong Zhao[1], Ning He[1], Liang Li[1], Asif Iqbal[2]
[1] College of Mechanical and Electrical Engineering, Nanjing University of Aeronautics and Astronautics, Nanjing 210016, P. R. China.
[2] Faculty of Integrated Technologies, Universiti Brunei Darussalam, Jalan Tungku Link, Gadong BE1410, Brunei Darussalam.

Abstract

The oxidation behavior of Ti6Al4V titanium alloy under laser irradiation in the conditions of atmospheric air and assisted oxygen delivery was studied. A nanosecond pulsed Y_b: glass fiber laser was used. The thickness of oxide layer, microstructure and phase composition of the material after laser irradiation were investigated. The characterization of the surface and subsurface microstructure, as well as the cross-sectional morphology were performed using scanning electron microscopy (SEM). The phase identification was performed using X-ray diffraction (XRD). The combined effects of accumulated laser fluence and reactive atmosphere on the oxidation behavior of Ti6Al4V were also studied in detail. With an increase in accumulated laser fluence, a porous and easily removable oxide layer gradually formed on the surface, while a compact oxide layer was also formed. At high accumulated laser fluence, the thickness of the porous oxide layer increased dramatically, while the change of thickness of compact oxide layer was not obvious. The reactive atmosphere also had a significant influence on the microstructure of the surface and subsurface layers. SEM and XRD results revealed existence of strong oxidation reactions that underwent in the condition of assisted oxygen delivery at a fixed accumulated laser fluence. The oxide layer was composed mainly of anatase and rutile titanium oxides.

Keywords: Laser-induced oxidation; Ti6Al4V; Reactive atmosphere; Surface morphology; Nanoparticles.

1 Introduction

Laser induced oxidation of metal surfaces has received considerable attention by the researchers in the last two decades due to its high spatial resolution, versatility and short processing time [1-4]. Laser induced oxidation of titanium and its alloys can be used in many fields, e.g., laser coloring and marking [4,5], laser surface modification [6,7], and synthesis of nanoparticles [8,9]. This technology has some significant technical application values [4,6-10].

In essence, laser induced oxidation of metals is a process of surface materials' rapid oxidation corrosion at high temperatures generated by laser radiation. This process is affected by many factors, e.g., laser process parameters, experimental environment, absorption coefficient and properties of the material itself. For the influence of laser process parameters, many researchers have investigated the microstructure of oxide layer obtained by nanosecond pulsed laser irradiation in atmospheric air [2-5,11-14]. The investigated features include the phase morphology, chemical composition, and thickness of the oxide layer. Pérez del Pino et al have revealed the formation of a bi-layer structure composed of a compact layer covered by a thin granulated layer when pure titanium was irradiated with an Nd:YAG laser in the air [11]. The thickness of this compact layer increased from 0.1 μm to 6 μm with an increase in accumulated laser fluence, while the thickness of the granulated layer increased from 0.4 μm to 4 μm. Adams et al have pointed out that coatings consisting of three distinct layers (TiO_2/TiO/Ti_6O+TiO_xN_{1-x}) were formed when pure grade 2 titanium was irradiated with a nanosecond fiber pulsed laser below the ablation threshold value of 844 J/cm^2 [12]. Antonczak et al. reported that nitrogen might have existed on the outer surface, which formed an optically active layer with titanium oxides (mainly TiO_2) [13]. The reaction atmosphere also has a non-ignorable influence on laser treatment of metals. However, the research in this aspect has mainly focused on the formation process and structure of nanoparticles [14,15]. There is a little research work available on the effect of atmospheric reaction on the microstructures of surface and subsurface, particularly under high accumulated laser fluence.

In this work, laser induced oxidation of Ti6Al4V alloys under the conditions of atmospheric air and assisted oxygen delivery was conducted. This study focuses on the microstructural changes of oxide layer surface and sub-layer surface in a wide range of laser beam energy

density and two different reactive atmospheres.

2 Experimental work

2.1 Substrate material

In this work, commercially available Ti6Al4V titanium alloy was used as the substrate material. The experimental samples with dimensions of 10 mm × 10 mm × 3 mm were cut from the monolithic block with an electrical discharge machine (EDM). The surface of the samples to be irradiated by the laser beam was polished with an automatic grinding/polishing machine using diamond slurries. After polishing, the surface roughness ranged between 34 and 42 nm as measured with a 3D confocal surface profiler (Phase Shift MicroXAM-3D, ADE). Before laser treatment, the samples were ultrasonically cleaned for 15 minutes in acetone and absolute ethyl alcohol to eliminate contaminations.

2.2 Laser treatment

A nanosecond pulse Y_b: glass fiber laser from IPG (YLP-1/100/20) was used in this research, having a wavelength of 1064 nm, maximum average output power of 20 W, beam quality factor of $M^2 \leq 1.5$, pulse duration of 100 ns, and pulse repetition rate of 20-200 kHz. The setup of laser induced oxidation experiments is shown in Figure 1. The diameter of the laser beam at the focus plane was approximately 57 μm. The workpiece was horizontally mounted on a two-axis (x- and y-axes) linear stage. A flexible nozzle was fixed in an inclined position atop the workpiece allowing for an adjustable flow of assist oxygen during the experiments.

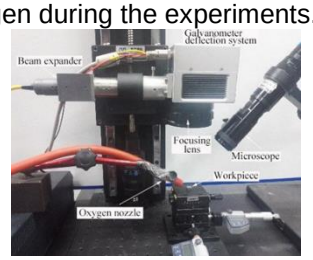

FIGURE 1. Experimental setup in respect of laser induced oxidation.

The pulse repetition rate and track displacement of laser were fixed at 20 kHz and 10 μm, respectively. The process parameters of laser induced oxidation of Ti6Al4V are shown in Table 1. The accumulated laser fluence is expressed as follows [13]:

$$F = \frac{2\sqrt{2}P}{\pi\omega_o V} \quad (1)$$

Where P is the average laser power, ω_0 is the radius of the laser beam at the focal plane, and V is the scanning velocity of the laser beam. The laser induced oxidation experiments were conducted both in atmospheric air and under assisted oxygen delivery. The oxygen flow rate was fixed at 5 L/min for the condition of assisted oxygen delivery.

TABLE 1. Process parameters of laser induced oxidation of the Ti6Al4V alloy.

No.	Power (W)	Velocity(mm/s)	Fluence (J/cm^2)	O_2 flow(L/min)
1	3.2	10	506	0
2	3.2	5	1011	0
3	3.2	1	5057	0
4	4.0	1	6321	0
5	3.2	10	506	5
6	3.2	5	1011	5
7	3.2	1	5057	5
8	4.0	1	6321	5

2.3 Characterization

Scanning electron microscope (SEM, Hitachi S4800) equipped with an energy dispersive spectrometer (EDS) was used to characterize the morphology of the surface and subsurface and microstructure of the cross-section after being irradiated with the laser beam. The subsurface was obtained through removing loose and porous surface layer by ultrasonic cleaning for about 10 minutes in acetone. X-ray diffraction (XRD, Bruker D8) was used to identify phases formed by laser irradiation.

3 Results and discussions

3.1 Morphology of surface and subsurface

Figure 2 shows the morphology of oxide layer surface and sub-layer surface after laser induced oxidation in atmospheric air with accumulated laser fluence varying from 506 J/cm^2 to 6321 J/cm^2. It is clear from Figure 2(a) that at the lowest accumulated laser fluence of 506 J/cm^2, the original surface after laser irradiation appears flat and compact with no apparent oxide particles. There are some obvious stripes and a network of micro-cracks found on the surface. It is speculated that the micro-cracks might have been caused by the release of residual stress, which was induced by high-temperature gradients during the cooling process after undergoing pulse laser irradiation [16]. EDS analysis, shown in Figure 4, reveals presence of around 26.41 at.% of oxygen elements on the surface, while 65.74 at.% of titanium, a small amount of aluminum (5.47 at.%) and vanadium (2.38 at.%) were also detected, indicating that a compact oxide layer is formed on the surface during laser irradiation. Comparing to EDS analysis in Fig. 3, the variation is attributed to the formation of oxides after the laser induced oxidation. After ultrasonic cleaning, no obvious

change in surface morphology was found except that the stripes looked fade, as shown in Figure 2(b). As the accumulated laser fluence was increased to 1011 J/cm^2, a small amount of granular oxides was formed on the surface, while there were also some flocculent oxides scattering randomly on the surface, as shown in Figure 2(c). High magnification image reveals that the size of granular oxides is very small (less than 0.1 μm) and the flocculent oxides are agglomerated by smaller oxide nanoparticles. This phenomenon of agglomeration is not strange and can be attributed to the high reactivity and susceptibility towards agglomeration of the nanoparticles [17]. There are two theories about the formation of nanoparticles during laser irradiation. Firstly, nucleation and growth of nanoparticles are occurring through atomic and/or molecular diffusion at the surface of the substrate [18]. Secondly, more researchers have pointed out that oxide nanoparticles are formed in plasma plume [8,14-15]. Furthermore, it is obvious that micro-cracks are becoming more obscure with the accumulated laser fluence increasing from 506 J/cm^2 to 1011 J/cm^2. This may be attributed to the melting of small cracks. After ultrasonic cleaning, the granular oxides and flocculent oxides were all removed except a small amount of oxide was adhered to the subsurface, see Figure 2(d). The subsurface is flat and compact. Moreover, the micro-cracks appear to be more obscure.

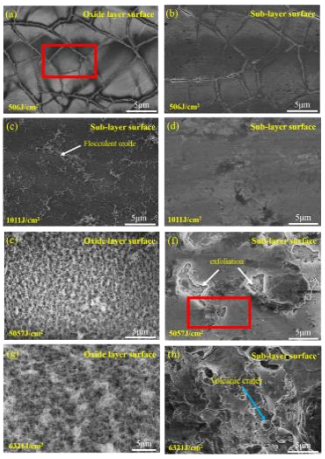

FIGURE 2. Morphology of the oxide layer surface and sub-layer surface irradiated in atmospheric air.

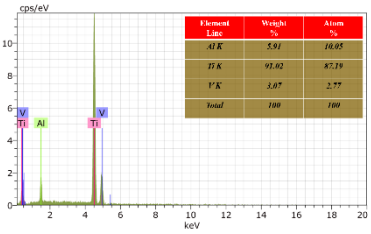

FIGURE 3. EDS analysis of the substrate.

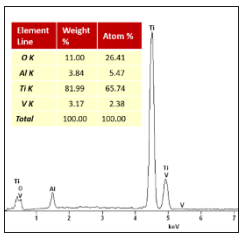

FIGURE 4. EDS pattern of the frame region shown in FIGURE 2(a).

As the accumulated laser fluence is increased abruptly from 1011 J/cm^2 to 5057 J/cm^2, the degree of oxidation is further deepened. Figure 2(e) shows that the surface is completely covered by flocculent oxides composed of oxide nanoparticles, forming a loose and porous oxide layer. Low magnification images indicate that this porous oxide layer is very flat. After ultrasonic cleaning, the loose and porous oxide layer was substantially removed as shown in Figure 2(f). However, the subsurface is no longer flat and a large amount of exfoliation was found there. Arkadiusz et al pointed out that this exfoliation was caused by relaxing shearing stress that occurs on the border between the alpha phase (Ti-O interstitial solid solution) and titanium [13]. EDS analysis shown in Figure 5 reveals presence of a large concentration of oxygen elements (around 46.74 at.%) on the subsurface along with 46.97 at.% of titanium, indicating that a compact oxide layer is also formed on the subsurface during the laser irradiation. As the accumulated laser fluence is increased further to 6321 J/cm^2, the oxide layer becomes more porous but remains flat, as is visible in the high and low magnification images (Figure 2(g)). However, SEM reveals that the subsurface is very rough and there are some micro-craters as well (Figure 2(h)). It is expected that these micro-craters were formed as a result of laser-induced explosive volume boiling and cavitation bubble generation [19]. This means that the subsurface material was at least melted during the laser irradiation or even vaporized.

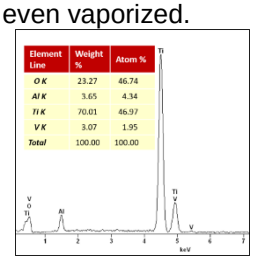

FIGURE 5. EDS pattern of the frame region shown in FIGURE 2(f).

Figure 6 shows the morphology of oxide layer surface and sub-layer surface irradiated in the condition of assisted oxygen delivery with the accumulated laser fluence varying from 506 J/cm^2 to 6321 J/cm^2. Different from the one irradiated in atmospheric air, the loose and

porous oxide layer was also formed at lower accumulated laser fluence (506 J/cm^2 and 1011 J/cm^2; Figure 6(a), 6(c)), while subsurface was flat and compact (Figure 6(b), 6(d)). This suggests that a stronger oxidation reaction has occurred in the condition of assisted oxygen delivery at the same fluence level. Low magnification images indicate that the porous oxide layer has a coralline-like structure at high accumulated laser fluence (5057 J/cm^2 and 6321 J/cm^2; Figure 6(e), 6(h)), while they are still observed as loose and porous in the high magnification images. Interestingly, the growth direction of those coralline-like structures is perpendicular to the laser scanning path and looks more stereoscopic with 6321 J/cm^2 of fluence. Unlike atmospheric air based irradiation, there was no significant exfoliation found on the subsurface when irradiated with 5057 J/cm^2 of fluence in the condition of assisted oxygen delivery (Figure 6(f)). The subsurface is still relatively flat but there is a large concentration of oxide adhering to the subsurface. At 6321 J/cm^2 of fluence, SEM image shows that the subsurface is extremely rough and that deep cracks have formed (Figure 6(h)). This suggests that the degrees of explosive volume boiling and cavitation bubble generation were more intense during laser irradiation under assisted oxygen delivery than those irradiated in the atmospheric air

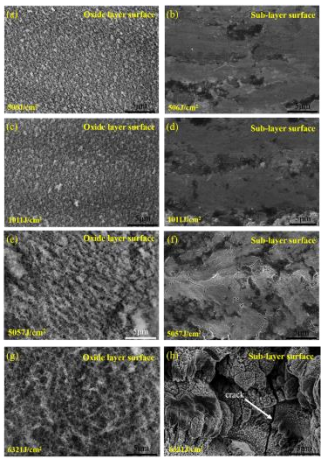

FIGURE 6. Morphology of the surfaces and sub-surfaces irradiated in the condition of assisted oxygen delivery.

3.2 Microstructure of the cross-section

In order to further investigate the microstructure of the surface layer and subsurface layer, SEM scans of the cross-section were taken. Figure 7 shows the morphology of the cross-section irradiated in both conditions of atmospheric air and assisted oxygen delivery. As shown in Figure 7(a), no visible oxide layer can be found on the surface when irradiated in atmospheric air with 506 J/cm^2 of fluence. This is attributed to the thickness of the oxide layer is practically beyond the resolution of the SEM equipment. When irradiated in the condition of assisted oxygen delivery with the same fluence, a dark and compact oxide layer was found, as shown in Figure 7(b). This compact oxide layer is regarded as the subsurface layer, and its thickness is approximately 1.5 μm. However, the porous oxide layer has disappeared. In light of the fact that the oxide layer is very loose and easy to remove, it can be deduced that the layer was probably removed by the flow and gradual contact of the resin during metallographic sample preparation. Furthermore, some large defects and micro-cracks were also found on the subsurface layer. It should be noted that the process of sample preparation might have caused the large defects. Moreover, it is obvious that micro-cracks on subsurface can penetrate into the titanium matrix for a few microns, which is in agreement with what is reported in the other literatures [6,16]. As the accumulated laser fluence is increased to 1011 J/cm^2, the compact oxide layer (subsurface layer) is also found in both the conditions of atmospheric air (Figure 7(c)) and assisted oxygen delivery (Figure 7(d)). Moreover, the thickness of the compact oxide layer obtained in assisted oxygen delivery condition (1.5 μm) is larger than that obtained in the condition of atmospheric air (0.5 μm). However, the change in the compact oxide layer thickness is not obvious when the accumulated laser fluence is increased from 506 J/cm^2 to1011 J/cm^2 in the condition of assisted oxygen delivery.

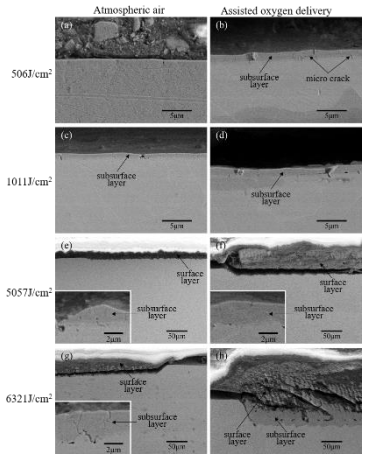

FIGURE 7. Morphology of the cross-sections irradiated in the atmospheric air and assisted oxygen delivery.

At 5057 J/cm^2 of accumulated laser fluence, the SEM image of the cross-section reveals presence of approximately 8 μm thickness of surface materials on the irradiated region when treated in the atmospheric air (Figure 7(e)). The low magnification image reveals that the compact oxide layer at subsurface is inhomogeneous and the maximum thickness reaches to 1.83 μm. When irradiated in the condition of assisted oxygen delivery with the

same fluence level (Figure 7(f)), the thickness of surface materials on the laser irradiated region increased enormously to approximately 18.2 μm, while the thickness of the compact oxide layer was approximately 2.3 μm. In addition, Figure 7(f) reveals that a dramatic oxidative expansion had been occurring during the irradiation process. At the highest accumulated laser fluence (6321 J/cm^2) in atmospheric air, the thicknesses of surface oxide layer and subsurface layer were further increased, reaching 22.04 μm and 3.2 μm respectively (Figure 7(g)). In the condition of assisted oxygen delivery, the thicknesses of the surface oxide layer and subsurface layer are increased rapidly to 109 μm and 61.2 μm, respectively (Figure 7(h)).

3.3 Phase composition

The XRD patterns of the four samples irradiated in atmospheric air with the accumulated laser fluence varying from 506 J/cm^2 to 6321 J/cm^2 are shown in Figure 8. It is obvious that the intensity of the main titanium peaks around 38.6° and 40.5° and decreases with an increase in accumulated laser fluence. At the lowest accumulated laser fluence (506 J/cm^2), the main phase is titanium, the diffraction peaks between 37° and 43° and two-theta are consistent with TiO. The diffraction peaking around 40° is consistent with Ti_2O. Moreover, the diffraction peaking around 57.5° is consistent with Al_2O_3, while the low-intensity diffraction peaking around 75° is attributed to Ti_2O. At 1011 J/cm^2 of fluence, one more diffraction peak appears around 25.3° as compared with the sample irradiated with 506J/cm^2 of fluence. This diffraction peak is consistent with anatase TiO_2. Parallel to the change in SEM results, the XRD results have changed dramatically at 5057 J/cm^2 of fluence. The diffraction peaks around 37° and 43° (TiO phase), 40° (Ti_2O or Ti_6O), 57.5° (Al_2O_3), and 75° (Ti_2O) disappears and the intensity of 25.3° diffraction peak (anatase TiO_2) falls. Moreover, a strong peak appears around 77°, which can be consistent with titanium. At the highest accumulated laser fluence (6321 J/cm^2), the main phase of the substrate surface is rutile TiO_2, while there is also a weak peak of anatase TiO_2 phase at around 25.3°.

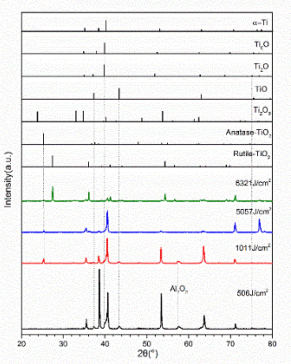

FIGURE 8. XRD patterns of the samples irradiated in atmospheric air.

Figure 9 shows the XRD patterns of the four samples irradiated in the condition of assisted oxygen delivery. Parallel to the change of SEM results, X-ray data also revealed some differences between the samples irradiated under the two conditions. At low accumulated laser fluences (506 J/cm^2 and 1011 J/cm^2), high valence oxides Ti_2O_3 (around 24°), anatase TiO_2 (around 25.3°) and rutile TiO_2 (around 36° and 54.3°) were found, while the diffraction peak of the low valence oxide Ti_2O had disappeared and the diffraction peaks of TiO phase (around 43°) and Al_2O_3 phase (around 57.5°) had become very low. These observations further prove the existence of strong oxidation effects in the condition of assisted oxygen delivery. At the high values of accumulated laser fluence (5057 J/cm^2 and 6321 J/cm^2), the diffraction peaks of titanium almost disappeared and the phase of the substrate surface was dominated by anatase TiO_2 and rutile TiO_2. In view of the large thickness of porous oxide at these two accumulated laser fluence values and its shielding effect to X-ray, it can be concluded that the porous oxide layer is composed of oxide nanoparticles, mainly including anatase TiO_2 and rutile TiO_2.

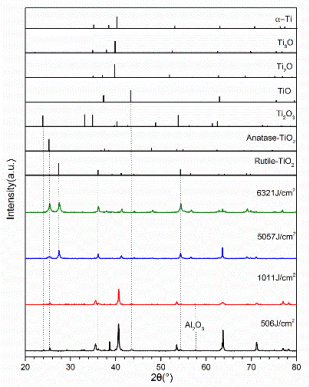

FIGURE 9. XRD patterns of the samples irradiated under the condition of assisted oxygen delivery.

4 Conclusions

Laser induced oxidation of Ti6Al4V titanium alloy was conducted with an industrial nanosecond pulsed Yb: glass fiber laser. The microstructural development, phase composition and thickness of the oxide layer were investigated. Under laser irradiation, a porous and easily removable surface oxide layer, mainly composed of anatase TiO_2 and rutile TiO_2, low valence oxide (TiO and Ti_2O) and Al_2O_3, was formed. The subsurface layer is a compact oxide layer mainly composed of anatase TiO_2 and rutile TiO_2.

The accumulated laser fluence has significant influence on the oxidation behavior of Ti6Al4V

alloy. In the same reaction atmosphere, the thickness of the surface layer increases with increasing the accumulated laser fluence, while the change of thickness of the subsurface layer is not obvious. The surface oxide layer becomes more and more porous as the accumulated laser fluence increases from 506 J/cm^2 to 6321 J/cm^2. The subsurface is affected by heat from laser beam and oxidation reaction. However, at high accumulated laser fluence of 6321 J/cm^2 in the condition of assisted oxygen delivery, a rough recast subsurface was formed due to explosive volume boiling and cavitation bubble generation.

The reaction atmosphere has a significant influence on the oxidation behavior of Ti6Al4V alloy. Compared with the samples irradiated in atmospheric air, a stronger oxidation reaction occurs in the condition of assisted oxygen delivery at the same level of fluence. When irradiated in the conditions of assisted oxygen delivery, the porous oxide layer was also formed even at a lower accumulated laser fluence of 506 J/cm^2. The thicknesses of both surface and subsurface layers are much larger than those irradiated in atmospheric air.

Acknowledgements
This work was supported by the National Natural Science Foundation of China [Grant No. 51705249], and the Natural Science Foundation of Jiangsu Province [Grant No. BK20160792].

References
[1] Palneedi H, et al. Laser irradiation of metal oxide films and nanostructures: applications and advances. Advanced Material. 2018; 30: 1705148.
[2] Pérez del Pino A, et al. Laser surface processing of titanium in air: influence of scan traces over lapping. Journal of Laser Applications. 2003; 15: 120-123.
[3] György E, et al. Structure formation on titanium during oxidation induced by cumulative pulsed Nd: YAG laser irradiation. Applied Physics A. 2004; 78: 765-770.
[4] Jwad T, et al. Laser induced single spot oxidation of titanium. Applied Surface Science. 2016; 387: 617-624.
[5] Jwad T, et al. Erasing and rewriting of titanium oxide colour marks using laser-induced reduction/oxidation. Applied Surface Science. 2018; 458: 849-854.
[6] Zimmermann S, et al. Improved adhesion at titanium surfaces via laser-induced surface oxidation and roughening. Materials Science and Engineering: A. 2012; 558: 755-760.
[7] Tian YS, et al. Research progress on laser surface modification of titanium alloys. Applied Surface Science. 2005; 242: 177-184.
[8] Ponnamma D, et al. Laser induced periodic surface structures on nano metal oxide filled polyvinylidene fluoride nanocomposites. Optik. 2019; 176: 372-383.
[9] Pallotti DK, et al. Laser ablation and deposition of titanium dioxide with ultrashort pulses at 527 nm. Applied Physics. 2015; 199: 445-452.
[10] Hoppius JS, et al. Femtosecond laser crystallization of amorphous titanium oxide thin films. Applied Physics Letter. 2018; 113: 071904.
[11] Pérez del Pino A, et al. Coloring of titanium by pulsed laser processing in air. Thin Solid Films. 2002; 415: 201-205.
[12] Adams DP, et al. Nanosecond pulsed laser irradiation of titanium: Oxide growth and effects on underlying metal. Surface Coating Technology. 2014; 248: 38-45.
[13] Antonczak J, et al. Laser-induced oxidation of titanium substrate: Analysis of the physicochemical structure of the surface and sub-surface layers. Applied Surface Science. 2015; 325: 217-226.
[14] Girault M, et al. Influence of the reactive atmosphere on the formation of nanoparticles in the plasma plume induced by nanosecond pulsed laser irradiation of metallic targets at atmospheric pressure and high repetition rate. Applied Surface Science. 2016; 374: 132-137.
[15] Girault M, et al. Modelling nanoparticles formation in the plasma plume induced by nanosecond pulsed lasers. Applied Surface Science. 2012; 258: 9461-9465.
[16] Espejo HM, et al. Substrate cracking in Ti-6Al-4V driven by pulsed laser irradiation and oxidation. Surface Coating Technology. 2017; 322: 46-50.
[17] Kakati M, et al. Synthesis of titanium oxide and titanium nitride nano-particles with narrow size distribution by supersonic thermal plasma expansion. Vacuum. 2008; 82: 833-841.
[18] Riabinina D, et al. Influence of pressure on the Pt nanoparticle growth modes during pulsed laser ablation. Journal of Applied Physics. 2010; 108: 034322.
[19] Guan YC, et al. Boiling effect in crater development on magnesium surface induced by laser melting. Surface Coating Technology. 2014; 252: 168-172.

Fundamental analysis on thermal characteristics of high-speed aerostatic spindle

Shumon Wakiya[1], Satsuki Yamazaki[1], Jumpei Kusuyama[2]
Dmytro Fedorynenko[2] and Yohichi Nakao[2]
[1]Graduate School of Mechanical Engineering
Kanagawa University
Yokohama, Kanagawa, JAPAN
[2]Department of Mechanical Engineering
Kanagawa University
Yokohama, Kanagawa, JAPAN

INTRODUCTION

In recent years, ultra-precision cuttings using micro milling cutter to produce parts with micro structural surfaces are being demanded. The parts with the micro structural surfaces are used for various fields based on the state-of-the-art technology, such as automobile, optical, energy, medical industries, for instance. An importance of ultra-precision machine tools for machining dies used for the molding processes of the precise components increases more than before. In the machining of the micro structural surfaces using micro milling cutter, high-speed and precise rotational motion of the machine tool spindle are indispensable to conduct the machining successfully. In the machining applications, aerostatic spindles are most commonly used.

However, in the range of the higher rotational speed such as over, for instance, 100,000 min^{-1}, the influence of the air viscosity on the heat generation cannot be neglected. As a result, the heat generation in the higher speed range causes thermal deformation of the spindle that degrades machining accuracy. In particular, the thermal deformation cannot be neglected in the ultra-precision machining aiming machining with the order of nanometers. Therefore, temperature variation of spindle due to the heat generation during high-speed spindle rotation must be suppressed. Therefore, it is very important to suppress heat generation by cooling the main body of spindle including the rotating shaft directly. An effective cooling performance can be expected by using water as a cooling fluid, because of the excellent thermal conductivity of water.

From the above reasons, in order to accomplish requiring high accuracy and efficient machining of fine components, research and development of the high-speed spindle for ultra-precision machining having superior thermal stability is essential. Accordingly, in this study, we are aiming to develop ultra-high speed aerostatic spindle having high thermal stability with the rated rotational speed: 100,000 min^{-1}. The spindle has a built-in motor to realize the ultra-high speed rotation. In this case, taking effective countermeasures to realize high thermal stability is essential, because not only the heat generation at the aerostatic bearings in the higher speed range but also the heat generation at the built-in motor affect thermal stability of the spindle. In our spindle design, effective cooling structures of the spindle casing as well as shaft bore in the rotating shaft are specifically designed. It should be mentioned that the diameter of the high-speed spindle is necessarily small. In this spindle, a special structure of shaft bore water cooling in the rotating shaft is supported by the aerostatic bearings and driven by the built-in motor is thus proposed.

In this paper, the thermal stability of the designed spindle is investigated using simulation studies. Specifically, the derived results based on the introduced lumped parameter model and finite-element model are presented.

STRUCTURE OF AEROSTATIC SPINDLE

Figure 1 shows the basic structure of the high speed aerostatic spindle that has been

developing in this study. Radial bearings are symmetrically arranged, and axial bearings support loads from both sides. This spindle has a built-in motor to achieve high speed and rotational accuracy. Cooling water is supplied to casing cooling structure, motor cooling structure and shaft cooling structure. In particular, a special structure for supplying cooling water into the rotating spindle shaft supported by aerostatic bearings is contrived.

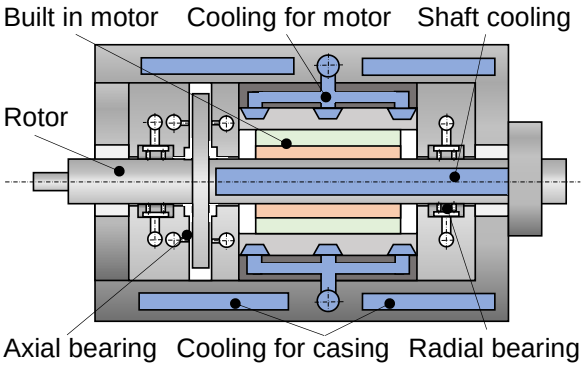

FIGURE 1. Cross-section of aerostatic spindle

HEAT SOURCES OF SPINDLE

Main heat sources of the developed spindle are attributed to the power loss of the built-in motor P_{mo} and the power loss P_a owing to the air viscosity during spindle rotation. These power losses cause to rise the temperature of spindle and lubricant. Each power losses are given as follows.

Power Loss of Built in Motor

The power loss of the built-in motor P_{mo} is given by Eq. (1), where P_{mo_o} and η denote the motor output and motor efficiency, respectively.

$$P_{mo} = P_{mo\_o}(1-\eta) \tag{1}$$

The power loss of the built-in motor P_{mo} divides into the power loss of rotor P_{mo_ro} and the power loss of stator P_{mo_st}. Rates of P_{mo_ro} and P_{mo_st} in the total power loss of the motor are approximately constant. If the rate of rotor part is given by x, the power loss of rotor part P_{mo_ro} and the power loss of stator part P_{mo_st} are given by Eq. (2), Eq. (3).

$$P_{mo\_ro} = xP_{mo} \tag{2}$$

$$P_{mo\_st} = (1-x)P_{mo} \tag{3}$$

Power Loss of Viscous Friction

The power loss due to the viscosity of lubricating air flowing through bearing gaps is significant, according to the increase of the spindle speeds. Even if the viscosity of air is greatly smaller than that of oil, the influence of air viscosity on the spindle rotation is significant, since the power losses of bearing increase in proportion to the square of the rotational speed of the spindle. The power losses of radial bearing and thrust bearing are given by Eq. (4), Eq. (5).

$$P_{th} = \frac{\pi\mu(R_o^{\,4} - R_i^{\,4})}{h_{th}}\omega^2 \tag{4}$$

$$P_{ra} = \frac{2\pi\mu R_{ra}^{\,3} L}{h_{ra}}\omega^2 \tag{5}$$

Here, h_{th} and h_{ra} indicate the bearing gaps of thrust bearing and radial bearing, respectively. In addition, the outer radius and the inner radius of axial bearings are denoted by R_o and R_i. The radius and length of radial bearing are given by R_{ra} and L. The viscosity of air and the angular speed of spindle are denoted by μ_a and ω. Therefore, in the range of ultra-higher rotational speed such as, for instance, more than 100,000 min^{-1}, the heat generation due to the air viscosity is conspicuous.

Moreover, the gross value of the power loss P_a due to viscosity is determined by the sum of the power losses of radial bearing and axial bearing as presented by Eq. (6).

$$P_a = P_{ra} + P_{th} \tag{6}$$

THERMAL STABILITY OF SPINDLE

From the heat generations mentioned above, the analysis results using the introduced lumped parameter model and the finite-element model are shown below.

LUMPED-PARAMETER MODEL

A temperature variation of each elements of the spindle is simulated by the introduced lumped-parameter model applied to air and each spindle parts. The temperature variations of air, rotor, and casing are given by Eqns. (7)- (9).

$$c_a m_a \frac{dT_a}{dt} = P_a - \alpha_{ro} S_{ro}(T_a - T_{ro}) - \alpha_c S_c(T_a - T_c) \tag{7}$$

$$c_{ro}m_{ro}\frac{dT_{ro}}{dt} = P_{mo\_ro} + \alpha_{ro}S_{ro}\left(T_a - T_{ro}\right) - \alpha_{sc}S_{sc}\left(T_{ro} - T_{w\_sc}\right) \quad (8)$$

$$c_c m_c \frac{dT_c}{dt} = P_{mo\_c} + \alpha_c S_c\left(T_a - T_c\right) - \alpha_{cc}S_{cc}\left(T_c - T_{w\_cc}\right) \quad (9)$$

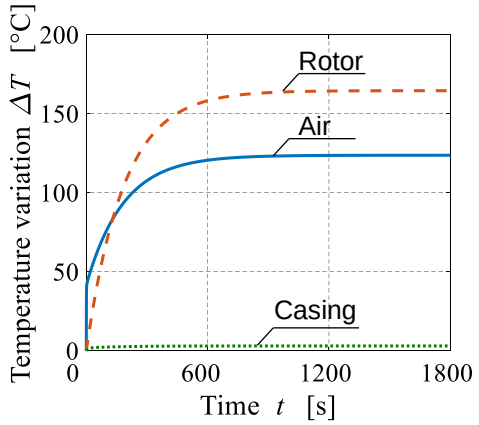

(a) Without shaft bore cooling

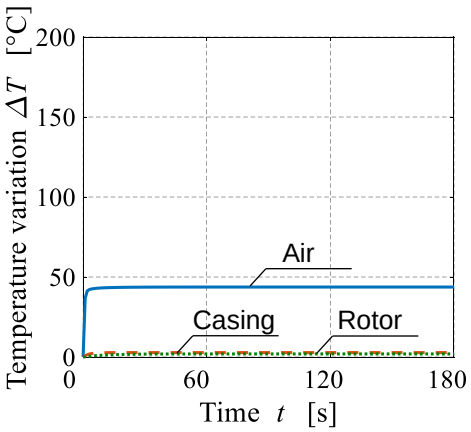

(b) With shaft bore cooling

FIGURE 2. Effect of shaft bore cooling on thermal stability and settling time

In Eqns. (7)- (9), *P*: the heat value, *T*: the temperature, *c*: the specific heat, *m*: the mass, α: the coefficient of heat transfer, *S*: the surface where heat transfer is considered, and *t*: the time. Subscriptions for the defined parameters are *a*: the air, *ro*: the rotor, *c*: the casing, *w*: the water, *mo*: the motor, *cc*: the casing cooling, *sc*: the shaft cooling, and *cj*: the cooling jacket. Figure 2 shows comparison of simulation results, the effect of shaft cooling on cooling is obvious. In the simulation studies, the initial conditions are defined as temperatures of air, rotor, casing, and cooling water are 20 °C, flow rate of air and cooling water are 2 L/min under a rotational speed of 100,000 min^{-1}. Table 1 shows that the shaft cooling is very effective to suppress the temperature rise of the spindle. Furthermore, the shaft cooling reduces the transient response as well.

TABLE 1. Simulation results of shaft bore cooling on thermal stability and settling time

	Without shaft cooling	With shaft cooling
Air ΔT [°C]	123.7	43.7
Rotor ΔT [°C]	164.3	2.7
Casing ΔT [°C]	3.1	1.9
time *t* [s]	1350	84

FINITE-ELEMENT MODEL

The temperature variation is simulated by finite-element model. In the initial conditions used are the same as the simulations by the lumped parameter model. Temperature distribution of the spindle in a steady state is then obtained as shown by Fig. 3. Figure 3(a) indicates that the temperature of the spindle is in a temperature range of from 19.850 to 234.524 °C. In contrary, Figure 3(b) shows a temperature range is from 19.850 to 33.220 °C if shaft-cooling is used.

From the simulation results using finite-element model as well as lumped-parameter model, it is verified how the shaft-cooling effectively reduces the temperature rise in the spindle. However, at the left end of the spindle shaft, the temperature rise cannot be effectively suppressed because the shaft-cooling structure does not reach at the shaft end. Temperature variation of this portion affects the machining accuracy of spindle.

In the simulation studies, the cooling conditions, namely the flowrate and temperature of water were constant. However, the temperature rise of the spindle changes depending on the cooling conditions. Accordingly, the simulations with different cooling conditions are carried out. Based on predicted temperature rise of the spindle shaft, the thermal deformation of the shaft is calculated, in relation to the cooling conditions. The simulation results are shown in Fig. 4.

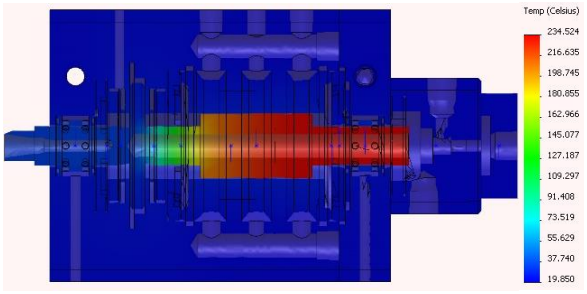

(a) Without shaft bore cooling

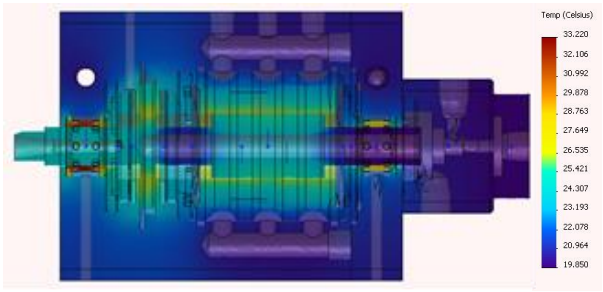

(b) With shaft bore cooling

FIGURE 3. Simulation results of temperature distribution

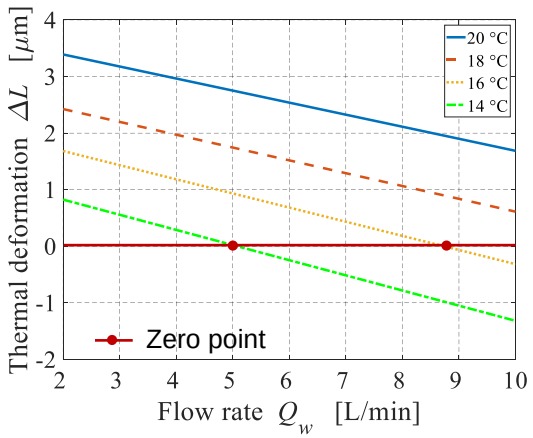

FIGURE 4. Thermal deformation of rotor in relation to temperature and flowrate of cooling water

From Fig. 4, the optimum cooling conditions can be derived. Specifically, the thermal deformation of the shaft becomes zero by using the optimum cooling conditions of temperature of cooling water 16 °C, and flowrate of cooling water 8.7 L/min, or another combination of the cooling condition, temperature of cooling water 14 °C, flowrate of cooling water 5 L/min.

CONCLUSION

In this paper, the temperature variation of the spindle and usefulness of shaft-bore cooling at a rotational speed of 100,000 min^{-1} are discussed by the lumped-parameter model and the finite-element model for aiming at developing high speed aerostatic spindle with better thermal stability. The results by each model show shaft-bore cooling have an extremely high cooling performance, and controlling cooling condition can suppress temperature rise of the rotor that directly affects the machining accuracy.

In the future work, actual spindle thermal characteristics will be investigated experimentally. The results will be compared with the simulation results.

This project is conducted based on the financial support by the NSK Foundation for Advancement of Mechatronics. Their supports are gratefully acknowledged.

REFERENCES

[1] The Japan Society of Mechanical Engineers. Ultra-precision Machining Technology. CORONA Publishing Co., Ltd. 1998; 1-2 (in Japanese).

[2] Ichiro Inazaki, Tohjiro Aoyama. Hydrostatic Bearing -Design and Application-. Kogyo Chosakai Publishing Co.,Ltd. 1998;12-23(in Japanese).

[3] Ryuichi Kawakami. Development of Air Spindles for Ultra Precision Machining. Fujikoshi Technical report, Vol. 50, No. 2. 1994; 58-70(in Japanese).

[4] Shinya Nakamura, Yoshiaki Kakino, Akira Muramatsu, Koichi Urano. An Analysis on Influence of Motor Heat Generation and Effect of Shaft-bore Cooling for Motor Integrated Spindle. Report of The Japan Society for Precision Engineering, Vol. 60, No. 7. 1994; 983(in Japanese).

[5] Hiroyuki Uchida, Masatoyo Sogabe. Linear Motor in Precision Engineering. Report of The Japan Society for Precision Engineering, Vol. 75, No. 2. 2009; 242-245(in Japanese).

CRACK PROPAGATION IN NANOCRYSTALLINE ALLOY SHEET BY LASER SPOT IRRADIATION

Hirotoshi Tagata[1], Keisuke Nagato[1], and Masayuki Nakao[1]
[1]Department of Mechanical Engineering,
The University of Tokyo,
Bunkyo-ku, Tokyo, Japan

INTRODUCTION

Recently, particularly in the field of industrial motors, the development of motors aiming at downsizing and high efficiency has been receiving increasing attention. One of the most significant factors that can improve the performance of these motors is the improvement of the physical properties of the motor core. As a material for the motor core, a soft magnetic material having high saturation magnetization and low core loss is desirable. One of the materials said to be useful as a motor core material is an amorphous alloy [1]. An alloy typically has a crystalline structure, but an amorphous alloy is an alloy material having no crystalline structure, which is obtained by quenching a liquid alloy faster than its crystallization rate. Owing to their low core loss, amorphous alloys are being used in the development of motors, and there have been cases in which the motor efficiency has been successfully increased [2]. Currently, nanocrystalline alloys with a higher saturation magnetization and lower core loss than amorphous alloys are attracting attention as new soft magnetic materials [3], and the development of ultra-high efficiency motors is expected with their use.

Typically, the average grain size of nanocrystalline alloys is less than 100 nm. These alloys are often produced by subjecting an amorphous alloy sheet processed by the single roll method to nanocrystallization heat treatment. Therefore, the nanocrystalline alloy is a thin material with a thickness of approximately several tens of μm, and is harder and more brittle than the amorphous alloy. Although many basic researches on magnetic properties and usefulness have been conducted since the development of nanocrystalline alloys [4] [5], the hardness and brittleness of nanocrystalline alloys are factors that have few studies in terms of practical use. Many sheet materials are processed into the desired shape by punching because punching is a highly productive processing method. However, nanocrystalline alloys may be so hard that the tool life may be shortened. In addition, due to its brittleness, the material gets cracked during mechanical contact processing, and there is concern that the yield rate may be reduced. Therefore, an appropriate processing method of the nanocrystalline alloy for practical use has not been established yet.

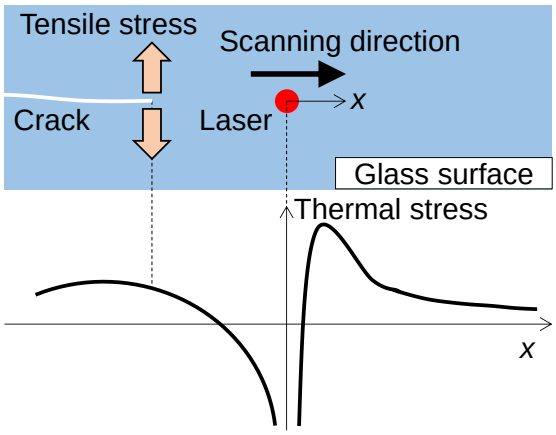

FIGURE 1. Simplest principle of laser scribing of glass and thermal stress field around the laser during simple laser scanning on no-crack glass.

On the other hand, glass is a typical material having high hardness and high brittleness. Moreover, flat glass is employed worldwide for industrial purposes. A laser scribing method has been established as a method of processing the shape of flat glass, and many studies have been conducted thus far from its basic principle to its application [6] [7]. Laser scribing is a processing method of forming a scribe line on a glass surface, or dividing the glass itself, by propagating a crack on the glass surface using the thermal stress caused by the local heating of a laser. Figure 1 illustrates the simplest explanation of this principle. When the glass is heated by a laser, the glass locally expands in the elastic deformation region, and a compressive stress field is formed to hold the expansion area. Additionally, in the vicinity of the compressive stress field, a tensile stress field is formed so that the stress of the whole material is balanced. When a crack tip of

the glass is present in this tensile stress field, a tensile stress acts on the crack tip in the crack opening direction. Then, when the stress exceeds the fracture toughness of the glass, a local fracture occurs and a crack develops. Laser scribing is the processing to continuously generate this destruction phenomenon through laser scanning. Based on its processing principle, laser scribing is a processing method suitable for materials with low fracture toughness, i.e., highly brittle materials.

However, the application of laser scribing of glass to nanocrystalline alloys is not simple. As with amorphous alloys, the structure of nanocrystalline alloys is not stable and crystallizes with excessive heating. Furthermore, they have a higher thermal conductivity and thinner thickness than that of glass. Therefore, the nanocrystalline alloy is a material more sensitive to heat than glass; thus, it is expected that the heat input condition of the laser will have a more severe effect. Moreover, the behavior of the nanocrystalline alloy during laser heating is also unclear.

Therefore, this study aims to demonstrate the applicability of laser scribing to nanocrystalline alloys. We observe the behavior of the nanocrystalline alloy irradiated using a laser, and conduct experiments to confirm the possibility of crack propagation. First, we observe the nanocrystalline alloy spot-irradiated using a laser and analyze its behavior during laser irradiation. Next, we spot the laser in front of the initial crack formed in the nanocrystalline alloy to confirm the progress of the crack. Finally, we perform real-time observation of the crack growth by spot irradiation and discuss the crack growth phenomenon in the nanocrystalline alloy.

EXPERIMENTAL

Figure 2(a) illustrates an outline of the experimental system. We used a Fe-based nanocrystalline alloy sheet. A laser microscope (LEXT OLS4500, OLYMPUS CO.) was used for observation of the surface of the nanocrystalline alloy and a high-speed camera (VW-9000, KEYENCE CO.) was used for the real-time observation of laser irradiation. The laser used was a single mode fiber laser with a wavelength of 1070 nm. Furthermore, as illustrated in figure 2(b), we defined the distance between the tip of initial crack and the center of laser irradiation as d_1, and the distance between the tip of developed crack and the center of laser irradiation as d_2.

In the observation of the surface of the nanocrystalline alloy, the laser spot diameter was

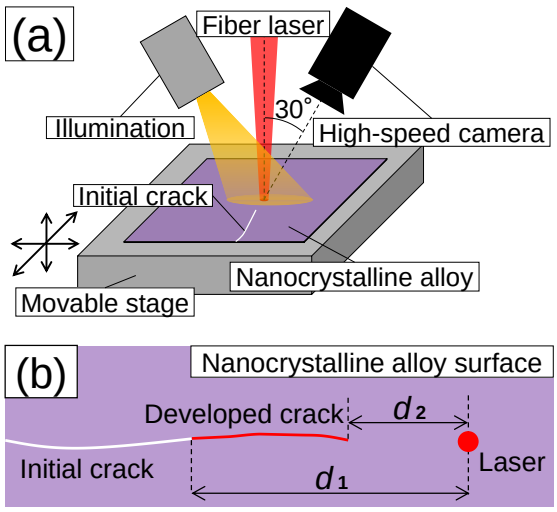

FIGURE 2. (a) Outline of experimental observation equipment and (b) definition of measurement values.

changed continuously while fixing the laser output to 10 W and the laser irradiation time to 10 ms. We irradiated the laser and observed the surface of the nanocrystalline alloy using the laser microscope.

In the crack extension experiment, the laser irradiation time was changed to 10 and 20 ms while fixing the laser output to 10 W and the laser spot diameter to 30 μm. We created an initial crack in the nanocrystalline alloy sheet, placed it on the xyz movable stage, and spotted the laser around the initial crack. We measured the values of d_1 and d_2 before and after the experiment using the laser microscope, and made real-time observation during laser irradiation using the high-speed camera.

RESULTS AND DISCUSSION

Observation

We observed the behavior of the laser spot irradiated part of the nanocrystalline alloy using a laser microscope. Figure 3 depicts the results. During this observation, the laser spot diameter was changed continuously while fixing the laser output to 10 W and the laser irradiation time to 10 ms.

The laser spot diameter was set to 30 μm, as depicted in figure 3(a). The laser-irradiated portion exhibited four major types of behavior in areas (i) to (iv) from the center to the outside. Area (i) directly received the laser light and exhibited a stripe pattern. In area (ii), the material was altered and granular structures of approximately several μm were observed. In area (iii), finer granular structures were observed than

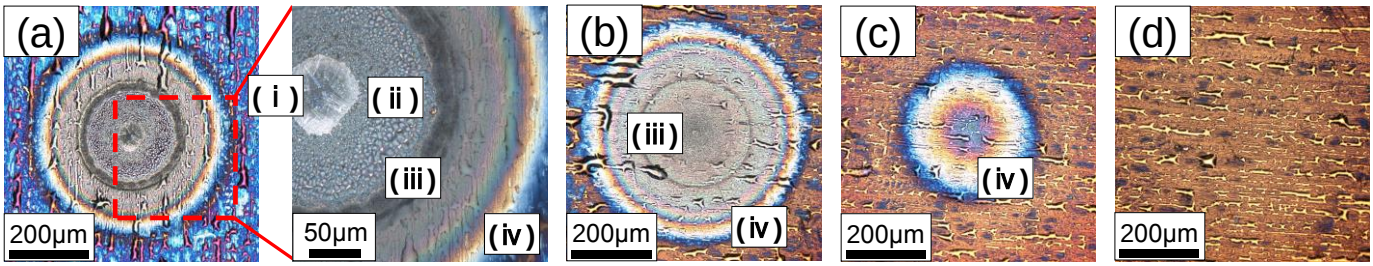

FIGURE 3. Laser microscope images of the laser irradiated area with a laser spot diameter of (a) 30 μm, (b) 780 μm, (c) 1020 μm and (d) 1270 μm.

in area (ii), and in area (iv), the color change of the material surface was observed.

The real-time observation revealed that areas (i) and (ii) were melted by the laser irradiation and then resolidified. In these two areas, area (ii) solidified first after the end of the laser irradiation, followed by the solidification of area (i). The difference in the timing of this solidification indicates different behavior. Although melting by laser irradiation did not occur in area (iii), it is expected that the material was degraded by heat. Area (iv) demonstrated no change in the material itself. A thin oxide film was formed on the surface of the nanocrystalline alloy during the heat treatment step, which resulted in a change in the surface color. It is expected that the laser heat scatters the oxide film originally formed on the surface, and then the oxide film is reformed into a circular shape.

Subsequently, we increased the spot diameter and reduced the energy density of the laser irradiation. The laser spot diameter was changed to 780 μm, as depicted in figure 3(b). Only areas (iii) and (iv) were observed at this spot diameter. This indicates that the energy density was lowered, such that the heat generated did not cause melting but caused deterioration of the material. The laser spot diameter was changed to 1020 μm, as depicted in figure 3(c). Only area (iv) was observed at this spot diameter. This indicates that the energy density was lowered, such that the heat generated did not cause deterioration of the material but reformed the oxide film. Then, as shown in figure 3(d), when the spot diameter was lowered to 1270 μm, no change could be observed.

From the above observations, it was found that melting, deterioration, and oxide film removal of the nanocrystalline alloy occurred owing to the difference in the energy density caused by the change in the spot diameter of the laser.

Experiment

We formed an initial crack in the nanocrystalline alloy sheet, and then performed an experiment to spot the laser around the crack to confirm the progress of the crack. In this experiment, the spot diameter was fixed at 30 μm and the laser output was fixed at 10 W. Figure 4 illustrates the progress of the crack,when irradiation time was set to 10 ms. It can be seen from figure 4(a) that when the laser was spot-irradiated in front of the initial crack, the crack propagated forward to the laser irradiation part. Additionally, it can be seen from figure 4(b) that when the laser was spot-irradiated diagonally in front of the initial crack, the crack propagated diagonally to the laser irradiation part. In any case, it was found that it is possible to develop an initial crack by laser irradiation.

The crack propagation phenomenon is a series of local fracture phenomena at the crack tip. Therefore, the crack propagation phenomenon can be discussed in terms of magnitude of stress and fracture toughness, that is, a crack develops when the stress exceeds the fracture toughness. When the stress range does not exceed the fracture toughness, the crack does not progress or the crack that has progressed stops. It is expected that the crack growth in nanocrystalline alloys can be considered as well. If the laser conditions are equal, the generated thermal stress field will also be equal. Therefore, when the crack develops under the same laser conditions, d2 is expected to take a constant value regardless of d1. When d1 is too large, it is assumed that the thermal stress at the crack tip does not exceed the fracture toughness and thus, the crack does not progress.

To confirm these hypotheses, we varied d_1 to measure d_2. The spot diameter was fixed to 30 μm, laser output was fixed to 10 W, and irradiation time was set to 10 and 20 ms.

Figure 5 depicts the measurement results. The conditions under which the crack did not progress are not plotted in the figure. When d_1 was too

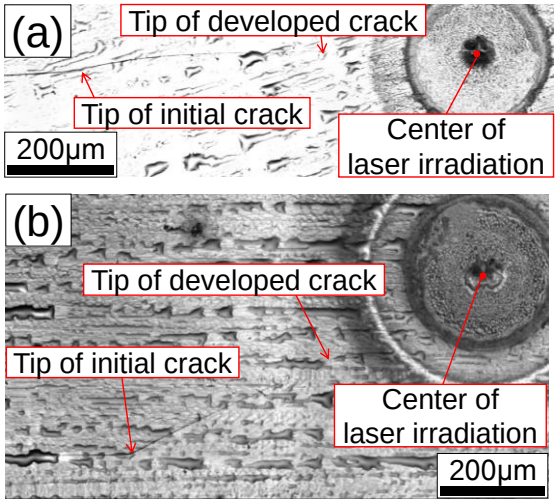

FIGURE 4. Crack propagation when irradiated to (a) the front of the crack, and (b) diagonally ahead of the crack.

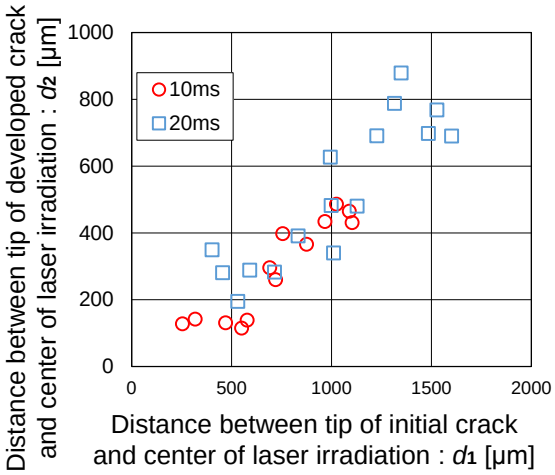

FIGURE 5. Relationship between d_1 and d_2 at irradiation times of 10 and 20 ms. d_1 is distance between tip of initial crack and center of laser irradiation, and d_2 is distance between tip of developed crack and center of laser irradiation.

large, the crack did not progress as hypothesized. On the other hand, under the condition in which the crack has progressed, $d2$ takes an approximately constant value when d_1 is small. However, the result is contrary to the hypothesis that d_2 increases as d_1 increases. A similar tendency is observed when the irradiation time is 10 and 20 ms. To consider this tendency, we made a real-time observation of how the crack progressed. Real-time observation was performed under two conditions of d_1 = 531 μm and 1348 μm at an irradiation time of 20 ms.

Figure 6(a) illustrates the appearance of crack propagation at d_1 = 531 μm. In this condition, the crack progressed 2.5 ms after the start of the laser irradiation. The nanocrystalline alloy is not molten at this point. Therefore, it is considered that the crack has progressed by the thermal stress of the laser heating in the elastic deformation region of the nanocrystalline alloy, that is, it can be considered that the crack has progressed based on the same principle as that of laser scribing of glass.

Figure 6(b) illustrates the appearance of crack propagation at d_1 = 1348 μm. In this condition, the crack progressed 41.5 ms after the start of the laser irradiation, that is, 21.5 ms after the end of the laser irradiation. The nanocrystalline alloy melted in the middle of the laser irradiation and solidified again after the end of the laser irradiation. Because only the laser irradiated portion locally melted and resolidified, the homogeneity in the nanocrystalline alloy was lost, and residual stress remained. It is considered that the crack progressed at the time when the residual stress exceeded the fracture toughness of the crack tip, that is, it is expected that the crack progressed based on a principle different from that of the laser scribing of glass.

Furthermore, by comparing the cases of the irradiation times of 10 and 20 ms, the tendencies of the graph were observed to be almost equal; however, in the case of the irradiation time of 20 ms, the crack progressed even if d_1 was larger. Thus, even if the irradiation time is increased, there is a difference only in the crack growth due to the residual stress. The larger the irradiation time, the larger is the melted part; hence, it is expected that the residual stress generated by melting and resolidification has increased.

From the above, it was found that there is an appropriate distance between the crack tip and the laser irradiation position to propagate the crack in the elastic deformation region of the nanocrystalline alloy by the same principle as that of the laser scribing of glass.

CONCLUSION

We conducted observations and experiments to demonstrate the applicability of laser scribing, which is a method of processing glass, to nanocrystalline alloys, which are not suitable for mechanical contact processing.

First, we observed the behavior of nanocrystalline alloys during laser irradiation using a laser microscope. The irradiated part exhibited four types of behavior. It was confirmed that changing the energy density changes the observed area.

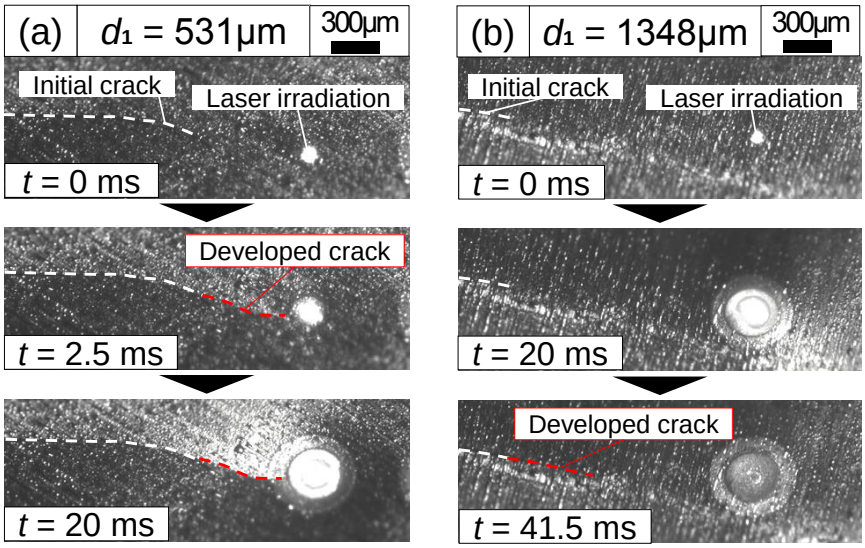

FIGURE 6. Appearances of crack propagation by real-time observation in the case of (a) d_1 = 531 μm and (b) 1348 μm. d_1 is distance between tip of initial crack and center of laser irradiation.

Next, we spotted a laser around the cracks in the nanocrystalline alloy to test whether the cracks progressed. As a result, it was confirmed that the crack tends to progress toward the laser irradiation position. Furthermore, the crack propagation phenomenon was observed by changing the initial crack tip and the laser irradiation position. When the crack tip and the laser irradiation position were close, the crack progressed immediately after the start of the laser irradiation. Similar to the laser scribing of glass, the thermal stress generated in the elastic deformation area of the nanocrystalline alloy causes the crack to propagate. When the laser irradiation position was far from the crack tip, the crack progressed after the end of the laser irradiation. Unlike in the laser scribing of glass, the residual stress generated by melting and resolidification of the irradiated part causes the crack to progress. When the laser irradiation position is farther from the crack tip, the generated stress does not exceed the fracture toughness of the crack tip and the crack does not progress. Based on these results, we can confirm that there is an appropriate laser irradiation position for the heat input condition to propagate the crack while maintaining the characteristics of the nanocrystalline alloy.

Thus, it is possible to develop a crack in the nanocrystalline alloy using the thermal stress caused by laser heating. In the future, we will also conduct laser scanning experiments instead of spot irradiation, and aim for the practical application of laser scribing to nanocrystalline alloys.

REFERENCES

[1] Hasegawa R. Applications of Amorphous Magnetic Alloys. Materials Science and Engineering A 2004; 375-377 90-97.

[2] Wang Z, Enomoto Y, Ito M, Masaki R, Morinaga S, Itabash H, Tanigawa S. Development of a Parmanent Magnete Motor Utilizing Amorphous Wound Cores. IEEE Transactions on Magnetics 2010; 46: 2.

[3] Herzer G. Modern Soft Magnets: Amorphous and Nanocrystalline Materials. Acta Materialia 2013; 61: 718-734.

[4] Kumar KS, Van Swygenhoven H, Suresh S. Mechanical Behavior of Nanocrystalline Metals and Alloys. Acta Materialia 2003; 51: 5743-5774.

[5] Meyers MA, Mishra A, Benson DJ. Mechanical Properties of Nanocrystalline Materials. Progress in Materials Science 2006; 51: 427-556.

[6] Buchanov VV,Kaptakov MO, Murav'ev EN,Revenko VI, Solinov EF. Theoretical Research of Laser Glass Cutting. Glass Physics and Chemistry 2018; 44: 254-259.

[7] Yamamoto K, Hasaka N, Morita H and Ohmura E. Influence of Glass Substrate Thickness in Laser Scribing of Glass. Precision Engineering 2010; 34: 55-61.

DEVELOPMENT OF COMPACT MAGLEV STAGE SYSTEM FOR NANOMETER-SCALE POSITIONING

Motohiro Takahashi, Hironori Ogawa, and Takanori Kato
Research and Development Group,
Hitachi, Ltd., Hitachinaka, Ibaraki, Japan

INTRODUCTION

This paper describes the development of a magnetic levitation (maglev) stage with a compact structure that can be installed for nanometer-scale positioning of an XY stage system.

Recently, high positioning accuracy is required for semiconductor manufacturing systems and ultra-precise machine tools. To improve positioning accuracy, it is efficient to support the table with a noncontact guide system to prevent guide friction and heat transfer from the lower table or base. An aerostatic guide is normally used for this purpose [1,2]; however, in vacuum condition, it is difficult to achieve high vacuum pressure without a differential vacuum system, and such a system enlarges the machine dimensions [3]. For this reason, a maglev stage was developed[4,5], and some have long strokes in a single direction [6]. The levitated masses of these conventional maglev stages which have several hundred mm stroke are commonly over 10 kg. And, total dimensions of maglev systems is too large to be installed as a fine stage on a coarse stage. In one study, a triangular compact maglev stage with a short stroke was developed, and a positioning resolution of 10 nm was confirmed [7]. However it's difficult to use this structure as XY-fine stage because of triangle layout of interferometers.

We aimed to develop a compact maglev stage for which the levitated mass is less than 1 kg and which is dramatically more lightweight than existing maglev stages. This compact feature is enabled by our newly suggested gravity compensation system with repellent force and planar motor structure. The developed stage system also has long strokes, such as 200 mm in X and Y directions on a horizontal plane. Further, bar mirrors can be installed on its table to measure and control table XY-position.

OVERALL STRUCTURE

Coarse-fine structure stages have frequently been used to fulfill requirements for both positioning accuracy and long strokes. The vibration canceller was developed as a coarse-fine structure stage that enables vibration reduction from the coarse stage [8]. However, heat transfer through the elastic hinge is a problem. To solve this problem, we developed a fine stage with noncontact support using maglev.

Figure 1 shows the overall structure of the developed coarse-fine stage system. A 6DOF maglev stage was installed as a fine stage on the coarse XY-stage with a conventional stuck structure, which is composed of a linear motor and linear guides. The coarse stage has strokes of 200 mm in both X and Y directions. Its table position, X and Y-tables in Figure 1, is measured by a linear scale. The table position of the fine stage is measured by capacitance sensors fixed at the table of the coarse stage, and after the levitation is stable, X, Y, and θz-axes measurements are changed to those measured by the laser interferometer, which is fixed at the base. This measurement system prevents error from the coarse stage from affecting fine-stage positioning accuracy in the XY-position.

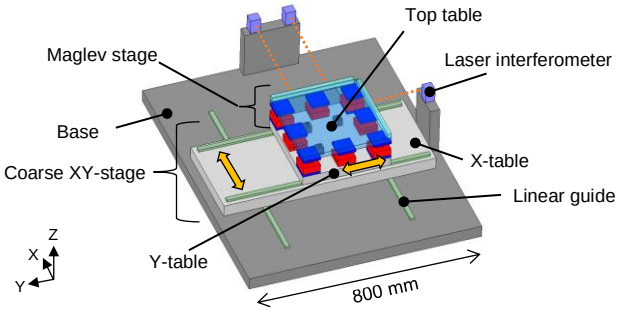

FIGURE 1. Overview of structure of developed coarse-fine stage system. Top-table position is measured from base.

CONFIGURATION OF MAGLEV STAGE

We developed a maglev stage with the following design concepts to create a compact structure:

(1) Reduce top-table mass to minimize the motor dimensions and enable a light weight and high responsiveness.
(2) Measure the top-table XY-position from the base to eliminate positioning error and isolate vibrations of the coarse stage.
(3) Install a motor in a symmetrical layout in view from the Z-axis to enable the same driving characteristics between the X and Y axes.

Figure 2 shows the configuration of the 6DOF fine stage with the maglev mechanism. The top table is levitated against the Y-table, which is the upper table of the coarse XY stage; this enables vibrations, heat transfer, and strain to be isolated from the coarse stage. The magnets and yokes of the voice coil motor (VCM) are installed in the surface below the top-table. The coils of the VCM are installed in the Y-table to prevent disturbances and heat generation from the power cable and coil current, respectively.

Bar mirrors, used for noncontact, long-stroke measurement of the top-table position in the X and Y directions with laser interferometers, are installed on the top table. Capacitance sensors, which measure displacement of sensor targets fixed on the top table, are installed on the Y-table to measure the 6DOF position of the top table. These laser interferometers and capacitance sensors are used for 6DOF feedback control of the fine maglev stage. Table 1 shows target specifications of the developed stage system. The main feature of this maglev stage is the planar table, in which bar mirrors for X, Y, and θz-axis measurement can be installed.

In addition, the compact structure of the fine stage enables the minimization of the moving mass of the coarse stage. Figure 3 shows the appearance of the developed coarse-fine stage system. The fine maglev stage is small enough to prevent increases in moving mass of the coarse stage.

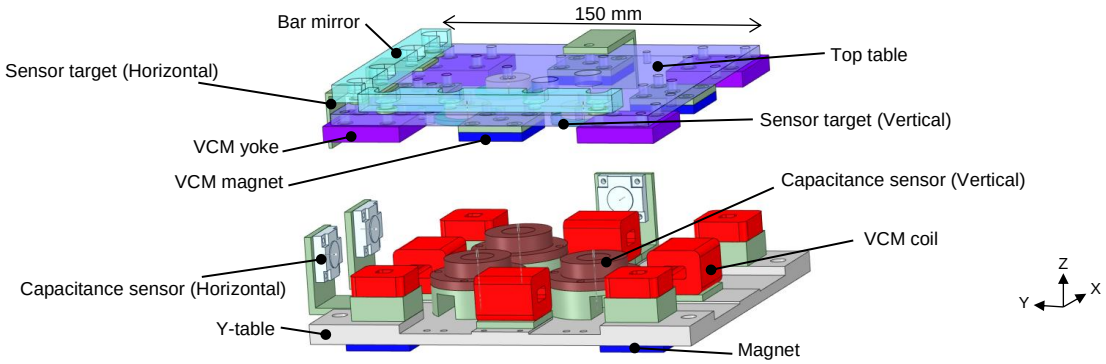

FIGURE 2. Configuration of 6DOF fine stage with maglev mechanism.

TABLE 1. Target specifications of fine 6DOF maglev stage with compact and lightweight structure.

Levitation mass		0.81 kg
Total mass of fine stage		2.3 kg
Dimensions		150×150×53 mm
Strokes	XY	±3 mm (±200 mm with course XY stage)
	Z	1 + (0~9.5) mm
Max. Acc.	XY	4.9 m/s^2
	Z	9.8 m/s^2
Sampling frequency		10 kHz
Resonance frequency		>500 Hz
Bandwidth		200 Hz

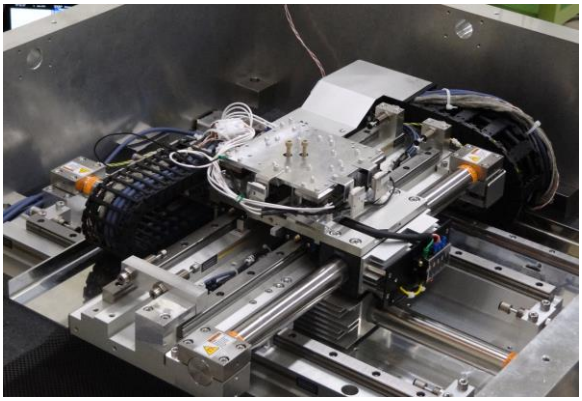

FIGURE 3. Appearance of the developed stage system which consists of 6DOF maglev fine stage and long-stroke XY coarse stage.

HORIZONTAL MOTOR DESIGN

In this study, magnets and yokes are installed in a planar layout to reduce the top-table mass and vertical dimensions and to enable high responsibility. Yoke volume, especially, increases levitated mass dramatically and should be used minimally. Then, a planar-shaped and simply structured VCM is designed using magnetic analysis.

Figure 4 shows the VCM structure of the horizontal axis and the results for its magnetic analysis. Figure 4 (a) shows the X-VCM structure, and Y-VCM has the same structure, which turns 90 degrees from the Y-axis to the X-axis. The magnetic field of the Z-direction is made by a neodymium magnet in the upper half of the coil unit. Thrust in the X-direction is made by the magnetic field and coil current of the Y-direction. As shown in Figure 4 (b), a strong magnetic field was shaped at the upper half of the coil unit. This VCM structure can be improved in efficiency, however we adapt this design to minimize the levitation mass and the Z-dimension of the levitated table.

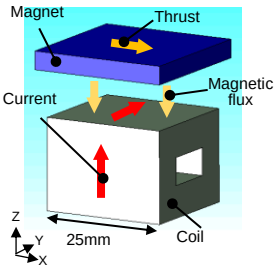

(a) Structure of X-VCM

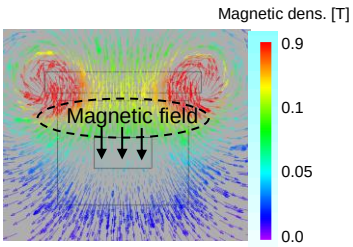

(b) Magnetic flux

FIGURE 4. Compact VCM designed with magnetic analysis to fulfill horizontal thrust requirements while remaining lightweight.

GRAVITY COMPENSATION AND Z-VCM

If the top table, with the mass of the magnets and yokes, is supported with only the Z-VCM thrust, its coil current causes dramatic heat generation on the X-table because the top table's gravity acceleration of 9.8 m/s^2 should be supported constantly. We adopted a gravity compensation mechanism using magnetic repellent force to support levitated mass without the coil current.

Figure 5 (a) shows the structure of the gravity compensator, which consists of two magnets facing each other with the same magnetic poles. As shown in Figure 5 (b), the magnetic field was shaped between two magnets, and this made vertical repellent force for gravity compensation. Not only the gravity of the levitated mass, but the vertical force caused by the moment during the acceleration and deceleration movements of the stage should also be compensated. The vertical VCM function is integrated with the described gravity compensator. This gravity compensator has stiffness in horizontal direction, however in case that the tracking error of the coarse stage is enough small, for example several μm, this stiffness hardly affects maglev control characteristics.

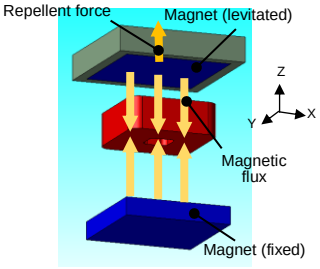

(a) Structure of gravity compensator

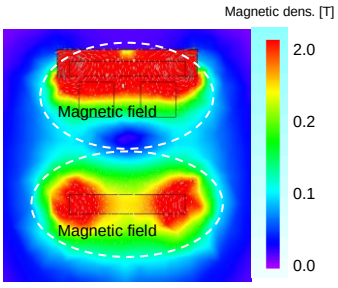

(b) Magnetic field generating repellent force

FIGURE 5. Gravity compensator with repellent force generated by two magnets facing opposite directions.

Figure 6 (a) shows the Z-VCM structure. The magnetic field, radially spread around the Z-axis, is shaped by magnets and yoke, which are used for the gravity compensator and attached to the surface below the top table. In addition, vertical thrust is generated by the coil current around the Z-axis. The magnetic field is strengthened by the magnet installed below for the gravity compensator. The strengthened magnetic field increases the thrust constant of the Z-VCM.

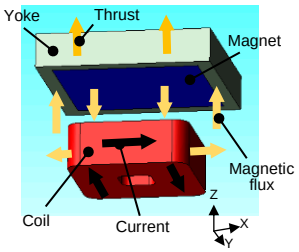

(a)Structure of Z-VCM

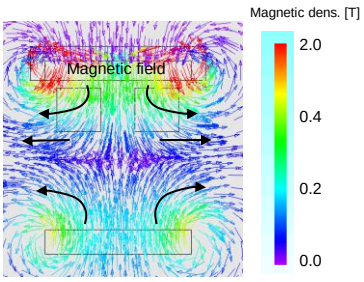

(b)Magnetic flux of Z-VCM

FIGURE 6. Z-VCM structure and its magnetic flux, shaped by magnet installed for gravity compensation.

CONTROL SYSTEM

According to Earnshaw's theorem, a maglev stage generally cannot maintain levitation without control. We configured 6DOF control for stable levitation.

Figure 7 shows a block diagram of the control system for positioning in the XY-plane and for the yawing motion around the Z-axis. Figure 7 (a) shows a layout of the capacitance sensor and VCM units in relation to the XY-planar control.

Y-axis thrust is calculated using displacement of the top table, measured by sensor Y. Then, VCM Y1 and Y2 are determined in the Y-PID controller. The X-axis position is calculated from the average of sensor X1 and X2. X-thrust is calculated in the same way as that of the Y-axis.

The θz angle is calculated from the difference between the sensor signals of X1 and X2. Thrust of the θz-axis is generated by the difference between X1 and X2 and Y1 and Y2.

Figure 8 shows the frequency response of the θz-axis from the VCM thrust to sensor signal. We confirmed that the characteristics match with the ideal theoretical model.

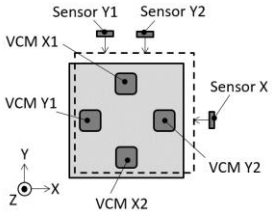

(a) X, Y, θ_Z-layout

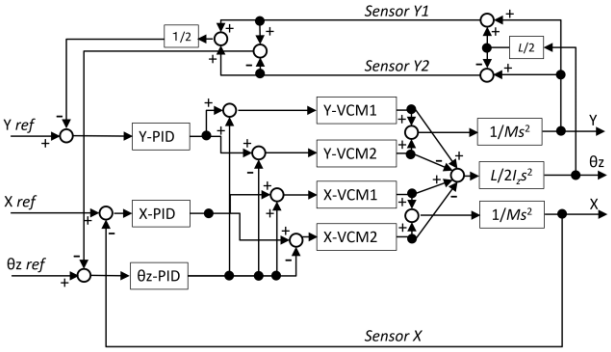

(b) X, Y, θ_Z-axes controller

FIGURE 7. Control system for positioning and yawing in horizontal plane.

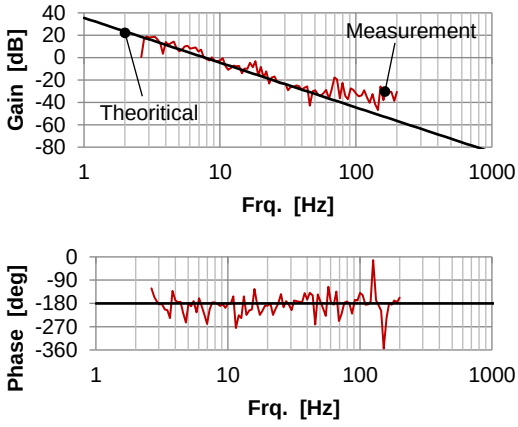

FIGURE 8. Frequency response of θz-axis measured with capacitance sensors X1 and X2.

Figure 9 shows the control system for vertical positioning and pitching motion. These controllers can be independent from the horizontal control system because interference between axes is small enough. This is because the top table altitude is limited to almost zero in order to reflect laser beams in the same directions as the interferometers.

Figure 10 shows the frequency response of the Z-axis. Resonance at 134 Hz limits the control bandwidth.

Table 2 shows the control gains of the PID controller; these are tuned with the frequency response measured by the capacitance sensor. The same characteristics are obtained in the X and Y-directions because of the symmetric structure and layout center in the Z-axis.

Figure 11 shows the closed loop characteristics of X-axis and Z-axis; these are the simulation results using identified models of frequency responses containing measured resonance peaks. The control bandwidth at 200 Hz was realized in the X-axis.

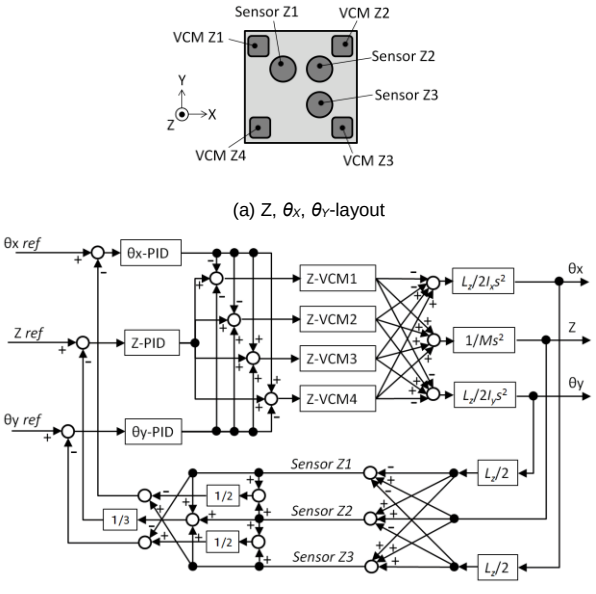

(a) Z, θ_X, θ_Y-layout

(b) Z, θ_X, θ_Y-axes controller

FIGURE 9. Control system for vertical positioning and pitching altitude.

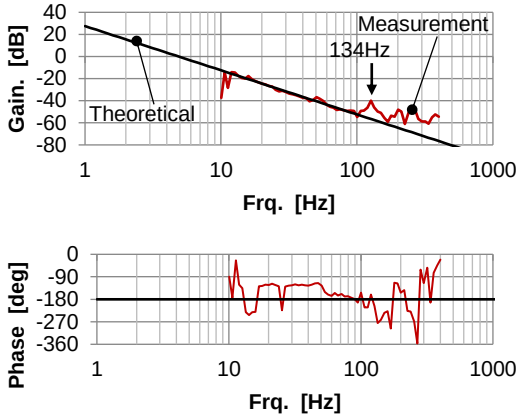

FIGURE 10. Frequency response of Z-axis measured with capacitance sensors Z1, Z2 and Z3.

TABLE 2. Control gains of maglev stage.

	X	Y	Z	θx	θy	θz
Proportional	9.0e5	9.0e5	4.0e4	6.0e6	6.0e6	5.0e6
Integral	1.1e8	1.1e8	1.3e6	1.5e8	1.5e8	1.3e8
Differential	4.8e3	4.8e3	6.4e2	9.5e4	9.5e4	8.0e4

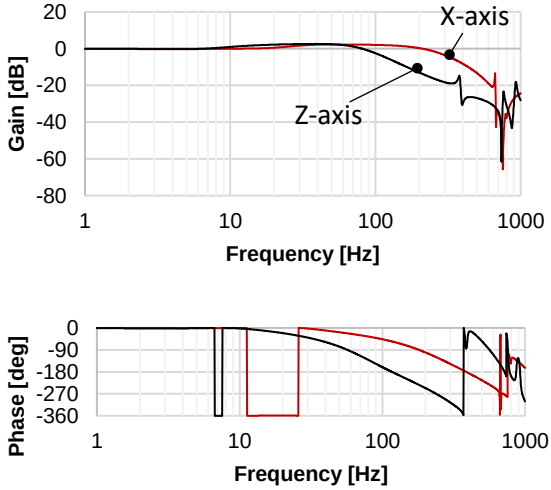

FIGURE 11. Simulation results of closed loop characteristics of X-axis and Z-axis feed-back control systems.

STATIC VIBRATION

We evaluated the static vibration of the levitated top table. Figure 12 shows vibration of the top table while the stage was levitated constantly. Figure 12 (a) shows vibration controlled with capacitance sensors in all axes. Fluctuation of low frequency, about 10 Hz, was observed, and the fluctuation's amplitude was about ±350 nm.

Figure 12 (b) shows vibration controlled with laser interferometers in the X, Y, and θz-axes and with capacitance sensors in the Z, θx, and θy-axes. Positioning error within ±10 nm was confirmed.

These results show the stage's capability of setting control parameters with high gains because of the decrease in the S/N ratio of the sensor noise.

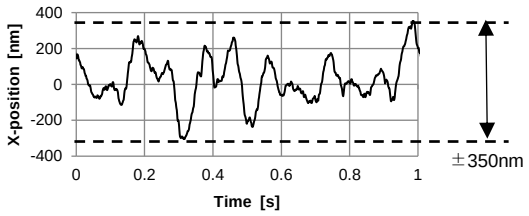

(a) Control with capacitance sensors

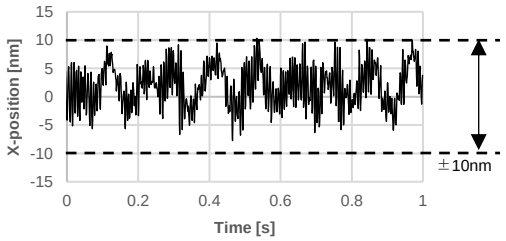

(b) Control with laser interferometers

FIGURE 12. Evaluation results of top table static vibration in X-axis. Top table was levitated constantly and controlled using capacitance sensors (a) or laser interferometers (b).

CONCLUSION

We developed a new maglev stage with a compact structure for a fine stage with a gravity compensator using repellent force. The compact VCM design enables a light weight for the levitated mass and a high responsiveness for the stage control. Through evaluating the developed stage, we confirmed its capability for nanometer-scale positioning.

FUTURE WORK

First, in this development, it appeared that the noise from the Z-axis capacitance sensors cause nanometer-scale vibration of the top table in XY-direction. More precise evaluation of the relationship between static vibration and sensor noise is planned for the future.

Second, robustness will be problem if the coarse stage moves faster than it does now. We will revise the stage structure, optimizing the VCM structure for higher thrust.

Finally, we will aim to optimize the frequency response to reduce tracking error and vibration after the stage moves more quickly. This optimization will be achieved by clarifying the relationship between the resonance of the structure and peak in frequency response.

REFERENCES

[1] Y. Tomita, M. Sugimine and Y. Koyanagawa, "Development of Six-Axis Precise Positioning System Driven by Surface Motor," JSME series C, Vol. 62, No. 597, 1996, pg. 1840–1847.

[2] M. Takahashi, H. Yoshioka and H. Shinno, "A Newly Developed Long-Stroke Vertical Nano-Motion Platform with Gravity Compensator," Journal of Advanced Mechanical Design, Systems, and manufacturing, Vol. 2, No. 3, 2008, pg. 356–365.

[3] K. Tanaka, "Development of 6DOF Magnetic Levitation Stage for Lithography Tool -Background and First Report-," JSPE, Vol. 75, No. 4, 2009, pg. 501–508.

[4] W.-J. Kim, D. L. Trumper and J. B. Bryan, "Linear Motor-Levitated Stage for Photolithography," CIRP Annals, Vol. 46, No. 1, 1997, pg. 447–450.

[5] D. Laro, "Through the Wall," MIKRONIEK, No.1, 2013, pg. 31-35.

[6] K. Tanaka, "Development of 6DOF Magnetic Levitation Stage for Lithography Tool -Proof of Concept (Second Report)- ," JSPE, Vol. 75, No. 5, 2009, pg. 605–611.

[7] W. Kim, S. Verma, and H. Shakir, "Design and precision construction of novel magnetic-levitation-based multi-axis nanoscale positioning systems," Precision Engineering, Vol. 31, 2007, pg. 337–350.

[8] M. Takahashi, H. Ogawa, and M. Odai, "A Study on Nanometer-Scale Vibration Canceller for Ultra Precision Positioning Stage," JSPE, Vol. 83, No. 10, 2017, pg. 956–961.

FORCE CONTROL FOR HYBRID ELECTRIC-PNEUMATIC ULTRA-PRECISION VERTICAL POSITIONING DEVICE

Tomohiro Tanaka[1], Youwei Xu[1], Tomonori Kato [1] and Kohei Shimazaki[1]
[1]Department of Intelligent Mechanical Engineering
Graduate School of Engineering
Fukuoka Institute of Technology

ABSTRACT
The purpose of this study is to construct a control method that can reduce the motor load by generating a vertical force by controlling the pressure of the balance cylinder in a hybrid electric-pneumatic ultra-precision vertical positioning device, and to estimate the machining force in the vertical direction using a disturbance force observer. In this paper, we investigated the relationship among the pressure in the balancing cylinder, driving current signal of the linear motor, and force in the vertical direction. We also attempted to generate and control the force by controlling the pressure in the balancing cylinder using a high-precision quick response pneumatic regulator (HPQR) developed in our previous research.

INTRODUCTION
There are multiple methods for the positioning of ultra-precision machining tools, such as aspherical lens generators, which are used for the mold processing of aspheric lenses. One such tool is a hybrid electric-pneumatic system that combines a pneumatic balancing cylinder as a gravity compensator and a cored electric linear motor to achieve both nanometer-level ultra-precise positioning and energy efficiency[1)]. In recent years, the authors have researched ways to enhance the function of the device by actively controlling the internal pressure of the balance cylinder of the hybrid electric-pneumatic ultra-precision vertical positioning device[2)].

During the cutting process using a working machine with a hybrid electric-pneumatic ultra-precision vertical positioning device, a linear motor is used to drive the stage and control the processing force applied to the material being processed. However, the maximum processing force that the device can output depends on the upper limit of the motor. In addition, a force sensor is required to monitor the external force generated in the vertical direction during machining. However, a larger-scale motor and force sensor settings are often not simple in terms of their structure and will increase the cost of the processing machinery.

The purpose of this research is to construct a control method that can reduce the motor load by generating a vertical force by controlling the pressure of the balance cylinder in a hybrid electric-pneumatic ultra-precision vertical positioning device, and to estimate the force generated in the vertical direction from the signals of the pressure sensor and the current sensor using a disturbance observer.

HYBRID ELECTRIC-PNEUMATIC ULTRA-PRECISION VERTICAL POSITIONING DEVICE
In practical working machinery, it is difficult to evaluate the relationship between the internal pressure fluctuation of the balance cylinder and the vertical positioning because of the influence of factors other than the vertical positioning axis and processing conditions. Therefore, in our laboratory, we manufactured an experimental device that simulates the vertical axis of an actual machine tool. The appearance of the experimental device is shown in Figure 1. The device is composed of a coreless-type linear motor (S250D, GHC), two pneumatic balancing cylinders with aerostatic linear bearings, and an absolute type linear scale (LIC4017,

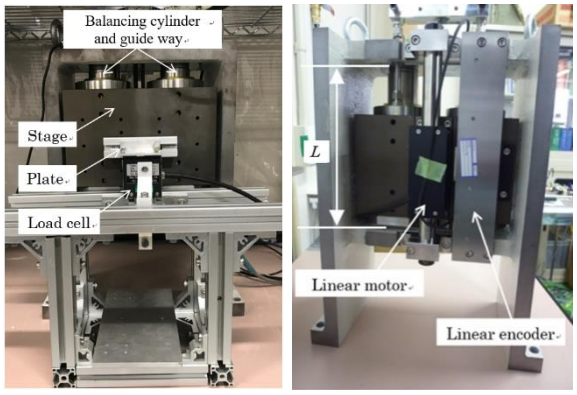

(a) Front view *(b) Back view*

FIGURE 1. Photographs of the experimental device

HEIDENHAIN) with a resolution of 1 nm. The unique characteristics of this device include its ability to suppress the friction, stick-slip, and heat generation owing to the adaption of a finely finished balancing cylinder surface with an aerostatic linear bearing and non-contact (coreless) type linear motor. A load cell (TCLZ-500NA, range of ± 500 N and resolution of 0.01 N) was used for the force measurement equipment.

PROPOSAL OF CYLINDER PRESSURE CONTROL METHOD FOR STAGE WEIGHT FLUCTUATION

When changing the machine tool using an electro-pneumatic hybrid method, the weight of the stage changes depending on the type of tool, and thus it is necessary to adjust the supply pressure to the cylinder to balance the stage weight and the compensation pressure. In this section, we propose a pressure control method to cope with any stage weight fluctuations by controlling the internal pressure of the cylinder such that the torque command reaches 0%.

A block diagram of the proposed control is shown in Figure 2. This system adds feedforward control to compensate for fluctuations of the torque command to the control of the high-precision quick response pneumatic pressure regulator (HPQR)[4]. The compensation pressure P_{cmp} is obtained by multiplying the torque command value T % by the gain K_t = −0.3854 kPa. By adding the compensation amount to the target pressure, the cylinder internal pressure is controlled such that the torque command reaches 0%.

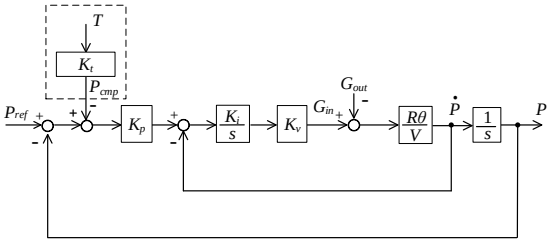

FIGURE 2. Block diagram of proposed method

EVALUATION TEST UNDER FLUCTUATIONS IN STAGE WEIGHT

To evaluate the effectiveness of the proposed method, comparative experiments were conducted using the DH regulator and the proposed method. The experiment setup is shown in Figure 3. The experiment was conducted according to the following procedure.

First, the stage upon which the weight is placed is stopped using a linear motor, and the internal pressure of the cylinder is adjusted such that the torque command reaches 0%. Then, 10 s after the start of the experiment, the weight is removed, and the internal pressure of the cylinder, the torque command, and the stage position are measured.

The results of the torque command are shown in Figure 4, and the results of the cylinder pressure are shown in Figure 5.

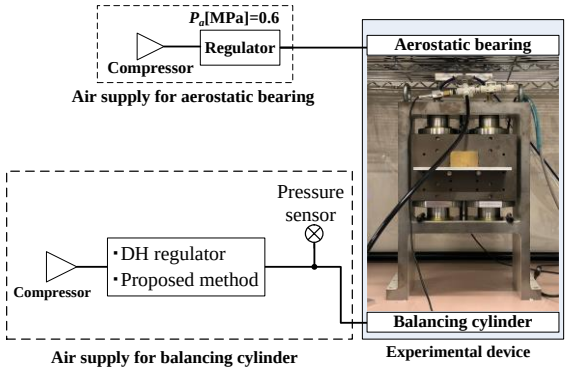

FIGURE 3. Experiment configuration

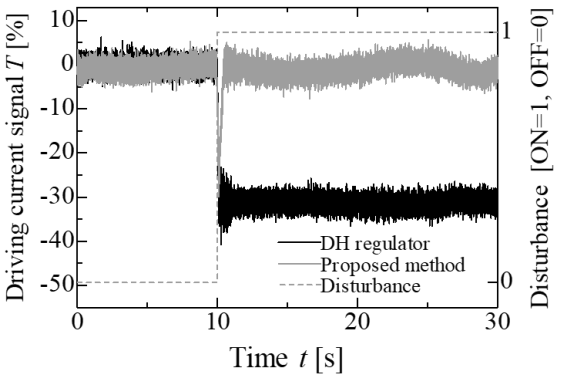

FIGURE 4. Experiment results of driving current signal

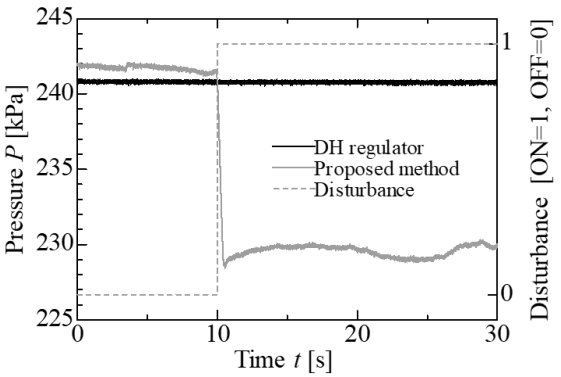

FIGURE 5. Experiment results of pressure

According to Figure 4,when the internal pressure of the cylinder is adjusted by the DH regulator, the torque command fluctuates by approximately 30% when the weight change is applied, and the load on the linear motor increases. By contrast, when the internal pressure of the cylinder is adjusted using the proposed method, it is possible to compensate for the influence of the weight fluctuation and instantly restore the torque command to 0%.

From the results of the internal pressure of the cylinder shown in Figure 5, when the DH regulator is used, the balance between the stage weight and the internal pressure of the cylinder is lost when the stage weight fluctuates, and the load on the motor increases. In the proposed method, the internal pressure of the cylinder is changed by approximately 12 kPa when the stage weight changes, and a pressure compensation is applied such that the torque command reaches 0%.

NEW PROCESSING AND EXTERNAL FORCE ESTIMATION METHOD USING DISTURBANCE OBSERVER

In existing processing methods that compensate for the stage weight with a balance cylinder and apply the processing by driving the stage with a linear motor, the driving current signal of the motor fluctuates when an external force is applied to the stage, causing a load on the motor. Therefore, we propose a new processing method that can reduce the motor load (Figure 6). With this method, the external force is first estimated, and the internal pressure compensation calculated from the estimated external force is added to the internal pressure P_B that balances with the stage weight to compensate the fluctuation of the driving current signal of the motor. The external force can be estimated from the internal pressure of the balance cylinder and driving current signal using the disturbance observer shown in Figure 7 (the driving current signal when providing the internal pressure P_B to the balance cylinder is the value of T_B). However, the relationship between the balance cylinder pressure, driving current signal, and force is not clear, and needs to be investigated.

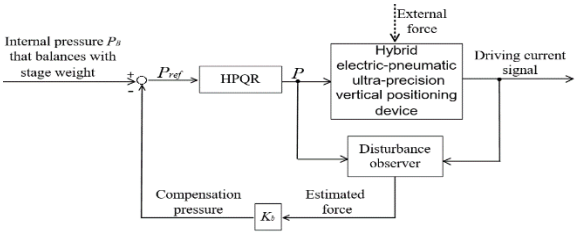

FIGURE 6. Proposed control method for cylinder pressure

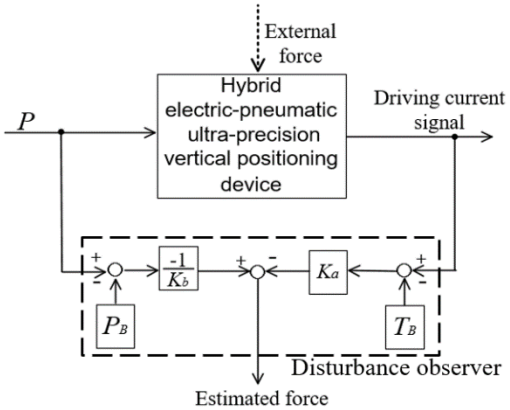

FIGURE 7. Block diagram for disturbance force observer

IDENTIFICATION EXPERIMENT OF THE RELATIONSHIP BETWEEN INTERNAL PRESSURE OF BALANCE CYLINDER AND VERTICAL FORCE

To clarify the relationship between the internal pressure of the cylinder and the force in the vertical direction, with the linear motor position control turned off, the stage and load cell are brought into contact, and the internal pressure of the balance cylinder is continuously changed from 228 kPa to approximately 166 kPa using the DH valve. The values of the generated force F_{Air} and internal pressure of the balance cylinder P were recorded using the DSP (MTT, S-BOX). In addition, the internal pressure and force of the cylinder were also measured when the internal pressure of the balance cylinder was stabilized at 30 s at 12 intervals of 5 kPa from 225 to 170 kPa.

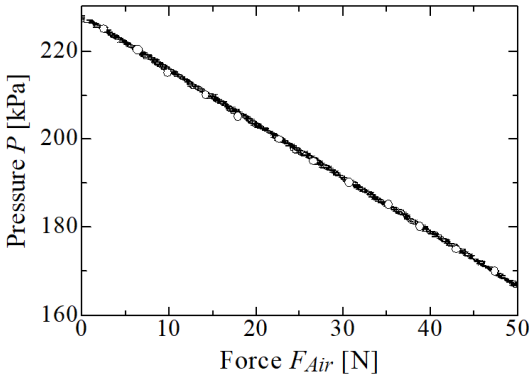

FIGURE 8. Experiment results of the relationship between the balancing cylinder pressure and force

The experiment results on the relationship between the internal pressure of the balance cylinder and the vertical force are shown in Figure 8. A linear relationship can be seen between the internal pressure of the balance cylinder *P* and the generated force F_{Air}. The relationship between *P* and F_{Air} can be approximated in equation (1) linearly.

$$P = -1.233 F_{Air} + 228.1 \quad (1)$$

IDENTIFICATION EXPERIMENT OF THE RELATIONSHIP BETWEEN DRIVING CURRENT SIGNAL AND FORCE OF LINEAR MOTOR

To clarify the relationship between the driving current signal of the linear motor and the force in the vertical direction, an experiment was conducted to investigate the relationship between the driving current signal by the position control of the linear motor and the force generated in the vertical direction while supplying internal pressure to balance the weight of the stage in the balance cylinder.

An internal pressure of approximately 228 kPa is supplied to the balance cylinder using HPQR, and the stage is stopped at the position (origin) where the plate contacts the load cell through a position control of the linear motor. The value of the generated force was recorded as approximately 10 s using the DSP. Subsequently, the stage was moved downward 5 μm and recorded for approximately 10 s in the same manner. This operation was repeated until the torque command reached -100%.

The results of the driving current signal and force obtained by the position control of the linear motor are shown in Figure 9. When the stage moves downward owing to position control of the linear motor, the driving current signal decreases and a force is generated. When the stage moves to a position of approximately -58 μm, the driving current signal decreases to approximately -100%, and a force of 30 N is obtained. The relationship between the driving current signal *T* and the force F_{Mot} generated in the vertical direction can be approximated through equation (2).

$$F_{Mot} = -0.31T + 0.51 \quad (2)$$

CONCLUSION AND FUTURE PLANS

In this study, we proposed a disturbance observer that estimates the generated force of the stage during machining, as well as a machining method that can reduce the motor load. It was confirmed that the relationship between the internal pressure of the balance cylinder and the force, and the relationship between the driving current signal of the linear motor and force, can be approximated into a linear function. The characteristics of the method used to control the force accurately through the HPQR were confirmed.

In a future study, the relationship between the internal pressure of the balance cylinder, the torque command value, and the force investigated in this study will be applied to the proposed method to estimate the force generated and verify the new processing method.

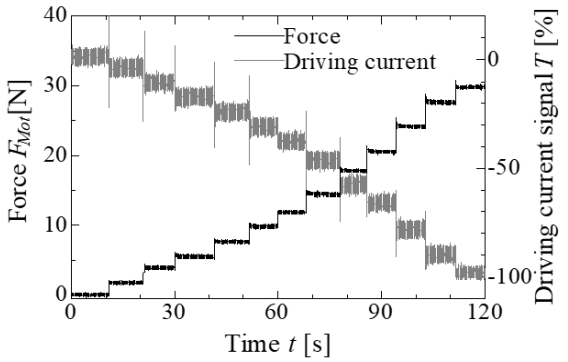

FIGURE 9. Experiment results of the force and driving current

REFERENCES

[1] Tanaka K., Status Quo Prospect of Ultra-precision machining, Journal of the Japan Welding Society, Vol. 70, No. 2, pp. 273-279, 2001.

[2] Tsukiyama, Y., Kato, T., Matsuo, K., Evaluation of energy consumption of hybrid electric-pneumatic ultra-precision vertical positioning device, The 10th JFPS International Symposium on Fluid Power 2017, 2D47, 2017.

[3] Kakinuma, Y., Sensorless cutting force monitoring technique and the application, Journal of the Japan Society for Precision Engineering, Vol. 83, No. 3, 2017.

[4] Kato, T., Higashijima, G., Yazawa, T., Otsubo, T., Tanaka, K., Proposal of disturbance-compensating and energy-saving control method of air turbine spindle and evaluation of its energy consumption, Precision Engineering, Vol. 43, pp. 439-447, 2016.

.

Study on an Active Vibration Isolation with respect to inertia variations

Jinsoo Choi[1], Kihyun Kim[1#], Jaehyun Park[2] and Seokwoo Lee[2] and Hyoyoung Kim[2]
[1]Department of Mechatronics Engineering
Korea Polytechnic Univ.
Siheung-si, Gyeonggi-do, South Korea
[2]Department of Manufacturing System R&D Group
Korea Institute of Industrial Technology
Cheonan-si, Chungcheongnam-do, South Korea

INSTRUCTIONS

As the modern industry develops, the precision of the system increases and the demand for the technology to control the vibration is also increasing. In this paper, active vibration isolation system (AVIS) are aimed to actively control the vibration of the target system. Traditional AVIS equipment does not consider the influence of the inertia changes due to the motion of the target system on the model. In most cases, the target system located at the top of the isolation equipment may have inertia that varies with application. The movement of the stage on the vibration isolation equipment, the robot arm, and the inertia may be changed depending on the application site. Changes in inertia can be associated with rotational motion, which can make the system unstable and the system's model can change. The change of the system model is that the gain cannot always be optimized when the gain value of the control applied in real time is constant, and located near the critical point of the existing system, the model is changed and the system may become unstable. This problem is limited by the gain value. To overcome these limitations, this active damping research aims to actively control the system by updating the model considering the effects of inertia change on the system. In this paper, the system for 6-DOF with an adaptive Linear Quadratic Gaussian (LQG) controller consists of 4-pneumatic isolators and 8 optimized VCMs. 4-position sensors for z, theta X, theta Y motions, an estimator for the other motions, and 8 geophone sensors for 6-DOF velocities are used. The AVIS is developed and validated with a dSPACE controller.

Active Vibration Isolation System

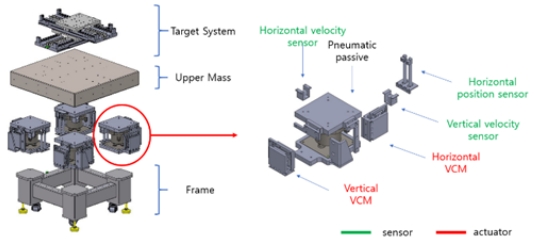

FIGURE.1 Schematic diagram of the hardware

Fig. 1 represents the developed system. Disturbances originating from the bottomed and target systems can be measured from a velocity and displacement sensor fixed to the top mass. The upper mass has pneumatic 4-point support, and the pneumatic passive, horizontal, vertical velocity sensor, vertical displacement sensor, horizontal and vertical actuators are modular. The modulated control isolates vibration between the bottom frame and the top mass. The actuator uses a voice coil motor (VCM) to convert electrical energy into mechanical translational motion. The target system is built as a linear stage that can easily mimic inertia changes and can apply inertia changes due to motion of the movers.

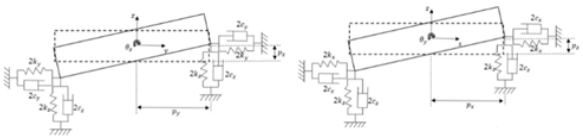

FIGURE.2 Schematic diagram of the passive isolation

Fig. 2 is the behavior of the system viewed from the YZ plane and the ZY plane. The degree of freedom of the system determines the 6-axis

motion, and each motion is determined by the distance between the center of gravity and the point supported by the isolator. In translational motion, total stiffness and damping are equal to the sum of stiffness and damping at each support point. The rotational motion is determined in proportion to the distance between the center of gravity and the point of support. In general, using pneumatic pressure to lower the natural frequency of the system does not consider the internal modes of the target system and the upper mass. By equalizing the target system and the upper mass to a rigid body, the system can take into consideration only the linear characteristics using the given constant parameters without considering the nonlinear characteristics. The proposed equation (1) is shown in Fig. 2 is a modeling equation. By using this, resonance frequency, transfer function, and output characteristics of the system can be grasped.

$$F_x = m\ddot{x}_p + c_x(\dot{x}_p - \dot{x}_b) + k_x(x_p - x_b) + c_x p_z \dot{\theta}_{y_p} + k_x p_z \theta_{y_b}$$

$$F_y = m\ddot{y}_p + c_y(\dot{y}_p - \dot{y}_b) + k_y(y_p - y_b) + c_y p_z \dot{\theta}_{x_p} + k_y p_z \theta_{x_b}$$

$$F_z = m\ddot{z}_p + c_z(\dot{z}_p - \dot{z}_b) + k_z(z_p - z_b)$$

$$M_{\theta_x} = I_{xx}\ddot{\theta}_{x_p} - c_y p_z(\dot{y}_p - \dot{y}_b) - k_y p_z(y_p - y_b) + (c_y {p_z}^2 + c_z {p_y}^2)\left(\dot{\theta_{x_p}} - \dot{\theta_{x_b}}\right) + (k_y {p_z}^2 + k_z {p_y}^2)(\theta_{x_p} - \theta_{x_b})$$

$$M_{\theta_y} = I_{yy}\ddot{\theta}_{y_p} + c_x p_z(\dot{x}_p - \dot{x}_b) + k_x p_z(x_p - x_b) + (c_x {p_z}^2 + c_z {p_x}^2)\left(\dot{\theta_{y_p}} - \dot{\theta_{y_b}}\right) + (k_x {p_z}^2 + k_z {p_x}^2)(\theta_{y_p} - \theta_{y_b})$$

$$M_{\theta_z} = I_{zz}\ddot{\theta}_{z_p} + (c_x {p_y}^2 + c_y {p_x}^2)\left(\dot{\theta_{z_p}} - \dot{\theta_{z_b}}\right) + (k_x {p_y}^2 + k_y {p_x}^2)\left(\theta_{z_p} - \theta_{z_b}\right) \quad (1)$$

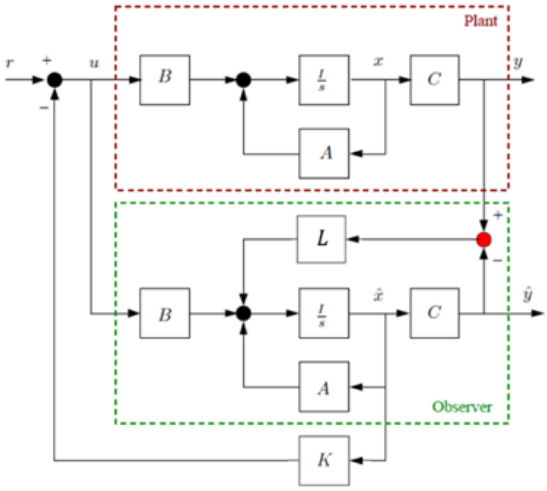

FIGURE.3 Block diagram of the state observer

Fig. 3 is the state variable of observer and plant. Control via state feedback can achieve the desired output by moving the pole of the plant to the desired position on the S-plane via pole placement. The plant can be represented in the form of a matrix of first-order derivative elements in the state space. A matrix is a plant matrix, B matrix is an input matrix, and C matrix is an output matrix. An observer with the same model as the plant follows the plant through the L gain, which outputs the state variable to determine the plant's output. The similarity of the output from the state variable with the actual output of the plant depends on the L gain. The problem of placing the poles of the L gain and the K gain generally improves performance as the position is farther away from the existing pole. However, since the performance of the actual equipment, the operation time of the controller, the performance of the actuator, the appropriate gain should be chosen through the relationship. Through the velocity sensor, the observer predicts the displacement. When the step input is applied, it is possible to determine the degree to which the state variable follows the velocity and displacement. The system is not always able to use sensors. The LQR requires all state variables, although the use of sensors may be difficult depending on the mechanical imperfections and the external environment, the price, and so on. Therefore, it is important to follow the displacement only with the velocity sensor. The closer the value of the actual sensor is, the more the output of the LQR can be outputted without using the actual sensor.

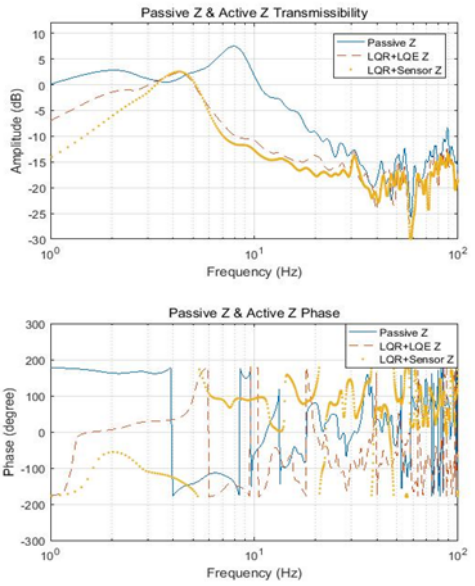

FIGURE.4 Transmissibility of Z axis

Next, in Fig.4, the transmissibility was output through the Bode plot in various states. The first is the passive state without the actuator and the second is the control performance through the state variable of the observer without using the sensor. The third is when sensor data without observer is directly controlled by LQR. The performance was best when the sensor data were directly received, but the difference was not significant when feedback was given to the observer. Thus, we can see the possibility of control through observer status feedback.

FIGURE.5 Proposed AVIS

Fig. 5 is the proposed AVIS. As in the modeling in Fig. 2, the system has 4-points of support by modularizing actuator, velocity and displacement sensors and passive using pneumatic pressure. The applied control algorithm used LQG and Fig. 3. Table. 1 is the z-axis inertia changed when the target system's movers are moved 100, 100, and 0 mm in x, y, and z axes from the A (center of gravity) point.

TABLE 1. Inertia Values

Center location	Inertia value of Z axis
A (0, 0, 0)	21.329 $kg \cdot m$^2
B (100, 100, 0)	27.582 $kg \cdot m$^2

The effect of the changed inertia on the system model is shown in Fig. 6. The performance of the model with updated inertia near the passive natural frequency is improved. Through the influence of inertia, it can be confirmed that the model update is required as the position of the movers is moved away from the origin. Also, if the characteristics of the target system are systems with large changes in inertia, model update can be an essential factor. In this paper, the target system is a stage mover, and its relative influence is low due to the small mass of the mover compared to the total mass. However, model changes can be an important factor depending on the target system because the inertia change can be relatively large depending on the change of the target system such as the robot arm and the machine.

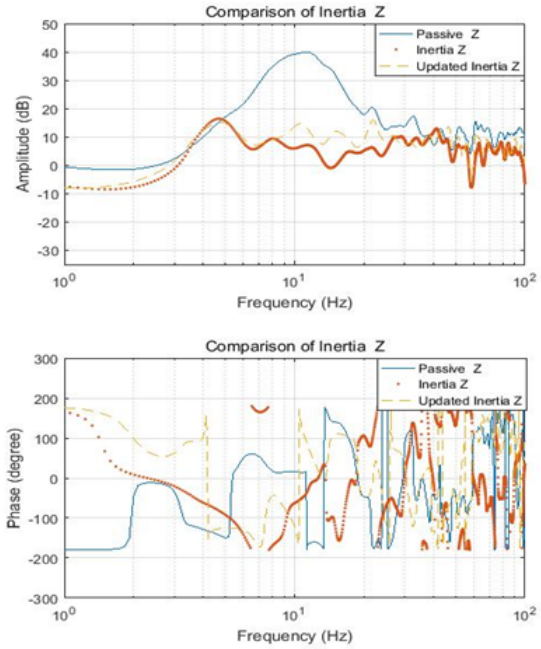

FIGURE.6 Comparison of Inertia Z

Conclusion

In this paper, we have studied the model change and active damping according to the inertia change of the target system. The frequency characteristics of the model update due to the inertia change of the target system mounted on the vibration damping table affect the control performance. Changes in the model are essential for the observer to follow the plant precisely, which is directly related to the control performance. The effect of observer state tracking on the control performance was investigated by comparing the performance of observer state variable and sensor measured value by state feedback. As a result, the influence of the inertia change on the plant model, the tracking accuracy of the observer,

and the influence on the control performance were confirmed, and the control performance according to the inertia change of the target system was confirmed.

Acknowledgement

This research was funded and conducted under 「the Competency Development Program for Industry Specialists」 of the Korean ministry of Trade, Industry and Energy(MOTIE), operated by Korea Institute for Advancement of Technology (KIAT). (HRD program for P00020007) and the Technology Innovation Program (10053248, Development of Manufacturing System for CFRP (Carbon Fiber Reinforced Plastics) Machining)

REFERENCES

[1] M-H, Kim., H-Y, Kim., H-C, Kim., D-Ahn, and D-G, Gweon., “Design and Control of a 6-DOF Active Vibration Isolation System Using a Halbach Magnet Array,” IEEE Transactions on Mechatronics., Vol. 21, No. 4, August 2016, pp. 2185-2196.

[2] Sang-Myeong. Kim,, Stephen, J., Elliott. and Michael. J. Brennan., “Decentralized Control for Multichannel Active Vibration Isolation,” IEEE TRANSACTIONS ON CONTROL SYSTEMS TECHNOLOGY, VOL. 9, NO. 1, JANUARY 2001.

[3] Markus, Their., Rudolf. Saathof., Andreas, Sinn., “Six Degree of Freedom Vibration Isolation Platform for In-Line Nano-Metrology,” IFAC., PapersOnLine 49-21 (2016) 149–156.

[4] M-G, Beker., A, Bertolini., J-F-J, van den Brand., H-J, Bulten., E, Hennes., and D-S, Rabeling., “State observers and Kalman filtering for high performance vibration isolation systems,” AIP Publishing., 034501 (2014); doi: 10.1063/1.4866659.

NOISE, RESOLUTION, AND SAMPLING RATE CHARACTERIZATION OF A LOW COST EDDY-CURRENT POSITION SENSING SYSTEM FOR BEARINGLESS MOTOR SUSPENSION CONTROL

Benjamin S. Weinreb[1,3], Minkyun Noh[2], Donald C. Fyler[3], and David L. Trumper[1]
[1]Department of Mechanical Engineering
[2]Kavli Institute for Astrophysics and Space Research
Massachusetts Institute of Technology
Cambridge, MA, USA
[3]The Charles Stark Draper Laboratory
Cambridge, MA, USA

INTRODUCTION

Bearingless motors are electric machines that combine suspension force and drive torque generating windings on a single stator. This provides the capability to both levitate and rotate a rotor, eliminating the need for mechanical bearings and allowing contact-free operation. Many bearingless motor varieties have been analyzed, built, and tested since they were first conceived in the 1980's [1].

Closed loop feedback control is usually required to achieve stable levitation of the rotor in a bearingless motor due to the inherent negative stiffness of an open loop magnetic suspension system [2]. This requires additional power electronics, sensors, and controls algorithms beyond what is typically needed for a conventional rotary electric machine. The selection, design, and configuration of these additional components is important to optimize both the cost and performance of a bearingless motor.

In this paper, we present additional analysis and experimental measurements of the low-cost eddy current position sensing system for bearingless motor suspension control presented in [3]-[5]. Particularly, we explore the tradeoff between sampling rate, sensor resolution, and noise characteristics of the sensor system. We show that we are able to increase the sensor sampling rate from 2 kHz to 5 kHz with acceptable resolution and noise performance. Additionally, we present experimental data showing the improvement in dynamic performance of the closed loop suspension system due to the increased sensor sample rate.

EDDY-CURRENT POSITION SENSING SYSTEMS FOR BEARINGLESS MOTORS

Stable rotor levitation in a bearingless motor often requires a measurement of the rotor position. Several types of non-contact sensors can be used to provide rotor position information, including eddy-current, capacitive, and optical sensors [6]. Eddy-current sensors are often used for magnetic levitation applications, as they are insensitive to debris and contaminants in the airgap, do not require electrical contact with the target, and can achieve sufficiently high resolution and stability [7]. Eddy-current sensing systems typically consist of a MHz frequency range AC-current excited sense coil, conductive target, and signal conditioning electronics. These sensors operate by detecting the inductive coupling between the sense coil and target, which varies as a function of the displacement.

There are several variations of eddy-current sensors that can be differentiated by their coil excitation and position dependent inductance variation detection methods. Many commercial eddy-current sensors, such as the Kaman Precision KD-2306, excite the sense coil with a fixed frequency AC signal and detect amplitude changes in the voltage across the coil to determine the change in inductance [8]. An alternate operating principle is to configure the coil as the inductor in an LC circuit and use closed loop control to drive the circuit to its resonant frequency. The displacement dependent sense coil inductance variation will result in LC resonant frequency variation, which can be detected by comparison to a reference frequency [9]. This self-resonant operating mode is employed by the Texas Instrument LDC 1101 inductance-to-digital converters described utilized in the sensing system described in this paper. Yet another class of eddy-current sensors make use of a coupled oscillation effect

to detect changes in sense coil inductance as the gap is varied. In these sensors, described in [10], the sense coil is configured as the inductor in an LC circuit which is coupled to an external oscillator through a resistor. Changes in the sense coil inductance result in a phase shift between the external oscillator frequency and the LC circuit frequency, which can be detected to determine the displacement.

LOW-COST EDDY CURRENT POSITION SENSOR SYSTEM OVERVIEW

The low-cost eddy current sensing system discussed in this paper was first presented in [3] and subsequently in [4] and [5]. In this section we will briefly review the system configuration and operating principle.

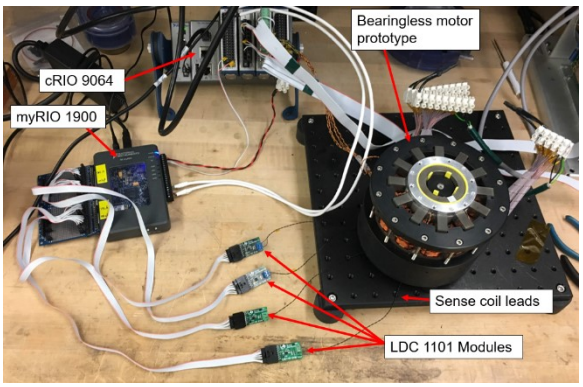

FIGURE 1. Experimental hardware configuration, including sensing system, real time controllers, and prototype bearingless motor.

As shown in Figure 1, the sensing system consists of four commercial Inductance-to-Digital Converter (LDC) Evaluation Modules (LDC1101EVM from Texas Instruments), four sensing coils (WR111180-36F5-B1 from TDK Corporation), and a myRIO real-time controller (myRIO-1900 from National Instruments). The LDC1101 modules are mixed signal circuits and their function is described in detail in [9]. The analog side drives an LC circuit consisting of the sense coil and a discrete capacitor to resonance. When the sense coil approaches a conductive target, eddy currents induced in the target generate a component of magnetic flux that opposes the flux generated by the coil current, thus reducing the sense coil's apparent inductance. The net result is that the LC circuit's resonant frequency will vary as a function of distance between the sense coil and target. The digital side of the LDC module determines the LC circuit's instantaneous resonance frequency by comparison to a provided reference frequency. The result is output to an external master device using SPI protocol.

SPI communication protocol is implemented on the FPGA of the myRIO real-time controller to interface with the LDC modules. The SPI transactions are configured to occur at a fixed sampling rate. Fixed rate SPI transactions equate to fixed rate sampling of the sensor output, which is important for implementing standard discrete-time feedback control.

IMPLEMENTATION IN BEARINGLESS MOTOR PROTOTYPE

The eddy-current sensing system is integrated with a previously developed bearingless motor prototype to provide radial position estimates for closed loop suspension control. This configuration, shown in Figure 1, is the same as that described in [5]. Specifically, the bearingless motor is a homopolar slice motor with an annular solid steel reluctance rotor. The sensor coils are installed on a central Delrin reference structure and positioned to sense the inner diameter of the rotor, as shown in Figure 2.

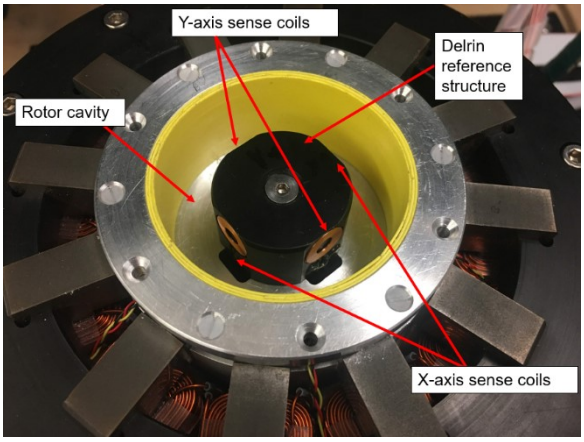

FIGURE 2. Sense coils and reference structure installed in bearingless motor prototype.

The outputs of the LDC modules attached to diametrically opposed pairs of sense coils are used to compute a differential measurement, which is then scaled by the calibrated sensor sensitivity to provide x-axis and y-axis position estimates.

EXPERIMENTAL RESULTS

In this section we present experimental measurements of sensor noise statistics and suspension loop frequency response for three different sensor sampling rates: 2 kHz, 3 kHz, and

5 kHz. The sensor sample rate is configured by writing values to a specific register on the LDC upon start-up as specified by the LDC 1101 documentation [9].

Figure 3a shows normalized histograms of the y-axis sensing module voltage at the three different sensor sampling rates, taken with the rotor fixed at approximately x = 0, y = 0. As in [3], the data was recorded with a cRIO real-time controller (cRIO-9064 from National Instruments) equipped with a 16-bit, ±10V, 370 kHz bandwidth analog input module (NI 9205 from National Instruments). The analog input module is configured to sample the data synchronously at the LDC sample rate. A series of 1.2x10^5 data points were recorded to generate each histogram. Additionally, the data is post-processed to remove the DC bias (in practice, the DC bias is removed with a fixed offset in software).

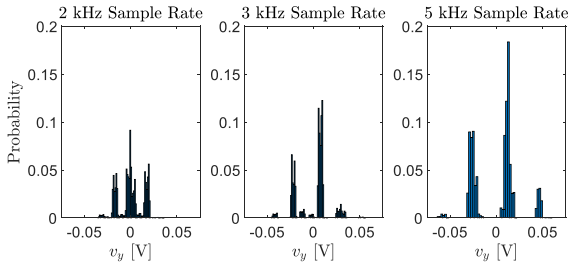

a) cRIO input signal noise histograms

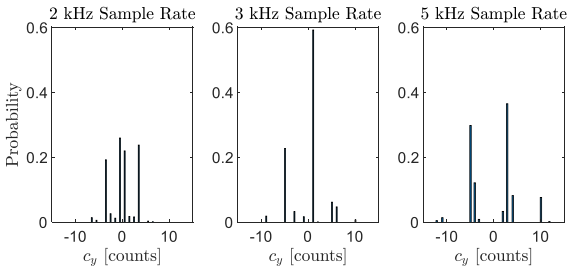

b) myRIO input signal noise histograms

FIGURE 3. Normalized histograms of sensor noise at various sensor sample rates.

The histograms in Figure 3a exhibit multimodal distributions, i.e, distinct multiple peaks. We postulate that such distributions result from quantization of the LDC's digital sensor output, and that the spread around each distinct peak is the result of additive analog noise injection between the myRIO DAC and cRIO ADC. Histograms generated directly from the LDC signal data sampled on the myRIO in the digital domain, as shown in Figure 3b, support this argument. Here we observe that the digital domain histograms consist of discrete delta functions whose positions correspond to those of the distinct peaks observed on the histograms of Figure 3a.

We observe from Figure 3 that the overall spread of each dataset increases with increasing LDC sampling rate. Table 1 shows the standard deviation, in mV, of the voltage measurement datasets for both the x and y axis modules at each sample rate. Each standard deviation is computed by taking a mean of the standard deviations of five 1.2x10^5 point datasets, and is presented with a 95% confidence interval. The position resolution for each axis at each frequency is also presented in Table 1. These are computed assuming a 12.0 V/mm x-axis sensor sensitivity and a 12.3 V/mm y-axis sensor sensitivity as measured in [5].

TABLE 1. Voltage noise statistics and sensor position resolution at various sensor sampling rates. All data presented with 95% confidence intervals assuming a t-distribution with n = 5.

Sensor Sample Rate	2 kHz		3 kHz		5 kHz	
Sensor Axis	x	y	x	y	x	y
Standard Deviation (mV)	10.5 ± 1.1	11.8 ± 1.3	12.8 ± 0.9	16.4 ± 2.0	21.0 ± 3.0	22.8 ± 1.8
Position Resolution (μm)	0.88 ± 0.10	0.96 ± 0.10	1.06 ± 0.07	1.33 ± 0.16	1.75 ± 0.25	1.85 ± 0.15

As shown in Table 1, the position resolution degrades as the sensor sampling rate increases. We hypothesize that this is because the digital side of the LDC computes the LC resonant frequency by counting the number of oscillations within the fixed sampling interval. Therefore, as the sampling rate increases, the LC frequency resolution of the sensor, which is proportional to the position resolution, will decrease. The discrepancy between the x and y axis resolution, particularly for the 3 kHz case, is likely due to the quantization of the LDC output. Each data point is a differential measurement from two LDC modules, each of which has a quantized output. At any given time, the output of each LDC is one of discrete numbers, i.e., codes, whose total quantity decreases and spacing increases as the sensor sample rate increases [11]. The spread of

a single LDC output depends on where the true sensor frequency falls relative to the division of the LDC's quantized codes. If the true frequency happens to fall close to the division between two codes, the output will oscillate between those two codes. If the true frequency is more centered within one code's range, however, the output can either remain in the single code or oscillate between said code and the codes both above and below. Thus, the resulting standard deviation has the potential to be magnitude dependent. We have observed that by slightly adjusting the position of the rotor, the histogram distribution and standard deviation could be changed, which further supports this explanation. Another possibility for the discrepancy is a time-varying stray capacitance coupling to the capacitor of the LC circuit, thus changing the LC resonant frequency.

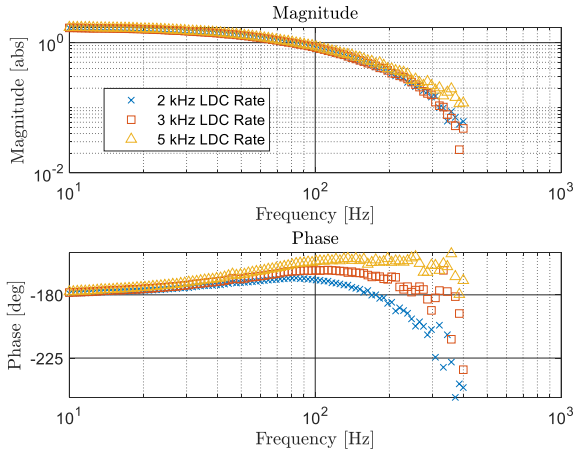

FIGURE 4. Bearingless motor protype loop return ratio for various LDC sampling rates.

The loop return ratio $L(j\omega)$ of the bearingless motor suspension loop was measured for each of the LDC sample rates and is shown in Figure 4. A discrete-time lead controller is implemented on the FPGA of the cRIO real time controller using LabVIEW 2018. The controller is implemented in a fixed rate loop running synchronously and at the same rate as the LDC. Coefficients for the discrete-time lead controller are computed by taking a Tustin transformation of a 70 Hz zero, 700 Hz pole continuous-time lead controller as described in [5]. A different set of discrete-time controller coefficients is computed for each LDC sample rate to ensure equivalent controller performance. The frequency response was measured with a dynamic signal analyzer (DSA) implemented on the cRIO running at 1 kHz.

The magnitude plots $|L(j\omega)|$ in Figure 4 are almost identical over frequencies around and below the crossover point, with the crossover occurring at approximately 79 Hz for all cases. The phase plots $\angle L(j\omega)$ in Figure 4 show that the phase delay at frequencies above 30 Hz reduces as the sample rate increases. The phase margins for the 2 kHz, 3 kHz, and 5 kHz cases are approximately 11.7º, 16.7º, and 21.8º respectively. This supports the argument made in [5] that the low phase margin for the 2 kHz case was driven by the time delay due to the relatively low sampling rate. By increasing the LDC sampling rate from 2 kHz to 5 kHz, we are able to almost double the phase margin at the expense of degrading the resolution by a factor of 2.

CONCLUSIONS

In this paper, we presented experimental measurements characterizing the low cost eddy-current position sensing system for a bearingless motor first presented in [3]. We demonstrated the inherent tradeoff between sensor position resolution and sampling frequency. An increase in the sampling rate from 2 kHz to 5 kHz results in degradation of the resolution by a factor of approximately 2. Depending on the application, this may be an acceptable tradeoff. We also presented an explanation for the shape of the sensor noise histograms and the discrepancy between the x and y axis measurements based on the LDC output quantization. Finally, we show that we are to almost double the suspension loop phase margin, which is approximately proportional to the damping ratio, by increasing the LDC sampling rate from 2 kHz to 5 kHz. Increasing the phase margin makes more aggressive tuning of the control, such as adding an integrator to eliminate steady state error, more feasible.

ACKNOWLEDGMENT

We thank the Charles Stark Draper Laboratory for funding the first author's graduate studies through the Draper Fellowship Program.

REFERENCES

[1] Chiba A, Fukao T, Ichikawa O, Oshima M, Takemoto M, Dorrell DG. Magnetic bearings and bearingless drives. Amsterdam London: Elsevier/Newnes; 2005.

[2] Schweitzer G, Maslen EH, editors. Magnetic bearings: theory, design, and application to rotating machinery. Dordrecht ; New York: Springer; 2009.

[3] Noh M, Gruber W, Trumper DL. Low-cost eddy-current position sensing for bearingless motor suspension control. In: 2017 IEEE International Electric Machines and Drives Conference (IEMDC). 2017. p. 1–6.
[4] Noh M, Gruber W, Speakman J, Gartner MJ, Trumper DL. Homopolar Bearingless Slice Motors Driving Reluctance Rotors. In: Proceedings of the 16th International Symposium on Magnetic Bearings. Beijing, China; 2018.
[5] Noh M. Homopolar Bearingless Slice Motors with Magnet-free Rotors for Extracorporeal Life Support [Doctoral Thesis]. [Cambridge, MA, USA]: Massachusetts Institute of Technology; 2018.
[6] Boehm J, Gerber R, Kiley NRC. Sensors for magnetic bearings. IEEE Transactions on Magnetics. 1993 Nov;29(6):2962–4.
[7] Nabavi MR, Nihtianov SN. Design Strategies for Eddy-Current Displacement Sensor Systems: Review and Recommendations. IEEE Sensors Journal. 2012 Dec;12(12):3346–55.
[8] KD-2306 Non-contact Displacement Measuring System User's Manual [Internet]. Kaman Precision Products; 2014. Available from:http://www.kamansensors.com/pdf_files/Kaman_KD-2306_User_Manual.pdf
[9] LDC1101 1.8-V High-Resolution, High-Speed Inductance-to-Digital Converter [Internet]. Texas Instruments; 2016. Available from: http://www.ti.com/lit/ds/symlink/ldc1101.pdf
[10] Passenbrunner J, Jungmayr G, Panholzer M, Silber S, Amrhein W. Simulation and optimization of an eddy current position sensor. In: 2015 IEEE 11th International Conference on Power Electronics and Drive Systems [Internet]. Sydney, Australia: IEEE; 2015. p. 171–6.
[11] Oberhauser C. Optimizing L Measurement Resolution for the LDC161x and LDC1101 [Internet]. 2016. Available from: http://www.ti.com/lit/an/snoa944/snoa944.pdf

ASPECTS OF DESIGN AND PERFORMANCE OF A THERMALLY ACTUATED LINEAR TRANSLATION STAGE

Chunjie Fan, DJ Hastings, Stuart T. Smith
Center for Precision Metrology
The University of North Carolina at Charlotte
Charlotte, NC 28223-0001, USA

OVERVIEW

This paper presents some design considerations for a thermally actuated, single degree of freedom flexure-based translation stage with 100 µm range and capable of operation in the presence of preloads up to 1000 N. The displacement of the thermal actuator (an aluminum tube) is based on the thermal expansion and contraction of the tube, which is controlled by induction heating for expansion, and mist (air and water) cooling for contraction. This system is controlled by a PID controller, and the displacement feedback uses an optical knife-edge sensor. Testing demonstrates that the system provides a stroke of 100 µm when pushing against a 0 N, 500 N and 1000 N preload force produced by a compression spring with settling time of around 30 seconds and up to 180 µm in 70 seconds. Circulating water cooling at each end of the actuator is used to maintain the rest of the translation stage structural components at room temperature to within ± 0.4 °C.

DESIGN AND PROTOTYPE

The goal is to provide a linear translation stage having a displacement range of greater than 100 µm and capable of driving loads of up to 1000 N. The overall design includes frame structure, flexure-based translation stage, preload structure, feedback sensor, heating system, cooling system (include thermal isolation) and control system. Fig. 1 shows the solid model of this thermal actuator with the feedback sensor that includes a knife mounted on the translation stage and an optical knife-edge sensor mounted on the frame structure.

Figure 2 shows a labeled photograph of the prototype thermal actuator. The heating system consists of an induction coil made from hollow copper wire surrounding the aluminum actuator tube. Water is pumped through the induction coil, and, therefore, maintains the outside of the actuator at room temperature.

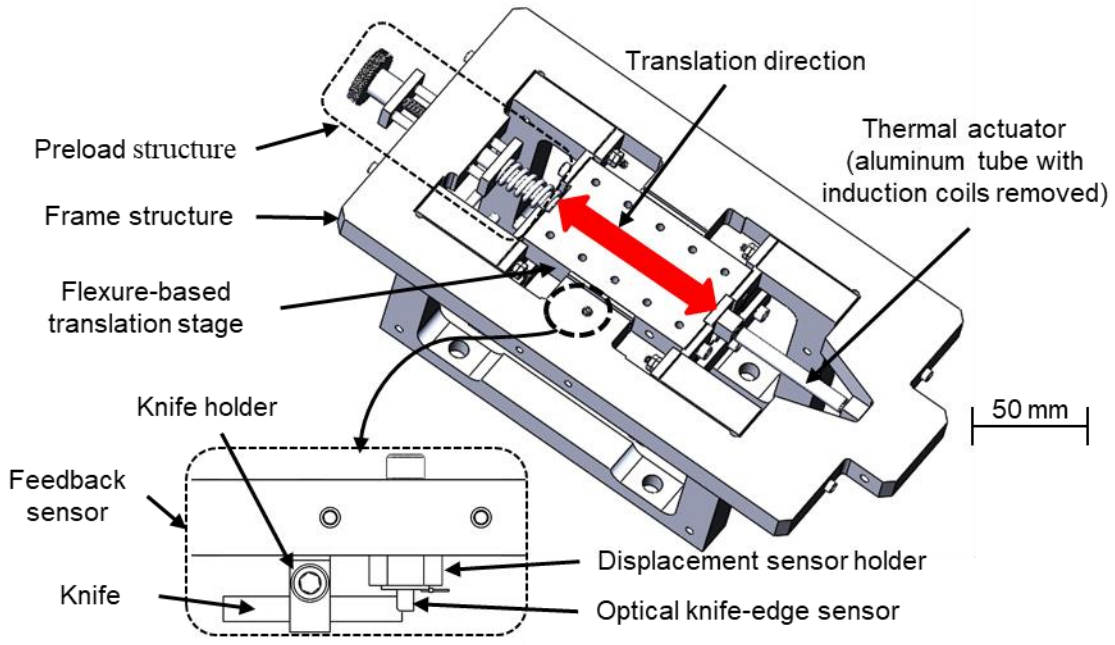

FIGURE 1. Solid model of the translation stage showing the thermal actuator with induction coil removed. Insite shows view of knife edge displacement sensor located on the underside of the stage.

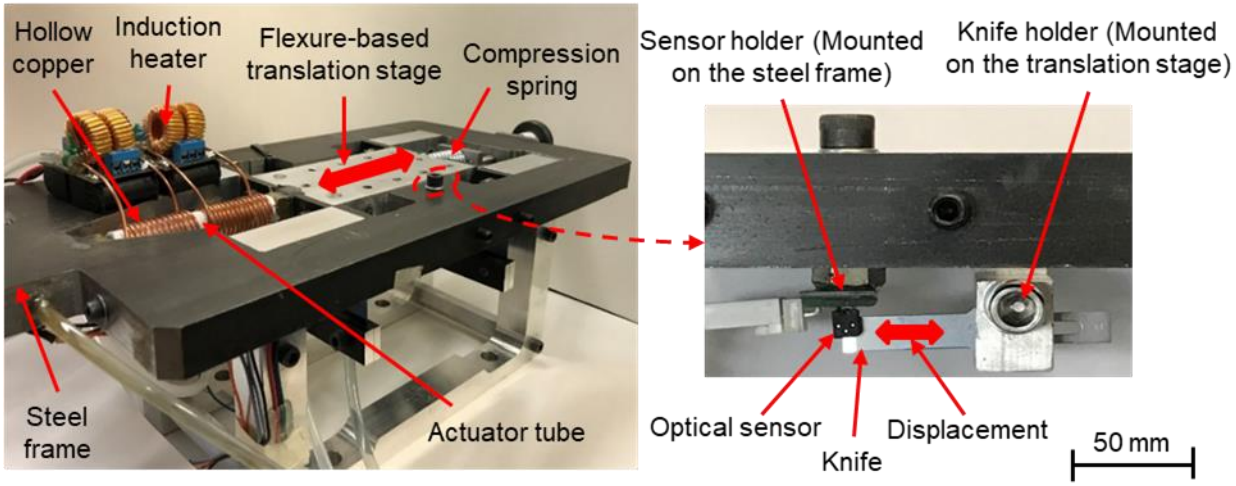

FIGURE 2. Prototype of the thermally actuated translation stage showing the thermal actuator surrounded by induction coil.

THERMAL ACTUATION

In principle, thermal actuators combine a number of unique attributes including simplicity of construction, large actuation force, compact, and can operate over a large range of temperatures. Direct electrical control of heat energy to the actuator tube can be achieved internally by resistive heating or externally via conduction and radiation from a heat source [1-9]. Currents for resistive heating can be produced by applying a voltage across the actuator or by eddy currents from an induction coil, this latter method being chosen for this study [10-11].

The induction heater comprises a tubular induction coil wound around the outside of the actuator tube, and cooling air or mist flowing through the inner diameter of the actuator tube. The tube is thermally isolated on both ends using additional water-cooling, that retains the temperature of the translation stage and frame. The wire for alternating current going through in the induction heater is a hollow copper coil to enable a flow of cooling water through the hole to maintain the coil at a desired temperature. This presentation is focused on the actuation performance observations.

OPTICAL SENSOR EVALUATION

Figure 3 and 4 involved the noise measurement of a Rohm RPI 0352E optical knife edge sensor used in this prototype. Given the low bandwidth requirements, the sensor can be filtered to an amplitude of around 3.4 mV corresponding to round 10 – 15 nm. Fig. 4 shows the position fluctuations of three different trials as a function of time while the translation stage was held stationary around 66.8 µm, and the position deviation is as small as 0.25 µm over 180 seconds period.

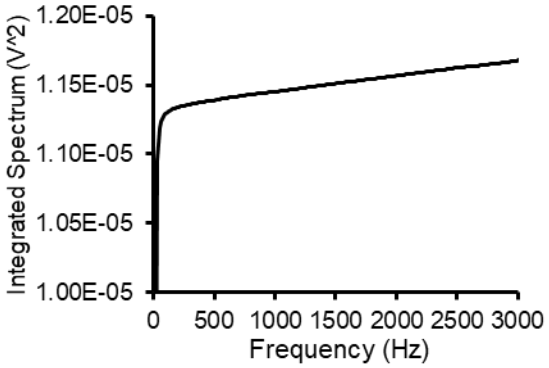

FIGURE 3. Noise measurement of the optical knife edge sensor.

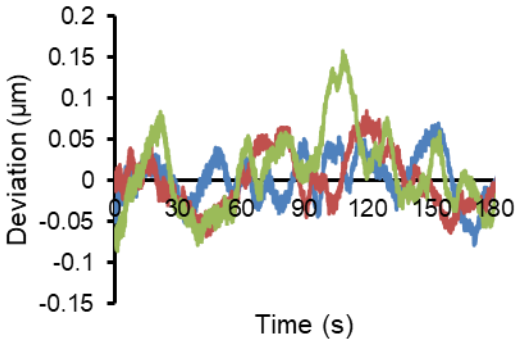

FIGURE 4. Stability tests of the optical knife edge sensor.

DYNAMIC RESPONSE

The 100 µm full range response times with position curves were evaluated. The heating system needs 30 seconds for covering the full range and cooling system need 180 seconds to go back the original position when cooling by air. In the second test, the cooling mist reduces the cooling time to 60 seconds. Fig. 5 shows the time-position curves. Pressure is maintained to be constant within the actuator tube, during heating only air flows through the tube, while during the cooling the water mist is switched on. The thermal time constants during heating cycle for this system are tested by using 0.25, 0.5, 0.75 and 1.00 duty cycle. From the step response data shown in Fig. 6, the time constant is around 60 seconds for open loop control.

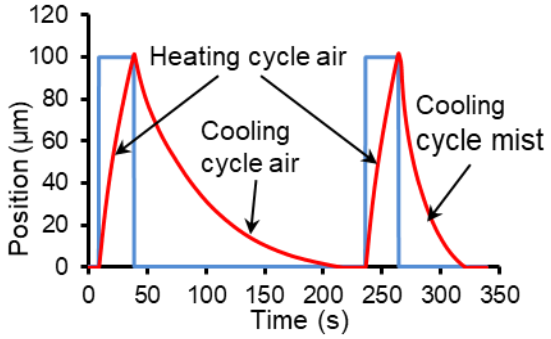

FIGURE 5. Time position response for heating cycle with air and cooling cycle with air or mist.

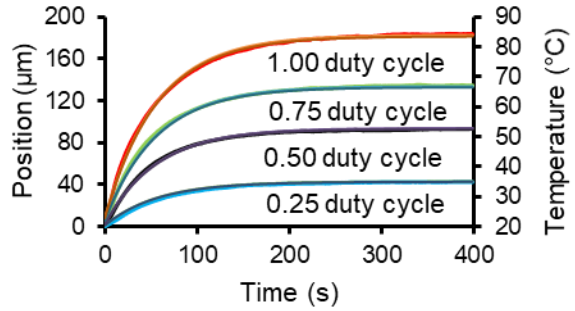

FIGURE 6. Time-position and time-temperature tests for 0.25, 0.50, 0.75 and 1.00 duty cycle show that the time constant for this open loop is around 60 seconds.

RESULTS AND CONCLUSIONS

Time and position curves were measured during a series of step demands fed to a PID controller, Fig. 7. The same procedure was repeated with preloads of 0 N, 500 N and then 1000 N. The rising time of the control system is around 15 seconds during heating and 30 seconds during cooling for 20 µm movement steps. The steady state control error after settling is within ±50 nm and the resolution is 13 nm, Fig. 8. The frame and stage temperatures are maintained to within 20.2 ±0.5 °C in these tests using a small reservoir tank, Fig. 9.

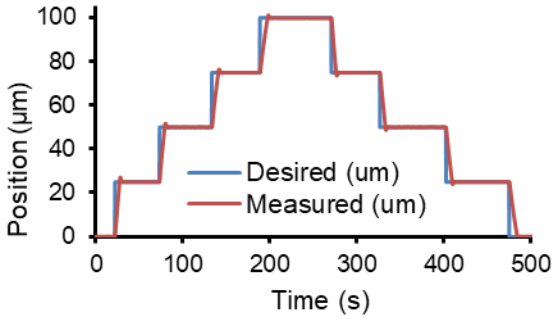

FIGURE 7. Displacement control test at 20 µm increments up to 100 µm.

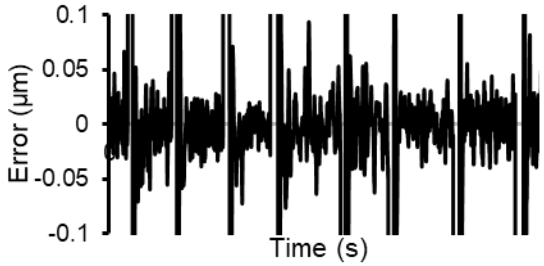

FIGURE 8. Error in the displacement at 20 µm increments up to 100 µm.

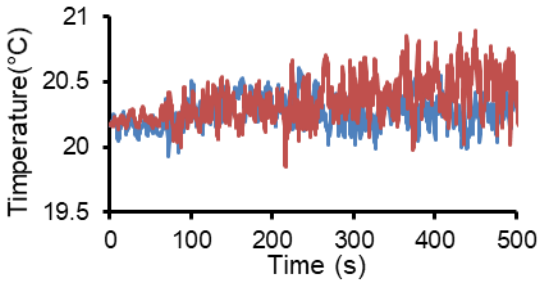

FIGURE 9. Temperature measurement of the flexure stage and frame.

FUTURE WORKS

Future work on the thermal actuator are to investigate the feasibility of manufacturing and realization of a compact system that can be integrated into system sizes between MEMS

devices and devices smaller than 25 mm x 25 mm in cross section. With a decrease in the overall dimensions of the actuator is the expectation that the dynamic properties will also decrease and create a more responsive system with a lower time constant while continuing to support loading in excess of 1000 N.

This paper focused on applications at a reservoir tank water around 20ºC. Future work will include systems that are operating at either elevated or reduced or constant temperatures. With this work will bring about additional opportunities for different metrology instruments due to exposure in the harsher environment.

Another topic for future work includes the validation of the calculated input current to verify the mathematical model of Maxwell's electromagnetic equations in this specific application, resulting in the eddy current power dissipation in a cylindrical conductive tube of finite length.

REFERENCES

[1] Y. Yamagata, T. Higuchi, N. Nakamura, and S. Hamamura, "A micro mobile mechanism using thermal expansion and its theoretical analysis. A comparison with impact drive mechanism using piezoelectric elements," in Micro Electro Mechanical Systems, 1994, MEMS'94, Proceedings, IEEE Workshop on, 1994, pp. 142-147: IEEE.

[2] S.T. Smith and R.M. Seugling, 2006, Review paper: Sensor and actuator considerations for precision, small machines, Precision Engineering, 30(3). 245 – 264.

[3] Y. Zhu, A. Corigliano, and H. D. Espinosa, "A thermal actuator for nanoscale in situ microscopy testing: design and characterization," Journal of micromechanics and microengineering, vol. 16, no. 2, p. 242, 2006.

[4] Y. Zhu and T.-H. Chang, "A review of microelectromechanical systems for nanoscale mechanical characterization," Journal of Micromechanics and Microengineering, vol. 25, no. 9, p. 093001, 2015.

[5] H. D. Espinosa, Y. Zhu, and N. Moldovan, "Design and operation of a MEMS-based material testing system for nanomechanical characterization," Journal of Microelectromechanical Systems, vol. 16, no. 5, pp. 1219-1231, 2007.

[6] R. Hickey, D. Sameoto, T. Hubbard, and M. Kujath, 2002, Time and frequency response of two-arm micromachined thermal actuators, J. Michromech. Microeng., 13, 40.

[7] L. Schönemann, O. Riemer, and E. Brinksmeier, "Control of a thermal actuator for UP-milling with multiple cutting edges," Procedia CIRP, vol. 46, pp. 424-427, 2016.

[8] G. A. Geithman and D. F. Olsen, "Induction heater and apparatus for use with stud mounted hot melt fasteners," ed: Google Patents, 1982.

[9] J.J. Snyder, 1993, Accurate, inexpensive, thermal expansion microtranslator, Rev. Sci. Instrum., 64, 1351 – 1354.

[10] H. Fujita, N. Uchida, and K. Ozaki, "A new zone-control induction heating system using multiple inverter units applicable under mutual magnetic coupling conditions," IEEE Transactions on Power Electronics, vol. 26, no. 7, pp. 2009-2017, 2011.

[11] D. Miyagi, A. Saitou, N. Takahashi, N. Uchida, and K. Ozaki, "Improvement of zone control induction heating equipment for high-speed processing of semiconductor devices," Magnetics, vol. 42, no. 2, pp. 292-294, 2006.

PREDICTION OF FEED DRIVE CONTROL PARAMETER EFFECT AT THE MACHINE TOOL CUTTING POINT DYNAMICS

Oier Franco[1], Xavier Beudaert[2], Kaan Erkorkmaz[1], and Jokin Munoa[2]
[1] Mechanical & Mechatronics Engineering
University of Waterloo
Waterloo, ON, Canada
[2] Dynamics and Control
IK4-Ideko
Elgoibar, Basque Country, Spain

ABSTRACT

Machine tools feed drives are mostly made of linear motors, ball screws or rack and pinion drives. The drive technology is selected according to the required travel length, dynamics, payload, positioning accuracy, price…

For medium and large size heavy duty milling machines, the electronically preloaded rack and pinion drive solution is commonly used, at least in one of the axis which handles the longest travel in combination with a high load. As opposed to the linear and ball screw drives, which concentrated most of the attention of the research community, the rack and pinion drives have seldom been studied in the literature. However, the rack and pinion feed drive system have several specificities that should be well understood to properly adjust the axis controller. First, two motors are used to generate the electronic preload that avoids the existing clearance between the pinions and rack, which generates the undesirable backlash effect. The preload level should be adjusted to fulfil the precision requirements without increasing the power consumption unnecessarily. Second, a specific proportional-integral controller is used to maintain the specified preload during the machine movements. Third, both motors have their own current and velocity control loops, but they are generally using a Master-Slave configuration for the position loop. Finally, compared to ball screws or linear drives, there are much more parameters to adjust for the regulation of a rack and pinion drive.

The objective of this study is to analyze the influence of the feed drive control parameters on the closed-loop response using measured Frequency Response Functions on a rack and pinion drive. Linear Fractional Transformations are used to simulate the linear components of the multi-input multi-output system. The considered inputs are the both motors torque and the generated external perturbations at the machine tooltip. Meanwhile, the outputs are measured by the rotary encoders of both motors, the linear encoder and an acceleration sensor located at the machine tooltip.

Experimental tests are carried out on a heavy duty machine with an electronically preloaded rack and pinion drive. The effect of the electronic preload on the dynamical response is measured. Then, knowing the position and velocity loops control structure, the effect of the feed drive parameter of the controllers can be simulated at the tooltip.

PROCEDURE TO DETERMINE LINEARITY DEVIATIONS OF A LARGE RANGE VERTICAL AXIS OF TOPOGRAPHY MEASUREMENT INSTRUMENTS USING SIMPLE STEP HEIGHT STANDARDS

Wilfried Bauer[1], Dorothee Hüser[2] and David Gerbert[1]
[1]Polytec GmbH
Polytec-Platz 1-7, 76337 Waldbronn, Germany
[2]Department of Surface Metrology
Physikalisch-Technische Bundesanstalt (PTB)
Bundesallee 100, 38116 Braunschweig, Germany

INTRODUCTION

There is a growing demand for a quality assessment of dimensional features of work pieces combining form and texture. A variety of optical measuring instruments is available for areal topography characterization with high accuracy. This is reflected in the upcoming standard ISO 25178-700 NWIP about calibration, adjustment and verification. In addition, some instruments provide a large scan range up to 70 mm in z-direction [1]. This article presents a low-cost method for characterizing the vertical axis of such instruments, which can be used for industrial routine calibration in the field.

To obtain the response curve of an axis usually requires costly setups with an interferometer or complex procedures employing material measures being positioned at many locations [2] of the measurement range or representing a multitude of steps [3]. The method of Kiyono et al. [2] shows that a response curve of the vertical axis can be obtained if a relation of the differential positions, i.e. heights, is maintained. To overcome the need of an external more accurate positioning stage Boedecker et al. [3] employ a material measure representing a multitude of steps. These artefacts require a costly calibration process and certificates are hardly obtained. In Leach et al. [4] a review is presented on procedures to measure metrological characteristics (MC) with a variety of material measures each representing one or few specific MC. They show step height standards, one of the kind employed by Boedecker et al. [3], see Fig. 9 in [4], and the depth setting type used during the investigations of the present article, see Fig. 8 in [4]. Guisca et al. [5] show linearity deviation studies that are performed by measurements of four different heights or depths values. Here, the amplification factor estimation is based on the relation between calibrated height values and measured height values, i.e. solely on the differential relation of positions. The residuals of a regression of this relation delivers a good estimate of the uncertainty of the linearity. However, if a systematic trend rather than random contributions of the non-linear behavior dominates, the absolute position of the location of the step heights with respect to one common origin is required.

With this article, we show that an estimate of linearity deviations can be carried out in field. This is achieved by employing a small number of steps or grooves on one artefact and with low cost positioning at few locations along the range of the vertical axis. The procedure is demonstrated using as example a white light interference microscope with the vertical axis being driven by an electro-magnetic actuator. Furthermore, the estimation of linearity deviations is verified with the aid of synthetically generated response curves of a sinusoidal linearity deviation characteristics.

MEASUREMENT STRATEGY

The German national institute PTB, for instance, provides material measures with five or six parallel grooves of varying depth in one object with the reference plane for all grooves being at the same level. This ensures the grooves having a fixed relationship with respect to each other.

The material measure is measured at different vertical positions (referred to as z-positions) along the measurement range with the distance between neighboring z-positions approximately being of the same size as the depth of the largest groove. Locating the depth setting object at the different z-positions may, for example, be realized by putting gauge blocks or other plane parallel objects underneath.

Be the number of grooves n_d (here it is $n_\mathrm{d} = 6$) and the number of positions the material measure is located be n_p, then $N = n_\mathrm{d} n_\mathrm{p}$ data points are obtained. For some positions we have performed

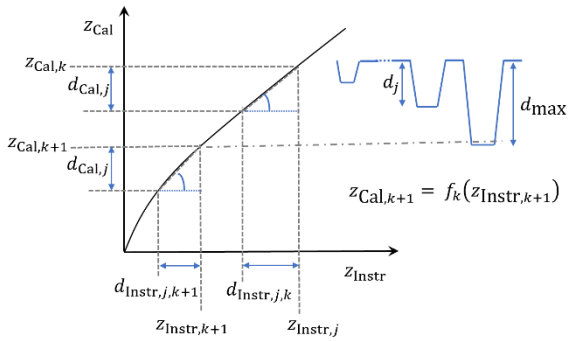

FIGURE 1. Principle of relating depth setting standards with the response curve of the vertical axis of a topography measurement instrument.

repetitive measurements, that the total number N is larger than $n_\mathrm{d} n_\mathrm{p}$. The PTB calibration certificate provides $j = 1, \dots, n_\mathrm{d}$ depth values for each of the grooves respectively $d_{\mathrm{Cal},j}$, the measurements deliver $k = 1, \dots, n_\mathrm{p}$ values for the vertical positions of the objects' reference plane location $z_{\mathrm{pos},k}$ and $l = 1, \dots, N$ depth values $d_{\mathrm{Instr},l}$.

ANALYSIS METHOD

The analysis method consists of two steps

1. Estimation of the corrected, i.e. calibrated, positions $z_{\mathrm{Cal},k}$ of the object location due to the calibrated values of the material measure.
2. Estimation of the scaling or amplification factor and the linearity deviation curve.

Step 1 is performed for each location $z_{\mathrm{pos},k}$. It uses a fit model function $f_k: z \mapsto f_k(z)$ of the response curve along the interval that is covered by the largest depth according to a priori knowledge, here we choose a parabola. For all measurements carried out at the location with the measured position $z_{\mathrm{pos},k}$, observed by the instrument the measured positions of the groove bottoms $z_{\mathrm{Instr},j(k)} = z_{\mathrm{pos},k} - d_{\mathrm{Instr},j(k)}$ and in case of step height standards the positions of the structure tops $z_{\mathrm{Instr},j(k)} = z_{\mathrm{pos},k} + d_{\mathrm{Instr},j(k)}$ are evaluated.
Furthermore, in case of depth setting standards, the sequence of positions is chosen such that the highest is the first and in case of step heights the lowest is the first. The first calibrated position $z_{\mathrm{Cal},1}$ is set equals the first measured position $z_{\mathrm{pos},1}$. The successing calibrated position is set to the value determined by the model function $z_{\mathrm{Cal},k+1} = f_k(z_{\mathrm{pos},k+1})$, which was obtained by fitting the target function as indicated in Fig. 1

$$z_{\mathrm{Cal},k} - d_{\mathrm{Cal},j} = f_k(z_{\mathrm{Instr},k} - d_{\mathrm{Instr},j(k)}). \quad (1)$$

Step 2, the estimation of the amplification factor α_z and the linearity deviation $r(z)$ is based on the model function

$$z_{\mathrm{Instr}} = \alpha_\mathrm{z}\, z + z_0 + r(z) \quad (2)$$

With α_z denoting the amplification factor, z_0 a constant offset and the function r the residual non-linearity. In ISO 25178-600, the maximum of the residuals is defined as linearity deviation $l_\mathrm{z} = \max\{r(z)\}$.

VERIFICATION OF THE PROCEDURE

For testing the procedure, sinusoidal linearity deviations of amplitudes $a_\mathrm{d} = 1\ \mu\mathrm{m}, 0.5\ \mu\mathrm{m},$ and $1.5\ \mu\mathrm{m}$ and wavelengths $\lambda = 30\ \mathrm{mm}$ and $70\ \mathrm{mm}$ along a measurement range of $35\ \mathrm{mm}$ have been generated

$$z_{\mathrm{Instr}} = \alpha_\mathrm{z}\, z_{\mathrm{true}} + a_\mathrm{d} \cos\left(\frac{2\pi}{\lambda}\,(z_{\mathrm{true}} + \Delta z)\right) \quad (3)$$

with α_z denoting the amplification factor, a_d the amplitude, λ the wavelength, and Δz the phase of the linearity deviation. Furthermore, as phase Δz the values 0 and $10\ \mathrm{mm}$ have been chosen. The regarded wavelengths are large compared to the measurement range so that parabolas are appropriate model functions $f(z_{\mathrm{Instr}}) = z_{\mathrm{Cal}}$ for intervals of $5\ \mathrm{mm}$, which is the depth of the largest groove of the material measure artefact.

Fig. 2 shows the residuals of the line fitted to all N pairs of data points $\left(z_{\mathrm{Instr},j(k)}, \left(z_{\mathrm{Cal},k} - d_{\mathrm{Cal},j}\right)\right)$ as red circles, while the blue squares show the residuals of the regression line fitted to N pairs $\left(z_{\mathrm{Instr},j(k)}, z_{\mathrm{true},j(k)}\right)$. Fig. 2 shows the result of a simulated data set with $\lambda = 70\ \mathrm{mm}$, $\Delta z = 10\ \mathrm{mm}$, $a_\mathrm{d} = 1.5\ \mu\mathrm{m}$ and $\alpha_\mathrm{z} = 0.99990$. The figure illustrates that simply regarding the residuals of a line fit to $d_{\mathrm{Instr},j(k)}$ vs. $d_{\mathrm{Cal},j}$, which are displayed as black diamonds, does not deliver a correct characterization of the linearity deviation of the instrument axis.
Comparing the residuals derived from the true positions with the residuals obtained by fitting with the estimated calibrated positions, only a very small deviation of below $10^{-4}\mu\mathrm{m}$ remains. The small finite deviation is mainly caused by the offset between the first measured position with respect to the unknown true value. Furthermore, a contribution to the deviation is due to the uncertainty of the model functions f_k.

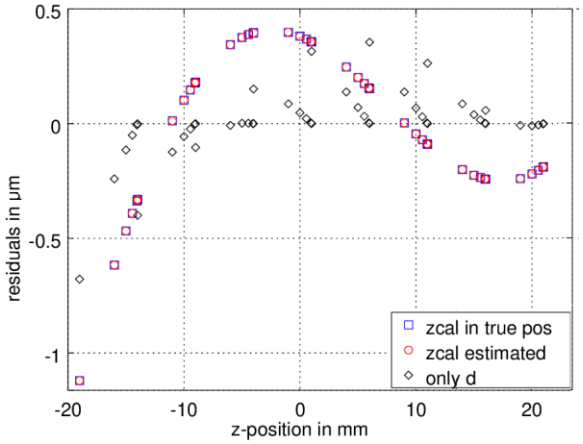

FIGURE 2. Simulation showing the linearity deviation as residuals from fitted regression lines, the blue squares obtained from instrumental values $z_{\mathrm{Instr},j(k)}$ as of Eq. (3) vs. true values and red circles vs. estimated values $z_{\mathrm{Cal},k} - d_{\mathrm{Cal},j}$. The black diamonds are the residuals of a regression line fitted to $d_{\mathrm{Instr},j(k)}$ vs. $d_{\mathrm{Cal},j}$.

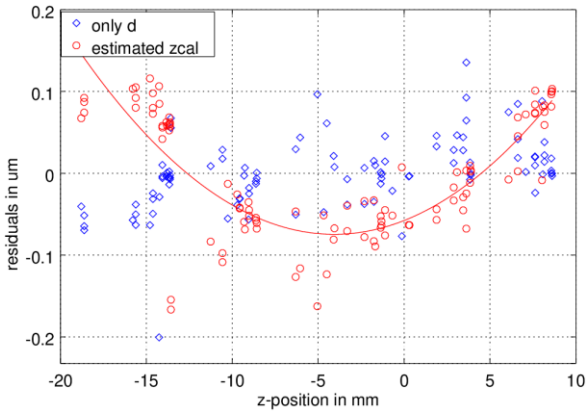

FIGURE 3. Measurement by a Polytec white light interferometer with blue diamond symbols showing the residuals of a regression line fitted to $d_{\mathrm{Instr},j(k)}$ vs. $d_{\mathrm{Cal},j}$ and red circles showing the result using absolute positions with estimated values $z_{\mathrm{Cal},k} - d_{\mathrm{Cal},j}$. The systematic trend of non-linearity visible for the red circles is emphasized by a parabola drawn as red curve.

MEASUREMENT RESULTS

The measurement example of Fig. 3 showing a result obtained by routine calibration of the instrument in the non-ideal field environment in industry illustrates that the procedure presented here can reveal systematic effects of non-linearity. This would be unrecognizable if only the relation between measured and calibrated values of the groove depths is regarded without any estimation of the absolute position within the range of the vertical axis. Two contributions to the uncertainty of the result have already been mentioned above: the ambiguity of the value for the first position $z_{\mathrm{Cal},1}$ and the uncertainty of the model functions f_k. The later has two components, first that the choice, here for instance the parabola, does not apply to the behavior of the instrument within each of the intervals sized the depth of the largest groove. Secondly, the uncertainties $u(d_{\mathrm{Cal}})$ of the depth values given in the certificate as well as the uncertainties $u(d_{\mathrm{Instr}})$ of the depth values measured by the instrument under investigation. Another contribution is the uncertainty of the whole artefact, which is mainly influenced by the flatness deviation of the reference surface. It results in the reference areas of the grooves not exactly lying at the same level. This type of systematic uncertainty has been modelled as bow with its maximum being $u_{\mathrm{bow}} = 0.3\ \mu\mathrm{m}$.

All these contributions have been included into a Monte Carlo simulation using the example of Fig. 2 and using the uncertainties $u(d_{\mathrm{Cal}})$ stated in the calibration certificate. As well, the depth uncertainty $u(d_{\mathrm{Instr}})$ of the example of Fig. 3 has been chosen as further contribution to the uncertainty budget. The uncertainty of the certified calibration values of the different depths differ according to their height, the deepest roove of 5 mm depth has a significantly larger uncertainty of $u(d_{\mathrm{Cal},6}) = 0.1\ \mu\mathrm{m}$ dominating the effect of influences of $u(d_{\mathrm{Cal}})$. Table 1 illustrates as example how an uncertainty budget can look like.

TABLE 1. Uncertainty contributions of the influencing components with uncertainties given in column 2, the sensitivities of the residuals of a linear response function model in column 3 and the resultant uncertainties of the residuals.

	$u(d_i)$	c	u_{r}
d_{Cal}	0.1 µm	0.5 . . 1	0.05 . . 0.1 µm
d_{Instr}	0.3 µm	0.4 . . 1	0.1 . . 0.3 µm
d_{bow}	0.3 µm	1.3	0.38 µm

The quantities of the second column display the uncertainty of the components $u(d_i) = u(d_{\mathrm{Cal}})$, $u(d_{\mathrm{Instr}})$, and $u(d_{\mathrm{bow}})$ respectively. The third column states the sensitivities by running the Monte Carlo simulation each time for only one of the three components yielding uncertainties u_r of the residuals of the regression line of z_{Instr} vs. z_{Cal} that are displayed in column four.

The combined uncertainty u_{r} of the linearity deviation when all three components are included to the Monte Carlo simulation ranges from

$u_r = 0.2\ \mu m$ to $0.4\ \mu m$ for the regarded example. This is independent of the choice of the amplification factor. We used different curvatures, spatial wavelengths of non-linearity of $\lambda = 30\ mm$ and $70\ mm$, and used different phase shifts $\Delta z = 0$ and $10\ mm$. Fig. 4 illustrates the influence of random uncertainty effects of $u(d_{Cal})$ and $u(d_{Instr})$ together with the systematic effect of a bow $u(d_{bow})$ deteriorating the determination of linearity deviations as systematic trend of the instrument's vertical positioning system.

CONCLUSION

It could be shown that an estimation of linearity deviations is possible using a fast low-cost method for industrial routine calibration in the field. This is realized by employing a small set of related depth setting standards with its grooves being on one common object. If the uncertainties of material measures and the random positioning uncertainty of the instrument are significantly smaller than the linearity deviation, a correction of non-linearity is possible. Simulations show how to distinguish systematic and random influences and prove that a response function can be obtained for small uncertainties of the material measure and the instrument's positioning.

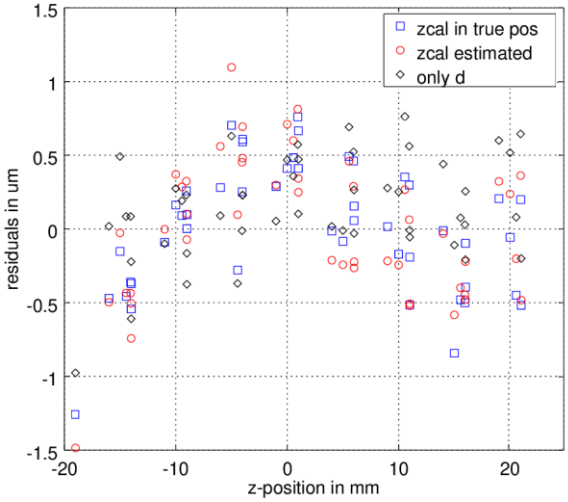

FIGURE 4. Simulation of Fig. 2 with uncertainty influences $u(d_{Cal}), u(d_{Instr})$ and $u(d_{bow})$ yielding a bias of the estimation of systematic linearity deviations.

REFERENCES

[1] Bauer, W, Special Properties of Coherence Scanning Interferometers for large Measurement Volumes, J. Phys.: Conf. Ser. 311 012030 (2011), doi:10.1088/1742-6596/311/1/012030.

[2] Kiyono S, Gao W, Zhang S, Arami T. Self-calibration of a scanning white light interference microscope. Opt. Eng. 39(10). 2000; 2720-2725; doi:10.1117/1.1290471.

[3] Boedecker S, Rembe C, Schmid H, Hageney T, Köhnlein T. Calibration of the z-axis for large-scale scanning white-light interferometers. J. Phys.: Conf. Ser. 311. 2011; 012027; doi:10.1088/1742-6596/311/1/012027.

[4] Leach R K, Giusca C L, Haitjema H, Evans C, Jiang X. Calibration and verification of areal surface texture measuring instruments. CIRP Annals 64(2). 2015; 797-813; doi:10.1016/j.cirp.2015.05.010.

[5] Giusca C L, Leach R K, Helery F, Calibration of the scales of areal surface topography measuring instruments: part 2. Amplification, linearity and squareness, Meas. Sci. Technol. 23 (2012) 065005 (11pp); doi:10.1088/0957-0233/23/6/065005.

Measurement Uncertainty Evaluation of Cosine Error-Free Surface Profile Measuring System

Xiangyu Guo[1], Jaemin Han[1], Joshua A Tarbutton[2] and ChaBum Lee[1]
[1]J. Mike Walker' 66 Department of Mechanical Engineering
Texas A & M University
College Station, Texas, USA
[2]Department of Mechanical Engineering and Engineering Science
University of North Carolina at Charlotte, Charlotte, NC, USA

INSTRODUCTION

This paper presents the uncertainty evaluation of a cosine error-free probe measuring system for precision-machined surface profiling, which is an aerostatic bearing spindle based non-contact displacement probe scanning process.

Cosine error (ε_c) occurs in a surface measuring system when the measurement axis and the axis of motion are misaligned, which is shown in Figure 1 and Eqs. 1-2, where L is the actual displacement, L' is the measured displacement, θ is the misalignment angle, and ε_c is the cosine error. This is a fundamental limitation to surface profile measuring accuracy.

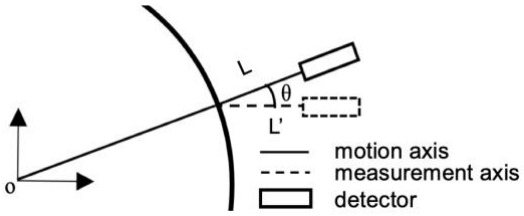

FIGURE 1. Cosine error schematic.

$$L' = L \cdot cos\theta \quad (1)$$

$$\varepsilon_c = L - L' = L(1 - cos\theta) \quad (2)$$

To eliminate cosine error, the detector (displacement probe) is required to be aligned normal to the measurement target surface.

The objective of the uncertainty evaluation presented here is to quantify the uncertainty for a surface measurement system that intentionally avoids cosine error. The paper is organized as follows. First, the measurement system is introduced. Second, the uncertainty contributors are classified and described. Third, the combined standard uncertainty is evaluated. Fourth, conclusions are presented.

COSINE ERROR FREE MEASURING SYSTEM

As mentioned, to establish a cosine error-free measuring system, the detector should be normal to the target surface profile during the entire measuring process. The required rotational degree of freedom is provided by an aerostatic bearing spindle in this study.

With the gas-lubricated bearing, the durability is high and axis of rotation errors are low. The cylindrical probe type capacitive sensors (CS) are used as the detectors and are mounted to the spindle. The effective sensing diameter is 5 mm and the gap between the CS and the target has a range of 500 μm.

One dimensional convex and concave surface targets with radii ranging from 45 mm to 100 mm are measured. The CS is aligned perpendicular to the spindle rotational axis, which is placed at the nominal radius of curvature, R, for the measurement target. Figure 2 [1] presents the (a) setup schematic and (b) photographs for a concave surface measuring example, where θ is the spindle rotating angle.

(a)

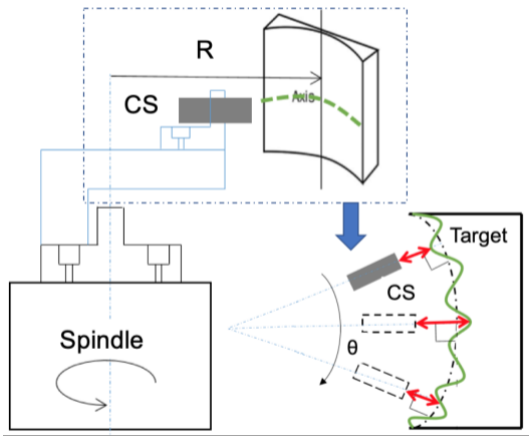

(b)

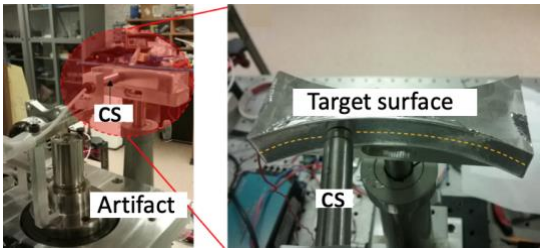

FIGURE 2. Sketch of the measuring system (a) and a concave surface measuring example of the real system setup (b). [1]

UNCERTAINTY SOURCES CLASSIFICATION

Four main uncertainty contributors are considered: instrumentation, installation, environment, and spindle rotation. Uncertainty evaluation can either be completed by statistical (Type A) or other means, such as instrument specifications and reference materials (Type B). [2]

In this case, installation and spindle rotation uncertainties are treated as Type A, while the instrumentation and the environmental uncertainties are treated as Type B.

UNCERTAINTY EVALUATIONS

Type A Evaluations

Repeated experiments are designed for both uncertainty contributors.

Installation Uncertainty Analysis

The installation uncertainties are related to the CS and the target offset or angular position. The surface profile error mainly results from three conditions, which are the probe offset error, probe angular alignment error and the target positioning offset error, where R = 52.4mm is the nominal radius.

In this study, the probe with an effective sensing area of ϕ 5 mm was used. To achieve the positioning accuracy easily, the varied range for offset is set as $\pm$ 100 μm and the angular deviation is set as $\pm$ 5 degrees. The experiment setup is shown in Figure 3. The probe is aligned with the spindle rotational axis first, the offset distance is set to be the same as the R of the measurement target. The offset is adjusted by using the micrometer in lateral and vertical direction. The tilt of probe is adjusted by using the indicator on the target surface. The surface is measured by 10 degrees interval

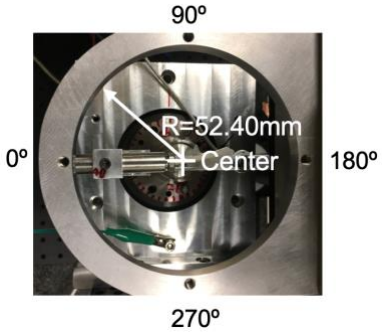

FIGURE 3. Installation uncertainty analysis experiment setup.

The illustration of each condition (a, b and c) as well as the test results (d, e and f) are shown in Figure 4. The measured surface profiles show the same trends over the range of the offset distance and tilted angle, the maximum deviations δ measured point were 4.21, 4.49 and 4.34 μm for each condition, and the measured standard deviations σ (averaged value of standard deviation from each measured point) among the initial and shifted or rotated back positions were 0.47, 0.78 and 0.48 μm individually.

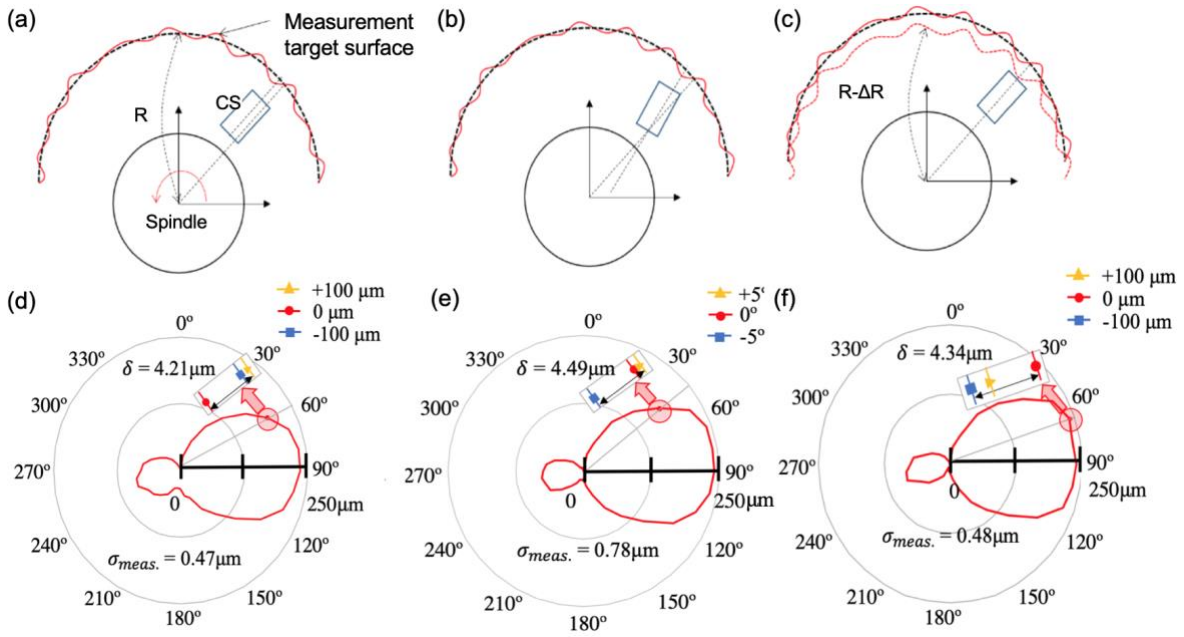

FIGURE 4. Installation error sources and corresponded test results: (a), (d) probe offset error, (b), (e) probe angular alignment error, and (c), (f) target positioning offset error.

Spindle Rotational Uncertainty Analysis

The spindle rotational error $S(\theta)$ was separated from the part (artifact) error $R(\theta)$ by a reversal method proposed by Donaldson and Brian. [3, 4] The results are shown in Figure 5, the spindle error S(θ) was 0.081 μm and its peak-to-valley (PV) value was 0.298 μm. [1]

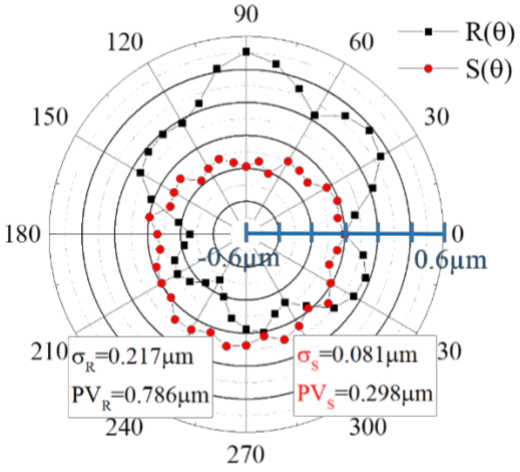

FIGURE 5. Spindle error separation results. [1]

Type B Uncertainty Evaluations

Instrumentation Uncertainty Analysis

The instrumentation error sources are the resolution of CS (Capacitec company) and the quantization error from the data acquisition instrument (National Instruments USB 6351). The sensitivity and the noise level (resolution) of the CS is 11.99 mV/μm and 0.05 μm separately, and the quantization error can be calculated from Eq. 3, which is 0.006 μm.

$$u_{\text{quantization}} = \frac{\text{output voltage range}}{2 \times 2^{16} \times \text{sensitivity}} = \frac{10\text{V}}{2 \times 2^{16} \times \frac{11.99\text{mV}}{\mu\text{m}}} = 0.006\ \mu\text{m} \quad (3)$$

Environmental Uncertainty Analysis

The lab temperature was stable at 23℃ with 1℃ temperature variation. The main environmental error sources are the thermal drift effects of the sensor and the aerostatic bearing spindle, the corresponded results are 0.008 and 0.009 μm, which are found from the references [5, 6].

Considering the air pressure level is well regulated and the whole experiment set-up is performed in a vibration-isolated granite table, those two factors are not considered. The humidity is also out of the consideration in this proposed measuring system.

System Uncertainty Evaluation

The whole system combined uncertainty is calculated from the root sum of squares of each

individual standard uncertainty. To scale the overall uncertainty, a 95 percent level of confidence is given by using the coverage factor k=2. The Measurement uncertainty evaluation of the proposed system depending on the detector type was estimated as 1.036 μm in Table 1.

Table 1. Uncertainty budget of the surface profile measurement.

Uncertainty source	Details	Uncertainty (μm)
Instrumentation error (Type - B uncertainty)	Capacitive sensor resolution	0.05
	Data acquisition quantization error	0.006
Installation error (Type - A uncertainty)	Probe offset error	0.47
	Probe angular alignment error	0.78
	Target positioning offset error	0.48
Environmental error (Type - B uncertainty)	Thermal drift (sensor) [5]	0.008
	Thermal drift (spindle) [6]	0.009
Spindle rotational error (Type – A uncertainty)	-	0.081
Total uncertainty	$\sqrt{0.05^2 + 0.006^2 + 0.47^2 + 0.78^2 + 0.48^2 + 0.008^2 + 0.009^2 + 0.081^2}$	1.036

FUTURE WORK

This evaluation can be applied to the multi-sensors measurement towards the hallow cylinder structure, like pipes, where each pair of sensors are placed opposed to each other and aligned normal to the inner and outer target surfaces. This measurement can provide not only the radius of each surface, but also the thickness, roundness as well as the concentricity information. With more high-level motion control, it also can be applied as an on-machine measurement (OMM) application.

CONCLUSION

The instrumentation error sources can be decreased by using higher resolution sensors like the laser displacement sensor and data acquisition instruments, the easily achieved positioning accuracy ensure that the system scans large area of surface fast and conveniently, and the aerostatic bearing spindle rotational error can be used to compensate the measured results. The overall uncertainty evaluation proves the reliability and accuracy of the non-contact cosine error-free measuring system for surface profiling. It also provides the possibility for further updating the measurement system to be a multi-sensors cylinder thickness and geometric tolerance measurement system or moreover as an OMM application.

ACKNOWLEDGEMENTS

The research was supported by the National Science Foundation (Award Number: CMMI 1663210) through Texas A&M University and (Award Number: CMMI 1663405) through University of North Carolina at Charlotte. The authors also acknowledge help suggestions from T. Schmitz, University of Tennessee, Knoxville.

REFERENCES

[1] ChaBum Lee, Joshua A.Tarbutton, Tony L. Schmitz. An Investigation of Cosine Error for Scanning Probe Measurements of Freeform Surfaces American Society for Precision Engineering, 2018.

[2] Stephanie Bell, A Beginner's Guide to Uncertainty of Measurement, United Kingdom, 2001.

[3] Donaldson, R.R., A simple method for separating spindle error from test ball roundness error, Annals of the CIRP, 21, 125–126, 1972.

[4] Bryan J, Clouser R, Holland E. Spindle accuracy. Am;149–164, 1967.

[5] Capacitec, Displacement sensing systems, Retrieved March 14, 2019 from https://www.capacitec.com/Products/Displacement-Sensing-Systems/Cylindrical-Probes.

[6] Bo Tan, Xinyong Mao, Hongqi Liu, Bin Li, Songping He, Fangyu Peng, Ling Yin, International Journal of Machine Tools & Manufacture, Vol. 82-83, pp. 11-20 (2014).

Effect of Particle Agglomeration Level in Reusing CMP Slurry at Various Pressures and Their Impact on Polishing Behavior

M. Kubota[1, 2], K. Takanashi[2], K. A. Dunn[1].
[1]College of Nanoscale Science & Engineering, SUNY Polytechnic Institute, Albany, NY, USA
[2]SUMCO Corporation, Imari, Saga, Japan

INTRODUCTION

The continued downscaling of semiconductor devices imposes increasingly stringent requirements on the quality of the silicon wafers themselves[1] to eliminate a source of surface defects that impact device performance. Particularly, wafer surface quality metrics including the flatness and the roughness are important for avoiding the defects in the final products[2, 3]. These surface perfections are achieved via chemical mechanical planarization (CMP) in the silicon wafer manufacturing process. CMP operations for forming the wafer surface are needed not only as an improvement in the removal rate and surface roughness, but also the minimization of the variation in these quantities across a wafer surface and among different batches. In most cases, these quality variations arise from deterioration of CMP consumables (pads[4, 5], conditioner[6], and slurry[7]). In this paper, the silica nanoparticles in CMP slurry for silicon wafer were selected for study.

The particles in CMP slurry are important for controlling the wafer surface quality because they provide both a chemical effect via surface oxidation[8, 9] and a mechanical effect removing the surface oxide layer of the work pieces[10, 11]. In generally, these particles behavior is investigated by Dynamic Light Scattering (DLS), Scanning Electron Microscopy (SEM) or Transmission Electron Microscopy (TEM)[12-15]. DLS can analyze the size of scattering centers in solution. However, these measurements may not accurately reflect the individual particle size diameter and the size distribution because these are affected by the concentration of solvent and surfactants. DLS therefore measures the size of agglomerates in solution. In contrast, SEM and TEM can observe individual particles in dried samples for accurate measurement of physical particle size. Measuring particles in solution is difficult in either SEM or TEM because of the vacuum conditions required for these instruments; even with specialized encapsulated liquid cells, imaging is still difficult due to the Brownian motion of the particles in liquid. Hence, DLS and SEM (TEM) offer only a limited understanding of the particles in slurry, if used in isolation. In previous study, the levels of particle agglomeration (AGL) were defined by comparison the average particle sizes between DLS and SEM[16]. the AGL was simply defined by

$$AGL = A_{DLS} - A_{SEM} \quad [1]$$

Here, A_{DLS} is the particle size average as measured by DLS, and A_{SEM} is the particle size average as measured from SEM images. And it was shows that there is a strong correlation between the AGL and polishing abilities such as removal rate and roughness with reusing of slurry under fixed polishing conditions. However, it has not been clarified that the AGL is useful metric for evaluating the polishing ability at other polishing conditions.

In this study, the behaviors of AGL at several pressure levels were investigated. Then, this metric was compared the surface quality metrics of silicon wafer such as removal rate and surface roughness.

EXPERIMENTAL

Polishing slurry (1 wt%, Colloidal silica particles, 25 mL, Allied high technology products INC) was continuously used for silicon coupon polishing (100, p-) in labscale CMP equipment (OptiPrep™ Polishing System, Allied High Technology Products INC. Platen / Head Rotation speed: 40 rpm / 41 rpm, Load: 85, 200, 342 g/cm2). The slurry samples were analyzed before polishing, and after 0.5, 5, 8, 10, 11, and 12 H of use. The wafer samples were analyzed after 30 min polishing using each reused times slurry.

Removal rate and surface roughness of the wafer samples were measured from the coupon by profilometer (Dektak 150 Surface Profiler, Veeco Instrument Inc.). The slurry particles were

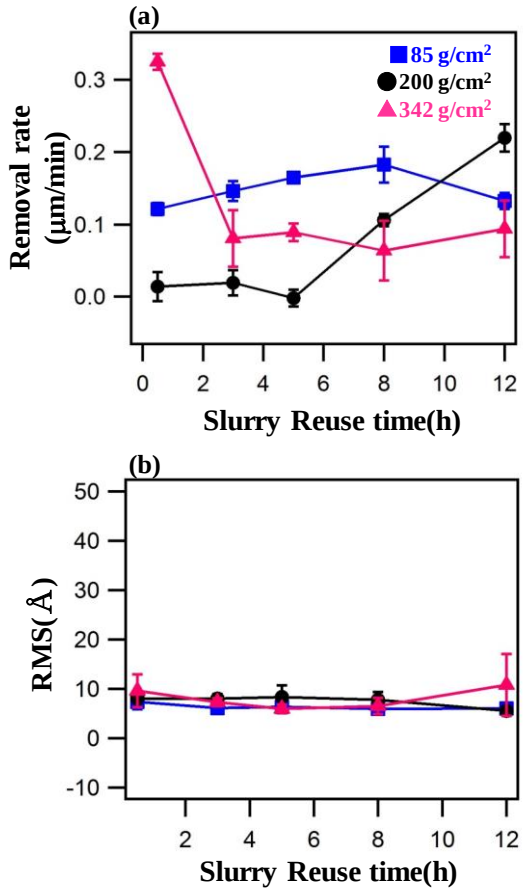

analyzed using an environmental scanning electron microscope (ESEM, FEI Nova

FIGURE 1. (a) Removal rate, (b) Surface Roughness with changing the slurry reuses time, squar is 85 g/cm^2, Circle is 200g g/cm^2 and triangle is 342 g/cm^2.

NanoSEM 600, FEI) for particle size and ZetaSizer (Nano-ZS, Malvern Panalytical Ltd.) for dynamic light scattering and Zeta potential measurements.

The particles in SEM images were manually identified and subsequently analyzed by ImageJ[17] using the FIJI build[18]. For this analysis, a background modification (Rolling 50 light) and binarization (8 bit) of the data were accomplished by auto setting the local threshold using the Otsu method[19] (radius 15). The areas of these particles were then calculated by ImageJ (Calculation range: Size 10-5000 pix, Circularity 0.75-1.00).

RESULTS AND DISCUSSIONS

The removal rate and roughness with each time and pressure are shown in Figure 1. Although the reuse time of slurry is typically used for the indicator for determined the endpoint of slurry in the manufacturing process, there are not any significant difference and tendency in the reuse time and the wafer surface qualities. Figure 2 shows the AGL with each reuse time and pressure. The AGLs show no obvious tendency with use as same as removal rate and roughness. On the other hand, the AGL at lower pressure tend to lower than at high pressure. It means that these particles more agglomerate when the pressure is increased at the same time of slurry reuse. At the high pressure, it is suggested that the particles are more pressed between the wafer surface and the polishing pad,

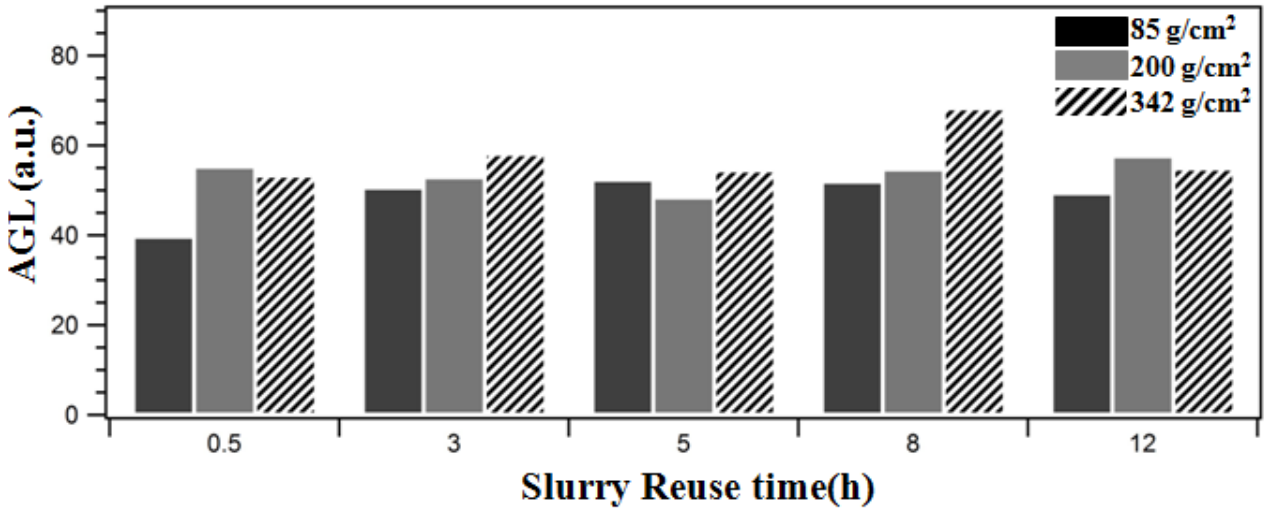

FIGURE 2. the AGL with each reuse time and pressure. Black is 85g/cm^2, gray is 200 g/cm^2 and the stripe is 342g/cm^2.

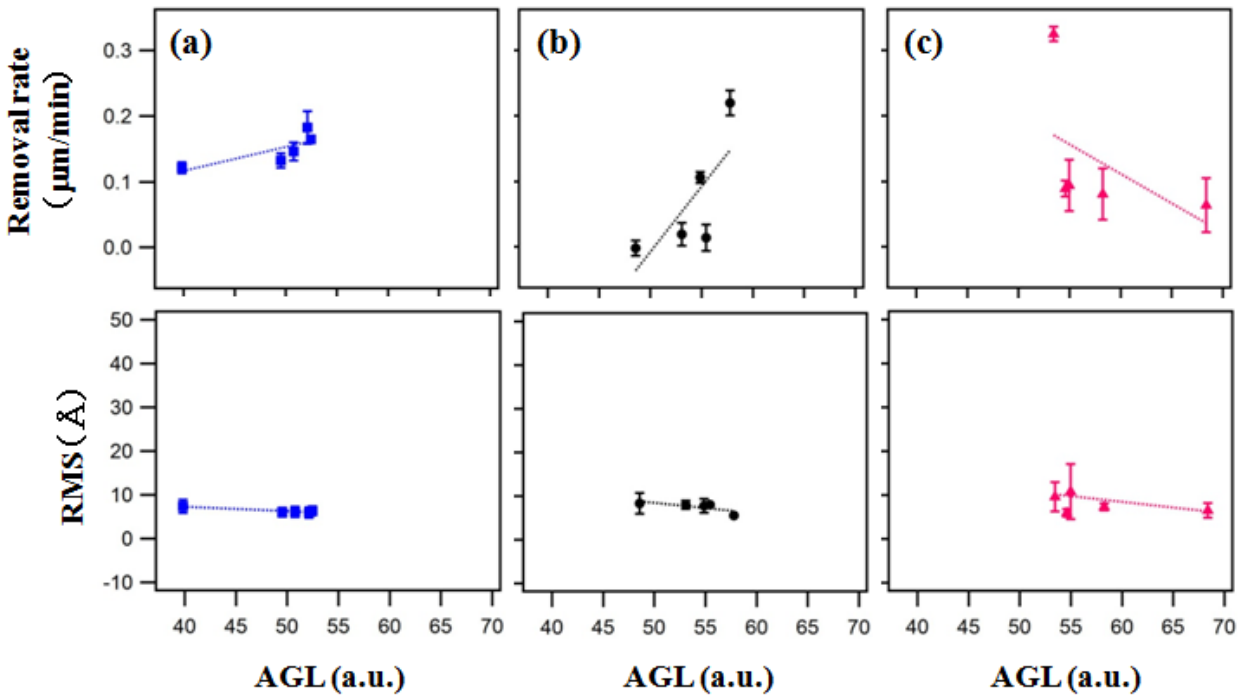

FIGURE 3. the removal rate (top row) and the roughness(bottom row) as a function of AGL. the pressure is (a) 85g/cm^2, (b) 200g/cm^2, (c)342g/cm^2.

as a result, the AGLs increases and the particles are more agglomerate.

The value of the AGLs with each reuse time and pressure are demonstrated in Figure 3 which shows the change in the removal rate and the surface roughness as function of AGL. The roughness at all pressure levels (85, 200, 342 g/cm^2) are decreased with increasing the AGL. In this experimental condition, the SEM images and particle size averages are suggested that the agglomerates are likely composed of one large particle with one or more small particles[16]. In an extreme case, a large particle could be completely surrounded by small particles in a flower-like arrangement. In this case, although the average agglomerate size (determined by DLS) has increased, it is in fact the smaller particles which are in contact with the polishing surface. This would be decrease the relative contact area, and as a result, the roughness became better when the AGL is increased at all pressure levels. On the other hand, the removal rate with increasing AGL shows different correlation between equal to or lower than 200 g/cm2 and 342 g/cm^2.The removal rate with increasing the AGL is increased at 85 and 200 g/ cm^2, and decreased at 342 g/ cm^2. The pushing amount of the particles is increased when the pressure is increased, and the contact area of particles on wafer surface is also increased[11]. In generally, the removal rate is determined by Preston formula[20].

$$Removal\ rate = Kp \cdot P \cdot V \qquad [2]$$

Here, *Kp* is the Preston constant determined by the polishing conditions and sub materials such as Pad hardness, slurry viscosity and so on, *V* is the relative speed to the wafer, and *P* is the relative pressure which can calculate by setting pressure and the contact area of particles. Hence, the removal rate is inversely proportional to contact area (A) in the same polishing conditions. The contact area (A) of these particles are calculated by

$$A = \sum_{n=1} 2\pi Z T_p X_n \sqrt{2D_n Z - Z^2} \qquad [3]$$

T_p is the number of all particles on wafer surface. In the presence of N different size particles, D_n is the radius for some different size of particles, and Xn is determined by the number of ratio of particles and these agglomeration levels if the same slurry is used. And Z is the depth of pushing amount of particles to wafer surface which is determined by polishing conditions and sub materials. In this experiment, the polishing

conditions except pressure are constant, and **TABLE 1.** The configuration for the simulation of the contact area of particles on wafer

same sub materials are used. Thus, Z is proportional to the setting pressure. The simulation for no agglomeration state and the agglomeration state are shown in Figure 4 and the calculated conditions are shown in Table 1. It is assumed that the distribution state of these particles is uniform in the slurry. In this case, the flower-like agglomerate particles are formed in the agglomeration state, thus, these Tp in this state is cannot be determined one value because of these several of three dimensional shapes and effect of pressure levels. Therefore, the ratio of Tp for no agglomeration state to agglomeration state ($T_{p\ (No\ agglomeration\ /\ agglomeration)}$) was chosen at 0.3-1.7. When the $T_{p\ (No\ agglomeration\ /\ agglomeration)}$ is less than 1.194, the contact area of agglomeration state is always smaller than the no agglomeration state at the same pushing amount. It means that the contact area is decreased if the AGL is increased. As a result the removal rate is increased with increase the AGL. It matches at 85, 200 g/cm^2. On the other hand, when the $T_{p\ (No\ agglomeration\ /\ agglomeration)}$ is larger than 1.194, the contact are of agglomeration state is always larger than the no agglomeration state. It means that the contact area is increased if the AGL is increased. As a result the removal rate is increased with increase the AGL. It matches at 342 g/cm^2. Hence, it is suggested that the contacted particle number is also changed with changing the pressure in the agglomeration state. And there are some thresholds of contacted particle number in the agglomeration state when the pressure is changed. And the positive or

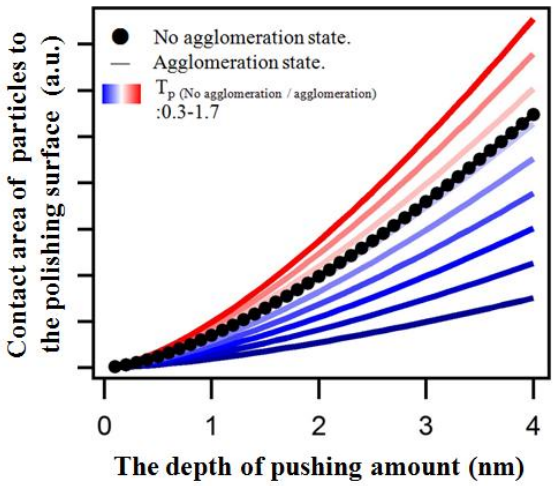

FIGURE 4. the contact area of particles to the polishing surface as a function of the depth of pushing amount of these particles. ● is no agglomeration state, - are agglomeration state with each $T_{p\ (No\ agglomeration\ /\ agglomeration)}$ is 0.3-1.7.

negative correlation of AGL to removal rate would be determined by $T_{p\ (No\ agglomeration\ /\ agglomeration)}$. And the slope of AGL to removal rate is shown by the difference the contact area between the no agglomeration state and the agglomeration state. It is means that the sensitivity of the variation of the removal rate to AGL. And it would be useful to select the stable polishing condition for the removal rate.

CONCLUSIONS

The wafer surface quality metrics (removal rate and roughness) was evaluated by the slurry reuse time and the AGL with each pressure levels. There are not significant tendency between the wafer surface quality metrics and the reuse time. It means that the reuse time is not good for evaluating the slurry conditions. On the other hand, there are some strong correlation between the polishing ability and the AGL. The roughness is always decreased when the AGL is increased because these particles are flower-like agglomeration, it cause decrease the relative contact area. As a result, the roughness became better with increasing the AGL. The removal rate is increased at 85, 200 g/cm^2 and decreased at 342g/cm^2 when the AGL is increased. These are explained by the pressure effect of not only the depth of pushing amount is increased but also the contacted particle number is changed. It would be suggested that the slope of the removal rate to AGL is useful to evaluate the sensitivity of the variation of the removal rate.

ACKNOWLEDGMENTS

This work was performed as part of a research agreement entitled “Change in silica nanoparticles during slurry use," funded and supported by State University of New York Polytechnic Institute and SUMCO Corporation.

REFERENCES

[1] Semiconductor Industry Association, “The International Technology Roadmap for Semiconductors (ITRS), 2013 edition,” http://www.itrs2.net/2013-itrs.html.
[2] C. S. Xu, et.al., Electrochem Solid-State Letter, 1 (1998), pp.181.
[3] Y.H. Xie, et.al., Physical Review Letters, 73 (1994), pp. 3006.
[4] D. Stein, et.al., Journal of Electronic Materials, 25 (1996), pp. 1623.
[5] B. Park, et.al., Journal of Materials Processing Technoogy, 203 (2008), pp. 287.
[6] M. Yi, et.al., Int J Adv Manuf Technol, 55 (2011), pp. 253.
[7] G. B. Basim, et.al., Journal of Colloid and Interface Science, 256.
[8] . F. Shimokawa, et.al., Precision Engineering in Japan, 77, 2 (2011), pp.162.
[9] T. Fujita, et.al., Precision Engineering in Japan, 74, 8 (2008), pp.815.
[10] F.W. Preston: The Theory and Design of Plate Polishing Journal of the Society of Glass Technology, 11(1927)214.
[11] L. Si, et al., J. Appl. Phys. 107, 2010, pp064310.
[12] X. Zhao, et al., Microelectronic Engineering, 87 (2010), pp.1716.
[13] H. Kim, et al., Jpn. J. Appl. Phys., 40 (2001), pp.1236.
[14] S. Jang, et al., Rev. Sci. Instrum., 87 (2016), pp. 046101.
[15] N. Chandrasekaran, et al., Mat. Res. Soc. Symp. Proc., 816 (2004), pp. K9.2.1.
[16] M. Kubota, et al., Materials Research Society Spring Meeting & Exhibit, QN08.08.33 (2019).
[17] . C. A. Schneider, et al., Nature methods, 9 (2012), pp. 671.
[18] J. Schindelin, et al., Nature methods, 9 (2012), pp. 676.
[19] N. Otsu, et al., IEEE Trans. Sys., Man., Cyber, 9 (1979), pp. 62.
[20]

SENSOR AND INSTRUMENTATION APPLIED TO SPINDLE HEALTH MONITORING

JaeMin Han and ChaBum Lee
J. Mike Walker 66' Department of Mechanical Engineering
Texas A&M University
College Station, Texas, USA

INTRODUCTION

There have been always many needs for machines which can achieve low power, high precision, high stability, and high-speed production in the industries. Moreover, machine tools which can realize high-speed machining and multi-tasking have increasing demands for advanced accuracy and productivity in production systems. At the heart of these machine tools, there is a spindle because of its characteristics. [1, 2]

In the up-to-date tooling, the spindle is the weakest part of the machine tool, however, this occupies appreciable part of the cost of the machine. Likewise, the spindle should be an essential component to decide machinability and productivity in machining such as drilling, milling, and grinding. Therefore, health monitoring of the spindle is the essential element to enhance the availability of the machine tools and achieve a robust machining process.

As a preliminary study, in this paper, the characteristics of the spindle which is made up of unknown inner structure were experimentally studied. Stiffness, natural frequency, and runout of the spindle shaft according to the location at front-end and back-end of it were measured. The 2-dimensional (X and Y axis) curved edge sensors (CES) setup for integrating into the back-end of the spindle were set and will be integrated on the spindle after calibration.

CURVED EDGE DIFFRACTION

The measuring limitation of the capacitive sensors (CS) as a result of the target surface (spindle shaft) was studied [3]. It was figured out that the sensitivity of the CS is exponentially increased when the radius of curvature is getting smaller which means that the characteristics of the CS are changed according to the shape of the target surface. This result indicates that it is inappropriate to measure such surface with the CS. For replacing this issue, a new instrumentation method on the basis of the curved edge diffraction (CED) is used [4, 5].

As illustrated in Figure 1, an electromagnetic (EM) wave incident on the curved edge brings about a transmitted wave, reflected wave, and edge diffracted wave and an edge excited wave which propagates along a surface ray. These surface ray fields also are excited at the shadow boundaries of the curved surface and a sum of the four waves may show the whole electric fields. This aggregation anticipates the scattering of the optical large platform and involves the use of spatial domain Fresnel integrals for the scattered or diffracted fields [6-8].

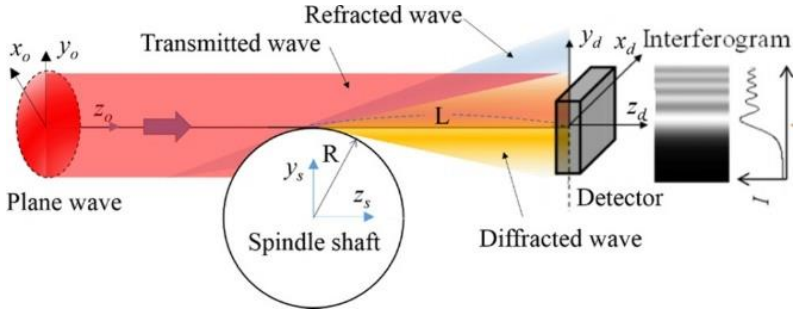

FIGURE 1. A schematic of curved edge sensors' principle [3]

Because of the difficulty and ambiguity in mathematical and computational ways in diffraction by a curved edge [9], an experimental approach to the CES taking advantage of CED characteristics has been conducted.

CHARACTERIZATION OF THE SPINDLE

In the real machining process, it is impossible to measure the front-end of the spindle. There is a method to measure the consumption power of the spindle however this only describes the estimate load value on the spindle. For measuring cutting force or other characteristics of machining, installing dynamometer on the table of machine tool is used. However, this method only used for research purpose and cannot be used in a real-time base.

For overcoming these obstacles, in this study, the way to measure at the back-end of the spindle is verified by comparing the characteristics between at the front-end and the back-end of the spindle.

Stiffness

Figure 2 shows the experimental setup for validating the characteristics of both ends of the air spindle which internal structure cannot be provided.

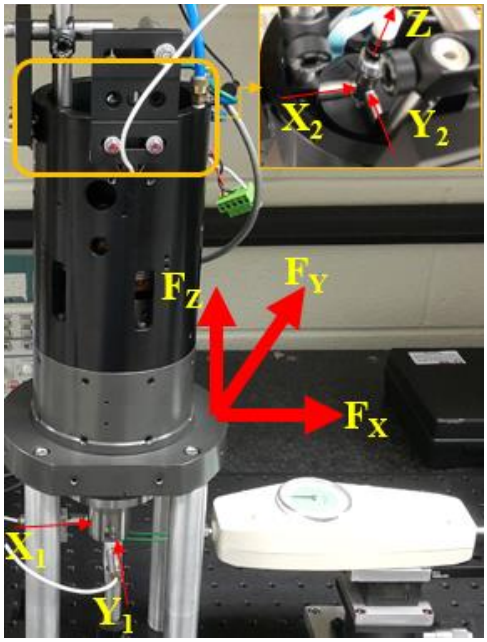

FIGURE 2. Experimental setup for comparing the difference between the front end and back end of the spindle.

Five CS (Capacitec) were used for gathering the stiffness of the spindle simultaneously. Two sensors (X1, Y1) represent the behavior of the front-end, another two sensors (X2, Y2) express the back-end's, and one sensor was installed for detecting the Z-axis direction.

$$k_1 = \begin{bmatrix} 1.3 & 21.7 & 0 \\ 52.6 & 1.2 & 0 \\ 0 & 0 & 250 \end{bmatrix} \quad \text{(1a)}$$

$$k_2 = \begin{bmatrix} -5.9 & 200 & 0 \\ 200 & -5.6 & 0 \\ 0 & 0 & 250 \end{bmatrix} \quad \text{(2a)}$$

Eq. 1 and 2 represent the stiffness matrix of the front and back end of the spindle, respectively. The stiffness at the back-end is expressed bigger than front-end's. It is expected and can be checked that the lateral (rotational) stiffness is smaller than the vertical (linear) stiffness because of the purpose of the air spindle.

Frequency Response

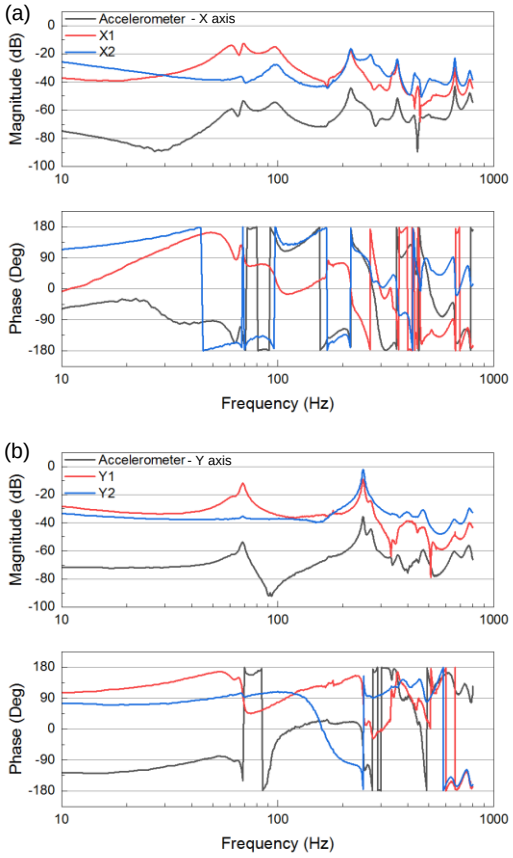

FIGURE 3. The result of the hammer test (a) X1 and X2, (b) Y1 and Y2.

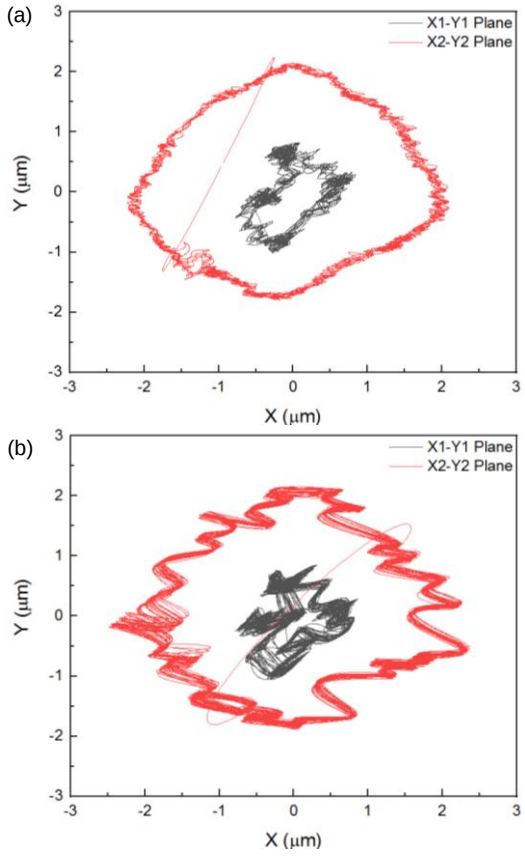

FIGURE 4. The spindle runout measured at (a) 240 rpm, (b) 1,200 rpm.

The impact response test was conducted with dynamic signal analyzer (Keysight 35670A), accelerometer, and CS. The four CS and accelerometer were placed around the spindle shaft along the r_X and r_Y directions. As shown in Figure 3, two frequencies, 70 Hz and 240 Hz, are found and these were related to angular and linear displacement. It is also seen that three methods for measuring the characteristics are similar. This explains that displacement sensor at the back end of the spindle can be utilized instead of the accelerometer.

Runout

The four CS were placed the same as the frequency response experiment setup. The output of the CS at both ends were compared with respect to the spindle rotational speed (at 240, 1200 rpm). As described in Figure 4, compare to the runout at the front-end, at the back-end of the spindle is easy to recognize the behavior because of the twice times magnified size of the runout.

However, it is well-known that the CS are sensitive to the lateral movement and radius of curvature of the target surface from the previous studies [3]. Spindle characterization at the back-end with CES should be conducted because there were large discrepancies between CS and CES outputs, especially in micrometer regions [5].

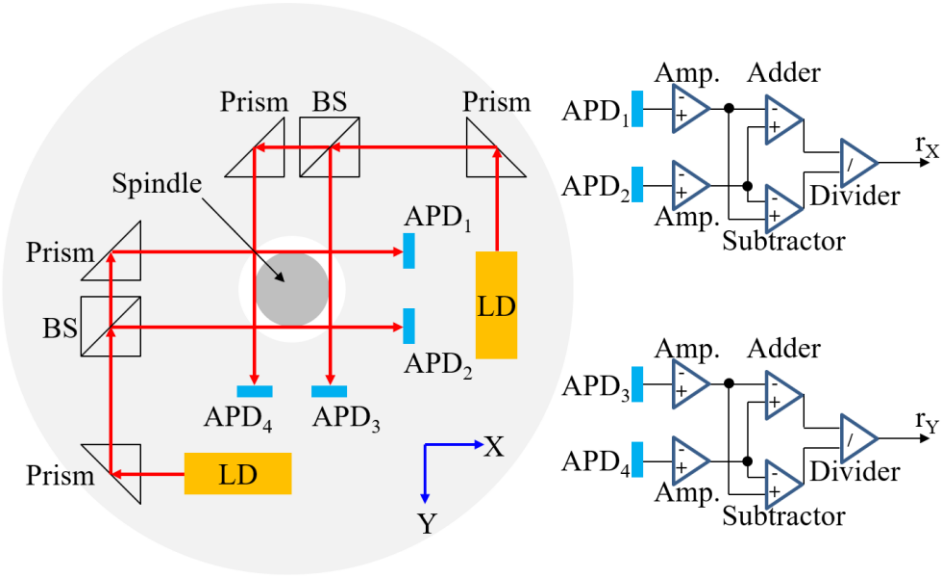

FIGURE 5. CES setup for integrating on spindle system.

CURVED EDGE SENSORS

Through the above-mentioned process, it was needed to check the behavior of the spindle at the back-end with CES. Based on the CED theory, the CES setup which is suitable for spindle metrology was made as illustrated in Figure 5. All of the optical components is placed on the rounded plate (Φ88.9mm). The two laser beams from each of the laser diodes are split into two by beam splitters (BS) respectively, and each of those laser beams is incident on the curved edge surface of the spindle shaft with a 90-degree interval (X and Y-axis).

The four-avalanche photo diode (APD, effective area 0.20 mm^2) receive the intensity of the beams which is pass through the shaft and the output signals of APDs are amplified by the operational amplifiers. The measurement bandwidth (Low pass filters) of this CES was set by 10kHz. Therefore, the displacement of the spindle shaft at the two axes, r_X and r_Y can be express as

$$r_X = S_X \frac{V_{APD2} - V_{APD1}}{V_{APD2} + V_{APD1}} \quad (2a)$$

$$r_Y = S_Y \frac{V_{APD4} - V_{APD3}}{V_{APD4} + V_{APD3}} \quad (2b)$$

where, SX and SY are the sensitivities of the CES at X and Y direction, respectively.

For the next step, the two-directional CES outputs will be gathered by the data acquisition system (NI) and calibrated within 100 μm scale by using the CS (10nm resolution) for reference. To calibrate properly, the target surface of the CS should be flat. The CES system will be integrated on the back-end of the spindle and the dynamic system identification of the spindle in the various condition such as at the specific velocity and during the machining process will be conducted. The above-mentioned process is currently under investigation.

CONCLUSION

Preliminary study for a novel method which is applicable to health monitoring of the spindle system in real-time based on the edge diffraction theory was carried out. Characterization of the air spindle measured at both ends of the spindle was performed for validating the effectiveness of the spindle behavior measurement at the back-end of the spindle. The results show that the proposed location can detect similar natural frequencies and magnify the behavior of the runout of the spindle at the front-end of the spindle.

The calibration of the CES output and the dynamic system identification of the spindle system with integrated CES system are currently under investigation.

REFERENCES

[1] A. H. Slocum. Precision Machine Design. Prentice-Hall, Inc. Englewood Cliffs, NJ: 1992.

[2] M. F. Spotts. Design of Machine Elements. Prentice-Hall, Inc. Englewood Cliffs, NJ: 1978.

[3] C. Lee, S.M. Mahajan, R. Zhao, S. Jeon. A curved edge diffraction-utilized displacement sensor for spindle metrology. Review of Scientific Instruments. 2016; 87

[4] C. Lee, R. Zhao, S. Jeon. A simple optical system for miniature spindle runout monitoring. Measurement. 2017; 102: 42-46.

[5] C. Lee, A. Zolfaghari, G-. Kim, S. Jeon. An optical measurement technique for dynamic stiffness and damping of precision spindle. Measurement. 2019; 131: 61-68.

[6] M. Born, E. Wolf. Principles of Optics: Electromagnetic Theory of Propagation, Interference, and Diffraction of Light, 6th ed. Pergamon Press. New York: 1980.

[7] A. Ishimaru. Wave propagation and Scattering in Random Media. IEEE, Piscataway. New York: 1997.

[8] B. A. Davis, G. S. Brown. Diffraction by a randomly rough knife edge. IEEE Trans. Antennas Propag. 2002; 50(12): 1769-1778.

[9] R. G. Kouyoumjian. A uniform geometrical theory of diffraction for an edge in a perfectly conducting surface. Proc. IEEE. 1974; 62(11): 1448–1461.

DESCRIPTION OF THE SHAPE OF ORDINATE DISTRIBUTION OF TWO-PROCESS PROFILE

Pawel Pawlus[1] and Rafal Reizer[2]
[1] Faculty of Mechanical Engineering and Aeronautics
Rzeszow University of Technology
Rzeszow, Poland
[2] Faculty of Mathematics and Natural Sciences
University of Rzeszow
Rzeszow, Poland

INTRODUCTION

Surfaces created by more than one process are functionally important. Most of them are two-process random textures. A plateau-honed cylinder surface is the most popular example of such topographies. It has a plateau-like surface part with a cross-hatch pattern. Proper honing reduces friction and wear. It also affects oil consumption of an internal combustion engine. Two-process random surfaces are also created in wear process, when the amount of wear is smaller than height of initial surface. It is more difficult to characterise completely two-process textures compared to one-process surface. An asymmetric ordinate distribution is the characteristic feature of two-process surface. It is connected with negative value of skewness Rsk and typically kurtosis Rku higher than 3. The material ratio curve is helpful in analyzing two-process textures. Now two competitive standards exist; they originated from an automobile industry. According to the ISO 13565-2 standard, a three-part division (peak, core and valley) of a profile is the basis of the material ratio assessment. Therefore five parameters describe the material ratio curve: the reduced peak height Rpk, the reduced valley depth Rvk, the core roughness depth Rk as well as the material ratios Mr1 and Mr2 – Figure 1a. This method, although designed to two-process profile can be applied also to one-process surface, because in each profile type, one can find peak, valley and core parts. However, for some profiles, this method can give false results [1] like not proper calculation of oil capacity A2 or of the Rk parameter.

In other approach (ISO 13565-3) the material ratio curve is presented on the Laplace-normal system. This method contrary to ISO 13565-2 standard can be applied only for two-process textures. In this case two regions of profile exist: peak (plateau) and valley. The probability plot of the cumulative distribution shows two straight lines of different slopes. The Rpq (plateau root-mean square roughness) parameter is the slope of a linear regression performed through the plateau region, the Rvq (valley root-mean square roughness) through the valley region [2] – Figure 1b . The intersection point of abscissa Rmq defines the separation of plateau and valley portions. For one-process surfaces of approximately Gaussian ordinate distribution only one straight line can be visible; its slope is equal to the Rq parameter. This method (Rq family) is more elegant than that presented in ISO 13565-2 standard (Rk group) and better characterizes two-process surface – because it has only two parts; is also good in discriminating between one- and two process surface. However, the method described in ISO 13565-3 standard is difficult in numerical implementation. This method is the base of two-process surface topography modeling. Two groups of parameters can be used not only in 2D profile, but also in 3D (areal) surface topography characterization.

Figure 1 presents graphical interpretation of parameters included in ISO 13565-2 and ISO 13565-3 standards.

PARAMETERS DESCRIBING THE SHAPE OF THE PROFILE ORDINATE DISTRIBUTION

Parameters characterizing the shape of the ordinate distribution should be non-dimensional.

Very often, especially for one-process profile this shape is characterized by skewness Rsk and kurtosis Rku. These parameters are sensitive on measuring errors errors and non-stable on surfaces (particularly Rku). For stratified surfaces there is typically strong correlation between these parameters – negative skewness corresponds to high kurtosis.

The emptiness coefficient Rp/Rt is the other parameter typically related to skewness. When surface is characterized by negative skewness,

the emptiness coefficient is smaller than 0.5 – when skewness is smaller, the emptiness coefficient is smaller. The alternative to the emptiness coefficient is Rp/Rv ratio. Rp is maximum profile peak height, Rv – maximum profile valley depth; however Rt is maximum height of the profile being the sum of Rp and Rv. The parameters Rp/Rt and Rk/Rt are more tribologically important than Rsk, because the Rv parameter characterizes the material volume, while Rp – volume of void (Figure 1c).

a

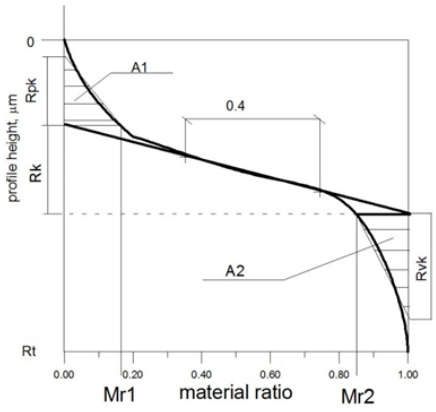

b

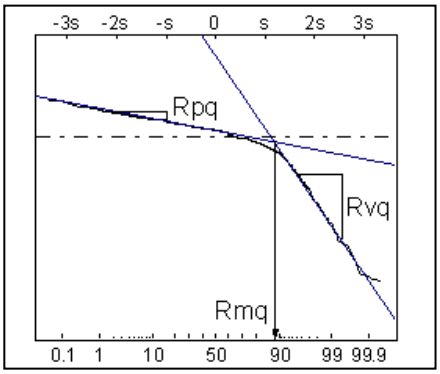

c

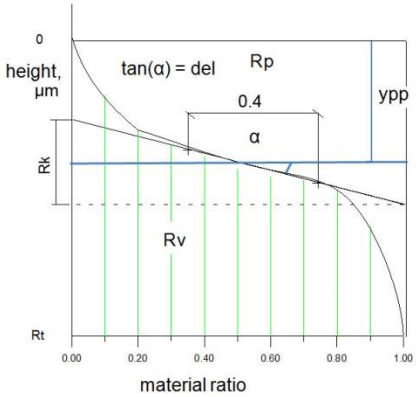

FIGURE 1. Parameters included in ISO 13565-2 (a) and ISO 13565-3 (b), graphical interpretation of parameters: Rp, Rv, Rt, ypp and del (c).

The parameter del describe the smallest slope of the normalized material ratio curve, ypp is the ordinate of the point of the smallest slope [3] (Figure 1c). The parameter max is the maximum % of the whole population in profile ordinate distribution curve. The normalized core roughness depth Rk/Rt is generally similar to del.

The other analyzed parameters are Rq/Ra and Δq/Δa. Rq is a root mean square deviation, while Ra an arithmetical mean deviation of a profile height. Δq is a root mean square slope, while Δa an average slope. These two parameters increase when the negative Rsk decreases. The Δq/Δa ratio depends not only on the shape of the ordinate distribution, but also on a horizontal profile parameter.

The alternative to Rsk and Rku are a and b parameters from BETA distribution [4].

$$a = \frac{Rv(RvRp - Rq^2)}{RtRq^2} \qquad (1)$$

$$b = \frac{Rp(RvRp - Rq^2)}{RtRq^2} \qquad (2)$$

From ISO 13565-3 standard the ratio Rpq/Rvq/Rmq was considered, too. In this case the Rmq material ratio was given is standard deviations s (in the 0-6 range).

The next two parameters are equivalents to the Rp/Rt and Rt/Rv parameters obtained on the base of the probability plot material ratio curve. The void area Rpa is:

$$Rpa = 0.5Rmq^2Rpq + 0.5(6 - Rmq)^2Rvq + (6 - Rmq)RmqRpq \qquad (3)$$

However the material area Rva is:

$$Rva = 0.5Rmq^2Rpq + 0.5(6 - Rmq)^2Rvq + RmqRvq(6 - Rmq) \qquad (4)$$

The total area Rta is:

$$Rta = 6[RmqRpq + (6 - Rmq)Rvq] \qquad (5)$$

The following ratios were analyzed: Rpa/Rva and Rpa/Rta.

Next parameter described the ratio of plateau height to valley height Ph/Vh:

$$\frac{Ph}{Vh} = \frac{RmqRpq}{(6 - Rmq)Rvq} \qquad (6)$$

The last parameter characterizes the ratio between the plateau height and total height Ph/Th:

$$\frac{Ph}{Th} = \frac{RmqRpg}{RmqRpq+(6-Rmq)Rvq} \qquad (7)$$

THE STUDY OF CORRELATIONS BETWEEN PARAMETERS

The values of the linear correlation coefficient between selected parameters characterizing the shape of the ordinate distributions of two-process profiles were computed. 36 profiles were modeled according to a procedure described on [5]. In addition 31 measured profiles were taken into consideration. They were measured by a white light interferometer Talysurf CCI Lite with 0.01 nm vertical resolution. The form was only removed without usage of a digital filter. They were 11 cylinder profiles after plateau honing, 10 cylinder profiles after one-process honing and then tribological test as well as 10 profiles after vapour blasting followed by lapping. In each case (for both simulated and measured profiles) the assessment lengths and sampling intervals were the same. Figure 2 shows examples of the analyzed profiles.

The results of correlation between parameters are listed in Table 1.

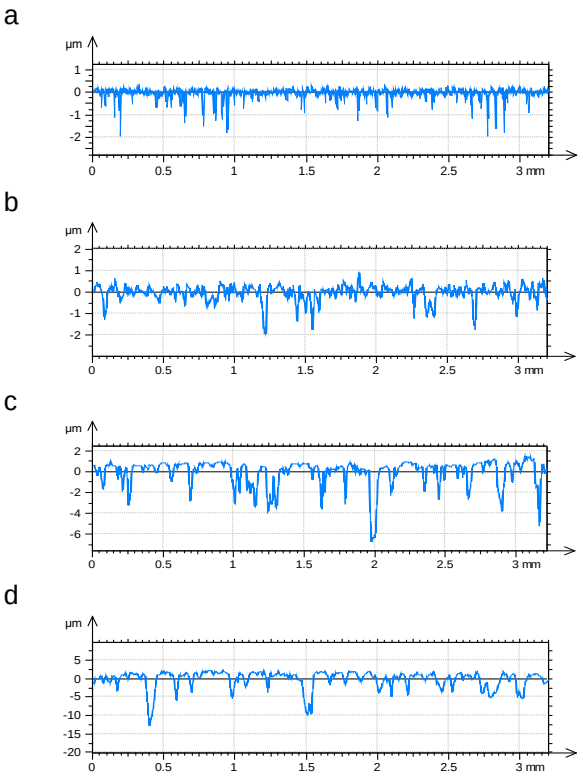

FIGURE 2. Examples of the analyzed profiles: modeled (a), after plateau honing (b) after one-process honing and operating (c), after vapour blasting and polishing (d).

TABLE 1. The values of the linear correlation coefficient r between parameters describing the shape of the ordinate distribution of two-process profiles.

Parameters	del	max	ypp	Rk/Rt	Rp/Rt	Rq/Ra	Δq/Δa	Rsk	Rku	Rp/Rv	a	b	Rpa/Rva	Rpa/Rta	Rpq/Rvq/Rmq	Ph/Vh	Ph/Th
del	1.00																
max	-0.63	1.00															
ypp	0.46	-0.57	1.00														
Rk/Rt	0.71	-0.44	0.12	1.00													
Rp/Rt	0.72	-0.65	0.59	0.78	1.00												
Rq/Ra	-0.43	0.30	0.10	-0.59	-0.54	1.00											
Δq/Δa	-0.50	0.68	-0.30	-0.57	-0.68	0.67	1.00										
Rsk	0.52	-0.32	-0.02	0.74	0.67	-0.96	-0.68	1.00									
Rku	-0.44	0.30	0.04	-0.57	-0.56	0.96	0.61	-0.96	1.00								
Rp/Rv	0.72	-0.59	0.58	0.80	0.99	-0.51	-0.62	0.65	-0.54	1.00							
a	0.03	-0.15	0.43	-0.04	0.20	0.18	-0.10	-0.12	0.14	0.22	1.00						
b	0.15	-0.38	0.52	0.23	0.42	0.14	-0.38	-0.05	0.20	0.40	0.12	1.00					
Rpa/Rva	0.72	-0.55	0.31	0.76	0.76	-0.57	-0.66	0.69	-0.59	0.74	0.01	0.22	1.00				
Rpa/Rta	0.72	-0.59	0.34	0.75	0.78	-0.61	-0.71	0.72	-0.63	0.76	0.02	0.23	0.99	1.00			
Rpq/Rvq/Rmq	0.86	-0.58	0.54	0.53	0.64	-0.34	-0.47	0.44	-0.38	0.63	0.07	0.17	0.81	0.80	1.00		
Ph/Vh	0.20	-0.42	0.81	-0.08	0.32	0.23	-0.22	-0.19	0.22	0.30	0.45	0.60	0.07	0.10	0.32	1.00	
Ph/Th	0.25	-0.49	0.83	-0.08	0.33	0.22	-0.23	-0.20	0.21	0.30	0.44	0.59	0.07	0.11	0.36	0.99	1.00

One can see from the analysis of Table 1 that the skewness Rsk is inversely proportional to the kurtosis Rku (the value of the r coefficient is 0.96). This is a characteristic feature of two-process surfaces; therefore this pair of parameter cannot describe the shape of the ordinate distribution of two-process textures. The Rku parameter is very strongly correlated with the Rq/Ra ratio (Figure 3).
Therefore this ratio can be interesting alternative to kurtosis Rku. Kurtosis is not stable on surface, sensitive to the presence of individual peaks or valleys, however stability of the Rq/Ra ratio is much better (the Ra and Ra parameters are statistical of small variation).

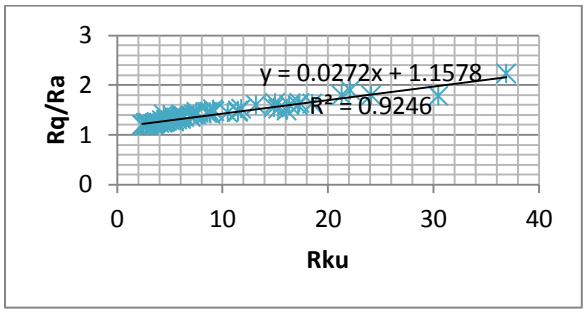

FIGURE 3. Dependence between Rku and Rq/Ra parameters.

The emptiness coefficient Rp/Rt is an alternative to skewness Rsk. It is proportional to some parameters like Rp/Rv and Rpa/Rva as well as Rpa/Rta. It was confirmed that Rp/Rt and Rpa/Rta as well as Rp/Rv and Rpa/Rva describe the same profile feature. It seems that profle can be described by the Rp/Rt and Rk/Rt pair (Figure 1c). However, these parameters were intercorrelated. The parameter del was strongly proportional to Rpq/Rvq/Rmq and other parameters, max was inversely correlated with del. The ratio of slopes $\Delta q/\Delta a$ was inversely proportional to Rp/Rt, Rsk as well as Rpa/Rva and Rpa/Rta. The parameters a and b were not statistically correlated with each other, they were proportional only to Pv/Vh and Pv/Th ratios.
The following pairs of parameters was selected to describe the shape of the ordinate distribution: the emptiness coefficient Rp/Rt and the ratio Rq/Ra. The first parameter is tribologically important, being the alternative to skewness Rsk. The second parameter Rq/Ra is better alternative to kurtosis Rku (Figure 3), because it is much more stable on surface than Rku. Moreover, the parameters Rp/Rt and Rq/Ra are not strongly intercorrelated (r = -0.54), contrary to pair Rsk-Rku. They describe various profile properties. The other possible pair of parameters are ypp-del. This set of parameters was selected earlier [3]. These parameters are statistically independent, (r=0.46), they describe various roughness properties (Figure 1c). The Rk/Rt ratio is similar to del, however it can be sometimes falsely estimated. Rpq/Rvq/Rmq can be alternative to del, while Ph/Th to ypp. Third possible pair are statistically independent parameters a and b.
The areal (3D) surface topography give more accurate information about surface texture than 2D profile parameters. The proposed parameters characterize two-process profiles. However the extension of the selected parameters can be also used in areal assessment. However it is necessary to eliminate spikes or isolated non-statistical valleys, for example by height truncation.

CONCLUSIONS

Statistical dependencies between various non-dimensional parameters characterized the shape of the ordinate distribution were analyzed on the basis of about 60 different two-process profiles. The pair of parameters: Rp/Rt and Rq/Ra were selected to completely describe this shape. The emptiness coefficient Rp/Rt is tribologically important, the Rq/Ra ratio is the stable alterative to the Rku parameter. The following pairs: ypp – del and a – b can be also used.
Extensions of the selected parameters can be also used in areal (3D) analysis.

REFERENCES

[1] Zipin B. Analysis of the Rk surface roughness parameter proposals. Precision Engineering. 1990; 12: 106-108.
[2] Malburg M.C., Raja J. Characterization of surface texture generated by plateau-honing process. CIRP Annals. 1993; 42: 637-640.
[3] Michalski J., Pawlus P. Characterization of the shape of the roughness profile ordinate distribution of honed cylinder surfaces. Wear. 1993; 161: 135-143.
[4] Whitehouse D.J. Beta functions for surface typology. Ann CIRP. 1978; 27: 491-493.
[5] Pawlus P. Simulation of stratified surface topographies. Wear. 2008; 264: 457-463.

EXPERIMENTAL CHARACTERIZATION OF LIGHTFIELD DIRECTING ARRAY ELEMENTS

Robert M. Panas[1], James M. Simonelli[2], Jordan Karburn[1], Vu Nguyen[1], Ken Enstrom[1], Jonathan B. Hopkins[2]
[1] Lawrence Livermore National Laboratory
Livermore, California, USA
[2]Department of Mechanical and Aerospace Engineering
University of California, Los Angeles
Los Angeles, California, USA

INTRODUCTION

We present on the experimental characterization of a recently fabricated high-bandwidth, high fill-factor micromirror array that can achieve analog, closed-loop control in three degrees of freedom (DOFs)—tip, tilt, and piston. The design capabilities of this device are in excess of the state of the art [1] with full digital control of tip/tilt/piston micro-mirrors (sufficient to steer the beam as well as provide phase coherence), large ranges of motion (up to 60 degrees of field of regard), high-speeds (repositioning at 10's of kHz), high fill factors (>98%, supporting high laser powers), and exactly constrained [2] so as to be highly insensitive to shock, vibration, and thermal variation. The flexure topology of this system was designed using Freedom and Constraint Topologies (FACT) approach [3], which allows the designer to consider a wide range of topologies and enables optimization of the final geometry.

The capabilities of the Lightfield Directing Array (LDA) are well aligned to next generation beamsteering needs, including those found in automotive lidar, free space optical communications, laser displays, optical sensors and laser-based manufacturing.

An operational array of Lightfield Directing Array (LDA) elements has previously been fabricated using a recently developed hybrid microfabrication, micro-additive manufacturing and microassembly technique [4]. This work covers recent efforts to characterize the performance of the mirror cell in both the static and dynamic domains.

METHODS

The characteristics of the LDA chip studied were via both static and dynamic tests. The static displacement, dynamics and sensing response of the paddle-only structure was first examined to confirm the LDA capability to controllably deflect. A fully assembly 3 paddle and mirror LDA cell was next studied for dynamics to confirm the predicted resonance modes. The dynamic response was measured using both an external laser rotation sensor and the integrated internal

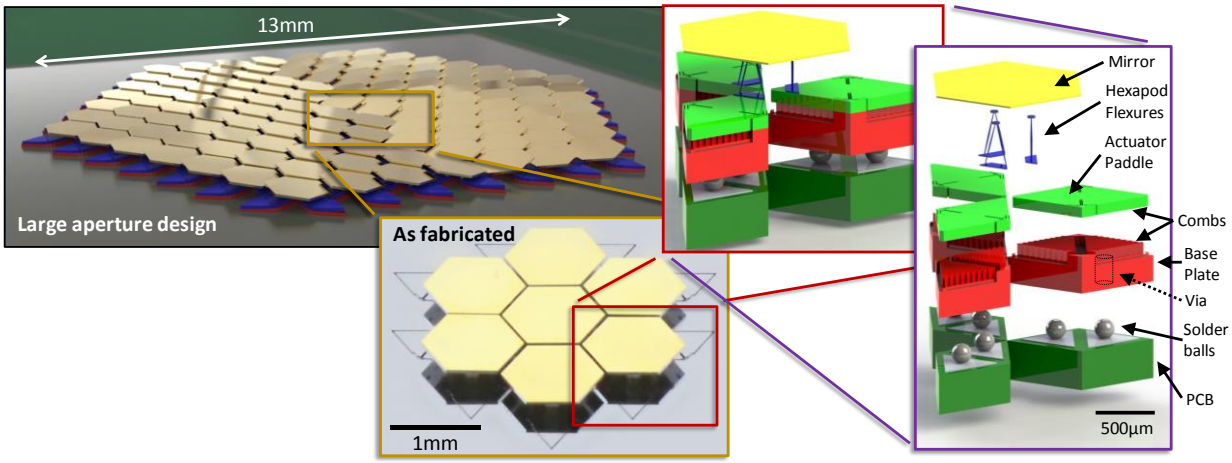

FIGURE 1: LDA MEMS Micromirror Array, showing large aperture mirror design rendering (top-left), operational 7 mirror sub-array image (bottom-left), and exploded view of unit cell layered architecture (right).

capacitive sensing. Finally the bode plot of the paddle only was measured using both the external and internal sensor. This provided fundamental confirmation of the sensing capability to operate as dynamic feedback.

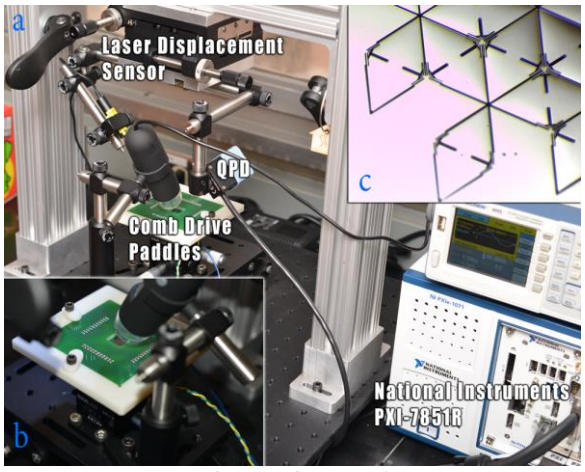

FIGURE 2: Experimental setup for measurement of paddle and mirror cell performance

PADDLE MEASUREMENTS

A 7-mirror array chip was used to study the paddle statics and integrated motion sensing capabilities. The MEMS design used the geometry parameters as described in [2]. The command signal generation and data acquisition were carried out by a National Instruments PXI-7851R FPGA/MIO. The paddle was driven via a high voltage command signal generated by a transimpedance amplifier composed of a AD829-LT6090 preamp-power amp combination and an AD797 as a virtual ground. The preamp-power amp combination sums the control signal from the PXI with an external modulation signal in order to drive the sensing through the actuation command. Both AD829 and LT6090 are inverting so the sum effect is non-inverting. Standard design efforts were taken with the transimpedance amplifier design to minimize the effect of parasitics and leakage currents including guard rings, and forgoing the topside ground pour. The rotation of the paddle was measured by a pen laser diode aligned to reflect off the surface of the paddle about 60° off vertical, as shown in Figure *FIGURE 2*. The diode laser light was a Mini Laser Center/Edge Finder aligned to a PDQ80A quadrant photodiode which provided lateral displacement information about the beam center. The rotation of the paddle was aligned to drive the laser diode beam centroid only vertically on the quadrant photodiode. The laser sensor was calibrated by translating the chip vertically and mapping this displacement against the quadrant photodiode reading. This provided a scale to the beam displacement observed on the quadrant photodiode, which was converted into a rotation via the known lever arm of approximately 0.1m. Error bars were calculated from the white noise measured on the QPD. The on-chip voltage was compared to the measured paddle deflection to generate the chart shown in Figure *FIGURE 3*.

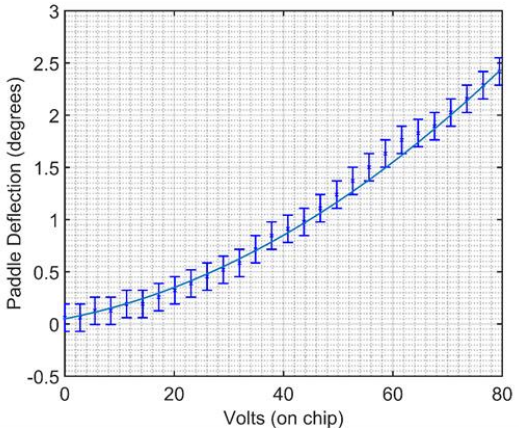

FIGURE 3: Static rotary displacement vs applied voltage for a single paddle.

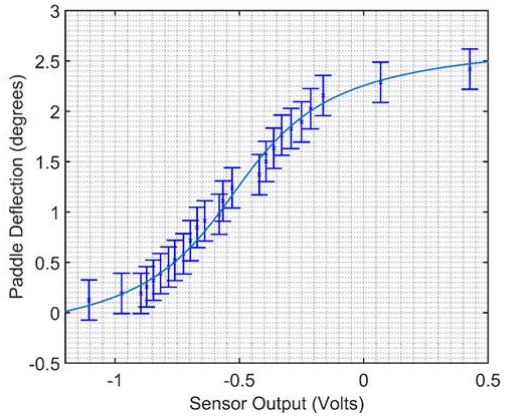

FIGURE 4: Static rotary displacement vs lock in amplifier output signal, the boosted output from the integrated sensor.

The rotary displacement plot shows several interesting properties. The data is fit to a V^2 curve, which shows the actuator physics is dominated by the comb drive effect. The best fit curve has a slight offset from zero of around 0.03°. The measurements were taken sequentially in increasing order, so they act as a map of thermal drift of the measurement frame. Rough estimates of the temperature variation

during the course of the experiment (1-2°C) for the roughly 1m scale aluminum measurement frame are consistent with angular drifts up around this scale. The bump in the data around 50-60V is also likely due to a temperature fluctuation during the experiment.

The integrated sensing output was captured simultaneously with the rotary displacement. A 1MHz-scale signal was injected into the command voltage and observed via measurement of the current flow. The current was measured by a transimpedance amplifier, while the output of the amplifier was passed through a (Stanford Research Systems SR 865A 4KHz DSP lock in amplifier which applied a 24dB/octave synchronous filter with a 40µs time constant on it. The resulting ratio of supplied voltage dither amplitude and phase compared to the measured current dither amplitude and phase provides a measurement of the comb capacitance. The measurement was passed through internal filters in the lock in amplifier and the resulting output voltage plotted against the measured paddle rotation as shown in Figure *FIGURE 4*. Error bars were generated in the same manner as Figure *FIGURE 3*, drawn from the noise in the quadrant photodiode angle sensor.

A first order physics estimate of the chip capacitance suggests the sensor output should scale roughly linearly with rotation. The data however shows a significant deviation from linearity. While this is acceptable from a calibration perspective, it is useful to postulate on the source of the non-linearity. The specific effects of the lock in amplifier on the signal are uncertain given that the system scales over a wide range of bias voltage and signal amplitude. The lock in amplifier filtering mechanisms may be adding impedance or slight voltage offsets to the signal that deviate over the range of operation. Alternately, the linear region observed from -0.9V to -0.1V may comprise the expected linear relationship, while fringe field or lock in nonlinearities dominate at the equilibrium and large displacement. Alternate non-lock in techniques are being evaluated to further study the position to capacitance mapping.

The Bode plot of the paddle only was measured using both the external and internal sensor. The experiment was carried out using the previously mentioned NI PXI-7851R data acquisition module, amplifier board and laser quadrant photodiode rotation sensor. A swept sine signal was generated in the PXI to drive the paddle. The lock in amplifier generated a modulation on the command signal to drive the internal capacitive sensing. The laser response on the quadrant photodiode was measured synchronously with the lock-in amplifier response. The data was post-processed to extract the bode plot ratio. The input and output signals were shifted to the frequency domain from which the amplitude and phase values were extracted to generate the Bode transmission. The lock in amplifier was known to inject additional delay and filtering components to the signal which did not occur for the laser sensing. This creates a difference in the dynamic response of the two signals. The effect was removed by applying the known internal filter to the laser sensor as shown in Figure *FIGURE 5*. The filtered laser sensor result can be compared directly to the capacitive sensing output.

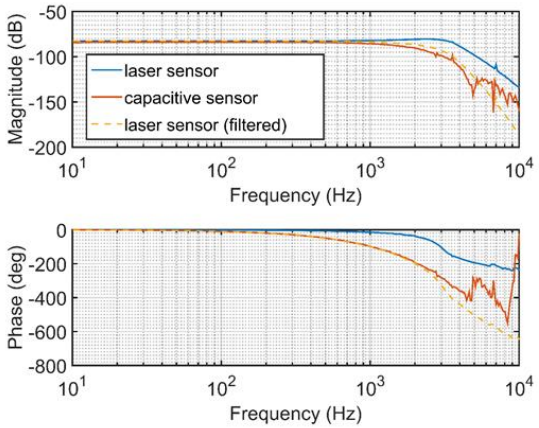

FIGURE 5: Paddle Bode plot captured by both the external laser sensor and internal capacitive sensor.

The unfiltered laser sensor response provides a clean measurement of the paddle dynamics, with a roughly 5dB gain increase at the resonant peak and a 2kHz natural frequency. The paddle has a high expected damping ratio due to the squeeze-film damping effect when the paddle rotation drives air out from the combs. The filtered laser sensor response matches closely with the capacitive sensor response up to about 4kHz where the lock in amplifier and data acquisition system reached its resolution limit.

The internal noise of the sensor was measured to determine whether this limit was the sensor or the electronics. The noise was measured by injecting small controlled motions into the paddle, and

comparing the laser sensing result against the capacitive sensing. The small motions caused the lock in amplifier to auto adjust its gain higher. The small motions could then be compared to the measured and calibrated laser sensor response to determine scale. The lock in amplifier signal scale was set to be equal to the average value of the laser sensor reading, which was approximately 2arcsec. The noise in the measurement between the small motions provided an upper bound on the capacitive sensor noise, as it is the combination of residual motion, the intrinsic sensor noise and the lock in amplifier noise. The small signal experiment showed a noise level around 0.2arcsec to first order estimate, as shown in Figure *FIGURE 6*. This corresponds to a dynamic range of 50udeg to 5deg, or around 100,000 (100dB). This suggests the noise limit observed in Figure *FIGURE 5* corresponds to the gains set for the

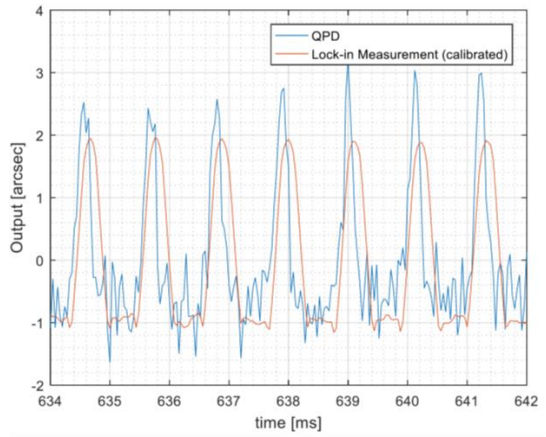

FIGURE 6: Small signal measurement showing a mapped comparison between the signal scale as measured at the limit of the laser sensor and the noise level in the capacitive sensor as measured between pulses.

experiment including the signal input scale and the lock in amplifier rather than a physical limit to the capacitive sensing.

CELL MEASUREMENTS

A separate chip was fabricated with a mirror attached to a set of 3 paddles in the standard unit cell form. This mirror cell was designed for small range of motion and high bandwidth operation. The dynamics of the mirror unit cell were studied to confirm the predicted resonant modes. The first test carried out on the mirror cell was a bode plot measurement using the previously described SR865A lock in amplifier to generate a swept sine input signal to one of the paddles and the previously described laser quadrant photodiode sensor to measure the rotational response of the mirror. The input frequency was swept from 10Hz

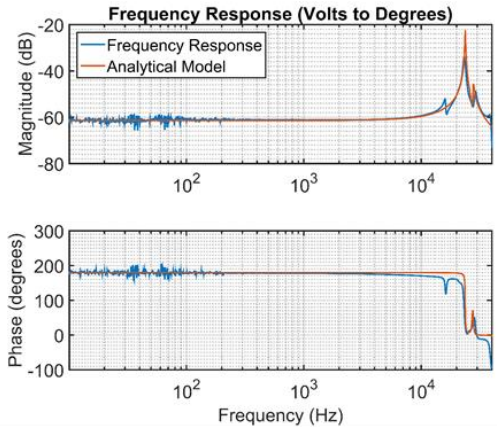

FIGURE 7: Bode plot of the single unit cell driven by the input of one of the paddles and measuring the output rotation of the mirror.

to 40kHz to collect the full plot shown in Figure *FIGURE 7*. The upper frequency bound was set by the limits of the swept sine input electronics.

A dynamic model of the mirror cell was generated and compared to the data as shown in the figure. The model was based in linear Timoshenko beam theory and implemented such that nominal geometric parameters could be input. From those inputs, a stiffness matrix for the whole system could be calculated. Similarly, a mass matrix could be calculated for the system based on the geometric parameters and material properties. A modified Rayleigh damping scheme was applied to obtain a damping matrix. Modal decomposition was performed on both the mass and stiffness matrices so that the damping of the individual modes could be independently adjusted. After appropriate scaling the matrices were transformed back and the traditional Rayleigh Damping equation was implemented as follows in Equation 1, where **C** is the net dynamic matrix, μ scales the mass matrix **M**, and λ scales the stiffness matrix **K**.

$$\mathbf{C} = \mu\mathbf{M} + \lambda\mathbf{K} \qquad (1)$$

The model was tuned to align the resonant frequencies, as there is uncertainty in the exact linkage stiffness for each build. The model proved accurate in predicting the one of the collocated pole-zero resonances around the peak. These are believed to be the other two degrees of freedom for the mirror cell. Only one

was being actively driven (tip) but the other two were able to be activated (tilt, piston) since two of the paddles were not being controlled. The model expects symmetric mirror cell geometry and thus shows only a single spike for the two undriven degrees of freedom. The other two measured resonant modes are likely split into discernable peaks due to fabrication variation which breaks the assumed symmetry.

ACKNOWLEDGEMENTS

This work was performed under the auspices of the U.S. Department of Energy by Lawrence Livermore National Laboratory under Contract DE-AC52-07NA27344 and by University of California, Los Angeles under subcontract B6629453. LLNL-ABS-777978.

REFERENCES

[1] Song, Y., Panas, R. M., & Hopkins, J. B. A review of micromirror arrays. Precision Engineering. In Press (2017).

[2] Hopkins, J. B.*, Panas, R. M.* (co-first author), Song, Y., and White C. D., "A High-speed Large-range Tip-tilt-piston Micromirror Array" *Journal of Microelectromechanical Systems*, Volume: 26, Issue: 1, September 2016, pp 196-205.

[3] Hopkins, J. B., & Culpepper, M. L. Synthesis of multi-degree of freedom, parallel flexure system concepts via Freedom and Constraint Topology (FACT)–Part I: Principles. Precision Engineering, 34(2), 259-270. (2010)

[4] Enstrom, K., Uphaus, T.M., Panas, R.M., and Harvey, C., “Microassembly Development for an Advanced Micromirror Array,” *Proceedings of the Annual Meeting of the American Society for Precision Engineering 32nd Annual Meeting*, Charlotte, NC, Oct 29-Nov 3, 2017.

SUB-WAVELENGTH PERIODIC SURFACE STRUCTURES FABRICATED BY TEMPORALLY FOCUSED FEMTOSECOND LASER

Zhiqiang Fu[1], Nan Zhang[1, 2], and Shih-Chi Chen[1*]
[1]Department of Mechanical and Automation Engineering
The Chinese University of Hong Kong
Shatin, N.T., Hong Kong SAR, China
[2]Institute of Modern Optics, Nankai University
Tianjin, China
[*]Email: scchen@mae.cuhk.edu.hk

In this paper, we present a new sub-wavelength precision laser micro-machining method by combining laser-induced periodic surface structures (LIPSS) and temporal focusing. LIPSS is a well-established method for fabricating sub-wavelength structures by controlling the energy fluence (φ), polarization, and number of pulses (N) of a spatially focused femtosecond laser [1]. To enhance the axial fabrication resolution and arbitrarily control the processing area, we use a digital micromirror device (DMD), i.e., a programmable blazed grating, to spatially disperse the femtosecond laser pulses and induce temporal focusing at the focal plane [2]. This effectively confines the axial range that LIPSS can be formed. Mathematical models have been derived to guide the system design. Fabrication experiments are performed to verify the performance of the proposed fabrication method.

PRINCIPLE OF LIPSS

LIPSS is a physical phenomenon which can be formed on almost any solid material surfaces when irradiated with laser pulses with a pulse duration from nanosecond to femtosecond time scale [3]. LIPSS has been widely implemented for surface modification and two-dimensional optical element fabrication since its first discovery in 1965 by Birnbaum [4]. With the development of ultrafast laser technology, femtosecond laser-induced periodic surface structures (fs-LIPSS) have attracted extensive interests in recent years due to the involved new physical processes and further improved fabrication results. The laser fluence (φ), polarization direction, number of pulses (N) and the ambient gas or liquid material's properties can affect the pattern of fs-LIPSS. For example, when a linearly polarized femtosecond laser is employed to form grating structures on a target surface, the laser fluence's variation can induce two distinctive structures: (1) high spatial frequency LIPSS (HSFL), whose periods are smaller than 0.4λ (λ is the central wavelength of the incident laser pulse); (2) low spatial frequency LIPSS (LSFL), whose periods are in the range of 0.4λ - λ. The orientations of LSFL are strongly influenced by the properties of the target which can be further divided into two categories. On the surface of strong absorbing materials (e.g., semiconductors and metals), the orientations of LSFL are always perpendicular to the laser polarization, which is called the LSFL-I type. For materials with large bandgaps, LSFL are always parallel to the incident laser polarization, which is called the LSFL-II type. The generally accepted formation mechanism of LSFL-I is the interference between the incident laser beam and the induced scattered waves or surface plasmon polaritons (SPP) [1, 5] on the rough sample surface.

SYSTEM CONFIGURATION

Figure 1 presents the optical configuration of the DMD-based temporal focusing system for LIPSS fabrication. The laser source is a Ti: sapphire femtosecond laser (Spitfire Pro, Spectra-physics Inc.) with a repetition rate of 1 kHz and an average power of 4.0 W. The laser beam first enters the Michelson interferometer to form double time-delayed laser beams. In one arm of the Michelson interferometer, a quarter-wave plate (QWP) is inserted to control the linear polarization of the femtosecond laser beam. The laser beams are diffracted by the DMD (DLP 4500, Texas Instrument). The multi-color beam in Fig. 1 indicates that different spectral components of the femtosecond laser beam are dispersed by the DMD and subsequently collimated by a tube lens with an effective focal length of 500 mm. After the tube lens, an objective lens (GCO-2133 40x, numerical aperture (NA) = 0.60, working distance (WD) = 3.330 mm) is used to recombine the different

spectral components. Temporal focusing is thus achieved, where a thin light sheet (2 - 10 μm thick) is formed at the focal plane of the objective lens, i.e., the focal plane is in conjugation with the DMD chip. Here, DMD is used both as a diffraction component and laser amplitude modulator at a modulation speed of 4.2 kHz. During the fabrication, the temporally and spatially focused light pulses strike the target surface and periodic surface structures with sub-diffraction-limit resolution are produced on the target surface in a parallel fashion.

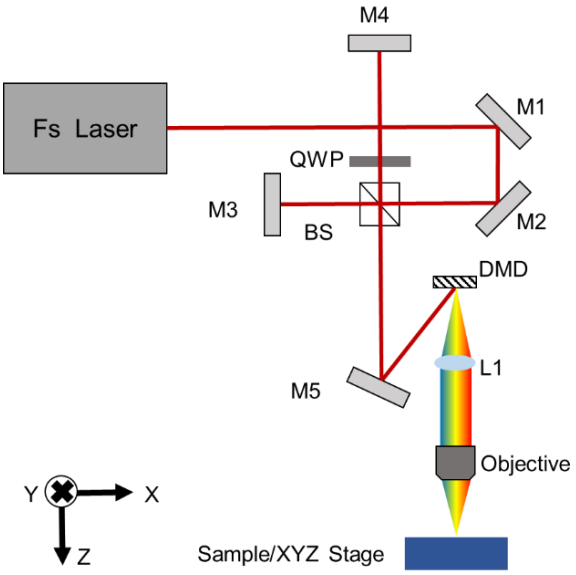

FIGURE 1. Optical configuration of the DMD-based temporal focusing LIPSS fabrication system; QWP: Quarter wave plate; DMD: Digital micro-mirror device; L1: Tube Lens; and M1 - M5: High reflectivity mirrors.

GENERATION OF TEMPORAL FOCUSING

In this paper, we generate LIPSS on silicon targets using a temporally focused femtosecond laser beam. DMD is used as a programmable diffraction element in the optical setup to achieve temporal focusing and arbitrarily control the processing area. The laser beam's incident angle on the DMD and the diffraction order's efficiency must be considered carefully. The micromirrors on DMD only have two states with tilted angles of $\pm\theta_b$ (θ_b= 12° [2]). The Bragg diffraction equation can be applied to analyze the diffraction of the femtosecond laser reflected from the DMD:

$$d(sin\theta_i + sin\theta_m) = m\lambda \qquad (1)$$

where θ_i is the incident angle; m is the diffraction order; θ_m is the diffraction angle for the m^{th} order's diffraction; λ is the central wavelength of femtosecond pulses ($\lambda = 800$ nm in our case); d is the effective pitch of the micromirrors (d = 10.8 μm in our experiments). To maximize the power efficiency of the temporally focused laser beam, the blaze condition, i.e., Eq. (2) should be satisfied:

$$\theta_i + \theta_m = 2\theta_b \qquad (2)$$

where θ_b is the tilting angle of the DMD mirrors, i.e., the blazed angle of the grating formed by the DMD. According to the optical setup shown in Fig. 2, θ_m = 0° , so θ_i = 24°. Based on Eq. (1), when the incident angle θ_i equals to 22.1°, the -5th order's diffracted light has a wave vector along the normal direction of the DMD. Therefore, in our experiments, the incident angle of the femtosecond laser on the DMD surface is set to be 22.1° and the -5th diffraction order is used to form temporal focusing pulses on silicon targets. In this case, the DMD is equivalent to a 470 lines/mm blazed grating [2].

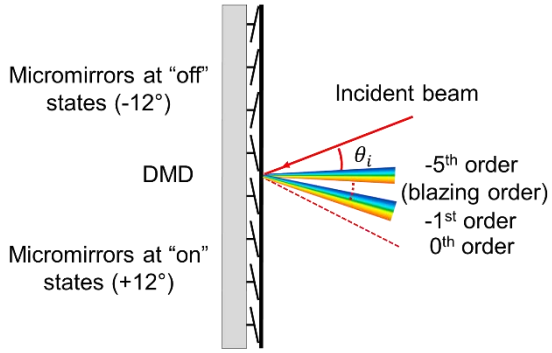

FIGURE 2. Schematic diagram of the DMD used as a diffraction element in the temporal focusing setup, where the -5th diffracted order satisfies the blazing condition and is selected to form temporal focusing pulses on the target surface.

EXPERIMENTAL RESULTS

In the first experiment, the monocrystalline (100) silicon target is irradiated by temporally focused femtosecond laser. To investigate the axial resolution of the temporal focusing based LIPSS fabrication system, the silicon target is placed at different axial positions ranging from 0 to 4 μm relative to the focal plane as illustrated in Fig. 1. The experimental results are presented in Fig. 3. During the experiments, all the micromirrors on the DMD are set to "on" states, i.e., DMD serves only as a blazed grating. The scanning speed of the target is set as 1.8 mm/s, and the laser fluence at the focal plane of the objective is 250 mJ/cm^2. The laser beams are set to vertical

polarization. From Fig. 3, one may observe that uniform periodic ripples with a period of 670 nm have been formed when the silicon surface is placed at the focal plane of the objective lens. However, when the silicon surface moves away from the focal plane, no obvious ablation occurs. The axial resolution of the temporal focusing fabrication system is thus estimated to be 2.0 µm, while the Rayleigh length of the same object lens is 7.2 µm.

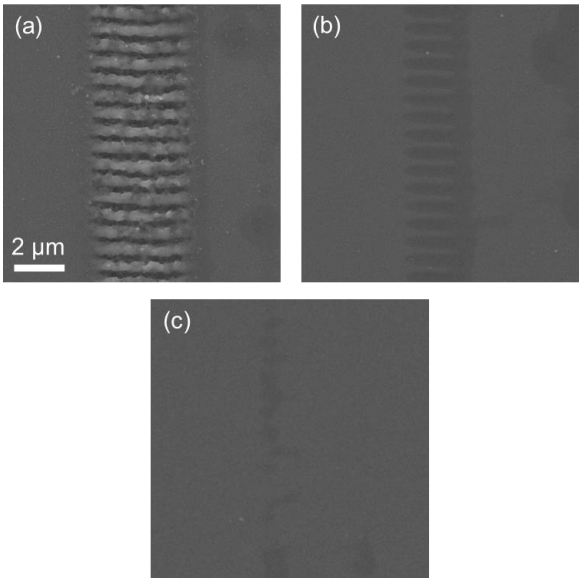

Figure 3. Fabrication results at different axial positions (a) ~ (c): 0 µm, 2 µm, 4 µm with the laser fluence of 250 mJ/cm^2 and the scanning velocity of 1.8 mm/s.

Next, we demonstrate the precise control of the LIPSS formation on selected areas via the DMD. First, we investigate the minimal size that can support the formation of LIPSS. The experimental results are shown in Fig. 4. Figures 4(a) - 4(f) show the silicon surface morphology after irradiated by the temporal focusing femtosecond laser when different patterns are loaded to the DMD. In Fig. 4, the silicon target is located at the focal plane of the objective, i.e., the DMD chip is imaged onto the silicon surface. Therefore, the intensity distribution on silicon surface is determined by the DMD pattern. By selectively setting the on/off states of the micromirrors on the DMD, periodic patterns oriented along the vertical direction with a duty cycle of 50% is formed on the DMD as shown in Fig. 4. After imaged onto the silicon surface, the periods of vertical periodic patterns of the DMD are 3.2 µm, 2.8 µm, 2.4 µm, 2.0 µm, 1.6 µm, and 1.2 µm respectively as shown in Fig. 4(a) - 4(f). During the fabrication, the silicon target is scanned at a constant speed of 0.58 mm/s, and the laser fluence is 640 mJ/cm^2. It can be observed from Fig. 4 that when the width of LIPSS formation region is larger than 800 nm, regular LIPSS can be formed. However, LIPSS becomes irregular when the width of the LIPSS formation area is 800 nm and entirely disappears when the width is below 800 nm, i.e., Fig. 4(f). So the minimal width that can support LIPSS formation is 800 nm, which is identical to the wavelength of the incident femtosecond laser.

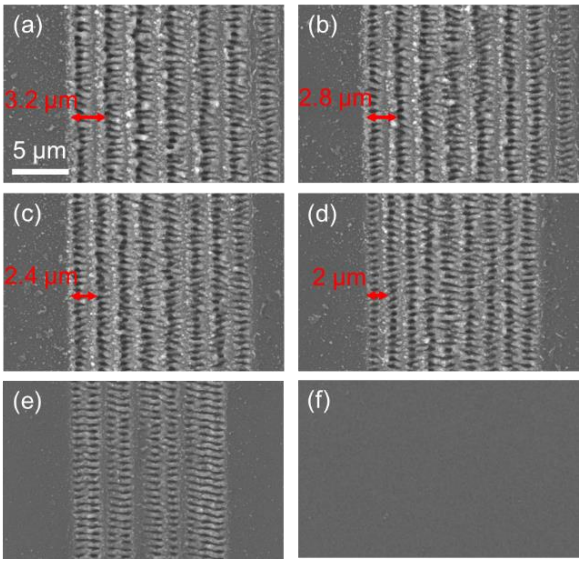

Figure 4. LIPSS fabricated by temporal focusing when periodic patterns with different periods are loaded onto the DMD. The periods of DMD patterns after imaged onto the silicon surface are 3.2 µm (a), 2.8 µm (b), 2.4 µm (c), 2.0 µm (d), 1.6 µm (e), and 1.2 µm (f) respectively.

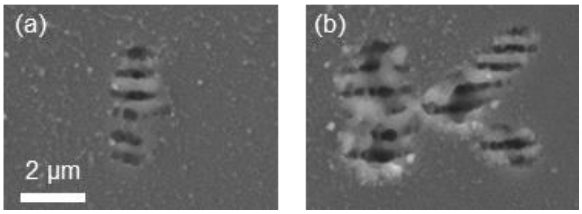

Figure 5. Demonstration of LIPSS fabrication at arbitrarily defined areas: (a) letter "I" and (b) letter "K".

Next, we demonstrate the generation of LIPSS on arbitrarily defined areas. This can be achieved by loading designed patterns to the DMD. The fabrication results are presented in Fig. 5. During the fabrication, the silicon target is irradiated by

the femtosecond laser with a fluence of 640 mJ/cm^2 and the exposure time of 20 milliseconds. From Fig. 5(a) and 5(b), one may observe that the LIPSS patterns are formed inside letter “I” and letter “K” respectively. The generated LIPSS are spatially confined in the selected regions by changing the patterns on the DMD.

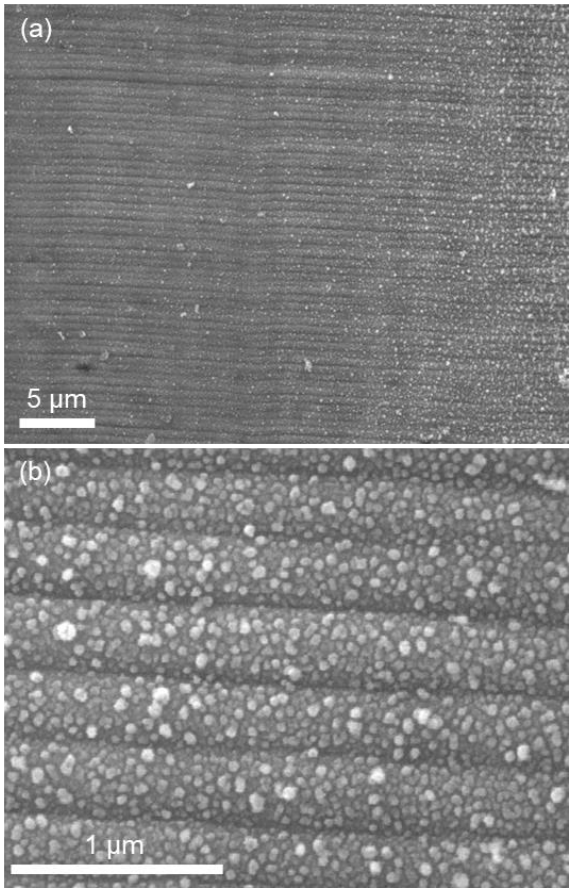

Figure 6. Fabrication results at different scales with double laser beams and orthogonal polarizations.

Finally, we use dual laser beams with orthogonal polarizations to produce LIPSS. The laser fluence of the beam with vertical polarization and horizontal polarization is the same at 170 mJ/cm^2, while the former reaches the target 2 picoseconds earlier. The scanning velocity is set to 0.31 mm/s. Figures 6(a) and 6(b) show the silicon surface morphology after irradiated by the temporal focusing dual femtosecond laser beams with orthogonal polarizations at different scales. It can be observed from Fig. 6(b) that uniform periodic ripples with a period of 330 nm can be formed. Such sub-wavelength periodic surface structures may have many unique optical and mechanical properties, i.e. hydrophilic, for a wide range of engineering applications.

CONCLUSION

In summary, we have presented a new LIPSS fabrication method with enhanced the axial resolution and arbitrarily programmable fabrication area, achieved by temporal focusing and the application of a DMD. By controlling the laser fluence (φ) and number of the applied pulses (N), i.e., the sample’s scanning speed, LIPSS can be induced on the silicon surface by a single temporally focused femtosecond laser beam. Experimental results show that (1) the minimal width that can support LIPSS formation is 800 nm; (2) the axial confinement of LIPSS is ~ 2 μm; and (3) the processing area can be arbitrarily defined by loading different patterns to the DMD. In addition, we have also demonstrated sub-diffraction limit nano-patterning (300 nm) using dual laser beams with orthogonal polarizations. This work has verified the performance of the DMD-based LIPSS fabrication method, which may find important applications in the nano-manufacturing area.

ACKNOWLEDGMENT

This work is supported by the HKSAR Research Grants Council (RGC), General Research Fund (GRF), (CUHK 14202815 & 14209081).

REFERENCES

[1] Bonse J, Höhm S, Kirner S, Rosenfeld A, and Krüger J. Laser-induced periodic surface structures— A scientific evergreen. IEEE Journal of Selected Topics in Quantum Electronics, 2017, 23(3).

[2] Gu C, Zhang D, Wang D, Yam Y, Li C, and Chen S. Parallel femtosecond laser light sheet micro-manufacturing based on temporal focusing. Precision Engineering, 2017, 50: 198-203.

[3] Van Driel H, Sipe J, Young J. Laser-induced periodic surface structure on solids: a universal phenomenon. Physical Review Letters, 1982, 49(26): 1955.

[4] Birnbaum M. Semiconductor surface damage produced by ruby lasers. Journal of Applied Physics, 1965, 36(11): 3688-3689.

[5] Sipe J, Young J, Preston J, and Van Driel H. Laser-induced periodic surface structure. I. Theory. Physical Review B, 1983, 27(2): 1141.

LIQUID CAPSULE-BASED PRESSURE SENSOR FOR PRECISION CARDIOVASCULAR MONITORING

Xiangyu Fan[1], Mindan Ren[1], Yan Huang[2], Ni Zhao[2], and Shih-Chi Chen[1*]
[1] Department of Mechanical and Automation Engineering
The Chinese University of Hong Kong
Shatin, N.T., Hong Kong SAR, China
[2] Department of Electronic Engineering
The Chinese University of Hong Kong
Shatin, N.T., Hong Kong SAR, China
[*]Email: scchen@mae.cuhk.edu.hk

This paper presents a new liquid capsule structure that enables alignment-relaxed continuous precision monitoring of epidermal pulse waves. Wearable pressure sensors are important as they enable long-term real-time epidermal pulse monitoring in a non-invasive and power-efficient way. However, most sensors are required to be precisely aligned with the optimal measurement spot, e.g., nearby the radial artery, for accurate signal acquisition, which causes inconvenience for untrained or elderly users.

INTRODUCTION

Epidermal pulse waves that originate from the blood pressure fluctuation in cardiac cycles contain important physiological information and are a good indicator of various cardiovascular diseases (CVDs). The pulse signals typically have three distinguishable peaks, i.e., percussion peak, dicrotic notch and dicrotic peak. With the aid of deep learning and signal processing, the underlying diagnostic information can be revealed from pulse signals. For wearable pulse monitoring, photoplethysmogram (PPG) sensors [1] and pressure sensors [2-4], have been widely studied. PPG sensors measure the blood volume fluctuation via illuminating the tissue and calculating the absorption of light in vasculatures. Pressure sensors detect the stress and deformation waves of the epidermis caused by blood flows in arteries. Although PPG sensor technologies are mature; yet they are not suitable for long-term continuous use due to their high power consumption (typically 10-100 mW). Reducing the required light power of PPG often comprises the signal quality, leading to low signal-to-noise ratio. Contrarily, pressure sensors are power efficient (typically tens of nW to several μW). Epidermal pulses measured by pressure sensors directly reflect the waveforms of arterial pressure, which provides abundant information for CVD diagnosis. Overall, the pressure sensors provide a more precise and energy-efficient solution for long-term pulse monitoring.

One important issue in pressure sensors is that the quality of the epidermal pulses measured by the pressure sensors depends heavily on the sensor placement. And high quality signals can be only obtained when the sensor is accurately aligned with the radial artery (i.e., < ±1.5 mm). Increasing misalignments between the sensor and the artery rapidly reduces the signal amplitude and waveform fidelity, leading to unreliable prediction of CVD risks (Figure 1) [4, 5]. Besides, the relative motion (e.g., slips) between the sensor and the skin results in distorted pulse signals. Generally, good pressure sensors should be compliant and tightly attached to the skin during measurements; this often causes inconvenience and discomfort due to the material limitation. In this paper, we present a new capsule-based pressure sensor that substantially relaxes the stringent alignment requirements between the sensor and the artery to over ± 6 mm, where the flexible capsule exploits the encapsulated liquid to uniformly transmit epidermal pulses to the embedded sensing elements.

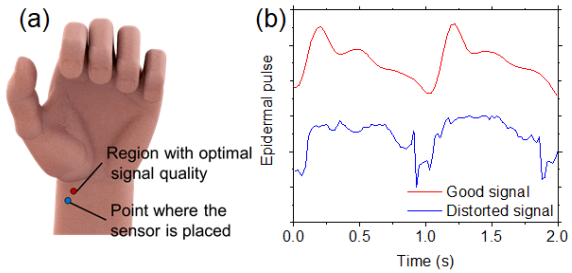

FIGURE 1. Effect of sensor misalignment on epidermal pulse signal quality. (a) Illustration of misalignment, defined as the distance between

the sensor location and the optimal measurement point. (b) Comparison between a good signal and a distorted signal, where good epidermal pulse signals resemble the arterial pressure waveform.

WORKING PRINCIPLE & MODELING

Pressure sensors detect optimal epidermal pulse signals when precisely positioned above the radial artery. The liquid capsule, as shown in Figure 2(a), is designed to preserve the signal quality even when the sensor is misaligned. This works as according to Pascal's law, a change in pressure at any point in an enclosed fluid at rest is transmitted undiminished to all points in the fluid. When applying a load at the bottom surface of the capsule structure, the pressure change is the same at all points in the embedded liquid. As a result, the sensing element senses equal pressure whether or not the load is applied at the center of the bottom surface. Figure 2(b) illustrates the detailed design of the liquid capsule pressure sensor (LCPS), where the capsule shell is made of flexible elastomer, and the top surface is fixed to a rigid glass slide. A piezoresistive sensing element is custom-designed and integrated in the center region between the glass slide and the top surface of the cavity.

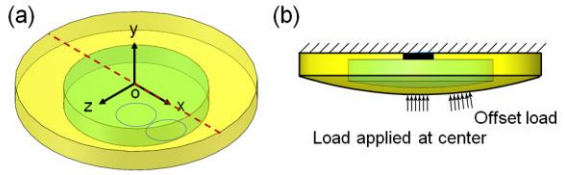

FIGURE 2. (a) Schematic of the liquid capsule structure. (b) Cross-section of the liquid capsule with embedded piezoresistive pressure sensor (i.e., LCPS). External loads applied at the center position and off-center position will induce the same pressure variation to the sensing element.

Figure 3 presents a finite element analysis (FEA) study to verify and assess the misalignment relaxation capability of the LCPS. In the simulation, an external load is sequentially applied to the center and off-center regions of the LCPS, as indicated in Fig. 2(b). The simulated pressure distribution (i.e., σ_{yy}) at the top surface of the cavity is presented in Fig. 3(a). Figure 3(b) plots the pressure distribution along the red dashed line, indicated in Fig. 3(a). From the results, one may conclude that the pressure distribution is uniform within the capsule and the embedded sensing element will detect similar pressures, i.e., 0.0226 kPa and 0.0180 kPa, in both cases.

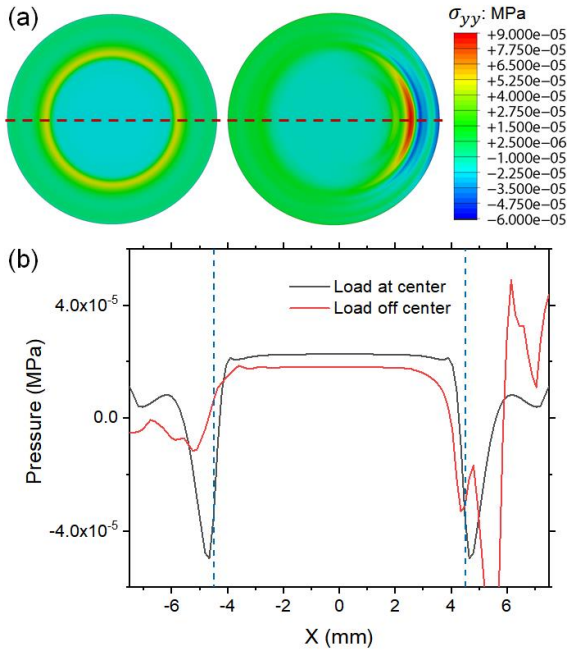

FIGURE 3. FEA simulation results of the LCPS under different loading conditions. (a) Pressure distribution (i.e., σ_{yy}) at the top surface of the capsule cavity; left: center loading; right: off-center loading. (b) Pressure distribution along the red dashed line. The sensing element is located at x = 0 mm.

Next, we develop a parametric model to study how design parameter variations (including capsule size, shell thickness, and modulus) can influence the sensor performance. Figure 4(a) presents the cross-section view of the LCPS model, where the load is applied to the center region, the top and side surfaces are assumed to be rigid, the embedded fluid is incompressible, and the bottom surface is assumed to be elastic, i.e., the tension of the bottom surface is linearly proportional to its strain. Based on the assumptions, the contour of the deformed bottom surface under different pressure loadings are calculated and presented in Fig. 4(b). From the results, one may find that when the applied pressure increases, the lowest point of the capsule membrane moves away from its original position; in the meantime, the pressure in the fluid increases such that the embedded senor detects the pressure variation.

Next, we investigate how shell stiffness can affect the LCPS performance; the results are presented in Fig. 4(c) and 4(d). Note that the stiffness of the capsule shell can be varied by selecting an

elastomer of different modulus or a shell thickness. From Fig. 4(c), we find the center displacement and the applied pressure do not have a linear relationship; this is because the total displacement is determined by both the tension in the capsule shell and the fluid pressure. The center displacement under loads represents the overall stiffness of the LCPS, i.e., k_{LCPS} = load/center displacement. Generally, k_{LCPS} should not be too stiff as stiff capsules prevent good conformation to the wrist contour and may potentially block the blood flow in the radial artery when high pressure is applied to the LCPS. Yet, from Fig. 4(d), one may observe that high shell stiffness can increase the LCPS sensitivity, i.e., higher capsule fluid pressure lead to higher electrical signals of the sensing element. Considering the capsule conformation capability and device sensitivity, a stiffness between 1.0 - 2.5 N/mm is recommended for optimizing the performance and maintaining the comfort level. Figure 4(e) - 4(f) study the LCPS performance as a function of capsule size; from the results, one may conclude that a capsule of smaller size has higher sensitivity. Importantly, the capsule size also defines the alignment relaxation range.

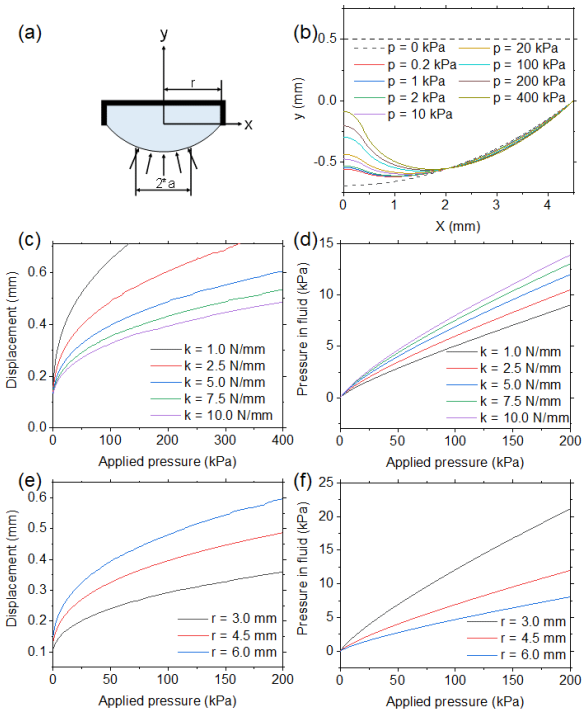

FIGURE 4. (a) Cross-section view of the LCPS model. (b) Membrane deformation under different pressure loadings (Default parameters: k = 5.0 N/mm and r = 4.5 mm). (c) Effect of capsule shell stiffness on shell displacement under different pressure loadings. (d) Effect of capsule shell stiffness on fluid pressure under different pressure loadings. (e) Effect of capsule size on shell displacement under different pressure loadings. (f) Effect of capsule size on fluid under different pressure loadings.

Based on the modeling results, the material of the capsule shell and the capsule size are determined. Polydimethylsiloxane (PDMS) that has a wide tunable range of modulus is selected to fabricate the capsule shell with a thickness of 400 μm. Considering the range of misalignment relaxation, device sensitivity, and overall comfort level, the radius of the capsule cavity is selected to be 6 mm.

FABRICATION OF LCPS

Figure 5(a) presents the fabrication process of the LCPS. The LCPS is fabricated in two steps. First, a piezoresistive carbon black-decorated knitted fabric is fabricated via dip-coating and drying processes and sealed between interdigitated electrodes on a circular glass plate and a polyethylene-naphthalate (PEN) film. (The PEN film is used for ensuring the sensor is electrically insulated and waterproof.) Next, the capsule base (or shell) is fabricated and filled with fluid. Lastly, the sandwiched sensor module and the capsule based is sealed.

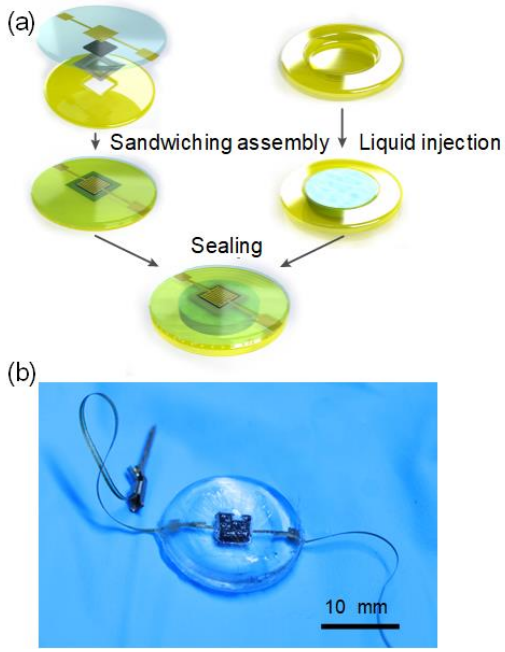

FIGURE 5. (a) Fabrication and encapsulation process of the LCPS. (b) Image of a completed LCPS, which has a diameter of 16 mm with a cavity of 12 mm diameter.

To fabricate the capsule base, PDMS is cast into a custom-fabricated steel mold. A 30:1 base to curing agent mixing ratio is used to achieve the targeted shell stiffness. After curing, the base is demolded and filled with glycerol. (Note that glycerol is selected for its nontoxicity and high boiling point at 290 ℃.) To join and seal the sensor module and the base, uncured PDMS is brushed uniformly to the base. The electrical connection to external circuits is achieved via two anisotropic conductive film (ACF) wires. Lastly, the sealing and the fabrication of the LCPS are completed after curing. Figure 5(b) presents an image of the completed device.

EPIDERMAL PULSE MEASUREMENT

In this section, we experimentally demonstrate that the LCPS achieves high fidelity for continuous pulse wave monitoring with significantly relaxed alignment requirements, i.e., undistorted signals can be collected when the LCPS is misaligned for as much as ±6 mm from the optimal measurement spot. We also report the pulse measurement results from an unpackaged piezoresistive sensor as a reference group. In the experiment, a precision source meter measures the current going through the device. Since the LCPS responds to pressure variation in a quasi-linear fashion, we use the measured currents to directly represent the pressure wave.

As shown in Fig. 6, to assess the alignment relaxation capability of the LCPS, we compare the sensor readings from different misaligned positions, i.e., a nine-point grid, where the center point refers to the aligned/optimal position, on the wrist as shown in Fig. 6(b). The selected locations cover an area of 12 × 12 mm^2. Figure 6(a) and 6(c) respectively present the measured pressure data from the LCPS and bare pressure sensor without the capsule. From Fig. 6(a), one may observe that the LCPS always records high-quality signals without distortion even when the LCPS is misaligned for as much as ±6 mm. In addition, in all nine measured points, the characteristic peaks of the pulse waves can be clearly identified. Contrarily, in Fig. 6(c), one can observe that both the amplitude and quality of the measured signals are inferior to those measured at the center point, i.e., the signals become severely distorted at non-center sites. These experiments have verified the capsule design as an effective solution to relax alignment requirements of flexible devices that measure epidermal pulse waves.

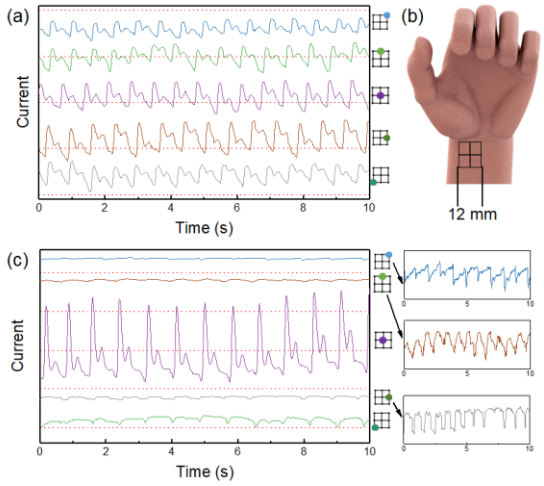

FIGURE 6. (a) & (c) Pulse measurements from the LCPS and bare piezoresistive sensor. (b) Illustration of the 12 × 12 mm^2 nine-point grid on the wrist, where the center (optimal) point is identified through careful calibration.

CONCLUSION

We have presented a new liquid capsule sensor platform to relax the stringent alignment requirements of flexible sensors for epidermal pulse tracking. Simulation and parametric models have been developed to identify the optimal design parameters of the capsule sensor, including the stiffness and size of the liquid capsule. Lastly, pulse wave measurements have been conducted at different locations to verify the alignment relaxation capability. The results suggest that the liquid capsule platform is a promising solution for all flexible sensors to relax alignment requirements for low-power, real-time and precise pulse monitoring.

ACKNOWLEDGMENT

This work is supported by the HKSAR Innovation and Technology Commission (ITC) Innovation and Technology Fund (ITF), MRP/056/17X.

REFERENCES

[1] Xu H, Liu J, Zhang J, Zhou G, Luo N, Zhao N. Flexible Organic/Inorganic Hybrid Near-Infrared Photoplethysmogram Sensor for Cardiovascular Monitoring. Advanced Materials. 2017; 29:1700975.

[2] Fan X, Huang Y, Ding X, Luo N, Li C, Zhao N, et al. Alignment-Free Liquid-Capsule Pressure Sensor for Cardiovascular

Monitoring. Advanced Functional Materials. 2018; 28:1805045.
[3] Luo N, Dai W, Li C, Zhou Z, Lu L, Poon CCY, et al. Flexible Piezoresistive Sensor Patch Enabling Ultralow Power Cuffless Blood Pressure Measurement. Advanced Functional Materials. 2016; 26:1178-87.
[4] Schwartz G, Tee BCK, Mei J, Appleton AL, Kim DH, Wang H, et al. Flexible polymer transistors with high pressure sensitivity for application in electronic skin and health monitoring. Nature Communications. 2013; 4:1859.
[5] Kao Y-H, Tu T-Y, Chao PC-P, Lee Y-P, Wey C-L. Optimizing a new cuffless blood pressure sensor via a solid–fluid-electric finite element model with consideration of varied mis-positionings. Microsystem Technologies. 2016; 22:1437-47.

METROLOGY OF NANO- AND MICRO-SCALE FEATURES CREATED WITH A LARGE-AREA INDENTING PROCESS – NANOCOINING

Nichole Cates Miller[1] and Stephen J. Furst[1]
[1]Smart Material Solutions, Inc.
Raleigh, NC, USA

INTRODUCTION

Although researchers have repeatedly highlighted how nanopatterning can revolutionize technologies ranging from displays to antimicrobial films, transferring these exciting innovations from lab-scale demonstrations to industrial-scale manufacturing has been a challenge, largely due to the lack of nanomanufacturing processes capable of patterning large areas at low cost. Nanocoining is unique in that it can quickly and seamlessly nanopattern the outside of drum molds used in roll-to-roll imprinting, thus enabling cost-effective, large-area nanomanufacturing. Nanocoining boasts patterning rates of more than 1000 mm^2/min, more than two orders of magnitude faster than competing technologies like electron-beam lithography. This process has the potential to benefit a variety of applications including displays, augmented and virtual reality, multispectral camouflage, wire-grid polarizers, and antimicrobial films to name a few [1,2,3].

Smart Material Solutions, Inc. (SMS) will discuss its recent progress towards improved indenting of nanopatterned metal molds and use of these molds to imprint polymer replicas. This paper will also present metrology of metal molds indented using a step-and-repeat process and ultrasonic indenting as well as polymer replicas created using batch and roll-to-roll processes.

Indenting Processes

This paper will discuss two indenting processes capable of nanopatterning the outside of a cylindrical drum mold: step-and-repeat indenting and ultrasonic nanocoining. Both processes start with the nanopatterning of a diamond die using traditional nanofabrication techniques like focused ion beam (FIB) milling. Indenting the die into a metal transfers the die's nanopattern into the metal surface as shown in Figure 1. The resulting metal molds can be used to rapidly nanopattern plastic films using roll-to-roll manufacturing processes (Figure 2).

FIGURE 1: Illustration of indenting.

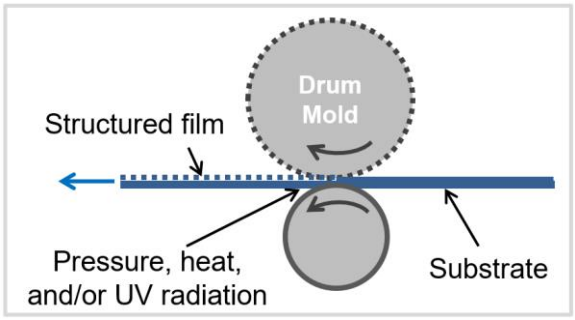

FIGURE 2: Illustration of roll-to-roll imprinting of a polymer film.

Step-and-Repeat Indenting

Step-and-repeat indenting refers to using two orthogonal axes and a spindle (theta) to create rows of indents by repeatedly indenting a nanopatterned die into metal and moving the diamond by the die width or height between each indent (Figure 3). This process has relatively low coverage rates of ~0.5 mm^2/min. Despite its low coverage rate, step-and-repeat indenting of metal foils can be a reliable method to create small master molds for lab-scale plate-to-plate imprinting desired by many R&D labs.

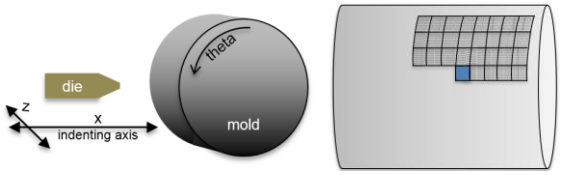

FIGURE 3: Illustration of step-and-repeat indenting setup.

Ultrasonic Nanocoining

Ultrasonic nanocoining is a high-speed indenting process that seamlessly patterns the outside of a cylinder. During nanocoining, an ultrasonic resonant actuator moves the nanopatterned diamond die in along an elliptical path such that it indents the rotating workpiece 50,000 times

per second (Figure 4). The spindle speed, actuator frequency, and elliptical path are controlled to match the tangential speeds of the die and the workpiece to prevent smearing during each indent.

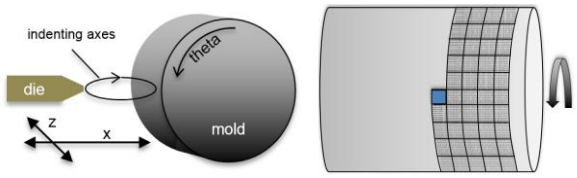

FIGURE 4: Illustration of ultrasonic nanocoining setup.

RECENT PROGRESS

SMS has made substantial progress with the nanopatterning of diamond dies, indenting of metal molds, and imprinting of functional polymer films. This progress is summarized below.

Diamond Nanopatterning

Nanopatterning of diamond is the first step in the nanocoining process. FIB milling can be used to fabricate a variety of features in diamond (see Figure 5). Nanofeatures with pitches below 150 nm, microfeatures up to a few microns in pitch, and hierarchical features comprised of nanofeatures on top of microfeatures have been patterned. Gratings with pitches below 150 nm as well as stochastic and arbitrary features have also been fabricated.

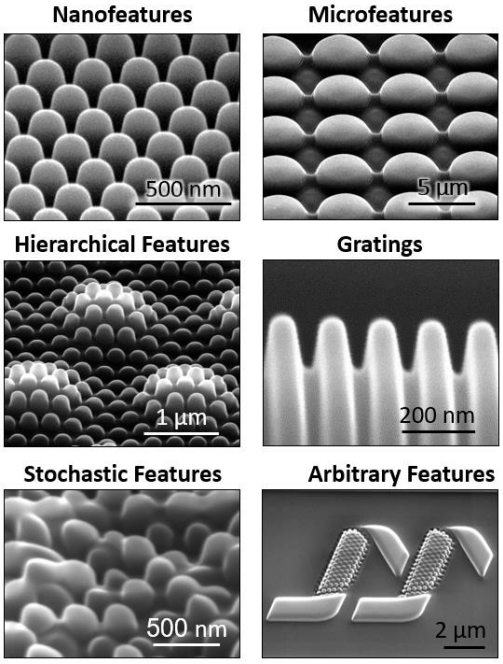

FIGURE 5: SEM images of features in diamond.

Indenting Processes

SMS has built a pilot line capable of indenting drum molds and metal foils using step-and-repeat indenting and ultrasonic nanocoining.

Step-and-Repeat Indenting

SMS has used step-and-repeat indenting to create arrays of nanofeatures on the outside of cylindrical drums and on metal foils. Figure 6 shows a photo, a scanning electron microscopy (SEM) image, and atomic force microscopy (AFM) image demonstrating the ability to create high-quality, albeit small-area, master molds using step-and-repeat indenting.

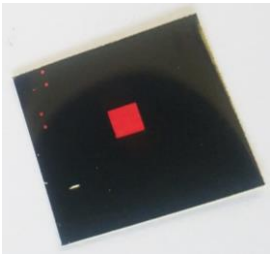

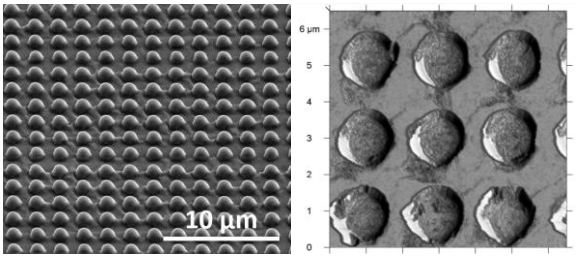

FIGURE 6: A photo (top), SEM image (bottom, left), and AFM image (bottom, right) of a small-area master mold made by step-and-repeat indenting of a metal foil.

Ultrasonic Nanocoining

In ultrasonic nanocoining, the spindle rotation speed, actuator frequency, and elliptical path must all be precisely controlled to prevent smearing of the features and ensure side-by-side tiling of the indents. The feature smearing and indent misalignment apparent in Figure 7 are a result of poor control over these variables. Improved control has led to precise tiling of indents like those shown in Figure 8.

AFM can assess 3D feature shapes. Figure 9 shows an AFM image of several features demonstrating low feature-to-feature variability. The closeup AFM images shown in Figure 10 of one feature shows some feature anisotropy, with more smearing in the upfeed direction than in the crossfeed direction as can be expected in

this dynamic indenting process. Future work will aim to minimize this anisotropy.

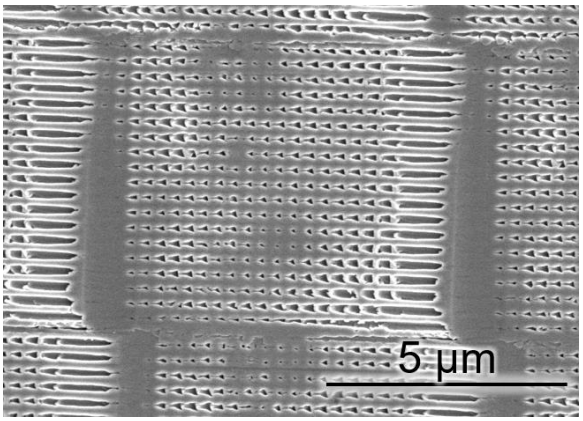

FIGURE 7: SEM image showing feature smearing due to a speed mismatch between the die and the workpiece during indenting.

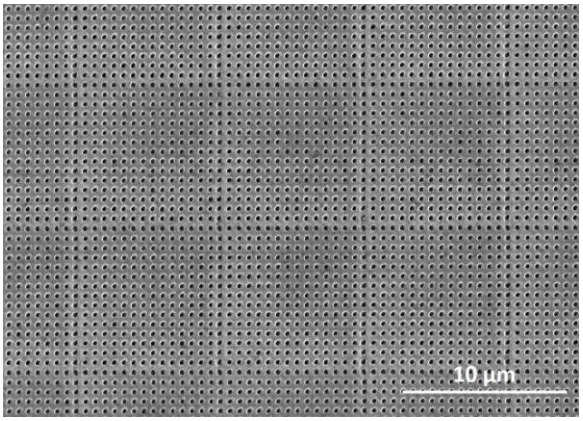

FIGURE 8: SEM image showing precise side-by-side tiling of indents of 600 nm features created using ultrasonic nanocoining.

.

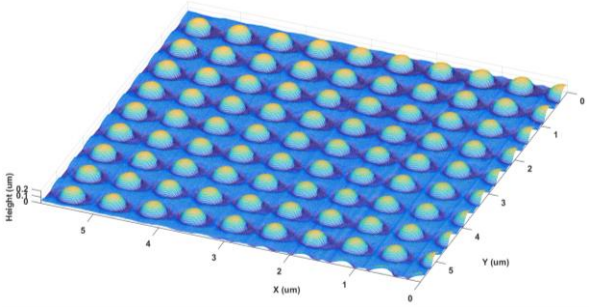

FIGURE 9: AFM image of a polymer replica made from a dynamically indented mold showing an array of indented features.

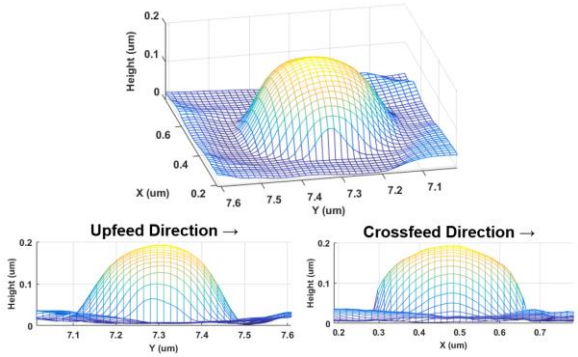

FIGURE 10: Closeup AFM images comparing the feature shape in the upfeed and crossfeed directions.

Polymer Imprinting

SMS's drum molds and flattened foil molds can imprint nanofeatures into polymer films using either UV nanoimprint lithography (UV-NIL) or thermal embossing.

In UV-NIL, the liquid precursors for a UV-curable polymer are placed in contact with the mold and exposed to UV radiation to cure the polymer. The UV-cured polymer, which is often supported on a polymer substrate for mechanical stability, retains the nanofeatures after its removal from the mold. UV-NIL has been used for both batch and roll-to-roll processing, as described below.

In thermal embossing, heat and pressure are applied to soften a thermoplastic polymer while it is in contact with a mold. Subsequent cooling solidifies the polymer, which retains the mold's nanofeatures. Although some batch and roll-to-roll thermal embossing has been performed with SMS molds and future thermal embossing is planned, thermal embossing with SMS's molds will not be discussed here.

Batch Processing

Batch UV-NIL was used to create nanopatterned polymer films by sandwiching several drops of a Norland Optical Adhesive (NOA 72 or NOA 85) between a metal mold and a polycarbonate substrate. A UV light cures the UV-curable polymer through the polycarbonate substrate. Once fully cured, the imprinted polymer is removed from the mold to nanopatterned films like the antireflective strip shown in Figure 11.

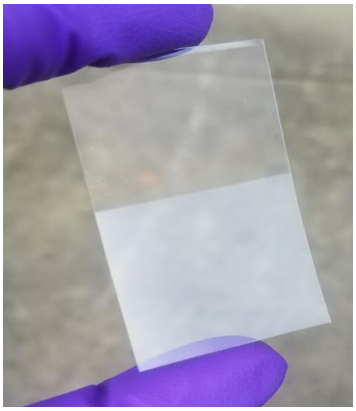

FIGURE 11: An anti-reflective, nanopatterned polymer film (top) next to a smooth polymer film (bottom).

Roll-To-Roll Processing

Roll-to-roll UV-NIL has been performed with SMS's nanopatterned molds by partners at the University of Massachusetts at Amherst's Center for Hierarchical Manufacturing (CHM). The CHM first used a nanostructured foil (Figure 12, top) to create a PDMS mold (Figure 12, middle) that was wrapped around a drum in a roll-to-roll setup and used to imprint nanofeatures a UV-curable polymer (NOA 65) onto a PET film (Figure 12, bottom).

SMS also recently fabricated a drum mold with a 6.5" outer diameter that contains strips of features with pitches of 300 nm, 600 nm, and 1 µm (Figure 13). The CHM will use this drum to seamlessly imprint polymer films using roll-to-roll UV-NIL. Future work will also include the creation of seamlessly nanopatterned sleeves for both UV-NIL and thermal embossing at the CHM.

CONCLUSIONS & FUTURE WORK

SMS has used step-and-repeat indenting to create small arrays of nanofeatures and ultrasonic nanocoining to seamlessly nanopattern cylindrical drum molds with outer diameters up to 6.5". Improved control over the spindle rotation speed, actuator frequency, and elliptical tool path has enabled precise tiling of the indents and reduced feature smearing, as evidenced by SEM and AFM. SMS's molds have been used to imprint UV-curable polymers in both batch and roll-to-roll imprinting processes. Future work will include the roll-to-roll imprinting of nanopatterns using SMS's seamless drums, patterning of seamless sleeves that can fit on existing air mandrels in roll-to-roll setups, and thermal embossing.

FIGURE 12: A nanostructured foil (top), PDMS stamp made from the foil (middle), and a polymer film replicated from the PDMS stamp on the CHM roll-to-roll UV-NIL setup (bottom).

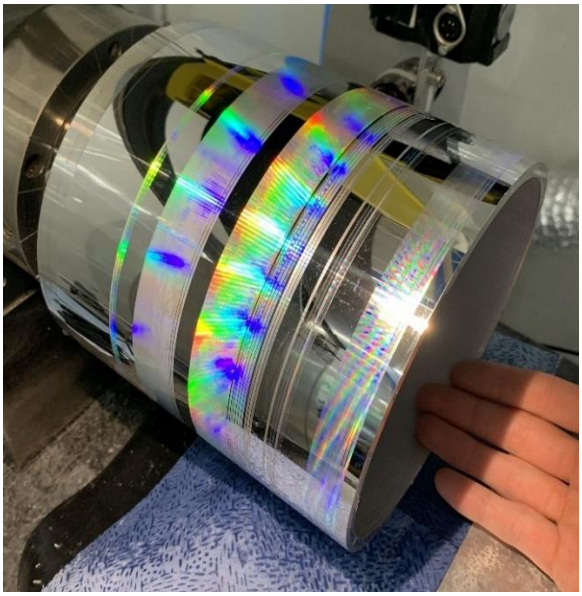

FIGURE 13: Drum mold with a 6.5" OD for use on the CHM R2R UV-NIL setup.

REFERENCES

[1] Chandra S, Franklin D, Cozart J, Safaei A, Chanda D. Adaptive Multispectral Infrared Camouflage. American Chemical Society Photonics. 2018; 5: 4513-4519.

[2] Panning E, Sanchez M. Special Section Guest Editorial: Novel Patterning Technologies. Journal of Micro/Nanolithography, MEMS, MOEMS. 2018; 17: 031201.

[3] Liu CH, Niu PL, Sung CK. Integrating anti-reflection and superhydrophobicity of moth-eye-like surface morphology on a large-area flexible substrate. Journal of Physics D Applied Physics. 2014; 47: 1.

WAFER SCALE EXFOLIATION OF MONOCRYSTALLINE MICRO-SCALE SILICON FILMS

Martin J. Ward and Michael A. Cullinan
Department of Mechanical Engineering
The University of Texas at Austin
Austin, Texas, United States of America

INTRODUCTION

Monocrystalline thin-film silicon combines highly desirable mechanical properties with CMOS compatibility and high performance which enables devices such as flexible solar cells or wearable electronics [1], [2] but has yet to be manufactured in a cost-feasible manner. Exfoliation is particularly cost-effective compared to other methods of creating thin-film Si, such as etching or mechanical grinding, which further increases the envelope of applications to includes things like IoT devices [3]. Silicon exfoliation involves peeling the top layer off a wafer, including any device built into the surface. This approach has the advantage of leveraging existing semiconductor fabrication techniques to produce flexible devices while other flexible device manufacturing methods require the development of completely new semiconductor manufacturing processes like organic thin-film transistors [4] which still do not match the performance of silicon.

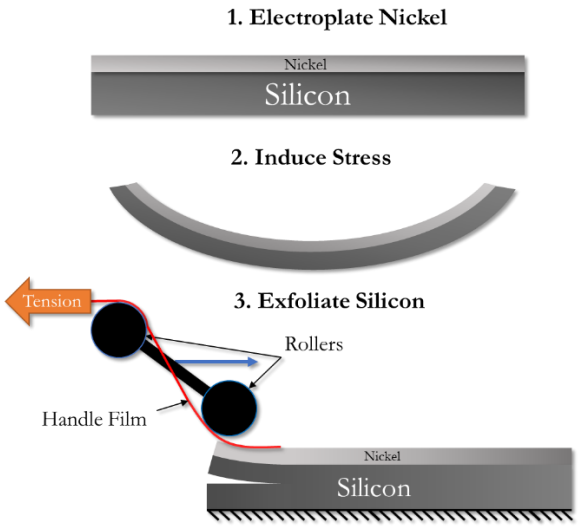

FIGURE 1. Exfoliation process flow.

The exfoliation process flow developed is shown in FIGURE 1. First, seed and adhesion layers are evaporated onto a wafer, on top of any previously fabricated devices. A 10-35 µm layer of nickel is then electrodeposited before a heat treatment process designed to induce a residual tensile stress in the nickel. This stress is just below the threshold for spontaneous exfoliation. Then a specific external load is applied to exfoliate the film while maintaining uniformity and regulating thickness.

A prototype tool to apply this external load has been constructed and tested to prove the viability of the process and identify critical areas of interest. Previous versions of this process used a wedge-shaped tool to apply extra stress near the crack front [5]. This produced both friction and vibrations which introduced roughness in the exfoliated surface. Other groups used a tape handle layer to apply a peeling force by hand [6]. When tested, this produced inconsistencies in the load and exfoliation results, but also final surface reduced roughness. To overcome these limitations, a tool that could create controlled peeling loads was created. The design and testing of this prototype has been described in detail here [7] and will be summarized for comparison throughout this paper. FIGURE 2 shows sample results from this tool. An upgraded version of the tool is being constructed and the areas of improvement focus on reducing vibrations, friction, and adding active force control and in line metrology.

ENHANCED EXFOLIATION TOOL DESIGN

Active Tension Control

Active tension control has already been added to the tool and can be seen in FIGURE 3. The system uses a pair of Airpel Anti-Stiction pneumatic cylinders to create a balanced load across the film. The cylinders are mounted on a load cell and share the same input pressure controlled by a ControlAir 900X E/P transducer. The input of the transducer is controlled by an Arduino running a PID loop with the load cell output as the control variable. Early tests show

that the system can maintain constant handle film tension at a desired setpoint between .1-90 N to within 10 mN during exfoliation.

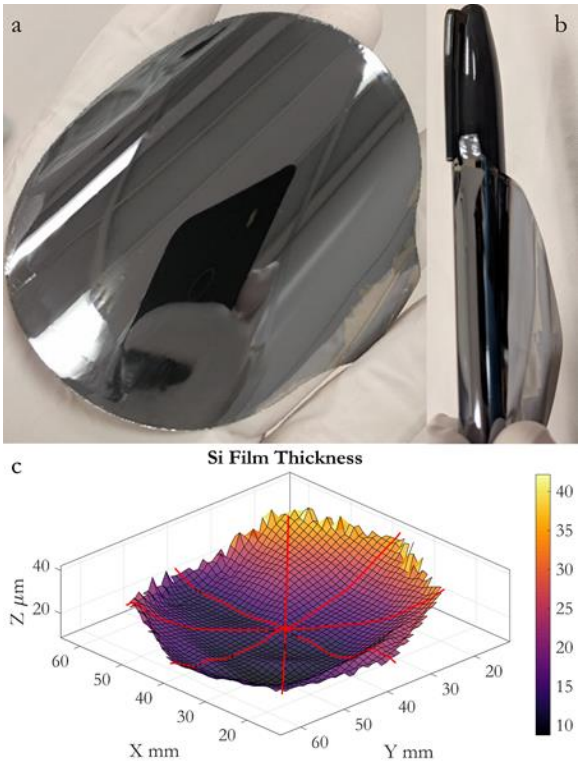

FIGURE 2. (a) Exfoliated film samples silicon side up with nickel backing at approximately 20 μm Si film thickness. (b) Bend radius demonstration. (c) Sample film thickness map.

Fracture Modeling

To better understand the ideal load for the tool to apply, a 2D fracture mechanics model was created and is described in detail in [8]. Previous work in the field of thin-film interfacial fracture mechanics indicates that a stable crack path in the substrate, parallel to the wafer surface occurs when the in-plane shear mode stress intensity, K_{II}, is equal to zero, and the opening mode stress intensity, K_I, is equal to a critical value, K_{Ic} [9]. It also indicates that there is a characteristic crack depth for a given elastic system. The theoretical system is defined by the material properties of the Si and Ni, the crack length, the film thickness, and the film stress. Analytical solutions from [10], [11] suggest that changing the applied load can skew the mode mix ratio and therefore the characteristic crack depth. An analytical solution to the loading conditions created by the tool was not feasible, so a parametric FEA model was created using ANSYS Fracture Tools that can be run iteratively to solve for the characteristic crack depth. Variation of the inputs was done using adaptive sampling to produce a Kriging metamodel with increased accuracy around the solution. This model can be used to predict the crack depth for a given system and will be used to calculate the ideal handle film tension load to create a uniform film while compensating for variations in the nickel film thickness.

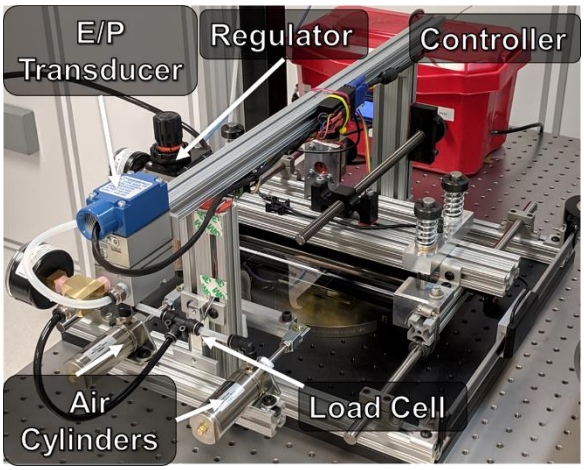

FIGURE 3. Partially upgraded exfoliation tool prototype with active pneumatic tensioning.

Metrology

The ability to measure and quantify the produced films is critical to improving the exfoliation processes. Fully characterizing this process requires thickness profile measurements for both the exfoliated film and the electro-deposited nickel across as large an area as possible. A curvature profile is also necessary to define the initial stress state using a modified Stoney's equation for (100) silicon wafers [12]. These measurement requirements present significant challenges due to the necessary vertical resolution, a few microns, and horizontal range spanning the entire 100 mm wafer. The unsupported silicon film is also very brittle and can only be handled with a backing layer, thus eliminating all available direct measurement methods. Previous methods from [7] were time consuming and involved moving the wafer between metrology stations multiple times throughout the exfoliation process to build surface maps of silicon and nickel film thickness and stress.

Adding inline metrology to the tool simplifies the exfoliation process flow and allows for direct compensation for variations in the nickel film thickness. It was desired to measure the film thickness to an accuracy of better than 500nm

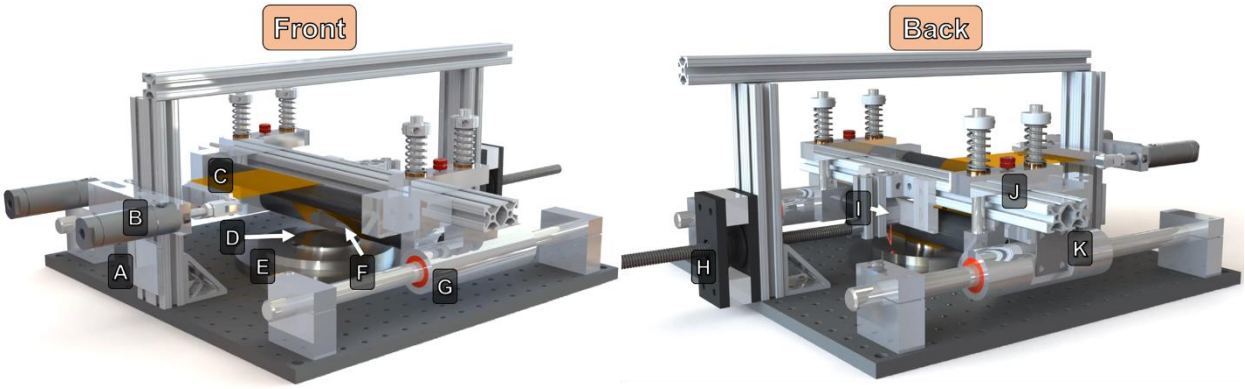

FIGURE 4. Render of enhanced exfoliation tool including laser distance sensor and improved motion stage showing: A, load cell; B, pneumatic tensioner; C, handle film; D, silicon wafer; E, vacuum chuck; F, exfoliated film; G, bushing assembly; H, actuator; I, laser distance sensor; J, roller height adjustment; K, flexure mount.

which necessitated a redesign of the stage. With a suitable stage design, a Micro-Epsilon optoNCDT 1420 laser displacement sensor will be mounted to the stage as seen in FIGURE 4. This will allow for height profile measurements to be taken before and after exfoliation to measure a profile for silicon and nickel film thickness provided the wafer thickness profile is measured in advance.

Stage Design

The previous prototype demonstrated errors in the vertical axis of approximately +/- 5 µm under the off-axis actuation load. The model indicated that the exfoliation process was not sensitive in this direction and this allowance was made to aid the rapid fabrication and testing of the first prototype. However, this error is not acceptable when incorporating inline metrology and reducing it could improve the surface finish. To improve the stage performance, a complete precision machine design analysis is being performed on the system and homogeneous transform matrix (HTM) models of the exfoliation and metrology loops have been constructed. From these it was determined that the vertical error was primarily due to excessive clearance in the four stage bushings. Preliminary results suggest the bushings will be replaced with low-clearance bushings in a housing with increased rigidity as well as increasing the rod diameter. In response to the increased stiffness of this configuration one set of bushings will be flexure mounted to avoid over-constraining the system.

Bushings were chosen over ball bearing linear guides to promote damping and reduce noise that could affect the surface finish of the silicon film. A cost-benefit analysis of air-bearings is also underway. It was also noted that the off-axis leadscrew actuator (visible in FIGURE 1) was causing an undesirable moment load that was exacerbating the bushing deflection. In response, the actuator was moved to be in line with the stage rails and wafer. A rendering of the proposed tool enhancements can be seen in FIGURE 4. Preliminary simulations indicate that these changes will bring the total vertical error motion below 0.5 µm.

Active Compensation

Combining the improvements to the stage, the inline metrology, the active tensioning system and the metamodel creates the opportunity for applying active compensation to the system. This means that a specific tension force profile can be input to the system to generate a desired silicon film thickness while compensating for measured deviations in the nickel thickness and stress. Key to accomplishing force compensation is designing and implementing a control system that can incorporate an inverse form of the metamodel and process the sensor data. The actual controller may be simple, but the system will require a significant amount of integration. *FIGURE 5* shows an example wafer profile of the measured uncompensated crack depth that resulted from the nickel film thickness and stress measurements shown as well as two different simulated crack profiles created by the two handle tension profiles. With this tool, uniform silicon films of a desired thickness can be made.

FUTURE WORK

Aside from the planned work described above; a thorough vibrational analysis of the system will be conducted to determine what improvements can be made to reduce the roughness of the film.

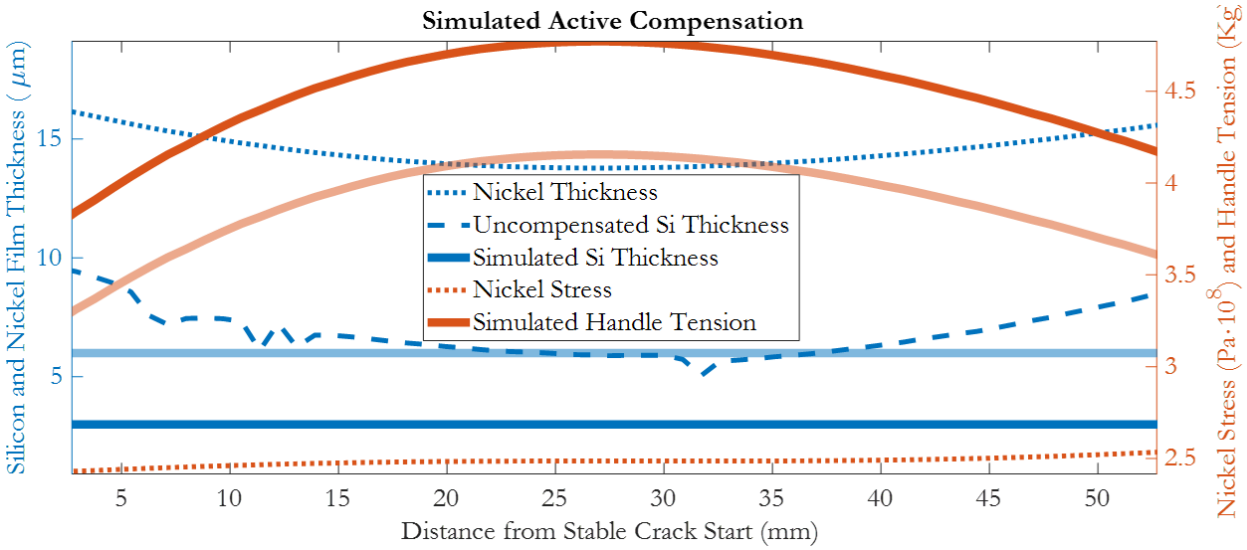

FIGURE 5. Example wafer profile measurement with simulated crack depth control and nickel thickness and stress compensation for two different desired silicon film thicknesses.

CONCLUSION

We have successfully demonstrated an exfoliation process to produce micron-scale single crystal silicon films over a wafer scale area. The construction of the exfoliation tool and model provides the basis for scalable, large-area, monocrystalline thin-film devices which will be improved upon with an enhanced version of the tool.

ACKNOWLEDGMENTS

The authors acknowledge and thank Dr. Kenneth M. Liechti for his invaluable expertise in the field of fracture mechanics and guidance during the development and review of this paper. The authors thank Kirsten Cole Christopherson and Miaomiao Yang for their efforts in completing these experiments. The authors would also like to thank Liam Conolly, Dipankar Behera, and Cheng Zhao for the informative discussions and technical expertise. This work is based upon work supported primarily by the National Science Foundation under Cooperative Agreement No. EEC-1160494 and NNCI-1542159. Any opinions, findings and conclusions or recommendations expressed in this material are those of the author(s) and do not necessarily reflect the views of the National Science Foundation.

REFERENCES

[1] M. Ying *et al.*, “Silicon nanomembranes for fingertip electronics,” *Nanotechnology*, vol. 23, no. 34, p. 344004, Aug. 2012.

[2] J. Kim *et al.*, “Stretchable silicon nanoribbon electronics for skin prosthesis,” *Nat. Commun.*, vol. 5, p. 5747, Dec. 2014.

[3] A. M. Hussain and M. M. Hussain, “CMOS-Technology-Enabled Flexible and Stretchable Electronics for Internet of Everything Applications,” *Adv. Mater.*, vol. 28, no. 22, pp. 4219–4249, Jun. 2016.

[4] H. Sirringhaus, “25th Anniversary Article: Organic Field-Effect Transistors: The Path Beyond Amorphous Silicon,” *Adv. Mater.*, vol. 26, no. 9, pp. 1319–1335, Mar. 2014.

[5] R. A. Rao *et al.*, “A novel low cost 25μm thin exfoliated monocrystalline si solar cell technology,” in *Photovoltaic Specialists Conference (PVSC), 2011 37th IEEE*, 2011, pp. 001504–001507.

[6] S. W. Bedell *et al.*, “Advanced flexible electronics: challenges and opportunities,” 2014, p. 90831G.

[7] M. Ward and M. Cullinan, “Design of Tool for Exfoliation of Monocrystalline Microscale Silicon Films,” *J. Micro Nano-Manuf.*, vol. 7, no. 1, pp. 011003-011003–7, May 2019.

[8] M. Ward and M. Cullinan, “A fracture model for exfoliation of thin silicon films,” *Int. J. Fract.*, Feb. 2019.

[9] M. D. Thouless, A. G. Evans, M. F. Ashby, and J. W. Hutchinson, “The edge cracking and spalling of brittle plates,” *Acta Metall.*, vol. 35, no. 6, pp. 1333–1341, Jun. 1987.

[10] Z. Suo and J. W. Hutchinson, “Steady-state cracking in brittle substrates beneath adherent films,” *Int. J. Solids Struct.*, vol. 25, no. 11, pp. 1337–1353, Jan. 1989.

[11] M. D. Drory, M. D. Thouless, and A. G. Evans, “On the decohesion of residually stressed thin films,” *Acta Metall.*, vol. 36, no. 8, pp. 2019–2028, 1988.
[12] G. C. A. M. Janssen, M. M. Abdalla, F. van Keulen, B. R. Pujada, and B. van Venrooy, “Celebrating the 100th anniversary of the Stoney equation for film stress: Developments from polycrystalline steel strips to single crystal silicon wafers,” *Thin Solid Films*, vol. 517, no. 6, pp. 1858–1867, Jan. 2009.

DESIGN OF A SIX-AXIS PARALLEL NANOPOSITIONER USING DECOUPLED FLEXURAL LEGS

Chenglin Li, Xiangbo Liu and Shih-Chi Chen*
Department of Mechanical and Automation Engineering
The Chinese University of Hong Kong
Shatin, N.T., Hong Kong SAR, China
*Email: scchen@mae.cuhk.edu.hk

In this paper, we present the design of a compliant six-axis parallel nanopositioner. The mechanism is designed based on a new method of decoupled flexural legs. The nanopositioner is actuated by six linear actuators, located below flexure mechanism on the same plane, achieving a compact device envelope. Static and dynamic positioning experiments have been devised and performed to characterize the range, resolution, and speed characteristics of the nanopositioner.

PARALLEL FLEXURE STAGES

Nanopositioners can move objects of different sizes and scales with nanometer level precision. Nanopositioners are important as they set limits on our ability to measure, manipulate, and manufacture physical systems. To realize nanometer level repeatability and precision, flexure bearings or compliant mechanisms are often used for their advantages (e.g., no wear between joint members and free of backlash etc.) over traditional mechanical linkages [1].

Nanopositioners often operate in multiple axes, thereby controlling the position and/or orientation of an object in one to six degrees of freedom (DOF). Many commercial multi-DOF nanopositioners achieve the required DOFs by serially stacking up single-axis stages. Although this design approach is straightforward and typically has a larger work space, the positioner becomes tall and bulky with compromised resolution due to high temperature sensitivity. On the other hand, multi-DOF nanopositioners can be designed in a parallel fashion, making the positioner compact, light-weight with improved dynamic performance. The parallel nanopositioners are usually custom-designed owing to their limited range, load capacity, and complex control solution.

In recent years, many multi-DOF parallel positioners have been developed for various applications. Two design methods are frequently used to develop such systems: (1) constraint-based design (CBD) [2], and (2) pseudo-rigid-body model (PRBM) [1]. For example, based on CBD, the HexFlex mechanism is developed, i.e., a monolithic six-axis compliant stage that can be easily fabricated via waterjet or wire electrical discharge machining (EDM). However, three custom-designed two-axis voice coil actuators are required to drive the HexFlex mechanism [3,4]. Using PRBM, a Stewart platform [5] can be transformed into a six-axis compliant stage driven by six linear actuators. Nevertheless, its 3-D flexural joints are difficult and expensive to fabricate [6]. In this paper, we present a new compliant mechanism design method based on decoupled flexural legs, demonstrated with a six-axis nanopositioner with improved performance.

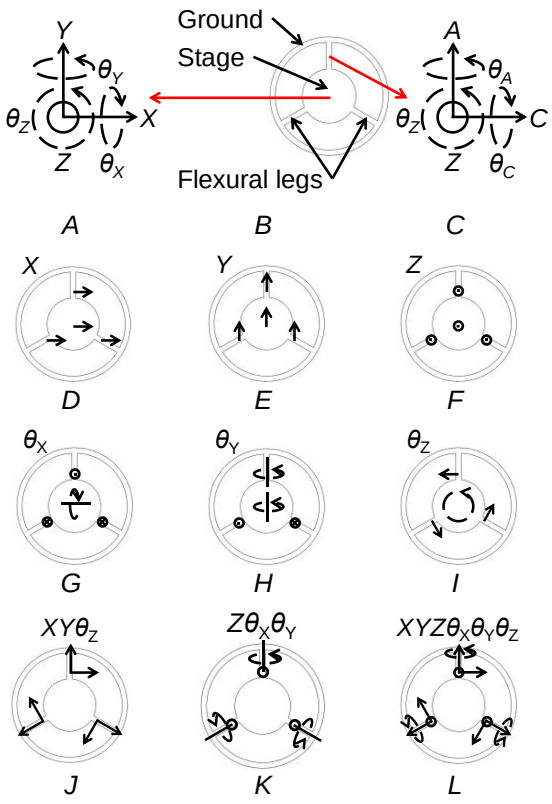

FIGURE 1. Schematic of a parallel flexure stage (B), consisting of a central stage and three flexural legs; global (A) and local (C) coordinates

set at the central stage and each leg respectively. Illustration of the motion decomposition (D~I) and composition (J~L)

Fig. 1B shows the schematic diagram of a parallel flexure stage, which consists a central stage, three equally-spaced flexural legs, and ground. The number of flexural legs (n) can be two or more depending on the design requirements. The global coordinate (Fig. 1A) is set at the central stage, and each flexural leg has a local coordinate (Fig. 1C), where A and C indicate the axial and circumferential directions, respectively. Fig. 1D - 1I illustrate the decomposition of the stage motions in all six axes, and notably only motions in the C, A, Z, and θ_A axes (in the local coordinates) are required for the flexural legs. Fig. 1J - 1L show examples of the multi-axis motion composition. For a six-DOF flexural stage (Fig. 1L), the flexural legs should have motions in the C, A, Z, and θ_A axes, while the θ_A DOF can be neglected as n (n ≥ 3) equally-spaced flexural legs with the Z DOF can achieve three out-of-plane rotations, e.g., rotations about different in-plane axes. Thus, flexural legs with three translational DOFs (TDOFs) are required to design six-axis parallel flexural stages.

DECOUPLED FLEXURAL LEGS

Generally, the design of appropriate flexural legs is the key step in designing a parallel mechanism. Here, we introduce a systematic approach to design multi-TDOF flexural legs by serially combining single-TDOF flexures. First, for one-TDOF flexural legs, we have the cantilever beam (CB), Fig. 2A, parallelogram (PA), Fig. 2B, and double parallelogram (DP), Fig. 2C, which are frequently used in CBD [7]. Besides, two additional one-TDOF flexures are considered, i.e., two cantilever beams joined collinearly at two fixed ends (CF), Fig. 2D, or two free ends (CC), Fig. 2E. As such, by serially combining the five different one-TDOF flexures, several different two-TDOF flexural legs and numerous three-TDOF flexural legs can be obtained. It is worthwhile to note that not all the generated flexural legs are suitable for fabrication and motion transfer. By using finite element analysis (FEA), we can determine best the flexural legs for different design requirements.

Figure 2 presents examples of two-TDOF or three-TDOF flexural legs: CC-CB (Fig. 2F~G), CB-CC (Fig. 2H~I), CB-CC-CB (Fig. 2J - 2L), and CB-CC-CF (Fig. 2M - 2O). To some extent, these flexural legs are “decoupled” due to the serial nature of the combination.

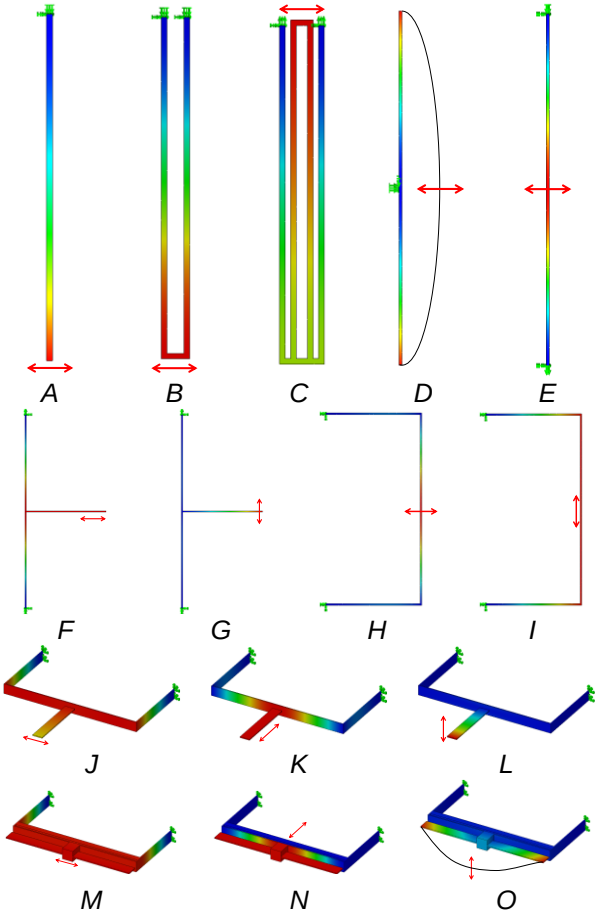

FIGURE 2. Examples of one-TDOF (A - E), two-TDOF (F - I), and three-TDOF (J - O) flexural legs

We can also analyze some of the existing parallel flexural stages using “flexural legs” concept. For example, the XY stage developed by Awtar [8] uses four DP-DP flexural legs, the HexFlex mechanism [3] uses three CC-CB flexural legs, and the μHexFlex mechanism [4] uses three CB-CC flexural legs. The reason that the HexFlex and μHexFlex can utilize three two-TDOF flexural legs to generate six-axis motions is that the width and thickness of the flexural beams have close values; as such the flexural legs are able to provide three TDOFs.

SIX-AXIS PARALLEL NANOPOSITIONER

To design a compact six-axis parallel nanopositioner, we first consider the best structure for actuation, and the CB-CC-CF flexural legs configuration (Fig. 2M - 2O) is selected. Fig. 3A presents the top view, global coordinate, and actuator layout of the six-axis parallel flexural stage, where actuators V_{C1}, V_{C2}, and V_{C3} are for in-plane motions ($X/Y/\theta_Z$), and actuators V_{Z1}, V_{Z2}, and V_{Z3} are for out-of-plane motions ($Z/\theta_X/\theta_Y$). Fig. 3B - 3G present the FEA

simulated results, which yields decoupled motions in all six axes, i.e., X, Y, Z, θ_X, θ_Y, and θ_Z. From the simulation, we can see that the in-plane and out-of-plane motions of the central stage are entirely decoupled.

Fig. 4C presents the CAD model of the six-axis parallel positioner, where the flexural stage is driven by six voice coil actuators (VCA) (NCC15-24-090-1X, H2W). The VCAs are used due to their high bandwidth (284 Hz) and high force output (18.1 N/amp). A decoupler mechanism (Fig. 4A) is affixed to the VCA, in order to ensure a pure Z motion input can be generated. A steering mechanism (Fig. 4B) is designed to transform the vertical motion into in-plane motion, allowing all VCAs to be positioned below the flexure stage. As shown in Fig. 4D, six capacitance probes are used to monitor the displacement of the central stage in all six axes in real time.

Figure 4D presents the prototype of six-axis nanopositioner with integrated actuators and sensors. The flexural stage is fabricated by wire-EDM and milling and made of 7075 aluminum alloy.

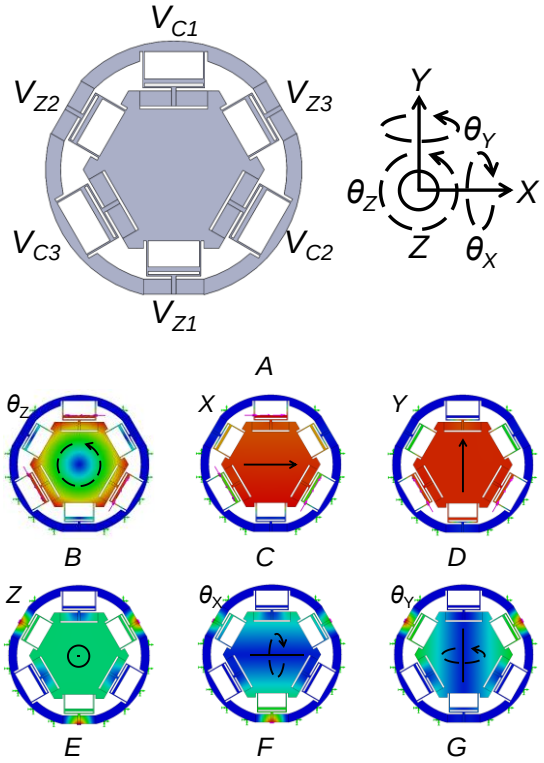

FIGURE 3. Top view (A) and simulated results (B - G) of the six-axis parallel flexural stage, demonstrating decoupled motions in all six axes

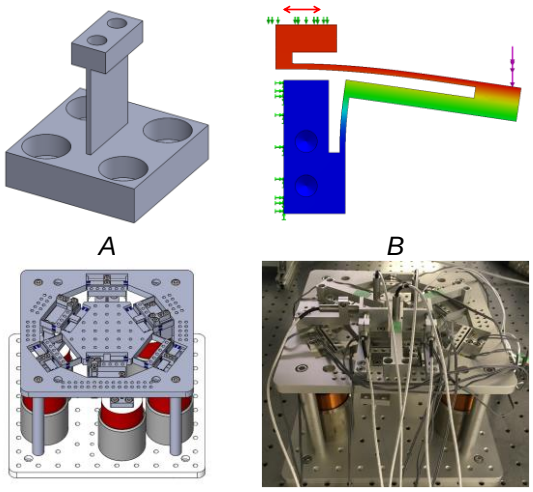

FIGURE 4. Decoupler for VCAs (A); motion steering mechanism (B) between the six-axis flexural stage and linear actuators; CAD model (C) and prototype (D) of the six-axis parallel nanopositioner

CHARACTERIZATION

To characterize the dynamic performance of the six-axis parallel positioner, an impulse response experiment has been conducted. Based on the measured displacement data from the capacitance probes, resonant frequencies in different axes are calculated by fast Fourier transform (FFT). Table 1 summarizes the performance specifications of the nanopositioner, including the resonant frequencies, strokes, and minimum step sizes in all six axes.

TABLE 1. Specifications of the six-axis parallel nanopositioner

	Freq.	Stroke	Min. step size
X	121 Hz	±80 μm	6 nm
Y	126 Hz	±60 μm	4 nm
Z	118 Hz	±70 μm	6 nm
θ_X	246 Hz	±900 μrad	150 nrad
θ_Y	216 Hz	±1700 μrad	120 nrad
θ_Z	188 Hz	±600 μrad	80 nrad

To characterize the cross-axis motion coupling effect, static displacement experiments were performed to identify the matrix, S_X, that maps the actuator input voltages, X_A, to the mechanism displacements, X_C. Six capacitance probes are fixed on a vibration isolation table to monitor the motions of the nanopositioner. Assuming small displacements, Eq. (1) and (2) can be used to obtain the matrix S_X [3]. The analytical solution of S_X is presented in Eq. (3), where a, b, c, d, e, f, g, and h are constant parameters related to the

characteristics of the VCAs and flexural stages. The analytical S_X indicates that the in-plane motions ($X/Y/\theta_Z$) and out-of-plane motions ($Z/\theta_X/\theta_Y$) are decoupled. Nevertheless, because of manufacturing errors and misaligned actuators and sensors, the measured S_X has deviations, and the motions in different axes are slightly coupled. The measured results are presented in Eq. (4). The units used in Eq. (1) - (4) are microns, microradians and millivolts.

$X_C = S_X X_A$, where

$$X_C = \begin{bmatrix} \Delta\theta_z & \Delta x & \Delta y & \Delta z & \Delta\theta_x & \Delta\theta_y \end{bmatrix}^{\mathrm{T}} \quad (1)$$

$$X_A = \begin{bmatrix} V_{C1} & V_{C2} & V_{C3} & V_{Z1} & V_{Z2} & V_{Z3} \end{bmatrix}^{\mathrm{T}}$$

$$X_A = S_X^{-1} X_C \quad (2)$$

$$S_X = \begin{bmatrix} a & a & a & 0 & 0 & 0 \\ -b & c & c & 0 & 0 & 0 \\ 0 & d & -d & 0 & 0 & 0 \\ 0 & 0 & 0 & e & e & e \\ 0 & 0 & 0 & -f & g & g \\ 0 & 0 & 0 & 0 & h & -h \end{bmatrix} \quad (3)$$

$$S_X = \begin{bmatrix} 0.158 & 0.154 & 0.149 & 0 & 0 & 0 \\ -0.029 & 0.008 & 0.008 & 0 & 0.013 & -0.015 \\ 0 & 0.020 & -0.020 & 0.012 & -0.009 & -0.009 \\ 0 & 0 & 0 & 0.015 & 0.021 & 0.021 \\ -0.128 & 0.067 & 0.073 & -0.401 & 0.273 & 0.299 \\ 0 & 0.139 & -0.109 & -0.030 & 0.450 & -0.480 \end{bmatrix} \quad (4)$$

POSITIONING EXPERIMENTS

We select the Z and θ_Z axes perform static positioning experiments for demonstrating the precision of the parallel positioner. In these experiments, the matrix, S_X^{-1}, is used in an open-loop controller, and the position signals are obtained from the six capacitance probes (C8/CPL190, Lion Precision, resolution: 20 nm). Figure 5 plots the measured displacements (left column) and off-axis errors (right column) versus open-loop displacement commands. The results show that the off-axis translational and rotational errors are reasonably small, i.e., within ±150 nm in $X/Y/Z$ axes, and ±3 μrad in $\theta_X/\theta_Y/\theta_Z$ axes. The precision can be further improved with closed-loop control.

Figure 6 presents the in-plane and out-of-plane positioning results for each axis under the PID control. In the experiments, the positioner is commanded to perform 1 μm and 10 μrad steps in the $X/Y/\theta_Z$ and $Z/\theta_X/\theta_Y$ axes in a sequential fashion, with each step held for about 15 seconds. As Fig. 6 shows, both in the in-plane and out-of-plane positioning experiments, the motion in one axis does not influence motions in other two axes. We have experimentally found that, under closed-loop control, the X, Y, Z, θ_X, θ_Y, and θ_Z axes have a resolution of 30 nm, 25 nm, 40 nm, 1.5 μrad, 1.4 μrad, and 1.0 μrad, respectively.

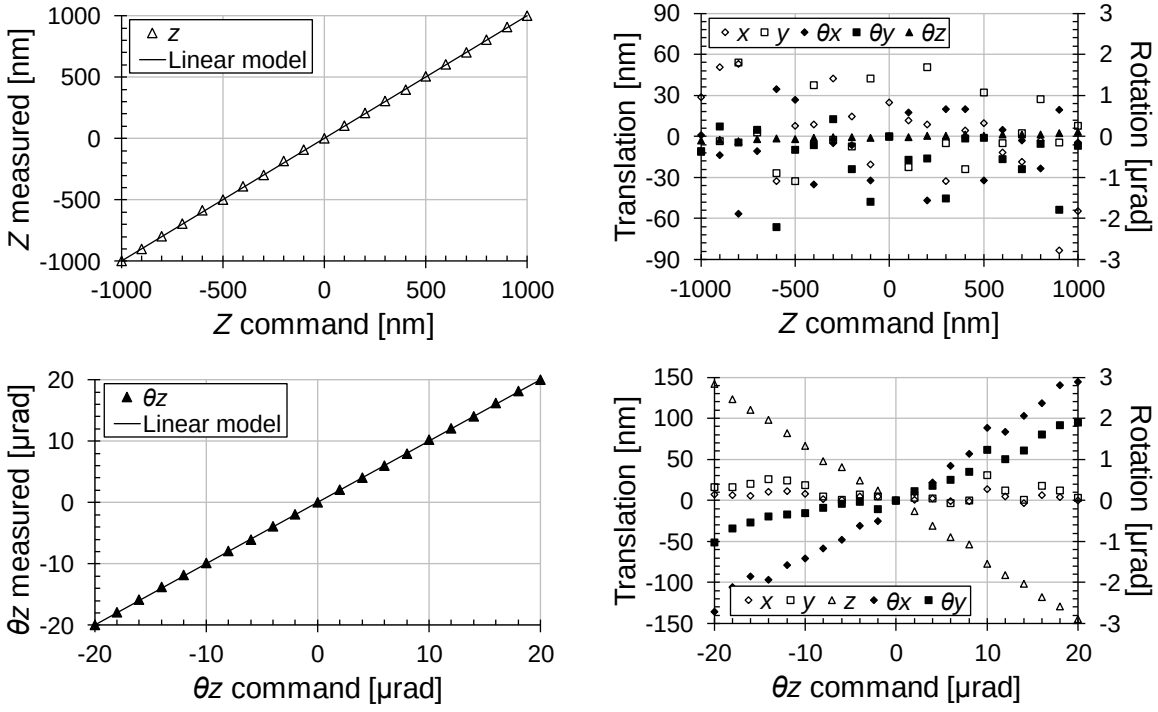

FIGURE 5. Z and θ_Z positioning results under open-loop control

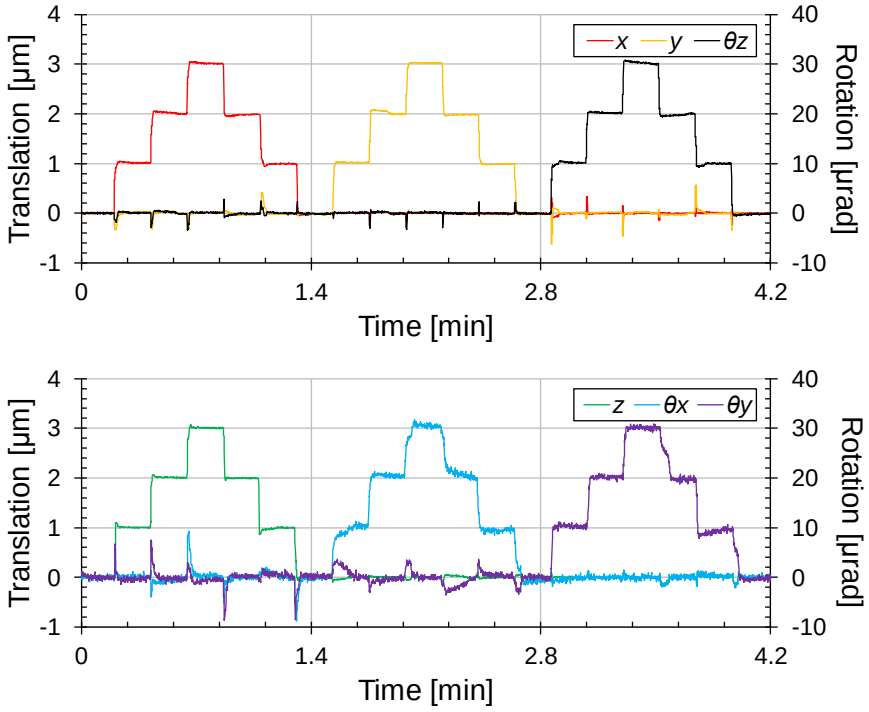

FIGURE 6. In-plane ($X/Y/\theta_Z$) and out-of-plane ($Z/\theta_X/\theta_Y$) positioning results, with PID control

CONCLUSION

We have presented the design and characterization of a flexure-based six-axis parallel positioner, demonstrating the new design method via combinations of decoupled flexural legs. The new six-axis parallel nanopositioner can be actuated by six linear VCAs and has decoupled in-plane and out-of-plane motions. Capacitance probes are used to monitor the displacement in all six axes in real time, and a resolution of ±40 nm in *X*/*Y*/*Z* axes, and ±1.5 µrad in $\theta_X/\theta_Y/\theta_Z$ axes has been achieved under closed-loop control. Dynamic performance of this flexural stage may be further improved by implementing deep learning-based control techniques [9].

ACKNOWLEDGMENT

This work is supported by the HKSAR Innovation and Technology Commission (ITC) Innovation and Technology Fund (ITF), ITS/077/17FP.

REFERENCES

[1] Howell L. Compliant Mechanisms. John Wiley and Sons Inc. New York: 2001.

[2] Blanding DL. Exact Constraint: Machine Design Using Kinematic Processing. ASME Press. New York: 1999.

[3] Culpepper ML, and Anderson G. Design of a Low-Cost Nano-Manipulator which Utilizes a Monolithic, Spatial Compliant Mechanism. Precision Engineering. 2004, 28(4), 469–482.

[4] Chen S, and Culpepper ML. Design of a Six-Axis Microscale Nanopositioner—µHexFlex. Precision Engineering. 2006, 30(3), 314–324.

[5] Stewart D. A Platform with Six Degrees of Freedom. Proceedings of the Institution of Mechanical Engineers. 1965, 180(1), 371–386.

[6] Wu T, Chen J, and Chang S. A Six-DOF Prismatic-Spherical-Spherical Parallel Compliant Nanopositioner. IEEE Transactions on Ultrasonics, Ferroelectrics, and Frequency Control. 2008, 55(12), 2544–2551.

[7] Li C, Wang J, and Chen S. Flexure-Based Dynamic-Tunable Five-Axis Nanopositioner for Parallel Nanomanufacturing. Precision Engineering. 2016, 45, 423–434.

[8] Awtar S, and Slocum AH. Constraint-Based Design of Parallel Kinematic XY Flexure Mechanisms. Journal of Mechanical Design. 2007, 129(8), 816–830.

[9] Liu X, Li C, and Chen S. Deep Learning-based Precision Control for Six-axis Compliant Nanopositioner. Proc. of the Annual Meeting of the ASPE, Pittsburgh, PA, USA, Oct. 2019.

MOTORIZATION OF A LARGE APERTURE AIR BEARING FOR USE IN A NEW X-RAY MICROSCOPE

Henry Arneson, Curt Preissner
Professional Instruments Company
Hopkins, Minnesota, USA

ABSTRACT
Professional Instruments specializes in designing motorizations for the most demanding applications. One such example is at the Advanced Photon Source (APS) at Argonne National Laboratory in Illinois, USA, cutting edge research is conducted using high energy X-ray beams. The upgrade of their new X-ray microscope, the Velociprobe, poses a unique challenge for a rotary stage. The stage requires extremely low error motions, high stiffness and a large aperture within the stage for instrumentation and routing of crucial wiring. The Blockhead air bearing spindles provide a nice solution to these requirements. They offer ultra-precision error motions and high stiffness in a compact package. Specifically, the 10R-606 Blockhead accommodates a large aperture in the middle of the bearing, originally intended for alignment of large optical axes. The motorization is just as critical because poor implementation of the motorization can induce unacceptable error motions. To fit the requirements for this application, collaboration with Aerotech was required to develop a bespoke motorization solution with minimal influence on error motions of the Blockhead. This paper discusses the unique motorization solution implemented on the 10R 606 Blockhead for use in the upgraded Velociprobe at the APS.

BACKGROUND
Since the 1970's, Professional Instruments Company has implemented brushless DC motors for use with our ultra-precision air bearings. Brushless DC motors are ideal because of their contactless operation, longevity, and ability to be directly driven on axis with the spindle. The compact size allows for close-coupling to the air bearing centerline minimizing the influence of nonsymmetrical forces on error motion. They also provide torque over a large speed range. Permanent magnets are mounted directly onto the rotor of the spindle and are actuated by alternating electromagnetic coils in the stator. Aerotech has extensive experience in demanding motorization systems for advanced industries such as semiconductor, photonics and ultra-precision. Collaboration with Aerotech was instrumental to providing a motorization system where there is negligible motor influence on spindle error motion.

Blockhead air bearing spindles offer high stiffness and accuracy within a compact footprint, making them applicable to a wide range of applications. The 10R-606 is a variant of our 10 inch Blockhead air bearing spindle. The large aperture of 154 mm in the middle of this bearing was originally built for open clearance of optics for precise alignment. The 10R-606 has specified total error motions of less than 50 nm with radial and axial stiffness are 0.35 and 0.6 kN/µm, respectively.

The APS is a premier US research facility where scientists and engineers use high brightness X-ray beams to probe the structures and functions of materials. The fast-scanning Velociprobe [1] is being modified to quickly scan large sample areas. The incorporation of this new capability into an existing structure required a compact design and the aperture of the 10R-606 allowed the sample scanning stages to be within the spindle rather than on top, which decreases the size of the complete motion assembly. The 10R-606 will provide ±1 arc second of positioning capability while providing a stable mount for the precision scanning stages within the cavity. Figure 1 shows the spindle in assembly with the Renishaw RESM 32768 line count encoder being installed.

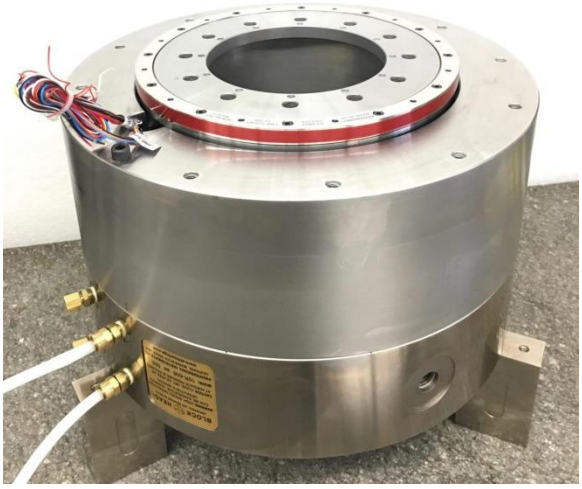

FIGURE 1. [Upside down] Motorized 10R 606 before the encoder enclosure is mounted. The encoder here is a Renishaw RESM with 32768 line counts and will allow for ±1 arc second positioning].

MOTORIZATION

Motorization of an air bearing spindle with little to zero motor influence on the nanometer-level requires extreme care in design and manufacturing. The motor must have sufficient pole pairs to minimize motor pole print through (to the error motions) without sacrificing too much torque. The influence of the motor coils must also be minimized because it can be significant to the error motion of the rotor. The S-240-43-A-ES model Aerotech motor was adapted to this spindle for this application. It utilizes aluminum laminations as opposed the usual silicon iron laminations to practically eliminate attractions between the rotor and the stator. While unwanted extra attraction forces can't be fully eliminated between rotor and stator, they are minimized by using lower flux levels, sinusoidal gap flux, stator winding with low harmonic content and slotless stator configuration.

Set up of this motor to the spindle is non-trivial because the smallest misalignments can lead to significant errors. The rotor, stator and encoder are then aligned precisely to the rotational axis of the spindle.

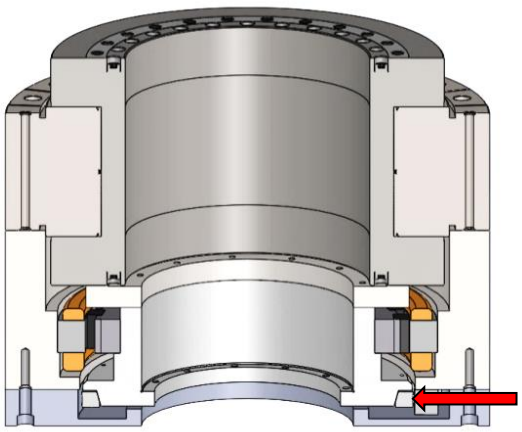

FIGURE 2. [Rightside up] Cross section of the motorized assembly with the encoder enclosure mounted. The arrow indicates the location of the Renishaw RESM encoder.

TESTING

Error motions of the spindle and motor assembly are evaluated using our special three-probe error separation set up. This hardware reliably tests spindles down to single digit nanometers over a variety of speed ranges [4]. A C9.5-2.0 Lion Precision capacitance probe is mounted directly to the stator and provides a stiff measuring loop. In this setup, the ball is approximately 130 mm above the working surface of the spindle. Precision jig ground pin holes are used to position the single probe to 3 unique angular positions. Probe positions (0°, 99.84375°, and 202.5°) were intentionally chosen because of their low harmonic content. Using three-probe error separation, detailed in Precision Spindle Metrology by Dr. Eric Marsh [3], the ball form error is separated from the error of the spindle which is necessary at this level of precision.

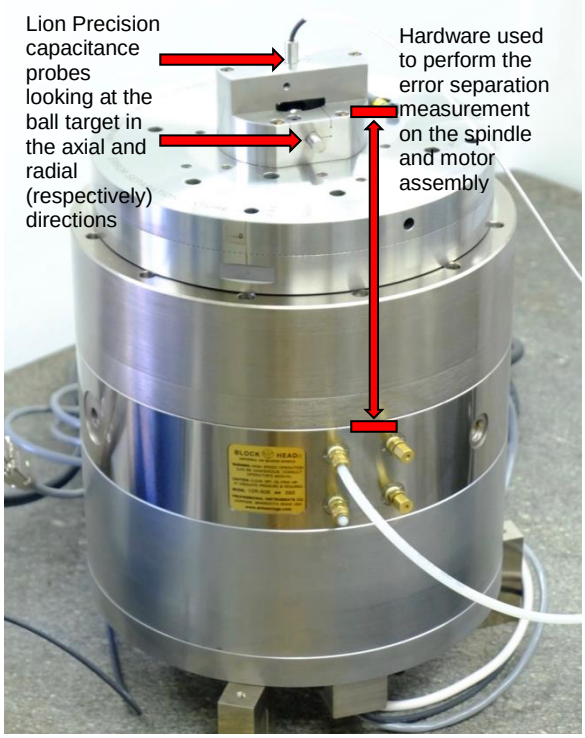
Lion Precision capacitance probes looking at the ball target in the axial and radial (respectively) directions
Hardware used to perform the error separation measurement on the spindle and motor assembly

FIGURE 3. Complete motorization assembly with the error separation hardware mounted. Note that the spindle is in its rightside up orientation and the error motion hardware (indicated by the arrow) is mounted to the stator].

RESULTS

The motor, using 13 electromagnetic pole pairs to operate, contributes minimal influence on the error motions of the complete assembly. The 10R 606, rated to 50 nm, far exceeds the specification, exhibiting total radial error motions of 19 nm and total axial error motions of 4 nm when tested at 120 rpm. This is shown in Figures 4 and 5 using the Lion Spindle Error Analyzer (SEA). One interesting observation is the presence of an almost undetectable sub-nanometer harmonic located at 13 undulations per revolution (UPR) shown in Figure 6. This is the only measurable motor influence on the spindle error motion. This small contribution to the error motion might be attributed to the 13 electro-magnetic pole pairs in the motor. Another set of error motion tests were conducted with the probe target mounted an additional 150 mm (280 mm total) above the surface of the spindle with only ~1 nm increase in the total error motions (Figure 5). A rough calculation shows that the spindle demonstrates roughly 1 nanoradian of tilt accuracy [3].

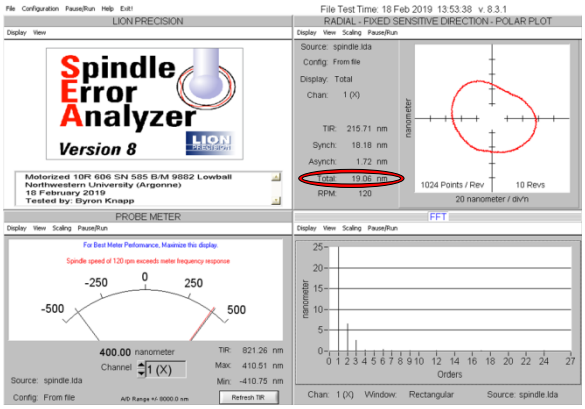

FIGURE 4. Radial error motion results at 130 mm above the spindle.

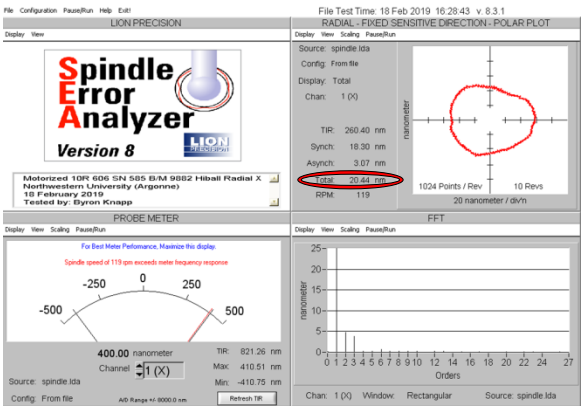

FIGURE 5. Radial error motion results at 280 mm above the spindle.

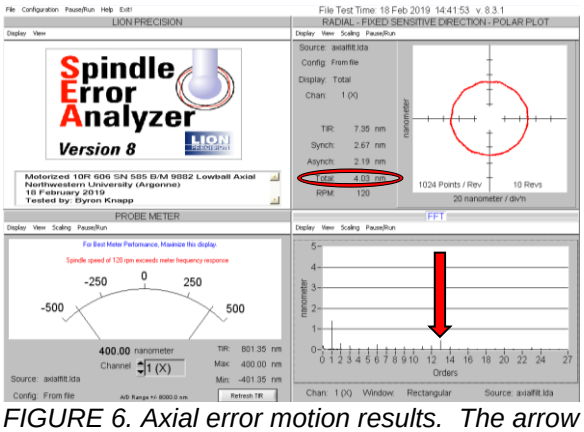

FIGURE 6. Axial error motion results. The arrow indicates the motor influence (less than 1 nm) on the error motion.

CONCLUSION

The upgrade of the Velociprobe at APS presents challenging mechanical design requirements. The spindle and motorization required are at the cutting edge of precision engineering. The large rotary system required nanometer level error motions and high stiffness in addition to having a large aperture to accommodate the extra instrumentation. The solution provided with the 10R-606 large aperture air bearing coupled with a specialized motor developed by Aerotech exceed these demands. The system also demonstrates incredible tilt accuracy of ~1 nanoradians.

REFERENCES

[1] Preissner, C. et al. (2017) Earth Wind and Fire: The new fast scanning Velociprobe. MEDSI 2016, DOI: 10.18429/JACoW-MEDSI2016-TUAA02

[2] U.S. Patent # 3,305,282, Hydrostatic Bearing Structure, Harold E. G. Arneson, Feb. 21, 1967.

[3] Marsh, Eric (2010) Precision Spindle Metrology.

EXPERIMENTAL ANALYSIS OF NICKEL ADHESION PROCESS DURING WIRE-SAWING OF ROCK IN VACUUM BY FRICTION TEST

Katsushi Furutani[1], Ryota Inukai[1], Tatsuaki Okada[2], Kazuto Saiki[3], and Hiroyuki Ohue[4]

[1]Toyota Technological Institute
Tempaku-ku, Nagoya 468-8511 Japan
[2]Institeu of Space and Astronautical Science (ISAS/ JAXA)
Chuo-ku, Sagamihara 252-5210 Japan
[3]Graduate School of Science, Osaka University
Toyonaka, Osaka 560-0043 Japan
[4]Research and Development Division, Tokusen Kogyo Co., Ltd.
Ono, Hyogo 675-1361 Japan

INTRODUCTION

In future planetary or asteroid explorations, wire-sawing is a solution for machining method for *In-situ* inspection. The authors have developed a wire-sawing machine on trial [1]. Electroplated nickel which fixes diamond abrasives on a core wire of a saw wire was adhered on the bottom of a machined groove on a rock as shown in Figure 1. The abrasives slipped on the nickel adhesion and the rock was removed little in vacuum. Then, the authors have measured the average temperature of a saw wire [2] and estimated the maximum temperature at the top of the abrasive [3]. It rose 55°C, which does not cause the nickel adhesion by softening [3]. The rest of factors is possibly the hardness difference between the rock and nickel and affinity.

In this paper, causes of the nickel adhesion due to the hardness difference and the affinity were investigated by friction tests.

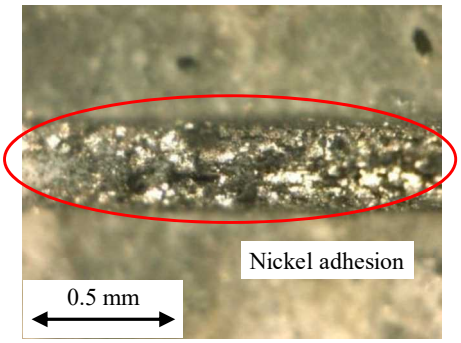

FIGURE 1. Bottom of machined groove in basalt.

EXPERIMENTAL SETUP AND METHOD

Figure 2 illustrates a friction tester for vacuum environment. Specimens were rubbed with a probe mounted at the end of a load cell in a vacuum chamber. The probe was moved with a motor-driven stage from the outside of the chamber. A normal load was adjusted by mounting a dead weight. Figure 3 shows a structure of a two-axis load cell with strain gauges. Two sets of parallel springs with a thickness of 1.25 mm were orthogonally combined. A two-active gauge method was used for each axis. The sensitivities were 13.6 and 23.8 με/N in the loading and friction directions, respectively.

Figure 4 shows a nickel sphere with a diameter of 8 mm and single diamond used as the probe tip. They are used for electroplating the abrasives on a saw wire and the abrasives, respectively. In the experiments mentioned later, the track width by

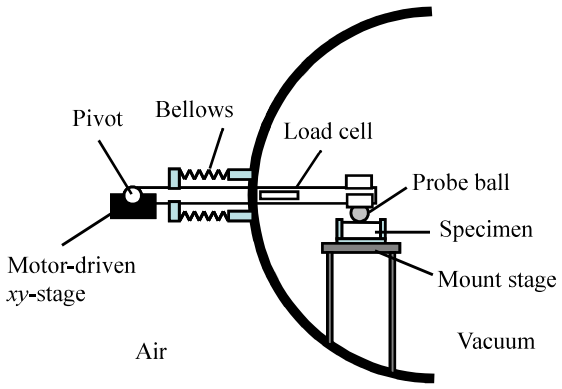

FIGURE 2. Friction tester for vacuum

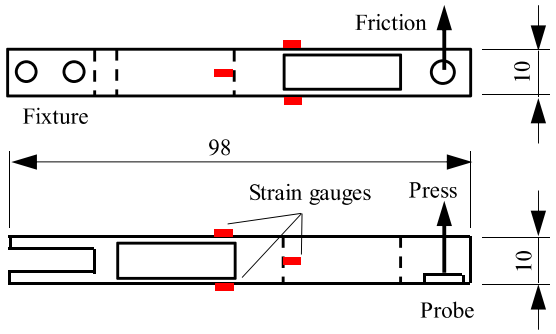

FIGURE 3. Top and side views of two-axis load cell with strain gauges.

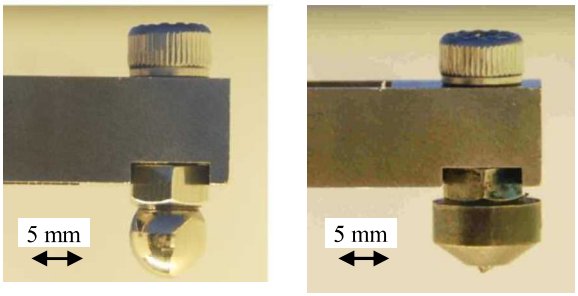

(a) Nickel sphere. (b) Diamond tip.
FIGURE 4. Friction test probes.

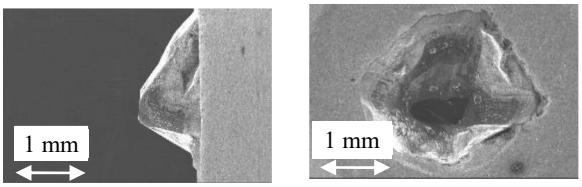

(c) Side view. (d) Bottom view.
FIGURE 5. Expanded view of diamond tip after electrical discharge machining with assisted electrode.

rubbing the nickel sphere was 0.5 mm so that the diamond tip was flattened to a 0.5-mm square by electrical discharge machining (EDM) with an assisted electrode [4]. They were glued onto a nut and fixed on the load cell with a bolt. Because the diamond tip was not worn at all after all the friction tests, it was not changed. The nickel sphere was changed at the beginning of every test. Plates made of glass (SiO_2) and alumina (Al_2O_3) which are major components of basalt, and basal itself were used for the specimens. All combinations were tested. The basalt and alumina plates were finished by buffing. The surface roughness of the basalt, glass and alumina plates was 2.7, 0.15 and 0.28 μmRa, respectively. The pore area on the basalt plate was 19%.

TABLE 1. Conditions for friction tests.

Load	2 N
Stroke	10 mm
Speed	10 mm/s (0.6 m/min)
Number of reciprocation	5000
Probe	Nickel ball, diamond
Specimen plate	Basalt, Nickel, Alumina, Glass
Environment	Air, Vacuum (3.5×10^{-3} Pa)

Table 1 shows the conditions for the friction tests. In the wire-sawing machine, the feeding length of the saw-wire was 10 m per reciprocating stroke and 150 m for 15 reciprocating strokes in total. To equalize the slipping distance, the stroke and number of reciprocations were 10 mm and 5000, respectively. Consequently, the total slipping distance was 100 m. The hertz stress at each abrasive was estimated as 144 MPa in wire-sawing. In case that the normal load was 2 N at which the normal load was stable, the hertz stress was 400-1200 MPa at the nickel sphere.

EXPERIMENTS

Firstly, a friction test between the nickel sphere and basalt was carried out. In air, the average normal and friction forces, and coefficient were 2.1 and 1.4 N, and 0.67, respectively. In vacuum, they were 2.3 and 0.8 N, and 0.35, respectively. The friction coefficient in vacuum was smaller than that in air. The excitation of resonance by stick-slip varied the normal load. By the components analysis by EDX (energy dispersive X-ray spectrometry), oxygen was detected on the surface of the nickel sphere tested in air. The toughness and hardness of an oxide were generally decreased and increased, respectively. In addition, the diamond is much harder than the others. Consequently, debris were generated. The basalt and nickel hardly adhered each other. The affinity between the basalt and nickel was low. In actual machining, worn nickel debris adhered cracks and pores on basalt.

Figure 6 shows the friction forces between the diamond tip and basalt. In air, the average normal and friction forces, and coefficient were 2.2 and 0.3 N, and 0.09, respectively. In vacuum, they

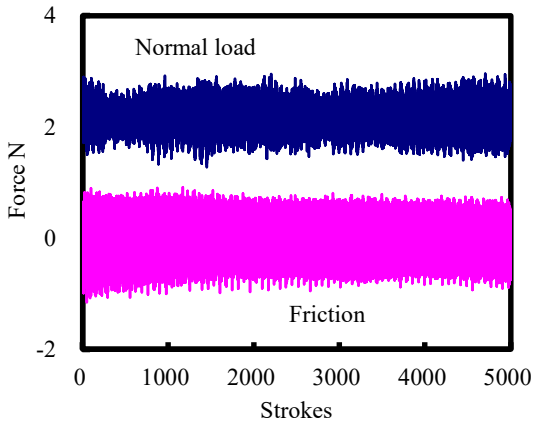

(a) In air.

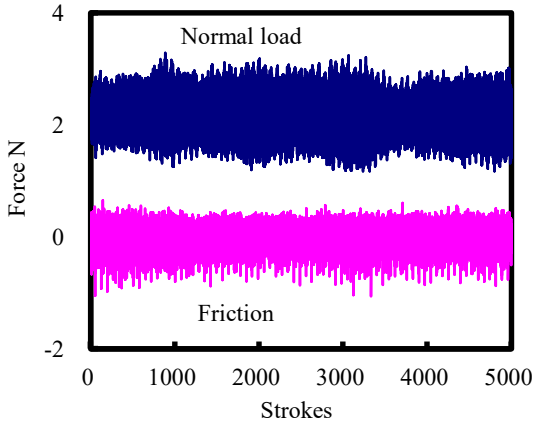

(b) In vacuum.

FIGURE 6. Friction between diamond tip and basalt surface.

were 2.1 and 0.2 N, and 0.14, respectively. In vacuum, the normal load was more fluctuated by unevenness of the surface, and the friction coefficient was small. Debris due to abrasive wear was adhered both on the diamond tip and basalt surface.

The surface of basalt after friction test in air was flat due to wear as shown in Fig. 7 (a). A larger amount of debris adhering by electrification was observed on the surface after friction test in vacuum as shown in Fig. 7 (b). The diamond tip slipped on the debris pressed with the diamond as shown in Fig. 8. The share force of the debris in vacuum was smaller than friction force by contacting the diamond and basalt directly.

The diamond abrasives possibly slip also on the adhered nickel in actual machining. To analyze

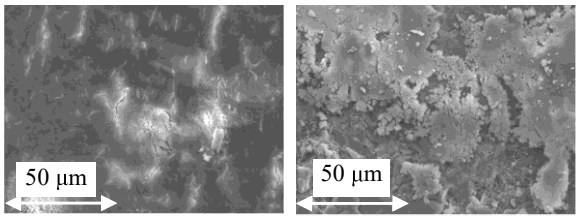

(a) In air. *(b) In vacuum.*

FIGURE 7. Basalt surface after friction test (vs. diamond).

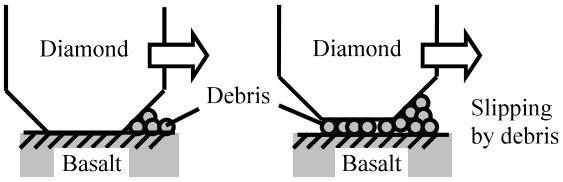

(a) In air. *(b) In vacuum.*

FIGURE 8. Influence of debris.

this, a friction test between the diamond tip and nickel plate was carried out under the same conditions shown in Table 1 except a reciprocation of 500 times. Figure 9 shows a nickel plate after a friction test in air. Worn nickel debris was observed on the whole track as shown in Fig. 9 (a). In particular, flakes of several tens of micrometers were observed on the boundaries of the track as shown in Fig. 9 (d). The surface was oxidized and oxygen was observed by EDX as shown in Fig. 9 (b). Figure 10 shows a nickel plate after a friction test in vacuum. In vacuum, metal is not oxidized and is still soft during machining [5]. Plastic flow of nickel was observed on the track, especially boundaries of the track as shown in Fig. 10 (d). Oxygen was seldom observed there as shown in Fig. 10 (b).

Figure 11 shows atomic percent of components on the rubbed nickel surface. After the friction test in air, oxygen was increased from 1.1 to 17.8% by the oxidation. However, it was not changed after the friction test in vacuum.

From the friction tests described above, the toughness and brittleness of nickel were increased by the oxidation so that it was removed with the diamond abrasives due to fracture. In vacuum, because there was no oxygen, nickel was not oxidized. Then, the toughness was not decreased and the surface was deformed as the plastic flow. Consequently, the diamond abrasive

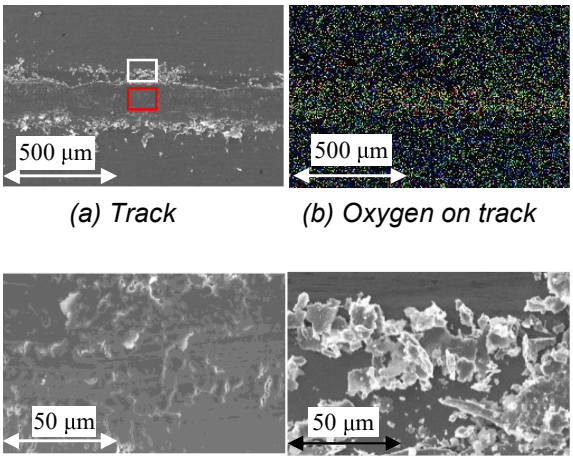

(a) Track (b) Oxygen on track

(c) Middle (red frame). (d) Boundary (white frame).

FIGURE 9. Nickel surface after friction test in air (vs. diamond).

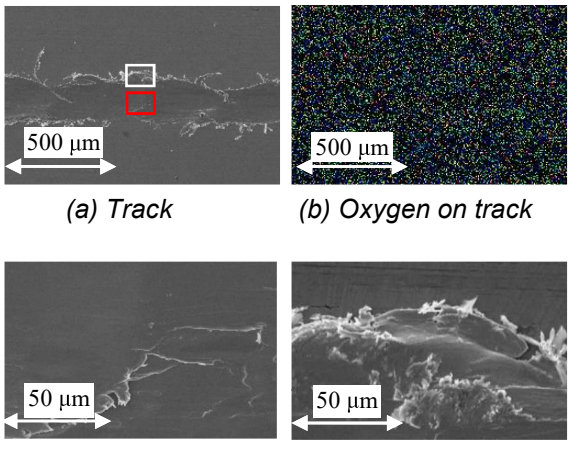

(a) Track (b) Oxygen on track

(c) Middle (red frame). (d) Boundary (white frame).

FIGURE 10. Nickel surface after friction test in vacuum (vs. diamond).

slipped on the adhered nickel covering the rock surface and the rock surface was not removed.

CONCLUSIONS

In this paper, the friction tests among nickel, diamond and basalt in air and vacuum were compared. The reason why the rock is hardly cut in vacuum is that nickel which is not oxidized in vacuum is hardly removed as debris during rubbing.

The authors thank Dr. Kensei Kaneko of Toyota Technological Institute (currently National Institute of Technology, Nagaoka College) for machining of the diamond tip by EDM.

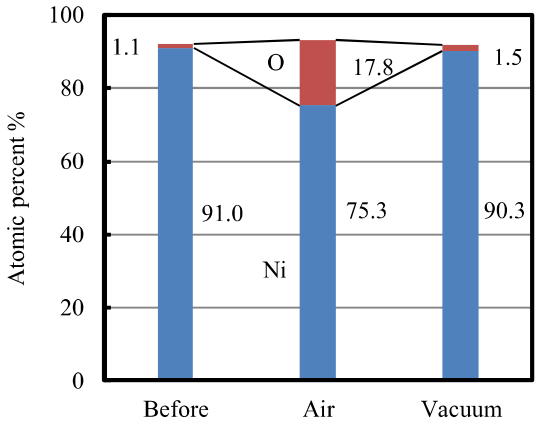

FIGURE 11. Atomic percent of components on rubbed surface of nickel with diamond.

REFERENCES

[1] Furutani K, Fukunaga S, Okada T, Saiki K, Ohue H. Effect of Vacuum on Wire-sawing as Preliminary Experiment to Lunar Exploration. Proceedings of 2011 Annual Meeting of American Society for Precision Engineering, Denver, CO. 2011; 349-352.

[2] Furutani K, Inukai R, Takano T, Okada T, Saiki K, Ohue H. Measurement of Saw Wire Temperature during Cutting of Rock in Vacuum. Proceedings of 2014 Annual Meeting of American Society for Precision Engineering, Boston, MA. 2014; 508-511.

[3] Furutani K, Inukai R, Takano T, Okada T, Saiki K, Ohue H. Estimation of Saw Wire Temperature during Machining of Rock in Vacuum. Proceedings of 2018 Annual Meeting of American Society for Precision Engineering, Las Vegas, NV. 2018; 273-276.

[4] Mohri N, Fukuzawa Y, Tani T, Saito N, Furutani K. Assisting Electrode Method for Machining Insulating Ceramics. CIRP Annals. 1996; 45 (1): 201-204.

[5] Tanaka Y, Ueguchi T. Grinding in Vacuum (4th Report). Journal of Japan Society for Precision Engineering. 1967; 33(4): 260-265.

STRUCTURED LIGHT SCANNING FOR ENDMILL MODELING

Timothy No, Michael Gomez, Ryan Copenhaver, and Tony L. Schmitz
Department of Mechanical, Aerospace, and Biomedical Engineering
University of Tennessee, Knoxville, TN, USA

INTRODUCTION

Multi-axis machining is a cornerstone manufacturing capability for discrete part production. Technology improvements are consistently pursued and implemented to increase productivity and efficiency. This includes new designs for: machines, controllers, spindles, holders, and tools. For endmills, design modifications to the cutting teeth include non-uniform spacing (or pitch), variable helix angle from one tooth to the next and along a single cutting edge, edge honing, and serrated edge geometry, among others. The purpose of these design updates are to affect chip formation and disturb the tooth-to-tooth chip thickness regeneration that serves as the mechanism for self-excited vibration, or chatter, in endmilling operations. While modeling of machining operations has received continuous international attention since the mid-20th century (see [1-3] for comprehensive overviews), relatively less effort has been expended on modeling the behavior of these non-standard geometry endmills, particularly those with serrated cutting edges. Notable exceptions include [4-8].

In this paper, a complete solution for modeling the behavior of non-standard edge geometry endmills is provided. The procedure includes: 1) structured light scanning to produce a solid model of the endmill; 2) identification of the spatial coordinates for the points that define the cutting edges; 3) analysis of those points to extract the cutting edge radius and angle at equally spaced slices along the tool axis; 4) simulation of the cutting force and tool/workpiece deflection using the measured edge geometry; and 5) periodic sampling of the simulation outputs to analyze stability.

SCANNING METROLOGY FOR EDGES

A primary challenge associated with modeling the performance of non-standard edge geometry endmills is that the design details are not generally available. To overcome this obstacle, the reverse engineering capabilities made possible by scanning metrology can be leveraged. One strategy for collecting point clouds from complex surfaces to develop the corresponding solid model is structured light, or fringe, projection. In this technique, a common approach is to project a pattern of parallel lines onto the surface in question. The reflected lines are distorted due to the surface geometry. The measurement system uses the relative positions of the projector and one or more cameras (two cameras is typical) together with the distorted lines to reconstruct the three-dimensional surface. While many commercial options are available, the GOM ATOS Capsule system was used for this research.

The measurements proceeded by first preparing the endmill surface using a removable anti-glare coating and attaching reference targets to the shank surface to enable multiple measurements to be stitched together and generate the solid model. Multiple scans were then completed to obtain the point cloud and 3D model. Figures 1-2 display results for an endmill from Walter Tools (part number 3D1163-6768616). Figures 3-4 present results for a Niagara endmill (part number N68949).

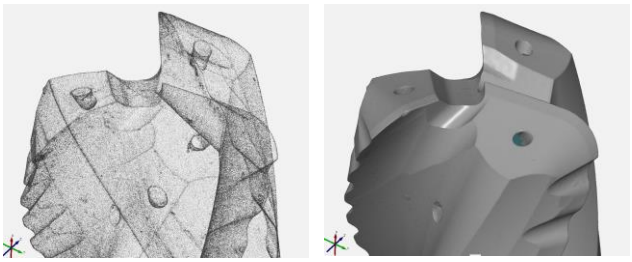

Figure 1. Point cloud (left) and model (right) for Walter Tools endmill obtained from scanning.

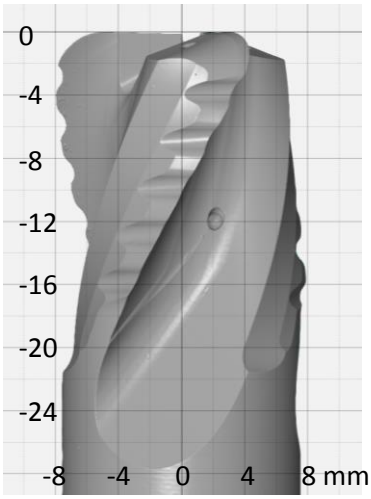

Figure 2. Scale for Walter Tool endmill to visualize edge geometry.

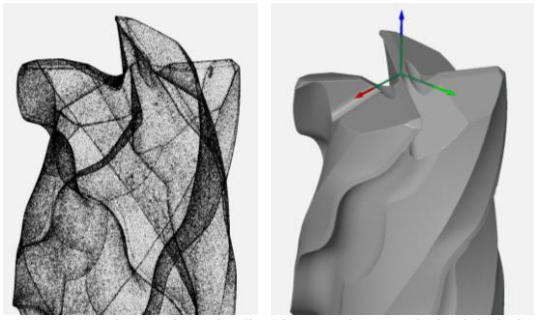

Figure 3. Point cloud (left) and model (right) for Niagara endmill.

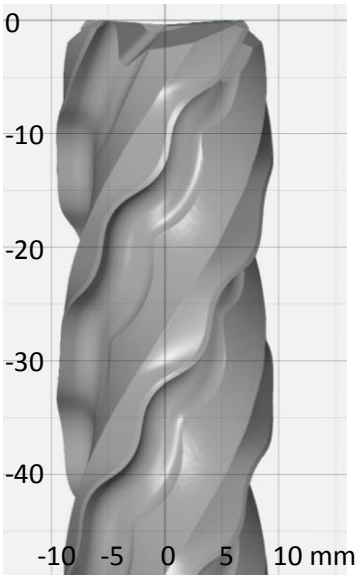

Figure 4. Scale for Niagara 3D model to visualize edge geometry.

The procedure used to extract the edge coordinates from the solid model included four steps.

- First, using the best fit cylinder to the tool shank and the fluted end's extreme point, the origin was established on the tool's center line.
- Second, the points located on the cutting edges were selected. This step required manual manipulation within the GOM software. In function, it was analogous to updating driving directions in Google Maps by dragging the original route to new roads.
- Third, the radius, r, and angle, ϕ, for each edge point was calculated. The teeth angles were normalized to a selected tooth and constrained to values between 0 and 360 deg; the z value (tool axis) was retained to obtain a triplet, {r, ϕ, z} for each point.
- Fourth, because the point density was higher than required for the time domain simulation, linear interpolation was used to obtain the triplet for axial slices located every 0.1 mm over the full flute length; see Fig. 5, which shows the origin, edge points, and axial slices for the Walter Tool endmill.

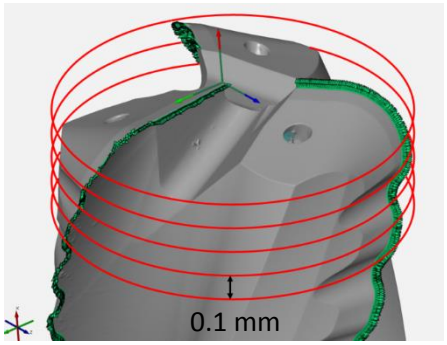

Figure 5. Cutting edge points and axial slices (not to scale) for linear interpolation. The origin is also identified (Walter Tool).

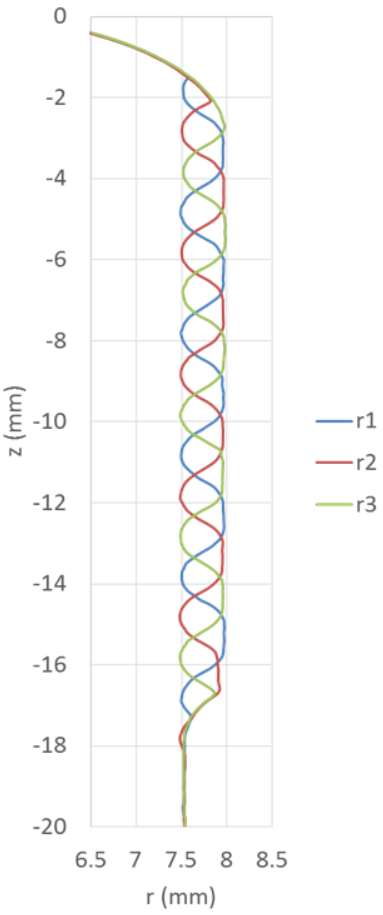

Figure 6. Radius value at each axial slice for all three endmill teeth (Walter Tool).

Example radius results for the Walter Tool endmill are provided in Fig. 6. It is observed that the specialized tool geometry incorporates large radius variation along the cutting edge and that these radius variations are phased from one tooth to the next (120 deg spacing between the peaks for the three teeth). For each tooth the angle variation from the nominal helix, $\Delta\phi$, was not significant. The mechanism for increased stability with this design is, therefore, the segmentation of the cutting edge into bands using the radius variation. This effectively reduces the axial depth of cut, while simultaneously increasing the chip thickness. Also, the point cloud data was used to determine the macro-geometry: 8 mm shank radius, 28.3 deg helix angle, and 2.785 mm bull nose radius.

Angle results for the Niagara endmill are provided in Fig. 7, where the angle variation is periodic and progressively offset by 90 deg between teeth. There is no appreciable radius variation in this case. The mechanism for increased stability with this design is, therefore, disruption of regeneration from one tooth to the next by the variable pitch. The point cloud data was used to determine the macro-geometry: 9.5 mm shank radius and 35.1 deg helix angle.

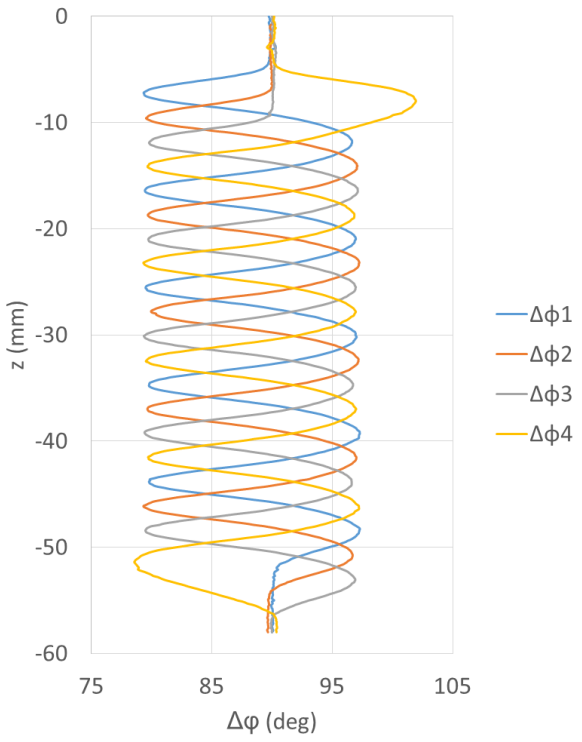

Figure 7. Deviations of teeth angles from nominal helix (Niagara).

TIME DOMAIN SIMULATION

Time domain simulation enables numerical solution of the coupled, time-delay equations of motion for milling in small time steps [1]. It is well suited to incorporating the inherent complexities of milling dynamics, including complicated tool geometries (runout, or different radii, of the cutter teeth, non-uniform teeth spacing, and variable helix) and the nonlinearity that occurs if the tooth leaves the cut due to large magnitude vibrations. The simulation applied here is based on the regenerative force, dynamic deflection model described in [1]. As opposed to analytical or semi-analytical stability maps that provide a global picture of the stability behavior, time domain simulation provides information regarding the local cutting force and vibration behavior for the selected cutting conditions. The simulation used in this study is described in the following paragraphs.

The strategy used to model the large radius variation for each tooth on the Walter Tool endmill (Fig. 6) was to define a nominal tooth shape with no serration and then incorporate the radial deviation as runout. It is observed in Fig. 6 that tooth 3 follows the nominal bull nose profile up to the shank diameter. The tooth 3 geometry was therefore selected as the reference up to -2.4 mm. The radius was set to a constant value of 7.974 mm (i.e., the value at -2.4 mm) for *z* values of -2.5 mm and beyond. The runout was then determined for each tooth as the difference between the reference profile and the actual radius value at each *z* interval. The peak-to-peak variation was 0.48 mm. For the Niagara endmill, the runout was small, but the intentional *z*-dependent pitch was incorporated by specifying the tooth angle at each *z* location using the interpolated data from the 3D model edge identification.

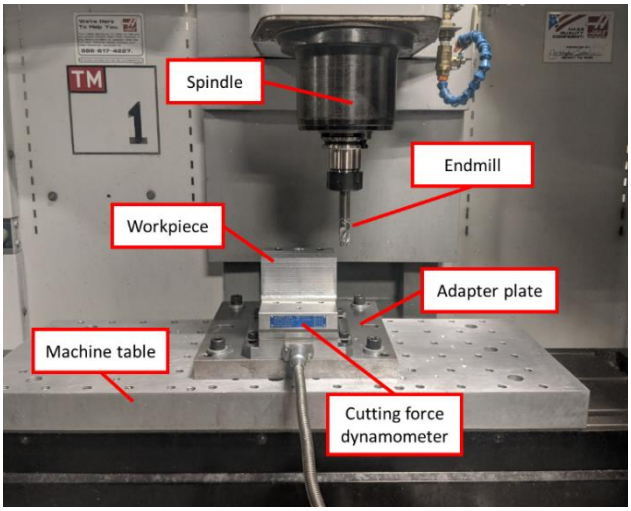

Figure 8. Experimental setup for milling force measurement.

EXPERIMENTAL SETUP

The experimental setup for milling force measurement is shown in Fig. 8. Trials were completed on a Haas TM-1 three-axis computer numerically controlled (CNC) milling machine. The 7075 aluminum workpiece was mounted on a cutting force dynamometer (Kistler 9257B) and the endmill was clamped in a collet holder and inserted in the CAT-40 spindle interface. For the Walter Tool endmill, tests were performed at axial depths of cut from 4 mm to 14 mm. The commanded feed per tooth for these down (climb) milling experiments was 75 µm/tooth, the spindle speed was 4000 rpm, and the radial depth of cut was 2 mm (12.5% radial immersion). The tool and workpiece frequency response functions, or FRFs, were measured by impact testing, where an instrumented hammer is used to excite the structure and the response is measured using a linear transducer (a low-mass accelerometer for this research). These were used in the simulation.

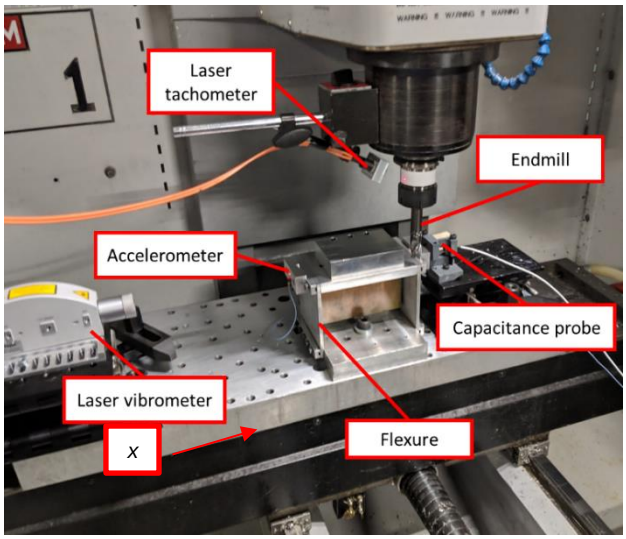

Figure 9. Experimental setup for stability testing.

For the Niagara endmill, tests were performed at axial depths of cut from 5 mm to 25 mm. The commanded feed per tooth for these down (climb) milling experiments was 100 µm/tooth, the spindle speed was 300 rpm, and the radial depth of cut was 1.9 mm (10% radial immersion). The FRFs were again measured and the modal parameters were extracted for use in the time domain simulation.

The setup for the Walter Tool endmill stability testing was similar to Fig. 8, but the aluminum alloy workpiece was mounted on a parallelogram, leaf-type flexure rather than the dynamometer (the flexible direction for the flexure was oriented parallel with the machine's *x* direction); see Fig. 9. Note that the workpiece (flexure) *x* direction was significantly more flexible than the tool or flexure *y* direction.

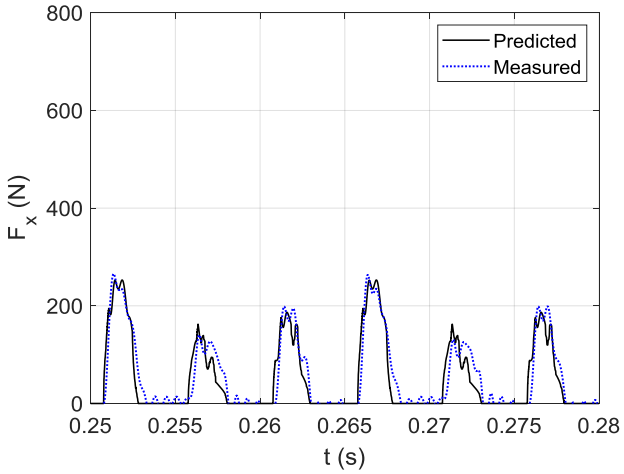

Figure 10. Measured and predicted force for b = 4 mm (Walter Tool).

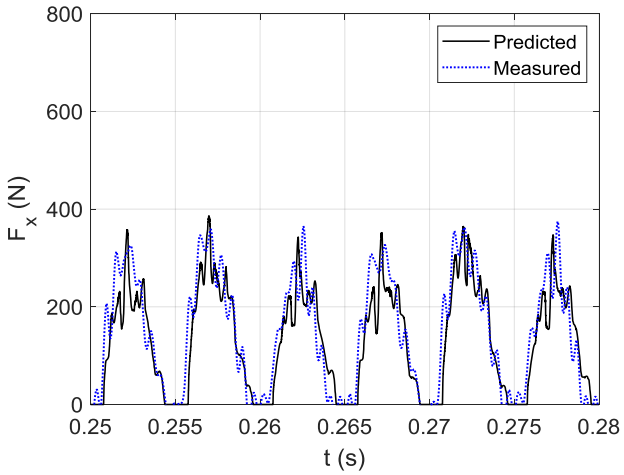

Figure 11. Measured and predicted force for b = 14 mm (Walter Tool).

RESULTS

Forces for Walter Tool endmill

Measured and predicted feed direction force values, F_x, for b = 4 mm and 14 mm are shown in Figs. 10-11. Good agreement is observed, although the dynamometer's structural dynamics added oscillations to the measured force. It is seen that the force progresses from a smoother profile while engaged in the cut for b = 4 mm to highly discontinuous at b = 14 mm. This is the result of the tool design which cuts with approximately 1 mm wide "bands" of limited axial depth, where the local radius is close to the shank diameter. These bands are separated on each cutting edge by the approximately 2.5 mm spatial period of the radius

variation along the tooth helix (see Figs. 2 and 6). As the axial depth increases, more bands are individually engaged (with a larger than commanded chip thickness) and the force is subsequently increasingly discontinuous even though all cuts are stable (forced vibration only).

Forces for Niagara endmill

Measured and predicted feed direction force values for *b* = 5 mm and 20 mm are shown in Figs. 12-13. As shown in Figs. 4 and 7, the spatial period for the pitch angle variation is approximately 10 mm. The force profile progresses from a typical down milling signal for *b* = 5 (Fig. 12), where the pitch angle variation is not fully incorporated, to nearly constant at *b* = 20 mm (Fig. 13), where two full spatial periods are engaged.

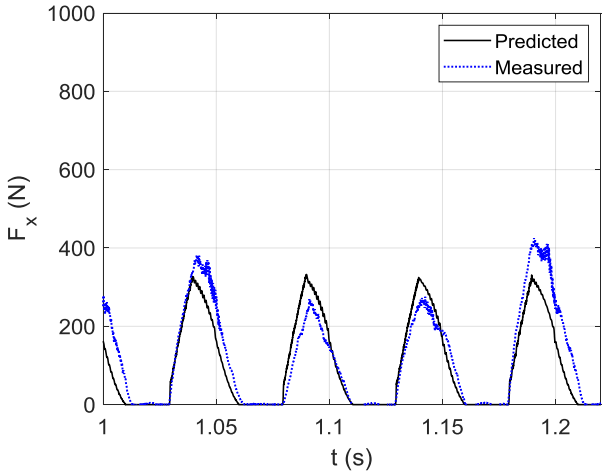

Figure 12. Measured and predicted force for b = 5 mm (Niagara).

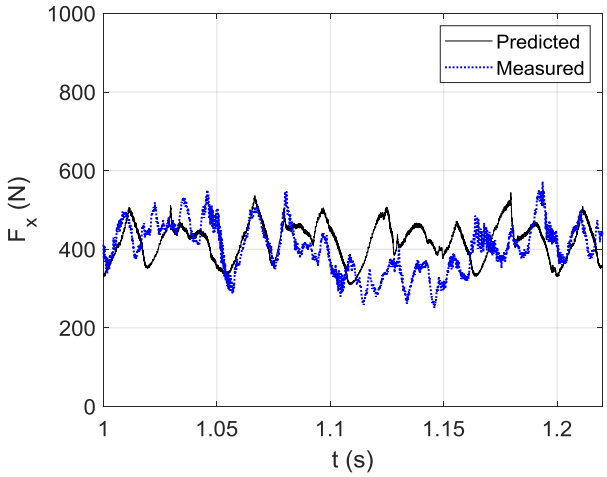

Figure 13. Measured and predicted force for b = 20 mm (Niagara).

Stability prediction and validation for Walter Tool endmill

Given the validated force results, stability testing was completed using the Fig. 9 setup. Workpiece (flexure) displacement and velocity predictions were generated using the time domain simulation. The down milling radial depth of cut was 3 mm and the commanded feed per tooth was 100 μm/tooth for all tests.

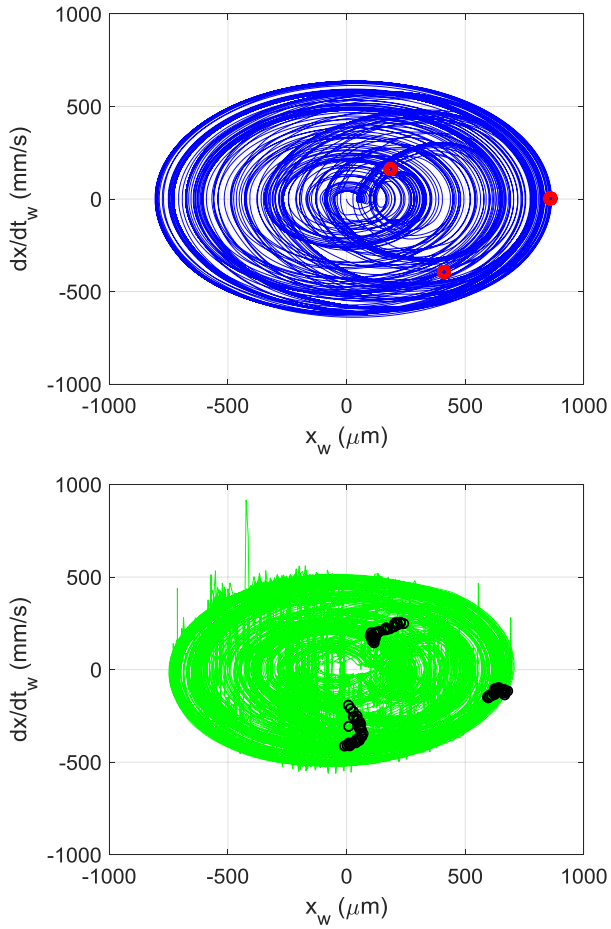

Figure 14. Poincaré maps for period-3 bifurcation at {2750 rpm, 10 mm}. (Top) predicted. (Bottom) measured. The local jumps in measured velocity are due to chips passing through the laser beam.

To establish stability, the workpiece *x* direction displacement and velocity signals were sampled once per revolution (i.e., at the spindle rotating frequency) [9]. The laser tachometer shown in Fig. 9 was used to generate the sampling signal. This periodic sampling approach was used to determine if the milling response was synchronous with the spindle rotation (or not) by constructing Poincaré maps (i.e., the periodically sampled displacement

was plotted versus the periodically sampled velocity) for both experiment and prediction. To interpret these Poincaré maps, if the cut is stable (i.e., it exhibits forced vibration only), the data repeats with each spindle revolution and the sampled points appear at one location. If self-excited vibration (i.e., regenerative chatter, or secondary Hopf bifurcation) occurs, however, an elliptical distribution of sampled points is observed due to the presence of both the (generally) incommensurate chatter frequency and the tooth passing frequency (and its harmonics). Additionally, period-*n* bifurcations can occur, where *n* represents the number of periods between repetition. A period-3 bifurcation, for example, exhibits motion that repeats every three rotations. Results are presented in Figs. 14-15 for two spindle speed-axial depth combinations, where the once-per-revolution samples (circles) are superimposed on the continuous *x* direction workpiece displacement, x_w, and velocity, dx/dt_w. Good agreement is observed in each case.

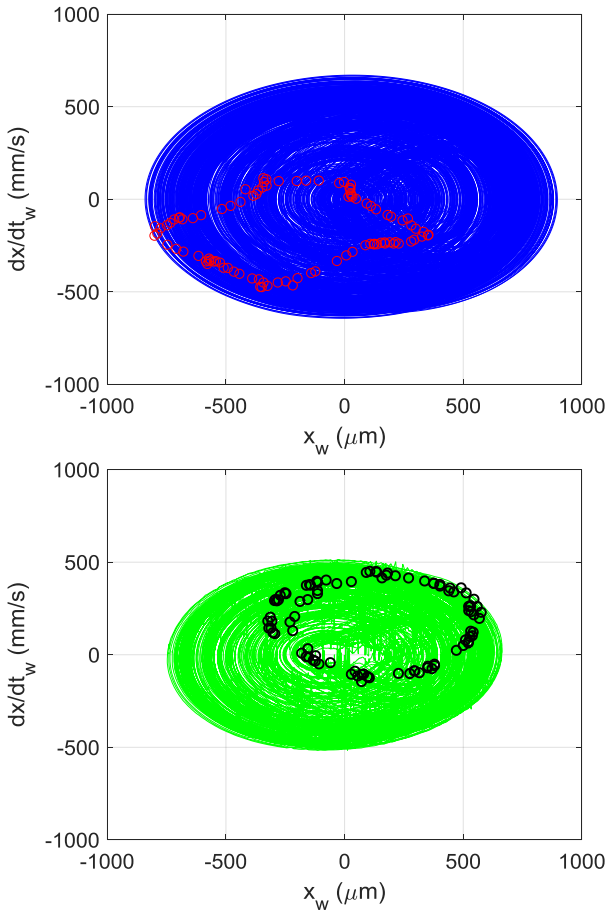

Figure 15. Poincaré maps for fully developed regenerative chatter (secondary Hopf bifurcation) at {2850 rpm, 10 mm}. (Top) predicted. (Bottom) measured.

CONCLUSIONS

This paper provides a reverse engineering solution for modeling the behavior of non-standard edge geometry endmills. Structured light scanning was used to produce a solid model of two different endmills. From these models, spatial coordinates for the points that define the cutting edges were extracted. The points were used to determine the cutting edge radius and angle at equally spaced points along the tool axis. The cutting edge geometry was then incorporated in a time domain simulation that was used to predict cutting force and tool/workpiece deflection for user-selected operating parameters.

ACKNOWLEDGEMENTS

This material is based on work supported by the National Science Foundation under Grant No. CMMI-1561221.

REFERENCES

[1] Schmitz, T.L. and Smith, K.S., 2009, Machining Dynamics: Frequency Response to Improved Productivity, Springer, New York, NY.

[2] Altintas, Y., 2012, Manufacturing Automation: Metal Cutting Mechanics, Machine Tool Vibrations, and CNC Design, Cambridge University Press.

[3] Altintas, Y. and Weck, M., 2004, Chatter stability of metal cutting and grinding, CIRP Annals-Manufacturing Technology, 53/2: 619-642.

[4] Wang, J.-J. and Yang, C.S., 2003, Angle and frequency force models for a roughing end mill with a sinusoidal edge profile, International Journal of Machine Tools and Manufacture, 43: 1509-1520.

[5] Merdol, S.D. and Altintas, Y., 2004, Mechanics and Dynamics of Serrated Cylindrical and Tapered End Mills, Journal of manufacturing Science and Engineering, 126: 317-326.

[6] Dombovari, Z., Altintas, Y., and Stepan, G., 2010, The effect of serration on mechanics and stability of milling cutters, International Journal of Machine Tools and Manufacture, 50: 511-520.

[7] Grabowski, R., Denkena, B., and Köhler, J., 2014, Prediction of process forces and stability of end mills with complex geometries, Procedia CIRP, 14: 119-124.

[8] Tehranizadeh, F., and Budak, E., 2017, Design of serrated end mills for improved productivity, Procedia CIRP, 58: 493-498.

[9] Honeycutt, A. and Schmitz, T., 2017, Milling stability interrogation by subharmonic sampling, Journal of Manufacturing Science and Engineering, 139/4: 041009.

LASER DOPPLER VIBROMETRY FOR MACHINING DYNAMICS ANALYSIS

Michael Gomez[1], Emma Betters[1], Jerome Eichenberger[2], Thomas S. Delio[3], and Tony L. Schmitz[1]
[1]Department of Mechanical, Aerospace, and Biomedical Engineering, University of Tennessee, Knoxville, TN, USA
[2]Polytec, Inc., Irvine, CA, USA
[3]Manufacturing Laboratories Inc., Las Vegas, NV, USA

INTRODUCTION

Optimizing machining operations in discrete part production remains a critical step in the realization of productivity enhancement, yield improvement, reject rate reduction, improved surface finish, increased part accuracy, and reduced tool wear. Production environments typically rely on the skill and experience of process planners and machinists to select tools and cutting conditions. Handbooks and tool catalogs are often applied as a resource, but these usually supply conservative cutting conditions that may reduce productivity due to suboptimal use of machining capability [1-3]. Because the vibration level depends on the relationship between the tooth passing frequency (i.e., the product of the rotating speed and number of teeth) and the system natural frequencies (e.g., the first bending mode of the endmill), spindle speed and, therefore, cutting speed selection is critical [1-2]. Due to these complications, an important ongoing research area is establishing effective methods for optimizing machining operations.

In this paper, in-process laser Doppler vibrometer measurements are used to assess stability and tool wear for milling a low carbon steel alloy. A comparison of the wear rate for stable resonant and non-resonant cutting speeds is also provided and correlated to the measured vibration signals.

LASER VIBROMETRY

The use of laser Doppler vibrometers (LDVs) as vibration transducers for machining dynamics analysis is common [4-9]. This provides noncontact measurement with high accuracy from a distance [5, 10-11]. LDVs measure motion using the Doppler frequency shift of the laser light reflected from the moving target surface [10].

The LDV used in this study was a Polytec OFV 5000 controller/OFV 534 laser head, which was able to simultaneously measure displacement and velocity. This enabled Poincaré maps to be generated that describe machining behavior graphically. The velocity decoder VD-09 and displacement decoder DD-900 provided ranges from 5 mm/s/V to 1 m/s/V and 50 nm/V to 5 mm/V [10]. A tracking filter was used due to "low backscattered light" [11]. The speckled nature of laser light on a diffuse surface can lead to brief moments when the amount of backscattered light is reduced. The tracking filter bridges these intervals using a phase-locked loop to provide clean data traces [10-11].

EXPERIMENTAL SETUP

The experimental setup for milling stability verification and tool wear is shown in Fig 1. The flexure and tool point dynamics were measured by impact testing, where an instrumented hammer (PCB 086C04) was used to excite the structure and the response was measured using a low mass accelerometer (PCB 352C23).

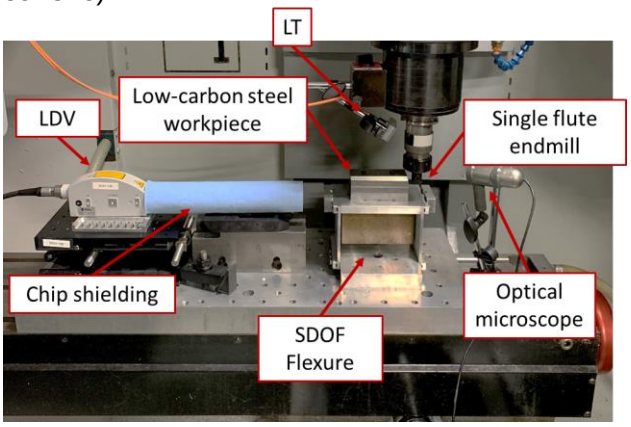

FIGURE 1. Experimental setup for milling stability and tool wear testing.

Cutting tests were performed on a Haas TM-1 computer numerically-controlled (CNC) vertical milling machine. A low carbon steel alloy workpiece was mounted on a parallelogram, leaf-type flexure. The compliant direction for the flexure was oriented parallel to the machine's x (feed) direction; see Fig. 2. A single flute, 19.05 mm diameter, 30 deg helix endmill was used to perform machining passes at a 4.76 mm radial depth of cut (25% radial immersion) and 2 mm axial depth of cut. Once-per-tooth sampling was achieved using a laser tachometer (LT), where a reflective target was attached to the rotating tool holder. In situ vibration signals were collected using

the LDV. An optical microscope (DinoLite Pro-AM4137) was used to record the flank wear width for the cutting edge (FWW) at regular intervals during the tool wear testing.

First, milling stability was predicted using a time domain simulation and then verified by the measured vibration signals obtained during the machining process. For the purposes of simulation, the tool was considered rigid with respect to the flexure. This assumption is confirmed by the frequency response function (FRF) measurements shown in Fig. 3 and the modal parameters listed in Table 1. Second, tests were carried out to monitor tool wear progression for resonant and non-resonant cutting speeds.

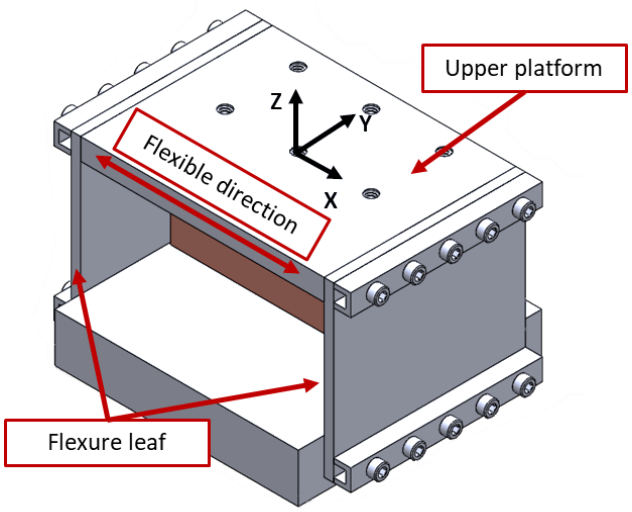

FIGURE 2. Single degree of freedom flexure.

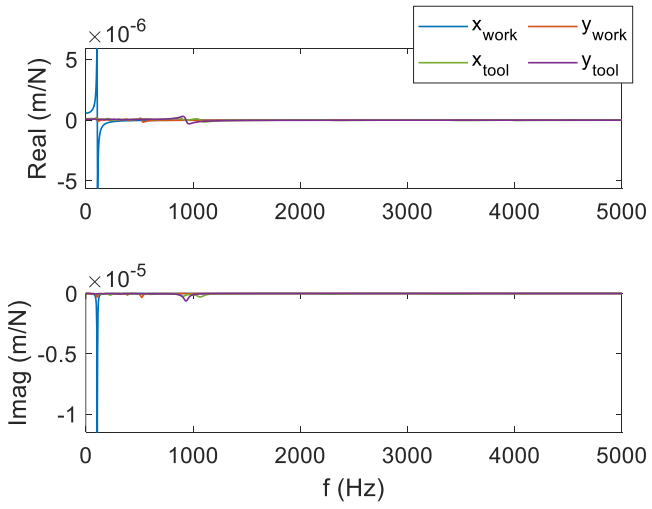

FIGURE 3. Measured FRFs of the tool and workpiece for the stability and tool wear testing.

TABLE 1. Modal parameters for milling simulations (mass, m, stiffness, k, and damping coefficient, c).

Direction	m (kg)	k (N/m)	c (N-s/m)
Tool			
x (feed)	0.88	5.0×10^7	1330
y	0.88	5.0×10^7	1330
Workpiece			
x (feed)	3.89	1.74×10^6	125
y	0.88	5.0×10^7	1330

RESULTS

Stability

A time domain simulation was used to predict the forces and displacements during milling. It was based on the "Regenerative Force, Dynamic Deflection" model described by Smith and Tlusty [12]. The simulation proceeded as follows.

- The instantaneous chip thickness was determined using the vibration of the previous and current teeth and commanded chip thickness at the selected tooth angle.
- The cutting force components were calculated as the product of the chip width (axial depth), chip thickness, and cutting force coefficients.
- The force was used to find the new displacement by modified Euler (numerical) integration of the second order, time delay differential equations of motion.
- The tooth angle was incremented and the process was repeated.

The simulation accounts for the non-linearity that can occur if the tooth leaves the cut due to large vibrations. It can also accommodate cutter teeth runout, variable teeth spacing, and variable helix angles [1, 12].

Stability testing was completed using the Fig. 1 setup. Workpiece (flexure) displacement and velocity predictions were generated using the time domain simulation and compared to measured signals. Stability lobe validation was achieved by selecting stable and unstable combinations of spindle speed and axial depth of cut and evaluating the behavior.

Simulations were completed over a grid of equally spaced points in spindle speed and axial depth. To establish stability, the workpiece x direction displacement and velocity signals were sampled once-per-tooth (i.e., at the tooth passing frequency) [8-9]. This periodic sampling approach was used to determine if the milling response was synchronous with the tooth passing frequency or not. Synchronous motion indicates stable behaviour, while anything else indicates unstable behaviour.

To automatically determine stability, a metric was applied where the absolute values of the differences in pairs of sequentially sampled points was summed

and then normalized to the number of sampled points. For forced (synchronous) vibration, the points repeat so this metric is ideally zero. For other behaviors, it is greater than zero [9]. Figure 4 shows a stability map produced using this metric. The dots indicate stable (forced vibration) performance. The circles identify period-2 bifurcations, where the motion repeats every other tooth passage (also referred to as period doubling bifurcations). The open area indicates all other bifurcation types, including secondary Hopf and higher-order period-n bifurcations (n = 3, 4, …). In Fig. 5, the stable behaviour (white zone) is separated from other bifurcation types by the stability limit (solid line). The test points are also identified.

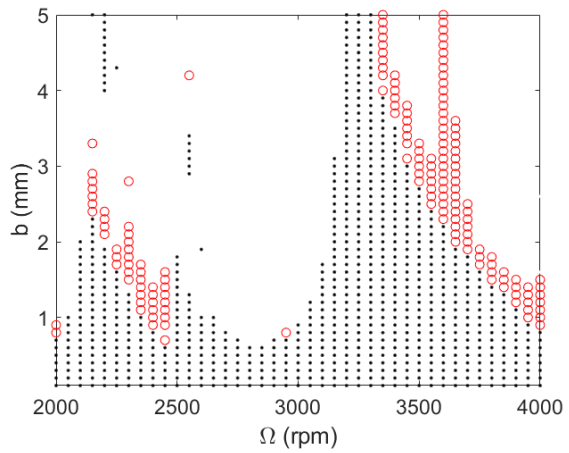

FIGURE 4. Predicted stability map for down milling at a 4.76 mm radial depth (25% radial immersion) and 150 μm/tooth feed using the Table 1 dynamics. The grid contains 2000 points.

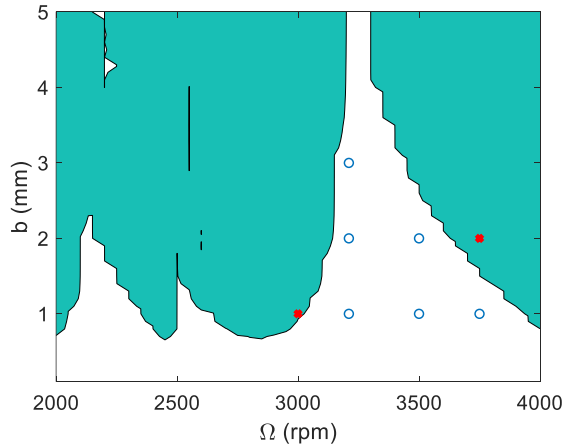

FIGURE 5. Predicted stability map with test points. Open circles were stable and filled were unstable.

The once-per-tooth sampling strategy was also used to produce Poincaré maps, where the time synchronized LDV displacement and velocity are plotted in the phase plane. The results of this approach are presented in Figs. 6-8 for the 2 mm axial depth of cut trials.

Figures 6 and 7 demonstrate stable cuts, where the once-per-tooth samples repeat. Note the change in scale between the two figures; the workpiece motion at resonance (i.e., where the tooth passing frequency is near the flexure's natural frequency) is much larger than the motion when not at resonance. However, both exhibit only a single grouping of points in the Poincaré map, which indicates forced vibration and stable operation.

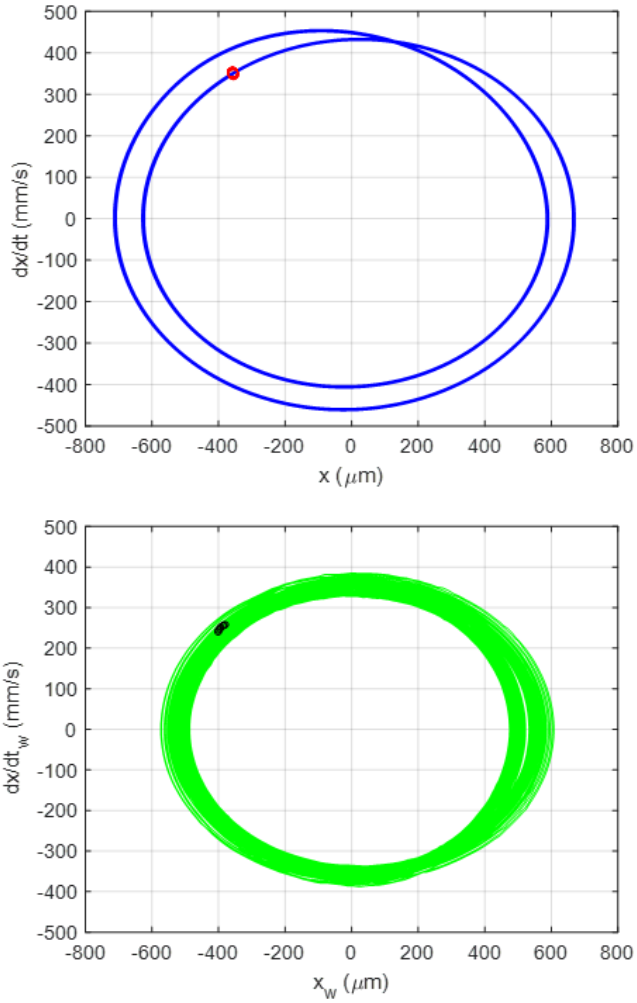

FIGURE 6. Poincaré maps for stable cutting at resonance {3210 rpm, 2 mm}. (Top) predicted. (Bottom) measured.

Figure 8, on the other hand, does not show a single grouping of periodically sampled points. Rather, an elliptical distribution is observed. This means that the behaviour changes from one tooth passage to the next. The elliptical shape is indicative

of a secondary Hopf bifurcation, or classic self-excited vibration caused by regeneration of the machined surface. In other words, the chip thickness for the current tooth depends on the commanded chip thickness (defined by the feed per tooth and cutter angle), the vibration state now, and the surface left behind by the previous tooth.

FIGURE 7. Poincaré maps for stable cutting away from resonance {3500 rpm, 2 mm}. (Top) predicted. (Bottom) measured.

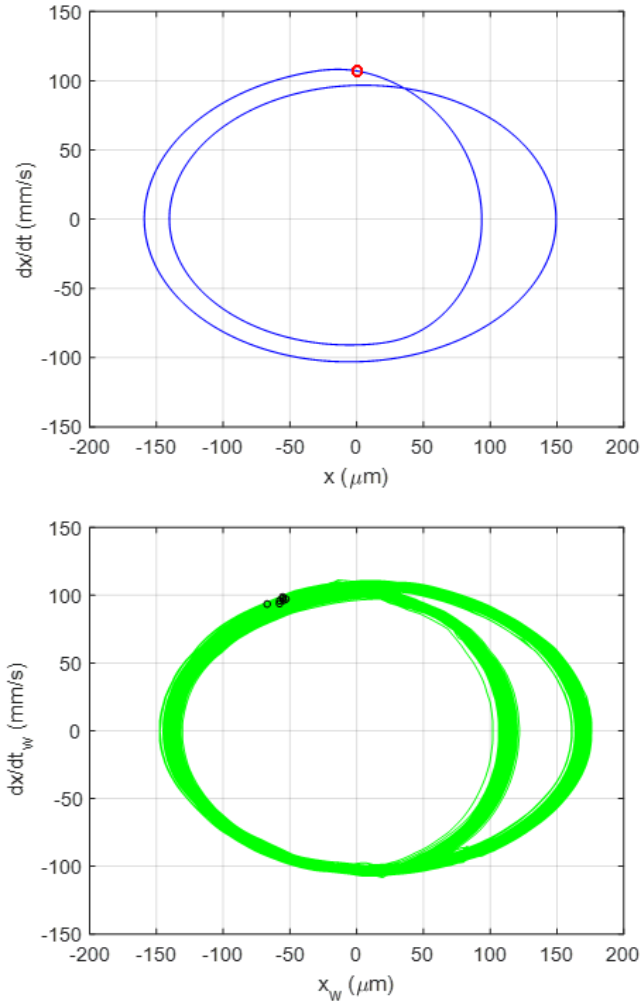

Tool wear

Tool wear tests were completed at two cutting speeds, with all other conditions held constant. The first set of tests was conducted at a stable cutting speed where the first harmonic of the tooth passing frequency matched the flexure's natural frequency (resonance). The second set was completed at a higher cutting speed (the first harmonic was above the flexure's natural frequency).

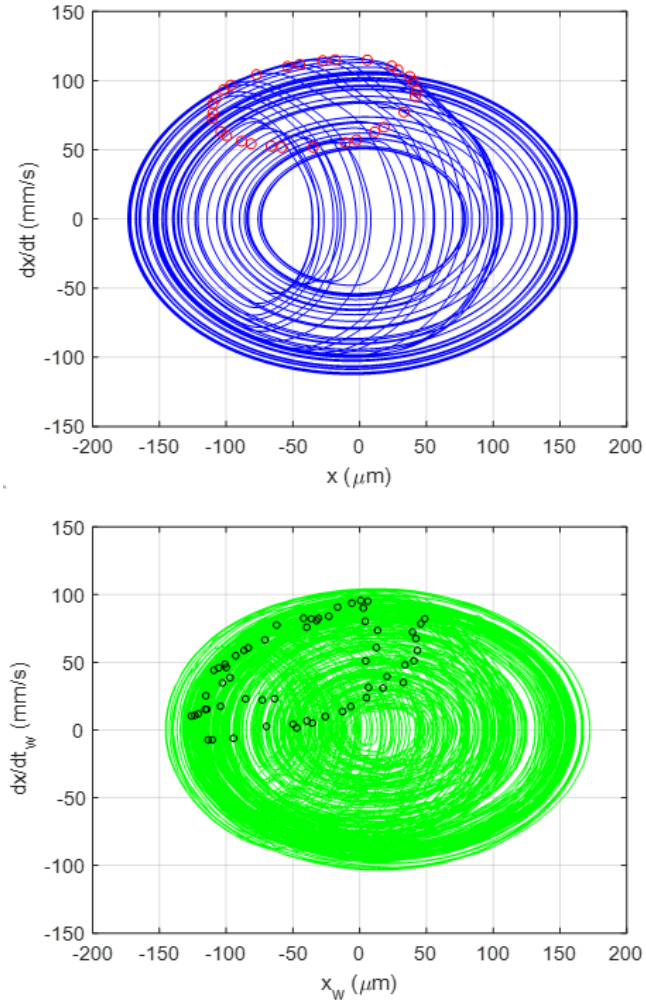

FIGURE 8. Poincaré maps for unstable cutting {3750 rpm, 2 mm}. (Top) predicted. (Bottom) measured.

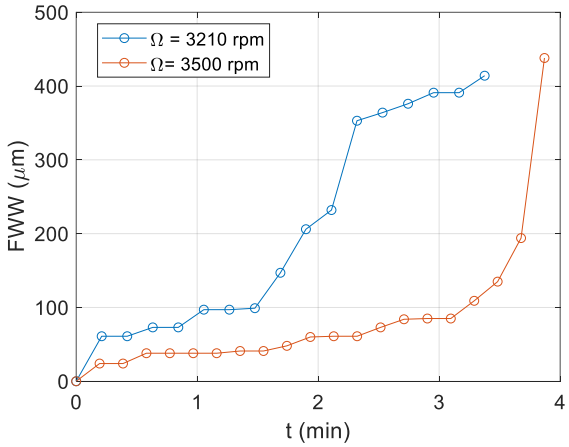

FIGURE 9. Maximum FWW progression as a function of time for all trials.

After each down milling pass, the FWW was measured. The maximum FWW was recorded for each pass and the results are summarized in Fig. 9. The volume per cut was approximately 967 mm^3 (101.6 mm × 2.0 mm × 4.8 mm). As expected, the FWW grows with increasing cutting time/volume for both cutting speeds. The images used to construct Fig. 9 are provided in Fig. 10. The progression of the flank wear is provided with FWW measurement values at four cutting time increments, t_c = {0, 1, 2, and 4} min.

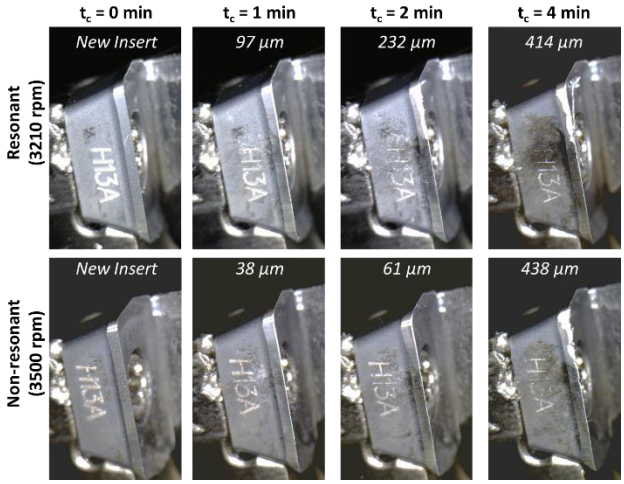

FIGURE 10. FWW progression. Images collected using the on-machine digital microscope. In the images, the rake face is on the right and the flank face is shown. The numerical FWW values are included at four cutting time intervals.

The interesting result from Fig. 9 is that a higher wear rate is obtained for the lower cutting speed. Specifically, the cutting tests at 3210 rpm reached a FWW of 300 µm (a traditional limiting value for carbide) in 2.2 min, while the 3500 rpm tests required 3.7 min. This is an unexpected result since the traditional Taylor tool life model relates the tool life to cutting speed using a simple power law; see Eq. 1, where V_c is the cutting speed, T is the tool life, and n and C are parameters that depend on the cutting conditions, work material, tool material and coating, and the tool life criterion [2]. This empirical relationship predicts that the higher cutting speed should yield a lower tool life. Clearly, the vibration magnitude difference between the resonant (3210 rpm) and non-resonant (3500 rpm) conditions also plays a role.

$$V_c T^n = C \quad (1)$$

To examine the tool life results further, the displacement and velocity levels were compared for the two tests. Figure 11 displays the synchronized displacement and velocity measured by the LDV for 3210 rpm. Figure 12 shows the results for 3500 rpm. It is seen that the vibration levels are approximately four times higher for the resonant condition at 3210 rpm. It is proposed that the increased magnitude caused the higher wear rate. Figures 11 and 12 both include displacement and velocity signals for new and worn cutting edges. It is seen that both signals indicate tool wear by the increase in magnitude.

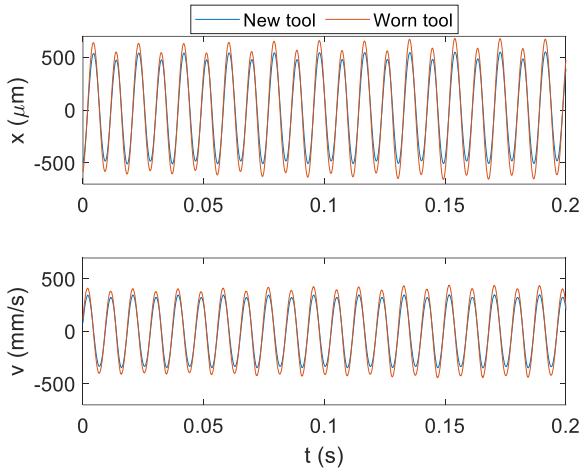

FIGURE 11. Stable, 3210 rpm cut results for x (feed) direction displacement (top) and velocity (bottom) for a new and worn tool insert.

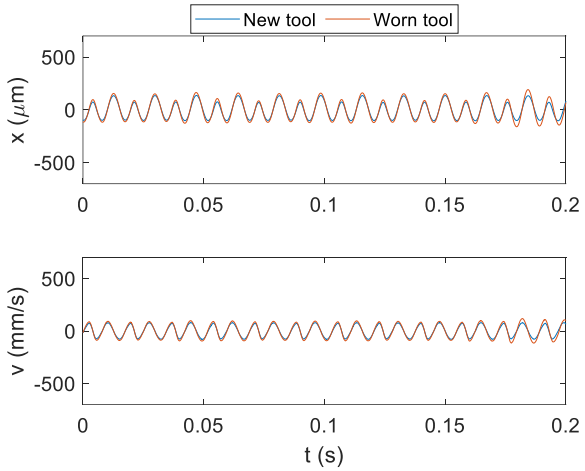

FIGURE 12. Stable, 3500 rpm cut for x (feed) direction displacement (top) and velocity (bottom) for a new and worn tool insert.

CONCLUSIONS

This paper presented stability and tool life studies using laser Doppler vibrometry as the process signal. It was shown that periodic sampling of the measured displacement and velocity signals could be used to

identify stable and unstable cutting conditions. Additionally, good agreement was obtained between predicted and measured behaviour.

During tool life testing, it was observed that the tool life increased with a higher cutting speed. This counter-intuitive behavior was attributed to a much larger vibration magnitude for the lower cutting speed. This higher magnitude was obtained because the lower cutting speed corresponded to a tooth passing frequency whose first harmonic matched the natural frequency for the flexure-based machining setup (resonant conditions).

In future work, additional tests will be performed to verify the preliminary results obtained in this study. The FWW progression with cutting time will be recorded for additional cutting speeds and the displacement and velocity will be measured to demonstrate that these signals can be used to indicate process health (stability and tool wear).

REFERENCES

[1] Schmitz, T.L. and Smith, K.S., 2009, Machining Dynamics: Frequency Response to Improved Productivity, Springer, New York, NY.

[2] Altintas, Y., 2012, Manufacturing Automation: Metal Cutting Mechanics, Machine Tool Vibrations, and CNC Design, Cambridge University Press.

[3] Pohokar, N.S. and Bhuyar, L.B., 2012, Optimization of tools for CNC machine: An explanation and overview, International Journal of Scientific & Engineering Research, 3/12: 1-9.

[4] Bediz, B., Uttara, K., Schmitz, T.L., Ozdoganlar, O.B., 2012, Modeling and experimentation for three-dimensional dynamics of endmills, International Journal of Machine Tools & Manufacture, 53/1: 39-50.

[5] Ozdoganlar, O.B., Hanshe, B.D., Carne, T.G., 2005, Experimental modal analysis for micromechanical systems, Experimental Mechanics, 46/6: 498-506.

[6] Özşahin, O., Budak, E., Özgüven, H.N., 2011, Investigating dynamics of machine tool spindles under operational conditions, Advanced Materials Research, 223/1: 610-621.

[7] Honeycutt, A., Schmitz, T.L., 2016, Experimental validation of period-n bifurcations in milling, Procedia Manufacturing, 5: 362-374.

[8] Honeycutt, A., Schmitz, T.L., 2016, A new metric for automated stability identification in time domain milling simulation, Journal of Manufacturing Science and Engineering, 138/7: 075401.

[9] Honeycutt, A., Schmitz, T.L., 2017, Milling stability interrogation by subharmonic sampling, Journal of Manufacturing Science and Engineering, 139/4: 041009.

[10] Polytec, 2016, OFV-5000 vibrometer controller datasheet, 1-12.

[11] Chan, A., 2011, Vocal fold vibration measurements using laser Doppler vibrometry, McGill University Master's Thesis, 3: 16-20.

[12] Smith, K.S. and Tlusty, J., 1991, An overview of modelling and simulation of the milling process, Journal of Engineering for Industry, 116/2: 169-175.

STUDY ON THE PROTECTIVE EFFECT OF BUILT-UP LAYER IN DRY CUTTING OF STAINLESS STEEL SUS304

SONG Xiaoqi[1], Yukio TAKAHASHI[1], HE Weiming[2] and Tohru IHARA[1]
[1] Department of Precision Mechanics,
Chuo University,
Tokyo, 112-8551, Japan
[2] School of Mechanical Engineering,
University of Shanghai for Science and Technology,
Shanghai, 200093, China

INSTROCTIONS

Stainless steels have a good combination of high strength, high corrosion and oxidation resistance and exceptional toughness at elevated temperature [1], which are widely used in the ship building, boiler, energy and chemical industries, construction industries, automobile industries and so on. However, they are very difficult to cut and belong to the iron based difficult-to-cut materials categories for the following reasons [2,3]: 1) their low thermal conductivity; 2) high work hardening rate; and 3) high chemical affinity to the cutting tool materials. These characteristics cause the high cutting temperature in the cutting zone even at low cutting speed. Cutting temperature generated during dry cutting of stainless steel SUS304 can reach about 610℃ at 40 m/min, and 800℃ at 100 m/min [4]. On the other hand, these characteristics also lead to intensive adhesive interaction at the tool and workpiece interface resulting in the Built-up Edge (BUE) formation, which is responsible for the poor surface quality and for the rapid tool wear [2,3,5,6]. Therefore, the research on the BUE formation has a significant meaning for cutting stainless steel in a more economical way.

BUE, mentioned in [1-3,5,6], strictly speaking, should be classified into three categories by its location: 1) built-up layer (BUL) on the tool rake face; 2) BUE around the cutting edge; 3) and flank built-up (FBU) on the tool flank face [7,8]. BUE appears at the low cutting speeds, e.g., 1–60 m/min for cutting carbon steels [8]. Because BUE can grow up to a noticeable size around the cutting edge, it can change the shape of cutting edge and affect cutting forces and surface quality. However, BUL is a thin and stable structure formed on the tool rake face at the higher cutting speeds [8] or formed while cutting difficult-to-cut materials [9-12]. Because the hardness of a BUL is higher than that of a workpiece, BUL can function as a protective layer during cutting. And it forms only on the tool rake face, therefore it has no or few effects on cutting forces and surface quality. To actively and purposely utilize it, BUL should not be treated as a predecessor of BUE; this opinion differs from those of studies in [13,14]. However, until the present time, the BUL/BUE formation in cutting of stainless steel have not been completely understood.

In our previous studies, the present authors conducted thermodynamic analysis of BUL/BUE formation to clarify its formation mechanisms in dry cutting of stainless steel SUS304 [15]. It was found that BUE appears at low cutting speed (5-20 m/min), and BUL forms on the tool rake face at cutting speed range 40-140 m/min. It was also verified that the proposed model can accurately predict the BUL/BUE formation conditions. However, the protective effect of BUL has not been completely discussed. Few studies have already reported that BUE has the protective effect during cutting of stainless steel [16,17]; however, the difference between BUL and BUE, and the detailed analysis of the influences of size of BUL/BUE on tool wear resistance have not been carried out.

In this study, a more detailed investigation on the BUL/BUE formation process and its influence on tool wear was performed to gain a deeper understanding on the protective effect of BUL in dry cutting of stainless steel SUS304. First, to study the BUL/BUE formation conditions and BUL/BUE formation mechanisms, dry cuttings of SUS304 under different cutting conditions were performed. Then, the protective effect of BUL, and relation between the size of BUL/BUE and tool wear was investigated. Finally, the influences of BUL/BUE on cutting forces and surface roughness, and the cutting conditions for actively and purposely utilizing BUL were also discussed.

EXPERIMENTAL PROCEDURE

Workpiece And Cutting Tools

Stainless steel SUS304 (1050℃×1min, WQ) was used as workpiece. The properties and chemical

TABLE 1. Material properties of SUS304

Yield point (MPa)	294
Tensile strength (MPa)	623
Elongation (%)	60
Reduction of area (%)	76
Hardness (HV)	175

TABLE 2. Chemical composition of SUS304 (%)

C	Si	Mn	P
0.06	0.4	1.49	0.035
S	Ni	Cr	Co
0.024	8.13	18	0.19

TABLE 3. Cutting parameters

Tool	TPGN160304, K10
Cutting speed V (m/min)	5 - 140
Feed rate f (mm/rev)	0.02, 0.05, 0.1
Depth of cut tu (mm)	1.0
Cutting time t (s)	1, 10, 30, 60, 120, 180, 240, 300
Rake angle α (°)	5
Flank angle γ (°)	6
Nose radius r (mm)	0.4
Wedge angle β (°)	60
Cutting edge angle κr (°)	91
Cutting fluid	Dry

composition of SUS304 are listed in **Table 1** and **Table 2**. And all workpieces were of length 200 mm and were cut from the same bar (diameter 40 mm). Uncoated cemented carbide inserts without chip breaker (rake angle 0° and flank angle 11°, TPGN160304, Tungaloy) were used for all the tests. The inserts were set on a tool holder having a seating surface with a rake angle 5° and flank angle 6° (CTGPR2020K3, Tungaloy). Therefore, the actual rake angle, flank angle after mounting are 5°, and 6°, respectively.

Experimental Set-up

A series of turning tests were performed using a CNC lathe machine (MULTUS B200, Okuma). The cutting parameters are listed in **Table 3**.

Cutting forces were measured by 3-component piezoelectric dynamometer (9129A, Kistler), and the finished surface was measured by a surface roughness tester (SJ-201, Mitutoyo). To study the BUL/BUE formation process and to measure tool wear, the tools after cutting were examined using scanning electron microscope (SEM, Quanta250, FEI) and laser scanning microscopy (LSM, OLS 4100, Olympus). The maximum height of adhesion (including BUL and BUE) above tool rake face h_1, contact length between adhesion and cutting tool L, and maximum depth of crater wear below tool rake face h_2 were also measured by LSM. A representative result is shown in **Fig.1**.

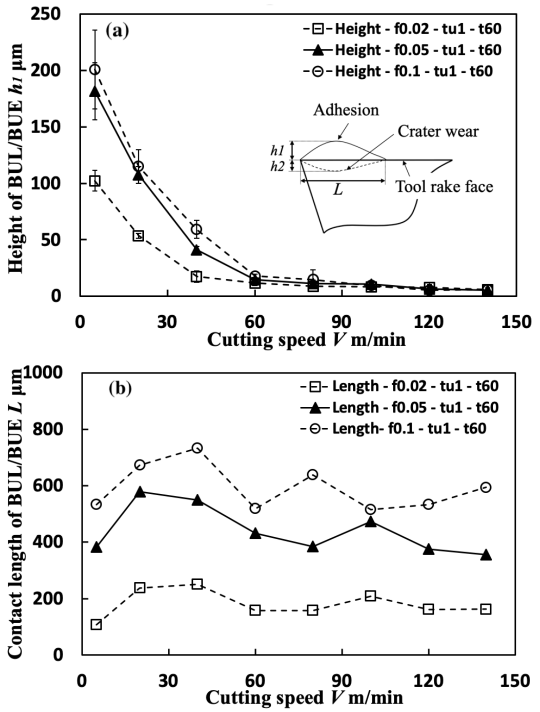

FIGURE 1. Variation of maximum height of adhesion above tool rake face h_1 and contact length between adhesion and cutting tool L after cutting 60 s under different cutting conditions.

RESULTS AND DISCUSSION

Investigation of Built-up Layer Formation

BUL and BUE Formation Conditions

In the first part of the results, the BUL and BUE formation conditions are investigated. To clarify of the adhesion (including BUL and BUE) formation, variations of maximum height of adhesion above tool rake face h_1 and contact length between adhesion and cutting tool L with cutting speed for three feed rates after cutting 60 s are shown in Fig.1. For example, SEM images of tool surface at 5, 40, 100, and 140 m/min, feed rate 0.05 mm/rev after cutting 60 s are shown in **Fig.2**. It can be confirmed that adhesion can form on tool surface under different cutting conditions. The highest adhesion appears at low cutting speed 5 m/min and its height decreases as cutting speed increases. The thin adhesion (its height is about 5 µm) can also appear at 140 m/min. Meanwhile, it is also observed that L at cutting speed above 20 m/min has only a slightly decreasing trend (Fig.1). These results indicate that, compared to its effects on L, cutting speed plays an important role on the variation of height of adhesion h_1. This phenomenon can be explained as the result of the increase of ductility and reduction of work hardening rate of workpiece at high cutting speed which causes the high cutting temperature [18]. It

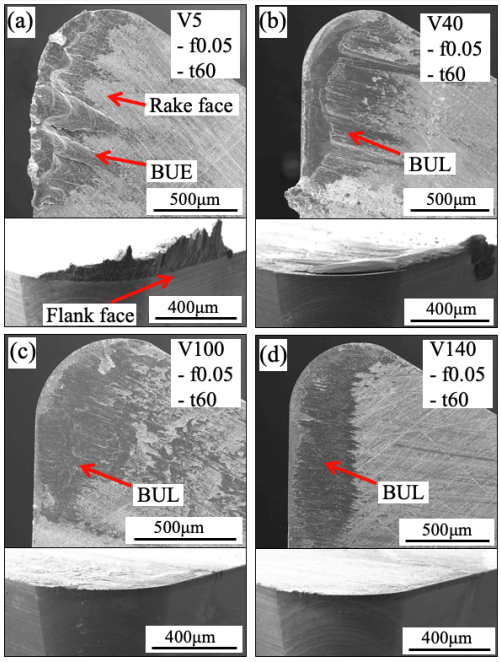

FIGURE 2. SEM images of cutting tool at cutting speed 5, 40, 100, and 140 m/min, feed rate 0.05 mm/rev after cutting 60 s.

is also verified that the feed rate can also play an important role on the size of adhesion (Fig.1).

To study the BUL/BUE formation conditions, the profiles of adhesion under different cutting speed are shown in **Fig.3**. it can be clearly seen that the cutting speed and feed rate exert significant influences on the morphology and location of adhesion, as reported in our previous study [15]. According to the proposed definition in [15], the BUL/BUE formation conditions in dry cutting of SUS304 are given as below: at low cutting speeds (5-20 m/min), BUE (h_1>100 μm) forms around the cutting edge. At cutting speeds equal to or above 40 m/min, BUL (h_1<100 μm), which resembles a water drop, forms on the rake face.

BUL Formation Mechanisms

To examine BUL formation mechanisms, LSM analysis was applied to gain a deeper insight into the BUL formation process at cutting speed equal to or above 40 m/min. For illustration, a sequence of four different contour maps in a time range between 1 and 60 s were chosen at cutting speed 40 and 80 m/min, feed rate 0.05 mm/rev, as shown in **Fig.4**. It can be verified that the BUL formation is a time-dependent phenomenon. At cutting time 1 s, the initial BUL quickly occurs at the middle of tool and chip contact zone. This process is the nucleus formation process [11,12,15]. After the initial BUL formed, BUL grows in the horizontal and vertical directions of tool rake face

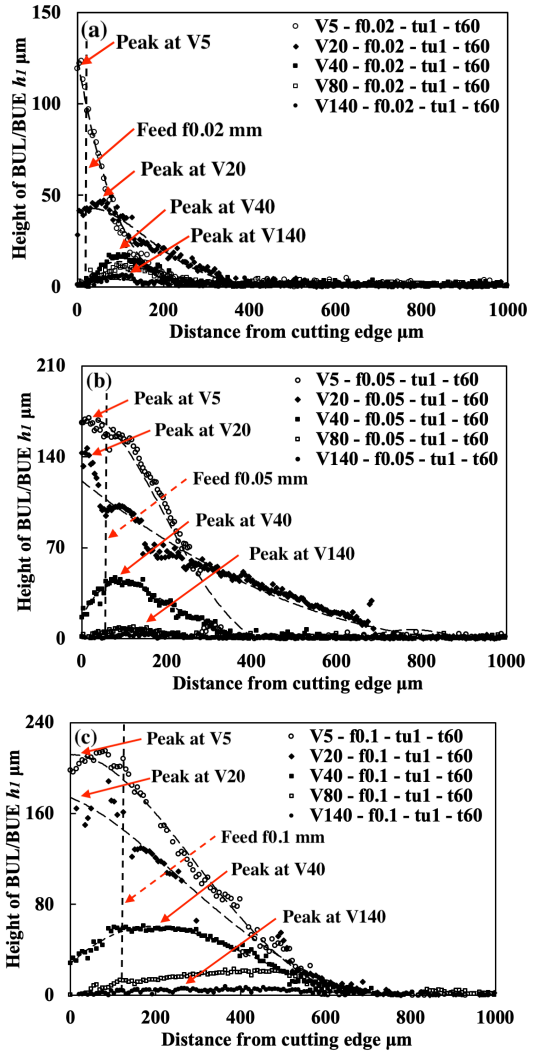
(a)
Peak at V5
Feed f0.02 mm
Peak at V20
Peak at V40
Peak at V140
V5 - f0.02 - tu1 - t60
V20 - f0.02 - tu1 - t60
V40 - f0.02 - tu1 - t60
V80 - f0.02 - tu1 - t60
V140 - f0.02 - tu1 - t60
Height of BUL/BUE h1 μm
Distance from cutting edge μm
(b)
Peak at V5
Peak at V20
Feed f0.05 mm
Peak at V40
Peak at V140
V5 - f0.05 - tu1 - t60
V20 - f0.05 - tu1 - t60
V40 - f0.05 - tu1 - t60
V80 - f0.05 - tu1 - t60
V140 - f0.05 - tu1 - t60
Height of BUL/BUE h1 μm
Distance from cutting edge μm
(c)
Peak at V5
Peak at V20
Feed f0.1 mm
Peak at V40
Peak at V140
V5 - f0.1 - tu1 - t60
V20 - f0.1 - tu1 - t60
V40 - f0.1 - tu1 - t60
V80 - f0.1 - tu1 - t60
V140 - f0.1 - tu1 - t60
Height of BUL/BUE h1 μm
Distance from cutting edge μm

FIGURE 3. Variation in the BUL/BUE profile with cutting speed at feed rate (a) 0.02, (b) 0.05, and (c) 0.1 mm/rev after cutting 60 s.

as the result of the accumulation of workpiece material (**Fig.5)**. And the peak of BUL's height moves from the middle of tool and chip contact zone to the cutting edge, as show in Fig.4. This process is called as the forward growing process [11,12,15]. As the cutting time increases to 30-60 s, the BUL's growth stops. The reason is that there is a balance between the accumulation and squeeze out of workpiece material. Figure 4 and Fig.5 clearly illustrate that a stable BUL can appear on the tool rake face without falling off. In what following, the protective effect of BUL is investigated.

Protective Effect of Built-up Layer

To study the protective effect of BUL, various tool wear tests were carried out. The cutting speed was varied in the range of 5-100 m/min. In **Fig.6**, the variations of flank wear with cutting speed and

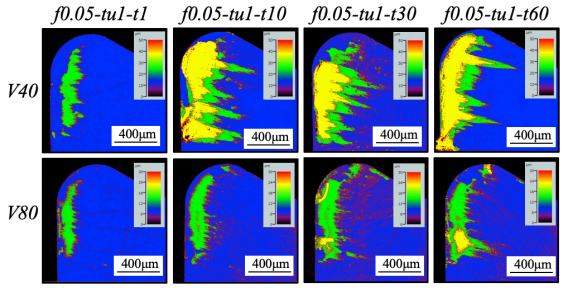

FIGURE 4. Contour maps of LSM analyses of the rake face at cutting speed 40, 80 m/min, feed rate 0.05 mm/rev after cutting 1, 10, 30, and 60 s.

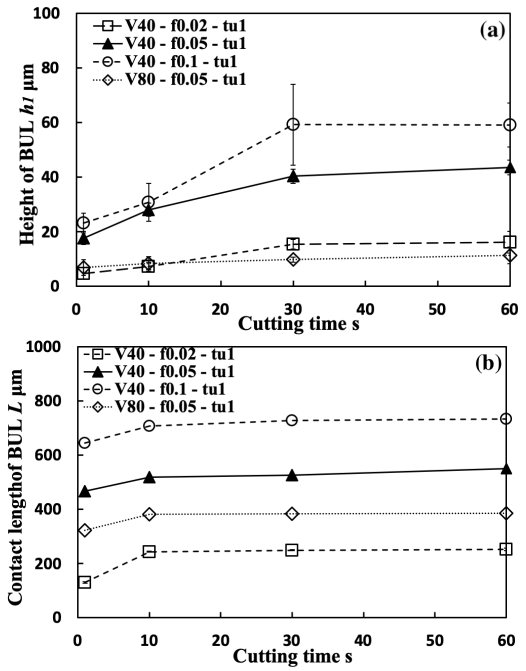

FIGURE 5. Variation of (a) height of BUL, and (b)contact length of BUL with cutting time for different feed rate at cutting speed 40,80 m/min.

cutting time are presented. The results shown in Fig.6 illustrate that flank wear is increasing with cutting speed and cutting time. However, it can be found that flank wear at 40 m/min is lower than it at 20 and 80 m/min in all the cases. This phenomenon can be explained as a result of the protective effect of BUL formed at 40 m/min, which can greatly reduce the average flank wear rate in the steady-state wear (from 60 s to 300 s) as shown in **Fig.7**. As discussed above, BUL, which resembles a water drop, is stable. And BUL is a work hardened workpiece, its hardness is higher than that of workpiece. Therefore, it can work as a protecting layer separating the tool from chip and replace the tool to perform actual cutting. On the other hand, BUE, formed at low cutting speed, is not stable. Because BUE falls off easily, tool

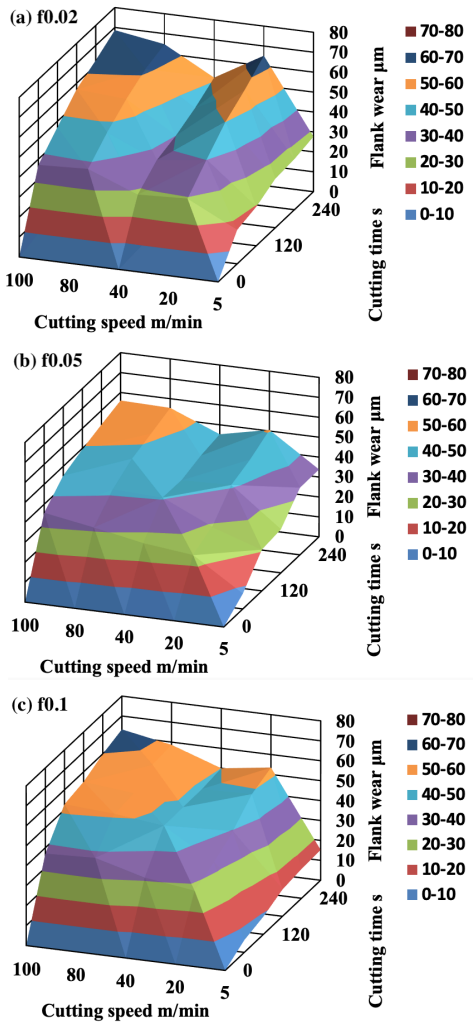

FIGURE 6. Variations of flank wear with cutting time under different cutting speeds for feed rate (a) 0.02 mm/rev, (b) 0.05 mm/rev, and (c) 0.1 mm/rev, depth of cut 1 mm.

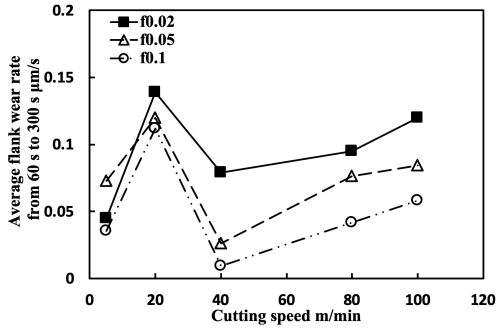

FIGURE 7. Variations of average flank wear rate from 60 s to 300 s with cutting speed.

wear occurs quickly. For example, variations of height of BUL/BUE with cutting time for feed rate 0.05 mm/rev are shown in **Fig.8**. The amplitude variation of height of BUE at 5, 20 m/min is very large, which indicates that BUE is not stable.

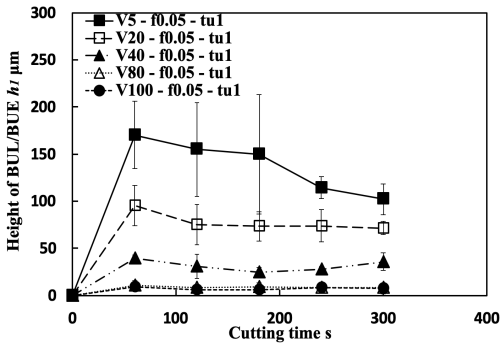

FIGURE 8. Variations of height of BUL/BUE with cutting time under different cutting speed for feed rate 0.05 mm/rev.

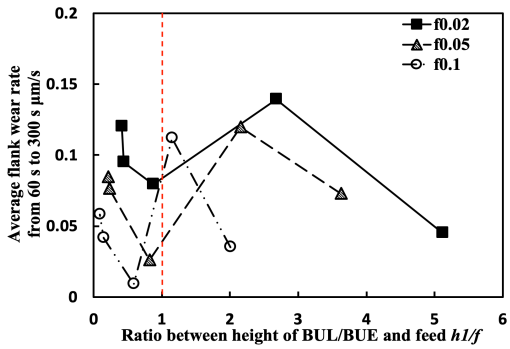

FIGURE 9. Relation between ratio of height of BUL/ BUE h_1 to feed f and average flank wear rate from 60 s to 300 s

In addition, the tool rake face is also protected by BUL. From the LSM analyses (Fig.4, Fig.8), it is verified that no crate wear is observed on the tool rake face in all the cases, which implies that BUL can protect the tool rake face from wear.

Generally, it is well known that flank wear (or flank wear rate) increases as cutting speed increases [2,3]. As shown in Fig.6, Fig.7 and Fig.8, it can be concluded that the stable BUL can decrease flank wear rate, and the height of BUL h_1 plays a great role on its wear reducing properties. To explain this, the relation between the height of BUL and average flank wear rate was investigated, which is displayed in **Fig.9**. Here, to get a more general conclusion, x axis is set as the ratio between h_1 with the feed *f*. It is confirmed that the protective effect of BUL happens when h_1/f is below 1, and it will decrease as h_1/f decreases to 0. In the work by Ahmed et al. [16], it was reported that the protective effect of BUE, which should be called as BUL in our opinion, happens at 60 m/min, depth of cut 0.5 mm in cutting of AISI304 with coolant. h_1/f is close to 0.6 in [16] (h_1 is about 60 μm, and feed rate *f* is 0.1 mm/rev). This result is in close agreement with the findings in this study. The difference is that in this study, the protective effect happens at 40 m/min, depth of cut 1mm.

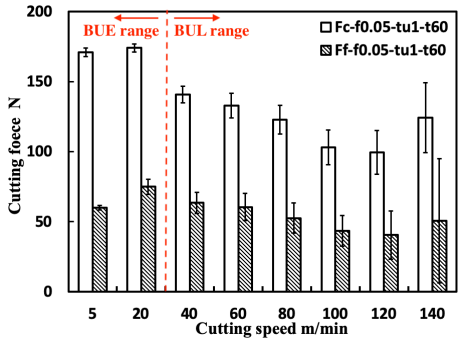

FIGURE 10. Variations of main cutting force Fc, and feed force Ff with cutting speed (average value during the steady cutting stage) for feed rate 0.05 mm/rev after cutting 60 s.

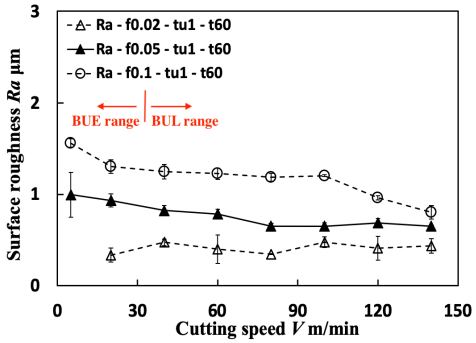

FIGURE 11. Variation of surface roughness Ra with cutting speed for various feed rate.

Examination of Influences of Built-up Layer

In order to actively and purposely utilizing BUL to realize the self-protective tool (SPT) in cutting of SUS304, the influences of BUL on cutting forces and surface roughness should also be studied.

Cutting Forces

Cutting forces during dry cutting of SUS304 were measured. For example, the results at cutting speed range 5-140 m/min, feed rate 0.05 mm/rev after cutting 60 s are summarized in **Fig.10**. The speed range over which BUL formed is shown as equal to or above 40 m/min. When BUE formed (the cutting speed range is below 20 m/min), the average main cutting force *Fc* and average feed force *Ff* are largest. When BUL formed, *Fc* and *Ff* exhibit a decreasing trend as cutting speed increases until 140 m/min. This is the result of the increase of workpiece ductility as cutting speed (or cutting temperature) increases. On the other hand, it is confirmed that BUL has few influences on the amplitude variation of cutting forces.

Surface Roughness

Figure 11 shows the variations of surface roughness *Ra* after cutting 60 s under different cutting speed. Here, there is no date at 5 m/min, 0.02

mm/rev, because the evaluated distance is too short. It can be observed that *Ra* has a slightly decreasing trend as the cutting speed increases. However, no significant variation of *Ra* can be observed when BUL formed at the cutting speed range 40 to 100 m/min. A possible reason for the almost same *Ra* when BUL formed is that BUL protect the tool and it reduce the variation of tool nose's shape during cutting.

Surface roughness *data* after cutting 60 and 300s under different cutting speed and feed rate are listed in **Table 4**. It can be seen that *Ra* increases as cutting time increases which is associated with the increase in the tool wear at 5, 100 m/min. At 40 m/min, no significant increase of *Ra* can be observed. This result is similar with the result in Fig.6. Therefore, it can be concluded that BUL formed at 40 m/min can not only protect the tool but also reduce the rise in *Ra* with cutting time and keep good precision. This behavior was also observed in dry cutting of hardened steel [9]. The difference is that in this study, the flank wear rate after cutting 60 s is very small when BUL formed. Considering experimental results above, it can be confirmed that we can actively and purposely utilize BUL to realize the SPT at 40 m/min in dry cutting of SUS304.

TABLE 4. Surface roughness values Ra and Rz after cutting 60 s and 300 s under different cutting speed and feed rate

Feed rate (mm/ rev)	Cutting speed (m/min)	Ra after cutting time t s (μm)		Rz after cutting time t s (μm)	
		60	300	60	300
0.02	5	×	×	×	×
	40	0.618± 0.042	0.620± 0.046	5.053± 1.101	4.778± 0.717
	100	0.478± 0.107	0.660± 0.028	3.335± 0.752	4.250± 0.438
0.05	5	0.725± 0.039	1.228± 0.486	4.658± 0.459	6.308± 2.135
	40	0.705± 0.036	0.565± 0.034	4.567± 0.036	3.895± 0.478
	100	0.623± 0.017	0.810± 0.008	3.723± 0.104	4.395± 0.158
0.1	5	1.108± 0.095	1.260± 0.042	6.838± 0.738	7.998± 0.598
	40	1.370± 0.046	1.333± 0.038	7.810± 0.171	7.673± 0.566
	100	1.225± 0.025	1.445± 0.044	6.478± 0.311	7.243± 0.281

CONCLUSIONS

The following conclusions can be drawn:

1. In dry cutting of SUS304, the morphology and location of BUL/BUE are different. BUE forms around the cutting edge at low cutting speeds (5-20 m/min). And BUL forms on the tool rake face at cutting speeds equal to or above 40 m/min.
2. The BUL formation has two processes: the nucleus process and forward growing process.
3. BUL has the protective effect, and the height of BUL plays a great role on its protective effect.
4. BUL has few influences on cutting forces and surface roughness.
5. It can be concluded that we can actively and purposely utilize BUL to realize the SPT at cutting speed 40 m/min in dry cutting of SUS304.

ACKNOWLEDGEMENTS

The authors wish to thank Machine Tool Engineering Foundation (Japan) for their financial support.

REFERENCES

[1] ASM Handbook, Volume 1, ASM Int., 1990.
[2] Trent, E.M. and Wright, P.K., Metal Cutting, 4th Edition, Butterworth-Heinemann, 2000.
[3] Shaw, M.C., Metal Cutting Principles, 2nd Edition, Oxford University Press, 2005.
[4] He, H., Li, H., et al., Int. J. Pre. Eng. Manu., 18, 10 (2017), 1387-1392.
[5] Selvaraj, D.P., Materials Today: Proceedings, 4 (2017), 11141–11147.
[6] Kaladhar, M., Ubbalah, K. V., et al., Int. J. of Mach. Machina. Mater., 12, 1-2 (2012), 178-192.
[7] Tomac, N., Tonnessen, K., et al., AMST'05 Adv. Manu. Sys. Tech., CISM Intern. Cent. Mech. Sci., 486, (2005), 183-192.
[8] Song, X.Q., Takahashi, Y., et al., Key Eng. Mat., 749, (2017), 39-45.
[9] Song, X.Q., Takahashi, Y., et al., Jour. Jap. Soc. Prec. Eng., 82, 9 (2016), 814-820 (in Japanese).
[10] Song, X.Q., Takahashi, Y. et al., LEM21 Proc., 56, (2017), 1-6.
[11] Song, X.Q., Takahashi, Y. et al., ASPE 33rd Proc., 70, (2018), 329-334.
[12] Song, X.Q., Takahasi, Y., et al., Jou. Jap. Soc. Prec. Eng., 83, 5 (2017), 445-452. (In Japanese)
[13] Koichi, H. and Tetsutaro, H., Memo. Fac. Eng., Hokkaido Uni., 12, 3(1969), 241-271.
[14] Gomez-Parra, A., Alvarez-Alcon, M., et al., Wear, 302, (2013), 1209-1218.
[15] Song, X.Q., Takahashi, Y. et al., Int. J. of Automation Tech., 13, 1 (2019), 13-21.
[16] Ahmed, Y. S., Fox-Rabinovich, G., et al., Materials, 10, 1230 (2017), 1-15.
[17] Ahmed, Y. S., Paiva, J. M., et al., Tribo. Inter., 137, (2019), 212-227.
[18] Usui, E. and Hoshi, K., Jour. Jap. Soc. Prec. Eng., 30, 350 (1964), 273-284 (in Japanese).

Direct control of machine tools using 3D-CAD

Koki Sagesaka[1], Yoshitaka Morimoto[1], and Akio Hayashi[2]
[1] Graduate Program in Mechanical Engineering
Kanazawa Institute of Technology Graduate School
Ohgigaoka Nonoichi Ishikawa, Japan
[2]Department of Mechanical Engineering
Kanazawa Institute of Technology
Ohgigaoka Nonoichi Ishikawa, Japan

INTRODUCTION

In recent years, multi-axis machine tools have become widespread, and machining of complicated shapes has become possible. In order to improve the machining accuracy, it is necessary to improve the accuracy of the machining program besides the high accuracy of the machine tool. By improving this accuracy, high-precision products can be produced. However, in practice, calculation errors and data conversion errors occur when transferring model drawings by 3D-CAD to the data for CAM, or when converting CAM data to a machining program for a machine tool, the processing accuracy decreases. Therefore, the reduction of the calculation error between these and the conversion data errors for machining leads to the improvement of the processing accuracy of complex shape.

In this research, in this research, we propose the direct control method based on the tool path generation from the model in 3D-CAD directly. Therefore, the improvement of the machining accuracy by eliminating calculation error and data conversion error by accessing control system of machine tool directly can be achieved. As a similar study to this research, there is a method of extracting the machining area from the difference between the material shape and the designed shape and generating a machining program. On the other hand, the feature of this research is to calculate the tool path in 3D-CAD. While 3D-CAD itself functions like a simulator, real-time path generation and real-time processing by direct control are performed [1].

In this report, we report a new path generation method by 3D-CAD, and its effectiveness by motion test of machine tool and actual machining test.

TOOL PATH GENERATION METHOD

The 3D-CAD used is SolidWorks. Since a VBA engine is standard installed in SolidWorks, a tool path generation program is created using this system.

As for the path generation method, parts and tools are placed in the assembly, the tool is moved so as to actual machining, and the tool coordinates at the time of contact with the parts are acquired as the tool path. Figure 1 shows the assembly layout of both tool and workpiece during route generation.

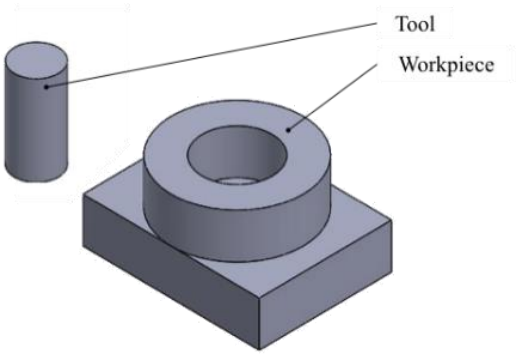

Figure 1. Schematic diagram for tool path generation of 3D-CAD model.

The acquired tool path is sent directly from 3D-CAD to the NC controller. Also, since the data format at the time of transmission is designed as same as the handled data in the NC controller, any conversion is not performed here either. Figure 2 (a) shows a tool path generation method using conventional CAD / CAM software and NC data transmission method to the NC machine tool. As mentioned above, it turns out that data conversion is performed each time. Figure 2 (b) shows the proposed direct control method for NC machine tools. Compared our method to the conventional method, it can be seen that the number of conversions and calculation passes of route data is reduced.

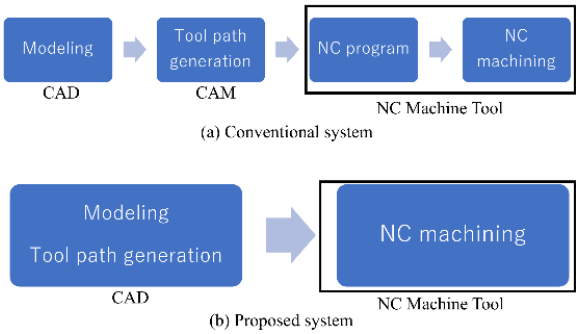

Figure 2. Machining system.

TOOL PATH GENERATION PROGRAM

Operation setting

When the program is executed, the path generation assembly, in which the machine tool table and tools are placed, is called, and the selected part data is inserted.

After placing the part data at the position on the table, where the parts are actually fixed on the machine tool, and entering the tool diameter, and click the Execution button to start path generation calculation. Figure 3 shows the example of the setting form.

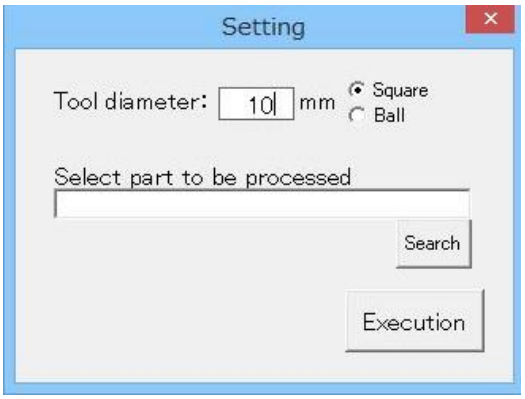

Figure 3. Setting form.

Calculation of tool path for rough machining

Rough machining tool path is calculated based on scanning line processing. As shown in Figure 4, the direction is changed each time until it goes out of the processing range, and the entire range is processed. When contacting parts with tool, as shown in Figure 5, raising the tool height above the maximum height of the parts and checking whether it can be lowered to the reference height without interference each time, the tool position is moved to the next point.

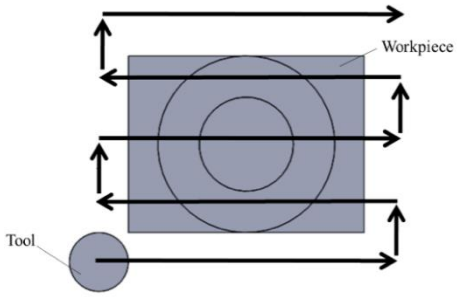

Figure 4. Tool path for rough cutting (XY plain).

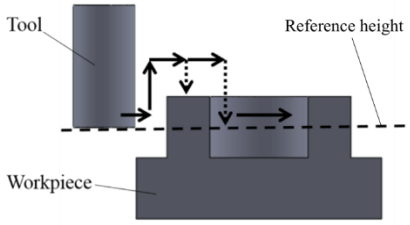

Figure 5. Tool path for rough cutting (XZ plain).

Calculation of tool path for finish machining

As for finish machining, two types of contour cutting and scan cutting were created. An operation example in case of the contour finish machining path calculation is shown in Figure 6, and another operation example in case of the scan line finish machining path calculation is shown in Figure 7. As shown in the two figures, in contour processing, the tool escapes to the direction opposite to the contact direction, in scan processing, it escapes to the height direction.

And the next contact coordinates are searched by arc motion. It can be thought that this makes the distance between contact coordinates uniform, which leads to the improvement of controllability and high accuracy [2].

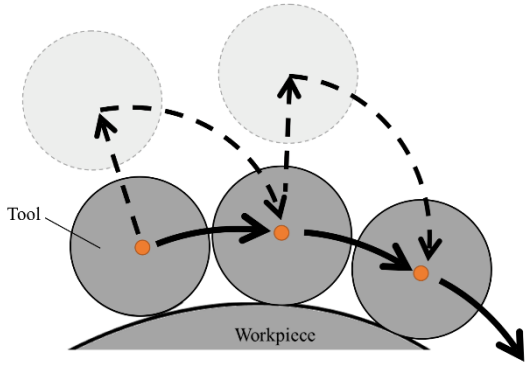

Figure 6. Contour cutting (XY plain).

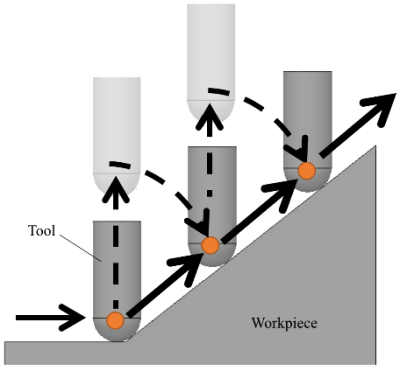

Figure 7. Scan cutting (XZ plain).

In addition, in the case of contour processing, there is a possibility that the uncut area may occur because the entire processing range is not scanned.
Therefore, the outline was recognized by applying simple mapping at the time of rough machining, so that the uncut area was eliminated. This mapping method is based on the digital image processing method.

MACHINE TOOLS USED AND CONTROL METHOD

Figure 8 shows the motion system of the developed machine tool. The machine tool is a desktop type machine tool [3], and the controller is an FPGA controller (cRIO-9022) manufactured by National Instruments. In addition, this machine tool has a structure in which the influence of gravity cannot be ignored because the drive units have the inclination angle. Therefore, stability and positioning accuracy were improved by performing position feedback from the linear position sensors attached to the drive units and velocity feedback from the rotary encoder attached to the servomotor [4]. The block diagram of the control system is shown in Figure 9.

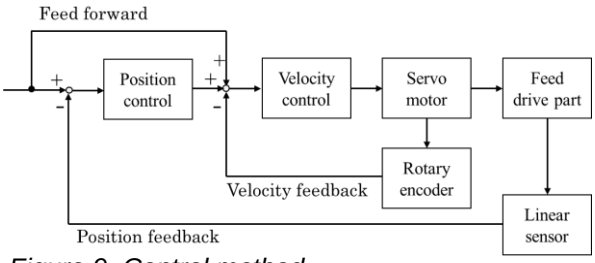

Figure 9. Control method.

Trajectory accuracy evaluation in the proposed method

In actually motion of the desktop machine tool, and the trajectory accuracy is evaluated from the value of the linear position sensor during motion test. The path to be calculated is set to a cylindrical shape with a diameter of 25 mm.
The results are shown in Figure 10. The left figure is the result by the conventional method. The measured blue line settles in ± 10μm.
The right one is the one by the proposed method. The measured orange line almost settles in ± 5μm. We can see that the proposed method traces the target shape more accurately. This is considered that the calculation error in the controller decreased because the distance between machining points in the proposed method is constant.

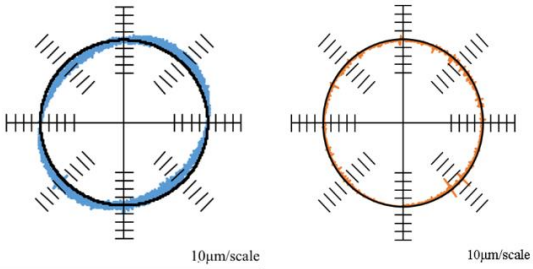

Figure 10. Measurement result of trajectory accuracy.

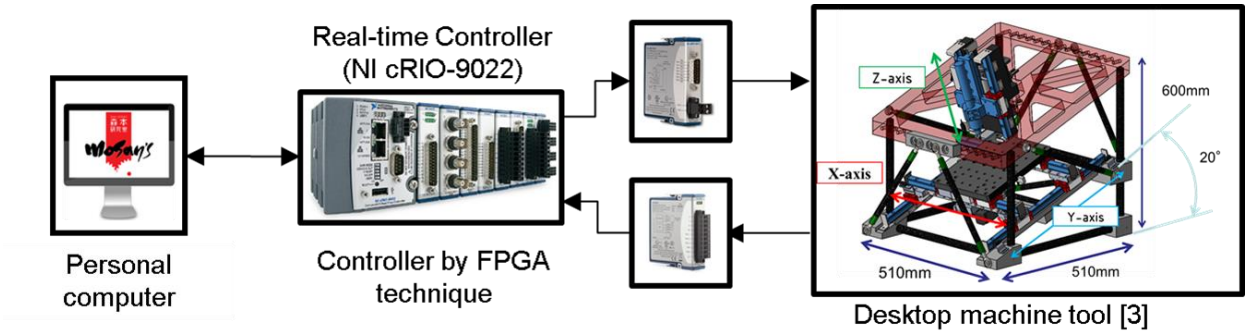

Figure 8. Control system of desktop machine tool.

Evaluation of accuracy by machining test

A shown in Figure 11, the target shape is designed based on the standard of JIS B6336-6 and evaluated from the measurement data of the dimensions. Aluminum alloy A5052 was used as the machining material. Roughing and contour finishing were performed using a ϕ6 carbide square end mill. The machined shape is shown in Figure 12 and the machining conditions are shown in Table 1.

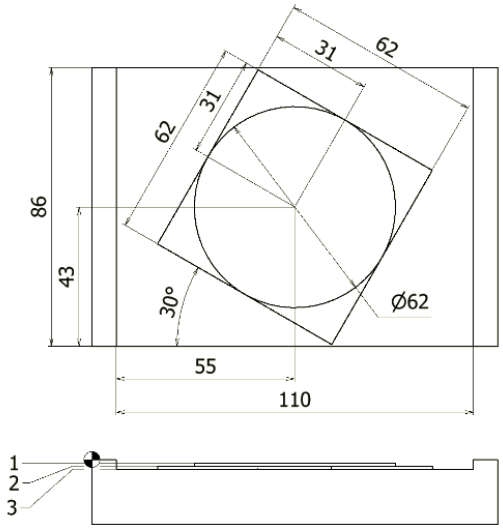

Figure 11. Target workpiece used in machining test.

TABLE 1. Machining conditions.

Spindle rotation (min^{-1})	20000
Feed rate (mm/min)	125
Pass depth (mm)	1
Stepover (%)	25

Figure 12 shows the machined workpiece with the measurement data of designed dimensions. The machining time was 100 minutes. The dimensions are measured at multiple locations using a vernier caliper, and the minimum and maximum values are listed. The width error at square column shows +0.05 to 0.07 mm, and the diameter error of th cylinder shows -0.02 to +0.05 mm. Also, some undulations can be confirmed on the machining side. This is considered that a certain amount of end mill deformation occurs due to cutting resistance during finish machining. In the cylindrical part, in addition to the inclination of the end mill, it is considered that an internal rotation error occurs. It is our future task to suppress these errors.

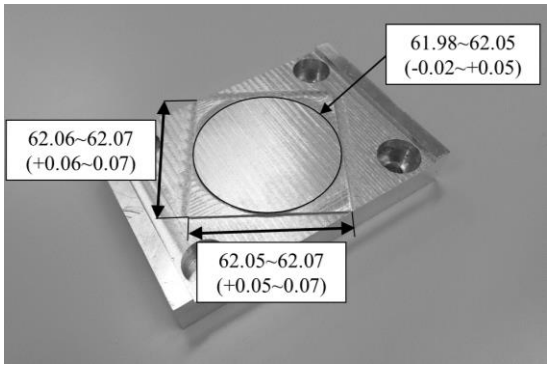

Figure 12. Machined result by proposed system.

CONCLUSION

1. We proposed direct control of a machine tool using 3D-CAD as a method of path generation and processing of machining without converting from the created model diagram.
2. The algorithm for realizing the proposed route generation was created and the processing accuracy was evaluated.
3. Investigate the error according to the processing conditions, and make correction to make improvement of processing accuracy a future issue.

REFERENCES

[1] Keiichi SHIRASE, Keiichi NAKAMOTO, Eiji ARAI and Toshimichi MORIWAKI. Autonomous Machine Tool to Realize Flexible Machining Operation Unconstrained by NC program - Direct Machining Operation Controlled by Flexible Process and Operation Planning System -. Journal of the Precision Machinery Society. 2004;70: 1449-1454.

[2] Osamu Hori et. Digital Image Processing. 2004. 177-190

[3] Satoshi IINO, Serenn SATO, Yoshitaka MORIMOTO, Ryo HIRONO, Naohiko SUZUKI, Yoshiyuki KANEKO. Development and performance evaluation of desktop machine tool. Euspen's 17th International Conference & Exhibition, 2017.

[4] Fumitoshi Sakai, Masatoshi Hikizu, Yoshitsugu Kamiya, Hiroaki Seki. Precision Positioning Which Contains Flexible Mechanical System: Fusion of Semi-closed and Full-closed Loop Control. Journal of the Precision Machinery Society. 2000;66: 1461-1466.

MACHINE LEARNING APPROACH PREDICTION OF STRESS-STRAIN CURVES FOR LOW-TEMPERATURE ANNEALED CARBON STEELS

Reona Ito[1], Keisuke Nagato[2], Takayoshi Niho[2] and Masayuki Nakao[2]
[1]Department of Technology Management for Innovation,
The University of Tokyo,
Bunkyo-ku, Tokyo, Japan
[2]Department of Mechanical Engineering,
The University of Tokyo,
Bunkyo-ku, Tokyo, Japan

INTRODUCTION

The mechanical properties of carbon steel, one of the common industrial materials, are determined by the morphology of its microstructure. Therefore, research is being conducted to predict the mechanical properties from the microstructures of materials such as grain size and form of phase in the materials [1,2]. As a popular example of predicting mechanical properties from the microstructure of materials, the Hall–Petch relation [3] has been proposed that can predict the yield stress of materials from the grain size.

However, it is known that mechanical properties of alloys containing multiple elements undergo complex transformation of their microstructures through processes such as heat treatments and other processing methods. Thus, in empirical ways, limits would appear for creating a prediction model that considers the complexity of transformations in microstructures caused by processing of materials. To overcome limitations arising from the complexity, it has been proposed that the mechanical properties of materials can be predicted using the machine learning approach methods that configures artificial neural networks (ANN). This method can create prediction models by training based on complex input information in the microstructures of the materials.

Setti [4] reported an accurate prediction of the stress-strain curves of titanium alloys, which are composed of different phases, by the machine learning approach. Using a similar approach, Adachi [5] predicted the stress-strain curve of ferrite-martensite dual phase (DP) steels by training the ANN with an input value of material genomes, such as volume fraction and micro-hardness of the ferrite phase. In those researches, the method for prediction of the stress-strain curves by the ANN mainly uses information of the microstructures in materials for training. Since the information of the microstructures in the material is complicated and has randomness, the mechanical properties should be predicted using the information or parameters at the process performed on the materials that are more accessible and have reliable data compared with the microstructural parameters.

In this research, we focused on the method to predict the stress-strain curves by the ANN-based machine learning approach using information of heat treatment processes for training.

METHOD

Data Acquisition for Machine Learning

The material used in this paper is 1045 AISI, common medium carbon steels. The specimens are cylinder-shaped with a diameter of 8 mm and a height of 12 mm. We conducted low-temperature annealing, which is usually implemented to make the material soft and remove the residual stress in the material. *FIGURE 1* shows a diagram of the heat treatment. In order to prevent significant oxidization of the material, all heat treatment processes were conducted in a vacuumed electric furnace. The temperature inside of the furnace was raised to T in 20 min regardless of the target temperature T. After the furnace temperature reached T, it was kept at T for time t and was cooled until the temperature in the furnace reached 400 °C at 1 °C per minute of the cooling rate. The furnace was turned off when the temperature reached 400 °C or less, and was air cooled to room temperature RT (approximately 20°C). Each value of the target temperature T and holding time t in the heat treatment conducted in this experiment are shown in the *TABLE 1*. The minimum value of T was set to 450 °C, which is sufficiently above the recrystallization temperature of 1045 AISI, and the maximum value was set to 750 °C. In the range of 450–750 °C, 550 °C, and 650 °C were

also selected for the heat treatment parameter *T*. The holding time *t* was set to three patterns of 30 min, 60 min, and 120 min.

Four types of heat treatments—A, B, C, D—shown in *TABLE 1* were implemented on the specimens in this experiment. After the specimens had been heat-treated, they were compressed by THERMECMASTOR Z (Fuji Electronic Industrial Co., LTD) to obtain the stress-strain curves for machine learning. The strain rate during the compression test was fixed at 0.001.

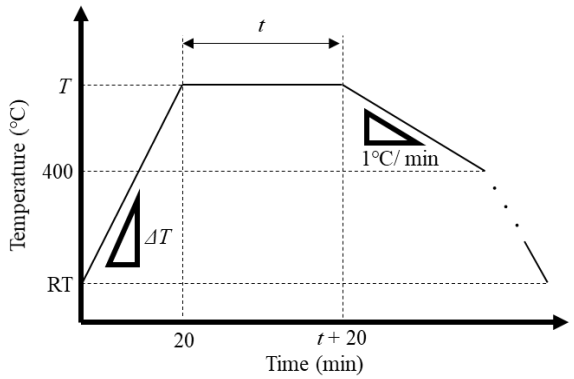

FIGURE 1. Process of heat treatment.

TABLE 1. Specific condition of heat treatment.

		t (min)		
		30	60	120
T (°C)	450	A	-	-
	550	-	B	-
	650	-	-	C
	750	D	-	-

Artificial Neural Network

The ANN used in this experiment was coded with Python 3.6 environment using *Tensorflow*, an open-source software library for machine learning [6]. The network's main structure was roughly divided into three parts, an input layer, hidden layers, and an output layer.

Four feature values, which had been inputted into an input layer, are shown in *FIGURE 2*: the strain value, target temperature *T* (°C), holding time *t* (min), and heating rate ΔT

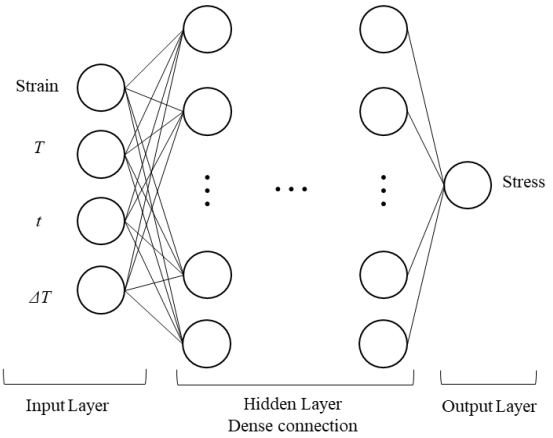

FIGURE 2. Schematic of the artificial neural network.

TABLE 2. Network number and number of nodes for each network.

Network No.	Number of Nodes 1st Hidden Layer	Number of Nodes 2nd Hidden Layer
1	100	-
2	500	-
3	1000	-
4	100	100
5	500	500
6	1000	1000

(°C/min), which are the parameters during the heat treatment process. Owing to the large difference in numerical size depending on the types of feature values (e.g., largest value of stress compared with that of strain), normalization of feature values had been subjected to each feature value such that the minimum value in each feature value is 0 and the maximum value is 1 before inputting them into an input layer. Further, 80% of the total dataset was used as the training data and the rest as validation data for the trained model to check the generalization performance. Batch training [7] was performed in the step of training and the size of the batch was set to 100. *TABLE 2* shows the number of hidden layers and nodes for each layer. The number of nodes in a single hidden layer was examined in three patterns of 100, 500, and 1000, and the number of layers in two patterns of 1 or 2 layers. A total of six patterns of networks (Network No. 1–6 in *TABLE 2*) were implemented in this experiment. Each node was densely connected (a single node is connected to all nodes in the next layer), and the type of activation function applied at all edges (connections of

nodes) was a rectified linear unit (ReLU). In addition, the *Dropout* algorithm [8] was used as the regularization method to prevent overfitting, and the value of the dropout-rate (one of the hyper-parameters in the dropout algorithm) for the nodes in the networks was fixed to 20%.

Mean squared error (MSE) was used for the objective function to optimize the ANN, and *Adam* [9] was selected as the optimization method for training. In the case of using Adam for an optimizer, it is necessary to set the learning rate. In this experiment, the learning rate was set to a constant value of 0.001. Moreover, the number of epochs for training was fixed with a constant parameter of 100.

Three stress-strain curves heat-treated with conditions A, C, and D, listed in *TABLE 1,* were used for training the ANN to predict the stress-strain curve that was subjected to the heat treatment B. To check the prediction accuracy of the trained model, a predicted curve was compared with an actual stress-strain curve obtained from the experiment.

RESULT AND DISCUSSION

Microstructures of specimens (5% nital-etched), which were heat-treated with conditions A and D observed with an optical microscope are shown in *FIGURES 3(a)***,** *(b)*. The microstructure of the specimen that was heat-treated in condition A (45 °C in 30 min, *FIGURE 3(a)*) is composed of a ferrite phase and a pearlite phase which ferrite and cementite phase are formed in stripes (enclosed in a square). On the other hand, the microstructure in a specimen heat-treated under condition D (750 °C in 30 min, *FIGURE 3(b)*) has a larger amount of ferrite phase compared with that under condition A. Moreover, most parts are assumed to be in the pearlite phase before the heat treatment are filled with the ferrite phase leaving the cementite phase clearly. Thereby, although the heat treatment did not perform clear phase transformations since the holding temperature *T* during the heat treatment did not exceed the α-γ phase transformation temperature of AISI1045 (greater than 750 °C), it is clear that the phase morphology in materials had been dramatically and intricately changed due to the heat treatment.

FIGURE 4 shows the stress-strain curves used for training the ANN obtained from the compression test. According to *FIGURE 4*, no obvious similarity was found in the curves. This implies that the profile of the stress-strain curves varied depending on each heat treatment condition. The three curves in *FIGURE 4* are adopted to train the six networks shown in *TABLE 2*.

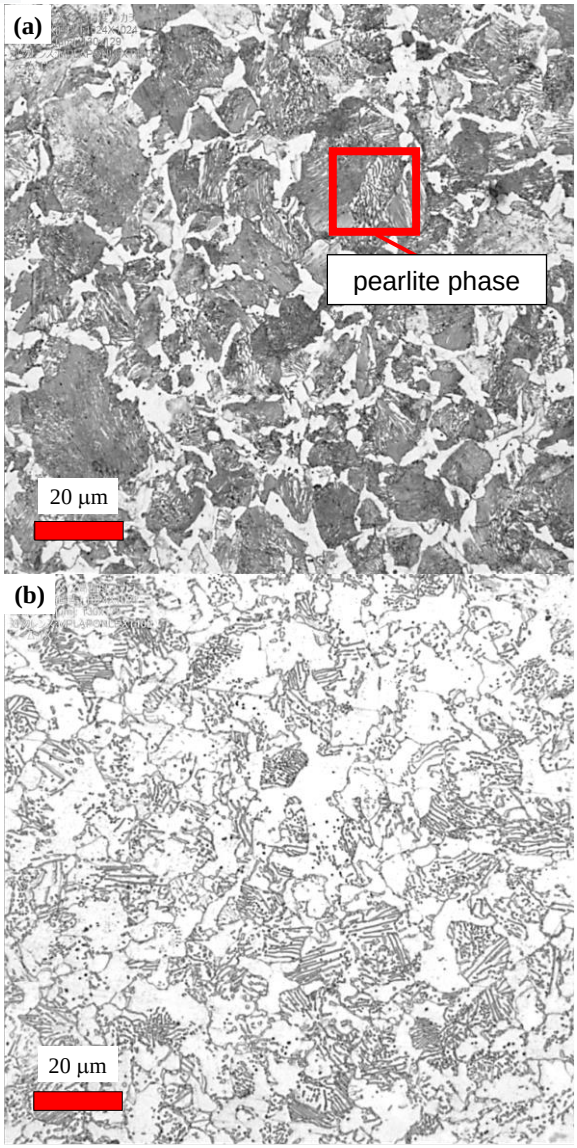

FIGURES 3. Microstructure of AISI1045 heat-treated at (a) 450 °C *in 30 min; (b) 750* °C *in 30 min.*

Moreover, the stress-strain curves heat-treated in condition B predicted by Network Nos. 1, 3, 5, and 6 are shown in *FIGURE 5(a)–(d)*. The stress-strain curve procured by the compression experiment are also shown in *FIGURE 5(a)–(d)*. The predicted curves by the single hidden layer networks with 100 and 1000 nodes (*FIGURE 5(a)* and *(b), respectively*) have large gaps between the curves obtained from the compression test.

According to *FIGURE 5(c)***,** the 500 nodes with the two hidden layer network structure are expected to be closest to the experimental curve. The learning curves of Network No. 5 are shown

in *FIGURE 6*, and it shows that the network had been trained enough without overfitting. Network Nos. 1 and 3 have single hidden layers, and it is speculated that these networks do not have enough complexity to describe the complicated transformation of mechanical properties through heat treatment. Moreover, despite the high complexity of Network No. 6, we can see the gaps between the predicted curve and an experimental curve. This may be caused by the over-fitting of the network.

The curve predicted by the trained Network No. 5 shown in the *FIGURE 5(c)* has a close profile compared with the experimental curve. However, the prediction accuracy after the strain value of 0.2 appears to be deteriorated. The cause of low prediction accuracy was assumed to be the unstable behaviors due to the contaminated training data owing to the formation of voids in the material at a large deformation.

Inoue [10] reported that the fraction of cementite in the pearlite phase causes voids in the material. As shown in *FIGURE 3(a)* and *(b)*, the annealed specimens have microstructures of ferrite and pearlite phases, and as the amount of strain increases, voids occur, and unstable fracture behaviors were introduced into the training data. Thus, the prediction accuracy of the stress-strain curve fell in the high strain range (0.2~).

As a result, it is possible to predict the stress-strain curves by using only the parameters of the heat treatment by machine learning, even for materials whose phase morphology changes complexly, as shown in *FIGURE 3*.

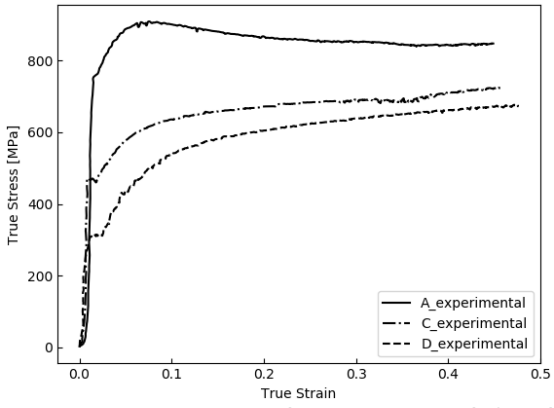

FIGURE 4. Stress-strain curves used for the training of the neural network obtained from the compression experiments for each heat treatment conditions.

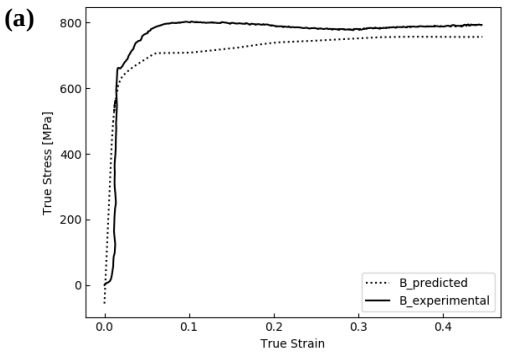

Network No.1 (100)

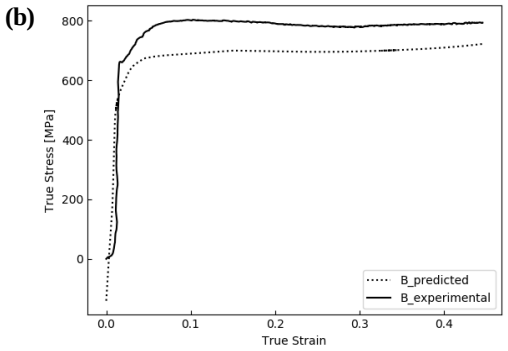

Network No.3 (1000)

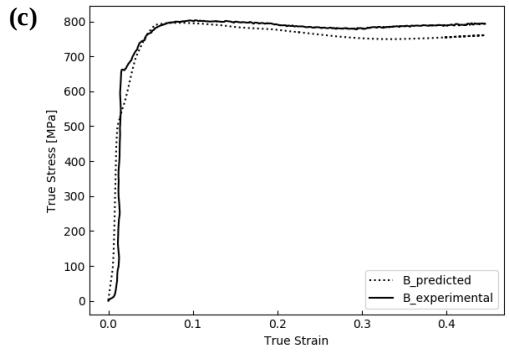

Network No.5 (500-500)

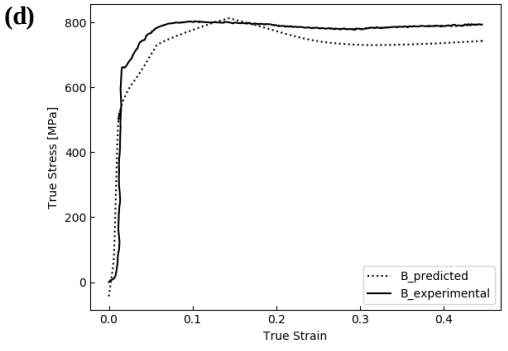

Network No.6 (1000-1000)

FIGURES 5. Predicted stress-strain curves by the trained model and experimental stress-strain curves at (a) Network No. 1, (b) Network No. 3, (c) Network No. 5, (d) Network No. 6.

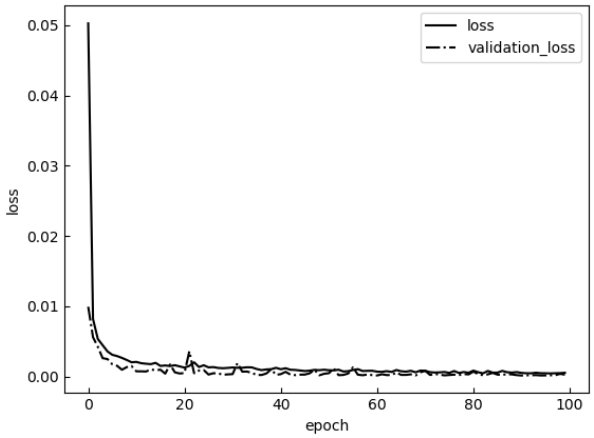

FIGURE 6. Value of MSE (loss) and validation loss vs number of epochs at Network No. 5 (500-500).

CONCLUSION

A compression test was performed on medium carbon steel AISI1045 subjected to four types of heat treatments.

Heat treatment was performed at different holding times from 450 °C (above recrystallization temperature) to 750 °C (below the α-γ phase transformation temperature). The microstructure of the heat-treated material was observed with an optical microscope, and it was found that although the phase transformation did not occur, the morphology of the ferrite phase and pearlite phase was significantly transformed.

Artificial neural networks (ANN) were trained by the data of three stress-strain curves (450 °C in 30 min, 650 °C in 120 min, 750 °C in 30 min) obtained by the compression tests. Using the trained ANN model, the stress-strain curve of the heat-treated carbon steel (550 °C in 60 minutes) was predicted by inputting the strain value, holding temperature, holding time, and temperature rising rate into the trained network. Finally, the network outputted the value of the stress.

The ANN trained in this research had six types and they were compared an accuracy of a prediction of stress-strain curve.

As a result, we found out that the network structure of the two hidden layers with 500 nodes for each layer predicted the closest stress-strain curve to an experimental curve, and it is possible to predict the stress-strain curve by only utilizing the heat treatment parameters by machine learning.

However, the prediction accuracy deteriorated after the strain value reached 0.2. This poor accuracy at the large deformation range was considered as a result from unstable behavior in the material caused by the voids, which formed due to the fracture of cementite in the pearlite phase.

The structure of the network that most accurately predicts the stress-strain curve depends on the dataset. Therefore, when the dataset is changed, the optimal model for predicting the stress-strain curve is different from that obtained in this study. This means that there is a limit to the types of stress-strain curves that can be predicted using the dataset used in this study. In the future, it is required to increase the variation of the stress-strain curves that can be predicted by designing the structure of the dataset.

REFERENCES

[1] Tekkaya A, Allwood J, Bariani P, Bruschi S, Cao J, Gramlich S, Groche P, Hirt G, Ishikawa T, Lobbe C, Lueg-Althoff J, Merklein M, Misiolek W, Pietrzyk M, Shivpuri R, Yanagimoto J. Metal Forming Beyond Shaping: Predicting and Setting Product Properties. CIRP Annals – Manufacturing Technology. 2015; 64: 629-653.

[2] Umemoto M. Relationships Between Microstructure and Mechanical Properties in Steels. Tetsu-to-Hagane. 1995; 81(3): 157-166.

[3] Hansen N. Hall-Petch Relation and Boundary Strengthening. Scripta Materialia. 2004; 51: 801-806.

[4] Setti S, Rao R. Artificial Neural Network Approach for Prediction of Stress-Strain Curve of near β Titanium Alloy. Rare Metals. 2014; 33: 249-257.

[5] High Dimensional Microstructure Data-driven Prediction of Stress-Strain Curve of DP Steels by Primary Artificial Intelligence. Tetsu-to-Hagane. 2016; 102(1): 47-55.

[6] Pedregosa F, Varoquaux G, Gramfort A, Michel V, Thirion B, Grisel O, Blondel M, Prettenhofer P, Weiss R, Dubourg V, Vanderplas J, Passos A, Cournapeau D. Scikit-learn: Machine Learning in Python. Journal of Machine Learning Research. 2011; 12: 2825-2830.

[7] Bishop C. Pattern Recognition and Machine Learning. Springer. New York: 2006.

[8] Srivastava N, Hinton G, Krizhevky A, Sutskever I, Salakhutdinov R. Dropout: A Simple Way to Prevent Neural Networks from Overfitting. Journal of Machine Learning Research. 2014; 15: 1929-1958.

[9] Kingma D, Ba J. ADAM: A Method for Stochastic Optimization. International Conference on Learning Representative. 2015.
[10] Inoue T, Kinoshita S. Strain Partitioning and Void Formation in Ferrite-Pearlite Steels Deformed in Tension. Tetsu-to-Hagane. 1976; 62(1): 90-99.

MANUFACTURING TECHNOLOGY OF METAMATERIAL WITH DOUBLE SQUARE LOOP ARRAY FILLED CONDUCTIVE CARBON INK FOR MICROWAVE ABSORPTION

T. J. Je[1,2], J. Y. Jeong[1,2], J. S. Han[1], D. S. Choi[1], J. H. Shin[3]
[1]Department of Nano Manufacturing Technology
Korea Institute of Machinery and Materials (KIMM)
[2]Department of Nano Mechatronics
University of Science and Technology (UST)
[3]Department of Materials Science and Engineering
Korea Advanced Institute of Science and Technology (KAIST)

INTRODUCTION

Microwaves are used as radars for detection of fighter aircrafts and battlefields. The conventional method which is applying a paint containing a large amount of iron powder has been mainly use to avoid detection radar. However, this method has problems such as increasing the energy consumption by heavy load due to the iron of high specific gravity, and high cost. To solve these problems, technologies for applying metamaterials have been recently studied.[1,2]

Metamaterials use artificial structures to implement functions that do not occur naturally. This material can be reduce the specific gravity and thickness of the microwave absorber. A CIC(conductive-insulator-conductive) structure is mainly applied to generate an absorption effect due to electromagnetic resonance of microwave passing through a metamaterial, and various micro/nano patterns such as cross, patch, closed loop, split loop are studied for the expand the range of absorption band of microwave.[3,4]

As part of these research, manufacturing technology of CIC structured metamaterial of flat surface having DSLA(double square loop array) by mechanical machining and filling processes was studied, and microwave absorption performance of this material was evaluated.

METAMATERIAL DESIGN

Fig. 1 shows a top view (a) and a cross-section (b) of a unit cell of a CIC structured metamaterial with a DSLA filled with a conductive ink. The shape dimensions of the unit cell, the sheet resistance of the conductive ink, and the dielectric constant of the PMMA are summarized in Table 1. This unit cell was designed by using genetic algorithm and referenced to design method of the DSLA previously studied by Ye Han.[5] This metamaterial have a reflection performance of under -10dB in the X-band(8~12GHz).

MANUFACTURING AND RESULTS

Mechanical Machining of Double Square Loop Array

A micro-endmilling process was applied to fabricate a DSLA on the PMMA substrate which

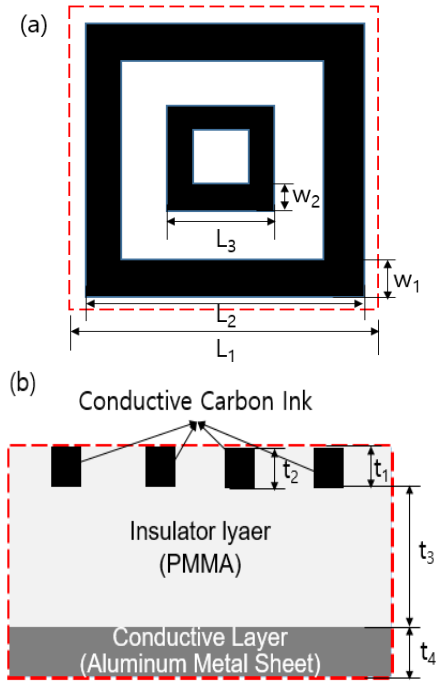

FIGURE 1. Unitcell of metamaterial which is consisting of conductive-insulator with conductive double square loop; (a) top view of the unitcell, (b) side of the unitcell

TABLE 1. The dimensions of the unit cell, sheet resistance of conductive ink, and the dielectric constant of PMMA

Item	Value
Period of unit cell(L_1)	4.791 mm
Outer loop size(L_2)	4.179 mm
Inner loop size(L_3)	2.470 mm
Outer loop width(w_1)	0.144 mm
Outer loop width(w_2)	0.350 mm
Outer loop thickness (t_1)	0.025 mm
Inner loop thickness (t_2)	0.025 mm
Insulator thickness(t_3)	2.5 mm
Surface resistance of conductive ink	6.871 ohm/sq

is insulator, and Fig. 2 shows an ultra-precision endmilling system with a position accuracy of 10nm used in this study. The rotation speed of the cutting tool was 50000rpm and the feed was 5mm/sec. In order to shorten the machining time, a micro endmill with a diameter of 100 μm was used for machining the outer loop having width of 145 μm, and endmill with a diameter of 200 μm was used for inner loop having width of 357 μm. The quality of the edge of the sidewall and bottom surface was optimized by applying the initial and final cutting depth to 2 μm, and the cutting depths between both steps were equally divided. Fig. 3 shows machined PMMA substrate with DSLs of 961 number, and measured images by using microscope. The width of outer loop was machined with 145.622 μm as shown in Fig. 3 (b) and inner loop was machined with 357.26 μm as shown in Fig. 3 (c). It was confirmed that the error was about 1.3% compared the design with machined loop.

Filling Process of Conductive Carbon Ink

In order to fabricate the DSLA with the designed value of sheet resistance, we use a manually mixed conductive carbon ink which has average sheet resistance of 7.3 ohm/sq at a thickness of 25 μm was used. As shown in Fig. 4, the conductive ink was sufficiently applied to the surface of machined PMMA substrate, and it cured at room temperature to minimize the deformation of the substrate. After the ink was completely cured, the remaining it except the ink filled in the DSLA was removed using a planing process. Aluminum sheet was attached to the back side of the substrate, Fig. 5 shows the finally fabricated CIC metamaterial with DSLA filled by conductive ink.

PERFORMANCE

The absorption performance of CIC structured metamaterial fabricated in this study was measured by using reflectance measurement system which has measuring range of X-band

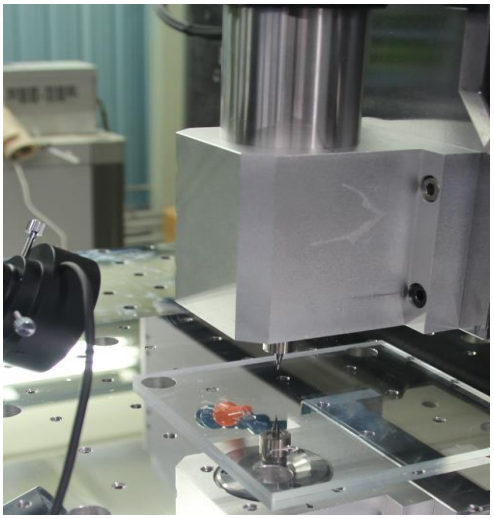

FIGURE 2. Micro-endmilling system for the machining of the double square loop array

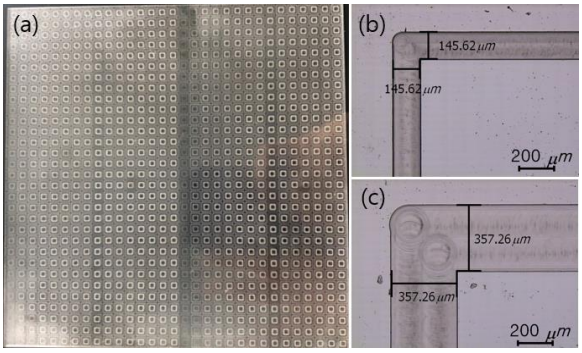

FIGURE 3. (a) The machined 150x150mm PMMA substrate with double square loop array and microscope images of the part of the double square loop; (b) outer loop, (c) inner loop

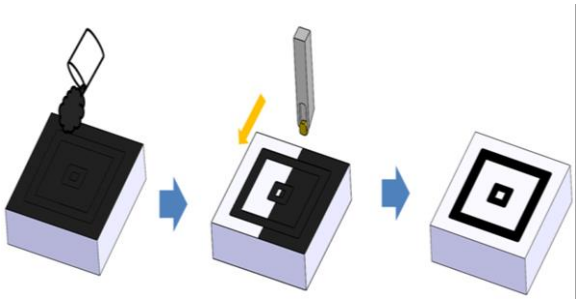

FIGURE 4. Filling process of the conductive carbon ink in the double square loop on insulator substrate

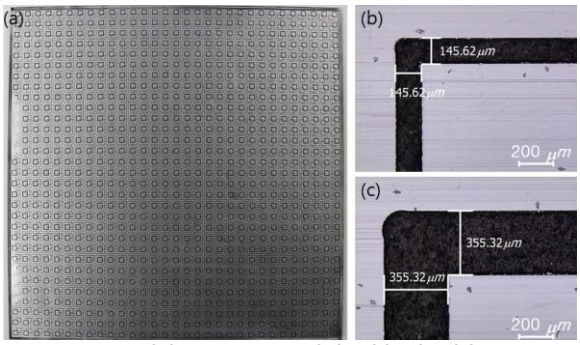

FIGURE 5. (a) Metamaterial with double square loop array filled by conductive ink and microscope images; (a) outer loop, (c) inner loop

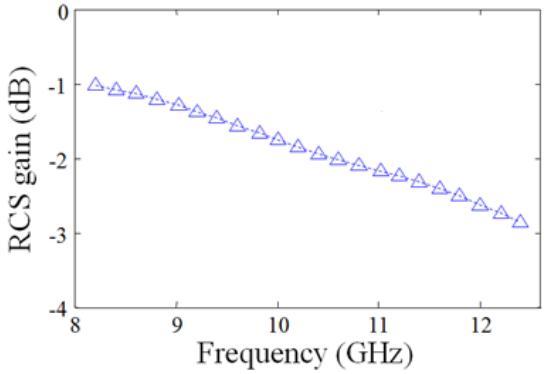

FIGURE 6. Measured RCS gain of the manufactured CIC metamaterial in X-band of micro wave

(8~12GHz). Fig. 6 shows the graph of measured value of RCS gain which is meaning reflectance. In the measured range of micro wave frequency, the reflectance was measured from -1 dB to -3 dB, and this result was different with designed value. However, it tends to decrease steadily with increasing frequency of microwave. It is considered that the electromagnetic resonance band of this metamaterial is shifted to the band of more than 12 GHz. This phenomenon can be attributed to errors in sheet resistance and irregularities in conductive ink, and it can be complemented by further research on a conductive ink.

CONCLUSION

In this paper, the manufacturing process of the CIC structured metamaterial which has conductive double square loop on the surface of it was studied. The double square loop array was machined by using micro-endmilling process on the PMMA substrate within 1 % of size error compared with designed shape. Then, the machined surface was applied by conductive ink which has 7.6 ohm/sq and it was cured in room temperature. The cured ink covering the substrate surface was taken off by using planing process. The reflectance of the fabricated metamaterial in X-band(8~12GHz) was measured from -1 dB to -3 dB, and the designed reflectance performance was not satisfied. However, it tends to decrease according to increasing frequency. Therefore, it is considered that the transition of the resonance band into high frequency more than X-band was generated by the error of the sheet resistance of filled conductive carbon ink into DSLA and irregularity. These issues will be addressed in future studies.

REFERENCES

[1] Z. Zhai, C. Zhan, Z. Li, C. Liang. A triple-band ultrathin metamaterial absorber with wide-angle and polarization stability. . IEEE Antennas and Wireless Propagation Letters. 2015; 14: 241-244

[2] Y. Zhang, et al. Broadband and tunable high-performance microwave absorption of an ultralight and highly compressible graphene foam. Journal of Advanced Material. 2015; 27: 2049-2053

[3] Y. Fan, et al. Ultra-thin and –broadband microwave magnetic absorber enhanced by phase gradient metasurface incorporation. Jornal of Physics D: Applied Physics. 2018; 51: 215001

[4] J. Yang, Z. Shen. A thin and broadband absorber using double-square loops. IEEE Antennas and Wireless Propagation Letters, 2007; 6: 388-391

[5] Y. Han, W. Che, C. Christopoulos, Y. Xiong, Y. Chang. A Fast and Efficient Design Method for Circuit Analog Absorbers Consisting of Resistive Square-Loop Arrays. IEEE Transactions on Electromagnetic Compatibility. 2016; 58: 747-757

ACKNOWLEGEMENT

“This work was supported by the Technology Innovation Program (20003945, Development of Core manufacturing technology of 4-axes ultra precision machining system and lens module for next-generation mobile lens having about 100nm shape accuracy) funded By the Ministry of Trade, Industry & Energy(MOTIE, Korea). This work also was supported by the Center for Advanced Meta-Materials(CAMM) funded by the Ministry of Science and ICT as Global Frontier Project(CAMM- No. 2019M3A6B3031046)”

NUMERICALLY CONTROLLED PLASMA CHEMICAL VAPORIZATION MACHINING USING ARRAY-TYPE ELECTRODE TOWARD HIGH-THROUGHPUT DETERMINISTIC MACHINING

Ken Nishida*, Shinya Okayama[1], Satoshi Matsuyama[1], Kazuto Yamauchi[1, 2], and Yasuhisa Sano[1]

[1]Department of Precision Science and Technology, Graduate School of Engineering, Osaka University, Suita, Osaka 565-0871, Japan

[2]Research Center for Ultra-Precision Science and Technology, Graduate School of Engineering, Osaka University, Suita, Osaka 565-0871, Japan

INTRODUCTION

Deterministic numerically controlled (NC) ultraprecision machining methods to realize nanometer-scale accuracy have been developed to satisfy the high-accuracy requirements of cutting-edge optical elements and electronic materials. Conventional deterministic NC machining is performed by scanning the machining head onto the entire work surface through feed-speed distribution that is calculated by deconvolution methods using pre-measured figure error distribution and a removal function of the machining head. Nanometer-scale accuracy can be obtained through these NC machining methods. For example, the thickness variation of a silicon-on-insulator (SOI) layer was reduced from 2.4 nm peak-to-valley (PV) to 0.9 nm PV by NC sacrificial oxidation [1]. However, the application of these methods is difficult for the mass production of materials such as semiconductor substrates; this is because the scanning part of the method tends to take a long time. Thus, we proposed the use of an array-type electrode instead of a single scanning electrode (Figure 1) for this process.

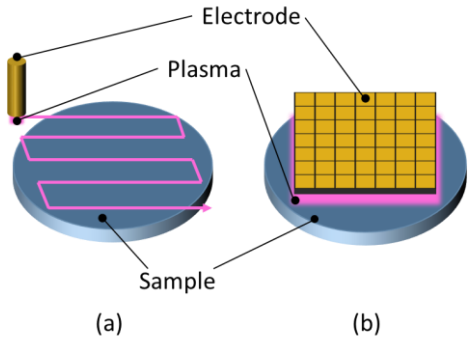

FIGURE 1. Schematic of numerically controlled plasma process with (a) single electrode, and (b) array-type electrode.

By controlling the plasma-on time of each electrode, simultaneous NC machining can be performed. We reported that the thickness variation of the SOI layer was reduced from 2.85 nm PV to 0.86 nm PV by NC sacrificial oxidation in only 40 min using an array-type electrode [2]. However, the sacrificial oxidation method is limited to the removal of amounts of less than 10 nm because of the thickness limitations of the oxidation process. Thus, we propose the application of an array-type electrode to the high-speed plasma etching method called plasma chemical vaporization machining (PCVM) [3,4]. In a plasma etching system, the stable and uniform supply of process gas and prompt ejection of reaction products should be important for the precise control of removal amounts. In this paper, we describe both a new machining procedure to meet the above demands and the results of basic experiments performed to this respect.

NEW MACHINING PROCEDURE

In order to avoid non-uniform etching, gas flow associated with the consumption of etching gas and the generation of reaction gas products, we proposed to use a “gas holding” method shown in Figure 2. In the gas-supply step, the processing gas is put into the chamber, opening only the gas-supplying valve. In the plasma-etching step, plasma is generated and the sample is processed without any gas flow. Finally, in the gas-exhaust step, plasma generation is turned off and the reaction products are exhausted, opening only the gas-exhaust valve. The cyclic etch process is performed by repeating these steps.

APPARATUS DESIGN

Figure 3 shows the schematic of the apparatus with an array-type electrode. This apparatus has 7 × 7 square electrodes with a length of approximately 4.8 mm; each electrode is switch

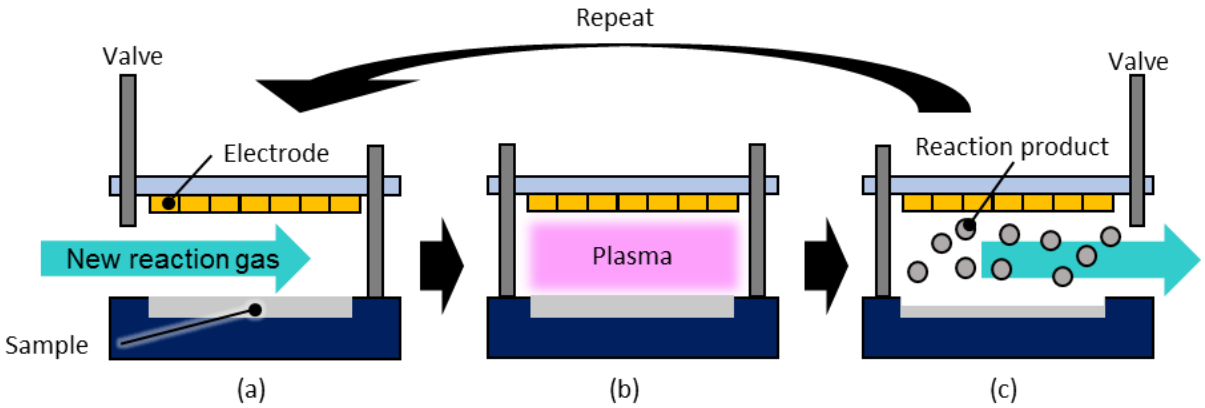

FIGURE 2. Schematic of cyclic etch process (a) Gas-supply step, (b) Plasma etching step, and (c) Gas-exhaust step.

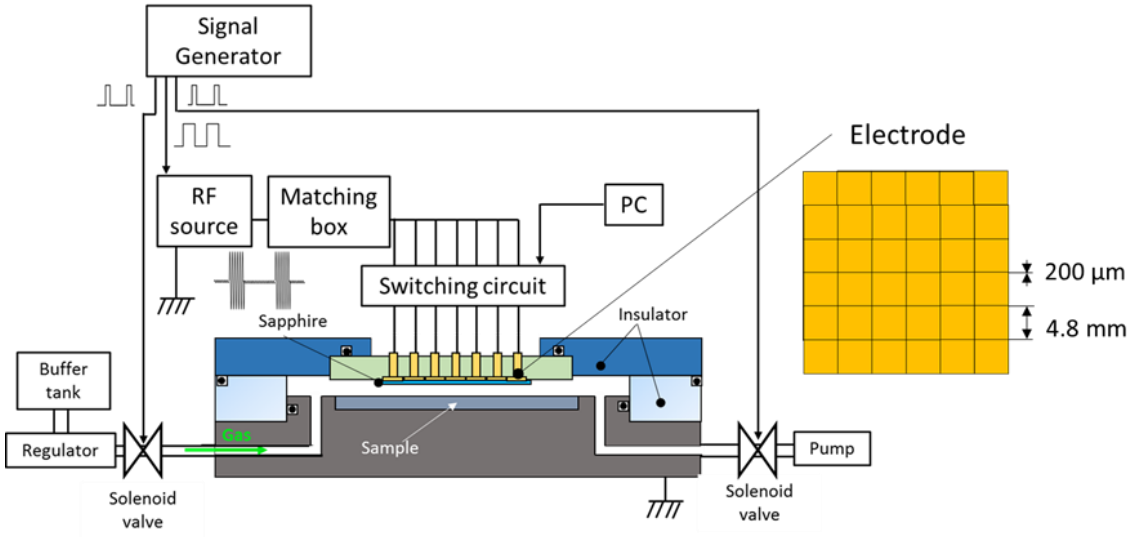

FIGURE 3. Schematic of apparatus with array-type electrode.

controlled by a PC for ON/OFF control of radio frequency (RF) power. In this method, plasma disappears when the electrical RF switch is turned off. The distance between the adjacent electrodes is 200 µm; if the distance is too small, the control of the ON/OFF switch can be lost due to capacitive coupling to proximate electrodes. However, if the distance is too large, non-processed areas can appear between the electrodes. The power frequency used was 13.56 MHz. We used the mixed gas He/SF_6, as a process gas. The distance between the electrodes and wafer was 1500 µm. There are two solenoid valves for the process control. One is a gas-exhaust valve located between the vacuum pump and the chamber, and the other is a gas-supply valve located between the gas mixing tank and the chamber. A multichannel signal generator can control individual on-off timing of the gas-exhaust valve, gas-supply valve, and RF power.

CONSIDERATION OF VALVE-OPENING TIME

First, we investigated the amount time necessary to exhaust reaction products. After supplying the process gas till the atmosphere pressure, the gas-exhaust valve was opened and the pressure in the chamber and the voltage of the signal to the valve were measured. Figure 4 shows the time dependence results of the pressure. The valve was opened without time lag when the valve received the signal from a signal generator. When the valve-opening time was 100 ms or more, it was enough to exhaust the reaction products in the chamber.

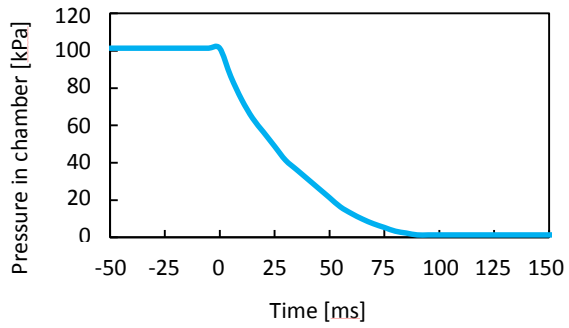

FIGURE 4. Time dependence of the pressure after the gas-exhaust valve is opened.

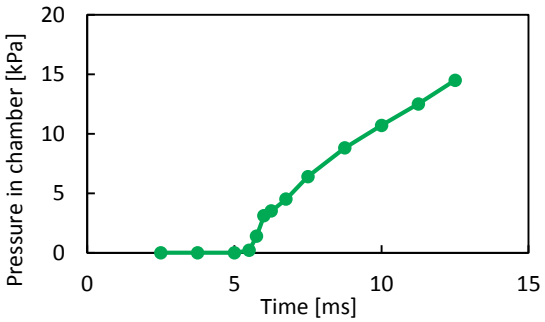

FIGURE 5. Time dependence of the pressure after the gas-supply valve is opened.

Second, we investigated the time required to supply the reaction gas. After evacuating the chamber, the gas-supply valve was opened during a period of time and the pressure in the chamber was measured; Figure 5 shows these results. It was found that it is possible to control the processing pressure by controlling the opening time of the gas-supply valve.

CONSIDERATION OF PLASMA-ON TIME

The plasma-ON time/cycle was investigated by an etching experiment using a Si wafer. The experimental conditions were as follows: RF power of 190 W, processing time of 5 min, electrode-sample distance of 1500 μm, chamber pressure of 3 kPa, reaction gas of He: SF_6 = 95:5, gas-supplying time of 6 ms/cycle, gas-exhausting time of 100 ms/cycle, and cycle time of 250 ms. Figures 6 (a) and (b) show the surface profiles when the plasma-ON time was 40 and 50 ms/cycle, respectively. When the plasma-ON time was 40 ms/cycle, an almost uniform processing amount was obtained. However, when the plasma-ON time was 50 ms, a larger removal depth was obtained at the electrode edge area than at the center area of the electrode. The maximum removal depth at the edge and the minimum removal depth at the center were measured in the case of each plasma-ON time; the results are shown in Figure 7. This result indicates that the maximum processing amount increases as plasma-ON time increases, whereas the minimum removal depth does not increase by more than approximately 1100 nm. Based on these results, we think that the reason for the saturation of the minimum removal depth is the consumption of SF_6 and the redepositing of the reaction products. The reason why the maximum removal depth increased even after consumption of SF_6 is that SF_6 is supplied from outside of the electrode area by the diffusion phenomena.

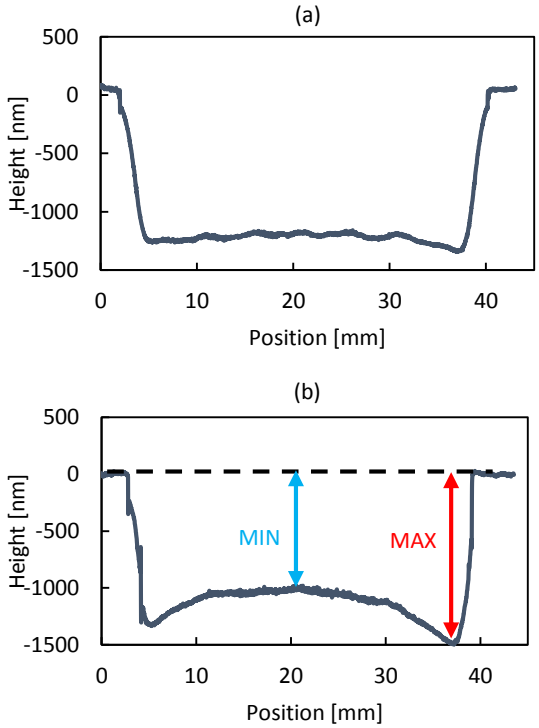

FIGURE 6. Surface profile after processing of (a) plasma-ON times of 40 ms and (b) 50 ms.

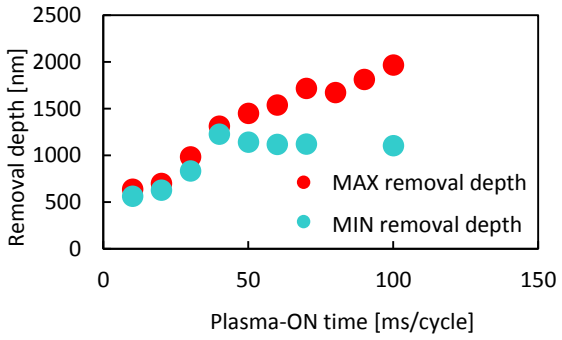

FIGURE 7. MAX and MIN removal depths in the case of each plasma-ON time.

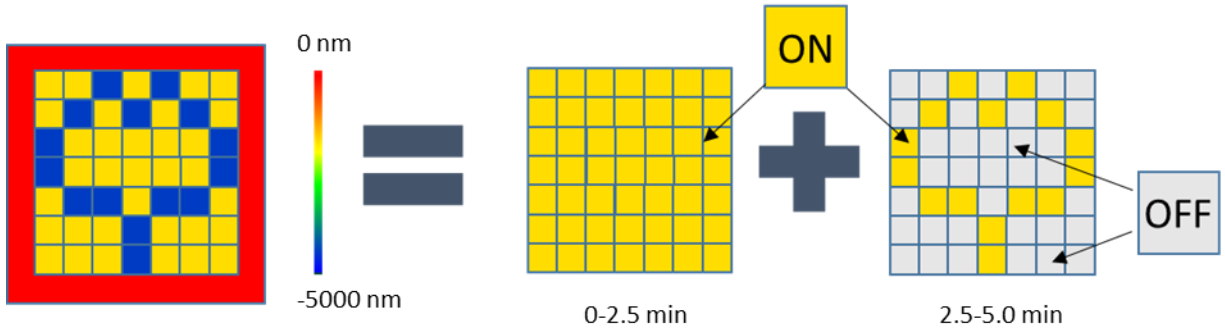

FIGURE 8. Target processing shape and electrode on-off pattern.

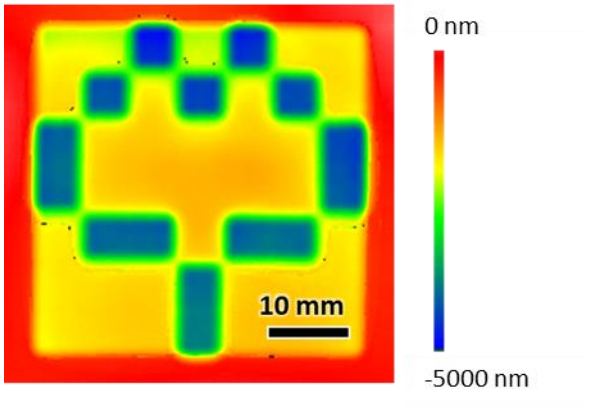

FIGURE 9. Removal depth distribution.

NC PROCESS DEMONSTRATION

Simultaneously, numerically controlled plasma chemical vaporization machining (NC-PCVM) was performed by controlling the process time of each electrode. Figure 8 shows the target processing shape. Experimental conditions were as follows: electrode voltage of 290 V, electrode-sample distance of 1500 μm, chamber pressure of 3 kPa, reaction gas of He: SF_6 = 95:5, gas-supplying time of 6 ms/cycle, gas-exhausting time of 100 ms/cycle, plasma-ON time of 40 ms/cycle, and a cycle time of 250 ms. Plasma was generated under all electrodes in the first 2.5 min and under only selected electrodes in the following 2.5 min. RF power was adjusted to maintain a stable applied voltage. Figure 9 shows the results of the removal depth distribution. It can be said that the actual processing shape is very similar to the target processing shape. It is also worth noting that the etching rate was about 800 nm/min, which is an extremely high speed for deterministic NC processing.

CONCLUSION

In order to improve the processing time of deterministic NC machining, we proposed an array-type electrode plasma generator capable of simultaneous NC-PCVM processing. We proposed a cyclic etch process composed of an etching step with plasma and a gas exchange step without plasma. After optimizing the process conditions, we successfully obtained the target processing amount distribution using 7 × 7 array-type electrodes. Further developments such as reducing the size of the electrode, increasing the number of electrodes, and improving the processing time could establish the array-type electrode as an NC processing device for mass-produced products.

REFERENCE

[1] Y. Sano, T. Masuda, S. Kamisaka, H. Mimura, S. Matsuyama, K. Yamauchi. Improvement of thickness uniformity of SOI by numerically controlled sacrificial oxidation using atmospheric-pressure plasma. IEEE Int. SOI Conf. 2008: 165–166.

[2] H. Takei, S. Kurio, S. Matsuyama, K. Yamauchi, Y. Sano. Development of array-type atmospheric-pressure RF plasma generator with electric on-off control for high-throughput numerically controlled processes. Rev. Sci. Instrum. 2016; 87: 105121.

[3] Y. Mori, K. Yamauchi, K. Yamamura, Y. Sano, Development of plasma chemical vaporization machining. Rev. Sci. Instrum. 2000; 71: 4627–4632.

[4] Y. Mori, K. Yamamura, Y. Sano. Thinning of silicon-on-insulator wafers by numerically controlled plasma chemical vaporization machining. Rev. Sci. Instrum. 2004; 75: 942-946.

Fundamental analysis on thermal characteristics of high-speed aerostatic spindle

Shumon Wakiya[1], Satsuki Yamazaki[1], Jumpei Kusuyama[2]
Dmytro Fedorynenko[2] and Yohichi Nakao[2]
[1]Graduate School of Mechanical Engineering
Kanagawa University
Yokohama, Kanagawa, JAPAN
[2]Department of Mechanical Engineering
Kanagawa University
Yokohama, Kanagawa, JAPAN

INTRODUCTION

In recent years, ultra-precision cuttings using micro milling cutter to produce parts with micro structural surfaces are being demanded. The parts with the micro structural surfaces are used for various fields based on the state-of-the-art technology, such as automobile, optical, energy, medical industries, for instance. An importance of ultra-precision machine tools for machining dies used for the molding processes of the precise components increases more than before. In the machining of the micro structural surfaces using micro milling cutter, high-speed and precise rotational motion of the machine tool spindle are indispensable to conduct the machining successfully. In the machining applications, aerostatic spindles are most commonly used.

However, in the range of the higher rotational speed such as over, for instance, 100,000 min^{-1}, the influence of the air viscosity on the heat generation cannot be neglected. As a result, the heat generation in the higher speed range causes thermal deformation of the spindle that degrades machining accuracy. In particular, the thermal deformation cannot be neglected in the ultra-precision machining aiming machining with the order of nanometers. Therefore, temperature variation of spindle due to the heat generation during high-speed spindle rotation must be suppressed. Therefore, it is very important to suppress heat generation by cooling the main body of spindle including the rotating shaft directly. An effective cooling performance can be expected by using water as a cooling fluid, because of the excellent thermal conductivity of water.

From the above reasons, in order to accomplish requiring high accuracy and efficient machining of fine components, research and development of the high-speed spindle for ultra-precision machining having superior thermal stability is essential. Accordingly, in this study, we are aiming to develop ultra-high speed aerostatic spindle having high thermal stability with the rated rotational speed: 100,000 min^{-1}. The spindle has a built-in motor to realize the ultra-high speed rotation. In this case, taking effective countermeasures to realize high thermal stability is essential, because not only the heat generation at the aerostatic bearings in the higher speed range but also the heat generation at the built-in motor affect thermal stability of the spindle. In our spindle design, effective cooling structures of the spindle casing as well as shaft bore in the rotating shaft are specifically designed. It should be mentioned that the diameter of the high-speed spindle is necessarily small. In this spindle, a special structure of shaft bore water cooling in the rotating shaft is supported by the aerostatic bearings and driven by the built-in motor is thus proposed.

In this paper, the thermal stability of the designed spindle is investigated using simulation studies. Specifically, the derived results based on the introduced lumped parameter model and finite-element model are presented.

STRUCTURE OF AEROSTATIC SPINDLE

Figure 1 shows the basic structure of the high speed aerostatic spindle that has been

developing in this study. Radial bearings are symmetrically arranged, and axial bearings support loads from both sides. This spindle has a built-in motor to achieve high speed and rotational accuracy. Cooling water is supplied to casing cooling structure, motor cooling structure and shaft cooling structure. In particular, a special structure for supplying cooling water into the rotating spindle shaft supported by aerostatic bearings is contrived.

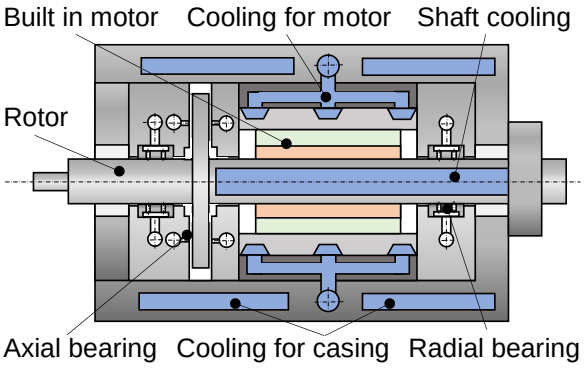

FIGURE 1. Cross-section of aerostatic spindle

HEAT SOURCES OF SPINDLE

Main heat sources of the developed spindle are attributed to the power loss of the built-in motor P_{mo} and the power loss P_a owing to the air viscosity during spindle rotation. These power losses cause to rise the temperature of spindle and lubricant. Each power losses are given as follows.

Power Loss of Built in Motor

The power loss of the built-in motor P_{mo} is given by Eq. (1), where P_{mo_o} and η denote the motor output and motor efficiency, respectively.

$$P_{mo} = P_{mo\_o}(1-\eta) \tag{1}$$

The power loss of the built-in motor P_{mo} divides into the power loss of rotor P_{mo_ro} and the power loss of stator P_{mo_st}. Rates of P_{mo_ro} and P_{mo_st} in the total power loss of the motor are approximately constant. If the rate of rotor part is given by x, the power loss of rotor part P_{mo_ro} and the power loss of stator part P_{mo_st} are given by Eq. (2), Eq. (3).

$$P_{mo\_ro} = xP_{mo} \tag{2}$$

$$P_{mo\_st} = (1-x)P_{mo} \tag{3}$$

Power Loss of Viscous Friction

The power loss due to the viscosity of lubricating air flowing through bearing gaps is significant, according to the increase of the spindle speeds. Even if the viscosity of air is greatly smaller than that of oil, the influence of air viscosity on the spindle rotation is significant, since the power losses of bearing increase in proportion to the square of the rotational speed of the spindle. The power losses of radial bearing and thrust bearing are given by Eq. (4), Eq. (5).

$$P_{th} = \frac{\pi\mu(R_o^{\,4} - R_i^{\,4})}{h_{th}}\omega^2 \tag{4}$$

$$P_{ra} = \frac{2\pi\mu R_{ra}^{\,3} L}{h_{ra}}\omega^2 \tag{5}$$

Here, h_{th} and h_{ra} indicate the bearing gaps of thrust bearing and radial bearing, respectively. In addition, the outer radius and the inner radius of axial bearings are denoted by R_o and R_i. The radius and length of radial bearing are given by R_{ra} and L. The viscosity of air and the angular speed of spindle are denoted by μ_a and ω. Therefore, in the range of ultra-higher rotational speed such as, for instance, more than 100,000 min^{-1}, the heat generation due to the air viscosity is conspicuous.

Moreover, the gross value of the power loss P_a due to viscosity is determined by the sum of the power losses of radial bearing and axial bearing as presented by Eq. (6).

$$P_a = P_{ra} + P_{th} \tag{6}$$

THERMAL STABILITY OF SPINDLE

From the heat generations mentioned above, the analysis results using the introduced lumped parameter model and the finite-element model are shown below.

LUMPED-PARAMETER MODEL

A temperature variation of each elements of the spindle is simulated by the introduced lumped-parameter model applied to air and each spindle parts. The temperature variations of air, rotor, and casing are given by Eqns. (7)- (9).

$$c_a m_a \frac{dT_a}{dt} = P_a - \alpha_{ro} S_{ro}(T_a - T_{ro}) - \alpha_c S_c(T_a - T_c) \tag{7}$$

$$c_{ro}m_{ro}\frac{dT_{ro}}{dt} = P_{mo\_ro} + \alpha_{ro}S_{ro}\left(T_a - T_{ro}\right) - \alpha_{sc}S_{sc}\left(T_{ro} - T_{w\_sc}\right) \quad (8)$$

$$c_c m_c \frac{dT_c}{dt} = P_{mo\_c} + \alpha_c S_c \left(T_a - T_c\right) - \alpha_{cc}S_{cc}\left(T_c - T_{w\_cc}\right) \quad (9)$$

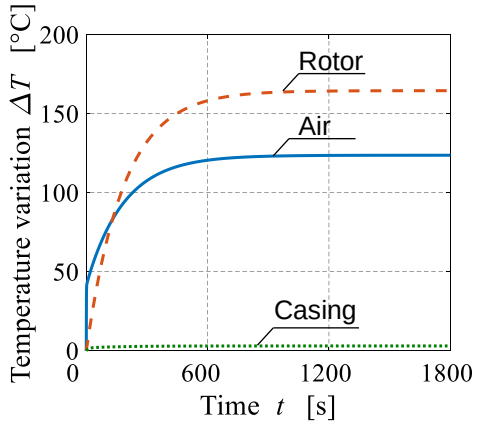

(a) Without shaft bore cooling

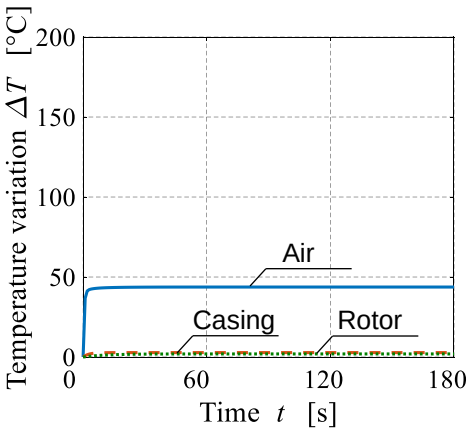

(b) With shaft bore cooling

FIGURE 2. Effect of shaft bore cooling on thermal stability and settling time

In Eqns. (7)- (9), *P*: the heat value, *T*: the temperature, *c*: the specific heat, *m*: the mass, α: the coefficient of heat transfer, *S*: the surface where heat transfer is considered, and *t*: the time. Subscriptions for the defined parameters are *a*: the air, *ro*: the rotor, *c*: the casing, *w*: the water, *mo*: the motor, *cc*: the casing cooling, *sc*: the shaft cooling, and *cj*: the cooling jacket. Figure 2 shows comparison of simulation results, the effect of shaft cooling on cooling is obvious. In the simulation studies, the initial conditions are defined as temperatures of air, rotor, casing, and cooling water are 20 °C, flow rate of air and cooling water are 2 L/min under a rotational speed of 100,000 min^{-1}. Table 1 shows that the shaft cooling is very effective to suppress the temperature rise of the spindle. Furthermore, the shaft cooling reduces the transient response as well.

TABLE 1. Simulation results of shaft bore cooling on thermal stability and settling time

	Without shaft cooling	With shaft cooling
Air ΔT [°C]	123.7	43.7
Rotor ΔT [°C]	164.3	2.7
Casing ΔT [°C]	3.1	1.9
time *t* [s]	1350	84

FINITE-ELEMENT MODEL

The temperature variation is simulated by finite-element model. In the initial conditions used are the same as the simulations by the lumped parameter model. Temperature distribution of the spindle in a steady state is then obtained as shown by Fig. 3. Figure 3(a) indicates that the temperature of the spindle is in a temperature range of from 19.850 to 234.524 °C. In contrary, Figure 3(b) shows a temperature range is from 19.850 to 33.220 °C if shaft-cooling is used.

From the simulation results using finite-element model as well as lumped-parameter model, it is verified how the shaft-cooling effectively reduces the temperature rise in the spindle. However, at the left end of the spindle shaft, the temperature rise cannot be effectively suppressed because the shaft-cooling structure does not reach at the shaft end. Temperature variation of this portion affects the machining accuracy of spindle.

In the simulation studies, the cooling conditions, namely the flowrate and temperature of water were constant. However, the temperature rise of the spindle changes depending on the cooling conditions. Accordingly, the simulations with different cooling conditions are carried out. Based on predicted temperature rise of the spindle shaft, the thermal deformation of the shaft is calculated, in relation to the cooling conditions. The simulation results are shown in Fig. 4.

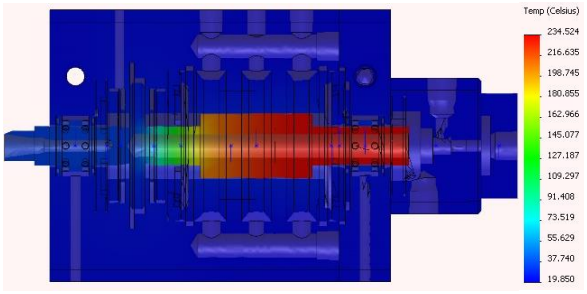

(a) Without shaft bore cooling

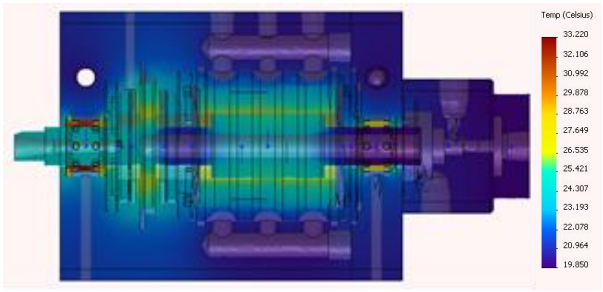

(b) With shaft bore cooling

FIGURE 3. Simulation results of temperature distribution

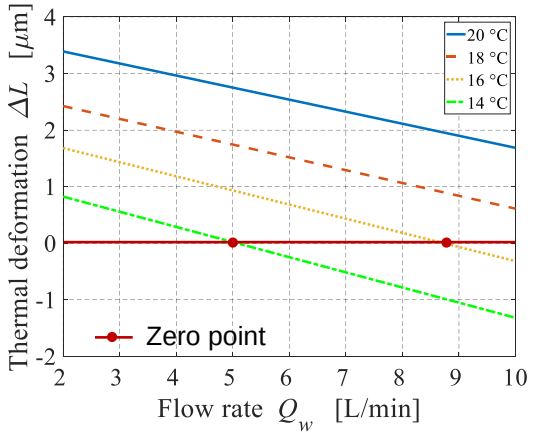

FIGURE 4. Thermal deformation of rotor in relation to temperature and flowrate of cooling water

From Fig. 4, the optimum cooling conditions can be derived. Specifically, the thermal deformation of the shaft becomes zero by using the optimum cooling conditions of temperature of cooling water 16 °C, and flowrate of cooling water 8.7 L/min, or another combination of the cooling condition, temperature of cooling water 14 °C, flowrate of cooling water 5 L/min.

CONCLUSION

In this paper, the temperature variation of the spindle and usefulness of shaft-bore cooling at a rotational speed of 100,000 min^{-1} are discussed by the lumped-parameter model and the finite-element model for aiming at developing high speed aerostatic spindle with better thermal stability. The results by each model show shaft-bore cooling have an extremely high cooling performance, and controlling cooling condition can suppress temperature rise of the rotor that directly affects the machining accuracy.

In the future work, actual spindle thermal characteristics will be investigated experimentally. The results will be compared with the simulation results.

This project is conducted based on the financial support by the NSK Foundation for Advancement of Mechatronics. Their supports are gratefully acknowledged.

REFERENCES

[1] The Japan Society of Mechanical Engineers. Ultra-precision Machining Technology. CORONA Publishing Co., Ltd. 1998; 1-2 (in Japanese).

[2] Ichiro Inazaki, Tohjiro Aoyama. Hydrostatic Bearing -Design and Application-. Kogyo Chosakai Publishing Co.,Ltd. 1998;12-23(in Japanese).

[3] Ryuichi Kawakami. Development of Air Spindles for Ultra Precision Machining. Fujikoshi Technical report, Vol. 50, No. 2. 1994; 58-70(in Japanese).

[4] Shinya Nakamura, Yoshiaki Kakino, Akira Muramatsu, Koichi Urano. An Analysis on Influence of Motor Heat Generation and Effect of Shaft-bore Cooling for Motor Integrated Spindle. Report of The Japan Society for Precision Engineering, Vol. 60, No. 7. 1994; 983(in Japanese).

[5] Hiroyuki Uchida, Masatoyo Sogabe. Linear Motor in Precision Engineering. Report of The Japan Society for Precision Engineering, Vol. 75, No. 2. 2009; 242-245(in Japanese).

Development of an abrasive-free polishing method for optical material using pure water and Ni catalyst

Daisetsu Toh[1], Ryosuke Ohnishi[1], Pho V. Bui[1], Ai Isohsahi[2], Satoshi Matsuyama[1], Yasuhisa Sano[1], and Kazuto Yamauchi[1,3]
[1]Department of Precision Science and Technology, Graduate School of Engineering, Osaka University Suita, Osaka, Japan
[2]Nanoscience and Nanotechnology Center, Institute of Scientific and Industrial Research, Osaka University Ibaraki, Osaka, Japan
[3]Research Center of Ultra-Precision Science and Technology Graduate School of Engineering, Osaka University Suita, Osaka, Japan

INTRODUCTION

Recently, short-wavelength lights of extreme ultraviolets (EUVs) and X-rays have attracted attention because of their excellent properties to achieve microscopy and/or lithography with an extremely high spatial resolution and a higher photon energy phenomenon [1,2]. In the short-wavelength range, reflective optics are generally utilized since they have a significantly large absorption loss. However, from the viewpoint of fabrication, the surfaces of optical components for EUVs and/or X-rays become difficult to manage because they require unprecedentedly high precision and smoothness. The level of smoothness demanded at the atomic level is a root-mean-square (rms) roughness at several tens of pico-meters and needs to be realized on free-form surfaces. The chemical mechanical polishing (CMP) method is currently utilized as a final surfacing method [3,4]. In CMP, a slurry is used that includes chemicals and abrasives. The workpiece surface is chemically modified and removed with abrasives [5,6]. Due to the usage of abrasives, physical damages onto the surface are unavoidable. The damaged layer significantly reduces the optical reflectance —especially in the short wavelength range [7]. In addition, the abrasives remaining on the surface after the CMP processing are difficult to remove and can cause yield reductions to the products.

We developed an abrasive-free polishing method, which is known as the catalyst-referred etching (CARE) method [8,9]. The CARE instrument is similar to a general planarization machine. A catalyst film on the surface of a polishing pad works as a reference plane, which enables the topmost sites of a sample to be removed chemically via a catalytic reaction. As a result, the sample surface is flattened.

Recently, Pt and pure water were utilized in CARE as a catalyst and an etchant, respectively. On the surface of crystalline quartz, an atomically well-ordered surface was obtained with a straight step-and-terrace structure, in which the height of the step is one bilayer, as shown in Figure 1 [10].

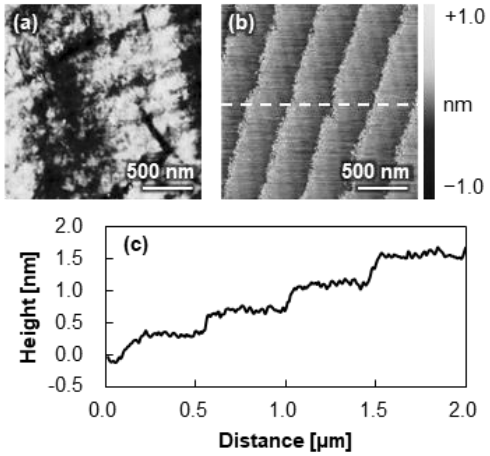

FIGURE 1. AFM images of (a) pre-processed surface of r-face quartz (PV: 3.431 nm, rms: 0.145 nm) and (b) CARE-processed surface of r-face quartz (P–V: 1.405 nm, rms: 0.131 nm). (c) The line profile of the height along the white dashed line in (b).The step height is approximately 0.34 nm, which corresponds to the height of one bilayer of the quartz crystal structure.

The mechanism of CARE in pure water was investigated via a simulation based on first-principles molecular dynamics. Figure 2 shows the schemes of the reaction pathway. First, the dissociative adsorption of a water molecule onto the catalyst is initiated. Next, Si adopts five-fold coordination, which weakens the Si–O bond in an intermediate state. Finally, the weak Si–O bond is cleaved via the transfer of the proton generated from the terminated OH to the back bond. There are two energy barriers in this reaction, with the first one corresponding to the dissociative adsorption of a water molecule [10].

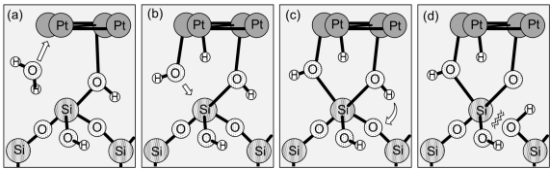

FIGURE 2. Schemes of the reaction pathway for the removal of topmost Si. The images show dissociative adsorption of a water molecule to Pt ((a)–(b)), OH adsorbs on topmost Si to form five-fold coordination ((b)–(c)), and cleavage of Si–O back bond by proton transfer ((c)–(d)).

Our recent study showed that the removal rate varies widely when other metal catalysts are used [11]. In particular, in the case of using a Ni catalyst, the removal rate is 10 times higher than that of using the Pt catalyst. Moreover, Ni has other advantages in that the cost is more effective and the metal contaminations of Ni after CARE processing are easy to remove by rinsing in an acidic solution, compared to the case of Pt. Ni is a promising catalyst in CARE. However, the removal rate of Ni catalyst decreases by more than 60 % within 30 minutes. This is because the Ni surface is oxidized easily in pure water, and the catalytic activity decreases. In this paper, we propose a stable utilization method to keep the Ni surface active.

PROPOSAL

A potential/pH diagram of Ni is shown in Figure 3(a) [12]. The vertical and horizontal axes show the potential of Ni and the pH of the solution, respectively. Each line indicates the equilibrium states of possible Ni compounds. The diagram reveals that various oxidation states of Ni appear when changing the potential. Below pH 7, Ni is plated under -0.31 V vs. standard hydrogen electrode (SHE), and dissolved over -0.31 V vs. SHE. Hereafter, the potentials are shown as their difference from the SHE. Therefore, in keeping the Ni surface catalytically active, we propose that Ni plating and dissolution can be repeated using an electrochemical method. The conceptual scheme of controlling the Ni surface condition is shown in Figure 3(b) and (c). In this method, we use a solution containing a high concentration of Ni ions as an etchant, and a polishing pad as an electrode. The V_{et} is the potential of the etchant and V_{el} is the potential of the electrode. First, before CARE processing, V_{el} is controlled to be lower than V_{et}, as shown in Figure 3(b). At this potential, electrons move from the electrode to the etchant. The Ni ions catch the electrons and are plated on the polishing pad. In this way, the Ni layer works as an active catalyst. Subsequently, to dissolve the Ni layer, V_{el} is controlled to be higher than the etchant potential as shown in Figure 3(c). Owing to this operation, the residual Ni is completely dissolved into the etchant. By repeating these steps, reactive Ni on the polishing pad is continually prepared.

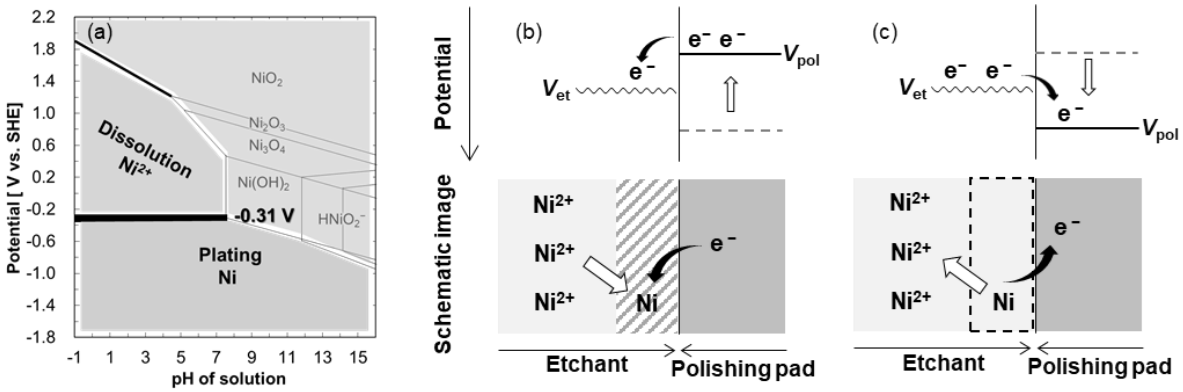

FIGURE 3. (a) Ni potential / pH diagram. (b) and (c) Conceptual scheme of controlling Ni surface condition; V_{et} and V_{pol} are the potential of the etchant and the polishing pad: (b) V_{pol} becomes lower than V_{et}, and Ni is plated. (c) V_{pol} becomes higher than V_{et}, and Ni is dissolved.

EXPERIMENT

First, to realize this method, we investigated and optimized the working electrode (WE) potentials for electroplating and dissolution of Ni film. Next, the properties of the method were evaluated from the standpoint of the removal rate stability and characteristics of the processed surface. The removal rate was evaluated through the difference of workpiece weights before and after processing.

The experimental setup is shown in Figure 4. The workpiece was placed inside the holder and pushed onto the catalytic pad with controlled pressure. The apparatus had a potentiostat consisting of three electrodes: a base electrode for electroplating the Ni catalyst on the polishing pad as a WE, and a Pt sheet and Ag/AgCl electrode as a counter electrode (CE) and reference electrode (RE). As a base electrode for Ni electroplating, a Au thin film with a thickness of about 100 nm, which is electrochemically stable and does not catalyze the CARE reaction, was deposited on a polyurethane pad by a magnetron sputtering. The $NiSO_4$ solution of 0.01 M with a pH of 5.5 was used as an electroplating solution. The WE potentials for plating and dissolution of the Ni film were appropriately decided at each experimental result and discussion. The work material employed was a quartz glass. Pressure and relative speed between the surfaces of the workpiece and catalyst were 40 kPa and 125 mm/s, respectively.

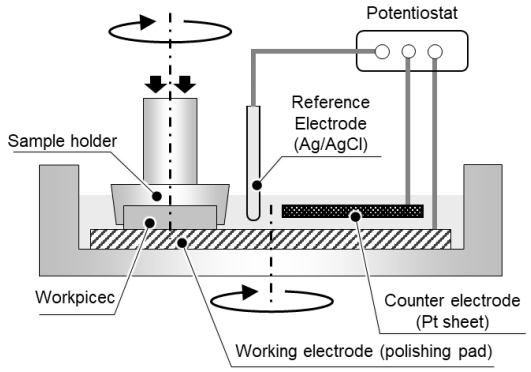

FIGURE 4. Schematic of the CARE machine which is similar to a general polishing machine, used in this study.

RESULT AND DISCUSSION

ELECTROPLATING

We investigated the removal rates under the potential, which is lower than the equilibrium potential of a reaction of $Ni \rightleftarrows Ni^{2+} + 2e^-$. As the potential became lower, the removal rate increased and reached the maximum at -0.8 V. This result shows that a fresh Ni surface is continuously prepared at the range. However, the removal rate decreased at potentials lower than -0.8 V. This is because in the potential range lower than -0.8 V, not only was Ni plated but also H_2 gas was generated, which could disturb the chemical interaction between surfaces of the workpiece and catalyst. The maximum removal rate was observed at -0.8 V, and this is the optimal potential for electroplating in this method.

ELECTRIC DISSOLUTION

In this method, the optimization of the dissolution condition is also needed. The Ni potential / pH diagram indicates that Ni dissolution proceeds under an oxidation condition. Under the oxidation condition, the removal rate decreases. From the viewpoint of processing efficiency, the dissolution time needs to be shortened. We investigated the relationship of the WE potential and the dissolution property of Ni. The experimental procedure is as follows: Au electrode, which is the base electrode for Ni electroplating, is dipped into the solution, and the open circuit potential of the Au electrode was measured. In our system, the potential was 0.4 V. Then, the WE potential was set to -0.8 V for Ni electroplating and was switched from plating to dissolution condition and kept there. Finally, we measured the open circuit potential again to determine whether the Ni film had been removed; Ni is identified as removed if the WE potential returns back to that of the Au electrode. In the case of the potential for dissolution at 0.6 V, the potential of WE returned back to that of the Au electrode at 0.4 V. We decided that the optimal WE potential for dissolution of Ni film was 0.6 V.

THE QUALITY THIS METHOD

We evaluated the processing characteristics of this method. The WE potentials for electroplating and dissolution of the Ni catalyst were set as -0.8 V and 0.6 V, respectively. The potential was switched every 20 s during the CARE processing. The workpiece surface before and after the processing was observed by atomic force microscope (AFM), with view areas of 1×1 μm^2. The removal rate was measured at every 120 min interval. Figures 5(a) and 5(b) show AFM images of the before and after processing, respectively. The roughness is drastically reduced, indicating that the surface is atomically smoothened. The removal rate using the

Ni catalyst with this method was 10 times higher than the one using the Pt catalyst under same processing conditions, and was stabilized over 8 h. This proposed method enables refreshment of the Ni surface and is confirmed to be a promising technique to appropriately utilize Ni as a superior catalyst than Pt from the standpoint of removal rate, stability, cost-effectiveness, and ease of post-cleaning.

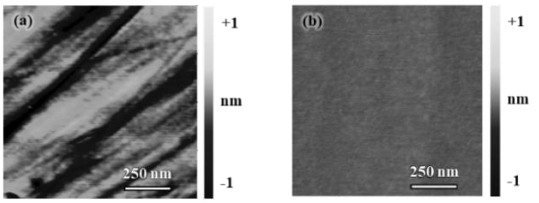

FIGURE 5. AFM images of (a) pre-processed surface (P-V: 3.238 nm, rms: 0.376 nm) and (b) CARE-processed surface (P-V: 1.046 nm, rms: 0.067 nm) of silica glass

SUMMARY

The removal rate using a Ni catalyst was higher than that using a Pt catalyst. However, it decreased with the processing time because the Ni surface was easily oxidized. Therefore, we proposed the electrochemical method to keep the Ni surface active. By repeating Ni plating and dissolution cycle, we stabilized the removal rate for at least 8 h and created an atomically flat surface on a SiO_2 surface.

REFERENCES

[1] A. Sakdinawat and D. Attwood, Nanoscale X-ray imaging. Nat. Photonics. 2010; 4: 840-848.

[2] R. Xie et al., A 7nm FinFET technology featuring EUV patterning and dual strained high mobility channels. Proc. IEDM art. 62nd IEEE International Electron Devices Meeting. 2017; 271-274.

[3] R. Komanduri, D. A. Lucca, and Y. Tani, Technological advances in fine abrasive processes. Ann. Manuf. Technol. 1997; 46: 545-596.

[4] R. B. Zantye, A. Kumar, and A. K. Sikder, Chemical mechanical planarization for microelectronics applications. Mater. Sci. Eng. R. Rep. 2004; 45: 89-220.

[5] J. Luo, and D. A. Dornfeld, Material removal mechanism in chemical mechanical polishing: Theory and modeling. IEEE Trans. Semicond. Manuf. 2001; 14: 112-133.

[6] M. Krishnan, J. W. Nalaskowski, and L. M. Cook Chemical mechanical planarization: Slurry chemistry, materials, and mechanisms. Chem. Rev. 2010; 110: 178-204.

[7] N. Saka, T. Eusner, J.-H, Chun. Nano-scale scratching in chemical-mechanical polishing. CIRP Annals - Manufacturing Technology. 2008; 57: 341-344.

[8] H. Hara, Y. Sano, H. Mimura, K. Arima, A. Kubota, K. Yagi, J. Murata, and K. Yamauchi Novel abrasive-free planarization of 4H-SiC (0001) using catalyst. J. Electron. Mater. 2006; 35: L11-L14.

[9] Y. Sano, K. Arima, and K. Yamauchi Planarization of SiC and GaN wafers using polishing technique utilizing catalyst surface reaction. ESC J. Solid State Sci. Technol. 2013; N3028-N3035.

[10] D. Toh, P. V. Bui, A. Isohashi, N. Kidani, S. Matsuyama, Y. Sano, and K. Yamauchi Catalyzed Chemical Polishing of SiO2 Glasses in Pure Water. Rev. Sci. Instrum. 2019; 90: 045115.

[11] D. Toh, A. Isohashi, P. V. Bui, T. Inada, Y. Nakahira, Y. Sano, S. Matsuyama, and K. Yamauchi Study on the catalytic activities of transition metals in the catalyst-referred etching of SiC. Book of Abstracts 11th European Conference on Silicon Carbide and Related Materials. 2016; 573-574.

[12] M. Pourbaix, Atlas of Electrochemical Equilibria in Aqueous Solutions, NACE, Houston; 1966

Fabrication of Micro Infrared Fresnel Lens Arrays by Virtual Spindle Based Tool Servo Diamond Turning and Precision Glass Molding

Lin Zhang, Wenchen Zhou, Allen Y. Yi*
Industrial and Systems Engineering
210 Baker Systems, 1971 Neil Ave
The Ohio State University
Columbus, Ohio 43210
*Corresponding author: yi.71@osu.edu

Abstract

Chalcogenide glasses are emerging as low-cost alternatives for infrared applications. These materials have promising characteristics that can improve both manufacturing processes and device performance. In this research, we aim to develop a novel manufacturing approach utilizing virtual spindle based tool servo diamond turning and precision glass molding to fabricate micro infrared Fresnel lens arrays in large-volume at low-cost. This novel diamond turning approach can realize rotation-axis transition to any specified position by combining multiple translational and rotational servo motions of the precision machine. During diamond turning, the discontinuous features of the Fresnel lens can be generated by transferring the rotation-axis from one local center to another. After the mold is diamond machined, molding is conducted on a commercial precision molding machine with optimized processing parameters. After the molded element is released, the profile of the replicated infrared element is measured using an interferometer. The results closely match the dimensions of the curvature of the lenslets on the mold. An experimental setup utilizing molded microlenses is used to validate the optical performance of the molded microlenses. This study demonstrates the feasibility of the proposed manufacturing process for improved fabrication efficiency of infrared elements and allows low-cost high-precision infrared micro-optics to be produced in high volume.

Keyword: Chalcogenide glass, virtual spindle based tool servo diamond turning, precision glass molding, micro Fresnel lens array

Design and fabrication of multi-element diffractive optical array for imaging applications

Wenchen Zhou, Tiantong Chen, Allen Y. Yi*
Department of Integrated Systems Engineering
The Ohio State University
210 Baker Systems, 1971 Neil Ave.
Columbus, Ohio 43210
*Corresponding author: yi.71@osu.edu

Abstract

Multi-layer diffractive optical elements (MLDOEs) are optical lenses which can correct chromatic aberrations while maintaining high diffraction efficiency. In this paper, an MLDOE array is designed and fabricated for imaging applications. Polymethylmethacrylate (PMMA) and polycarbonate (PC) are selected as the materials of the MLDOE array. A specially designed fiducial feature which ensures the precise assembly of the lenses is fabricated together with the diffractive elements. Ultraprecision diamond machining is adopted for fabrication of the elements. The application of this MLDOE into imaging systems can shrink the size of the system and achieve a high resolution at the same time.

IDENTIFICATION FOR THE FEED DRIVE DYNAMICS OF A 5-AXIS LASER DRILLING MACHINE VIA IN-PROCESS DATA

Chia-Pei Wang, Kaan Erkorkmaz, and John McPhee
Mechanical & Mechatronics Engineering
University of Waterloo
Waterloo, ON, Canada

INTRODUCTION

Laser drilling is an advanced drilling technique in aerospace industry, e.g. drilling the cooling holes in turbine engines. Percussion drilling and on-the-fly drilling are two major techniques for producing holes on freeform shaped parts. Percussion drilling is simple and widely used in industry. The nozzle is stationary while sending laser pulses. After the hole is penetrated, the nozzle moves to the next hole location. The problem of the percussion drilling is high local thermal loading which may deteriorate the part quality. In contrast, in the on-the-fly drilling, the nozzle is continuously moving through all the holes and sending only one pulse at a time until all the holes are penetrated. Such strategy leaves sufficient time for cooling, and results in better part quality. More information about laser drilling technique is available in a recent state-of-the-art review [1].

However, in the on-the-fly drilling process, since the nozzle is sending laser pulses while moving, the accuracy of the 5-axis simultaneous motion becomes a crucial problem [1]. As a result, currently the percussion drilling is still adopted in industry. Hence this paper aims at developing a virtual model of the machine dynamics such that the drilling accuracy can be predicted and possible to be compensated. And this approach should directly use the in-process data such that it would not cause additional downtime.

MACHINE CONFIGURATION

Figure 1 shows a 5-axis laser drilling machine which will be investigated in this paper. X and Y axes are placed on top of the machine frame and holding the laser system. These two linear axes are actuated by linear motors which are suitable for high speed motion. Z, B, and C axes form a serial kinematic chain. Z axis is actuated by a ball screw drive which has good performance of rejecting disturbances such as the dynamic coupling forces. B and C axes are a set of tilting rotary table both driven by direct drive motors.
This type of machine configuration has several dynamic characteristics listed as follows. X and Y axes can be simply assumed as independent feed drives due to the orthogonal configuration. However, the kinematics and dynamics of Z, B, and C axes are inherently coupled and nonlinear. Besides, there are substantial position dependent torque ripples acting as disturbances owing to utilizing direct drive motors. Regarding the above issues, the dynamic models are illustrated in the next section.

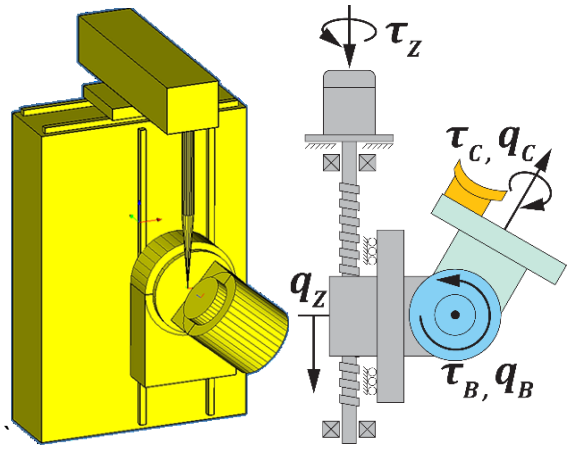

(a) (b)

Figure 1. A 5-axis laser drilling machine. (a) The machine configuration; (b) Z-B-C kinematic chain.

DYNAMIC MODEL OF MECHANICAL DRIVES

The Z, B, and C axes are assembled as a serial kinematic chain. The multi-body dynamics can be derived using the Euler–Lagrange equations of motion resulting in

$$\begin{cases} \tau_Z = P_{Z_1}\ddot{q}_Z + P_{Z_2}\cos(q_B)\,\dot{q}_B{}^2 \ldots \\ \tau_B = P_{B_1}\ddot{q}_B + P_{B_2}\sin(q_B) \ldots \\ \tau_C = P_{C_1}\ddot{q}_C + P_{C_2}\ddot{q}_B \sin(q_C) \ldots \end{cases} . \qquad (1)$$

The rotary axes make the dynamics non-linear and coupled. The lengthy equations can be written in matrix notation as:

$$\boldsymbol{\tau} = \boldsymbol{M}(\boldsymbol{q})\ddot{\boldsymbol{q}} + \boldsymbol{B}(\boldsymbol{q}, \dot{\boldsymbol{q}}) + \boldsymbol{\tau}_f + \boldsymbol{\tau}_r. \qquad (2)$$

$\boldsymbol{M}(\boldsymbol{q})$ is the mass matrix and $\boldsymbol{B}(\boldsymbol{q}, \dot{\boldsymbol{q}})$ contains the Coriolis, centrifugal, and gravitational terms. $\boldsymbol{\tau}_f$

and $\boldsymbol{\tau}_r$ are friction and position dependent ripples respectively. $\boldsymbol{q}$ represents the measured position or angle of each drive. $\boldsymbol{\tau}$ is the measured motor current which can be viewed as the equivalent motor torque related by motor constants. It should be noted the motor constants are unknown parameters and are embedded in the right hand side of the equations. The above equation can be extended to include the dynamics of X and Y axes which are assumed as SISO model due to the orthogonal configuration. To simplify the illustration, X and Y axes will not be discussed in the later sections.

The friction of each joint can be described by Stribeck curve:

$$\tau_f = \tau_C + (\tau_S - \tau_C)e^{-|\dot{q}/v_s|}. \quad (3)$$

Direct drive motors exhibit substantial position dependent ripples acting as one kind of external disturbance [2]. The ripples in one axis can be described as

$$\tau_r = A_r(1 + \alpha_r|\sin(q + \varepsilon_r)|)\sin(q\omega_r + \phi_r). \quad (4)$$

A_r, ω_r, and ϕ_r are the magnitude, frequency, and the phase of the ripple. Due to the imperfection of the motor assembly, the misalignment would make the magnitude of the ripple inconsistent. Therefore, $(1 + \alpha_r|\sin(q + \varepsilon_r)|)$ is introduced to capture this issue. For linear motors, this term should be discarded.

IDENTIFICATION

The procedure of the identification for the above dynamic models is proposed as follows. First, the collected data $\boldsymbol{q}, \dot{\boldsymbol{q}}, \ddot{\boldsymbol{q}}$, and $\boldsymbol{\tau}$ are pre-processed by a velocity threshold which discards the data with low velocity motion where non-linear friction may involve. Therefore, only the steady-state friction remains. The observation matrix $\boldsymbol{W}$ can be derived by differentiating the equations of motion, Eq. (**2**), with respect to the identification parameter set $\boldsymbol{\chi}_L$ [3].

$$\boldsymbol{W}(\boldsymbol{q}, \dot{\boldsymbol{q}}, \ddot{\boldsymbol{q}}, \boldsymbol{\chi}_{NL}) = \frac{\partial}{\partial \boldsymbol{\chi}_L}[\boldsymbol{M}(\boldsymbol{q})\ddot{\boldsymbol{q}} + \boldsymbol{B}(\boldsymbol{q}, \dot{\boldsymbol{q}}) + \boldsymbol{\tau}_r + (\boldsymbol{\sigma_2}\dot{\boldsymbol{q}} + \boldsymbol{\tau_C} sign(\dot{\boldsymbol{q}}) + \boldsymbol{\tau_{Stribeck}})], \quad (5)$$

$\boldsymbol{\chi}_L$ contains all the parameters that can be used to Eq. (**2**) without leaving the parameter itself in $\boldsymbol{W}(\boldsymbol{q}, \dot{\boldsymbol{q}}, \ddot{\boldsymbol{q}}, \boldsymbol{\chi}_{NL})$. The parameters excluded from $\boldsymbol{\chi}_L$ are classified under $\boldsymbol{\chi}_{NL}$.

$\boldsymbol{\chi}_L$ includes the parameters in the multibody dynamic model $\boldsymbol{M}(\boldsymbol{q})$ and $\boldsymbol{B}(\boldsymbol{q}, \dot{\boldsymbol{q}})$, viscous friction coefficient $\boldsymbol{\sigma_2}$, the Coulomb friction $\boldsymbol{\tau_C}$, the stiction $\boldsymbol{\tau_S}$, and the torque ripple magnitude $\boldsymbol{A_r}$. $\boldsymbol{\chi}_{NL}$ contains ω_r and ϕ_r in the torque ripple model and v_s in the Stribeck curve. Eq. (**5**) can be derived in the linear Least Squares sense:

$$\boldsymbol{\tau} = \boldsymbol{W}(\boldsymbol{q}, \dot{\boldsymbol{q}}, \ddot{\boldsymbol{q}}, \boldsymbol{\chi}_{NL})\boldsymbol{\chi}_L + \boldsymbol{error}. \quad (6)$$

A global optimization method, Particle Swarm Optimization (PSO), is applied to find $\boldsymbol{\chi}_{NL}$. In every iteration of PSO, each particle chooses a set of design variables for determining $\boldsymbol{\chi}_{NL}$. Then, $\boldsymbol{\chi}_L$ is inherently estimated by the pseudo inverse of $\boldsymbol{W}$ in the form

$$\widehat{\boldsymbol{\chi}_L} = \boldsymbol{W}^{\dagger}\boldsymbol{\tau} = (\boldsymbol{W}^{\boldsymbol{T}}\boldsymbol{W})^{-1}\boldsymbol{W}^{\boldsymbol{T}}\boldsymbol{\tau}. \quad (7)$$

The estimated motor input $\hat{\boldsymbol{\tau}}$ can be obtained by

$$\hat{\boldsymbol{\tau}} = \boldsymbol{W}\widehat{\boldsymbol{\chi}_L}. \quad (8)$$

The 2-norm of error $\|\boldsymbol{\tau} - \hat{\boldsymbol{\tau}}\|_2$ is minimized for each particle with a prescribed $\boldsymbol{\chi}_{NL}$. Thus, the objective function of PSO is designed as

$$\min_{\boldsymbol{\chi}_{NL}} \sum_{i=1}^{j} \|\boldsymbol{\tau} - \hat{\boldsymbol{\tau}}\|_2. \quad (9)$$

Through the above iterative approach, $\widehat{\boldsymbol{\chi}_L}$ and $\widehat{\boldsymbol{\chi}_{NL}}$ can both be found with the minimized error of motor inputs estimation. Such approach is capable of solving problems with nonlinear parameters with efficiency due to the combined use of LS and PSO.

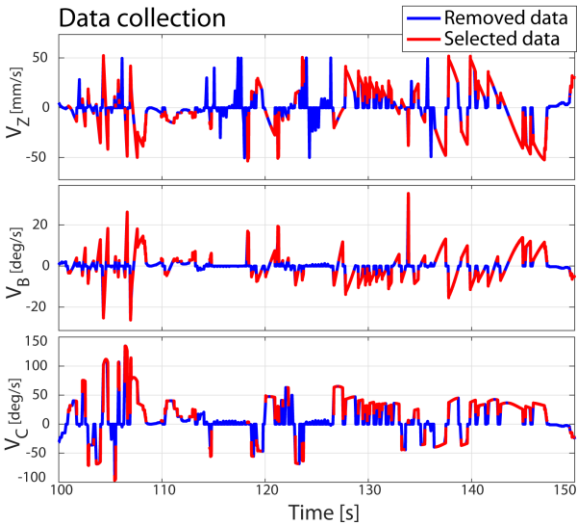

Figure 2. Collected data during a percussion laser drilling process.

EXPERIMENTAL RESULTS

The proposed method has been applied to a 5-axis laser drilling machine, as shown in Figure 1. Figure 2 shows the data collected during a percussion drilling process for producing turbine engine components. To prevent the overfitting problem, the normalized 2-norm of error, $\|\boldsymbol{\tau} - \hat{\boldsymbol{\tau}}\|_2/\|\boldsymbol{\tau}\|_2$, with respective to time are plotted in Figure 3 to ensure that the identification is

convergent. The normalized 2-norm of error converges on around 3.4% when it is longer than around 50 seconds.

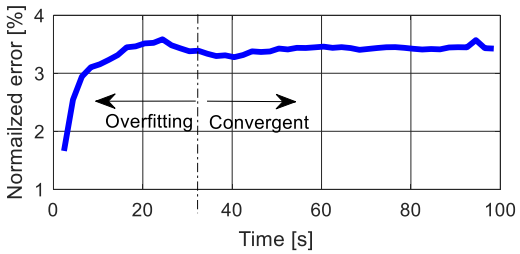

Figure 3. Convergence of the estimation.

In order to validate the effect of using the MIMO dynamic model, a SISO model which discards the dynamic coupling terms is also built to be compared. Figure 4 shows the identification result of B-axis. During acceleration and deceleration periods, the SISO model has significant estimation error due to ignoring the dynamic coupling terms. The result proves the necessity of using MIMO dynamic models for 5-Axis machine dynamic modelling.

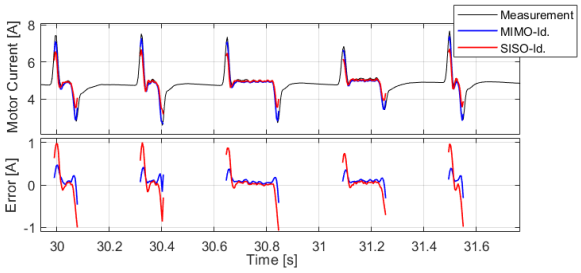

Figure 4. MIMO and SISO multibody dynamic model, B-axis.

Figure 5 shows a comparison between using and without using torque ripple model in C-axis. The torque ripple is shown to be an apparent disturbance causing substantial current variation. Therefore, the torque ripple is necessary to be identified such that other dynamic characteristics will not be corrupted with this effect. Figure 6 shows the estimated torque ripple overlapping with the extracted ripple data from the measured motor current. It shows that the frequency of ripples is consistent, and the magnitude varies with the angle probably due to the imperfect motor assembly. This magnitude variation is also captured by the proposed model.

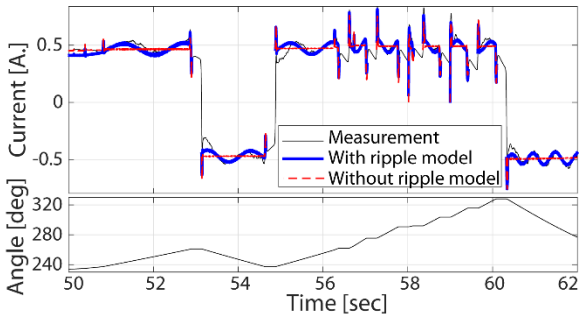

Figure 5. Identification result, C-axis.

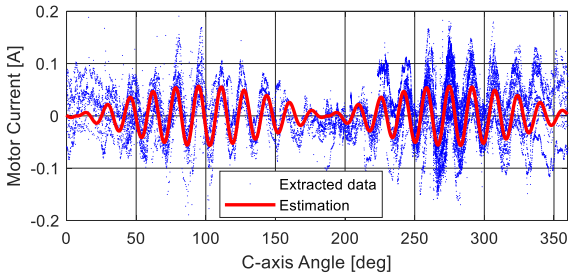

Figure 6. Torque ripple estimation, C-axis.

Figure 7 shows the estimated steady state friction overlapping with the extracted friction data from the measured motor current. Due to the fact that the data are collected from a real drilling process, not from dedicated experiments, steady state condition, i.e. constant velocity, is not satisfied. Nevertheless, this result still substantially captures the friction characteristic.

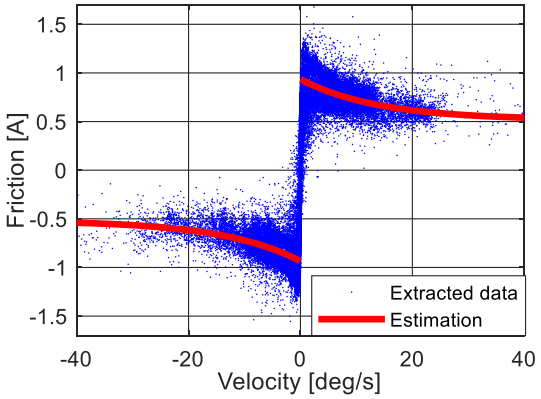

Figure 7 Steady state friction estimation, B-axis.

The estimated dynamic model is then further combined with the controller's model such that tracking errors of each drive can be simulated. The results are shown in Figure 8.

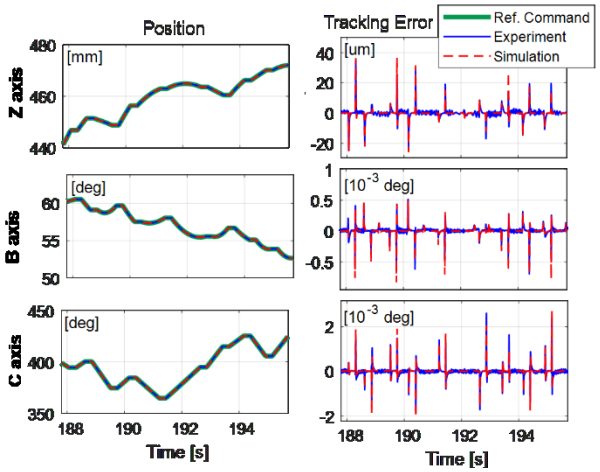

Figure 8 Tracking error simulation based on the estimated dynamic model.

CONCLUSIONS

In this paper, a parameter identification method is proposed for building virtual models of machine tool drives. The approach is practical for the industry because it directly utilizes the in-process data during the production without executing dedicated experiments. Numerous dynamic characteristics are considered, including multi-rigid-body dynamics, torque ripples, and Stribeck effect, such that the methodology can be applied to 5-axis machine tools with rotary axes. The result shows that various dynamic characteristics can be identified and decoupled. The tracking error can be simulated such that the drilling accuracy can be predicted and possible to be compensated.

ACKNOWLEDGEMENT

This research was supported by Natural Sciences and Engineering Research Council of Canada (NSERC) under the CANRIMT Strategic Research Network Grant NETGP 479639-15.

REFERENCES

[1] Alzaydi A. Trajectory generation and optimization for five-axis on-the-fly laser drilling: a state-of-the-art review. Optical Engineering. 2018; 57: 12.

[2] Kamalzadeh A, Erkorkmaz K. Accurate tracking controller design for high-speed drives. Int. J. Mach. Tools Manuf. 2007; 47: 1393-1400.

[3] van Tuijl N, et al. A new method of rapid rigid-body parameter identification of MIMO systems. 7th International Conference on Virtual Machining Process Technology (VMPT). 2018.

GRINDING A WORKPIECE TO SUB-MICRON ROUNDNESS IN A 100 YEAR OLD GRINDER

Dave Arneson, Mel Liebers, and Christopher Arneson
Professional Instruments Company
Hopkins, Minnesota, USA

ABSTRACT

Older machines can be used to grind workpieces to very good roundness by retrofitting them with precision air bearing spindles. The Blockhead design was originally intended for this very purpose. In this work we demonstrate the ability to grind a test piece round to better than 0.1 micron or 4 millionths of an inch, which is considered by most to be the threshold of super-precision grinding. Nowadays a modern machine can grind shapes and hold dimensions that are impossible on an old grinder, but in cases where a straight cylinder is desired, it can be much more economical to simply replace the existing spindles with precision air bearing spindles such as the Professional Instruments 4R Blockhead.

INTRODUCTION

The universal grinder used in this test was originally built by Brown and Sharpe in 1918 is shown in Figure 1. It was purchased by Professional Instruments in 1955 and has been in continuous use ever since. Although we now have 10 recent model CNC cylindrical grinders, we still keep this machine around for doing short run high accuracy grinding jobs, where a CNC grinder would actually take more time than this trusty old grinder does. Furthermore, retrofitting this machine is much more environmentally friendly than buying a new machine.

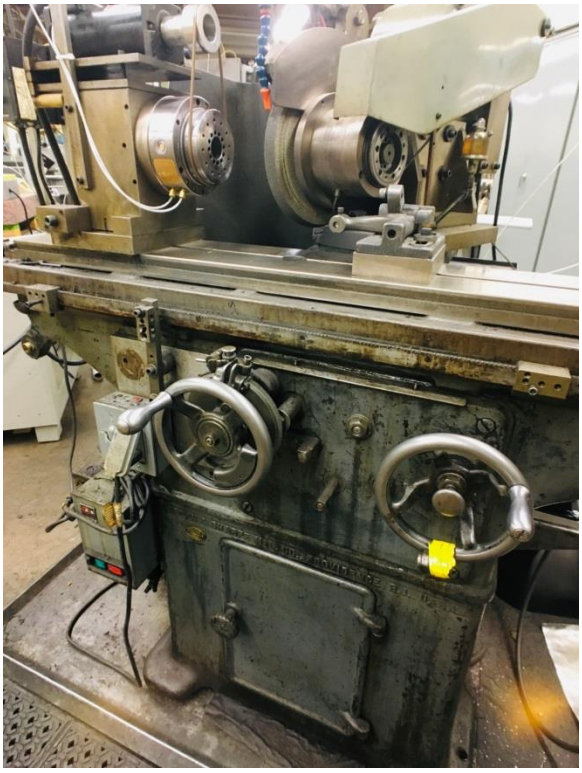

FIGURE 1. 100+ year old Brown and Sharpe No. 1 universal grinder with air bearing wheelhead and workhead.

FIGURE 2. Upgrading our grinders with air bearing spindles make them capable of grinding to 0.1 micron roundness.

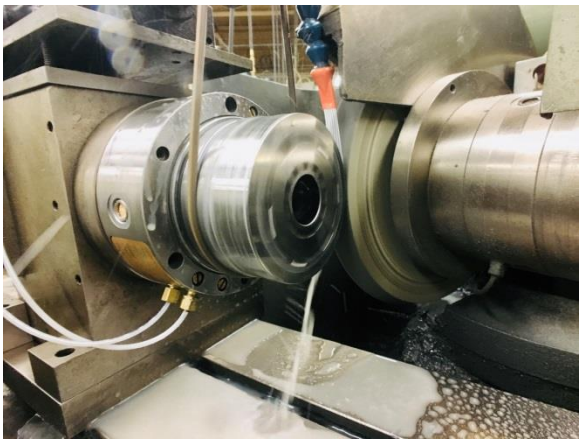

FIGURE 3. Air bearing wheelhead grinding a case hardened steel C1117 (60 Rc) testpiece with an air bearing workhead.

METHODOLOGY

Both workhead and the wheelhead were retrofit with 4R Blockhead air bearing spindles. The compact size and simple construction of the Blockhead design allow for this spindle to be used in a variety of situations [1] and it is ideally suited to be retrofit into existing machines. The central stiffness of Blockhead spindles allow for light cuts which makes grinding extremely round parts possible. The workhead is mounted to a tip-up fixture which addresses the issue of dialing in flexible parts that tend to sag and distort during centering. The motor driving the workhead is on a spring-loaded mount in addition to having the belt tension act in the non-sensitive direction.

Another important thing we did was adding an inverter drive to the drive motor so we can run the wheel spindle a little bit slower. This machine tends to vibrate when the spindle is run at line frequency, 60 Hz, just lowering that to 54 Hz improves things substantially [2]. This gives us a 1900 RPM wheel speed which is acceptable for the small amounts of stock removal we do on typical parts in this machine.

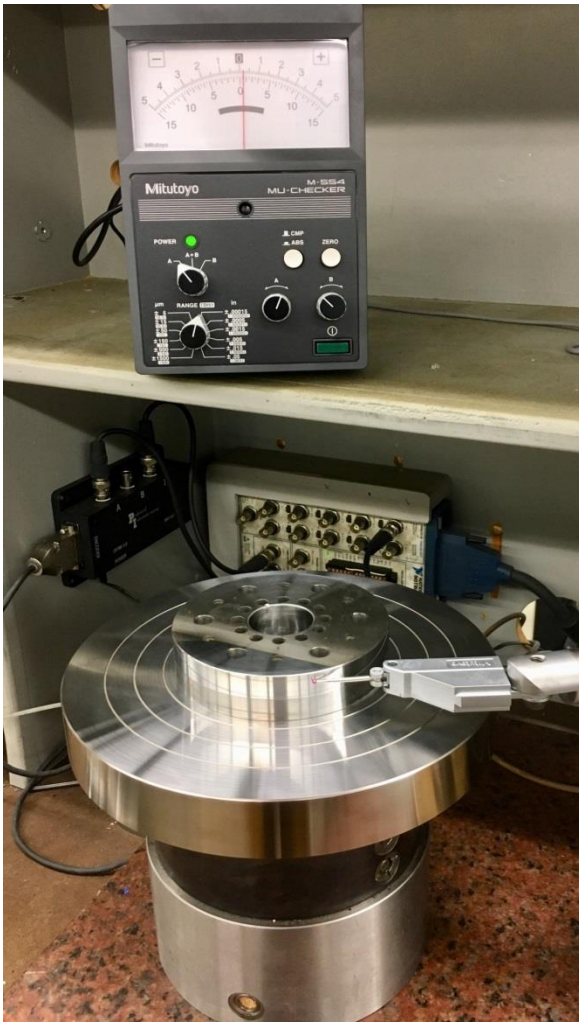

FIGURE 4. Roundness tester developed in cooperation with Professor Eric Marsh at Penn State.

METROLOGY

Roundness is measured with a bespoke roundness instrument using an air bearing spindle (4R Blockhead) and lever-head LVDT indicator (Mitutoyo 519-522) with ruby tip. The analog output of the amplifier (Mitutoyo 519-552A) is sampled by 16-Bit data acquisition hardware (National Instruments USB-6212) using the encoder signal. The analysis software was developed by students at Penn State's MDRL under the direction of Professor Eric Marsh.

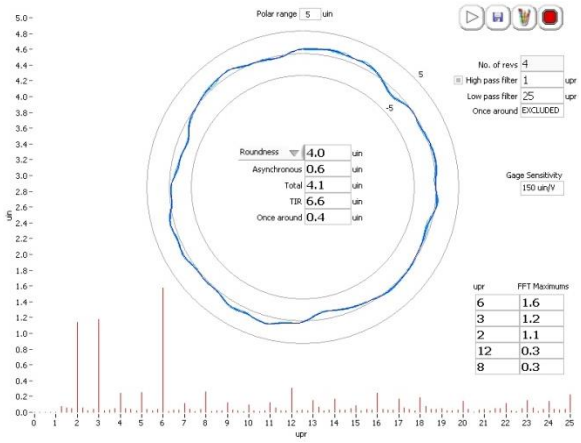

FIGURE 5. Roundness is 4.0 µin (0.10 µm) of a part ground on 100+ year old Brown & Sharpe No. 1 universal grinder retrofit with air bearing spindles.

RESULTS

According to Studer, the Swiss company known for making the very best cylindrical grinders in the world, their standard workhead can achieve 0.4 micron roundness and if you special order they can provide a workhead capable of 0.2 microns [3]. That makes us pretty happy with our result of 4 microinch roundness, or 0.1 micron. Note also that the lower orders—2, 3, and 4 UPR—are extremely low magnitude which is desirable.

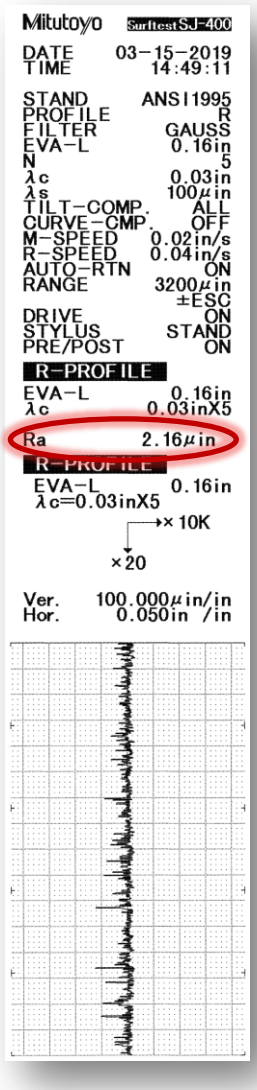

FIGURE 6. Roughness of a part ground on the Brown & Sharpe No. 1. Ra 2.2 µin (0.05 µm).

CONCLUSIONS

Whilst modern CNC cylindrical grinders can be a wise investment, thought should be given to whether or not it is absolutely necessary before spending upwards of $300,000. Retrofitting old grinders with air bearing wheelhead and workhead spindles can in some cases be an economical alternative, and on certain parts yield results equal to or better than what you can achieve on the best commercially available machines.

REFERENCES

[1] U.S. Patent # 3,305,282, Hydrostatic Bearing Structure, Harold E. G. Arneson, Feb. 21, 1967

[2] Knapp BR (1999) Benefits of Grinding with Variable Workspeed. Thesis Master of science. The Pennsylvania State University.

[3] Studer, The Art of Grinding ://pdf.directindustry.com/pdf/studer/s41/26168-658165-_10.html

CERAMIC ADDITIVE MANUFACTURING OF A SIMPLE PLANO MIRROR

Bradley H. Jared, Junoh Choi, Adam W. Cook, William Reinholtz, Michael P. Saavedra, David J. Saiz, Christian Arrington, Kalin Baca
Sandia National Laboratories
Albuquerque, NM

High performance optical systems are commonly placed in extreme environments which produce strict constraints relative to size, weight, and power. Precision processes are also necessary for optical component fabrication due to surface form and finish requirements. As a result, design solutions are commonly sub-optimal, overly complex, expensive and difficult to fabricate and assemble. Additive manufacturing (AM) has recently garnered significant interest across a host of applications and industries intent on increasing design freedom and reducing the cost and lead-time for small quantity, high value fabrication lots. AM's use in optical systems, however, has been relatively restrictive. As-printed dimensional tolerances for AM processes often exceed 1-2% of a part's base dimension (e.x. 100μm for a 10mm part) which is significantly larger than the micron tolerances commonplace for optical components. Further, as-printed surface roughness can exceed 10μm, i.e. two to three orders of magnitude rougher than many finish requirements. Nevertheless, opportunities exist to leverage AM for optical systems, especially aggressively light-weighted reflective optics.

The feasibility of using AM to produce optical components has been demonstrated in the literature [1]. Prior work at Sandia [2] has also been encouraging as lead time for a mirror assembly was reduced almost an order of magnitude compared to traditional fabrication and procurement routes. Such rapid fabrication highlights AM's potential to meet rapid response criteria necessary for optical components serving critical mission applications. Further benefits of AM for reflective optical components, however, are also being considered. Integration of additional mirror features (ex. mounts, sunshades, tubes) into the monolithic structure is also being considered to eliminate mirror deformations associated with assembly.

DESIGN

A relatively simple, single-sided plano mirror element, roughly 1in in diameter, was designed for fabrication and development activities, Figure 1. While design complexity is a commonly cited benefit for additive manufacturing, the complexity of ceramic AM parts is more restrictive for than for typical metal or polymer processes and parts. One restriction lies in the need to apply a uniform thickness to all part

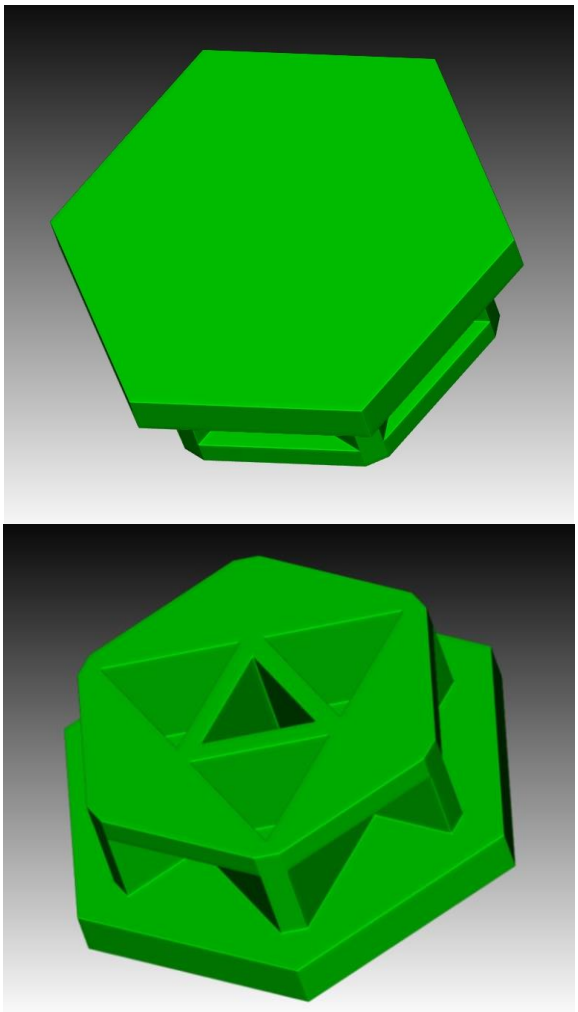

FIGURE 1. Solid model design of the plano mirror element. Top view (top) and rear view (bottom).

features. This insures uniform de-binding and sintering of the printed material to reduce material cracking and delamination. This is not a restriction of the printing process but related to de-binding and sintering kinetics, and therefore is a fundamental restriction for any ceramic part, not just those that are printed. Similarly, part size is limited for ceramic AM as de-binding and sintering processes become prohibitively long and unstable for larger parts.

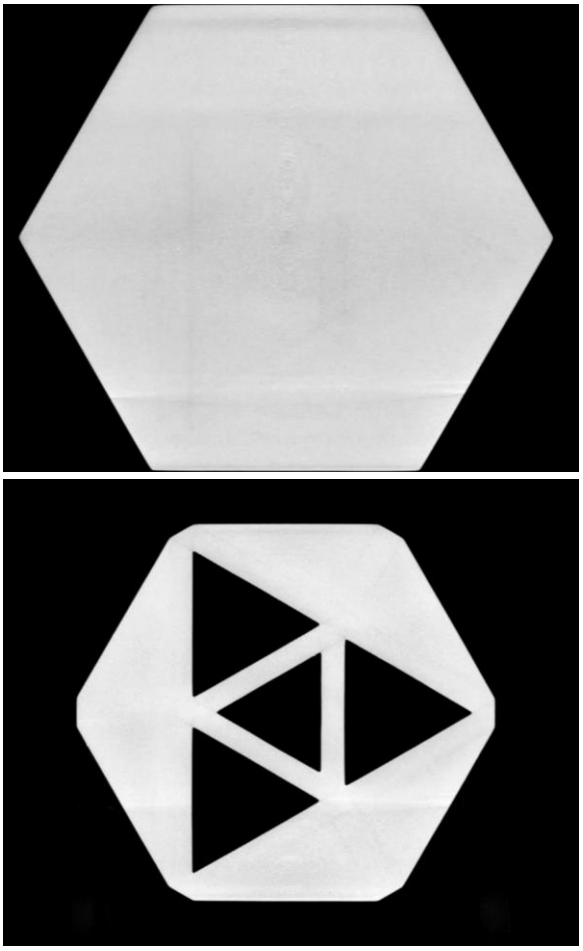

FIGURE 2. XY cross sections of sintered mirror elements in the top structure (top) and in the base mount (bottom) using computed tomography.

FABRICATION

The use of novel, ceramic materials for a monolithic optical structure is being developed due to their higher modulus of elasticity and lower coefficient of thermal expansion than traditional metals. Fabrication of the mirror element was thus performed in alumina by Lithoz based on their proprietary lithography-based ceramic manufacturing (LCM) process [3]. They performed both printing and post-process de-binding and sintering. One key advantage of the LCM compared to prior work using direct write printing [2] is the ability to print overhang features; a capability leveraged in the mirror design to generate integrate part stiffeners. Final part density is quite good, exceeding 90% density. Figure 2 provides two images of the part cross section obtained via computed tomography.

After printing and sintering, the mirror surface was ground and polished, Figure 3. Two approaches are being explored to generate a reflective optical surface from the ground and polished printed surface. The first is to apply a thin film adhesion layer of chromium and copper followed by electroplating of a uniform nickel layer ~100 μm in thickness, Figure 4. The nickel enables a machinable surface to be diamond

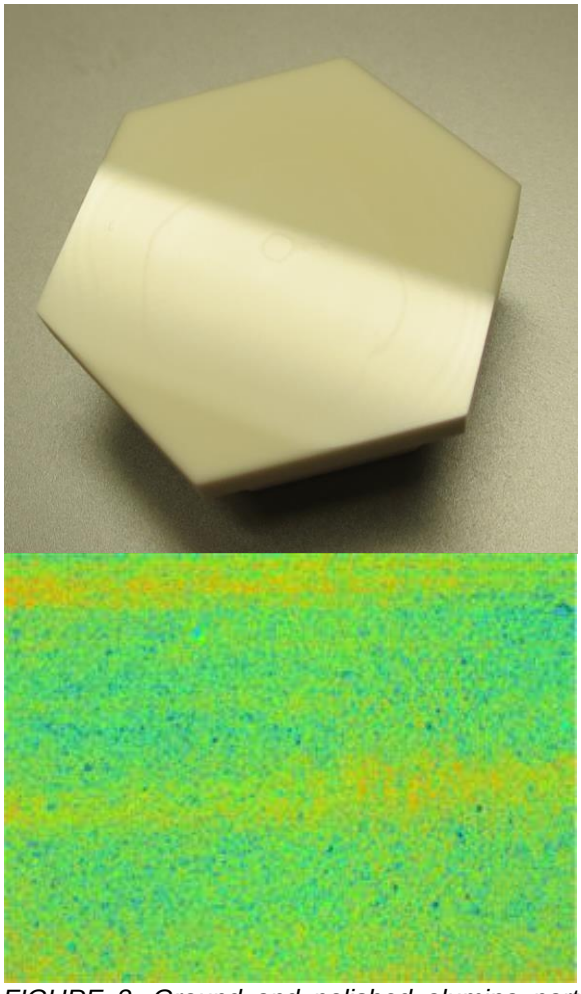

FIGURE 3. Ground and polished alumina part after LCM. Part view (top), and surface finish (bottom).

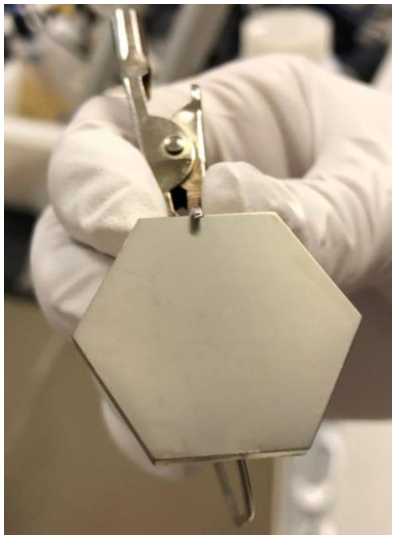

FIGURE 4. Nickel plated optical surface prior to diamond turning.

turned to generate the final plano mirror surface. Here, the polished surface is relatively rough, 0.45µm Sa in Figure 3, to enhance the interfacial bonding of the thin metal adhesion layer and Ni plating. The second approach involves depositing silicon nitride onto the polished LCM surface. A thin film deposition of chrome and pure aluminum is then applied to generate the optical surface for the visible spectrum.

CONCLUSIONS

A development effort has explored an additively manufactured ceramic plano mirror. Progress has been made, but ceramic AM remains a challenging and an immature process for the fabrication of optical components. Additive manufacturing clearly provides opportunities to both reduce the fabrication cycle times for ceramic components and to introduce new levels of complexity into part geometries. Key fundamental challenges in processing ceramic materials, namely de-binding, sintering and accounting for part shrinkage / distortion; however, are neither avoided or alleviated by additive manufacturing.

ACKNOWLEDGMENTS

Sandia National Laboratories is a multimission laboratory managed and operated by National Technology and Engineering Solutions of Sandia LLC, a wholly owned subsidiary of Honeywell International Inc. for the U.S. Department of Energy's National Nuclear Security Administration under contract DE-NA0003525. This document has been reviewed and approved for unclassified, unlimited release, SAND2019-10673 A.

REFERENCES

[1] Sweeney M, Acreman M, Vettese T, Myatt R, Thompson M. Application and testing of additive manufacturing for mirrors and precision structures. Proceedings SPIE 9574, Material Technologies and Applications to Optics, Structures, Components, and Sub-Systems II, September 2015.

[2] Jared B, Chavez T, Saiz D, Reinholtz W, Winrow E, Saavedra M, Choi J, Cook A, Diantonio C, Additive Manufacturing of Reflective Optical Components, Proceedings for the Annual Meeting of the American Society for Precision Engineering, Charlotte, NC, 2017.

[3] Lithoz LCM Technology, http://www.lithoz.com/en/additive-manufacturing/lcm-technology.

.

Volumetric Data Analysis: Inspection and Experimental Design for Additive Manufacturing

Zhaohui Geng[1], and Bopaya Bidanda[1]
[1]Department of Industrial Engineering
University of Pittsburgh
Pittsburgh, PA, United States

INSTRUCTIONS

3D printing (3DP), also known as additive manufacturing (AM), is a transformative manufacturing technology that can directly create 3-dimensional physical parts from CAD design. [1] Traditional manufacturing processes, such as machining processes, often require a careful analysis of the CAD model and a detailed process planning strategy to produce a product. Even though these classical manufacturing processes are widely adopted by manufacturing industries for mass production, the process planning step can be involved and time consuming based on the geometric complexity of the products. This time can be ignored for mass production. However, it can be quite significant when considering highly customized or geometrically complex products for small-to-medium batch of products. Sometimes, the initial design must be decomposed to subassembly due to the inner structure or complex shape; while, the products cannot even be produced due to the complexity of the features and limitation of process capability. 3DP can heavily reduce such huge amount of efforts and provide feasibility and flexibility to produce complex structural products. The nature of how AM works is that the final products are crated through adding material layer by layer. In this way, the 3-dimensional production is reduced to generate a pile of lower-dimensional, 2-d, thin plates. The complex outer surfaces are reduced to the stack-up of thin plates with different shapes, while the inner structures are reduced to the hollow features within the plate. In this way, AM outperforms traditional manufacturing in terms of analytical difficulty, design complexity, internal structural design, and, further, throughput time for small batch production.

However, the adoption of 3DP techniques is limited by some of its restrictions, such as accuracy, cost, production time, etc. Even though 3DP can produce parts with many great attributes, such as complex shapes, inner structures, which cannot be attained by traditional manufacturing processes, the lower accuracy of the products limits its applicability. Many efforts have been made in the 3DP community to improve AM's accuracy and applicability, however, most of them fail to capture the nature of 3DP. That is, instead of directly producing features in traditional manufacturing processes, 3DP creates the products through adding material lay by layer. For example, in order to produce a box-shaped product, classical machining processes can directly produce six flat outer surfaces. As for 3DP, the bottom and upper surface of the products can be directly printed, while the other surfaces are just the byproduct of the surrounding edges of square thin plates. It is valid to use current-state-of-the-art statistical quality control tools, such as profile monitoring, to control the machining process through measuring the surfaces separately. Yet, it is unreasonable and inapplicable to use tools to monitor or control the printing parameters for the side surfaces in this simple example. Also, the features definition can be useless if we consider different printing orientations. So, the designed features cannot be detected by the 3D printer, which is significantly different from classical manufacturing processes. Therefore, it requires a different analytical tool designed for 3DP that can be used for production parameter optimization or quality improvement.

In this paper, we propose a novel framework designed for inspection of 3DP process, called

volumetric data analysis. It bridges the gap of 3-dimensional data and statistical models and provides the analytical traceability for 3-dimensional closed-shape data. The first part of the paper is devoted to survey current-state-of-the-art off-line quality control techniques for 3DP. Next, the volumetric data analysis framework is proposed and connections to useful statistical models for 3DP are briefly presented. The requirements for components of the volumetric data analysis are presented and future work directions are discussed. At last, a novel classification methodology for manufacturing processes is proposed.

Literature Review

In this section, we review the current analysis models and quality engineering techniques for manufacturing in general and 3DP, specifically. Also, based on the unique nature of 3DP, the research gaps of these models will be stated.

Shape-Based Statistical Techniques for Manufacturing Processes

In the literature, geometric data are often treated with profile data in the field of statistical process control (SPC) or shape/form data in statistical shape analysis (SSA) [2]. In manufacturing, most of the papers are using profile monitoring to deal with profile data. Profile monitoring is one subject of multivariate statistical process control method. The idea is to use a parametric or nonparametric model to describe the data cloud as the functional form. The model is first fitted to the data and then multivariate SPC methods can be applied based on monitoring of thee model parameters. If both the response and covariates are coordinate or shape-related 3-dimensional data, then the response can be one of the three coordinates and the other two will be the covariates. Detailed review work in profile monitoring can be seen in Woodall et al. [3], Woodall [4], and Noorossana et al. [5] Yet, there's some limitations of these techniques when applied to 3DP. First, profile monitoring requires a functional form between response variable and covariates. However, for 3DP inspection, our objective is to make inference of or monitor the whole data clouds collected from product, which are closed-shaped, for process optimization or control. Even though we could write the functional form as $z = f(x, y)$, this form is inappropriate for closed-shape data. On the other hand, profile monitoring can only be applied to 2-dimensional or 3-dimensional surfaces, and usually, the each fitted model is infinitely large and independent. As discussed before, the analysis of the whole point cloud is more reasonable and useful for 3DP.

The other field of methods is based on SSA. del Castillo and Colosimo [6] firstly introduce SSA based ANOVA analysis to manufacturing applications for process improvement. Their technique is based on shape data obtained by measuring the parts at specific landmarks, points of special interests, or unique characteristics. A generalized procrustes algorithm is implemented to transform the landmarks to pre-shape space, where the mean shape is estimated and ANOVA Ftest can be conducted to compare different process settings. However, the limitations of this methodology applied to high precision manufacturing processes. Firstly, landmarks should be found and matched for each target product. Usually, landmarks are manually selected and matched, however, for 3DP inspection, thousands to millions of points are generated according to random sampling procedures, which are hard to get landmarks. Also, within SSA, the similarity in shape is free of rotation, translation, and isometric scaling effects. However, for a manufacturing setting, even though rotation and translation will not influence the product, the scaling factors and the dimensions of a feature are heavily affecting the quality characteristics.

Other models, such as the Gaussian process model [7] is more flexible to deal with nonlinear surface fitting regarding to the geometric data. However, this model, again, is used for surface data, instead of volumetric data. Also, the Gaussian process model may not be feasible to handle point cloud of the size that are generated by scanning machines.

Statistical Quality Control Techniques for 3DP

AM-oriented statistical analysis has attracted much attention during the past few years. In this research, we only focus on offline analysis and monitoring for AM. Thin plate parts printed by AM have been analyzed and predicted using various statistical. [8, 9, 10] Wang et al. [10] also provide a compensation scheme to reduce deviation between printed parts and design for thin plate objects. However, the analysis for printing freeform design cannot be fully analyzed using their model.

On the other hand, with the current trend of AM, continuous production, metrological methodology

for AM process is needed for both process control and optimization. Since it is an emerging topic, few studies have been done. Recently, Zang and Qiu [11, 12] propose a novel Phase I/II monitoring of nonlinear profile data for AM. Their algorithm integrates the spirits of conventional profile monitoring methods and SSA. At the beginning, a nonparametric smoothing procedure fits the surface data to a smooth surface. Then, they generate an equally spaced grid to cover the entire design space, which is similar to the idea of landmark in SSA. The grid for each surface is used for registration of all surfaces, and then, used for generating the mean surface. Finally, a statistic for profile monitoring is defined as the maximum deviation of each surface from the mean surface. However, their study failed to capture the nature of AM process. That is, instead of producing profiles or features, AM directly creates the products through adding material layer by layer. Also, even though their objective is close to SSA, the grids generated in their model cannot be seen as landmarks. The algorithm uses equally space points, which cannot guarantee to have the same number of corresponding points for all surfaces. Thus, it lacks the connection to other useful analytical tools in SSA.

Volumetric Data Analysis

As shown in previous sections, current-state-of-the-art statistical methodologies for geometric data, such as profile monitoring and SSA, have their limitations when applied to 3DP. That is, profile monitoring is limited for surfaces and SSA is heavily and restrictedly based on corresponding landmarks. Therefore, we propose a novel algorithm to deal with these limitations, shown in Fig. 1. The overall algorithm can be divided into two steps: point clouds registration and mean surface estimation.

Volume Registration

Image registration is well studied in computer vision, while surface registration is trending in the profile monitoring. However, for the point cloud of the printed parts, 2-dimensional registration or 3D one profile registration algorithm is not enough. Therefore, a volumetric level registration algorithm is needed. The key idea of volumetric registration is closed to surface registration, however, instead of only registration of one surface, the parts point cloud can be registered either by the whole outer surfaces, of which the special case is iterative closest points algorithm, or by the datum features.

As for the whole outer surface algorithm, point cloud of one part can be arbitrarily selected as the reference volume. The point clouds of other parts can be registered to the reference volume. The basic idea of such registration algorithm is to find the rigid transformation parameters in order to minimize the overall deviation of the surfaces from the reference surfaces. Within this algorithm, we could manually set larger weights to the important surfaces, such as key features or datum features.

On the other hand, manufacturing knowledge should be considered in the registration process. Since the datum features are closely related to the manufacturing and the inspection processes, it is more suitable to register the point cloud according to them. Assignment of datum features is an important problem for 3DP. The datum features may not be obvious from AM machine point of view, while, considering hybrid methods integrating AM with other manufacturing processes, determination of the datum features becomes inevitable. The algorithm we consider in this study require datum features already assigned or determined. Then, the volume point cloud is registered according to the registration of the corresponding datum features.

While the conventional registration algorithm for point cloud is available, such as iterative closet points, etc., these algorithms are often computationally and, also, analytically difficult for the next step, mean surface estimation. Therefore, we could use the grid-matching algorithm for volumetric registration. First, a nonparametric model is generated based on the data point on each surface needed to be register from each point cloud. To fit the nonparametric surfaces, the volumetric data need to be first segmented into features. These features can be either manually selected or segmented through segmentation algorithms. Then, a grid for each feature is generated according to the equal distance, which is the ratio of minimax envelope of the feature, for example, the minimax square envelope. Due to the envelope is greater in area than the true feature, some grid points can be out of the feature, while some may have values in one part and may not have values in others. Therefore, an ‘or’ logic operator is required to generate corresponding points, that is only the points that have values in all parts is recorded in the grids. With grid points generated, a grid-

matching algorithm is proposed to register all the surfaces. The grid-matching algorithm can be either based on the grids for all surface, whose output are co-centroid volumes; while, considering the nature of manufacturing, a more reasonable solution is to register the volume data according to the grid-matching of the points on datum features.

Mean Surface Estimation and Inference

After the surfaces are registered according to grid-matching algorithm, it is much easier to find the mean surfaces. Firstly, the data points constitute the mean surface, or averaged point cloud, can be easily calculated through the sample mean for each corresponding grid points of different surfaces. The mean surface can be fitted by these average data cloud through a nonparametric surface fitting algorithm. Then, more importantly, for many engineering applications, such as tolerance analysis, process capacity analysis, etc., the variational behavior for the mean surface model is needed to be derived and analyzed. It is possible to find the statistical behavior of the averaged data cloud and then the mean surface. The averaged data points are inherently the 3D random processes, which can be correlated. We could use bootstrapping methods to find out the statistical behavior and confidence interval or tolerance interval for the mean surface estimator.

VDA Based Inspection Analysis for 3DP

As shown above, VDA is ready for whole body inspection analysis for 3DP. However, conventional statistical methods, such as ANOVA and SPC, can be only applied to univariate or, at most, multivariate random variables. However, for VDA framework, the 3D closed-form mean surface is the estimator for the nominal design. Therefore, for analytical tractability and simplicity, the surface models are needed to map to real valued random variables or random vectors. That is, the random vector, $\boldsymbol{X}$, maps the surface model and mean surface model from the space of 3D closed-form volume, $\mathcal{H}$, to k dimensional real vectors, $\mathbb{R}^k$.

Examples, such as the maximum absolute deviation or first n absolute deviations or the sum of deviations, can be used to test and compare statistical performance. The major concern is the value of k. Many studies in high dimensional statistics are devoted to dimensional reduction methods, such as Lasso, principle component analysis. One possible solution to this study is to implement nonlinear dimensional reduction methods in manifold learning. With the random variable available, it can be directly available for ANOVA analysis, which can be used to compare different AM settings or optimize them, such as printing orientation, and Phase I and Phase II monitoring for process control. Distribution of test statistics for VDA-ANOVA and process monitoring can be approximated by statistical resampling methods, such as bootstrapping.

The objective of VDA-DOE is to test whether the geometric differences from parts which are printed from various settings can be identified and, further, to find out the optimal setting combinations. The simple case in DOE is Here, the different AM settings are treatments and, between treatments, parts from the same design can be with different biases or variance. Point clouds for each treatment are generated based on the same geometric designs with various features. SSA based ANOVA [5] and profile monitoring based statistical method [10] will be used for comparison of statistical performance, such as level of significance and power. It worth notice that the test statistic for VDAANOVA is based on the whole point cloud. Yet, for the other methods, multiple comparison tests are needed, since they are based on each of the feature or surfaces.

Summary and Future Work

In this paper, the major difficulty for analyzing of the inspection data of 3D printing process is first discussed. Current-state-of-the-art techniques fail to capture the unique nature of 3DP, layer-by-lay fabrication. Then, the novel framework, volumetric data analysis, is proposed to bridge the gap between the closed-shape point cloud and available statistical analyzing techniques.

Future research will focus on conducting the experiments on design specific parameters for 3DP, for example, the printing orientation. VDA provide a scientific path to analyze such parameters, which traditional methods cannot be used. Also, each component of the VDA framework will be investigated in detail. So far, the components, such as grid-generation algorithm, registration algorithm, that we propose can be implemented. However, they need to be well studied to enhance the accuracy and performance of the model. For grid-generation algorithm, we state an equal-space, whose

distance is based on a ratio of the envelope. However, it can be improved if the dense of the grid is a function of the complexity of the local features. That is, the more complex the feature is, the denser the grid points should be. For example, let the local curvature of the surface represent the complexity, the grid points should be denser in the area with high curvature. Thus, the local dense of the grid points, or the distance between the grid points, should be a ratio of the envelope, also, it should be monotone increasing with respect to the curvature and positive lower bounded.

On the other hand, the performance in terms of accuracy should be compared between ICP-based VDA and grid-based VDA. That is which one provides a higher accuracy, to generate the grid after registration based on ICP or to generate the grid and use the grid to register the point clouds.

Even though the volumetric data analysis is still at its early age, since many aspects can be improved in the future, it provides a new way to think about manufacturing processes and an opportunity to analyze the products geometric data. Volumetric data can be analyzed in a more reasonable way using VDA, compared to classical feature-based analysis.

Classification of Manufacturing Processes

3DP has a unique nature comparing to classical manufacturing processes. As shown above, the features of the products generated by 3DP may not be identified by the printer. Instead, most features are just the 'byproducts' of the thin layers. Therefore, we propose a novel way to classify manufacturing processes: feature generation processes, semi-feature generation processes and volume generation processes. This classification methodology is based on what and how the processes create the products. It can be helpful to select appropriate metrology equipment and analytical tools.

Feature generation processes cover most of the current wide adopted machining processes. These machining processes can directly generate the features of the products. For example, the drilling process can generate a hole feature, while the cutting process can generate a flat surface. In this category, traditional point-based metrology tools, such as gauge, or manual CMM, are useful. In this categories, classical DOE methodologies, such as ANOVA, can be implemented to seek for the best production settings; traditional process monitoring techniques, such as control charts, can be used to monitor and control the process.

Volume generation processes, on the other hand, do not generate features directly. Instead, most of the features are created as 'byproduct' of the processes. Obviously, all 3DP processes belong to this category. Based on this nature, 3D scans of the whole volume should be used for metrology purposed. And VDA based methodologies are perfect for the point clouds collected by 3D scans.

The semi-feature generation processes are in the middle of the feature- and volume generation processes. All the features are generated by the processes; however, the feature-generations are not totally independent. Die-based manufacturing, such as die casting, die forging, are in this category. Both traditional metrology and 3D scans can be used for different purposes. And, a mixture of both classical methodologies and VDA should work for this category.

REFERENCES

[1] Gibson I, Rosen D W, Stucker B. Additive manufacturing. Springer. Boston: 2014.

[2] Dryden I L, Mardia K V. Statistical shape analysis with applications in R. John Willey & Sons Ltd. New York: 2016.

[3] Woodall W H, Spitzner D J, Montgomery D C, Gupta S. Using control charts to monitor process and product quality profiles. Journal of Quality Technology. 2004; 36; 309-320.

[4] Woodall W H. Current research on profile monitoring. Production. 2007; 17; 420-425.

[5] del Castillo E, Colosimo B M. Statistical Shape analysis of experiments for manufacturing processes. Technometrics. 2011; 53; 1-15.

[6] del Castillo E, Colosimo B M, Tajbakhsh S D. Geodesic Gaussian processes for the parametric reconstruction of a free-form surface. Technometrics. 2015; 57; 89-99.

[7] Huang Q, Nouri H, Xu K, Chen Y, Sosina S, Dasgupta T. Statistical prediction modeling and compensation of geometric deviation of three-dimensional printed products. Journal of Manufacturing Science and Engineering. 2014; 136; 061008.

[8] Huang Q, Zhang J, Sabbaghi A, Dasgupta T. Optimal offline compensation of shape shrinkage for three-dimensional printing processes. IIE Transactions. 2015; 47; 431-441.

[9] Wang A, Song S, Huang Q, Tsung F, In-plane shape-deviation modeling and

compensation for fused deposition modeling processes. IEEE Transactions on Automation Science and Engineering. 2017; 14; 968-976.
[10] Zang Y, Qiu P. Phase I monitoring of spatial surface data from 3D printing. Technometrics. 2018; 60; 169-180.
[11] Zang Y, Qiu P. Phase II monitoring of free-form surfaces: an application to 3D printing. Journal of Quality Technology. 2018; 50; 379-390.

Effect of laser-assisted diamond turning (Micro-LAM) on non-optimally oriented calcium fluoride crystal

Charan Bodlapati[1], Jayesh Navare[1], Dmytro Zaytsev[1], Di Kang[1], Hossein Mohammadi[1],Deepak Ravindra[1], Megan Arlt[1], Hossein Shahinian[1]
[1]Micro-LAM , Inc
5960 S Sprinkle Rd
Portage, Michigan, USA

INTRODUCTION

In this paper we investigate the effect of laser-assisted diamond turning, hereafter referred to as the µ-LAM process, on the form and surface cosmetics of non-optimally oriented single crystal calcium fluoride (CaF_2). The µ-LAM process is a technology that enables the simultaneous use of laser emission during single point diamond turning (SPDT). The laser is passed through the diamond and the irradiance of the laser on the machining zone facilitates the cutting action of the diamond tool due to the local heating and " thermal softening" of the material during the cut [1, 2 and 3].

The SPDT process has enabled the easy production of freeform and aspherical optics. These optics have found vast applications in fields of optical imaging, illumination, etc. It is imperative for the SPDT process to produce parts with form errors less than a quarter of the operating wavelength of the light.

Calcium fluoride (CaF_2) has higher transmission in both IR and UV wavelength ranges. It has a very high Abbe number, which makes fabrication of achromat optics with CaF_2 very feasible. It is particularly well suited for manufacturing lenses, prisms and mirrors for dark field imaging systems, large-scale microlithography systems and excimer lasers [4].

Studies on machining different single crystal materials suggest that crystal orientation of the workpiece material affects shear angle and cutting forces [5], thereby affecting overall surface quality. Single crystal materials like CaF_2 exhibit brittle fractured zones on the surface when machined; This behavior is attributed to different crystal orientations having different cleavage planes. This work focuses on the effect of laser assisted diamond turning of µ-LAM process on aesthetics and form of non-optimally oriented CaF_2 crystal.

EXPERIMENTAL METHOD

To study the effect of the µ-LAM process on the surface form and cosmetics of CaF_2, an experimental approach was undertaken. A concave sample was machined. The crystal orientation of the CaF_2 sample was determined to be <211>, in the plane normal to the cutting direction. The orientation of the sample was determined using a Siemens D5000 X-ray diffractometer. The machining was done on an ultraprecise diamond turning lathe, a Nanotech 250 ultraprecision lathe. The setup is shown in FIGURE 1. A set of diamond cutting experiments using the µ-LAM process and conventional SPDT were performed.

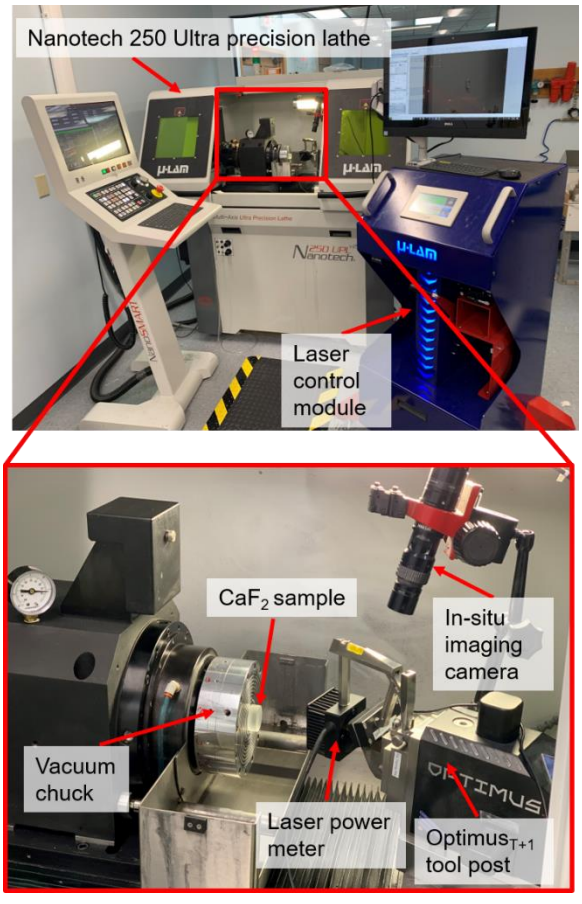

FIGURE 1. Experimental Setup

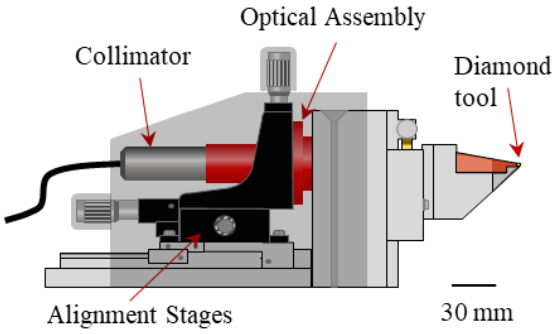

FIGURE 2. Optimus$_{T+1}$ Tool Post

Optimus$_{T+1}$ Tool Post

The Optimus$_{T+1}$ is a specially made tool post, that incorporates an optical assembly designed to deliver an IR laser beam (1064nm wavelength) through the diamond cutting tool, see FIGURE 2.

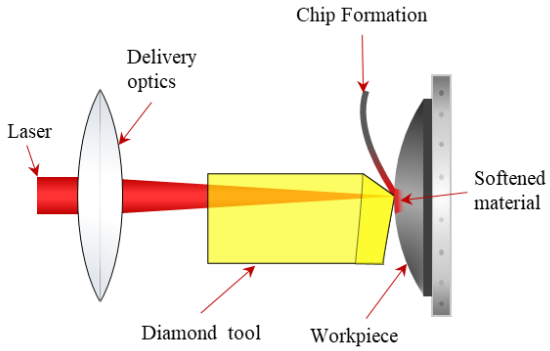

FIGURE 3. The delivery of laser emission at the cutting edge of the diamond tool

The laser delivered by the optical system within the tool post is focused near the cutting edge of the diamond tool, see FIGURE 3. This highly focused spot of the laser at the cutting edge provides the local heat that enables the material "softening" mentioned in the introduction.

Test Sample

A concave sample comprised from single crystal CaF_2 with <211> crystal orientation was used. The sample is 35 mm in diameter and 75mm ROC.

Metrology

The form measurements were done using a Taylor Hobson LuphoScan® 260 HD. This instrument is a multi-wavelength scanning interferometer. Piston, tilt and power were removed during data analysis. RMS was the metric used for the metrology data. The RMS corresponds to the root mean square deviation of points on the measured surface.

Diamond Cutting Tools

Single crystal synthetic diamond tools manufactured by K&Y Diamond® were used for all the cutting tests. Tools with 0.3 mm nose radius with 10º primary clearance and -35° rake angle was used for the study. The -35° rake angle provides the necessary compressive stresses during the cutting of the brittle crystals.

SPDT conditions

A set of cutting experiments with conventional diamond turning and with the µ-LAM process was performed. Each test was repeated three times. In each of the performed experiments two cuts were done. Before each cut, a setup stud was cut to correct for tool offsets in the horizontal (X) and vertical (Y) directions. The final X and Y tool offsets were less than 1 µm. Moreover, no tool waviness compensation was used for the tool path generation. The machining parameters are listed in Table 2.

Table 1. Machining parameters of the samples

Sample	RPM	Feed (mm/min)	DOC (µm)	Laser power (W)
CaF_2	4500	3.4	2	2.4
CaF_2	4500	3.4	2	0

Three experiments each were done using the cutting parameters shown in Table 2. Both tests used odorless mineral spirits as coolant. These tests were aimed to establish a direct comparison between the achievable form and surface cosmetics when diamond turned conventionally to that of the µ-LAM process.

RESULTS

The cutting tests were done with a spindle balance of less than 1 nm PV deviations in the spindle position. In each test the surface of the samples were measured using the LuphoScan. The sample was inspected for cosmetics by shining a 15W dual light on it.

Form measurements

FIGURE 4 (a), (b) depict the form errors imparted on the CaF_2 sample cutting with conventional diamond turning and the µ-LAM process,

respectively. The measurement data of the parts suggest that the form error is slightly better when the μ-LAM process was used. FIGURE 4 also shows that astigmatism on the part is much lower when the μ-LAM process was used under identical vacuum pressure on the chuck.

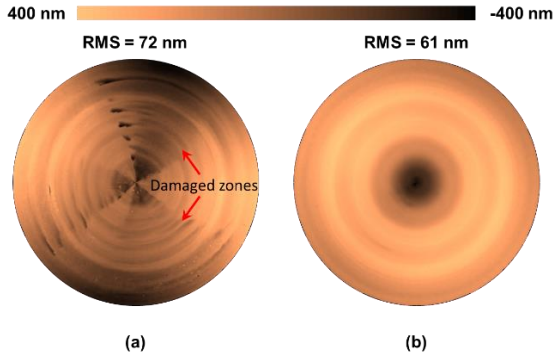

FIGURE 4. Form error measurements for the CaF_2 sample; (a) conventional diamond turning (b) μ-LAM process

Cosmetics

The good agreement between the RMS values of the measurements of the parts cut in the absence of the laser, i.e. FIGURE 4(a) and the presence of the laser, i.e. FIGURE 4(b), is complemented by the fact that large surface defects near the center are nearly gone on the sample machined with the μ-LAM process. These defects are a consequence of the single crystal structure of the CaF_2 sample. Their absence on the sample in FIGURE 5(b) demonstrates how the laser enhances the ductile cutting of the CaF_2 material. FIGURE 5(a) shows relatively intense brittle fractured zones on the sample.

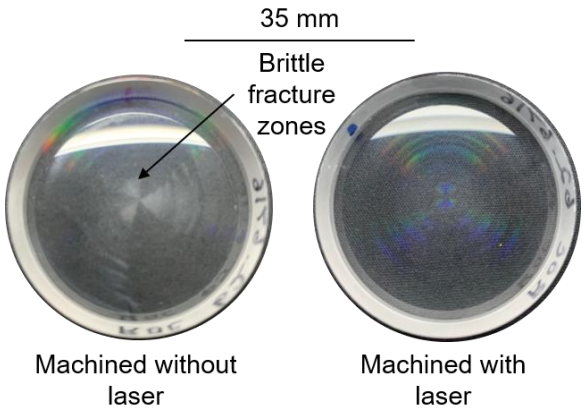

FIGURE 5. CaF_2 sample. (a) without μ-LAM (b) with μ-LAM

DISCUSSION

The feasibility of μ-LAM process on CaF_2 has been previously reported in [6] for a <111> crystal orientation. However, the effect of laser was more prevalent in the case of non-optimally oriented CaF_2 crystal discussed in this paper. Crystal orientation of a sample determines the fracture toughness along the cleavage planes. When brittle fracture occurs in the sample, definite brittle fracture zones can be seen along the cleavage planes. For the sample that was cut with conventional diamond turning, clear defects and zones exhibiting brittle fracture were observed. The improved surfaces of the materials with the addition of the μ-LAM process, implies that the local heating of the laser facilitates the ductile cutting of the <211> CaF_2 under study. This result confirms the material "softening" effect of the laser on the workpiece.

As mentioned earlier, the part machined with the μ-LAM process, showed to have smaller non-rotationally symmetric irregularities. The sample machined using the μ-LAM process had approximately 15% of the astigmatism and 5% of the trefoil irregularity of that machined with conventional diamond turning. Such non-rotationally symmetric errors are thought to be magnified with higher cutting forces, thus leaving the conclusion that the overall forces during machining the sample using the μ-LAM process are lower. This could be explained best as assuming a higher level of ductile material removal using the μ-LAM process.

CONCLUSION

The capability of machining non-optimally oriented calcium fluoride crystal that is inherently brittle in nature using the μ-LAM process was compared with conventional diamond turning. Even though the laser, a significant heat source, is propagated through the diamond tool, the μ-LAM can achieve improved form and cosmetics on the machined surface.

As future investigations on μ-LAM of CaF2, different crystalline orientation as well as tooling geometries will be investigated. Furthermore, optimizations in reducing the tool wear as a function of the distribution of the laser beam is of utmost interest.

REFERENCES

1. Shahinian, Hossein., Navare, Jayesh., Zaytsev, Dmytro., Ravindra, Deepak. *Micro laser assisted diamond turning of precision silicon optics*. Optical engineering, 2019. 58(9), 092607.

2. Shahinian, Hossein & Zaytsev, Dmytro & Navare, Jayesh & Su, Yang & Kang, Di & Ravindra, Deepak. *Micro Laser Assisted Machining (μ-LAM) of Precision Optics*. (2018) OT1A.5. 10.1364/OFT.2019.OT1A.5.

3. Kang, Di., Navare, Jayesh., Su, Yang., Zaytsev, Dmytro., Ravindra, Deepak and Shahinian, Hossein. *Observations on Ductile Laser Assisted Diamond Turning of Tungsten Carbide*. (2019). Optical Design and Fabrication 2019 (Freeform, OFT), OSA Technical Digest Optical Society of America.

4. Ewing, D.J., *Excimer Lasers at 30 years.* 2003. Opt. Photonics News 14. p. 26-31.

5. Lee, W.B., Sandy, To & Cheung, C. *Effect of crystallographic orientation in diamond turning of copper single crystals.* (2000). Scripta Materialia - SCRIPTA MATER. (42) p. 937-945.

6. Shahinian, Hossein., Navare, Jayesh., Zaytsev, Dmytro., Kode, Sai., Azimi, Farzad & Ravindra, Deepak. *Effect of laser-assisted diamond turning (Micro-LAM) on form and finish of selected IR crystals*. (2018). 33rd Annual Meeting of American Society of Precision Engineering.

ACCURACY ANALYSIS ON WELD SPECIFICATIONS USING CONFOCAL MICROSCOPY

Mario O. Valdez, Roy S. Sikkink, Carlos R. Arguero, D. Eric Keim, Linda E. Cassidy
Production Agency Quality
Los Alamos National Laboratory (LANL)
Los Alamos, NM, USA

INTRODUCTION

Aerospace applications such as satellites and space probes require long-lasting power sources to maintain power over the life of the mission. It is critical that these power sources are robust enough to adequately provide the proper wattage in the harsh environment of space without maintenance and intervention. A popular power source satisfying these criteria is the radioisotopic thermoelectric generator (RTG), which use radioactive materials to generate heat as they decay into non-radioactive materials. The heat from the decay is then converted into electrical power utilizing the Seebeck Effect [1], [2].

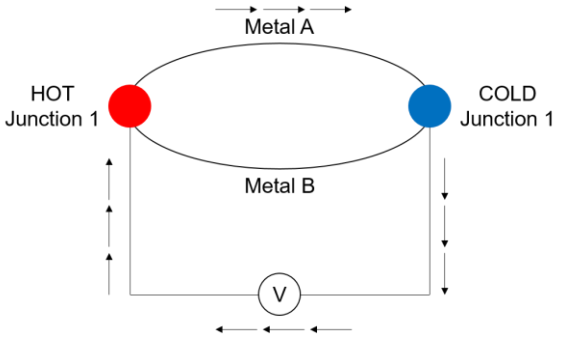

FIGURE 1. Schematic of the Seebeck Effect.

BACKGROUND

The radioactive materials that fuel an RTG are contained within an encapsulated heat source. In this work, we examine a heat source with a triple-encapsulated and hermetically-sealed radioactive oxide fuel. The 1st and 3rd encapsulations are sealed via a gas tungsten arc welding method, while the 2nd encapsulation uses an electron beam welding method. Each of these welds requires dimensional inspection to verify compliance with the product specifications. While classical dimensional metrology techniques such as hard gaging and fine-wire can verify acceptance/rejection criteria, they do not provide adequate verification for requirements that require absolute data (i.e. numerical values). To remedy this issue, we require a measurement system capable of collecting and post-processing continuous data.

In the work described below, we outline a calibration process for a measurement system which utilizes confocal microscopy as its measurement principle, contextualized within the framework of an accuracy study for application to weld specifications. We develop an error indication model as a function of the predictable biases, along with an estimate of the associated uncertainty model. We describe the design of a calibration artifact and associated fixturing, and the process for performing a calibration. Finally, we provide some insights into the future of the accuracy study.

MEASURANDS

A procedural approach to evaluating measurement uncertainty must begin with identification and specification of the measurands of interest. As defined by the *International Vocabulary of Metrology* (VIM), the measurand is *"the quantity intended to be measured"* [3]. The heat source product specification identifies two final weld characteristics, concavity and undercut, which require dimensional inspection and evaluation of measurement data (FIGURE 2).

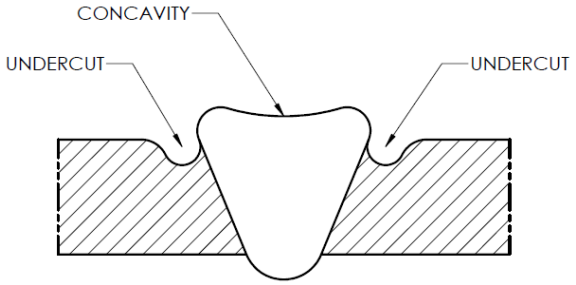

FIGURE 2. Cross-sectional definition of a weld. (The solid white area represents the weld, while the hatched area indicates the base metal.)

As the planned realization of these measurands is through confocal microscopy at shop-floor conditions, their definitions must be such that uncertainty is minimized and systematic errors can be accounted for and corrected.

Weld Concavity

Weld concavity is defined as *"the maximum distance from the face of a concave fillet weld perpendicular to a line joining the weld toes."* [4]. FIGURE 3 depicts the weld concavity as the distance/depth, d_{con}.

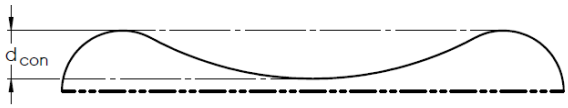

FIGURE 3. Weld concavity.

Weld Undercut

Weld undercut is defined as *"a groove in the base metal along both sides of the weld that is not completely filled during the welding process."* [4]. FIGURE 4 depicts the weld undercut as the distance/depth, d_{und}.

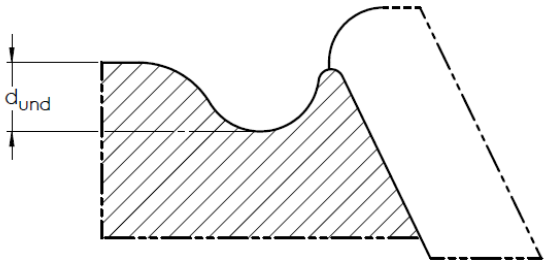

FIGURE 4. Weld undercut. (The hatched area on the left indicates base metal, while the solid white area on the right indicates the weld.)

Workpiece Concavity

The workpiece concavity is related to the geometry of the final encapsulation; it is not an inherent feature of the weld itself but rather a result of the forces which occur during the welding process. In regards to this phenomenon, the workpiece concavity is defined as *"the maximum distance between the point just inboard of the weld and the center point of the workpiece profile."* FIGURE 5 depicts a cross-sectional visualization of workpiece concavity.

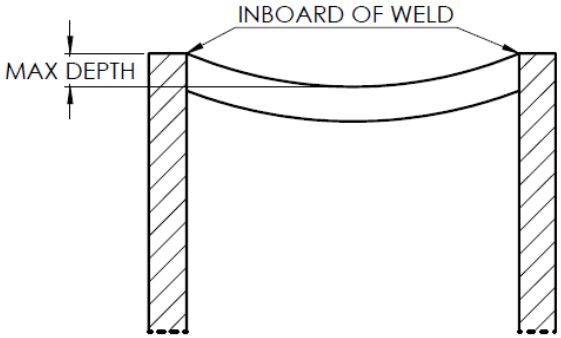

FIGURE 5. Workpiece concavity. (The hatched areas and solid white area represent components of the workpiece, joined by a weld at the interface.)

CALIBRATION

Traditionally, it is challenging to ensure positional accuracy in a 3-axis system, particularly along the optical axis (i.e., z axis) where scanning is performed by a different physical mechanism. Additionally, a lack of established standardization potentially raises ambiguities in the ability to properly calibrate the instrument. As an alternative, we seek to apply standardization which currently exists for measurement instruments with similar characteristics. The ISO 10360 series, and in particular, ISO 10360-8, is the industry-accepted calibration method for coordinate measurement systems (CMSs) with optical distance sensors [5].

The technical objectives of the standard are as follows:

- To test the error indication of a calibrated length using an optical distance sensor; and
- To test the errors of the optical distance sensor.

This is allowed for the following types of sensors:

- Point measuring sensors; and
- Area measuring sensors (i.e., laser point scan, laser line scan, fringe projection, etc.)

In applying these principles the tests will provide direct traceability to the unit of length, and thus provide information on how the CMS will perform on similar length-dependent measurements.

Error Indication Model

To establish the uncertainty for traceability of the calibration per the technical objectives of ISO 10360-8, an error indication model is required. To meet this requirement, the error indication model must account for influence quantities from the instruments, calibration artifact, and extrinsic factors. However, it impossible to account for all the influence quantities; therefore only the predictable biases are accounted for.

The error indication model is a function of the following influence quantities,

$$E = f(L,\ S, \alpha_s, \Delta T_{art},\ \delta\alpha, \delta T, \varphi, R) \qquad (1)$$

where the functional parameters are the mean length of the measurement instrument, L; the step size of the calibration artifact, S; the CTE of the measurement system scale, α_s; the temperature deviation from 20℃ of the calibration artifact, $\Delta T_{art} = T_{art} - 20℃$; the difference in CTE between the calibration artifact and measurement system scale, $\delta\alpha = \alpha_{art} - \alpha_s$; the difference in temperature between the calibration artifact measurement system scale, $\delta T = T_{art} - T_s$; the misalignment between the measured direction of the calibration artifact and axis being measured, φ; and the effective lateral resolution for the X/Y axes or effective uncertainty of the sensor for the Z axis, R.

With the known functional parameters, the error indication model is shown in Appendix A, Eq. A-1. In quasi-correlation to ISO 10360-8, the error indication model can be utilized as the maximum permissible length measurement error, more specifically Eq.2,

$$E = E_{Uni:j:ODS,MPE} \qquad (2).$$

For clarity, the subscript implies the following: Uni, unidirectional length measurements; j, measuring conditions of the CMS; ODS, indicates that it is associated with the optical distance sensor; and MPE, the maximum permissible error.

Uncertainty Model

Estimating the measurement uncertainty via the principles outlined in the *Guide to the Expression of Uncertainty in Measurement* (GUM) [6] requires an empirical mathematical model of the measurand. The establishment of the error indication model meets this criteria. Therefore, the uncertainty model is a function of the products of the sensitivity coefficients and standard uncertainties from Eq.1.,

$$u(E) = f\left(\frac{\partial E}{\partial L}\cdot u_L, \frac{\partial E}{\partial S}\cdot u_S, \dots, \frac{\partial E}{\partial R}\cdot u_R\right) \qquad (3).$$

Furthermore, to capture the entire measurement process, rather than individual influence quantities, Eq.3 must be added in quadrature to express the combined standard uncertainty. The full uncertainty model is shown as Eq.A-2 in Appendix A, along with a tabulation of the standard uncertainties for the functional parameters.

Finally, the expanded uncertainty is determined at the 95% confidence level; however, Eq.3 is equivalent to the uncertainty of the calibration process,

$$U_{95} = 2u(E) = U_{cal} \qquad (4).$$

CALIBRATION PROCESS

For the calibration process, both a physical calibration artifact and calibration fixture were developed. The artifact satisfies the requirement for a reference artifact per the technical objectives of ISO 10360-8, whereas the fixture aids in minimizing certain predictable biases (e.g., misalignment in the measurements of the calibration artifact (cosine error)).

Artifact and Fixture

We developed a calibration artifact with the intent of calibrating the measurement instrument in all three axes. The artifact design includes features of length for the X and Y axes as well as features of depth for the Z axis. The artifact was manufactured internally, and is made of ASTM A2 Tool Steel ($\alpha = 6.5 \times 10^{-6}$ /°F) with ground surfaces, stress relief, and laser marked zones for consistent calibration. The calibration fixture was made by an external vendor from AL 6061 Aluminum and features a tramming resolution of 0.001" over a 9.25" length (0.006°), and a magnetized fixture arm for stability during calibration. The artifact is intended for unidirectional calibration, see FIGURE 6, where measurements for Z are in tandem with those of either X or Y.

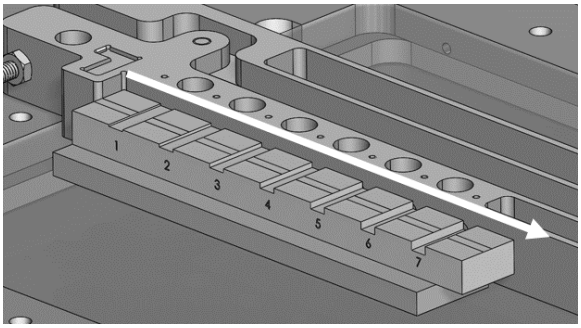

FIGURE 6. Artifact and calibration fixture.

Raw data from the measurement sets of the calibration fixture are compared to the reference values provided from the calibration certificate.

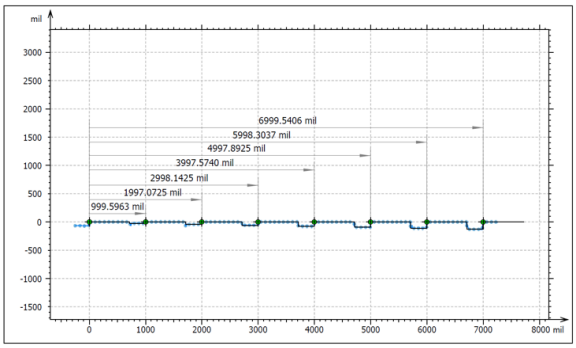

FIGURE 7. Reference values and measured value comparison using semi-automated feature recognition.

By incorporating the reference values from the calibration certificate into a CAD model of the artifact, determination of measurement zones can be partially automated through software-based feature recognition. This significantly reduces processing time for each data set while still allowing for manual verification. Development of this process for the calibration artifact in turn provided additional insight for applying a similar methodology to features of the actual part.

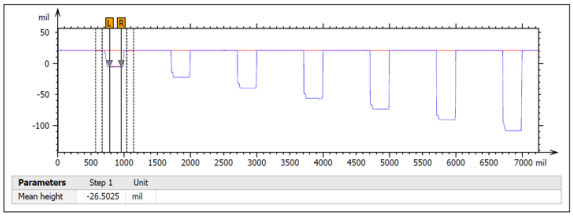

FIGURE 8. Manual analysis of measurements.

Once the calibration measurements were completed, the systematic encoder corrections were performed where the measurement results are now only affected by the random variations in the measurement process albeit small residual systematic or transient variations.

Initial measurements in the calibration process yielded an error of…

CONCLUSION

We extended the calibration principles of ISO 10360-8 to a measurement system which utilizes confocal microscopy. Previous calibration was subjective and lacked standardization, thus making it impossible to follow the acceptance testing and verification procedures of an industry-accepted standard. To ensure traceability, an error indication model and uncertainty model were developed via the principles established in the GUM. Additionally, a calibration artifact and calibration-specific fixture were developed to assist in the calibration of the measurements instrument. As a result, validation of the calibration is ensured and the traceability chain is unbroken.

FUTURE WORK

Completion of the accuracy study will require additional testing on actual parts. This will provide information on the capability of the measurements as to whether there is acceptance, acceptance with exception, or rejection of the measurement process. The preferred method will be a Gage Repeatability and Reproducibility (GR&R) study to identify the statistical uncertainty contributions, specifically from the instrument (repeatability), appraisers/operators (reproducibility), and interactions (part*appraiser/operator). Analysis of Variance (ANOVA) techniques have been well-established to provide this information. For assurance of quasi-standardization, testing and evaluations will follow industry-accepted practices [7], [8]. Finally, validation of the accuracy study will conclude with an uncertainty budget evaluation of the contributing factors and evaluation of the measurement process capability as a whole.

ACKNOWLEDGEMENTS

The authors would like to thank Los Alamos National Laboratory (LANL) for funding this research as well as the National Nuclear Security Administration (NNSA).

APPENDIX A: ERROR INDICATION MODEL AND UNCERTAINTY MODEL

To establish traceability and validation of the calibration measurements, an uncertainty evaluation is required to meet these criteria. For determination of the calibration uncertainty pertaining to the confocal measurement system, an error indication model is developed via the principles suggested by the *Guide to the Expression of Uncertainty in Measurement (GUM)*. Accounting for the predictable biases, the error indication model is

$$E = L\cos(\varphi)\left[1 + \alpha_s \Delta T_{art} + (\delta\alpha)\Delta T_{art} + \alpha_s(\delta T) + (\delta\alpha)(\delta T)\right] - S(1 + \alpha_s \Delta T_{art}) - R \tag{A.1}$$

From Eq. A-1, the uncertainty model (in this case the combined standard variance) is modeled via the uncertainty propagation law,

$$u^2(E_{cal}) = \left(\frac{\partial E}{\partial L}\cdot u_L\right)^2 + \left(\frac{\partial E}{\partial S}\cdot u_S\right)^2 + \left(\frac{\partial E}{\partial \alpha_s}\cdot u_{\alpha_s}\right)^2 + \left(\frac{\partial E}{\partial \Delta T_{art}}\cdot u_{\Delta T_{art}}\right)^2 + \cdots \\ \cdots + \left(\frac{\partial E}{\partial \delta\alpha}\cdot u_{\delta\alpha}\right)^2 + \left(\frac{\partial E}{\partial \delta T}\cdot u_{\delta T}\right)^2 + \left(\frac{\partial E}{\partial \varphi}\cdot u_{\varphi}\right)^2 + \left(\frac{\partial E}{\partial R}\cdot u_R\right)^2 \tag{A.2}$$

where the sensitivity coefficients, $\partial E/\partial x_i$, are shown in Eq. A-3,

$$\frac{\partial E}{\partial L} = \cos(\varphi)\left[1 + \alpha_s \Delta T_{art} + (\delta\alpha)\Delta T_{art} + \alpha_s(\delta T) + (\delta\alpha)(\delta T)\right] \qquad \frac{\partial E}{\partial S} = -(1 + \alpha_s \Delta T_{art})$$
$$\frac{\partial E}{\partial \alpha_s} = L\cos(\varphi)\,(\Delta T_{art} + \delta T) - S\Delta T_{art} \qquad \frac{\partial E}{\partial \Delta T_{art}} = L(\alpha_s + \delta\alpha) - S\alpha_s$$
$$\frac{\partial E}{\partial \delta\alpha} = L(\Delta T_{art} + \delta T) \qquad \frac{\partial E}{\partial \delta T} = L(\alpha_s + \delta\alpha)$$
$$\frac{\partial E}{\partial \phi} = -L\sin(\phi)\left[1 + \alpha_s \Delta T_{art} + (\delta\alpha)\Delta T_{art} + \alpha_s(\delta T) + (\delta\alpha)(\delta T)\right] \qquad \frac{\partial E}{\partial R} = -1 \tag{A.3}$$

The standard uncertainties needed for uncertainty model, Eq. A.2, are tabulated below with their respective probability distribution functions.

Table 1. Standard uncertainties for calibration error uncertainty model.

Source	Type	Distribution Function	Standard Uncertainty
L	A	Normal	$u_L = s_L = \sqrt{\frac{1}{n}\sum_{i=1}^{n}(L_i - \bar{L})^2}$
S	A	Normal	$u_S = s_S = \sqrt{\frac{1}{n}\sum_{i=1}^{n}(S_i - \bar{S})^2}$
α_s†	B	Uniform	$u_{\alpha_s} = \frac{0.2\alpha_s}{\sqrt{3}}$
ΔT_{art}	B	Arcsine/Normal	$u_{\Delta T_s} = \sqrt{\left(\frac{\Delta T_{art}}{\sqrt{2}}\right)^2 + \left(\frac{U(\Delta T_{art})_{sen}}{2}\right)^2}$
$\delta\alpha$‡	B	Uniform	$u_{\delta\alpha} = \sqrt{\left(\frac{0.1\alpha_{art}}{\sqrt{3}}\right)^2 + \left(\frac{0.2\alpha_s}{\sqrt{3}}\right)^2}$
δT	B	Normal	$u_{\delta T} = \sqrt{\left(\frac{U(T_{art})_{sen}}{2}\right)^2 + \left(\frac{U(T_s)_{sen}}{2}\right)^2}$
φ*	B	Uniform	$u_{\varphi} = \frac{a}{\sqrt{3}}$
R**	B	Uniform	$u_R = \frac{a}{\sqrt{3}}$

† - The measurement system scale material is 6061-Al so industry-acceptable variations is ±20% for aluminum alloys.
‡ - The calibration artifact material is XXXX, where industry-accepted variations are ±10% for steel alloys.
* - The misalignment angle is determined after the calibration artifact is trammed.
** - The lateral resolution is the radius of the spot size of the confocal sensor pen, that is a is taken from the product specification.

REFERENCES

[1] D. M. Rowe, CRC Handbook of Thermoelectrics, 1 st. ed., Boca Raton: CRC Press, 1995.

[2] D. M. Rowe, Thermoelectrics Handbook: Macro to Nano, 1 st. ed., Boca Raton: CRC Press, 2005.

[3] BIPM, "JCGM 200:2012 - International Vocabulary of Metrology - Basic and General Concepts and Associated Terms," BIPM, Paris, 2012.

[4] "American Welding Society," [Online]. Available: https://www.aws.org/.

[5] ISO, "Geometrical Product Specifications (GPS) - Acceptance and Reverfication Test for Coordinate Measuring Systems (CMS) - Part 8: CMMs with Optical Distance Sensors," ISO, Geneva, 2013.

[6] BIPM, "JCGM 100:2008 - Evaluation of Measurement Data - Guide to the Expression of Uncertainty in Measurement," BIPM, Paris, 2008.

[7] "A.I.A.G - Chrysler Corp., Ford Motor Co., General Motors Corp.," Automotive Industry Action Group, Michigan, 2010.

[8] "VDA Volume 5: Capability of Measurement Processes," Verband der Automobilindustrie, Frankfurt, 2010.

Authors Index

Anton, Jayson 111
Arguero, Carlos 501
Arlt, Megan 319, 497
Arneson, Christopher 301, 484
Arneson, David 264, 484
Arneson, Henry 427
Arneson, Sam 310
Arrington, Christian 488
Arumugam, Kumar 225
Assoufid, Lahsen 111
Austin, Sydney 24
Bauer, Wilfried 376
Behera, Dipankar 314
Betters, Emma 43, 283, 441
Beudaert, Xavier 375
Bhattacharya, Sambit 63
Bidanda, Bopaya 491
Bodlapati, Charan 319, 497
Bordatchev, Evgueni 84, 325
Brinksmeier, Ekkard 69
Brown, Thomas 157
Bui, Pho 474
Cao, Yongzhi 199
Cassidy, Linda 501
Catalucci, Sofia 145
Caviness, Alex 225
Cayll, David 244
Chabot, Joshua 115
Chao, Leon 166
Chen, Ni 254
Chen, Shih-Chi 18, 139, 209, 403, 407, 422
Cherukuri, Harish 295
Cheung, Chi-Fai 220
Chizari, Samira 24
Cho, Joon 244
Choi, Doo-Sun 232, 463
Choi, Jinsoo 362
Choi, Junoh 488
Connolly, Liam G. 238
Cook, Adam 488
Copenhaver, Ryan 435
Cullinan, Michael 32, 238, 244, 314, 417
Cvijanovic, Srdjan 84
Dagel, Daryl 61
Davies, Angela 295
Delio, Thomas 441
Devitt, Andrew 95
Dong, Xin 127
Dörgeloh, Timo 69
Dowski, Edward 175
Dumanli, Alper 133, 181
Dunn, Kathleen A. 385
Ebihara, Yusuke 26
Eichenberger, Jerome 441
Ellis, Jonathan 157
Enomoto, Toshiyuki 274
Enstrom, Kenneth 398
Erkorkmaz, Kaan 304, 375, 480
Ertas, Bugra 90
Evans, Christopher 295
Fan, Chunjie 371
Fan, Xiangyu 407
Farzaneh, Amin 24
Feng, Pingfa 279
Franco, Oier 375
Fu, Zhiqiang 403
Furst, Stephen 412
Furutani, Katsushi 431
Fyler, Donald 366
Geng, Zhaohui 491
Gerbert, David 376
Gomez, Michael 435, 441
Greis, Noel 63
Groen, Alex 304
Gu, Le 199
Guo, Ping 75
Guo, Shusen 199
Guo, Xiangyu 380
Haddad, Darine 166
Hamer, Tyler 115
Han, JaeMin 259, 380, 390
Han, Jun Sae 232, 463
Harada, Sena 274
Harder, Ross 111
Hastings, DJ 371
Hatridge, Michael ..... *
Hayashi, Akio 453
He, Ning 254, 337
Her, Tsing-Hua 225
Hopkins, Jonathan 24, 32, 106, 398
Huang, Yan 407
Hueser, Dorothee 376
Iqbal, Asif 337

Isa, Mohammed 151
Isohashi, Ai 79, 474
Ito, Reona 331
Ivanoff, Thomas 61
Jared, Bradley 61, 488
Jayatilaka, Gehan 32
Je, Tae-Jin 232, 463
Jeong, Ji-Young 232, 463
Jiang, Jiali 171
Jiang, Jiang 63
Joao, Delfim 325
Jonghwa, Shin 463
Kae, Doki 191, 195
Kang, Di 319, 497
Kang, Dongwoo 127
Karburn, Jordan 398
Kato, Tomonori 358
Kearney, Steve 111
Keim, D. Eric 501
Kim, Gyuha 259
Kim, Hyo Young 362
Kim, Jong-Jae 184
Kim, Kihyun 362
Kim, Won-jong 100
Knapp, Byron 264
Kodaka, Seiya 289
Koepke, Joshua 61
Koh, Daegwon 184
Kubota, Mami 385
Küpper, Moritz 84
Ladner, Ian 32, 244
Leach, Richard 145, 151
Lee, ChaBum 259, 380, 390
Lee, Seok Woo 362
Lee, Sun-Kyu 184
Lemon, John 37
Li, Chenglin 139, 422
Li, Da 220
Li, Haozheng 249
Li, Hongchuan 199
Li, Hongsheng 139
Li, Liang 254,337
Li, Simi 279
Li, Zhenjun 254
Liang, Rongguang 162
Liao, Wei-Hsin 75
Liebers, Melvin 484
Lim, Miles 24
Lin, Fuyan 171
Liu, Xiangbo 139, 422
Luo, Chenyang 32
Madison, Jonathan 61
Marangoni, Rafael 166
Mashrafi, Sheikh 111
Matsuyama, Satoshi 79, 466, 474
McPhee, John 480
Miller, Nichole 412
Milliken, Nicolas 84, 325
Mishra, Sandipan 54
Mitchell, John 61
Miyake, Hiroaki 195
Mohammadi, Hossein 319, 497
Mooney, Tim 111
Morimoto, Yoshitaka 453
Munoa, Jokin 375
Nagato, Keisuke 26, 49, 235, 331
Nakao, Masayuki 26, 49, 235, 331
Nakazato, Ayaka 191
Naples, Neil 268
Navare, Jayesh 319, 497
Newell, David 166
Newman, Tara 225
Nguyen, Vu 398
Nguyen, Vu 18, 100
Niho, Takayoshi 331
Nishida, Ken 466
No, Timothy 204, 435
Noakes, Mark 43
Nogueira, Monica 63
Noh, Minkyun 366
Nycz, Andrzej 43
Oakdale, James 18
Ohnishi, Ryosuke 79, 474
Ohyama, Kenta 49
Okamura, Toshihde 235
Okayama, Shinya 466
Okwudire, Chinedum 127
Olea, Gheorghe 250
Oss, Dan 264
Panas, Robert 106, 398
Park, Jaehyun 362
Park, Sangki 184
Park, Seongjin 232
Pascall, Andrew 106
Patel, Kevin 295
Pawlus, Pawel 214, 394
Piano, Samanta 145, 151
Preissner, Curt 427
Qian, Jun 111
Ravindra, Deepak 319, 497
Reinholtz, William 488
Reizer, Rafal 214, 394
Ren, Mindan 209, 407
Riemer, Oltmann 69

Rocha, Andrew 157
Rock, Stephen 54
Roy, Nilabh 314
Saavedra, Michael 488
Sagesaka, Koki 453
Saha, Sourabh 18, 244
Saiz, David 61, 488
Sano, Yasuhisa 79, 466, 474
Satake, Urara 274
Schlamminger, Stephan 166
Schmitz, Tony 43, 63, 204, 283, 435 441
Schoenemann, Lars 69
Seifert, Frank 166
Sencer, Burak 133, 181
Senin, Nicola 145
Shabahang, Farzaneh 225
Shahinian, Hossein 319, 497
Shannon, Tucker 181
Shaw, Lucas 24
Shi, Bing 111
Shi, Xianbo 111
Shim, Jaeyoon 184
Shimazaki, Kohei 358
Shkoruta, Aleksandr 54
Shu, Deming 111
Sikkink, Roy 501
Simonelli, James 398
Sims-Waterhouse, Danny 151
Smith, Scott 43
Smith, Stuart 225, 371
Sohn, Alexander 162
Song, Xiaoqi 447
Song, Yuanping 32
Suguru, Mototani 191, 195
Sun, Frederick 106
Sun, Tao 199
Tajima, Shingo 181
Takahashi, Motohiro 352
Takahashi, Nana 26
Tanaka, Tomohiro 358
Tangari Larrategui, Martin 157
Tarbutton, Joshua 380
Temmler, André 84
Tendo, Haruto 26
Tian, Xiaobo 162
To, Albert 37
Toh, Daisetsu 79, 474
Tohru, Ihara 447
Tomizawa, Morio 235
Torii, Akihiro 191, 195
Tran, Hai 37
Trumper, David 115, 121, 366
Tutunea-Fatan, Remus 84, 325
Valdez, Mario 501
Villarraga-Gómez, Herminso 259
Vlasea, Mihaela 304
Vlugter, Pieter 12
Wakiya, Shumon 343
Wang, Chia-Pei 480
Wang, Daodang 162
Wang, Dien 18
Wang, JianJian 75
Wang, Ping 249
Wang, Xiaogang 139
Ward, Martin 417
Weiming, He 447
Weinreb, Benjamin 366
Wen, Chenyang 209
West, Justin 43, 283
Willenborg, Edgar 84
Wu, Yang 254
Xu, You 358
Xu, Zhiqiang 199
Yamauchi, Kazuto 79, 466, 474
Yang, Yang 75
Ye, Peiqing 171
Yi, Allen 268, 479
Yukio, Takahashi 447
Zaytsev, Dmytro 319, 497
Zeng, Long 279
Zhang, Chuanwei 199
Zhang, Hui 171
Zhang, Lin 478
Zhang, Nan 403
Zhang, Yanqi 157
Zhang, Yong 171
Zhao, Guolong 337
Zhao, Ni 407
Zhao, Wei 337
Zhou, Lei 121
Zhou, Wenchen 479
Zhou, Zekai 37

*No abstract included

Volume 71
ISBN 978-1-887706-78-0